Frequency Multiplier Based on Nonlinear Defective Photonic Crystal

Yi Dai[1], **Shao-Bin Liu**[1], **Xiang-Kun Kong**[1,2], **Hai-Feng Zhang**[1],
Hui-Chao Zhao[1], **and Chen Chen**[1]

[1]College of Electronic and Information Engineering
Nanjing University of Aeronautics and Astronautics, Nanjing 210016, China
[2]Jiangsu Key Laboratory of Meteorological Observation and Information Processing
Nanjing University of Information Science and Technology, Nanjing 210044, China

Abstract— This paper presents a proposal of taking nonlinear material as the structural defects in one-dimensional photonic crystals. The performance of this structure is simulated by using finite-difference time-domain method and transfer matrix method. The simulation results show that the investigated structure can work as frequency multiplier. In this paper, we introduce nonlinear defective photonic crystals in order to enhance the second harmonic wave and achieve relatively high second harmonic conversion efficiency. By adjusting the parameters of the defective photonic crystals, the position of the defect modes overlap in the position of the fundamental wave ($\lambda_{FW} = 1064\,\text{nm}$) and the harmonic wave ($\lambda_{SH} = 532\,\text{nm}$).

1. INTRODUCTION

Photonic crystals (PCs) [1–3] have gained worldwide interest due to their unique electromagnetic properties and potential applications [4, 5] in the last two decades. PCs are artificially fabricated periodic structure in which the dielectric constant varies periodically in one, two, or three spatial directions. They have many novel physical properties, which provide a good way to control the propagation of electromagnetic (EM) waves due to the existence of photonic band-gaps (PBG). The PBG means that the propagation of EM waves of certain frequencies is forbidden. When a single defect layer is introduced into the PCs, defect mode will appear in PBG and such defect modes is also periodic. Nonlinear optics [6] describes the behavior of light in nonlinear material, which the polarization of the material responds nonlinearly to the electric field of the light. Typically, laser light is sufficiently intense to modify the optical properties of a material system. Essentially, almost all the material can have nonlinear optical response in case of intense light. Researchers have been made many efforts to enhance the second-order harmonic generation of nonlinear materials [7–11]. When the nonlinear material is introduced to the defective PCs, nonlinear processes, such as harmonic generation, optical bistability [12] will emerge. Second harmonic generation (SHG) occurs as a result of the part of the atomic response that scales quadratically with the strength of the applied optical field. Shi et al. [9] demonstrated the great enhancement of SHG in the defective PCs. Ren et al. [10] investigated giant enhancement of SHG in the finite PC with a single defect and dual-localized modes. Dolgova et al. [11] verified the enhancement of SHG in PCs with single and coupled microcavities.

In this paper, we construct the nonlinear photonic crystal structures [10] alternating between nonlinear and linear layers. When we increase the thickness of the central nonlinear layer, SHG can be enhanced greatly. By using the finite difference time domain (FDTD) method [13] and the transfer matrix method (TMM) [14], we simulated the electromagnetic waves propagating through the proposed structures. Giant enhancement of SHG is predicted in numerical simulation. Such a kind of structures can be expected as high-efficiency nonlinear photonic devices. We utilize the investigated structure to make a frequency multiplier.

2. PHYSICAL MODELS

We consider a one-dimensional nonlinear PC created by alternating between nonlinear and linear materials. Fig. 1(a) shows a finite perfect periodic PC. It is composed of alternately stacked N-L layers surrounded with L medium, where N and L indicate the nonlinear and linear layers. $LiNbO_3$ crystal is chosen as the nonlinear material. The parameters of the designed perfect PC are as follows: thicknesses and refractive indices of the N and L and layers are $0.304\,\mu\text{m}$, $0.351\,\mu\text{m}$, 2.157, 1.0, respectively. In order to introduce the defect, we change the thickness of the central N layer from $0.351\,\mu\text{m}$ to $0.737\,\mu\text{m}$ as shown in Fig. 1(b).

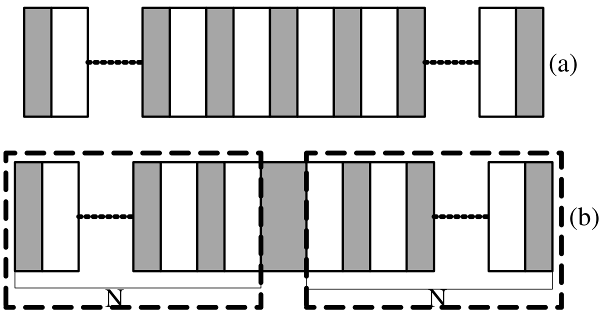

Figure 1: Geometric structure of PC. (a) Perfect periodic PC, (b) defective PC.

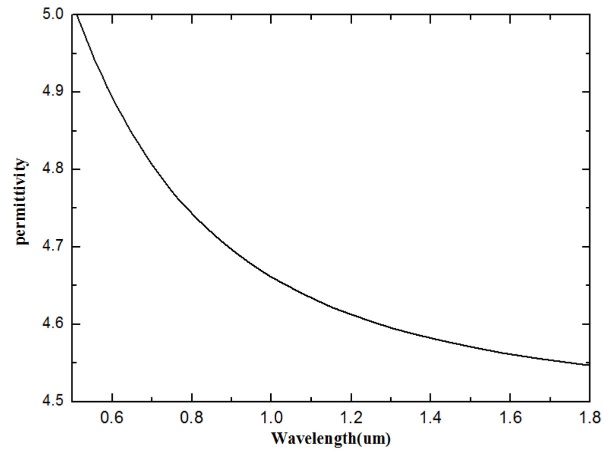

Figure 2: Permittivity in the wavelength range of 0.15–0.18 μm.

Nonlinear materials ($LiNbO_3$) is a dispersive material, the dispersion effect of its relative dielectric constant ε versus frequency ω should be taken into account in the calculations. Normally, the dispersion in $LiNbO_3$ should be expressed by a multiple second order Lorentz poles model, and $\omega(\varepsilon)$ can be expressed as

$$\omega(\varepsilon) = a + \frac{b-a}{1-j\omega\tau} \tag{1}$$

where a, b, and τ are fitting constants, and they are chosen to be 6.2, 4.49, and 1.77×10^{16} s , respectively. Fig. 2 shows that in the wavelength range of 0.5–1.8 μm.

In these structures, the nonlinearity is modeled in the relation $D = \varepsilon_0 \varepsilon E$, where

$$\varepsilon = n^2 = \left(n_0 + n_2 |E|^2\right)^2 \simeq n_0^2 + 2n_0 n_2 |E|^2 \tag{2}$$

where the linear refractive index n_0 is dimensionless, and the nonlinear refractive index n_2 has units of $\mathrm{m}^2/\mathrm{v}^2$. We use the finite-difference time-domain method [15] to solve three-order nonlinear medium.

3. SIMULATION AND RESULTS

Firstly we simulate the frequency-domain waveform of a bulk nonlinear material layer with a Gaussian beam illumination as illustrated in Fig. 3. The fundamental wave frequency is chosen to be 250 THz, and the third-harmonic wave appears at 750 THz. As shown in Fig. 2, the harmonic amplitude is about 3.5% of the fundamental amplitude.

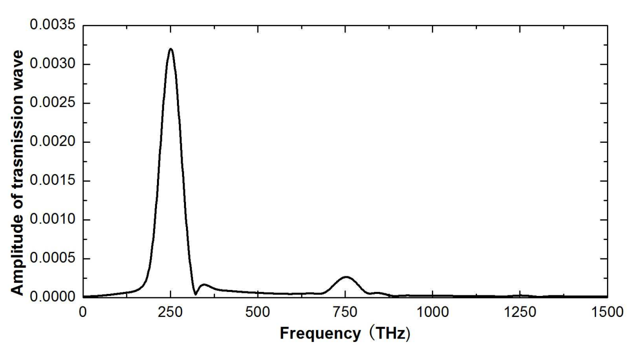

Figure 3: Frequency-domain waveform of third-harmonic generation in a bulk nonlinear material.

In this paper, we can enhance the second-order harmonic wave by utilizing the nonlinear defective PCs. According to the results in [10], high-order harmonic wave can be enhanced by introducing the nonlinear defective layer in PC structures. Electromagnetic wave can't directly propagate through the PCs for the PBG. If PCs have a defect layer, electromagnetic wave can be limited in the defect and reflected back and forth repeatedly. These localized electromagnetic waves are superimposed, and the amplitude of the electromagnetic waves will be improved greatly. The refractive index of the nonlinear medium is related to the intensity of electric field. It can be also looked as a very strong electromagnetic wave. So enhancement of high order harmonic wave can be realized. Now, we introduce a single defect into the PCs. And the nonlinear material is introduced into a defect layer. We calculated the transmission spectrum of the structure $(NL)^7N(LN)^7$ by using TMM.

Figure 4(a) shows the transmission spectrum versus free space wavelength for a 29-layers perfect PC. When we introduce a single defect layer by changing the thickness of the central layer from 0.304 µm to 0.737 µm, defect mode will appear in PBG and such defect modes is also periodic. As the nonlinear material can generate harmonic wave, we introduce the nonlinear material to the defect layer of PC structures. By adjusting the parameters of the defective PCs, the position of the defect modes overlap in the position of the fundamental wave (the wavelength of FW, 1064 nm) and the harmonic wave(the wavelength of SH, 532 nm). As shown in Fig. 4(a), the transmittance of the perfect PC at the wavelength of FW and the wavelength of SH approach zero, meaning that there is no localized modes within the PBG's. As shown in Fig. 4(b), when the transmittance of the defective PC at the wavelength of FW and the wavelength of SH arrive at the maximum value. There are two sharp peaks around and within two discrete PBG. These results confirm that a single defect can give rise to the simultaneous dual-localized modes at the fundamental wave and the second harmonic wave. We found that such dual-localization feature should cause the giant enhancement of SHG. We utilize the proposed structure to make a frequency multiplier.

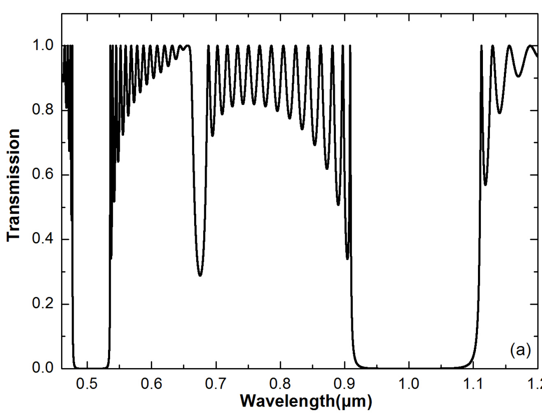

(a)

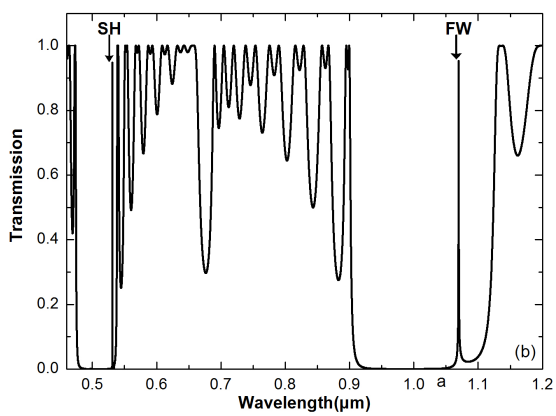

(b)

Figure 4: Transmission spectrum of (a) the perfect PC and (b) the defective PC.

4. CONCLUSIONS

We present a one-dimensional defective photonic crystal containing the nonlinear medium. The performance of this structure is simulated by using finite-difference time-domain (FDTD) method and transfer matrix method (TMM). Giant enhancement of second harmonic generation is predicted in numerical simulation. The simulation results show that the investigated structure can work as frequency multiplier.

ACKNOWLEDGMENT

The authors are grateful for the support from the Chinese Natural Science Foundation (Grant No. 60971122), the Jiangsu Province Natural Science Foundation (Grant No. BK2011727), Funding of Jiangsu Innovation Program for Graduate Education (Grant No. CXZZ11_0210 & CXZZ11_0211) and Funding for Outstanding Doctoral Dissertation in NUAA (Grant No. BCXJ11-05).

REFERENCES

1. Sajeev, J., "Strong localization of photons in certain disordered dielectric superlattices," *Physical Review Letters*, Vol. 58, No. 23, 2486–2489, 1987.
2. Eli, Y., "Inhibited spontaneous emission in solid-state physics and electronics," *Physical Review Letters*, Vol. 58, No. 20, 2059–2062, 1987.

3. Joannopoulos, J. D., R. D. Meade, and J. N. Winn, *Photonic Crystals: Modeling the Flow of Light*, Princeton University Press, Princeton, NJ, 1995.
4. Lin, S. Y., E. Chow, V. Hietala, et al., "Experimental demonstration of guiding and bending of electromagnetic waves in a photonic crystal," *Science*, Vol. 282, No. 5387, 274–276, 1998.
5. Sakai, O., et al., "Properties of electromagnetic wave propagation emerging in 2-D periodic plasma structures," *IEEE Transactions on Plasma Science*, Vol. 35, No. 5, 1267–1273, 2007.
6. Boyd, R. W., *Nonlinear Optics*, Academic, Boston, MA, 1992.
7. Scalora, M., M. J. Bloemer, A. S. Manka, et al., "Pulsed second-harmonic generation in nonlinear, one-dimensional, periodic structures," *Physical Review A*, Vol. 56, No. 4, 3166, 1997.
8. Sasaki, F., S. Haraichi, and S. Kobayashi, "Linear and nonlinear optical properties of pseudoisocyanine J aggregates in distributed feedback microcavities," *IEEE Journal of Quantum Electronics*, Vol. 38, No. 7, 943–948, 2002.
9. Shi, B., Z. M. Jiang, and X. Wang, "Defective photonic crystals with greatly enhanced second-harmonic generation," *Optics Letters*, Vol. 26, No. 15, 1194–1196, 2001.
10. Ren, F. F., R. Li, C. Cheng, et al., "Giant enhancement of second harmonic generation in a finite photonic crystal with a single defect and dual-localized modes," *Physical Review B*, Vol. 70, No. 24, 245109, 2004.
11. Dolgova, T. V., et al., "Giant optical second-harmonic generation in single and coupled microcavities formed from one-dimensional photonic crystals," *JOSA B*, Vol. 19, No. 9, 2129–2140, 2002.
12. Danckaert, J., et al., "Dispersive optical bistability in stratified structures," *Physical Review B*, Vol. 44, No. 15, 8214, 1991.
13. Wang, S. Y., S. B. Liu, and L. W. Li, "Finite-difference time-domain studies of low-frequency stop band in superconductor-dielectric superlattice," *Chinese Physics B*, Vol. 19, No. 8, 084101, 2010.
14. Wang, L.-G., H. Chen, and S.-Y. Zhu, "Omnidirectional gap and defect mode of one-dimensional photonic crystals with single-negative materials," *Physical Review B*, Vol. 70, No. 24, 245102–245108, 2004.
15. Goorjian, P. M. and A. Taflove, "Direct time integration of Maxwell's equations in nonlinear dispersive media for propagation and scattering of femtosecond electromagnetic solitons," *Optics Letters*, Vol. 17, No. 3, 180–182, 1992.

Collapse of Nonlinear Dust Sound Pulses in Dusty Plasma Waveguides

M. E. Bustos De La Rosa[1], **V. Grimalsky**[1], **S. Koshevaya**[1], **and A. Kotsarenko**[2]

[1]CIICAp, Autonomous University of State Morelos (UAEM)
Av. Universidad 1001, Cuernavaca, ZP 62209, Mor., Mexico
[2]Center of Geoscience, UNAM, Campus UNAM, Juriquilla, ZP 76230, Qro., Mexico

Abstract— Nonlinear monopulses of dust sound waves in dusty plasma waveguides bounded by dielectrics are investigated. The dusty plasma includes the positive ions as a light component and the negative dust as a heavy one. The dusty plasma with different masses of dust particles is considered. The set of hydrodynamic equations for the dust jointly with the Poisson one are used. The Boltzmann distribution is valid for the ions. The boundary conditions are applied at the smooth interfaces. When the moderate volume nonlinearity manifests, near the interfaces the variations of the dust concentration reach extremely high values, and the collapse of the dust sound waves occurs.

1. INTRODUCTION

The dusty plasmas in space, the Earth's ionosphere, in volcano dust clouds, and under laboratory conditions now are under investigations [1–5]. An important property of dusty plasmas is the support of various waves and oscillations, both linear and nonlinear ones [3–8]. The dusty plasmas can be bounded and can be the waveguides for plasma waves. In the bounded plasma waves the oscillations of the surface charge take place [2, 6]. Even in the case when the volume nonlinearity is small, the variations of the dust concentration near interfaces can reach essential values. Moreover, because the dust concentration is principally nonnegative, the surface nonlinearity cannot be considered as moderate.

In the present report the nonlinear monopulses of dust sound waves in the dusty plasma waveguides bounded by dielectrics are investigated. The waves propagate along OZ-axis, see Fig. 1. The dusty plasma includes the positive ions as the light component and the negative dust as the heavy component. The set of hydrodynamic equations for the dust, namely, the continuity equation and the equation for the momentum jointly with the Poisson one are used. The Boltzmann distribution is used for the ions. The electric and hydrodynamic boundary conditions are applied at the interfaces. The initial condition for the electric potential is monopulse-like. The simulations have demonstrated that the monopulses of small amplitudes are the subject to the wave dispersion and the diffraction. But when the moderate nonlinearity manifests, the pulse dynamics changes drastically. Namely, near the interfaces the variations of the dust concentration reach extremely high values, where the collapse of the dust sound waves occurs.

2. BASIC EQUATIONS

Consider the dusty plasma, layer $0 < x < L_x$, bounded by two dielectrics of the permittivities $\varepsilon_{1,2} > 1$ at $x < 0$ and $x > L_x$, see Fig. 1. The dusty plasma includes positively charged ions $(+e)$ and negative charged dust particles $(-Q)$. The temperature of ion fluid is T_i, one of the dust is T_d. It is assumed that $T_d \ll T_i$. Note that T_d is the temperature of the collective motion of the dust particles but not the temperature within each particle. The mass of the ion is m_i, the mass of the dust particle is $m_d \gg m_i$. Generally the dust particles can possess different masses in different regions: $m_d = m_d(x)$.

The set of hydrodynamic equations for the dust fluid concentration n_d and the velocity $\mathbf{v_d}$ is [2, 3, 9, 10]:

$$\frac{\partial n_d}{\partial t} + div(n_d\vec{v}_d) = 0, \qquad \frac{d\vec{v}_d}{dt} \equiv \frac{\partial \vec{v}_d}{\partial t} + (\vec{v}_d\cdot\nabla)\vec{v}_d = \frac{Q}{m_d}\nabla\varphi - \frac{T_d}{m_d n_d}\nabla n_d. \tag{1}$$

The ion concentration n_i obeys the Boltzmann distribution:

$$n_i = n_{i0}\times\exp\left(-\frac{\varphi}{\varphi_{Ti}}\right), \quad \text{where} \quad \varphi_{Ti} = \frac{k_B T_i}{e}. \tag{2}$$

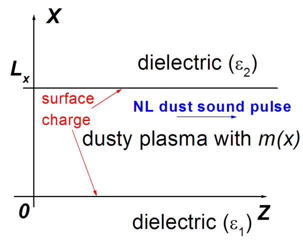

Figure 1: Geometry of the problem.

Here n_{i0}, n_{d0} are unperturbed concentrations, in the neutral state there is $e \times n_{i0} = Q \times n_{d0}$.

Equation (1) should be added by the Poisson equation for the electric potential φ (in absolute units):

$$\Delta\varphi + 4\pi e n_{i0} \times \exp\left(-\frac{\varphi}{\varphi_{Ti}}\right) = 4\pi Q n_d. \tag{3}$$

The basic equations have been reduced to the undimensional form. The following units have been used for prepare of undimensional values like φ_{Ti} for the potential, $l_n \equiv r_{Di} = (k_B T_i / 4\pi e^2 n_{i0})$ for distances, $t_n = (m_{d0}/4\pi Q^2 n_{d0})^{1/2}$ for time. The parameter m_{d0} is some typical value of the dust particle mass. As the result the basic equations are:

$$\begin{aligned} &\frac{\partial n}{\partial t} + div(n\vec{v}) = 0, \quad \frac{\partial \vec{v}}{\partial t} + (\vec{v}\cdot\nabla)\vec{v} = \frac{1}{m}(\nabla\varphi - T\cdot\nabla\log n), \\ &\frac{\partial \vec{u}}{\partial t} + (\vec{v}\cdot\nabla)\vec{u} = \vec{v}; \quad m \equiv m(x-u_x), \quad \Delta\varphi + \exp(-\varphi) - n = 0. \end{aligned} \tag{4}$$

Here n, $\mathbf{v}$, $\mathbf{u}$ are undimensional dust concentration, velocity, and displacement; $T = (T_d/T_i) \times (e/Q) \ll 1$; the undimensional dust mass is $m \sim 1$. One can see that the dependence of mass on the coordinate results in an additional mechanism of nonlinearity. In calculations the value of $T \neq 0$ is used, because in the limiting case $T = 0$ it is necessary to consider the motion of the surface charge separately. Our results are independent on the value of T, when $T < 0.01$.

Within the dielectrics at $x < 0$ and $x > L_x$ the Laplace equation is valid:

$$\Delta\varphi = 0. \tag{5}$$

The system is uniform in y-direction so $\partial/\partial y = 0$. Therefore, the dust velocity $\mathbf{v}$ has only the two components v_x, v_z.

The volume equations have been added by boundary conditions at $x = 0$ and $x = L_x$. Namely, the electric potential φ and the electric induction should be continuous at $x = 0$ (analogously at $x = L_x$):

$$\varphi(x=+0) = \varphi(x=-0), \quad \frac{\partial\varphi}{\partial x}(x=+0) = \varepsilon\frac{\partial\varphi}{\partial x}(x=-0). \tag{6}$$

Also, because it is considered the case $T \neq 0$, it should be $v_x(x=+0) = 0$. Otherwise, in the limiting case $T \to 0$ the surface dust concentration should be considered separately. Note that the interface is assumed as smooth, so the tangential component of the dust velocity is $v_z(x=+0) \neq 0$.

To solve the equations, the explicit 3-layer finite difference schemes have been applied for n, v_x, v_z, u_x. For the Poisson equation the fast Fourier transform has been used:

$$\begin{aligned} &\varphi(x,z) = \sum_l \Phi_l(x)\sin(k_l z); \quad k_l = \frac{\pi l}{L_z}, \quad l = 1, 2\ldots \\ &\frac{d^2\Phi_l(x)}{dz^2} - \left(1 + k_l^2\right)\Phi_l(x) = F_l; \quad \text{where} \quad F(x,z) \equiv n - (\exp(-\varphi) - \varphi = \sum_l \Phi_l(x)\sin(k_l z); \end{aligned} \tag{7}$$

The boundary conditions (6) are rewritten as:

$$\frac{d\Phi_l}{dx} - \varepsilon_1 k_l \Phi_l = 0, \quad x = +0; \quad \frac{d\Phi_l}{dx} + \varepsilon_2 k_l \Phi_l = 0, \quad x = L_x - 0. \tag{8}$$

Equations (7), (8) have been solved by the finite differences within the region $0 < x < L_x$ with several iterations, which show a good convergence.

3. RESULTS OF SIMULATIONS

The linearized Eqs. (4), (5) and the boundary conditions (6) possess a solution as the waveguide modes of dusty sound waves. These waves are mostly the oscillations of the surface charge near the interfaces $x = 0$, $x = L_x$. In the linear case one should consider the dust concentration as $n = 1+\tilde{n}$, $|\tilde{n}| \ll 1$. But it is physically impossible to get the value of $n < 0$. Therefore, a manifestation of nonlinearity near the surfaces is more essential than in the volume.

Equations (4), (5) added by boundary conditions (6) have been simulated. It is possible to solve these equations under the proper initial conditions. Namely, the initial monopulses of almost rectangular shape and of moderate maximum values $|a_0| \ll 1$ have been considered:

$$\begin{aligned} &\varphi(z,x,t=0) = -a_0 \exp\left(-\left(\frac{z-z_1}{z_0}\right)^6\right) < 0; \quad \tilde{n}(z,x,t=0) = \Delta\varphi + \exp(-\varphi) - 1 > 0; \\ &v_z(z,x,t=0) = -\frac{\varphi}{m(x)^{1/2}} > 0; \quad v_x(z,x,t=0) = u_x(z,x,t=0) = 0. \end{aligned} \tag{9}$$

The following distribution of the masses of the dust particles has been used:

$$m(x) = m_1 + (m_2 - m_1) \cdot \left(\exp\left(-\left(\frac{x-L_x}{x_q}\right)^4\right) + \exp\left(-\left(\frac{x}{x_q}\right)^4\right)\right) \tag{10}$$

Namely, the values of the masses are m_1 and m_2 in the center of the waveguide and at the boundaries, respectively.

Under small initial amplitudes the pulse of the dust sound wave is subject to strong diffraction and dispersion. The nonlinearity is unessential there, both at the surface and within the volume. But at higher but moderate amplitudes the dynamics of the pulses changes, see Figs. 2–4. For all the Figures, the initial distribution of the perturbation of the concentration $\tilde{n}$ is chosen the same: $a_0 = 0.14$, see Fig. 2(a). The used parameters are: $z_0 = 20$, $L_x = 16$, $x_q = 1$, $\varepsilon_1 = \varepsilon_2 = 4$.

The sharp peaks of the dust concentration near the surfaces are formed, which are localized both in longitudinal (Z) and transverse (X) directions. The maximum values of $\tilde{n}$ are 40...50 times higher then in the volume. The nonlinearity ceases to be moderate near the surface. Moreover,

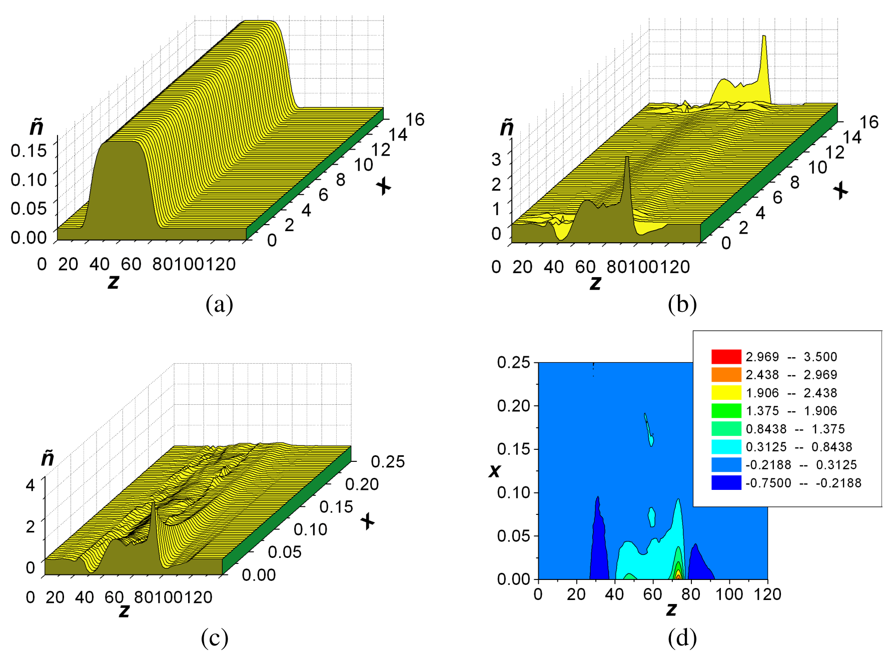

Figure 2: The collapse of the monopulse of the dust sound wave. A distribution of perturbation of the undimensional dust concentration $\tilde{n}$ is given. The maximum initial amplitude is $a_0 = 0.14$. Part (a) is the initial distribution for $t = 0$, parts (b), (c), (d) are for $t = 21$ in different representations. The values of the particle masses are $m_1 = 1$, $m_2 = 0.5$.

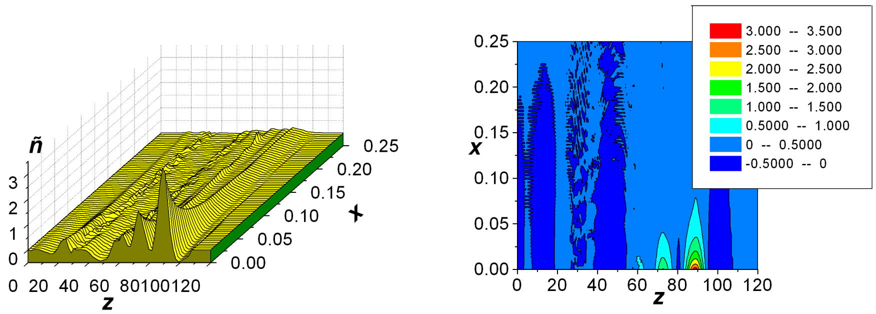

(a) (b)

Figure 3: The collapse of the monopulse of the dust sound wave. The maximum initial amplitude is $a_0 = 0.14$. Parts (a), (b) are for $t = 28$. The values of the particle masses are $m_1 = 0.5$, $m_2 = 1$.

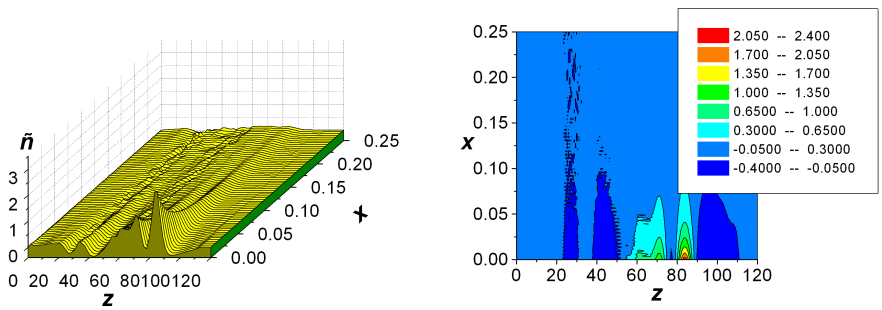

(a) (b)

Figure 4: The collapse of the monopulse of the dust sound wave. The maximum initial amplitude is $a_0 = 0.14$. Parts (a), (b) are for $t = 32$. The values of the particle masses are $m_1 = m_2 = 1$ (the uniform waveguide).

under this level of a_0 and higher, see Eq. (9), the calculations overflow. It is possible to interpret this phenomenon of the sharp growing and the narrowing of the dust concentration near the surface as a manifestation of the wave collapse [9, 11]. At the undimensional dust temperatures $T < 0.01$ the dynamics of surface dust sound waves does not depend on the value of this temperature.

The wave dynamics depends on the values of the dust particle mass at the boundaries. One can see from Fig. 2 that the collapse occurs at smaller times when the lighter particles are near the boundaries: $m_2 < m_1$. Figs. 3 and 4 are for the same masses of the particles near the boundaries, $m_2 = 1$. The collapse occurs earlier for the nonuniform distribution of masses $m_1 \neq m_2$ within the waveguide, compare Fig. 3 (smaller masses in the center, $m_1 = 0.5$) and Fig. 4 (the same masses of the particles within the waveguide, $m_1 = 1$).

There is an explanation of the formation of the peaks of the dust concentration. When the excess concentration is present at $t = 0$, the electric field $E_x < 0$ occurs near the interface $x = 0$. This leads to the presence of the normal component of the velocity $v_x < 0$ at the front end of the rectangular pulse. Therefore, the accumulation of the dust particles and the formation of pointed above sharp peaks occur at the interfaces.

The decrease of the waveguide thickness L_z can stabilize the dynamics of the nonlinear waves.

4. CONCLUSIONS

The evolution of initial rectangular pulses of dust sound waves in the plasma waveguides with dielectrics has demonstrated the essential surface nonlinearity near the interfaces. Under moderate values of the input amplitudes, the values of the dust concentrations near the surfaces reach high values, and the formation of narrow peaks of the dust concentration occurs. The nonlinearity near the surface ceases to be moderate, the compression of these pulses both in longitudinal and transverse directions takes place, and the wave collapse can be observed. The dynamics of the wave collapse depends on the distribution of the masses of the particles within the waveguide.

The estimated temporal and spatial scales have demonstrated that it could be possible an appearance of the investigated phenomena of the nonlinear wave collapse in the dust objects under volcano eruptions.

ACKNOWLEDGMENT

The authors are grateful to SEP-CONACyT (Mexico) for a partial support of our work.

REFERENCES

1. Fortov, V. E., A. V. Ivlev, S. A. Khrapak, A. G. Khrapak, and G. E. Morfill, "Complex (dusty) plasmas: Current status, open issues, perspectives," *Physics Reports*, Vol. 421, No. 1, 1–103, 2005.
2. Shukla, P. K. and A. A. Mamun, *Introduction to Dusty Plasma Physics*, IoP Publ., Bristol, UK, 2002.
3. Verheest, F., *Waves in Dusty Space Plasmas*, Kluwer, Dordrecht, Netherlands, 2001.
4. Shukla, P. K. and A. A. Mamun, "Solitons, shocks and vortices in dusty plasmas," *New Journal of Physics*, Vol. 5, 17.1–17.37, 2003.
5. Popel, S. I., S. I. Kopnin, I. N. Kosarev, and M. Y. Yu, "Solitons in Earth's dusty mesosphere," *Advances in Space Research*, Vol. 37, No. 1, 414–419, 2006.
6. Ostrikov, K. N., M. Y. Yu, and L. Stenflo, "Surface waves in strongly irradiated dusty plasmas," *Phys. Rev. E*, Vol. 61, No. 2, 782–787, 2000.
7. Kopnin, S. I. and S. I. Popel, "Dust acoustic mode manifestations in Earth's dusty ionosphere," *AIP Conference Proceedings*, Vol. 799, 161–164, 2005.
8. Popel, S. I., A. P. Golub', T. V. Losseva, R. Bingham, and S. Benkadda, "Evolution of perturbation in charge-varying dusty plasmas," *Phys. Plasmas*, Vol. 8, No. 5, 1497–1504, 2001.
9. Infeld, E. and G. Rowlands, *Nonlinear Waves, Solitons and Chaos*, CUP, Cambridge, UK, 2000.
10. Lifshitz, E. M. and L. P. Pitaevskii, *Physical Kinetics*, Pergamon, London, UK, 1981.
11. Ostrovsky, L. and A. Potapov, *Modulated Waves: Theory and Applications*, The Johns Hopkins University Press, New York, 2002.

Effects of Plasma Formation on Reflection of Laser Light in Ablation of Metals in Air

O. Benavides, **L. de la Cruz May**, and **A. Flores Gil**
Universidad Autónoma del Carmen, Cd. del Carmen, Campeche, Mexico

Abstract— In this work, we study the total reflectivity of mechanically polished metals samples. In our experiment, a Q-switched Nd:YAG laser that generates 50-ns pulses at a wavelength of 1064 nm is used for ablation of a sample. To measure the total hemispherical reflectivity we use an ellipsoidal light reflector technique. The total hemispherical reflectivity is studied as a function of laser fluence in the range of 0.1–100 J/cm^2. The experiments are performed in air at the atmospheric pressure.

1. INTRODUCTION

Processing of materials through laser ablation [1] is widely used in fabrication of devices for photonics [2, 3], plasmonics [4], optoelectronics [5], photovoltaics, microfluidics, and solar energy harvesting [6–9]. Despite a large number of studies on nanosecond laser ablation, the reflection of high-intensity nanosecond laser pulses is still a poorly studied issue.

The reflection of intense laser pulses by metals was first studied by Bonch-Bruevich et al. [10], where a substantial drop of the total reflectivity during submicrosecond spikes in a millisecond Nd-glass laser pulse was experimentally found. For studying reflection, the authors used an integrating sphere technique that allowed measuring the total reflectivity (both specular and diffuse components). Basov et al. [11] studied the total reflection of 15-ns Nd-laser pulses from Cu, Sn, and Al in a laser intensity range of 3×10^7 to 3×10^{10} W/cm^2 and reported a sharp decrease of the total reflectivity to ~ 0.1 for ablation in a vacuum. Dymshits [12] studied the reflection of a 30-ns Nd-laser pulse from a thin aluminum film ablated in vacuum. The reflected laser light was collected over a solid angle of about 1 sr. Vorob'ev [13] carried out a comparative study on the hemispherical total reflection of 45-ns ruby laser pulses in ablation of Cu in air and vacuum. Both time-resolved and time-integrated experiments showed a substantial decrease of the total reflectivity at the plasma formation threshold. At laser fluence above about 15 J/cm^2, the time-integrated reflectivity of copper was measured to be about 0.3 and 0.2 in vacuum and air, respectively. At present, nanosecond Nd:YAG laser is the most widely used laser for ablation of materials as compared with other nanosecond lasers. In many applications, nanosecond laser ablation of materials is carried out in air of atmospheric pressure. However, as seen from previous works [10–13], the reflection/absorption of the nanosecond Nd:YAG laser pulses for ablation of the materials in air has not been yet studied despite a crucial role of the reflection/absorption in ablation.

2. EXPERIMENTAL PROCEDURE

Figure 1 shows the experimental setup used in this study. For ablation of the samples we use an Nd:YAG laser that produces 1.3 J in a 50-ns FWHM (Full Width at Half-Maximum intensity) pulse. The main laser beam is focused onto the sample with a lens. Reflected laser light is collected using an ellipsoidal light reflector technique [13, 14].

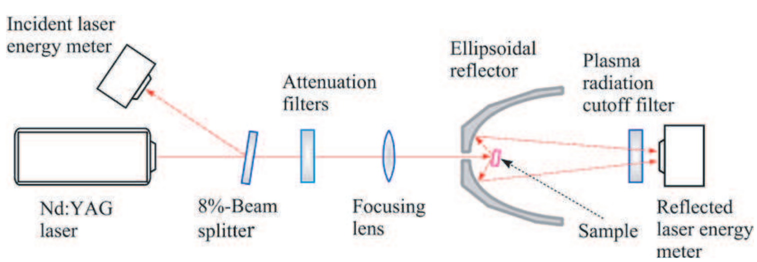

Figure 1: Experimental setup for studying reflection of the laser light in ablation of a metal sample.

The studied sample is placed in an internal focal point of the ellipsoidal reflector. To reduce laser light backscattering through the entrance hole in the reflector, the sample is tilted at 19 degrees.

Energy of the reflected laser pulse, E_{refl}, is measured using an energy meter located in the external focal point of the reflector. A cutoff filter is placed in front of this energy meter for blocking the plasma radiation. Energy of the laser pulse incident upon the sample, E_{inc}, is measured using an 8%-beamsplittter and energy meter. Using this method, the hemispherical total reflectivity, R, (a sum of specular and diffuse components of the reflected light) can be found as $R = E_{refl}/E_{inc}$. The laser fluence, F, incident upon the sample is varied by inserting attenuation filters and changing the distance between the focusing lens and sample. The total reflectivity is studied in the range of laser fluences between 0.1 and 100 J/cm^2. The reflectivity measurements were performed in air of the atmospheric pressure. The sample was translated after each laser shot in order to expose an undamaged surface area for the next laser shot. Along with the reflectivity measurements, both surface damage and plasma formation thresholds are also determined. The surface damage threshold is found as the lowest laser fluence resulting in a surface damage that can be discerned under an optical microscope. The plasma formation threshold is determined by detecting the onset of a bright violet flash from the irradiated spot [15] using a photomultiplier (PMT) with a filter that blocks wavelengths longer 0.45 μm. The studied metals are mechanically polished bulk silver and molybdenum.

3. RESULTS AND DISCUSSION

The total reflectivity as a function of laser fluence in ablation of silver and molybdenum in air of the atmospheric pressure is shown in Fig. 2. It is seen that the reflectivity of the studied metals remains constant at low laser fluences. At these low fluences, the irradiated surface does not undergo any surface damage and the reflectivity values are 0.92 and 0.62 for silver and molybdenum, respectively. These reflectivity values agree with available table values of the room-temperature reflectivity for mechanically polished surfaces [16, 17]. The plots of $R(F)$ in Fig. 2 show that the reflectivity begins to decrease rapidly at a threshold fluence of 3.3 and 2.4 J/cm^2 for silver and molybdenum, respectively. These threshold fluences of a sharp reflectance drop coincide with the measured plasma formation thresholds within the experimental uncertainty. In our study, the plasma formation thresholds averaged over ten measurements were found to be 3.2, and 2.5 J/cm^2 for silver and molybdenum, respectively. The values of the damage threshold were found to be only slightly lower than those for the reflectivity drop. As can be seen in Fig. 2, as the laser fluence increases further, the reflectivity drops (to about 0.17 and 0.11 for silver and molybdenum, respectively) and then remains unchanged with further increasing fluence.

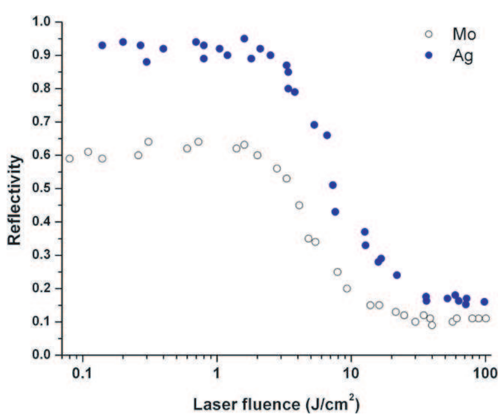

Figure 2: The total reflectivity of silver and molybdenum as function of laser fluence for ablation in 1-atm air.

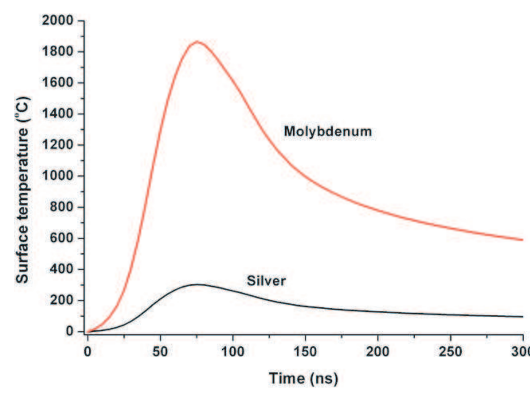

Figure 3: Surface temperature of silver and molybdenum samples as function of time at the plasma formation threshold laser fluence.

The above observations indicate the correlation between the reflectivity drop and plasma formation. In general, the reflectivity reduction can be caused by Drude's temperature dependence of the optical constants and absorption of laser light in a laser-induced plasma. In order to ascertain the role of Drude's temperature dependence of the optical constants on the reflectivity, we computed the surface temperature, T_{surf}, of the samples at the plasma formation threshold fluences using the following formula [18]

$$T_{surf}(t) = \frac{(1-R)\sqrt{a}}{k\sqrt{\pi}} \int_0^t \frac{I(t-\tau)}{\sqrt{\tau}} d\tau + T_0$$

where a is the thermal diffusivity, k is the thermal conductivity, I is the intensity of the incident laser light, t is the time, T_0 is the initial temperature, and τ is the integration variable. The dependencies $T_{surf}(t)$ computed for Ag ($R = 0.92$, $k = 410\,\mathrm{W\cdot m^{-1}\cdot K^{-1}}$, $a = 1.696 \times 10^{-4}\,\mathrm{m^2/s}$) and Mo ($R = 0.62$, $k = 135\,\mathrm{W\cdot m^{-1}\cdot K^{-1}}$, $a = 5.263 \times 10^{-5}\,\mathrm{m^2/s}$). The computed dependencies $T_{surf}(t)$ are shown in Fig. 3, where it is seen that the maximum surface temperature is about 305 and 1865°C for silver and molybdenum, respectively. These surface temperature values are significantly smaller than the melting points of studied metals (962 and 2617°C for silver and molybdenum, respectively). To find out the role of the temperature dependence of the optical constants on the reflectivity, we calculated the surface temperature, T_{surf}, of the samples at the plasma formation threshold fluences using the following formula derived in Ref. [18] for the case when the transverse dimensions of the laser spot are large compared to the depth of heat diffusion during the time of the laser pulse and the optical absorption coefficient of the irradiated material is large.

Modeling of the temperature dependence of the reflectivity for silver [19] showed that the reflectivity of silver slightly decreases as the temperature rises up to the melting point.

Therefore, the sharp reflectivity drop observed in our study cannot be explained by the temperature dependence of the optical properties. Our observation that the plasma formation thresholds of the studied metals are very close to their reflectivity drop thresholds leads us to believe that the observed reflectivity drop is associated with a plasma shielding effect. The fact that the plasma formation occurs in our experiment at a low surface temperature indicates that the surface imperfections of the sample play an important role in inducing an optical breakdown. For example, surface micro/nanostructural defects commonly present on mechanically polished surfaces can be locally heated to a high temperature due to plasmonic absorption [20–22] and plasmonic nanofocusing [23]. These "hot nanospots" on cold (on average) surface can be sources of both thermally ionized species and thermionically emitted electrons, which due acceleration through inverse-bremsstrahlung mechanism can trigger an avalanche air optical breakdown. When the plasma forms in front of the irradiated sample, the reflection and absorption of laser light by the sample dramatically changes due to absorption of the laser light in the plasma. For ablation into the background gas, the reflection/absorption of laser energy by the sample is more complicated than in the vacuum due to generation of laser-supported absorption waves (laser-supported combustion wave and laser-supported detonation wave) [24, 25]. Under these conditions, the reflection of the laser beam occurs from a sample-plasma system [13]. Assuming negligible laser light scattering from particulates ejected from the sample and negligible reflections at both air/air-plasma and air-plasma/vapor-plasma boundaries, the laser beam reflection will occur as schematically shown in Fig. 4. Although the plasma reduces the laser energy that arrives at the sample surface, it can contribute to energy deposition into the sample through the transfer of a fraction of its stored thermal energy to the sample [13, 15, 26].

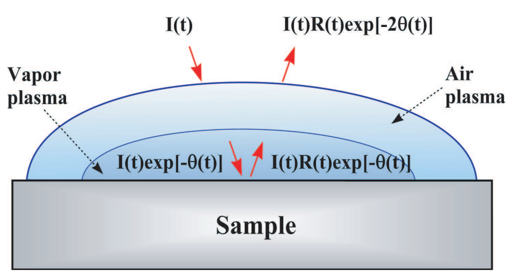

Figure 4: Reflection of the laser pulse from the sample-plasma system: $I(t)$ is the incident laser pulse intensity; $I(t)\exp[-\theta(t)]$ is the laser pulse intensity that arrives at the sample surface, here $\theta(t)$ is the total optical thickness of the plasma; $I(t)R(t))\exp[-\theta(t)]$ is the laser pulse intensity reflected from the sample surface; $I(t)R(t))\exp[-2\theta(t)]$ is the laser pulse intensity that comes out from the sample-plasma system.

Previously, a number of theoretical models that include the absorption of laser radiation in the plasma produced by ablation into vacuum and background gas [27–34] have been developed.

However, satisfactory understanding of reflection/absorption of the laser energy is still lacking and the value of the laser energy absorbed by the sample actually remains a parameter of intuitive choice. We believe that our experimental data can be useful for further advancing theoretical models of the nanosecond laser ablation.

4. CONCLUSIONS

In this work, the total reflectivity of the mechanically polished Mo and Ag samples in ablation by nanosecond Nd:YAG laser pulses in air of the atmospheric pressure is experimentally studied as a function of laser fluence in the range of $0.1–100\,\mathrm{J/cm^2}$. Our experiment shows that at laser fluences below the plasma formation thresholds the reflectivity of the studied metals remains virtually equal to the table room-temperature reflectivity values for mechanically polished surfaces. The total reflectivity of the studied metals begins to drop at the laser fluence of the plasma formation threshold. With increasing laser fluence above the plasma formation threshold, the reflectivity drops sharply to a low value (to about 0.17 and 0.11 for silver and molybdenum, respectively) and then remains unchanged with further increasing laser fluence. The computation of temperature of the irradiated surface at the plasma formation threshold fluence shows that the surface temperature is substantially below the melting point that indicates an important role of the surface nanostructural defects in the plasma formation on the real sample due to their enhanced heating caused by both plasmonic absorption and plasmonic nanofocusing.

REFERENCES

1. Anisimov, S. I. and B. S. Luk'yanchuk, *Phys. Uspekhi*, Vol. 45, 293, 2002.
2. Bäuerle, D., *Laser Processing and Chemistry,* 3rd Editon, Springer, Berlin, 2000.
3. Chrisey, D. B. and G. K. Hubler, ed., *Pulsed Laser Deposition of Thin Films*, Wiley, New York, 1994.
4. Marla, D., U. V. Bhandarkar, and S. S. Joshi, *J. Appl. Phys.*, Vol. 109, 021101, 2011.
5. Cheng, J.-Y., M.-H. Yen, C.-W. Wei, Y.-C. Chuang, and T.-H. Young, *J. Micromech. Microeng.*, Vol. 15, 1147, 2005.
6. Li, L., M. Hong, M. Schmidt, M. Zhong, A. Malshe, B. H. In'tveld, and V. Kovalenko, *CIRP Annals — Manufacturing Technology*, Vol. 60, 735, 2011.
7. Kelly, R. and J. E. Rothenberg, *Nucl. Instrum. Methods Phys. Res. B*, Vol. 7–8, 755, 1985.
8. Wang, Z. B., M. H. Hong, B. S. Luk'yanchuk, et al., *Appl. Phys. A*, Vol. 79, 1603, 2004.
9. Zorba, V., N. Boukos, I. Zergioti, and C. Fotakis, *Appl. Opt.*, Vol. 47, 1846, 2008.
10. Bonch-Bruevich, A. M., Y. A. Imas, G. S. Romanov, M. N. Libenson, and L. N. Mal'tsev, "Effect of a laser pulse on the reflecting power of a metal," *Sov. Phys. Tech. Phys.*, Vol. 13, No. 5, 640–643, 1968.
11. Basov, N. G., V. A. Boiko, O. N. Krokhin, O. G. Semenov, and G. V. Sklizkov, "Reduction of reflection coefficient for intense laser radiation on solid surfaces," *Sov. Phys. Tech. Phys.*, Vol. 13, No. 1, 1581–1582, 1969.
12. Dymshits, Yu. I., "Reflection of intense radiation from a thin metal film," *Sov. Phys. Tech. Phys.*, Vol. 22, No. 7, 901–902, 1977.
13. Vorob'ev, A. Y., "Reflection of the pulsed ruby laser radiation by a copper target in air and in vacuum," *Sov. J. Quantum Electron.*, Vol. 15, No. 4, 490–493, 1985.
14. Vorobyev, A. Y. and C. Guo, "Reflection of femtosecond laser light in multipulse ablation of metals," *J. Appl. Phys.*, Vol. 110, No. 4, 043102, 2011.
15. Vorobyev, A. Y., V. M. Kuzmichev, N. G. Kokody, P. Kohns, J. Dai, and C. Guo, "Residual thermal effects in Al following single ns- and fs-laser pulse ablation," *Appl. Phys., A Mater. Sci. Process.*, Vol. 82, No. 2, 357–362, 2006.
16. Kaye, G. W. C. and T. H. Laby, *Tables of Physical and Chemical Constants*, 11th Edition, Longmans, London, New York, 1956.
17. Touloukian, Y. S. and D. P. De Witt, ed., *Thermophysical Properties of Matter. Thermal Radiative Properties,* Vol. 7, IFI/Plenum, New York-Washington, 1970.
18. Ready, J. F., *Effects of High-power Laser Radiation*, Academic Press, New York, London, 1971.
19. Ujihara, K., *J. Appl. Phys.* Vol. 43, 2376, 1972.
20. Vorobyev, A. Y. and C. Guo, "Enhanced absorptance of gold following multi-pulse femtosecond laser ablation," *Phys. Rev. B*, Vol. 72, No. 19, 195422, 2005.

21. Vorobyev, A. Y. and C. Guo, "Femtosecond laser blackening of platinum," *J. Appl. Phys.*, Vol. 104, No. 5, 053516, 2008.
22. Eversole, D., B. Luk'yanchuk, and A. Ben-Yakar, "Plasmonic laser nanoablation of silicon by the scattering of femtosecond pulses near gold nanospheres," *Appl. Phys., A Mater. Sci. Process.*, Vol. 89, No. 2, 283–291, 2007.
23. Tan, S. J. and D. K. Gramotnev, "Heating effects in nanofocusing metal wedges," *J. Appl. Phys.*, Vol. 110, No. 3, 034310, 2011.
24. Radziemski, L. J. and D. A. Cremers, ed., *Laser-induced Plasmas and Applications*, Marcel Dekker, Inc., 1989.
25. Wen, S.-B., X. Mao, R. Greif, and R. E. Russo, "Laser ablation induced vapor plume expansion into a background gas. II. Experimental analysis," *J. Appl. Phys.* Vol. 101, No. 2, 023115, 2007.
26. Bulgakova, N. M., V. P. Zhukov, A. Y. Vorobyev, and C. Guo, "Modeling of residual thermal effect in femtosecond laser ablation of metals. Role of gas environment," *Appl. Phys., A Mater. Sci. Process.*, Vol. 92, No. 4, 883–889, 2008.
27. Singh, R. K. and J. Narayan, "Pulsed-laser evaporation technique for deposition of thin films: Physics and theoretical model," *Phys. Rev. B Condens. Matter*, Vol. 41, No. 13, 8843–8859, 1990.
28. Peterlongo, A., A. Miotello, and R. Kelly, "Laser-pulse sputtering of aluminum: Vaporization, boiling, superheating, and gas-dynamic effects," *Phys. Rev. E Stat. Phys. Plasmas Fluids Relat. Interdiscip. Topics*, Vol. 50, No. 6, 4716–4727, 1994.
29. Ho, J. R., C. P. Grigoropoulos, and J. A. C. Humphrey, "Computational study of heat transfer and gas dynamics in the pulsed laser evaporation of metals," *J. Appl. Phys.* Vol. 78, No. 7, 4696–4709, 1995.
30. Amoruso, S., "Modeling of UV pulsed-laser ablation of metallic targets," *Appl. Phys., A Mater. Sci. Process.*, Vol. 69, No. 3, 323–332, 1999.
31. Bulgakov, A. V. and N. M. Bulgakova, "Thermal model of pulsed laser ablation under the conditions of formation and heating of a radiation-absorbing plasma," *Quantum Electron.*, Vol. 29, No. 5, 433–437, 1999.
32. Bulgakova, N. M. and A. V. Bulgakov, "Pulsed laser ablation of solids: Transition from normal vaporization to phase explosion," *Appl. Phys., A Mater. Sci. Process.*, Vol. 73, No. 2, 199–208, 2001.
33. Bulgakova, N. M., A. V. Bulgakov, and L. P. Babich, "Energy balance of pulsed laser ablation: Thermal model revised," *Appl. Phys., A Mater. Sci. Process.*, Vol. 79, Nos. 4–6, 1323–1326, 2004.
34. Chen, Z. and A. Bogaerts, "Laser ablation of Cu and plume expansion into 1 atm ambient gas," *J. Appl. Phys.*, Vol. 97, No. 6, 063305, 2005.

Volume Scattering Influence on MARSIS and SHARAD Data Inversion

Marco Restano, Giovanni Picardi, and Roberto Seu
Department of Information, Electrical and Telecommunication Engineering (DIET)
University of Rome "Sapienza", Italy

Abstract— The Mars Advanced Radar for Subsurface and Ionosphere Sounding (MARSIS) and the Shallow Radar (SHARAD) are currently operating on Mars transmitting an HF chirp signal to retrieve information regarding the Martian crust structure. An important task to be performed is the data inversion, i.e., the permittivity estimation of the detected subsurface layers. In order to be properly performed, degrading effects on attenuation estimation and geometric term correction have to be understood. This paper aims to simulate a few representative scenarios, using the Finite-Difference Time-Domain formulation, pointing out the volume scattering influence on MARSIS and SHARAD data. Influence on both attenuation estimation and geometric term correction will be discussed.

1. INTRODUCTION

The inversion process proposed for the Martian south pole [1] relies on investigations performed over flat areas selected according to the Mars Orbiter Laser Altimeter (MOLA) data in order to avoid surface clutter presence that could mask subsurface reflections. Power backscattered by surface and subsurface interfaces is used to evaluate crust attenuation by means of a dual channel analysis performed after compensating no flat geometries using Physical and Geometric Optics backscattering models [2]. Nonetheless, both attenuation and geometry evaluation are strongly influenced by volume scattering produced during the propagation in the crust. A one dimensional Finite-Difference Time-Domain (FDTD) simulator [3] has been implemented evaluating the volume scattering influence on data inversion parameters for scenarios made up of parallel interfaces as proposed by [4]. Power losses, anomalies on attenuation estimation and effects on pulses shape, related to the geometric term correction, are discussed providing new criteria to select and correct data to be used in the inversion process.

2. MARSIS AND SHARAD AS SUBSURFACE SOUNDING RADARS

The MARSIS instrument [5] is a low-frequency, nadir-looking, pulse-limited radar sounder using unfocused synthetic aperture radar (SAR) techniques. The sounder operates in the 1.3–5.5 MHz range over four frequency bands of 1MHz bandwidth. In order to acquire data with a sufficient signal-to-noise ratio, MARSIS emits a 1 MHz bandwidth chirp signal of 250 μs duration. To prevent the subsurface returns from being masked by the sidelobes of the first specular surface reflection, Hanning weighting function was selected to reduce the sidelobes level. The expected ground penetration (depending on the composition of the crust) is 5 to 9 km. A typical frame showing power returns from surface (P_s) and subsurface (P_{ss}) interfaces is reported in Fig. 1, $\Delta\tau$ can be used to retrieve the layer thickness once its composition is known. The SHARAD instrument is similar to MARSIS. It achieves a better vertical resolution using a 10 MHz bandwidth chirp signal of 85 μs duration. The carrier frequency is 20 MHz. The expected ground penetration of the instrument is 1 km.

3. DATA INVERSION EQUATION

MARSIS data inversion is accomplished using the following equation [1]:

$$R^2_{12,z} - \Gamma_s = -\frac{P_s}{P_{ss}} + \frac{f_s}{f_{ss}} + K_{\mathrm{dB}}$$
$$\text{where} \quad K_{\mathrm{dB}} = \left[\frac{f_1|_{\mathrm{MHz}}}{f_1|_{\mathrm{MHz}} - f_2|_{\mathrm{MHz}}}\right] \cdot \left[\left(\left.\frac{P_s}{P_{ss}}\right|_{f_1} + \frac{f_s}{f_{ss}}\right) - \left(\left.\frac{P_s}{P_{ss}}\right|_{f_2} + \frac{f_s}{f_{ss}}\right)\right] \tag{1}$$

where Γ_s is the surface Fresnel reflectivity $R^2_{12,z}$ is the reflection coefficient of the interface at the depth z, $\frac{P_s}{P_{ss}}$ is the surface to subsurface power ratio, $\frac{f_s}{f_{ss}}$ is the ratio between the geometric correction terms, which deals with the geometric structure of the surface and the subsurface and K_{dB} is the attenuation between surface and subsurface when $f_1 = 4\,\mathrm{MHz}$ and $f_2 = 3\,\mathrm{MHz}$. Similar equations can be used on SHARAD data after having half-splitted the 10 MHz bandwidth obtaining the two channels needed to evaluate the K_{dB} term. An example of backscattering models from [2] can be seen in Fig. 2.

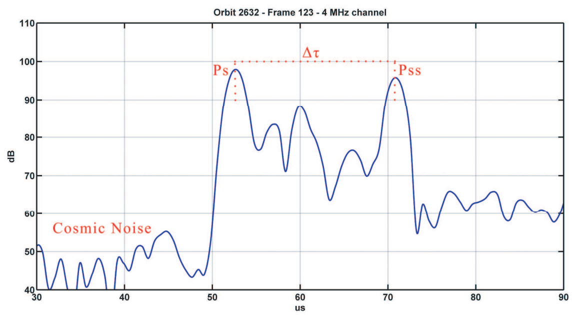

Figure 1: Typical MARSIS frame.

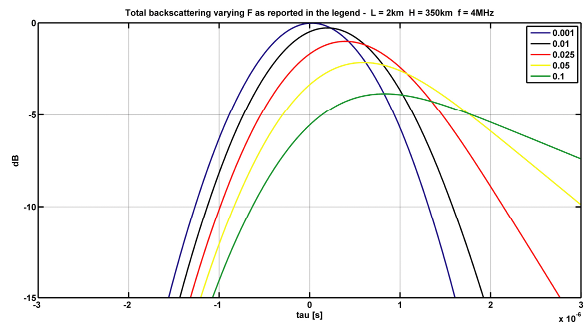

Figure 2: Backscattering vs. roughness (F), for fixed values of correlation length L, altitude H and frequency f.

4. FDTD MODELING

The adopted 1D-FDTD algorithm divides the problem geometry into a spatial grid of cells where electric and magnetic field components as well as constitutive parameters (like permittivity and permeability) are placed at certain discrete positions in space and it solves Maxwell's equations in time at discrete time instances δt. The 1D-FDTD proposed to model the subsurface propagation by [3] is the following:

$$E_z^{n+1}(i) = C_{eze}(i) \times E_z^n(i) + C_{ezhy}(i) \times \left[H_y^{n+\frac{1}{2}}(i) - H_y^{n+\frac{1}{2}}(i-1)\right] + C_{ezj}(i) \times J_{iz}^{n+\frac{1}{2}}(i) \tag{2}$$

$$H_y^{n+\frac{1}{2}}(i) = C_{hyh}(i) \times H_y^{n-\frac{1}{2}}(i) + C_{hyez}(i) \times \left[E_z^n(i+1) - E_z^n(i)\right] + C_{hym}(i) \times M_{iy}^{n+\frac{1}{2}}(i) \tag{3}$$

In particular, n denotes the current time step δt and i is the cell index on the one dimensional grid having width δx. $C_{eze} \ldots C_{hym}(i)$ account for the permittivity, permeability and conductivity along the grid, their expression can be found in [3].

5. AIM OF THE PROPOSED WORK

In order to understand the volume scattering influence on the data inversion, the simulation of scenarios having structures influencing $\frac{P_s}{P_{ss}} \frac{f_s}{f_{ss}}$ is needed. Using a 1D-FDTD code is not possible to simulate tilted layers, however, data inversion has been performed so far on a South Polar region that is free of surface clutter according to MOLA data and do not present a significant power contribution in lateral Doppler filters, that account for tilted layers [6]. So, the proposed simulations will be focused on parallel layers. The reference scenario will be composed by air, ice ($\varepsilon_r = 3.15$), basalt ($\varepsilon_r = 8$). The ice will extend for 2 km so reproducing the $\Delta\tau \sim 20\,\mu\mathrm{s}$ value registered by experimental data. No attenuation (only real permittivity values are adopted) is considered for two reasons: firstly, because south pole present some dust mixed with ice in the upper portion of the polar cap that is supposed to not significantly attenuate the transmitted wave [4], and secondly, starting from $K_{\mathrm{dB}} = 0$ the $\frac{P_s}{P_{ss}}$ is required to be the same for the two channels, since the interfaces are flat and not rough (that would introduce frequency dependency).

So, this choice would be useful to separate the volume scattering effect from the attenuation effect, also underlining the impact on the attenuation estimation that volume scattering, considered as created by layers in the ice that are unresolved by radar resolution, would wave on P_s and P_{ss}. Since experimental frames always present returns between those coming from the air/ice (P_s) and ice/rock (P_{ss}) interfaces (Fig. 1) is worth questioning in which cases such returns could drain power modifying the P_{ss} recorded level. Moreover, it not clear the volume scattering frequency dependency since both channels share the same range resolution having equal bandwidth. As [4] pointed out, CO_2 layers present in the first 10 m of the polar surface will influence the backscattered power. In this case, MARSIS range resolution will not be able to reveal them maintaining the shape of the surface response belonging to the ice layer. Finally, the degrading effect on the geometric term correction will be shown.

6. SIMULATIONS

Simulations will reproduce MARSIS transmitted signal, similar considerations would be applicable to SHARAD once the 10 MHz bandwidth is half-splitted in two channels. FDTD stability is guaranteed respecting the Courant-Friedrichs-Lewy (CFL) condition, which requires that the time increment δt has a specific bound relative to the lattice space increments, such that $\delta t \leq \delta x/c$ while 20 cells per wavelength have been set to perfectly reproduce the propagating chirp spectrum. It is important to underline that the speed of light will be $c \neq c_0$ in the various layers being dependent on their permittivity, $c = c_0/\sqrt{\varepsilon_r}$. So, the CFL has been verified for both channels in case of scenarios having permittivity values ranging from 1 (air) to 8 (rocks) finding the required pair (δt; δx). Verifying such a CFL condition allows to propagate both 3 and 4 MHz channels in the above mentioned reference scenario obtaining the same P_s/P_{ss}value (2.66 dB as required by theory) and verifying $K_{\mathrm{dB}}= 0$ as needed.

To explain volume scattering frequency dependency the reference scenario has been modeled adding 2 groups of layers: the first group is composed by 2×50 m layers having permittivity equal to 5 separated by 50m of ice while the second group is composed by 2×100 m layers of the same permittivity spaced by 100 m of ice. In optics these structures are better known as periodic stratified mediums. The simulated scenario and results are reported in Fig. 3.

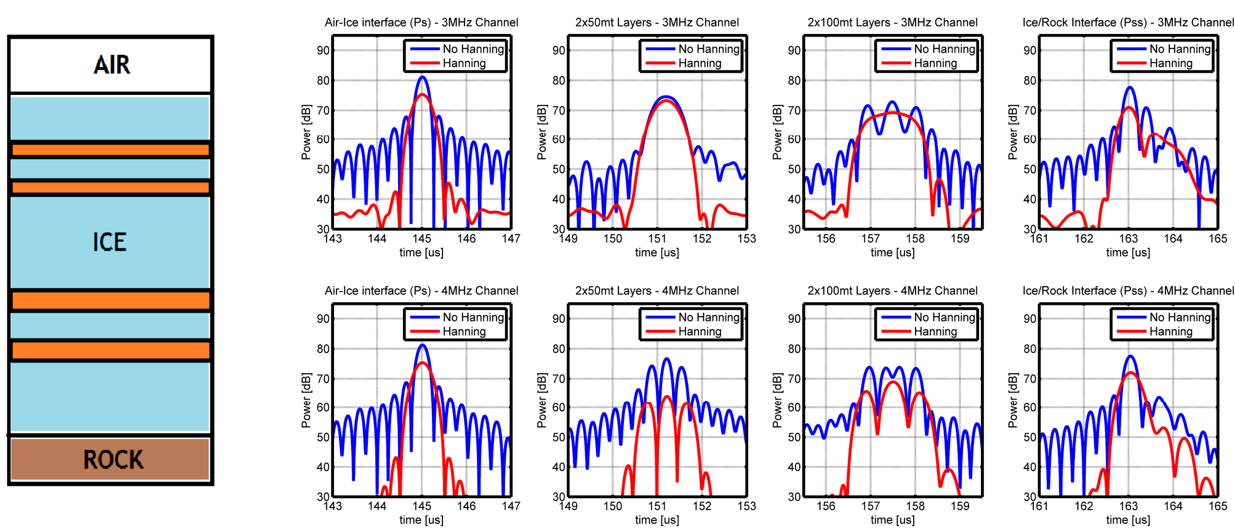

Figure 3: Reference Scenario including 2 groups of layers having ε_r= 5. Transmission and reception take place in the air.

Layers extending more than range resolution, like the air/ice and ice/rock ones, are correctly resolved by range compression at both channels. The $\varepsilon_r = 5$ layers having thickness below the resolution are better evidenced, but not resolved, by the channel having a wavelength in the medium shorter than their extension. As reported by Fig. 3 in the 3 MHz case, 2×50 m layers are totally unresolved, as their extension is limited compared to both resolution and wavelength in the medium, anyway, they continue influencing the basckscattered power. It is important to point out that, for scenarios modeled under the assumptions made, frequency dependency arise whenever layers are no more resolved by the radar resolution. Moreover, volume power backscattered by the stratified medium is very high also introducing frequency dependency on P_{ss} and so leading to a wrong attenuation evaluation using (1).

The results obtained have been verified by a theoretical analysis of the reflection coefficient for periodically stratified media, based on the formulation developed by [7].

Another important case to be inferred accounts for layers close to the air/ice and ice/basalt interfaces. There is the possibility that their returns close to the interfaces could be visible before applying the Hanning weighting and not after, so influencing the shape of the P_s, P_{ss} in the weighted compression and consequently misleading the geometric correction algorithm as stated by [8] that would tend to correct a flat-shaped interface return as a rough one, using the theoretical curves in Fig. 2, so introducing an error in the data inversion equation. A scenario made adding two layers to the reference scenario is reported in Fig. 4 showing the influence on the P_{ss} shape after weighting. A full analysis regarding such effect can be found in [8], for different values of permittivity and thickness.

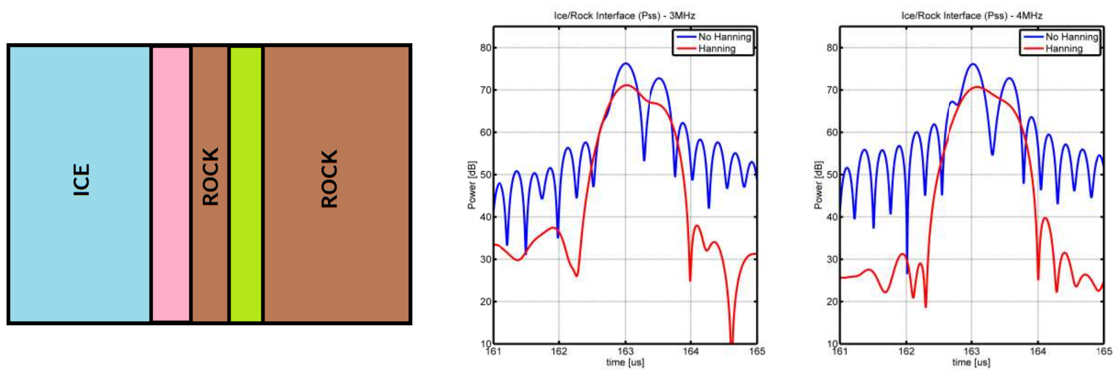

Figure 4: Pulse shape degradation due to rocky layers close to the ice/rock interface.

Moreover, taking into account the power reflection coefficient formula for a single interface:

$$\rho^2 = \left(\frac{n_2 - n_1}{n_2 + n_1}\right)^2 \tag{4}$$

It is important to notice that some ambiguity can exists because of the exponentiation presence. For instance, the pair of permittivity values [3.15, 2] brings to a reflection coefficient equal to 0.11 that is also the same given by [3.15, 5]. These two pairs could exist both in a real scenario. Running two simulations adding, in the ice, a wide layer resolved by the radar resolution having $\varepsilon_r = 2$ for the first simulation and $\varepsilon_r = 5$ for the second the same result is obtained (Fig. 5). It is worth noticing anyway that no variation on P_{ss} is evidenced cause the returns level is very low, 10 dB from P_s and P_{ss}. So, the inversion would bring to the same result of the reference scenario. In Fig. 3, volume level was higher because of the periodic structures.

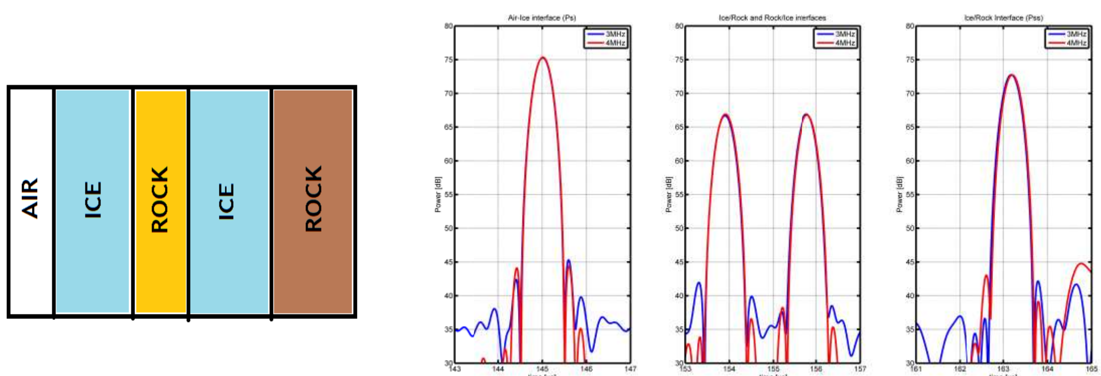

Figure 5: Example of ambiguous scenario.

As reported by [4], CO_2 ice layers can be found in the upper part of the south polar icy crust. The thickness of such layers is considered to be limited to a few meters. So, the pulse will not change its shape but the power, P_s, could be influenced differently for MARSIS channels as indicated by previous simulations. If a frequency dependency exists, attenuation estimation will be corrupted.

To assess such influence, the reference scenario has been modified introducing a 10 m CO_2 layer having real permittivity equal to 2.4 (as proposed by [4]) between the air-ice interface. FDTD simulations have been verified by theory [9] reporting the results in Fig. 6. It is important to note that the P_s value is clearly frequency dependent but P_{ss} is not. Once again, the attenuation will be wrongly evaluated leading to a wrong data inversion. Since no periodic stratification is present and the P_{ss} pulse shape is not distorted, no clues of such effect will be found on experimental data apart from the frequency dependency of the P_s. For this reason only data frames from flat surfaces having the same power should be selected for data inversion.

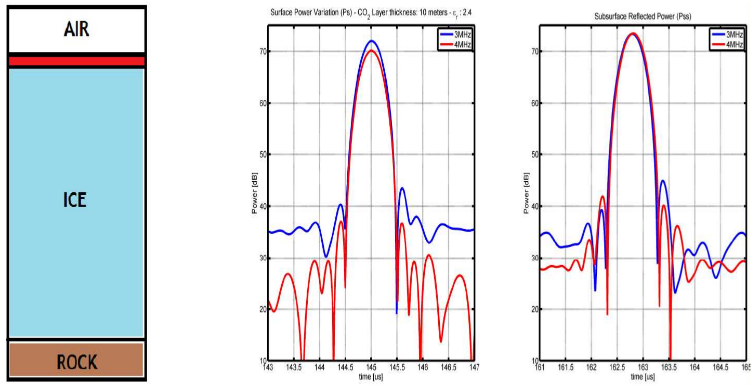

Figure 6: CO_2 superficial stratification influence on P_s.

7. CONCLUSIONS

Volume scattering influence on power backscattered by air/ice and ice/basalt interfaces has been inferred using a 1D-FDTD simulator. Several scenarios have been simulated according to trends reported by experimental data. Data inversion equation has been reported and the effect of volume scattering has been discussed for both recorded power levels (P_s, P_{ss}) and attenuation estimation. Summarizing the obtained results, it seems clear that attenuation cannot be always correctly evaluated. Effects on pulse shape influencing the geometric correction algorithm have been also pointed out. A selection procedure should select experimental data frames having a volume level around -10 dB from P_s and P_{ss} in order to avoid a degrading influence on the P_{ss} value and shape. Moreover, assuming a flat surface for the area under investigation, Ps values at both channels shall be the same, avoiding the presence of CO_2 layers. Such constrains will surely increase the data set stability for data inversion. The proposed simulator is fast and easily implementable representing an important tool to support both the theoretical as well as experimental data analysis.

REFERENCES

1. Picardi, G., et al., "MARSIS data inversion approach: Preliminary results," *Proc. of 2008 IEEE Radar Conference*, Vol. 1, 1–4, Rome, Italy, May 2008.
2. Picardi, G., D. Biccari, R. Seu, et al., "Performance and surface scattering models for the Mars advanced radar for subsurface and ionosphere sounding (MARSIS)," *Planetary and Space Science*, Vol. 52, 149–156, 2004.
3. Elsherbeni, A. and V. Demir, *The Finite-Difference Time-Domain Method for Electromagnetics With MATLAB Simulations*, Scitech Publishing Inc., Chapters II, V & Apprendix A, January 2009.
4. Mouginot, J., W. Kofman, A. Safaeinili, C. Grima, A. Herique, and J. J. Plaut, "MARSIS surface reflectivity of the south residual cap of Mars," *Icarus*, Vol. 201, No. 2, 454–459, 2009.
5. Flamini, E., "Sounding Mars with SHARAD & MARSIS", *Proc. of 2007 IEEE 4th International Workshop on Advanced Ground Penetrating Radar*, Vol. 1, 246–251, Naples, Italy, June 207, 2007.
6. Restano, M., A. Masdea, G. Picardi, and R. Seu, "Doppler analysis for data inversion and image processing in the MARSIS experiment," *Proc. of 2011 IEEE Microwaves, Radar and Remote Sensing Symposium*, Vol. 1, 153–156, Kiev, Ukraine, August 2011.
7. Born, M. and E. Wolf, *Principles of Optics*, 6th Edition, 66–69, Pergamon Press, 1983.
8. Restano, M., A. Masdea, G. Picardi, and R. Seu, "Weighting network influence on the geometric term correction in MARSIS data inversion," *Proc. of 2012 IEEE International Radar Symposium*, Vol. 1, 213–217, Warsaw, Poland, May 2012.

Electromagnetic Susceptibility Analysis of Printed Circuits Board (PCB) and Their Impact to IEC 61000-4-3

R. Linares y Miranda, J. H. Caltenco Franca, and R. Peña Rivero
Instituto Politécnico Nacional, SEPI-ESIME-Zacatenco, Laboratorio de Compatibilidad Electromagnética
Av. IPN, S/N, Unidad Profesional Adolfo López Mateos, Edif. Laboratorios Pesados 1
Col. Lindavista, México, DF, C.P. 07836, México

Abstract— As consequence of the requirements of electronic equipment with IEC61000-4-3 standard, studies of immunity to radio frequency electromagnetic fields in Printed Circuits Board (PCB) tracks must be developed, taking into account the geometry and configuration in order to apply mitigation techniques induced currents. In this paper, a method for predicting the induced current in PCB tracks of digital electronic systems is presented. The results of the prediction are compared to measurements, which are very similar. This contribution may be used as a design tool for electromagnetic compatibility compliance of immunity test in PCB.

1. INTRODUCTION

In electronic systems, numerous devices and different structures, such as: wire, cables, Printed Circuit Board (PCB) trace, chip pins, ground plane and others, can act as unintentional antennas in the presence of electromagnetic energy of radio frequency (RF). The RF can be either radiated from intentional or unintentional sources. The intentional sources can be: powerful radio transmitters, wireless network devices (Wi-Fi, Bluetooth), mobile phones, PDAs, or intentionally generated for malicious reasons. The unintentional sources can: natural sources (atmospheric, lightning, electrostatic discharges) or men made sources (all that are electrically operated) [1–3]. The unintentional antennas can serve to couple RF energy into the core circuit. The RF energy that is coupled by the system can induce unwanted currents, which cause various disturbances; this energy is an Electromagnetic Interferences (EMI), also called Radio Frequency Interference (RFI). On other hand, high performance integrated circuits (IC's), such as microprocessors, which have very small feature sizes and are clocked at frequencies well into the GHz range while operating at reduced voltage levels. Although this has improved the ability and performance of modern systems have also increased their susceptibility to EMI radiated [4, 5]. The electrical charge required in transistor switching decreases with relatively smaller IC feature size; this implies, that voltage levels required to make the device to switch is reduced, making it easier to disturb the circuit with lower RF signal levels (EMI). Also as switching speed of the IC's increases and the supply voltage scales down, the noise margin becomes smaller and they are more susceptible to EMI. All this allows external disturbances to degrade the signal integrity more easily.

For the commercial part, that is the real world; it is said that a device, equipment or system meets compliance assessment of Electromagnetic Compatibility, if their susceptibility to radiated emissions not exceeds the strength electric field levels that in IEC 61000-4-3 [6] standard are specified. However, since currently the integrated circuits operate at very low energy levels, the standard IEC's level allow EMI problems to be presented. It is absolutely clear that the devices, equipment and systems with new technologies today have susceptibility levels are lower than those set out in the standard [7]. Then is necessary to develop methodologies for predicting the induced currents in PCB trace, which are the interference paths. This paper a method for predicting the induced current in PCB traces of digital electronic systems is presented. The results of the prediction are compared to measurements, which are very similar. This contribution may be used as a design tool for electromagnetic compatibility compliance of immunity test in PCB.

2. EQUATIONS OF THE INDUCED CURRENT IN PCB TRACE

The susceptibility effects in PCB trace are related with electromagnetic field illumination, therefore, the problem consists of describing the voltages and currents induced in the trace in terms of the inducing field [8]. The current $i = (z, t)$ at a point along a trace is defined, as the charge flow across the cross section of the conductor at that point; and the voltage at that point. So, the induced voltage $v = (z, t)$, is defined for a horizontal line as the integral of the electric field along a vertical trajectory from that point on the conductor to the ground or some reference point. The expression

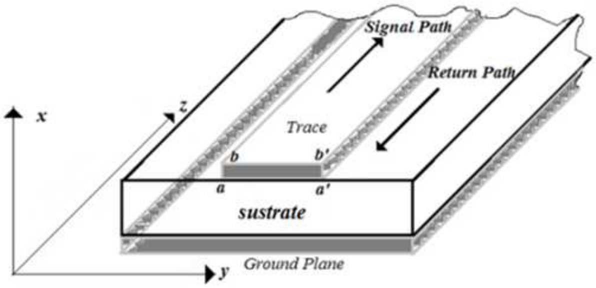

Figure 1: Printed circuit board trace.

that determines this phenomenon is the Faraday's law, which can be applied to determine the effects on a PCB trace, as shown in Figure 1. Then we have:

$$\int_{C_l} \vec{E} d\vec{l} = -\frac{d}{dt}\int_{S_l} \vec{B} d\vec{S} \tag{1}$$

With the help of Figure 1 and Faraday's law we have:

$$\int_a^{a'} \vec{E}_l dl + \int_{a'}^{b} \vec{E}_t d\vec{l} + \int_b^{b'} \vec{E}_l d\vec{l} + \int_{b'}^{a} \vec{E}_t d\vec{l} = \frac{d}{dt}\int_{S_l} \vec{B}\cdot\vec{a}_n d\vec{S}, \tag{2}$$

where E_t is the electric field transverse of the cross section in the xy-plane and E_l is the longitudinal field along the surface of the conductors. In this processes, incidents phenomenon fields and of the dispersed fields is presented. The incidents fields are generated by a source from a determinate distance and the fields dispersed are due to induced currents in the conductors. The total field is the sum of both fields, incidents and dispersed, therefore one have

$$\vec{E}_t = \vec{E}_t^i + \vec{E}_t^S; \quad \vec{E}_l = \vec{E}_l^i + \vec{E}_l^S; \quad \vec{B} = \vec{B}^i + \vec{B}^s \tag{3}$$

Since the currents are in the direction "z", the potential can be determined by

$$V_i^S(z,l) = -\int_a^{a'} \vec{E}_l^S d\vec{l}; \quad V_i^S(z+\Delta z, l) = -\int_b^{b'} \vec{E}_l^S d\vec{l} \tag{4}$$

As the PCB under study is a transmission line, the induced fields are reflected in the ends of the line as voltages and currents, which can be determined by the telegrapher's equations, which are:

$$\frac{\partial V(z,t)}{\partial x} + RI(z,t) + L\frac{\partial I(z,t)}{\partial x} = V_F(z,t) \quad \frac{\partial I(z,t)}{\partial x} + GV(z,t) + C\frac{\partial V(z,t)}{\partial x} = I_F(z,t) \tag{5}$$

Then

$$I_F = -G\int_a^{a'} \vec{E}_t^i \vec{dl} - C\frac{\partial}{\partial t}\int_a^{a'} \vec{E}_t^i \vec{dl} \tag{6}$$

So that:

$$\vec{H}^i = \frac{1}{\eta}\vec{a}_\beta \times \vec{E}^i = \frac{\vec{E}_0}{\eta}\left(h_x\vec{a}_x + h_y\vec{a}_y + h_z\vec{a}_z\right) e^{-j(\beta_x+\beta_y+\beta_z)}, \tag{7}$$

where

$$\begin{aligned}
&\beta_x = -\beta\cos\theta_p; \quad \beta_y = -\beta\sin\theta_p\cos\phi_p; \quad \beta_z = -\beta\sin\theta_p\sin\phi_p \\
&h_x = -\cos\theta_E\sin\theta_p; \quad h_y = \cos\theta_E\cos\theta_p\cos\phi_p - \sin\theta_E\sin\theta_p; \\
&h_z = \cos\theta_E\cos\theta_p\sin\phi_p + \sin\theta_E\sin\phi_p.
\end{aligned}$$

Thus is satisfied that $h_x^2 + h_y^2 + h_z^2 = 1$.

In the case of plane wave incident a PCB with a trace and ground plane, the image field can be analyzed as a reflected wave. Then the voltage at the PCB is the sum of the fields generated in the trace and the ground plane. Considering that the incident and reflected field have the same angle (Snell's law), we have that the fields are

$$\vec{E}^i = E_0\left(e_x^i\vec{a}_x + e_y^i\vec{a}_x + e_z^i\vec{a}_x\right)e^{-j(\beta_x+\beta_y+\beta_z)};\quad \vec{E}^r = E_0\left(e_x^r\vec{a}_x + e_y^r\vec{a}_x + e_z^r\vec{a}_x\right)e^{j(\beta_x+\beta_y+\beta_z)}. \tag{8}$$

For case that the ground plane position is $y = 0$ the tangential fields are:

$$e_z^r = -e_z^i = -e_z;\quad e_y^r = -e_y^i = -e_y$$

where $e_x = \sin\theta_E\sin\theta_p$; $e_y = -\sin\theta_E\cos\theta_p\cos\phi_p - \cos\theta_E\sin\theta_p$; $e_z = -\sin\theta_E\cos\theta_p\sin\phi_p + \cos\theta_E\cos\phi_p$.

Thus is satisfied that $e_x^2 + e_y^2 + e_z^2 = 1$.

As the PCB under study is a transmission line, incident field components are in directions "x" and "z", since the component in $y = 0$, then their expressions are:

$$\begin{aligned} E_z^{total} &= E_z^i + E_z^r = -2jE_0e_z\sin(\beta_z x)e^{-j(\beta_y y+\beta_z z)} \\ E_x^{total} &= E_x^i + E_x^r = -2jE_0e_x\sin(\beta_x x)e^{-j(\beta_y y+\beta_z z)} \end{aligned} \tag{9}$$

Thus evaluating $V_{FT}(l)$ and $I_{FT}(l)$ we have:

$$V_{FT}(l) = \int_0^L \cosh\left[\gamma(l-\tau)\right]\left[E_z^i(d,\tau) - E_z^i(0,\tau)\right]d\tau - \int_0^d E_x^i(x,l)\,dx + \cosh(\gamma l)\int_0^d E_x^i(0,l)\,dx \tag{10}$$

$$I_{FT}(l) = -\int_0^l \sinh\left[\gamma(l-\tau)\right]Z_c^{-1}\left[E_z^i(d,\tau) - E_z^i(0,\tau)\right]d\tau - \sinh(\gamma l)\,Z_c^{-1}\int_0^d E_x^i(0,l)\,dx \tag{11}$$

The current at the end of the transmission line is: $I(0) = \frac{V_{FT}(l) - Z_l I_{FT}(l)}{D}$, where $D = 10\beta[(Z_0Z_s + Z_0Z_l)\cos(\beta s) + j(Z_0Z_s + Z_0Z_l)\sin(\beta s)]$.

Then the induced currents due incident fields is

$$\begin{aligned} I(s) &= \frac{-j\sin\left(\beta\frac{b}{2}\right)\left\{Z_0\sin(\beta s) + jZ_s[1-\cos(\beta s)]\right\}}{10\beta\left[(Z_0Z_s + Z_0Z_L)\cos(\beta s) + j\left(Z_0^2 + Z_sZ_L\right)\sin(\beta s)\right]} \\ I(s) &= \frac{-j\sin\left(\frac{\omega}{v_p}\frac{b}{2}\right)\left\{Z_0\sin\left(s\frac{\omega}{v_p}\right) + jZ_s[1-\cos\left(s\frac{\omega}{v_p}\right)]\right\}}{10\beta\left[(Z_0Z_s + Z_0Z_L)\cos\left(s\frac{\omega}{v_p}\right) + j\left(Z_0^2 + Z_sZ_L\right)\sin\left(s\frac{\omega}{v_p}\right)\right]}. \end{aligned} \tag{12}$$

For low frequency we have

$$\beta\frac{b}{2} \to 0,\quad \sin\left(\beta\frac{b}{2}\right) \approx \beta\frac{b}{2};\quad \beta s \to 0,\quad \sin(\beta s) \approx \cos(\beta s) \approx 1$$

where

$$\beta_0 = \frac{2\pi}{\lambda},\quad \beta_r = \frac{\omega}{c}\sqrt{\varepsilon_r}$$

As "bs" is the area that forms the trace and the ground plane, it has:

$$I = E\frac{bsZ_0\beta}{Z_0(Z_s + Z_L) + j(Z_0^2 + Z_sZ_L)\beta s} = E\cdot\frac{bs}{Z_s + Z_L} \tag{13}$$

3. RESULTS

The experimental part was carried out with a PCB with the dimensions specified in Table 1. The measured and simulated response of the induced voltage on a PCB is shown in Figure 2. The measurement was performed with a GTEM cell and simulation with SPICE. The applied electric field was 3 V/m inside the GTEM cell.

Dielectric constant of the substrate $\varepsilon_r = 4.7$	substrate thickness $h = 1.58\,\mathrm{mm}$
Trace width $a = 2.22\,\mathrm{mm}$	Trace thickness $t = 0.3508\,\mathrm{mm}$
Trace length $l = 150\,\mathrm{mm}$	Impedance $Z_0 = 50\,\Omega$

Table 1: PCB dimension.

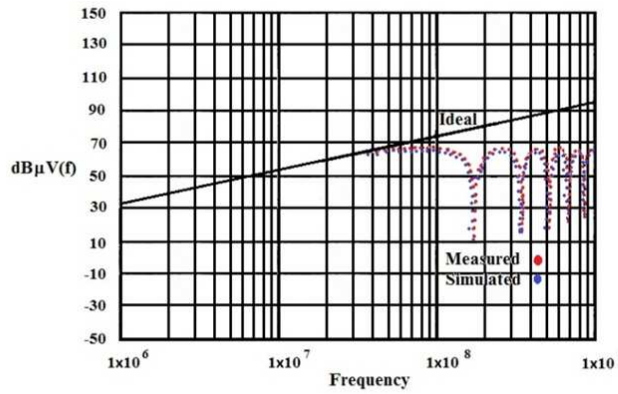

Figure 2: Voltage induced in a printed circuit board.

4. DISCUSSION AND CONCLUSIONS

In the results the ideal behavior is compared with measurement and simulation of a transmission line exposed to an external electric field. In the graph of Figure 2, the simulated and measured the overlapping, so that no difference is noted.Therefore is concluded that the model may be predict the levels of induced electric field that can affect the behavior of a circuit, especially if it is digital. This behavior is appropriate to analyze the signal integrity. It is also noted that the results of the second order resonance, in the first instance give information of the decoupling of the transmission line. With the first resonance can determine where the first decoupling occurs, which in this case is outside the PBC, since coaxial cables of 0.6 m to capture the signal are used. This is the part of the measurement system that is required to analyze in order to be completely sure of the effects. According to the results the standard IEC 61000-4-3 is covered perfectly, since the induced field is below of limits. The objective was achieved with develop of a model to predict the electric field induced on PCB.

ACKNOWLEDGMENT

Consejo Nacional de Ciencia y Tecnología (CONACYT), México, Project 124091, Comisión de Operación y Fomento de Actividades Académicas.

REFERENCES

1. Montrose, M. I., *Printed Circuit Board Design Techniques for EMC Compliance: A Handbook for Designers*, 2nd Revised Edition, John Wiley & Sons Inc., 2000.
2. Bogatin, E., *Signal Integrity: Simplified*, Prentice Hall Professional, 2004.
3. Taylor, C. D., R. S. Satterwhite, and C. W. Harrison, "The response of a terminated two-wire transmission line excited by a non-uniform electromagnetic field," *IEEE Trans. Antennas Propag.*, Vol. 13, No. 6, 987–989, Nov. 1965.
4. Ben Dhia, S., M. Ramdani, and E. Sicard, *Electromagnetic Compatibility of Integrated Circuits: Techniques for Low Emission and Susceptibility*, Spinger, 2006.
5. IEC 61967-2, "Integrated circuits — Measurement of electromagneticemissions, 150 kHz to 1 GHz — Part 2: Measurement of radiatedemissions — TEM cell and wideband TEM cell method," *International Electrotechnical Commission (IEC)*, 2005.
6. IEC EN61000-4-3, "Testing and measurement techniques — Radiated, radio-frequency, electromagnetic field immunity test, third edition. International," *International Electrotechnical Commission (IEC)*, Geneva, Switzerland, 2006.
7. IEC 61000-4-20, "Electromagnetic compatibility (EMC), Part 4: Testing and measurement techniques, Section 20: Emission and immunity testing in transverse electromagnetic (TEM) waveguides," *International Electrotechnical Commission (IEC)*, Geneva, Switzerland, 2003.
8. Li, S. R., Y. Li, Z. Sun, and F. Wang, "Electromagnetic susceptibility model of discontinuous microstrip circuits under plane wave illumination," *Progress In Electromagnetics Research M*, Vol. 25, 223–237, 2012.

3-phase VSC Modifications for Symmetrical and Asymmetrical Operation

Seyed Mahdi Fazeli, **Wooi Ping Hew**, **Nasrudin Bin Abd Rahim**,
Boon Teck Ooi, and **Jeyraj Seelvaraj**
UMPEDAC, Level 4, Wisma R & D UM, University of Malaya, Kuala Lumpur 59990, Malaysia

Abstract— The paper describes minor modifications required of 3-phase voltage-source converters (VSCs) to accommodate the negative and zero-sequences of asymmetrical operation. It also proposes the Individual-Phase Decoupled P-Q Control which has 2 independent degrees of freedom for each of the 3 phases. They enable asymmetrical operation to be controlled from the a-b-c frame without having to transform to the d-q frame and without having to use symmetrical component concepts. The methods are applied to a D-STATCOM and the concepts are validated by simulations using PSCAD/EMTDC.

1. INTRODUCTION

Existing methods, [1–5], of dealing with asymmetry make use of positive sequence and negative sequence 3-phase decoupled P-Q control. In the Individual-phase Decoupled P-Q Control method, it is not necessary to transform from a-b-c frame to the d-q frame and the equally abstract concepts of symmetrical components is not used.

This convenience is made possible by developing fast response, single-phase phase-locked loops (S-PLL) so that the in-phase and the quadrature components of the phase voltages are identified to implement the 6 decoupled P-Q controllers (P_a^*, Q_a^*), (P_b^*, Q_b^*) and (P_c^*, Q_c^*). Equally important is the development of fast single-phase active power measurement (SPM) units so that P_a, P_b, and P_c are measured for negative feedback control.

The methods are applied to a D-STATCOM which is tasked to equalize the complex power of the sending-end side in spite of imbalance on the load-side. The concepts are validated by simulations using PSCAD/EMTDC.

2. SWITCHING FUNCTION ANALYSIS OF ZERO SEQUENCE

If the VSC shown in Fig. 1 is required to accommodate the zero-sequence current, the mid-point between the upper and lower buses has to be grounded so that the zero-sequence current can flow to the ground. The mid-point voltage in Fig. 1 is labeled as $v_y(t)$.

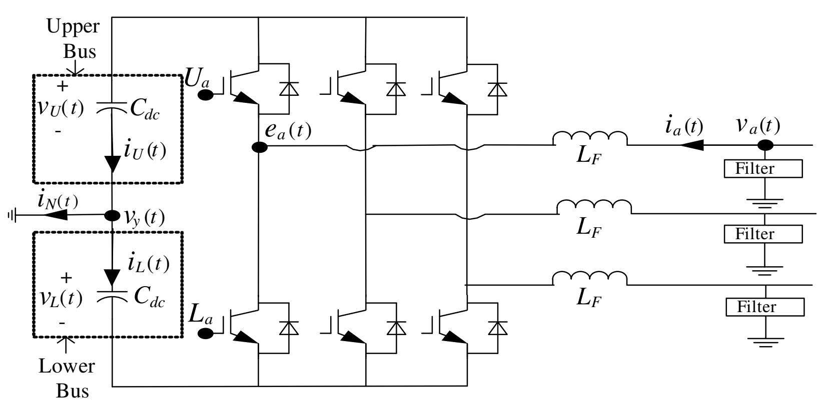

Figure 1: Three-phase voltage-source converter.

2.1. DC-side Currents and Voltages

The insulated-gate bipolar transistors (IGBT) and anti-parallel diodes of each leg of the VSC in Fig. 1 are assumed to be as ideal ON/OFF switches. The anti parallel diode enables bi-direction current flow through the ON switch. The symbols U and L designate Upper and Lower respectively.

The upper and lower bus currents are the sums of the current contributions from the 3 phases,

$$i_U(t) = 0.5[(S_a(t)+1)i_a(t) + (S_b(t)+1)i_b(t) + (S_c(t)+1)i_c(t)] \quad (1)$$
$$i_L(t) = 0.5[(S_a(t)-1)i_a(t) + (S_b(t)-1)i_b(t) + (S_c(t)-1)i_c(t)] \quad (2)$$

Note that applying Kirchhoff's current law at the node of $v_y(t)$

$$i_N(t) = i_U(t) - i_L(t) \quad (3)$$

Equations (1) and (2) can be rewritten as:

$$i_U(t) = i_M(t) + 0.5 i_N(t) \quad (4)$$
$$i_L(t) = i_M(t) - 0.5 i_N(t) \quad (5)$$

where

$$i_M(t) = 0.5[S_a(t)i_a(t) + S_b(t)i_b(t) + S_c(t)i_c(t)] \quad (6)$$

From definition of the zero sequence current

$$i_0(t) = \frac{[i_a(t) + i_b(t) + i_c(t)]}{3} \quad (7)$$

From (7), $i_N(t) = 3 \times i_0(t)$. The interpretation from (4) and (5) is: on admission into the VSC, the zero-sequence current or neutral current after entering the VSC divide into two, $0.5 i_N(t)$, one half flowing along the upper bus and the other half along the lower bus and merge again at the mid-point of the buses.

2.2. Charging of dc Capacitors

The voltages across the upper and lower buses with capacitors of size C are based on the charging equations:

$$C_{dc}\frac{dv_U(t)}{dt} = i_U(t) = i_M(t) + 0.5 i_N(t) \quad (8)$$
$$C_{dc}\frac{dv_L(t)}{dt} = i_L(t) = i_M(t) - 0.5 i_N(t) \quad (9)$$

Adding (18) and (19)

$$C_{dc}\frac{d[v_U(t) + v_L(t)]}{dt} = 2 i_M(t) \quad (10)$$

From (10) it is clear that $[v_U(t) + v_L(t)]$ is charged by $2i_M(t)$ and is not affected by $i_N(t)$. On the other hand, from (8) and (9) when $i_N(t)$ has a dc component, the average voltage of the upper and lower buses become unbalanced.

Figure 2 shows the simulated voltages and currents in the dc side of the VSC under slight imbalance whereas ripples from PWM switching have been filtered. Fig. 2(a) shows the currents of the upper bus (see (4)) and the lower bus (see (5)) which contain 50 Hz components of the zero-sequence and 100 Hz components of single-phase power. Fig. 2(a) also shows the 50 Hz neutral current. Fig. 2(b) shows the bus-to-bus voltage $[v_{dc}(t) = v_U(t) + v_L(t)]$ (see (10)) which is a dc constant with a 100 Hz ripple. But it is free of the 50 Hz of the zero-sequence current. Fig. 2(c) shows a dc average together with 50 Hz and 100 Hz components in the voltages of the upper and lower buses (see (8) and (9) respectively). In Fig. 2(c), the average voltages of the upper and lower buses are not significantly imbalance because the zero-sequence is at the steady-state stage. In the long term, the accumulation of dc off-sets in the zero-sequence current in transient events can cause imbalance.

3. DOUBLE FREQUENCY POWER IN VSC

Unless the double frequency components of individual single-phases ac power are cancelled by symmetrical balance, they appear as a double frequency ripple riding on the constant dc voltage in $v_{dc}(t)$. This has been attributed to the negative sequence but a correction needs to be made because the double frequency pulsation is inherent in all single-phase power. Therefore, the zero sequence voltage and current together also gives rise to the double frequency dc voltage ripple [9].

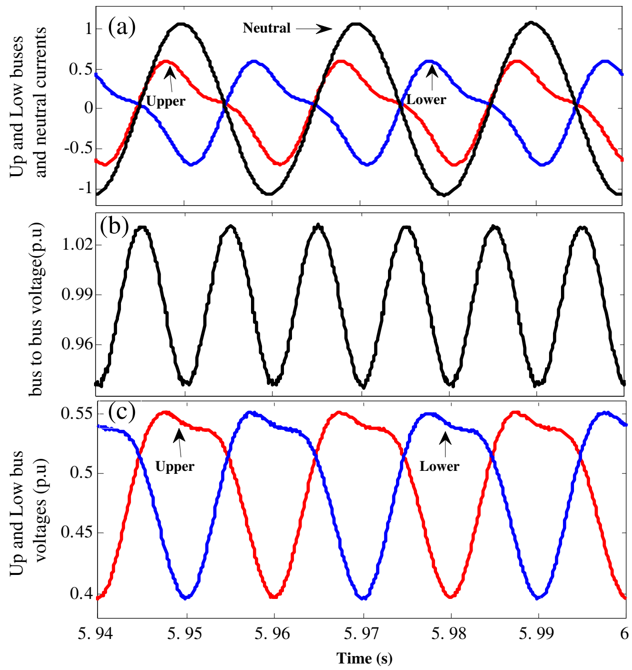

Figure 2: DC-side voltages and currents: (a) currents of upper and lower buses and neutral; (b) bus-to-bus voltage $[v_{dc}(t) = v_U(t) + v_L(t)]$; (c) voltages of upper and lower buses.

In Sinusoidal Pulse Width Modulation (SPWM), the fundamental component of the pulsed voltage at the terminal of the a-phase of the VSC is:

$$v_a(t) = \frac{m_a(t)v_{dc}(t)}{2V_{tr}} \tag{11}$$

where $m_a(t)$ is the modulating signal and V_{tr} is the peak of the triangle carrier. In view of the double frequency fluctuation in the dc link voltage, $v_{dc}(t)$, the output voltage is no longer the linearly amplified form of the modulating signal $m_a(t)$.

If the control signal of the a-phase of the VSC is $M_{SPWM-a}(t)$, the linear amplifier property of the VSC is restored by measuring $v_{dc}(t)$ and modifying the modulating signal as:

$$m_a(t) = \frac{M_{SPWM\text{-}a}(t)V_{dc\text{-}REF}}{v_{dc}(t)} \tag{12}$$

With this compensation

$$v_a(t) = \frac{M_{SPWM\text{-}a}(t)V_{dc\text{-}REF}}{2V_{tr}} \tag{13}$$

As this technique is well known and widely applied since [11] for example, no further elaboration is necessary.

4. INDIVIDUAL-PHASE DECOUPLED P-Q CONTROL

4.1. Single-phase Decoupled P-Q Control

The original time functions of the a-phase voltage and current are:

$$v_a(t) = \mathrm{Im} V_a e^{j(\omega t+\theta_{V\text{-}a})} = V_a \sin(\omega t + \theta_{V\text{-}a}) \tag{14}$$

$$i_a(t) = \mathrm{Im} I_a e^{j(\omega t+\theta_{I\text{-}a})} = I_a \sin(\omega t + \theta_{I\text{-}a}) \tag{15}$$

Phasor representations of them are:

$$\bar{V}_a = V_a e^{j\theta_{V\text{-}a}} = V_{pa} + jV_{qa} \tag{16}$$

$$\bar{I}_a = I_a e^{j\theta_{I\text{-}a}} = I_{pa} + jI_{qa} \tag{17}$$

where the subscripts p and q are respectively the in-phase and in-quadrate components of the sinusoidal time-varying components of voltage and current.

By definition, the complex power is:

$$\bar{S}_a = P_a + jQ_a = (V_{pa} + jV_{qa})(I_{pa} - jI_{qa}) \tag{18}$$

When a single-phase phase-locked loop (S-PLL) is synchronized to the a-phase voltage waveform, using of the S-PLL which acquires $(\omega t + \theta_{V\text{-}a})$ as reference for the sinusoidal time-varying functions, the phasor representation of (16) simplifies to:

$$\bar{V}_a = V_{pa} \tag{19}$$

Continuing to use the S-PLL, by injecting a controlled current of the a-phase as

$$\bar{I}_a{}^* = \left(I^*_{pa} - jI^*_{qa}\right) \tag{20}$$

the controlled complex power is

$$P^*_a + jQ^*_a = V_{pa}\left(I^*_{pa} - jI^*_{qa}\right) \tag{21}$$

The symbol (*) is used to denote a control variable.

In order to arrive at the controlled complex power of (21), the S-PLL generates the in-phase function $\sin(\omega t + \theta_{V\text{-}a})$ and in-quadrature function $\cos(\omega t + \theta_{V\text{-}a})$. Active power P^*_a and the reactive power Q^*_a control of the a-phase consists of multiplying I^*_{pa} and I^*_{qa} to $\sin(\omega t + \theta_{V\text{-}a})$ and $\cos(\omega t + \theta_{V\text{-}a})$ respectively to form the control signal

$$M_{SPWM\text{-}a}(t) = I^*_{pa}\sin(\omega t + \theta_{V\text{-}a}) - I^*_{qa}\cos(\omega t + \theta_{V\text{-}a}) \tag{22}$$

Although the voltage-source converter (VSC) outputs voltage pulses, a variety of methods, such as "dead-beat control" which make use feed forward and feedback, are available so that (35) is implemented.

Decoupled control of the complex powers for b-phase (P^*_b, Q^*_b) and c-phase (P^*_c, Q^*_c) are also achieved by multiplying (I^*_{pb}, I^*_{qb}) and (I^*_{pc}, I^*_{qc}) to the in-phase and in-quadrature functions generated by the S-PLL of the b- and c-phase respectively.

5. SINGLE-PHASE MEASUREMENT UNITS

5.1. Single-phase Phase-locked Loop (S-PLL)

Figure 3(a) is the schematic of the S-PLL of this paper. The R-L-C notch filter [12], shown in Fig. 3(b), eliminates the double frequency component in the output of the "detection stage" of the phase-locked loop. The components L and C are tuned to eliminate the double frequency $2f_0 = 100\,\text{Hz}$. R is designed to ensure that there is sufficient attenuation of of frequencies at $2f_0(1 \pm 0.05)\,\text{Hz}$. This is because the line frequency is allowed deviation of 5%. The Bode diagram of the magnitude in Fig. 4(a) shows that attenuation below $-25\,\text{dB}$ at 5% deviation can be designed using the notch filter. Unlike a low pass filter in traditional S-PLL, the high frequency end of the spectrum is kept intact and therefore the speed of response is fast. The simulation of Fig. 4(b) shows that the response to step change is well within 10 ms.

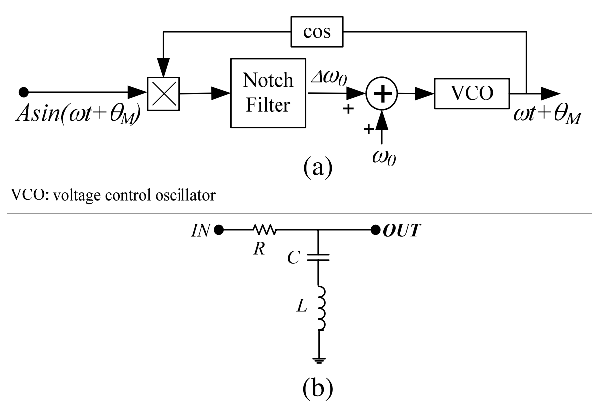

Figure 3: (a) Single-phase PLL based on a notch filter; (b) notch filter.

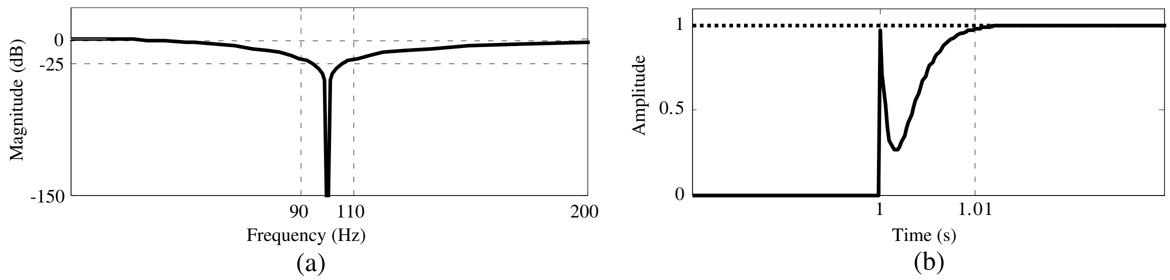

Figure 4: Notch filter. (a) Frequency response; (b) step response.

5.2. Single-phase Active Power Measurement

Instantaneous active power is measured by electronically multiplying $v(t) \times i(t)$ and removing the double frequency term by a notch filter as illustrated in Fig. 5.

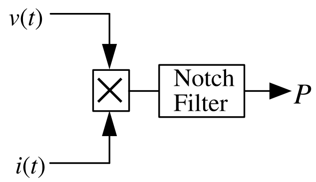

Figure 5: Active power measurement.

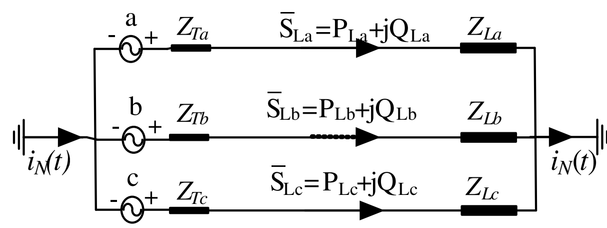

Figure 6: 3-phase network.

6. IMPLEMENTATION OF INDIVIDUAL-PHASE DECOUPLED *P-Q* CONTROL

Figure 8 shows a balanced 3-phase ac voltage source at the sending-end connected to unequal load impedances Z_{La}, Z_{Lb}, Z_{Lc} by balanced transmission-line impedances (Z_{Ta}, Z_{Tb}, Z_{Tc}). The complex powers of the loads, $\bar{S}_{La}$, $\bar{S}_{Lb}$, $\bar{S}_{Lc}$, are unequal. The neutrals of the wye (Y) connections are-grounded so that there is zero-sequence current under imbalance. The transmission line impedances are large so that there is voltage droop at the point of common connection (PCC).

The complex powers can be equalized by redistributing the active powers of the unequal loads, P_{La}, P_{Lb}, P_{Lc}, between the transmission lines so that each transmission line carries the average

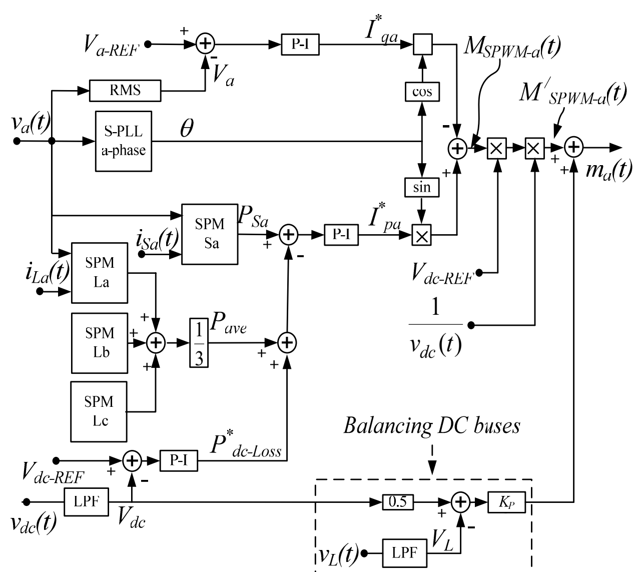

Figure 7: Block diagram decoupled *P-Q* control of the *a*-phase.

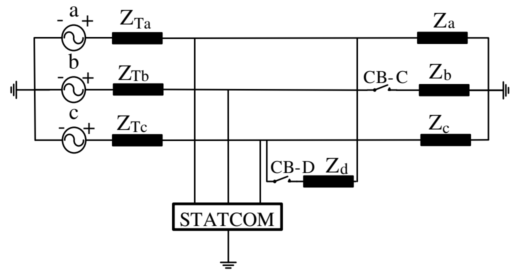

Figure 8: System of simulation test.

power of the 3 loads, P_{ave}, that is:

$$P_{ave} = \frac{P_{La} + P_{Lb} + P_{Lc}}{3} \tag{23}$$

This can be accomplished by a complex power compensator. The compensator injects Individual-Phase complex powers at the PCC:

$$\begin{aligned} \bar{S}^*_{Ca} &= P^*_{RDa} + jQ^*_{Ca} \\ \bar{S}^*_{Cb} &= P^*_{RDb} + jQ^*_{Cb} \\ \bar{S}^*_{Cc} &= P^*_{RDc} + jQ^*_{Cc} \end{aligned} \tag{24}$$

where

$$\begin{aligned} P^*_{RDa} &= P_{La} - P_{ave} \\ P^*_{RDb} &= P_{Lb} - P_{ave} \\ P^*_{RDc} &= P_{LC} - P_{ave} \end{aligned} \tag{25}$$

Because the total active power for compensator always is zero, here, a system such as a D-STATCOM can be considered as complex power compensator.

The Q-control $(Q^*_{Ca}, Q^*_{Cb}, Q^*_{Cc})$ of each phase of the D-STATCOM is used to regulate the output ac voltage magnitude at the PCC.

Figure 9 shows the function blocks leading to the SPWM input of the a-phase of the D-STATCOM: $M_{SPWM\text{-}a}(t)$ of (22) and $m_a(t)$ of (12). The function blocks of the b-phase and the c-phase are similar. The following blocks are common to all the three phases: (i) the computation of the average load active power, P_{ave}, (23); (ii) the formation of the loss of the D-STATCOM, $P^*_{dc\text{-}loss}$; (iii) the compensation of the dc voltage ripple by multiplication of $(V_{dc\text{-}Ref}/v_{dc}(t))$ (located between $M'_{SPWM\text{-}a}(t)$ and $M_{SPWM\text{-}a}(t)$); (iv) Balancing the DC bus voltages.

The ac voltage magnitude V_a is compared with the ac voltage reference. The error after passing the proportional-integral gain (P-I) block becomes I^*_{qa} which is multiplied to $\cos(\omega t + \theta_{V\text{-}a})$ (obtained from the S-PLL) to form one component of $M_{SPWM\text{-}a}(t)$.

In P-control, the average active load power P_{ave} of (23) (formed from SPM measurements of the active powers of all the phases at the load side) is applied as one component of active power reference. The other component is $P^*_{dc\text{-}loss}$, the active power required to replenish ohmic losses of the D-STATCOM so as to regulate the bus-to-bus voltage at $V_{dc\text{-}REF}$. The combined power reference $(P_{ave} + P^*_{dc\text{-}loss})$ is compared with transmission line power P_{Sa} and the error after passing a proportional-integral gain (P-I) block becomes I^*_{pa} which is multiplied to $\sin(\omega t + \theta_{V\text{-}a})$ to form the other component of $M_{SPWM\text{-}a}(t)$.

$M_{SPWM\text{-}a}(t)$ is multiplied by $[V_{dc\text{-}Ref}/v_{dc}(t)]$ to compensate for the dc voltage fluctuation (see (26)). Finally, the zero-sequence signal $i_{bal}(t)$ (see (21) to (23)) is added to balance the dc voltages of the upper and lower buses .

7. VALIDATION BY SIMULATIONS

A continuous simulation test ($0.0\,\text{s} \leq t < 6.0\,\text{s}$) has been conducted on the system of Fig. 8 with the D-STATCOM of Fig. 1. Originally, Circuit Breakers CB-C is closed and CB-D is open. Loss of a load is simulated by opening CB-C during $4.0\,\text{s} \leq t < 5.0\,\text{s}$. The simulation results are chosen to

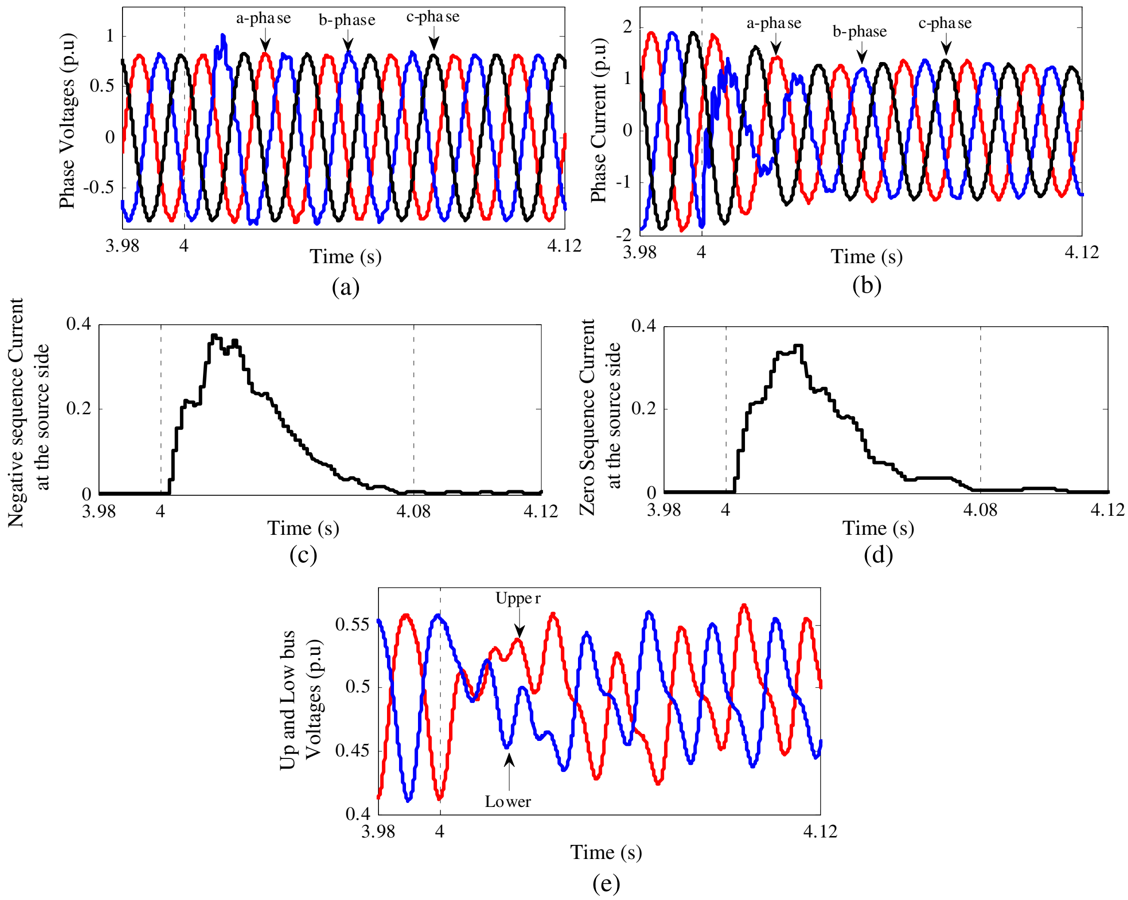

Figure 9: Simulation results before and after $t = 4.0$ s. (a) ac voltages; (b) ac currents; (c) negative sequence current at the source side; (d) zero sequence current at the source side; (e) upper and lower bus voltages.

show that voltages and the currents of the transmission lines are balanced at the Point of Common Coupling (PCC). Implicitly, the balanced voltages and currents imply balanced active and reactive powers of the three phases. The active and reactive powers of the individual phases are balanced.

7.1. Simulation Test Results

At $t = 4.0$ s, CB-C is opened to simulate loss of the load, Z_b. Figs. 9(a) and (b) show the voltages and currents. The transmission line currents decrease because the source voltages supply power to only 2 of the 3 load impedances. In order to high-light the fast response (transient duration about 80 ms), the negative-sequence and the zero sequence of the- currents are computed from the simulated currents and displayed in Figs. 9(c) and (d). Fig. 9(e) displays the upper $v_U(t)$ and lower $v_L(t)$ dc bus voltages proving that scheme for Balancing the DC buses in Fig. 9 is successful.

8. CONCLUSIONS

The paper has described modifications by which the 3-phase voltage-source converter is suited to interface with the ac power system under asymmetrical operating conditions. Analysis is presented to show how the zero-sequence passes through the VSC and how dc capacitor voltage imbalance due to the zero sequence is eliminated by negative feedback. A compensation scheme is applied to counter the double frequency voltage pulsation across the dc buses. The method of Individual-Phase Decoupled P-Q Control enables both symmetrical and asymmetrical operation to be controlled from the straight forward a-b-c reference frame, without the need to use the complication of symmetrical component analysis.

ACKNOWLEDGMENT

This research is supported by the Research Grant ERGS/FASA 1/2011 ER027-2011A from the Ministry of Higher Education Malaysia.

REFERENCES

1. Awad, H., J. Svensson, and M. Bollen, "Practical implementation of delayed signal cancellation method for phase-sequence separation," *IEEE Transactions on Power Electronics*, Vol. 19, No. 3, 837–846, 2004.
2. Awad, H., J. Svensson, and M. J. Bollen, "Tuning software phase-locked loop for series-connected converters," *IEEE Transactions on Power Delivery*, Vol. 20, No. 1, 300–308, 2005.
3. Li, Y., D. M. Vilathgamuwa, and P. C. Loh, "Microgrid power quality enhancement using a three-phase four-wire grid-interfacing compensator," *IEEE Transactions on Industry Applications*, Vol. 41, No. 6, 1707–1719, 2005.
4. Svensson, J., M. Bongiorno, and A. Sannino, "Practical implementation of delayed signal cancellation method for phase-sequence separation," *IEEE Transactions on Power Delivery*, Vol. 22, No. 1, 18–26, 2007.
5. Bongiorno, M., J. Svensson, and A. Sannino, "Effect of sampling frequency and harmonics on delay-based phase-sequence estimation method," *IEEE Transactions on Power Delivery*, Vol. 23, No. 3, 1664–1672, 2008.
6. Hatano, N. and T. Ise, "Control scheme of cascaded H-bridge STATCOM using zero-sequence voltage and negative-sequence current," *IEEE Transactions on Power Delivery*, Vol. 25, No. 2, 543–550, 2010.
7. Karimi-Ghartemani, M. and H. Karimi, "Processing of symmetrical components in time-domain," *IEEE Transactions on Power Systems*, Vol. 22, No. 2, 572–579, 2007.
8. Aredes, M. and E. H. Watanabe, "New control algorithms for series and shunt three-phase four-wire active power filters," *IEEE Transactions on Power Delivery*, Vol. 10, No. 3, 1649–1656, 1995.
9. Aredes, M. and E. H. Watanabe, " Three-phase four-wire shunt active filter control strategies," *IEEE Transactions on Power Electronics,* Vol. 12, No. 2, 311–318, 1997.
10. Enjeti, P. N. and W. Shireen, "A new technique to reject DC-link voltage ripple for inverters operating on programmed PWM waveforms," *IEEE Transactions on Power Electronics*, Vol. 7, No. 1, 171–180, 1992.
11. Chen, W. K., *The Circuits and Filters Handbook*, 1st Edition, 2161–2192, CRC, USA, 1995.
12. Hsieh, G. C. and J. C. Hung, "Phase-locked loop techniques. A survey," *IEEE Trans. Industrial Elec.*, Vol. 43, No. 6, 609–615, Dec. 1996.

Design Optimization of the Exponentially Tapered Microstrip Impedance Matching Sections Using a Cost Effective 3-D-SONNET-based SVRM with the Particle Swarm Intelligence

Mehmet Ali Belen, Salih Demirel, Filiz Güneş, and Ahmet Kenan Keskin
Department of Electronics and Communication Engineering
Yıldız Technical University, Istanbul, Turkey

Abstract— Non uniform transmission lines are extensively used as impedance-matching sections in microwave circuits. Non uniform transmission lines are widely examined in the literature with the pioneering works [1–3]. In this work, exponential tapered microstrip line are realized by the microstrip lines with the exponentially tapered widths and a robust design optimization procedure is put forward to match a complex load to a given another complex impedance within a bandwidth.

In the first stage of the design procedure, a cost effective 3-D SONNET-based Support Vector Regression Machine (SVRM) model of the microstrip line is completed. The 3D EM-based SVRM microstrip model provides the accurate and fast characterization of the equivalent transmission line in terms of the characteristic impedance Z_0 and the dielectric constant ε_{eff} within the continuous domain of the microstrip width W, substrate parameters (ε, h) and in the work the input variable domain is defined by $\{0.1\,\mathrm{mm} \leq w \leq 4.6\,\mathrm{mm},\ 2 \leq \varepsilon_r \leq 10,\ 0.1\,\mathrm{mm} \leq h \leq 2.2\,\mathrm{mm},\ 2\,\mathrm{GHz} \leq f \leq 14\,\mathrm{GHz}\}$ in an efficient manner. In the modeling process, the substantial reduction (up to 64%) is obtained utilizing sparseness of SVRM in the number of expensive fine discretization training data with the negligible loss in the predictive accuracy using the quasi-TEM microstrip synthesis formulas as the coarse model that allow to identify the regions of the design space requiring denser sampling.

The impedance transformation of anexponential tapered microstrip transmission segment in the differential length $\Delta\ell$ with the variable $Z_0(x)$ and $\varepsilon_r(x)$ is formulated in the second stage. The total length of the transmission line ℓ, the governing parameter α of the exponential variation and maximum value of the width are determined as output of the Particle Swarm Optimization (PSO). The objective of the PSO is to minimize the magnitude of the difference between the desired and input impedances over a defined bandwidth.

In the final stage of the work, a worked example is presented which is design of input matching network of a low-noise amplifier using the exponential tapered microstrip line.

1. INTRODUCTION

Exponential tapered microstrip linesare widely used in radio frequency and microwave circuits. In this work, a microstrip line with exponentially tapered widthis used as a matching section for given impedance along the required bandwidth. The problem is set an optimization problem where the optimization variables are the length ℓ, the governing parameter α of the exponential variation and maximum value of the width $w_{\max}$ and the Particle Swarm Optimization (PSO) algorithm is used a search and optimization tool within the problem domain. Furthermore, a cost effective 3-D SONNET-based Support Vector Regression Machine (SVRM) model of the microstrip line is employed to provide the accurate and fast characterization of the equivalent transmission line in terms of the characteristic impedance Z_0 and the dielectric constant ε_{eff} within the continuous domain of the microstrip width w, substrate parameters ε_r, h and in the work the input variable domain is defined by $\{0.1\,\mathrm{mm} \leq w \leq 4.6\,\mathrm{mm},\ 2 \leq \varepsilon_r \leq 10,\ 0.1\,\mathrm{mm} \leq h \leq 2.2\,\mathrm{mm},\ 2\,\mathrm{GHz} \leq f \leq 14\,\mathrm{GHz}\}$ in an efficient manner [4]. In the modeling process, the substantial reduction (up to 64%) is obtained utilizing sparseness of SVRM in the number of expensive fine discretization training data with the negligible loss in the predictive accuracy using the quasi-TEM microstrip synthesis formulas as the coarse model that allow to identify the regions of the design space requiring denser sampling.

The impedance transformation of the microstrip segment in the differential length $\Delta\ell$ which can be assumed as uniform, is formulated using its variable $Z_0(x)$ and ε_{eff} obtained from the output of the SVRM model in the next section. The total length of the transmission line ℓ, the governing parameter α of the exponential variation and maximum value of the width $w_{\max}$ are determined using PSO provided that the input impedance is equal to the given impedance along the required bandwidth.

Finally, a low-noise amplifier is designed with input and output matching circuits made up exponentially tapered microstrips and the resulted gain, noise input mismatching characteristics are analyzed and AWR simulation is also given.

2. MICROSTRIP MATCHING CIRCUITS

Exponential tapered microstrip lines are quite often used as impedance transformers, resonators and filters at microwave frequencies. These have the advantages of broader band impedance matching when used as impedance transformers and larger rejection bandwidths when used as resonators and filters.

2.1. Modeling of Matching Network with Exponentially Tapered Line

For a dissipation less uniform transmission line with characteristic impedance Z_0 load impedance Z_L and input impedance Z_{in} at a distance ℓ to the load can be calculated from

$$\frac{Z_{in}}{Z_0} = \frac{Z_L + jZ_0 \tan(\beta x)}{Z_0 + jZ_L \tan(\beta x)} \tag{1}$$

On the other hand impedance of an exponentially tapered microstrip transmission line would be a function of distance x. Therefore characteristic impedance becomes $Z_0(x)$. The characteristic impedance distribution of the exponentially tapered transmission line (Fig. 1) may be represented by

$$w(x) = w_{\max} e^{(-\alpha x)} \tag{2}$$

$$Z_{in}(w_i, x) = \begin{cases} Z_L & x = 0 \\ Z_{in}(w_{\max}, \alpha, \ell) & x = \ell \end{cases} \tag{3}$$

If one assumes the line has uniform characteristic impedance $Z_0(w_i, x) = \text{const.}$ over the incremental distance Δx and line width w_i then using (1)

$$\frac{Z_{in} + \Delta Z_{in}}{Z_0(w_i, x, f_i)} = \frac{Z_{in}(w_i, x, f_i) + jZ_0(w_i, x, f_i) \tan[\beta(w_i, x, f_i)]}{Z_0(w_i, x, f_i) + jZ_{in}(w_i, x, f_i) \tan[\beta(w_i, x, f_i)]} \tag{4}$$

where $Z_{in}(w_i, x) + \Delta Z_{in}$ is the input impedance of the microstrip line with the width w_i and the length Δx at the x position loaded by $Z_{in}(w_i, x)$. Transformation from the microstrip geometry and the substrate to the equivalent line parameters of Z_0, ε_{eff} is made by the cost effective 3-D SONNET-based Support Vector Regression Machine (SVRM) model of the microstrip line [4]. Thus the cost of the PSO optimization process can be defined by the minimum of the following function:

$$\text{Cost} = \text{minimum} \sum_{i}^{m} |R_{in}(W_{\max}, \alpha, \ell, f_i) - R_{inreq}(f_i)| + |X_{in}(W_{\max}, \alpha, \ell, f_i) - X_{inreq}(f_i)| \quad i = 1, 2, \ldots, m \tag{5}$$

As it is seen in Fig. 2 algorithm will use the input variables and data to start the SVRM network in order to obtain Z_0 and ε_{eff} values for Δx_i; $i = 1, 2, \ldots N$ (*Number of segments*) segments

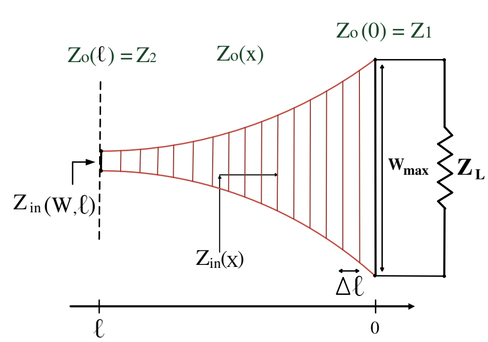

Figure 1: Characteristic impedance distribution of the exponentially tapered microstrip transmission line.

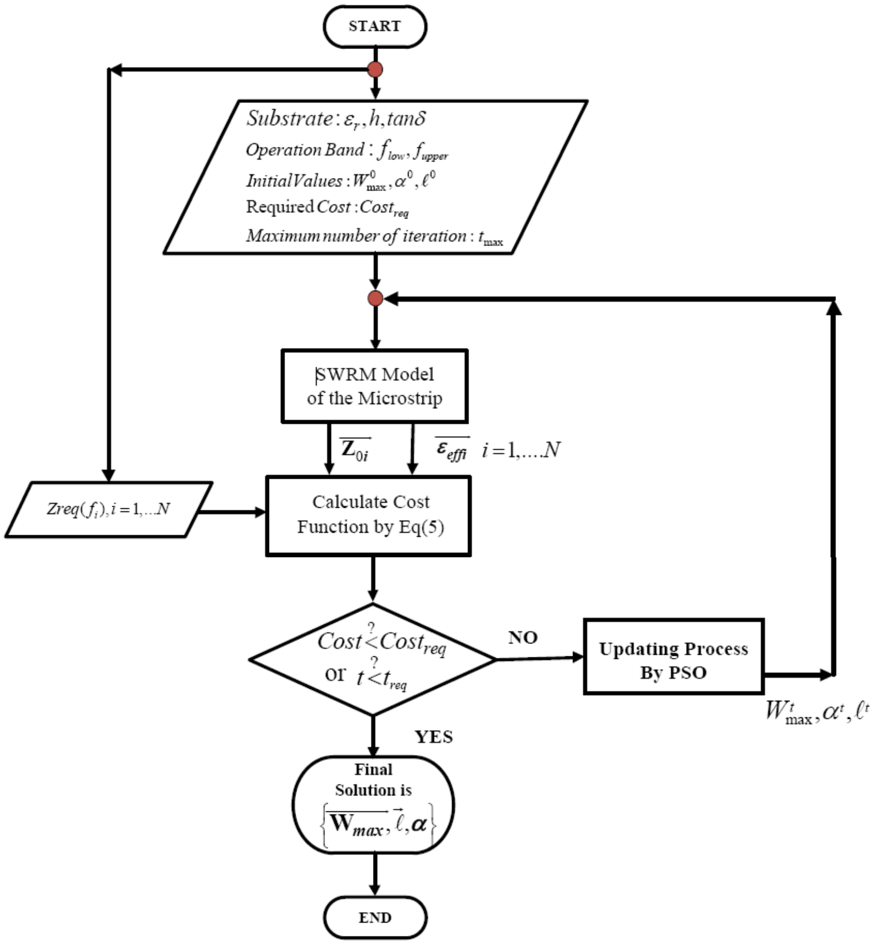

Figure 2: Block diagram of design optimization of the exponentially tapered microstrip matching section with the cost-effective 3D EM-based support vector microstrip model.

corresponding to α and w_i's, then this current set will be updated by using Particle Swarm Optimization method till the final α and w's of the exponential tapered microstrip line satisfies the required impedance values. Thus, the total length of the transmission line ℓ, the governing parameter α of the exponential variation and maximum value of the width $w_{\max}$ are determined as output of the Particle Swarm Optimization (PSO). The objective of the PSO is to minimize the difference between magnitudes of the desired impedances and the impedances values obtained from SVRM model over the defined bandwidth.

3. WORKED EXAMPLE

In this part of the work, it is aimed to design an exponentially tapered line structure for design of a matching circuit for application in 11–13 GHz bandwidth with the certain impedance values that had been shown in Table 1. Designs variables will be used as input variables for optimization algorithm and the values of optimization variables will be given as input for SVRM network in order to acquire the best exponentially tapered line structure parameters for our matching problem. For worked example purpose, NE3511S02 is selected as a high technology low-noise transistor in the front-end amplifier design. The impedance values that had been shown in Table 1 are obtained from performance characterization [5] of the selected transistor for the desired bandwidth while $G_{Treq} = 12\,\text{dB}$, $V_{in} = 1.5$ and $F = 0.7\,\text{dB}$, the substrate that had been used for our design is R03006 ($\varepsilon_r = 6.15$, $H = 1.28\,\text{mm}$, $\tan\delta = 0.035$) for the microwave amplifiers. The parameters and their values that had been used during our designing process can be given as follow, $Z_s = Z_L = 50\,\Omega$, differential length $\Delta\ell = \ell/100$, variables length $1\,\text{mm} < \ell < 10\,\text{mm}$, governing parameter α of the exponential variation $0.01 < \alpha < 1$, maximum value of the width $0.1\,\text{mm} < w < 10\,\text{mm}$.

In Table 2 the w, ℓ and α values of the designed input and output matching circuit for our worked example are shown. In Fig. 3 the layout of the designed matching circuits are presented.

Also in Fig. 4 the impedance variation of the designed structures that obtained from proposed algorithm for input and output matching circuits are shown and compared with the results from the performance characterization results in AWR environment.

The full circuit, including all the parasitic and matching/biasing/stabilizing networks, was initially simulated using AWR. The performance figs, based on this simulation, are presented in Figs. 5(a), (b). The LNA shows a Transducer power gain (S_{21}) of 12 dB, noise-figure (NF) of

Table 1: Desired goals of the microstrip tapered matching circuits for the LNA.

f (GHz)	Load Impedance of Input Matching Network Z_L^{IMC} (Ω)				Source Impedance of the Output Matching Network Z_S^{OMC} (Ω)			
	Target R_L	PSO+ SVRM R_L	Target X_L	PSO+ SVRM X_L	Target R_S	PSO+ SVRM R_S	Target X_S	PSO+ SVRM X_S
11	24,9523	23.69	13,9367	12.33	20,6699	19.01	21,5704	21.01
12	23,6061	22.79	11,0415	11.2	19,9586	17.67	14,0143	17.06
13	22,5549	22.105	8,04718	10.06	19,7733	16.75	6,66023	14.76

Table 2: Parameters of the input and output matching exponentially tapered microstrip lines.

Section	$w_{\max}$ (mm)	$w_{\min}$ (mm)	ℓ (mm)	α
Input Matching	5.98	1.71	3.284	0.381
Output Matching	3.675	2.897	1.895	0.126

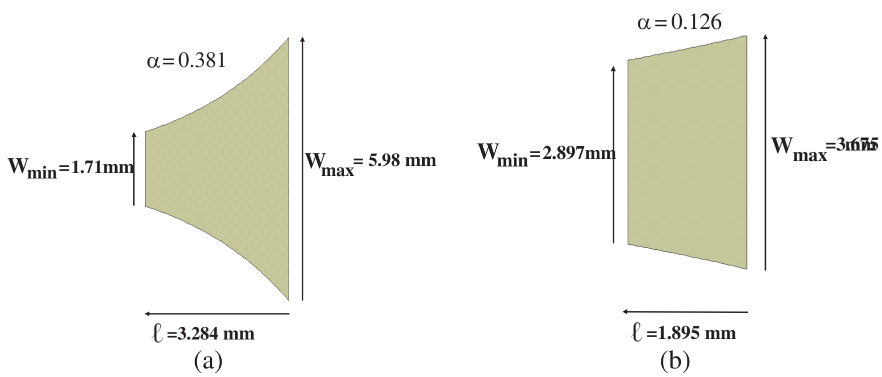

Figure 3: Exponentially tapered microstrip lines. (a) Input matching. (b) Output matching.

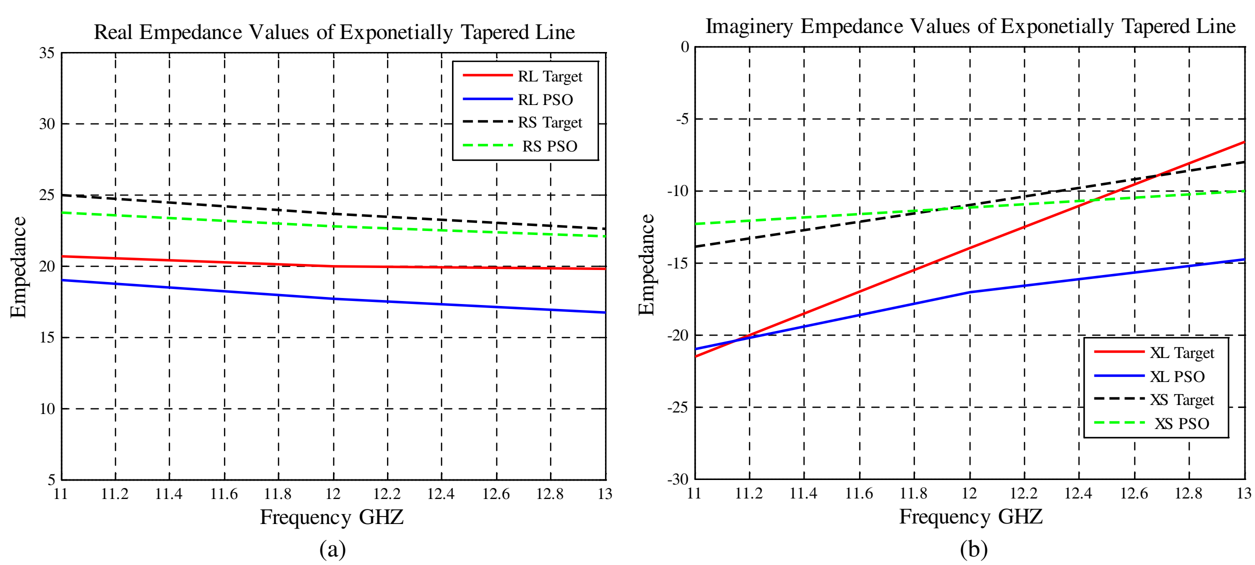

Figure 4: Exponentially tapered microstrip lines. (a) IMC: Z_L^{IMC} (Ω). (b) OMC: Z_S^{OMC} (Ω).

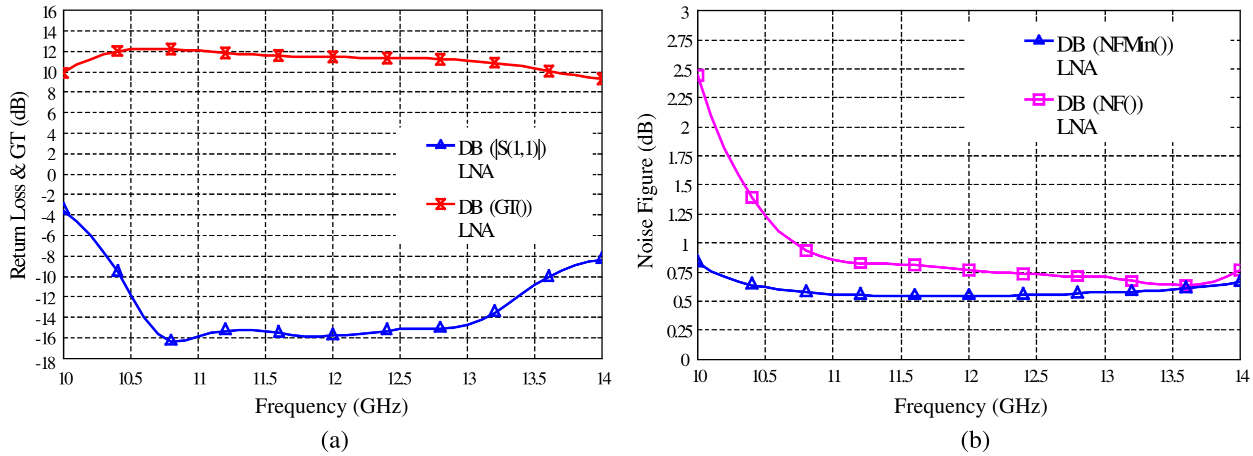

Figure 5: (a) Return loss & transducer gain. (b) Noise figure.

0.85 dB, input return loss (S_{11}) of less than -15.0 dB in the frequency range of 11–13.0 GHz.

4. CONCLUSION

In this work, an exponentially tapered microstrip microwave matching circuits for an amplifier design which all the necessary parameters describing for the microstrip lines can be obtained from the output subject to the potential performance of the employed transistor. Geometry of the exponentially tapered microstrip lines on a substrate $\vec{W}$, $\vec{\ell}$, α are used as the Design Variables within their technological limitations and Particle Swarm Optimization algorithm is utilized as the optimization tool. At the end of a speedy optimization process, the targeted performances are caught by the solution spaces $\{\vec{W}, \vec{\ell}, T, \varepsilon_r, H, \tan\delta\}$ applicable by the microstrip line technology. Besides proposed design method is verified by the circuit simulators.

REFERENCES

1. Ahmed, M. J., "Impedance transformation equations for exponential, cosine-squared, and parabolic tapered transmission lines," *IEEE Trans. Microwave Theory Tech., MTT*, Vol. 29, 67–68, 1981.
2. Hamade, A. H., A. B. Kouki, and F. M. Ghannouchi, "An efficient approach suitable for the analysis and design of non-uniform transmission lines," *Microwave Opt. Technol. Letters*, Vol. 3, 146–150, 1995.
3. Duoleng, W. and R. Chengli, "Analysis of lossless nonuniformtransmission lines with power-law characteristic impedance function," *Microwave Opt. Technol. Letters*, Vol. 17, 195–197, 1998.
4. Keskin, A. K., "Design of an ultra-wide band microstrip amplifier using 3D SONNET based SVRM with particle swarm optimization," MSC Thesis, Turkish, 2012.
5. Güneş, F., M. Güneş, and M. Fidan, "Performance characterization of a microwave transistor," *IEE Proceedings — Circuits Devices and Systems*, Vol. 141, No. 5, 337–344, 1994.

Space Gravity Optimization Applied to the Feasible Design Target Space Required for a Wide-band Front-end Amplifier

Nihal Kılınç, Peyman Mahouti, and Filiz Güneş
Department of Electronics and Communication Engineering
Yıldız Technical University, Istanbul, Turkey

Abstract— In this paper, the Space Gravity Optimization (SGO) algorithm is presented as a new meta-heuristic optimization tool to determine Feasible Design Target Space (FDTS) for a microwave amplifier subject to the potential performance of the employed transistor. In this optimization problem, the search space is four-dimensioned consisting of the real and imaginary parts of the source and load terminations of the transistor and the position of each asteroid gives the candidate solution. Asteroids with the less cost values will have a higher amount of masses than the others. In this algorithm, the speed and acceleration of the asteroid having the maximum amount of the mass will be assumed to be equal to zero while other asteroids with lesser masses will be forced to have accelerations and speeds due to the gravity field of the heaviest asteroid. This results in change the coordinates and the costs of the asteroids. Thus, the solution space of the problem domain will be searched until the iteration reaches to its maximum value or the cost value of the heaviest asteroid is equal or less than the required cost value. In the final part of the work, the proposed SGO approach is implemented to determine. The FDTS of a selected microwave low noise transistor and the numerical results will be compared with their analytical counterparts [1]. Furthermore performance of the SGO algorithm is compared with those of the Particle Swarm Optimization [2], Honey Bee Mating optimization algorithms [3] and advantages and disadvantages are concluded.

1. INTRODUCTION

One of the recently proposed nature inspired intelligence algorithms that have shown great potential and good perspective for the solution of highly nonlinear engineering optimization problems is the Space Gravity Optimization algorithm that had been proposed by Ying-Tung Hsiao and his team in [8]. In this method, dimension of the search space is equal to the number of the optimization variables and the position of each asteroid corresponds to the candidate solution of the problem. In each iteration mass of each asteroid is taken to be equal to the inverse of its cost, thus the asteroid with the minimum cost will have the maximum amount of the mass and its acceleration and velocity will be assumed to be equal to zero in each Galaxy. Thus this asteroid will apply the gravitational force to the rest asteroids resulting in changes in their masses due to change in their positions. The solution corresponding to the asteroid with the maximum mass within the universe consisting of the galaxies will be outputted as the final solution.

In this work, the SGO algorithm will apply to solve the highly nonlinear performance equations of the transistor to determine the source and load terminations for the maximum gain $G_{T\max}$ constrained by the required noise F_{req} and input VSWR V_{inreq}.

In the next section, the objective of the problem will be established by giving the performance equations; the third section will give the SGO algorithm, the worked example takes place in the fourth section, the paper end the conclusions.

2. THE FEASIBLE DESIGN TARGET SPACE

The FDTS consists of the (Noise Figure F, Input VSWR V_{in}, Maximum $G_{T\max}$) triplets and the corresponding source $Z_{S\max}$ and load $Z_{L\max}$ impedances depending on the operation point (V_{DS}, I_{DS}, f) of the device. Here F, G_T and V_{in} are given by the following nonlinear equations, respectively:

$$F = F(Z_S) = F_{\min} + \frac{R_n \left|Z_S - Z_{opt}\right|^2}{\left|Z_{opt}\right|^2 R_S} \tag{1}$$

$$G_T = G_T(Z_S, Z_L) = \frac{4R_S R_L \left|z_{21}\right|^2}{\left|(z_{11} + Z_S)(z_{22} + Z_L) - z_{12}z_{21}\right|^2} \tag{2}$$

$$V_{in} = V_{in}(Z_S, Z_L) = \frac{1 + \rho_{in}}{1 - \rho_{in}}, \quad \text{where } \rho_{in} = \left|\frac{Z_{in} - Z_S^*}{Z_{in} + Z_S}\right|^2 \leq 1 \tag{3}$$

The physical realization conditions which must be satisfied by the Z_S and Z_L terminations can be given as

$$\Re e\{Z_{in}\} = \Re e\left\{z_{11} - \frac{z_{12}z_{21}}{z_{22}+Z_L}\right\} > 0, \tag{4}$$

$$\Re e\{Z_{out}\} = \Re e\left\{z_{22} - \frac{z_{12}z_{21}}{z_{11}+Z_S}\right\} > 0, \tag{5}$$

$$F \geq F_{\min}, \quad V_i \geq 1, \quad G_{T\min} < G_T \leq G_{T\max} \tag{6}$$

The objective of the optimization is to minimize the following cost function:

$$\begin{aligned} Cost = \text{minimum}\Big\{ & e^{-a\,G_T(R_S,X_S,R_L,X_L)} + b\,|F(R_S,X_S) - F_{req}| \\ & + c\,|V_{in}(R_S,X_S,R_L,X_L) - V_{inreq}| \Big\} \end{aligned} \tag{7}$$

where G_T, F, V_{in} are given by the Eqs. (1), (2), (3), respectively and (4), (5), (6) can be considered as the constrained which should satisfied by the (Z_S, Z_L) solution pairs. In (7), a, b and c are the weighting coefficients which are chosen during the process by trial.

3. SPACE GRAVITY OPTIMIZATION

In this section of the work, the Space Gravity optimization method with its parameters for our optimization problem will be explained. The SGO algorithm can be described as in following steps.

3.1. Define Input Parameters

Input data consists of the two parts: The first part is the input data of the problem which are the scattering and noise parameters of the selected transistor; the second part includes the user-defined parameters of the algorithm.

The first part consists of the Scattering and Noise parameters of the selected transistor.

The second part includes the user-defined parameters of the algorithm:

- The Maximum iteration number or the index of galaxy N_{GA}
- The Maximum number of coordinate change N_{UPGR}
- The number of the asteroids N_{AST}
- The jth coordinate parameter of the i'th asteroid X_{ij}
- The Velocity of the ith asteroid for jth parameter V_{ij}
- The Acceleration of the ith asteroid for jth parameter a_{ij}
- Range of detection r_d
- Strength of the gravity field G

3.2. Define the Fitness and the Constraints of the FDTS problem

Fitness of the FDTS problem is given by Eq. (7) with this inequality constraints are given by Eqs. (3)–(5).

3.3. Define the Galaxy and Its Asteroid Population

In this algorithm you can simply think we will search whole universe for the biggest object. Since the universe (solution space) is incredibly huge, it will be wise to divide the universe in to the smaller parts which we name galaxies. In SGO each iteration step will be consider as a galaxy where it will have a certain number of asteroid population (N_{AST}) as it shown if below:

$$Universe = \begin{bmatrix} Galaxy_1 \\ Galaxy_2 \\ Galaxy_{N_{GA}} \end{bmatrix} \quad Galaxy = \begin{bmatrix} AST_1 \\ AST_2 \\ AST_{N_{AST}} \end{bmatrix} \tag{8}$$

Each asteroid will have a coordinate set for its own

$$AST_i = (R_L, R_S, X_L, X_S) \tag{9}$$

$$R_L = C_1 rand(.) \tag{10}$$

$$R_s = C_2 rand(.) \tag{11}$$

$$X_L = C_3 rand(.) - C_4 rand(.) \tag{12}$$

$$X_S = C_5 rand(.) - C_6 rand(.) \tag{13}$$

$C_{1,2,3,5}$ are the upper and $C_{4,6}$ is the lower boundary constrain for problem.

3.4. Finding the Heaviest Asteroid in Galaxy

As its said before each asteroid Eq. (10) will have a certain cost value of itself

$$\begin{aligned} Cost_{AST_i} = \Big\{ & e^{-aG_T(R_{Si},X_{Si},R_{Li},X_{Li})} + b\left|F(R_{Si},X_{Si}) - F_{req}\right| \\ & +c\left|V_{in}(R_{Si},X_{Si},R_{Li},X_{Li}) - V_{inreq}\right|\Big\} \quad i = 1,2,\ldots,N_{AST} \end{aligned} \tag{14}$$

Algorithm will sort the entire asteroid population in the galaxy by the cost value of them. The asteroid with the biggest mass AST_B will be taken as an object with no velocity and acceleration in the center of that galaxy while all other asteroid will have a random velocity and acceleration as it shown in Eqs. (15), (16)

$$\begin{aligned} V_{ij} &= C_1 rand(.), \quad V_{Bj} = 0 \\ a_{ij} &= [Cost_i - Cost_i(j+rd)] + [Cost_i(j-rd) - Cost_i] \quad i = 1(R_L), 2(R_S), 3(X_L), 4(X_S) \end{aligned} \tag{15}$$

3.5. Updating the Coordinates of the Asteroids of A Galaxy

Since each of smaller asteroids in previous step has an acceleration and velocity for itself, their coordinates will have to change accordingly to these values as follows:

$$V_{ij} = V_{ij} + G * a_{ij} \quad i = 1,2,3,\ldots,N_{AST} \tag{16}$$

$$x_{ij} = x_{ij} + V_{ij} \quad j = R_L, R_S, X_L, X_S \tag{17}$$

After this algorithm will recalculate all the asteroids in the galaxy in case of that any of the smaller asteroids might have a better value that the current biggest asteroid in that case the newer biggest asteroid will be selected and all the previous steps will be repeated again and again until the upgrading attempts reach N_{UPGR} number of times for the selected galaxy. In the end the biggest asteroid will be registered as the center or the star of that galaxy.

3.6. Finding the Heaviest Asteroid in the Universe

In previous step, it is mentioned that there will be a star or a center for each galaxy. In this step algorithm will sort all these stars according to their cost values and will chose the star with the smallest cost value as the center of universe or the best solution for our optimization problem.

3.7. Stopping Criteria

If any star from the galaxy population has an equal or less cost value from the required cost value or the number of Galaxy/iteration had reached to its maximum value N_{GA} algorithm will stop the search and take the best star as the center of the universe.

4. WORKED EXAMPLE

In the worked example, SGO is applied to gain maximization subject to $F_{\min}(f)$ and V_{ireq} with respect to the input and output terminations for the transistor NE3512S02 in an operation frequency band of 2–18 GHz. In Fig. 1 Gain value of the selected transistor that had been obtained via numerical methods and the results from SGO algorithm for different values of Vin with DC bias of 2 V 5 mA had been showed. As it is seen in Fig. 1 the results of analytic methods are same with the results from SGO algorithm which shows the high performance of SGO algorithm.

Table 1: Benchmarking results of the algorithms.

Algorithm	Obtained Minimum Cost Value	Execution Time (sec) for Best Result	Iteration for Best Result
HBMO	0.02	93	21
SGO	0.2	77.5	23
PSO	0.1	85	21

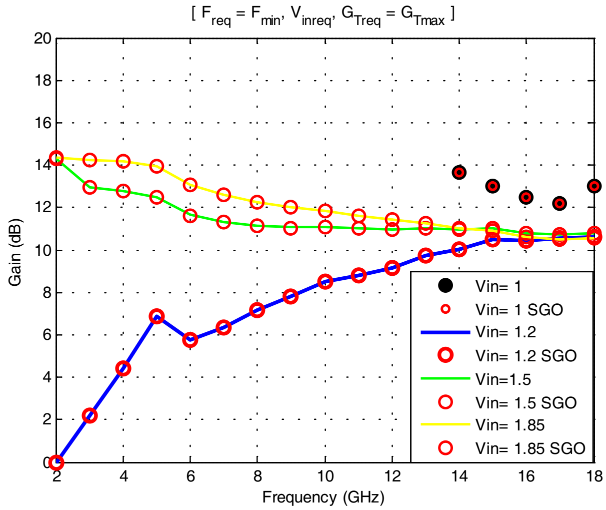

Figure 1: Gain Variations for different Vin values for 2 V, 5 mA.

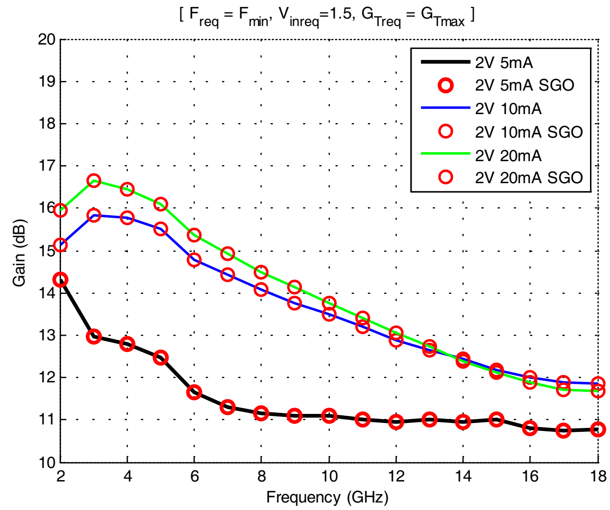

Figure 2: Gain Variations for different bias conditions.

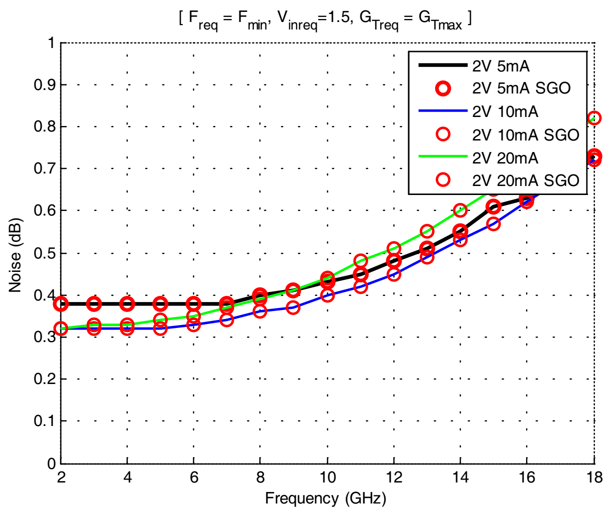

Figure 3: Noise Variations for different bias conditions.

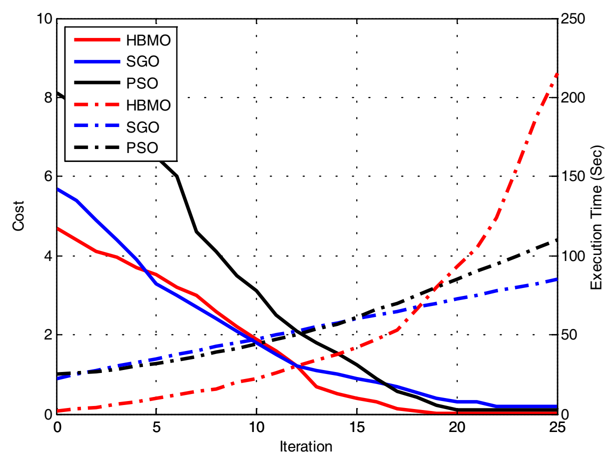

Figure 4: Cost and Calculation Time variation for iterations.

5. CONCLUSION

SGO is an algorithm which is as simple as PSO and simpler than the HBMO. In the other hand, it uses less memory compared to the other algorithms in our application. As it seen in Figures 1–4 and Table 1, SGO algorithm can find a cost value near to the global minimum cost value much faster than the other algorithms, and it can be concluded that this time difference can be used to increase the accuracy by a simple the local optimizer.

REFERENCES

1. Güneş, F., M. Güneş, and M. Fidan, "Performance characterisation of a microwave transistor," *IEE Proceedings — Circuits, Devices and Systems*, Vol. 141, No. 5, 337–344, 1994.
2. Güneş, F., U. Özkaya, and S. Demirel, "Particle swarm intelligence applied to determination of the feasible design target for a low-noise amplifier," *Microwave and Optical Technology Letters*, Vol. 51, No. 5, 1214–1218, May 2009.
3. Mahouti, P., F., Güneş, and S. Demirel, "Honey-bees mating algorithm applied to feasible design target space for a wide-band front-end amplifier," *2012 IEEE International Conference on Ultra-wideband*, 251–255, 2012.
4. Karaboa, N., K. Güney, and A. Akdal, "Null steering of linear antenna arrays with use of modified touring ant colony optimization algorithm," *Int. J. RF and Microwave CAE*, Vol. 12, 375–383, 2002.

5. Galehdar, A., D. V. Thiel, A. Lewis, and M. Randall, "Multiobjective optimization for small meander wire dipole antennas in a fixed area using ant colony system," *Int. J. RF and Microwave CAE*, Vol. 19, 592–597, 2009.
6. Güney, K. and M. Onay, "Bees algorithm for design of dual-beam linear antenna arrays with digital attenuators and digital phase shifters," *Int. J. RF and Microwave CAE*, Vol. 18, 337–347, 2008.
7. Güney, F., U. Özkaya, and S. Demirel, "Particle swarm intelligence applied to determination of the feasible design target for a low-noise amplifier," *Microwave and Optical Technology Letters*, Vol. 51, No. 5, 1214–1218, May 2009.
8. Hsiao, Y. T., C. L. Chuang, J. A. Jiang, and C. C. Chien, "A novel optimization algorithm: Space gravitational optimization," *IEEE International Conference on Systems, Man and Cybernetics Waikoloa*, Hawaii, Oct. 10–12, 2005.

Impact of Uncompensated Ionospheric Distortions on MARSIS Data

Marco Restano, Giovanni Picardi, and Roberto Seu
Department of Information, Electrical and Telecommunication Engineering (DIET)
University of Rome, "Sapienza", Italy

Abstract— The Mars Advanced Radar for Subsurface and Ionosphere Sounding (MARSIS) currently operating on Mars needs a fine ionospheric correction in order to deliver products useful for geological investigations. Ionosphere influence can be assessed using a new approach based on the finite-difference time-domain (FDTD) method. The proposed work aims to underline the errors introduced by a not perfect knowledge of the ionospheric electron density profile on the chirp signal range compression. Such effect has a great impact on the data inversion process that aims to estimate the permittivity of the subsurface detected interfaces.

1. INTRODUCTION

MARSIS provided products useful to visualize the subsurface structure of the Martian crust. Another important goal to be pursued is the data inversion [1], that is the evaluation of the permittivity values associated with the subsurface detected layers. Data inversion is accomplished by evaluating, via a two channels approach, quantities related to crust attenuation, surface and subsurface geometry and power scattered by the detected interfaces. The final product delivered after SAR processing is highly dependent on the ionosphere compensation. Not perfectly compensated data would provide erroneous power levels and a wrong geometric interpretation jeopardizing the entire data inversion process. So far, ionosphere phase related distortions have been theoretically modeled using the Chapman density function [2]. They introduce an S/N and a side lobe level (SLL) degradation after matched filtering along with a delay and a pulse shape distortion [3].

The finite-difference time-domain (FDTD) method can be used to study the propagation of MARSIS chirp signal into a plasma modeled according to a desired electron density profile adding a new important benefit to the simulation methods available to understand GPR signals in this context. A 1D-FDTD code is enough to model both plasma and collision frequencies. The implemented simulator discretizes the wave equation using finite differences and models the plasma according to the approach suggested by [4] that perfectly matches the distortions evaluated by [5].

2. IONOSPHERE CHARACTERIZATION

So far, the Chapman model has been used to compensate MARSIS data approximating the ionosphere electron density profile using the relation described by Equation (1) that represents a reasonable approximation, valid only for single ionospheric layers [6]:

$$\mathbf{N}(\mathbf{z}) = \mathbf{N}_0 \exp\left(\frac{1}{2}\left(1 - \frac{\mathbf{z}-\mathbf{z}_0}{\mathbf{L}} - \exp\left(-\frac{\mathbf{z}-\mathbf{z}_0}{\mathbf{L}}\right)\right)\right) \tag{1}$$

where $\mathbf{N}_0$ is the maximum electron density, $\mathbf{z}_0$ is the altitude at which $\mathbf{N} = \mathbf{N}_0$ and $\mathbf{L}$ is the width of the layer. Recent studies [6, 7] regarding Martian ionosphere propose the electron density profiles reported in Figure 1. The main layer, labeled M2, is produced by photo-ionization of carbon dioxide molecules, the most abundant atmospheric constituent, and by solar extreme ultraviolet (EUV) photons. The M2 layer can be adequately represented as a Chapman layer (Figure 2). Several other processes can create additional plasma layers at lower altitudes. First, a less dense layer, called M1 layer is found at 100–110 km altitude, 20 km below the M2 layer. Some plasma in the M1 layer is produced by photo-ionization by solar soft X-rays, but the majority is produced by electron impact ionization. Since the solar soft X-ray spectrum is very variable, the properties of the M1 layer are also extremely variable. The layer is significantly enhanced during solar flares. Second, a layer attributed to meteoroid influx is sporadically present around 85 km altitude. Third, the precipitation of high-energy particles, such as cosmic rays and solar energetic particles, can produce plasma at altitudes below the M2 layer. This layer, made up of electrons produced by energetic particle precipitation, is known as 'EP' layer. The nightside and the dayside ionosphere differ significantly due to the absence of ionizing solar irradiance on the nightside. Only the Meteoric and EP layers are expect to be present on the nightside.

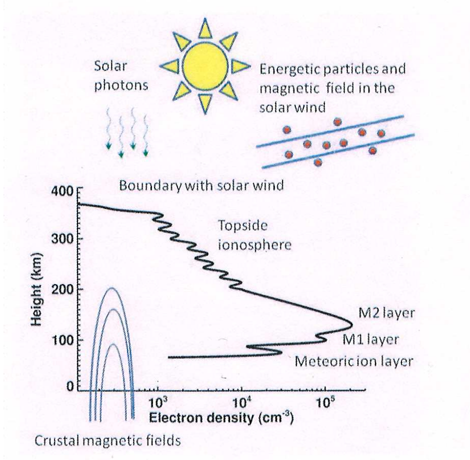

Figure 1: Main features and forcings associated with the ionosphere of Mars [6].

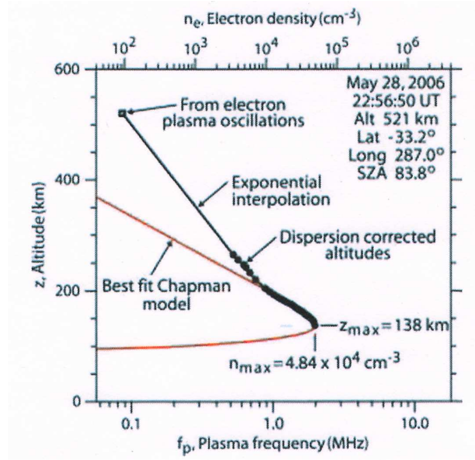

Figure 2: Chapman model fitting on experimental data [6].

The experimental data reported in Figure 2 are acquired by MARSIS during ionosphere sounding operations. A signal passes through the ionosphere, experiencing attenuation and phase distortion, only if the transmitted frequency is higher than the ionosphere plasma frequency related to the electronic density by the formula:

$$\mathbf{f}_p(\mathbf{z}) = 8.98\sqrt{\mathbf{N}_e\left(\mathbf{z}\right)} \tag{2}$$

The ionospheric sounder [8] operates at altitudes greater than 800 km in a mode that sweeps the entire 0.1–5.5 MHz range. During the ionospheric sounding, the transmitter sends a 91 µs tone at 127 pulses per second rate. Reflected pulses, having frequency components below the local plasma frequency, reveal the plasma frequency value at a certain height (Figure 2).

It is important to remark that lower electron density layers (M1, meteoric, EP) located below the Chapman modeled M2 layer will not be discovered by MARSIS because the M2 layer will mask them having an higher plasma frequency and so reflecting the wave prior that such layers can be reached by the propagating signal. Since Chapman model used so far to compensate MARSIS data is valid only to approximate a single ionospheric layer, experimental data could be influenced by a not perfect compensation especially on dayside when multilayered electron densities profiles similar to the one reported in Figure 1 are present.

3. FDTD IONOSPHERE MODELING

The adopted 1D-FDTD algorithm divides the problem geometry into a spatial grid of cells where electric and magnetic field components as well as constitutive parameters (like permittivity and permeability) are placed at certain discrete positions in space and it solves Maxwell's equations in time at discrete time instances $\boldsymbol{\delta}\mathbf{t}$. The 1D-FDTD proposed to model the ionosphere propagation by [4] is the following:

$$P_z'^{n}(i) \;=\; P_z'^{n-2}(i) + 2\delta t\left[\varepsilon_0\omega_p^2(i)E_z^{n-1}(i) - \upsilon_c P_z'^{n-1}(i)\right] \tag{3}$$

$$\begin{aligned} E_z^n(i) \;=\;& 2E_z^{n-1}(i) - E_z^{n-2}(i) + \frac{(c\delta t)^2}{\delta x^2}\left[E_z^{n-1}(i+1) - 2E_z^{n-1}(i) + E_z^{n-1}(i-1)\right] \\ & -\frac{c^2\delta t\mu_0}{2}\left[P_z'^{n}(i) - P_z'^{n-2}(i)\right] \end{aligned} \tag{4}$$

where P is the electric polarization, E is the electric field, $\omega_p^2 = N_e e^2/(\varepsilon_0 m_e)$, υ_c is the collision frequency accounting signal absorbtion, n denotes the current time step δt and i is the cell index on the one dimensional grid having width δx. This approach, based on vector wave equation has the advantage that only one grid is required for calculation ($\vec{H}$ is not present in the vector wave formulation) saving the memory requirement.

4. MARSIS AS A SUBSURFACE SOUNDING RADAR

The MARSIS instrument [8] is a low-frequency, nadir-looking, pulse-limited radar sounder using unfocused synthetic aperture radar (SAR) techniques. The sounder operates in the 1.3–5.5 MHz range over four frequency bands of 1 MHz bandwidth. In order to acquire data with a sufficient signal-to-noise ratio, MARSIS emits a 1 MHz bandwidth chirp signal of 250 µs duration. Moreover, to prevent the subsurface return from being masked by the sidelobes of the first specular surface reflection, Hanning weighting function was selected to reduce the sidelobes level. The expected ground penetration (depending on the composition of the crust) is 5 to 9 km. A typical frame showing power returns from surface (P_s) and subsurface (P_{ss}) interfaces is reported in Figure 3, $\Delta\tau$ can be used to retrieve the layer thickness once its composition is known.

5. AIM OF THE PROPOSED WORK

Ionosphere [9] affects the propagating signal introducing attenuation and phase distortion that lead, after matched filtering, to an S/N loss, a pulse widening and to an increase of sidelobe level. The degrating effect is higher as the frequency components approach the plasma frequency. Higher plasma frequency values are recorded on dayside reaching a 2.5 MHz value while a maximum of 1 MHz is recorded during nightside. An example of ionosphere related distortion after matched filtering is reported in Figure 4. The adopted ionosphere compensation procedures are based on the Chapman model described in Figure 2. Recently evaluated ionospheric profiles suggest a more complex ionospheric behavior including several layers, especially at dayside (Figure 1). The goal of this work is to simulate the dayside propagation using the recently discovered ionospheric profiles evaluating the influence of M1, Meteroid and EP layers located below the M2 layer, that is the only layer correctly compensated by the Chapman model. This analysis will assess the eventual need of another compensation scheme to be adopted on MARSIS data. An application on experimental data will be provided.

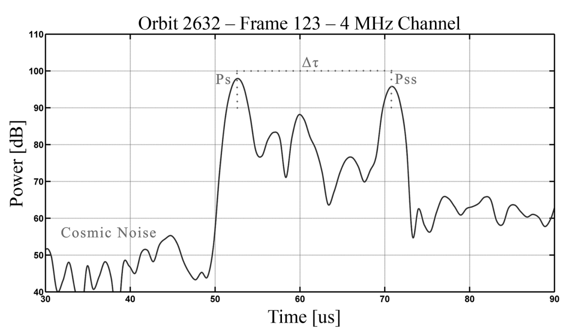

Figure 3: Typical MARSIS frame.

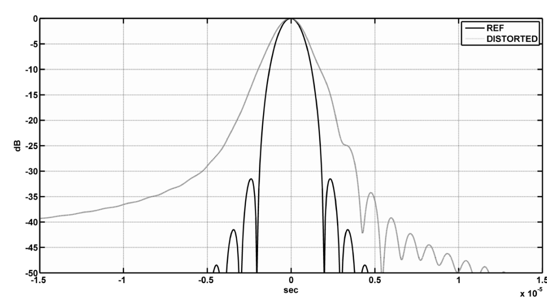

Figure 4: Ionosphere distortion effects on a chirp compression [9].

6. SIMULATIONS

Since a theoretical analysis is considered, there is no need to reproduce the exact ionosphere thickness. One-way phase distortions are evaluated. Attenuation analysis can be found in [6]. FDTD simulated dayside electron density profiles are modeled according to those based on Mars Express Radio Science Experiment (MaRS) data recently proposed by [7] and having excellent accuracy. MARSIS higher channels (3, 4 and 5 MHz) are simulated applying Hanning weighting as on MARSIS data. FDTD stability is guaranteed respecting the Courant-Friedrichs-Lewy (CFL) condition, which requires that the time increment δt has a specific bound relative to the lattice space increments, such that $\delta t \leq \delta x / c$ while 20 cells per wavelength have been set to perfectly reproduce the propagating chirp spectrum.

Among the various profiles proposed by [7], only the most recurring ones have been selected to be reproduced in the FDTD analysis over a length of 100 km (scale 1 : 3). They are reported in Figure 5. In the first profile, 'M2' (10% of cases), the topside electron density decrease with a single scale height. In the second, 'M2+TOP' (25% of cases), the topside electron density decrease with a two scale heights. In the last one, 'M2+TOP+M1' (25% of cases), the M1 layer is added including the effects of Meteoric and EP layers. So, MARSIS channels have been simulated by transmitting a 1 MHz chirp bandwidth. Upon receiving, the range compression has been performed without applying any compensation scheme to underline the distortion, that is evaluated as the −4 dB additional widening with respect to the reference undistorted compression. An example of both compressions is depicted in Figure 4.

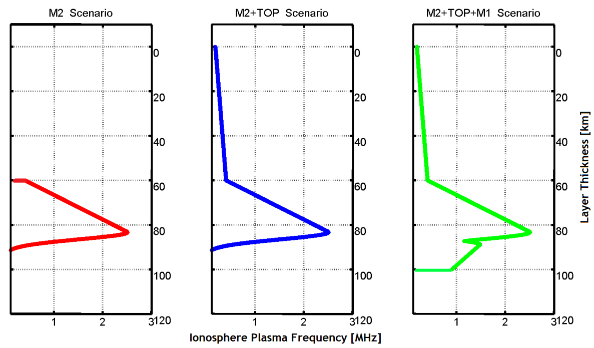

Figure 5: Simulated ionospheric profiles from [7].

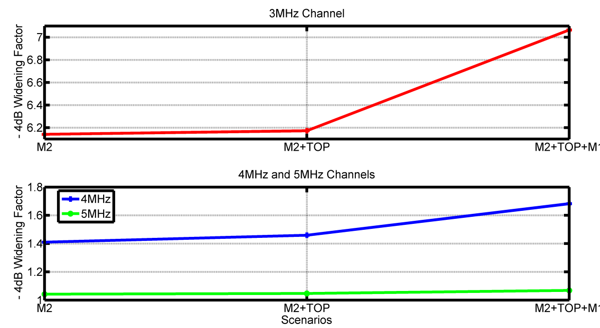

Figure 6: Loss of widening for each simulated scenario.

Simulations results are reported in Figure 6. As can be easily seen, the 3 MHz channel is the most distorted because of its proximity to the maximum plasma frequency value (around 2.5 MHz), similarly the 5 MHz is slightly distorted being the farthest. On daytime, MARSIS operates using two channels (4 and 5 MHz) to avoid being severely distorted by the ionosphere. Proposed results show that top layer influence is very limited being its plasma frequency very low with respect to the transmitted carriers while M1 influence may represent an issue, especially at 4 MHz. Since compensation schemes based on Chapman model, that can be approximated by a Gaussian function [6] or by a uniform layer [3] for simplicity, only take into account the M2 layer, having the topside electron density decreasing with a single scale height, there is the possibility that both double scaled height layer and M1 layer will not be perfectly compensated, leading to a rough range compression that will impact on the data inversion dataset in terms of power recorded from the detected interfaces (P_s, P_{ss}), pulses shape (that is related to the geometric correction) and distance between the recorded reflections related to subsurface layers thickness ($\Delta\tau$).

Nighttime profiles could present some residuals of the M2/M1 layers while the Meteoric/EP layers continue to be present as on daytime. Considering the nighttime ionospheric profiles proposed by [10] it is possible to adopt a compensation based on 3 layers of uniform shape, so having a constant plasma frequency over the extension of each layer. The first layer models the topside, the second one the M2/M1 residuals while the third will model the Meteoric/EP layer. In Figure 7, such compensation is compared with the official MARSIS L2 data level for the nighttime frame 124 orbit 2632, tuning layers extension and plasma frequency values to reach the maximum contrast (defined as the standard deviation on the mean value) on signal compression, as required by the ionosphere compensation procedure [3]. Surface and subsurface peaks show the same width in the 2 cases while different thicknesses and subsurface power levels, related to $\Delta\tau$ and P_{ss} respectively, can be seen.

Since the contrast value obtainable using the 3 layers approach has almost the same value as the L2 reference it is worth questioning which trend is the more accurate since differences could not be negligible for data inversion.

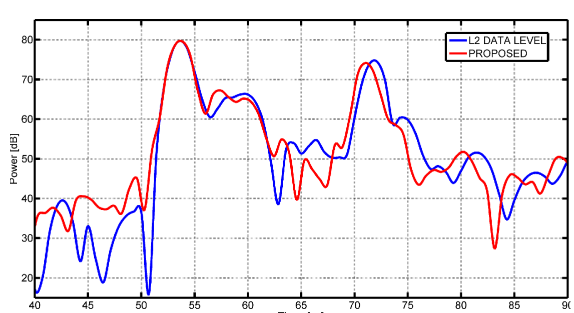

Figure 7: Compensation schemes comparison.

7. CONCLUSIONS

Starting from the recently proposed ionospheric density profiles an analysis has been performed using the finite-difference time-domain (FDTD) method to assess the ionosphere influence on experimental data involved in the data inversion process. Dayside ionosphere induced degradation on pulse shape has been analyzed for MARSIS 3, 4 and 5 MHz channels. A possible compensation scheme has been proposed using nighttime acquired data from the Martian south pole, a surface clutter-free region presenting frames suitable for data inversion. Next works will focus on the eventual need to include this compensation in selecting data for the inversion process.

REFERENCES

1. Picardi, G., et al., "MARSIS data inversion approach: Preliminary results," *Proc. of 2008 IEEE Radar Conference*, Vol. 1, 1–4, Rome, Italy, May 2008.
2. Chapman, S., "Absorption and dissociative or ionising effects of monochromatic radiation in an atmosphere on a rotating earth," *Proc. of the Physical Society*, Vol. 43, No. 1, 1047–1055, London, Jan. 1931.
3. Biccari, D., G. Picardi, and R. Seu, "Adaptive compensation of Mars ionosphere dispersion in the MARSIS experiment," *Proc. of 2001 IEEE International Geoscience and Remote Sensing Symposium*, Vol. 6, 2557–2559, Sydney, Australia, Jul. 2001.
4. Nickisch, L. J. and P. M. Franke, "Finite-difference time-domain solution of Maxwell's equations for the dispersive ionosphere," *IEEE Antennas and Propagation Magazine*, Vol. 34, No. 5, 33–39, Oct. 1992.
5. Picardi, G., et al., "Mars ionosphere data inversion by MARSIS surface and subsurface signals analysis," *Proc. of 2008 IEEE Radar Conference*, Vol. 1, 1–5, Rome, Italy, May 2008.
6. Withers, P., "Attenuation of radio signals by the ionosphere of Mars: Theoretical development and application to MARSIS observation," *Radio Science*, Vol. 26, No. 2, Apr. 2011.
7. Withers, P., et al., "A clear view of the multifaceted dayside ionosphere of Mars," *Geophysical Research Letters*, Vol. 39, L18202, 2012.
8. Jordan, R., et al., "The Mars express MARSIS sounder instrument," *Planetary and Space Science*, Vol. 57, 1975–1986, 2009.
9. Restano, M., M. Mastrogiuseppe, A. Masdea, G. Picardi, and R. Seu, "Ionosphere compensation and stepped frequency processing in the MARSIS experiment," *Proc. of 2011 IEEE Microwaves, Radar and Remote Sensing Symposium*, Vol. 1, 149–152, Kiev, Ukraine, Aug. 2011.
10. Withers, P., et al., "Observations of the nightside ionosphere of Mars by the Mars express radio science experiment (MaRS)," *Geophysical of Geophysical Research*, Vol. 117, A12307, 2012.

Subsurface Geometry Influence on Radar Returns in the Orbiting Ground Penetrating Radar Context

Marco Restano, Giovanni Picardi, and Roberto Seu
Department of Information, Electrical and Telecommunication Engineering (DIET)
University of Rome "Sapienza", Italy

Abstract— The Mars Advanced Radar for Subsurface and Ionosphere Sounding (MARSIS) and the Shallow Radar (SHARAD) are low frequency, pulse limited ground penetrating radars selected to investigate the Mars subsurface as payloads of the ESA Mars Express and NASA MRO missions respectively. Radar echoes coming from both surface and subsurface are strongly affected by geometry. The proposed work aims to produce a theoretical analysis for the various scenarios of interest, evaluating the impact on the data inversion process that aims to estimate the dielectric constant of materials composing the different detected sub-superficial interfaces.

1. INTRODUCTION

MARSIS [1] and SHARAD [2] primary scientific objective is to map the distribution and depth of water reservoirs in both liquid and solid forms in the upper kilometres of the Martian crust. MARSIS is a low-frequency (0.1–5.5 MHz) nadir-looking pulse limited radar sounder and altimeter with ground penetration capabilities. Taking into account the ionosphere plasma frequency, MARSIS operates using the following carrier frequencies: 1.8, 3, 4 and 5 MHz. The transmitted bandwidth is equal to 1 MHz providing a vertical resolution of about 150 m in the air. Among the available sounding configurations, the SS3 subsurface sounding mode has been selected using two frequency channels to investigate the Martian crust returning data in 3 separated Doppler filters. The SHARAD instrument is similar to MARSIS achieving a better vertical resolution using a 10 MHz bandwidth chirp signal of 85 µs duration over a 20 MHz carrier frequency. The expected ground penetration is 5 to 9 km for MARSIS and 1km for SHARAD depending on crust composition. A MARSIS typical frame showing power returns from surface (P_s) and subsurface (P_{ss}) interfaces is reported in Figure 1, $\Delta\tau$ can be used to retrieve the layer thickness once its composition is known. Figure 2 reports a typical SS3 dual channel frame, a collection of such frames, over a stationary area, is needed to perform the data inversion process.

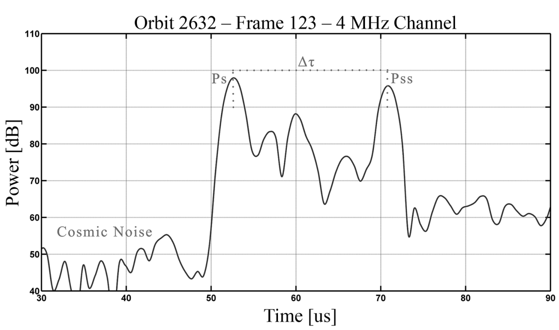

Figure 1: Typical MARSIS frame.

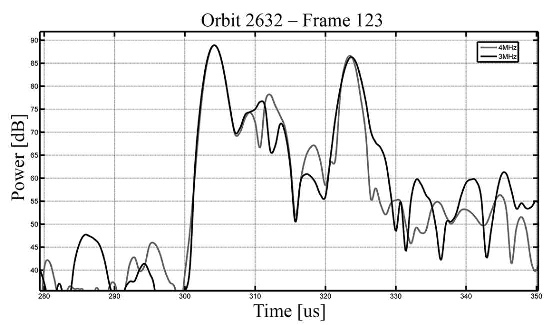

Figure 2: Typical SS3 dual channel frame.

2. DATA INVERSION EQUATION

The data inversion process [1] aims to estimate the dielectric constant of materials composing the different detected interfaces by the evaluation of values of permittivity that would generate the observed radio echoes. The data inversion equation has been described by the following relation:

$$R_{12,z}^2 - \Gamma_s = -\frac{P_s}{P_{ss}} + \frac{f_s}{f_{ss}} + K_{\mathrm{dB}} \tag{1}$$

with

$$K_{\mathrm{dB}|f_1} = \frac{f_1}{(f_1 - f_2)} \cdot \Delta\frac{P_s}{P_{ss}} = \frac{f_1}{(f_1 - f_2)} \cdot \left[\left(\frac{P_s}{P_{ss}} + \frac{f_s}{f_{ss}}\right)_{f_1} - \left(\frac{P_s}{P_{ss}} + \frac{f_s}{f_{ss}}\right)_{f_2}\right] \quad (f_1 > f_2) \tag{2}$$

where Γ_s is the surface Fresnel reflectivity, $R^2_{12,z}$ is the reflection coefficient of the interface at the depth z, P_s/P_{ss} is the surface to subsurface power ratio, f_s/f_{ss} is the ratio between the geometric correction terms, which deals with surface and subsurface geometry and K_{dB} is the attenuation between surface and subsurface when considering the 4 MHz and 3 MHz channels (as in Figure 2). MARSIS data inversion aims to estimate the parameters in (1) in order to deduce the subsurface dielectric constant by the $R^2_{12,z}$ of the detected interfaces, being the power ratio P_s/P_{ss} and $\Delta P_s/P_{ss}$ given by observations and Γ_s by other instruments on previous missions to Mars. The same procedure can be adopted using SHARAD data once its 10 MHz bandwidth is half-splitted in two channels. Mars polar regions are the most suitable to perform data inversion showing plenty of sub-superficial structures. Polar areas are mainly composed of ice (pure or mixed with rock dust), with the possible presence of superficial stratifications including CO_2 [3].

3. BACKSCATTERING MODELS

Taking into account the classical studies on the validity conditions of the backscattering models, the Kirchhoff theory can be used to estimate the backscattering contribution for gently undulating surfaces (large scale model) while the Small Perturbation Method can be applied to slightly rough surfaces (small scale model). From a statistical point of view [4], the surface height can been modelled as a Gaussian random process, where σ_{h1} is the surface RMS height. Under the hypothesis of Kirchhoff approximation the average scattered power at time τ has been computed for the large scale model by taking the average of the product of the scattered electric field with its complex conjugate:

$$\langle E_s(\tau)E_s^*(\tau)\rangle = \Gamma_s(\theta)\frac{1}{4h^2}\cos^2\theta\left(P_c(\tau)+P_{nc1}(\tau)-P_{nc2}(\tau)\right) \tag{3}$$

where h is the distance from the radar to the mean surface, θ is the angle of incidence, P_c is the coherent (specular) scattering component and $P_{nc1}(\tau) - P_{nc2}(\tau) = P_{nc}(\tau)$ is the non coherent (diffuse) scattering component. In particular:

$$\begin{aligned}
P_c(\tau) &= \frac{1}{1+F}\cdot\exp\left(-(2k\sigma_{h1}\cos\theta)^2\right)/1+F)\cdot\exp\left(-\tau^2/2{\tau_p}^2(1+F)\right)\\
P_{nc1}(\tau) &= \frac{\beta}{\sqrt{1+2F}}\cdot\sqrt{\frac{\pi}{2}}\cdot\exp\left(\frac{\beta^2}{2}\right)\cdot\exp\left(-\beta\cdot\left(\frac{\tau}{\tau_p\sqrt{1+2F}}\right)\right)\cdot\mathrm{erfc}\left[\frac{1}{\sqrt{2}}\left(\beta-\frac{\tau}{\tau_p\sqrt{1+2F}}\right)\right]\\
P_{nc2}(\tau) &= \frac{\beta}{\sqrt{1+F}\cdot\sqrt{1+2F}}\cdot\sqrt{\frac{\pi}{2}}\cdot\exp\left(-(2k\sigma_{h1}\cos\theta)^2\right)/1+F)\cdot\exp\left(\beta^2\cdot\frac{1+F}{2}\cdot(1+2F)\right)\\
&\quad\cdot\exp\left(-\beta\cdot\left(\frac{\tau}{\tau_p\sqrt{1+2F}}\right)\right)\cdot\mathrm{erfc}\left[\frac{1}{\sqrt{2}}(\beta\sqrt{\frac{1+F}{1+2F}}-\frac{\tau}{\tau_p\sqrt{1+F}})\right]
\end{aligned} \tag{4}$$

Both $P_c(\tau)$ and $P_{nc}(\tau)$ depend on the normalized project roughness $F = \frac{1}{2}\frac{\sigma^2_{h1}\cos^2\theta}{(c\tau_p/2)^2}$ and the surface parameter β given by $\beta = \frac{c\tau_p}{2h}\frac{\sqrt{1+2F}}{m_s^2\cos\theta}(1-\exp(-(2k\sigma_{h1}\cos\theta)^2)$ where c is the speed of light, k is the wave number, B_w is the bandwidth, $\tau_p = 0.37/B_w$, m_s is the rms slope related to the correlation length L and the roughness σ_{h1} by the relation $m_s = \sqrt{2}(\frac{\sigma_{h1}}{L})$.

This closed form describing the average scattered power has been derived assuming a Gaussian correlation coefficient and a Gaussian pulse spectrum which corresponds to a Gaussian shape of the compressed pulse.

Imposing MARSIS signal parameters, $L = 2$ km, $H = 350$ km and $f = 4$ MHz the backscattering is reported for several σ_{h1} (F parameter) in Figure 3. It is important to consider the shape variation from the Gaussian one ($F \leq 0.01$) related to a flat geometry as the roughness increase ($F \geq 0.01$).

4. FDTD MODELING

The adopted FDTD algorithm [5] divides the problem geometry into a spatial grid of cells where electric and magnetic field components as well as constitutive parameters (like permittivity and permeability) are placed at certain discrete positions in space and it solves Maxwell's equations in

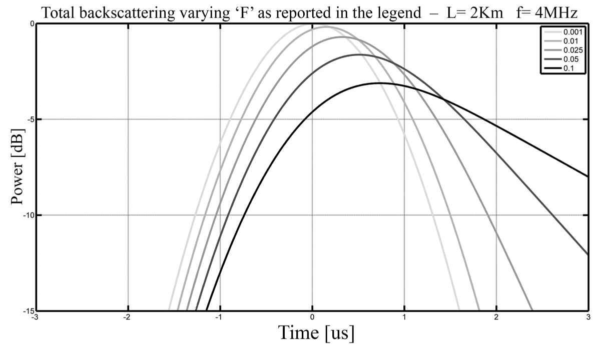

Figure 3: Backscattering models.

time at discrete time instances. Maxwell formulation is reported in the following form:

$$\nabla \times \vec{H} = \varepsilon \frac{\delta \vec{E}}{\delta t} + \sigma^e \vec{E} + \vec{J}_i \tag{5}$$

$$\nabla \times \vec{E} = -\mu \frac{\delta \vec{H}}{\delta t} - \sigma^m \vec{H} - \vec{M}_i \tag{6}$$

which is composed by two vector equations taking into account conduction and impressed components. Each equation can be decomposed into 3 scalar equations for the 3D space including time and space derivatives. To run the FDTD algorithm, the time and space derivatives are approximated by finite differences. Afterwards, a set of equations is constructed in order to calculate the values of fields at a future time instant from the values of fields at a past time instant, therefore, a time marching algorithm that simulates the progression of the fields in time is obtained. The full formulation can be found in [5].

Convolutional perfectly matched layer (CPML) has been adopted to absorb evanescent waves while the Courant-Friedrichs-Lewy (CFL) condition has been verified for all the permittivity values adopted in the simulated scenario to guarantee the stability of the simulation. 20 cells per wavelength have been set to perfectly reproduce the propagating chirp spectrum. Near Field-Far Field transformation has been implemented according to the formulation proposed by [6] along with the scattering field formulation, so reproducing a plane wave entering the simulated scenario.

5. THE PROPOSED SIMULATIONS

3D simulations are considered. Since high processing resources are required, both chirp signal and scenarios have been designed to guarantee accurate results while limiting the simulation times. The backscattering model introduced in (3) has been considered to reproduce in FDTD a correlation length of 1 m and a roughness ranging from 0 (flat geometry) to 6.4 m over a 70 m by 70 m surface. The emitted waveform is a chirp signal having 50 µs duration and 4 MHz bandwidth over a 6 MHz carrier. It is transmitted over a plane wave entering the scenario and received in the air at Far Field after the propagation in the crust. Afterwards, chirp compression is performed along with Hanning weighting as on MARSIS/SHARAD data. The reference attenuation-free scenario is composed by air, CO_2 and ice. It is important to carefully set the layers depth in order to respect the chirp resolution in the crust (related to wave speed in the medium) avoiding the overlapping of both surface and subsurface responses which would bring to a distorted shape [7]. Consequently, a depth of 150 m has been set for both CO_2 and ice layers.

Both chirp signal and surface/subsurface geometry have been designed according to (3) in order to always receive a Gaussian pulse shape that decreases its power level as the roughness increases (like for $F < 0.01$ in Figure 3). This assumption, possible to be found in experimental data, will clarify another degrading effect being non-attenuating (so frequency independent: $\left.\frac{P_s}{P_{ss}}\right|_{f_1} = \left.\frac{P_s}{P_{ss}}\right|_{f_2}$) materials ($CO_2$/ice) simulated. It is important to underline that the attenuation given by (2) is null for such materials only if both surface and subsurface are flat ($\frac{f_s}{f_{ss}} = 0$) or perfectly roughness compensated. So, flat geometry also implies frequency independency.

Two groups of simulations are proposed, considering the roughness presence only on surface or subsurface. Band splitting has been implemented to underline the roughness-related frequency dependency. The first group of simulations, regarding a rough surface and a flat subsurface, is reported in Figures 4–5 for P_s and P_{ss} respectively. P_s (Figure 4) decreases for increasing roughness as predicted by (3) while frequency dependency arises with increasing roughness as reported by the band splitting trends. The H-BAND (6–8 MHz) is more influenced by roughness, having shorter wavelengths, than the L-BAND (4–6 MHz). P_{ss} decreases (Figure 5) as P_s, being slightly influenced by the surface roughness on its way back to the receiver, but frequency dependency is very limited as reported by the band splitting analysis. The second group of simulations, regarding a flat surface and a rough subsurface, is reported in Figures 6–7 for P_s and P_{ss} respectively. P_s value (Figure 6) is stable and frequency independent in all the simulations being the surface flat. P_{ss} value (Figure 7) shows a frequency dependency similar to the one reported in (Figure 4).

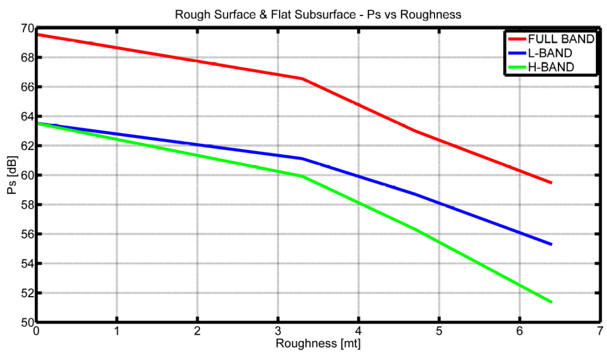

Figure 4: Rough surface and flat subsurface — P_s.

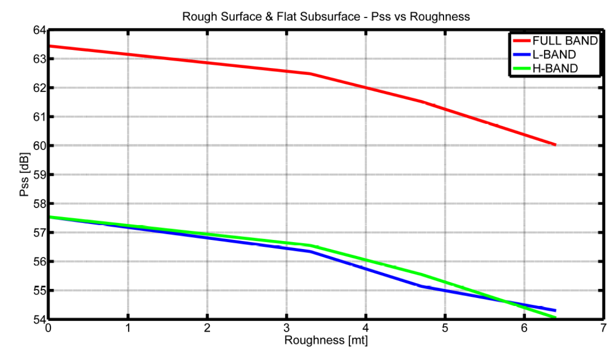

Figure 5: Rough surface and flat subsurface — P_{ss}.

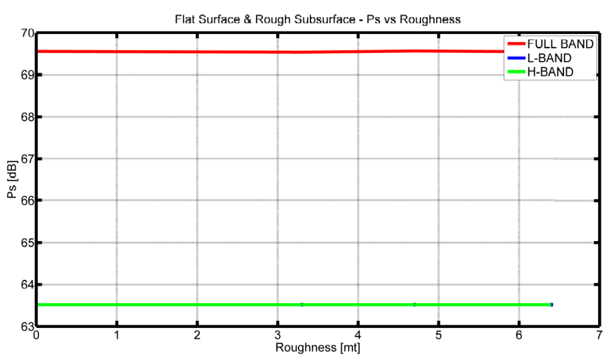

Figure 6: Flat surface and rough subsurface — P_s.

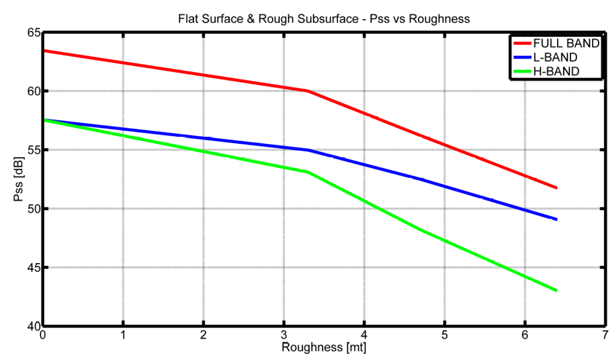

Figure 7: Flat surface and rough subsurface — P_{ss}.

Reported values are valid only for a qualitative analysis, such as the parameters used to model the proposed scenario. However, even though MARSIS frames can be roughness compensated using Mars Orbiter Laser Altimeter (MOLA) data as proposed by [7], no information regarding the Martian subsurface geometry is available apart from the returns recorded in the 3 available Doppler filters accounting for the sub-superficial layers tilt [8]. So, data inversion should be based on frames in which frequency dependency is very limited or null, that would indicate no layer attenuation and no roughness for both surface and subsurface. Otherwise, even the Gaussian pulses related to the non-attenuating simulated scenario would not be reliable because such pulses could be wrongly associated to flat geometries, and the frequency dependency to the attenuation presence, misleading the data inversion process based on (1).

6. CONCLUSIONS

A 3D-FDTD simulator has been proposed to qualitatively analyze the degrading effects introduced by surface and subsurface roughness on data inversion performed by radars like MARSIS and SHARAD on a specific class of frames.

The analysis evidenced the possibility that frequency dependency introduced by a rough surface/sub-surface could be interpreted as layer attenuation being pulse shape related to a rough geometry not always modified with respect to the Gaussian one related to a flat geometry.

A 2D-FDTD simulator could be implemented to reproduce Martian scenarios at the scale needed by MARSIS and SHARAD but it would only allow a surface geometry compensation because no information regarding the subsurface geometry is available.

Since a full compensation of data is not obtainable, the only possibility to perform a reliable data inversion lies in an accurate frames selection that should discard trends showing severe frequency dependency in the two channels.

REFERENCES

1. Picardi, G., et al., "MARSIS data inversion approach: Preliminary results," *Proc. of 2008 IEEE Radar Conference*, Vol. 1, 1–4, Rome, Italy, May 2008.
2. Seu, R., et al., "SHARAD, a shallow radar sounder to investigate the red planet," *Proc. of 2008 IEEE Radar Conference*, Vol. 1, 1–4, Rome, Italy, May 2008.
3. Mouginot, J., W. Kofman, A. Safaeinili, C. Grima, A. Heriquea, and J. J. Plaut, "MARSIS surface reflectivity of the south residual cap of Mars," *Icarus*, Vol. 201, 454–459, 2009.
4. Picardi, G., D. Biccari, R. Seu, et al., "Performance and surface scattering models for the Mars advanced radar for subsurface and ionosphere sounding (MARSIS)," *Planetary and Space Science*, Vol. 52, 149–156, 2004.
5. Elsherbeni, A. and V. Demir, *The Finite-difference Time-domain Method for Electromagnetics with MATLAB Simulations*, Scitech Publishing Inc., Jan. 2009.
6. Luebbers, R. J., K. S. Kunz, M. Schneider, and F. Hunsberger, "A finite-difference time-domain near zone to far zone transformation," *IEEE Transactions on Antennas and Propagation*, Vol. 39, No. 4, Apr. 1991.
7. Restano, M., A. Masdea, G. Picardi, and R. Seu, "Weighting network influence on the geometric term correction in MARSIS data inversion," *Proc. of 2012 IEEE International Radar Symposium*, Vol. 1, 213–217, Warsaw, Poland, May 2012.
8. Restano, M., A. Masdea, G. Picardi, and R. Seu, "Doppler analysis for data inversion and image processing in the MARSIS experiment," *Proc. of 2011 IEEE Microwaves, Radar and Remote Sensing Symposium*, Vol. 1, 153–156, Kiev, Ukraine, Aug. 2011.

Consequences of Electromagnetic Stimulation on Hydraulic Conductivity of Soils

A. Farid, S. Azad, J. Browning, and E. Barney-Smith
Boise State University, USA

Abstract— Hydraulic conductivity is a measure of the rate at which water flows through porous media. Because of the dipole properties of water molecules, any electric field can affect hydraulic conductivity. In this study, the effect of radio-frequency (RF) waves on hydraulic conductivity is investigated. This is important both for the geophysical measurement of hydraulic conductivity as well as remediation using electromagnetic waves. Bentonite clay and sandy samples are tested in rigid-wall, cylindrical permeameters and stimulated using a CPVC-cased monopole antenna vertically centered in the permeameters. The permeameters are encased within RF cavities constructed of aluminum mesh in order to prevent interference from outside and to confine the RF wave to the medium. Falling-head and constant-head tests are performed to measure the hydraulic conductivity of the clayey and sandy soil samples, respectively. The results show a correlation between the change in the hydraulic conductivity and the characteristics of the RF stimulation. The change is, however, different for sandy and clayey soils.

1. INTRODUCTION

The use of RF waves can enhance various transport mechanisms within soils. Research in the food industry has proven that an RF electric field can enhance diffusion and the mass transfer rate [1]. During other research on the use of RF waves to enhance soil remediation [2], the authors realized the hydraulic conductivity was altered. The hydraulic conductivity of a saturated soil is dependent on the unit weight and viscosity of the permeant fluid (in this case water) as well as on the intrinsic permeability of the porous media, which is in turn dependent on the pore- and grain-size distribution as well as porosity. The hydraulic conductivity is also a function of the level of water-saturation in the medium [3]. Understanding the relation between RF stimulation and hydraulic conductivity could have a broad use in geoenvironmental and geotechnical applications such as contaminant remediation in soils, grout injection, and landfill-liner design.

2. METHODOLOGY

To experimentally model the effect of RF waves on hydraulic conductivity, a series of bench-top tests was conducted using rigid-wall permeameters. In this work, the permeameters were customized to measure the change in the hydraulic conductivity due to an RF wave launched into the medium contained within the permeameter. A vertical monopole probe is used to measure the electric field within the experimental setups. The laboratory-scale setup was modeled using COMSOL Multiphysics software, and the simulated electric field was validated against the experimentally measured Z component of the electric field.

3. EXPERIMENTAL SETUP

Rigid-wall, cylindrical permeameters were prepared using acrylic and CPVC material to prevent interference with the RF wave. Figure 1 shows schematics of the setups. The permeameter used for the clayey sample has a diameter of 152 mm and a height of 190 mm, containing soil samples of 76 mm in length (L). The entire body of the permeameter is contained within a 200-mm $\times$ 200-mm $\times$ 230-mm RF cavity constructed of aluminum mesh. The permeameter was filled with soil in three layers, each 2.54 cm (1 in.) thick, until it filled the desired 76 mm (3 in.) length of the soil sample (L). The water used for this test was deaerated and deionized. The effect of RF waves on the natural water existing in the environment can be different. However, at this stage of the study, a controlled environment is necessary. It is understood that the cations existing in the clay structure can be washed away by the flow of deionized water with a volume equal to multiple times the sample's void volume. Nevertheless, repeated flow through the same clay sample during the preliminary experiments did not show any sudden change in the hydraulic conductivity. Deaerated water was used to eliminate air entrapment in the soil when the flow direction was changed downward to study the RF effect while flow direction was varied.

Sand experiments are similar to clay experiments, except the size of the sample is different. The permeameter for the sand experiment had a diameter of 100 mm and length of 250 mm, containing soil samples of 150 mm in length (L). In order to measure the flow rate, Q (m^3/s), water flowing out of the plastic drainage tube was collected in a 500-mL graduated cylinder at measured durations, t.

The monopole antenna, used to launch RF waves, was made of an RG8 coaxial cable with 50 mm of its conducting shield stripped, cased within a CPVC tube, submerged into the medium. A continuous-wave (CW) RF signal was generated using an Agilent Model # E4400B signal generator and amplified using an amplifier (RF Lambda Model # 100LM8, manufactured by Amplifier Research). The entire system (i.e., antenna, soil medium, and cavity) was impedance matched with the 50-Ω amplifier using a matching network. The matching network consists of two two-gang variable capacitors built in a BUD box (an aluminum box to contain the EM waves). The impedance measurement was performed using an Agilent N9320A vector network analyzer.

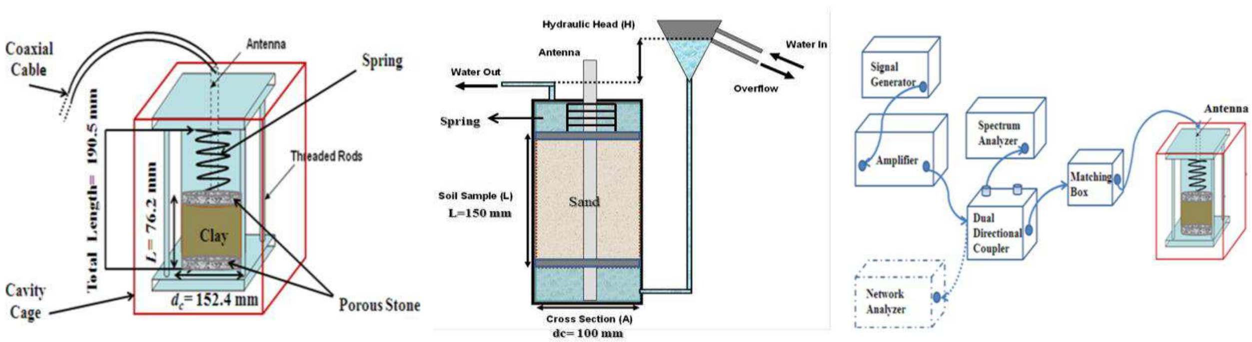

(a) (b) (c)

Figure 1: Schematic of rigid-wall, cylindrical permeameter (d_c: soil sample diameter, L: length of soil sample) designed for EM stimulation of: (a) clayey samples, (b) sandy samples, and (c) schematic of instruments and setup.

4. SUMMARY AND RESULTS

4.1. Bentonite Clay Sample, Falling-Head-Test [4]

The RF stimulation was conducted on the Bentonite sample with a 30-W input power carried out within 3 consecutive days. The tests were implemented at frequencies of 80, 94, and 153 MHz. Pre-stimulation, the hydraulic conductivity was allowed to stabilize to values roughly between 0.75×10^{-7} cm/s and 1.1×10^{-7} cm/s, typical of clay [5]. During the first half hour of RF excitation, the stimulation (dashed line in Figure 2(a)) caused a sharp decrease in the hydraulic conductivity through the clay. The reduction of k in this period of stimulation was different for each frequency. At 153 MHz, the permeability of the sample decreased from 1×10^{-7} cm/s to about 2.6×10^{-8} cm/s, a reduction to 1/4 of the initial unstimulated hydraulic conductivity. The sharp decline in k at the frequencies of 80 and 94 MHz were about 4/5 and 1/2 of the initial unstimulated values, respectively. RF stimulation (dashed lines) was continued about 6 hours in each cycle. Right after the sharp reduction in k, some degree of relaxation occurs during the stimulation. The frequency of 153 MHz results in a much larger reduction of k compared to the other two frequencies. This could be related to the resonance and radiation pattern at this frequency and relaxation mechanisms of water molecules in response to RF waves. In other words, cavities of various sizes, and in turn various resonant frequencies, are necessary to truly evaluate the RF-frequency effect — independent of cavity size and corresponding resonance — on hydraulic conductivity. Termination of RF stimulation (solid lines in Figure 2(a)) caused an increase to a value greater than the average pre-stimulation hydraulic conductivity of the clay sample, referred to as rebound. This rebound relaxes after 10–12 hours.

To evaluate the effect of the RF power and electric-field intensity on the reduction of the clay sample's k, the stimulated experiment was replicated at 153 MHz but at three power levels (10, 20, and 30 W). The experiment was continued for 33 hours. In each cycle of RF stimulation from on (dashed lines) to off (solid lines), the duration of the stimulation was constant, and the RF power level was gradually reduced in subsequent cycles. Figure 2(b) reveals that higher electric-field intensities result in larger reductions in the permeability. Figure 2(b) also shows the average stable value of k versus the RF power. It appears that the reduction in the average hydraulic conductivity of the clay sample will be smaller at lower RF power. The power level of 30 W achieves the most reduction in the clay permeability, to 2/5 of the initial value.

4.2. Sand Sample Constant-Head Test [6]

The RF stimulation was conducted on the sand sample with a 20-W input power carried out within 60 hours. The test was implemented at a frequency of 153 MHz. Pre-stimulation, the hydraulic conductivity was allowed to stabilize to a value roughly at 2.19×10^{-4} cm/s (Figure 3), typical for sand [5]. During the first hour of RF excitation, the RF stimulation (dashed lines in Figure 3) caused an increase in the hydraulic conductivity through the sand. In the first cycle of the stimulation, the permeability increased from 2.19×10^{-4} cm/s to about 2.5×10^{-4} cm/s, an increase of 14%. RF stimulation was continued about 20 hours in each cycle. Within 5 hours after the sharp increase in k, some degree of relaxation occurs during the stimulation. Termination of RF stimulation (solid lines of Figure 3) caused a sudden decrease in the hydraulic conductivity until it stabilized at its typical value of k, after about 5 hours. It took about 15 hours for the unstimulated hydraulic conductivity to stabilize at typical k values. Then a second cycle of RF stimulation started with similar results.

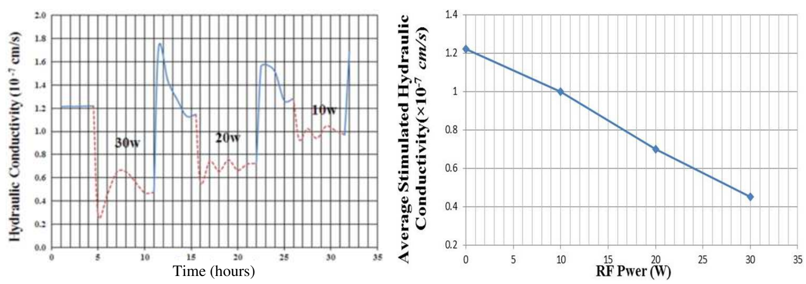

(a) (b)

Figure 2: (a) Change in hydraulic conductivity at a constant frequency of 153 MHz and power levels of 30, 20, and 10 W (solid line: unstimulated; dashed line: RF-stimulated) and (b) average change in hydraulic conductivity versus RF power level.

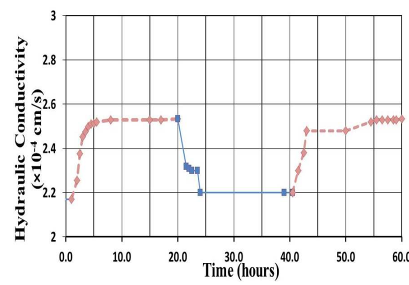

Figure 3: Variation of hydraulic conductivity of a sand sample under RF stimulation, power output of 20 W (solid line: unstimulated; dashed line: RF-stimulated) at a frequency of 153 MHz.

5. EXPERIMENTALLY VALIDATED SIMULATION

Acquiring the full 3D vector electric field is necessary. The permeameter containing the soil, water, resonant cavity, and coaxial antenna was modeled using COMSOL Multiphysics. The RF effect on flow was considered. However, even though water affects the EM waves, the effect from the laminar flow on the EM waves was neglected. Hence, this model was used only to enable the visualization of the EM field without simulating the seepage flow. Typical electrical properties of water and Bentonite clays were assigned to the model [7].

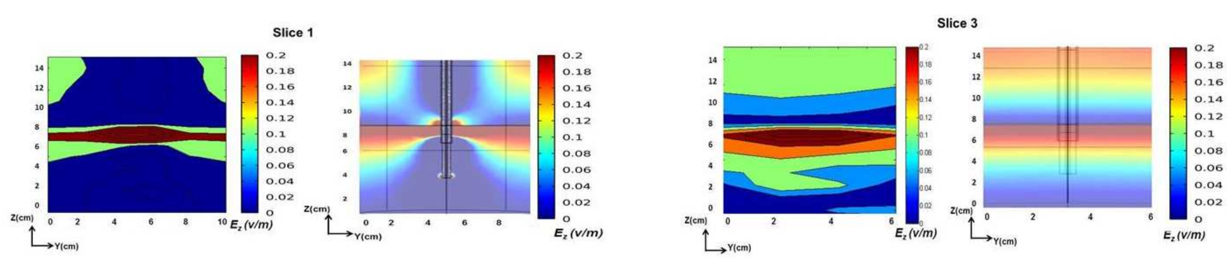

(a) (b)

Figure 4: Contour maps of experimentally measured *amplitude* (left) and simulated *Z component* using COMSOL Multiphysics (right) of electric field on: (a) centric Slice 1 through the center and (b) Slice 3, 4 cm from the center.

Then the electric field was mapped in the test region using a 3D computer-controlled translation table. The experimental measurements were used to validate the Z component of the simulated electric field. Typical slices are shown in Figure 4. As seen, the equivalent slices provide the same pattern of the electric field. The probe is not a calibrated probe. Hence, experimental measurements are representatives of the electric-field pattern, and absolute values do not match.

6. MECHANISMS BEHIND EM EFFECT ON HYDRAULIC CONDUCTIVITY

A potential mechanism that can cause the alteration in the permeability of the soil samples is dielectrophoresis (DEP). In order to measure the force applied to the water, flowing through the soil, saturated soil (with a bulk dielectric constant) should not be viewed as the background. In other words, the background would be the dry soil skeleton, and the particles would be the water molecules. This is not the traditional view of dielectrophoresis. However, for our evaluation of dielectrophoresis as the potential mechanism behind the RF-stimulation effect, this viewpoint can be justified. Since the dielectric constant of the particles (water molecules in this case, $\varepsilon_p^* \approx 81$) is higher than that of the medium (dry Bentonite clay in this case, $\varepsilon_m^* = 2.38$), dielectrophoresis would exert a force to the particles (water molecules) moving them toward the area of lower electric-field intensities. The dielectrophoretic force was calculated using simulated electric fields, using a code developed in MATLAB interface. The three components of the simulated electric field developed using COMSOL were imported as a matrix into MATLAB. The imported matrices contained the three electric-field components at all nodes on a 100-mm × 100-mm horizontal grid and 120-mm × 170-mm vertical grid on the cross-sectional (horizontal) and depth (vertical) slices, respectively. A MATLAB script (*m.file*) was then developed using a central finite-difference method to calculate the gradient of the squared electric field, $\nabla|E|^2$, based on the following discretized equation where r is the particle diameter and ε_m^* and ε_p^* are the dielectric permittivity of the particles and background.

$$\begin{aligned}\vec{F}_{DEF} &= 2\pi r^3 \varepsilon_m^* \mathrm{Re}\left\{\frac{\varepsilon_p^* - \varepsilon_m^*}{\varepsilon_m^*}\right\} \vec{\nabla}\,|E|^2_{(i,j,k)} = 2\pi r^3 \varepsilon_m^* \mathrm{Re}\left\{\frac{\varepsilon_p^* - \varepsilon_m^*}{\varepsilon_m^*}\right\} \\ &\quad \left(\frac{|E|^2_{i,j+1,k} - |E|^2_{i,j-1,k}}{2dx} + \frac{|E|^2_{i+1,j,k} - |E|^2_{i-1,j,k}}{2dy} + \frac{|E|^2_{i,j,k+1} - |E|^2_{i,j,k-1}}{2dz}\right) \qquad (1)\end{aligned}$$

Figure 5 shows the X and Z components of the dielectrophoretic force on the depth and cross-sectional slices for the clay and sand samples, respectively. According to Figure 5(b), the Z-component of the simulated force is negative in the soil domain and positive closer to the water domain. In other words, the direction of the simulated dielectrophoretic force is in the negative Z-direction (i.e., downward) within the majority of the soil domain and reverses approaching the top of the soil. The resultant of these two is always downward regardless of the flow direction (i.e., resists upward flow and helps downward flow). However, the change in the direction of F_{DEP} within the sample could act as a barrier for the seepage flow regardless of the flow direction. As mentioned, regardless of the seepage flow, a reduction in the k of the clay sample is always experimentally observed. This cannot conclusively prove or refute the hypothesis about the role of dielectrophoresis on the experimentally observed reduction of hydraulic conductivity of clay by EM waves, which is independent of the seepage flow direction.

On the other hand, it can be observed that the value of F_{DEF} force in the clay sample is four times larger than in the sand sample. Moreover, the same simulated force vector direction was observed for the sand while an increase in hydraulic conductivity was observed during the experimental investigation, which results in a disagreement between the direction of the dielectrophoretic force and alteration of flow rate. On the other hand, the X-component of the force creates a force that drags the water away from or toward the center of the permeameter (Figure 5(a)). The magnitude of the horizontal component is almost 1/40 the vertical component of dielectrophoretic forces, for both soil samples. The energy absorbed by the water could reduce the viscosity and hence increase the hydraulic conductivity of the sand. However, the cation complex in the clay could be the factor causing the reduction of the hydraulic conductivity of the clay.

The temperature of the medium was recorded. The temperature was recorded at 1-minute intervals for a test at one of the applied frequencies (153 MHz) at 30 W of power. The total temperature variation at that frequency over about 11 hours of RF stimulation was only 1.6°C. The temperature variation between the center and boundary of the cylindrical soil sample was only 0.1°C. Therefore, even though the temperature change and gradient can cause a minor convective flow, the small temperature increase within the medium may not be strong enough to create such strong convective flow, causing the change in k — especially in clay. In addition, a convective flow due to the generated heat would not cause the relaxation and rebound behavior observed in both sand and clay samples.

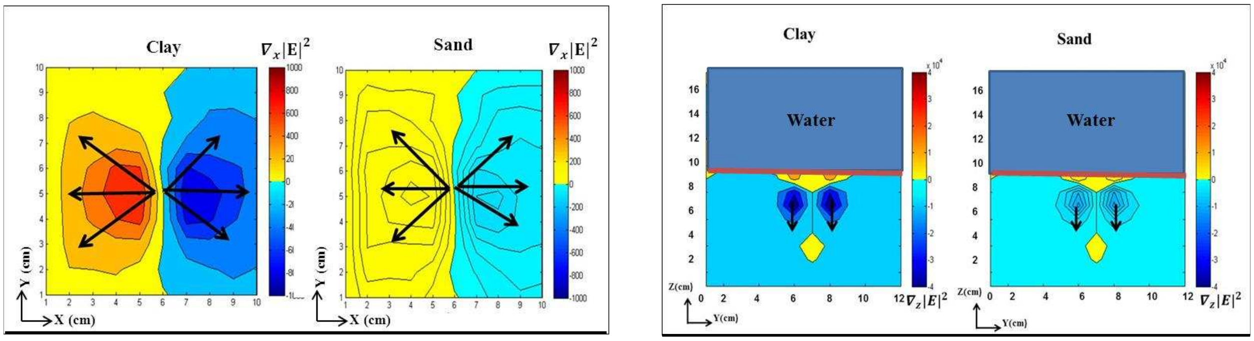

(a) (b)

Figure 5: Dielectrophoretic force: (a) X component ($\nabla_x|E|^2$) on a cross-sectional slice, 5 cm from bottom of permeameter; and (b) Z component ($\nabla_z|E|^2$) on a depth slice, 0 cm from antenna.

7. CONCLUSION

This work demonstrated two opposite effects by RF waves on the hydraulic conductivity of clayey and sandy soils. Dielectrophoresis can be the cause of rapid reduction in the hydraulic conductivity of clay. However, even though dielectrophoresis exists in sand, it is much weaker and dominated by other factors such as energy absorbed by water, resulting in an increase in its hydraulic conductivity.

ACKNOWLEDGMENT

This project was supported by the National Science Foundation through the Interdisciplinary Research (IDR) program, CBET Award No. 0928703.

REFERENCES

1. Lima, M. and S. K. Sastry, "The effects of ohmic heating frequency on hot-air drying rate and juice yield," *Journal of Food Engineering*, Vol. 41, No. 2, 115–119, 1999.
2. Azad, M., H. Sangrey, A. Farid, J. Browning, and E. Barney-Smith, "Electromagnetic stimulation of two-phase transport in water-saturated media for geoenvironmental applications," *ASTM, Geotechnical Testing Journal*, Vol. 13, No. 1, 97–106, January 2013.
3. Das, B. M., *Principles of Geotechnical Engineering*, Cengage Learning, 666, 2006, ISBN-10: 0495411302.
4. Association of Standard, Testing, and Materials (ASTM D5084-10), *Standard Test Methods for Measurement of Hydraulic Conductivity of Saturated Porous Materials Using a Flexible Wall Permeameter*, Book of Standard, Vol. 04.08, 2006, DOI: 10.1520/D5084-10.
5. Fetter, C. W., *Applied Hydrogeology*, 4th Edition, Prentice-Hall, Upper Saddle River, NJ, USA, 2001.
6. ASTM D2434-68, *Standard Test Method for Permeability of Granular Soils (Constant Head)*, Book of Standard, Vol. 04.08, DOI: 10.1520/D2434-68R06, 2006.
7. Von Hippel, R., *Dielectric Materials and Application*, 371, John Willey & Sons Inc., New York, 1969.

UWB SAR Landmine-enhanced Imaging Based on Aspect-frequency Characteristics Using Sparse Representation

Fu-Lai Liang, Yu-Ming Wang, Qian Song, Han-Hua Zhang, and Zhi-Min Zhou
College of Electronic Science and Engineering
National University of Defense Technology, Changsha, Hunan 410073, China

Abstract— Ultra-wideband Synthetic Aperture Radar (UWB SAR) has the characteristics of wide aspect angle and wide frequency band, which can provide with aspect-frequency dependence about targets. In this paper, a new landmine-enhanced imaging method using sparse representation is proposed based on the analysis of aspect-frequency dependence. Firstly, subaperture and subband images sequence preserves the aspect-frequency dependence information. The Gabor atoms are selected to construct the dictionary for its convenient description of different structures in the image. The weighting value for each pixel is calculated by parameters extracted atoms. The electromagnetic simulation demonstrates the validation of the proposed method.

1. INTRODUCTION

Ultra-wideband synthetic aperture radar (UWB SAR) has the characteristics of low-frequency band, large bandwidth and wide accumulated angle. These characteristics guarantee better soil or foliage penetration, high resolution of SAR images, and richer aspect and frequency dependent information of targets, making UWB SAR a promising method for detecting landmines from a safe standoff distance [1–3].

The traditional SAR image mainly shows the intensity of reflectivity from targets. Thus, the weak targets such as the landmine are easy to be masked by the strong clutters with the structures such as trihedral and dihedral. Besides, since little prior knowledge of targets is used in traditional SAR imaging, the targets are treated the same as the clutters. So there exist a lot of clutters in the traditional SAR image. These drawbacks make it a tough problem to detect landmine in the traditional SAR image. Aimed at this problem, the aspect-frequency characteristics of targets contained in UWB SAR data are brought into SAR imaging to enhance targets and suppress clutters.

In this paper, we concentrate our attention on landmine-enhanced imaging. In Section 2, we make analysis on the aspect-frequency characteristics of landmine. For convenience, the landmine is simplified into cylinder with the same size. There exist evident distinctions between the landmine and trihedral reflector. Based on the analysis, a new landmine-enhanced imaging method based on sparse representation is proposed in Section 3. In this method, the characteristics of targets are extracted by sparse representation. The parameters of the extracted atoms can quantify these characteristics. The weighting value for landmine-enhanced imaging is created by several selected parameters of atom. Electromagnetic simulation results demonstrate the validation of the proposed method.

2. ANALYSIS ON ASPECT-FREQUENCY CHARACTERISTICS

In traditional SAR imaging, the multi-aspect and multi-frequency signatures are integrated to form a single image, thereby losing some of the explicit aspect and frequency dependence. In contrast, subaperture and subband technique divides the collected returns into several subapertures and subbands, and then form image with the aspect and frequency dependence preserved. Thus, each pixel has a matrix to describe its aspect and frequency dependence.

For UWB SAR, the centric frequency is low and the frequency band is wide. So it is a hard job to construct analytical model of targets. The finite-difference time domain (FDTD) method for numerical calculation is an effective way to simulate data under various conditions for UWB SAR [4, 5]. In this paper, we simulate the SAR echo of targets by FDTD, and then the analysis on aspect-frequency characteristics is based on the FDTD simulation echo.

We employ the FDTD method to simulate the scattering data of a scene including a landmine (simplified into a cylinder) and a 0.3 m trihedral. The frequency bandwidth is 2 GHz, from 0.5 GHz to 2.5 GHz. The elevation angle is 60°, the aspect angle is from $-45°$ to $45°$. The distance between the two targets is 1.414 m. The diameter and height of the cylinder are 0.3 m and 0.1 m, respectively.

Figure 1 shows the aspect-frequency dependence matrix of pixels corresponding to the landmine and the trihedral. There exist two dominant ridges in aspect-frequency dependence matrix of landmine (as Figure 1(a) shows). But the main characteristics of trihedral are two peaks in Figure 1(b).

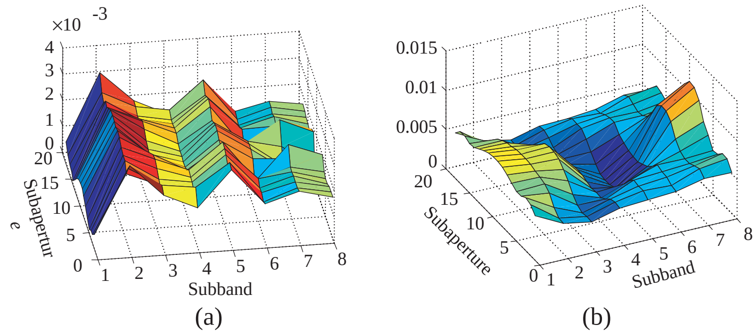

Figure 1: The aspect-frequency characteristics of typical targets. (a) Landmine. (b) Trihedral.

3. LANDMINE-ENHANCED IMAGING BASED ON SPARSE REPRESENTATION

3.1. Theory of Sparse Representation

Image sparse representation is often used to extract features of images. The aspect-frequency dependence matrix of each pixel can also be seen as an image. Sparse representation can be considered as a process of acquiring the minimums number of coefficients of atoms α_i, which can be written as

$$\min_{\alpha} \|\alpha\|_0 \quad s.t. \quad f = D\alpha \tag{1}$$

where $\alpha = [\alpha_1, \alpha_2, \dots, \alpha_I]$.

Basis Pursuit (BP) method [6, 7] is often adopted for solving Equation (1). But BP is computationally expensive. So reducing calculation is a research emphasis for improving this method. Matching Pursuit (MP) method is often adopted for its high computational efficiency [8].

3.2. Construction of Dictionary

The key of sparse representation is the construction of appropriate dictionary. Many dictionaries have been proposed for sparse representation, such as dictionary of DCT, curvelet and Gabor. Gabor is widely used for its nice and convenient description of different constructions in the image. So we choose Gabor atoms to construct the dictionary in this paper. Gabor atoms are defined as follows.

$$\begin{aligned} g(x, y, a, b, f, \theta, x_0, y_0) &= \frac{1}{ab} \exp\left[-\pi\left(\frac{x_t^2}{a^2} + \frac{y_t^2}{b^2}\right)\right]\left[\exp(j2\pi f x_t) - \exp\left(-\frac{\pi^2}{2}\right)\right] \\ x_t &= (x - x_0)\cos\theta + (y - y_0)\sin\theta \\ y_t &= -(x - x_0)\sin\theta + (y - y_0)\cos\theta \end{aligned} \tag{2}$$

where a and b are scale factors, x_0 and y_0 are shift factors, f is tuning factor, and θ is rotation angle.

From Table 1 we can know that the extraction of ridges requires that the scale of atom along some direction should be large enough but the scale along the vertical direction is small. So it is computation expensive to directly make sparse representation by the dictionary without consideration of the prior information of targets. Thus, dictionary is constructed by several subdictionaries can reflect the structures contained to reduce the redundancy of dictionary. The subdictionaries are shown as follows.

- Subdictionary D_i of aspect-invariance components.

  In order to well reflect aspect-invariance components, large a is adopted and f is set a low value. And then the atoms have the characteristics of $\theta = 0$ or $\theta = \pi$. That is to say, the atoms are also aspect-symmetrical.

Table 1: The meaning of parameters of atoms.

α	Intensity of extracted structures
θ	Metric of symmetry. $\theta = 0$ and $\theta = \pi/2$ mean the symmetry in azimuth and range direction, respectively.
x_0	Position of the center of atom along azimuth direction. It gives the azimuth angle.
y_0	Position of the center of atom along frequency direction. It gives the main frequency components.
a	Size of atom along azimuth direction. Large a means aspect-invariance.
b	Size of atom along range direction. Large b means weak frequency-dependence.
f	Amplitude undulation of atom.

- Subdictionary D_g of directive components along aspect.

  Targets such as dihedral and cone exhibit explicit aspect-directive. The atoms in this subdictionary has small a.
- Subdictionary D_I of peak components

  Targets like the trihedral have explicit structure of peaks. In this subdictionary, atoms with small a and b are adopted.

3.3. Landmine-enhanced Imaging

From the above analysis, we can know that the peaks and ridges can be described by atoms with different scale factors and rotation angle. As Figure 2 shows, the peaks are represented by two atoms whose scale factors are both 6 pixel in subapreture and subband direction. However, the ridges are represented by two atoms whose subapreture scale factors are large but subband scale factors are small. The rotation angles of atoms belonging to landmine are 0, but rotation angles of atoms belonging to trihedral are $\pi/2$.

The extracted atoms show the quantitative analysis of targets, which can be used for enhancement of specific target and classification of targets. In this paper, we concentrate on the method

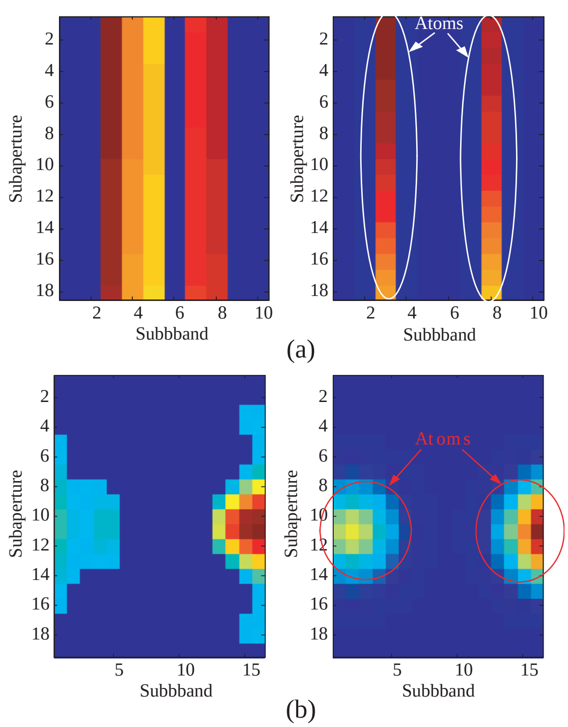

Figure 2: Atoms for image sparse representation. (a) Landmine. (b) Trihedral.

of landmine enhancement. Figure 3 gives the flow of landmine-enhanced imaging method. Firstly, the subaperture and subband images sequence are acquired. And then, the aspect-frequency dependence matrix of each pixel is preprocessed for improving the sparsity of main structures. The simplest method is to remove the small value of the matrix by the hard threshold. Sparse representation is then performed on the preprocessed results. The mean value of azimuth scale factors of the first two atoms is chosen as the weighting value of each pixel. Thus, the landmine can be enhanced. Further more, the traditional full aperture and full band image is formed by subaperture and subband images sequence. Finally, the landmine-enhanced imaging result is generated by the product of the traditional full aperture and full band image and landmine-enhanced weighting value.

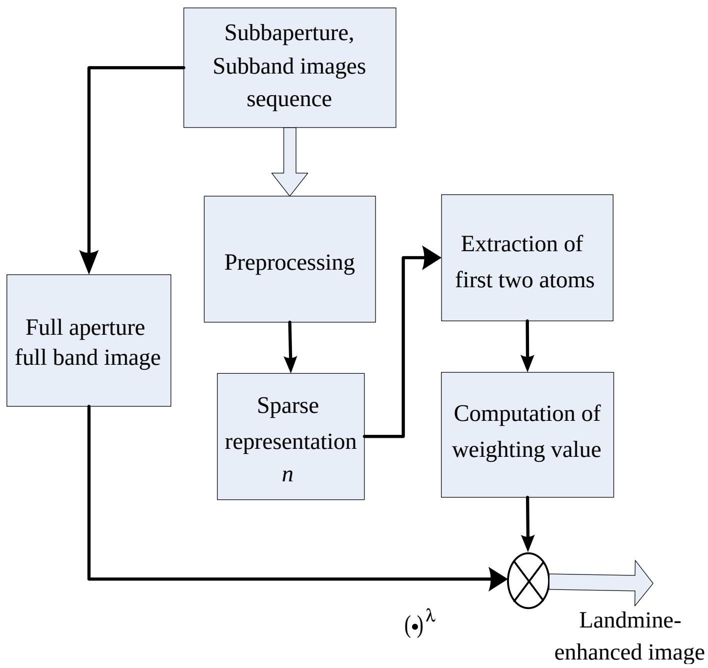

Figure 3: Flow of landmine-enhanced imaging based on sparse representation.

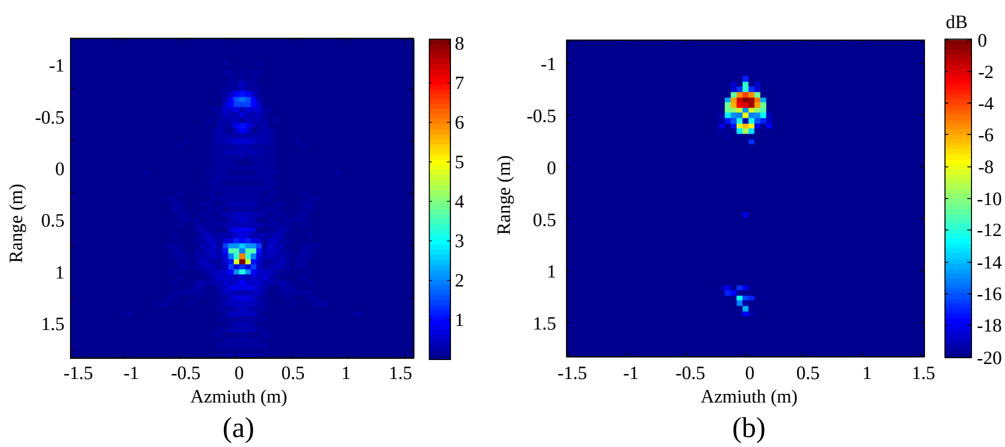

Figure 4: Comparison of results. (a) traditional SAR image. (b) Landmine-enhanced imaging result.

4. NUMERICAL RESULTS

We apply the proposed landmine-enhanced imaging method on the electromagnetic scene which has been mentioned in Section 2.

As Figure 4(a) shows, the landmine in traditional SAR image is much weaker than trihedral. Since the enhanced imaging is performed pixel-to-pixel, the coarse imaging grid is adopted in order to reduce the computation cost.

In the enhanced-imaging result shown in Figure 4(b), the landmine becomes much stronger than the trihedral. Actually, the trihedral has been well suppressed. The residue is caused by sidelobe of trihedral. The proposed method is valid.

5. CONCLUSIONS

In this paper, a new landmine-enhanced imaging method based on aspect-frequency characteristics using sparse representation is proposed. The analysis on aspect-frequency dependence shows that the landmine and the other target, i.e., trihedral, have different structures, which can be extracted by sparse representation. The parameters of the extracted atoms can be used in landmine-enhanced imaging. The results in this paper are based on the electromagnetic simulation, which will be extended to real data processing in the future.

REFERENCES

1. Jin, T. and Z. Zhou, "Ultrawideband synthetic aperture radar landmine detection," *IEEE Transactions on Geoscience and Remote Sensing*, Vol. 45, 3561–3573, 2007.
2. Andrieu, J., F. Gallais, V. Mallepeyre, V. Bertrand, B. Beillard, B. Jecko, et al., "Land mine detection with an ultra-wideband SAR system," *Proc. SPIE*, Vol. 4742, 237–247, 2002.
3. Yang, J., X. Huang, T. Jin, J. Thompson, and Z. Zhou, "Synthetic aperture radar imaging using stepped frequency waveform," *IEEE Transactions on Geoscience and Remote Sensing*, Vol. 50, 2026–2036, 2012.
4. Zhang, Y.-Q. and D.-B. Ge, "A unified FDTD approach for electromagnetic analysis of dispersive objects," *Progress In Electromagnetics Research*, Vol. 96, 155–172, 2009.
5. Hu, X.-J. and D.-B. Ge, "Study on conformal FDTD for electromagnetic scattering by targets with thin coating," *Progress In Electromagnetics Research*, Vol. 79, 305–319, 2008.
6. Candes, E. J., J. Romberg, and T. Tao, "Robust uncertainty principles: Extract signal reconstruction from highly incomplete frequency information," *IEEE Trans. Inf. Theory*, Vol. 52, 489–509, 2006.
7. Wei, S. J., et al., "Sparse reconstruction for SAR imaging based on compressed sensing," *Progress In Electromagnetics Research*, Vol. 109, 63–81, 2010.
8. Bergeaud, F. and S. Mallat, "Match pursuit of images," *International Conference on Image Processing*, Vol. 1, 53–56, Washington DC, USA, 1995.

Robust Compressive Imaging Approach to Through-wall Imaging Radar Based on Stepped-frequency and Virtual Aperture

Pengyu Wang, Qian Song, Jian Wang, and Zhimin Zhou
College of Electronic Science and Engineering
National University of Defense Technology, Changsha, Hunan 410073, China

Abstract— Due to the sparsity of the targets behind walls, the compressive sensing (CS) theory has been successfully applied to the through-wall imaging (TWI) radar. Based on the techniques of stepped-frequency (SF) and virtual aperture (VA), a scheme of realizing the SFVA CS-based TWI radar (SFVACS-TWIR) system is put forward in this paper. For improving the robustness of CS reconstruction, the multi-measurement iterative pixel discrimination (MM-IPD) approach is also introduced. The data from both the simulated and experimental SFVACS-TWIR systems are presented to demonstrate the effectiveness of MM-IPD in SFVACS-TWIR.

1. INTRODUCTION

Through-wall imaging (TWI) radar has gained much attention in recent years due to its broad civilian and military applications. With the techniques of ultra-wideband (UWB) and aperture synthesization [1], it can receive high resolutions in both cross- and down-range directions except some disadvantages, such as a long time of data collection, a huge amount of data, and a high computational complexity. When the data collection time prolongs, the targets may change positions, and their movements may cause smearing and blurring in the processed image [2]. For many applications of TWI radar, their main goals are not to reconstruct the radar-received signals but rather to create an image of the target space behind walls. That means the targets can be supposed to be point-like reflectors at discrete spatial positions. Moreover, the target number is much smaller than the total number of discrete spatial positions determined by the spatial resolution. This sparsity just satisfies the premise of applying a new technique, known as compressive sensing (CS) [3, 4]. In past several years, the CS theory has received remarkable development, and it has been successfully applied to TWI radar despite some unsolved challenges before a real CS radar system comes true [2, 5]. To actualize a real CS-based radar system, the generation of random measure matrix has to be thoroughly solved by hardware design. Comparing the existing random measure matrices, the matrix randomly constructed with 0 and 1 seems quite suitable, because the element 0 and 1 just correspond to the off and on of the circuit. Furthermore, the techniques of stepped-frequency (SF) and virtual aperture (VA) also provide the convenience for CS-based radar to implement random measurements. In this paper, we mainly concentrate on the design scheme of a real CS-based TWI radar system using SFVA technique (named SFVACS-TWIR system hereafter). In addition, the through-wall attenuation usually makes the signal-to-noise ratio (SNR) of target echoes reduce to below 0 dB. Noise violates the sparsity precondition and makes CS reconstruction inaccurate or even unrealizable. To achieve robust reconstruction in low SNR conditions, the approach called multi-measurement iterative pixel discrimination (MM-IPD) is also introduced [6]. With iterative CS processing and pixel serials clustering, the MM-IPD can reach the robust reconstruction, namely obtain the accurate positions of the targets behind walls.

The remainder of this paper is organized as follows. Section 2 describes the design scheme and signal model of the SFVACS-TWIR system. In Section 3, the MM-IPD approach is discussed. Simulated and experimental results are given in Section 4. Finally, conclusions drawn are presented in Section 5.

2. SYSTEM SCHEME AND SIGNAL MODEL OF SFVACS-TWIR

2.1. System Scheme

The SFVACS-TWIR system which is to be designed is derived from the forward looking ground penetrating radar designed by national university of defense technology [7]. Except for array length and antenna type, the work pattern of transmit-receive system should be considerably redesigned. The key constraint on system actualization is how to implement random measurement with hardware. Apparently, the random measure matrix consisting of 0 and 1 is a proper selection for its one-one correspondence with circuit switch [2, 8, 9]. Ref. [9] has provided the way of constructing the random measure matrix by randomly selecting M rows of an identity matrix, where M should satisfy the requirement of CS reconstruction. Both the simulated and experimental results have verified its effectiveness.

With the techniques of SF and VA, the SFVACS-TWIR system can obtain target echo of arbitrary frequency and transmit-receive channel, namely implement random measurement via hardware. For enhancing the system stability, the signal generator should work in the mode of ordinal frequency sweep and the frequency scanning number υ should be a positive integer. That means M should equal to υK, where K is the total frequency number. Accordingly, the style of random measure matrix is determined by the work mode of VA which depends on fast switch and logical controller. Fig. 1(a) shows the work mode of the SFVACS-TWIR system. When the SF signal is transmitted consecutively, the fast switches randomly switch from one to another according to the sequence preset by logical controller. Fig. 1(b) shows the sketch map of the SFVACS-TWIR system. The switch between different transmit-receive channels is under the control of the logical controller.

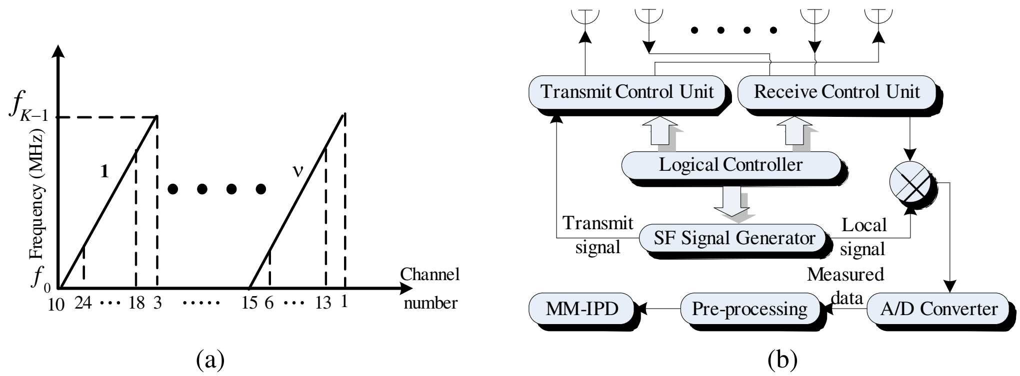

Figure 1: SFVACS-TWIR system, (a) work mode, (b) sketch map.

2.2. Signal Model

Figure 2 shows the simplified signal model of the SFVACS-TWIR system and the corresponding coordinates. Suppose that the antenna array which consists of two transmitters and N receivers is set along the X direction with height H and distance d_r away from the wall. For the pth target, suppose $S[m, n, k]$ represents the signal of the kth frequency f_k received with the mth transmitter and nth receiver.

$$S[m,n,k]=\sum_{p=0}^{P-1}\sigma_p \exp\left[-j4\pi f_k R\left(p,m,n\right)/c\right],\quad (m=1,2;\ n=1,\ldots,N) \tag{1}$$

where σ_p is the reflection coefficient of target T_p, P is the total number of target, and c is the speed of electromagnetic (EM) wave in the vacuum. $R(p, m, n)$ stands for the propagation distance between the antenna pair and target T_p. Moreover, wall thickness d and its relative permittivity ε_r are supposed to be known. According to Snell's law, refraction happens when EM wave travels

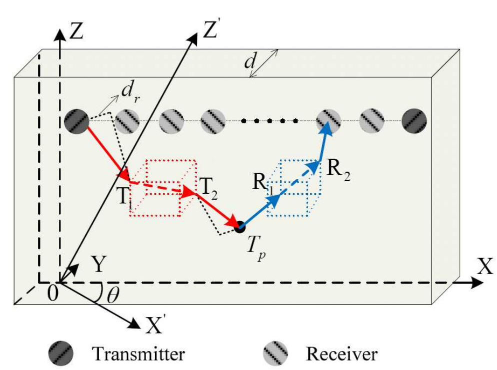

Figure 2: Simplified signal model of the SFVACS-TWIR system.

through air to wall and wall to air. T_1 and T_2 respectively represent the refraction points of the transmit path on the air-wall interface and wall-air interface, whereas R_1 and R_2 correspond to the receive path.

Although it is difficult and complex to calculate the coordinates of point T_1, T_2, R_1 and R_2, Ref. [2] inspires us that it can be solved with the technique of coordinate rotation [10]. Comparing with the approximate signal model used by most conventional imaging algorithms, this accurate model can effectively reduce the reconstruction error of CS, such as positioning error and integrate sidelobe ratio reduction of each recovered target.

3. THE MULTI-MEASUREMENT ITERATIVE PIXEL DISCRIMINATION APPROACH

The remarkable result of CS reveals that a signal x of length J is sparse in the domain $\Psi_{J\times J}$, it can be robustly reconstructed via only some random projections of the signal onto a random matrix Φ which is called measure matrix. More precisely

$$y = \Phi x = \Phi\Psi\alpha \tag{2}$$

If only k components of α are non-zero, x is called k-sparse. In the real environments, y is usually contaminated by noise, and thus Eq. (2) should be rewritten as follows:

$$y = \Phi x + w = \Phi\Psi\alpha + w = \Theta\alpha + w \tag{3}$$

where w is the additive white Gaussian noise with the variance σ^2, then α can be robustly reconstructed by solving the following optimization problem

$$\hat{\alpha} = \arg\min(||\Theta\alpha - y||_2^2 + \lambda||\alpha||_1) \tag{4}$$

where λ is called regularization parameter which can be estimated by the generalized cross validation (GCV) approach [11]. But in the low SNR conditions, GCV is unable to guarantee λ will converge to the optimal. Based on our experience of GCV, the nonoptimal estimation arises frequently. For TWI radar, through-wall attenuation usually reduces the SNR to below 0 dB despite background subtraction techniques [2].

Aiming at robust reconstruction, the multi-measurement iterative pixel discrimination (MM-IPD) approach is introduced [6]. As mentioned in Ref. [6], the MM-IPD is on the basis of the statistical separability of the reconstructed amplitudes between target and clutter. Namely, target has a consistent nonzero center of the recovered amplitude series, while clutter usually converges to a near-zero value. To measure the constructed image quality, two variables are defined: sparsity of reconstructed image $\mathrm{I}_{\mathrm{S}}^{l} = ||\hat{\alpha}^{l}||_{\mathrm{S}}$ and standard deviation of the reconstructed image $\mathrm{I}_{\mathrm{SD}}^{l} = ||\hat{\alpha}^{l}||_{\mathrm{SD}}$, where $\hat{\alpha}^{l}$ denotes the reconstruction of lth CS and clustering processing. Actually, $\mathrm{I}_{\mathrm{S}}^{l}$ stands for the target number whose amplitude exceeding the mean value of $\hat{\alpha}^{l}$, whereas $\mathrm{I}_{\mathrm{SD}}^{l}$ represents the standard variance of $\hat{\alpha}^{l}$. With the growth of SNR and iteration number, $\mathrm{I}_{\mathrm{S}}^{l}$ (or $\mathrm{I}_{\mathrm{SD}}^{l}$) will converge to some consistent values. The procedure steps of MM-IPD are shown as follows.

1) The CS imaging space is meshed, and the dictionary Ψ is generated;
2) The original measure matrix Φ is used to obtain the measured data y;
3) The measure submatrix Φ_l is generated by randomly selecting several rows from Φ;
4) the measure subset y_l is randomly extracted from y via Φ_l;
5) If $l = 0$, λ is estimated by GCV with Φ_l, y_l, and Ψ, otherwise jump to step 6;
6) $\hat{\alpha}_l$ is given by solving Eq. (4) with Φ_l, Ψ, λ, and y_l;
7) If $l = 1$, $\hat{\alpha}^{l} = \hat{\alpha}_l$; otherwise, $\hat{\alpha}^{l} = \text{Clustering}\ ([\hat{\alpha}_1, \ldots, \hat{\alpha}_l])$;
8) $\Delta\mathrm{I}_{\mathrm{S}} = |\mathrm{I}_{\mathrm{S}}^{l} - \mathrm{I}_{\mathrm{S}}^{l-1}|/\mathrm{I}_{\mathrm{S}}^{l}$ and $\Delta\mathrm{I}_{\mathrm{SD}} = |\mathrm{I}_{\mathrm{SD}}^{l} - \mathrm{I}_{\mathrm{SD}}^{l-1}|/\mathrm{I}_{\mathrm{SD}}^{l}$ are calculated;
9) If either $\Delta\mathrm{I}_{\mathrm{S}} > \varepsilon_{\mathrm{S}}$ or $\Delta\mathrm{I}_{\mathrm{SD}} > \varepsilon_{\mathrm{SD}}$ where ε_{S} and $\varepsilon_{\mathrm{SD}}$ are decision thresholds (e.g., -10 dB), $l = l + 1$ and return to step 3, otherwise, iteration terminates.

4. RESULTS AND DISCUSSIONS

To demonstrate the effectiveness of the MM-IPD approach on SFVACS-TWIR system, both the simulated and experimental results are presented. Except special declarations, all the images are normalized amplitude images in the logarithmic scale within a limit ranging from -3 dB to 0 dB.

The SNR is defined as the power ratio of signal to noise in the raw echo domain and the wall parameters are assumed to be known: $d = 0.2\,\mathrm{m}$ and $\varepsilon_r = 4$. Fig. 3 shows the simulated results of SFVACS-TWIR system with nonideal walls. There are five point-like targets randomly positioned in the 2-dimensional space. Fig. 3(b) gives the single CS result of the data without noise. When the SNR equals to $-10\,\mathrm{dB}$, the reconstructed result begins to deteriorate. Except for some clutters, one target is even lost (see Fig. 3(c)). By contrast, the MM-IPD exhibits more robustly, all the targets are reconstructed (see Fig. 3(d)).

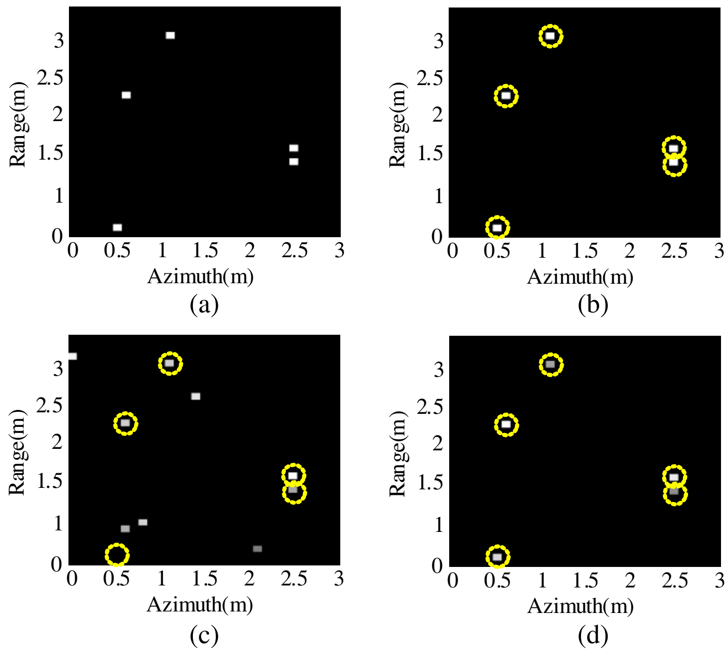

Figure 3: Simulated results of SFVACS-TWIR, (a) target space, (b) single CS with no noise, (c) single CS with noise (SNR $= -10\,\mathrm{dB}$), (d) MM-IPD with noise (SNR $= -10\,\mathrm{dB}$).

According to the abundant experimental results of TWI in the microwave anechoic chamber, the SFVACS-TWIR system is operated in frequency range from 0.5 GHz to 1.5 GHz with 5 MHz frequency step. Fig. 4(a) shows the system antenna array consisted of 14 plane ridged horn antennae. The antenna array is constructed as similarly as Fig. 2. There are four metal trihedral corner reflectors (MTCR) with side length being 0.2 m is positioned on the ground behind the wall. The wall parameters have been estimated and measured beforehand, namely $d = 0.2\,\mathrm{m}$ and $\varepsilon_r = 4$ respectively. According to the CS theory, we set the scanning frequency number υ as 3, which means the proportion of the measured data used for CS reconstruction to the complete data is only 12.5%.

Figure 5 shows the results processed by single CS and MM-IPD. As the through-wall attenuation reduces the SNR of the received echoes, which makes it difficult for single CS processing to achieve robust reconstruction. Though the target receives successful recovery, there exist some clutters. By contrast, the MM-IPD approach behaves more robustly. Except for target's robust reconstruction, the clutters receive effective suppression.

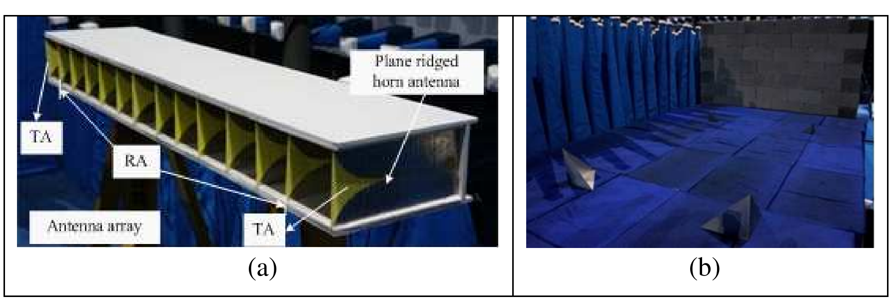

Figure 4: Experiment of the SFVACS-TWIR system, (a) antenna array, (b) target scene.

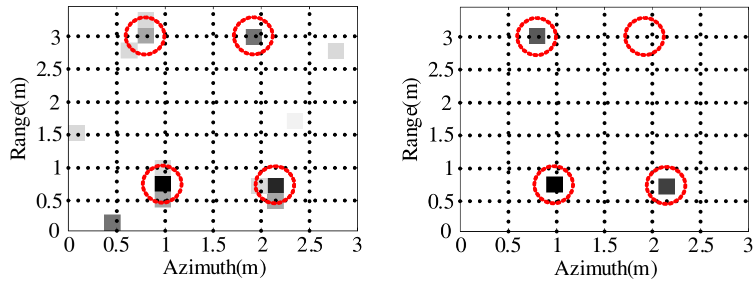

Figure 5: Experimental results of SFVACS-TWIR, (a) single CS, (b) MM-IPD.

5. CONCLUSION

Based on the techniques of stepped-frequency and virtual aperture, the scheme for realizing the CS-based TWI radar system has been discussed in this paper. To achieve robust reconstruction, the MM-IPD approach has been applied to the SFVACS-TWIR system. Firstly, the accurate signal model of the SFVACS-TWIR system is analyzed. Secondly, the MM-IPD approach is discussed. Thirdly, both simulated and experimental results are presented to demonstrate the effectiveness of the MM-IPD. Though the SFVACS-TWIR system doesn't belong to real CS radar system, it has explored a way for the realization of CS radar.

REFERENCES

1. Ahmad, F. and M. Amin, "Noncoherent approach to through-the-wall radar localization," *IEEE Trans. Aerosp. Electron. Syst.*, Vol. 42, No. 4, 1405–1419, Oct. 2006.
2. Huang, Q., L. Qu, B. Wu, and G. Fang, "UWB through-wall imaging based on compressive sensing, "*IEEE Transactions on Geoscience and Remote Sensing*, Vol. 48, No. 3, 1408–1415, Mar. 2010.
3. Donoho, D., "Compressed sensing," *IEEE Trans. Inf. Theory*, Vol. 52, No. 4, 1289–1306, Apr. 2006.
4. Candès, E., J. Romberg, and T. Tao, "Robust uncertainty principles: Exact signal reconstruction from highly incomplete frequency information," *IEEE Trans. Inf. Theory*, Vol. 52, No. 2, 489–509, Feb. 2006.
5. Yoon, Y.-S., "Through-the-wall radar imaging using compressive sensing," *2010 IEEE International Conference on Acoustics Speech and Signal Processing (ICASSP)*, 2806–2809, Mar. 2010.
6. Wang, P., Q. Song, and Z. Zhou, "A physics-based landmine discrimination approach with compressive sensing," *Progress In Electromagnetics Research*, Vol. 135, 37–53, 2013.
7. Jin, T., J. Lou, and Z. Zhou, "Extraction of landmine features using a forward-looking ground penetrating radar with MIMO array," *IEEE Transactions on Geoscience and Remote Sensing*, Vol. 50, No. 10, 4135–4144, Oct. 2012.
8. Yoon, Y.-S. and M. G. Amin, "Compressed sensing technique for high-resolution radar imaging," *Proc. SPIE*, Vol. 6968, 69681A.1–69681A.10, May 2008.
9. Gurbuz, A. C., H. M. James, and R. S Waymond, "A compressive sensing data acquisition and imaging method for stepped frequency GPRs," *IEEE Transactions on Signal Processing*, Vol. 57, No. 7, 2640–2650, 2009.
10. Wang, P., T. Jin, and Q. Song, "Analysis of accurate signal propagation model for through-wall imaging radar using compressive sensing," *International Conference on Signal Processing, Communication and Computation 2013 (ICSPCC 2013)*, Kunming, Yunnan, China, Aug. 2013 (Under Reviewer).
11. Batu, O. and M. Cetin, "Parameter selection in sparsity-driven SAR imaging," *IEEE Transactions on Aerospace and Electronic Systems*, Vol. 47, No. 4, 3040–3050, Oct. 2011.

Model for Determination of Territorial Distribution of Surface Radio Refractivity

M. Zilinskas[1,2], M. Tamosiunaite[3], S. Tamosiunas[2,4], E. Brilius[2], and M. Tamosiuniene[3]

[1]Department of Radio Communication
Communications Regulatory Authority of the Republic of Lithuania, Lithuania
[2]Faculty of Physics, Vilnius University, Lithuania
[3]Semiconductor Physics Institute of Center for Physical Sciences and Technology, Lithuania
[4]Institute of Applied Research, Vilnius University, Lithuania

Abstract— An atmospheric refractive index is not constant in a long length of the path. Atmospheric refractive index for radio waves over the selected area can be calculated using the air pressure, temperature and relative humidity data, measured in the area. In most cases, such information is collected only in main cities. Therefore, a method is required that allows calculations of the atmospheric refractive index, using data collected in the surrounding areas. A new specific model for determination of radio refractivity is presented. It is based on determination of the unknown value using three known values from the surrounding areas. Geographically, these reference points make a triangle. Inside the triangle, using the proposed method, the radio refractivity can be calculated when only the coordinates of the locality, its altitude, and the meteorological parameters measured in three surrounding localities are known. The model was tested using average monthly values of meteorological parameters; therefore several days in different seasons were selected for analysis in order to assess the possible deviation from the true value of *N*. The differences in the values determined using new model and the model proposed by ITU were less than one percent in all months except July and September. It was concluded that the average monthly relative humidity values should be calculated separately for day-time and night-time hours due to the large daily fluctuations in relative humidity in July.

1. INTRODUCTION

A ratio of radio wave propagation velocity in free space and its velocity in an atmosphere is an atmospheric radio refractive index n. Refractive index is not constant in the atmosphere and its space-time distribution results in scattering, sub-refraction, super-refraction, ducting, and absorption phenomena [1]. These changes are negligible. However, they strongly influence the radio wave propagation due to the long length of the path. On purpose to make these changes more noticeable, the term of radio refractivity, *N*, is used. N-value shows a number in parts per million, how much the refractive index exceeds unit. This parameter is very important in design of telecommunication systems. It depends on the temperature, pressure, and humidity of air. The characterization of tropospheric N variability has great significance to radio communications, aero-space, environmental monitoring, disaster forecasting, etc. [2]. For instance, worse propagation conditions lead to increased fading on communication links and consequently decreased power levels at receiver [2]. The method for determination of N-value has been proposed by International Telecommunication Union (ITU) [3]. In this model, the data of air temperature, pressure, and relative humidity are used. However, the meteorological parameters, required in the ITU method, are measured only in limited number of localities. Therefore it is a need to develop a model for determination of N in the localities, where such local meteorological data are not available, so it could be calculated using meteorological data, measured in the surrounding localities.

2. DETERMINATION OF RADIO REFRACTIVITY

In [3–7], the radio refractivity N is expressed as:

$$N = (n - 1) \times 10^6, \tag{1}$$

where n is an atmospheric radio refractive index.

As was mentioned in [7], the estimation of the refraction effect in troposphere is possible only by modeling the troposphere medium. According to [2–4], the expression (2) might well be used for all frequencies up to 100 GHz with an error less than 0.5%. This means that the value of N can be defined only by properties of the troposphere:

$$N = \frac{77.6}{T}\left(p + 4810\frac{e}{T}\right), \tag{2}$$

where T (K) is a temperature; p (hPa) is an atmospheric pressure; e (hPa) is a partial water vapor pressure. The refractivity is dimensionless size and it is expressed in N-units.

The atmospheric refractivity consists of two parts, which are a dry term $N_{\mathtt{dry}}$ and a wet term $N_{\mathtt{wet}}$:

$$N = N_{\mathtt{dry}} + N_{\mathtt{wet}}, \tag{3}$$

The dry term is due to non-polar nitrogen and oxygen molecules; it is proportional to pressure, p, and therefore, related to the air density [2]. The wet term is proportional to vapor pressure and dominated by polar water contents in the troposphere [2]. The importance of the liquid water and water vapor in the atmosphere, when the measurements are carried in the air, are highlighted in [10]. At the Sea level, the average value of $N \approx 315$ [4] is used. The relationship between the partial water vapor pressure e and the relative humidity $H(\%)$ is presented in [4].

3. DEVELOPMENT OF A NEW MODEL

If the N-value is estimated using formula (2), the values of meteorological parameters should be known. However, these data are not always measured at a point. Data measured at the further points is not suitable, because meteorological conditions in Lithuania (and in other European countries as well) are very variable. Therefore, we propose a new specific model for calculation of N inside some area, confined by surrounding areas in which the required values are known. It is based on the unknown value determination using three known values. Some locations are used as a reference points for the model. Geographically, these reference points make a triangle. Inside the triangle, using the proposed method, the radio refractivity can be calculated when only the coordinates of the locality, its altitude, and the meteorological parameters, measured in some surrounding reference points, are known. The essence of the method is to calculate the average value of the triangle vertices, depending on the coordinates of test point in the triangle. The sinus, cosine, and similar triangles theorems have been used for development of the model. Refractivity values in the locality other than the reference points, according to the proposed model, can be calculated in two ways: directly, using known three refractivity values in the surrounding cities, or determining meteorological parameters using the meteorological data, measured in surrounding localities and then calculating the N. This makes the proposed model very flexible and more accurate.

A schematic picture of the theoretical model is presented in Fig. 1, where x is the maximum value of the known parameters, y is the middle value of the known parameters, and z is the minimum value of the known parameters; a is the distance between the points with the maximum and middle values of the parameters; b is the distance between the points with the maximum and minimum values of the parameters; j is the distance between the point with the minimum value and the point where the parameter value is determined; f is the distance between the point with the maximum value and the point where the parameter value is determined; h is the distance between the point with the middle value of the parameter and the point where the parameter value is determined; W is the value of the parameter (it can be N, H or T), which should be found. The method is not suitable for calculation of the values in the points that comes out of the area, defined by the triangular boundaries. The drawback of the model is requirement that unknown value must be lower than the peak value of the triangular and higher than the minimum value of the triangle apex. However, large variations between the points are uncommon if the distances are small.

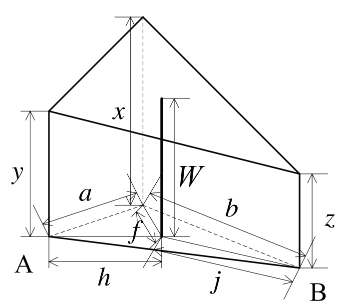

Figure 1: The schematic picture of the model.

The application of this model begins from measurements of the distances between the W-point and the apexes of the described triangle. All longitude and latitude coordinates may be found using possibilities of "Google Maps" [8]. The distance e between the points A and B can be determined by this relation (4):

$$e = \cos^{-1}\left(\cos(a_x)\sin(a_x)\cos(a_x)\cos(b_x)\cos(a_x a_y - b_y)\right) r, \tag{4}$$

where a_x, a_y, b_x, b_y are the coordinates of the points A and B, expressed in radians: latitude and longitude of A and latitude and longitude of B respectively; r is the Earth ellipsoid radius, going from the center to the equator.

The next step is gathering of meteorological data. In this paper, the meteorological data (measured on 02:00, 05:00, 08:00, 11:00, 14:00, 17:00, 20:00, and 23:00 o'clock) of the year 2012 [9] have been used. All meteorological values were averaged, except values of temperature, which was used directly.

After these two steps, the W-value can be found as:

$$W = z + \frac{t - (t-d) f \frac{\sin(180-\zeta)}{a\sin(\zeta)-\vartheta}}{f \frac{\sin(\vartheta)}{\sin(180-\zeta)} + j}, \tag{5}$$

where ζ, ϑ, t and d are the following substitutions:

$$\zeta = \cos^{-1}\left(\frac{j^2 + f^2 - b^2}{2fj}\right), \quad \vartheta = \cos^{-1}\left(\frac{a^2 + f^2 - h^2}{2fa}\right), \tag{6}$$

$$t = x - z, \quad d = y - z. \tag{7}$$

The atmospheric pressure has been determined using the Barometric formula (8):

$$p = p_0 \left(1 - \frac{0.0065 h_1}{T + 0.0065 h_1 + 273.15}\right)^{5.257}, \tag{8}$$

where p is the atmospheric pressure in the locality (hPa), p_0 is the average monthly value of pressure at the Sea level (hPa), h_1 is the height above the Sea level of the locality (m), T is the temperature (°C).

The pressure at the Sea level is known from the measures in Klaipeda (this city is located in Seacoast of Lithuania). The average monthly values have been used. The calculations were made using average monthly values of meteorological parameters; therefore several days in different seasons were selected for analysis in order to assess the possible deviation from the real value of N. The differences in the values determined using new model and the model proposed by [3] were less than one percent in all months except July and September. The largest difference between the N-values determined using the monthly average of H and the N-value determined using the real value of H measured at a point has been observed in Pagegiai (see Table 1). In this locality, the average H of 80% was in July 2012. The values of H, measured on 02:00, 05:00, 08:00, 11:00, 14:00, 17:00, 20:00, and 23:00, were 89; 88; 86; 63; 46; 74; 87, and 91% respectively. For example, the deviation of N-value from the monthly average was 34% in July. This is the main reason for the discrepancy of results in July.

The results show, that the average monthly relative humidity values should be calculated separately for day-time and night-time hours due to the large daily fluctuations in relative humidity in July. In September the difference was smaller than in July, but higher than one percent (about

Table 1: The differences (in N-units) between the N-values determined using new model and the model presented in [3].

Date and time	Kaunas	Pagegiai	Siauliai	Telsiai	Klaipeda	Vilnius
15.01.2012 17:00	−0.556	−0.728	−0.846	1.288	−1.210	0.132
05.03.2012 11:00	−0.973	−1.994	−2.077	4.870	0.252	−0.223
10.07.2012 14:00	38.690	46.412	37.789	10.173	17.550	17.311
17.09.2012 02:00	−7.137	−7.559	−11.452	−6.669	0.909	−4.619
22.11.2012 18:00	−6.694	0.338	−0.373	1.643	0.692	−6.313

3%). The measured value of H was higher than the monthly average value. This could result in higher than usual deviation from the real value.

The greater will be the distance separating two areas, the higher will be the probability that the N-value will strongly differ. This assumption was made because the temperature, relative humidity and pressure often have different trends and average monthly values in different geographic areas. According to analysis of the model, use of the relative humidity monthly averages can sometimes lead to wrong refractive index values. Nevertheless, the model is applicable for calculation of radio refractivity with a good accuracy, when primary weather parameters are correct. Also, the triangle apexes should be as close as possible to the W-point. The most accurate results will be achieved, when the triangle will cover areas of the same climatic divisions.

According to a data of French National Geographic Institute, Lithuania's Capital Vilnius is located close to the Geographical Center of Europe. Therefore, this model may be useful to the neighboring countries located in Europe.

The average N-values in Vilnius in the months of the year 2012 at different times of the day are presented in Fig. 2. The data presented in Fig. 2 show that N was the highest during the warm season; the largest N variations within a day was also observed during the warm season.

Lithuanian meteorological station network does not cover borders of country. Therefore, data collected in Lithuanian Meteorological Stations does not cover the whole country. For this reason, the research continued. The meteorological data measured in the neighboring countries will be used for the future verification of this model.

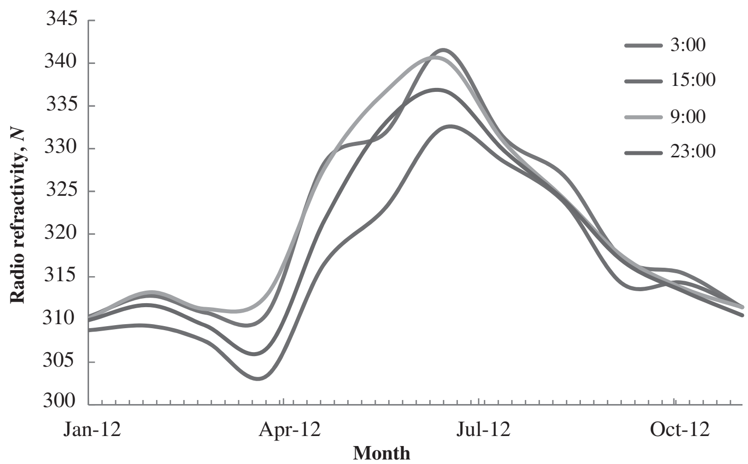

Figure 2: The N-values in Vilnius in different months of the year 2012 at different times of the day.

4. CONCLUSIONS

The testing and analysis of the new model, proposed in the paper, show that it is applicable for calculations of the radio refractivity with good accuracy, when the requirement of correct primary parameters is satisfied. The average monthly relative humidity values should be calculated separately for day-time and night-time hours, due to the large daily fluctuations in relative humidity in July. The correct calculation of the N during the warm season of year is more complicated than in the cold season.

REFERENCES

1. Adeyemi, B., "Surface water vapor density and tropospheric radio refractivity linkage over three stations in Nigeria," *Journal of Atmospheric and Solar-Terrestrial Physics*, Vol. 68, 1105–1115, 2006.
2. Ali, S., S. A. Malik, K. S. Alimgeer, S. A. Khan, and R. L. Ali, "Statistical estimation of tropospheric radio refractivity derived from 10 years meteorological data," *Journal of Atmospheric and Solar-Terrestrial Physics*, Vol. 77, 96–103, 2012.
3. "The radio refractive index; its formula and refractivity data," *Recommendation ITU-R*, 453-9, 2003.

4. Freeman, R. L., *Radio System Design for Telecommunications*, Wiley-Interscience, New York, 2007.
5. Zilinskas, M., M. Tamosiunaite, M. Tamosiuniene, E. Valma, and S. Tamosiunas, "Gradient of radio refractivity in troposphere," *PIERS Proceedings*, 603–607, Moscow, Russia, August 19–23, 2012.
6. Tamosiunaite, M., M. Zilinskas, M. Tamosiuniene, and S. Tamosiunas, "Atmospheric attenuation due to humidity," *Electromagnetic Waves*, V. Zhurbenko, Ed., Chapter 8, 157–172, InTech, 2011.
7. Olasoji, Y. O. and M. O. Kolawole, "Seasonal effect on atmospheric refractivity in diverse terrains," *Journal of Environmental Science and Engineering*, Vol. 5, 1537–1541, 2011.
8. Google Maps, maps.google.lt.
9. Reliable prognosis, www.rp5.lt.
10. Li, J., L. Guo, L. Lin, Y. Zhao, Z. Zhao, T. Shu, and H. Han, "A dual-frequency method of eliminating liquid water radiation to remotely sense cloudy atmosphere by ground based microwave radiometer," *Progress In Electromagnetics Research*, Vol. 138, 629–645, 2013.

HEMS with Wireless Power Transmission and Energy Harvesting

Takashi Yoshikawa
Kinki University Technical College, Kasugaoka, Nabari, Mie 518-0459, Japan

Abstract— HEMS (Home Energy Management System) is the most important technology for saving energy. Because conventional HEMS is always mounted into wall of the house so can't satisfy the location free situation, HEMS is not spreading into the public life. Then I propose the novel concept of HEMS which is based on the sensor network technology. Sensor network nodes can be moved everywhere at anytime. This system is characterized as the free from communication wire. But its power source is battery. So we have to change the battery frequently. So as to get rid of the maintenance of changing battery, I introduce the energy harvesting into sensor network nodes. Room illumination and the temperature difference between human body and room atmosphere are regarded as the circumference energy resources. And we can get such energy by using Solar cell and Peltier element. We have to get more than 100 μW power as the average of consumption power of sensor network node by energy harvesting (room illumination and the difference of temperature). Then I've examined the amount of power. Account for room illumination, 100 μW can be obtained under the condition of 200 lx. And account for the difference of temperature, 20 μW can be obtained under the temperature. Considering room condition, the room illumination does not always exist for every room, and the difference of temperature always exist. But 20 μW is not enough for the system. Then I've tried to add the extra energy for using magnetic resonance typed wireless power transmission. The target specification for it is transmitting distance is more than 1 m and transmitting loss is more than 0.1% and the diameter of receiving coil must be less than 10 cm for realizing practical HEMS. In this paper we present the calculation result for satisfying the target specification for using different size coils (transmitting coil is very large and receiving coil is very small).

1. INTRODUCTION

In recent days, the demand for saving energy consumption is increasing steadily. HEMS (Home Energy Management System) is expected as one of the promising technologies to satisfy the demand. But it is now introduced only by few people, not spreading into the majority.

The reasons are considered that the initial cost of HEMS equipment is very high and they are not movable, besides the fact that many people are not interested in saving energy. Thus, we have proposed to introduce a sensor network system into HEMS. We have planned to equip the energy harvesting function into the sensor network nodes in order to get rid of batteries and AC power supply cables, where the energy harvesting is defined as the technology that uses the environment energy such as light, heat, vibration and so on.

But the problem is that those energies do not exist stably in real life. Hence, we consider the wireless power transmission is the best way to get the energy into the sensor network nodes because it is an anytime chargeable technology with no wire. Then we have studied the Resonant-type Wireless Power Transmission applying for HEMS as the technology for transmitting comparatively high power in the middle range.

The Resonant-type Wireless Power Transmission is proposed by Prof. André Kurs (MIT) in 2007 [1]. In that paper the conceptual calculation using coupling mode theory is described but practical detailed calculation is not described.

After that the design method is proposed by Prof. Ikuo Awai (Ryukoku University in Japan) based on filter theory in 2010 [2]. These theoretical approaches are complete but they are difficult to calculate using direct parameter as coil form and so on. Then we have derived the formula of transmitting efficiency by equivalent circuit in 2011[3]. And we have proposed the way of introducing wireless power transmission into HEMS in that paper. We have focused that power transmitting distance can be mere than 1 m. We have performed this aim by adding repeating coil between the transmitting coil and the receiving coil [4]. But this way has the difficulty of arrangement. Then we have tried to calculate other two ways for that. One is to use the spiral coil and the other is the way of using large coil for transmitter and small coil for receiver [5]. Ive describe all of the consideration mentioned above in this paper.

2. HEMS FOR ENERGY HARVESTING

We aim at wireless HMES by using sensor network node having energy harvesting power supplier. The work what to attain that is to clarify the consumption power for sensor network nodes and to consider how to get the power by using energy harvesting.

At first we have examined the energy consumption for sensor network node. We have made the prototype (Fig. 1) of sensor network node for HEMS and experiment the consumption power for each element as sensor, RFIC, MPU.

There are many kinds of HEMS (Table 1), for example, only monitoring HEMS or monitoring and controlling apparatus HEMS. The consumption energy is various for each HEMS. Then we have categorized HEMS and examined the consumption energy for each HEMS. The results are shown in Table 2.

Table 2 shows the average value of the consumption power because the sensor nodes work with sleep mode.

Figure 1: Prototype photograph of sensor network node.

Table 1: HEMS category.

	Model 1	**Model 2**	**Model 3**
Type	Monitoring	Monitoring	Monitoring
Sensor	Basic (Temp., Humidity, Illumination)	Basic Sensor Power Meter Motion	Basic Sensor Vital Sensor
Location	Fixed	Fixed	Movable
	Model 4	**Model 5**	**Model 6**
Type	Controlling	controlling	Controlling
Sensor	Basic Sensor Power Meter Motion Sensor	Basic Sensor Vital Sensor	Basic Sensor Power Meter Motion Sensor
Location	Fixed	Movable	Fixed

Table 2: Consumption power for HEMS.

Model	Power(mW)	T(ms)	1	2	3	4	5		6	
Sleep	4.50E-03	–								
Comm.	42	3								
RF	22.5	30								
Temp. Sens.	22.5	1	○	○	○	○	○	○	○	○
Moist. Sens.	0.073	8000		○	○	○	○			
Illumi. Sens.	22.5	1	○	○	○	○	○	○	○	○
Motion Sens.	0.002	–	○	○		○	○		○	Location
Door Sens.	22.5	1	○	○		○	○		○	
Acc. Sens.	21.6	1000						○		○
Vital Sens.	10.1	1000			○			○		○
Used Pow Mon	43.5	10		○		○	○		○	
Control	200	24				○	○		○	
Comm times			1	1	1	2	2	3	2	30
Moni./Ctrl			Moni.	Moni.	Moni.	Ctrl.	Ctrl	Moni.	Ctrl	Moni.
Fix/Mov.			Fix	Fix	Mov.	Fix	Fix	Mov.	Fix	Mov.
Duty (min)			30	10	30	10	10	30	3	30
Ave. used Pow (μm)			6.98	9.65	10.91	18.98	18.98	23.47	48.10	35.49

Moreover considering to the converting energy for charge and discharge and power conditioning, the demanded power from the harvesting energy is estimated as 100 μW in the region of Model 4 and Model 5 HEMS.

Next we have examined harvesting energy to supply for the consumption energy. There are many kinds of harvesting energy in the environment of the house, for example illumination light, heat, vibration, and so on. Referring to the living environment, harvesting energy is estimated as following. Illumination light energy is estimated as 35 μW, thermal energy is estimated as 35 μW, and vibration energy is estimated as 60 μW respectively (Table 3).

Table 3: Harvesting energy in living environment.

	Generated power	Duty	Average Power
Illumination	320 μm	11%	35 μm
Thermal	35 μm	100%	35 μm
Vibration	3 mW	2%	60 μm

As the results, it is impossible that only one kind of harvesting energy can supply full consuming energy. In that reason wireless power transmission is the most useful for this application.

3. WIRELESS POWER TRANSMISSION FOR HEMS

3.1. Resonant-type Wireless Power Transmission

Since validity of the resonant-type wireless power transmission was reported by MIT [1] in 2007, many researchers have started the study on the relating technologies. This technology is expected to transmit higher power for larger distance than the conventional technology that can transmit by less than few mm or cm by electromagnetic induction. We have studied to introduce a resonant-type wireless power transmission into HEMS. Our aim is to ensure the feasibility of a practical HEMS system. To attain it, we have measured the power transmitting characteristics in the case of 100 [mm] diameter coil for the practical HEMS. The measurement system is drawn in Fig. 2 and its picture is shown in Fig. 3.

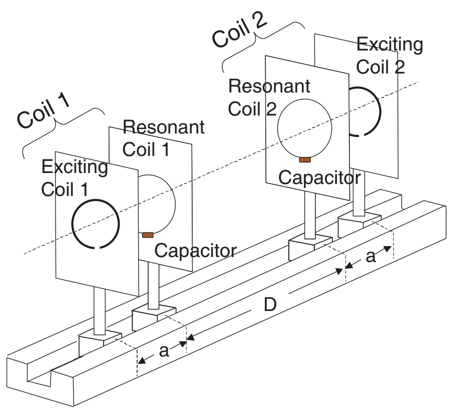

Figure 2: Resonant-type WPT measurement system.

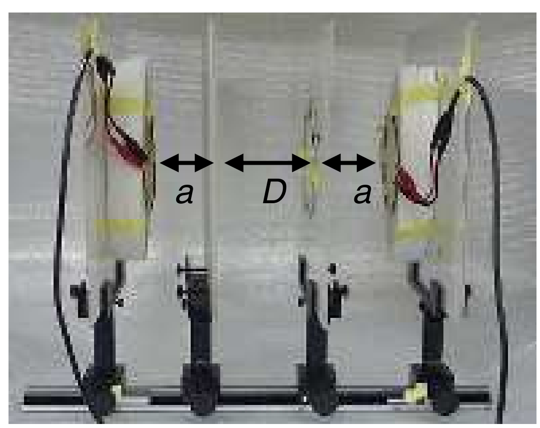

Figure 3: Photograph of measurement system.

This system consists of four coils, that is, two resonant coils and two exciting coils. The resonant coils are 100 mm diameter loops by $\phi 1.6$ wire with 220 [pF] mica capacitor at the loop end. The two resonant coils make a reciprocal transmitter and receiver located with the distance D.

And the exciting coils are adjusted by distance a to attain the circuit matching based on the band pass filter theory [2]. Measurement is performed for various distance $D = 0.0\,5$m, 0.1 m, 0.15 m, 0.2 m by sliding the coil along to the optical stage. Measurement of transmitting efficiency S_{21} follows the procedure below. (Detail is shown in Ref. [6]) On the other hand, We have derived the equation (1) for calculating transmitting efficiency S_{21} using equivalent circuit in Fig. 4. Calculating result and experimental result are shown in Fig. 5 and Fig. 6. Those results are in good agreement.

$$S_{21} = \frac{-2j\omega^3\sqrt{Z_{01}Z_{02}}MM_1M_2(Z_1Z_2+\omega^2M^2)}{\left[\begin{array}{l}\{(Z_{01}+j\omega L_0+R_0)(Z_1Z_2+\omega^2M^2)+\omega^2M_1^2Z_2\} \\ \{(Z_{02}+j\omega L_0+R_0)(Z_1Z_2+\omega^2M^2)+\omega^2M_2^2Z_1\}+\omega^6M^2M_1^2M_2^2\end{array}\right]} \tag{1}$$

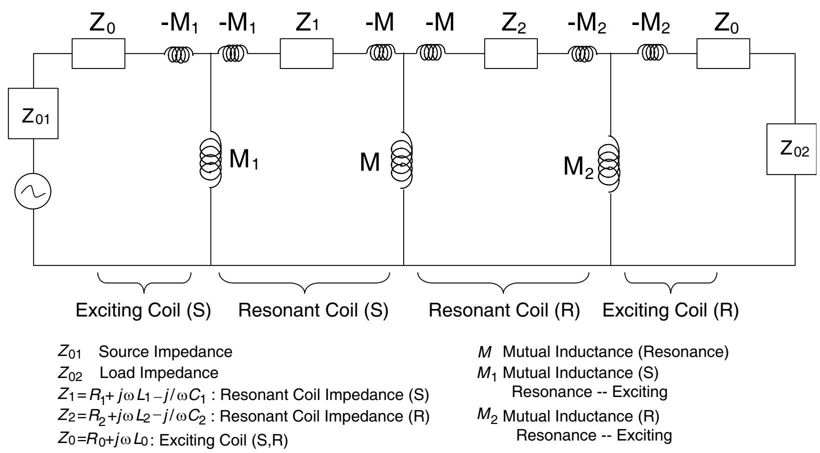

Figure 4: Equivalent circuit of resonant-type WPT.

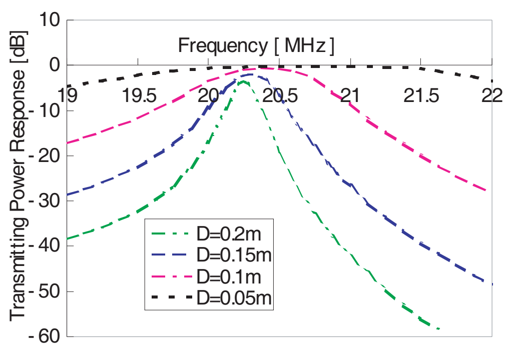

Figure 5: Measured transmitting characteristics.

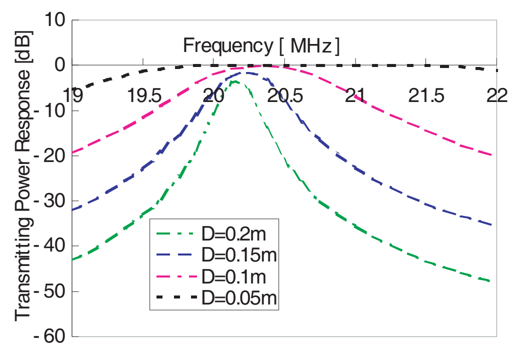

Figure 6: Calculated transmitting characteristics.

3.2. Introducing Extra Resonance Coil

As we have confirmed the validity of our calculation method, we calculated the transmitting efficiency accounting for the farther distance transmission with the equivalent circuit method. The result is shown in Fig. 7. Referring to practical use of HEMS, transmitting distance must be more than 1 [m]. Fig. 7 shows the transmitting efficiency is drastically reduced according to the distance. Then two resonance coils are insufficient. Considering the use of HEMS, one or two extra resonant coil (repeating coil) must be inserted between initial two resonant coils [6], and showing the calculated results in Fig. 8.

3.3. Various Coil Shape

We have shown the validity of introducing extra coils, but system is complex because this way needs many resonant coils and we have to adjust the location of those coils. So we have considered the effect of various coil shape. In addition to the equivalent circuit method, we have set to calculate with numerical code WIPL-D, which is a 3D electro magnetic moment method calculation package, so the problems containing complex shape can be solved. The transmitting efficiency up to 1 [m] for various shape coils is calculated using numerical code WIPL-D shown in Fig. 9. Fig. 9 shows the transmitting efficiency for spiral coil (Fig. 10) and square and circular loop coils as the resonant coil for the longest side of each coil is 0.1 [m]. The resonant frequency for each coil is adjusted at around 22 MHz equipping with suitable capacitor. Transmitting distance is extended over 1 [m] under HEMS condition (Transmitting efficiency is larger than 0.13%) in use of spiral coil.

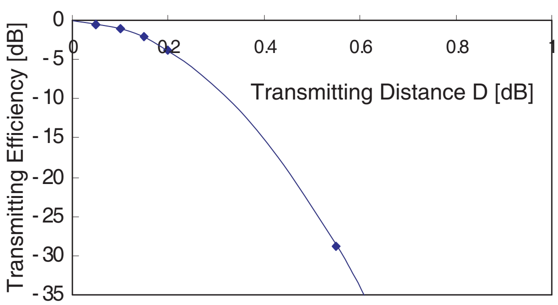

Figure 7: Farther transmitting calculation.

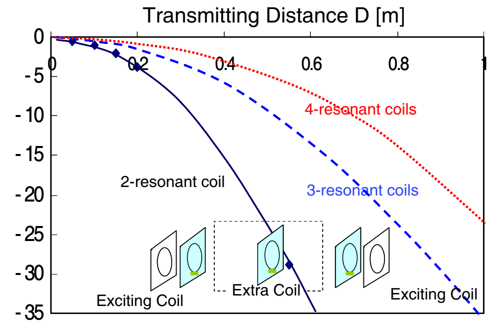

Figure 8: Transmitting characteristics in the case of inserting extra resonant coils.

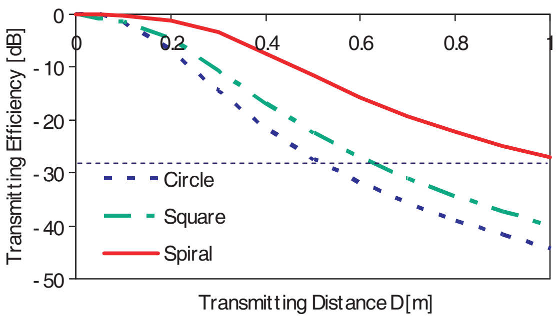

Figure 9: Transmitting efficiency of spiral coil.

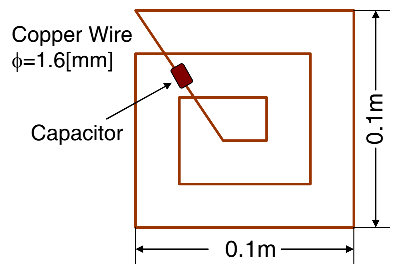

Figure 10: Configuration of the spiral coil.

3.4. Various Size Coils

The idea occurred to us if we use much larger transmitting coil comparing with receiving coil the magnetic flux divergence can be reduced at further distance between their coils. Then we have modeled ten times larger transmitting coil (1 m diameter) than small one (Fig. 11). This model is harmonized well with HEMS. Because smaller receiving coil is usually located at less than 2 m from the floor, we only mount the larger transmitting coil under the floor. The calculated result with WIPL-D is shown in Fig. 12.

We can get very good result in Fig. 12. The way for various size coils shows more than 7 dB larger transmitting efficiency at 1 m than other ways. Furthermore we have calculated the extension where transmitting loss is less than 30 dB. The distance is 1.9 [m] at the center of the large coil and 1.8 [m] above the circle of the large coil.

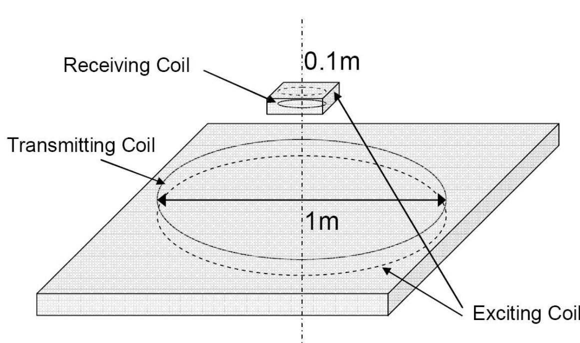

Figure 11: Various coil arrangements.

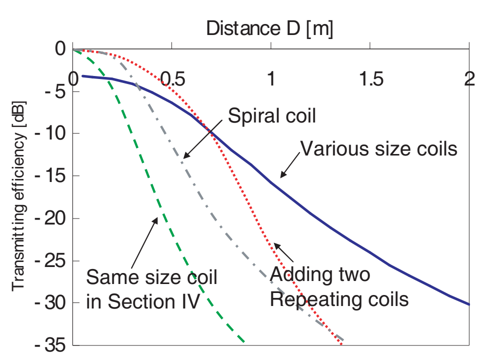

Figure 12: Transmitting efficiency for various coil arrangements.

4. CONCLUSION

We study the way for the no wire HEMS. The most important technology is regarded as wireless power transmission so as to supply the consumption power into sensor network nodes wirelessly.

Then we have considered the vest way of the coil shape and coil arrangement in the case of using resonance-typed wireless power transmission. The way of repeating coil, various shape coils, various size (10 times) coil is considered. As the result, the transmitting efficiency at the way of various size coils is largest than the other ways, arriving at -15 dB far over the efficiency satisfying HEMS condition as -30 dB. Moreover this way is suitable for HEMS at the view point of coil arrangement. We have concluded the way of various size coils is most practical way for HEMS.

REFERENCES

1. Kurs, A., A. Karalis, R. Moffatt, J. D. Joannopoulos, P. Fisher, and M. Soljai, "Wireless power transfer via strongly coupled magnetic resonances," *Science*, Vol. 317, No. 5834, 83–86, 2007.
2. Awai, I., "Analysis of resonant-type wireless power transmission by BPF theory," *IEICE Technical Report*, AP-2009-169, 81–86, Dec. 2009; *General Conference Proceedings*, BS-9-6, Mar. 2010.
3. Yoshikawa, T. and I. Awai, "HEMS with resonant-type wireless power transmission," *IMWS-IWPT9-1 Proceedings*, 167–170, Mar. 13, 2011.
4. Yoshikawa, T. and I. Awai, "A novel design for HEMS consisting of sensor network nodes with energy harvesting and wireless power transmission," *AIEM*, Vol. 2, No. 1, 11–15, 2012.
5. Yoshikawa, T. and S. Saraya, "HEMS assisted by a sensor network having an efficient wireless power supply," *IEEE Trans. on Magnetics*, Vol. 49, No. 3, 974–977, 2012.
6. Komori, T. and I. Awai, "A simple design for resonant-type wireless power-transmission system," *2010 IEICE General Conference Proceedings*, BS-9-8, Mar. 2010.

A New CPW-fed Circularly Polarized Square Slot Antenna Design with Inverted-L Grounded Strips for Wireless Applications

Erol Karaca and Mesut Kartal
Istanbul Technical University, Maslak, İstanbul 34469, Turkey

Abstract— This paper presents a new Circularly polarized square slot antenna (CPSSA) with a coplanar wave guide (CPW) feed. The proposed antenna contains inverted-L Grounded strips around the corners. Circular polarization mechanism is related with the L-shaped strips, vertical staircase shaped feed line extension and the thin tuning strip. Compared to most of the previously reported CPSSA structures, the axial ratio bandwidth is increased and also the size of the antenna becomes smaller. The presented compact antenna has $40 \times 40 \times 0.8\,\text{mm}^3$ dimensions. The operation bandwidth for VSWR < 2 is from 3.45 to 8.59 GHz and exhibits a 53.67% (4.73–8.20 GHz) 3 dB Axial ratio bandwidth. Throughout this letter, the improvement process of the axial ratio (AR) and S_{11} properties are discussed in detail.

1. INTRODUCTION

In the past few years, rapid development in wireless communication brings need for high data rate and multimedia applications. Antenna design topic takes attention as presented different designs in [1–15]. Communication systems require integrated antennas of low cost, compact size and broadband support with low profile [2]. In all antenna classifications circularly polarized (CP) antennas, because of reducing polarization mismatch and multipath fading, becomes the most desirable antenna type [11]. Coplanar waveguide is advantageous for providing just a single metallic layer, wide bandwidth, easy integration with solid-state active devices and small mutual coupling between two adjust lines [9].

Table 1: Comparison of characteristics of some CPSS antennas reported with the proposed antenna in this paper.

	BW (VSWR < 2) (MHz)	Total BW (VSWR < 2) (MHz)	BW (AR < 3 dB) (MHz)	Total BW (AR < 3 dB) (MHz)	3 dB AR %	Dim. (mm)
Ref. [1]	2681–6381	3700	3000–6100	3100	71.11%	40×40×0.8
Ref. [2]	2000–7071	5071	2030–5120	3090	86.4%	60×60×0.8
Ref. [3]	1600–3055	1455	2300–3030	730	27.4%	60×60×0.8
Ref. [4]	2023–3421	1398	2075–3415	1340	48.8%	60×60×0.8
Ref. [5]	2671–13000	10329	4900–6900	2000	32.2%	60×60×0.8
Ref. [6]	1575–1600; 1900–2200	325			8.4%; 19.24%	70×70×1.6
Ref. [7]	865				18%	70×70×1.6
Ref. [8]	1420–2559	1139	1739–2437	698	33.4%	60×60×1.6
Ref. [9]	1604–2450	846	1840–2080	240	12.4%	70×70×1.6
Ref. [10]	2041–3159	1118	2200–2600	400	17%	100×100×1.6
Ref. [11]	1960–3260; 3610–6980; 7870–11240	8040	4600–6100	1500	28.03%	40×40×0.8
Ref. [12]	1890–2690; 4040–6750; 7830–11520	7810	2112–3056; 5292–5837	1489	36%; 9%	40×40×0.8
Ref. [13]	1772–2591	819	1880–2560	680	30.6%	100×100×1.6
Ref. [14]	1800–4500	2700	2250–3750	1500	50%	$R = 31$; $r = 22$; $h = 3$
Ant 3	3450–8590	5140	4730–8200	3470	53.67%	40×40×0.8

Designs with various patch shapes and different feed lines have been presented to increase both impedance bandwidth and axial ratio bandwidth in [1–15]. The structures are presented with their characteristics and dimensions in Table 1. Most of the previously reported antennas have large sizes or have either narrow impedance bandwidth or 3 dB axial ratio bandwidth. Three inverted L shaped strips are used in different corners to have circular polarization similarly to this design in [1, 2]. 2 L shaped strips on the cross corners are used in [3–5]. In [4], a lightning shaped feed line structure is used to both increase impedance bandwidth and AR bandwidth. Embedding two spiral slots in order to create current circulation for circular polarization is also presented in [6]. In [7], protruding a T shaped strip perpendicularly to the feed line, thin prolongation makes the antenna operates with CP. Also in a different design, two E shaped slits in opposite corners of the ground plane are designed to have CP [8]. A cross patch inclined diagonally placed at the center of the square slot presented in [9]. In [10], widened L-type strip along the diagonal line of the square slot is researched. In [11], 2 T shaped and 1 F shaped strips are implemented. Fork shaped feed line and rectangular indentations are used to perform circular polarization mechanism in [12]. On the other hand, asymmetric CPW feed line from a corner of the slot is presented in [13]. Differently, in [14] a hexagonal slot is designed with 2 L-Shaped strips grounded at cross corners. In [15], a monopole type antenna is presented, this reference do not show circular polarization but inspires the other designs for the feed line structures.

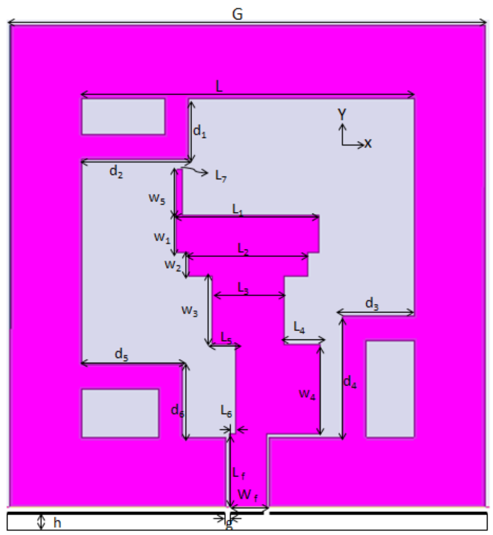

Figure 1: Geometry of the proposed CP antenna (units are in millimeters). $G = 40$, $L = 28$, $L_1 = 12$, $L_2 = 10$, $L_3 = 6$, $L_4 = 3.1$, $L_5 = 2$, $L_6 = 0.55$, $L_7 = 0.5$, $L_f = 6.3$, $W_1 = 3$, $W_2 = 2$, $W_3 = 5.6$, $W_4 = 7.4$, $W_5 = 3.8$, $W_f = 3.1$, $d_1 = 5$, $d_2 =9$, $d_3 = 6$, $d_4 = 10$, $d_5 = 8.5$, $d_6 = 6$, $g = 0.3$, $h = 0.8$.

In this paper, our purpose is to design a circularly polarized square slot antenna (CPSSA) for broadband systems where the CP bandwidth refers to the frequency range in which both AR¡3 and VSWR < 2 are met. The proposed antenna supports circular polarization from 4.73 to 8.20 GHz exhibiting 53.67% fractional bandwidth. In terms of VSWR < 2 impedance matching, the antenna supports from 3.45 to 8.59 GHz. The proposed antenna is appropriate to show circular polarization capability for IEEE 802.11a (5.15–5.35 GHz and an additional band of 5.725–5.825 GHz), and HiperLAN2 (5.47–5.725 GHz) standards [11].

2. ANTENNA DESIGN AND CONFIGURATION

The proposed single layer circularly polarized square slot antenna geometry is presented in Fig. 1. As can be shown, the antenna consists of a square ground plane with length of G, vertical staircase shaped structure and a thin tuning strip. The antenna is printed on a FR4 dielectric substrate with a thickness of 0.8 mm having tanδ = 0.02 loss tangent and permittivity $\varepsilon_r = 4.4$. Square dimensions are designed to be $G \times G$ ($G = 40$ mm). The antenna is fed by a 50 Ω CPW with a single strip W_f with 3.1 mm width and two identical gaps of width $g = 0.3$ mm. The feed line is terminated with a standard SMA connector. The widths of the L shaped strips were preselected as 2 mm to simplify the antenna design.

Two main purposes are enhancing the impedance bandwidth and axial ratio bandwidth have been analysed in this study. The single strip of the CPW feed line is extended with staircase shaped rectangular extensions and a thin tuning strip. All these parameters (W_1, W_2, W_3, W_4, W_7) and the identical gaps g effects the impedance matching. Additionally, 3 L shaped strips help to enhance impedance matching also in the lower purposed frequency band interval. On the other hand, circular polarization operation simply relates with 3 Inverted L-shape strips grounded in the 3 corners of the square slot. Finally, from the experimental simulation study the thin strip close to the upper left corner L shape strip enhances greatly the axial ratio bandwidth performance.

3. PARAMETRIC STUDY OF THE ANTENNA

By using Ansoft HFSS software, optimized parameters are investigated for the good performance with extensive simulation process. As can be seen in Fig. 2, 4 prototypes of the antenna are defined. In Ant 0, the structure contains only a rectangular patch. Ant 1 includes staircase shaped rectangular extensions to the feed line. In Ant 2, 3 L shaped strips are grounded at 3 corners. Finally in Ant 3, a thin tuning strip having 0.5 mm width and 3.8 mm length is added to the left upper side staircase shaped extensions of the feed line.

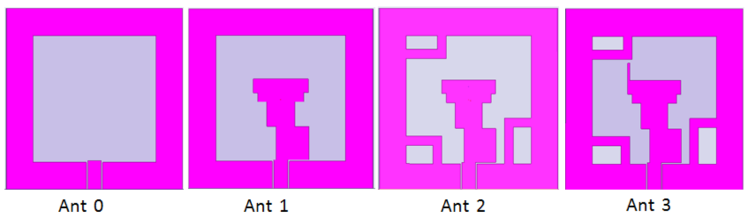

Figure 2: Four improved prototypes of the antenna.

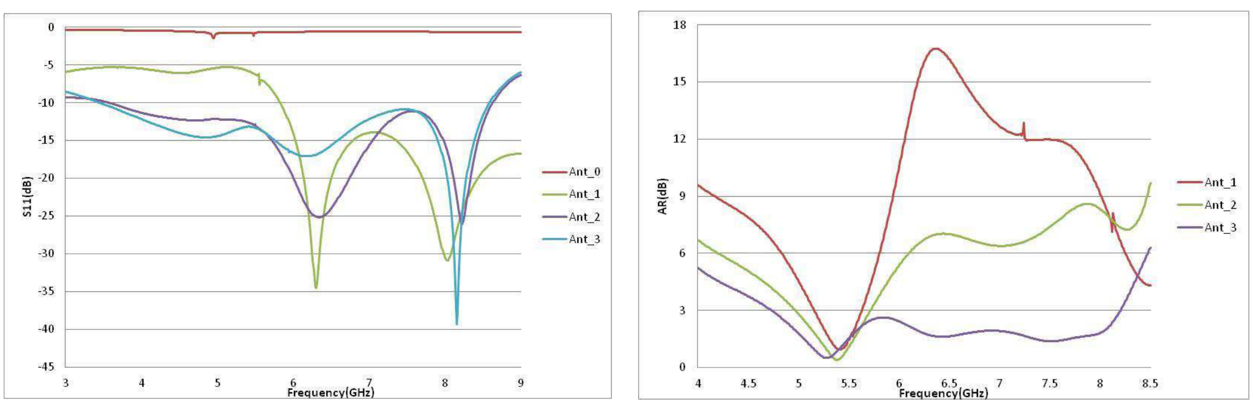

Figure 3: Simulated S_{11} and 3 dB axial ratio bandwidth for the Ant 0 to 3.

The simulated results of the S_{11} and 3 dB axial ratio bandwidths of the 4 prototype antennas are shown in Fig. 3. As can be seen from the S_{11} graph, adding the staircase rectangular extensions to the feed line, Ant 1 achieves impedance matching by showing S_{11} under -10 dB for the frequencies between 5.83 GHz to 9.00 GHz. In Ant 2, 3 L shaped strips are in conjunction with the extended feed line structure of Ant 2 supplies S_{11} from 3.57 to 8.63 GHz. Finally in Ant 3, the tuning strip enhances the impedance bandwidth by increasing the coupling with the feed line extension with the left top corner L shaped strip line. On the other hand, as compared the antennas in ARBW performance, Ant 1 shows AR < 3 dB in a small band between 5.16 and 5.62 GHz. However, Ant 1 does not support impedance matching at this band. In Ant 2, with the effect of 3 L-shaped strips ARBW performance enhanced the frequency band between 4.97 and 5.71 GHz. However in Ant 2, in the ARBW frequency interval, impedance matching is also supported. So as a result, in a frequency band in which AR < 3 dB condition is met, may not satisfy the impedance matching in the same frequency band and vice versa. In Antenna 3, the tuning strips effects the surface current distribution in the structure in a way to show CP characteristics in a wide frequency band from 4.73 to 8.20 GHz. Impedance matching is also supported for this band for Ant 3. Characteristics of the 3 improved antennas are summarized in Table 2.

Table 2: Summary of simulated characteristics of the three improved antennas ($W_f = 3.1$, $g = 0.3$, $h = 0.8$, $G = 40$, $L = 28$, $L_1 = 12$, $L_2 = 10$, $L_3 = 6$, $L_4 = 3.1$, $L_5 = 2$, $L_6 = 0.55$, $W_1 = 3$, $W_2 = 2$, $W_3 = 5.6$, $W_4 = 7.4$).

	$d1$	$d2$	$d3$	$d4$	$d5$	$d6$	$w5$	$l7$	BW (VSWR < 2)	3 dB ARBW
Ant 1	0	0	0	0	0	0	0	0	5830–9000	5160–5620
Ant 2	5	9	6	10	8.5	6	0	0	3570–8630	4970–5710
Ant 3	5	9	6	10	8.5	6	3.8	0.5	3450–8590	4730–8200

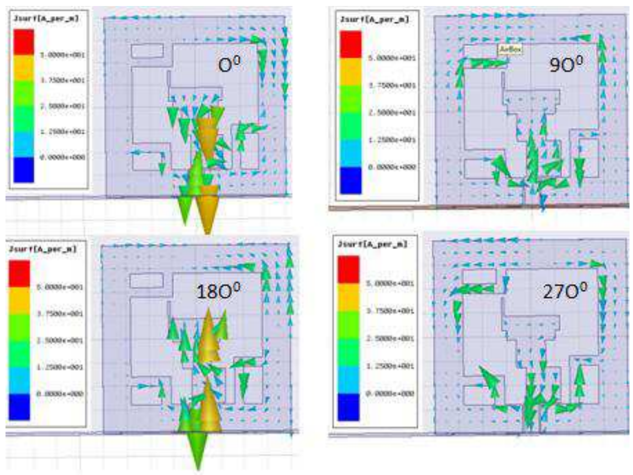

Figure 4: Surface current distribution at 5.2 GHz.

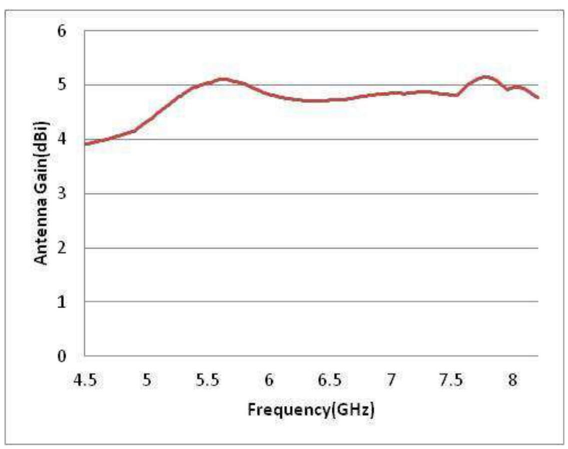

Figure 5: Simulated gain distribution of Ant 3.

Time-varying surface current distribution for Ant 3 at 5.2 GHz is simulated and the results can be seen at Fig. 4. As expected for the CP characteristic, the surface current distribution in 180° and 270° are equal in magnitude and in opposite direction as compared with the surface current distribution in 0° and 90° respectively. Right hand circular polarization (RHCP) can be radiated if the current rotates in clockwise direction. On the other hand, the simulated peak gain for Ant 3 between the frequencies 4.73 and 8.20 GHz where both ARBW< 3 dB and $S_{11} < -10$ dB conditions are met, as can be seen in Fig 5. The simulated radiation pattern graphs at 5.2, 5.6 and 5.77 GHz frequencies can be seen in Fig. 6. The radiation pattern is right hand polarization (RHCP) for $Z > 0$ and left hand polarization (LHCP) for $Z < 0$.

Compared to the previously reported circularly polarized square slot antenna (CPSSA) structures, the proposed antenna is smaller than [2–10] and same dimensions with [1, 11, 12] references. It is so interesting that the proposed antenna shows circular polarization (3 dB axial ratio bandwidth) at totally 3470 MHz bandwidth. The obtained result is wider than the reference antennas from [1] to [15]. This is also better than the [1–4] having similar CP design technique, in total

3dB Axial Ratio bandwidth. In the meaning of VSWR¡2 radiation bandwidth, the antenna supports a wider bandwidth then [1–4, 6–10, 12–15] references. However, [5, 11] references show wider impedance matching than the proposed antenna. Compact size brings advantage to be used in mobile terminals for Wi-Fi Applications.

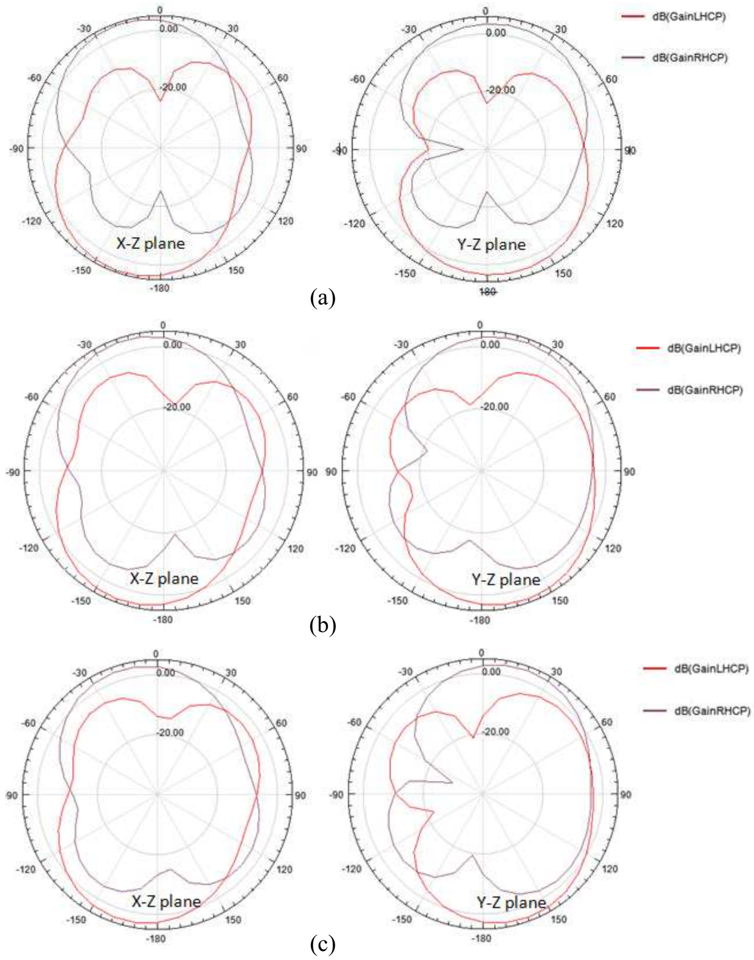

Figure 6: Simulated radiation pattern of the proposed antenna at frequencies (a) 5.2 GHz, (b) 5.6 GHz, (c) 5.77 GHz.

4. CONCLUSION

A new circularly polarized square slot antenna has been presented with this study. It proposes a compact structure having dimensions of $40 \times 40 \times 0.8\,\text{mm}^3$. The proposed structure shows impedance bandwidth between 3.45 GHz and 8.59 GHz, also supports CP characteristic as 53.67% (4.73–8.20 GHz) fractional bandwidth. The simulation results show that when L shaped strips, staircase shaped and the thin tuning strip feed line extensions are used, both impedance bandwidth and 3 dB axial ratio bandwidths can be increased. The thin tuning strip has effectively widened the 3 dB axial ratio bandwidth, in addition to slightly increase the impedance bandwidth. The maximum gain of the antenna is also high enough in the desired bandwidth. As a result of these properties, the proposed antenna is to be deployed in wireless technology supported devices.

REFERENCES

1. Rezaieh, S. A. and M. Kartal, "Broadband CPW-fed circularly polarized square slot antenna with inverted-L strips for wireless applications," *Microwave and Optical Technology Letters,* Vol. 54, No. 6, 1399–1402, Jun. 2012.
2. Felegari, N., J. Nourinia, C. Ghobadi, and J. Pourahmadazar, "Broadband CPW-fed circularly polarized square slot antenna with inverted-L shape grounded strips," *IEEE Antennas and Wireless Propogation Letters,* Vol. 10, 274–277, 2011.

3. Size, J. Y. and C. C. Chang, "Circularly polarized square slot antenna with a pair of inverted-L grounded strips," *IEEE Antennas and Wireless Propogation Letters,* Vol. 7, 149–151, 2008.
4. Size, J. Y., C. I. G. Hsu, Z. W. Chen, and C. C. Chang, "Broadband CPW-fed circularly polarized square slot antenna with lightening-shaped feedline and inverted-L grounded strips," *IEEE Transactions on Antennas and Propogation,* Vol. 58, No. 3, 973–977, Mar. 2010.
5. Pourahmadazar, J., C. Ghobadi, J. Nourinia, N. Felegari, and H. Shirzad, "Broadband CPW-fed circularly polarized square slot antenna with inverted-L strips for UWB applications," *IEEE Antennas and Wireless Propogation Letters,* Vol. 10, 369–372, 2011.
6. Chen, C. and E. K. N. Yung, "Dual-band dual-sense circularly-polarized CPW-fed slot antenna with two spiral slots loaded," *IEEE Transactions on Antennas and Propogation,* Vol. 57, No. 6, 1829–1833, Jun. 2009.
7. Size, J. Y., K. L. Wong, and C. C. Huang, "Coplanar waveguide-fed square slot antenna for broadband circularly polarized radiation," *IEEE Transactions on Antennas and Propogation,* Vol. 51, No. 8, 2141–2144, Aug. 2003.
8. Du, S. and Q. X. Chu, "A CPW-fed broadband circularly-polarized square slot antenna with E-shaped slits in ground plane," *Proceedings of the 39th European Microwave Conference,* Rome, Italy, Oct. 2009.
9. Chou, C. C., K. H. Lin, and H. L. Su, "Broadband circularly polarised crosspatch-loaded square slot antenna," *Electronics Letters,* Vol. 43, No. 9, Apr. 2007.
10. Chen, Y. B., X. F. Liu, Y. C. Jiao, and F. S. Zhang, "CPW-fed broadband circularly polarised square slot antenna," *Electronics Letters,* Vol. 42, No. 19, Sep. 2006.
11. Rezaieh, S. A. and M. Kartal, "A new triple band circularly polarized square slot antenna design with crooked T and F-shape strips for wireless applications," *Progress In Electromagnetics Research,* Vol. 121, 1–18, Oct. 2011.
12. Rezaieh, S. A., M. Abbak, and I. Akduman, "A circularly polarized square slot antenna for wireless applications," *19th Telecommunications Forum TELFOR 2011*, Belgrade, Serbia, Nov. 2011.
13. Size, J. Y., J. C. Wang, and C. C. Chang, "Axial-ratio bandwidth enhancement of asymmetric-CPW-fed circularly-polarised square slot antenna," *Electronics Letters,* Vol. 44, No. 18, Aug. 2008.
14. Zhou, S. W., P. H. Li, Y. Wang, W. H. Feng, and Z. Q. Liu, "A CPW-fed broadband circularly polarized regular-hexagonal slot antenna with L-shape monopole," *IEEE Antennas and Wireless Propogation Letters,* Vol. 10, 1182–1185, 2011.
15. Chen, H. D. and H. T. Chen, "A CPW-fed dual-frequency monopole antenna," *IEEE Transactions on Antennas and Propogation,* Vol. 52, No. 4, 978–982, Apr. 2004.

Investigation of Preliminary Breakdown Pulses in Lightning Waveforms

Kamyar Mehranzamir, Behnam Salimi, and Zulkurnain Abdul-Malek
Institute of High Voltage and High Current (IVAT), Faculty of Electrical Engineering
Universiti Teknologi Malaysia (UTM), Johor Bahru, Malaysia

Abstract— The cloud-to-ground lightning contains one or more sporadic discharges. These cloud discharges usually include a pre-starting process which is called the preliminary breakdown (PB) before a leader initiation. These breakdown processes are not well understood because of the stochastic characteristics of the lightning flashes. Several models have been introduced to categorise the lightning waveforms. The BIL model is an early model which has been used to investigate the lightning flashes in different regions from more than 50 years ago till now. This model is closely successful in depicting incipient processes of the cloud-to-ground lightnings. Although the BIL model is useful as a general depiction, the details of the breakdown process differ from study to study and hence it is not completely standardized. In this paper, the preliminary breakdown pulse (PBP) train is analysed in cloud-to-ground (CG) lightning waveforms recorded in Malaysia using a broadband antenna.

1. INTRODUCTION

Cloud to ground lightning is a process which is initiated within the clouds. This process contains changes in the electric field configuration. These discharges eventuate to streamers, leaders and finally to the return strokes (RSs). There are several descriptions for CG lightning process [1–3]. Clarence and Malan [1] introduced the BIL model, the first and simplest description of the processes for South African lightnings. They have reported the characteristic features of preliminary breakdown pulse trains in negative cloud-to-ground flashes. After that several researchers such as Kitagawa and Brook [4], Beasley et al. [5], Brook [6], Cooray and Scuka [7], Cooray and Jayaratne [8] have done several studies on the PB pulse trains. The pulse trains contain the essential information of the electrical breakdown which leads to the return strokes. Therefore the breakdown characteristics could be extracted from the pulse trains. According to the previous studies, the PBP trains vary in different geographical regions. It means the meteorological conditions may have influence on the breakdown process of the lightning. Consequently, there may be a variety in the initial breakdown processes and characteristics in the clouds at the different regions. For this reason, it is important to analyse and compare the features of the pulse trains in different geographical areas. A few studies have been done on the lightning flashes in equatorial regions, therefore more researches are still needed. This research investigates on the characteristics of the lightning waveforms captured in Johor, Malaysia in years 2012 and 2013.

2. LIGHTNING THEORETICAL MODEL

Clarence and Malan defined BIL model, which is the earliest and simplest description of the breakdown processes in a lightning flash. In the BIL model, the flash processes are initiated by three sequential sections. Initial breakdown (B) is the first step which lasts for some milliseconds contains intense electromagnetic radiations. This breakdown section followed by a quiet intermediate stage with little radiations compare with the first stage. The intermediate stage (I) lasts up to several hundred milliseconds which ends with the stepped leaders (L). The stepped leader again radiates more intensive electromagnetic radiations lasting a few milliseconds. The stepped leader stage finally ends with a very intensive return stroke (RS). According to the previous studies [1, 2], the BIL model is quite successful in depicting the discharge processes in the cloud to ground lightning. Although the BIL model is useful as a general description for the lightning characterization, the manner of the breakdown phenomenon differs in the thunderstorms. Therefore the behaviour of the lightning flashes varies from study to study, so it is not completely standardized. In the previous studies, it was assumed the breakdown consists of vertical discharges between a negative charge centre and a lower positive one. There is some dispute whether the BIL model is able to express correctly the breakdown processes in a lightning flash [4, 5]. The BIL model was supported by several researches such as Harris and salman [20], but some researches such as Beasley et al. [5] and Proctor [21] found that the BIL model is not completely fitted to the lightning flashes in some measurements. Makela et al. [10] done another studies on the preliminary breakdown pulses later and they showed that their observations were fitted to the BIL model [13–19].

3. SYSTEM DESCRIPTION AND MEASUREMENTS

The measuring system consists of a parallel plate antenna to capture the vertical component of the electric field, a buffer circuit, a Global Positioning System (GPS) for time synchronising, a digital oscilloscope (Lecroy WaveRunner 400 MHz), and a personal computer (connected to the oscilloscope) for analysing purpose. The setup was installed at a location which was 132 m above the sea level and 30 km away from the Tebrau Straits. Johor is a state located in the southern portion of Peninsular Malaysia which is close to the equator (1.4 N, 103 E) and has a tropical rainforest climate with a monsoon rain season from November until February blowing from the South China Sea. The average annual rainfall is 1778 mm with average temperatures ranging between 25.5 C (78 F) and 27.8 C (82 F) [12–14, 16].

Figure 1 shows the schematic of the installed system for capturing lightning flashes. The buffer circuit was connected between the broadband antenna and the digital oscilloscope using RG58 coaxial cables. The trigger setting of the oscilloscope was such that signals of both polarities could be captured. The sampling rate was set to 50 MS/s with the total length of recorded waveforms being 500 ms. The trigger level was set at between 500 mV and 2 V.

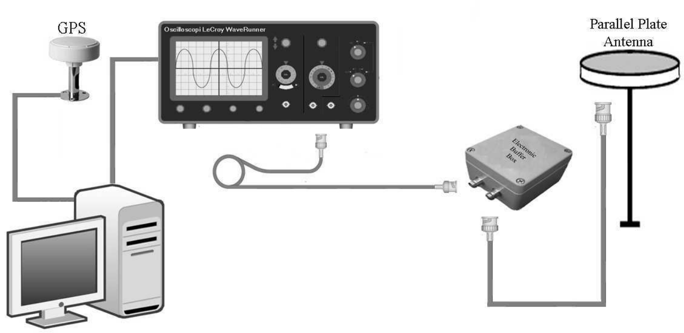

Figure 1: The schematic of the installed system.

4. RESULTS

This study only analyses the PBs which precede the cloud to ground flashes in a certain period. Data collection were started in November 2012 and continued to May 2013. Over 8000 flashes were captured by the broadband antenna. In this paper only the captured flashes in March and April 2013 were investigated.

A total numbers of 2000 flashes were captured during these two months. From the total of 1760 (88%) captured flashes with detectable PB pulse trains in the data set gathered in Malaysia, 1364 (77.5%) recorded flashes were found to be consistent with the BIL model. Figure 2 displays one typical pattern of electric field changes preceding the first negative cloud to ground flash. This lightning flash can be investigated in different aspects. In terms of the pulse train duration, the duration of the breakdown stages to the first return stroke takes around 22 ms. In terms of the

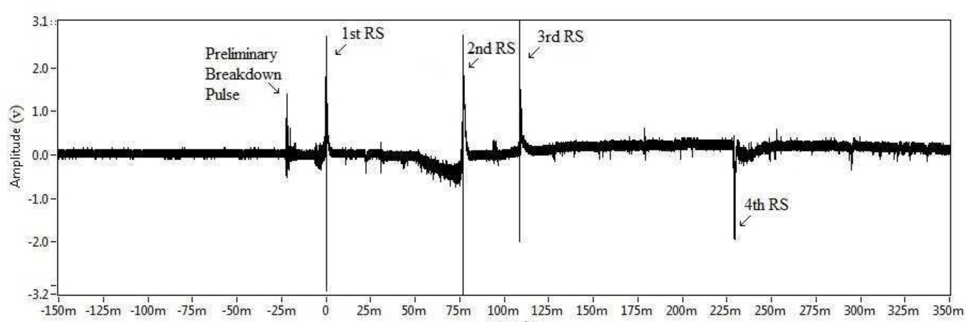

Figure 2: The could to ground lightning flash electric field.

magnitude; the amplitude of the first return stroke is much higher than the maximum point of the PBP train. On the other hand the PBP and the first return stroke have the same polarity but these specifications are not fixed to all the captured flashes due to the stochastic behaviour of the lightning waveforms even in a similar thunderstorm.

The close up of the time frame between the PBP and the first return stroke (RS) is presented in Figure 3. As the BIL stages are clearly specified in Figure 3, this lightning flash is compatible with the BIL model. Around 400 captured flashes were found to have irregular waveforms compared to the BIL model.

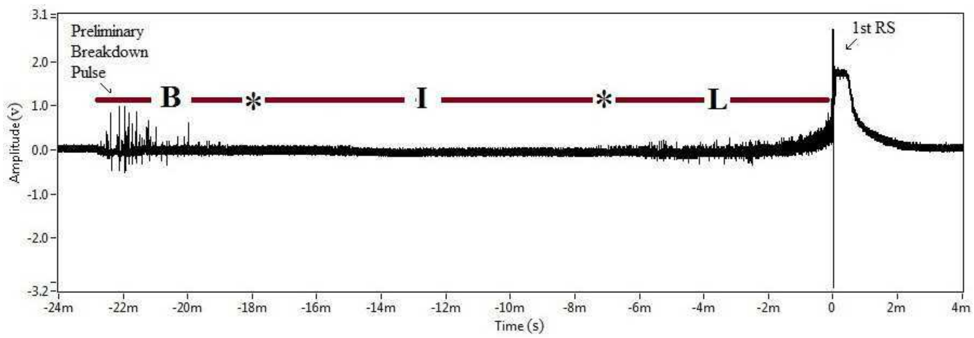

Figure 3: The close up of the preliminary breakdown-first return stroke section in Figure 2.

Figure 4 shows one captured flashes which is not fitted to the BIL model. This type of waveforms may create some confusion in our attempt to investigate the breakdown process of the lightning flashes. The intermediate (I) section has a duration of zero in this waveform. The PBP train duration is near 7 ms. Figure 5 is the close up of time duration between the starting the Preliminary breakdown and the first return stroke. This type of signals are considered as intricate cases. Figure 6 presents the pie chart of the PBP duration according to the captured flashes in Malaysia. It can be concluded from the pie chart, above 50% of the flashes have the pulse train durations between 20–30 ms. These statistics differ from study to study and they also depend more on the geographical region of the lightning measurement.

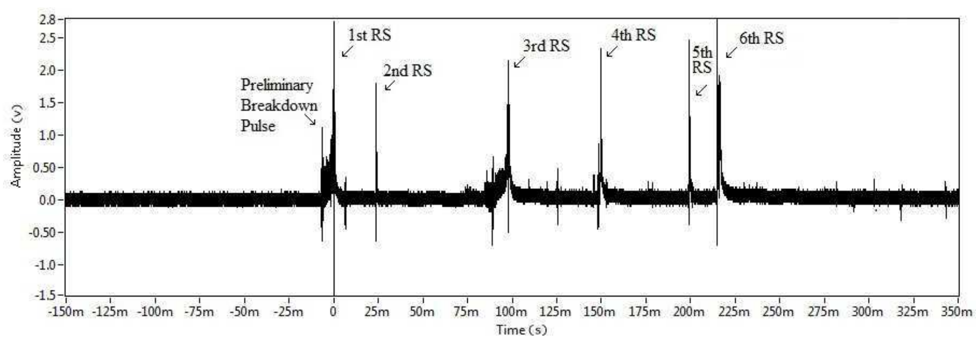

Figure 4: The could to ground lightning flash electric field.

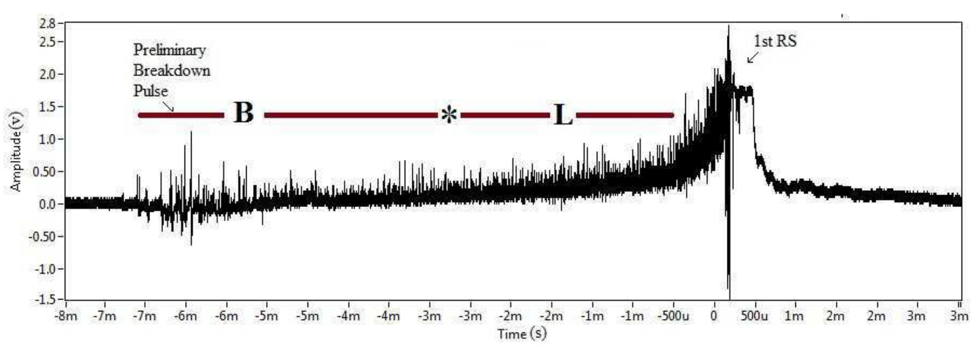

Figure 5: The close up of the preliminary breakdown-first return stroke section in Figure 4.

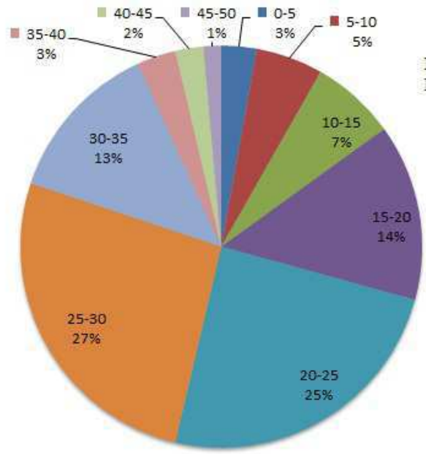

Preliminary Breakdown Pulse (PBP) Duration (ms) and No. of Flashes (%)

0-5	3
5-10	5
10-15	7
15-20	14
20-25	25
25-30	27
30-35	13
35-40	3
40-45	2
45-50	1

Figure 6: Pie Chart of the average duration of PB pulse train.

5. CONCLUSION

This study focused more on the preliminary breakdown happened within the cloud to ground flashes. The preliminary breakdown process were analysed in around 2000 captured waveforms in two months (March and April) in Malaysia. Only a few researches have been done in equatorial regions such as Malaysia on the lightning discharges. The statistics obtained during the measurements showed that the preliminary breakdown pulse duration took 20–30 ms in average. The results of this study are almost compatible with the BIL model. Further studies should also be conducted to investigate the relation between the preliminary breakdown pulses and the first return strokes in terms of the amplitude, ratio and polarity.

ACKNOWLEDGMENT

Authors wish to thank Ministry of Science, Technology and Innovation (MOSTI) and Universiti Teknologi Malaysia (Research Vote Nos. 4S004, 4S045, 00H41).

REFERENCES

1. Clarence, N. D. and D. J. Malan, "Preliminary discharge processes in lightning flashes to ground," *Quarterly Journal of the Royal Meteorological Society*, Vol. 83, 161–172, 1957.
2. Galvan, A. and M. Fernando, "Operative characteristics of a parallel-plate antenna to measure vertical electric fields from lightning fields from lightning flashes," Report UURIE 285-00, Uppsala University, 2000.
3. Rakov, V. A., M. A. Uman, G. R. Hoffman, W. M. Micheal, and M. Brook, "Burst of pulses in lightning electromagnetic radiation: Observations and implications for lightning test standards," *IEE Trans. Electromagn. Compat.*, Vol. 38, No. 2, 156–164. 1996.
4. Kitagawa, N. and M. Brook, "A comparison of intracloud and cloud-to ground lightning discharges," *J. Geophys.*, 1189–1201, 1960.
5. Beasley, W., M. A. Uman, and P. L. Rustan, "Electric fields preceding cloud to ground lightning flashes," *J. Geophys.*, 4883–4902, 1982.
6. Brook, M., "Breakdown electric fields in winter storms," *Res. Lett. Atmos. Electr.*, 47–52, 1992.
7. Cooray, V. and V. Scuka, "What attracts a lightning to ground," *Proceedings of the 10th International Conference on Atmospheric Electricity*, Osaka, Japan, 1996.
8. Cooray, V. and R. Jayaratne, "What directs a lightning flash towards ground," *Sri Lankan J. Phys.*, Vol. 1, 2000.
9. Gomes, C. and V. Cooray, "Radiation field pulses associated with the initiation of positive cloud to ground lightning flashes," *J. Atmos. Sol. Terr. Phys.*, Vol. 66, 1047–1055, 2004.
10. Makela, J. S., N. Porjo, A. Makela, T. Tuomi, and V. Cooray, "Properties of preliminary breakdown process in Scandinavian lightning," *J. Atmos. Sol. Terr. Phys.*, 2008.
11. Nag, A. and V. Rakov, "Pulse trains that are characteristic of preliminary breakdown in cloud-to-ground lightning but not followed by are not followed by return stroke pulses," *Journal of Geophysical Research*, Vol. 113, 2008.

12. Salimi, B., Z. Abdul-Malek, S. J. Mirazimi, and K. Mehranzamir, "Investigation of short base line lightning detection system by using time of arrival method," *Intelligent Informatics*, Vol. 182, 141–147, Springer, Berlin, Heidelberg, 2013.
13. Noor Azlinda, A., M. Fernando, Z. A. Baharudin, V. Cooray, H. Ahmad, and Z. Abdul Malek, "Characteristics of narrow bipolar pulses observed in Malaysia," *Journal of Atmospheric and Solar-terrestrial Physics*, Apr. 2010.
14. Rhodes, C. and P. R. Krehbiel, "Interferometric observations of a single stroke cloud-to-ground flash," *Geophysical Research Letters*, Vol. 16, 1169–1172, 1989.
15. Mashak, S. V., H. N. Afrouz, and Z. Abdul-Malek, "Simulation of lightning flash in time of arrival (TOA) method by using three broadband antennas," *SME2011*, Madrid, Nov. 2011.
16. Mashak, S. V., H. N. Afrouzi, and Z. Abdul-Malek, "Simulation of lightning flash and detection using in time of arrival (TOA) method based on four broadband antennas," *ICI2011*, Bandung, Nov. 2011.
17. Gomes, C. V. and C. Jayaratne, "Comparison of preliminary breakdown pulses observed in Sweden and Sri Lanka," *J. Atmos. Sol. Terr. Phys.*, Vol. 60, 975–979, 1998.
18. Ogawa, T., "Initiation of lightning in Clouds," *Journal of Atmospheric Electricity*, 121–132, 1993.
19. Ushio, T., Z. I. Kawasaki, K. Matsuura, and D. Wang, "Electric fields of initial breakdown in positive ground flash," *Journal of Geophysical Research*, Vol. 103, 14135–14140, 1998.
20. Harris, D. J. and Y. E. Salman, "The measurement of lightning characteristics in Northern Nigeria," *Journal of Atmospheric and Solar Terrestrial Physics*, Vol. 34, 775–786, 1972.
21. Proctor, D. E., R. Uytenbogaardt, and B. M. Meredith, "VHF radio pictures of lightning flashes to ground," *Journal of Geophysical Research*, Vol. 93, 12683–12727, 1988.

Lorentz Contraction, Apparent or Real

Nils H. Abramson
Industrial Metrology, Royal Institute of Technology, Stockholm 10044, Sweden

Abstract— The Michelson Morley interference experiment of 1887 indicated that the velocity of light is independent of the velocities of source and observer. This surprising result was in conflict with earlier calculations. To make theory and experiment in agreement Lorentz stated a contraction of rigid objects parallel to velocity. We discuss if this contraction is real or caused by the interference method of measurement. Our approach is to introduce a sphere of observation based on ultra short light pulses combined to ultra short observations. When the experimenter travels at high velocity this sphere is according to Lorentz contracted into an oblate ellipsoid. According to our proposed theory the sphere is instead elongated into a prolate ellipsoid. The result of this effect is that stationary objects appear contracted. Our results are in full agreement to Einsteins Special Theory of Relativity. To support our statements we introduce a novel method to measure the length of a travelling object that is independent of interferometry.

1. THE MICHELSON MORLEY EXPERIMENT (MM)

Figures 1–4 demonstrate in a graphic way the conventional way to explain the null result of the MM experiment [1] as compared to our novel way using the elongation of the sphere of observation.

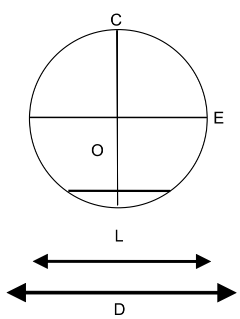

Figure 1: The MM experiment.

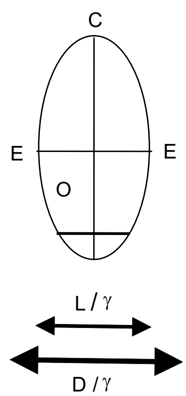

Figure 2: Lorentz contraction.

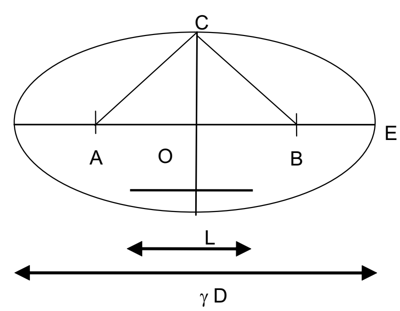

Figure 3: Elongation of the sphere into the ellipsoid of the "holodiagram".

Figures 1 and 2 display the basic principle of the Michelson Morley (MM) interference experiment [1] used to test if the velocity of light (c) is influence by the velocity of earth (v). In the stationary interferometer of Fig. 1 the distance OCO is equal to OEO. We have inscribed this interferometer into a sphere which we name a sphere of observation. An analogy to this experiment is that when (v) is zero light pulses travelling OCO and OEO should arrive at the same time.

Theoretical calculations show that if (c) was influenced by (v), the time to travel OEO (t_v) should be longer than the time (t_0) for OCO. Such was not the result of the experiment and therefore Lorentz and Einstein [2] stated that the length OE and all other lengths parallel to velocity was contracted by $1/\gamma$ in such a way that the delay of the light was compensated for (Fig. 2). This statement was made without knowing any mechanical or physical reason for this effect.

Citation [3] from R. Feynman: "Although the contraction hypothesis successfully accounted for the negative result of the experiment, it was open to the objection that it was invented for the express purpose of explaining away the difficulty, and was too artificial."

2. THE SPHERE OF OBSERVATION

Our novel explanation is that contrary to a real Lorentz contraction there is an elongation of the sphere of observation (Fig. 1) into the ellipsoid of observation (Fig. 3) caused by the distance that

B travelled from A during the time light passes ACB. Such an ellipsoid of observation has been introduced as a tool to evaluate holographic interference fringes [4] it has also been photographed by light-in-flight recording [5] and published as one of the ellipses of the hoodiagram [6]. The moiré effect of these ellipses have been used to explain fringes in holographic interference [7].

There is as an accepted fact in relativity that it is not possible for a traveller to observe a constant velocity without measurements of the outside world. It is also accepted that the distance OC does not change because such a velocity. Thus, the time it takes for light to pass ACB (t_v) must be longer than passing OCO (t_o). For he traveller not to observe this difference his clocks therefore must be slowed by t_o/t_v and his seconds elongated by = CB/CO = γ (Fig. 3). Where $\gamma = ct_0/ct_v$ and $ct_0^2 = ct_v^2 - vt_v^2$, resulting in:

$$\frac{t_v}{t_0} = 1/\cos\alpha = \frac{1}{\sqrt{1 - \frac{(vt_v)^2}{(ct_v)^2}}} = \frac{1}{\sqrt{1 - \frac{v^2}{c^2}}} = \gamma$$

The elongation of the sphere into an ellipsoid is not observed by the traveller because any plane intersection of an ellipsoid appears circular when observed from any of its focal points [6].

The explanation is that from the focal point such an intersection is viewed from exactly such an angle that the ellipse appears circular and the object Lorentz contracted. The increased path lengths caused by the transformation are not observed by the traveller because the length of his Meter parallel to (v) is increased just as much as his Second, of which the latter has been proved by the well known time dilation.

Thus, we state that the Lorentz contraction is not real but only a measuring error caused by the elongation of the measuring tool. When the traveller uses the ellipsoid to measure stationary objects he makes an error because he does not know the transformation of the sphere into the ellipsoid, resulting in that the stationary object by the traveller appears contracted by $1/\gamma$ (Fig. 4). This result agrees with the fact that our Meter is defined as the distance light passes in a certain fraction of a second and using this meter for measurements again results in that objects appear contracted for measurements parallel to velocity.

Constant (c) results in that observers at A and B of Fig. 3 both find themselves in the centre of the same expanding and contracting spherical waves. As this is impossible we have stated that instead they are in each of the two focal points of the same ellipsoid. If A represents a point on a stationary train and B a point on a travelling train both will use the same ellipsoid to measure objects on the others train. Outgoing light is tilted from OC to AC (The headlight effect). Incoming light is tilted OC to BC (magnifying).

3. THE SHADOW METHOD

To demonstrate our statement we propose a different method to measure the length of a travelling object. Our new method is independent of the velocity of light and of time (Fig. 5). The source of an ultra short light pulse A is at infinite distance from the object B-C which at relativistic velocity (v) passes in front of a stationary photographic plate D-E, which is infinitely close to the object. After exposure the recorded shadow of the object is developed and its length is measured on the photographic plate. The set up of Fig. 5 is fully symmetric and there are no electric signals

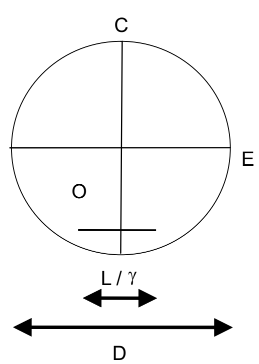

Figure 4: Apparent contraction.

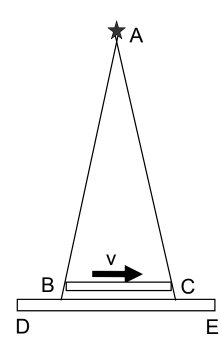

Figure 5: The shadowing method for measuring length.

involved, therefore it is clear that the recorded shadow of the object B-C represents the true length of the travelling object.

If, however, instead a Lorentz contraction was recorded, we could repeat the experiment with B-C stationary and D-E passing at (v). This way the shadow of BC would be recorded on the photographic emulsion of the contracted DE. Later on when the shadow on the stationary DE is developed and measured we would record an elongation of B-C because DE is now back to its original length. This result would be against the principle of relativistic theory. Thus, our thought experiment demonstrates that there is no true contraction of the travelling object, again proving that the Lorentz contraction is not real but only apparent.

4. CONCLUSIONS

Introduction of the ellipsoids of observation produces a simple geometric explanation of several optical phenomena, e.g., the elongation by velocity of the sphere of observation into an ellipsoid produces the real reason to the null result of the MM experiment: the distance from one focal point to the other via any point on the surface of an ellipsoid is constant.

The sphere is expanding as a wave until it reaches an observer at which instant the first light is transformed into an ellipsoid of infinite eccentricity, as a ray or a particle. Thus, it is the observer that causes the transformation. If the sphere consists of one single photon which is absorbed by an observation, this ray is absorbed and there is no reason to a sudden collapse of the sphere.

The sphere of observation is also a sphere of simultaneity because everything happening on its surface appears to the observer to happen at the same time, which by the observers' velocity is elongated into an ellipsoid of simultaneity. At light velocity, the time will thus to the travelling observer appear to be standing still, which also well agrees with Einsteins time dilation.

The two focal points A and B of the infinitely stretched ellipsoid are closely related as they do not *know* that they have left their birth place O of Fig. 3. Thus, they represent two entangled points in space, which appear to have identical points of time and space. As energy can not travel faster than light, the information existing at both focal points can only be information about random processes, that is useless until compared ordinary information from A to B.

REFERENCES

1. Michelson, A. and E. Morley, "On the relative motion of the earth and the luminiferous ether," *American Journal of Science*, Vol. 34, 333–34, 1887.
2. Einstein, A., "On the electrodynamics of moving bodies," *Ann. Phys.*, Vol. 17, 891, 1905.
3. Feynman, R., *Lectures on Physics*, California Institute of Technology, 15-5, 1963.
4. Abramson, N., "The Holo-diagram: A practical device for the making and evaluation of holograms," *Engineering Uses of Holography*, Strathclyde, 1968 and *Appl. Opt.*, Vol. 8, 1235–1240, 1969.
5. Abramson, N., "Light-in-flight recording: High-speed holographic motion picture of ultrafast phenomena," *Appl. Opt.*, Vol. 22, 215–232, 1983.
6. Abramson, N., J. Boman, and B. Bonnevier, "Plane Intersections of rotational ellipsoids," *Amer. Math. Monthly*, Vol. 119, No. 4, 336–339, 2006.
7. Abramson, N., "Moiré patterns and hologram interferometry," *Nature*, Vol. 231, 65–67, 1971.

High Speed BOCDA Measurement of Strain Distribution by Longitudinal Sweep Method

K. Washiyama[1], **M. Kishi**[1], **Z. He**[2], **and K. Hotate**[1]

[1]Department of Electrical Engineering and Information Systems
University of Tokyo, Japan
[2]Shanghai Jiao Tong University, Shanghai, China

Abstract— This paper describes a high-speed fiber optic distributed strain measurement, utilizing Brillouin scattering caused in the optical fiber. We proposed and developed Brillouin Optical Correlation Domain Analysis (BOCDA) system for the distributed measurement, in which the strain dependence of the Brillouin frequency shift (BFS) can be measured position-selectively along the optical fiber. The BOCDA has advantages, compared with the time domain pulsed-lightwave technologies, such as high spatial resolution and high speed measurement with random accessibility to arbitrary multiple points along the optical fiber. In this research, we newly propose a BOCDA system, in which fully distributed measurement can be realized in a high speed, by overcoming the restriction caused by a lock-in detection that were indispensable in the basic BOCDA system. A fully distributed BFS measurement has been performed in 50 msec., and repeated distributed measurement with a speed of 12 traces/sec. has also been demonstrated.

1. INTRODUCTION

Research on smart structures and smart materials has been more and more attractive recently. As sensing technology for realizing the structures and materials, optical fiber sensing based on Brillouin scattering is quite promising due to its capability of distributed strain and/or temperature measurement along an optical fiber. Pulsed-lightwave schemes have been mainly proposed and studied as the distributed measurement mechanism. However, these have difficulty in realizing ultimate performances, such as high spatial resolution and high speed measurement. To overcome these difficulties, we have proposed and developed Brillouin Optical Correlation Domain Analysis (BOCDA) systems [1], which utilizes the continuous lightwave with manipulating its correlation or interference characteristic for position-selective excitation of the stimulated Brillouin scattering along the fiber.

The BOCDA has already achieved the superior functions, such as 1.6 mm spatial resolution [2] and 1 kHz measurement speed for the Brillouin gain spectrum shaping [3]. Additionally, we have proposed and demonstrated simultaneous distributed measurement of strain and temperature along a polarization maintaining optical fiber with 10 cm resolution [4]. Another feature of this system is random accessibility to the arbitrary multiple points along the sensing optical fiber. Some applications, however, do not require the random accessibility, but require fully distributed measurement with quite a high measurement speed.

In this research, we propose a BOCDA system, in which a high speed fully distributed measurement can be realized. Repeated fully distributed measurement with a speed of 12 traces/sec. has been demonstrated.

2. HIGH SPEED BOCDA SYSTEM WITH LONGITUDINAL SWEEP METHOD

Figure 1 shows a BOCDA system proposed and fabricated in this research. A 1.55 μm laser diode (LD) is used as a light source, whose output is divided into two ways as shown in Figure 1.

One lightwave is launched into a single side-band lithtwave modulator (SSBM) to shift the frequency downward by the Brillouin frequency shift (BFS), which is around 11 GHz in silica optical fibers. This is launched into the sensing fiber as the probe lightwave for the stimulated Brillouin scattering. The other is amplified by an erbium doped fiber amplifier (EDFA) and launched into the sensing fiber at the opposite end as the pump lightwave. It is the point in the BOCDA system to modulate the laser in its frequency, which realizes the position-selective excitation of the stimulated Brillouin scattering at the correlation-peak position along the fiber, as shown in Figure 1. By simply changing the modulation frequency, the position can be scanned to achieve the distributed measurement.

In the BOCDA system for this study, we adopted the "longitudinal sweep method" for the high speed fully distributed measurement, in which the mean frequency difference between the

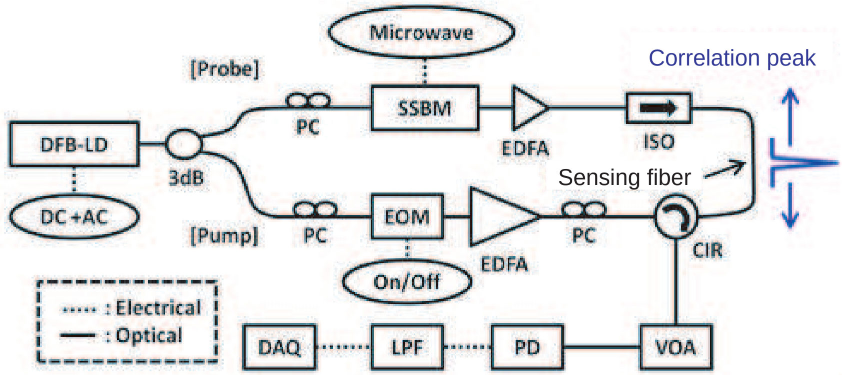

Figure 1: High speed BOCDA distributed strain measurement system with the longitudinal sweep method.

pump and probe lightwave and the frequency of the laser FM for sweeping the sensing position are simultaneously changed, as shown schematically in Figure 2, in order to obtain the distribution of the Brillouin gain spectrum (BGS) along the entire sensing fiber in a short time. While the frequency difference between the pump and probe lightwave is swept one time, the sweep of the sensing position is repeated multiple times.

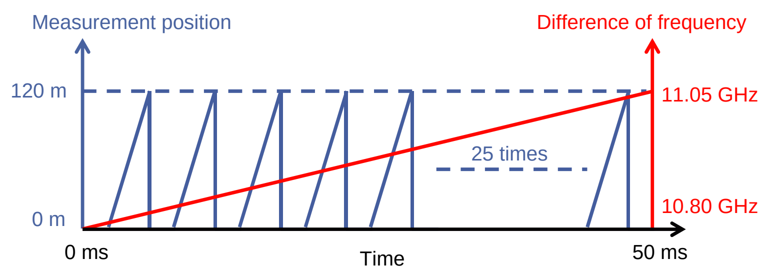

Figure 2: Operation of the longitudinal sweep method.

In our preceding study on the longitudinal sweep method, time constant of the lock-in amplifier, which is indispensable to selectively obtain the stimulated Brillouin scattering increment in the probe lightwave, restricted the measurement speed [5, 6]. In another study on the method, there was difficulty in making the precise waveform to control the laser frequency, because it adopted a time-division pump-probe generation scheme [7].

In this study, we newly proposed the system to overcome these difficulties as shown in Figure 1. In the system, the lock-in detection is not used, but a data subtraction scheme is introduced. The two data sets for the pump-on case and the pump-off case are subtracted with each other as shown in Figure 1 to obtain the probe increment corresponding to the stimulated Brillouin scattering gain. Additionally, this system is based on the basic BOCDA system, in which the time-division pump-probe generation scheme is not adopted.

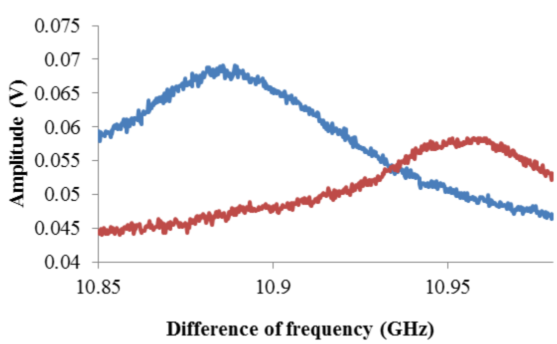

Figure 3: Brillouin gain spectrum obtained by the BOCDA system shown in Fig. 1.

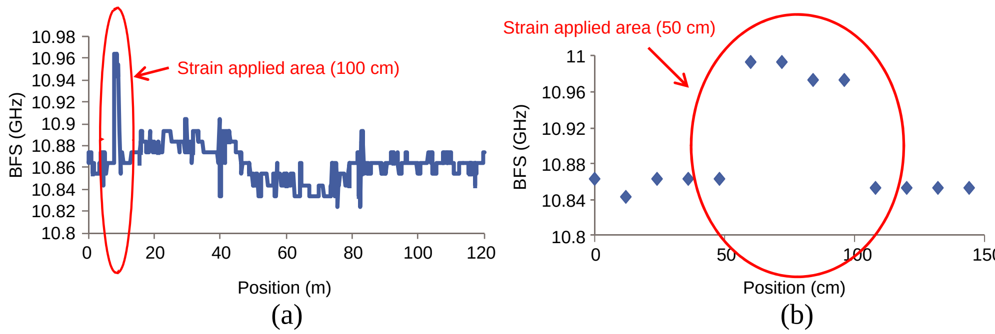

Figure 4: Measureunt of the BFS distribution along the sensing optical fiber of 120 m length with 50 msec. total measurement speed. (a) Full length BFS measurement, and (b) demonstration of 50 cm spatial resolution.

In order to realize the function of the position selective measurement in the correlation domain technique, a low pass filter or an integration circuit is required [1]. In the system shown in Figure 1, an electronic low pass filter (LPF) is introduced after the detector for that purpose, instead of the time constant in the lock-in amplifier for the basic BOCDA systems [1–3].

Figure 3 shows the BGS spectrum shapes successfully obtained by the BOCDA system. In Figure 3, one is obtained at the loose fiber portion, which shows the BFS around 10.88 GHz, and the other is for the strain-applied portion, which shows the BFS around 10.96 GHz.

3. EXPERMENTAL RESULTS OF HIGH-SPEED DISTRIBUTED MEASUREMENT

Figure 4(a) shows the BFS distribution measured along the entire sensing optical fiber of 120 m length. The measurement speed of 50 msec. has been achieved for one fully distributed measurement in the system. The strain-applied portion of 100 cm length is clearly measured at around 10 m position of the fiber. Figure 4(b) shows the other experiment, in which the strain-applied portion of 50 cm length is clearly detected, which means that the spatial resolution of the system is better than 50 cm.

Next, repeated measurement of the strain distribution along the entire length of the fiber has been demonstrated in the proposed BOCDA system as shown in Figure 5.

Though the measurement speed has been a little bit reduced due to the limitation in control speed of the equipments such as the waveform generator used for sweeping the measurement position, the repetition rate of 12 traces/sec. has been achieved in the BOCDA system as shown in Figure 5. This figure shows the high speed repeated distributed measurement at around the dynamic strain applied portion. Dynamic strain of 1 Hz has been applied along a 50 cm section, which has been successfully detected by the system.

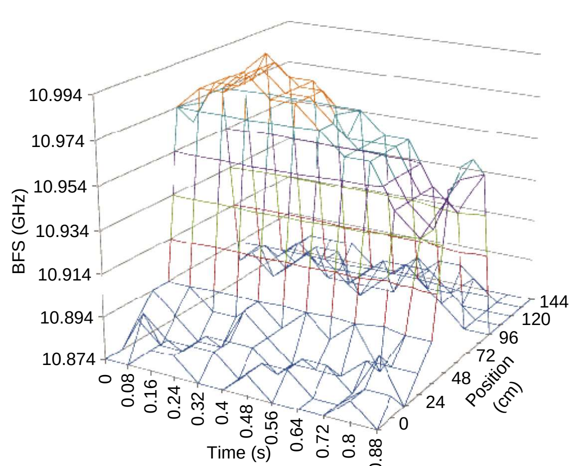

Figure 5: High speed repeated measurement of the BFS distribution around the fiber portion where the dynamic strain of 1 Hz is applied. Twelve traces of the distribution has been measured per one second with 50 cm spatial resolution along the entire length of 120m sensing optical fiber.

Figure 6 shows the measurement of the dynamic strain applied along the sensing optical fiber as a function of time. Dynamic measurements at the strain applied portion and at the strain free portion shown in Figure 5 are depicted in Figures 6(a) and (b), respectively. Dynamic strain of 1 Hz has been clearly shown in Figure 6(a).

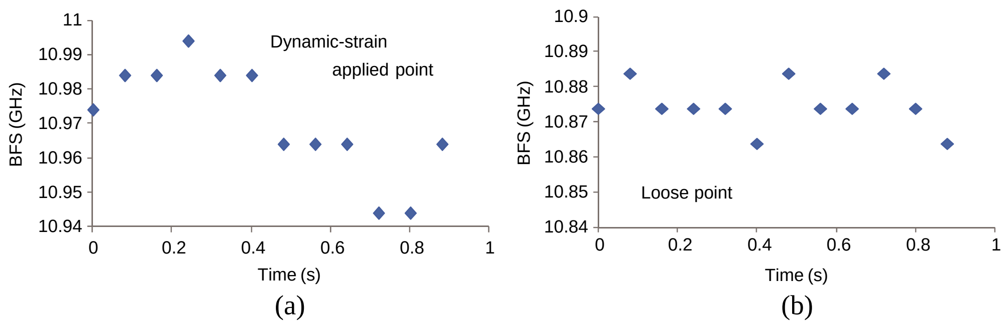

Figure 6: Measurement of the dynamic strain applied along the sensing optical fiber as a function of time. Dynamic measurements (a) at the strain applied portion, and (b) at the strain free portion shown in Figure 5.

4. CONCLUSION

The BOCDA system with the longitudinal sweep method has been proposed and demonstrated to achieve a high speed fully distributed strain measurement along the entire sensing optical fiber. In the fabricated system, one distributed measurement with 50 cm spatial resolution along the 120 m length sensing fiber was performed in 50 ms. Additionally, the high speed repeated distributed strain measurement along the fiber has also been demonstrated with 12 traces/sec. speed, with applying 1 Hz dynamic strain at a 50 cm length fiber portion.

The BOCDA with the longitudinal sweep method having no lock-in amplifier has been proved to have the potential to increase the measurement speed in the fully distributed strain measurement along the fiber.

REFERENCES

1. Hotate, K. and T. Hasegawa, "Measurement of Brillouin gain spectrum distribution along an optical fiber using a correlation-based technique — Proposal, experiment and simulation," *IEICE Trans. on Electronics*, Vol. E83-C, No. 3, 405–412, 2000.
2. Song, K.-Y., Z. He, and K. Hotate, "Distributed strain measurement with millimeter-order spatial resolution based on Brillouin optical correlation domain analysis," *OSA Optics Letters*, Vol. 31, No. 17, 2526–2528, 2006.
3. Song, K.-Y. and K. Hotate, "Distributed fiber strain sensor at 1 kHz sampling rate based on Brillouin optical correlation domain analysis," *IEEE Photonics Technology Letters*, Vol. 19, No. 23, 1928–1930, 2007.
4. Zou, W., Z. He, and K. Hotate, "Demonstration of Brillouin distributed discrimination of strain and temperature based on a polarization-maintaining optical fiber," *IEEE Photonics Technology Letters*, Vol. 22, No. 8, 526–528, 2010.
5. Zou, W., Z. He, and K. Hotate, "Realization of high-speed distributed sensing based on Brillouin optical correlation domain analysis," *OSA/CLEO/IQEC*, CMNN5, 2009.
6. Zou, W., Z. He, and K. Hotate, "Distributed dynamic-strain sensing based on Brillouin optical correlation domain analysis," *The 8th Pacific Rim Conf. on Lasers and Electro-Optics (CLEO PR 2009)*, WE1-5, Shanghai, Sep. 30, 2009.
7. Song, K. Y., M. Kishi, Z. He, and K. Hotate, "High-repetition-rate distributed Brillouin sensor based on optical correlation-domain analysis with differential frequency modulation," *OSA Optics Letters*, Vol. 36, No. 11, 2011.

Magnetic Characterization of Interfering Objects in Resonant Inductive Coupling Wireless Power Transfer

E. Bou[1], **D. Vidal**[1], **R. Sedwick**[2], **and E. Alarcon**[1]

[1]Technical University of Catalonia UPC BarcelonaTech, Spain
[2]University of Maryland, US

Abstract— Resonant Inductive Coupling (RIC) Wireless Power Transfer is a key technology to provide an efficient and harmless wireless energy channel to consumer electronics, biomedical implants and wireless sensor networks. However, there are two factors that are limiting the applicability of this technology: the effects of distance variation between transmitter and receiver and the effects of interfering objects. While distance variation in WPT has been thoroughly studied, the effects of conductive interfering objects in resonant inductive coupling links are still unclear.

When a conductive element is in the vicinity of a RIC link, both the transmitter and the receiver can experiment a change on their resonant frequencies as well as their impedances. This can greatly affect the efficiency of such WPT link causing it to a) make the transmitter and/or receiver act as a pass-band filter and b) loose part of the transmitter magnetic field through coupling to the interfering object. Depending on the natural resonant frequency of the object and the distances between this object and the transmitter and receiver antennas, this can affect significantly the RIC wireless power transfer link. In this article, we characterize the Magnetic behavior of a resonant inductive coupled link in the presence of a conductive interfering object using a Finite Element Field Solver (FEKO). Several distances between interference and transmitter/receiver are analyzed providing a design space exploration and applicability study of this link.

1. INTRODUCTION

Resonant Inductive Coupling (RIC) Wireless Power Transfer is foreseen as one of the key technologies to satisfy the energy requirements of a network of battery-less/ambient-powered electronic devices. Towards the applicability of resonant inductive coupling to a network of devices, the effects of multiple devices acting as interfering objects should be studied. Due to the resonance of Resonant Inductive Coupled Wireless Power Transfer, these systems are very sensitive to conductive objects in close proximity, which interact with the transmitter and/or the receiver, modifying its impedance and resonant frequency.

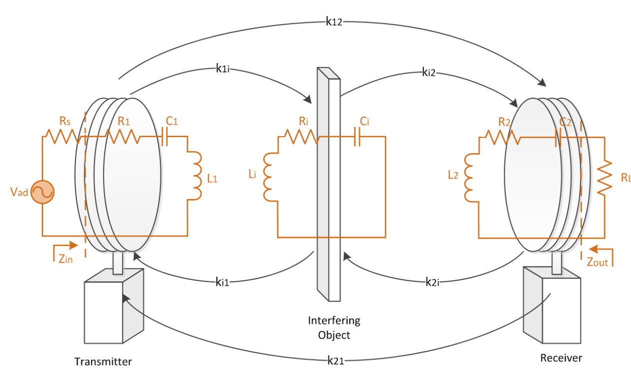

Figure 1: Block diagram of WPT system.

In this paper, we 1) propose an analytical circuit-based approach to study the effects of interfering objects on a Resonant Inductive Coupled Link, 2) explore the behavior of this model taking into account the resonant frequency of the interfering object and the coupling between the interference and transmitter/receiver coils and 3) verify the obtained results through a magnetic characterization of this link using a Finite Element Field Solver Software (FEKO).

2. CIRCUIT-BASED ANALYTICAL MODEL

To explore the effects of an interference, the interfering object is approximated by an RLC circuit that models the frequency response of its impedance (which depends on the object geometry, size and material) and the coupling coefficients ($k_{1i}, k_{i1}, k_{i2}, k_{2i}$) which model the magnetic behavior of the interference, this is, the amount of magnetic field that is effectively transferred between the interfering object and the transmitter/receiver coils.

Once this is known, the transfer functions of transmitter, receiver and interfering object can be defined respectively as:

$$\begin{aligned} G_1 &= \frac{I_1}{V_1} = \frac{j\omega C_1}{1 + j\omega C_1 R_1 - \omega^2 L_1 C_1} \\ G_2 &= \frac{I_2}{V_2} = \frac{j\omega C_2}{1 + j\omega C_2 R_2 - \omega^2 L_2 C_2} \\ G_i &= \frac{I_i}{V_i} = \frac{j\omega C_i}{1 + j\omega C_i R_i - \omega^2 L_i C_i} \end{aligned} \tag{1}$$

where ω is the frequency at which the system operates and ω_1, ω_2 and ω_i are the resonant frequencies of transmitter, receiver and interfering object respectively. G_{1i}, G_{i1}, G_{2i}, G_{i2} are defined as the transfer functions from the transmitter/receiver to interfering object and from the interfering object to transmitter/receiver, representing the amount of power that arrives to the transmitter and receiver from the interfering object and the other way around. Finally, G_{12}, G_{21} represent the power coupled directly from transmitter to receiver and from receiver to transmitter respectively.

$$\begin{aligned} G_{1i} = G_{i1} &= \frac{V_{i1}}{I_1} = \left(\omega k_{1i}\sqrt{L_1 L_i}\right)^2 \\ G_{2i} = G_{i2} &= \frac{V_{i2}}{I_2} = \left(\omega k_{2i}\sqrt{L_2 L_i}\right)^2 \\ G_{12} = G_{21} &= \frac{V_{21}}{I_1} = \left(\omega k_{12}\sqrt{L_1 L_2}\right)^2 \end{aligned} \tag{2}$$

Once the gain functions are known, the currents at transmitter (I_1), receiver (I_2) and interfering object (I_i) can be found as:

$$\begin{aligned} V_1 &= V_{ad} + I_i G_{i1} + I_2 G_{21} \\ I_1 &= V_1 G_1 \\ I_i &= V_i G_i = (I_1 G_{1i} + I_2 G_{2i}) G_i \\ I_2 &= V_2 G_2 = (I_1 G_{12} + I_i G_{i2}) G_2 \end{aligned} \tag{3}$$

Solving this system of equations yields the output current at the receiver:

$$I_2 = I_1 \frac{G_2 G_{12} + G_i G_2 G_{1i} G_{i2}}{1 + G_i G_2 G_{2i} G_{i2}} \tag{4}$$

the current at the interfering object:

$$I_i = I_1 \frac{G_i G_{1i} + G_i G_2 G_{12} G_{2i}}{1 + G_i G_2 G_{2i} G_{i2}} \tag{5}$$

and finally, the source current I_1:

$$I_1 = V_{ad} \frac{G_1}{1 + G_1 G_{i1} \frac{(G_i G_{1i} + G_i G_2 G_{12} G_{2i})}{1 + G_i G_2 G_{2i} G_{i2}} + G_1 G_{21} \frac{(G_2 G_{12} + G_i G_2 G_{1i} G_{i2})}{1 + G_i G_2 G_{2i} G_{i2}}} \tag{6}$$

The power dissipated in the first coil (transmitter), the power dissipated in the second coil (receiver), the power transferred to the load and the power lost due to the interfering object can be defined as:

$$P_1 = \frac{|I_1|^2}{2} R_1; \quad P_2 = \frac{|I_2|^2}{2} R_2; \quad P_L = \frac{I_2^2}{2} R_L; \quad P_i = \frac{I_i^2}{2} R_i \tag{7}$$

where R_1, R_2, R_L and R_i are the real part of Z_1, Z_2, Z_L and Z_i respectively. Once the power dissipated and transferred are known, the efficiency, defined as the power transferred to the load divided by the total power of the system, is found as:

$$\eta = \frac{P_L}{P_1 + P_2 + P_L + P_i} \tag{8}$$

3. BRIDGING THE CIRCUIT-MODEL TO MAGNETIC FIELDS

While the functional forms of the equations defined above are quite complex, the factors that define the impact of the interfering object can be qualitatively understood to be:

- Resonant frequency of the interfering object with respect to the resonant frequency of the system: $\Delta f = \frac{f_i - f_o}{f_o}$. The smaller the $\Delta f'$ is, the greater the effect of the interfering object will be. This is due to the fact that near resonance the reactive component of the impedance is greatly reduced, allowing for more current to ow and more power to be consumed by the resistive component.
- Resistance of the interfering object with respect to the load resistance: $R' = \frac{R_i}{R_L}$: if $R_i \ll R_L$, the system's input and output impedances (Z_{in} and Z_{out}) are driven by the interfering objects impedance, thus shifting the frequency response of the system depending upon Δf. If $R_i \gg R_L$ the effect of the interfering object is negligible.
- Distance and axial orientation between interference and transmitter/receiver, this is, coupling between interference and transmitter ($k_{i1} = k_{1i}$) and receiver ($k_{i2} = k_{2i}$). High values of coupling mean that the magnetic field is more effectively transmitted to the interfering object, which causes an increase of losses through coupling to the interfering object.

For simplicity, we suppose a RIC link in which transmitter and receiver share the same resonant frequency $\omega_o = \omega_1 = \omega_2$. Figures 2, 3, 4 showcase the effects explained above for a link resonating at $f_o = 240.8\,\text{MHz}$ made of two coils of 1-turn 16 cm diameter with $R_1 = R_2 = R_{i,\Omega} = 60.9\,\Omega$, $L_1 = L_2 = L_i = 5.99\,\mu\text{H}$, $C_1 = C_2 = C_i = 0.0734\,\text{pF}$, $R_L = 70.2\,\Omega$ and $R_i = 45.5\,\Omega$.

In Figure 2, the interfering object is placed before the transmitter at several distances, represented as multiples of the antenna diameter: $-1.25D$, $-1D$, $-0.75D$, $-0.5D$, $-0.25D$. In this case, the interfering object is mostly coupled to transmitter ($k_{1i} = k_{i1} \neq 0$, $k_{i2} = k_{2i} \simeq 0$). It can be seen that the frequency response of the power available from the source is modified due to the presence of the interfering object and that the effect of a near object ($d_{i1} < 0.5D$) increases the power received at the interference and, at the same time, decreases the power received at load. Finally, if the distance $d_{1i} > 1D$, the effect of the interfering object is negligible. This is due to a low coupling $k_{1i}(d_{i1})$.

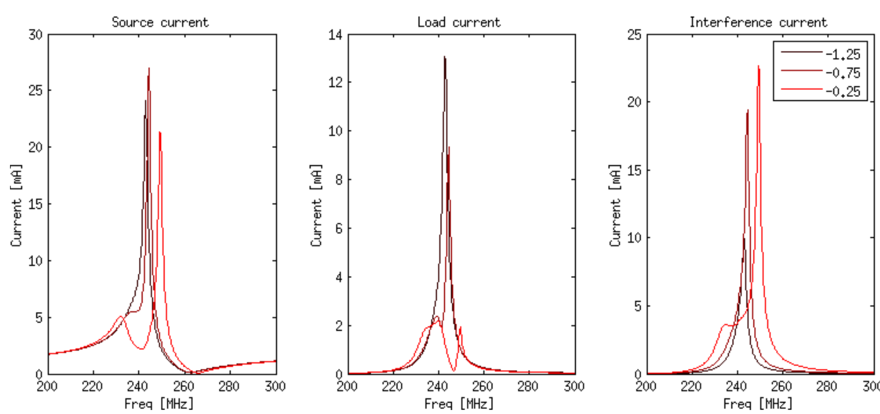

Figure 2: Currents in transmitter, load and interference. FEKO simulation. Transmitter coupled.

Figure 3 illustrates the same scenario but with the interfering object placed between transmitter and receiver. It can be seen that, when the interfering is in close proximity to the transmitter $d = 0.25D$, the source impedance is modified and the frequency response of the source current shifts and presents multiple peaks, thereby presenting an overcoupled response. Regarding the

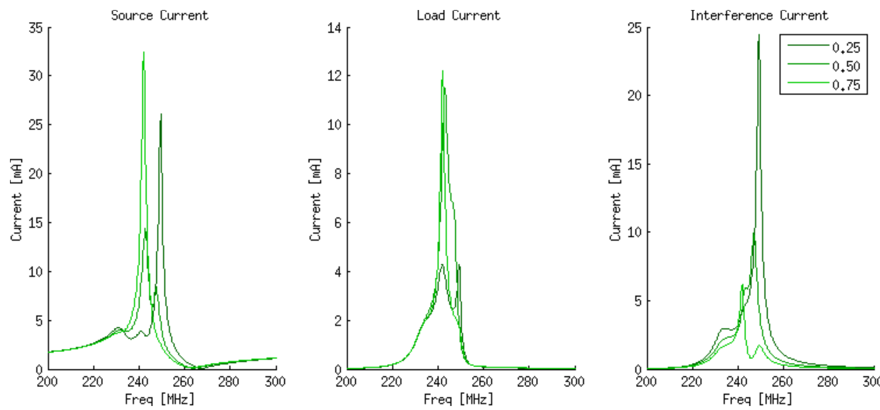

Figure 3: Currents in transmitter, load and interference. FEKO simulation. Transmitter and receiver coupled.

current at the load (receiver), we can see that it is maximum when the interfering object is placed between transmitter and receiver $d = 0.5D$ and that the current is higher than in the case of the same system operating without any interference. This is due to the interfering object acting as a relay between transmitter and receiver. Since the impedance of the interfering object is lower than the impedance of the load, more power is effectively transferred to the load. Finally, when the interfering object is closer to the receiver ($d = 0.75D$) it receives less power and its effect upon the power transfer link is causing an impedance mismatch at the receiver.

Finally, Figure 4 illustrates the situation in which the interfering object is placed only near the receiver $d = 1.25D, 1.50D, 1.75D$ and $2D$. We can see that the effect upon the source power is negligible ($k_{i1} = k_{1i} \simeq 0$) and that, for large distances $d > 1D$, the effect of the interfering object upon the current the load receives is very small.

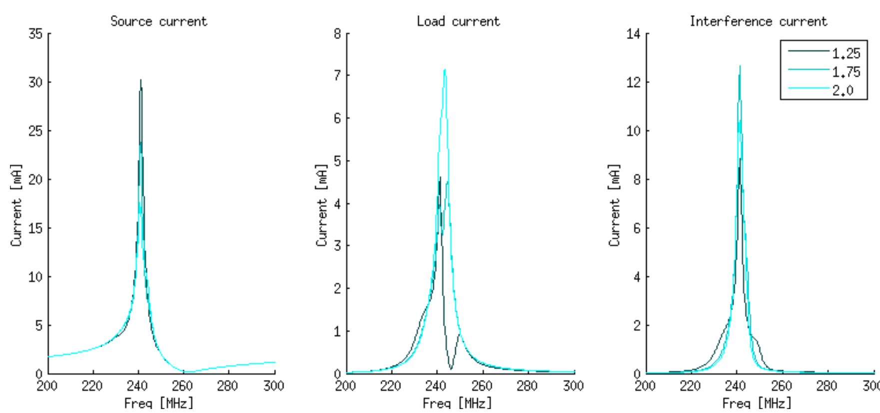

Figure 4: Currents in transmitter, load and interference. FEKO simulation. Receiver coupled.

4. MAGNETIC CHARACTERIZATION

In this section, a magnetic characterization of a RIC link in the presence of an interfering object obtained by a Finite Element Field Solver FEKO is presented to validate the prior design-oriented model-based results. This link is made of a 1-turn 16 cm diameter coils with $R_1 = R_2 = R_{i,\Omega} = 58.8\,\Omega$, $L_1 = L_2 = L_i = 5.99\,\mu\text{H}$, $C_1 = C_2 = C_i = 0.075\,\text{pF}$. A load is added to the second coil $R_L = 33.3\,\Omega$ and a smaller one ($R_i \ll R_L$) to the interfering object $R_i = 0.1R_L$.

Figure 5 compares the magnetic field of a RIC link without any interfering object (a) to the one with an interfering object only coupled to the transmitter (b) and (c). In this case, two effects can be observed: first, the magnetic field that effectively arrives to the load (receiver) is smaller. This is due to an impedance mismatch caused by the interfering object, which reduces the power provided by the source coil. Second, the interfering object, now in close proximity to the transmitter, receives most of the magnetic field, which is caused by a smaller interfering object resistance ($R_i \ll R_L$) and a higher coupling $k_{i1} = k_{1i} > k_{12} = k_{21}$.

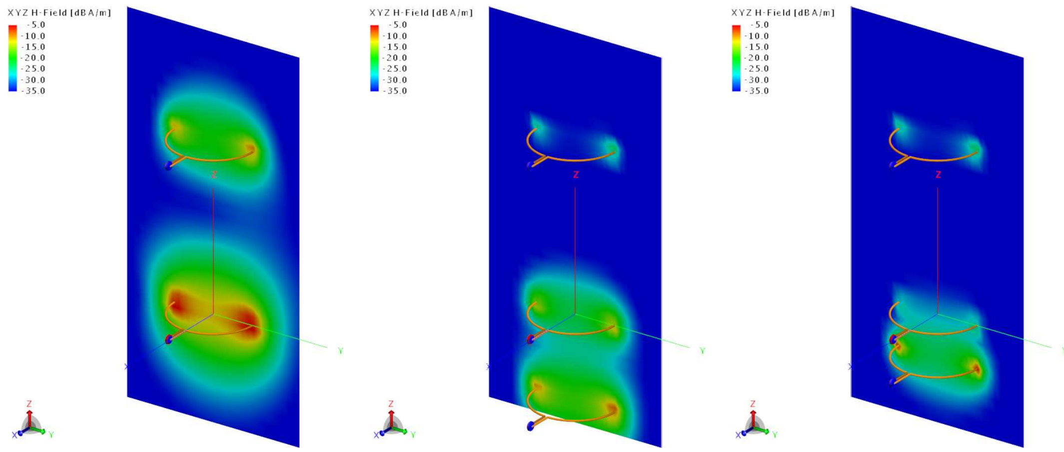

(a) No Interference (b) d_{i1} =–1m, d_{i2} =–3 m (c) d_{i1} =–0.5m, d_{i2} =–2.5 m

Figure 5: Magnetic field distribution of a RIC link with a resonant interfering object near the transmitter.

Figure 6 explores the effect of an interfering object between transmitter and receiver for three diferent distances: near the transmitter (a), in between (b) and near the receiver (c).

- If the interfering object is near the transmitter (case a), the effect is similar to the one described in Figures 5(b) and 5(c): the source impedance is modified, thereby decreasing the power available from the source and more power is coupled to the interfering object. However, in this case, the effect is diminished by the fact that part of the field that is effectively transferred to the interfering object is later transferred to the receiver, increasing the magnetic field at the load.
- If the interfering object is in between transmitter and receiver (case b), the magnetic field that is coupled to the receiver is increased with respect to the one obtained without any interfering object (Figure 5(a)). The interfering object is, in this case, acting as a relay. This result agrees with the increase of the current at the receiver shown in Figure 3. For this to happen, several things have to occur: first, the interfering object impedance has to be low in order to retransmit efficiently. Secondly, the interference has to be resonant at the same frequency of the system $\omega_i = \omega_o$. Third, the interfering object has to be sufficiently far away from the transmitter and receiver in order to minimize the impedance mismatch.
- If the interfering object is near the receiver (case c), the magnetic field at the receiver is lowered due to an impedance mismatch caused by the close proximity of interfering and receiver coils. Since the coupling between transmitter and interfering object is not negligible, the source power is also modified.

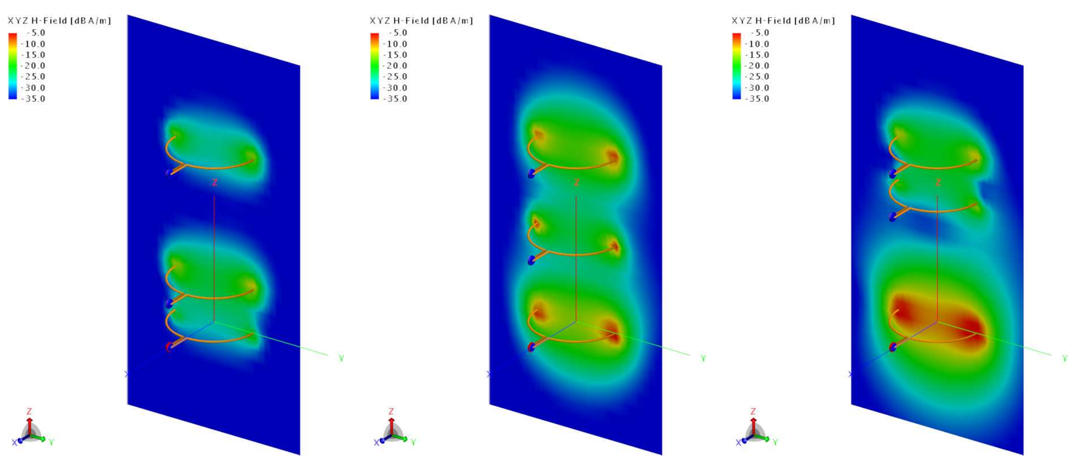

(a) d_{i1} =0.5 m, d_{i2} =1.5 m (b) d_{i1} =1 m, d_{i2} =1 m (c) d_{i1} =1.5 m, d_{i2} =0.5 m

Figure 6: Magnetic field distribution of a RIC link with a resonant interfering object between transmitter and receiver.

Finally, Figure 7 shows the effect of the interfering object far from the transmitter ($k_{i1} = k_{1i} \simeq 0$) and in close proximity to the receiver ($k_{i2} = k_{2i} \neq 0$). Since the coupling between interference and source is very small, the source power is not affected by it. On the other hand, the receiver does experience an impedance mismatch, which results in less power transferred to it, and some of the power coupled to the receiver is later transferred to the interfering object, this is, the receiver acts as a high-loss relay between the source coil and the interfering object.

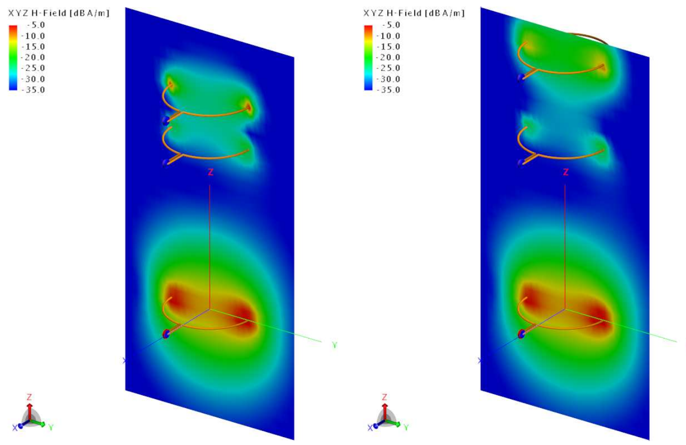

(a) d_{i1} =2.5 m, d_{i2} =0.5 m (b) d_{i1} =3 m, d_{i2} =1 m

Figure 7: Magnetic field distribution of a RIC link with a resonant interfering object near the receiver.

5. CONCLUSIONS

In this work, the effects of an interfering object on a Resonant Inductive Coupling Link have been studied analytically from a circuit-centric model-based point of view and then characterized magnetically using a Finite Element Field Solver Software (FEKO). Several scenarios have been analyzed and studied, namely a) interfering object near the transmitter, b) interfering object between transmitter and receiver and c) interfering object near the receiver; emphasizing the factors that cause a severe degradation of the wireless power transfer link. Finally, for the case in which the interfering object is between the transmitter and receiver, the assumed operating conditions resulted in the interfering object acting as a boosting relay rather than degrading the system performance. A reasonable set of conditions for which this would occur were presented, but not formally investigated.

ACKNOWLEDGMENT

Partial funding by projects TEC2010-15765 and RUE CSD2009-00046 (Consolider-Ingenio 2010), from the Spanish ministry of Science and Innovation is acknowledged.

REFERENCES

1. Kurs, A., A. Karalis, and R. Moffat, "Wireless power transfer via strongly coupled magnetic resonances," *Science*, Vol. 6, 83–86, Jun. 2007.
2. Kurs, A., J. Joannopoulos, and M. Soljacic, "Efficient wireless non-radiative mid-range energy transfer," *Annals of Physics*, Vol. 323, 34–48, 2008.
3. Kiani, M. and M. Ghovanloo, "The circuit theory behind coupled-mode magnetic resonance-based wireless power transmission," *IEEE Transactions on Circuits and Systems I: Regular Papers*, Vol. 59, No. 9, 2065–2074, 2012.
4. Kiani, M., U.-M. Jow, and M. Ghovanloo, "Design and optimization of a 3-coil inductive link for efficient wireless power transmission," *IEEE Transactions on Biomedical Circuits and Systems*, Vol. 5, No. 6, 579 –591, Dec. 2011.
5. Ahn, D. and S. Hong, "Effect of coupling between multiple transmitters or multiple receivers on wireless power transfer," *IEEE Transactions on Industrial Electronics*, Vol. 60, Jul. 2013.
6. Bou, E., E. Alarcon, R. Sedwick, and P. Fisher, "Interference analysis on resonant inductive coupled wireless power transfer links," *IEEE International Symposium on Circuits and Systems*, May 2013.

Inductive Power Transmission by Toothed Drive Belt

H.-J. Roscher and K. Wolf
Fraunhofer Institute for Machine Tools and Forming Technology (IWU)
Chemnitz/Dresden, Germany

Abstract— Toothed drive belts are widely used in both drive and conveyor technologies.

Integrating active elements like sensors and actuators into toothed drive belts opens up more possibilities for the use of toothed drive belts in both assembly automation and handling technology applications.

The traditionally used drag chains can be eliminated by using the toothed drive belt to transmit electricity to and from the units connected by it.

Further advantages are that this concept reduces the moving mass and that it allows for a contactless inductive electricity supply at the point of use.

It is also simple to transmit the electricity from the toothed drive belt to the unit requiring the electricity if the unit in question is firmly fixed to the toothed drive belt.

The concept of conducting electrical current with toothed drive belts necessitates the integration of conductors into the belt. The conductors act as the secondary coil of a transformer.

This transformer is plagued by high secondary leakage inductance because of the geometrical conditions resulting from the long conductors in the belts.

The effect of secondary leakage inductance can be limited by using resonance in the power supply.

The possibility to improve the efficiency of the conductors, by reducing their ohmic resistance, is limited by the extremely high flexibility requirements. The high flexibility requirements can only be satisfied when the diameter of the conductors is very small.

To ensure energy efficient electricity transmission from the supply to the point of use, the voltage drop in relation to the connection voltage must be kept to a minimum.

The solution to ensure good energy efficiency of the system is to use inductive energy transmission from the toothed drive belt to a switchable capacitor which acts as energy storage.

The capacitor must be rechargeable with the smallest possible current while only increasing the mass of the moving components marginally. Double layer capacitors are particularly well suited for this purpose, because of their high energy density. They also enable, with ease, the storage of regenerated energy typically produced when motorised units act as brakes.

In order to minimise the current flowing in the conductors, the operation of the equipment must be managed in such a way that there is enough time to recharge the capacitors.

1. INTRODUCTION

By integrating active elements, such as sensors or actuators [1], it is possible to extend the application of toothed drive belt systems to the fields of assembly automation and handling systems.

Using the toothed drive belt also as a tool for electrical energy transmission makes it unnecessary to use drag chains for electricity supply to assemblies as an energy consumer. These assemblies are firmly fixed with the toothed drive belt. Another advantage is that moving mass decreases. Contactless inductive energy feed-in is required to keep the system as free of maintenance as possible. Consequently, energy feed-in using toothed drive belts [2] based on contact has not been applied yet.

The investigations described in this publication were carried out within the context of the eniPROD project [4].

1.1. Electrical Aspects of the Integration of Conductor Loops

For contactless inductive transmission of electrical energy by means of toothed drive belts, it is necessary to integrate the conductor loops as a partial coil of a transformer.

As a rule, feed-in and consumption of energy may be performed contactlessly. The commonly used reversing operation mode of the linear toothed drive belt accommodates the demand for high efficiency. In this case, energy may be tapped in a conductor-bound manner. The individual conductor loops, which now form the secondary coil of the transformer, can be switched freely. This fact is, for instance, relevant in a parallel connection of juxtaposed conductor loops to decrease the ohmic resistance, since ohmic resistance substantially influences efficiency. We compared commonly used steel flexes for reinforcement of the toothed drive belt with special copper flexes of high tensile strength and fatigue strength under reversed bending stresses. Taking identically conductive cross-sections of both flexes the common steel flexes exhibited substantially greater resistance per length. Consequently, it is also critical to use these steel flexes as live conductors due to efficiency The ratios are elucidated in the table below.

Table 1: DC resistance of flexes, copper round wire by comparison.

Conductor material	**Wire cross-section** in mm^2	**Resistance** in Ohm/m
Copper round wire	1×0.142	0.12
Copper flex high tensile	$19 \times 0.00785 = 0149$	022
Steel flex	$9 \times 0.0154 = 0138$	14

Furthermore, the steel flexes mentioned above must not form any short-circuit coils. To maintain the required fatigue strength under reversed bending stresses, it is necessary to keep the conductor diameter of the conductor loops relatively small. For this reason, the additional losses inside the conductor loops due to current displacement below 100 kHz are minor.

2. MAGNETIC CIRCUIT

The arrangement of transformers to be implemented consists of a feed-in primary coil and at least one conductor loop that surrounds the generated flux of the toothed drive belt as completely as possible, with a contact point for energy consumption. The feed-in coil is compactly set out on a core. This core partially or totally surrounds the toothed drive belt in a contactless manner and has to direct the alternating magnetic flux. Resulting from the geometric ratio — strung-out conductor loops in the toothed drive belt — the magnetic coupling coefficient between primary and secondary coils, an important transformer characteristic, particularly in arrangements with open core, is relatively small in contrast to the limit One. However, it is possible to dimension a feed-in with open core and conductor loops in the area of the core branch length independently of the belt width. This way, it can be more easily inserted structurally. We obtain the simplest structure with feed-in conductors inserted at the belt edge by means of a U core carrying the primary coil. However, the coupling coefficient is small. The tendency is for transmission efficiency to increase as a function of the coupling coefficient. It should be noted that an efficiency of 884% was achieved even with a coupling coefficient of 0.14. Furthermore, this result was possible in an air-core coil arrangement, dimensioned for 5 kW transmission power to charge an accumulator [3]. When doing this, resonance mode is unavoidably necessary to compensate for high leakage inductance values as a result of the low coupling coefficient.

Table 2 demonstrates the coupling coefficients of selected magnetic circuit arrangements. $L1$ stands for primary and $L2$ for secondary inductance, $L3$ and $L4$ are auxiliary variables determined metrologically to calculate the coupling coefficient. Fig. 1 shows the test set up used.

Table 2: Coupling coefficients of magnetic circuit arrangements.

Magnetic circuit	*Secondary coils*	*Inductances [μH], f=10kHz*				*Coupling coefficient*	*Cores (Epcos)*
		L1	*L2*	*L3*	*L4*		
U 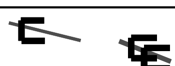 *U ‖ U*	*4* *4*	***4.9***	***56***	***64.7***	***57***	***0.12*** ***0.16***	***U93*** ***N27***
U + I 	*4*	***69***	***119.3***	***318.5***	***36.6***	***0.78***	***UI126*** ***N87***
U + U 	*4*	***81.1***	***131.8***	***368.7***	***56***	***0.76***	***UU93***
	2 *4*	***53.9*** ***53.9***	***29.2*** ***104.3***	***132.3*** ***258.3***	***33.5*** ***58.9***	***0.62*** ***0.66***	***UU126*** ***UU126***

* Primary coil (4 windings) not shown in diagrammatic view

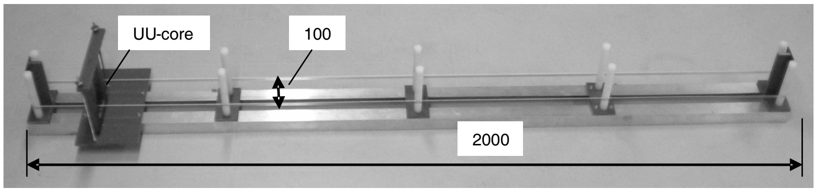

Figure 1: Test setup for energy transmission characteristics.

It should be noted that the coupling coefficient decreases with increasing length of the linear toothed drive belt. Consequently, open magnetic circuits are critical in terms of efficiency.

Losses mainly result from ohmic total resistance of the secondary conductor loops in relation to the ohmic load resistor and the losses of the transformer's ferrite core.

To achieve a very high efficiency, keep the voltage drop at conductor resistance due to current consumption of the secondary consumer in contrast to its nominal supply voltage minimal!

3. INCREASE IN EFFICIENCY BY SECONDARY ENERGY STORAGE

A capacitor energy storage, which is switched between inductive energy transmission path and consumer, can make possible a high total efficiency due to decoupling in the current. Above all, the capacitor is recharged with the lowest possible current, as demonstrated by the calculation below! Furthermore, the capacitor makes it possible to store the braking energy of motive consumers easily.

In Equation (1) for efficiency, R_D stands for the loss resistance of the conductor loops and R_S for the relatively small value for the storing capacitor. The capacitor with capacitance C is recharged from initial voltage U_{CA} to final voltage U_{CE} . Charging current I_L is a rectified sinusoidal current (average amount). Equation (2) defines the required recharging time, Equation (3) the collectible energy W_N of the recharged capacitor.

$$\eta = \frac{W_N}{W} = \frac{1}{1+\frac{W_V}{W_N}} = \frac{1}{1+\frac{\pi^2}{8}\cdot\frac{2\,(R_D+R_S)\cdot\bar{I}_L}{(U_{CA}+U_{CE})}} \tag{1}$$

$$t_L = \frac{C}{\bar{I}_L}\,(U_{CE}-U_{CA}) \tag{2}$$

$$W_N = \frac{C}{2}\left(U_{CE}^2-U_{CA}^2\right) \tag{3}$$

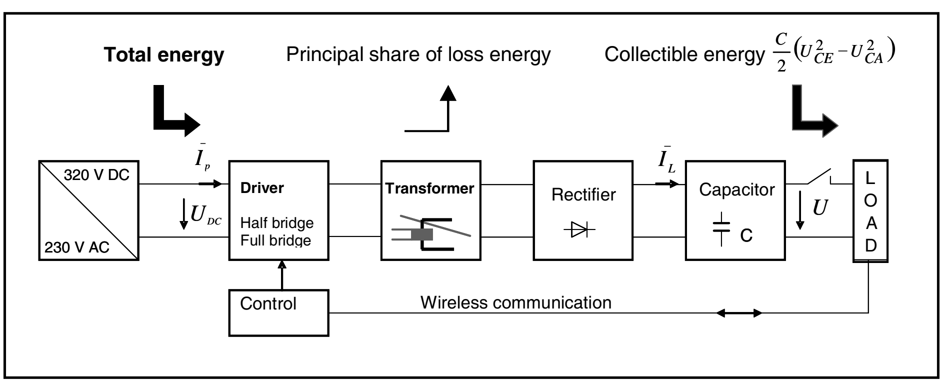

Figure 2: Topology.

Figure 2 illustrates the topology of contactless energy transmission via toothed drive belt in connection with power electronic elements.

An operation mode optimised for long recharge times provides low currents in the conductor loops inside the toothed drive belt. It provides low-loss recharge of the storage capacitor. If the capacitor is dimensioned in a larger size to add a margin of safety, then the required recharge time does not substantially increase, since the voltage loss to be compensated for as a result of discharging is reduced. As capacitive energy storage devices, not only electrolytic capacitors, but also Electric

Double Layer Capacitors (EDLC), which are especially favourable in terms of capacitance per mass, may be used. These, however, demand a series connection with balancing of voltage due to the typical maximal voltage of 25 V of the individual component. For this reason, they are of interest in a low volt design of the load circuit, such as for power supply of EC motors.

Recharging of the storage capacitor during energy consumption clearly reduces the recharge time but only if the consumer current does not substantially exceed the recharge current. In this regard, a high volt design of the load circuit is more suitable than a low volt one.

The loss share out of the moving mass of the storage capacitor, for instance from lifting work, has to be taken into consideration in the efficiency of the energy transmission path. Table 3 summarises the parameters relevant to the specification of the design.

Table 3: Voltage levels secondary, energy store and charge times.

Voltage level secondary	**Energy storage secondary** ΔW: 650 W x 1s and U: -10%		**Recharge time** **(Current)** **Charging Power**	**Efficiency electrical**
	Type	Mass		
High Volt 320 V DC	Electrolyte capacitor 2x 15 mF/350 V and simultaneous Charging with 1 A	ca. 4 kg	1 s + 1 s (1 A) 320 W	
High Volt 320 V DC	Electrolyt capacitor 5x 15 mF/350 V	ca. 10 kg **mechanical work 100 Ws/m** **for vertical movement**	2.1 s (1 A) 320 W	
Low Volt 48 V DC	EDLC > 3 ... **5 F** **(ΔU = - 2.8 V; 5,8%)**	0.6 kg	14 s (1 A) 28 s (0,5 A) 48 W bzw. 24 W	0.90 * 0.95 *
Low Volt 24 V DC	EDLC > 12 F ... 16 F	0.3 ... 1 kg	29 s (1A) 24 W	

* $R_D + R_S$ = 4 Ohm

3.1. Energy Buffer with Electric Double Layer Capacitors

An EC motor of 40 V nominal voltage (50 V maximal voltage) was defined as the consumer for an exemplary energy transmission path. For this voltage level, Electric Double Layer Capacitors (EDLCs) are predetermined as energy storage devices. They have to be cascaded because their operating voltage is less than 25 V. As a result, we built up a capacitor bank tailored to the ongoing experiments with 46 V nominal voltage (total voltage of the cascade), 10 kWs basic energy and at least 600 Ws energy output capacity. Due to the high specific current capacity and the fact that the nominal voltage is close to the maximal voltage of the capacitor bank ($21 \times 2.28\,\mathrm{V} = 47.9\,\mathrm{V}$), additional functions for short circuit and overvoltage protection were included in the circuit

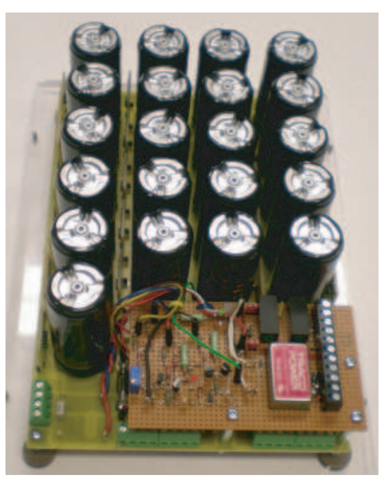

Figure 3: Experimental setup of the energy buffer with electric double layer capacitors (EDLCs).

Thus, we currently have available an intrinsically safe capacitor bank, whose operation is largely without external control. For a load cycle with 600 Ws energy output, voltage loss is 14 V. A greater loss is permitted in terms of 46 V nominal voltage of the capacitor bank and 40 V nominal motor voltage. Assuming optimised operating parameters of the drive and recuperation of braking energy, which until now has not been utilised capacitor bank capacitance can be diminished. Consequently, mass and volume can be at least halved in the future.

3.2. Power Switch Step

AC supply voltage (AC mains voltage) (230 V AC) is highly efficiently transmitted into a triggering voltage, which is adapted to the transmission path's characteristics. This transmission is executed by means of a resonance converter in LLC half bridge circuit. The transformer with a ferrite core surrounding the toothed drive belt for feed-in is a part of the circuit as a component with inductive effect. A value of 400 V was set as the limit of the DC supply voltage of the converter. We selected the bridge circuit out of the secondary rectification options given in Fig. 4, because two secondary coils would demand too many conductor loops in the toothed drive belt.

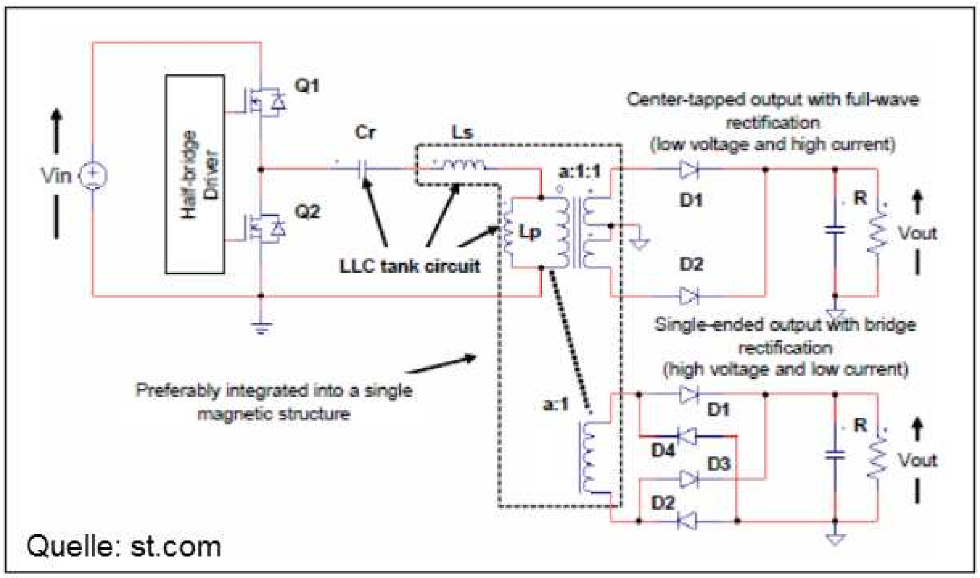

Figure 4: Block diagram of the LLC half bridge resonance converter. Quelle: Courtesy from.

The below-mentioned table includes an overview of the power loss rates during energy transmission from converter to capacitor bank. The relatively high losses in the conductor loops result from too low a conductor loop number and, in consequence, too high a resonance step-up of the conductor loop current.

Table 4: Losses.

Power input primary	103.4 W 60 kHz ;C2p = 3x 47 nF	78 W 75 kHz ;C2p = 2x 47 nF
Total power loss	21.7 W	17.3 W
Mean recharge current	2.05 A	1.63 A
r.m.s. current in conductor loops (measurement)	3.9 A !	3.14 W
Losses in conductor loops + feed wires (0.9 Ohm + 0.05 Ohm)	14.5 W	9.4 W
Losses from rectification (DC measurement with mean recharge current)	2 W (2.05 A*0.98 V)	1.5 W (1.63 A*0.93 V)
Losses in supercaps (charging)	0.55 W	0.35 W
Losses in ferrite core, MOSFETs, resonant circuit capacitors	ca. 4.7 W	ca. 6W **(75 kHz !)**

4. RESULTS

The parameters listed below were recorded using a toothed drive belt arrangement at a 28 m reversing distance. The available number of conductor loops only allowed for the installation of 4 secondary coils in the circuit. For higher efficiency, one needs more coils. The capacitor C2p is the secondary switching for the formation of a parallel resonant circuit. The AC input voltage of the LLC half bridge resonance converter was 325 V (230 V * sqrt2).

Table 5: Parameters of the energy transmission path.

C2p (Parallel resonant circuit with conductor loops)	3x 47 nF	2x 47 nF
Actual frequency **Capacitor bank voltage > 40 V**	60 kHz	75 kHz
Power input primary	103.4 W	78 W
Mean input current	0.318 A	0.24 A
Recharge time 40 V…45 V	31 s (6.2 s/V)	39 s (7.8 s/V)
Input energy	3203 Ws	3042 Ws
Increase in energy and mean recharge current in the supercaps **10 F @ 40 V and 10.3 F @ 45 V**	2429 Ws 2.05 A 63.5 As/31 s	2429 Ws 1.63 A 63.5 As/39 s
Efficiency of recharging	75.8 %	79.8 %

The energy of 2429 watt seconds corresponds to the energy demand of four load cycles per 600 Ws. Nominal voltage of the EC motor is 40 V. It is permitted to run it up to 50 V. Assuming 46.5 V charging voltage of the capacitor bank, energy consumption of 600 Ws for one load cycle results in a capacitor bank discharge by 1.4 V.

ACKNOWLEDGMENT

These investigations were carried out as a part of the project "Energy-Efficient Product and Process Innovation in Production Engineering" (eniPROD®) The Cluster of Excellence "Energy-Efficient Product and Process Innovation in Production Engineering" (eniPROD®) is funded by the European Union (European Regional Development Fund) and the Free State of Saxony.

REFERENCES

1. Voigt, U. and W. Wegner, *Zahnriemenrobotik — Eine neue Entwicklungsrichtung bei Norditec*, 11. Tagung, "Zahnriemengetriebe", Institut für Feinwerktechnik und Elektronik-Design der TU Dresden, 2006.
2. Schechinger, B., "Daten- und energieübertragung mit zahnriemen," 10, Fachtagung Zahnriemengetriebe, Institut für Feinwerktechnik und Elektronik-Design der TU Dresden, 2005.
3. Villa, J., J. Sallan, A. Llombart, and J. Sanz, "Design of a high frequency inductively coupled power transfer system for electric vehicle battery charge," *Applied Energy* Vol. 86, 355–363, 2009.
4. eniPROD, "Energieeffiziente produkt- und prozessinnovationen in der produktionstechnik," gefördert von der Europäischen Union aus Mitteln des Europäischen Fonds für regionale Entwicklung (EFRE) sowie aus Landesmitteln des Freistaats Sachsen.

A 1-kW Wireless Power Transfer Link for Welding Rollers

R. Trevisan[1] **and A. Costanzo**[2]

[1]DEI, University of Bologna, IMA Industries Srl, Italy
[2]DEI, University of Bologna, Italy

Abstract— This paper proposes an innovative approach to inductive wireless power transfer links based on a contactless energy transfer device. The key parts of the device, that are a rotary transformer and its windings, are presented. Since many configurations are possible, in terms of number of turns, wire, and compensation, different configurations are also discussed. Two setups able to transfer up to 1.3 kW in a contactless fashion are also prototyped and tested as replacements for slip rings used to supply welding roller resistors of automatic machineries. Experimental measures carried out on the test bench are used to validate the analytical model and the finite element simulations of the wireless power transfer link. Trade-offs emerge from the setups, in particular concerning efficiency and electro-magnetic compatibility. As a consequence, the choice of the optimal configuration depends on the final application.

1. INTRODUCTION

Traditionally, electrical joints between static and rotatable parts of automatic machinery are realized by mean of sliding contacts, usually slip rings. Older materials employed in sliding contact manufacturing were subject to early degradation, leading to unacceptable increase in the contact resistance [1]. In order to overcome this phenomenon and improve contacts' reliability, some studies toward innovative brush plates were made [2]. In spite of that, rotatable joints represent a common point of failure, because their lifetime is strongly related to the cumulated number of revolutions. For this reason, contactless rotary joints would significantly increase the overall machine's reliability, reducing costs of maintenance and the consequent downtimes. Contactless rotatable joints may widely replace the unreliable slip rings employed in rotary organs of automatic machines. A system based on a rotatable transformer fulfills such requirement. Indeed, an inductive contactless channel was proposed to achieve power transfer between stationary and rotatable parts of tool machines or robots [3]. A pot-core transformer is composed by two physically separated half cores, as shown in Fig. 1. Separation of the halves allows the rotation of the one in respect to the other, as the static and the rotary part of a slip ring [4].

In this paper, we propose a *wireless power transfer link* based on a pot-core transformer to be used as replacement for the slip rings usually applied to supply welding roller resistors. Two different setups are also presented and their measured performances are compared.

2. INDUCTIVE CET SYSTEMS

Inductive CET systems based on pot-core transformers are usually composed by a switching power supply, the inductive coupler (i.e., the rotatable transformer, which comprises the half cores and the windings), and the application load [5]. Optionally, a rectifying stage might be required between the rotary part of the transformer and the load. The main goal of such system is its ac-ac efficiency,

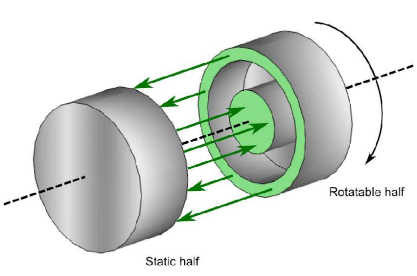

Figure 1: 3D image of two pot half cores and magnetic flux lines.

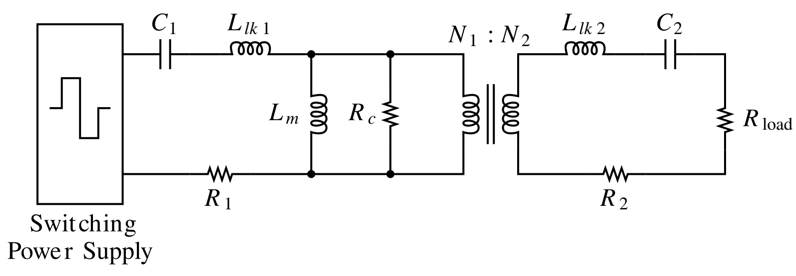

Figure 2: Equivalent representation of the inductive CET device.

which can be expressed as:

$$\eta = \frac{P_{\text{load}}}{P_{\text{in}}} = \left| \frac{n}{\frac{n^2(Z_2+R_{\text{load}})}{Z_m} + 1} \right|^2 \frac{R_{\text{load}}}{\text{Re}[Z_{\text{in}}]}, \tag{1}$$

$$n = \frac{N_1}{N_2}, \quad Z_i = j\omega L_i + \frac{1}{j\omega C_i} + R_i, \quad i = 1, 2, \tag{2}$$

$$Z_m = \frac{j\omega L_m\, R_c}{j\omega L_m + R_c}, \quad Z_{\text{in}} = Z_1 + \frac{n^2(Z_2 + R_{\text{load}})Z_m}{n^2(Z_2 + R_{\text{load}}) + Z_m}. \tag{3}$$

A circuit equivalent representation of the CET link, is shown in Fig. 2, where the quantities to compute the system efficiency are outlined. In (1) P_{load} is the power delivered to R_{load} and P_{in} is the power available at the Switching Power Supply port, in sinusoidal excitation condition. To effectively account for the strong dependence of system efficiency on the physical parameters of the pot core and of its windings, a systematic design procedure need to be implemented.

2.1. Rotatable Transformer

To ensure the physical separation of the rotatable transformer of Fig. 1, a small air gap (0.6 mm in our case) between the ferrite cores is realized. The air gap does not break the magnetic flux path, though significantly reduces the coupling coefficient of the transformer [6].

An estimation of the core's inductances can be obtained by the approach presented in [7]. Single reluctances are computed starting from geometrical and magnetic properties of the core such as radii, widths, heights, and permeability. The electrical equivalent circuit is then solved to calculate primary, secondary, and mutual inductances, as known from magnetics theory [8].

Despite the better coupling of pot-core transformers, compared to loosely coupled inductive power transfer (LCIPT) devices, compensation of leakage inductances would further improve its efficiency. Four different arrangements (SS, SP, PS, and PP) of the compensation capacitances are possible, depending on the positioning of each capacitance in series (S) or in parallel (P) to the primary or secondary winding, respectively [9]. Theoretically, SS compensation represents the best choice because it does not depend on the load, and therefore is the only considered in the following. Series capacitors usually compensate the self-inductance by the well-known relationship:

$$C_1 = \frac{1}{\omega^2 L_1}, \quad C_2 = \frac{1}{\omega^2 L_2}\,. \tag{4}$$

2.2. Windings

In order to allow relative rotation, hence physical separation of the halves, the windings must be detached as well. Thus, two different winding topologies are possible: *adjacent* windings and *coaxial* windings [10]. In the former topology each windings is placed in its own half core, whereas in the latter windings are concentric. In this work, we choose the coaxial winding topology, because of its greater reliability under mechanical vibrations.

A number of parasitic effects need to be included in the CET design to obtain accurate prediction of its performance. First of all, the well-known *skin effect* which results in an increase in the wire resistance when ac currents at high-frequencies circulate through them [11]. Second, wires stacked in layers, the ones above the others, also suffer from the *proximity effect*, that contributes to reduce the effective wire's current cross-section due to the induced magnetic field from adjacent conductors [12]. Many works estimate the equivalent ac resistance of windings in magnetic components, when skin-effect and proximit-effect losses are considerable, such as [13, 14]. We have obtained a strong reduction of these effects by choosing stranded wire, also called *litz wire*. Sullivan in [15] proposes a method to optimise the number of strands in a litz wire, by considering wire's thickness as well as core's geometries. Given the dc resistance of the winding R_{dc}, its dc + ac resistance can be estimated as follows:

$$R_{\text{dc+ac}} = R_{\text{dc}} \left(1 + \frac{\pi^2 \omega^2 \mu_0^2 N^2 n^2 d_c^6 k}{768 \rho_c^2 b_c^2}\right), \tag{5}$$

in which the current is supposed sinusoidal and ω is the radian frequency, n the number of strands, N the number of turns, d_c the diameter of the copper in each strand, ρ_c the resistivity of the copper, b_c the breadth of the window area of the core, and k a factor usually equal to one.

3. CET DEVICE EXPERIMENTAL SETUPS

Slip rings of welding rollers commonly employed in automatic machines represent reasonable components to be replaced with a wireless power transfer links. Therefore, we set up a prototypal test bench able to transfer up to 1.3 kW through a CET device to a resistive load. Because of the wide variety of configurations in terms of number of turns, wire types, and compensating capacitances, we decided to test two different setups in order to seek the optimal trade off between efficiency, feasibility, reliability, and compatibility. The following considerations emerge:

1. The equivalent input inductance should not be cancelled, otherwise the power inverter that supplies the CET device would require an additional inductor to achieve resonant commutation of its switches.
2. The copper losses increase with the winding wire length. Hence, the fewer turns, the better.
3. The ferrite losses increase with the magnetic flux density. Hence, the more turns, the better.
4. The voltage magnitude across C_1 (or C_2) decreases with the inverse of the capacitance, thus decreases with the increase in the inductance. Hence, the more turns, the better.

The two setups that we will discuss below, named *setup 18/17* and *setup 27/24*, use the same P66/56 3C81-ferrite core and 50-kHz switching frequency, whereas they adopt different windings, capacitances, and number of turns. The 3C81 material is a MnZn soft ferrite suitable for power applications at frequencies up to 200 kHz, with minimal losses around 60°C [16]. We pursued the following design priority constraints for the setups.

3.1. Setup 18/17

Minimal copper loss constraint is pursued. The litz strand section is ideal for 50-kHz signals, and the number of strands is maximised. Thick wires imply a small number of turns, that results in greater ferrite losses. 18 turns of 500×0.1-mm strand litz wire for the primary winding represent a good compromise at 50 kHz to prevent saturation. The number of turns (17) of the secondary winding is chosen to obtain a suitable voltage on the load. According to Eq. (4), the small inductances of this setup result in big compensating capacitances, thus high voltage ratings (almost prohibitive). For this reason, we decided not to include any compensation in this case.

3.2. Setup 27/24

Minimal EMI emission constraint is pursued. The highly-distorted current waveform of a purely-inductive CET system (e.g., of setup 18/17) may induce electro-magnetic incompatibilities. Adding primary compensation results into two benefits: 1. *LC* filtering network on current's harmonics; 2. partially compensation of inductance. Since the load is fixed, only primary compensation can be adopted. In this case, its value can be computed as follows:

$$C_1 = \frac{1}{\omega \operatorname{Im}\left[Z_2' + j\omega L_{lk1} + R_1\right]}, \quad Z_2' = \frac{n^2\left(j\omega L_{lk2} + R_2 + R_{\text{load}}\right)\ Z_m}{n^2\left(j\omega L_{lk2} + R_2 + R_{\text{load}}\right) + Z_m}, \tag{6}$$

With respect to the considerations above, a good compromise is represented by 27/24 turns of 84×0.18-mm strand litz wire and $C_1 = 100\,\text{nF}$. Despite the higher copper losses of 27/24 turns, lower EMI and lower ferrite losses are expected.

4. RESULTS

The setups described above are used to validate the analytical model presented, including the finite element simulations of the pot-core transformer.

First, electrical parameters of the circuit-equivalent model are compared with the results of the FEM simulation. Then, a systematic set of measurements are carried out. The FEM software used to simulate the transformer is Finite Element Method Magnetics (FEMM) free software [17]. Comparisons among electrical parameters of the analytical model, FEM simulation based on the physical quantities of the CET link, and the experimental measurements are summarized in Table 1 and in Table 2 for the setup 18/17 and the setup 27/24, respectively. Measures of the efficiency at the given conditions are also shown, and the input impedance of the CET link is plotted in Fig. 3 for the two configurations.

Table 3 provides a short comparison between the tested setups. Although either configuration is able to transfer more than 1 kW of electrical power by loosing less than 5% in ferrite and copper losses, the second setup also guarantees low EMI with moderate additional efforts in terms of circuit

Figure 3: Electrical parameters of setup 18/17.

	Analytical	**FEM**	**Measured**	**Units**
R_1	54.6	–	–	mΩ
R_2	47.2	–	–	mΩ
L_{lk1}	0.028	0.030	0.048	mH
L_{lk2}	0.025	0.027	0.010	mH
L_m	0.303	0.296	0.269	mH
η	–	–	0.977	·

Figure 4: Electrical parameters of setup 27/24.

	Analytical	**FEM**	**Measured**	**Units**
R_1	255	–	–	mΩ
R_2	174	–	–	mΩ
L_{lk1}	0.063	0.068	0.065	mH
L_{lk2}	0.050	0.053	0.049	mH
L_m	0.682	0.671	0.670	mH
η	–	–	0.956	·

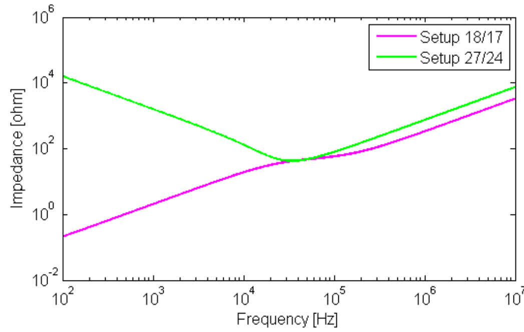

Figure 5: Input impedance of the CET link.

Table 1: Comparison between setups.

	Setup 18/17	**Setup 27/24**
Complexity	Low	Medium
Ferrite losses	Medium	Low
Copper losses	Very Low	Medium
Efficiency	Very High	High
EMI	High	Low

complexity. Further tests should be carried out in order to verify the effective electro-magnetic compatibility of the proposed solutions. Finally, the plots of the measured input and output power waveforms are shown in Fig. 4 and Fig. 5 for setup 18/17 and setup 27/24, respectively. The bad shape of the power waveforms in setup 18/17 warns that severe EMI may occur. In case of extensive wiring of the automatic machine, such interference might become a serious issue and must be taken into account. Yet, the setup 27/24 represents a suitable solution for EMI, despite the slight inefficiency with respect to setup 18/17.

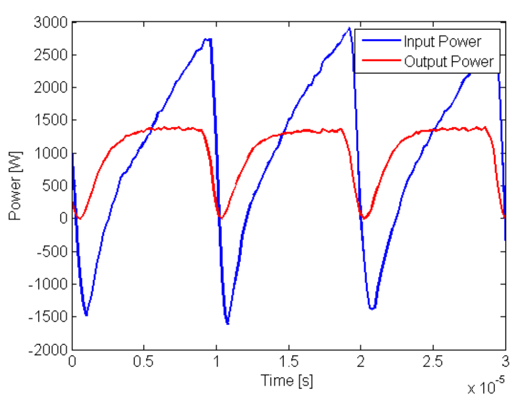

Figure 6: Power waveforms of setup 18/17.

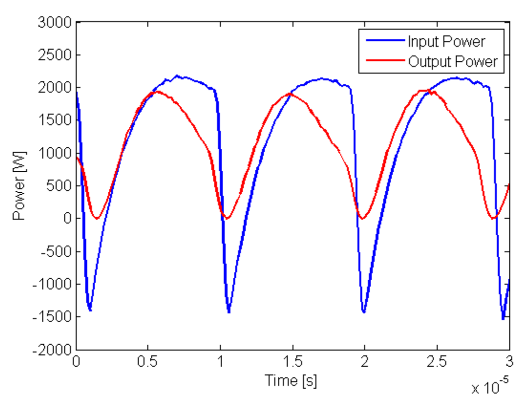

Figure 7: Power waveforms of setup 27/24.

5. CONCLUSIONS

We have introduced a solution for a wireless power transportation link, to transfer up to 1.3 kW, which represent a valid replacement for slip rings employed in welding rollers of automatic machines. We have adopted an analytical design procedure starting from a reference circuit equivalent scheme of the CET link. The design results are checked by a suitable set of measurements carried out on the prototype confirming the accuracy of the analytical models adopted. Two different solutions are compared to outline the different trade-offs that may be required in different CET application scenarios.

REFERENCES

1. Antler, M., "Survey of contact fretting in electrical connectors," *IEEE Trans. Compon., Hybrids, Manuf. Technol.*, Vol. 8, No. 1, 87–104, 1985.
2. Sawa, K., S. Kakino, K. Endo, G. Ou, and H. Hagino, "Degradation process of a sliding system with Au-plated slip-ring and AgPd brush for power supply," *Proc. 51st IEEE Holm Conf. on Electrical Contacts*, 312–317, Chicago, IL, 2005.
3. Esser, A. and H.-C. Skudelny, "A new approach to power supplies for robots," *IEEE Trans. Ind. Appl.*, Vol. 27, No. 5, 872–875, 1991.
4. Papastergiou, K. D. and D. E. Macpherson, "An airborne radar power supply with contactless transfer of energy — Part I: Rotating transformer," *IEEE Trans. Ind. Electron.*, Vol. 54, No. 5, 2874–2884, 2007.
5. Moradewicz, A. J. and M. P. Kazmierkowski, "Contactless energy transfer system with FPGA-controlled resonant converter," *IEEE Trans. Ind. Electron.*, Vol. 57, No. 9, 3181–3190, 2010.
6. Papastergiou, K., D. Macpherson, and F. Fisher, "A 1 kW phase-shifted full bridge converter incorporating contact-less transfer of energy," *Proc. 2005 Power Electronics Specialists Conf.*, 83–89, Recife, Brazil, 2005.
7. Perrottet, M., "Transmission électromagnétique rotative d'énergie et d'information sans contact," Ph.D. Dissertation, Département d'Électricité, École Polytechnique Fédérale de Lausanne, Lausanne, Switzerland, 2000.
8. McLyman, C. W. T., *Transformer and Inductor Design Handbook*, 3rd Edition, CRC Press, 2004.
9. Wang, C.-S., O. H. Stielau, and G. A. Covic, "Design considerations for a contactless electric vehicle battery charger," *IEEE Trans. Ind. Electron.*, Vol. 52, No. 5, 1308–1314, 2005.
10. Smeets, J., D. Krop, J. Jansen, and E. Lomonova, "Contactless power transfer to a rotating disk," *Proc. 2010 IEEE Int. Symp. Industrial Electronics*, 748–753, Bari, Italy, 2010.
11. Brown, M., *Power Supply Cookbook*, Newnes, 2001.
12. Lotfi, A. and F. Lee, "A high frequency model for litz wire for switch-mode magnetics," *Conf. Rec. 1993 IEEE Industry Applications Society Annu. Meeting*, Vol. 2, 1169–1175, Toronto, ON, 1993.
13. Dowell, P., "Effects of eddy currents in transformer windings," *Proc. of the Inst. of Elect. Eng.*, Vol. 113, No. 8, 1387–1394, 1966.
14. Ferreira, J. A., "Improved analytical modeling of conductive losses in magnetic components," *IEEE Trans. Power Electron.*, Vol. 9, No. 1, 127–131, 1994.
15. Sullivan, C. R., "Optimal choice for number of strands in a litz-wire transformer winding," *IEEE Trans. Power Electron.*, Vol. 14, No. 2, 283–291, 1999.
16. Ferroxcube, *Soft Ferrite and Accessories 2009 Data Handbook*, Ferroxcube, 2009.
17. Meeker, D. C., "Finite element method magnetics," 2012, Available: http://www.femm.info.

Obstacle Detection Method Using Array Antenna for Coupled-resonant Wireless Power Transfer

H. Yamada, K. Miwa, H. Hirayama, N. Kikuma, and K. Sakakibara
Department of Computer Science and Engineering, Nagoya Institute of Technology, Japan

Abstract— This paper proposes a method of obstacle detection for coupled-resonant wireless power transfer. 2×2 array antenna is used for power transmission and obstacle detection. Standard deviation of transmission coefficient and reflection coefficient is used as an index of detection. Feasibility of the proposed method is verified through numerical simulations.

1. INTRODUCTION

Recently, research and development on coupled-resonant wireless power transfer (WPT) is getting large interests [1]. It is expected that power transfer for electric vehicle (EV) is turned into practical use. However, there is a possibility that an interposed obstacle, such as a drink can, is heated to cause fire because the WPT system for EV handles power of kW order. Therefore, it is necessary to detect an interposed obstacle between transmitting and receiving coils.

In this paper, we propose a method of obstacle detection by using array antennas. Feasibility of the proposed method is verified through numerical simulation using method of moments (MoM).

2. POWER TRANSFER USING ARRAY ANTENNA

In order to extend power transmission area, using two-dimensional array antenna is proposed [2]. The proposed method utilizes 2D array antenna not only for power transmission but also for obstacle detection. The consideration model using array antennas is shown in Fig. 1. Transmitting (TX) and receiving (RX) antennas consist of 2×2 array antenna. Each element antennas are square-shaped two-turn loop coils. The coil is made of 1 mm-radius copper wire. Side of the square is 25 cm. The gap between the adjacent element antennas is 6 cm. At the port of the transmitting coils (port 1–4), voltage sources (1 V, 50 Ω) and tuning capacitors of 38.8 pF are connected in series. At the port of the receiving coils (port 5–8), 50 Ω loads and tuning capacitors are connected in series. The capacitance of the tuning capacitors is determined to resonate at 13.56 MHz for each element antenna. For power transmission, power is distributed for four TX element antennas and collected from four RX element antennas.

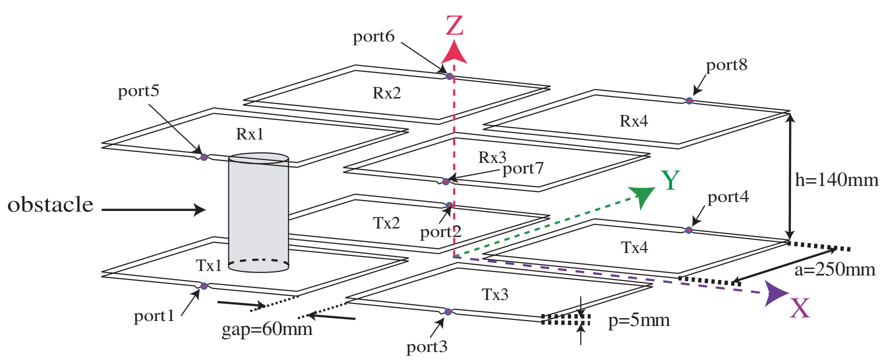

Figure 1: Consideration model.

3. METHOD OF DETECTION

Let us assume that an obstacle is interposed between TX and RX as shown in Fig. 1. If there is no obstacle, reflection coefficients for all four TX antenna become same value. Transmission coefficient between facing TX and RX element antennas for four combinations become also same value. However, when an obstacle is interposed between TX and RX antennas, variation is caused among four transmission or reflection coefficients because magnetic field is disturbed.

The proposed method utilizes this variation by using standard deviation (SD) of transmission or reflection coefficients. SD for reflection coefficient σ_r and SD for transmission coefficient σ_t are examined:

$$\sigma_r = \sqrt{\frac{1}{N}\sum_{i=1}^{N}(s_{i,i} - \overline{s_r})^2} \tag{1}$$

$$\sigma_t = \sqrt{\frac{1}{N}\sum_{i=1}^{N}(s_{i+N,i} - \overline{s_t})^2} \tag{2}$$

where N shows number of element antennas, in this case $N = 4$. $s_{i,j}$ shows S parameters between port i and j. $\overline{s_r}$ shows average of S_{11}, S_{22}, S_{33}, S_{44}. $\overline{s_t}$ shows average of S_{51}, S_{62}, S_{73}, S_{84}.

4. ANALYSIS AND RESULTS

4.1. Effect of Position of Obstacle

To verify the ability of the proposed method, we conduct MoM simulation. As an obstacle, a drink can and a coin is assumed. Six obstacle models are used as shown in Fig. 2. All obstacle models are hollow cylinder made of aluminum.

Height \ Radius	Drink can radius	Coin radius
Drink can height	r, h h=12.22cm r=3.3cm model1	h=12.22cm r=1.33cm model4
Half height of drink can	h=6.11cm r=3.3cm model2	h=6.11cm r=1.33cm model5
Coin height	h=0.181cm r=3.3cm model3	h=0.181cm r=1.33cm model6

Figure 2: Size of obstacle model.

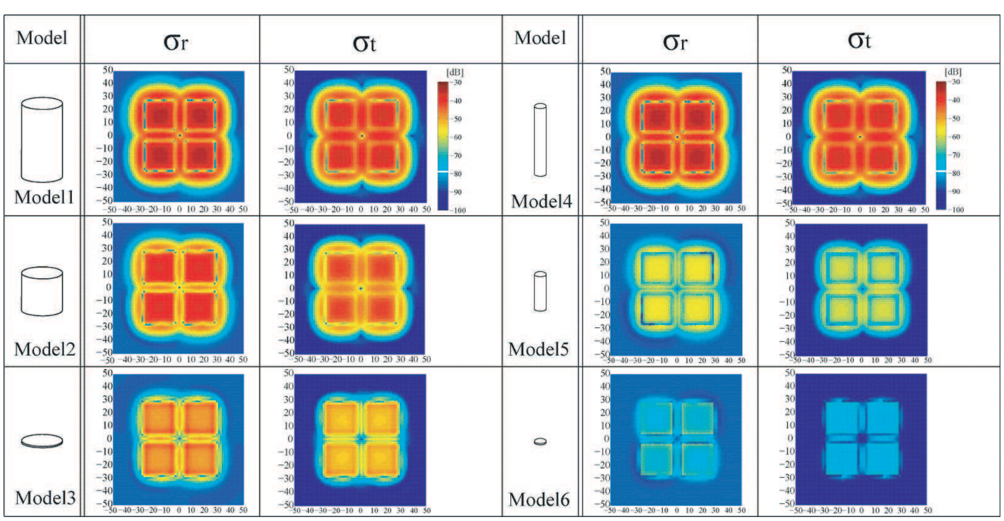

Figure 3: Effect of obstacle position on SD.

First, effect of position of the obstacle on the SD is analyzed by using MoM. Position of the obstacle is swept within the square region ($-60\,\mathrm{cm} < (x, y) < 60\,\mathrm{cm}$) above the TX antenna. The distance between the TX and RX antennas is set to 14 cm.

Figure 3 shows simulation result. SD without the obstacle is -79 dB, which is indicated by white line in the color bar. Therefore, obstacle can be detected if SD exceeds -79 dB. For the model 1–5, obstacle can be detected except some region, where obstacle is just under the coil and just center of the array antenna. Model 6 was not detected for any position because this model is too small to detect the disturbance of the field.

When the obstacle is located just center of the array antenna, variation of the transmission or reflection coefficient for all antennas become same value. Therefore obstacle can not be detected. In order to understand the mechanism why obstacle can not be detected when it is just under the coil, magnetic field vector distribution without obstacle is shown in Fig. 4. Direction of magnetic field vector inside and outside of the coil becomes opposite. Thus, effect of disturbance due to the obstacle is canceled. This reason is similar to the null zone of RFID tag [3].

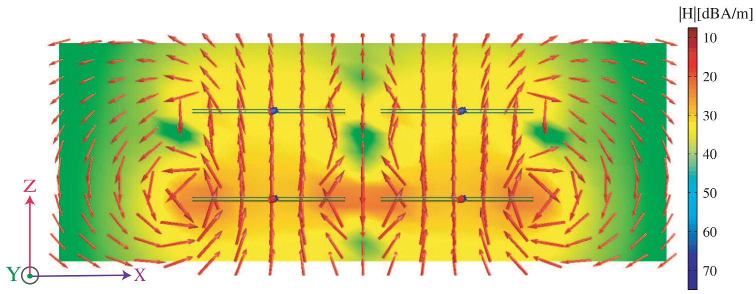

Figure 4: Magnetic field vector distribution without obstacle.

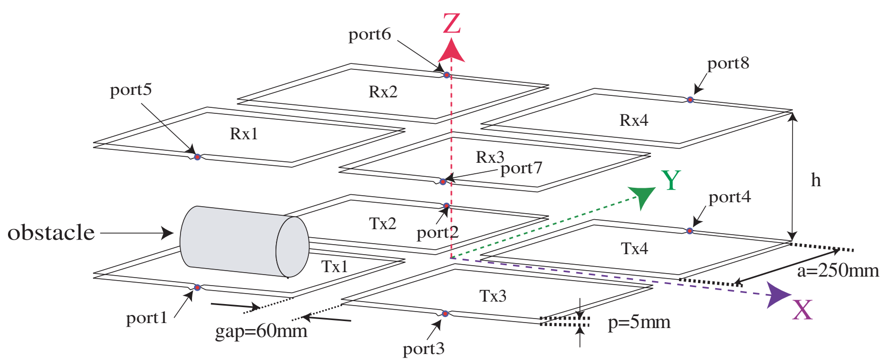

Figure 5: Consideration model for distance characteristic.

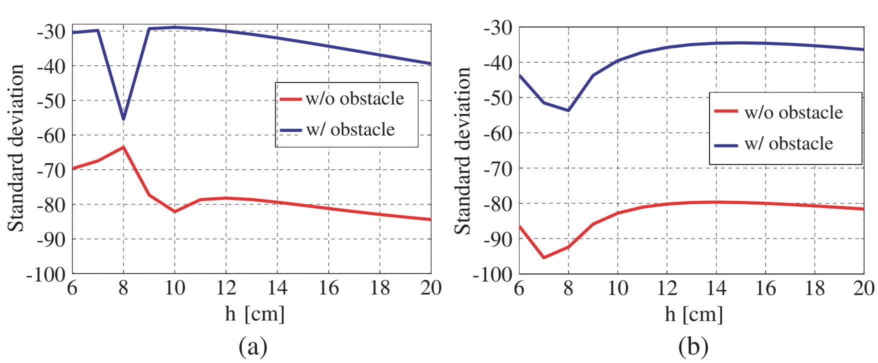

Figure 6: Effect of distance between TX and RX on SD. (a) SD using reflection coefficient σ_r. (b) SD using transmission coefficient σ_t.

4.2. Effect of Distance between TX and RX

Second, effect of distance between TX and RX on SD is examined. Fig. 5 shows consideration model. Distance h between the TX and RX antennas is varied from 6 cm to 20 cm. Model 1 is assumed as an obstacle. In this model, obstacle is laid above the TX1. Fig. 6 shows SD with and without obstacle. Margin for obstacle detection is determined by the difference between the minimum value of SD with the obstacle and the maximum value of SD without the obstacle. Margin for σ_r and σ_t is 8 dB and 26 dB, respectively. SD for transmission coefficient has larger margin to detect obstacle than SD for reflection coefficient. Mutual coupling among element antennas can be reason of this.

5. CONCLUSION

Obstacle detection method for coupled-resonant wireless power transfer is proposed. Standard deviation of transmission coefficient and reflection coefficient is used as an index of detection. MoM simulation demonstrated feasibility of the proposed method. Advantage of the proposed method is that antennas for power transmission is used also for obstacle detection.

To evaluate effect of displacement of TX and RX antenna is further study.

REFERENCES

1. Kurs, A., A. Karalis, R. Moffatt, J. Joannpoulos, P. Fisher, and M. Soljacic, "Wireless power transfer via strongly coupled magnetic resonances," *Science Magazine*, Vol. 317, No. 5834, 83–86, Jul. 2007.
2. Miwa, K., H. Mori, N. Kikuma, H. Hirayama, and K. Sakakibara, "A consideration of efficiency improvement of transmitting coil array in wireless power transfer with magnetically coupled resonance," *Proc. of WPTC 2013*, 13–16, May 2013.
3. Hirayama, H., N. Kikuma, and K. Sakakibara, "A new scheme to avoid null zone for HF-band RFID with diversity combining of loop antennas," *IEICE Trans. on Commun.*, Vol. E93-B, No. 10, 2666–2669, Oct. 2010.

Ultrawideband Radar Future Directions and Benefits

James D. Taylor
148 Breezy Bay Drive, Ponte Vedra, FL 32081, USA

Abstract— Practical applications and benefits can guide future ultrawideband (UWB) radar development objectives. Application driven research could produce UWB radar techniques to detect and identify small, low contrast objects from their shape, composition and return spectrum characteristics. Previous experimental work has shown the possibilities for exploiting side and forward scattered signals as a way to detect objects which have small backscatter due to geometry (size and shape) and a low object/medium index of refraction contrast. Potential applications include ways to detect small biological tumors, plastic mines, defects in structures or parts in medicine, manufacturing control and improved materials penetrating radar imaging. A combination of radar and tomographic approaches could increase the possibilities a small target detection and identification. Tangible benefits could include applications for medical imaging which can give small clinics the capabilities of a large hospital.

1. INTRODUCTION

Ultrawideband radar has demonstrated possibilities for high resolution remote sensing and materials penetrating applications. Each year the available research literature presents a better understanding of how UWB signals travel through media, reflect and scatter [1–4]. This paper presents some suggestions for practical applications driven UWB radar research.

2. UWB RADAR PROPAGATION DIFFERENCES

2.1. Conventional Narrowband Radar Theory

The conventional narrowband radar approach treats targets as a reflector with an effective geometric surface (*radar cross section* in m^2) reflecting energy back to the radar set, or scattering it to other bistatic and multistatic receivers. With no shift in the signal waveform/frequency content and long duration signals this approach works for conventional narrowband (sinusoidal signal) radar performance predictions. Radar signal bandwidths greater than 25 percent of center frequency with small spatial resolution introduces a new set of considerations not described by conventional radar theory.

2.2. UWB Radar Theory

Nonsinusoidal UWB radio signals change waveform and spectrum on transmission, target interaction and reception due to differentiation at each conversion from electrical to electromagnetic waves and vice versa. Predicting and modeling the waveform changes and return signal spectra could provide the basis for increased detection sensitivity and promote medical, nondestructive testing and other practical applications. Terence Barrett describes this concept in *Resonance and Aspect Matched Adaptive Radar (RAMAR)* [5]. The ability to search for objects with a spatial resolution of the same size or smaller than the object introduces new considerations in signal detection through multiple sequential returns and permits the possibility of object imaging [2–4].

3. FUTURE UWB RADAR RESEARCH DIRECTIONS

3.1. Overview

Progress in UWB radar technology suggests some ideas for research, systems design and practical applications. These research area include: improved UWB propagation theory; better UWB radar architectures; multisensor integration; higher order signal processing; and combining multistatic and tomographic methods [6].

3.2. Improved UWB Propagation Theory

UWB short duration nonsinusoidal signals change waveform during transmission, reception and reflection. Better UWB radar design will require improved UWB signals analysis methods based on time domain approaches. Improved development of UWB propagation theory will greatly help developing future applications. Advanced models for high resolution scattering from objects smaller than the spatial resolution can guide multistatic detection system design [3, 12, 13]. Guidelines for developing effective signal waveforms which also comply with governmental spectrum frequency and power restrictions can provide a valuable resource for avoiding electromagnetic interference issues [14, 15].

3.3. Advanced UWB Radar Architectures

Depending on the applications and performance objectives, future UWB radar architectures could include the features in Table 1. A system architecture including all of the advanced features would look like Figure 1(a).

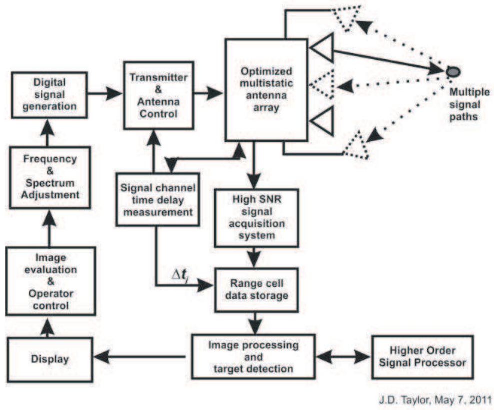

(a) Future UWB Radar Architecture

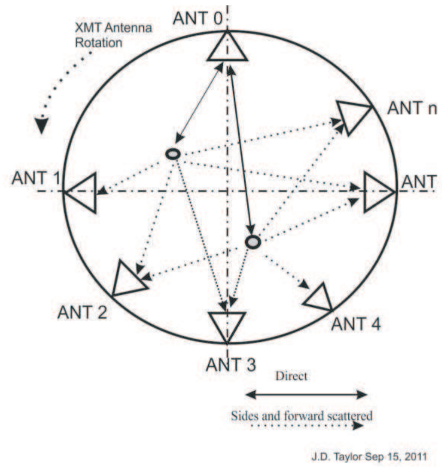

(b) Multistatic imaging and tomographic array

Figure 1: (a) Advanced UWB radar architecture including the features of Table 1. (b) A multistatic UWB radar and tomography antenna array for small object detection receives side scattered energy to augment directly reflected and direct path tomographic object detection.

Table 1: Future UWB radar architecture improvements.

DESIGN FEATURE	BENEFIT
Unsymmetrical antenna array	Optimal information content [3]
Self-calibrating channel time delays	Improved high resolution imaging [3]
Variable range bin signal integration	Improved SNR and detection at all ranges [3]
Range gating to restrict measurement range	Interference elimination in medical and other measurements [2, 3]
Holographic signal processing	Improved imaging [3]
Variable and adaptive waveform transmitters	Increased target return by matching the signal spectrum to target resonances [1, 3, 5, 13]
Step frequency radar	High resolution with long range performance [2, 3]
Random noise signals	Extended range [2, 3]
Bistatic and multistatic radar operation	Improved small target detection and imaging [3]
Time domain analysis	Improved signal and system design [1–3]
Unknown signal detection methods	Improved sensitivity with distorted signals [3]
Higher Order Signal Processing	Target identification through spectral shifting [1]

3.4. Multisensor Integration

Combining UWB radar with UV, millimeter wave, and other sensors could provide the basis for improved remote sensing applications for medical, security, defense and other purposes [13].

3.5. Higher Order Signal Processing

The wide spectrum of UWB signals presents new possibilities for target identification by examining the frequency content of radar returns. In Chapter 9 of *Introduction to Ultrawideband Radar Systems*, van Blaricum describes the Singularity Expansion Method (SEM) for examining the effects of target geometry on UWB returns. In Chapter 11, Sheby and Marmarelis describe Higher Order Signal Processing (HOSP) using bispectral or kernel analysis to increase radar performance by charaterizing radar returns from different materials. Combining these effects with high resolution imagery could provide new remote sensing capabilities in materials penetrating applications [1].

3.6. Waveform Modification

Adjusting the transmitted waveform to match the target response can improve the chances of target detection [5]. The radar architecture of Figure 1(a) includes a capability to analyze the return and change the transmitted waveform to match the signal to the target resonances for an enhanced target return signal.

3.7. Combined Multistatic Radar and Tomographic Methods

Combining UWB radar with microwave tomographic techniques could provide improved detection of small, low contrast objects in medical imaging and tumor detection. Objects have a single frequency bistatic scattering pattern angular width $\theta_b = \lambda/d$ where d indicates the linear target dimension in a particular plane [6]. For the ultrawideband case, a signal with a bandwidth b or pulse duration τ, the linear dimension d could have a size close to, or larger than the range resolution $\Delta r = c\tau/2 = c/2b$. This condition could produce significant side scatter from a UWB signal. This suggests that a multistatic antenna array to collect reflected and side scattered signals could increase the possibilities for detecting and imaging small or low contrast objects for medical and other applications. Applying tomographic techniques and spectral analysis to the signal received at the opposite antenna could aid in detecting small or low contrast targets. Figure 1(b) shows a combined UWB radar and microwave tomographic concept with either a static or rotating antenna array.

4. CURRENT AND FUTURE UWB RADAR MEDICAL APPLICATIONS

UWB radar based scanners could provide small medical clinics with imaging and diagnostic capabilities currently available in hospitals. For a practical applications objective, imagine a medical scanner (internal imaging system) controlled by a computer through a USB port [6]. Some current examples of UWB radar medical applications include.

4.1. The Sensiotec Virtual Medical Assistant^{TM} Patient Monitor

UWB radar can penetrate human tissue and provide instantaneous measurements of heart and lung movements. Figure 2(a) shows the Sensiotec radar sensor bed panel for measuring heart and respiration rates. The bed panel UWB radar has a 4 GHz center frequency with a ~ 2 ns pulse length and ~ 50 nanowatt radiated power. The estimated price of $3500 (July 2010) makes this a

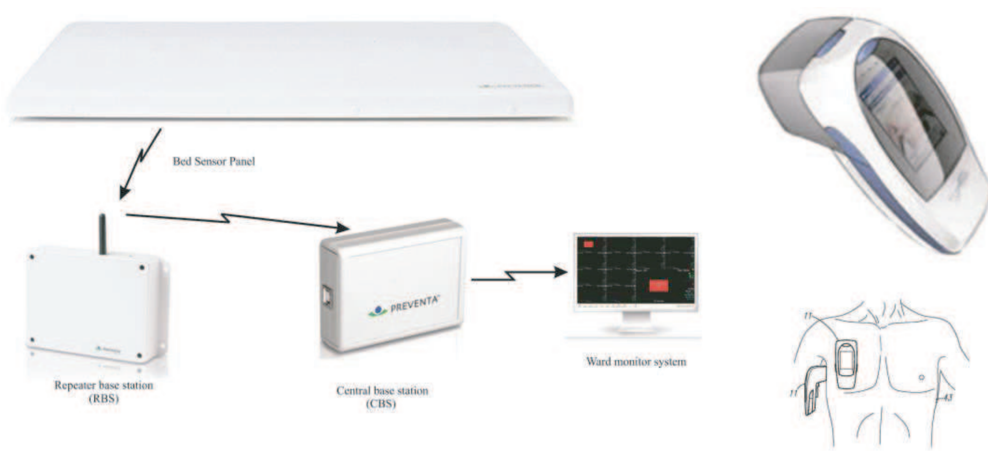

(a) Sensiotec Virtual Medical Assistant^{TM} Patient Monitor (b) The PneumoScan® pneumothorax detection system

Figure 2: Examples of current UWB radar medical applications: (a) The Sensiotec Virtual Medical Assistant^{TM} uses UWB radar to measure heart rate and respiration. (b) The Pneumoscan® uses UWB radar to detect bleeding within the chest cavity. (Permission of Sensiotek and Pneumoscan© Sensiotec and Pneumoscan).

cost effective solution to improving overall hospital care and efficiency [9, 10].

4.2. The PneumoScan® Pneumothorax Detector

Trauma or infection can cause pneumothorax, a condition which fills the chest cavity with blood and can cause death if not treated promptly. Emergency medical personnel need a quick way to detect pneumothorax without X-ray or CT scans. PneumoSonics Inc. developed the PneumoScan® handheld pneumothorax detector for emergency medical personnel. It uses UWB radar pulses to measure the relative positions of the chest wall and lungs. The hand held device shown in Figure 2(a) contains a UWB radar probe, a control unit containing the power source and processing system to analyze incoming data. After analyzing measurements, it gives the user an immediate indication of any pneumothorax and the location [11, 12].

5. DEVELOPMENT OBJECTIVES FOR FUTURE UWB RADAR RESEARCH

Directing UWB radar development objectives to detecting small biological tumors, plastic mines, defects in structures or parts in medicine, manufacturing control and materials penetrating imaging can yield great benefits for future practical applications. A combination of radar and tomographic approaches could increase the possibilities a small target detection and identification. Continued progress in understanding the theory of UWB back, side and forward scattering could produce a UWB radar based scanner for diagnosis in small clinics and remote areas. It could help emergency medical technicians to detect serious internal injuries quickly. Applications directed to developing UWB radar based imaging and diagnostic systems can provide inexpensive medical imaging systems for small and remote medical clinics worldwide.

REFERENCES

1. Taylor, J. D., ed., *Introduction to Ultra-wideband Radar Systems*, CRC Press, Boca Raton, FL, USA, 1995.
2. Taylor, J. D., ed., *Ultra-wideband Radar Technology*, CRC Press, Boca Raton, FL, USA, 1995.
3. Taylor, J. D., ed., *Ultrawideband Radar Applications and Design*, CRC Press, Boca Raton, FL, USA, 2012.
4. Astanin, L. Y. and A. A. Kostylev, *Ultrawideband Radar Measurements and Processing*, The Institution of Electrical Engineers, Stevanage, Herts, UK, 1997.
5. Barrett, T., *Resonance and Aspect Matched Adaptive Radar (RAMAR)*, World Scientific Publishing, 2012.
6. Taylor, J. D., "Ultrawideband radar progress," *Proc. IEEE Radar Conference 2012*, Atlanta, GA, 2012.
7. Wicks, M. C., J. D. Norgard, and T. N. Cushman, "Adaptive tomographic sensors for below ground imaging," *IEEE Aerospace and Electronic Systems Magazine*, Vol. 25, No. 5, 24–28, 2010.
8. Howland, P. E., H. D. Griffiths, and C. J. Baker, "Chap 7: Passive bistatic radar systems," *Bistatic Radar: Emerging Technology*, M. Cherniakov, ed., John Wiley & Sons, West Sussex, UK, 2008.
9. Farrell, M., "Nine technologies to ease pain of getting old," *Forbes*, July 1, 2010, http://www.forbes.com/2010/07/01/technology-for-the-elderly-entrepreneurs-technology-mit_2.html.
10. Sensiotec Inc., "Preventa vital," 2011, http://www.sensiotec.com/products/vital.php.
11. LLNL, "Fast detection of a punctured lung," *LLNL Science and Technology Review*, October 2007, https://www.llnl.gov/str/Oct07/pdfs/10_07.1.pdf.
12. Wilder, S., D. Theobold, R. B. Fell, and R. L. Yoder, "Non-invasive pneumothorax detection and apparatus," United States Patent Application Publication (10) Pub. No.: US 20100222663 Al, September 2, 2010.
13. Wickes, M. E., E. Mokole, S. Blunt, R. Schneible, and V. Amuso, eds., *Principles of Waveform Diversity and Design*, Scitech Publishing, Raleigh, NC, 2010.
14. Hamran, S.-E., "Radar performance of ultra wideband waveforms," *Radar Technology*, 410, G. Kouemou, ed., INTECH, Croatia, 2009, http://www.intechopen.com/books/radar-technology/radar-performance-of-ultra-wideband-waveforms.
15. Mirshafiei, M., M. Abtahi, P. Larochelle, and L. A. Rusch, "Pulse shapes that outperform traditional UWB antenna/waveform combinations," *IEEE Globecom 2010 Proceedings*, 2010.

Advances in Imaging of Archaeological Structures Using GPR

S. Piro[1] **and D. Goodman**[2]

[1]ITABC, CNR, P. O. Box 10, Monterotondo Sc., Roma 00015, Italy
[2]Geophysical Archaeometry Laboratory, LA, CA, USA

Abstract— For most archaeological prospections with GPR, detection is the most important aspect of the surveys. If enough density of profiles is recorded across a site, structural information can also be obtained regarding the buried features. Shallow and narrow features may require a very fine line density to get detected. If the profile spacing is large, shallow areas can have no microwaves penetrating the region. At greater penetration depths however, the unsampled region decreases. If small targets are buried close to the ground surface, detection of these features may require a finer line spacing then objects which are buried slightly deeper and within the penetration depth of the antenna.

A method for presenting GPR data from archaeological sites is needed to show these minute changes. Rather than showing the changes in reflected energies along the vertical — radargram — slices of the ground, it is more useful to map horizontal changes of reflected energy across a site. In this case small, but consistent reflections above the background noise can be visualized by using time slice analysis. There are a variety of imaging and analyses that must be implemented to solve the multitude of subsurface conditions in the archaeological field survey. Among a few of the necessary imaging techniques and analysis to be briefly introduced in this presentation: Time slices, Isosurface rendering and Overlay Analysis.

1. INTRODUCTION

Nonetheless, shallow and narrow features may require a very fine line density to get detected. Shown in Fig. 1 is a generalized description of the “unsampled” region vs. the profile spacing”.

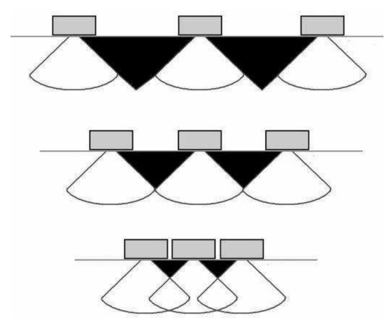

Figure 1: Profile spacing vs. unsampled area.

If the profile spacing is large, shallow areas can have no microwaves penetrating the region. At greater penetration depths however, the unsampled region decreases. If small targets are buried close to the ground surface, detection of these features may require a finer line spacing then objects which are buried slightly deeper and within the penetration depth of the antenna. This thinking somewhat goes against what we believe about GPR: the shallower something is the better chances we can detect it. This is obviously not the case if buried materials are very shallow and a sufficient line density is not employed in the field survey.

The smallest detectable size of archaeological materials is in general dependent on the frequency of the transmitting antenna. Smaller antennas can resolve smaller objects better than larger lower frequency antennas. Large antenna can detect very small objects, although the significance of the reflections from those small objects may not be realized by the naked eye on a single radargram profile. These reflections may be so minute that the changes may not be easily visualized. For instance, imaging a buried archaeological debris field, perhaps containing higher concentrations of small fragments of ancient habitation, e.g., flint chips or other materials, may show some scattered energies on the radargrams which may only be one or two digital values different then in areas where no debris are located. Unless a fortunate colour transform is used, it is unlikely that these small reflections will ever be noticed within the radargram — vertical slice — dataset. An alternative method for presenting GPR data from archaeological sites is needed to show these minute changes. Rather than showing the changes in reflected energies along the vertical — radargram — slices of the ground, it is more useful to map horizontal changes of reflected energy across a site. In this case small, but consistent reflections above the background noise can be visualized by using time slice analysis.

2. IMAGING TECHNIQUES FOR ARCHAEOLOGY

There are a variety of imaging and analyses that must be implemented to solve the multitude of subsurface conditions in the archaeological field survey, in Ref. [1]. Among a few of the necessary imaging techniques and analysis to be briefly introduced in this chapter are:

Time slices — mapping of reflection anomalies across a site and at various depths.

Isosurface rendering — showing equal amplitude surfaces in a 3D dataset by rendering the data, e.g., applying shading to the surface to give a 3D effect.

Overlay Analysis — collecting (strong) reflectors from individual time slice map and overlaying the results on a single, comprehensive 2D time slice.

The process of time slice analysis is not new, and the implementation of this method for archaeological applications is presented after, in Refs. [2, 3]. They found from archaeological imaging, that using radargrams that were binned or spatially averaged in the vertical and horizontal windows and then interpolated to create 3D volumes, provided much more visually useful images for reading the continuity of subsurface reflection anomalies. Particularly at archaeological sites where subsurface structures may not be buried at equal depths (reflection times) and to reduce radar clutter, thicker slices of the radargrams provide very useful images of the subsurface.

One of the natural effects of time slicing radargrams, and mapping the changing in amplitude across them, is that this in itself acts as a background filter. Often, GPR radargrams can have significant banding noise caused by equipment designs as well as reverberations from ground surface. It is difficult to see changes in the large ground surface waves, or any part of the radargram where banding background noises are significant. By slicing the data, the banding noise is actually naturally removed since only deviations from the averaged background noise are being detailed. GPR practicioners often will apply a series of filtering operations before beginning the time slice analysis, included of which is background removal. Background filtering is generally blindly applied to the radargrams first before time slice slicing. This filter can have the unfortunate effect of removing features which are more or less parallel to the radar profile. If a linear feature like a Roman wall were being imaged then a possibility of deleting this wall could occur when the structures are parallel to the profile direction. In the data presentation for archaeological sites, radargrams that are unfiltered for the background are often more useful for creating subsurface images.

Migrated data are often used at archaeological sites where the microwave velocities can be determined, subsurface features and stratigraphy are well defined, and where hyperbolic reflection patterns dominate a site. In some instances however, migrated radargrams can often reduce the relative amplitude of small targets at a site. Detection is usually the most important objective. The fact of a small target having a larger footprint because it has not been migrated is sometimes more useful when time slice images are made. These small features appear larger than they really are and can be detected. It is not unusual to use several sets of processed and unprocessed radargrams to extract different and essential information regarding an archaeological site.

The most important factor in generating time slices, generally has little in the way of dealing with the signal processing of the radargrams, but rather, depends upon image processing. In some cases the time slices are presented in either a linear, square root, or logarithm transforms, to delineate various features which have a large dynamic range in recorded reflection intensity. Also, custom transforms are generated to amplify a particular reflection within a dataset, which may be the archaeological targets of interest. It is not always the case that the targets of interest are the strongest reflectors, they may be the mid-range to lowest reflection anomalies mapped across a site. In addition, minimum and maximum thresholding is often applied to the time slice maps to enhance or reduce background noises. Within each separate time window chosen, the full range of colours is generally applied between the relative lowest and strongest reflector. The relative amplitude time slices, can show the relative features within each time window more clearly, however, the importance of these anomalies when compared to the strongest reflections in the entire dataset can be lost. For this reason, a series of time slices are sometimes displayed using an absolute reference amplitude in order to show the true recorded reflection amplitudes between different reflection times at a site. Finally, in order to convert time slices into actually depth slices, requires knowledge of the microwave velocities at the site.

3. CASE HISTORY AIALI SITE (GROSSETO, ITALY)

The place named Aiali is situated on lowland between the medieval town of Grosseto and the roman town of Roselle in the Tuscany region. This site has been studied since 2006 employing different surveying methods including remote sensing satellite and aerial photography, field walking surveys and geophysical surveys (magnetic, resistivity, GPR) in Ref. [4]. The main goals of the survey consisted of obtaining information about location, depth and dimensions of possible remains and providing interpretable information to archaeologists for characterizing the types of building that might be present. This site was also considered propitious for testing the potential of dense grid strategies as well as different 3d processing schemes over a complex Roman site.

Data were recorded inside four areas (A, B, C, D) at 50 cm profile spacing at Aiali. Once the basic raw radargrams were conditioned, the squared amplitude of the radar pulses were then averaged spatially every 25 cm along the profile and averaged in time over 6 ns time windows. Consecutive time slices were generated at about 50% overlap between adjacent levels to better show transitions of the reflection anomalies, in Ref. [5] .

GPR time slice images for the combined site CD are shown in Fig. 2. Shallow time slices indicate that the reflections to the tops of wall of a destroyed Roman villa are quite shallow and begin to appear on the third slice that is from 17–34 cm below the ground surface. A utility pipe that crosses the site can be identified by a faint linear reflection in a deeper slice from 43–60 cm. An overlay analysis of the site using all the time slice information from 17–112 cm (skipping the top

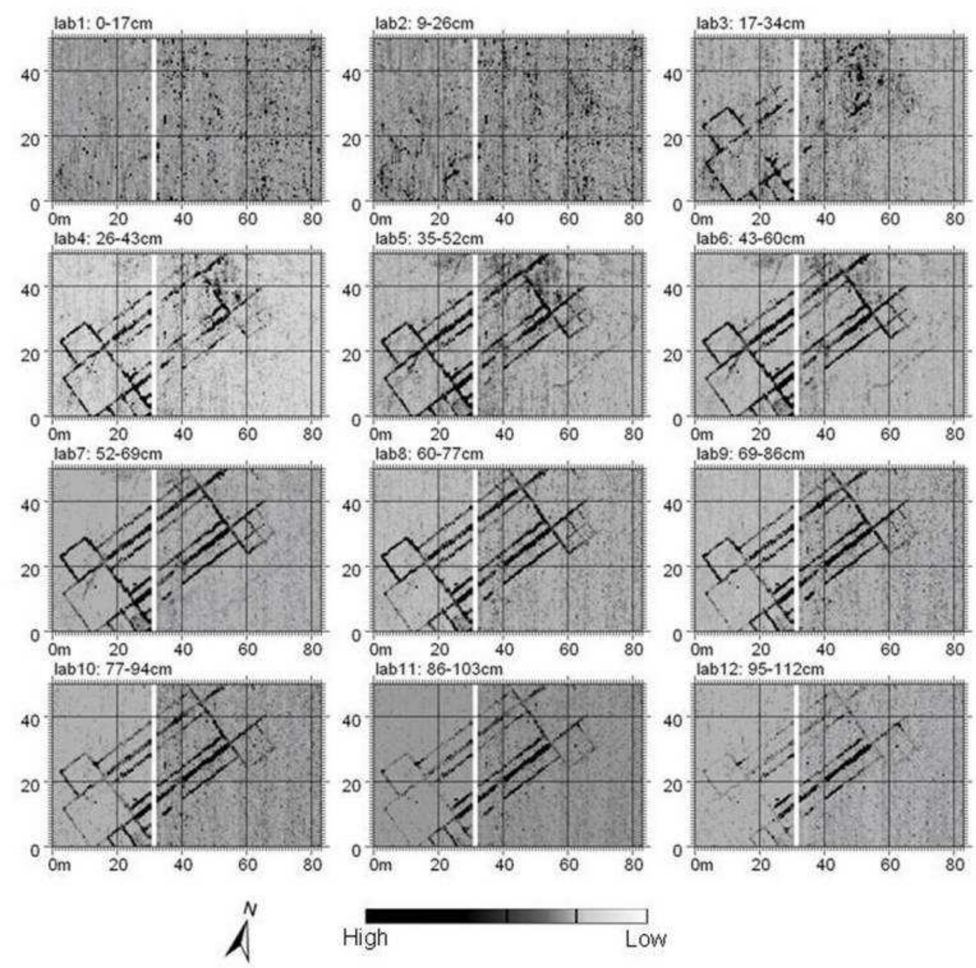

Figure 2: The complete time slice dataset computed the Aiali site. A nominal velocity of 7cm/ns was used to convert the time slices to estimated depth slices.

surface information)is shown in Fig. 3. The overlay image is shown with one background filtered radargrams indicating the strong — reverberating wall reflections that were recorded. Because the wall reflections have a strong contrast with the surrounding areas, an isosurface amplitude render showing shapes of the remnant wall structures of the destroyed villa could be created, Fig. 4.

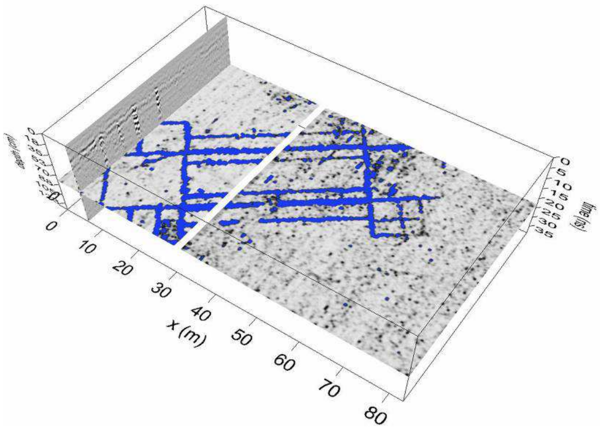

Figure 3: Overlay analysis showing all the reflectors from 40–81 cm along with an example background filtered radargram showing the strong wall reflections from the destroyed foundations of the villa.

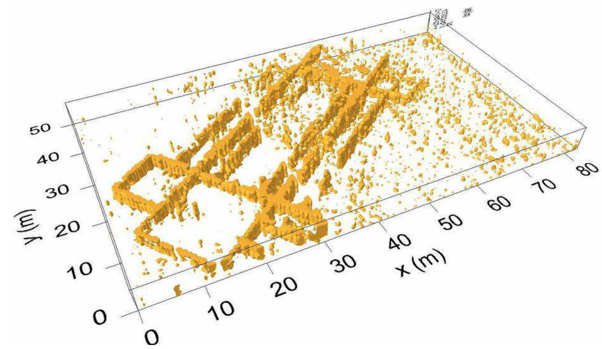

Figure 4: Isosurface rendering of all the reflection greater than 40% the peak response recorded in the volume for the destroyed Roman villa discovered at the Aiali site.

For the Aiali site, the GPR survey results, along with those made from other remote sensing methods, will be able to assist the archaeologists in reconstructing and preserving the "digital" knowledge of the site. Whether or not the site will be delineated as an important archaeological monument and the lands acquired from the farmers to prevent further destruction, is left for future generations to determine.

REFERENCES

1. Goodman, D. and S. Piro, *GPR Remote sensing in Archaeology*, Springer Ed., 2013, ISBN 978-3-642-31856-6, ISBN 978-3-642-31857-3 (eBook), DOI 10.1007/978-3-642-31857-3.
2. Goodman, D. and Y. Nishimura, *Antiquity,* Vol. 67, 349–354, 1993.
3. Malagodi, S., L. Orlando, S. Piro, and F. Rosso, *Archaeological Prospection*, Vol. 3, 13–23, 1996.
4. Campana, S. and S. Piro, *Seeing the Unseen. Geophysics and Landscape Archaeology*, Ed. by Campana and Piro, CRC Press, Taylor & Francis Group, Oxon, UK, 2009, ISBN 978-0-415-44721-8.
5. Goodman, D. and S. Piro, *Seeing the Unseen. Geophysics and Landscape Archaeology*, Ed. by Campana and Piro, CRC Press, 297–302, Taylor & Francis Group, Oxon, UK, 2009, ISBN 978-0-415-44721-8.

High Resolution Imaging with a Holographic Radar Mounted on a Robotic Scanner

L. Capineri[1], **I. Arezzini**[1], **M. Calzolai**[1], **C. Windsor**[2], **M. Inagaki**[3], **T. Bechtel**[4], **and S. Ivashov**[5]

[1]Department of Information Engineering, University of Florence, Florence 50139, Italy
[2]116 New Road, East Hagbourne, OX11 9LD, UK
[3]Walnut Ltd., 1-19-13, Saiwaicho, Tachikawa, Tokyo 190-0002, Japan
[4]Department of Earth and Environment, Franklin & Marshall College, Lancaster, PA, USA
[5]Remote Sensing Laboratory, Bauman Moscow State Technical University, Moscow, Russia

Abstract— Ground penetrating radars operating at high frequency are currently used for subsurface investigation. The data are generally collected by manual scans and this is a time consuming process and it is also affected by errors in spatial positioning of the data. In this work, we present an innovative approach by devising a robotic scanner that is remote controlled. The robot scanner operates with a high resolution 3.6–4.0 GHz multi-frequency holographic radar antenna of RASCAN type. The paper describes the advantages of this new instrument in different applications fields (civil engineering, archaeology, land mine detection) with high resolution images of shallow objects and virtually zero set up time for the experiments.

1. INTRODUCTION

The holographic radar of RASCAN 4/4000 type has been demonstrated as a useful instrument for producing images with high spatial resolution from subsurface dielectric constant discontinuities [1]. The comparison of the incident monocromatic field and the reflected field from a buried shallow object is the basic holographic principle that in this case is implemented at five microwave frequencies between 3.6 and 4.0 GHz. The measured phase variations between the incident and received fields at different locations on the scanning surface create a sinusoidal modulated baseband signal that can be used to produce gray scale images. From an electromagnetic viewpoint these images are not complete holograms because RASCAN-4 provides only the amplitude information of recorded signals while the actual hologram is complex. However the images have a spatial resolution that is about a $\lambda/4$, where λ is the wavelength in the investigated material at the emitted frequency f_i [2]. Generally the holographic radar transmits and receives signals at different discrete frequencies in order to avoid null responses from targets at depths and frequencies that produce phase values that cancel the two sinusoidal functions [1]. The standard method for scanning a surface is the manual scan similar to that used for high frequency impulse GPR: This is a rather time consuming task as the experiments need a spatially-referenced grid along which the antenna head is moved manually. The line grid can be inscribed on a thin dielectric mat (Plexiglas, rubber, or paper). This accessory is certainly useful but use is limited to rather small areas of investigation (typically less than 1 square meter) and require a skilled and concentrated operator to avoid deviations in the manual movement of the antenna head. Larger surfaces of several square meters are difficult to scan manually with accuracy and require a long time to set-up the reference system. A different approach to overcome this limitation is the development of a robotic scanner where the holographic radar head is moved automatically with high spatial accuracy (better than 1 mm) guaranteed by the optical encoders connected to the mechanical movements. An area is covered by the composition of a lateral fast (50 cm/s) movement and the advancement slow (programmable speed from 2 to 5 mm/s) motion by two wheels connected to DC motors. This approach is particularly suitable for the compact and light weigh (400 grams) holographic radar head that must be moved fast.

In this way the robot scanner can spatially oversample the reflected field and produce averaged low noise images of subsurface objects, while the operator remotely designates the area to be investigated. A research field where robot scanners have been developed is humanitarian demining [3–7]. Development of this new microwave subsurface scanner mounted on a robotic platform will also aid in the rapid diffusion of robotic products into daily life, which will also decrease the price of these technologies. The complete system is depicted in Figure 1.

2. APPLICATION TO RAPID SURVEYING OF A CONCRETE PAVEMENT

A common application of subsurface radar is scanning of concrete pavements for detection of reinforcing bars or mesh, and other buried structures. An investigation was required on an old concrete

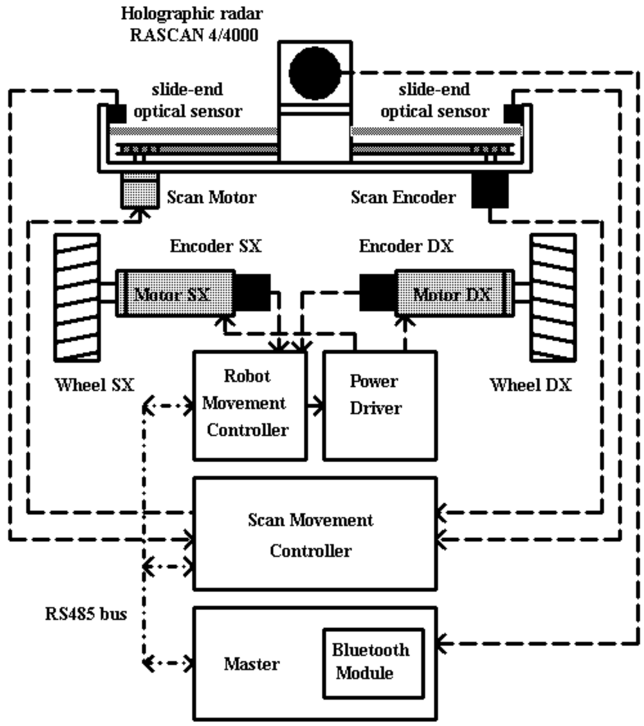

Figure 1: Block schematic of the robotic scanner with holographic radar. The three electronic units communicate in real-time by a standard RS-485 bus (dot-dashed line). Power DC lines and encoder connections are shown by the dashed line.

pavement where the metal reinforcing grid was at about 60 mm depth. Because some cracks are visible on the surface, the survey intended to check for structures underneath the mesh. The construction details of the pavement were lost, and detection of reinforcing bars with a commercial pacometer instrument was unsuccessful in the presence of the continuous magnetic field from the shallow mesh. The robot scanner was used to acquire an image of 1 m length by 33 cm width with 5 frequencies (3.6; 3.7; 3.8; 3.9; 4.0 GHz), with spatial sampling 2 mm and advancement motion speed of 2 mm/s. Hence the length of 1 m is covered in 500 s. This is the total time for doing the survey because no extra time was needed to set-up the experiment.

Figure 2: Robotic scanner operating on a concrete pavement. Note the separation line between two concrete pours.

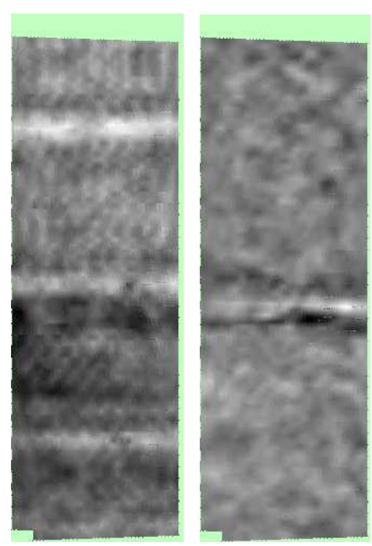

Figure 3: Parallel (a) and cross polar (b) holographic radar images at 3.7 GHz. Pixel size 2 mm, image dimension 1 m × 0.33 m.

The images were acquired from both the parallel- and cross-polarized transmitter-receiver antenna pairs. The two images corresponding to 3.7 GHz were selected because they show with better contrast the presence of buried structures. In Figure 2 the robotic scanner is in operation on the concrete pavement.

From the parallel image in Figure 3, we can detect three horizontal features about 30 cm apart. The central one was the only horizontal feature detected by the cross-polar channel at the same position; this central feature can be easily interpreted by visual inspection of Figure 2 as the separation line between two concrete pours. The upper and lower horizontal features in the parallel output channel are certainly buried structures underneath the metal mesh, that at this frequency, given the depth of the mesh, is invisible, and thus does not interfere with the holographic response of the two deeper structures. Planned repetition of this survey on other nearby areas will finalize the interpretation about the nature of these two features that are likely to be reinforcing bars.

3. CONCLUSIONS

In this paper we present a robotic scanner for high resolution imaging with holographic radar. The high-spatial resolution allows use of the robotic scanner at high frequencies (> 2 GHz) that require a sampling tighter than at most a quarter of the wavelength in the soil or material under investigation.

The robotic scanner is currently used in different applications: Detection of low dielectric contrast objects like plastic landmines, for rapid scan of floors after an earthquake or other natural disaster, investigation of historical structures, or for searching for hidden dinosaur tracks in the rocks of paleontological sites. Moreover, for these applications a light-weight robotic scanner (less than 6 kg) is suitable to avoid loading of sensitive surfaces with the weight of a human operator.

REFERENCES

1. Ivashov, S. I., V. V. Razevig, I. A. Vasiliev, A. V. Zhuravlev, T. D. Bechtel, and L. Capineri, "Holographic subsurface radar of RASCAN type: Development and applications," *IEEE Journal of Selected Topics in Earth Observations and Remote Sensing*, Vol. 4, No. 4, 763–778, December 2011.
2. Ivashov, S. I., L. Capineri, and T. D. Bechtel, *Holographic Subsurface Radar Technology and Applications*, in book *UWB Radar Applications and Design*, edited by J. J. Taylor, 421–444, CRC Press, Taylor & Francis Group, 2012, ISBN 978-1-4200-8986-8.
3. MacDonald, J., J. R. Lockwood, J. Fee, T. Artshuler, T. Broach, L. Carin, R. Harmon, C. Rappaport, W. Scott, and R. Weaver, "Alternatives for landmine detection," RAND, Santa Monica, CA, 2003.
4. Habib, M. K., *Humanitarian Deming: Innovative Solutions and Challenge of Techonlogy*, ARS Publisher, 2008.
5. Habib, M. K., "Humanitarian demining: Reality and the challenge of technology the state of the arts," *International Journal of Assistive Robotics and Systems*, Saga, Japan, 2007.
6. Havlik, S., *Land Robotic Vehicles for Deming, Humanitarian Demining*, I-Tech Education, 2008.
7. Santana, P., J. Barata, and L. Correia, "Sustainable robots for humanitarian demining," *International Journal of Advanced Robotics Systems, (special issue on Robotics and Sensors for Humanitarian Demining)*, Vol. 4, No. 2, 206–218, 2007.
8. Colon, E., P. Hong, J. C. Habumuremyi, I. Doroftei, Y. Baudoin, H. Shali, D. Milojevic, and J. Weemaels, "An integrated robotic system for antipersonal mines detection," *Control Engineering Practice*, Vol. 10, No. 11, 1283–1291, 2002.

Analytical Approach for RASCAN Radar Images of Dinosaur Footprints through Basic Experiments

M. Inagaki[1], **T. Bechtel**[2], **L. Capineri**[3], **S. Ivashov**[4], **and C. Windsor**[5]

[1]Walnut Ltd., 1-19-13, Saiwaicho, Tachikawa, Tokyo 190-0002, Japan
[2]Department of Earth and Environment, Franklin & Marshal College, Lancaster, PA, USA
[3]Department of Information Engineering, University of Florence, Florence 50139, Italy
[4]Remote Sensing Laboratory, Bauman Moscow State Technical University, Moscow, Russia
[5]116, New Road, East Hagbourne, OX11 9LD, UK

Abstract— The existence of a footprint fossil indicates that some discontinuity occurred at the footprint plane during sedimentation. RASCAN holographic radar reveals the plan shape of shallow buried objects. A simple experiment showed that a clod of loam soil buried in powdered loam soil was recognizable in a radar image. Another experiment showed that a thin film inserted between dielectrically similar materials also provides recognizable reflection. Finally, blind tests were performed for realistic surrogates for dinosaur footprints. The radar image has no recognizable pattern for the case of microscopic air gap at the footprint parting plane. However, when the air gap was replaced by very thin clay film, the shape of the toes became recognizable. Thus, there may be some cases in which some discontinuity during sedimentation makes the shape of a dinosaur footprint fossil recognizable by holographic radar.

1. INTRODUCTION

A dinosaur footprint, which is not the creature itself, but a mold of markings made by the activites of the creature, represents a trace fossil. A RASCAN holographic radar image taken at *Parco dei Lavani* site (Italy) shows that some reflection related to dinosaur footprints is produced inside rock body [1] (Figure 1). Generally speaking, the reflection circumstance inside sedimentary rock is not necessarily cooperative to GPR. Nevertheless, a small blow of a hammer may unveil a footprint with amazingly fine shape. This indicates that some discontinuity occurred at the footprint plane during sedimentation even if the rock appears homogeneous. The possibility of revealing the shape of trace fossils by radar is analytically investigated using simple experiments.

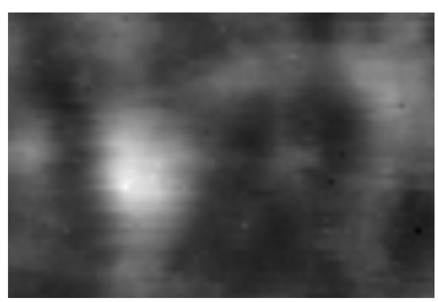

Figure 1: Partially exposed dinosaur footprint and its holographic radar image.

2. RASCAN HOLOGRAPHIC RADAR

RASCAN holographic radar provides plan subsurface images which can reveal the shape of buried objects. Although an impulse radar records reflected wave strengths and travel times as direct values, holographic radar does indirect values determined by the degree of phase coincidence between incident and reflected waves. As a result effect from strong surface reflections can be avoided. Therefore RASCAN can produce clear images especially at shallower depths. RASCAN operates at 5 discrete continuous wave frequencies from 3.6 to 4.0 GHz with two receiving antennae in parallel and cross polarizations relative to the transmitter. As a result, two sets of five images are obtained. At least one image among ten is expected to provide a fine view by realizing the optimum combination of the permittivity of the medium and the distance from antenna to the target.

3. SMALL DIFFERENCE IN PERMITTIVITY

Electromagnetic waves reflect at the boundary between layers with different permittivity. The intensity of reflection decreases with smaller difference of permittivity. Reflected waves become unrecognizable below some intensity threshold, and reflections cease at zero difference Obviously, identical materials have identical specific permittivity. Permittivity of soils varies strongly with water content. However, slowly dried loam forms clods and instantly dried loam forms powder. These two soils then have identical mineralogy and water content, but different texture due to different history, and are expected to have slightly different permittivity.

Loam soil was left to dry naturally for about four years after full saturation, finally forming cohesive lumps or clods. Some of the clods were smashed to make granular powder. Three clods were placed in a container and buried in the powder. Figure 2 shows the clods before buried in the powder. RASCAN holographic radar was scanned over the test bed. Figure 3 is a radar image of the scan. Next the powdered loam soil was replaced by dry sand, and RASCAN holographic radar was scanned again. Figure 4 is a radar image of the clods-in-sand scan.

Figure 2: Clods of dried loam soil in the test bed.

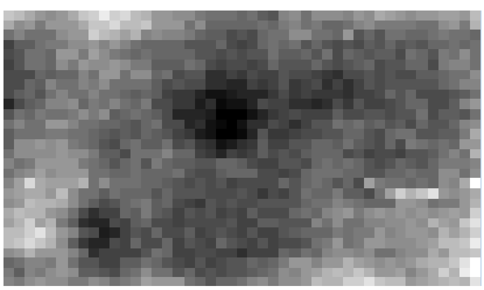

Figure 3: RASCAN holographic radar 3.8 GHz parallel polarization image of the clods buried in powdered loam soil.

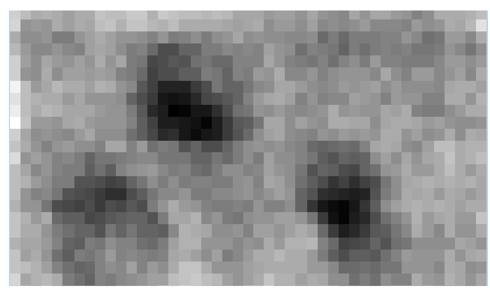

Figure 4: RASCAN holographic radar 3.8 GHz parallel polarization image of the clods buried in sand.

In Figure 3 the right clod is very hard to recognize. However, the upper and the left clods are both subtly recognizable. In Figure 4 it is obvious that all the clods are fully recognizable. This fine sensitivity of holographic radar for even small difference in permittivity might be helpful to determine the presence and shape of hidden dinosaur footprints.

4. EFFECT OF THIN LAYERS

A base material in which a thin layer of some impurity is inserted produces reflections at this thin layer. If the layer is too thin, the reflection will not be recognizable. However, the reflection becomes stronger with increasing impurity layer thickness and finally reaches a recognizable level [2]. Experiments were carried out for some materials with different impurity layers. Rubber plates and vinyl chloride plates were used as the base materials. An air gap was used as the impurity layer. The permittivity is 8.3 for rubber, 2.7 for vinyl chloride and 1 for air. Figure 5 shows a test body using rubber plates. The left body has no gap and the right body has a small air gap. The air gap is set by lifting the uppermost rubber plate (10 mm thickness) with paper slips piled as spacers placed under the both sides of the plate. Each paper slip has 100 μm thickness, so the gap can be increased in this increment. This method was applied in the same manner using vinyl chloride plates as the base material, but with the thickness of upper part 12 mm instead of 10 mm. The

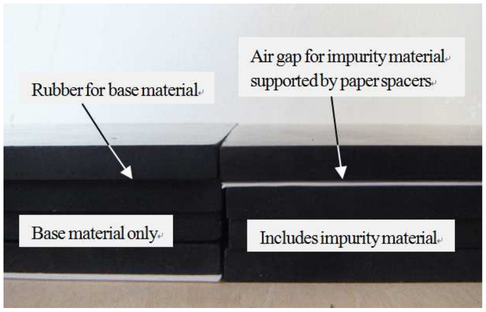

Figure 5: Test body for contrast experiment.

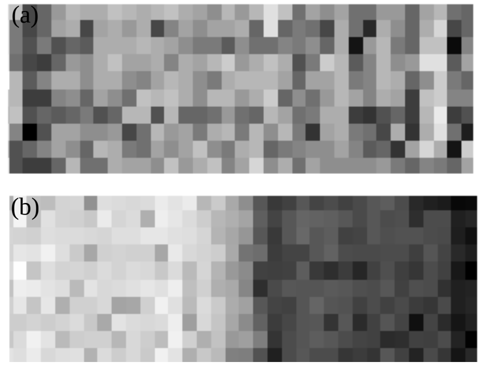

Figure 6: Holographic radar images. Air gap is (a) 200 µm and (b) 1 mm.

test body was scanned by RASCAN holographic radar with air gap varying from 200 µm to 9 mm. The left and right bodies become sufficiently identical when the gap is more than 1 mm for rubber, and 3 mm for vinyl chloride. Figure 6 shows holographic radar images with 200 µm gap (top) and 1 mm gap (bottom). The top image indicates no contrast difference and the bottom image clearly shows the difference.

The intensity contrast between the right body and left body were calculated and plotted on Figure 7 for rubber and Figure 8 for vinyl chloride. This means that the contrast of permittivity and the thickness of impurity layer are both important factors. In Figure 7 (rubber) 4 GHz data seem to represent the best distance from antenna to the target among five frequencies. The contrast is very small at less than 1 mm thickness and it almost linearly increase from 1 mm through thicker gaps. In Figure 8 (vinyl chloride) 3.6 GHz data represent the best distance. The contrast linearly increases from 3 mm to thicker gap. These results indicate that the impurity layer may help to reveal the shape of buried target by holographic radar.

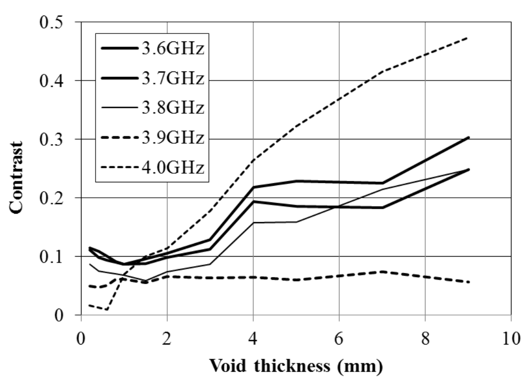

Figure 7: Image contrast to basic material with the thickness of impurity thin film layer. (Basic material = Rubber, Impurity material = Void).

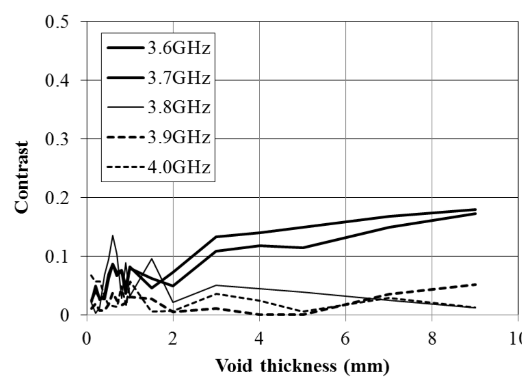

Figure 8: Image contrast to basic material with the thickness of impurity thin film layer. (Basic material = Vinyl chloride, Impurity material = Void).

5. HOLOGRAPHIC RADAR IMAGES BASED ON ACTUAL DINOSAUR FOOTPRINTS

Artificial footprints were carved on water saturated loam soil in a test bed. After leaving for three weeks to dry, the test bed was covered with dry powdered loam soil. The depths of the footprint planes are approximately 30 mm. Figure 9 shows the footprints before covering. The holographic radar image is shown in Figure 10. Despite of small permittivity contrast the three footprints are all recognizable. Separation of three toes is imperfectly attained at the leftmost footprint. No separation is observed at the other footprints.

The radar scan was performed again after changing the covering material from loam soil to sand above the center and rightmost footprints. The result is shown in Figure 11. The reflection was intensified for footprints covered with sand. The toes are also separately recognized. The increase of contrast is important not only for better recognition but also for precision of the shapes.

Figure 9: Image contrast to basic material with the thickness of impurity thin film layer. (Basic material = Rubber, Impurity material = Void).

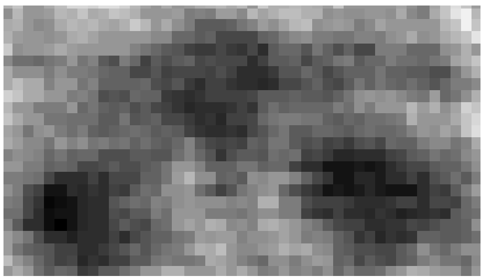

Figure 10: Image contrast to basic material with the thickness of impurity thin film layer. (Basic material = Rubber, Impurity material = Void).

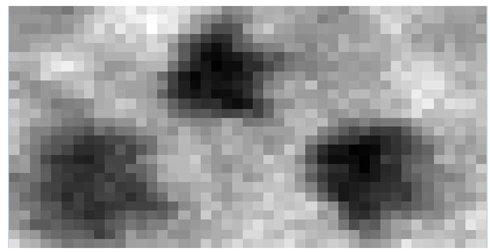

Figure 11: Image contrast to basic material with the thickness of impurity thin film layer. (Basic material = Rubber, Impurity material = Void).

Figure 12: Anamoepus cast with clay film coating.

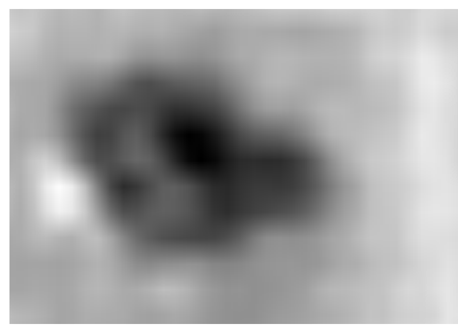

Figure 13: RASCAN 3.8 GHz cross polarization image for clay film on the cast-mold interface.

Finally a test piece was produced by a cast taken of an actual dinosaur footprint (Anamoepus) from the Early Jurassic rocks of Dinosaur State Park in Connecticut, USA [3]. The cast was done with a quick dry lime plaster consisting of calcium carbonate and silica sand and oven-dried. The cast was then covered with a layer of plaster to make a tight-fitting mold. A hidden test was carried out. The hidden footprint is located about 3 cm depth. The mold and cast were scanned first with nothing but the microscopic air gap separating them, and this produced no recognizable contrast pattern. However, when the mating surface was painted with a very thin clay-water mixture (See Figure 12), and allowed to dry overnight (air dry, not oven dry), a shape strongly resembling the track appears (See Figure 13). Note that the long middle toe is clear, and the shape of the heel is obvious, but the outer toes are subtle at best.

6. CONCLUSIONS

RASCAN holographic radar showed fine sensitivity to small differences in permittivity and to thin layers of impurity material. Dinosaur footprints are sometimes found as trace fossils preserving realistic shapes. This usually means that the rock layer containing the trace fossils has experienced a special history of sedimentation that created a subtle permittivity difference suitable to the application of the holographic radar. Low noise imaging in the shallower subsurface is a unique feature of RASCAN holographic radar [4], and provides a way to detect and image the shape of dinosaur hidden footprints. This capability of RASCAN radar may add to the already-demonstrated applications in archaeology and inspections of civil structure such as delamination of pavement.

REFERENCES

1. Leonardi, G. and P. Mietto, eds., *Dinosauri in Italia: le orme giurassiche dei Lavini di Marco (Trentino) e gli altri resti fossili italiani*, 494, Accademia editoriale, Pisa, Italy, 2000.
2. Inagaki, M., "Quantitative proof of interference," *IWAGPR 2009*, Granada, Spain, 2009.
3. Capineri, L., V. Razevig, S. Ivashov, F. Zandonai, C. Windsor, M. Inagaki, and T. Bechtel, "RASCAN holographic radar for detecting and characterizing dinosaur tracks," *IWAGPR 2013*, Nantes, France, July 2–4, 2013.
4. Ivashov, S., V. Razevig, V. Vasiliev, A. Zhuravlev, T. Bechtel, and L. Capineri, "Holographic subsurface radar of RASCAN type: Development and applications," *IEEE Journal of Selected Topics in Applied Earth Observations and Remote Sensing*, Vol. 4 , 763–777, 2011, ISSN: 1939-1404, doi:10.1109/JSTARS.2011.2161755.

Bringing up the Bodies: High Resolution and Target Definition Using GPR

Erica Utsi
Utsi Electronics Ltd., UK

Abstract— Ground Penetrating Radar (GPR) is an extremely useful non-destructive testing (NDT) and detection technique applied in many different spheres of activity from the common ones of utility detection, concrete investigation, road monitoring and archaeology to the more rarely used ability for forensic and security investigations. Target detection and imaging are inter-related both in terms of the frequency of antenna used and the survey parameters applied. Even for strong reflectors, the density of data collected can make a significant difference to identification, particularly where this is based on pattern recognition.

The definition capability of a 4 GHz antenna used primarily in structural investigations is described. Taking as an example the two graves discovered beneath the floor of the Cosmati Pavement in front of the High Altar of Westminster Abbey, this paper examines the evidence for extant skeletal remains in GPR data generated using a 4 GHz antenna. These results are then compared with results from a more traditional lower frequency antenna (400 MHz) used for the detection of graves within the Abbey (including the two beneath the mosaic pavement) in forensic searches for missing persons believed to have been buried in open ground and in the archaeological investigation of an area known to contain mediaeval graves. Although faunal remains have been found in such searches, the recognition of weak reflectors such as human remains more often relies upon the recognition of associated material rather than the signals returned by the bodies themselves. The reasons for this are briefly discussed.

The potential effect of increasing data density is discussed with particular reference to the data (4 GHz and 400 MHz) from Westminster Abbey and suggestions made as to how the effect of more intensive survey might assist in the identification of buried human remains, whether in a legitimate grave or not.

1. INTRODUCTION

Ground Penetrating Radar (GPR) is recognised as an extremely useful investigative tool in a wide range of applications, many of which are ultimately related to safety [2]. The largest single use of the technology is the detection of utilities, generally in advance of construction but the method is also commonly applied to many other subsurface investigations such as concrete investigation, road monitoring, structural integrity, glaciology, mining, archaeology and even occasionally forensic searches (cf, for example, http://www.mappingtheunderworld.ac.uk/; http://www.trl.co.uk/facilities/mobile_test_equipment/ground_penetrating_radar.htm) [1].

2. HIGH FREQUENCY, HIGH DEFINITION

There are a number of applications where high frequency GPR is useful, notably in detecting delamination in the near surface of roads or in built structures such as bridges, supermarket tiled floors or within historic monuments (Figure 1). Another common application is locating structural elements such as reinforcement bars in concrete (e.g., [16]).

Although traditionally frequencies of the order of 2 GHz have been used for these purposes, higher frequency options are now being deployed with resultant improved detection and target

Figure 1: 4 GHz antenna being used on a historic bridge inside the Forbidden City, Beijing.

imaging within the near surface. Measurements using a 4 GHz antenna can detect delamination of less than 1 mm [15].

3. HIGH FREQUENCY INVESTIGATION

In recent years there has been increasing interest in high definition GPR surveys, creating dense data sets with resultant improved target definition. This has been particularly useful in archaeological investigations where horizontal imaging is usually the principal clue to the nature of the extant remains [8, 12].

The principal factors in creating recognisable features from GPR imaging are the wavelengths emitted by the radar and the sampling frequency of the investigation both along the line of travel of the radar and also between successive survey transects (cf, [3]). Although it is clearly advantageous to use as small a wavelength as possible, this limits the possible depth of investigation and also carries the implication of greater resources being required in order to maximise the imaging potential.

In 2004, the Collegiate Church of St Peter, Westminster, more commonly known as Westminster Abbey, decided to restore the 13th Century mosaic in front of the High Altar, traditionally the coronation site. The original stone Abbey was built in the 11th Century, but the current building dates back to the reconstruction by Henry III in the 13th Century although it is known to include some remnants of the original stone building. The brief for the GPR survey was therefore to investigate the internal structure of the mosaic prior to restoration; check for near surface delamination; map any remains from the former Abbey; and search for a substantial royal vault. After trialling antennas of 400 MHz, 1 GHz and 4 GHz, the 4 GHz was used for the first two of these and the 400 MHz for the latter two.

The results of the survey demonstrated the intricacy of construction, revealed previous repairs, including some changes to the patterning of at least two elements and also confirmed the existence of two abbots' graves, one previously known although brief historical references to the burial of two 13th Century abbots in this vicinity exist ([12], Figures 2 and 3).

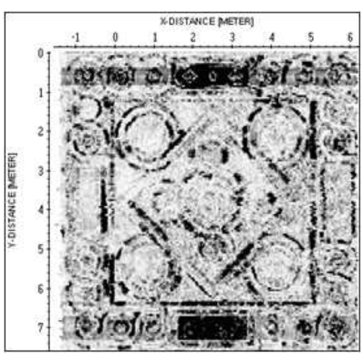

Figure 2: Horizontal time slice extracted from the 4 GHz investigation of the Cosmati Pavement showing interfaces between different stone elements and the location of two tombs [12].

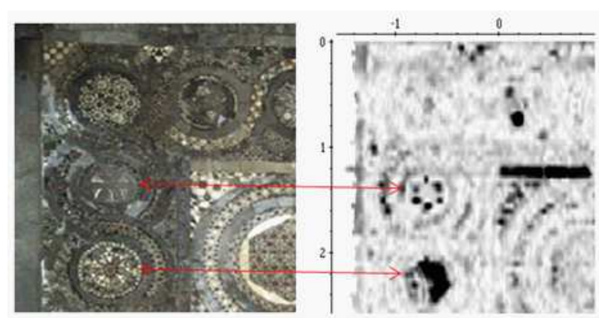

Figure 3: Historical repairs, as evidenced by changes in the decorative elements and the partial replacement of a linear outline [12].

Three questions arise from this work. Firstly to what extent is it possible to identify the tomb contents on the basis of signal patterning? Secondly is it possible to detect weaker reflectors such as human remains, if any? Lastly, to what extent can the same methodology be applied to other subsurface investigations? The first of these was tackled, in part, at the time. Time slices extracted from the 3-dimensional data block suggested the presence of a chalice and paten at the head of the northern tomb, in accordance with traditional burial practice. GPR-Max 2d and 3d was used to model a typical chalice and paten and the results modified until the signals matched those at the head of the tomb (Giannopoulos). It is evident, however that there is more material in the grave (cf, Figures 5 & 6).

In order to understand the nature of the remains in the tomb, it is helpful to start with the strong reflectors. Comparison of time slices from the 4 GHz data with that data generated by the 400 MHz reveals that whereas both tombs are clearly visible at high frequency, only the northern tomb is as clear at the lower, suggesting that that the strong signal reflector in the south tomb is

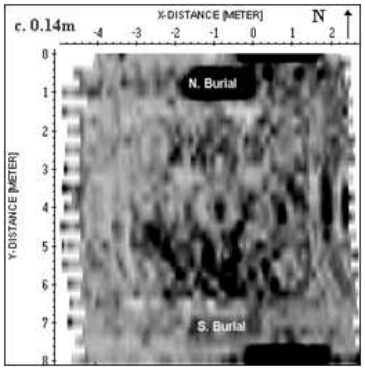

Figure 4: Time slice taken from the 400 MHz survey of the Cosmati Pavement showing the two burials (cf, with Figure 2), from [14].

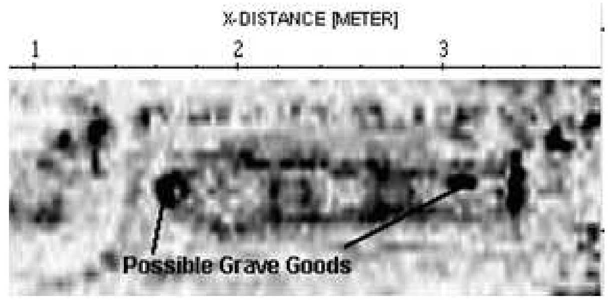

Figure 5: Close up of the northern tomb showing grave goods (probably metallic) and weaker reflectors [12].

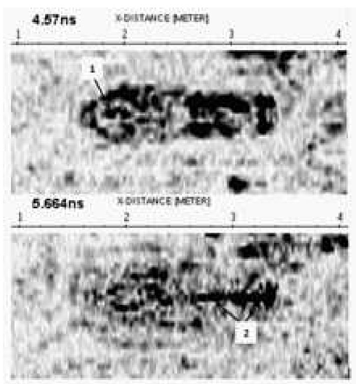

Figure 6: Top (1) and Bottom (2) of a possible crozier or Abbot's staff lying at an angle from head to foot suggesting the presence of human remains.

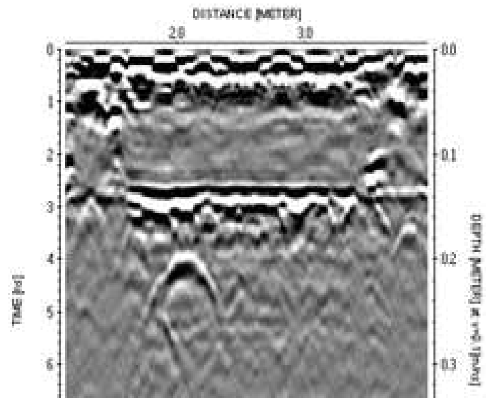

Figure 7: Vertical profile of the southern grave showing one strong reflector at the head of the tomb and a series of weaker reflectors towards the foot [12].

physically small (compare Figure 4 with Figure 2). In the 4 GHz data, it proved impossible to find a level at which the southern tomb showed uniform or near-uniform strong signal reflections across the whole surface. One likely reason for this is the traditional use of Fuller's Earth to backfill the grave. As decomposition sets in, the backfill settles generating an uneven slender void. The weaker reflections would therefore indicate where the backfill is still in contact with the stone above [14]. Assuming that this interpretation is correct, it appears likely that air is the principal reflector not only in the northern tomb, but in both. Although it is clear that more work remains to be done in terms of identifying the different elements in the northern grave, the horizontal patterning so far obtained does not suggest reflection from bones, for example (see Figure 5). That there are extant human remains in both graves is, however, extremely likely as evidenced by the angle of the possible crozier in the northern tomb (Figure 6) and the levels at which the strong and weak reflectors are positioned relative to each other along the southern grave (Figure 7). The existence of these remains is recognized by implication rather than by direct signal reflection and the graves revealed by the voids and associated artefacts rather than the bodies themselves.

4. FORENSIC SEARCHES FOR HUMAN REMAINS

There is evidence to suggest that GPR is much better at detecting recently deceased bodies than corpses which have been reduced to bone. Although human tissue and bone are naturally weak signal reflectors, it is possible, for example, to use a high frequency GPR to detect either hand or heart movements on the other side of a barrier. Experimental research into the detection of both human and pig corpses has demonstrated that GPR can detect recently interred remains [5, 9]. If for no other reason, the presence of fluid within the decomposing remains should yield sufficient difference in electromagnetic properties for successful detection in most soils.

However, once buried, the decomposing corpse interacts with the soil around it. Liquids drain, flesh decomposes and bones calcify. Over time, the electromagnetic difference between the corpse and the surrounding soil will diminish. Graves containing skeletons are not easy to detect using GPR, for which reason current English Heritage guidance on geophysical investigation advises that GPR responses to grave detection are likely to be poor except where the interment is associated with stone coffins [6]. An example of a recent survey of a cathedral cloister where trial excavation had previously revealed the existence of mediaeval graves is shown in Figure 8. The lack of detection by the GPR is consistent with the bodies having been buried in shrouds. No voids, stone containers or artefacts were associated with the burials.

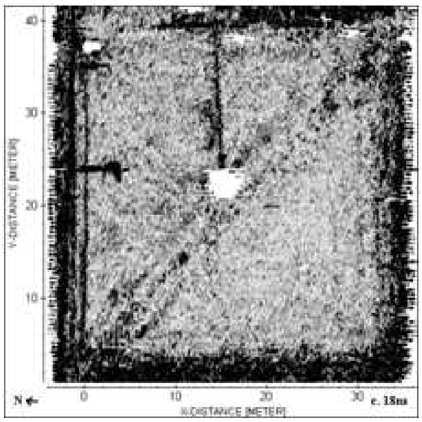

Figure 8: Time slice at c. 18 ns from a cathedral cloister where mediaeval burials are known to exist in the NE corner and should be visible at this depth. There is no indication of burials in the GPR data.

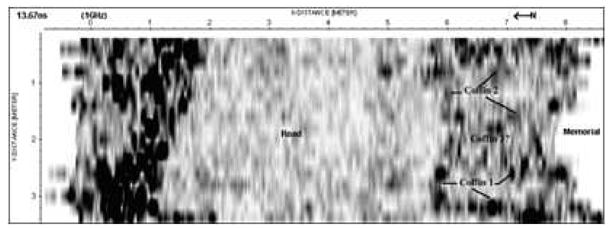

Figure 9: Time slice from a Forensic survey of a graveyard showing the extant remains of coffins rather than their contents.

The point at which burials become effectively invisible has not been established but there is evidence to suggest that it takes many years for all traces to be eliminated. There is at least one forensic case for which remains were traced 14 years after the person went missing. However, it was disturbed ground that the radar data identified rather than bodily remains (Openshaw, Pers. Comm.). Similarly, when carrying out a search for a missing person, believed to have been interred illegally within a cemetery, the legal burials were detectable from the remains of the coffins, rather than from their contents (Figure 9). The only way of identifying the illegal burial in that instance was by association with excess retained moisture. It makes intrinsic sense that burial within a container or within some material that retains fluids will aid detection.

5. DATA DENSITY, SURVEY TECHNIQUE AND THE USE OF HIGHER FREQUENCY ANTENNAS

Following the surveys of the Cosmati pavement in Westminster Abbey, the Dean and Chapter commissioned a series of surveys of the main Abbey floors. Previous surveys had failed to identify the majority of the graves even though these were mostly associated with built tombs and voids. Trials of 400 MHz, 1 GHz and 4 GHz antennas demonstrated the efficacy of the first and last but also demonstrated that attenuation of the 1 GHz signals was greater comparatively than the 4 GHz. However soil research has demonstrated that whereas electrical losses vary linearly with frequency, magnetic losses peak at around 1 GHz [10, 11]. This explains not only why the performance of the 1 GHz was less efficient but also why previous GPR surveys had been unsuccessful since, based on the depth of investigation, 1 GHz appeared to be an ideal frequency. Since the majority of the graves lay beyond the 10 ns range of the 4 GHz, the 400 MHz antenna was used to map the graves. In order to increase target definition as much as possible, the spacing between successive survey transects was decreased from the traditional 0.5 m (cf, Jones, 2006) to 0.25 m. This has been shown to increase target definition significantly, effectively bringing them into focus [13].

One implication of this is that the 4 GHz surveys previously completed, should be re-visited since the 5 cm transect spacing applied is effectively equivalent to the 50 cm spacing used with a 400 MHz antenna and the resulting data can therefore be considered to be aliased. This raises the possibility of a better understanding of the grave contents, including the weaker reflectors.

The other conclusion is that antenna frequency should never be assumed. There is a tendency in archaeological and forensic investigations to opt for antennas of c. 500 MHz central frequency, with the occasional use of lower frequency antennas particularly in damp environments and to accept the resultant target definition. Obviously it is desirable to ensure adequate depth penetration but it is possible to use higher frequency antennas outdoors, even in damp conditions. The forensic case illustrated in Figure 9 is one such case. Given the improvement in potential target definition and the possibility of using multi-channel radars, even for operation at 4 GHz, there is a case for trialling a wider variety of antenna frequencies.

6. CONCLUSION

The obvious implication is that forensic searchers looking for recently buried human remains should not necessarily aim to detect the bodies themselves but instead target associated stronger reflectors. These might be containers, grave goods, voids, leaked liquids or disturbed ground. The longer the period of time from the interment to discovery, the truer this maxim becomes.

Another strategy which deserves to be researched is the application of different frequencies, specifically higher frequencies on known human or animal remains to investigate to what extent and under what conditions weaker reflectors can be identified. The resource implications in terms of forensic search are not as great as they once were, given the number of multi-channel GPRs now available.

Finally, target definition should be considered carefully in planning forensic searches. Increasing the frequency should be considered where practical and, where a lower frequency is applied, reduction of the sampling interval between successive survey transects will mitigate some of the loss of definition. In this connection, it is hoped to examine the cloister example given above using a higher frequency of antenna and a reduced transect spacing.

REFERENCES

1. Conyers, L. B. and D. Goodman, *Ground-penetrating Radar: An Introduction for Archaeologists*, London, 1997.
2. Daniels, D. J., "Ground penetrating radar," Institution of Electrical Engineers, London, 2004.
3. Dennis, T. J., "Imaging geophysical data — Taking the viewer into account," *Archaeological Prospection*, Vol. 11, 2004.
4. Giannopoulos, A., "GPRMax 2-dimensional and 3-dimensional modelling software," Available at www.gprmax.org.
5. Hunter, J. and M. Cox, *Forensic Archaeology: Advances in Theory and Practice*, 27–61, Routledge, London, 2005.
6. Jones, D. M., *Geophysical Survey in Archaeological Field Evaluation*, 28, English Heritage Publishing, Swindon, 2008.
7. Openshaw, S., pers. com, Bentham Geoconsulting, Wennington, Lancashire, LA2 8NP, UK.
8. Sala, J. and N. Linford, "Processing stepped frequency continuous wave GPR systems to obtain maximum value from archaeological data sets," *Near Surface Geophysics*, Vol. 10, No. 1, 3–10, Feb. 2012.
9. Schultz, J. J., A. B. Falsetti, C. A. Pound, M. E. Collins, S. K. Koppenjan, and M. W. Warren, "The detection of forensic burials in Florida using GPR," *GPR 2002, Ninth International Conference on Ground Penetrating Radar, SPIE*, S. K. Koppenjan and H. Lee, Eds., Vol. 4758, Santa Barbara, 2002.
10. Serbin, G., D. Or, and D. G. Blumber, "Thermodi-electric effects on radar backscattering from wet soils," *IEEE Transactions on Geoscience and Remote Sensing*, Vol. 39, 897–901, 2001.
11. Thomas, A. M., N. Metje, C. D. F. Rogers, and D. N. Chapman, "Ground penetrating radar interpretation as a function of soil response complexity in utility mapping," Daniels, J. J. and C. Chen, Eds., *GPR 2006, the Proceedings of the 11th International Conference on Ground Penetrating Radar*, Columbus, Ohio, USA, Jun. 19–22, 2006.
12. Utsi, E., "Improving definition: GPR investigations at westminster abbey," *GPR 2006, the Proceedings of the 11th International Conference on Ground Penetrating Radar*, J. J. Daniels and C. Chen, Eds., Ohio State University, Columbus, Ohio, Jun. 19–22, 2006.
13. Utsi, E., "GPR as an imaging device: Some problems and potential solutions," *GPR 2010, Proceedings of the 13th International Conference on Ground Penetrating Radar*, R. Persico, L. Crocco, L. Orlando, and M. Pieraccini, Eds., Lecce, Jun. 21–25, 2010.

14. Utsi, E., "The shrine of edward the confessor: A study in multi-frequency GPR investigation," *Near Surface Geophysics*, Vol. 10, No. 1, 65–75, 2012.
15. Utsi, V., "Minimum delamination width for GPR," M. Forde, Ed., *Proceedings of the 10th International Conference Structural Faults and Repair*, London, 2003.
16. Utsi, V. and E. Utsi, "Measurement of reinforcement bar depths and diameters in concrete," *GPR 2004, Proceedings of the 10th International Conference on Ground Penetrating Radar*, E. Slob, A. Yarovoy, and J. Rhebergen, Eds., Vol. 2, 659–662, Delft, 2004.

Concrete Imaging without Information of Incident Field

Toshiyuki Tanaka, **Toshifumi Moriyama**, **and Takashi Takenaka**
Graduate School of Engineering, Nagasaki University, Nagasaki 852-8521, Japan

Abstract— This paper discusses about the imaging of a concrete structure without information of incident field. An inverse scattering approach based on the field equivalence principle is extended to apply for reconstruction of spatial profiles of electric parameters in the concrete structure. Numerical simulations of a reinforcing-bar or a cavity investigation in the concrete structure from only total field data measured on the observation surface are performed in order to show the effectiveness of the proposed inversion method.

1. INTRODUCTION

Maintenance and management of concrete structures are important to prevent serious accidents. Among a variety of diagnostic approaches ground penetrating radar (GPR) [1] is a non-destructive diagnosis technique for inspection without affecting the current state or any damage to the existing structures. GPR emits an electromagnetic pulse which is radiated into a concrete structure and part of the wave is reflected by reinforcing-bars and defects such as voids in the structure. GPR processes the reflected data to detect or locate them. The use of a tomographic technique for GPR is expected to give more information of the concrete structure than radar-based techniques, e.g., a size of a reinforcing bar and, the shape and dielectric parameter of defects. Inverse scattering analyses which are the basis of microwave tomography usually assume the knowledge of incident fields. The field radiating from a transmitting antenna of GPR just above a concrete surface is different from the field of GPR located far from the concrete structure since the antenna characteristics are changed due to interaction between the antenna and the structure, so that it is difficult to know accurately the incident field penetrating into the concrete structure.

In this paper, imaging of a concrete structure without information of incident field is discussed. An inverse scattering approach based on the field equivalence principle [2, 3] is extended to apply for reconstruction of spatial profiles of electric parameters (relative permittivity and conductivity) in the concrete structure. If a measurement surface is closed, a problem equivalent to the original scattering problem for the interior region enclosed by the measurement surface can be set up. In the case of concrete evaluation, however, it is impossible to measure the fields on a whole closed surface. Usually transmitting and receiving antennas are limited to one side of a concrete structure. Since a pulsed incident wave does not reach the place far enough from the wave source in a finite observation time, it is not necessary for the measurement surface to be a closed surface. Equivalent surface currents in the equivalent problem are determined by the tangential component of the electric and the magnetic fields on the measurement surface. These equivalent surface currents generate the same electromagnetic field in the region below the measurement surface as does the original incident pulse and yield a null field in the region above the measurement surface. Note that the equivalence holds only when the original source in the region above the measurement surface is removed while the original scatterers remain below the surface. If the original scatterers are replaced by different objects, then there appear non-zero electromagnetic fields in the region above the measurement surface. This allow us to formulate the inverse scattering problem as a minimization problem with a cost function consisting of a magnitude of electromagnetic fields in the region above the measurement surface. Genetic Algorithm (GA) was used for the method of the imaging [4–8]. Numerical simulations of a reinforcing-bar or a cavity investigation in the concrete structure from only total field data measured on the observation surface are performed in order to show the effectiveness of the proposed inversion method.

2. FORMULATION

Figure 1 shows the geometry of the problem. Figures 1(a) and (b) are the original problem and the equivalent problem, respectively. Primary source is arranged in the air. We divide the whole space into two regions denoted by Ω and $\bar{\Omega}$ as shown Figure 1. The boundary is denoted by one closed curve which consists of a linear broken line and three chain lines. The electromagnetic wave emitted from primary source is measured on the boundary during a time interval $[0,\, T]$, where T is duration time. However, it is impossible to measure the fields in concrete. Usually transmitting

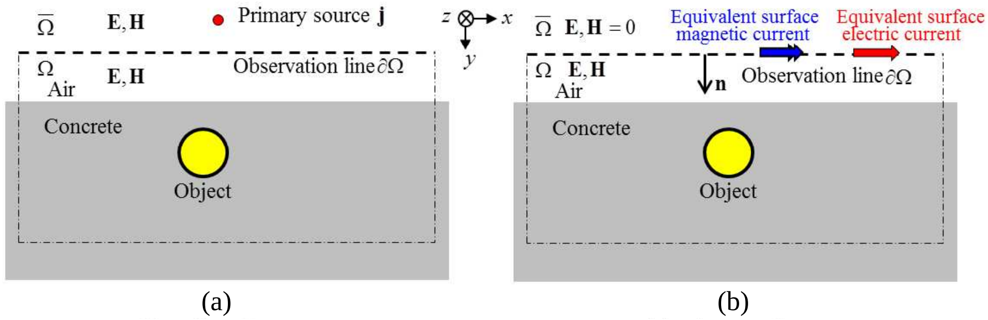

Figure 1: Geometry of the problem. (a) Original problem. (b) Equivalent problem.

and receiving antennas are limited to one side of a concrete structure. If the distance between the primary source and any point on chain lines is far enough, the pulsed incident wave can't arrive to chain lines. Therefore it is enough for us to measure electromagnetic fields on the broken line (the observation line $\partial\Omega$). For simplicity, two-dimensional case is examined, i.e., the electric parameters of the object depend only on the x and y directions, and a short pulsed wave is generated by an electric current source $\mathbf{J}(\mathbf{r},t) = J_z(\mathbf{r},t)\hat{z}$ flowing along the z-direction, where $\mathbf{r} = (x,\, y)$ and $\hat{z}$ is the unit vector in the z-direction. We assume that the source is turned on at time $t = 0$ and any electromagnetic field doesn't exist before time $t = 0$. We apply the field equivalence principle as shown in Figure 1(b).

The impressed primary source $\mathbf{J}$ is assumed to be in the region $\bar{\Omega}$, while the concrete structure to be estimated is in the region Ω. The equivalent surface currents $\mathbf{s}$ are given by the tangential components of the measured total fields over the surface $\partial\Omega$ as

$$\mathbf{s} = \begin{pmatrix}\eta J_z\\ M_x\\ M_y\end{pmatrix}\delta_{\partial\Omega} = \begin{pmatrix}\eta\left[n_x H_y - n_y H_x\right]\\ -n_y E_z\\ n_x E_z\end{pmatrix}\delta_{\partial\Omega} = \begin{pmatrix}-\eta H_x\\ -E_z\\ 0\end{pmatrix}\delta_{\partial\Omega}, \tag{1}$$

where $\delta_{\partial\Omega}$ is a delta function representing a source concentrated on the surface $\partial\Omega$, and n_x and n_y are the components of the unit vector $\hat{n}$ inward normal to $\partial\Omega$. $\eta\,(=\sqrt{\mu_0/\varepsilon_0})$ is the characteristic impedance of free space The electromagnetic fields $\mathbf{u}^T = (E_z^{eq}\ \ \eta H_x^{eq}\ \ \eta H_y^{eq})$ of the equivalent problem are the solution of Maxwell's equations,

$$\left(\bar{A}\frac{\partial}{\partial x} + \bar{B}\frac{\partial}{\partial y} - \bar{C}\frac{\partial}{\partial\,(ct)} - \bar{D}\right)\mathbf{u} = \mathbf{s}, \tag{2}$$

$$\bar{A}=\begin{pmatrix}0&0&1\\0&0&0\\1&0&0\end{pmatrix},\quad \bar{B}=\begin{pmatrix}0&-1&0\\-1&0&0\\0&0&0\end{pmatrix},\quad \bar{C}=\begin{pmatrix}\varepsilon_r(\mathbf{r})&0&0\\0&\mu_r(\mathbf{r})&0\\0&0&\mu_r(\mathbf{r})\end{pmatrix},\quad \bar{D}=\begin{pmatrix}\eta\sigma(\mathbf{r})&0&0\\0&0&0\\0&0&0\end{pmatrix} \tag{3}$$

In the equivalent problem, the primary source is removed and the original concrete structure is remained. In addition, it is not necessary to consider obstacles yielding unwanted clutter located in the exterior region $\bar{\Omega}$. The equivalent surface current produces the same total field in the interior region Ω as does the primary source, while null field in the exterior region, i.e.,

$$\mathbf{u}(\mathbf{r},t) = \begin{cases}\mathbf{v}(\mathbf{r},t) & \mathbf{r}\in\Omega\\ 0 & \mathbf{r}\in\bar{\Omega}\end{cases}\ \text{(for the original concrete structure)} \tag{4}$$

If we replace the original concrete structure by the different concrete structure,

$$\mathbf{u}(\mathbf{r},t) \neq \begin{cases}\mathbf{v}(\mathbf{r},t) & \mathbf{r}\in\Omega\\ 0 & \mathbf{r}\in\bar{\Omega}\end{cases}\ \text{(for the different concrete structure).} \tag{5}$$

where $\mathbf{v}(\mathbf{r},t)$ denote the original fields generated by the primary source $\mathbf{j}$. This allow us to formulate the inverse scattering problem as a minimization problem with a cost function consisting of a magnitude of electromagnetic fields in the region $\bar{\Omega}$ above the observation line $\partial\Omega$. We introduce following functional of the electrical parameters:

$$G(\mathbf{p}) = \sum_{n=1}^{N} \int_0^T \int_{\bar{\Omega}} |\mathbf{u}_n(\mathbf{r}, t)|^2 \, d\mathbf{r} dt, \tag{6}$$

where $\mathbf{p} = (\varepsilon, \mu)$ is the parameter vector to be estimated. The vectors $\mathbf{u}_n(\mathbf{r}, t)$ represents the equivalent fields for a current estimated parameter $\mathbf{p}$ due to the nth equivalent surface current $\mathbf{s}_n$, $n = 1, \ldots, N$. N is the number of sources. Note that the surface current $\mathbf{s}_n$ is given by the total fields $\mathbf{v}_n(\mathbf{r}, t)$ measured on $\partial\Omega$ for the concrete structure with true parameter $\mathbf{p}^{true}$ due to the nth illuminating source $\mathbf{j}_n$.

3. NUMERICAL SIMULATIONS

Numerical simulation is carried out to estimate the size and the position of a reinforcing bar or a cavity in an unknown concrete structure. The total field $\mathbf{v}(\mathbf{r}, t)$ is calculated with the finite-difference time-domain method. The concrete is homogeneous with relative permittivity $\varepsilon_r = 7.7$ and conductivity $\sigma = 0.068\,\mathrm{s/m}$. The computational region is a $6.4\lambda \times 6.4\lambda$. The upper region $3.2\lambda \times 6.4\lambda$ is the air and the lower region $3.2\lambda \times 6.4\lambda$ is the concrete. Where λ is the wavelength in free space corresponding to the highest frequency contained in the primary source:

$$\mathbf{j}_1 = I(t)\, \delta(\mathbf{r} - \mathbf{r}_1)\, \hat{\mathbf{z}}, \tag{7}$$

where $\mathbf{r}_1$ is the location of the primary source and the number of the primary source is one. The source is put in the center of the x direction and 3.2 cm ($10\Delta y$) above the concrete surface. The time factor is

$$I(t) = \frac{d^3}{dt^3} \exp\left[-\alpha^2 (t - \tau)^2\right] \tag{8}$$

and where $\tau = \beta\Delta t$, $\alpha = 4/\tau$, and $\beta = 132$ with time step $\Delta t = 0.98(\Delta x / c\sqrt{2})$ and cell size $\Delta x = \Delta y = \lambda/10\sqrt{10}$. The observation line $\partial\Omega$ locate 1.6 cm ($5\Delta y$) above the concrete surface. We redefine the functional for simulations as follows:

$$G_1(\mathbf{p}) = \frac{\int_0^T \int_{L_{out}} |\mathbf{u}_1(x, y_{out}, t)|^2 \, dx dt}{\int_0^T \int_{L_{in}} |\mathbf{u}_1(x, y_{in}, t)|^2 \, dx dt}, \tag{9}$$

where L_{out} and L_{in} are the estimation line parallel to the concrete surface in the region $\bar{\Omega}$ and Ω, respectively. y_{out} is 3.2 cm ($10\Delta y$) above the concrete surface and y_{in} is 0.96 cm ($3\Delta y$) above the concrete surface. Eq. (9) is normalized by the non-zero field in the region Ω to evaluate the amplitude of the zero-field in the region $\bar{\Omega}$. Since electromagnetic waves are propagate continuously, if the electromagnetic fields on L_{out} become zero, it can be considered that the electromagnetic fields in $\bar{\Omega}$ are zero. Also we define the fitness:

$$F(\mathbf{p}) = \exp\{-G_1(\mathbf{p})\} \tag{10}$$

If the parameter vector $\mathbf{p}$ same to the true distribution $\mathbf{p}^{true}$, it is $\mathbf{u}_1(x, y_{out}, t) = 0$, namely $F(\mathbf{p}^{true}) = 1$.

3.1. Example (a): Detect of a Circular Cavity

A circular cavity exists in the concrete. The radius of the cavity is 1.6 cm and the depth from the concrete surface is 6.4 cm. The concrete is assumed homogeneous. Figure 2 shows a change of the fitness for the relative permittivity of concrete with no cavity and true conductivity. From Figure 2, we found that the relative permittivity given the maximum of the fitness match up nicely with true permittivity. For this reason, we can use the true permittivity for internal estimate of the concrete structure. A genetic algorithm (GA), which is a global optimization technique, is applied to the maximization of the fitness (10). The electric parameters of the concrete are $\varepsilon_r = 7.7$ and $\sigma = 0.068\,\mathrm{s/m}$. The chromosome consists of three genes: the location x, the depth y and the radius r of a cavity. The electric parameter $\mathbf{p}$ in the cavity specified by the chromosome is set to $\varepsilon_r = 1$ and $\sigma = 0$. The configuration details of Real-Coded GA are as follows: the number of population is 20, the mutation rate is 0.03 and the elitism is adopted. The GA search stops when the maximum fitness does not change during 20 generations. A correct estimated result was provided for all 20 times of trials to be shown in Table 1. For discretization error and computation error, the maximum fitness is not equal to 1.0.

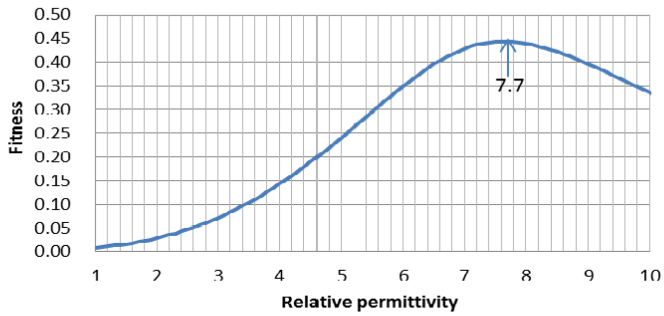

Figure 2: Change of the fitness for the permittivity.

Table 1: A cavity estimated by GA.

	average of maximum fitness	average of fitness	x	y	r	average number of	average number of different chromosome
20 trials	0.949692905	0.839315	116	86	5	40.75	281
ture value	0.949692905	-	116	86	5	-	-

3.2. Example (b): Detect of a Reinforcing Bar

A reinforcing bar exists in the concrete. The radius of the re-bar is 1.6 cm and the depth from the concrete surface is 6.4 cm. The chromosome consists of three genes: the location x, the depth y and the radius r of a re-bar. The electric parameter $\mathbf{p}$ in the re-bar specified by the chromosome is set to $\sigma = 10^7$. Other GA parameters are same to example (a). Table 2 is shown the result of 50 trials for a reinforcing bar. 45 of 50 times succeeded in an estimate and 5 times failed. We found that the exploration falls into two local minimums. For all trials, $y + r = 91$ holds. That is, the distance from the upper surface of re-bar is same. It is a future problem to improve exploration precision by adopting this in algorithm of GA.

Table 2: A cavity estimated by GA. (a) In the case of correct estimation (45/50). (b) In the case of fail estimation (5/50).

(a)

	average of maximum fitness	average of fitness	x	y	r	average number of generations	average number of different chromosome
45 trials	0.949192	0.795998	116	86	5	36.3	207.6
ture value	0.949192	-	116	86	5	-	-

(b)

trial number	maximum fitness	average of fitness	x	y	r	number of generations	number of different chromosome
13, 14, 20, 49	0.721026	0.6538468	116	82	9	25	134
18	0.592847	0.473844	116	79	12	36	178
ture value	0.949192	-	116	86	5	-	-

4. CONCLUSIONS

We discussed about the imaging of a concrete structure without information of incident field by using of the equivalence principle. Real-Coded GA was used for the method of the imaging. By numerical simulations of a reinforcing-bar or a cavity investigation in the concrete structure, the effectiveness of the present method was clarified. The future works are the exploration of two or more objects and the reconstruction using measured data.

ACKNOWLEDGMENT

This work was supported by Grant-in-Aid for Scientific Research (C: 23560572).

REFERENCES

1. He, X. Q., Z. Q. Zhu, Q. Y. Liu, and G. Y. Lu, "Review of GPR rebar detection," *PIERS Proceedings*, 804–813, Beijing, China, Mar. 23–27, 2009.
2. Takenaka, T. and T. Moriyama, "Inverse scattering approach based on the field equivalence principle: Inversion without a priori information on incident fields," *Optics Letters*, Vol. 37, 3432–3434, Aug. 2012.
3. Moriyama, T., T. Tanaka, and T. Takenaka, "Time reversal imaging without information of incident field," *2013 URSI Commission B, EMTS*, May 2013.
4. Meng, Z. Q., T. Takenaka, and T. Tanaka, "Image reconstruction of two-dimensional impenetrable objects using genetic algorithm," *Journal of Electromagnetic Waves and Applications*, Vol. 13, No. 1, 95–118, 1999.
5. Caorsi, S., A. Massa, and M. Pastorino, "A computational technique based on a real-coded genetic algorithm for microwave imaging purposes," *IEEE Trans. Geosci. Remote Sensing*, Vol. 38, 1697–1708, Jul. 2000.
6. Huang, C. H., H. C. Lu, C. C. Chiu, T. A. Wysocki, and B. J. Wysocki, "Image reconstruction of buried multiple conductors by genetic algorithms," *International Journal of Imaging Systems and Technology*, Vol. 18, 276–281, Oct. 2008.
7. Li, F., X. Chen, and K. Huang "Microwave imaging a buried object by the GA and using the S_{11} parameter," *Progress In Electromagnetics Research*, Vol. 85, 289–302, 2008.
8. Tanaka, T., T. Matsuoka, T. Takenaka, and T. Moriyama, "Estimation of reinforcing bars by using real GA with discrete chromosomes" *PIERS Online*, Vol. 7, No. 5, 466–470, 2011.

An Experimental Study of Through-the-Wall Radar for Lifesign Detection

Betul Yilmaz[1], **Sevket Demirci**[1], **Enes Yigit**[2], **and Caner Ozdemir**[1]

[1]Department of Electrical-Electronics Engineering, Mersin University, Mersin, Turkey
[2]Vocational School of Technical Sciences, Mersin University, Mersin, Turkey

Abstract— In this study, an experimental study on Through-the-Wall radar imagery was accomplished for the purpose of imaging life-sign symptoms. The proposed system is based on a stepped frequency continuous wave radar with the help of a Vector Network Analyzer (VNA-Agilent E5071B ENA), antenna (C-band), and the control computer. Breathing and heartbeat information is extracted from the backscattering electromagnetic field exploiting a change detection routine. The experimental results show that both breathing and the heartbeat signatures from real human beings are gathered.

1. INTRODUCTION

Through-the-Wall Radar (TWR) is an emerging technology which is very useful for detecting and identifying unknown objects behind walls. It can be used in different applications ranging from survivor detection in rescue, hostage operations, to people localization in anti-terrorist operations or life detecting under earthquake rubble [1]. Recently, microwave Doppler radars were developed for remote sensing of heartbeat and breathing [2]. Both heartbeat and breathing motions may cause changes in frequency, phase, amplitude and arrival time of returned signal from a living human-body. These responses; however, may attenuate drastically due to the thickness and the electrical properties of the wall material. Therefore; getting successful radar based detection of heartbeat or breathing is usually considered to be a challenging task. In this study, we have exploited a stepped frequency continuous wave radar system that has a very large fractional bandwidth (50%). Thus, change detection (CD) algorithms are capable of detecting life signs of human beings behind walls. Breathing is a periodical behavior over a certain interval of time. The difference signals can be achieved by the subtraction of two consecutive data sets. The difference signal occurs as the breathing's periodic behavior on the two dimensional time varying range profile diagram.

This study is organized as follows: Section 2 briefly describes the radar measurement system and configuration. In Section 3, the through-wall human breathing and heartbeat detection experiments with the experimental set-up are presented. Finally, the last section provides the conclusion with ideas for future work.

2. RADAR SYSTEM DESCRIPTION

In the experiments, we have utilized a monostatic configuration in front of a concrete wall that has a thickness of 30 cm. As a sensor, a C-band pyramidal horn antenna was used while the frequency of the Agilent E5071B ENA vector network analyzer (VNA) was varied from of 3 to 5 GHz for 201 linearly stepped points. The experimental radar system is shown in Fig. 1.

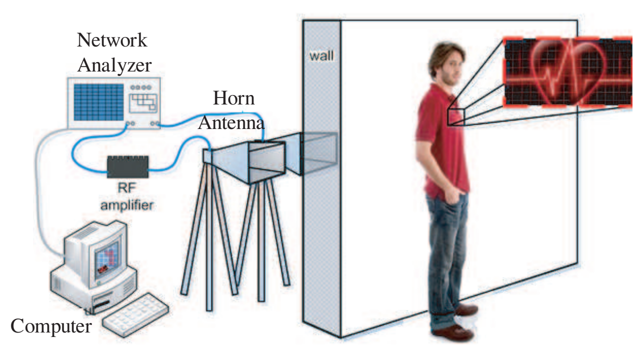

Figure 1: Measurement schematic.

3. MEASUREMENT RESULTS

In the first experiment, a 26 year old man stood still behind the wall. The distance between him and the wall was about 30 cm. The response from a normally breathing man was collected over a period of 20 seconds while the man was standing still. It is well known that the movement of a person's chest causes varying radar returns with different back-scattering amplitudes. To be able to plot this change in the environment, a differential range profile was generated by subtracting the consecutive range profiles of the scene. With this construct, static objects such as the wall or any fixed object inside the room are filtered out and only the dynamic objects; i.e., changes in the scene are displayed. This change detection operation produced the radar images that are shown in Fig. 2. This time-varying differential range-profiles of the breathing man are then consecutively displayed to have a two-dimensional (2D) image as plotted in Fig. 2(a). The changes around the 30 cm range distance can be easily detected for all time instants in the image.

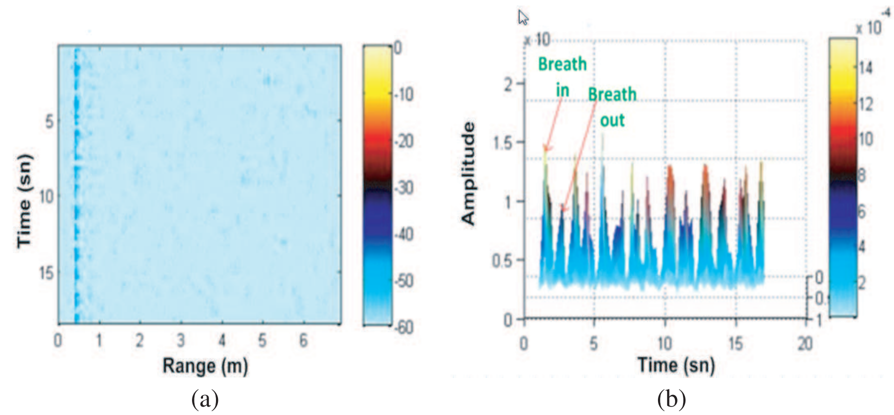

Figure 2: Radar images for breathing person: (a) 2D image constructed by consecutively displaying the differential range-profiles, (b) slice of the resulted image that corresponds to the 30 cm range.

In Fig. 2(b), the response at 30 cm range is drawn with respect to the observed time interval. A total of 7 breathing (for the 16 seconds period) were detected using the figure that is consistent with nominal breathing values for a healthy human. In the second experiment, heartbeat detection has been studied. For this purpose, the person stood still just behind the wall holding his breath for a period of 16 seconds. The experimental set-up and the parameters were kept the same with the previous experiment. The resulting radar images are given in Fig. 3. Since the person was not breathing (so his chest was on rest), the only change in the scene was his beating heart. The resultant time-varying range-profiles that have weaker reflection when compared to the breathing experiment were detected and plotted in Fig. 3(a) as a two-dimensional radar image. Again, changes about 30 cm range distance are distinguishable in the image around -50 dB amplitude level. Plotting the response at 30 cm range distance with respect to the observed time interval produces the plot in Fig. 3(b). In this figure, the peaks corresponds the heartbeats of the person. We have counted a total of 17 peaks that corresponds to 64 pulses/min. This result is again consistent with nominal values of 60 to 80 beats/min for a healthy man.

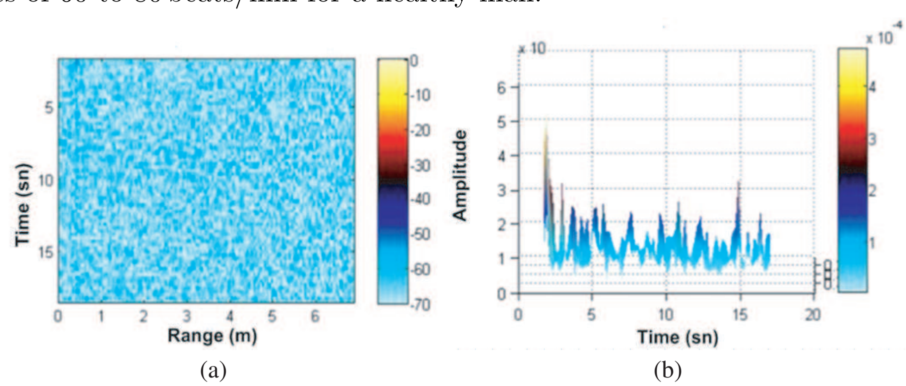

Figure 3: Radar images for heartbeat: (a) 2D image constructed by consecutively displaying the differential range-profiles, (b) slice of the resulted image that corresponds to the 30 cm range .

4. CONCLUSION

In this paper, we have successfully demonstrated the ability of radar to be applied in through the wall detection of life sign symptoms. The proposed method using the change detection algorithm effectively detects and locates the position of the human and periodic motion of breathing and heartbeat. The experimental results show that detected breathing and heartbeat rates are consistent with nominal values for a healthy man. Our method has high accuracy and is easy to implement. This methodology can be easily adapted to search and locate survivors buried under earthquake wreckage and similar applications.

REFERENCES

1. Ferris, D. D. and N. C. Currie, "A survey of current technologies for through-the-wall surveillance (TWS)," *Proc. SPIE*, Vol. 3577, 62–72, 1998.
2. Ivashov, S. I., V. V. Razevig, A. P. Sheyko, and I. A. Vasilyev, "Detection of human breathing and heartbeat by remote radar," *PIERS Proceedings*, 663–666, Pisa, Italy, 2004.

Microwave Diode on the Base of Symmetrically and Asymmetrically Doped Semiconductor Heterojunction

A. Sužiedėlis[1], **S. Ašmontas**[1], **A. J. Kundrotas**[1], **J. Gradauskas**[1], **A. Lučun**[1], **A. Čerškus**[1], **V. Nargelienė**[1], **T. Anbinderis**[2], **and P. Anbinderis**[2]

[1]Center for Physical Sciences and Technology, Savanoriu Ave. 231, LT-02300 Vilnius, Lithuania
[2]Elmika Ltd, Naugarduko St. 41, LT-03227 Vilnius, Lithuania

Abstract— Microwave diodes on the basis of semiconductor heterojunction are considered as an alternative for Schottky junction diode. Preliminary experimental results of DC and high frequency parameters of the planar GaAs/$Al_xGa_{1-x}As$ isotype heterojunction diodes with symmetrically doped narrow- and wide-gap semiconductors are presented. New design of the heterojunction diode with different doping of the n-GaAs and n-$Al_{0.2}Ga_{0.8}As$ semiconductor epitaxial layers is considered as well.

1. INTRODUCTION

Microwave Schottky-diode detectors are the most sensitive devices in a wide range of electromagnetic radiation wavelength. However, poor stability and reliability of the detectors necessitate search for new alternatives to the Schottky diodes. One of such alternative is microwave diode on the base of semiconductor heterojunction. Bulk nature of the active region of the diode, with heterojunction situated far away from the surface promises better stability and reliability of the microwave diode. Planar design of the heterojunction diode makes possible to use it both in the microwaves and infrared [1].

The n-type semiconductor heterojunction of GaAs/$Al_xGa_{1-x}As$ was created in MBE grown structure. Both sides of the heterojunction were doped by the same value of donor density $N_d = 10^{16}\,\mathrm{cm}^{-3}$. $Al_xGa_{1-x}As$ compound semiconductor with different AlAs mole fraction x was used for the heterojunction diode fabrication. Optimal composition of the $Al_xGa_{1-x}As$ compound was determined with the $x = (0.2 \div 0.25)$ as concerns the voltage sensitivity of the heterojunction microwave diode [2]. However, optimal design of the heterojunction microwave diode is under consideration: symmetric doping of the GaAs and AlGaAs layers of the heterojunction results in greater electrical resistance of the junction. This, in turn, leads to the lower voltage sensitivity and lower operational speed of the microwave diode.

New design of the n-GaAs/n-$Al_xGa_{1-x}As$ is considered in this report with different doping level of the sides of the heterojunction. Optimal design of the heterojunction is proposed after simplified analysis of energetic band structure of the n-GaAs/n-$Al_{0.2}Ga_{0.8}As$ heterojunction.

2. DESIGN OF THE PLANAR HETEROJUNCTION MICROWAVE DIODE WITH SYMMETRIC DOPING

Energy band structure of the n-GaAs/n-$Al_{0.2}Ga_{0.8}As$ heterojunction is presented in Fig. 1. The band structure was calculated using Poisson equation. The surface states at the GaAs/AlGaAs interface are ignored for the simplicity. Cross-sectional view of the MBE grown structure is shown on the picture as well. Both GaAs and AlGaAs layers are doped with $N_d = 10^{16}\,\mathrm{cm}^{-3}$ donor density. The adjacent contact layers n^+-GaAs and n^+-$Al_{0.2}Ga_{0.8}As$ are doped to the value of $N_d = 3 \cdot 10^{18}\,\mathrm{cm}^{-3}$ donor density. The heterojunction diode is majority charge carrier device, and there is an energy barrier in conduction band of the heterojunction for electrons. The height of the barrier in the heterojunction equals to 0.183 eV.

Active region of the heterojunction diode is shown in Fig. 2. Semiconductor mezastructure with metal contacts of the microwave diode is transferred onto a dielectric polyimide film. The heterojunction microwave diode is cut from the diode matrix and mounted in a strip line using conductive epoxy.

3. EXPERIMENTAL RESULTS OF THE HETEROJUNCTION DIODE WITH SYMMETRIC DOPING

Measurements of I-V characteristics of the diodes were performed using Agilent Semiconductor parameter analyzer. Fig. 3 depicts I-V characteristic of the microwave diode with the n-GaAs/n-$Al_{0.2}Ga_{0.8}As$ heterojunction measured at room temperature. The forward current flows through

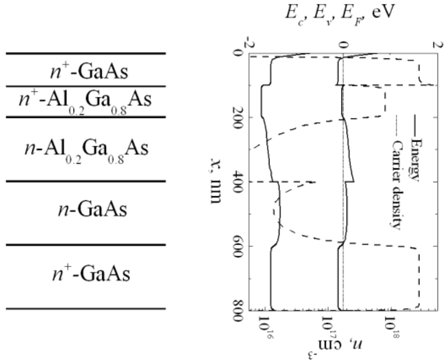

Figure 1: Crossection of n-GaAs/n-Al$_{0.2}$Ga$_{0.8}$As heterojunction structure and its energy band diagram with electron density distribution.

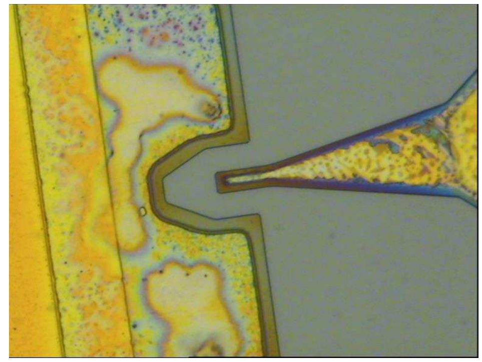

Figure 2: Active region of the heterojunction diode.

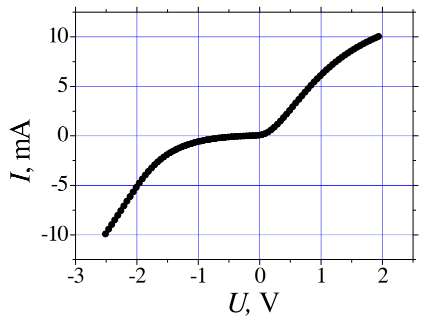

Figure 3: I-V characteristic of the microwave diode on the base of n-GaAs/n-Al$_{0.2}$Ga$_{0.8}$As heterojunction.

the diode when negative potential is applied to the right contact of the diode that is shown in Fig. 2. The right metallic contact is situated at the top of the heterostructures.

The heterojunction diode revealed the asymmetric I-V characteristic with current saturation in forward direction at higher voltages. The current saturation is absent for the reverse direction. Reason for the current increase at reverse bias may be the current leakage in the active region of the diode aside the energy barrier. Tunneling of electrons through the barrier is unlikely to occur due to the substantial width of the barrier at low doping of semiconductors, however thermally activated tunneling of charge carriers can take place at higher voltage. The forward branch of the I-V characteristic at low voltage was approximated using graded gap model of heterojunction [3]. The fitting parameters were chosen: barrier height φ_b, barrier width l and non-ideality factor n of the exponential I-V characteristic. The best fit theory to the experimental data was achieved when $\varphi_b = 0.33\,\mathrm{eV}$, $l = 12\,\mathrm{nm}$ and $n = 1.70$. The differential resistance of the diode at zero voltage was $1300\,\Omega$.

Detection properties of the heterojunction microwave diode were measured in K_a, W and D frequency ranges using Scalar network analyser produced by Elmika Ltd. The voltage power characteristic of the diode was linear up to hundreds of microwatts of microwave power in waveguide (see in Fig. 4). Increase of the microwave power resulted in sublinear voltage power characteristic. Voltage sensitivity of the heterojunction diode at low frequencies ($26 \div 30\,\mathrm{GHz}$) was $\sim 2000\,\mathrm{V/W}$ as can be seen in Fig. 5. The voltage sensitivity decreased with frequency increase following the law of $1/f^2$. This frequency dependence of voltage sensitivity supports our previous done presumption concerning nature of the detected voltage in n-GaAs/n-Al$_x$Ga$_{1-x}$As heterojunction: the detected voltage decrease is determined by frequency dependence of intervalley electromotive force in n-Al$_x$Ga$_{1-x}$As on frequency [4].

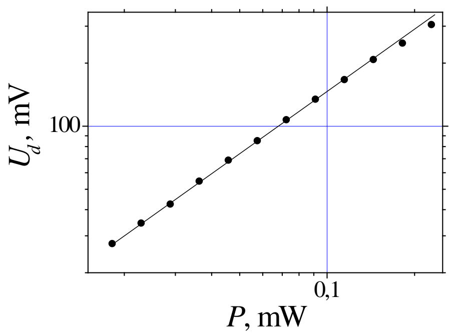

Figure 4: Voltage power characteristic of the microwave diode on the base of n-GaAs/n-$Al_{0.2}Ga_{0.8}As$ heterojunction at $f = 26$ GHz. A line is guide for eyes of the linear dependence of detected voltage on microwave power.

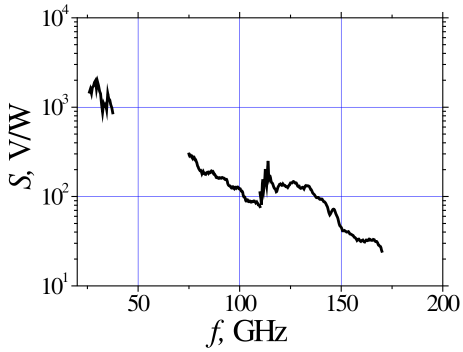

Figure 5: Frequency dependence of voltage sensitivity of the microwave diode on the base of n-GaAs/n-$Al_{0.2}Ga_{0.8}As$ heterojunction.

4. THEORETICAL CONSIDERATION OF NEW DESIGN OF THE HETEROJUNCTION DIODE WITH ASYMMETRIC DOPING

Here we present some ideas concerning the improvement of parameters of the heterojunction diode. First of all we intend decrease electrical resistance of the diode increasing doping level of the n-$Al_xGa_{1-x}As$ or n-GaAs region of the heterojunction. The design of the MBE grown semiconductor structure with n^+-$Al_{0.2}Ga_{0.8}As$/n-GaAs heterojunction, its energy band diagram and electron density distribution in the heterostructure are presented in Fig. 6. Donor density in the n^+-GaAs contact layers was chosen to be $3 \cdot 10^{18}\,\mathrm{cm}^{-3}$. The same doping level was in the n^+-$Al_{0.2}Ga_{0.8}As$ layer. The n-GaAs layer was lightly doped with donor density $N_d = 10^{15}\,\mathrm{cm}^{-3}$.

This design of the heterostructure requires 4 epitaxial layers (compare with 5 for the symmetric heterojunction in Fig. 1). The barrier width of the n^+-$Al_{0.2}Ga_{0.8}As$/n-GaAs heterojunction is more than one order less comparing with the symmetrically doped heterojunction. The narrower energy barrier should result in lower differential electrical resistance of the heterojunction diode that, in turn, should improve operational speed of the diode. More doped n^+-$Al_{0.2}Ga_{0.8}As$ region of the heterojunction let us to expect less influence of the intervalley electromotive force to the detected voltage in the heterojunction microwave diode. Therefore, weaker frequency dependence of the detected voltage can be expected for the microwave diode with the asymmetrically doped heterojunction.

Now consider asymmetrically doped heterojunction of n^+-GaAs/n-$Al_{0.2}Ga_{0.8}As$. This design of the heterostructure for the microwave diode let us to reduce the number of epitaxial layers to

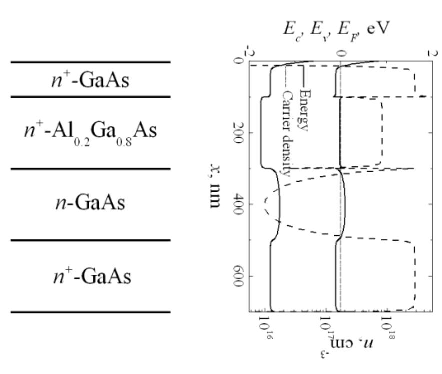

Figure 6: Crossection of n^+-$Al_{0.2}Ga_{0.8}As$/n-GaAs heterojunction structure and its energy band diagram with electron density distribution.

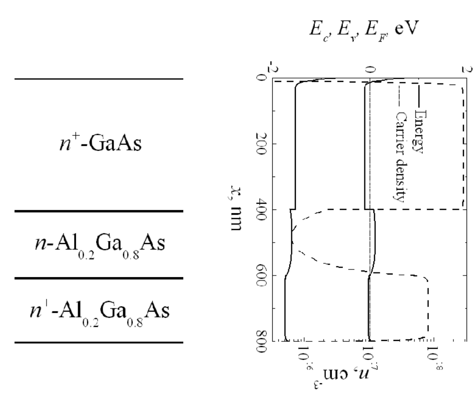

Figure 7: Crossection of n^+-GaAs/n-$Al_{0.2}Ga_{0.8}As$ heterojunction structure and its energy band diagram with electron density distribution.

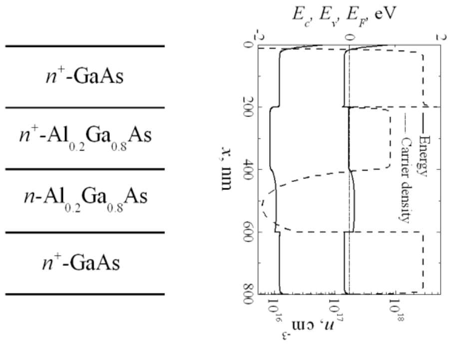

Figure 8: Crossection of n-Al$_{0.2}$Ga$_{0.8}$As/n^+-GaAs heterojunction structure and its energy band diagram with electron density distribution.

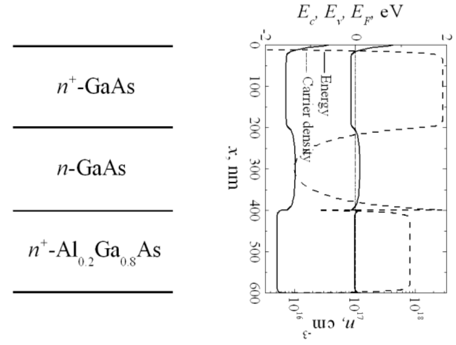

Figure 9: Crossection of n-GaAs/n^+-Al$_{0.2}$Ga$_{0.8}$As heterojunction structure and its energy band diagram with electron density distribution.

3. Fig. 7 depicts the cross-section of the heterojunction, its energy band structure and electron distribution in conduction band. Comparison of the energy band diagram of the n^+-GaAs/n-Al$_{0.2}$Ga$_{0.8}$As heterojunction with that of the n^+-Al$_{0.2}$Ga$_{0.8}$As/n-GaAs let us to conclude that the first one contains more simple heterojunction of step-like shape without two dimensional electron gas sheet in the n^+-GaAs layer and without narrow depletion layer in the heterojunction. The later circumstance let us to expect lower value of electrical capacitance of the n^+-GaAs/n-Al$_{0.2}$Ga$_{0.8}$As heterojunction and, thus, greater operational speed of the microwave diode. In case of the n^+-Al$_{0.2}$Ga$_{0.8}$As/n-GaAs heterojunction the current flows in forward direction when negative potential is applied to the surface of heterostructure and, the other way, in case of the n^+-GaAs/n-Al$_{0.2}$Ga$_{0.8}$As heterojunction the forward current flows when positive potential is applied to the surface of heterojunction (surface of heterojunctions is situated at point $x = 0$). Therefore, the polarity of the detected voltage in microwave diodes on the base of those different heterostructures should be opposite if the detected voltage arise due to microwave currents rectification in the heterojunctions.

The heterojunction microwave diode with great operational speed should be expected when it is fabricated on the base of heterostructure that is shown in Fig. 8. This heterojunction is inverted variant of the heterojunction that is depicted in Fig. 7. Therefore the polarity of the detected voltage of the microwave diode fabricated on the base of the n-Al$_{0.2}$Ga$_{0.8}$As/n^+-GaAs heterojunction should be expected to be opposite to that of the microwave diode on the base of n^+-GaAs/n-Al$_{0.2}$Ga$_{0.8}$As heterojunction if the detected voltage is determined by microwave currents rectification. Possible rise of intervalley elctromotive force in n-Al$_{0.2}$Ga$_{0.8}$As layer [4] should differently influence the detected voltage:in one case the intervalley emf should add to the detected voltage due to the rectification in anoter case it should be subtracted.

Finally, we present the design of heterostructure with n-GaAs/n^+-Al$_{0.2}$Ga$_{0.8}$As heterojunction that is shown in Fig. 9. This heterostructure contains the n-GaAs/n^+-Al$_{0.2}$Ga$_{0.8}$As heterostructure that is inverted variant of then^+-Al$_{0.2}$Ga$_{0.8}$As/n-GaAs heterojunction that is shown in Fig. 6. The energy band structure is similar in both cases. However, the heterojunction n-GaAs/n^+-Al$_{0.2}$Ga$_{0.8}$As design can be realized using minimal epitaxial layers number that is reduced to 3. One more feature of the last two heterostructures should be pointed out. The heterostructures presented in Fig. 8 and Fig. 9 contain the n^+-n junctions of the same semiconductor: Al$_{0.2}$Ga$_{0.8}$As in Fig. 8 and GaAs in Fig. 9. The n^+-n junctions of specific configuration were used for the microwave radiation detection in wide frequency range from microwaves up to infrared radiation [5, 6].

In conclusion, we can predicate the use of isotype GaAs/AlGaAs heterojunction for sensitive detection of microwave radiation and hope that as a majority carrier device, the microwave diode on the base of the isotype heterojunction, could fairly compete with Schottky diode.

ACKNOWLEDGMENT

This work was supported by Agency for Science, Innovation and Technology (grant No. 31V-37) in the frame of High Technology Development Program for 2011–2013. Authors are thankful to Angele Steikuniene and Gytis Steikunas for sample preparation.

REFERENCES

1. Gradauskas, J., A. Suziedelis, S. Asmontas, E. Sirmulis, V. Kazlauskaite, A. Lucun, and M. Vingelis, "Sensitive planar semiconductor detector from microwave to infrared applications," *IEEE Sensors Journal*, Vol. 10, No. 3, 662–667, 2010.
2. Sužiedėlis, A., S. Ašmontas, A. J. Kundrotas, J. Gradauskas, A. Čerškus, V. Nargelienė, and T. Anbinderis, "Planar heterojunction diode for millimeter waves detection," *PIERS Proceedings*, 927–930, Moscow, Russia, August 19–23, 2012.
3. Cheung, D. T., S. Y. Chiang, and G. L. Pearson, "A simplified model for graded-gap heterojunctions," *Solid-State Electron.*, Vol. 18, 263–266, 1975.
4. Sužiedėlis, A., S. Ašmontas, A. J. Kundrotas, V. Nargelienė, and J. Gradauskas, "Voltage sensitivity of point-contact GaAs/AlGaAs heterojunction microwave detector," *Phys. Scr.*, Vol. 85, 035702 (5pp), 2012.
5. Ašmontas, S. and A. Sužiedėlis, "New microwave detector," *Int. Journ. Infr. Millimeter Waves*, Vol. 15, No. 3, 525–538, 1994.
6. Sužiedėlis, A., J. Gradauskas, S. Ašmontas, G. Valušis, and H. G. Roskos, "Giga- and terahertz frequency band detector based on an asymmetrically-necked n-n^{+}-GaAs planar structure," *J. Appl. Phys.*, Vol. 93, No. 5, 3034–3038, 2003.

A Waveguide-to-microstrip Line Transition in Multi-layered Structure for 77 GHz Band Automotive Radar Applications

C. H. Tsai and S. J. Chung
Institute of Communications Engineering, National Chao-Tung University, Hsinchu 30010, Taiwan

Abstract— In this paper, a novel waveguide-to-microstrip line transition in the multi-layered substrate which is operated at 77 GHz forward-looking automotive collision warning radar band, is presented. The proposed waveguide-to-microstrip line transition is fed by a standard WR10 rectangular waveguide, the power is coupled from the waveguide into the patch which is located at the center of waveguide and transmit to antenna. Compare to the conventional W-band waveguide-to-microstrip line transition, the feeding direction of the proposed transition is inverse to those conventional design. The design of freedom of conventional type transition is limited cause by this fed direction. Moreover, the stacked-layer structure's via size and spacing is restrict by the fabrication rule, via size and spacing is different in each dielectric layer, thus, the complexity of the design increase. Finally, the proposed waveguide-to-microstrip line transition is well design, this design possess several advances such as small size, low cost, and could easy introduced in the automobile radar application.

1. INTRODUCTION

Owing to the rapidly increasing number of vehicles, the traffic safety becomes an important issue at the modern society. To improve the transportation efficiency and traffic safety, the Intelligent Transport Systems was developed and become more popular [1]. The radar is the key technology in Intelligent Transport System, which opens up new perspectives of comfort and safety features in future automobiles. The automotive radar is operated in two frequency bands, one is the 24 GHz band, and the other one is the 77 GHz band. The 77 GHz band is getting popular is recent years owing to the range and angle resolution in 77 GHz radar is better than that in 24 GHz radar. In the millimeter wave circuitry design, the waveguide-to-microstrip line transition plays an important role was due to the antenna and measurement equipment were using waveguide as transmission line and in PCB was using microstrip line, in order to connect antenna or VNA to the RF circuit, thus, a well-designed waveguide-to-microstrip line transition is needed.

Compare to the conventional W-band waveguide-to-microstrip line transition [1–3], the feeding direction of the proposed transition is inverse to those conventional design, the freedom of design is limited cause by this fed direction. Moreover, the stacked-layer structure's via size and spacing is restrict by the fabrication rule, via size and spacing is different in each dielectric layer, thus, the complexity of the design increase. Finally, the proposed waveguide-to-microstrip line transition is well design and verified by measurement, this design possess several advances such as small size, low cost, and could easy introduced in the automobile radar application.

2. MULTI-LAYERED WAVEGUIDE-TO-MICROSTRIP LINE DESIGN

In this design, the antenna substrate is a triple-layered structure (3 metal layer, 2 dielectric layer) which is shown in Fig. 1(a), the thickness of layer M1/2/3 are 5/2.7/20 mil, respectively. The 20 mil layer is antenna layer, the 5 mil layer is circuit layer, the L_1 is metal layer of microstrip line and RF circuit, L_2 and L_3 is ground and antenna layer, respectively. The dielectric layer is using the low loss Taconic TLP series substrate. The triple-layered design can separate the radiating elements and RF circuits to the front and back side which creates more room to place more antenna elements and RF component. The principle of the energy coupled from waveguide to micrstrip line is similar to the conventional coaxial probe to waveguide transition [4]. Fig. 2 is the top view of the proposed transition, a patch-like probe was place at the center of the waveguide with width W and length L. In order to couple energy from waveguide to microstrip line, a back-short wall at the lower waveguide end is needed, the length between back-short wall and the probe is $\lambda_g/4$. Fig. 2 shows the magnetic field distribution in the waveguide, it can clearly observed that in the center frequency, the maximum H-field occur at back-short point and minimum at the probe area which induced the maximum current at probe and resulting the maximum power transmission.

The impedance matching can be achieved by adjusting the patch width W, length L, and line width d. After tuning the parameters of W, L, and d, the 10-dB impedance bandwidth can be

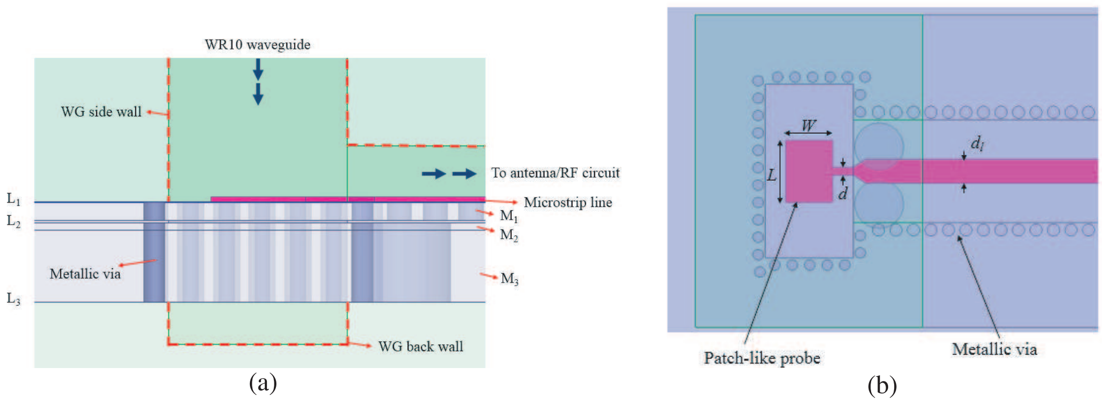

Figure 1: The schematic of the proposed multi-layered waveguide-to-microstrip line transitions. (a) Side view. (b) Top view.

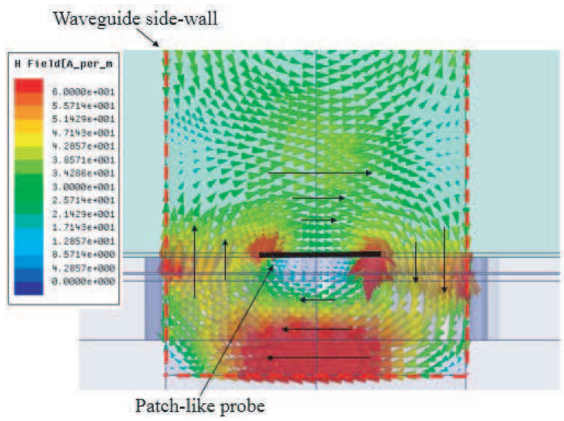

Figure 2: Magnetic field distribution of the fundamental mode at 77 GHz.

achieved at 71.6 $\sim$ 84.6 GHz, the 15-dB impedance bandwidth is about 75.4 $\sim$ 82.6 GHz with the loss about 0.9 dB maximum, with the values of $W = 0.9$ mm, $L = 0.67$ mm, and $d = 0.11$ mm as shown in Fig. 3. Moreover, the effects of L are invested and shown in Fig. 4. From the Fig. 4 it can be observed that the impedance bandwidth increase with increasing L. It have to be mentioned that although the bandwidth of $L = 0.9$ is similar to $L = 1$, the upper frequency of $L = 0.9$ is higher than $L = 1$, it's more suitable for using in 76 $\sim$ 81 GHz automotive radar band. Finally, the photo of the fabricated transition is shown in Fig. 5.

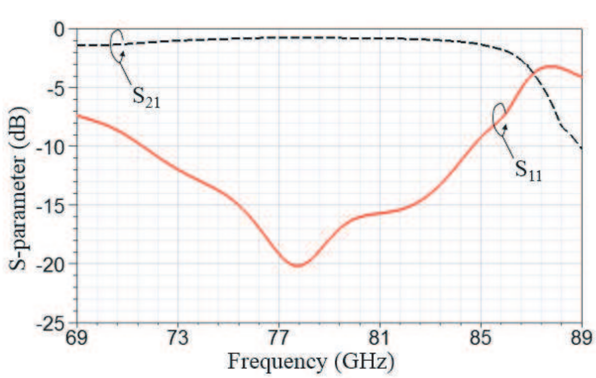

Figure 3: The simulated S-parameters of the proposed transition.

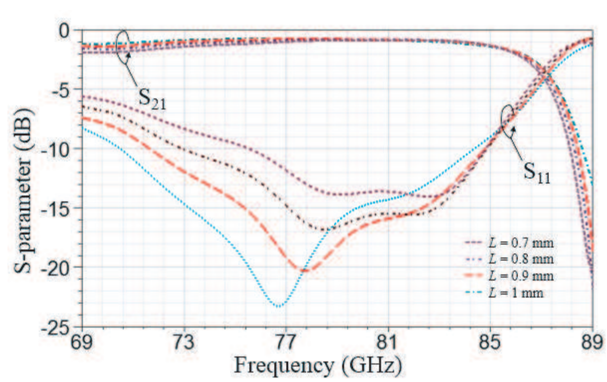

Figure 4: The simulated S-parameters for varying the length L of the patch-like probe.

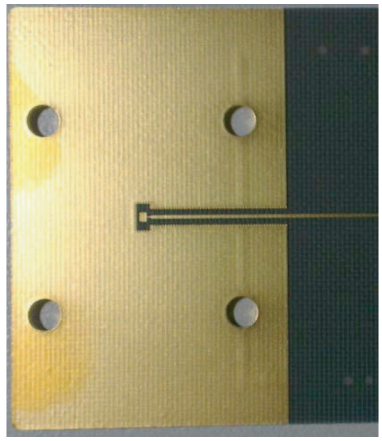

Figure 5: Photograph of the proposed transition.

3. CONCLUSIONS

A novel waveguide-to-microstrip line transition in the multi-layered substrate is proposed. Compare to the conventional W-band waveguide-to-microstrip line transition, the feeding direction of the proposed transition is inverse to those conventional design. The design of freedom of conventional type transition is limited cause by this fed direction. The 10-dB impedance bandwidth of proposed transition can be achieved at $71.6 \sim 84.6$ GHz, the 15-dB impedance bandwidth is about $75.4 \sim 82.6$ GHz with the loss about 0.9 dB.

ACKNOWLEDGMENT

This work was partly supported by Ministry of Economic Affairs under Grant 101-EC-17-A-03-S1-195.

REFERENCES

1. Iizuka, H., K. Sakakibara, and N. Kikuma, "Millimeter-wave transition from waveguide to two microstrip lines using rectangular patch element," *IEEE Trans. Microw. Theory Tech.*, Vol. 55, 899–905, 2007.
2. Murase, K., K. Sakakibara, N. Kikuma, and H. Hirayama, "Design of via-less planer microstrip-to-waveguide transition with choke structure," *IEEE iWAT*, 63–66, 2008.
3. Sakakibara, K., M. Hirono, N. Kikuma, and H. Hirayama, "Broadband and planar microstrip-to-waveguide transitions in millimeter-wave band," *International Conference on ICMMT*, Vol. 3, 1278–1281, 2008.
4. Seo, K., "Study of planar microstrip-to-waveguide transitions in millimeter-wave band," Ph.D. Dissertation, Dept. of Computer Science and Eng., Nagoya Univ., Nagoya, Japan, 2011.

Dispersion Properties of Subwavelength Grating SOI Waveguides

Jiří Čtyroký[1], Pavel Kwiecien[2], and Ivan Richter[2]

[1]Institute of Photonics and Electronics AS CR, v.v.i., Chaberská 57, 182 51 Prague 8, Czech Republic
[2]Department of Physical Electronics, Faculty of Nuclear Sciences and Physical Engineering
Czech Technical University in Prague, Břehová 7, 11519 Prague 1, Czech Republic

Abstract— Segmented subwavelength grating waveguides can be effectively applied to fabricate optical waveguides with very different properties using a standard silicon-on-insulator fabrication technology with one-lithographic step only. The subwavelength grating waveguides can be interpreted as a waveguide with the refractive index reduced by interlacing high-index Si segments with a low-index material (silica or a suitable polymer). However, for real applications, the mode field confinement and the dispersion properties of such waveguides have to be known with much greater accuracy than this simple approximation allows. In this contribution, we present results of a full-vector 3D modeling of subwavelength grating waveguides using our in-house Fourier modal methods. Dependencies of both phase and group effective indices of Bloch modes in the wide wavelength range on the geometrical parameters of the waveguides are presented. Three typical values of Si thickness used in SOI technology are considered, namely 200 nm, 220 nm, and 260 nm. Our results are important for the design of SOI waveguide devices in a number of applications as mode transformers and couplers, nonlinear optical devices, sensors, etc..

1. INTRODUCTION

Silicon-on-insulator (SOI) is one of the most promising platforms for implementation of advanced integrated photonic structures and devices. High refractive index contrast between the silicon waveguide "core" and SiO_2 or polymer "cladding" media allows utilizing very small waveguide bending radii of the order of a few micrometers so that a very high density of integration of photonic devices can be reached on a silicon chip. On the other hand, because of a very high refractive index contrast, even a rather small surface roughness can cause intolerable scattering loss and back-reflections. Using state-of-the-art fabrication technologies, the silicon waveguide refractive index can hardly be substantially modified. An elegant and technologically feasible solution to circumvent these limitations while keeping the advantages of a high index-contrast of silicon waveguides was recently reported by the group of authors [1–6]. The idea is based on the formation of the subwavelength-sized structures with materials of different refractive indices which propagating light "perceives" as an "effective medium" with an averaged refractive index. This approach is not new [7, 8] but in [1–6] it has been creatively applied to the field of SOI waveguides and integrated photonic devices.

In our present contribution we analyze waveguiding properties of segmented subwavelength grating (SWG) waveguides. The principle of subwavelength grating waveguides allows fabrication of waveguides with a wide range of effective refractive indices ranging from the substrate (SiO_2) refractive index up to that of the silicon nanowire, and with different group velocities using a relatively simple single-step nanolithographic process. As it has been shown both theoretically and experimentally [3, 9], very efficient and ultra-broadband couplers can be designed to couple the SWG waveguide with a silicon nanowire.

The SWG waveguides are longitudinally periodic, supporting propagation of Bloch modes. The dispersion properties of these modes are determined by the content of the high-index material — silicon — and by the ratio of the wavelength and the period length, and can thus be easily varied by the design in a broad range. For applications of SWG waveguides in nonlinear optical devices, the dispersion properties are of fundamental importance. With this in mind, we also investigate a combination of the SOI slot waveguide [10, 11] with the "standard" SWG waveguide [3] — the slot SWG waveguide.

2. SEGMENTED SWG WAVEGUIDE

The basic arrangement of segmented SWG waveguides is shown in Figure 1. The standard SWG waveguide in Figure 1(a) is formed by a periodic array of small blocks of silicon separated by the surrounding (substrate or superstrate) medium — in our case SiO_2. In the slotted waveguide Figure 1(b), each Si block is split into two parts with a deeply subwavelength gap between them.

As we will see, for the (quasi)-TE polarization that we consider here, the mode field is strongly confined in the gap between the Si blocks, similarly as in the slot waveguides [10–12].

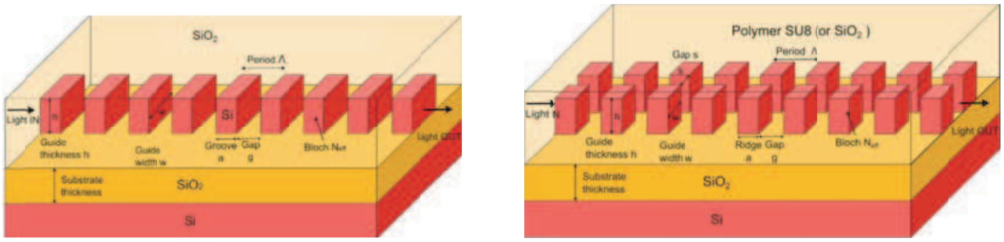

(a) (b)

Figure 1: (a) SWG waveguide, (b) slot SWG waveguide.

To simplify the analysis we will suppose that the bottom SiO_2 (BOX) layer is thick enough so that the influence of the supporting silicon substrate can be neglected. Different approaches can be used to analyze the waveguide properties. Probably the simplest approach is based on the effective medium theory [7, 8]. However, as we have shown recently [13], even the higher-order approximation taking into account the anisotropy of the effective medium does not provide acceptable results, and the same is true for 2-D approximations. Here we present results obtained with our full-vector 3-D modeling software tools developed in-house on the basis of the Fourier modal method [14, 15].

The propagation constants and the field distributions of the (guided) Bloch modes are calculated using the scattering matrix approach by solving the linear eigenvalue problem

$$\begin{pmatrix} \mathbf{0} & \mathbf{S}_{12} \\ \mathbf{I} & -\mathbf{S}_{22} \end{pmatrix} \cdot \mathbf{B} = \begin{pmatrix} -\mathbf{S}_{11} & \mathbf{I}+\mathbf{S}_{12} \\ \mathbf{I}+\mathbf{S}_{21} & -\mathbf{S}_{22} \end{pmatrix} \cdot \mathbf{B} \cdot (\mathbf{I}+\mathbf{\Gamma})^{-1}, \tag{1}$$

where matrix $\mathbf{S}$ with submatrices $\mathbf{S}_{11}, \mathbf{S}_{12}, \mathbf{S}_{21}, \mathbf{S}_{22}$ is the scattering matrix of one period of the SWG waveguide. The columns of matrix $\mathbf{B}$ contain the complex amplitudes of local normal modes at the particular cross-section of the waveguide structure that combine into the individual Bloch modes, and $\mathbf{\Gamma}$ is a diagonal matrix with elements $\Gamma_{mn} = \delta_{mn} \exp(ik_0 N_{B,m} \Lambda)$; here $k_0 = 2\pi/\lambda$, $N_{B,m}$ is the effective refractive index of the m-th Bloch mode, and Λ is the length of the SWG waveguide period. The group effective index of the (fundamental guided) Bloch mode N_B is then calculated using the well-known formula $N_{Bg} = N_B - \lambda dN_B/d\lambda$. Realizing that for the grating considered as an 1-D photonic crystal the "first Brillouin zone" corresponds to the interval of propagation constants $-K/2 < k_0 N_B < K/2 = \pi/\Lambda$, it follows that the effective index of the propagating Bloch mode in the first ("dielectric") band must satisfy the condition $n_s < N_B < \lambda/(2\Lambda)$, where n_s is the substrate refractive index. The bottom limit ensures field confinement of the guided mode, the upper limit represents the forbidden band edge (or equivalently, the limit of Bragg reflection from the grating).

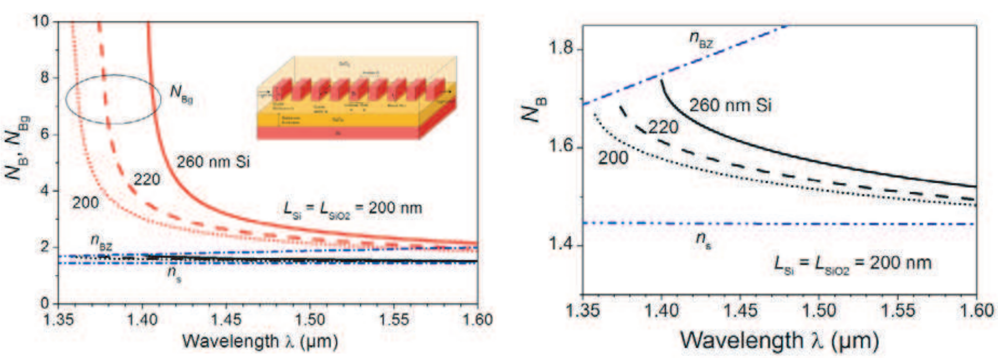

(a) (b)

Figure 2: (a) Group and (b) phase effective indices of Bloch modes in a SWG waveguide. Period length 400 nm, filling fraction 1 : 1, Si thickness 260 nm (solid lines), 220 nm (dashed) and 200 nm (dotted). Dash-dotted lines indicate the substrate (n_s) and Brillouin zone (n_{BZ}) limits. Fig. 2(b) differs from Fig. 2(a) only in the vertical scale.

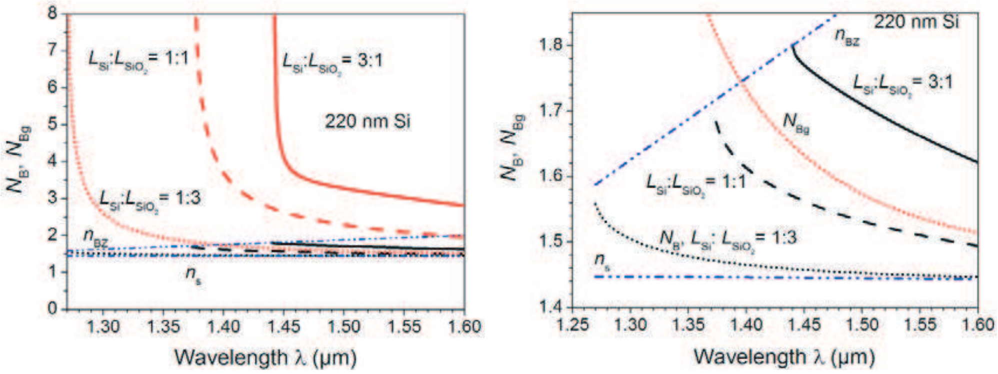

(a) (b)

Figure 3: (a) Group and (b) phase effective indices of Bloch modes in SWG waveguides. Period length 400 nm, filling fractions 3 : 1, 1 : 1 and 1 : 3, Si thickness 220 nm. Other symbols same as in Fig. 2.

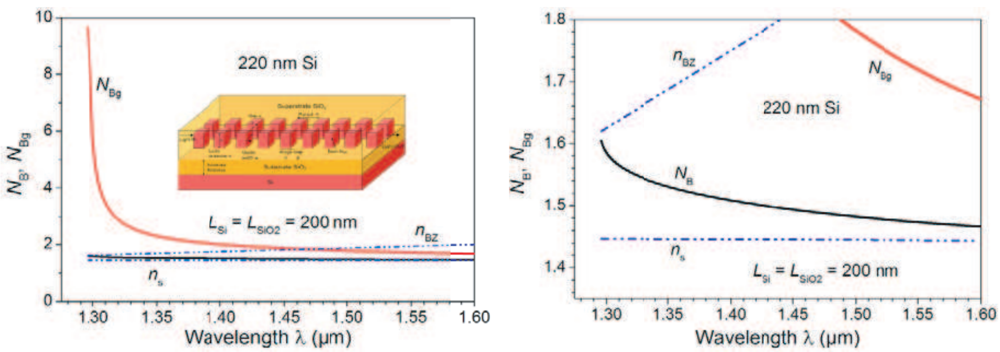

(a) (b)

Figure 4: Group and phase effective indices of Bloch modes in a slot SWG waveguide. Period length 400 nm, filling fraction 1 : 1, Si thickness 220 nm. Other symbols same as in Fig. 2.

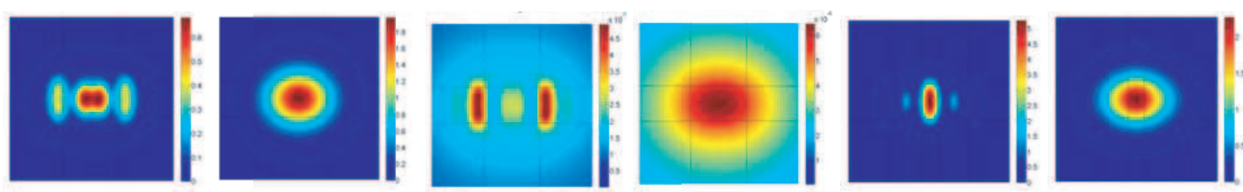

(a) (b) (c) (d) (e) (f)

Figure 5: Power density distributions of Bloch modes at different cross-sections of the SWG waveguides with 220 nm thick Si layer and $\Lambda = 400$ nm. (a), (c), (e) — in the middle of Si block, (b), (d), (f) — in the middle of the gap; (a), (b) — Si:gap ratio 1 : 3, $\lambda = 1.3\,\mu$m; (c), (d) — Si:gap ratio 1 : 9, $\lambda = 1.55\,\mu$m; (e), (f) — slot SWG waveguide, $\lambda = 1.3\,\mu$m. The size of each plotted area is $500 \times 500\,\text{nm}^2$.

3. NUMERICAL RESULTS

Calculated dispersion curves of SWG and slot SWG waveguides are presented in Figs. 2 to 4. Fig. 2 shows the dispersion curves of the SWG waveguide 350 nm wide with thesame lengths of the Si block and the gap, of 200 nm; the period is thus $\Lambda = 400$ nm. Three standard thicknesses of the silicon layer (silicon block height) are considered, namely 260 nm, 22 nm and 200 nm. In Fig. 3 we demonstrate the influence of the Si:gap ratio. It has qualitatively similar effect as the silicon layer thickness; the total fraction of silicon in the waveguide is namely changed in a similar way.

As it could be expected, as the effective index N_B approaches the Brillouin zone limit n_{BZ} (i.e., the band gap of the periodic structure), the group index dramatically increases, and the waveguide operates in the "slow-wave regime".

Figure 5 shows the variability of the power density distribution (the real part of the longitudinal component of the Poynting vector) of the fundamental guided Bloch mode in different SWG waveguides. Very strong confinement in the slot SWG waveguide (Fig. 5(e)) and weak confinement in the waveguide with low Si content (Figs. 5(c), (d)) are apparent.

4. CONCLUSIONS

We have shown by 3-D full-vector numerical modeling that modification of design parameters of segmented SWG waveguides leads to very significant changes in their dispersion properties. Both very weakly and very strongly guiding waveguides operating in the standard as well as in the "slow-wave" regime can be easily designed and fabricated. Having in mind also the feasibility of efficient broadband coupling of SWG waveguides with silicon nanowires, we could perhaps expect that photonic structures based on SWG waveguides might find applications also in some of the areas reserved so far for devices based on photonic crystals.

ACKNOWLEDGMENT

This work was financially supported by the Czech Science Foundation under project P205/10/0046.

REFERENCES

1. Bock, P. J., P. Cheben, J. H. Schmid, J. Lapointe, A. Delage, S. Janz, G. C. Aers, G. C. D. X. Xu, A. Densmore, and T. J. Hall, "Subwavelength grating periodic structures in silicon-on-insulator: A new type of microphotonic waveguide," *Optics Express,* Vol. 18, 20251–20262, 2010.
2. Bock, P. J., P. Cheben, J. H. Schmid, J. Lapointe, A. Delage, D. X. Xu, S. Janz, A. Densmore, and T. J. Hall, "Subwavelength grating crossings for silicon wire waveguides," *Optics Express,* Vol. 18, 16146–16155, 2010.
3. Cheben, P., P. J. Bock, J. H. Schmid, J. Lapointe, S. Janz, D. X. Xu, A. Densmore, A. Delage, A., B. Lamontagne, and T. J. Hall, "Refractive index engineering with subwavelength gratings for efficient microphotonic couplers and planar waveguide multiplexers," *Optics Letters,* Vol. 35, 2526–2528, 2010.
4. Glesk, I., P. J. Bock, P. Cheben, J. H. Schmid, J. Lapointe, and S. Janz, "All-optical switching using nonlinear subwavelength Mach-Zehnder on silicon," *Optics Express,* Vol. 19, 14031–14039, 2011.
5. Schmid, J. H., P. Cheben, P. J. Bock, R. Halir, J. Lapointe, S. Janz, et al., "Refractive index engineering with subwavelength gratings in silicon microphotonic waveguides," *IEEE Photonics Journal,* Vol. 3, 597–607, 2011.
6. Glesk, I., P. J. Bock, P. Cheben, J. H. Schmid, J. Lapointe, and S. Janz, "Picosecond all-optical switching using nonlinear Mach-Zehnder with silicon subwavelength grating and photonic wire arms," *Opt. Quantum Electron.,* Vol. 44, 613–621, 2012.
7. Rytov, S. M., "Electromagnetic properties of a finely stratified medium," *Sov. Phys. JETP,* Vol. 2, 466-475, 1956.
8. Lalanne, P. and J. P. Hugonin, "High-order effective-medium theory of subwavelength gratings in classical mounting: Application to volume holograms," *J. Opt. Soc. Am. A,* Vol. 15, 1843–1851, 1998.
9. Čtyroký, J., P. Kwiecien, and I. Richter, "Analysis of couplers between photonic nanowires and subwavelength grating waveguides," *Proc. SPIE*, Vol. 8781, 1–9, 2013.
10. Alloatti, L., D. Korn, C. Weimann, C. Koos, W. Freude, and J. Leuthold, "Second-order nonlinear silicon-organic hybrid waveguides," *Optics Express,* Vol. 20, 20506–20515, 2012.
11. Pfeifle, J., L. Alloatti, W. Freude, J. Leuthold, and C. Koos, "Silicon-organic hybrid phase shifter based on a slot waveguide with a liquid-crystal cladding," *Optics Express,* Vol. 20, 15359–15376, 2012.
12. Jágerská, J., N. Le Thomas, R. Houdré, J. Bolten, C. Moormann, T. Wahlbrink, J. Čtyroký, M. Waldow, and M. Först, "Dispersion properties of silicon nanophotonic waveguides investigated with Fourier optics," *Optics Letters*, Vol. 32, 2723–2725, 2007.
13. Kwiecien, P., I. Richter, and J. Čtyroký, "Comparison of 2D and 3D Fourier modal methods for modeling subwavelegth-structured silicon waveguides," presented at *Photonics Prague 2011*, Prague, 2011.
14. Čtyroký, J., "3-D bidirectional propagation algorithm based on Fourier series," *J. Lightwave Technol.*, Vol. 30, 3699–3708, 2012.

15. Čtyroký, J., P. Kwiecien, and I. Richter, "Fourier series based 3D Bi-directional propagation algorithm for integrated photonics," presented at the *18th European Conference on Integrated Optics ECIO 2012*, Sitges, Barcelona, Spain, 2012.

Power Spectra of a Radio Wave Diffracted by Random Electron Density Irregularities

G. V. Jandieri[1] **and A. Ishimaru**[2]

[1]Georgian Technical University, Georgia
[2]University of Washington, USA

Abstract— The scintillation spectral features of multiply scattered radio waves in turbulent magnetized plasma with electron density fluctuations are investigated analytically and numerically. An example is based on the anisotropic Gaussian and power-law spectra. The results are applied to the F-region ionosphere. Minimums of the power spectrum are calculated for the Gaussian spectrum in the principle plane. Scintillation level is estimated for different anisotropy factor and the angle of inclination of prolate irregularities with respect to the external magnetic field.

Peculiarities of the electromagnetic waves propagation in randomly inhomogeneous media have been intensively studied [1]. Anisotropic irregularities have different nature, particularly plasma irregularities in the Earth's ionosphere are aligned with the geomagnetic fields [2]. The fluctuations in phase (scintillation) of radio waves passing through the ionosphere are caused by spatial irregularities in the electron density. Evolution of the angular distribution of ray intensity at light propagation in random medium with prolate irregularities has been investigated [3] using the smooth perturbation method. It has been shown that the spatial power spectrum (SPS) of a multiple scattered radiation at oblique illumination of random medium by mono-directed incident radiation has a double-peaked shape. Numerical simulation has been carried out by Monte-Carlo method. The features of the SPS of scattered radiation in magnetized anisotropic plasma in the complex geometrical optics approximation and in smooth perturbation method have been investigated in [4, 5].

The temporal spectrum of scattered radio waves and peculiarities of the evolution of the SPS of multiply scattered radiation in randomly inhomogeneous anisotropic plasma caused by electron density fluctuations analytically and numerically is investigated in this paper using the smooth perturbation method. The Fresnel oscillations are considered taking into account diffraction effects and the movement of rigid plasma irregularities. The evaluation of a double-peak shape in the SPS of multiple scattered radio waves is analyzed at oblique illumination of turbulent plasma by mono-directed incident radiation. Numerical calculations are carried out for both anisotropic Gaussian and power-law correlations functions in the principle and perpendicular planes for the F-region ionosphere using the experimental data.

1. FORMULATION OF THE PROBLEM

Electric field in magnetized turbulent plasma with anisotropic electron density irregularities satisfies wave equation:

$$\left(\frac{\partial^2}{\partial x_i \partial x_j} - \Delta\delta_{ij} - k_0^2 \varepsilon_{ij}(\mathbf{r})\right)\mathbf{E_j}(\mathbf{r}) = 0. \tag{1}$$

Absorption in the layer is negligible for high frequency incident wave and components of second-rank tensor ε_{ij} of the collisionless magnetized plasma are [6]: $\varepsilon_{xx} = 1 - v(1-u)^{-1}$, $\varepsilon_{yy} = 1 - v(1 - u\sin^2\alpha)\cdot(1-u)^{-1}$, $\varepsilon_{zz} = 1 - v(1 - u\cos^2\alpha)(1-u)^{-1}$, $\tilde{\varepsilon}_{xy} = -\tilde{\varepsilon}_{yx} = v\sqrt{u}\cos\alpha(1-u)^{-1}$, $\tilde{\varepsilon}_{xz} = -\tilde{\varepsilon}_{zx} = -v\sqrt{u}\sin\alpha(1-u)^{-1}$; where α is the angle between $\mathbf{k}_0$ and $\mathbf{H}_0$ vectors; $\omega_p(\mathbf{r}) = [4\pi N(\mathbf{r})e^2/m]^{1/2}$ is the plasma frequency, $u = (eH_0/mc\omega)^2$ and $v(\mathbf{r}) = \omega_p^2(\mathbf{r})/\omega^2$ are the magneto-ionic parameters, $\Omega_H = eH_0/mc$ is the electron gyrofrequency. Wave field we introduce as $E_j(\mathbf{r}) = E_{0j}\exp(\varphi_1+\varphi_2+ik_\perp y+ik_0 z)$ $(k_\perp \ll k_0)$. Variation of dielectric permittivity are caused by electron density fluctuations $v(\mathbf{r}) = v_0[1+n_1(\mathbf{r})]$; $\varepsilon_{ij}(\mathbf{r}) = \varepsilon_{ij}^{(0)} + \varepsilon_{ij}^{(1)}(\mathbf{r})$. First component represents zeroth-order approximation, the second term is random function of the spatial coordinates, $|\varepsilon_{ij}^{(1)}(\mathbf{r})| \ll 1$. Fluctuations of complex phase are of the order $\varphi_1 \sim \varepsilon_{ij}^{(1)}$, $\varphi_2 \sim \varepsilon_{ij}^{(1)2}$. The parameter $\mu = k_\perp/k_0$ is calculated from the set of differential equation for the phase φ_0 [3–5].

Information about the irregularity electron density spectrum (the so-called "wavenumber spectrum"), the irregularity velocity, and the equivalent thickness of the scattering plasma layer can be deduced using conventional diffraction theory. A scintillation spectrum with Fresnel oscillations is considered for both anisotropic Gaussian and power-law wavenumber models. To compare the one-dimensional in-situ results, $P_N(k_x)$, with the scintillation results, $P_{SN}(k_x)$, a three-dimensional wavenumber spectrum of electron density irregularities should be integrate [7]

$$P_{SN}(k_x) = 2\pi v_0^2 k_0^2 L \int\limits_{-\infty}^{\infty} dk_y V_N(k_x, k_y, k_z = 0) \sin^2\left(\frac{k_x^2 + k_y^2}{k_f^2}\right). \tag{2}$$

where $v_0 = \omega_{p0}^2/\omega^2$, L is a thickness of plasma layer. The Fresnel oscillations are smeared by the finite thickness of the irregular layer. This effect can be calculated for a one-dimensional model and weak scattering. The one-dimensional received spatial power spectrum, $P_S(k_x, L)$, with plasma layer having finite thickness can be calculated from Equation (2) for arbitrary spatial power spectrum of the phase fluctuations

$$P_S(s, L) = 2 \int\limits_{-\infty}^{\infty} dx W_\varphi(x, s, L) \left\{1 - \frac{2}{k_0 L} \frac{1}{x^2} \sin\left(\frac{k_0 L}{2} x^2\right) \cos\left[2\left(\frac{k_0}{k_f}\right)^2 (x^2 + s^2)\right]\right\}, \tag{3}$$

where $W_\varphi(x, s, L)$ is the two-dimensional power spectrum of the correlation function of phase fluctuations $\langle\varphi_1(\mathbf{r})\varphi_1^*(\mathbf{r} + \rho)\rangle$, $\rho = \{\rho_x, \rho_y\}$ is a distance between two observation points, $x = k_x/k_0$, $s = k_y/k_0$.

For the transition from the three-dimensional function to the one-dimensional one we shall use the assumption of "frozen-in" irregularities, moving without evolution with a velocity V normal to the direction of the wave. We assume that irregularities drift across the beam of the radio signals without changing their shapes. If rigid plasma irregularities are moving in the Y direction (YZ is the principle plane) with apparent velocity V_y transverse to the line of sight path, the power spectrum $P_S(\nu, L)$ and scintillation level S_4 (seroth moment) which is a measure of the scintillation rate are computed from the power spectrum [7]

$$\begin{aligned} P_\varphi(\nu, L) &= \frac{2\pi}{V_y} \int\limits_0^{\infty} dk_x W_\varphi\left(k_x, k_y = \frac{2\pi\nu}{V_y}, L\right), \quad P_S(\nu, L) = 4 P_\varphi(\nu, L) \sin^2\left(\frac{\nu}{\nu_f}\right)^2, \\ S_4^2 &= \int\limits_0^{\infty} d\nu P_S(\nu, L). \end{aligned} \tag{4}$$

The Fresnel frequency, $\nu_f = V_y/(\pi\lambda z)^{1/2}$, is directly proportional to the drift velocity V_y transverse to the radio path and inversely proportional to the Fresnel radius, $(\lambda z)^{1/2}$, where λ is the radio wavelength and z is the mean distance between the observer and the irregularities. The sinusoidal term in (4) is responsible for oscillations in the scintillation spectrum.

Transverse correlation function of a scattered field $W_{EE^*}(\rho) = \langle E(\mathbf{r})E^*(\mathbf{r}+\boldsymbol{\rho})\rangle$ has the following form [3]

$$W_{EE^*}(\boldsymbol{\rho}, k_\perp) = E_0^2 \exp\left[\frac{1}{2}\left(\left\langle\varphi_1^2(\mathbf{r})\right\rangle + \left\langle\varphi_1^{2*}(\mathbf{r}+\boldsymbol{\rho})\right\rangle\right) + \langle\varphi_1(\mathbf{r})\varphi_1^*(\mathbf{r}+\boldsymbol{\rho})\rangle + 2\mathrm{Re}\,\langle\varphi_2\rangle\right] \cdot \exp(-i\rho_y k_\perp), \tag{5}$$

where E_0^2 is the intensity of an incident radiation. In the ray-(optics) approximation describing multiple scattering in random media the condition $\sqrt{\lambda L} \ll l_\varepsilon$ is fulfilled, but it neglects the diffraction effects. If a distance L traveling by the wave in random plasma is substantially big, $L \gg (l_\varepsilon/\lambda)$, diffraction effects become essential. The smooth perturbation method is a more general method for the solution of diffraction effects if parameter λ/l_ε is small. SPS of scattered field in case of an incident plane wave is easily calculated by Fourier transform of the transversal correlation function of a scattered field [1]. If the angular spectrum of an incident wave has a finite width and its maximum is directed along the Z-axis, SPS of scattered radiation is given by [3]:

$$I(k) = \int\limits_{-\infty}^{\infty} dk_\perp \int\limits_{-\infty}^{\infty} d\rho_y W_{EE^*}(\rho_y, k_\perp) \exp\left(ik\rho_y - k_\perp^2\beta^2\right), \tag{6}$$

where β characterizes the dispersal of an incident radiation (disorder of an incident radiation).

Correlation functions of the phase fluctuations for arbitrary second order moment of electron density fluctuations in the YZ plane and in the direction perpendicular to the principle plane are:

$$\begin{aligned} W_{\varphi}^{(1)}(\xi,\eta,L) &= \tilde{\Omega}_5 \int_{-\infty}^{\infty} ds \int_{-\infty}^{\infty} dx \frac{x^2 + P_j^2(\mu+s)^2}{(\delta_4 + x^2)^2} V_N\left(x, s, -2\frac{\Phi_2}{\Phi_3}\right) \exp(-i\xi x - i\eta s) \\ W_{\varphi}^{(2)}(\xi,\eta,L) &= \tilde{\Omega}_1 \int_{-\infty}^{\infty} ds \int_{-\infty}^{\infty} dx V_N(x,s,-G) \exp(-i\xi x - i\eta s), \end{aligned} \tag{7}$$

where: $\xi = k_0\rho_x$, $\eta = k_0\rho_y$, $\tilde{\Omega}_1$, $\tilde{\Omega}_5$ and 3D spatial spectrum of electron density fluctuations are complicated function of the non-dimensional wavevectors and polarization coefficients [6]:

$$P_j = \frac{2\sqrt{u}(1-v)\cos\alpha}{u\sin^2\alpha \pm \sqrt{u^2\sin^4\alpha + 4u(1-v)^2\cos^2\alpha}}, \quad \Gamma_j = -\frac{v\sqrt{u}\sin\alpha + P_j uv\sin\alpha\cos\alpha}{1-u-v+uv\cos^2\alpha},$$

Plus sign and index $j = 1$ correspond to the extraordinary wave, minus sign and index $j = 2$ to the ordinary wave.

2. NUMERICAL CALCULATIONS

Incident electromagnetic wave has a frequency 40 MHz ($k_0 = 0.84\,\mathrm{m}^{-1}$). Plasma parameters on the altitude $z = 300$ km are: $u_0 = 0.0012$, $v_0 = 0.0133$, $\sigma_N^2 = 10^{-4}$. The Fresnel radius and the Fresnel wavenumber $k_f = (4\pi/\lambda z)^{1/2}$ are equal to 1.5 km and $2.4\,\mathrm{km}^{-1}$, respectively. Observations show [2] that drift velocity 60–140 m/s is characteristic for ionospheric irregularities on the altitudes 300 km. A velocity 100 m/s caused by the steady drifting with the horizontal wind of scattering irregularities embedded in the ionosphere will be used in numerical calculations for both Gaussian and power-law spectra. Anisotropic Gaussian three-dimensional power spectrum of electron density fluctuations for which the correlation contours are ellipsoids is given by [4]

$$V_N(k_x,k_y,k_z) = \sigma_N^2 \frac{l_{\parallel}^3}{8\pi^{3/2}\chi^2} \exp\left(-\frac{k_x^2 l_{\perp}^2}{4} - p_1\frac{k_y^2 l_{\parallel}^2}{4} - p_2\frac{k_z^2 l_{\parallel}^2}{4} - p_3 k_y k_z l_{\parallel}^2\right), \tag{8}$$

where: $p_1 = (\sin^2\gamma_0 + \chi^2\cos^2\gamma_0)^{-1}[1 + (1-\chi^2)^2\sin^2\gamma_0\cos^2\gamma_0/\chi^2]$, $p_2 = (\sin^2\gamma_0 + \chi^2\cos^2\gamma_0)/\chi^2$, $p_3 = (1-\chi^2)\sin\gamma_0\cos\gamma_0/2\chi^2$, σ_N^2 is the variance. This function contains anisotropy factor of irregularities $\chi = l_{\parallel}/l_{\perp}$ (ratio of longitudinal and transverse linear scales of plasma irregularities) and inclination angle γ_0 of prolate irregularities with respect to the external magnetic field.

Measurements of satellite's signal parameters passing through ionospheric layer and measurements aboard of satellite show that in F-region of the ionosphere irregularities have power-law spectrum with different spatial scales. Generalized correlation function for power-law spectrum of electron density irregularities with a power-law index p has been proposed in [8]. For $p > 3$ spatial power-law spectrum has the following form:

$$W_N(\mathbf{k}) = \frac{\sigma_N^2}{\pi^{5/2}}\Gamma\left(\frac{p}{2}\right)\Gamma\left(\frac{5-p}{2}\right)\sin\left[\frac{(p-3)\pi}{2}\right]\frac{l_{\parallel}^3}{\chi^2\left[1 + \ell_{\perp}^2\left(k_{\perp}^2 + \chi^2 k_{\parallel}^2\right)\right]^{p/2}}, \tag{9}$$

Calculations using Equation (3) was performed assuming a power-law spectrum with the index of 4. The results of these calculations are plotted in Figure 1(a). The break point is at $k_x/k_f = 0.995$. The gap in the power spectrum increases in proportion to the anisotropy factor χ. Figure 1(b) depicts the dependence of the SPS of scattered ordinary wave for the spectrum (8) in the direction perpendicular to the principle plane. Longitudinal characteristic linear scale of plasma irregularities $l_{\parallel} = 2$ km, $\chi = 18$, the inclination angle of prolate irregularities with respect to the external magnetic field $\gamma_0 = 10^0$, $\alpha = 20^0$, distances between the observation points are $\rho_x \approx \rho_y = 500$ m. Numerical calculations show that varying thickness of a plasma slab from 12 km up to 190 km, the first oscillation minimum ν_1 occurs at: 127 mHz, and the following minimums occur at: 230 mHz, 338 mHz, 441 mHz (Figure 1(b)).

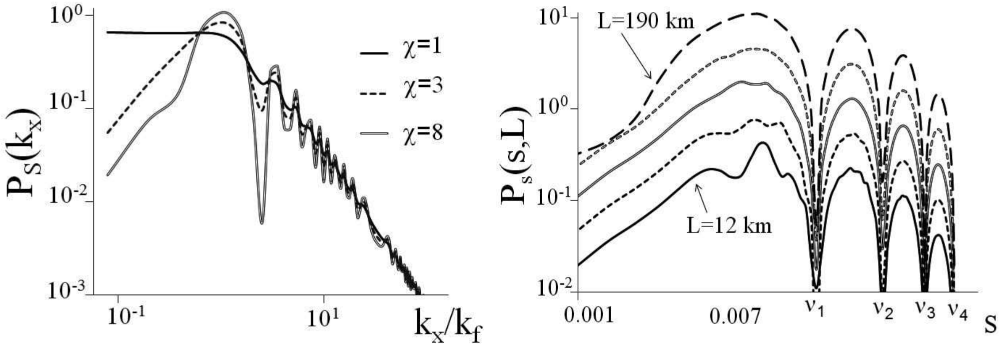

(a) (b)

Figure 1: (a) The log-log plots of the scintillation spectrum in the X direction for the power-law spectrum of electron density fluctuations and different anisotropy factor χ; (b) also the log-log curves of the SPS of phase fluctuations for Gaussian spectrum versus non-dimensional wavenumber parameter s and different thickness of a plasma slab $L = 12\,\mathrm{km} \dots 190\,\mathrm{km}$.

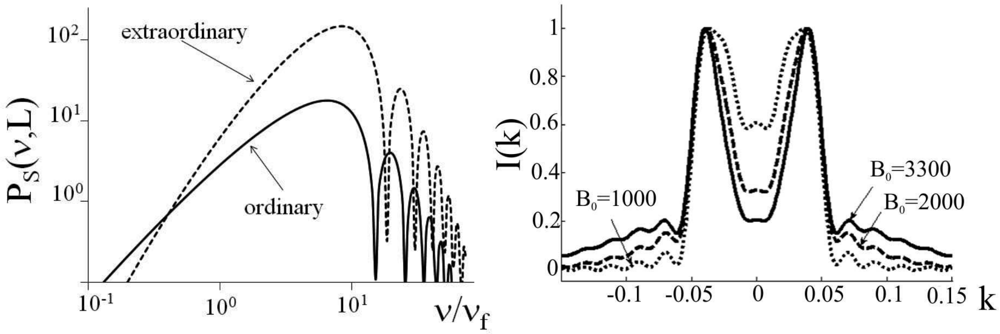

(a) (b)

Figure 2: (a) The normalized power spectrum of both the ordinary and extraordinary waves as log-log plots versus parameter ν/ν_f at $\chi = 5$ and with $T = 250$, $\alpha = 40^0$, $\gamma_0 = 10^0$; (b) the SPS of scattered ordinary wave as a function ofthe SPS of scattered ordinary wave as a function of k for $\alpha = 20^0$, $p = 3.2$, $l_{\|} = 10\,\mathrm{km}$, $B_0 = 1000$, 2000, 3000.

A phase switch depends on the ratio between scintillation frequency ν and the Fresnel frequency $\nu_f = V_y/(\pi\lambda z)^{1/2}$. We suppose that the drift velocity transverse to the radio path is equal to $V_y = 100\,\mathrm{m/s}$. Numerical calculations have been carried out for scattered ordinary (o-wave) and extraordinary (e-wave) waves scattered in the principle plane and anisotropic Gaussian spectrum at $\nu_f = 38\,\mathrm{mHz}$. If prolate plasma irregularities are stretched along the external magnetic field ($\gamma_0 = 0^0$) the behavior of the ordinary and extraordinary waves is the same. Maximum of the power spectrum is at 39 mHz. Increasing angle $\gamma_0 = 10^0$ power spectrum for the o-wave reaches maximum at $\nu_{\max}^{(o)} = 36.4\,\mathrm{mHz}$, for e-wave at $\nu_{\max}^{(e)} = 45.1\,\mathrm{mHz}$. Temporal spectrum for o-wave have minimums at the frequencies: 68 mHz, 96 mHz, 118 mHz, 136 mHz; for e-wave at: 76 mHz, 107 mHz, 131 mHz, 152 mHz. These frequencies satisfy the relations: $1 : \sqrt{2}$, $1 : \sqrt{3}$, $1 : \sqrt{4}$ and so on, which is in a good agreement with the scintillation spectrum when the Fresnel scintillations are observed [2]. Location of these minimums can be used to determine k_f and ν_f. Numerical calculations show that variation of the angle γ_0 at fixed parameter χ weakly influence on the scintillation index S_4, while at $\gamma_0 = 0^0$ (highly elongated irregularities) increasing the degree of elongation χ from 5 up to 10, the scintillation level S_4 decreases twice from 0.56 (large scintillation level) to 0.28 (small scintillation level). Hence, the influence of anisotropy of plasma irregularities on S_4 is stronger than inclination angle of prolate irregularities with respect to the external magnetic field.

Figure 2(b) represents the "Double-humped effect" of scattered ordinary wave in magnetized plasma versus wavenumber k in the direction perpendicular to the principle plane for the power-law spectrum with $\mu = 0.05$, $\alpha = 20^0$, $\beta = 10$, $l_{\|} = 10\,\mathrm{km}$, $\chi = 350$, power-law index $p = 3.2$ and different $B_0 = \sigma_n^2 \sqrt{\pi} T k_0 L / 4\chi$. Numerical analyses show that depth of a gap in the SPS increases in 61% travelling 2300 km by radio wave in turbulent plasma.

REFERENCES

1. Ishimaru, A., "Wave propagation and scattering in random media," Vol. 2, *Multiple Scattering, Turbulence, Rough Surfaces and Remote Sensing*, IEEE Press, Piscataway, New Jersey, USA, 1997.
2. Gershman, B. N., L. M. Eruxhimov, and Yu. Ya. Yashin, *Wavy Phenomena in the Ionosphere and Cosmic Plasma*, Moscow, Nauka, 1984 (in Russian).
3. Gavrilenko, V. G., G. V. Jandieri, A. Ishimaru, and V. G. Jandieri, "Peculiarities of spatial spectrum of scattered electromagnetic waves in anisotropic inhomogeneous medium," *Progress In Electromagnetics Research B*, Vol. 7, 191–208, 2008.
4. Jandieri, G. V., A. Ishimaru, V. G. Jandieri, A. G. Khantadze, and Z. M. Diasamidze, "Model computations of angular power spectra for anisotropic absorptive turbulent magnetized plasma," *Progress In Electromagnetics Research*, Vol. 70, 307–328, 2007.
5. Jandieri, G. V. and A. Ishimaru, "Some peculiarities of the spatial power spectrum of scattered electromagnetic waves in randomly inhomogeneous magnetized plasma with electron density and external magnetic field fluctuations," *Progress In Electromagnetics Research B*, Vol. 50, 77–95, 2013.
6. Ginzburg, V. L., *Propagation of Electromagnetic Waves in Plasma*, Gordon and Beach, New York, 1961.
7. Rufenach, C. L., "Power-law wavenumber spectrum deduced from ionospheric scintillation observations," *Journal of Geophysical Research*, Vol. 77, No. 25, 4761–4772, 1972.
8. Shkarofsky, I. P., "Generalized turbulence space-correlation and wave-number spectrum-function pairs," *Canadian Journal of Physics*, Vol. 46, 2133–2153, 1968.

Aperture Averaging of Focused Multi-Gaussian Beams

Canan Kamacıoğlu[1], **Yahya Baykal**[2], **and Erdem Yazgan**[3]

[1]Department of Mechatronics Engineering, Çankaya University, Ankara, Turkey
[2]Department of Electronic and Communication Engineering, Çankaya University, Ankara, Turkey
[3]Electrical and Electronics Engineering, Hacettepe University, Ankara, Turkey

Abstract— We investigate the behavior of the power fluctuations of the focused annular and flat-topped beams when a realistic receiver possessing a finite sized aperture is employed in turbulent atmospheric optics links. Employing our previously derived formulation for the power scintillation index, the variations of the power scintillations and the receiver aperture averaging factor of the focused annular and flat-topped beams are scrutinized. Receiver aperture averaging factor is deduced from the ratio of power scintillation index detected by a finite sized aperture to that obtained by a point aperture. Influence of the receiver aperture radius, the propagation length, the structure constant, the inner and the outer beam sizes for an annular type incidence, flatness parameter for a flat-topped incidence and the focusing parameter for the multi-Gaussian beam in general, on the power scintillation and the receiver aperture averaging factor are studied. It is found that for the focused multi-Gaussian beams, the effect of the receiver aperture averaging factor increases as the aperture radius increases for larger link lengths. Additionally, for the annular incidences in turbulence, the effect of the receiver aperture averaging factor is stronger for larger inner beam source sizes. At a fixed receiver aperture radius, receiver aperture averaging becomes more effective when the structure constant becomes larger. When focused multi-Gaussian beams are compared to their collimated counterparts, it is seen that the receiver aperture averaging is more beneficial for the focused annular and focused flat-topped beams. At large link lengths, increase in the receiver aperture radius decreases the power scintillations.

1. INTRODUCTION

Scintillations are the intensity fluctuations occurring in the received optical beam caused by the turbulent nature of the atmosphere. The scintillations deteriorate the received signal, thus there are many studies in the literature to decrease the scintillations. The improvement of the scintillations can be obtained by using focused beams in the optical communication link [1, 2]. The aperture averaging is one of the methods used to decrease the scintillations. The effects of the aperture averaging are studied in the context of the laser beam propagation in turbulent atmosphere [3]. The receiver aperture averaging effects for the plane wave are studied by Tatarskii [4]. Closed-form representation of the receiver aperture averaging effect is obtained for a focused beam wave in turbulent atmosphere where Gaussian weighting function for the receiver aperture is utilized [5]. The propagation of flat-topped Gaussian beams is investigated when a realistic receiver is used that possess a finite sized aperture in turbulent atmospheric optics link [6].

In this study we have calculated the power scintillation index and the receiver aperture averaging factor of focused multi-Gaussian beams propagating in weak atmospheric turbulence. In obtaining the results, we have utilized our formulation for the power scintillation index of flat-topped beams [6]. We have examined the effect of focusing on the power scintillations and the receiver aperture averaging factor when annular and flat-topped profiles are employed as incidence. We have also compared the power scintillation and the receiver aperture averaging factor of focused and collimated multi-Gaussian beams.

2. FORMULATION

The incident field for multi-Gaussian beam is [7]

$$u(\mathbf{s}) = \sum_{n=1}^{N} A_n \exp\left(-k\alpha_n |\mathbf{s}|^2\right) \tag{1}$$

where $\mathbf{s} = (s_x, s_y)$ is the source transverse coordinate, N is the number of Gaussian beams, A_n is the complex amplitude and $\alpha_n = 1/(2k\alpha_{sn}^2) + j/(2F)$, $k = 2\pi/\lambda$ is the wave number with, λ is the wavelength, F is the focusing parameter, $j = \sqrt{-1}$ and α_{sn}^2 is the source size. The field of a focused annular beam is formed by the difference of two Gaussian beams (i.e., $N = 2$) with amplitudes

$A_1 = -A_2$ and $\alpha_1 = 1/2k\alpha_{s1}^2 + j/(2F)$, $\alpha_2 = 1/2k\alpha_{s2}^2 - j/(2F)$. Focused flat-topped Gaussian beam is obtained by superposing two or more Gaussian beams of different amplitudes and different source sizes so that $A_n = \frac{(-1)^{n-1}}{N}\frac{N!}{n!(N-n)!}$ and $\alpha_n = 1/2k\alpha_{sn}^2 + j/(2F)$.

The power scintillation index, $m_p^2 = \langle P^2\rangle/\langle P\rangle^2 - 1$ and the receiver aperture averaging factor, G_R of multi-Gaussian beams at the receiver plane having a circular aperture are calculated by using Eqs. (10) and (11) of Ref. [6] in which the incidence given in Eq. (1) is employed. Here P is the optical power at the receiver plane and $\langle\,\rangle$ denotes the ensemble average taken over the medium statistics. The receiver aperture averaging factor is [6]

$$G_R = \frac{m_p^2}{m_p^2\big|_{R=0}} \tag{2}$$

where $m_p^2|_{R=0}$ is the scintillation index for a point aperture.

3. RESULTS

In this study we have analyzed the effect of the focusing parameter on the power scintillation and the receiver aperture averaging factor of annular and flat-topped beams against various parameters such as the propagation length L and the receiver aperture radius R at different inner beam source sizes, α_{s2} for the annular case, flatness parameter, N for the flat-topped Gaussian case, structure constant, C_n^2 for multi-Gaussian beams.

Figures 1–3 show the power scintillation and the receiver aperture averaging factor of focused annular beams and Figs. 4–6 show the power scintillation and the receiver aperture averaging factor of focused flat-topped Gaussian beams. In all the figures, the wavelength is taken as $\lambda = 1.55\,\mu\text{m}$ and for all the mentioned focused beams the focal lengths are equal to the propagation distance, i.e., $F = L$. Fig. 1 shows the receiver aperture averaging factor versus the receiver aperture radius for different inner beam source sizes at $L = 3\,\text{km}$ where the source size of the primary beam is taken as $\alpha_{s1} = 3\,\text{cm}$. It is seen from Fig. 1 that for focused annular beams, as the receiver aperture radius increases, the receiver aperture averaging effect increases. At a fixed receiver aperture radius, focused annular beams having larger secondary beam source size possess smaller receiver aperture average factors. In Fig. 2, the receiver aperture averaging factor versus the receiver aperture radius of collimated and focused annular beams at different propagation lengths is plotted where $C_n^2 = 2.2 \times 10^{-15}\,\text{m}^{-2/3}$, $\alpha_{s1} = 2\,\text{cm}$, $\alpha_{s2} = 1.5\,\text{cm}$ are taken. It is seen from Fig. 2 that the focused annular beams increases the effect of the receiver aperture averaging at a fixed propagation length. When the propagation length increases from $L = 3$ km to $L = 4\,\text{km}$, the receiver aperture averaging factor becomes stronger at larger receiver aperture sizes for both collimated and focused cases. If the collimated and focused annular beams are compared, it is observed that the receiver aperture averaging factor is more effective on the focused annular beams. These comparisons show that using focused annular beam as an incident beam improves the effect of the receiver aperture averaging.

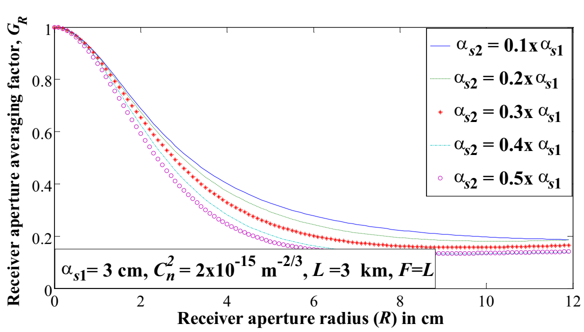

Figure 1: Receiver aperture averaging factor of annular beams versus receiver aperture radius for various secondary beam source sizes at $C_n^2 = 2 \times 10^{-15}\,\text{m}^{-2/3}$, $L = 3\,\text{km}$ and $\alpha_{s1} = 3\,\text{cm}$.

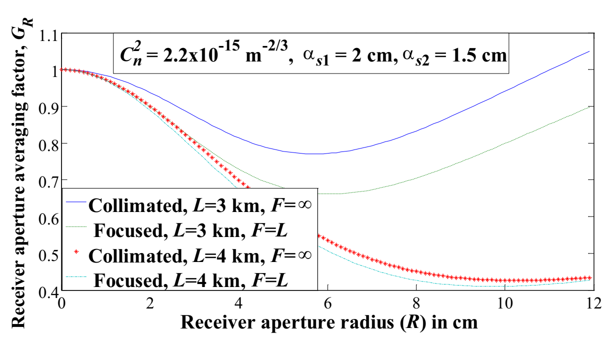

Figure 2: Receiver aperture averaging factor of annular beam versus receiver aperture radius for different propagation lengths at $C_n^2 = 2.2 \times 10^{-15}\,\text{m}^{-2/3}$, $\alpha_{s1} = 2\,\text{cm}$, $\alpha_{s2} = 1.5\,\text{cm}$.

In Fig. 3, the power scintillations of focused annular beams having different structure constants are analyzed versus the propagation length in which the source size of the primary beam, the source size of the secondary beam and the receiver aperture radius are taken as $\alpha_{s1} = 3\,\mathrm{cm}$, $\alpha_{s2} = 1.5\,\mathrm{cm}$ and $R = 9\,\mathrm{cm}$, respectively. It is observed from Fig. 3 that for small propagation lengths, the power scintillations of focused annular beams increase as the propagation length increases until a certain propagation length is reached. However, when the propagation length is further increased, the power scintillations start to decrease. At a fixed propagation length, again until a certain propagation length, the power scintillation increases as the structure constant increases. Again, when the propagation length is further increased, this trend reverses at the fixed propagation length. Power scintillation versus propagation length at different receiver aperture radii for the focused flat-topped beams is analyzed in Fig. 4 where the source size, flatness parameter and structure constant are taken as $\alpha_s = 5\,\mathrm{cm}$, $N = 4$, $C_n^2 = 2 \times 10^{-15}\,\mathrm{m}^{-2/3}$, respectively. The power scintillations of the focused flat-topped beams are seen to increase for a while as the propagation length increases. However, after a large propagation length, this trend reverses.

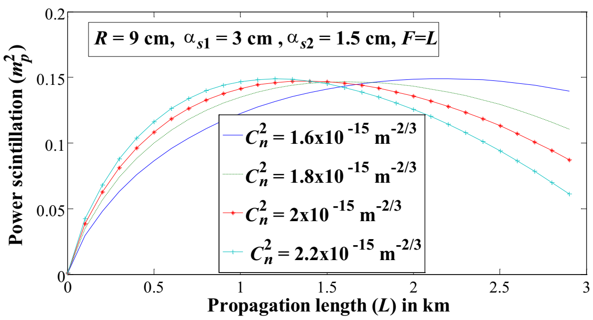

Figure 3: Power scintillation of annular beams versus propagation length for different structure constants at $R = 9\,\mathrm{cm}$, $\alpha_{s1} = 3\,\mathrm{cm}$, $\alpha_{s2} = 1.5\,\mathrm{cm}$.

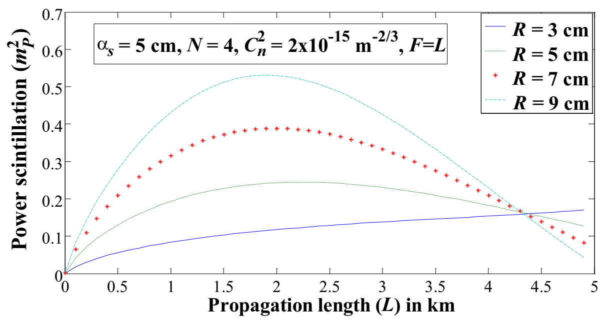

Figure 4: Power scintillation of flat-topped beams versus propagation length for different receiver aperture sizes at $\alpha_s = 5\,\mathrm{cm}$, $N = 4$ and $C_n^2 = 2 \times 10^{-15}\,\mathrm{m}^{-2/3}$.

Figure 5 shows the relation between the receiver aperture averaging factor and the radius of the receiver aperture for the focused flat-topped Gaussian beams for varying C_n^2 values at $L = 4\,\mathrm{km}$, $N = 6$ and $\alpha_s = 3\,\mathrm{cm}$. It is observed from Fig. 5 that for the focused flat-topped Gaussian beams, the improvement of the receiver aperture averaging is strong for the large structure constant values at increasing aperture sizes. For smaller structure constants for focused flat-topped beams the receiver aperture averaging does not occur. Fig. 6 shows the power scintillation versus the propagation length of collimated and focused flat-topped Gaussian beams at different receiver aperture radii for $\alpha_s = 6\,\mathrm{cm}$ and $N = 2$. It is seen from the Fig. 6 that focused beams are attractive since they have smaller power scintillations than the collimated beams at each propagation length. Power scintillation first starts to increase as the propagation length increases for both focused and collimated cases. However, when the propagation length reaches a certain distance, this trend reverses. The reversing in the trend starts from smaller propagation length for the focused beams.

When the power scintillations are compared against the receiver aperture sizes, it is concluded

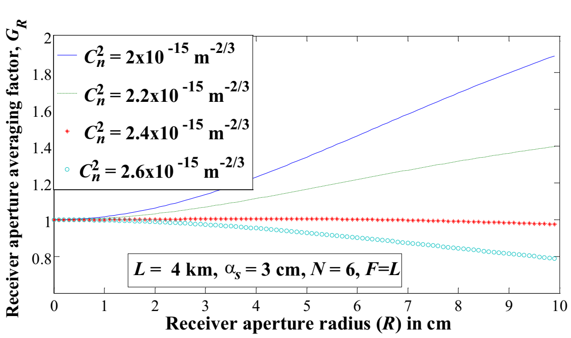

Figure 5: Receiver aperture averaging factor of flat-topped beams versus receiver aperture radius for different structure constants at $L = 4\,\mathrm{km}$, $N = 6$ and $\alpha_s = 3\,\mathrm{cm}$.

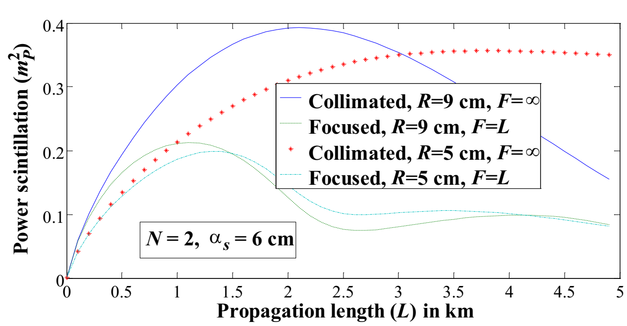

Figure 6: Power scintillation of flat-topped beams versus propagation length at different receiver aperture sizes for $N = 2$ and $\alpha_s = 6\,\mathrm{cm}$.

that larger receiver apertures have larger power scintillations at smaller propagation lengths. This trend also reverses with the effect of the aperture averaging for large propagation lengths. These comparisons show that a focused flat-topped Gaussian beam offers certain advantages over the collimated cases.

4. CONCLUSION

We have examined the power scintillation and the receiver aperture averaging factor of focused multi-Gaussian beams and the effect of focusing to reduce scintillations and to increase the effect of the aperture averaging. It is found that the improvement in the effect of the receiver aperture averaging is more in the focused cases than the collimated beams. The effect is stronger as the receiver aperture size increases. At small propagation lengths, power scintillation increases as the structure constant increases for focused multi-Gaussian beams. However, this mentioned behavior exhibits reverse trend at large propagation lengths. For the focused annular cases the receiver aperture averaging is more beneficial when the secondary beam source sizes increase. It is concluded that focusing has benefits since the focusing effect increases the influence of the receiver aperture averaging. We observed that if the structure constant, inner and outer beam source sizes are fixed, focused annular beams improve the system performance because of the strong effect of the aperture averaging. Also, the focused flat-topped beams are more advantageous than the collimated cases since the power scintillation is less and the effect of aperture averaging is strong for the focused cases.

REFERENCES

1. Eyyuboğlu, H. T. and Y. Baykal, "Scintillations of cos-Gaussian and annular beams," *JOSA A*, Vol. 24, 156–163, 2007.
2. Eyyuboğlu, H. T. and Y. Baykal, "Scintillation characteristics of cosh-Gaussian beam," *Appl. Opt.*, Vol. 46, 1099–1106, 2007.
3. Lutomirski, R. F. and H. T. Yura, "Aperture-averaging factor of a fluctuating light signal," *J. Opt. Soc. Am.*, Vol. 59, 1247–1248, 1969.
4. Tatarskii, V. I., *The Effects of the Turbulent Atmosphere on Wave Propagation*, National Technical Information Service, 1971.
5. Wang, S. J., Y. Baykal, and M. A. Plonus, *J. Opt. Soc. Am.*, Vol. 73, 831–837, 1983.
6. Kamacıoğlu, C., Y. Baykal, and E. Yazgan, "Averaging of receiver aperture for flat-topped incidence," *Opt. Laser Technol.*, DOI 10.1016/j.optlastec.2013.04.01.
7. Baykal, Y., H. T. Eyyuboğlu, and Y. Cai, "Scintillations of partially coherent multiple Gaussian beams in turbulence," *Appl. Opt.*, Vol. 48, 1943–1954, 2009.

Real Beam vs. Synthetic Aperture Radar for Slope Monitoring

Massimiliano Pieraccini
Department of Information Engineering, University of Florence, Via Santa Marta, 3 Firenze 50139, Italy

Abstract— In the last years ground-based radar interferometry has become a popular technology for displacement monitoring of landslides and slopes in open-pit mines. Several research groups and companies have worked on it, and currently two quite different technologies are emerging: real beam radar and synthetic aperture radar. The aim of this paper is to discuss the fundamental differences of the two techniques, with emphasis on the principles rather than on particular implementations and commercial products.

1. INTRODUCTION

The first embryonic idea of SAR (Synthetic Aperture Radar) is probably due the mathematician Carl A. Wiley [1] that in 1951 described a "Doppler Unbeamed Search Radar". It was not a SAR as known today, nevertheless it provided the basis of a radar with improved angular resolution using the Doppler shift of a travelling antenna. Other developments were done in 1950s, but they were covered by military secret. The civil history of SAR begins in 1960, when the idea was first acknowledged publicly [2]. Today SAR is the standard for satellite radars, as they require the best possible angular resolution for focussing on the earth surface operating from an orbit [3]. Since 1990s with the launch of ERS-1 (1991), JERS-1 (1992), RADARSAT-1 and ERS-2 (1995) [4, 5], satellite-based SAR has been able to exploit the phase information of images for detecting ground displacements. These developments had an early follow-up in analogue ground-based radar systems in the late '90s.

In 2003 Tarchi et al. [6] proposed for the first time to exploit Ground Based SAR Inteferometry for slope monitoring. Since those early days of ground based SAR, the technique has been developed and tested in the field for about a decade [7–10] until its consolidation as a commercial equipment [11–14]. At the same time, more traditional radars with physical aperture antennas have been proposed and used with the same purpose [15]. Currently the two different technologies (Real Beam and Synthetic Aperture) are both popular as instruments for displacement monitoring of natural and engineered slopes. Just for reference, IBIS [11] of IDS company and LisaLab [9] of Ellegi are radars for slope monitoring based on synthetic aperture, SSR of GroundProbe [15], MSR of Reutech and GPRI of Gamma Remote Sensing [16] are radar systems based on physical aperture antennas.

The aim of this paper is to discuss the fundamental differences of the two techniques with emphasis on the principles rather than on specific implementations and commercial products.

2. GROUND BASED RADAR INTERFEROMETRY FOR SLOPE MONITORING

Landslides and slopes of open pit mines can be remotely monitored by a ground-based inteferometric radar installed in a position where it can have a suitable view of the unstable area (Figure 1).

This equipment images its field of view with a range resolution ΔR related to the operated bandwidth B, given by

$$\Delta R = \frac{c}{2B} \tag{1}$$

with c speed of light. In each resolution cell the component Δr along the view direction of the terrain movement Δs is detected by exploiting the differential phase information $\Delta\phi$ of the radar signal:

$$\Delta r = \frac{\lambda}{4\pi}\Delta\varphi \tag{2}$$

with λ wavelength.

3. REAL BEAM AND SYNTHETIC APERTURE

Generally speaking, a radar is able detect the distance (range) and the direction of a target, transmitting and receiving electromagnetic waves. The distance is obtained by evaluating the time of flight of a returning electromagnetic pulse (alternatively using compressed or synthetic pulses,

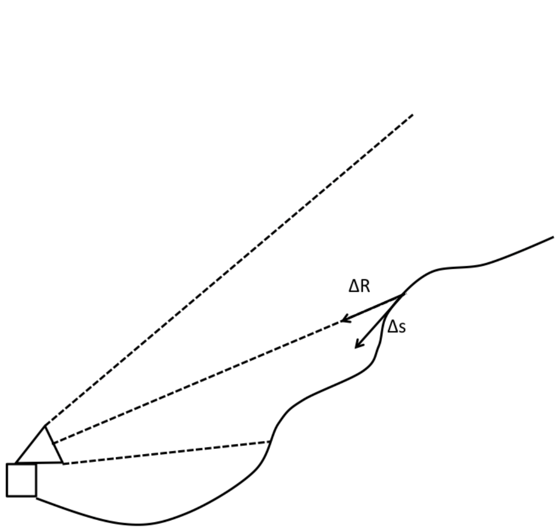

Figure 1: Ground based radar installation for slope monitoring.

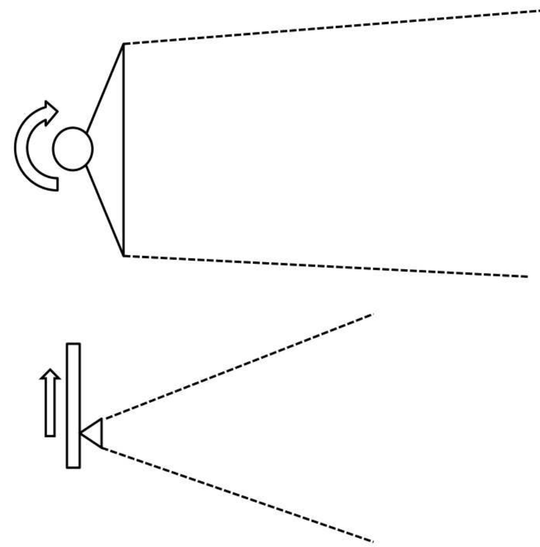

Figure 2: Real beam antenna and synthetic aperture.

but a discussion about this is beyond the aim of this paper). The direction of target is obtained using a real beam or a synthetic aperture. In the first case a large high gain (i.e., very directive) antenna is rotated to scan all directions, in the second case a small low-gain antenna is moved along a guide in order to “simulate” a larger antenna (Figure 2).

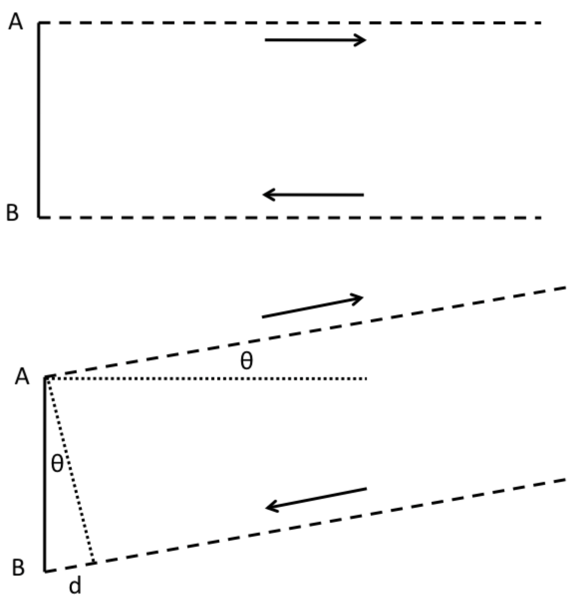

Figure 3: Angular resolution for a real beam antenna.

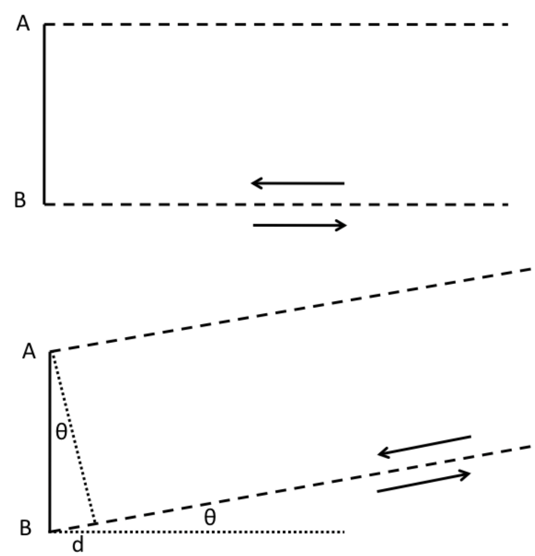

Figure 4: Angular resolution for a synthetic aperture radar.

A remarkable feature of this second solution is that it gives the directivity performances of a physical antenna large L, by scanning a $L/2$ length. In other words a synthetic antenna is in size a half of a real beam antenna. This can be demonstrated rigorously [17], but also by an intuitive way. Indeed, physically what allows to separate two signals incoming from different targets in front of an antenna is their difference of path: when this is greater that wavelength the signals are separable. A physical antenna transmit (or receive) concurrently by all its elements, so with reference to Figure 3 when transmit from point A receive also from point B and the largest difference path between a target in front of the antenna and a target at angle θ is $d = L\sin(\theta)$.

On the contrary, in the case of a synthetic aperture the antenna receives (or transmits) separately from each point along the aperture, so when it transmits from A receive only from A and the largest difference path is twice d as the backscattered wave travel twice the same path.

This is the reason because the size of a synthetic antenna is a half of a physical antenna, keeping constant its directivity. Radars for monitoring slopes are bulky and heavy equipment and their size is constrained by logistic reasons, therefore a synthetic aperture has performances improved of a factor 2 in terms of angular resolution, other things being equal. The higher spatial resolution of synthetic aperture radar may result in an increased capability of detecting localized slope movements (if used at the same working distance of a real beam radar) or in an extension of the operating distance of the radar. This pro has, obviously, some cons. A rotating antenna can scan 360°, while an antenna along a linear guide has a view that theoretically could be 180°, but in practice is about 90° due to the fact that a physical antenna has a beam that sure cannot cover 180°. In principle, the linear guide of synthetic aperture radar or the moving small antenna could be rotated as a physical antenna, but this is rarely done [16]. In fact, the experience shows that such a feature is not a real advantage for typical slope monitoring applications. Since radar does purely measure the components of the 3D displacement vector along its line of sight, the sensitivity to movements of radar depends on how parallel its line of sight is to the 3D displacement direction. Therefore the 360° scan capabilities of real beam radar would be a real advantage in monitoring scenarios characterized by circular shape slope geometries with the radar unit installed in the middle of that scenario, but these conditions are not very common.

In principle, both real and synthetic apertures could provide vertical or horizontal cross-range resolution, but in the practice synthetic radars are designed to have only horizontal angular resolution and to obtain vertical resolution from exploiting the fact that slope is a bi-dimensional surface and therefore 3D acquisition capability is in effect redundant. Indeed, in a real slope it is very improbable that two different targets have same range and horizontal angle (i.e., azimuth). Furthermore, if a 3D model (Digital Elevation Model) of the monitored area is available, the radar image can easily projected on this, resulting an effective 3D visualization. A DEM can be obtained by means of a laser scanner, or also using the same radar. In effect, as it is common by satellite, also a ground-based SAR can produce a DEM just performing two scans with a known baseline [18, 19].

4. NARROW BEAM VS. WIDE BEAM

Another fundamental difference between real beam e synthetic aperture is that the first scans the field of view with a narrow beam, the second irradiates always all the targets. This has the following remarkable consequences.

4.1. Steep Slope Limits

The typical arrangement for monitoring a slope by ground based radar is shown in Figure 5.

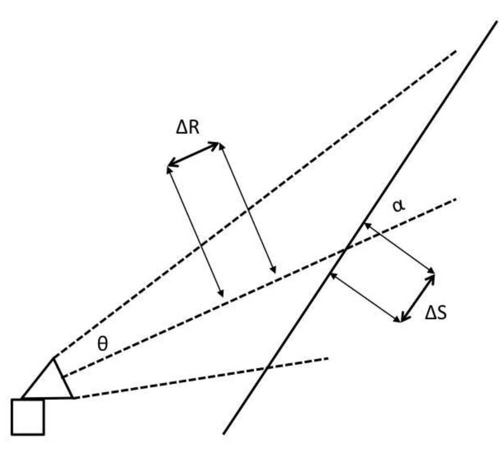

Figure 5: Sketch of a radar installation for slope monitoring.

A wide beam radar obtains spatial resolution ΔS_w along the slope, projecting its range resolution

ΔR

$$\Delta S_w = \frac{\Delta R}{\cos(\alpha)} \tag{3}$$

On the contrary narrow beam radar is able to exploit its directivity and it can provide a spatial resolution on the slope, given by

$$\Delta S_n = \frac{2\theta R}{\tan(\alpha)} \tag{4}$$

As ΔR typically is much smaller that θR, for slope not too steep spatial resolution given by (3) is better than resolution of a narrow beam radar (4). But when the slope is steep, Δs_w can became very large (it tends to infinity for $\alpha = 90°$). In order to evaluate this possible problem in a realistic case we consider: $\Delta R = 0.75$ m (corresponding to 200 MHz, the licensed bandwidth for this kind of applications), $R = 500$ m, $\theta = 0.0075$ rad (i.e., a real aperture of 2 m with $\lambda = 0.03$ m), then $\Delta s_w > \Delta s_n$ only if $\alpha > 72°$ that is a very steep slope.

4.2. Dynamic Range

As well known, a key requirement for the electronics of a radar is a high dynamic range for acquiring close and far targets. In other words a high radar cross section target close to the radar can blind it by saturating the receiver. In the case of narrow beam, this can be prevented switching off (or decreasing the gain) of the receiver when beam impinges the disturbing target. This is not possible with synthetic radar, that so has to rely exclusively on the dynamic performances of receiver. For early radar, this could be an insurmountable problem, but indeed current receiver have a discrete dynamic margin with respect to the range of the typical signal backscattered by natural and engineered slopes. Obviously a big excavator or haul trucks operating at a few meters from the equipment can be a problem, but at the same way it is an issue for narrow beam radar due to secondary lobes of any real antenna.

4.3. Moving Clutter

Real beam and synthetic aperture radar are affected differently by moving clutter as tracks or mining equipment in the slope. Since real beam radar has an almost instantaneous acquisition, when the beam impinges the disturbing target, the relative resolution simply gives a wrong signal. A synthetic aperture radar perform a sort of average that spread across the image the disturbance, reducing the overall signal to noise ratio, but affecting not a single pixel.

4.4. Multiple Targets in Range

Another essential difference between the two radar technique, is when multiple targets are in the same line of view, for example when a metallic cables on pylons across the scenario. In these cases a real beam radar could detect only the strongest target (the metallic cable, in the example), on the contrary a synthetic aperture radar, due to its own working principle, focuses in all the range.

4.5. Scan Time

A narrow beam radar operates scanning the area of interest line by line, while a synthetic aperture radar traveling along a horizontal guide, acquires the whole scenario in a single pass, therefore it can operate much faster. Typical scan time of modern commercial synthetic aperture radars are of the order of 2 minutes for a full resolution image at 2.5 km of operating distance, compared to 15–30 minutes for typical scan times of modern real beam radar scanning the same area of a SAR system. In principle, a physical antenna could be shaped in order to give an asymmetric beam, narrow in horizontal direction and wide in vertical direction, so also real beam radar could image the whole scenario with a single pass, fast as a synthetic radar. Indeed, this feature is not very common but has been tested [16]. A short scan time is an important figure for almost three reasons: 1) reduction of signal de-correlation due to the not-stationary atmospheric conditions inside; 2) larger phase unambiguity range, therefore higher detectable displacement velocity; 3) higher sensitivity to the detection of slope failure on-set, that could be sampled at higher speed. Of course even real beam radars can reduce the scan time if they needs, but only at the price of a reduction of the area coverage.

5. CONCLUSION

Real Beam and Synthetic Aperture radars obtain angular resolution with techniques quite different. Narrow beam radar relies on load and bulky precision mechanical systems able to move a large physical antenna, while Synthetic Aperture can make use of a positioning system smaller and lighter with mechanical requirements less severe, at the price of stricter requirements for the electronic system in terms of band and dynamic range.

Real Beam is surely a more traditional radar technology, but Synthetic Aperture allows faster and lighter systems with a greater stand-off distance (due to better angular resolution). It can make the difference for critical slope monitoring, where alarms are generated in case of impending failures and on-time detection of acceleration is crucial.

REFERENCES

1. Love, A. W., "In memory of Carl A. Wiley," *IEEE Antennas and Propagation Society Newsletter*, 17–18, Jun. 1985.
2. Cutrona, L. J., W. E. Vivian, E. N. Leith, and G. O. Hall, "A high-resolution radar combat-intelligence system," *IRE Transactions on Military Electronics*, 127–131, Apr. 1961.
3. Curlander, J. C. and R. N. McDonough, "Synthetic aperture radar: Systems and signal processing," *Wiley Series in Remote Sensing and Image Processing*, 1991.
4. Borgeaud, M., J. Noll, and A. Bellini, "Multi-temporal comparisons of ERS-1 and JERS-1 SAR data for land applications," *Geoscience and Remote Sensing Symposium, 1994, IGARSS'94*, Vol. 3, 1603–1605, 1994.
5. Srivastava, S. K., T. I. Lukowski, R. B. Gray, N. W. Shepherd, and R. K. Hawkins, "RADARSAT: Image quality management and performance results," *Canadian Conference on Electrical and Computer Engineering*, Vol. 1, 21–23, 1996.
6. Tarchi, D., N. Casagli, R. Fantib, D. Leva, G. Luzi, A. Pasuto, M. Pieraccini, and S. Silvano, "Silvano Landslide monitoring by using ground-based SAR interferometry: An example of application to the Tessina landslide in Italy," *Engineering Geology*, Vol. 68, 15–30, 2003.
7. Pieraccini, M., L. Noferini, D. Mecatti, C. Atzeni, G. Teza, A. Galgaro, and N. Zaltron, "Integration of radar interferometry and laser scanning for remote monitoring of an urban site built on a sliding slope," *IEEE Transactions on Geoscience and Remote Sensing*, Vol. 44, No. 9, 2335–2342, Sep. 2006.
8. Noferini, L., T. Takayama, M. Pieraccini, D. Mecatti, G. Macaluso, G. Luzi, and C. Atzeni, "A new algorithm for analysing Ground-based SAR data with diverse temporal baseline," *IEEE Transactions on Geoscience and Remote Sensing*, Vol. 46, No. 6, 1614–1622, Jun. 2008.
9. Antonello, G., J. Fortuny, D. Tarchi, N. Casagli, C. Del Ventisette, L. Guerri, G. Luzi, F. Mugnai, and D. Leva, "Microwave interferometric sensors as a tool for space and time analysis of active volcano deformations: The Stromboli case," *Second Workshop on Use of Remote Sensing Techniques for Monitoring Volcanoes and Seismogenic Areas, 2008, USEReST 2008*, 1–6, Nov. 11–14, 2008.
10. Mecatti, D., G. Macaluso, A. Barucci, L. Noferini, M. Pieraccini, and C. Atzeni, "Monitoring open-pit quarries by interferometric radar for safety purposes," *2010 European Radar Conference (EuRAD)*, 37–40, Sep. 30–Oct. 1, 2010.
11. Wang, W. S., D. C. Tian, J. H. Sun, L. Jiang, and H. B. Rao, "The application of IBIS-L remote monitoring system for micro deformation of terrain in dam safety monitoring," *Applied Mechanics and Materials*, Vol. 239–240, 552–559, Dec. 2012.
12. Bozzano, F., I. Cipriani, P. Mazzanti, and A. Prestininzi, "Displacement patterns of a landslide affected by human activities: Insights from ground-based InSAR monitoring," *Natural Hazards*, Vol. 59, No. 3, 1377–1396, 2011.
13. Farina, P., L. Leoni, F. Babboni, F. Coppi, L. Mayer, and P. Ricci, "IBIS-M, an innovative radar for monitoring slopes in open-pit mines," *Proceedings, Slope Stability 2011: International Symposium on Rock Slope Stability in Open Pit Mining and Civil Engineering*, Vancouver, Canada, Sep. 18–21, 2011.
14. Severin, E., L. Eberhardt, S. Leoni, and S. Fortin, "Use of ground-based synthetic aperture radar to investigate complex 3-D pit slope kinematics," *Proceedings, Slope Stability 2011: International Symposium on Rock Slope Stability in Open Pit Mining and Civil Engineering*, Vancouver, Canada, Sep. 18–21, 2011.
15. Noon, D., "Slope stability radar for monitoring mine walls," *Mining Risk Management Conference*, 1–12, Sidney, 2003.
16. Werner, C., A. Wiesmann, T. Strozzi, A. Kos, R. Caduff, and U. Wegmiuler, "The GPRI multi-mode differential interferometric radar for ground-based observations," *9th European Conference on Synthetic Aperture Radar, EUSAR*, 304–307, Apr. 23–26, 2012.

17. Soumekh, M., *Synthetic Aperture Radar Signal Processing with MATLAB Algorithms*, John Wiley & Sons, 1999.
18. Pieraccini, M., G. Luzi, and C. Atzeni, "Terrain mapping by ground-based interferometric radar," *IEEE Transactions on Geoscience and Remote Sensing*, Vol. 39, No. 10, 2176–2181, 2001.
19. Noferini, L., M. Pieraccini, D. Mecatti, G. Macaluso, G. Luzi, and C. Atzeni, "DEM by ground based SAR interferometry," *IEEE Letters on Geoscience and Remote Sensing*, Vol. 4, No. 4, 2007.

An Approach for on Body Concealed Weapon Detection Using Continuous Wavelet Transform

A. Atiah[1] **and N. J. Bowring**[2]

[1]Alzaetona University, Libya
[2]Manchester Metropolitan University, UK

Abstract— Continues Wavelet Transform (CWT) applied to the scattering response of on body concealed weapons. A series of experiments were conducted to test the system which involved on and off body objects such as, knives, handheld guns. Experimental results illustrated the success of the approach in analyzing the LTR signature. Spectral response for every target could be seen as a distribution in which the energy level and life-time depended on the target material and geometry and gives powerful information of the target unique signature.

1. INTRODUCTION

During the last few years the demand to remotely and automatically detect concealed weapons at the entrance of public places such as airport and government buildings has been a major security challenge. This approach is not currently available by the application of access control technologies or imaging systems which are time consuming and do not preserves the privacy of people. In order to detect and classify an unknown concealed object by remote sensing, certain electrical properties of the object to be detected are required. The transient scattering returns of a radar target was first modeled by SEM [1]. The CNR behaviour in linear time invariant system models was formulated the first mathematical model to represent the LTR using the independent resonance frequencies of the target which described as:

$$y(t) = \sum\nolimits_{t=1}^{M} A_m \cos\left(\omega_m t + \varphi_m\right) \exp\left(-\alpha_m t\right), \quad t > T_L \tag{1}$$

where T_L describes the start of the LTR, and M is the number of resonance modes are required to describe the time signal. The natural modes consist of amplitude A_m and phase (φ_m), and the CNR ($\omega_m t + \varphi_m$).

The form of the LTR is dependent upon the time form of the illuminating pulse, since $y(t)$ in Equation (1) is the impulse response of the target, the LTR can be expected to have the time form.

$$R(t) = X(t) \otimes y(t) \tag{2}$$

This represents a convolution process, from which the LTR has the form:

$$R(\omega) = X(\omega) y(\omega) \tag{3}$$

Illuminating the target by an UWB short pulse excites a sufficient number of resonances (M) of the unlimited set of CNRs with sufficient time resolution in time domain data. Since LTRs are aspect independent it should be possible to extract the same LTRs of the target from any incident angle related to target corresponding impulse response [3, 4]. For discrimination of the concealed objects based on the natural resonance frequencies accurate extraction at these frequencies from a measured transient response is very important [5]. Prony's method [7] suggests target resonance extraction to be directed upon the interval of late time response, if the nearby objects are included in the extraction, fairly accurate CNR extraction is achieved. Prony's method thus requires that accurate late time commencement evaluation is critical for the overall accuracy of target resonance extraction. Late time responses are target dependent and theoretically independent of polarization state and target orientations. Knowledge of the model order is critical in some filtering methods such as E-pulse and Generalized Pencil of Function (GPoF) [7, 8] and in the subsequent calculations for poles and residues algorithms. If the model order is underestimation, this can cause loss of poles in the calculations. Similarly, resonant modes are unlikely to be excited or weakly excited in all incident aspects and states of polarization due to a dependency on residues. It is apparent from the complexity of the methods and algorithms involved that another method is required for the extraction of the resonant modes. In fact, analytical solutions to transient electromagnetic problem involve huge mathematical calculations are imperfect for some canonical problems. An alternative choice, stemming from signal processing perspective is to apply Joint TF analysis. The Wavelet transform is introduced as alterative approach to overcome the STFT resolution limitation, a detailed explanation of the wavelet theory could be found in [12]. In fact, in this paper the CWT approach is proposed to extract the target signature and represent the LTR in time frequency domain. The CWT provides coefficients in which the degree of correlation is proportional to the peaks or amplitude. Another perspective is that the analysed signal decomposes into a superposition of scaled mother wavelets by the wavelet transform. In order to extract the target signature that appears in the late time response it is desirable to use good time resolution in the ETR and good frequency resolution in the LTR.

2. CONTINOUS WAVLET TRANSFORM

Many mother-wavelets are utilized for varies implementation and applications. The best known are Morlet, Daubechies and Haar wavelets. Also of great importance are the coiflet, symlet, Mexican and Hat wavelets. A CWT can analyse a signal into a set of limited basis functions, which can uncover transient features in the signal. Wavelet analysis is the contravention up of a signal into dilated and translated versions of the original mother wavelet. The wavelet should be oscillatory, have amplitudes that speedily tends its decay to zero, and has at least one vanishing moment [13, 14]. In this work, the chosen mother is Morlet wavelet because of its advantages and features such as, it's fine tuning to the desired frequency band, good resolution and localization in time and frequency domain, capability of detection and extraction oriented features [15]. Morlet wavelet mother is a sinusoidal signal modulated by a Gaussian wave. This wavelet is particularly useful for filtering out the Background noise of the target response.

$$CWT_x(t,\alpha,h)=\frac{1}{\sqrt{\alpha}}\int_{-\infty}^{+\infty}x(\tau)h\left(\frac{t-\tau}{\alpha}\right)d\tau \tag{4}$$

Here the mother wavelet is known as $h(t)$ and is localized in time, the continuously varying scaling parameter is a. The CWT transforms a one dimension time domain signal $x(t)$ is plotted into a two dimensional space across scale a and time scale t. The CWT can be considered a member of Time-Scale Distribution (TSD) series. if we set $\alpha=\frac{f_0}{f}$ where f_0 centre frequency of $h(t)$, for the TF analysis application, the subsequent distribution can be written as [13, 14]

$$CWT_x(t,f,h)=\sqrt{\frac{f}{f_0}}\int_{-\infty}^{+\infty}x(t)h\left(\frac{t-\tau}{f_0}\right)d\tau \tag{5}$$

The magnitude of the CWT is called as the Scalogram (SC).

$$|CWT_X(T,F,H)|^2 \tag{6}$$

The mother wavelet needs to satisfy certain mathematical criterion. A complex or real-value function $h(t)$ is defined as a wavelet if,

$$\int_{-\infty}^{\infty}h(t)dt=0 \tag{7}$$

This shows that a wavelet must have a zero dc component, i.e., zero average value in the time domain. This indicates that in the frequency domain the signal must be oscillatory. Admission Condition is another condition that a wavelet has to mollify, which is given by [15] as:

$$\int_{-\infty}^{\infty}|H(f)|^2\frac{df}{|f|}=1 \tag{8}$$

Here: $H(f)=$ is the Fourier Transform of $h(t)$. It can be shown that the signal $x(t)$ can be obtained from the following equation [15]

$$x(t)=\int_{-\infty}^{\infty}\int_{-\infty}^{\infty}CWT(\tau,\alpha,h)h\left(\frac{t-\tau}{a}\right)d\tau\frac{da}{a^2} \tag{9}$$

A large number of wavelets meet the Admission Condition only if $h(t)$ satisfies the Admission Condition. The Morlet wavelet is one of the most frequent used wavelets that does this and is given by [16], as

$$h(t) = e^{jW_0 t} e^{-t^2/2} \tag{10}$$

To discover whether the multi-resolution property of the CWT is appropriate for investigating transient scattering consequently, the CWT gives a good time resolution but poor frequency resolution when a is small (high frequency as $a = f_0/f$), but good frequency and poor time resolution when a is large, i.e., low frequency [20, 23]. In subsequent sections practical measurements will be reported. The main purpose is to conduct an in-depth study of the experimental results corresponding to the samples of different dimensions of complex targets.

3. EXPERMENTAL WORK

Figure 1 show the lay-out of the equipment for the experimental detection of concealed objects at standoff distances the picture taken from inside the chamber room in which the target stands and oriented. Important are two identical antennas. These have a lower cut-off frequency of around 0.25 GHz by which the LTR fundamental frequency of the most firearms is covered [21].

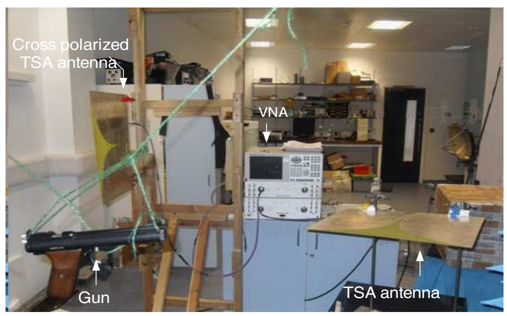

Figure 1: Experimental setup.

The VNA drives the transmitting antenna which converts the transmitted signal into incident field and captures the backscattered data from the receiving antenna. To obtain the LTR of the object, the target measurements are processed to reduce or eliminate undesired parameters such as the antennas coupling field, background noise, unwanted reflections (known as the clutter field) and the antennas response. Elimination of these fields from the measured S_{21} gives the frequency response of the object. The elimination of undesired background noise and antenna coupling and errors will be treated first by background subtraction and antenna deconvolution. The back scattering impulse response S_{21} was measured by VNA and separately analyzed by MATLAB code. The collected data was transformed into time domain by applying the IFFT on this frequency response produce the object's impulse response. From this impulse response, the object's LTR can be extracted. The accuracy of the proposed approach is verified by taking the measurements many times, so that the results can be trusted when applied to other objects.

4. KNIFE

First, a practical experiment was carried out using a knife with length of 12 cm and width of PEC part was 1.0 cm and the dielectric part was 1.5 cm, the depth of the dielectric part was 0.5 cm and the PEC part was 0.1 cm. The LTR of this target is plotted in Figure 2 in which the late time response life time is about 6 ns. This LTR represents all of the fundamental frequencies of the dominant LTR modes. Figure 3 shows the CWT.

The fundamental frequency and TFD modes lie between 0.5 and 1 GHz and those represents the unique signature of this target by which it could be identified. The observation shows the high energy levels of the PEC part of the knife and low energy levels corresponding to the dielectric part of this target. The energy levels represent the response of this target according to its reradiated energy corresponding to its LTR target signature.

5. SMALL HANDGUN

The second complex object to be tested was an Olympus pistol handgun. The results for the LTR, CWT and frequency response can be seen in Figures 4 and 5. The gun is more complex and generally

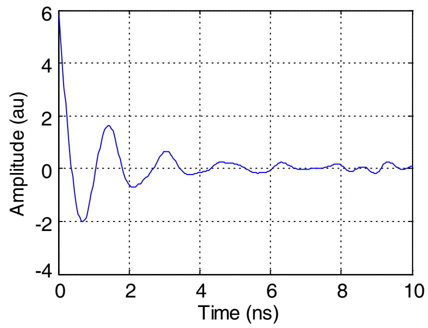

Figure 2: LTR of knife.

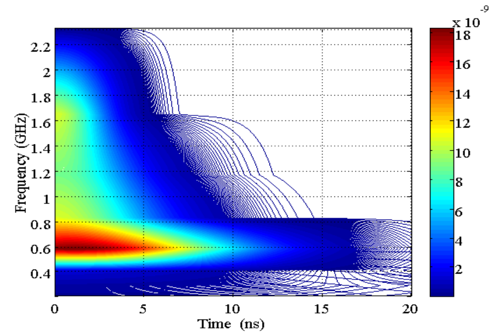

Figure 3: CWT of knife.

complex geometry object than the simple wire and knife, so its LTR lifetime is more complicated and has more modes. The first fundamental resonance frequency of this handgun is appearing at 0.61 GHz as shown in Figure 4. It's quite clear that the LTR of the gun is more complex and it has more resonance modes than simple objects. The LTR of the handgun is clearly visible as the damped oscillations after the reflection of the excitation pulse (sharp peak). Complexity of the LTR related to the multi target edges, in other words the LTR modes are clearly dependent on the target geometry. Figure 5 shows the target CWT analysis, all of the LTR resonant frequencies could be clearly observed as energy levels. After observing the LTR global resonance frequency, it can be seen that the target does not have many resonance modes as the knife, in other words the LTR life time of this target is shorter.

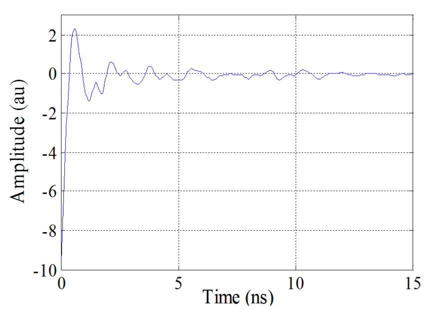

Figure 4: LTR of small handgun.

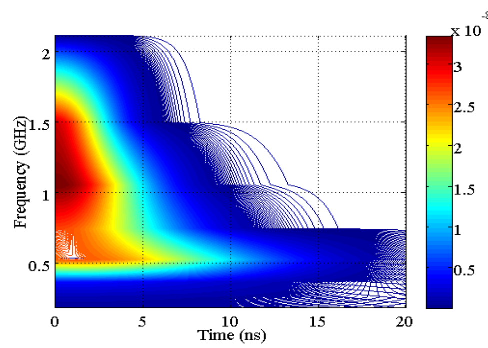

Figure 5: CWT of small handgun.

6. CWT PERFORMANCE OF ONBODY CONCEALED WEAPONS

In the last section, analyses of the response from wires of different dimensions have been presented using CWT time frequency analysis. The practical results show that CWT analysis is very promising and can be used as an alternative means for studying the transient scattering of onbody concealed weapons and to gain further physical insights into the process. In particular, the occurrences of LTR resonances are clearly observed in the TF domain. In this section, transient re-radiating from real target objects such as knives or handguns sited beneath clothes covering the human body will be analysed and studied, and the different dielectric properties will be considered. The purpose here is to study the interaction between the target and the human body in the TF domain. The CWT time frequency domain analysis of scattering from the human body only, a concealed knife onbody and a concealed gun onbody are considered respectively. The aim is to study in the TF domain how the interactions between the target and the medium interface affect the LTR response.

7. HUMAN BODY RESPONSE IN TF DOMAIN

Backscatters from the human body will be analysed using the CWT. A real human body stood 2 m away from the transmitting and receiving antennas from which a sweep frequency of operating bandwidth is transmitted toward the human body and the backscatter data captured by the VNA via the receiving antenna. Figures 6 and 7, shows the time domain response and CWT response of the human body only.

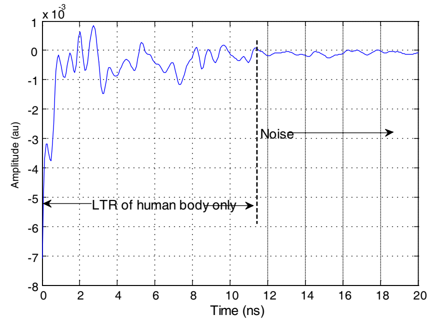

Figure 6: Response of human body only.

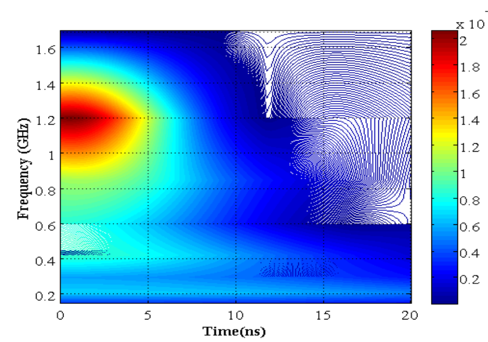

Figure 7: CWT of human body only.

As shown in Figure 6, the late time response scattering events are clearly observed in the TD. Because of the human body's dielectric properties, the re-radiated backscattered data is very weak and since the nature of the frequency is dependent on the human tissue dielectric properties, the refraction angle $\emptyset_t^0$ and the transmitted pulse phase velocity is frequency dependent and varied accordingly [20, 23]. As a result of that the pulse hits the proposed target on very small deference on frequency and time. The magnitude of the re-radiated energy shown in Figure 7 is small since the transmitted pulse is attenuated as it propagates within the lossy dielectric of the human body.

8. ONBODY CONCEALED KNIFE

In this experimental measurement a kitchen knife of length $L = 12\,\text{cm}$ and width $d = 1.2\,\text{cm}$, was attached to the human body and the data captured according to the experimental setup stated earlier. Figure 8 presents the time domain of the LTR resonance scattering event sequence of the target, while the CWT performance is presented in Figure 9.

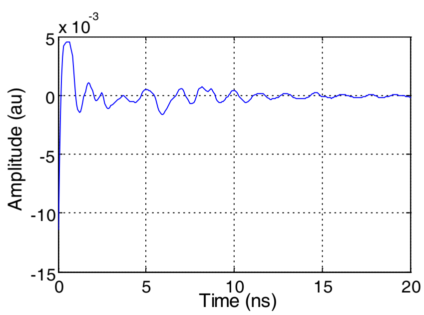

Figure 8: LTR of onbody knife.

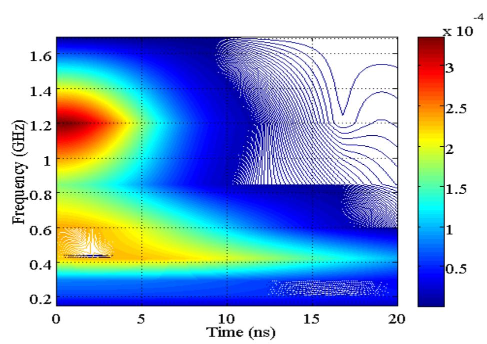

Figure 9: CWT performance of onbody knife.

Compared to the response of lossy human body, alone, the transmitted and received backscattered data is travelling through three mediums, free space (air), human body (lossy dielectric material properties) and the PEC target. The angle of refraction is very similar to that for the land mind detection and could be calculated to be [2],

$$\theta_r = \tan^{-1}\left(\sqrt{\frac{\varepsilon_r \varepsilon_0}{\varepsilon_0}}\right)^0 \tag{11}$$

The backscattered data is more complicated compared to experimental examples studied earlier; the scattered response of the different media interferes with each other and the LTR of the concealed object is masked as shown in the Figure 8. The LTR scattering sequences of this complex medium illustrate that the scattering objects interacted with each other. The CWT analysis of the target signature is given in Figure 9. Comparing the CWT for the knife (Figure 3), lossy human body only, (Figure 7) and the on body knife (Figure 9), it can be clearly seen that the time frequency intensity patterns for the on body knife retain the characteristics observed for the knife only. These energy levels corresponding to the dominant modes of the LTR concealed target.

9. ONBODY CONCEALED GUN

In this section, a real handgun was attached to a human body. Again the re-radiated data was measured by the VNA via the receiving antenna. The time domain scattering event sequence and frequency domain data of the scattering target data are presented in the following Figures 10 and 11. In a manner similar to the test with the on body knife, the non-zero conductivity of a lossy dielectric (human body) attenuates the electromagnetic wave and only the first few dominant scattering phenomena in the low frequency region are observed in frequency domain. However Figure 11 clearly shows that the CTW for the on body handgun contains high energy levels which are related to the presence of the gun (see Figure 7 and Figure 11). However, further investigation is required to confirm the nature of each resonance mode. The CWT performance regarding practical detection of on body concealed weapons shows that in the time frequency domain the spectrum a characteristic signal for both the knife and the handgun could be extracted. This shows that the spectral density is a very powerful means to represent target complexity and geometry. Thus it can be confirmed that the CWT response was related to the concealed target and could be a very powerful tool in the detection of any on body concealed objects.

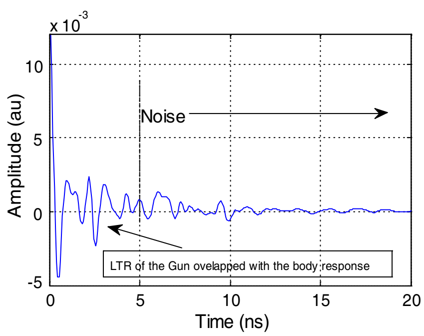

Figure 10: LTR of onbody gun.

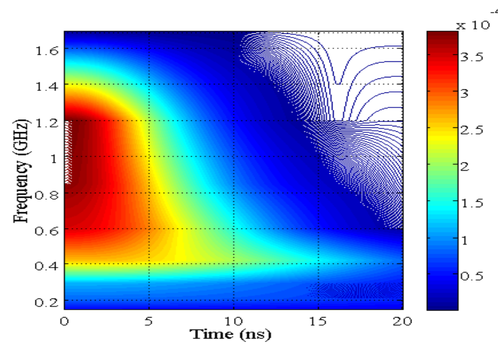

Figure 11: CWT performance of onbody gun.

10. CONCLUSION

New approach for concealed weapon detection based on a CWT applied to the scattering response of a target being detected has been successfully tested. In the TF domain, the occurrence of the frequency components can be easily observed which also provide further insight into transient scattering. The behaviors of TFD using different target signature of a well-known scattered such as the simple wire were examined. In particular, CWT performance showed it to be capable of revealing the major scattering events. The LTR signature of each object was accurately extracted and presented in the TF domain for a knife and small handgun. It is also found that TF analysis can be used as an alternative tool to study transient electromagnetic scattering behavior and extract the unique signature of concealed weapons. The application of TF analysis to the transient scattering from on body concealed weapons was also considered. The signature of both an on body knife and on body handgun was demonstrated the feasibilities of using TFDs to study transient scattering from on body concealed targets. The CWT's experimental performance regarding detection of on body concealed weapons showed that in the TFD the spectral response for every target could be seen as a distribution in which the level and life-time depended on the target material and geometry. The spectral density provides very powerful information concerning target complexity and geometry. As a result of that it can be confirmed that the CWT response is directly identifies the response of the unknown concealed target and could be a very powerful tool in the detection of any on body concealed object.

REFERENCES

1. Baum, C., "The singularity expansion method," *Transient Electromagnetic Fields*, Vol. 10, 129–179, Springer, Berlin, 1976.
2. Balanis, C. A., *Advanced Engineering Electromagnetics,* Wiley, New York, 1989.
3. Sarkar, T. K., S. Park, J. Koh, and S. M. Rao, "Application of the matrix pencil method for estimating the SEM (singularity expansion method) poles of source-free transient responses

from multiple look directions," *IEEE Transactions on Antennas and Propagation*, Vol. 48, 612–618, 2000.

4. Harmer, S., D. Anderws, N. Bowring, N. Rezgui, and M. Southgate, "Ultra wide band detection of onbody concealed weapons using the out of plane polarized late time response," *Proceedings of the SPIE*, Vol. 7485, 748505-748505–8, 2009.
5. Harmer, S., D. Andrews, N. Rezgui, and N. Bowring, "Detection of handguns by their complex natural resonant frequencies," *IET Microwaves, Antennas* & *Propagation*, Vol. 4, 1182–1190, 2010.
6. Dudley, D., "Comments on SEM and the parametric inverse problem," *IEEE Transactions on Antennas and Propagation*, Vol. 33, 119–120, 1985.
7. Van Blaricum, M. and R. Mittra, "A technique for extracting the poles and residues of a system directly from its transient response," *IEEE Transactions on Antennas and Propagation*, Vol. 23, 777–781, 1988.
8. Liu, J.-H. and H.-T. Kim, "Comments on extraction of natural frequencies od radar target from a measured response using E-pulse techniques," *IEEE Transactions on Antenna and Propagation*, Vol. 53, 3853–3855, 2005.
9. Hua, Y. and T. Sarkar, "Generalized pencil-of-function method for extracting poles of an EM system from its transient response," *IEEE Transactions on Antennas and Propagation*, Vol. 37, 229–234, 1989.
10. Heyman, E. and L. Felsen, "A wavefront interpretation of the singularity expansion method," *IEEE Transactions on Antennas and Propagation*, Vol. 33, 706–718, 1985.
11. Heyman, E., G. Friedlander, and L. Felsen, "Ray-mode analysis of complex resonances of an open cavity [radar targets]," *Proceedings of the IEEE*, Vol. 77, 780–787, 2002.
12. Shirai, H. and L. Felsen, "Wavefront and resonance analysis of scattering by a perfectly conducting flat strip," *IEEE Transactions on Antennas and Propagation*, Vol. 34, 1196–1207, 1986.
13. Kaiser, G., *A Friendly Guide to Wavelets*, Birkhauser, Boston, 60–64, 1994.
14. Young, R. K., *Wavelet Theory and Its Applications*, 1st Edition, 13–20, Springer, USA, 1992.
15. Torrence, C. and G. P. Compo, "A practical guide to wavelet analysis," *Bull. Am. Meteorol. Soc.*, Vol. 79, 61–78, 1998.
16. Rioul, O. and P. Flandrin, "Time-scale energy distributions: A general class extending wavelet transforms," *IEEE Transactions on Signal Processing*, Vol. 40, 1746–1757, 2002.
17. Hlawatsch, F. and G. Boudreaux-Bartels, "Linear and quadratic time-frequency signal representations," *IEEE Signal Processing Magazine*, Vol. 9, 21–67, 1992.
18. Rioul, O. and P. Flandrin, "Time-scale energy distributions: A general class extending wavelet transforms," *IEEE Transactions on Signal Processing*, Vol. 40, 1746–1757, 2002.
19. Sadiku, M. O., C. M. Akujuobi, and R. C. Garcia, "An introduction to wavelets in electromagnetics," *IEEE Microwave Magazine*, Vol. 6, 63–72, 2005.
20. Debanth, L., *Wavelets and Signal Processing*, Birkhauser, 2003.
21. Wei, Q., J. Xin, S.-Q. Liu, and Y.-H. Wu, "SAR interference signal feature vector extraction and simulation based on wavelet packet analysis," *IEEE 2nd International Conference on Signal Processing Systems*, Vol. 3, 284–287, Dalian, 2010.
22. Atiah, A. and N. Bowring, "Design of flat gain UWB tapered slot antenna for onbody concealed weapons detections," *Piers Online*, Vol. 7, No. 5, 491–495, 2011.
23. Le-Tien, T., H. Talhami, and D. T. Nguyen, "Target signature extraction based on the continuous wavelet transform in ultra-wideband radar," *Electronics Letters*, Vol. 33, 89–91, 1997.

Examples of UV Measurements under 400 kV Powerlines in Finland

Rauno Pääkkonen[1], **Leena Korpinen**[2], **and Fabriziomaria Gobba**[3]

[1]Finnish Institute of Occupational Health, Tampere, Finland
[2]Department of Electronics and Communications Engineering
Tampere University of Technology, Tampere, Finland
[3]Department of Public Health Sciences, University of Modena and Reggio Emilia, Italy

Abstract— The aim of our study is to investigate UV exposure under 400 kV powerlines in Finland through sample measurements as a typical case study. The Finnish exposure limit value at work for weighted ultraviolet radiation (UV-BC) is 30 J/m^2 per eight hours of exposure (based on European directive (2006/25/EU)), which is not applicable to solar radiation. This means as instantaneous irradiance about 1 mW/m^2. We measured UV-BC weighted radiation and calculated a daily dose, which is about 10 percent of the Finnish exposure limit value. However, technical means are also needed in Scandinavia against ultraviolet sun exposure. These means are the use of sun protective lotions, reasonable clothing, sunglasses, avoiding direct sunshine in midday, using shadow etc..

1. INTRODUCTION

Ultraviolet (UV) radiation is part of the electromagnetic spectrum emitted by the sun. Whereas UVC rays (wavelengths of 100–280 nm) are absorbed by the atmospheric ozone, most radiation in the UVA range (315–400 nm) and about 10% of the UVB rays (280–315 nm) reach the Earth's surface. Both UVA and UVB are of major importance to human health. Small amounts of UV are essential for the production of vitamin D in people, yet overexposure may result in acute and chronic health effects on the skin, eye and immune system.

Ultraviolet radiation exposure in Finland is relatively low compared to that found in many other European countries such as Italy or Spain. However, Nordic skin tone is often lighter than that found in other parts of Europe, and thus the risk of adverse effects from radiation exposure can also exist in Finland. Approximately 30 percent of Finnish persons have skin type I-II, and most Finns have skin type III. Therefore, at least 30 percent of Finns have a relatively high risk of sunburn if they are exposed to solar radiation in summer in Finland [1]. In Finland more than 1200 persons receives a melanoma every year that means that the prevalence of melanoma is 8–9/100 000 person [4]. The prevalence of melanoma is increasing also over the whole western world, and therefore the sunburns should be avoided. The most significant occupations for solar radiation exposure is farming, construction, service and maintenance activities, and also many other outdoor work especially in summer time [5–7].

It is a popular misconception that only fairskinned people need to be concerned about overexposure to the sun. Darker skin has more protective melanin pigment, and the incidence of skin cancer is lower in darkskinned people. Nevertheless, skin cancers do occur with this group and unfortunately they are often detected at a later, more dangerous stage. The risk of UV radiation-related health effects on the eye and immune system is independent of skin type [8, 9].

The Finnish exposure limit value at work for weighted ultraviolet radiation (UV-BC) is 30 J/m^2 for eight hours of exposure (based on European directive (2006/25/EU)), [2] which, however, is not applicable to solar radiation. The ACGIH (American Conference of Industrial Hygienists) has recommended a value of 1 mW/m^2 over eight hours that equals to 30 J/m^2 over eight hours [3]. In Finland, it is not usual to measure ultraviolet radiation, and then there is a need to develop both measurement facilities and information on social media. Nowadays there are available more and more simple ultraviolet index meters, but the user must know what the indices mean, what the skin types are, what the sun protection factor means and how clothing and sunglasses diminish exposure to solar radiation. Ultraviolet index is a global index that in Finland is at maximum about 5–7, when globally the index varies 0–18 [10].

The aim of our study was to investigate UV exposure under 400 kV powerlines in Finland through sample measurements. Our aim was to get basic data for exposure evaluation.

2. MATERIALS AND METHODS

We measured UV-BC weighted radiation with a Solar PMA2100 meter equipped with a safety probe PMA2120 (factory-calibrated in 2010). Figure 1 shows an example of our measurements. We also measured UV index by using a new Oregon Scientific EB612 meter.

Figure 1: Taking sample UV measurements under 400 kV powerlines on a sunny summer day.

Figure 2 shows the area in which we took measurements under 400 kV powerlines.

Figure 2: The place in which we took measurements under 400 kV powerlines.

3. RESULTS

We measured a dose of 0.65 J/m^2 over one hour, and dose of 1.23 J/m^2 over three hours and 51 minutes. We also measured instantaneous values of irradiance to be 2–150 mW/m^2. Table 1 shows our instantaneous measurements. Time of the measurements was in the middle of the day (11:00–15:00) 20 July in Tampere Region, and these values represent Finnish maximum values.

Figure 3 shows UV index measurement results over a July day. Maximum value for the index was 7, and the value was more than 6 over 4.5 hours.

Table 1: The instantaneous UV measurements under power line.

Case	UV measurements mW/m^2	Measurement situation
1	55	cloudy
2	112	sunny
3	127	sunny
4	148	towards the sun
5	5.0	away from the sun
6	2.0	towards the ground
7	3.0	reflection from aluminum paper on ground
8	55 . . . 65	in shadow, the sun behind clouds

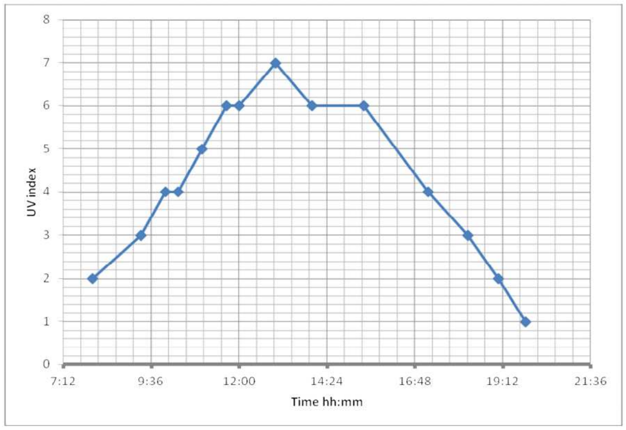

Figure 3: Measured UV index in Tampere region in July.

4. DISCUSSION AND CONCLUSION

If we calculate daily dosage from our measurements, we receive exposure of less than $3\,\mathrm{J/m^2}$, or about 10 percent of the Finnish exposure limit value at work for weighted ultraviolet radiation (UV-BC), which is $30\,\mathrm{J/m^2}$ over eight hours of exposure (based on European directive (2006/25/EU)) [2]. Then, it is probable that these values are not exceeded other time of the day or the summer. In any case, it means, that limit values are not exceeded in Finland.

The instantaneous values of irradiance were between 2–$150\,\mathrm{mW/m^2}$. This exceeds, for example, the maximum value recommended by the ACGIH (American Conference of Industrial Hygienists) [3], which is $1\,\mathrm{mW/m^2}$ over eight hours. This also means that in Finland, the dose at which a light-skinned person is at risk of erythema can be reached and exceeded if protective measures, such as entering a shaded area or applying sunscreen, are not employed. In Finland, the recommended midsummer exposure is less than one hour for type II skin. Similar evaluation can be reached using ultraviolet index [11].

Therefore, technical means are also needed in Scandinavia against ultraviolet sun exposure. These means are the use of sun protective lotions, reasonable clothing, sunglasses, avoiding direct sunshine in midday, using shadow etc.. Clouds and shade reduced the intensity of ultraviolet radiation to half, which means that the exposure time can be doubled or the risk is reduced to half [9]. WHO lists following personal actions [9]:

- **Limit Time in the Midday Sun**

  To the extent possible, limit exposure to the sun during 10 a.m. and 4 p.m.
- **Watch for the UV Index**

  This helps you plan your outdoor activities in ways that prevent overexposure to the sun's rays (Figure 3). Take special care to adopt sun safety practices when the UV Index predicts exposure levels of moderate (index 3–5) or above.
- **Use Shade Wisely**

  Seek shade when UV rays are the most intense.
- **Wear Protective Clothing**

  A hat with a wide brim offers good sun protection for your eyes, ears, face, and the back or your neck. Sunglasses that provide 99 to 100 percent UV-A and UV-B protection will greatly reduce eye damage from sun exposure. Tightly woven, loose fitting clothes will provide additional protection from the sun.
- **Use Sunscreen**

  Apply a broad-spectrum sunscreen of SPF 15+ liberally and re-apply every two hours, or after working, swimming, playing or exercising outdoors.

To conclude, we made a small case analysis on ultraviolet exposure dose, radiance and UV-index, and we noticed that these work in harmony when evaluating the practical exposure limitations against solar radiation in Finland. The ultraviolet dose in middle Finland is less than $5\,\mathrm{J/m^2}$ (over a day), irradiance less than $200\,\mathrm{mW/m^2}$ and ultraviolet index less than 7.

REFERENCES

1. Säteilyturvakeskus, *Ultraviolettisäteily Ja Ihminen*, 12 p, Vammalan Kirjapaino Oy, Helsinki, 2008 (in Finnish).
2. "Directive 2006/25/EC of the European parliament and of the council of 5 April 2006 on the minimum health and safety requirements regarding the exposure of workers to risks arising from physical agents (artificial optical radiation) (19th individual Directive within the meaning of Article 16(1) of Directive 89/391/EEC)," *Official Journal of the European Union*, 2006.
3. ACGIH (American Conference of Industrial Hygienists), *2008 TLVs and BEIs*, *Threshold Limit Values for Chemical Substances and Physical Agents* & *Biological Exposure Indices*, 252, Cincinnati, Ohio, 2008.
4. Hannuksela, M., "Melanooma eli tummasolusyöpä," Terveyskirjasto, Duodecim, Helsinki, 2009 (in Finnish), http://www.terveyskirjasto.fi/terveyskirjasto/tk.koti?p_artikkeli=hpa00029.
5. Gobba, F. and A. Modenese, "Occupational risk related to optical radiation exposure in construction workers," *Giornale Italiano di Medicina del Lavoro ed Ergonomia*, Vol. 34, No. 3, 144–146, 2012.
6. Thieden, E., S. Collins, S. Philipsen, G. Murphy, and H. C. Wulf, "Ultraviolet exposure patterns of Irish and Danish gardeners during work and leisure," *Photobiology*, *British Journal of Dermatology*, Vol. 153, 795–801, 2005.
7. Siani, A., G. Casale, R. Sisto, A. Colosimo, C. Lang, and M. Kimlin, "Occupational exposures to solar ultraviolet radiation of vineyard workers in Tuscany (Italy)," *Photochemistry and Photobiology*, Vol. 87, 925–934, 2011.
8. WHO, "Health effects of ultraviolet radiation," 2013, http://www.who.int/uv/health/en/.
9. WHO, "Sun protection," 2013, http://www.who.int/uv/sun_protection/en/.
10. UNEP, "Global Solar ultraviolet index, practical guide," 2002, http://www.unep.org/pdf/Solar_Index_Guide.pdf.
11. Finnish Meteorological Institute, "Ultraviolet index," 2013, http://en.ilmatieteenlaitos.fi/uv-index?p_p_id=WebProxyPortlet_WAR_WebProxyPortlet_INSTANCE_sf1X&p_p_lifecycle=1&p_p_state=normal&p_p_mode=view&p_p_col_id=column-4&p_p_col_count=2&_WebProxyPortlet_WAR_WebProxyPortlet_INSTANCE_sf1X_edu.wisc.my.webproxy.URL=http%3A%2F%2Fcdn.fmi.fi%2Flegacy-fmi-fi-content%2Fproducts%2Fglobal-ultraviolet-index%2Findex.php.

Stochastic Electromagnetic Plane-wave Pulse with Non-uniform Correlation Distribution

Chaoliang Ding and Liuzhan Pan
Department of Physics, Luoyang Normal University, Luoyang 471022, China

Abstract— Stochastic electromagnetic plane-wave (SEPW) pulse with non-uniform correlation distribution is introduced. The realizability condition for such pulse is derived. It is found that the evolution properties of the intensity and the degree of polarization of a SEPW pulse with non-uniform correlation distribution in dispersive media are much different from those of a SEPW pulse with uniform correlation distribution.

1. INTRODUCTION

In the past decades, stochastic beam with uniform correlation distribution (e.g., Schell-model correlation) has been studied extensively due to its important applications in various fields, such as free-space optical communications, material thermal processing, particle trapping, optical projection, inertial confinement fusion, remote detection, imaging applications and nonlinear optics [1–3]. Recently, more and more attention is being paid to a stochastic beam with special correlation distribution [4–9]. Gori et al. proposed the sufficient condition for devising genuine correlation function of a stochastic scalar or electromagnetic beam [4, 5]. Based on the model suggested by Gori et al., Lajunen and Saastamoinen introduced a partially coherent beam with spatially varying correlation properties (i.e., non-uniform correlation distribution) [6]. Tong and Korotkova explored the behavior of a stochastic beam with non-uniform correlation distribution in isotropic random media [7], and introduced a stochastic electromagnetic beam with non-uniform correlation distribution [8]. Mei et al. investigated the polarization properties of a stochastic electromagnetic beam with non-uniform correlation distribution in turbulent atmosphere [9].

All the above-mentioned literatures are confined to stationary beams. In the past decade, a non-stationary stochastic light named partially coherent pulse has been studied widely [10–20]. Such pulse was introduced by Pääkkönen et al. [10] and Lin et al. [11], respectively. Propagation properties of a partially coherent pulse in dispersive media and nonlinear media were reported in [12, 13]. The methods for generating a partially coherent pulse were proposed in [14, 15]. Lancis et al. discussed the space-time analogy for partially coherent plane-wave-type pulses [16]. Ghost interference and ghost imaging with partially coherent pulse were reported in [17, 18], respectively. Scattering of a partially coherent pulse was reported in [19]. The polarization properties of a stochastic electromagnetic pulse (also named electromagnetic partially coherent pulse) on propagation were studied in [20–23]. More recently, Lajunen and Saastamoinen introduced a partially coherent plane-wave pulse with non-uniform correlation distribution and studied its propagation in dispersive media, and they have found that the maximum peak of the pulse energy can be accelerating or decelerating, and self-focusing effects are also possible on propagation [24]. In this letter, we introduce a stochastic electromagnetic plane-wave (SEPW) pulse with non-uniform correlation distribution, and explore the intensity and the polarization properties of such pulse in dispersive media. Some interesting results are found.

2. THE REALIZABILITY CONDITION FOR A SEPW PULSE WITH NON-UNIFORM CORRELATION DISTRIBUTION

In the space-time domain, the second-order statistical properties of a SEPW pulse can be characterized by the mutual coherence matrix defined as [1, 2, 20, 21]

$$\overset{\leftrightarrow}{\Gamma}(t_1,t_2) = \begin{pmatrix} \Gamma_{xx}(t_1,t_2) & \Gamma_{xy}(t_1,t_2) \\ \Gamma_{yx}(t_1,t_2) & \Gamma_{yy}(t_1,t_2) \end{pmatrix}, \tag{1}$$

where $\Gamma_{\alpha\beta}(t_1,\, t_2) = \langle E_\alpha^*(t_1) E_\beta(t_2)\rangle$, $(\alpha,\, \beta = x, y)$, here the asterisk denotes the complex conjugate and the angular brackets denote ensemble average, $E_\alpha(t)$ represents the component of the random electric vector at time t along α direction. According to [5], in the temporal domain, a sufficient condition for the non-negative definiteness of the mutual coherence matrix can be expressed as

$$\Gamma_{\alpha\beta}(t_1,t_2) = \int p_{\alpha\beta}(v) H_\alpha^*(t_1,v) H_\beta(t_2,v) dv,\ \ (\alpha,\beta = x,y), \tag{2}$$

where $p_{\alpha\beta}$ is a non-negative, Fourier-transformable function and H_α is an arbitrary kernel. By choosing suitable $p_{\alpha\beta}$ and H_α, one can define a wide variety of temporal coherence functions for a partially coherent pulse.

In order to introduce a SEPW pulse with non-uniform correlation distribution, we choose $p_{\alpha\beta}$ and H_α as follows

$$p_{\alpha\beta}(v) = \frac{B_{\alpha\beta}\omega_0 T_{c\alpha\beta}^2}{2\sqrt{\pi}} \exp\left[-\frac{1}{4}\omega_0^2 T_{c\alpha\beta}^4 v^2\right], \tag{3}$$

$$H_j(t, v) = A_j \exp\left[-\frac{t^2}{2T_0^2}\right] \exp\left[-i\omega_0 v \left(t - t_{cj}\right)^2\right], \quad (j = \alpha, \beta), \tag{4}$$

where ω_0 is the carrier frequency, A_α and A_β are the amplitudes of the x and y components of the electric field, T_0 represents the pulse duration, $T_{c\alpha\beta}$ is the r.m.s source correlation between E_α and E_β determining the degree of coherence of a pulse. t_{cx} and t_{cy} are real-valued two-dimensional vectors describing off-axis shifts of the correlation maximum, which leads to a situation where the correlations are highest around t_{cx} and t_{cy}. $B_{\alpha\beta} = |B_{\alpha\beta}| \exp(i\varphi_{\alpha\beta})$ is the correlation coefficient between x and y components of the electric field and $\varphi_{\alpha\beta}$ is the phase difference. Substituting Eqs. (3) and (4) into Eq. (2), we obtain the elements of the mutual coherence matrix of a SEPW pulse with non-uniform correlation distribution as follows

$$\Gamma_{\alpha\beta}(t_1, t_2) = A_\alpha A_\beta B_{\alpha\beta} \exp\left[-\frac{t_1^2 + t_2^2}{2T_0^2}\right] \times \exp\left\{-\frac{1}{T_{c\alpha\beta}^4}\left[(t_2 - t_{c\beta})^2 - (t_1 - t_{c\alpha})^2\right]^2\right\}. \tag{5}$$

To generate a physically realizable pulse, the mutual coherence matrix must be Hermitian and non-negative definite. The former restriction leads to the following relations

$$\Gamma_{\alpha\beta}(t_1, t_2) = \Gamma_{\beta\alpha}^*(t_2, t_1), \tag{6}$$

$$B_{xx} = B_{yy} = 1, \ |B_{xy}| = |B_{yx}|, \ \phi_{xy} = \phi_{yx}, \ T_{cxy} = T_{cyx}. \tag{7}$$

According to [5, 8], to satisfy the latter restriction, the following relations

$$p_{xx}(v) \geq 0, \ p_{yy}(v) \geq 0, \ p_{xx}(v)p_{yy}(v) - p_{xy}(v)p_{yx}(v) \geq 0, \tag{8}$$

must be satisfied besides that $p_{\alpha\beta}$ is the non-negative, Fourier-transformable function.

Substituting Eq. (3) into Eq. (8), we find that the first two inequalities always hold and the third inequality leads to

$$T_{cxx}^2 T_{cyy}^2 \exp\left[-\frac{1}{4}\kappa^2 v^2 \left(T_{cxx}^4 + T_{cyy}^4\right)\right] \geq |B_{xy}|^2 T_{cxy}^4 \exp\left[-\frac{1}{2}\kappa^2 v^2 T_{cxy}^4\right]. \tag{9}$$

If we set $v = 0$ and $v \to \infty$, we can obtain the following two inequalities

$$T_{cxx}^2 T_{cyy}^2 \geq |B_{xy}|^2 T_{cxy}^4, \quad \frac{1}{2}\left(T_{cxx}^4 + T_{cyy}^4\right) \leq T_{cxy}^4. \tag{10}$$

The combination of the two inequalities in Eq. (10) leads to the following double inequality

$$\sqrt[4]{\frac{1}{2}\left(T_{cxx}^4 + T_{cyy}^4\right)} \leq T_{cxy} \leq \sqrt{\frac{1}{|B_{xy}|} T_{cxx} T_{cyy}}. \tag{11}$$

The form of the realizability condition for a SEPW pulse with non-uniform correlation distribution is somewhat similar to that for a stationary electromagnetic beam with non-uniform correlation distribution [8].

If we choose $p_{\alpha\beta}$ and H_α as follows

$$p_{\alpha\beta}(v) = \frac{B_{\alpha\beta} T_{c\alpha\beta}}{2\sqrt{\pi}} \exp\left[-\frac{1}{4}T_{c\alpha\beta}^2 v^2\right], \tag{12}$$

$$H_j(t, v) = A_j \exp\left[-\frac{t^2}{2T_0^2}\right] \exp\left[-ivt\right], \quad (j = \alpha, \beta), \tag{13}$$

then substituting Eqs. (12) and (13) into Eq. (2), we obtain the elements of the mutual coherence matrix of a SEPW pulse with uniform correlation distribution as follows [20–23]

$$\Gamma_{\alpha\beta}(t_1,t_2)=A_\alpha A_\beta B_{\alpha\beta}\exp\left[-\frac{t_1^2+t_2^2}{2T_0^2}-\frac{1}{T_{c\alpha\beta}^2}(t_1-t_2)^2\right]. \tag{14}$$

3. PROPAGATION OF A SEPW PULSE WITH NON-UNIFORM CORRELATION DISTRIBUTION IN THE SECOND-ORDER DISPERSIVE MEDIA

In this section, we study the propagation of a SEPW pulse in the second-order dispersive media. Propagation of the elements of the mutual coherence matrix in the dispersive media can be studied by the generalized Collins formula in the temporal domain [11, 25]

$$\begin{aligned}&\Gamma_{\alpha\beta}(t_1,t_2,z)\\&=\frac{\omega_0}{2\pi B}\iint\Gamma_{\alpha\beta}(t_{10},t_{20})\exp\left\{\frac{i\omega_0}{2B}\left[A\left(t_{10}^2-t_{20}^2\right)+D\left(t_1^2-t_2^2\right)-2\left(t_{10}t_1-t_{20}t_2\right)\right]\right\}dt_{10}dt_{20},\end{aligned} \tag{15}$$

where A, B, C, and D are the elements of the temporal matrix of the dispersive media. Here we have assumed that the time coordinate is measured in the reference frame moving at the group velocity of the pulse.

The temporal matrix for the second-order dispersive media of length z is given as [11, 25]

$$\begin{pmatrix}A & B\\ C & D\end{pmatrix}=\begin{pmatrix}1 & \omega_0\beta_2 z\\ 0 & 1\end{pmatrix}, \tag{16}$$

where β_2 represents the group velocity dispersion coefficient.

The intensity is obtained as $I(t,z)=\mathrm{Tr}\,\overleftrightarrow{\Gamma}(t,t,z)$ and the degree of polarization (DOP) is expressed as

$$P(t,z)=\sqrt{1-\frac{4\mathrm{Det}\,\overleftrightarrow{\Gamma}(t,t,z)}{\left[\mathrm{Tr}\,\overleftrightarrow{\Gamma}(t,t,z)\right]^2}}. \tag{17}$$

Applying Eqs. (5) and (15)–(17), we calculate in Fig. 1 the normalized intensity distribution of a SEPW pulse with non-uniform correlation distribution on propagation in dispersive media with $T_0=15\,\mathrm{ps}$, $T_{cxx}=9\,\mathrm{ps}$, $T_{cxy}=20\,\mathrm{ps}$, $B_{xy}=0.2$, $\beta_2=25\,\mathrm{ps}^2/\mathrm{km}$, $A_x=A_y=1$. One finds from Fig. 1 that the intensity is focused during propagation, and the maximum peak is laterally shifted when $t_{cx}=t_{cy}\neq 0$, which is similar to the behavior of a partially coherent plane-wave pulse with non-uniform correlation distribution on propagation in dispersive media [24]. Fig. 2 shows the shift of the maximum peak of the intensity on propagation. As can be see from Fig. 2, the absolute value of the shift of the maximum peak increases on propagation, and saturates at sufficiently large distance, which is similar to the behavior of a stationary electromagnetic beam with non-uniform correlation distribution on propagation in free space [8]. Furthermore, the absolute value of the shift approaches to different values at large distance for different values of t_{cx} and t_{cy}, while it approaches

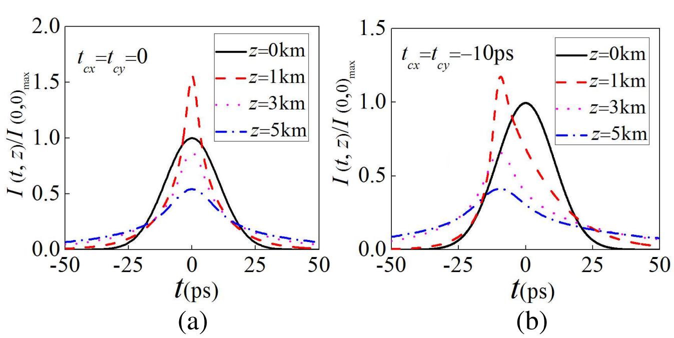

Figure 1: Normalized intensity distribution of a SEPW pulse with non-uniform correlation distribution in dispersive media on propagation.

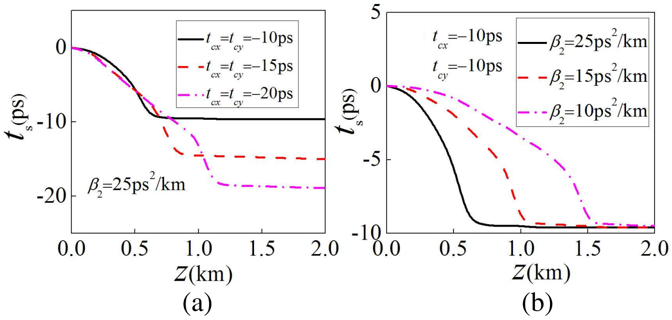

Figure 2: Shift of the maximum peak of the intensity on propagation.

to the same value for different values of β_2 although it increases more rapidly on propagation for large β_2.

Figure 3 shows the DOP of a SEPW pulse with non-uniform correlation distribution on propagation in dispersive media with $t_{cx} = t_{cy} = 0$. For the convenience of comparison, the corresponding result of a SEPW pulse with uniform correlation distribution is also shown in Fig. 3(a). One finds from Fig. 3 that the behavior of the degree of polarization of a SEPW pulse with non-uniform correlation distribution on propagation is much different from that of a SEPW pulse with uniform correlation distribution. For a SEPW pulse with uniform correlation distribution, the DOP increases monotonically on propagation and saturates at large distance. For a SEPW pulse with non-uniform correlation distribution, the DOP initially displays a downward trend at small propagation distance but after reaching a dip starts to increase on propagation, and saturates at large distance, and it is interesting to find that the DOP increases more rapidly on propagation for large β_2, while it approaches to the same value at large distance for different values of β_2.

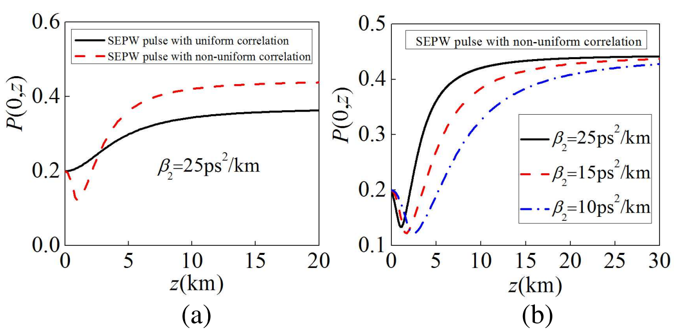

Figure 3: DOP of a SEPW pulse with non-uniform or uniform correlation distribution on propagation in dispersive media.

4. CONCLUSIONS

In conclusion, we have introduced a new class of electromagnetic pulse named SEPW pulse with non-uniform correlation distribution and have discussed its realizability condition. We have found that the evolution properties of a SEPW pulse with non-uniform correlation distribution on propagation are much different from those of a SEPW pulse with uniform correlation distribution, and we can modulate the intensity and polarization properties of a SEPW pulse by manipulating its correlation function.

ACKNOWLEDGMENT

This work is supported by the National Natural Science Foundation of China under Grant Nos. 61275150, 61078077, 61108090 & 11274005, Natural Science Foundation of Henan Province under Grant Nos. 112300410062 & 13A140797, the Huo Ying Dong Education Foundation of China under Grant No. 121009, the Key Project of Chinese Ministry of Education under Grant No. 210081, and the Project Sponsored by the Scientific Research Foundation for the Returned Overseas Chinese Scholars, State Education Ministry.

REFERENCES

1. Mandel, L. and E. Wolf, *Optical Coherence and Quantum Optics*, Chapter 5, Cambridge University Press, Cambridge, 1995.
2. Wolf, E., *Introduction to the Theory of Coherence and Polarization of Light*, Chapter 5, Cambridge University Press, Cambridge, 2007.
3. Andrews, L. C., R. L. Phillips, and C. Y. Hopen, *Laser Beam Scintillation with Applications*, Part II, SPIE Press, Washington, 2001.
4. Gori, F. and M. Santarsiero, *Opt. Lett.*, Vol. 32, 3531, 2007.
5. Gori, F., V. R. Sanchez, M. Santarsiero, and T. Shirai, *J. Opt. A: Pure Appl. Opt.*, Vol. 11, 085706, 2009.
6. Lajunen, H. and T. Saastamoinen, *Opt. Lett.*, Vol. 36, 4104, 2011.
7. Tong, Z. S. and O. Korotkova, *Opt. Lett.*, Vol. 37, 3240, 2012.
8. Tong, Z. S. and O. Korotkova, *J. Opt. Soc. Am. A*, Vol. 29, 2154, 2012.
9. Mei, Z. R., Z. S. Tong, and O. Korotkova, *Opt. Express*, Vol. 20, 26458, 2012.
10. Pääkkönen, P., J. Turunen, P. Vahimaa, A. T. Friberg, and F. Wyrowski, *Opt. Commun.*, Vol. 204, 53, 2002.
11. Lin, Q., L. G. Wang, and S. Y. Zhu, *Opt. Commun.*, Vol. 219, 65, 2003.
12. Lajunen, H., J. Turunen, P. Vahima, J. Tervo, and F. Wyrowski, *Opt. Commun.*, Vol. 255, 12, 2005.
13. Lajunen, H., V. Torres-Company, J. Lancis, E. Silvestre, and P. Andres, *Opt. Express*, Vol. 18, 14979, 2010.
14. Lajunen, H., J. Tervo, J. Turunen, P. Vahimaa, and F. Wyrowski, *Opt. Express*, Vol. 11, 1894, 2003.
15. Torres-Company, V., G. Mínguez-Vega, J. Lancis, and A. T. Friberg, *Opt. Lett.*, Vol. 32, 1608, 2007.
16. Lancis, J., V. Torres-Company, E. Silvestre, and P. Andrés, *Opt. Lett.*, Vol. 30, 2973, 2005.
17. Torres-Company, V., H. Lajunen, J. Lancis, and A. T. Friberg, *Phys. Rev. A*, Vol. 77, 043811, 2008.
18. Shirai, T., T. Setälä, and A. T. Friberg, *J. Opt. Soc. Am. B*, Vol. 27, 2549, 2010.
19. Ding, C. L., Y. J. Cai, O. Korotkova, Y. T. Zhang, and L. Z. Pan, *Opt. Lett.*, Vol. 36, 517, 2011.
20. Huang, W. H., S. A. Ponomarenko, M. Cada, and G. P. Agrawal, *J. Opt. Soc. Am. A*, Vol. 24, 3063, 2007.
21. Ding, C. L., L. Z. Pan, and B. D. Lü, *New J. Phys.*, Vol. 11, 083001, 2009.
22. Yao, M., Y. J. Cai, O. Korotkova, Q. Lin, and Z. Y. Wang, *Opt. Express*, Vol. 18, 22503, 2010.
23. Voipio, T., T. Setälä, and A. T. Friberg, *J. Opt. Soc. Am. A*, Vol. 30, 71, 2013.
24. Lajunen, H. and T. Saastamoinen, *Opt. Express*, Vol. 21, 190, 2013.
25. Dijaili, S. P., A. Dienes, and J. S. Smith, *IEEE J. Quantum Electron.*, Vol. 26, 1158, 1990.

Nonlinear Dissipative Dynamics and Optical Properties of Quantum Dots for Nanomedicine

V. D. Krevchik[1], **V. I. Volchikhin**[1], **I. I. Artemov**[1], **M. B. Semenov**[1], **R. V. Zaitsev**[1], **A. V. Razumov**[1], **A. K. Aringazin**[2], and **K. Yamamoto**[3]

[1]Penza State University, Russia
[2]Eurasian National University, Kazakhstan
[3]International Medical Center, Japan

Abstract— The aim of this work is theoretical and experimental study of the effect of doping for semiconductor quantum dots on their photoluminescence (PL), which has important applications both for nanomedicine and nanoelectronics devices to create the controlled properties. An experimental study of the surface treatment effect for quantum dots (QDs) of CdSe on their photoluminescence (PL) has been fulfilled. It is shown that the highest intensity of photoluminescence yield QD with surface treated by the donor electron impurity. The role of the QD doping by impurities has been theoretically studied. It is shown that the PL intensity in this case can be increased considerably. The development of the 1D-dissipative tunneling theory for structures with quantum dots in the system of combined AFM/STM in an external electric field at a finite temperature has been proposed. The probability of the 1d-dissipative tunneling in a double-well model oscillator potential in the external electric field with accuracy of the pre-exponential factor has been calculated. Theoretical investigation of features for the field dependence of the tunnel probability is allowed to offer the controlled growth method of colloidal gold QD, based on the transformation of the oscillator double-well potential in the external electric field. The applicability of nanoscale dots (QD) from colloidal gold for nanomedicine has been discussed. For example, QD from colloidal gold are used as carriers of drugs, as well as for the diagnosis and treatment of cancer. Optical response for QD from colloidal gold (surface enhanced Raman spectroscopy) is 200 times brighter than for semiconductor quantum dots. Optical and transport properties of the doped semiconductor QDs with bio-conjugated shells can be used as fluorescent labels for imaging of biological objects and in nanomedicine for the diagnosis and treatment of a number of serious diseases, including cancer.

1. INTRODUCTION

The last few years the number of experimental and theoretical research in the field of optics for nanostructures with impurity centers has dramatically increased. Success in the development of methods for the synthesis of fluorescent nanocrystals (quantum dots (QDs)) with desired properties and methods for functionalizing of the QD-surface has opened ways of the new class of fluorophores creation for many biological and medical applications. Fluorescent nanocrystals are detected as individual objects with usage of conventional fluorescence microscopes that can help to visualize the processes at the single molecule. The advantage of nanocrystals in comparison with organic fluorophores is their high brightness due to the large value of the absorption coefficient, a unique high photostability and the narrow, symmetrical peak of emission. The wavelength of photoluminescence (PL) for nanocrystals is strictly dependent on their size, and for all colors of nanocrystals the excitation of only one radiation source is necessary. Such unique properties of nanocrystals make its as ideal fluorophores for ultrasensitive, multicolor detection in biological and medical diagnosis that requires registration of many parameters simultaneously.

2. THE FLUORESCENCE INTENSITY OF THE QUANTUM DOTS IN THE WATER DEPENDS ON THE SURFACE PROCESSING

Various materials, such as semiconductor, metals and lattices are used for synthesize the quantum dots with recent nano-technology. Many kinds of characters on the quantum dots have been reported on quantum dot films of semiconductor and electron packed metals. One of the important characters, we focus on the surface treatment of the quantum dot. The cyto-toxicity is reported to depend on the surface processing. That is the interaction of the surface of the molecules of the cell and the surface of the quantum dot plays a key roll for the safety for human being and the environment. The size of the aggregation also depends on the surface treatment. The intensity of the fluorescent light and the surface treatment of the quantum dot will be studied in this report.

2.1. Material and Methods

Red colored quantum dot and yellow colored quantum dot was made as from Cadmium and selenium by the hot soap method with trioctylphosphine oxide (TOPO). Then, the shells of both of the quantum dots were covered with mercapto-zinc. Here, we obtain the quantum dots that are not solvable to the water. Then, the surface of the quantum dots, TOPO were exchanged by the water solvable molecules such as 11-mercapto-undecanoic acids and mercapto-glycerol. Vero cell, the kidney cell of the African green monkey, was cultured with the standard methods. Fluorescent microscope system (OLYMPUS) was used for the observation. Measurement of the photo-luminescent spectra with the time course was done by JASCO fluorescence spectrophotometer. Measurement of the zeta potential and the particle size was done by zeta potential and particle size measurement system (SYSMEX).

2.2. Results and Discussion

The more the emission light is dosed, the larger the fluorescent intensity of the quantum dot becomes, which is known as the light memory effect [1]. This effect was found not in the water but in the dry film at first. We have found this memory effect also occurs in the water with the appropriate surface processing of the quantum dot. This effect does not continue infinitely. That is after a while, the intensity of the fluorescent come to the maximum and, after that, comes down. The wavelength of the fluorescent light becomes short in the meantime. One of the ideas for the movement of the wavelength of the fluorescent to the short wave length is the light etching. It is reported the quantum dot of the mercapto-cadmium can be produced with the laser light etching from the bulk material. In our case of cadmium seren quantum dot, it might also true. But we have not any data for the evidence of the difference of particle size yet. Another idea for the effect would be the oxidization of the quantum dot by laser light dose. The electron might skip away from the surface might lead to the oxidization from the outside of the quantum dot. So far now, we use the Cd/Se quantum dot with the ZnS processed as the surface of the particle. As this nano-particle is not water soluble, we use mercapto undecanoic acids, mercapto glycerol, and mercapto amine for the surface processing to get the hydrophilicity. We measured the zeta potential of the surface of these three different treated quantum dot. The quantum dot treated with the mercapto undecanoic acids is negatively charged, that with the mercapto amine is positively charged and that with the mercapto glycerol is the neutral. The quantum dot treated with mercapto-organic acidthe showed the highest intensity of the fluorescent light, the quantum dot treated with mercapto glycerol the middle, and the quantum dot treated with mercapto-organic amine, the lowest intensity. Zeta potential from the minimum to the maximum is just the reverse order with the intensity of the fluorescent light, (from strong to weak). It seems the surface electric potential has the key role for the fluorescent intensity. Different surface treatment will result in the different zeta potential of the quantum dot. In the previous study, we have reported the cyto-toxicity is also depend on the surface treatment rather than the inside, the quantum dot itself. The conjugation of the quantum dot with the bio-molecule such as protein, sugar and nucleic acids will change the zeta potential which lead to speculate that the measurement of the zeta potential of the bio-molecule predict roughly the fluorescent intensity of the conjugated bio-molecule quantum dot complex.

2.3. The Electron Donor Agent and the Intensity of the Fluorescent Light

We added the electron donor agent in order to see if the intensity of the fluorescent light of the quantum dot will become strong. We used sodium azide for the electron donor agent. We used the quantum dot, the surface of which was treated with mercapto-undecanoic acids for this experiment. In this study, we have some evidence of the importance of the surface electric potential of the quantum dot to get the strong fluorescent light. We have studied to add the electron scavenger agents into the water solution of containing the water soluble quantum dots. The fluorescent light became very weak. Under this condition, we added the electron donor agents and found the recover of the strong fluorescent. One of the application for this effect is the way to recover the fluorescent light and to find the quantum dot tagged cell in the organ with the microscope.

3. THE INFLUENCE OF TWO-DIMENSIONAL DISSIPATIVE TUNNELING ON PROBABILITY FOR TWO-PHOTON IONIZATION OF D-CENTER IN A SYSTEM OF TWO INTERACTING QUANTUM MOLECULES

Currently, two-photon (TF) spectroscopy is widely used for studying of the band structure in low-dimensional systems [1, 2] as a non-destructive method for the information readout in three-dimensional optical memory devices [3], to study the coherence properties of radiation [4], and also in many other applications. Development of technology for creation of quantum molecules (QM) (tunnel-coupled QDs) requires broadening of the TF-spectroscopy possibilities, in particular, in relation to investigation of the dissipative tunneling features. Usage of the science of quantum tunneling with dissipation to study the interaction of QM with contact medium is productive, because, despite the use of the instanton approach it is possible to get the main results in an analytical form for the effects of environment on the tunneling process, which it is not possible in other often used approaches. One of the aims of this work is the theoretical study of TF impurity absorption in QM, under 2D-dissipative tunneling in the presence of an external electric field.

3.1. The Two-photon Impurity Absorption Spectra Features for Quantum Molecules

Probability of two-photon ionization for D(-)-center in quantum dot $W(2\omega)$ with the parabolic confinement potential under influence of external electric field with account of the Lorentz broadening for energy levels of virtual and final states in QD, can be written as

$$\begin{aligned} W(2\omega) = {} & B_0 \sum_{n_1,\, n_2,\, n_3} \frac{\left[(\beta^{-1}(n_1+n_2+n_3+1/2) - W_0^* + \eta^2)^2 + \hbar^2\Gamma_0^2/E_d^2\right] X^{-2}}{\left[(\beta^{-1}(n_1+n_2+n_3+1/2) - W_0^* + \eta^2 - X)^2 + \hbar^2\Gamma_0^2/E_d^2\right]((n_2/2)!(n_3/2)!)^2} \\ & \times \left\{ \frac{\exp(x_0^{*2}/a_0^{*2})\Gamma(\beta(\eta^2 - W_0^*)/2 + 7/4)}{\pi(\beta(\eta^2 - W_0^*)/2 + 3/4)\Gamma(\beta(\eta^2 - W_0^*)/2+1)} \left[(\beta(\eta^2 - W_0^*)/2 + 3/4)\right.\right. \\ & \times \left.\left. (\psi(\beta(\eta^2 - W_0^*)/2 + 7/4) - \psi(\beta(\eta^2 - W_0^*)/2 + 1)) - 1\right]\right\}^{-1} \\ & \times 2^{-5(n_1+n_2+n_3)-3} \cdot n_1! n_2! n_3! \left| \int_0^\infty dt (1 - e^{-2t})^{-1/2} \exp\left[-(\beta(\eta^2 - W_0^*) + n_2 + n_3 + 3/2)t\right.\right. \\ & \times \sum_{m=0}^{[n_1/2]} (-1)^m f(x_0^*, t) \frac{\exp(f(x_0^*, t)/4)}{m!(n_1 - 2m - 1)!} \left[x_0^*(n_1 - 2m - 1) \sum_{k=0}^{[(n_1-2m-1)/2]} \frac{f(x_0^*, t)^{-k}}{(n_1 - 2m - 2k - 1)!k!} \right. \\ & \left.\left.\left. - a_0^*(n_1 - 2m) \sum_{k=0}^{[(n_1-2m)/2]} \frac{f(x_0^*, t)^{1-k}}{2(n_1 - 2m - 2k)!k!} \right]\right]\right|^2 \times \frac{\Gamma_0}{(3\beta^{-1}/2 - W_0^* + \eta^2 - X)^2 + \hbar^2\Gamma_0^2/E_d^2}, \end{aligned} \tag{1}$$

where $B_0 = 2(a_0^*\beta\lambda_0)^4(a_d\alpha^*)^2\hbar I_0/E_d$; λ_0 — the local field coefficient; α^* — the fine structure constant with account of dielectric permittivity; I_0, ω — intensity and the light frequency, correspondingly; $X = \hbar\omega/E_d$ — the photon energy in units of effective Bohr energy; $f(x_0^*, t) = x_0^{*2}(2e^{-t} + e^{-2t})/a_0^{*2}$; $\psi(x)$ — logarithmic derivative for Γ — function. The calculation process has identified the following selection rules: the optical transitions from the impurity level are possible only to the size-quantized states of QD with even quantum numbers n_2, n_3 and with the value of the quantum number $n_1 = n_1' + 1$ ($n' = 0, 1, 2 \ldots$). The tunnel probability $\Gamma_0 = B\exp(-S)$ for quantum molecule has been calculated in frames of the tunneling with dissipation theory.

3.2. Features of the TF-impurity Absorption under 2D-dissipative Tunneling

Figure 1 shows the calculated dependence of the TF-ionization probability of the $D^{(-)}$-center in system consisting of two interacting QM from the magnitude of the external electric field under 2D-dissipative tunneling. It can be seen from Fig. 1 that for the field dependence of the TF-impurity absorption probability corresponds the characteristic kink point — bifurcation — as a result of change in the dissipative tunneling regime from synchronous to asynchronous. It is evident, too, that in a small neighborhood of the bifurcation point, the regime of quantum beats, associated with the existence of competing solutions under search of 2D-instanton, can be realized. It can be seen, that with increase of coupling constant α the bifurcation point is shifted to the region of more strong fields (cf. Fig. 1(a) and Fig. 1(b)), due to the symmetry change of 2D-potential by increasing of the Coulomb repulsion for the tunnel particles. A similar situation occurs with decreasing temperature (parameter ε_T) (cf. Figs. 1(c) and 1(b)). With reduction of the parameter ε_T the 2D-tunnel probability is reduced and hence, the more high value of the external electric field is required to the increase of the potential asymmetry. Thus, the effects of bifurcations and quantum beats are strongly depended on such parameters of 2D-tunneling, as temperature and the interaction constant of tunnel particles. The role of the external electric field is reduced to the restoration of 2D-potential asymmetry, which is necessary for the appearance of 2D-bifurcations.

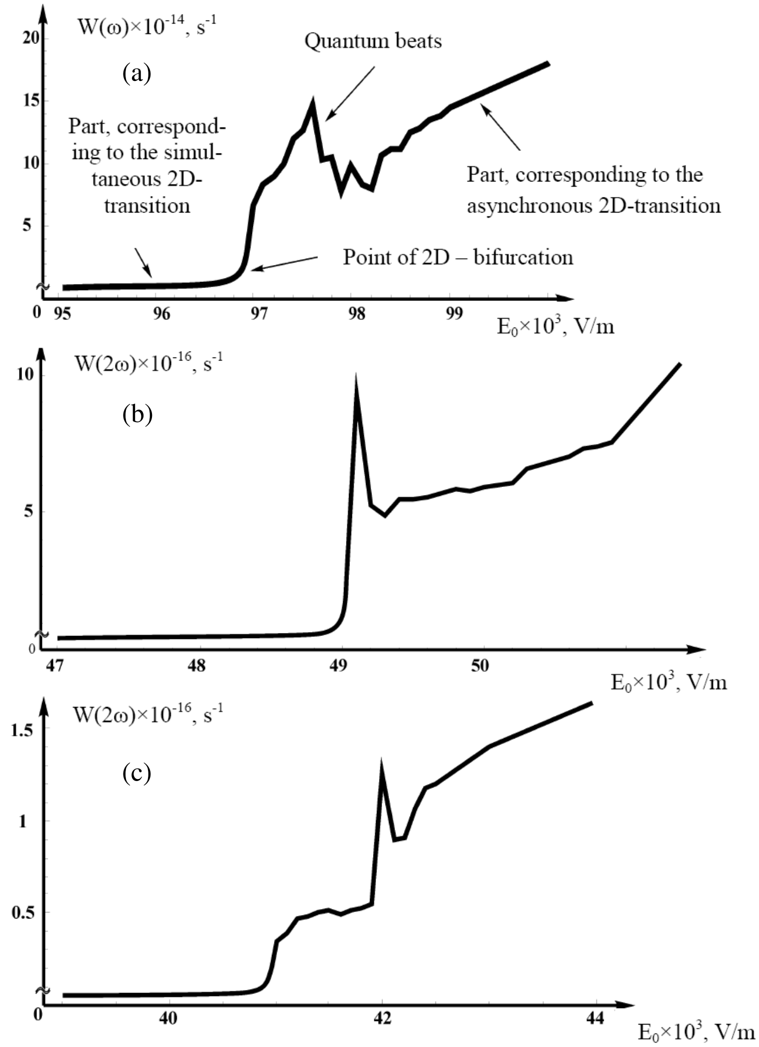

Figure 1: The dependence of TF-ionization probability for $D^{(-)}$-center in system, consisting of two interacting QM from intensity of external electric field E_0 at $U_0^* = 250$, $a_0 = 1$, $b_0 = 1.5$, $\eta_i = 7$, $\varepsilon_L = 1$, $\varepsilon_C = 1$: $a - \alpha = 0.38$, $\varepsilon_T = 1$; $b - \alpha = 0.37$, $\varepsilon_T = 1$; $c - \alpha = 0.37$, $\varepsilon_T = 1.5$.

4. CONCLUSION

Thus, optical and transport properties of the doped semiconductor QD with bio-conjugated shells can be used as fluorescent labels for visualization of biological objects and in nanomedicine for diagnosis and treatment of a number of serious diseases, including cancer. The experimental check of the predicted effects, such as 2D-bifurcations and quantum beats in the field dependence of the TF-ionization probability for $D^{(-)}$-center in system, consisting of two interacting QM, is also planned. The predicted effect can be used in high-precision devices of opto-and nano-electronics with controllable characteristics.

REFERENCES

1. Kurita, A., Y. Kanematsu, and T. Kushida, "Observation of optical memory effect due to interference of multiply scattered light by using a focused beam," *Journal of Luminescence*, Vol. 98, No. 1, 325–329, 2002, DOI: 10.1016/S0022-2313(02)00287-9.
2. Caldeira, A. O. and A. J. Leggett, "Influence of dissipation on quantum tunneling in macroscopic systems," *Phys. Rev. Lett.*, Vol. 46, No. 4, 211–214, 1981.
3. Larkin, A. I. and Yu. N. Ovchinnikov, "Quantum tunneling with dissipation," *JETP Letters*, Vol. 37, No. 7, 322–325, 1983.
4. Ivlev, B. I. and Yu. N. Ovchinnikov, "The decay of metastable states in the presence of close-barrier trajectories," *JETP*, Vol. 93, No. 2(8), 668–679, 1987.

5. Benderskii, V. A., E. V. Vetoshkin, E. I. Kats, and H. P. Trommsdorff, "Competing tunneling trajectories in a 2D potential with variable topology as a model for quantum bifurcations," *Phys. Rev. E*, Vol. 67, 026102, 2003.
6. Dahnovsky, Yu. I., V. D. Krevchik, V. Ya. Krivnov, M. B. Semenov, and K. Yamamoto, edited, *Transfer Processes in Low-dimensional Systems*, 690, UT Research Institute Press, Tokyo, Japan, 2005.
7. Leggett, A. J., A. K. Aringazin, M. B. Semenov, V. D. Krevchik, Yu. N. Ovchinnikov, K. Yamamoto, editors, "Controllable dissipative tunneling. Tunnel transfer in low-dimensional systems," 495, Fizmatlit, Moscow, 2011–2012.
8. Aringazin, A. K., Yu. I. Dahnovsky, V. D. Krevchik, M. B. Semenov, A. A. Ovchinnikov, and K. Yamamoto, "Two-dimensional tunnel correlations with dissipation," *Physical Review B*, Vol. 68, 155426, 2003.

Effects of Extremely High Frequency EMI on Growth and Some Parameters of Wheat Seedlings Nuclei

L. A. Minasbekyan and M. R. Darbinyan
Department of Biophysics, Yerevan State University, 1 Alek Manukyan St, Yerevan 0025, Armenia

Abstract— Low intensively EHF EMI capable to cause the replay of the biological system, appearing on all level of the organizations of the alive organism. Initial unit of the biological influence of EMI is the lipid layers of membrane, which stimulate peroxidation of lipids.

The phospholipids (PL) content of nuclear soluble fraction and membrane of wheat seedlings have been investigated. Under treatment of soak seeds by EM mm-waves of different frequency, to the 3-D day of germination occur redistribution in PL composition of seedlings nuclear subfraction. EM mm-waves influence not only on the PL content of nuclear envelope, but act and on the chromatin conformation, DNA melting parameters and DNA methylation, and by this path controlling of permeability of nuclear membrane and its surface charge.

We have study as well as electrokinetic property of intact nuclei from wheat seeds control and treated by different EMI (extremely high frequency) in the range 45–53 GHz, *in vitro* and *in vivo*. Nuclear envelope and its charge play significant role in the transport of macromolecules between nucleus and cytoplasm through nuclear pore complexes. The significant effect was observed at exposition of 20 min treated *in vitro* intact nuclei. This exposition led to the increasing of EKP that evidence that EMI change surface charge on the nuclei. The biological effective frequencies are narrow range 49–53 GHz with the expressed resonant frequencies close to 50.3 GHz and 53 GHz are revealed. On the basis of our study we suggested that EMI of this diapason increase of preservation system of living organisms. Biological replay directs to the surviving of organisms and in an adaptive reaction of organism against to the stress of physical factors of environment.

1. INTRODUCTION

In recent years because of wide introduction in a field of human activity a new types of communications (including cellular communication) and sending devices, the problem of electromagnetic safety assume extremely importance. Cellular answers to a biotic and abiotic stress it is expressed in change of an expression of some genes as a result of which there can be a denaturation of proteins [1] and change of phospholipids contents [2]. In this study the phospholipids (PL) content of nuclear soluble fraction and envelope of wheat seedlings have been investigated. Redistribution in PL composition of wheat seedlings nuclear subfraction has been obtained under treatment by EM mm-waves of different frequency. EM mm-waves influencing on the PL content of nuclear envelope can act and on the chromatin conformation, DNA melting parameters and DNA methylation, and by this path to control permeability of nuclear membrane and form its surface charge.

It is supposed that many structural changes which have arisen owing to such stressful impact generally have epigenetic character [3]. The purpose of this work was to reveal changes in the contents of phospholipids in the nuclear membrane and soluble nuclear fraction under the influence of extremely high frequency electromagnetic irradiation EHF EMI during germination of wheat seeds that will can to throw light on mechanisms of mm-waves influence with a live organism at cellular level.

The biological effective frequencies are narrow range 49–53 GHz with the expressed resonant frequencies close to 50.3 GHz and 53 GHz are revealed. On the basis of our study we suggested that EMI of this diapason increase of preservation system of living organisms. Biological replay directs to the surviving of organisms and in an adaptive reaction of organism against to the stress of physical factors of environment. The results of our study confirm the dependence between functional state of nuclei and its surface charge, which is influence and even can control permeabilization of nucleic membrane and even gene expression.

2. MATERIALS AND METHODS

Seed Germination. Seeds of hexaploid wheat: Tr. aestivum L. of Arshaluys variety presoaked for the night, then sow on trays and growing in a thermostat at temperature 26°C within 72 hours. For receiving irradiated by mm-waves seedlings presoaked for the night seeds irradiated with not thermal low-intensively EMI. The source of irradiation is served by generator of high-frequency signals of EMI G4-141 (made in the USSR) in a range of 45 GHz–53 GHz. Radiation carried out during 20 mines in capacity of radiation 0.64 mV/cm^2.

Nuclei Isolation and Fractionation. Nuclei from 3 day etiolated wheat seedlings received according to the Blobel and Potter method [4]. The precipitated nuclei repeatedly washed and received fraction of the pure intact nuclei then carried out fractionation on nuclear membranes and soluble nuclear fraction [5].

Phospholipid Extraction and Quantification. Phospholipids from soluble nuclear fraction and a nuclear envelope extracted by method of Folch as it was described in [5], and quantity of separated phospholipids' fractions estimated by the content of inorganic phosphorus according to the Ames method [6].

3. RESULTS AND DISCUSSION

Earlier we investigated changes of physical and chemical parameters of a nuclear membrane at various physiological conditions. It is shown that change of a physiological condition influences both the general electrokinetic potential of nuclei, and on the phospholipids content in nuclear sub-fractions that is reflected in the total contents of anionic phospholipids [2, 5, 7].

Results of experiments show that the phospholipids (PL) content in a **nuclear membrane** of seedlings to the 3-d day after 20 mines irradiation by EHF EMI at frequency of 50 GHz remains almost invariable against a control seedlings (see the Fig. 1(a)). Processing of the presoaked seeds by mm-waves of 50.3 GHz frequency during 20 mines led to increase of content of such PL, as PC and PE for 7% and 2% respectively (Fig. 1(a)). Higher frequencies of EHF EMI — 53 GHz, at the same exposition of treatment lead to increase in content of PC and PE at 8% and 9% correspondingly and to reduction a share of PA in a nuclear membrane almost in 3 times (see Fig. 1 and) which play important role both for structure and permeability of a nuclear membrane [5, 8]. Such sharp change can lead to considerable changes of properties of a nuclear membrane that earlier was discussed by us [5].

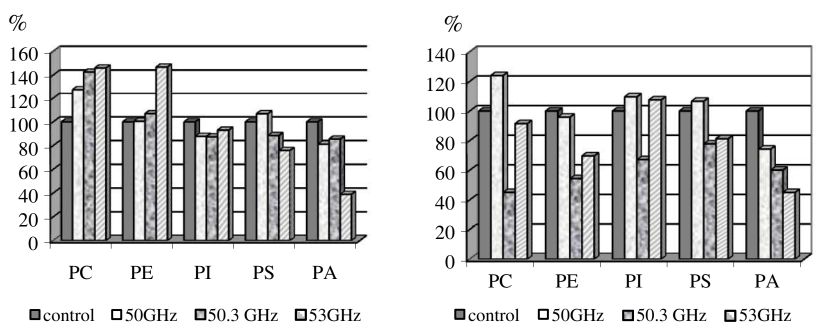

(a) (b)

Figure 1: A content of phospholipids fraction in % (from the general contents) of (a) nuclear membrane and (b) soluble nuclear fraction of the wheat seedlings in control and treated by different frequencies of mm-waves seeds to the 3rd days after single processing.

Processing by EHF EMI leads to changes in the PL content of nuclear envelope and soluble nuclear fraction. Have been observed the changes in the PL content of **soluble nuclear fraction** of seedlings on the 3-d day after single influence of EHF EMI at 50 GHz frequency during 20 min as it presented in Fig. 1(b). At the level of a whole organism we received positive influence of EHF EMI (probably, temporary) on physiological processes of an wheat seeds [9], however at cellular level in reply to an external stress there are structural changes on cellular level, which can have subsequently negative impact.

Treatment by mm-waves with frequency of 50.3 GHz also influences on PL content in composition of soluble nuclear fraction. As the data of experiments testifies about EHF EMI with frequency of 50.3 GHz has overwhelming influence on growth of seedlings [9], and modify PL content of soluble nuclear fraction (see Fig. 1(b)).

Influence of mm-waves by frequency of 53 GHz leads to increase of total quantity of PL in content of soluble nuclear fraction of seedlings nuclei and occur the changes in the ratio separate PL fractions (Fig. 1(b)). Such touch redistribution in content of individual PL that can lead to the conformational reconstruction between active and inactive chromatin compartments [1, 10, 11].

Thus under the influence of EHF EMI increase of the total content of anionic PL from 62% to 81% in nucleic soluble fraction concerning a control variant (see the Table), that can lead to chromatin decondensation as it is known from literature that addition of negatively charged lipids in vitro lead to the chromosome decondensation [12]. Increase of the total content of neutral PL and simultaneous sharp reduction of PA share in a nuclear membrane testifies in favor of that there is a smoothing of a surface and falling of the general superficial charge of nuclei.

Table 1: Content of neutral and anionic phospholipids of seedlings nuclear subfractions to the 3-d day after treatments by mm-waves (in % of total content).

Nucleic fraction		**Total content of PL (in %)**			
		control	**50 GHz**	**50.3 GHz**	**53 GHz**
Nucleic membrane	**neutral**	**35.34**	**40.01**	**43.57**	**51.72**
	anionic	**64.66**	**60.31**	**56.43**	**48.28**
Soluble nuclear fraction	**neutral**	**37.92**	**40.61**	**19.21**	**29.74**
	anionic	**62.08**	**59.42**	**80.79**	**70.26**

By changing the quality of the nuclear membrane and soluble nuclear fraction obtained next picture, as shown in Table 3. If we sum all the neutral phospholipids and separately anionic phospholipids of the nuclear membrane, we get a certain regularity: increase in the number of neutral and decrease anionic PL in content of the nuclear membrane. In contrast, in the soluble fraction observed decrease of neutral and the increase of anionic phospholipids. Such redistribution of the contents under the influence of EHF EME on nuclear subfractions may entail formation a difference of potential between the inner and outer surfaces of the nuclear membrane and cause a conformational change in the matrix and permeability of the nuclear membrane. According to the model offered by us about the mechanism of permeability of a nuclear membrane [13], reduction of a superficial charge of a nuclear membrane owing to content fall anionic PL led to reduction of potential difference between a surface of a nuclei and its inside layers that, in turn, can lead to reduction of transport activity of a membrane. At processing of mm-waves at frequencies in 50 GHz and 50.3 GHz also are observed reduction of anionic PL content in the composition of nuclear membrane. Probably, what exactly reduction of **anionic** PL in content of nuclear membrane has protective reaction of a cell in reply to action of stressing factors. Some authors marked sharp activation of free-radical reactions in a cells under a stress at the initial stage [14, 15], and in this case reduction of anionic PL as a part of a nuclear membrane (see the Table) compensates transport activity — by thus path playing a buffer role on the cellular level for a whole organism.

REFERENCES

1. Van de Vosse, D. W., Y. Wan, R. Wozniak, and J. D. Aitchinson, "Role of nuclear envelope in genome organization and gene expression," *Willey Interdisciplinary Reviews: Systems Biology and Medicine*, Vol. 3, No. 2, 147–166, 2011.
2. Minasbekyan, L. A., Z. V. Yavroyan, M. R. Darbinyan, and P. O. Vardevanyan, "Changes in the content of phospholipids in nuclear subfractions of wheat seedlings under influence of of gibberellic acid," *Rus. J. of Plant Physiology*, Vol. 55, No. 3, 412–418, 2008.
3. Yuan, G.-C., "Linking Genome to epigenome," *Wiley Interdisciplinary Reviews: Systems Biology and Medicine*, Vol. 4, No. 3, 297–309, 2012.
4. Blobel, G. and V. R. Potter, "Nuclei from rat liver: Isolation method that combines purity with high yield," *Science*, Vol. 154, 1662–1665, 1966.
5. Minasbekyan, L. A., Z. V. Yavroyan, M. R. Darbinyan, and P. O. Vardevanyan, "Comparative characteristics of phospholipid content in nucleic subfractions during embryos germination," *Russ. J. of Plant Physiology*, Vol. 51, No. 5, 784–789, 2004.
6. Ames, B. N., "Assay of inorganic phosphate, total phospholipid and phosphatases," *Meth. Enzymol.*, Vol. 8, 115–118, 1966.
7. Minasbekyan, L. A., S. A. Gonyan, M. A. Parsadanyan, and P. O. Vardevanyan, "The RNA — Export and electrokinetic potential of nucleus surface during germination of cereal embryos," *Rus. J. of Plant Physiology*, Vol. 49, No. 2, 250–254, 2002.

8. Wang, Z., C. Xu, and C. Benning, "TGD4 involved in endoplasmic reticulum-to-chloroplast lipid trafficking is a phosphatidic acid binding protein," *The Plant Journal*, Vol. 70, No. 4, 614–623, 2012.
9. Vardevanyan, P. O., A. V. Nerkararyan, L. A. Minasbekyan, and T. K. Khaltackchyan, "Comparative analyse of wheat and amarant sensitivity to the influence of EHF EMI," *International Conference*, Vol. 2, 107–110, Michurinsk, Russia, 2008.
10. Minasbekyan, L. A., V. P. Kalantaryan, and P. O. Vardevanyan, "Influence of low-intensively electromagnetic irradiation on the wheat seedlings chromatin fractions," *Brilliant Light in Life and Material Sciences*, V. Tsakanov and H. Wiedemann, Ed., 199–203, Springer, Dordrecht, 2007.
11. Kwon, S. H. and J. L. Workman, "The changing faces of HP1: From heterochromatin formation and gene silencing to euchromatic gene expression," *BioEssays*, Vol. 33. No. 4, 280–289, 2011.
12. Kuvichkin, V. V., "DNA-lipid interactions in vitro and in vivo," *Bioelectrochemistry*, Vol. 58, 3–12, 2002.
13. Minasbekyan, L. A., H. Badalyan, and P. H. Vardevanyan, "Correlation between aqueous pore permeability and surface charge of wheat seedlings nuclei," *Brilliant Light in Life and Material Sciences*, V. Tsakanov and H. Wiedemann, Ed., 205–211, Springer, Dordrecht, 2007.
14. Kreslavski, V. D., D. A. Los, S. I. Allakhverdiev, and V. V. Kuznetsov, "Signaling role of reactive oxygen species in plants under stress," *Rus. J. of Plant Physiol.*, Vol. 59. No. 2, 141–154, 2012.
15. Nazari M., M. Amiri, F. H. Mehraban, and H. Z. Khaneghah, "Change in antioxidant responses against oxidative damage in black chickpea following cold acclimation," *Rus. J. of Plant Physiology.*, Vol. 59, No. 2, 183–189, 2012.

Increasing of Fermentative and Antiinflamatory Activity of the Pleurotus Ostreatus (Jacq.:Fr.) Kumm. Culture by Modification of Growth Conditions by MM-waves

I. A. Avagyan[1], **S. G. Nanagulyan**[1], **and L. A. Minasbekyan**[2]

[1]Department of Botany and Mycology, Yerevan State University
1 Alek Manukyan St, Yerevan 0025, Armenia
[2]Department of Biophysics, Yerevan State University
1 Alek Manukyan St, Yerevan 0025, Armenia

Abstract— Epidemiological studies have indicated that almost all cases of cancer are associated with environmental factors including foods. Mushrooms have recently become attractive as health beneficent foods. Mushrooms have been used traditionally to treat many types of cancers. In mushroom's content there are such valuable compounds as the isoflavones genestein, β-glucans, glioxal-oxidase et al.. Plants contain isoflavones in primarily in glucoside forms and need in β-glucosidase which converts glucoside isoflavones in more potent aglicone forms. The unique feature of mushrooms in their content of β-glucosidase enzyme and various type of active peroxidases.

We have examined the most popular edible wood-decaying mushroom — *Pleurotus ostreatus* (Jacq.:Fr.) Kumm., which is wide-spreading in the forests, under influence of such an abiotic factor as the extremely high frequency waves in the interval of 45–53 GHz during 20 and 40 min on the 7-th day of mycelial culture's growth. The some conditions of such treatment led to significant rising of the peroxidase activity in mycelia culture homogenate. After the treatment of culture at the 3-th and 4-th days we examined the influence these waves on physiological parameters of the growth, changes in the protein content and fermentative activity. Such treatments and conditions will allow us to produce mushrooms with high content of active enzymes and high protein content without genetically transformation, which provides us with high valuable pharmaceutical raw materials.

We study antiinflammatory property obtained extracts from mushroom cultures with increased fermentative activity. Antiinflammatory activity of mushroom's extract investigate on the model of ear acute inflammation stimulated by xylol on white underbred rat-male. Antiinflammatory activity estimated by mass difference after 90 min of administration of the fresh extract from mushroom's culture, treated by various frequency of mm-waves. As evidence our investigations intraperitoneal introduction of extracts in a dose 2.5 ml/kg led to the decreasing of induced by xylol ear swelling compare with control up to 85%. Obtained data evidence about high antiinflammatory activity of extracts from culture of wood-decaying mushroom's, due to increased fermentative systems, having antioxidant activity and be able to inhibited ferments, participated in synthesis and metabolism of prostaglandins.

1. INTRODUCTION

Recently, much importance search of drugs containing a set of active compounds that can affect on the various links in the development of chronic inflammatory diseases. This is due to an increased interest to the natural sources of medicinal substances, which having a rich composition of biologically active compounds are a potential and relatively safe source for a new anti-inflammatory drug. Most of medicinal plant contain biologically active compounds, among which special attention have phenol compounds, saponins, terpenoids and fatty acids.

Antiviral drugs based on fungi consist in the ability to block the viral enzyme, synthesis or adsorption of viral nucleic acid, and the introduction of viruses in the mother cells, as well as indirectly — in the immunostimulatory activity of polysaccharides or other complex molecules. In this work, we used different frequencies of extremely high frequency of electromagnetic irradiation with aim to obtain mushrooms cultures with increased fermentative activity by the modulation of its growth conditions of growth on the peptone media. On the base of observed data we suggested application of mushroom cultures by EHF EMI for resolving of problem raw source for pharmaceuticals in the abundant volume by accessible and easy path (methods).

2. MATERIALS AND METHODS

Anti-inflammatory activity of mushroom's extract was carried out on the model of ear acute inflammation stimulated by xylol on white underbred rat-male with weight approximately 150–180 g. The weight of inflamed ear induced by xylol exceeds of no inflamed ear from the same rat. The extracts from mushroom culture for intraperitoneal introduction prepared in a dose of 2.5 mg/kg. Anti-inflammatory activity estimated by mass difference of inflamed and control ears after 90 min of intraperitoneal administration of fresh extracts from mushroom's culture, treated by different frequency of mm-waves in diapason from 45–53 GHz with exposition in 20 min and 40 min. On the difference of weights of these pair of rats ears tips also judge about influence of an extracts on inflammatory process.

Fermentative activity. Peroxidase activity was estimated by Baden [1], activity of β-glucosidase was estimated according to protocols in [2].

3. RESULTS AND DISCUSSION

Basidial macromycetes are not only value food, but can use as source of biological active compounds as the genestein, β-glucans, glioxal-oxidase et al.. The influence of the non-thermal extremely high frequency electromagnetic waves in the interval of 45–53 GHz on mycelial culture's β-glycosidase and peroxidase activity of wood decaying mushroom shown on Fig. 1 and Fig. 2 [3, 4].

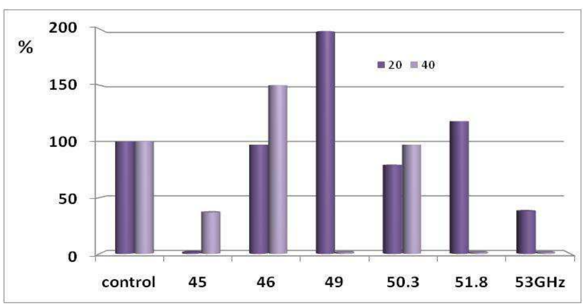

Figure 1: Activity of β-glycosidase varies with frequency and exposition time of EHF EMI.

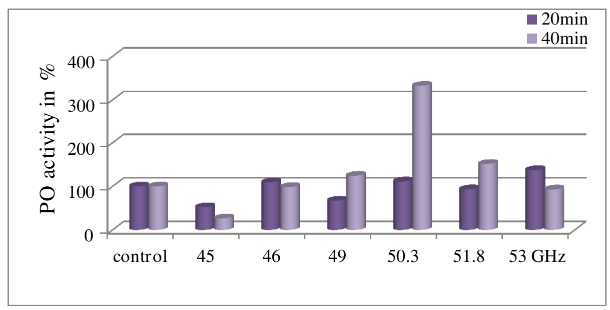

Figure 2: Peroxidase activity depended from frequency and exposition time of EHF EMI.

The mushroom is rich by β-glucosidase and peroxidases, as it necessary for synthesis and cleavage of lignin and polysaccharides of chitin and their derivatives. The structure of secondary cell wall of wood-rot mushroom — *Pleurotus ostreatus* consist from chitin, which is contain glucans and lignin (a polymer of phenylpropanoids). Phenol compounds exhibit strong antibacterial, antiviral and antioxidant activity, and possess neuroprotective and anti-tumor effect. Therefore, we have assumed that the extract from fresh culture of the mushroom Pleurotus ostreatus will be effective in use as anti-inflammatory drug. Study on determination of anti-inflammatory activity of the extracts of mushroom was carried out on models of rat ear acute inflammation induced by xylol.

Intraperitoneal introduction of an extract of the before cutting off of tips of both ears, is accompanied by reduction of the acute induced by a xylol that is shown in reduction of a difference between rat ears weight in different degree in comparison with a control extract from not irradiated culture of a mushroom. Distinctions in influence of an extracts depending on frequency of extremely high frequencies electromagnetic radiation (EHF EMR) of preliminary processing cultures are observed Fig. 3.

Then the inflammation of an ear induced by a xylol at a rat by whom it has preliminary been intraperitoneal injection of an extracts both from not irradiated and the irradiated mm-waves culture of a mushroom reduces an inflammatory acute by 85% (Fig. 3). Such effective influence of this extractfrom treated by mm-waves culture of mushrom may be explained by sharp increase of peroxidase activity in culture of a mushroom, as it is presented on Fig. 2.

The increase of activity peroxides (PO) testifies about activation of oxidizing processes also can be caused by formation in the irradiated system of a plenty peroxides of hydrogen, strengthening of free-radical processes conducting to the changes in properties of membrane. These changes can be result as direct influence EHF EMR on membrane, and, mediated through influence on mater.

Thus, the data indicate that the extract of the wood-rot mushroom has a pronounced anti-inflammatory activity, which is likely due to the presence of identified in the extract of the enzyme

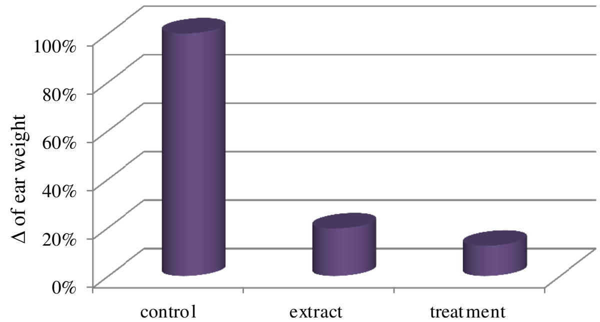

Figure 3: Decreasing in differences between rat ears dependent from preliminary introduction extract treatment by EHF EMI.

systems, which according to obtained data showing strong antioxidant activity and may inhibit the activity of enzymes involved in synthesis and biotransformation of prostaglandins. Moreover anti-inflammatory activity of extracts from mushroom culture increasing after treated the cultures during growth by mm-waves of different frequency, particularly in the range 45–53 GHz.

ACKNOWLEDGMENT

This research was partly supported by the National State Committee on Science of the Ministry of Education and Science of the Republic of Armenia, Grant (13A-1g29) to I. A. and the Armenian National Science and Education Fund to I. A.& L. M. (plant-3261).

REFERENCES

1. Baden, D. G. and M. D. Corbet, "Peroxidases produced by the marine sponge Iotrochota birotulata," *Comp. Biochem. Physiol.*, Vol. 64B, No. 3, 279–283, 1979.
2. Riou, C., L.-M. Salmon, M.-J. Vallier, Z. Günata, and P. Barre, "Purification, characterization, and substrate specificity of a novel highly glucose-tolerant β-glucosidase from *Aspergillus oryzae*," *Applied and Environmental Microbiology*, Vol. 64, No. 10, 3607–3614, 1998.
3. Minasbekyan, L. A., S. G. Nanagulyan, and I. A. Avagyan, "Increasing of β-glucosidase activity of Pleurotus ostreatus cultures on replay of stress influence," *Immunopathology, Allergology, Infectology*, No. 1, 26–27, 2009.
4. Avagyan, I. A., A. V. Nerkararyan, L. A. Minasbekyan, and S. G. Nanagulyan, "Influence of mm-waves on growth and fermentative activity of *Pleurotus ostreatus* mushroom culture," *Micologiya i Phytopatologiya*, No. 6, 77–83, 2011.

Influence of Near Earth Electromagnetic Resonances on Human Cerebrovascular System in Time of Heliogeophysical Disturbances

E. A. Sazanova[1], **A. V. Sazanov**[2], **N. P. Sergeenko**[2], **V. G. Ionova**[3], **and Yu. Ya. Varakin**[3]

[1]Clinical Hospital of Russian Academy of Sciences, Moscow, Russia
[2]Pushkov Institute of Terrestrial Magnetism, Ionosphere and Radio Wave Propagation (IZMIRAN), RAS
Moscow, Russia
[3]Scientific Center of Neurology RAMS, Moscow, Russia

Abstract— The physical processes influencing on cerebrovascular shifts at people are discussed in this work. It is supposed, that in a storm initial stage the stochastic resonance can be one of physical mechanisms of influence of external weak periodic signals against noise. External electromagnetic fluctuations can synchronize or desynchronize rhythms of electromagnetic fluctuations of cells of a brain and blood. Ionosphere indignations lead to fluctuations of frequencies and the periods of Alfen's ionosphere resonator which in turn can influence on rhythms of components of an organism, first of all on a brain and rheological properties of blood, as in experiences in vitro, and in vivo.

The hypothesis is checked also, that one of the internal reasons of observed biotropic effects is level increase of catecholamines and changes of viscosity properties of blood.

1. INTRODUCTION

Influence of electromagnetic disturbances in near Earth space, including atmosphere and biosphere, is proved in works of many researchers (reviews for example, [1]). During heliogeophysical storms of solar and magnetosphere origins, it be aggravated many diseases in human population — up to lethal outcomes. Professional reliability of persons, labile to influence of heliogeophysical disturbances decreases also which is especially shown in situations of extreme risk. Problems of adaptation of the person in conditions of heliogeophysical disturbances are actual, both on the Earth, and in space.

In the present paper attempt to compare such physical characteristics of an environment, as bioeffective frequencies of ionosphere resonators with own frequencies of a human body is undertaken. On the other hand it is researched time correlation between of heliogeophysical indexes and indicators of blood which reflect a condition of reulatory mechanisms providing optimisation of haemocirculation in the whole organism, that is especially important, in cerebrovascular system of the person.

2. THE IONOSPHERE ELECTROMAGNETIC RESONANCES, CAPABLE TO INFLUENCE ON STATE OF HEALTH OF PEOPLE

As statistics of the clinical indicators reflecting subjective state of health of people during heliogeophysical processes, databank of "Moscow Ambulance" on number of hospitalisation of people with cerebro-vascular shifts were considered. For diagnostics of heliogeophysical activity numbers of a stream of a solar radio emission on length of a wave 10.7 sm, intensity of ionosphere indignations and geomagnetic activity according to supervision IZMIRAN (Moscow) were used.

101 cases of the increasing number of calls in "Ambulance" during disturbances has been analysed. The facts of increase in number of "Ambulance" calls of people with vascular infringements have been compared with the moments of flashes and the beginning magnetic and ionosphere indignations. 29 cases from 101 were not possible to identify with heliogeophysical events, $\sim 50\%$ of cases of increase in number of calls correspond on time either solar flash, or the beginning magnetic or ionosphere storms; and, the greatest number of the raised quantity of calls corresponds to the beginning ionosphere indignations.

The carried out analysis shows, that there is statistically authentic communication of medical indicators with ionosphere indignations (26 cases) in F2 layer more, than with solar (10 cases) and geomagnetic storms (13 cases). And the agent of this influence, apparently, are the ionosphere resonators, good quality depends on an ionosphere condition.

We think the theories based on the approach to an organism as to difficult nonlinear self-oscillatory system, subject to resonant influence [2] are of interest. Such approaches give the chance to use the theory of fluctuations to many processes in an organism.

From all spectrum of the electromagnetic field observed on a surface of the Earth, biologically operating factor is in that frequency range where level of intensity of a field the greatest, and differences of intensity from quiet conditions to indignant are great enough. To such conditions a range of ultralow frequencies satisfies in which there is "the transparency window" of ionospheres. Electromagnetic waves with such frequencies freely reach the Earth, and their intensity increases during storms in tens times [3]. In a low-frequency range, except the micropulsations, generated by processes in magnetosphere of the Earth, and Shuman's resonances, in a wave guide the Earth — the ionosphere, also the resonator for Alfen's waves with the frequency of fluctuations depending on a thickness and electronic concentration of an ionosphere is formed. The first resonant frequency the Alfen's resonator is 0.5–3 Htz depending on an ionosphere condition. For example, in [4] the spectrum with three accurate peaks more to the left of Shumans peak — 1.32 Htz, 2.86 Htz, 4.84 Htz is resulted. Alfen's and Shuman's ionosphere resonant structure of a spectrum of an atmospheric noise background are regularly observable feature of background electromagnetic noise. In [4] it is shown, that parameters of resonant structure are appreciably supervised by ionosphere structure in a point of supervision and this fact apparently provides higher correlation of medical statistics with ionosphere parameters in comparison with geomagnetic and solar characteristics.

Now we will address to internal frequencies of an organism. An organism — system self-oscillatory and nonlinear. It means existence of system of resonators, the nonlinear terminator of increase of fluctuations and a feedback between the resonator and an energy source. The nervous system more often is responsible for a feedback in scales of all organism, as system with the greatest speed of a signal transmission. In scales such oscillatory systems as the nervous, blood system, heart, — a feedback carry out electrochemical processes and mechanical movement.

In Table 1 rhythms of a brain which are fixed both electroencephalographs, and magnetometers [5] are presented. The rhythms in Table 1 is characteristic for the healthy person. Alpha rhythm changes (reduction of its amplitude, aperiodicity) and presence delta — and teta-rhythms in a wakefulness condition are considered as symptoms of defeat of a brain.

In Table 2 own frequencies of blood system, comparable on size with bioeffective frequencies of an environment, and in Table 3 — resonant frequencies of a brain of the person and frequency of Shuman and Alfen ionosphere resonators are resulted.

It is interesting, that bioeffective frequencies for a brain 2 and 1 too have appeared connected with resonances of electromagnetic noise of an ionosphere, but not with Shuman's frequencies (see Table 3). From 3 it is visible, that the second and third harmonics of a resonance of brain nervous structures can be really caused the first harmonics of fluctuations in Alfen's ionosphere_resonator.

Thus, it is possible the following chain of events — variations of electronic concentration in a peak of F2 layer during time ionosphere indignations lead to fluctuations of frequencies and the

Table 1: Amplitude and frequency of rhythms of a brain on data of electroencephalography.

Name	**Frequency, Htz**	**Amplitude, mkV**
delta — rhythm	0.3–4	50–500
teta — rhythm	4–8	10–30
Alpha rhythm	9–13	30–60
Betta-1 — rhythm	13–25	3–10
Betta-2 — rhythm	25–35	
Gamma — rhythm	35–100	5–15

Table 2: Own frequencies of blood system and number of harmonics, comparable with bioeffective frequencies of an environment.

	Experimental data (frequency of the response, Htz; n-a harmonic
a vein	0.02 ($n = 3$); 0.06 ($n = 2$) [6]
an artery	0.2 ($n = 1$); 0.5–0.6 ($n = 1$) [6]
a capillary	1–2 ($n = 2$); 5–6 ($n = 1$) [6, 7]

Table 3: Resonant frequencies of a brain of the person and frequency of Shuman and Alfen ionosphere resonator. n — numbers of harmonics.

Bioeffective frequencies, Htz	**Resonant frequencies of ionosphere electromagnetic noise, Htz**
5–7.6 ($n = 1$)	7.8 ± 1.5 (Shuman's, $n = 1$)
2.5–3.8 ($n = 2$)	3.5 ± 1.25 (Alfen's, $n = 2$)
1.3–1.7 ($n = 3$)	1.75 ± 1.25 (Alfen's, $n = 1$)

periods ionosphere Alfen's the resonator which in turn can influence rhythms of components of an organism.

3. STATISTICAL COMMUNICATION OF HELIOGEOPHYSICAL DISTURBANCES WITH INFRINGEMENTS IN CEREBROVASCULAR SYSTEM OF THE PERSON

3.1. Material and Methods

Parameters of blood of 62 practically healthy men examined in process of screening of the population of Moscow, were received in Scientific center of neurology RAMS in quiet conditions and in time of heliogeomagnetic perturbations. It was not observed cerebrovascular pathology, attributes of ischemic illness of heart in examined subjects (according to the data from examination and ECG). The subjects were of follows age: 40–49 years — 42%, 50–59 years — 48.4% and 60–64 years — 9.6%. The examined persons was not connected to a professional harmfulness (chemical and toxic manufacture, the action of electromagnetic fields and radio-frequency radiations were excluded). In all examined persons defined viscosity of an integral blood (VK).

Variation of catecholamins of plasma: noradrenalin (NA), adrenalin (A), dofamin (DA) were measured in 73 men in different heliogeomagnetic conditions.

The received results are summarised and analysed depending on heliogeophysical characteristics. At mathematical processing the Student criterion was used, reliable considered differences at $p < 0,05$.

3.2. Results of Research

The results of examination have shown, that investigated haemorheological parameters tend to increase in time of heliogeomagnetic perturbations [8]. In a Fig. 1(a) dynamics of medial values VK per quiet days, for one–two days before storm, during perturbations and three days after storm are submitted.

As it is visible from a figure, viscosity of an integral blood per quiet days did not overstep the bounds of normal oscillations, while the majority of the viewed parameters begins to change already before the beginning magnetic storm.

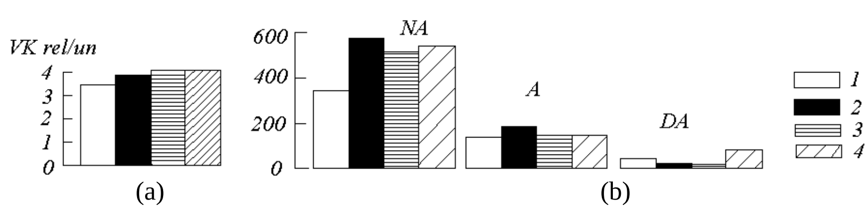

Figure 1: (a) Dynamics of viscosity of an integral blood (VK) medial values of healthy men, (b) dynamics of changes of concentrations of catecholamins of a blood plasma at the healthy people in per quiet days (1), one–two days before storm (2), during perturbations (3) and three days after storm (4).

The viewing of changes of catecholamins in a blood of the healthy people has revealed detrusions of investigated parameters in time of heliogeophysical paroxysms in comparison with quiet days (Fig. 1(b). During perturbations, 2 days prior to storm and in 2 days after storm a level NA raises ($p < 0.05$). In the disturbances periods the level A at the healthy persons also grows, with more grown until storm. Thus the concentration DA 2 days prior to storm and in time of storm decreases, accordingly on 51.7% and 60.6%. And in 2 days after storm grows more than in 2 times.

The carried out analysis has shown, that there is a stressful reaction at development of the resonant phenomena that conducts to occurrence in blood of "stress hormones" — catecholamins and glucocorticoids which it is direct or indirect influence activation of factors of system of curling of blood, first of all activating aggregative activity of cellular elements of blood, and also cause spasm development in vessels of microcirculatory channels, up to full deenergizing of a blood-groove in capillaries, exceeding admissible time parameter that can lead to development of the centers of an ischemia in a brain fabric.

This thesis is checked on samples of the register of a stroke of Scientific center of neurology (1255 cases, from them 590 men and 665 women), the of Moscow spent among the population.

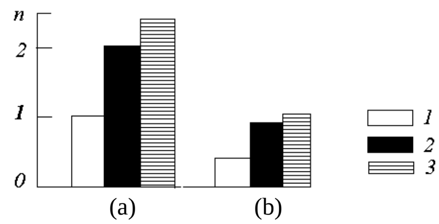

Figure 2: (a) Analysis of number of strokes and (b) death rates from it, according to the register of strokes in quiet heliogeophysical conditions (1), before (2) and during (3) storms.

On Fig. 2 are resulted generalised on all groups of patients of the histogram of distributions of frequency of a stroke and death rate from it. The increase of these indicators is visible already during indignation preparation in near Earth space. The further growth of characteristics during the periods of development of the indignation is obvious.

From spent above the analysis it is visible, that changes of concentration of neurotransmiters, viscosity of blood, and also the stroke cases, connected with strengthening heliogeophysical activity, in most cases occur already prior to the beginning of actually magnetic storm. It allows to assume, that changes of amplitude of a geomagnetic field don't operate on a human body at initial stages of indignations. It is supposed, that the stochastic resonance can be such physical mechanism. At development of the resonant phenomena there is a stressful reaction with activation of simptoadrenalin systems that promotes catecholamins concentration increase. Neurotransmiters activated curtailing system of blood also increase_proagregregativ of blood potential.

It is necessary to notice, that in the literature also direct influences of magnetic storms as on a brain fabric, and blood system (through nanomagnetic in systems of an organism and ferriferous blood cells — erythrocytes) also are discussed.

4. CONCLUSION

The results received above allow to assume, that, apparently, one of leading mechanisms of influence of heliogeophysical disturbance on cerebro-vascular system of the person are their effects on properties of blood and changes of concentrations of catecholamins. Ionosphere and geomagnetic indignations can serve as the indicator of influences of physical processes during time heliogeophysical disturbances on health of people.

It is obvious, that ambiguity of reaction of difficult nonlinear systems what the human body is, on weak external heliogeophysical influences depends not only on properties of the influencing factor, but also from a condition of the system. Change healthy people properties of the blood, connected with disturbances, are reversible. At sick people in the presence of the pathological processes developing at vascular system of a head — from the main arteries to channels of microcirculatory, are created conditions for development various on severity level cerebrovascular infringements, up to — a stroke.

REFERENCES

1. Komarov, F. I., T. K. Breus, S. I. Rapoport, V. N. Oraevskii, Yu. L. Gurfinkel, F. Halberg, G. Cornelissen, and S. I. Chibisov, "Medicobiological effects of solar activity," *Vestn. Ross. Akad. Med. Nauk*, No. 11, 37–49, 1994.
2. Uzdenskij, A. B., "Realization in cages of resonant mechanisms of biological action ultralow magnetic fields," *Materials of 2nd International Conference on Electromagnetic Fields and Health of the Person*, 43, Moscow, September 20–24, 1999,
3. Akasofu, S.-I. and S. Chapman, "An account of the wave and particle radiations from the quiet and the active sun, and of the consequent terrestrial phenomena," *Solar-Terrestrial Physics*, 509, Clarendon, Oxford, 1972.

4. Beljaev, P. P., S. V. Polyakov, V. O. Rapoport, and V. Ju. Trahtengerts, "Experimental researches of resonant structure of a spectrum of an atmospheric electromagnetic noise background in a range short period geomagnetic pulsations," *Radiophysics*, Vol. 32, No. 6, 663–672, 1989.
5. Povorinski, J. A. G. and V. A. Zabolotnyh, *The Text-book on Clinical Electroencephalography*, Medical Literature, 2000.
6. Oshe, A. I. and K. C. Urusov, "Electrochemical metabolism model," *Electromagnetic Fields in Biosphere*, Vol. II, 133–144, 1989.
7. Grigorev, J. G., et al., "Electromagnetic safety of the person," *The Russian National Committee on Protection from Non-ionized Radiation*, Moscow, 1999.
8. Varakin, Y. Y., V. G. Ionova, G. V. Gornostaeva, E. A. Sazanova, and N. P. Sergeenko, "Effects of heliogeomagnetic disturbances on haemorheological parameters of human," *PIERS Proceedings*, 1583–1586, Xi'an, China, March 22–26, 2010.

MRI Imaging of the Physiology of Fungal Pathogens in Cultivated Plants

E. Hutová[1], K. Bartušek[2], R. Kořínek[2], and R. Pokorný[3]

[1]Department of Theoretical and Experimental Electrical Engineering
Brno University of Technology, Technicka 12, Brno 612 00, Czech Republic
[2]Institute of Scientific Instruments, Academy of Sciences of the Czech Republic
Kralovopolska 147, Brno 612 64, Czech Republic
[3]Department of Crop Science, Breeding and Plant Medicine (FA)
Mendel University in Brno, Zemedelska 1, Brno 613 00, Czech Republic

Abstract— The imaging of the physiology of fungal pathogens is currently feasible by means of the microscopic technique or the photographic approach. However, these methods do not provide dependable results, mainly because their description of the physiology of pathogens is either too detailed or lacks the necessary aspects. The authors of this paper have analyzed the possibility of visualizing the physiology of pathogen mycelia via the MRI method. This approach provides an overall image of the pathogens and enables the mapping of the plant infestation stage. MRI imaging also appears to be a suitable tool to support further research of the pathogens and their influence on the attacked plants or other biological material.

1. INTRODUCTION

Plant pathology is a discipline that examines plant diseases and attempts to improve the chances for the survival of plants confronted with the effects of unfavorable environmental conditions and parasitic microorganisms. The digital analysis of the data describing the pathology of a plant has found wide application because the traditional determination of the plant pathogens is based only on the morphological characters that can be measured. The characters that can be investigated with a microscope or stereomicroscope are regarded as microscopic, and those which are recognizable without such devices can be denoted as macroscopic.

Using the microscopic approach, we are capable of mapping the individual elementary structural components of phytopathogens. However, to acquire information concerning the overall appearance of the given pathogen, we need to utilize the method of photographic imaging, which requires specialized knowledge of pathogens and their properties or effects on the nutrient medium.

2. PLANT MATERIAL

In the experiment, we used 2 types of fungal phytopathogens, namely *Colletrotichum acutatum* and *Fusarium sp.*, which had been produced at the Department of Crop Science, Breeding, and Plant Medicine (FA), Mendel University in Brno. These fungal phytopathogens are among the main diseases of cultured plants in the Czech Republic. In laboratory conditions, the fungi are grown on the potato-dextrose agar (PDA). The rate of growth in *Colletrotichum acutatum* is approximately 7.5 mm per day at 25°C. These pathogens can be identified on the basis of their morphological characteristics (shape and size of the conidias), using immunodiagnostic techniques (PTA ELISA) and molecular genetic methods (PCR with specific primers ITS4 and CaINt2, the ITS sequences of DNA) 1.

Colletotrichum acutatum is the major pathogen of fruit crops, causing economically important losses of temperate, subtropical and tropical fruits worldwide. *Colletotrichum acutatum* may overwinter as mycelium and/or appressoria in or on different parts of the host. The conidia are water-born and spread in a humid environment, the risk of infection thus being the highest during the wettest periods of the growing season. Current strategies for the management of this fungus comprise the exploitation of cultivar resistance, cultural, chemical, and biological control methods, and preventive strategies such as disease-forecasting models 2.

Most *Fusarium* species are soil fungi and have a world-wide distribution. Some are plant pathogens causing root and stem rot, vascular wilt, or fruit rot. Other species cause storage rot and are important mycotoxin producers. Several species, notably *F. oxysporum*, *F. solani* and *F. moniliforme*, are recognized as being pathogenic to man and animals, causing mycotic keratitis, onychomycosis and hyalohyphomycosis, especially in burn victims and bone marrow transplant patients 4.

Figure 1: Infested strawberry fruits.

Figure 2: Mycelium of the Phytophthora.

Figure 3: Infested ears of seedcorn.

3. METHOD

The general aim of the experiment was to perform in vivo measurement of the fungus early colonies by means of MRI techniques, and the entire process comprised several stages. Subsequently, we compared the acquired MR images weighted by proton density (PD) with the relaxation times T_1, T_2, and the last phase of the experiment consisted in determining the changes of the basic magnetic field B_0 caused by the magnetic susceptibility of the fungus colonies. The acquired results will be used for the examination of growth focused on mycelia. To measure the T_2 relaxation, we applied the spin echo (SE) method. The measurement of the T_1 relaxation was realized using inversion recovery (IR) and rapid acquisition with relaxation enhancement (RARE). All the described experiments were performed on the 9.4 T (Bruker) MRI systems operated by the Institute of Scientific Instruments, Academy of Sciences of the Czech Republic, Brno. The measured data were in the time and frequency domains assessed in the MAREVISI (8.2), and the approximation of data for determining the relaxation times was performed in MATLAB (7.11.1) [4].

4. RESULTS

The imaging of the complex physiology of fungal phytopathogens on a nutrient medium appears to be a comparatively demanding task, which could nevertheless be easily solved using the MRI imaging technique. The images below indicate that the visualization of a Petri dish conducted by means of the MRI enables us to gain a more comprehensive insight into the mapping of the physiology of fungal pathogens in cultured plants. In this respect, a very significant factor consists in the possibility of differentiating the pathogen tissue and its conidia from the actual growth medium (PDA). Differences between the images of the Coletotrichum fungal pathogen are shown in Figs. 8 and 9. The actual pathogen nests are marked in red and with the number 1, and

Figure 4: Colletotrichum — RARE-T_1+T_2 — map.

Figure 5: Colletotrichum — MSME_bas.

the nutrient medium (PDA) is labelled with the number 2. A brief visual comparison will reveal that the pathogen is well distinugished from the agar, but the photographs do not contain any information related to the properties of the pathogen.

Thus, no data are available on the pathogen structure, which could otherwise be obtained via microscopic imaging or other similar techniques. Yet we can still utilize the MRI approach to acquire the desired information. With this method, it is also possible to perform subsequent evaluation of the pathogen, whose size can then be determined by means of the MAREVISI program. An even more detailed and significant difference is obvious from a comparison of the Fusarium pathogen images (Figs. 10 and 11); the pathogen conidia, which are vividly apparent in Fig. 11, cannot be identified at all in the photograph. It is thus clearly demonstrated how the conidia penetrate through the nutrient medium, and this process is a concrete example of the intergrowth of a pathogen through an infested plant. Without any damage to the plant, we would not be able to acquire the described information. The processing of the information performed via the MAREVISI and MATLAB program will provide us with detailed data on the pathogen and the nutrient medium. The examples of detailed imaging carried out by means of a camera (Fig. 12) indicate that this technique is not suitable for the scanning of the pathogen structure. Not providing any detailed information, the approach is virtually of reference value only.

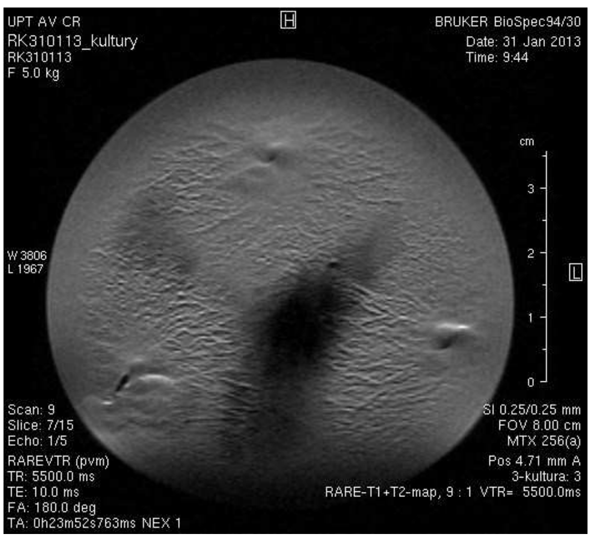

Figure 6: Fusarium — RARE-$T_1 + T_2$ map (pvm).

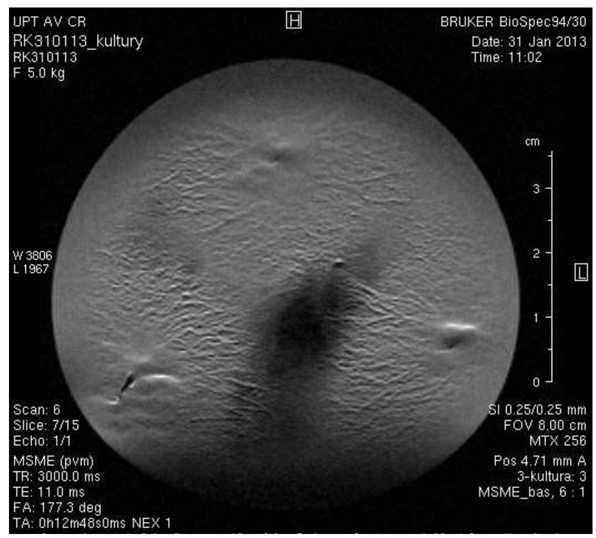

Figure 7: Fusarium — MSME_bas (pvm).

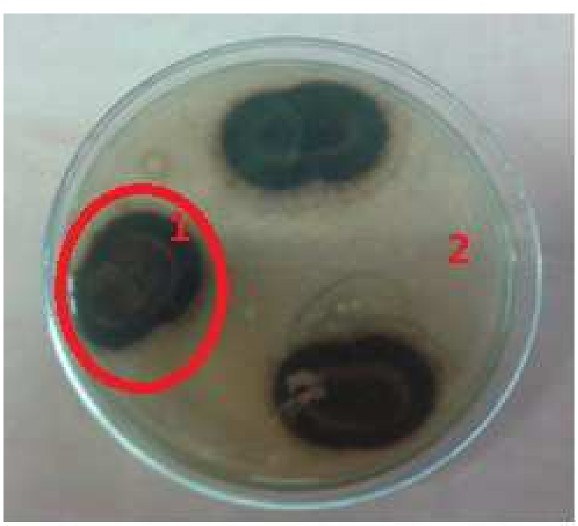

Figure 8: Colletoterichum in a Petri dish — camera scanning.

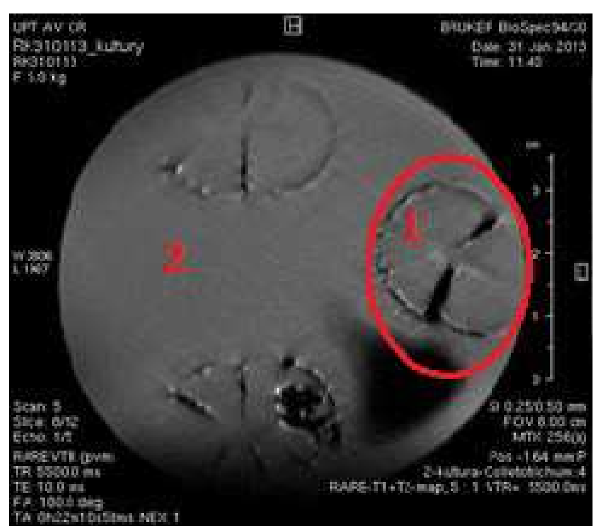

Figure 9: Coletotrichum: An MRI image.

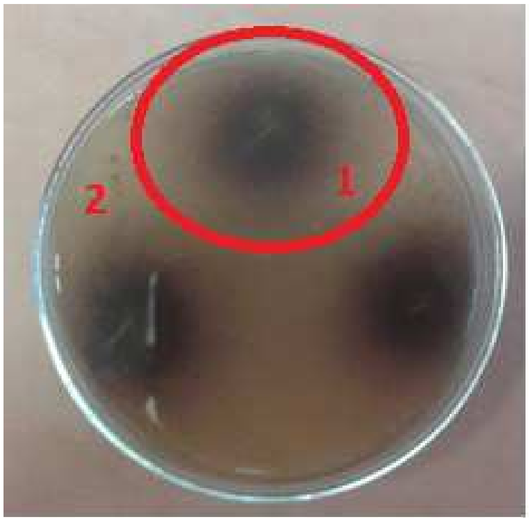

Figure 10: Fusarium in a Petri dish — camera scanning.

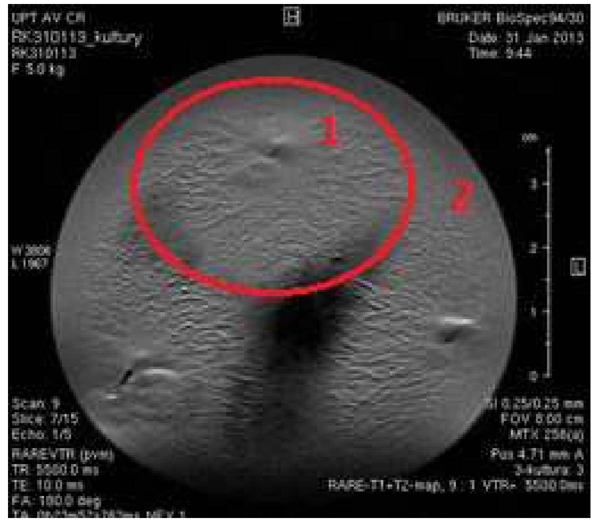

Figure 11: Fusarium: An MRI image.

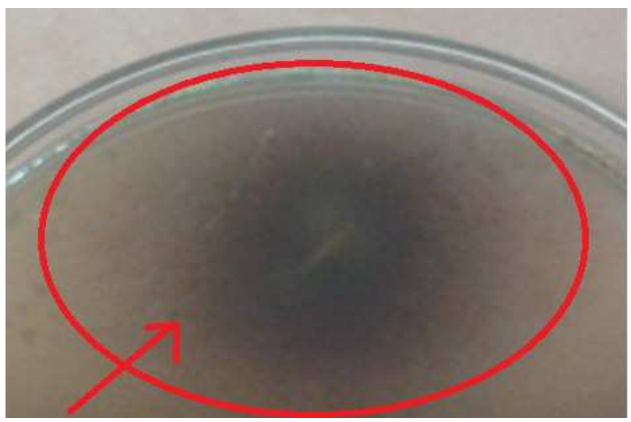

Figure 12: A detailed view.

5. DISCUSSION AND CONCLUSION

The results acquired on the basis of the experiment described in the paper have pointed to new horizons for the MRI and its applications within plant phytopathology. Although, in the basic sense, these perspectives include the actual imaging of the physiology and the subsequent description of various types of fungal pathogens, there is also the possibility of using the MRI method to visualize the initial stages of plant infestation with a fungal pathogen. It is assumed that further research in this field will analyze the impact of pathogen presence on the overall status and vitality of the damaged plant. In the introductory sections of this paper, the authors described the life cycle of pathogens. The MRI approach could be used to prove an attack by an temporarily inactive pathogen.

The main disadvantage of pathogen imaging by means of the MRI method consists in the long measuring period. In this context, it should be noted that rapid and descriptive imaging of pathogens can still be performed by partial visualization based on microscopic techniques.

ACKNOWLEDGMENT

This paper was supported within a project of the Education for Competitiveness Operative Programme, No. CZ.1.07.2.3.00.20.0175 (Electro-researcher), and a project of the BUT Grant Agency, No. FEKT-S-11-5.

REFERENCES

1. Lukáš, J. "Využití obrazové analýzy v rostlinolékařské praxi," *Metodika pro Úvar Státní Správy*, VÚVR, Praha, 2008.

2. Wharton, P. S. and J. Diéguez-Uribeondo, "The biology of Colletotrichum acutatum," *Anales del Jardín Botánico de Madrid*, Vol. 61, No. 1, 3–22, 2004.
3. Agrios, G., *Plant Pathology*, 5th Edition, Elsevier Academic Press, London, 2005.
4. Mikulka, J., E. Gescheidtová, P. Marcoň, K. Bartušek, and A. Šprláková, "Evaluation of tissue properties in MR images," *PIERS Proceedings*, 339–342, Moscow, Russia, August 19–23, 2012.

Comparison and Display of the Water Contained in Early Somatic Embryos

E. Hutova[1], **R. Korinek**[2], **K. Bartusek**[2], **and L. Havel**[3]

[1]Department of Theoretical and Experimental Electrical Engineering
Brno University of Technology, Technicka 12, Brno 612 00, Czech Republic
[2]Institute of Scientific Instruments, Academy of Sciences of the Czech Republic
Kralovopolska 147, Brno 612 64, Czech Republic
[3]Department of Crop Science, Breeding and Plant Medicine (FA)
Mendel University in Brno, Zemedelska 1, Brno 61300, Czech Republic

Abstract— This paper compares two methods that allow determining the total volume of water that occurs in early somatic embryos (ESEs). The first measurement was the measurement of proton density (PD) of early somatic embryos. This measurement was performed using MRI views (ISI ASCR Brno). The second technique was the weighing of dry sample of ESEs (Mendel University, Brno). These two methods were compared and the correlation coefficient of the two techniques was 0.816. Another important issue of the experiment was comparing the images of ESEs which were to show the biological processes in ESEs used relaxation times T_1 and T_2 to show the transition between the plant and the culture substrate.

1. INTRODUCTION

Magnetic resonance imaging (MRI) is a non-invasive tool applied by many researchers to study molecules. The MRI approach is frequently used not only in medicine, but also in biological, biochemical, and chemical research. In plant biology, MRI is utilized to support the research of water and mineral compounds transported within a plant [1, 2], the determination of plant metabolites [3, 4], the investigation of cellular processes [5], and the examination of the growth and development of plants [6]. MRI is also instrumental towards monitoring water changes in early somatic embryos of spruce (ESEs) [7]. These embryos constitute a unique plant model system applicable for the study of various types of environmental stresses (including metal ions) under well-controlled experimental conditions [8–10].

2. PLANT MATERIAL AND CULTIVATION CONDITIONS

A clone of early somatic embryos of the Norway spruce (Picea abies/L./ Karst.) marked as 2/32 and a clone of the Blue spruce (Picea pungens Engelm.) designated as PE 14 were used in our experiments. The cultures were maintained on a semisolid (Gelrite Gellan Gum, Merck, Germany) half-strength LP medium [11] with modifications [12]. The concentration of 2,4-dichlorofenoxyacetic acid and N^6-*benzyladenine was* 4.4 and 9 µM, respectively [13]. *The pH value was adjusted to* 5.7–5.8 before autoclaving (121°C, 100 kPa, 20 min). The organic part of the medium, excluding saccharose, was sterilized by filtration through a 0.2 µm polyethylensulfone membrane (Whatman, Puradisc 25 AS). The cultivation was carried out in Petri dishes (diameter 50 mm). The sub-cultivation of stock cultures was carried out in 2-week intervals; the stock and experimental cultures were maintained at the temperature of 23 ± 2°C in a cultivation box kept in a dark place. The experiment started with colonies of early somatic embryos which weight was about 3 mg. Ten colonies per one Petri dish were cultivated. After 2 weeks the colonies of early somatic embryos were harvested and after fresh weight determination they were dried at 105°C to stable weight. Thirty colonies were used for weighing and statistical analysis.

3. METHOD

The general aim of the experiment was to perform in vivo measurement of the ESEs using MRI techniques, and the entire process comprised several stages. Within the first step, a comparison was carried out of the volumes of water in the cultures (proton density measurement using a 4.7 T system) with the volumes of water determined upon the weight changes observed after desiccation of the sample. Subsequently, we compared the acquired MR images weighted by proton density (PD) and relaxation times T_1, T_2, and the last stage of the experiment consisted in determining the changes of the basic magnetic field B_0 caused by the magnetic susceptibility of ESEs. The acquired results will be used for the examination of growth focused on ESEs contaminated with heavy metals. To measure the T_2 relaxation, we applied the spin echo (SE) method; the measurement of the T_1 relaxation was realized using inversion recovery (IR) and rapid acquisition with relaxation enhancement (RARE). All the described experiments were performed on the 4.7 T (Magnex) and 9.4 T (Bruker) MRI systems operated by the Institute of Scientific Instruments, Brno. The MAREVISI (8.2) and MATLAB (7.11.0) programs were used for the processing.

4. RESULTS

A comparison of the volumes of water in the embryos measured via the above-discussed methods can be seen in Figs. 1 and 2. While the measurement using desiccation and subsequent weighting was conducted at MENDELU, the proton density measurement with the SE technique was performed at the ISI Brno.

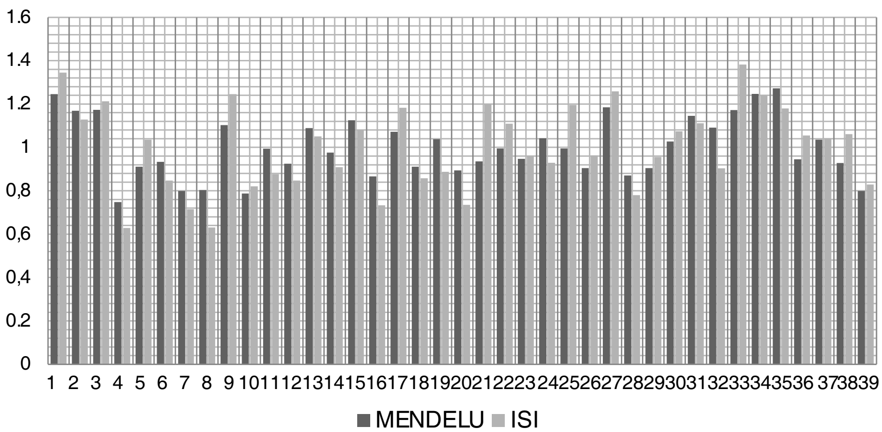

Figure 1: Comparison of the normalized values of the samples 1-39 measured at the ISI and MENDELU.

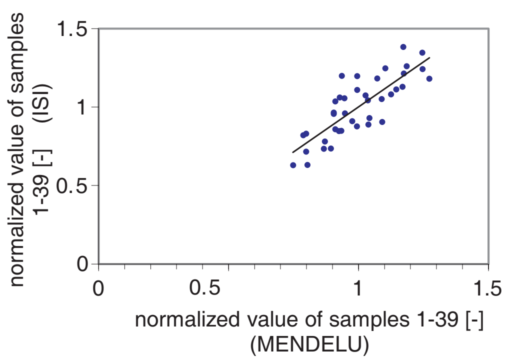

Figure 2: Normalized value of the samples measured at the ISI and MENDELU.

The data from MENDELU and the ISI were normalized to the mean value for all the samples examined. The correlation coefficient of the volumes of water measured by both methods is 0.816. The proton density, relaxation times T_1 and T_2, and B_0 maps of the embryos measured using the 4.7 T and 9.4 T MRI systems are shown in Figs. 3, 4, and 5.

The difference of the magnetic field between the embryos and the medium ($\Delta B_0 = 16.92\,\mu\mathrm{T}$) was established from the map of the magnetic field B_0. To measure the magnetic field B_0 map, we applied the gradient echo method ($\Delta T_E = 5\,\mathrm{ms}$, 9.4 T MRI system). Susceptibility difference ($\Delta\chi = 1.8 \cdot 10^{-6}$) is calculated from ΔB_0 (Fig. 6). Susceptibility difference is difference between susceptibility of embryos and substrate. A comparison of the relaxation times T_1 and T_2 in the embryos and the substrate can be seen in Table 1. The measurement was performed with the 4.7 T and 9.4 T MRI systems.

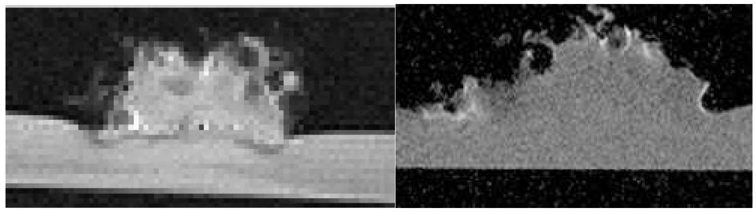

(a) (b)

Figure 3: Images of the PD of the ESEs. (a) 4.7 T magnet, (b) 9.4 T magnet.

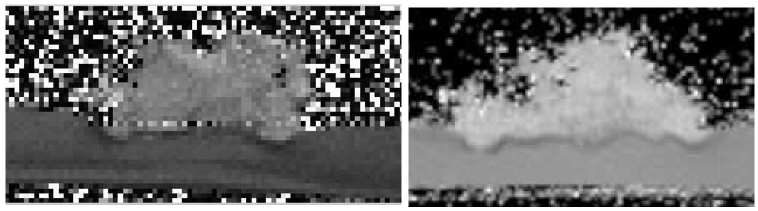

(a) (b)

Figure 4: Images of the T_1 map of the ESEs. (a) 4.7 T magnet, (b) 9.4 T magnet.

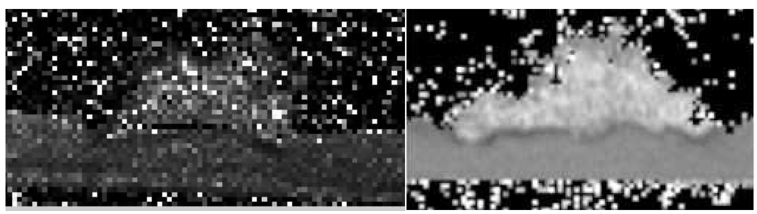

(a) (b)

Figure 5: Images of the T_2 map of the ESEs. (a) 4.7 T magnet, (b) 9.4 T magnet.

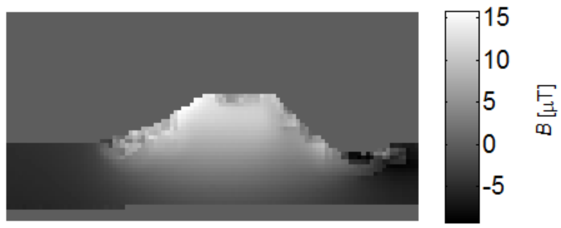

Figure 6: Map of the magnetic field ΔB_0 in a measured sample; the 9.4 T MRI system.

Table 1: Table of the relaxation times T_1 and T_2 in the ESEs and the substrate.

B_0 field	T_1 [ms]	T_2 [ms]	Method
ESEs			
4.7 T	748	64	IR/SE
9.4 T	1540	90	RARE/SE
Substrate			
4.7 T	492	36	IR/SE
9.4 T	988	51	RARE/SE

5. DISCUSSION AND CONCLUSION

The authors utilized two methods to carry out a comparison of the volumes of water in early somatic embryos. The first technique consists in MRI-based proton density (PD) measurement of the sample. The second method requires double weighting of the embryos before and after desiccation. The difference in weight is equal to the volume of water in the embryos. The correlation coefficient between the normalized results measured via both methods was 0.816; the results after the normalization of the mean value of the determined volumes shown in Figs. 1 and 2 exhibit differences. Generally, MRI may be used as an effective approach to non-invasive measurement of water in organic structures.

The above-mentioned differences between the volumes are caused by several factors: a) the volume of water is also evaluated for the area affecting the substrate (nutrient medium), b) low sensitivity of the RF coil, c) imperfect image segmentation. With the second method, the removal of embryo from the substrate can accompanied by accidental withdrawal of a larger amount of material than is necessary for the subsequent desiccation and weighing. The use of a higher magnetic field in combination with a small RF coil having high sensitivity can improve the signal-to-noise ratio (SNR) and, consequently, provide higher resolution and thinner slices. Table!1 shows the relaxation times T_1 and T_2 of the samples in different magnetic fields. The change of the relaxation times T_1 and T_2 on the boundary between the embryo and the substrate are of interest for the investigation of biological processes.

ACKNOWLEDGMENT

This paper was supported within a project of the Education for Competitiveness Operative Programme, no. CZ.1.07.2.3.00.20.0175 (Electro-researcher), and a project of the BUT Grant Agency, no. FEKT-S-11-5.

REFERENCES

1. Scheenen, T. W. J., F. J. Vergeldt, A. M. Heemskerk, and H. Van As, "Intact plant magnetic resonance imaging to study dynamics in long-distance sap flow and flow-conducting surface area," *Plant Physiol.*, Vol. 144, No. 2, 1157–1165, 2007.
2. Ionenko, I. F., A. V. Anisimov, and N. R. Dautova, "Early changes of water diffusional transfer in maize roots under the influence of water stress," *Biol. Plant.*, Vol. 54, 488, 2010.
3. Pu, Y. Q., F. Chen, A. Ziebell, B. H. Davison, and A. J. Ragauskas, *Bio. Energy Res.*, Vol. 2, 198, 2009.
4. Zulak, K. G., A. M. Weljie, H. J. Vogel, and P. J. Facchini, *BMC Plant Biol.*, Vol. 8, 2008.
5. Lambert, J., P. Lampen, A. von Bohlen, and R. Hergenroder, "Two- and three-dimensional mapping of the iron distribution in the apoplastic fluid of plant leaf tissue by means of magnetic resonance imaging," *Anal. Bioanal. Chem.*, Vol. 84, 231, 2006.
6. Glidewell, S. M., M. Moller, G. Duncan, R. R. Mill, D. Masson, and B. Williamson, *New Phytol.*, Vol. 154, 197, 2002.
7. Supalkova, V., J. Petrek, J. Baloun, V. Adam, K.Bartusek, L. Trnkova, M. Beklova, V. Diopan, L. Havel, and R. Kizek, "Multi-instrumental investigation of affecting of early somatic embryos of spruce by cadmium(II) and lead(II) ions," *Sensors*, Vol. 7, 743, 2007.
8. Marcon, P., K. Bartusek, J. Mikulka, and M. Cap, "Magnetic susceptibility measurement using 2D magnetic resonance imaging," *Measurement Science and Technology*, Vol. 22, No. 10, 2011.
9. Petrek, J., J. Vitecek, H. Vlasinova, R. Kizek, K. J. Kramer, V. Adam, B. Klejdus, and L. Havel, *Anal. Bioanal. Chem.*, Vol. 383, 576, 2005.
10. Vítečik, J., V. Adam, J. Petřek, J. Vacek, R. Kizek, and L. Havel, "Esterases as a marker for growth of BY-2 tobacco cells and early somatic embryos of the Norway spruce," *Plant Cell Tissue Organ Cult.*, Vol. 79, 195–201, 2004.
11. Von Arnold, S. J., "Improved efficiency of somatic embryogenesis in mature embryos of Picea abies (L.)," *Plant Phys.*, Vol. 128, 233–244, 1987.
12. Havel, L. and D. J. Durzan, "Apoptosis during diploid parthenogenesis and early somatic embryogenesis of Norway spruce," *Int. J. Plant Sci.*, Vol. 157, 8–16, 1996.
13. Vlasinova, H., M. Mikulecky, and L. Havel, "The mitotic activity of Norway spruce polyembryonic culture oscillates during the synodic lunar cycle," *Biol. Plant*, Vol. 47, 475–476, 2003.

Methods for the Sensing of Ionosphere Changes

M. Hanzelka, P. Fiala, and M. Friedl
Department of Theoretical and Experimental Electrical Engineering
Brno University of Technology, Technická 3082/12, Brno 616 00, Czech Republic

Abstract— The impact of the environment upon living organisms constitutes a crucial problem examined by today's science. In this context, research institutes worldwide have analyzed diverse positive and negative factors affecting the biological system of the human body. One such factor consists in the influence of the surrounding electromagnetic field. This paper presents the results of investigation focused on ionosphere parameter changes and their effect on the basic function of the nervous system. It is a well-known fact that the frequency of the so-called alpha waves of brain activity [1] ranges within 6–8 Hz. Changes in the electromagnetic and chemical composition of the Earth's surface may cause variation of signals in the above-defined frequency region of 6–8 Hz. Detailed examination of the overall impact of environmental factors upon the human organism is performed within a large number of medicinal disciplines. The research presented in this paper is concentrated on the sensing and detection of changes in the region of very low frequencies of the electromagnetic field; the authors apply both theoretical and experimental procedures to define the effects influencing brain activity.

1. INTRODUCTION

The low-level measurement of low frequencies (0.01–10 Hz) performed to evaluate the effect of magnetic fields on the human organism can be regarded as an interdisciplinary branch of science that embraces different types of research.

The set of provinces subsumed within the discussed subject comprises elementary research disciplines such as particle physics, geophysics, astrophysics, and metrology, which are all related to the investigation of the ionosphere and magnetosphere. Moreover, medical fields and problems, for example neurology and circadian rhythms, are also included in the scope of contributing elements. By further extension, the low-level measurements are interesting from the perspectives of theoretical electrical engineering and research of magnetic fields.

At this point, is is important to consider applied research disciplines, for example the measurement and radar technology in the following ranges: the ULF (Ultra Low Frequency Band: 300 Hz–3 kHz), SLF (Super Low Frequency Band: 30 Hz–300 Hz, and ELF (Extreme Low Frequency Band: 0.1 Hz–30 Hz). The group of auxiliary subjects or activities includes mathematical modelling of electromagnetic effects, the basics of biomedical research and biological feedback, and the influence of low-level magnetic fields on the human organism. The role of the above-mentioned disciplines is complemented by the fact that human beings do not exist as solitary entities but rather live in a wider community, which is influenced by each of its members. If the external magnetic fields influenced a human being to such an extent that they would change their behaviour within the social community at a higher level of statistical significance, it would be necessary to employ various questions of economics, mainly the evolution of economic value as a market phenomenon based on human behaviour and decision making. Scientists and researchers are currently preparing to solve special tasks related to the objectivization of the impact of low-level magnetic fields upon the human organism; such impact will be examined from the perspective of physical harm to cells [2] and mental condition of humans [3–6].

The current status of knowledge in this field is relatively unsatisfactory, and certain hasty conclusions have been made and found application even in hygienic standards. An example of such standards is the guideline issued by the Council of Europe and implemented by the ICNIRP (International Commission on Non-lonizing Radiaction Protection) in 1999 to establish the boundary values of magnetic flux in relation to the speed of magnetic field changes for very slowly changing currents. More concretely, this guideline introduces the value of 50 mT/s as the maximum magnetic flux change acceptable in an environment with a variable magnetic field at the frequency of 1 Hz and characterized by a permanent presence of humans. This value is many millions higher than the largest changes hitherto measured during the so-called magnetic storms, in which the Earth was exposed to charged particles from the Sun.

2. ORIENTATION OF THE METHODS FOR DETECTING IONOSPHERE DISTURBANCES

According to the conclusions of secondary research, there is mutual interaction between low-level electric or magnetic fields irradiated both by humans and the geomagnetic system of the Earth. However, this interaction can be scientifically validated only with difficulty [4, 7]. Some of the reasons for this situation may be the inadequate cohesion between the complex description of a human being, his/her biological feedback related to the internal and external electromagnetic fields, the scope of interdisciplinary scientific knowledge, and the complicated structure of devices designed for the measurement of low-level ULF, SLF, ELF of electric, magnetic, and electromagnetic fields [8]. This paper presents a portion of the research conducted in this province by the DTEEE, FEEC BUT; the research is built upon the current knowledge of low-level magnetic fields generated the geomagnetic system of the Earth and the solar system. The authors of this article have focused their attention on examining the effect of the changes of the geomagnetic system of the Earth that are due to solar activity. In this context, the research was also centered on proving the existence of the effect as a result of geomagnetic storms, which substantially influence low-level magnetic fields affecting the human organism, including its behavioural patterns and decisioning.

The actual analysis of the description of the effect could be performed from the outside. The magnetosphere of the Earth is a section of space where the motion of ionized particles influenced by Earth's magnetic field becomes evident. In the direction towards the Sun, the outer boundaries of the magnetosphere, the magnetopause, are located at the distance of approximately 10 radii of the Earth; in the opposite direction, the magnetosphere stretched beyond the orbit of the Moon. The position of the magnetopause is given by the precondition of equal pressure of the solar wind and magnetic field of the Earth:

$$\rho v^2 = \frac{B^2}{2\mu}, \tag{1}$$

where ρ is the density of electrically charged particles in the solar wind, v their instantaneous velocity, B the magnetic flux density, and μ the permeability of the environment ($\mu = \mu_0\mu_r$), where μ_0 is the permeability of vacuum, μ_r the relative permeability. The solar wind consists of the following components: electrically charged particles known as electrons, positively charged ions, $95^{\circ\circ}/_{\circ}H^+$, almost $5^{\circ\circ}/_{\circ}$ of He^{++}, and heavier ions. The wind conductivity causes a magnetic field. The solar wind flows past the magnetopause but does not penetrate the magnetosphere. As solar wind particles move at a supersonic speed, there occurs the so-called bow shock at the boundary of the plasmapause. At higher latitudes, cusps appear; these cusps separate the closed lines of force of the Earth's magnetic field from the open ones, which descend from the Sun. At the locations of these cusps, the electrically charged particles may penetrate the magnetosphere (the polar aurora) [9].

The environment in close vicinity of the Earth changes progressively; if we assume the direction away from the surface of the Earth, then the ionosphere, which consists of ionized particles, is located already at the altitude of 80 km. The greater the distance from the Earth's surface, or from the boundary of the ionosphere, the more ionized the gas in the interstellar environment is. In this space, the plasma with a higher mobility of the electrically charged particles starts to progressively dominate.

The most significant information to be acquired from the research into the status of the ionosphere is the electron concentration at a certain altitude above the Earth's surface. The electron concentration is established by means of ion probes. Such probes operate on the same principle as classic electromagnetic locators. A short electromagnetic pulse is sent upwards from a surface transmitting antenna, and the time for the signal to return to the transmitting antenna is measured. The electromagnetic wave bounces back in the ionosphere exactly at the altitude where its frequency equals the plasma frequency f_{pl}. Waves having a higher frequency, $f > f_{pl}$, pass through the plasma environment. The reflection altitude can be evaluated from the time delay of the return of the reflected wave. The maximum frequency of the signal which will reflect from the given layer is denoted as the critical frequency f_{kr}; the signals with a higher frequency $f > f_{kr}$ pass through the layer.

The indicator of the solar activity level is the flow of radio emission from the Sun at the wavelength of $\lambda = 10.7\,\text{cm}$ ($f = 2.8\,\text{GHz}$) [10]. Owing to the external electric and magnetic fields outside the region of the Earth, a wide variety of oscillations and waves at acoustic, radio, and optical frequencies may propagate through the plasma. This effect is connected with the oscillation of ions. Although the frequency range is considerable, the low-frequency spectrum appears to be the most suitable option for further research. The low-frequency wave lies in the acoustic band and is referred to as the magnetoacoustic wave, whose typical frequency is the ion plasma frequency [11].

The detection of changes in geomagnetic field disturbances could be performed by means of the so-called Schumann resonances. Until recently, this oscillation was at the frequency of $f_{sch} = 7.83\,\text{Hz}$; this frequency changes as a result of the impact exerted by phenomena such as solar wind or greenhouse gases. In 1953, Professor W. O. Schumann of Munich university, Germany, had found out that the cavity between the ionosphere and the Earth's surface could be interpreted as a spherical resonator. After Schumann's results were published in the *Technische Physik* journal, Dr. Ankermueller, a medical specialist, immediately related the resonances to brain wave rhythm (EEG). In 1954, the measurements conducted by W. O. Schumann and Herbert Koenig, who was to become Schumann's successor, confirmed the pulsation of the Earth at the frequency of $f = 7.83\,\text{Hz}$. Koenig then validated the correlation between the Schumann resonances and brain wave rhythms [12].

3. RESEARCH OF GEOMAGNETIC EFFECTS

In polar areas, the solar wind particles captured by the Earth's magnetic field travel along the lines of force to the upper layers of the atmosphere. Here, together with the ultraviolet radiation from the Sun, they excite and ionize neutral atoms. The excited atoms emit a distinctive glow, thus creating the well-known polar aurora. The ionized atoms are captured by magnetic lines of force and travel along them freely. But these are all only traditional facts. The desciption becomes somewhat more interesting with Cluster-based data [11]. It has been proved that the magnetic lines of force move and change; the elementary mode is caused by the revolution of the Earth. The lines of force close to the Earth are of approximately dipole character and revolve together with the Earth (this does not hold the more distant lines, which are elongated to form the "magnetic tail", Figure 1. On the day side (towards the Sun), the close lines of force are compressed by the solar wind more towards the Earth's surface; on the night side (away from the Sun), the same lines of force are farther from the Earth. Thus, there occurs oscillation of the lines of force caused by the rotation of the Earth. But this is not the only manner in which a line of force may start to oscillate. For example, the energy released during the switching of the magnetic lines of force in the curls at the sides of the magnetosphere causes the ultra-low frequency oscillation of the lines of force, the Gulf Stream, and motion of the Earth's magma.

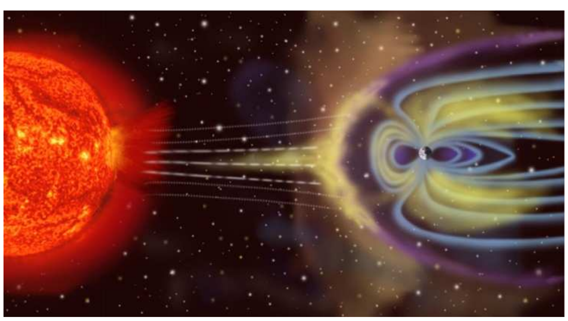

Figure 1: Magnetosphere, source [11].

The simple idea is that heavy ions are hung on a line of force like small weightings on a dangling string, along which they can move freely. Some ions receive a substantial amount of energy from the moving line of force, and the ions are ejected from the polar region either to a higher line of force or outside the Earth's gravitational field. The hypothesis of the described mechanism clarifies, for the first time, the high velocities of the ions along the lines of force of the Earth's field (the so-called parallel velocity). This velocity is in the direction of electron drift provided by the incident wave-particle from the direction of the Sun and at resonance; all these aspects are necessary to facilitate the excitation of instability. The concrete principle is the EIC (Excitation of the electrostatic ion cyclotron) instability [13].

4. DESIGN OF THE EXPERIMENTAL MEASUREMENT

The physical quantities for the discussed problem of the electromagnetic field as a wave (intensity of the electric and magnetic fields) are measured by methods and devices such as search coils, fluxgate magnetometers based on the principle of saturation, electric antennas, or electron beam drift (the $\mathbf{E} \times \mathbf{B}$ drift).

The physical quantities from the area of particle energy (density, energy) are measured using classical techniques such as Langmuir probes (employment of the probe to collect charged particles in isothermic and anisothermic plasma at intermediate pressures in the presence of a magnetic field), retarding potential analysers, electrostatic analysers, semiconductor and time-of-flight detectors [14].

The measurement of low-level magnetic and electromagnetic signals in the ULF, SLF, and ELF bands is a unique scientific discipline. The ULF, SLF, and ELF waves exhibit wavelengths of thousands of kilometers. The wavelength is $\lambda = v/f$, with units of [m; m/s, Hz], where v is the speed of the wave propagation in space, λ the length of the wave, and f its frequency. For an electromagnetic wave, v is the mean speed of light in vacuum.

In order to ensure the required sensitivity and operation in the ULF, SLF and ELF frequency bands, it is suitable to use a ferrite antenna, whose dimensions are significantly smaller than the wavelength of the incident electromagnetic wave. In such antennas, the phase φ_E of the

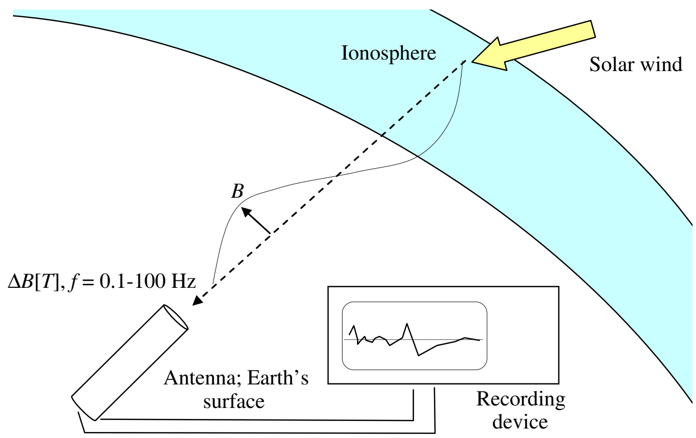

Figure 2: Schematic arrangement of the problem of detecting the changes in the Earth's ionosphere.

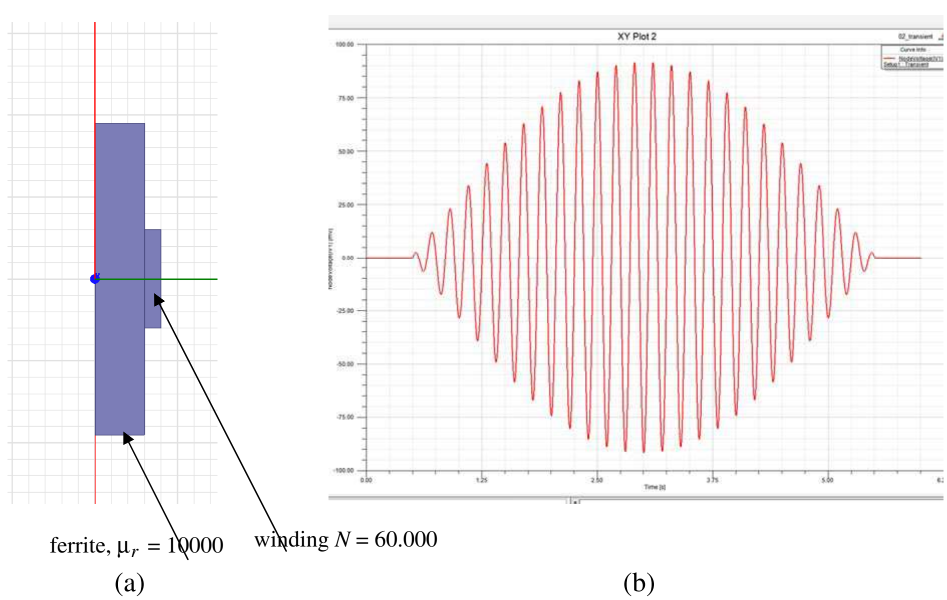

Figure 3: The numerical model of fefrite antenna (a) for detecting the changes in the Earth's ionosphere, (b) result of electric voltage induction for $\mathbf{\Delta B} = 5\,[\mu\mathrm{T}]$, $f = 0.1$–$100\,\mathrm{Hz}$.

electric field intensity E is practically identical at every point of the antenna, even when the incident electromagnetic wave is not planar. The directional characteristics of such antennas can be measured in the near electromagnetic field. Figure 2 shows the experiment focused on the application of a ferrite antenna for the detection of changes in the Earth's ionosphere, its numerical model and result in Figure 3 [15].

5. CONCLUSION

The outcome of the research will be compared with the hypotheses and results already published internationally; the main aim is to demonstrably measure the differences between instantaneous condition of the Earth's ionosphere as monitored at various locations of the planet.

With respect to the scope and interdisciplinary character of the research, we can expect that the scientific contribution of examining geomagnetic storms and the changes of low-level magnetic fields will consist mainly in the characterization of their effects upon the human organism, the biological feedback generated by some parts of the organism, behaviour of individuals or parts of communities, and decision making in the economic area.

The prepared experiments and measurement should prove the influence of the above-mentioned aspects on the human emotional system and thus point to the hitherto applied boundary values of magnetic flux density B in relation to the alterations of the magnetic field for very slowly changing electric currents and possible impact of these currents on human beings permanently present in such environment.

ACKNOWLEDGMENT

The research described in the paper was financially supported by a grant of the Czech Science Foundation (GACR 13-09086S), project of the BUT Grant Agency, No. FEKT-S-11-5/1012, and projects from the Education for Competitiveness Operative Programme Nos. CZ.1.07.2.3.00.20.0175 and CZ.1.07/2.3.00/30.0005.

REFERENCES

1. Ferris, J., "The brain generates an electric field that influences its own activity," *Scientific American Mind*, Vol. 21, No. 10, 2010, published online: October 28, 2010, doi:10.1038/scientificamericanmind1110-10a.
2. Stuchly, M. S., 2000.
3. Scorretti, R., N. Burais, L. Nicolas, and A. Nicolas, "Modeling of induced current into the human body by low-frequency magnetic field," *IEEE Transactions on Magnetics*, Vol. 41, No. 5, May 2005, Dostpnáz: 10.1109/TMAG.2005.846276.
4. Carrubba, S. and A. A. Marino, "The effects of low-frequency environmental-strength electromagnetic fields on brain electrical activity: A critical review of the literature," *Electromagnetic Biology ang Medical*, Vol. 27, No. 2, 83–101, Department of Orthopaedic Surgery, LSU Health Sciences Center, P. O. Box 33932, Shreveport, LA 71130-3932, United States, 2008.
5. Hashish, A. H., M. A. El-Missiry, H. I. Abdelkader, and R. H. Abou-Saleh, "Assessment of biological changes of continuous whole body exposure to static magnetic field and extremely low frequency electromagnetic fields in mice," Department of Physics, Faculty of Science, University of Mansoura, Mansoura 35516, Egypt Department of Zoology, Faculty of science, University of Mansoura, Mansoura 35516, available online, February 21, 2008, Dostupnáz: doi:10.1016/j.ecoenv.2007.10.002.
6. Gobba, F. M., A. Bargellini, M. Scaringi, G. Bravo, and P. Borella, "Extremely low frequency-magnetic fields (ELF-EMF) occupational exposure and natural killer activity in peripheral blood lymphocytes," Modena (MO), Italy Chair of Hygiene, Department of Public Health Sciences, University of Modena and Reggio Emilia, Via Campi 287, 41100, Modena (MO), Italy, 0048-9697/$ — see front matter ©2008 Elsevier B.V. All rights reserved.
7. Cocco, P. and R. J. Reiter, "Urinary 6-sulfatoxymelatonin excretion in humans during domestic exposure to 50 hertz electromagnetic fields," *Neuroendocrinology Lellers*, Vol. 26, No. 2, 136–142, published: April 2005, ISSN: 0172-780X.
8. Rose, L., "Review and assessment of select us space security technology proposals," Department of Materials Engineering, University of British Columbia, 309-6350 Stores Road, Vancouver, British Columbia, Canada v6t 1z4. 0265-9646/$ — see front matter ©2008 Elsevier Ltd. All rights reserved, Dostupníz: doi:10.1016/j.spacepol.2008.09.007.

9. Cohen, M. B., "ELF/VLF phased array generation viafrequency-matched steering of a continuous hfionospheric heating beam," Dissertation for the degrre of doctor of philosophy, October 2009.
10. www.nasa.gov.
11. Korepanov, V., G. Lizunov, O. Fedorov, Y. U. Yampolsky, and I. Ivchenko, "Ionosat — ionospheric satellite cluster," Lviv Centre of Institute of Space Research, Laboratory for EM Investigations, 5-a, naukova str., Lviv 79000, Ukraine, Received October 31, 2006; received in revised form February 25, 2008; accepted February 27, 2008, Dostupná z: doi:10.1016/j.asr.2008.02.022.
12. Gray, J. A., *The Neuropsychology of Anxiety: An Enquiry into the Functions of the Septo-Hippocampal System*, Oxford Univ. Press, Oxford, U.K., 1982.
13. Agrimson, E., S. Kim, N. Angelo, and R. Merlino, "Effect of parallel velocity shear on the electrostatic ion-cyclotron instability in filamentary current channels," Department of Physics and Astronomy, The University ofIowa, Iowa City, Iowa 52242, Received March 31, 2003; accepted July 1, 2003.
14. Barchanski, A., M. Clemens, H. Gersem, and T. Weiland, "Efficient calculation of current densities in the human body induced by arbitrarily shaped, low-frequency magnetic field sources," Received May 18, 2005; received in revised form August 10, 2005; accepted September 13, 2005, available online November 11, 2005, Dostupnáz: doi:10.1016/j.jcp.2005.09.009.
15. Steinbauer, M., P. Fiala, K. Bartušek, and Z. SzabÓ, "Experiments with accuracy of air ion field measurement," *PIERS Proceedings*, 1062–1066, Hangzhou, China, March 24–28, 2008.

Thermal Conductivity and Heat Capacity Measurement of Biological Tissues

J. Hrozek[1], D. Nespor[1], and K. Bartusek[2]

[1]Deptartment of Theoretical and Experimental Electrical Engineering, Brno University of Technology
Kolejni 2906/4, Brno 612 00, Czech Republic
[2]Institute of Scientific Instruments, Academy of Sciences of the Czech Republic
Kralovopolska 147, Brno 612 64, Czech Republic

Abstract— This paper deals with a measurement of temperature dependencies of thermal properties only by one measure system. Specific heat and thermal conductivity are two general thermal properties subscribed here. Thermal properties of each matter are dependent on their own temperature and are various in whole temperature range. Temperature dependencies of many commercial materials are well known. But temperature dependencies of biological tissues are very bad to find. However knowledge of these parameters is very important for the thermal processes computer simulation. The methodology described here is based on deficiencies of current measuring devices and methods. The thermal conductivity of biological tissues is measured with special needle (very thin and quite long) called the needle probe. This method has some good known deficiencies which are described in this paper. Specific heat is measured with Differential Scanning Calorimetry (DSC). The DSC is conventional method without serious deficiencies. Big disadvantage of current thermal properties measurement is in necessary using of both methods, i.e., two devices must be used. Methodology described here is based on simultaneous measurement of thermal conductivity and specific heat. It is the main advantage of our methodology. Measure system was tested only for measuring of thermal conductivity of 1% agar and for one steady state temperature. Next part of research will be focused on specific heat measurement and temperature dependencies of both physical quantities contained here. Results of temperature dependencies measurement will be used in computer simulation for hypothermia cancer destroying.

1. INTRODUCTION

The thermal conduction and the specific heat are two most important thermal properties of each matter for computer simulation. However these parameters could be very different in whole temperature range. Knowledge of these temperature dependencies is very important for correct results obtaining. For example see Figures 1(a) and (c) where temperature dependencies of stainless steel AISI 302 are shown.

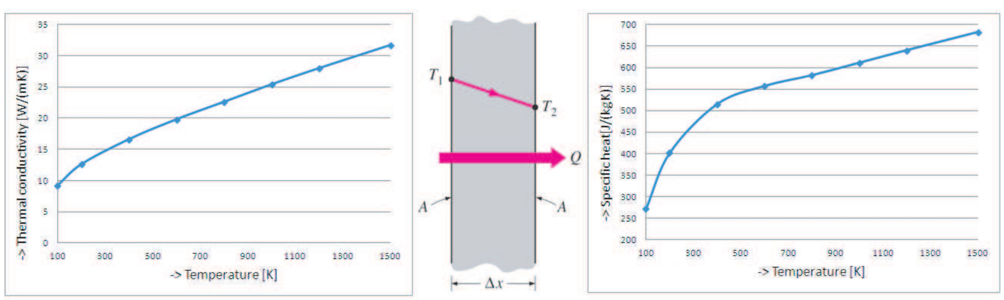

(a) (b) (c)

Figure 1: (a) Thermal conductivity. (b) Heat transfer scheme. (c) Specific heat.

We need to know temperature dependencies of the bio-material thermal properties. These properties will be used for real experiment of hypothermia optimization. We have to use two physical approaches for obtaining of all important data. The first one is calculation of thermal conductivity from known parameters of system, see Equation (1) and Figure 1(b). It's necessary to have only small temperature gradient $T_1 - T_2$ about 1 K for exact determination of the thermal conductivity by the temperature in $1/2$ of Δx.

$$Q = k \cdot A \cdot \frac{T_1 - T_2}{\Delta x} \quad \Rightarrow \quad k = \frac{Q \cdot \Delta x}{A \cdot (T_1 - T_2)}, \tag{1}$$

where Q is heat transfer [W], k is thermal conductivity [W/(m·K)], A is area [m^2], T_1, T_2 are temperatures on both sides of material [K], Δx is thickness [m].

The second physical approach is the calorimetry. The main principle of the calorimetry is in heat transferring from first matter of known weight to second matter of known weight. We need temperature steady state for reading of specific heat by this temperature. The principle of the calorimetry is obvious from the Equation (2).

$$Q_1 = Q_2 \quad \Rightarrow \quad C_1 \cdot m_1 (T_1 - T) = C_2 \cdot m_2 (T - T_2) \quad \Rightarrow \quad C_2 = \frac{C_1 \cdot m_1 (T_1 - T)}{m_2 (T - T_2)}, \tag{2}$$

where C_1, C_2 are specific heats of both matters [kJ/(kg·K)], m_1, m_2 are weights [kg], T_1, T_2 are initial temperatures [K], T is the final stable temperature [K]. Equation (2) could be expressed like Equation (3) corresponds with our experiment configuration on Figure 2.

$$C_P = \frac{Q}{m \cdot (T - T_2)}, \tag{3}$$

where C_P is specific heat capacity at constant pressure, Q is heat [W], m is weight [Kg].

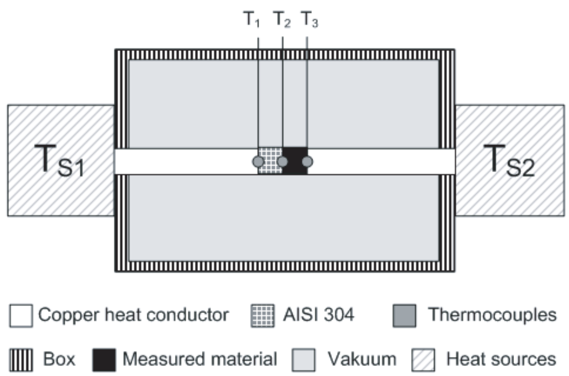

Figure 2: Scheme of thermal conductivity and specific heat measurement.

2. MEASUREMENT OF THERMAL CONDUCTIVITY

The laboratory preparation was made from a Plexiglas box, thermocouples type E, vacuum valve, two 15 cm copper heat conductors, 0.5 cm stainless steel AISI 304 heat resistor with known temperature dependencies, capsule with 0.5 cm of agar gel displayed in Figure 3 and box for crushed ice.

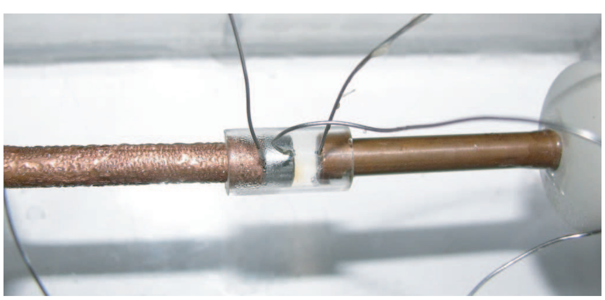

Figure 3: Detail of capsule.

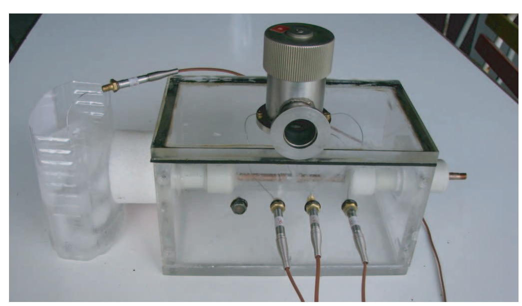

Figure 4: Measure system.

Laboratory preparation is displayed in Figure 4. A vacuum within the Plexiglas box is necessary for good insulation.

The laboratory preparation was stored in constant temperature about 18°C before the measuring → temperature of whole system was 18°C. Measuring was started at time 0 s if the crushed ice was filled into box. Temperatures T_1, T_2 and T_3 were measured with thermocouples type E connected to digital thermometer. Values were saved to the computer. Temperatures T_1, T_2 and T_3 were continuously measured as long as was the system came to steady state. The steady state was came 30 min after beginning of measuring. Temperatures of three boundaries were used for calculation of thermal conductivity at this moment. $T_1 = 1.4°\text{C}$, $T_2 = 2°\text{C}$ and $T_3 = 17.2°\text{C}$. These values were substitute to Equation (1) and the result is shown below:

$$\begin{aligned} |Q| &= k \cdot A \cdot \frac{T_1 - T_2}{\Delta x} = 14 \cdot 2.85 \cdot 10^{-5} \cdot \frac{1.4-2}{0.005} = \underline{\underline{0.0475\ J}} \\ k &= \frac{Q \cdot \Delta x}{A \cdot (T_1 - T_2)} = \frac{0.0475 \cdot 0.005}{2.85 \cdot 10^{-5} \cdot (17.2-2)} = \underline{\underline{0.55\ \frac{W}{m \cdot K}}} \end{aligned} \tag{4}$$

Thermal conductivity $0.55\,\text{W}/(\text{m} \cdot \text{K})$ at circa 15°C responds to known thermal conductivity of 1% agar gel. Two regulated heat sources will be added on both sides of laboratory preparation in next time research. This change allows setup the heat conductor temperature in wide temperature range. Measurement of specific heat will be also possible then.

3. COMPUTER SIMULATION

A physical model for verification good function of laboratory preparation was created in COMSOL multiphysics. Steady state temperatures along the whole composition are shown in Figure 5.

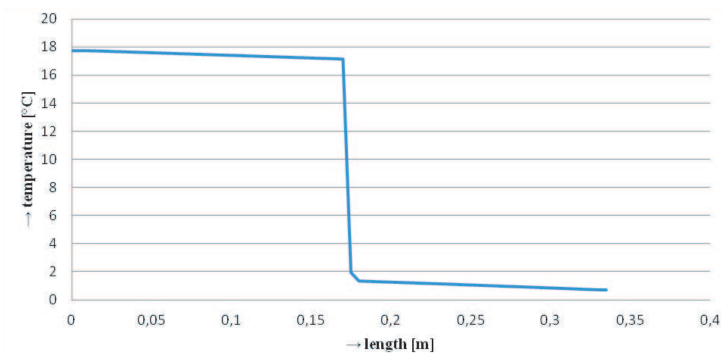

Figure 5: Steady state temperatures along the whole composition.

4. RESULTS

Real experiment with our laboratory preparation gave us thermal conductivity of 1% agar gel sample. Obtained value $0.55\ \text{W}/(\text{m} \cdot \text{K})$ at circa 15°C responds to known values.

5. CONCLUSIONS

The main goal of research discrabed in this paper is temperature dependecies meeasurement of bio-material thermal properties. This properties are very important for next computer simulation for optimization of hypothermia. The laboratory preparation measures the thermal conductiviti at one steady state temperature. Two added regulated heat sources will enable measure thermal conductivity of sample in wide temperature range. This improvement will enable measurement of specific heat also. Next part of research will be focused on simultaneously measurement of temperature dependencies of bio-material thermal properties. Final part of this research will be focused on cryosurgery optimization.

REFERENCES

1. Incropera, F., et al., *Fundamentals of Heat and Mass Transfer*, 6th Edition, 1024 Pages, Wiley, 2006, ISBN 978-0-471-45728-2.
2. Cho, Y., *Bioengineering Heat Transfer: Advances in Heat Transfer*, 443 Pages, Academis Press Limited, London, 1992, ISBN 0-12-020022-8.
3. Zhmakin, A. I., *Fundamentals of Cryobiology: Physical Phenomena and Mathematical Models*, 280 Pages, Springer, Berlin, 2009, ISBN 978-3-540-88784-3.
4. Akay, M., *Biomedical Engineering: Volume 1 and 5*, John Wiley and Sons, Hoboken, New Jersey, 2006, ISBN-13: 978-0-471-24967-2.
5. Hrozek, J., D. Nespor, and K. Bartusek, "Temperature dependencies measurement, proposal and preparing," *PIERS Proceedings*, 357–360, Kuala Lumpur, Malaysia, March 27–30, 2012.

Multi-resolution Analysis Technique for Lung Cancer Detection in Computed Tomograpic Images

Muhammad Usman[1], **Muhammad Shoaib**[2], **and Mohamad Rahal**[1]

[1]Department of Electrical Engineering, University of Hail, P. O. Box 2440, Hail, Saudi Arabia
[2]Department of Mathematics, University of Hail, P. O. Box 2440, Hail, Saudi Arabia

Abstract— This research proposed a multi-resolution based Lung parenchyma segmentation method to segment the lung lobes at accuracy levels acceptable for clinical applications. The methodology incorporates statistical models together with multi-resolution analysis techniques in order to enhance the accuracy of the overall system. In this research, the image quality and accuracy of detecting the cancer affected area are the key factors. The assessment of image quality and improvements are depending on the enhancement stage where different techniques have been used. Mainly Gabor filter and Fourier Transforms have been used for image enhancement and Pixel Percentage and Mask Labelling techniques have been used for detecting the area of interest.

1. INTRODUCTION

Lungs cancer ranked fourth in the number of deaths related with cancer in Saudi Arabia. In most cases Lung cancer does not show any symptoms in the initial stages. It is often suspected initially from chest x-ray or Computed Tomography (CT) scans done to evaluate a cough or chest pain. Several researchers have recommended Computer Aided Diagnosis (CAD) systems which facilitate early detection of lung cancer nodules at more curable stages. The First stage of those CAD systems requires the segmentation of the Lung parenchyma from the CT or x-ray Scan images. Improper segmentation of the Lung parenchyma will highly affect the accuracy of the Lung nodule detection or lung diseases classification algorithms. This research proposed a multi-resolution based Lung parenchyma segmentation method to segment the lung lobes at accuracy levels acceptable for clinical applications [1–3]. Several researchers have recommended Computer Aided Diagnosis (CAD) systems which facilitate early detection of lung cancer nodules at more curable stages. The First stage of those CAD systems requires the segmentation of the lung parenchyma from the CT or x-ray Scan images. Improper segmentation of the lung parenchyma will highly affect the accuracy of the lung nodule detection or lung diseases classification algorithms [4, 5]. This project proposes a noble multi-resolution based lung parenchyma segmentation method to segment the lung lobes at accuracy levels acceptable for clinical applications. The methodology incorporates statistical models together with multi-resolution analysis techniques in order to enhance the accuracy of the overall system. In this research, the image quality and accuracy of detecting the cancer affected area are the key factors. The assessment of image quality and improvements are depending on the enhancement stage where different techniques have been used. Mainly Gabor filter and Fourier Transforms have been used for image enhancement and Pixel Percentage and Mask Labelling techniques have been used for detecting the area of interest.

2. RESULTS AND DISCUSSION

The CT scan Data set is obtained from Early Lung Cancer Action Program (ELCAP) data base. Different lung segmentation algorithms were applied to test the database and it has showed that it is suitable for our study. A novel probablistic and multi-resolution based lung segmentation algorithm was tested. For the probablistic modeling we have employed Hidden markovian models. A Hidden Markov Model (HMM) is a statistical model in which the system being modelled is assumed to be a Markov process with unobserved states. HMMs are used to characterize the statistical properties of a signal. They have been used successfully in speech and face recognition for a number of decades and are now being applied to medical imaging. We have employed a block based segmentation method. The chest CT scan lung images are divided into super pixels and feature vectors are extracted for each block. These feature vectors were obtained from the multi-resolution analysis stage. To generate an observation sequence using HMM, an initial state must be chosen according to the initial state distribution; then an observation sequence should be chosen according to the probability distribution in the initial state. Many feature selection techniques have been tested in medical images, the most common being the use of intensity values. But in our case we used the features extracted from the multi resolution analysis to generate the initial states. In order to train the HMM, the image super pixels need to be of the same size. Using HMMTrain built-in function in MATLAB the state transition and emission probability matrixes were generated. The lung segmentation methods investigated in the previous stages could easily be applied on the latter stage of this project, to verify how the segmentation affects the lung nodule detection accuracy.In this research, to obtain more accurate results we divided our work into the following three stages:

A. Image Enhancement stage: to make the image better and enhance it from noising, corruption or interference. The following three methods are used for this purpose: Gabor filter (has the best results), Auto enhancement algorithm, and FFT Fast Fourier Transform (shows the worst results for image segmentation).

B. Image Segmentation stage: to divide and segment the enhanced images, the used algorithms on the ROI (Region of Interest) of the image (just two lungs, the methods used are: Thresholding approach and Marker-Controlled Watershed Segmentation approach (this approach has better results than thresholding).

C. Features Extraction stage: to obtain the general features of the enhanced segmented image using Binarization and Masking Approach.

Lung cancer detection system adopted in this research contains four basic stages. The first stage starts with taking a collection of CT images (normal and abnormal) from the available Database from IMBA Home (VIA-ELCAP Public Access) [6]. The second stage applies several techniques of image enhancement, to get best level of quality and clearness. The third stage applies image segmentation algorithms which play an effective rule in image processing stages, and the fourth stage obtains the general features from enhanced a segmented image which gives indicators of normality or abnormality of images.

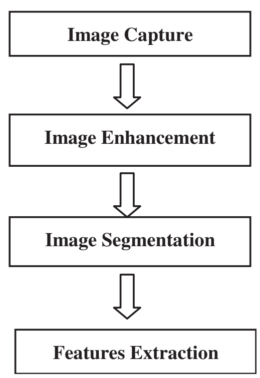

Figure 1: Lung cancer image processing stages.

2.1. Image Enhancement

The image Pre-processing stage starts with image enhancement; the aim of image enhancement is to improve the interpretability or perception of information included in the image for human viewers, or to provide better input for other automated image processing techniques. Image enhancement techniques can be divided into two broad categories: Spatial domain methods and frequency domain methods. Unfortunately, there is no general theory for determining what "good" image enhancement is when it comes to human perception. If it looks good, it is good. However, when image enhancement techniques are used as pre processing tools for other image processing techniques, the quantitative measures can determine which techniques are most appropriate [7]. In the image enhancement stage we used the following three techniques: Gabor filter, Auto-enhancement and Fast Fourier transform techniques.

2.2. Image Segmentation

Image segmentation is an essential process for most image analysis subsequent tasks. In particular, many of the existing techniques for image description and recognition depend highly on the segmentation results [8]. Segmentation divides the image into its constituent regions or objects. Segmentation of medical images in 2D, slice by slice has many useful applications for the medical professional such as: visualization and volume estimation of objects of interest, detection of abnormalities (e.g., tumours, polyps, etc.), tissue quantification and classification, and more. The goal of segmentation is to simplify and/or change the representation of the image into something that is more meaningful and easier to analyse. Image segmentation is typically used to locate objects and boundaries (lines, curves, etc.) in images. More precisely, image segmentation is the process of assigning a label to every pixel in an image such that pixels with the same label share certain visual characteristics. The result of image segmentation is a set of segments that collectively cover the entire image, or a set of contours extracted from the image (edge detection). All pixels in a given region are similar with respect to some characteristic or computed property, such as colour, intensity, or texture. Adjacent regions are significantly different with respect to the same characteristic(s). Segmentation algorithms are based on one of two basic properties of intensity values: discontinuity and similarity. The first category is to partition the image based on abrupt changes in intensity, such as edges in an image. The second category is based on partitioning the image into regions that are similar according to a predefined criterion. Histogram threshold approach falls under this category [9].

2.2.1. Threshold Approach

Threshold is one of the most powerful tools for image segmentation. The segmented image obtained from threshold has the advantages of smaller storage space, fast processing speed and ease in manipulation, compared with gray level image which usually contains 256 levels. Therefore, thresholding techniques have drawn a lot of attention during the past 20 years. Thresholding is a non-linear operation that converts a gray-scale image into a binary image where the two levels are assigned to pixels that are below or above the specified threshold value. In this research, Otsu's method that uses (gray thresh) function to compute global image threshold is used. Otsu's method is based on threshold selection by statistical criteria. Otsu suggested minimizing the weighted sum of within-class variances of the object and background pixels to establish an optimum threshold. Recalling that minimization of within-class variances is equivalent to maximization of between-class variance. This method gives satisfactory results for bimodal histogram images. Threshold values based on this method will be between 0 and 1, after achieving the threshold value image will be segmented based on it. Figure 4 shows the result of applying threshold technique.

2.2.2. Marker-controlled Watershed Segmentation Approach

Marker-driven watershed segmentation technique extracts seeds that indicate the presence of objects or background at specific image locations. Marker locations are then set to be regional minima within the topological surface (typically, the gradient of the original input image), and the watershed algorithm is applied [10]. Separating touching objects in an image is one of the most difficult image processing operations, where the watershed transform is often applied to such problem. Marker-controlled watershed approach has two types: External associated with the background and Internal associated with the objects of interest. Image Segmentation using the watershed transforms works well if we can identify or "mark" foreground objects and background locations, to find "catchment basins" and "watershed ridge lines" in an image by treating it as a surface where light pixels are high and dark pixels are low. Figure 5 shows a segmented image by watershed. According to the experimental subjective assessment during the segmentation stage, Marker-Controlled Watershed Segmentation approach has more accuracy 5.165%) and quality than thresholding approach (81.835%).

2.3. Features Extraction

Image Features Extraction stage is an important stage that uses algorithms and techniques to detect and isolate various desired portions or shapes (features) of a given image. To predict the probability of lung cancer presence, the following two methods are used: **binarization** and **masking**, both methods are based on facts that strongly related to lung anatomy and information of lung CT imaging.

2.3.1. Binarization Approach

Binarization approach depends on the fact that the number of black pixels is much greater than white pixels in normal lung images, so we started to count the black pixels for normal and abnormal images to get an average that can be used later as a threshold, if the number of the black pixels of a new image is greater than the threshold, then it indicates that the image is normal, otherwise, if the number of the black pixels is less than the threshold, it indicates that the image in abnormal.

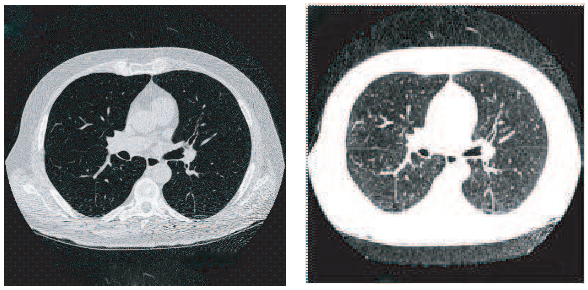

(a) (b)

Figure 2: Image enhancement using Gabor filter. (a) Original image. (b) Enhanced image using Gabor filter.

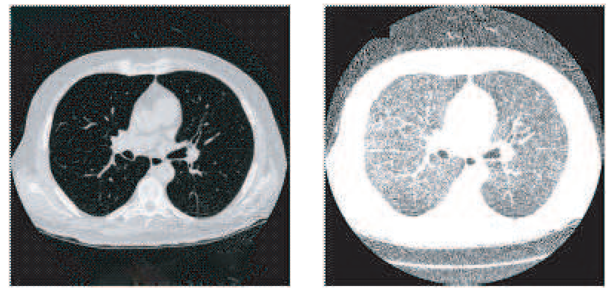

(a) (b)

Figure 3: Image enhancement using FFT. (a) Original image. (b) Enhanced image using FFT.

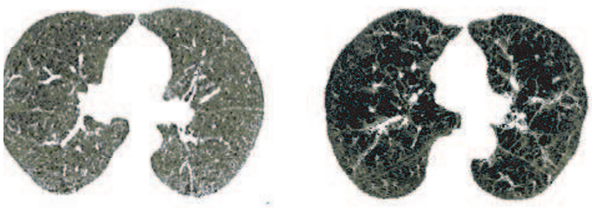

(a) (b)

Figure 4: Image segmentation using threshold technique. (a) Enhanced image using Gabor. (b) Threshold segmented image.

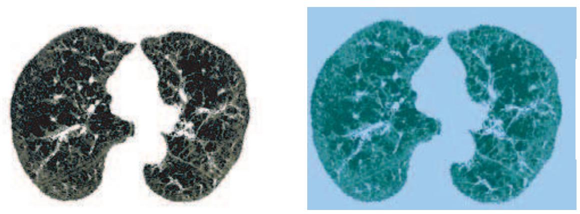

(a) (b)

Figure 5: Normal enhanced image by Gabor filter and its segmentation using marker-controlled Watershed approach. (a) Enhanced image by Gabor. (b) Segmented image by Watershed.

The threshold value that is used in this research is 17178.48 and the True acceptance rate (TAR) is (92.86%) and False acceptance rate (FAR) is (7.14%).

2.3.2. Masking Approach

Masking approach depends on the fact that the masses are appeared as white connected areas inside ROI (lungs), as they increase the percent of cancer presence increase. The appearance of solid blue colour indicates normal case while appearance of RGB masses indicates the presence of cancer, the TAR of this method is (85.7%) and FAR has (14.3%). Figure 6 shows normal and abnormal images resulted by implementing Masking approach using MATLAB.

Combining Binarization and Masking approaches together will lead us to take a decision whether the case is normal or abnormal according to the mentioned assumptions in the previous two approaches, we can conclude that image that has number of black pixels greater than white ones, indicates normality, and otherwise it indicates abnormality.

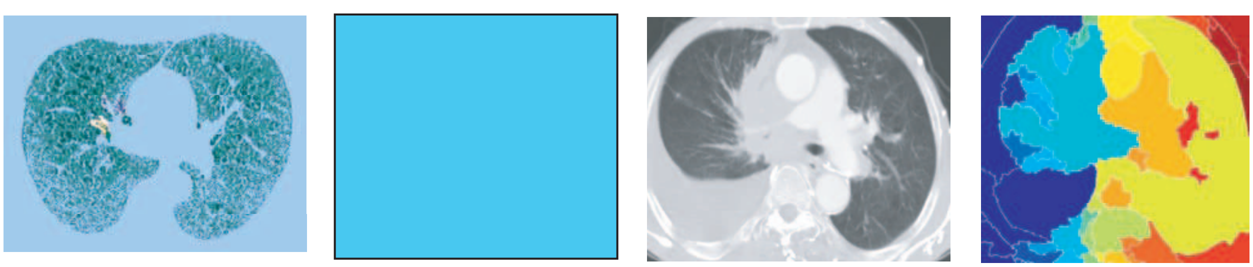

(a) (b) (c) (d)

Figure 6: Normal and abnormal images using Masking approach. (a) Normal image enhanced by Gabor, segmented by Watershed. (b) The resulted image indicates normality. (c) Abnormal image. (d) The resulted indicates abnormality.

3. CONCLUSION

An image improvement technique is developing for earlier disease detection and treatment stages; the time factor was taken in account to discover the abnormality issues in target images. Image quality and accuracy is the core factors of this research, image quality assessment as well as enhancement stage which were adopted on low pre-processing techniques based on Gabor filter within Gaussian rules. The proposed technique is efficient for segmentation principles to be a region of interest foundation for feature extraction obtaining. The proposed technique gives very promising results comparing with other used techniques. Relying on general features, a normality comparison is made. The main detected features for accurate images comparison are pixels percentage and mask-labelling with high accuracy and robust operation.

REFERENCES

1. El-Baz, A., A. A. Farag, R. Falk, and R. La Rocca, "Detection, visualization and identification of lung abnormalities in chest spiral CT scan: Phase-I," *International Conference on Biomedical Engineering*, Cairo, Egypt, December 1, 2002.
2. El-Baz, A., A. A. Farag, R. Falk, and R. La Rocca, "A unified approach for detection, visualization and identification of lung abnormalities in chest spiral CT scan," *Proceedings of Computer Assisted Radiology and Surgery*, London, 2003.
3. Zhao, B., G. Gamsu, M. S. Ginsberg, L. Jiang, and L. H. Schwartz, "Automatic detection of small lung nodules on CT utilizing a local density maximum algorithm," *Journal of Applied Clinical Medical Physics*, Vol. 4, No. 3, Summer 2003.
4. Krishan, A., "Evaluation of Gabor filter parameters for image enhancement and segmentation," *Electronic Instrumentation and Control Engineering*, 126, Thapar University, Master, Punjab, 2009.
5. Lee, S. L. A., A. Z. Kouzani, and E. J. Hu, "Empirical evaluation of segmentation algorithm for Lung Modelling," *IEEE International Conference on Systems, Man and Cybernetics*, Singapore, 2008.
6. Lung Cancer Database, Available at: https://eddie.via.cornell.edu/cgibin/datac/signon.cgi, accessed July 2012.
7. Ceylan, M., Y. Özbay, O. Nuri Uçan, and E. Yildirim, "A novel method for lung segmentation on chest CT images: Complex-valued artificial neural network with complex wavelet transform," *Turk. J. Elec. Eng. & Comp. Sci.*, Vol. 18, 613–624, 2010.
8. Kakar, M. and D. R. Olsen, "Automatic segmentation and recognition of lungs and lesion from CT scans of thorax," *Computerized Medical Imaging and Graphics*, Vol. 33, No. 1, 72–82, January 2009, ISSN 0895-6111, 10.1016/j.compmedimag.2008.10.009.
9. Nunes É, D. O. and M. G. Pérez, "Medical image segmentation by multilevel thresholding based on histogram difference," Presented at *17th International Conference on Systems, Signals and Image Processing*, 2010.
10. Otsu, N., "A threshold selection method from gray-level histograms," *IEEE Transactions on Systems, Man, and Cybernetics*, Vol. 9, No. 1, 62–66, 1979.

Novel Magnetic Lens for Static Magnetic Field Enhancement

Fei Sun[1, 2] **and Sailing He**[1, 2]

[1]Centre for Optical and Electromagnetic Research
Zhejiang Provincial Key Laboratory for Sensing Technologies
JORCEP, East Building #5, Zijingang Campus, Zhejiang University, Hangzhou 310058, China
[2]Department of Electromagnetic Engineering, School of Electrical Engineering
Royal Institute of Technology (KTH), S-100 44 Stockholm, Sweden

Abstract— We design a passive lens for static magnetic field enhancement by using transformation optics. In our previous study, our attention is focused on two dimensional (2D) structures. In this paper, we extend our design to three dimensional (3D) structures and good static magnetic field enhancement performance has also been verified by using 3D finite element method (FEM). This novel magnetic lens can greatly enhance the static magnetic field without additional power consumption from a weak background magnetic field, which may have potential applications in magnetic resonance imaging (MRI) and other compact high-field-magnet systems.

1. INTRODUCTION AND METHOD

High artificial static magnetic field will give a critical impact on the future of mankind. With the help of high static magnetic field, we can get an image with better resolution in magnetic resonance imaging (MRI), which means that we can find diseased cells earlier and get lesion location more precisely. By means of high static magnetic field, gene drug can be sent to the deeper tissues of human body for treatment. Up to now, the strongest artificial static magnetic field we human being can create is no more than 45 T (created at the National High Magnetic Field Laboratory in the United States, which consumes an electrical power of about 30 MW in a small air bore with a diameter of only 32 mm [1, 2]). In many cases, we need some special devices (referred as magnetic lenses) to farther enhance the static magnetic field without additional power consumption from a weak background magnetic field [3]. These devices will have applications in compact high-field-magnet systems [4].

We have designed a magnetic lens based on space-folded transformation optics (TO), which is a compact passive device and can greatly enhance the background magnetic field (e.g., if the background field is 1 T, the magnified field can reach 50T in a large 2D free space region) [5]. The performance of the proposed 2D lens has been verified in our previous paper [5]. In this paper, our attention is focused on studying the performance of the 3D magnetic lenses based on space-folded TO. The designed lens is a ring with inner radius R_1 and outer radius R_2 in x-y plane and infinitely long in z axis. The material parameters of this lens can be written as [5]:

$$\mu=\begin{cases}\mathrm{diag}\left(1,1,\left(\frac{R_3}{R_1}\right)^2\right), & \rho\in[0,R_1)\\ \mathrm{diag}\left(\frac{\rho-R_2\frac{R_1-R_3}{R_2-R_3}}{\rho},\frac{\rho}{\rho-R_2\frac{R_1-R_3}{R_2-R_3}},\left(\frac{R_2-R_3}{R_2-R_1}\right)^2\frac{\rho-R_2\frac{R_1-R_3}{R_2-R_3}}{\rho}\right), & \rho\in[R_1,R_2]\\ \mathrm{diag}(1,1,1), & \rho\in(R_2,\infty)\end{cases}\tag{1}$$

where $\rho=\sqrt{x^2+y^2}$. R_3 is a parameter which determines the enhancement factor, e.g., if the weak background magnetic field is 1 T, the enhanced magnetic field in the center region of the device ($\rho<R_1$) is R_3/R_1. We should note the designed lens is infinitely long in z axis. However in practice, we cannot fabricate an infinite device. Thus in the following simulation, we only simulate a lens with finite height $h=0.5$ m in z direction. Our simulation is based on 3D finite element method [6]. As shown in Fig. 1, even if the height of the lens in z direction is finite, it still keeps very good magnetic field enhancement performance. When the weak background static magnetic field 1 T incidents from z direction onto the lens, and we can see, we can obtain an enhanced magnetic field about 25 T in the center part of the lens. The more interesting is that the enhanced magnetic field is almost uniform. In the following, we will try to reduce the material parameters of the device, which will make it more easily to be realized and applied in MRI or other practical

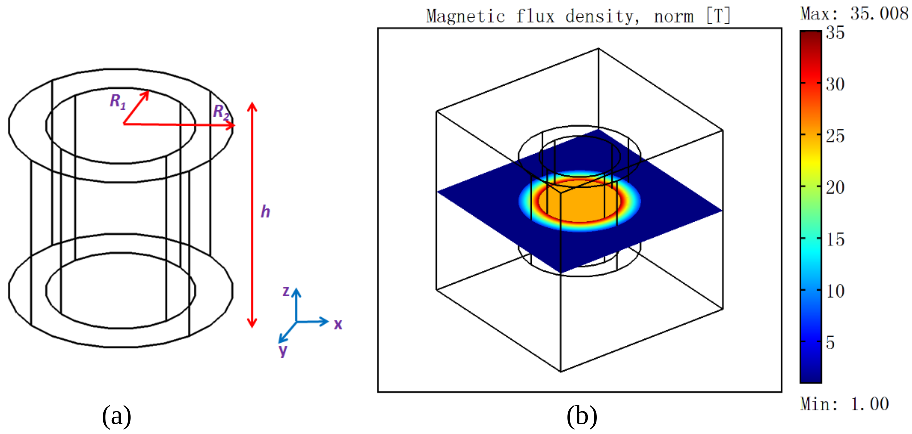

Figure 1: (a) The geometric structure of the lens. (b) 3D FEM simulation result. The parameters of the magnetic lens is $R_1 = 0.2\,\mathrm{m}$, $R_2 = 0.3\,\mathrm{m}$, $R_3 = 1\,\mathrm{m}$ and $h = 0.5\,\mathrm{m}$. The background magnetic flux incidents from z direction with amplitude 1 T onto the lens. We plot the magnetic flux distribution on a cross section of the lens which passes through the center of the lens. The material parameters of the lens are described by Eq. (1).

systems. Considering the magnetic flux incidents from z direction, thus only the permeability in z direction plays a leading role of our lens. The parameters described by Eq. (1) can be reduced as:

$$\mu = \begin{cases} \mathrm{diag}\left(1, 1, \left(\frac{R_3}{R_1}\right)^2\right), & \rho \in [0, R_1) \\ \mathrm{diag}\left(1, 1, \left(\frac{R_2-R_3}{R_2-R_1}\right)^2 \frac{\rho - R_2 \frac{R_1-R_3}{R_2-R_3}}{\rho}\right), & \rho \in [R_1, R_2] \\ \mathrm{diag}(1, 1, 1), & \rho \in (R_2, \infty) \end{cases} \tag{2}$$

The performance of the reduced magnetic lens has also been verified by FEM (see Fig. 2). The simulation result shows that if the magnetic flux incidents from z direction, only the permeability in z direction of the lens influences the performance of the lens. As shown in the Fig. 2, the reduced lens still keeps good performance and the enhanced magnetic field in the center region of the lens is still highly uniform, which is required in MRI. We should also mention that if we want to apply our lens to a practical MRI system, there are still two more obstacles should be overcome: one obstacle is μ_z in the region $R_1 <= \rho <= R_2$ is negative (see Eq. (2)) which still cannot be achieved under current technology. The other is μ_z in the region $\rho <= R_1$ (see Eq. (2)) is not air (unlike

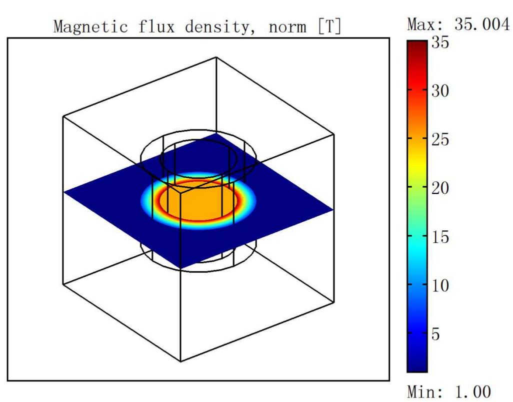

Figure 2: The 3D FEM simulation result: we keep the same geometric parameters as the Fig. 1. The magnetic flux incidents from z direction with amplitude 1 T onto the lens. The material parameters of the lens are described by Eq. (2). We only plot the magnetic flux distribution on a cross section of the lens which passes through the center of the lens.

the 2D case). We will further study how to overcome these obstacles in the following work.

2. SUMMARY

Based on transformation optics and folded-space transformation, a compact 3D passive magnetic lens has been proposed, which can achieve a greatly high magnetic field enhancement without additional power consumption. The more important is the enhanced static magnetic field is highly uniform which may have potential applications in MRI and other compact high-field-magnet systems.

ACKNOWLEDGMENT

Fei Sun thanks the China Scholarship Council (CSC) No. 201206320083.

REFERENCES

1. Brandt, B. L., S. Hannahs, H. J. Schneider-Muntau, G. Boebinger, and N. S. Sullivan, "The national high magnetic field laboratory," *Physica B*, 294–295; 505–511, 2001.
2. Choi, S., J. Yoon, B. Lee, M. Won, J. Ok, Z. Y. Zhang, T. Kiyoshi, S. Matsumoto, and S. Lee, "Magnetic lens effect using Gd-Ba-Cu-O bulk superconductor in very high magnetic field," *Appl. Phys. Lett.*, Vol. 111, 07E728, 2012.
3. Zhang, Z. Y., S. Matsumoto, S. Choi, R. Teranoshi, and T. Kiyoshi, "Superconductivity and its applications," *Physica C*, Vol. 471, 1547–1549, 2011.
4. Zhang, Z. Y., S. Matsumoto, S. Choi, R. Teranoshi, and T. Kiyoshi, "Comparison of different configurations of NbTi magnetic lenses," *Supercond. Sci. Technol.*, Vol. 24, 105012, 2011.
5. Sun, F. and S. He, "Create a uniform static magnetic field over 50 T in a large free space region," *Progress In Electromagnetics Research*, Vol. 137, 149–157, 2013.
6. The Finite Element Simulation, Conducted by Using Commercial Software COMSOL Multiphysics, http://www.comsol.com/.

Impact of Electromagnetic Field Generated nearby High Voltage Alternating Current Transmission Lines on Prooxidant-antioxidant Balance in Selected Internal Organs of Rats

P. Sowa[1], **K. Sieron-Stoltny**[2], **G. Cieslar**[3], **and A. Sieron**[3]

[1]Institute of Power System and Control, Silesian University of Technology, Poland
[2]Department of Physical Medicine, Medical University of Silesia, Katowice, Poland
[3]Department and Clinic of Internal Diseases, Angiology and Physical Medicine
Medical University of Silesia, Poland

Abstract— In the study the impact of whole-body exposure to 50 Hz electromagnetic field generated nearby those lines on prooxidant/antioxidant balance in selected internal organs of male rats was estimated, by means of analysis of the contents of markers of membrane lipid peroxidation and oxidative stress: malone dialdehyde (MDA) and total oxidant capacity (TOC), respectively, as well as the activity of antioxidant enzymes: superoxide dismutase (SOD), catalase (CAT), glutathione peroxidase (GPx), glutathione reductase (GR) and glutathione S-transferase (GST), in homogenates of kidney, heart and lung tissue. The experiment was performed on 20 male Wistar rats, in mean age of 10 weeks, divided into 2 equal groups (consisting of 10 animals), subjected to long-term exposure to electromagnetic field or to sham-exposure, respectively. Rats from examined group were exposed to electromagnetic field with physical parameters generated by typical high voltage electric current transmission lines ($f = 50\,\text{Hz}$, $E = 10\,\text{kV/m}$), 22 hours a day (with a break between 800 and 1000) for 28 succeeding days. Rats from control group were exposed for 28 succeeding days to sham-exposure, during which they stayed in identical as examined animals environmental conditions, excluding the influence of electromagnetic field. During the exposure rats were stayed in plastic cages placed between two round electrodes of experimental system supplied with an alternating current. After the end of a cycle of 28 daily exposures to electromagnetic field or sham-exposures (control rats), animals were starved by 24 hours, then anaesthetized and next the abdominal cavity was opened and samples of kidney, heart and lung were taken. In the homogenates prepared from the obtained samples the contents of TOC and MDA, as well as the activity of SOD, CAT, GPx, GR and GST were measured. The biochemical analyses were performed by means of routine spectrophotometric and kinetic methods. As a result of repeated exposures, in electromagnetic field-exposed group of rats in kidney tissue homogenates a significant increase in the contents of TOC and in the activity of SOD and GPx, as well as a significant decrease in the activity of GR and GST was observed, in heart tissue homogenates a significant decrease in the contents of TOC and in the activity of GST, as well as a significant increase in the activity of GPx was found, while in lung homogenates a significant increase in the contents of MDA and in the activity of CAT was confirmed, as compared to control sham-exposed rats. On the basis of the obtained results it was found, that 4-week lasting exposure of rats to electromagnetic field with physical parameters generated by high voltage alternating current transmission lines causes a slight intensification of oxidant processes in the tissue of examined internal organs with accompanying compensatory, multidirectional changes of antioxidant enzymes activity, enabling the maintenance of prooxidant/antioxidant balance only in heart tissue.

1. INTRODUCTION

Nowadays human population is permanently exposed to electromagnetic fields with industrial frequency generated by high voltage alternating current transmission lines, both in living places and in occupational conditions. It was proved in many experimental studies that electromagnetic fields with various physical parameters could intensify a generation of reactive oxygen species with subsequent disturbances of a balance between an intensity of oxidant processes and capacity of antioxidant defense system depending on the activity of antioxidant enzymes [1–6]. This toxic phenomenon called oxidative stress, results in stimulation of the process of membrane lipids peroxidation, leading in a consequence to development of apoptosis and cell death [7–11].

As in attainable literature there are lacking papers dealing with the influence of the mentioned above form of electromagnetic field on the intensity of prooxidant processes and the activity of antioxidant enzymes in tissues of internal organs of living organisms, the aim of the study was to estimate the impact of electromagnetic field with industrial frequency generated by high voltage alternating current transmission lines (frequency $f = 50\,\text{Hz}$, intensity $E = 10\,\text{kV/m}$) on prooxidant/antioxidant balance in kidney, heart and lung of male rats, by means of analysis of the contents of markers of membrane lipid peroxidation and oxidative stress: malone dialdehyde (MDA) and total oxidant capacity (TOC), respectively, as well as the activity of antioxidant enzymes: superoxide dismutase (SOD) (EC 1.15.1.1), catalase (CAT) (EC 1.11.1.6), glutathione peroxidase (POX) (EC 1.11.1.9.), glutathione reductase (GR) (EC 1.6.4.2) and glutathione S-transferase (GST) (EC 3.1.2.7.) in homogenates of those organs.

2. MATERIAL AND METHODS

The experiment was performed on 20 male Wistar rats, in mean age of 10 weeks with mean initial body mass of $180 \pm 7.5\,\text{g}$ before the beginning of the experiment. In order to estimate the impact of electromagnetic field with frequency of 50 Hz generated between two electrodes of experimental system supplied with an alternating current rats were divided into 2 equal groups (consisting of 10 animals) subjected to long-term exposure to electromagnetic field or to sham-exposure, respectively.

During the experiment the animals were kept in a special plastic cages, in optimal environmental conditions (stable humidity of air: 60% and temperature: 21°C, 12-hour light-dark cycle). They were fed with standard laboratory pellet food for rodents Labofed B and had unlimited access to drinkable water.

All procedures involving animals were carried out in accordance with the Animals Scientific Procedures Act, published by the U.S. National Institute of Health (1985) and were accepted by the Committee of Bioethics of Medical University of Silesia in Katowice (permission No. 65/2008)

During the exposure animals were placed in a special plastic cage (10 animals in one cage), that did not disturb applied electromagnetic field and allowed the possibility of free movement. Rats from examined group were exposed to electromagnetic field with physical parameters emitted by typical high voltage electric current transmission lines ($f = 50\,\text{Hz}$, $E = 10\,\text{kV/m}$), which was generated between 2 electrodes of experimental exposure system, placed in the distance of 50 cm from each other, 22 hours a day (with a break between 8^{00} and 10^{00}), for 28 succeeding days. Rats from control group were subjected for 28 succeeding days to sham-exposure, during which they stayed in identical as examined animals environmental conditions, excluding the influence of electromagnetic field, as between electrodes no voltage was generated.

After the end of a cycle of 28 daily exposures to electromagnetic field or sham-exposures (control rats), animals were starved by 24 hours and then anaesthetized with use of a mixture of *xylazine* (10 mg/kg *ip*) and *ketamine* (100 mg/kg *ip*). Next after surgical opening of chest and collecting total amount of blood from the left heart ventricle, the abdominal cavity was opened and samples of kidney, heart and lung were taken. In the homogenates prepared from the obtained samples the contents of markers of oxidative stress (TOC) and membrane lipid peroxidation (MDA), as well as the activity of selected antioxidant enzymes: SOD, CAT, POX, GR and GST were measured. The biochemical analyses were performed by means of kinetic and spectrophotometric methods by: Ohkawa, Ohishi and Yagi [12], Erel [13], Oyanagui [14], Aebi [15], Paglia and Valentine [16], Meister and Anderson [17] and Habich [18], respectively.

3. RESULTS

The results of measurements of the contents of markers of oxidant processes and activities of antioxidant enzymes in homogenates of tissues of particular internal organs (kidney, heart and lung) in both groups of rats, with statistical analysis are presented in Tables 1–6.

In electromagnetic field-exposed rats in kidney tissue homogenates a significant increase in the contents of TOC and in the activity of SOD and POX, as well as a significant decrease in the activity of GR and GST was observed, as compared to control, sham-exposed rats. No statistically significant changes in the contents of MDA and in the activity of CAT were noticed.

In electromagnetic field-exposed rats in heart tissue homogenates a significant decrease in the contents of TOC and in the activity of GST, as well as a significant increase in the activity of POX was observed, as compared to control, sham-exposed rats. No statistically significant changes in the contents of MDA and in the activity of SOD, CAT and GR were noticed.

In electromagnetic field-exposed rats in lung homogenates a significant increase in the contents of MDA and in the activity of CAT was confirmed, as compared to control, sham-exposed rats. No statistically significant changes in the contents of TOC and in the activity of SOD, POX and GR were noticed.

Table 1: The contents of markers of oxidant processes: MDA and TOC in homogenates of kidney tissue in electromagnetic field-exposed rats and in control, sham-exposed rats, with statistical analysis.

Parameter	**Electromagnetic field-exposed group of rats**	**Control sham-exposed group of rats**	**Statistical significance**
	Mean value ± SD	Mean value ± SD	
Malone dialdehyde MDA [μmol/g protein]	4.81 ± 1.99	3.45 ± 1.41	$p = 0.051$
Total Oxidant Capacity TOC [μmol/g protein]	$\mathbf{5.39 \pm 1.38}$	10.13 ± 1.82	$\mathbf{p < 0.001}$

Table 2: The activity of antioxidant enzymes: SOD, CAT, POX, GR and GST in homogenates of kidney tissue in electromagnetic field-exposed rats and in control, sham-exposed rats, with statistical analysis.

Parameter	**Electromagnetic field-exposed group of rats**	**Control sham-exposed group of rats**	**Statistical significance**
	Mean value ± SD	Mean value ± SD	
Superoxide dismutase SOD [NU/mg protein]	$\mathbf{239.20 \pm 25.40}$	217.00 ± 16.69	$\mathbf{p = 0.025}$
Catalase CAT [kIU/g protein]	136.60 ± 13.54	141.80 ± 15.27	$p = 0.457$
Glutathione peroxidase POX [IU/g protein]	$\mathbf{48.18 \pm 4.26}$	40.88 ± 3.58	$\mathbf{p < 0.001}$
Glutathione reductase GR [IU/g protein]	$\mathbf{58.11 \pm 5.44}$	92.72 ± 2.78	$\mathbf{p = 0.030}$
Glutatione S-transferase GST [IU/g protein]	$\mathbf{0.86 \pm 0.42}$	2.91 ± 0.27	$\mathbf{p < 0.001}$

Table 3: The contents of markers of oxidant processes: MDA and TOC in homogenates of heart tissue in electromagnetic field-exposed rats and in control, sham-exposed rats, with statistical analysis.

Parameter	**Electromagnetic field-exposed group of rats**	**Control sham-exposed group of rats**	**Statistical significance**
	Mean value ± SD	Mean value ± SD	
Malone dialdehyde MDA [μmol/g protein]	4.42 ± 0.49	4.58 ± 0.97	$p = 0.592$
Total Oxidant Capacity TOC [μmol/g protein]	$\mathbf{0.74 \pm 0.26}$	1.60 ± 0.36	$\mathbf{p < 0.001}$

Table 4: The activity of antioxidant enzymes: SOD, CAT, POX, GR and GST in homogenates of heart tissue in electromagnetic field-exposed rats and in control, sham-exposed rats, with statistical analysis.

Parameter	**Electromagnetic field-exposed group of rats**	**Control sham-exposed group of rats**	**Statistical significance**
	Mean value ± SD	Mean value ± SD	
Superoxide dismutase SOD [NU/mg protein]	66.79 ± 3.66	65.26 ± 7.56	$p = 1.000$
Catalase CAT [kIU/g protein]	57.10 ± 7.99	62.46 ± 12.39	$p = 0.176$
Glutathione peroxidase POX [IU/g protein]	$\mathbf{1.61 \pm 0.10}$	1.15 ± 0.20	$\mathbf{p < 0.001}$
Glutathione reductase GR [IU/g protein]	17.33 ± 1.41	19.82 ± 1.98	$p = 0.876$
Glutatione S-transferase GST [IU/g protein]	$\mathbf{0.12 \pm 0.09}$	0.30 ± 0.91	$\mathbf{p < 0.001}$

Table 5: The contents of markers of oxidant processes: MDA and TOC in homogenates of lung tissue in electromagnetic field-exposed rats and in control, sham-exposed rats, with statistical analysis.

Parameter	**Electromagnetic field-exposed group of rats**	**Control sham-exposed group of rats**	**Statistical significance**
	Mean value ± SD	Mean value ± SD	
Malone dialdehyde MDA [μmol/g protein]	$\mathbf{2.07 \pm 0.44}$	1.50 ± 0.29	$\mathbf{p < 0.001}$
Total Oxidant Capacity TOC [μmol/g protein]	4.51 ± 0.98	4.48 ± 1.70	$p = 0.974$

Table 6: The activity of antioxidant enzymes: SOD, CAT, POX, GR and GST in homogenates of lung tissue in electromagnetic field-exposed rats and in control, sham-exposed rats, with statistical analysis.

Parameter	**Electromagnetic field-exposed group of rats**	**Control sham-exposed group of rats**	**Statistical significance**
	Mean value ± SD	Mean value ± SD	
Superoxide dismutase SOD [NU/mg protein]	40.14 ± 5.87	39.39 ± 6.14	$p = 1.000$
Catalase CAT [kIU/g protein]	$\mathbf{25.18 \pm 3.48}$	20.80 ± 3.40	$\mathbf{p = 0.023}$

Parameter	Electromagnetic field-exposed group of rats	Control sham-exposed group of rats	Statistical significance
Glutathione peroxidase POX [IU/g protein]	3.73 ± 0.94	$4.50 \pm 1,17$	$p = 0.091$
Glutathione reductase GR [IU/g protein]	37.85 ± 5.06	35.40 ± 6.37	$p = 0.280$
Glutatione S-transferase GST [IU/g protein]	4.49 ± 1.67	4.03 ± 0.91	$p = 1.000$

4. CONCLUSIONS

Long-term, 4-week lasting exposure of rats to electromagnetic field with physical parameters generated by high voltage alternating current transmission lines causes a slight intensification of oxidant processes in the tissues of examined internal organs with accompanying compensatory, multidirectional changes of antioxidant enzymes activity, enabling the maintenance of prooxidant/antioxidant balance only in heart tissue.

ACKNOWLEDGMENT

This project was supported by grant No. N N511 351737 from the Polish Ministry for Science and Higher Education.

REFERENCES

1. Paluszak, J., P. Sosnowski, and K. Mikrut, "Influence of variable magnetic field on antioxidant enzymes activity in rat blood," *Acta Bio-Optica et Informatica Medica*, Vol. 5, No. 1, 1–5, 1999.
2. Del Carratore, R., E. Morichetti, C. Della Croce, and G. Bronzetti, "Effect of magnetic fields on rodent monooxygenase enzymes," *Bioelectromagnetics*, Vol. 16, No. 5, 324–329, 1995.
3. Kula, B., A. Sobczak, and R. Kuska, "Effects of static and ELF magnetic fields on free radical processes in rat liver and kidney," *Electromagnetic Biology and Medicine*, Vol. 19, No. 1, 99–105, 2000.
4. Kula, B., A. Sobczak, and R. Kuska, "A study of the effects of static and extremely low frequency magnetic fields on lipid peroxidation products in subcellular fibroblast fractions," *Electromagnetic Biology and Medicine*, Vol. 21, No. 2, 161–168, 2002.
5. Cieslar, G., J. Malyszek-Tumidajewicz, P. Sowa, and A. Sieron, "Impact of static electric field on prooxidant-antioxidant balance in rats," *COMPEL*, Vol. 31, No. 4, 1212–1223, 2012.
6. Cieslar, G., J. Zalejska-Fiolka, E. Birkner, S. Kasperczyk, and A. Sieron, "Influence of long-lasting exposure to weak variable magnetic field on activity of antioxidant enzymes in rats," *Physica Medica*, Vol. 20, Suppl. 1, 25–27, 2004.
7. Itoh, K., T. Ishii, N. Wakabayashi, and M. Yamamoto, "Regulatory mechanisms of cellular response to oxidative stress," *Free Radical Research*, Vol. 31, No. 4, 319–324, 1999.
8. Cadenas, E. and K. Davies, "Mitochondrial free radical generation, oxidative stress and aging," *Free Radical Biology and Medicine*, Vol. 29, No. 3-4, 222–230, 2000.
9. Burcham, P. C., "Genotoxic lipid peroxidation products: Their DNA demaging properties and role in formation of endogenous DNA adducts," *Mutagenesis*, Vol. 13, No. 3, 287–305, 1998.
10. Hisamitsu, T., K. Narita, and T. Kasahara, "Induction of apoptosis in human leucemic cells by magnetic fields," *Japan Journal of Physiology*, Vol. 47, No. 3, 307–310, 1997.
11. Wolf, F. I., A. Torsello, B., Tedesco, S. Fasanella, A. Boninsegna, M. D'Ascenzo, C. Grassi, G. B. Azzena, and A. Cittadini, "50-Hz extremely low frequency electromagnetic fields enhance cell proliferation and DNA damage: Possible involvement of a redox mechanism," *Biochimica et Biophysica Acta*, Vol. 1743, Nos. 1–2, 120–129, 2005.

12. Ohkawa, H., N. Ohishi, and K. Yagi, "Assay for peroxides in animal tissues by thiobarbituric acid reaction," *Analytical Biochemistry*, Vol. 95, No. 2, 351–358, 1979.
13. Erel, O., "A new automated colorimetric method for measuring total oxidant status," *Clinical Biochemistry*, Vol. 38, No. 12, 1103–1111, 2005.
14. Oyanagui, Y., "Evaluation of assay methods and establishment of kit for superoxide dismutase activity," *Analytical Biochemistry*, Vol. 142, No. 2, 290–296, 1984.
15. Aebi, H., "Catalase in vitro," *Methods in Enzymology*, Vol. 105, 121–126, 1984.
16. Paglia, D. and W. Valentine, "Studies on the quantities and qualitative characterization of erythrocyte glutathione peroxidase," *Journal of Laboratory and Clinical Medicine*, Vol. 70, No. 1, 158–169, 1967.
17. Meister, A. and M. E. Anderson, "Glutathione," *Annual Review of Biochemistry*, Vol. 52, 711–760, 1983.
18. Habig, W. H. and W. B. Jakoby, "Assays for differentiation of glutathione S-transferases," *Methods in Enzymology*, Vol. 77, 398–405, 1981.

System Information Therapy in the Management of Pain: A Pilot Study

Paolo Baron[1], **Giuseppe Bucci**[1], **Alfio Rinaudo**[1], **Roberto Rocco**[1],
Eugenio Sclauzero[1], **and Alberto Foletti**[2,3]

[1]General Practictioners, Regione Friuli Venezia Giulia, Italy
[2]Institute of Translational Pharmacology, National Research Council — CNR
Via Fosso del Cavaliere, 100, Rome 00133, Italy
[3]Deartment of Innovative Technologies
University of Applied Sciences of Southern Switzerland — SUPSI
Galleria 2, Manno 6928, Switzerland

Abstract— Dealing with pain is an important daily part of current medical practice. Biophysical methods by use of medical devices (such as Med Select 729 in this trial) allows to perform very personalized treatment using endogenous signals of the patient leading to the definition of a System Information Therapy (SIT) approach. An open labeled clinical trial was designed to assess the effectiveness of a biophysical treatment compared to a common anti inflammation drug (ibuprofen) and compared to placebo. Methods: patients has been divided in three groups: **Group 1** System Information Therapy patients receiving two steps of treatment by the Med Select 729 medical device: 1st step delivered with a program called regulation therapy with recording of endogenous input signals at the painful region and delivery of therapeutic output signals at systemic level by mean of an electromagnetic mattress on which the patient lied — 2nd step delivered with the program called pain therapy: recording endogenous input signals at the painful region and delivery of therapeutic output signals at the pain site, moreover a copy of therapeutic signals has been recorded on a commercial available aqueous system (Nomabit Base). **Group 2** Pharmacological therapy: receiving ibuprofen 600 mg twice a day for 10 days. **Group 3** Placebo group: receiving only Nomabit Base solution as placebo. A total of 66 patients was enrolled: 26 in System Information Therapy group (17 f, 9 m), 23 in the pharmacological group (11 f, 9 m); 17 in the placebo group (12 f, 5 m). Evaluation of follow up was performed by a visual analogue scale at the beginning, after one week, after one month, and after three months. After one week biophysical therapy shows similar effect than ibuprofen and after one month the statistical significance was $\chi^2 = 12.153$ with $p < 0.02$. In conclusion the biophysical therapy protocol demonstrated the same effectiveness than usual pharmacological therapy with ibuprofen at first week reaching statistical significance after one month of administration and maintaining the effect at tree month. System information therapy seems, therefore, to be an effective and safe method in the management of pain in current medical practice representing a possible resource especially for patients with chronic disease and multiple comorbidities in order to reduce drug overload.

1. INTRODUCTION

Practitioners has to cope daily with many kind of pain related diseases. Pain usually expresses maladaptive response to stress. Stress can be defined as a condition or state in which a perceived discrepancy between afferent stimuli and a well-defined range of allostasis activates adaptive responses trying to reduce this possible discrepancy. Allostasis describe the dynamic adaptive process aimed to keep stability while coping with both internal of external challenges. Allostasis describe the dynamic adaptive process aimed to maintain the most effective condition of the whole organism at any moment: therefore it is intrinsically time varying according to different combinations of both inner and external conditions. Allostatic load is the sum of allostatic response exciding physiological attitude of the organism at a certain time. Allostatic load occur when activation of allostatic response are continuously settled [1–3]. Pain is part of almost any adaptive response in the acute diseases yielding a fastening in recovery of allostasis. Pain is part of the maladaptive responses in chronic diseases leading to a worsening of allostatic load and slowing recovery [4–6]. In this framework it is clear that coping with pain has to be considered not only from a symptomatic viewpoint but also from a systemic perspective [7–10]. Biophysical methods by use of electro-medical devices allows to deliver treatment using endogenous electromagnetic signals and is therefore consistent with the developing concept of personalized medicine [11, 12]. In the last decays a progressive fall of reductionism had leaded to the concept of Systems biology and, only very recently, to the concept of Systems Medicine. In the framework of Systems Medicine it is clear that some features and behaviour of the system as a whole are not the sum of the single parts but arise from emergent characteristics due to the complexity of living organisms. Consistently with the raising concept of System Medicine [7–10] is raising the concept of System Information Therapy [13] as an integrative clinical tool able to allows the treatment of patients with biophysical methods operating at once by endogenous and external electromagnetic signals. Indeed livings organisms are endogenously producing electromagnetic signals and make fruitful use of them in the coordination of their internal processes and in cell to cell coordination [14–16]. On the other hand the clinical use of electromagnetic therapies has long history with evidence of anti-inflammatory effects of electronic signals [17]. System Information Therapy approach allows to achieve at once a systemic and a local effect [18] leading to a reduction of allostatic load as clinically detectable by evaluation of fluctuating asymmetry, a clinical marker of stress [19], as reported in a previous study [20]. In this pilot study we also implemented the transfer of electromagnetic signals to an aqueous system in agreement with previous finding on cellular, bacterial, plants and human models [21–26]. The idea of performing a single treatment with biophysical therapy making at the same time a record of the signals on a commercial available aqueous system allows to perform a single treatment in a single day and to continue the treatment by the daily sublingual administration of drops of the recorded aqueous solution (a commercial available aqueous solution of micro elements: Nomabit Base). This could also provide support to the feasibility of the Electro Magnetic Information Transfer (EMIT) through aqueous system [26] in clinical use.

2. METHODS

A pilot clinical trial was designed to assess the effectiveness of a biophysical treatment recorded on an aqueous system compared to a common anti inflammation drug (ibuprofen) and compared to placebo. A total of 66 patient (40 females and 26 males) was enrolled in the study, that was performed in the respect of the declaration of Helsinky, upon delivery of an informed consent. 66 patients was divided into 3 groups as follow: 26 in the Biophysical therapy group (17 f, 9 m), 23 in the pharmacological group (11 f, 9 m); 17 in the placebo group (12 f, 5 m). Visual Analogue Scale (VAS) score was recorded at the beginning, after one week, after one month.

2.1. Group 1

Group 1 was the System Information Therapy group and was treated by a 2 step protocol using a commercial available electro-medical device Med Select 729 (by Wega, Germany). Meanwhile a copy of the output therapeutic signals were recorded on a commercial available aqueous system (Nomabit Base) placing the solution into a special output coil built-in for this purpose in the Med select device. The aqueous solution of Nomabit Base was self-administered daily to the patient in order to allows to the therapeutic information recorded to be delivered once a day. The drops were taken according to a weekly plan starting on Monday with a single drop and raising of one drop a day up to 6 drops on Saturday, no therapy was taken on Sunday an then the protocol started again from one to six drops during each following week.

2.2. Group 2

Group 2 was the Pharmacological therapy group: ibuprofen 600 mg twice a day, on full stomach, for 10 days, was administered to each patient of this group.

2.3. Group 3

Group 3 was the Placebo group. The patients of this group was receiving only Nomabit Base solution as placebo, therefore not placed into the Med Select to be selectively recorded, and administered with the same protocol as in the System Information Therapy group.

3. RESULTS

Evaluation and follow up was performed by a Visual Analogue Scale (VAS) at the beginning, after one week, and after one month. Criteria of evaluation of VAS self-rating modification in the follow up was the following: Reduction ≥ 2 Points in VAS score was considered as improved; Reduction $= 1$ Points in VAS score was considered as unchanged; Reduction ≤ 0 Points in VAS score was considered as worsen. After one week System Information Therapy shows similar effect than ibuprofen as reported in Figure 1.

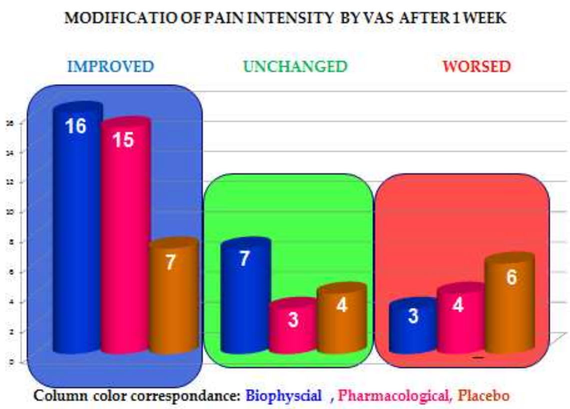

Figure 1.

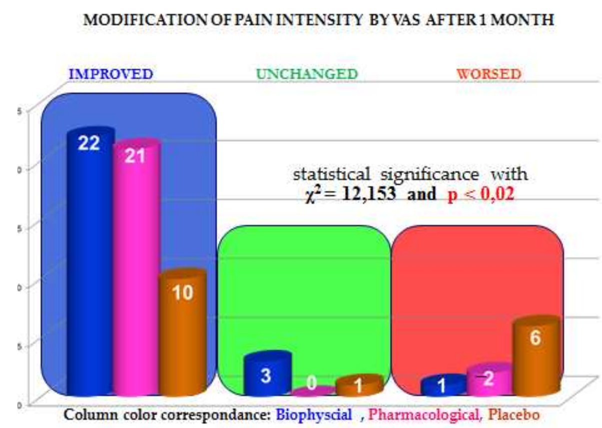

Figure 2.

Data reported after one month reach a statistical significance with $\chi^2 = 12.153$ and $p < 0.02$ as showed in Figure 2 demonstrating that biophysical therapy is as effective as pharmacological treatment with ibuprofen in respect to placebo in the management of pain.

4. DISCUSSION

System Information Therapy demonstrated to be an effective and efficient method in pain relief according to the modification of self-rating of pain collected by mean of the Visual Analog Scale VAS. System Information Therapy showed the same effectiveness of the non-steroidal anti-inflammatory drug Ibubrofen administered in the dose of 600 mg. twice a day in respect to the use of a placebo. System Information Therapy and Ibuprofen were efficient in pain rating reduction as reported at the first follow up assessment after one week while placebo was not as reported in Figure 1. System Information Therapy and Ibuprofen was efficient also in pain rating reduction at the second follow up assessment after one month while placebo was not. A complete statistical significance is achieved by both Biophysical and Pharmacological group in respect to placebo at the end of the first month with $\chi^2 = 12.153$ with $p < 0.02$ (Figure 2). The available data suggest that Biophysical therapy mimic the dynamics of the Pharmacological treatment and is long lasting in their effects. Interestingly a very low amount of worsen cases was reported in the biophysical group ad especially no side effect was referred. Moreover many patients of the Biophysical group reported feeling of a general relaxation following the treatment as presumably to be due to a systemic effect of the biophysical therapy besides the effect on pain. Importantly the use of a single recording procedure during the System Information Therapy allowed to perform a unique treatment of the patient, lasting only 20 minutes, saving time and cost due to repetition of the treatment. Biophysical treatment therefore was time effective and cost effective. The treatment fulfill the requirement to be considered as a personalized medication because the pattern of signals are recorded on the site of the pain, such pattern of endogenous electromagnetic signal being unique for any single person at any single time, this way the procedure is actually tailored on the patient. Moreover the recording of the output signals on the aqueous system, a commercial available solution of micro elements Nomabit Base (by Named, Italy) is consistent with the previous findings [21–26] and demonstrate the clinical feasibility of such a procedure as a useful integrative tool in general practice as reported by further studies in agreement with the hypotheses that aqueous system could be able to record, store, and transfer biophysical active information to biological targets [27–30]. Further clinical trials are certainly requested to confirm and widen the data presented in this preliminary pilot study and someone are already in process to better define the clinical areas besides pain in which a biophysical strategy could improve quality of life to the increasing number of patients with chronic diseases and multiple comorbidities that require to be treated effectively and safely reducing the number of drugs to be used especially for the management of pain. Biophysical therapies could help to manage some symptoms related to no life-threatening diseases reducing global allostatic load and therefore cooperating to reduce total morbidity and mortality as reported from successful aging studies [31, 32].

5. CONCLUSION

In this pilot study on the management of pain in general practice System Information Therapy demonstrated the same effectiveness than an usual pharmacological therapy with ibuprofen, in respect to placebo. The effectiveness was already disclosed at the end of first week reaching statistical significance after one month of treatment. System Information Therapy should therefore be considered as an effective and safe method in the management of pain in current medical practice.

REFERENCES

1. McEwen, B. S. and E. Stellar, "Stress and the individual. Mechanisms leading to disease," *Arch Intern Med.*, Vol. 153, No. 18, 2093–2101, 1993.
2. Seeman, T. E., B. H. Singer, J. W. Rowe, R. I. Horwitz, and B. S. McEwen, "Price of adaptation — Allostaic load and its health consequences. MacAthur studies of successful aging," *Arch. Intern. Med.*, Vol. 157, No. 19, 2259–2268, 1997.
3. McEwen, B. S., "Stress, adaptation and disease. Allostasis and allostatic load," *Ann. N. Y. Acad. Sci.*, Vol. 840, 33–44, 1998.
4. McEwen, B. S. and T. Seeman, "Protective and damaging effects of mediators of stress. Elaborating and testing the concepts of allostasis and allostatic load," *Ann. N. Y. Acad. Sci.*, Vol. 896, 30–47, 1999.
5. McEwen, B. S. and J. C. Wingfield, "The concept of allostasis in biology and biomedicine," *Horm. Behav.*, Vol. 43, No. 1, 2–15, 2003.
6. Glein, D. A., N. Goldman, Y.-L. Chuang, and M. Weinstein, "Do chronic stressors lead to physiological dysregulation? Testing the theory of allostatic load," *Psychosomatic Med.*, Vol. 69, No. 8, 769–776, 2007.
7. Ahn, A. C., M. Tewari, C.-S. Poon, and R. S. Phillips, "The clinical applications of a system approach," *PLoS Medicine.*, Vol. 3, No. 7, e209, 2006.
8. Ahn, A. C., M. Tewari, C.-S. Poon, and R. S. Phillips, "The limits of reductionism in Medicine: Could system biology offer an alternative?," *PLoS Medicine*, Vol. 3, No. 6, e208, 2006.
9. Carlson, R. J., "Holism and reductionism as perspectives in medicine and patient care," *West J. Med.*, Vol. 131, 466–470, 1979.
10. Federoff, H. G. and L. O. Gostin, "Evolving from reductionism to holism: Is there a future for system medicine?," *JAMA*, Vol. 302, No. 9, 994–996, 2009.
11. Henney, A. M., "The promise and challenge of personalized medicine: Aging populations, complex diseases, and unmet medical need," *Croat. Med. J.*, Vol. 53, No. 3, 207–210, 2012.
12. Louca, S., "Personalized medicine — A tailored health care system: Challenges and opportunities," *Croat Med J.*, Vol. 53, No. 3, 211–213, 2012.
13. Foletti, A., "Managing biological complexity in the framework of systems medicine: The possible key role of systems information therapy by biophysical methods in integrating medical practice," *Proceedings of the 1st International Symposium "Biophysical Aspects of Complexity in Health and Disease"*, 20–21, Milan, Italy, Mar. 26, 2010.
14. Liboff, A. R., "Toward an electromagnetic paradigm for biology and medicine," *J. Altern. Complement. Med.*, Vol. 10, No. 1, 41–47, Review, 2004.
15. Cifra, M., J. Z. Fields, and A. Farhadi, "Electromagnetic cellular interaction," *Prog. Biophys. Mol. Biol.*, Vol. 105, No. 3, 223–246, 2010.
16. Rossi, C., A. Foletti, A. Magnani, and S. Lamponi, "New perspectives in cell comunication: Bioelectromagnetics interactions," *Seminar Cancer Biol.*, Vol. 21, No. 3, 207–214, 2011.
17. Odell, Jr., R. H. and R. E. Sorgnard, "Anti-iflammatory effects of electronic signals treatment," *Pain Physician.*, Vol. 11, No. 6, 891–907, 2008.
18. Liboff, A. R., "Local and holistic electromagnetic therapies," *Electromagn. Biol. Med.*, Vol. 26, No. 4, 315–325, 2007.
19. Parson, P. A., "Fluctating asymmetry: An epigenetic measurement of stress," *Biol. Rev. Camb. Philos. Soc.*, Vol. 65, No. 2, 131–145, 1990.
20. Foletti, A. and S. Grimaldi, "Systems information therapy and the central role of the brain in allostasis," *J. Phys.: Conf. Ser.*, Vol. 329, 012027, 2011.
21. Jerman, I., M. Berden, and R. Ruźic, "Biological influence of ultraweak supposedly EM radiation from organisms mediated through water," *Electro. and Magnetobiology*, Vol. 15, No. 3, 229–244, 1996.

22. Kreisl, P., "Test on the transduction of acetic acid information via an electronic amplifier," *Acta Medica Empirica*, Vol. 47, No. 3, 17–24, 1998.
23. Jerman, I., R. Rużic, R. Krašovec, M. Škarja, and L. Mogilnicki, "Electrical transfer of molecule information into water, its storage, and bioeffects on plants and bacteria," *Electromagn. Biol. Med.*, Vol. 24, No. 3, 341–353, 2005.
24. Heredia-Rojas, J. A., A. C. Torres-Flores, A. O. Rodriguez-De la Fuente, B. D. Mata-Cardenas, L. E. Rodriguez-Flores, M. P. Barron-Gonzales, A. C. Torres-Pantoja, and G. M. Alcocer-Gonzales, "Entamoeba histolytica and Trichomonas vaginalis: Trophozoite growth inhibition by metronidazole electro-transferred water," *Exp. Parasitol.*, Vol. 127, No. 1, 80–83, 2011.
25. Heredia-Rojas, J. A., A. C. Gomez-Flores, A. O. Rodriguez-De la Fuente, E. Monreal-Cuevas, A. C. Torres-Flores, L. E. Rodriguez-Flores, M. Beltcheva, and A. C. Torres-Pantoja, "Antibicrobial effect of amphotericin B electronically-activated water against Candida Albicans," *African J. Microbiology Res.*, Vol. 6, No. 15, 3684–3689, 2012.
26. Foletti, A., M. Ledda, E. D'Emilia, S. Grimaldi, and A. Lisi, "Eperimental finding on the electromagnetic information transfer of specific molecular signals mediated through aqueous system on two human cellular models," *J. Altern. Complement. Med.*, Vol. 18, No. 3, 258–261, 2012.
27. Thomas, Y., M. Schiff, L. Belkadi, P. Jurgens, L. Kahhak, and J. Benveniste, "Activation of human neutrophils by electronically transmitted phorbol-myristate acetate," *Medical Hypotheses*, Vol. 54, 33–39, 2000.
28. Smith, C. W., "Quanta and coherence effects in water and living systems," *J. Altern. Complement. Med.*, Vol. 10, No. 1, 69–78, 2004.
29. Widom, A., Y. Srivastava, and V. Valenzi, "The biophysical basis of Benveniste experiments: Entropy, structure, and information in water," *Int. J. Quantum. Chem.*, Vol. 110, No. 1, 252–256, 2010.
30. Foletti, A., S. Grimaldi, A. Lisi, M. Ledda, and A. R. Liboff, "Bioelectromagnetic medicine: The role of resonance signaling," *Electromagn Biol Med.*, Vol. 2, 2013, in press.
31. Seeman, T. E., B. S. McEwen, J. W. Rowe, and B. H. Singer, "Allostatic load as a marker of cumulative biological risk: MacArthur studies of successful aging," *Proc. Natl. Acad. Sci. USA*, Vol. 98, No. 8, 4770–4775, 2001.
32. Karlamangla, A. S., B. H. Singer, B. S. McEwen, J. W. Rowe, and T. E. Seeman, "Allostatic load as a predictor of functional decline. MacArthur studies of successful aging," *J. Clin. Epidemiol.*, Vol. 55, No. 7, 696–710, 2002.

The Thermal Analysis of Some Light Sources

A. Yasin Citkaya[1], **S. Selim Seker**[1], **and Osman Cerezci**[2]

[1]Department of Electrical-Electronic Engineering, Bogazici University, Bebek, Istanbul 34342, Turkey
[2]Department of Electrical-Electronic Engineering, Sakarya University, Esentepe, Sakarya 54187, Turkey

Abstract— The assessment of exposure level due to commonly used light sources needs specific attention in today's technology of lighting. The main reason behind this concern is that if exposure levels are not known, the biological results and necessary safety limits cannot be determined with accuracy. In this regard, this study has aimed to design, implement, analyze and solve partial differential equations related to diffusion and Bioheat equations. The study also provides experimental real-time data that makes the research more reliable. Subsequently, risk management policies can be established utilizing the thermal response of skin tissue and the associated health hazards.

1. INTRODUCTION

Lamp designs are undergoing a continuous evolution, utilizing newer and more powerful sources of optical radiation. Because of the rapid growth in usage of new types of special-purpose light sources in medicine, science and consumer applications, there is no doubt that importance on optical radiation exposure limits will increase day by day. This brings the growing need for codes of practice for all potentially hazardous optical sources [1]. The first step to be taken in this respect should indefinitely be the determination of light sources with potential adverse health effects.

Incandescent, fluorescent, compact fluorescent lamps (CFL), High Intensity Discharge (HID) sources including mercury vapor, metal halide, High Pressure Sodium (HPS), Low Pressure Sodium (LPS) are the common light source types. Many indoor lighting sources in general use, such as fluorescent, quartz halogen and even tungsten filament incandescent lamps, emit UVA, UVB and sometimes even UVC wavelengths. Intensities of some emissions are of similar magnitude to those in sunlight. Findings in literature show that chronic exposure may pose risks through cumulative UV exposure to skin and eyes, especially for photosensitive patients [2].

Studies of UV risk accumulated from indoor lighting sources have primarily focused on the possible relationship between fluorescent room lighting and increasing prevalence of melanoma [3]. Spectral measurements reported by Cole [4], addressing possible risks of UV from indoor lighting, were limited to fluorescent sources.

2. THEORETICAL BACKGROUND

The absorption of light in tissue causes a local elevation in temperature. Tissue heat transfer due to the deposited light is described by the Bioheat Transfer Equation, which was first introduced by Pennes [5] to model heat transfer in perfused tissue as:

$$\delta_{ts}\rho C\frac{\partial T}{\partial t}+\nabla\cdot(-k\nabla T)=\rho_b C_b\omega_b(T_b-T)+Q_{met}+Q_{ext} \tag{1}$$

On the right hand side of the equation, first term describes the thermal conduction, second term describes the convective effects of blood flow represented as a heat sink proportional to tissue perfusion [5] excluding effects of large blood vessels, and the last term is the absorbed power density from the optical source. Note that for a phantom with no perfusion, w_b would be set to 0. Boundary conditions and the related parameters for the Bioheat transfer equation is described by the reference [6].

An exact representation of light propagation in skin requires a model that characterizes the spatial distribution and the size distribution of tissue structures, their absorbing qualities and their refractive indexes [7]. The finite element method (FEM) which it is used in this work, allows for good approximations of complex boundaries. The FEM provides a systematic methodology by which the solution, in the case of our example, the temperature field, can be determined by a computer program, which actually is essential since thousands of nodes are usually needed to obtain a reasonably accurate solution.

3. COMPUTER SIMULATIONS

The numerical procedure developed for the solution of the bio-heat equation analyzes the dynamics of spatial-temporal temperature distribution $T(x, y, x, t)$ in biological tissues. An opto-thermal model of the skin obtained from different sources has been implemented in computer software program, such that the tissue, with a volume of $5\,\mathrm{mm} \times 5\,\mathrm{mm} \times 4\,\mathrm{mm}$, is considered to be composed of six layers from the optical point of view where some limitations are inevitable due to the multilayered structure. In the model specified, the tissue initial temperature is fixed at 36.6°C, and air temperature fixed at 25°C. Figure 1 shows the composed multilayered skin model in software program.

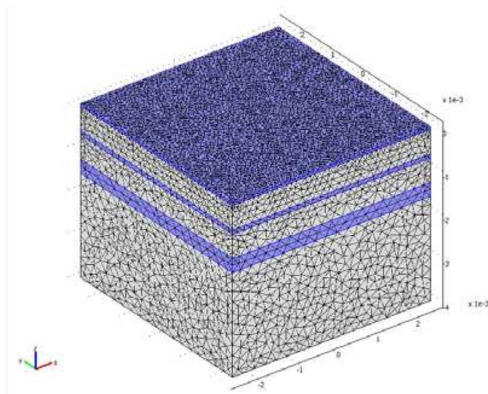

Figure 1: Meshed model of skin tissue created for computer simulation. (Layers in order from outside to inner: 1 — epidermis, 2 — upper dermis, 3 — blood plexus, 4 — lower dermis, 5 — subcutaneous fat, and 6 — muscle).

Thermal behavior of skin tissue that is exposed to light source is analyzed through the numerical method which utilizes Finite Element Method (FEM) by solving the diffusion and Bioheat equations under the effect of dominating boundary conditions. Regarding the light sources simulated, spectral information from production data is implemented in the model. In this numerical study, two Infra-Red lamps: one is red, other is clear, are chosen. For the multilayer skin model depicted in Figure 1. Ref. [7] is used for parameters of multilayered skin tissue model [7]. Having completed the modeling steps in the Finite Element Solver software by creating geometries, putting up the parameters and defining the boundary and sub domain settings, it is now time to run the simulations.

Simulation results for two different InfraRed light sources (red and clear) are summarized with respect to time in Figure 2. These results clearly show that temperature distribution inside the tissue is generally non-monotonic function of depth, due to varying optothermal parameters of tissue layers, like absorption coefficient, heat conductivity and so on. Temperature increase in tissue is also no-doubt dependent on exposure time and source power. As the exposure duration

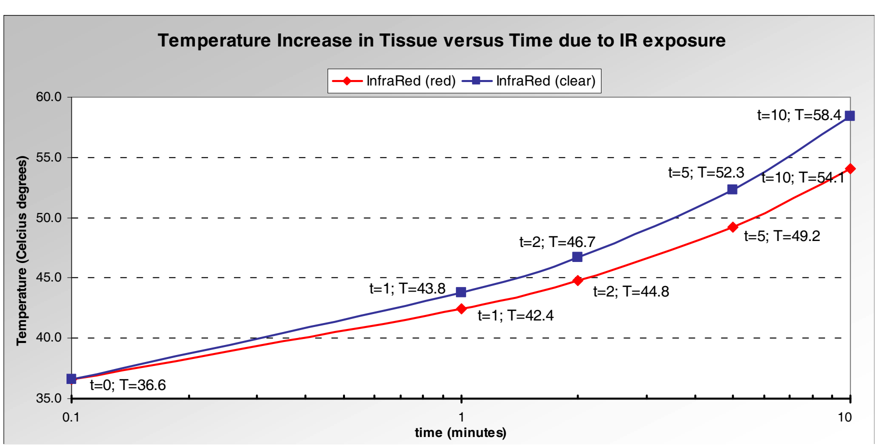

Figure 2: Graphical comparison of the simulation results obtained with two light sources at different times (time axis is represented with logarithmic scale).

increases, maximum temperature induced on tissue increases. When it comes to effects of two different InfraRed light sources, one clear and other with a red filter, it can be noticed that two light sources have different thermal effects on tissue even though the lamp output powers are set to be equal. It is also apparent that as exposure duration gets longer, difference in maximum temperature induced in tissue models increases and gets more significant for the two different types of light sources. Hence, the obtained results are in line with the expected results in such a way that red filtered lamp should and actually do cause less temperature increase in tissue.

4. EXPERIMENTAL STUDY

In order to make more and meaningful contributions with this study, different light sources from everyday usage are chosen in order to illustrate the effects of spectral variations and also the durational impact on temperature increases. Additionally, the effect of distance between light sources and tissue is verified via a comparative study made with the same light source. The experimental setup, graphically shown in Figure 3, consists of a light source directed to in vitro biological tissue (namely chicken meat covered with skin), and the thermal interaction between them is monitored via a thermal camera. In order to simulate a living tissue with blood perfusion in effect, in vitro tissue samples are kept in a water bath at 37°C. Distance between tissue and light source, d_1, is set to 30 cm and thermal camera is held at a distance d_2 of 50 cm for the best visual results, because of the limitation from the focus distance of camera which is 40 cm.

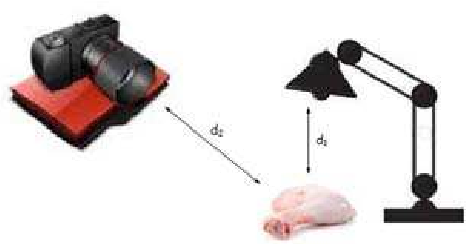

Figure 3: Graphical representation of the experimental setup.

First experiments are done with the InfraRed lamps, whose thermal effects are simulated beforehand with Finite Element Solver program. Then distance d_1 is increased to 50 cm, where experimental data is obtained for verification of distance variation effect. Next, other lamps, namely UV, Incandescent, LED, CFL and Halogen, are chosen to illustrate the results for various thermally induced tissues.

5. DISCUSSION

Numerical model for the multilayered skin tissue that is exposed to InfraRed lights, where the model is designed to enable the solution equations described earlier with specific boundary conditions using FEM via a computer software program, yielded spatial temporal distribution results. Same light sources are also used in the experiment to induce temperature increase on the biological tissue so to enable better understanding of both numerical and experimental results by first comparison and then verification of the results if possible. A summary of the maximum temperatures induced on tissue samples are given in Figure 4. This comparative study is realized by taking the maximum temperatures induced on tissues, because thermal camera is only able to monitor the surface temperature distribution.

As it can be clearly seen from Figure 4, obtained results are quite in-line with each other, such that the temperature curves behave in the same way for both experimental and numerically obtained results. From Figure 4, it can be inferred that there is about 2% difference between the results, which is generally in acceptable limits. Deep analysis of comparative study of the results will reveal possible reasons for this difference in results, for example numerical model contains blood perfusion effect, whereas experimental study is done on in-vitro samples which lack that property. With this comparison between the results, it has also been verified that although specific assumptions and simplifications have been made in modeling step, the simulation results obtained are free of modeling error and compatible with real samples.

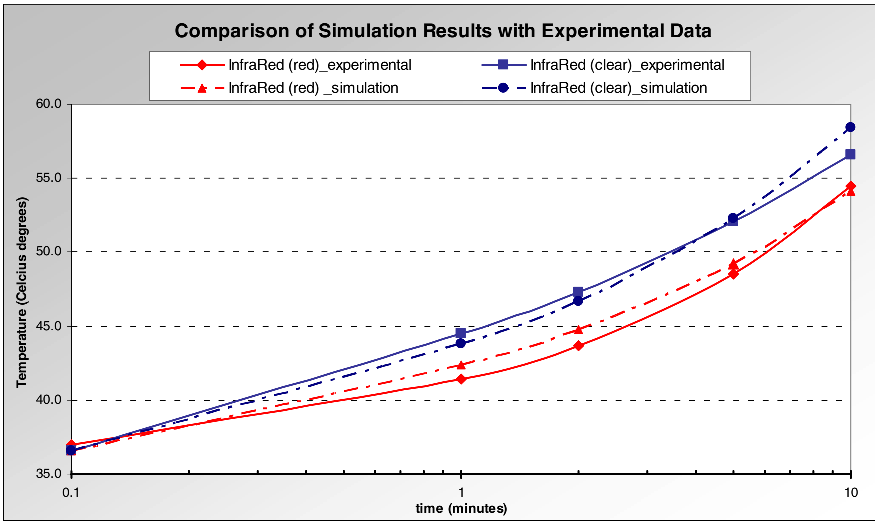

Figure 4: Comparison of simulation results with experimental data obtained for InfraRed Lamps.

One experiment is carried out at 50 cm distance between tissue and lamp (InfraRed light with red filter). It should not be so surprising that as exposure distance rises, maximum induced temperature gets low. Hence, it becomes easy to conclude that less photo thermal damage occurs at large exposure distances. In this regard, safety limits can be defined to minimize the hazardous effects of light.

People are exposed to various kinds of light in everyday, so studying the effects of different artificial light sources will demonstrate realistic conclusions for the daily exposure. To reach this goal, several experiments are conducted with different lamps, and thermal behavior of tissue is monitored via thermal camera.

Experimental results obtained can be used to compare the thermal effects of different light sources. Those with high power outputs, such as IR, Halogen and UV, some of which are designed for usage especially in heating applications, display higher temperature increases during the exposure period. On the other hand, LED and CFLs, today's energy efficient replacements for the most common home-use lamp Incandescent, seem to have little thermal effects on the tissue. Since this minimal effect can be foreseen, some of the experiments are conducted at quite lower tissue initial temperatures of 30°C. Even if the initial tissue temperature is set to a degree which is between air temperature and normal body temperature, these lamps have shown negligible effects on tissue samples in terms of temperature increase. Experiment with the incandescent lamp reveals that there is a minor increase (1°C after 10 minutes of exposure) in skin temperature. The reason can be explained in terms of light efficiency of the lamp compared with other sources at the same output power. Incandescent lamps have relatively low efficiency, as a result of which the surrounding air temperature increases. It has been observed that incandescent light causes the air temperature to increase. When it comes to the question why it has been less effective on increasing the tissue temperature, a reasonable explanation would be the reflector factor. What is more, it can be inferred that as duration of exposure is increased from 1 min to 5 min and 10 minutes, the maximum temperature increase rate gets smaller, that is to say induced maximum temperatures will eventually reach to steady state level as a result of continuous exposure.

In the experiments, it has also been observed that some light sources cause temperature increase in the surrounding air, which has also affected the thermal induction in skin tissue.

6. CONCLUSION

This study has provided a better knowledge of the thermal behavior of skin tissue under exposure to artificial light sources. The scope of work can also be extended in future with similar studies to investigate the health implications of light sources on eye, which is under direct exposure to light and surely one of the most sensitive part of human body. Considering the lack of scientific studies on heating effects of light sources on human skin and the lack of definition of safety limits for light exposure, thermal analysis carried out in this work will be useful to get a step forward in the ultimate goal of providing safety exposure limits, so that general public, who are consciously or unconsciously exposed to different light sources in everyday life, can be made aware to take precaution.

ACKNOWLEDGMENT

This work is supported by Bogazici University Research Foundation Project Code: 5698.

REFERENCES

1. International Commission on Non-ionizing Radiation and Protection, "Guidelines on limits of exposure to broad-band incoherent optical radiation (0.38 to 3 μm)," *Health Physics*, Vol. 73, No. 3, 539–554, 1997.
2. Harber, L. C., G. B. Whitman, R. B. Anstrong, and V. A. Deleo, "Photosensitivity diseases related to interior lighting," *Ann. N. Y. Acad. Sci.*, Vol. 453, 317–327, 1985.
3. Elwood, J. M., "Could melanoma be caused by fluorescent light? A review of relevant epidemiology," *Recent Results Cancer Res.*, Vol. 102, 1986.
4. Cole, C., P. D. Forbes, R. E. Davies, and F. Urbach, "Effect of indoor lighting on normal skin," *Ann. N. Y. Acad. Sci.*, Vol. 453, 305–316, 1985.
5. Datta, A. and V. Rakesh, *An Introduction to Modeling of Transport Processes*, Cambridge, 2010.
6. "Directive 2006/25/EC of the European Parliament and of the council of 5 April 2006 on the minimum health and safety requirements regarding the exposure of workers to risks arising from physical agents (artificial optical radiation) (19th individual directive within the meaning of article 16 (1) of directive 89/391/EEC)," *Official Journal L*, Vol. 114, 38–59, Apr. 27, 2006, http://eur-lex.europa.eu/LexUriServ/LexUriServ.do?uri=CELEX:32006L0025:EN:HTML.
7. L'Etang, A. and Z. Huang, "The effect of laser wavelength in the simulation of laser generated surface waves in human skin model," *Proceedings of the 28th IEEE EMBS Annual International Conference*, 4140–4143, New York City, USA, 2006.

Characteristics of an Optical Bowtie Nanoantenna

Ahmed Abbas, Mostafa El-Said, and Samir F. Mahmoud
Electronic and Communication Engineering Department, Cairo University, Egypt

Abstract— The performance of Bow-Tie gold nanoantenna placed on glass substrate is studied. Upon illuminating such nanoantenna by a Gaussian pulse, the received electric field across the antenna gap is monitored and plotted against frequency using the CST software. Meanwhile the complex impedance defined as the ratio of longitudinal E to the transverse H within the gap is monitored. It is shown that the electric field across the gap displays a peak value at the same frequency that corresponds to impedance resonance. A transmission line model is proposed, by which we can predict the dependence of the resonant frequency on the Bow-tie length and the gap between its arms.

1. INTRODUCTION

Optical nanoantennas have recently found several applications in areas such as near field probing in optical microscopy, nanometric optical tweezers, and biomedical applications [1, 2]. The optical nanoantenna is composed of a resonant length of rare metal, such as silver or gold, placed on glass or any dielectric layer. There is a fundamental difference between wire antennas in the radio frequency (RF) range and the optical range. Metallic wire antennas in the RF spectrum behave as almost perfectly conducting wires. As a consequence, the current wave developed on such wires propagate at the same velocity as that in the outer free space. In contrast, at Infrared or optical frequencies, metals no longer behave as perfect conductors. Instead, they are characterized as dielectrics with frequency dependent complex permittivity [3, 4]. Metals, such as Silver, Gold and Aluminum display permittivities with negative real part. This negative permittivity cause localized Plasmon to form at the metal-dielectric interface with little penetration in metal or the embedding dielectric. Another important consequence is that the current wave on the metal travels at a much slower velocity than that in the surrounding dielectric or the outer free space. This leads to compact antenna whose length is much shorter than a free space wavelength.

A nanoantenna of Bow-tie shape is depicted in Fig. 1. The plane of interface between the metal and dielectric is the y-z plane. A Plasmon mode on this metal-dielectric interface is a TM wave [3, 4] with the magnetic field H lying totally on the interface along the x-direction. The electric field has both transverse E_z and longitudinal E_y components. There is a standing wave along the antenna length (along y) and the (complex) phase constant of the wave is given by:

$$\beta = k_0\sqrt{\frac{\epsilon_m \epsilon_d}{\epsilon_m + \epsilon_d}}, \tag{1}$$

where k_0 is the free space wavenumber ($= \omega/c = 2\pi/\lambda_0$), while ε_m and ε_d are the relative permittivity of the metal and dielectric material respectively. Noting that $\mathrm{Re}(\varepsilon_m)$ is negative and greater in magnitude than ε_d at the frequencies of interest, we infer that β is $> k_0\sqrt{\epsilon_d}$. Furthermore if $\mathrm{Re}(\varepsilon_m+\varepsilon_d)$ approaches zero, β will attain very high values. This will reflect on the resonant antenna length which will be much shorter than the free space wavelength.

In the next section, we present simulation results for the longitudinal electric field across the Bow-tie gap versus the applied frequency of the light wave that illuminates the antenna. We define an impedance Z_g, as the longitudinal E field to transverse H field in the gap. We present simulated results of Z_g versus frequency with the gap spacing 'g' as a parameter. In Section 3 we propose a simple transmission line model for the nanoantenna that accounts for the gap length and end effects.

2. SIMULATION RESULTS

The CST commercial software is used to obtain the nanoantenna response to an incident Gaussian pulse. The longitudinal electric field E_y in the gap between the antenna arms is plotted versus the applied frequency with the antenna half length 'L' as a parameter in Fig. 2. The field displays a peak value at $f = 214$, 230, and 256 THz, corresponding to 'L' = 175, 150, and 125 nm respectively. The gap spacing 'g' is fixed at $g = 10$ nm. In Fig. 3, the Real and imaginary parts of the impedance

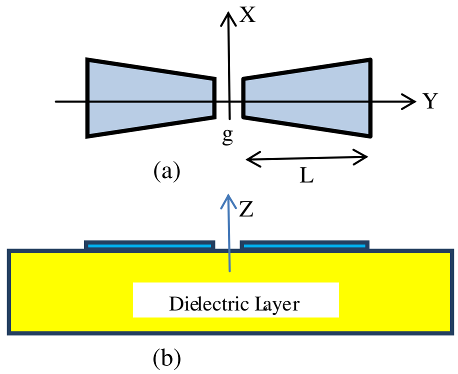

Figure 1: Nanoantenna made of metal on dielectric layer. (a) Top view. (b) Side view.

$Z_g = E_y/H_x$ are plotted versus frequency for 'L' = 125 nm and g = 10 nm. It is noted that E_y displays a peak at the same resonant frequency where $\mathrm{Re}(Z_g)$ is maximum and $\mathrm{Im}(Z_g) = 0$. Similar results for Z_g were obtained for 'L' = 150 and 175 nm (not shown) and lead to the same conclusion stated above.

Simulation results for the resonant frequency of Bow-tie antenna as a function of the gap 'g' for a given 'L' is shown in Fig. 4. The resonant frequency corresponds to maximum E_y in the gap and real impedance Z_g. It is clear that the resonant frequency shows blue shift as 'g' increases. These results have the same trend as those reported in [3].

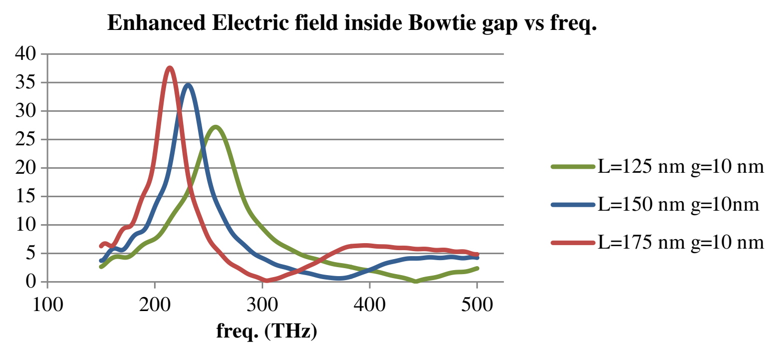

Figure 2: The longitudinal E_y field in the gap versus frequency with antenna length 'L' as a parameter.

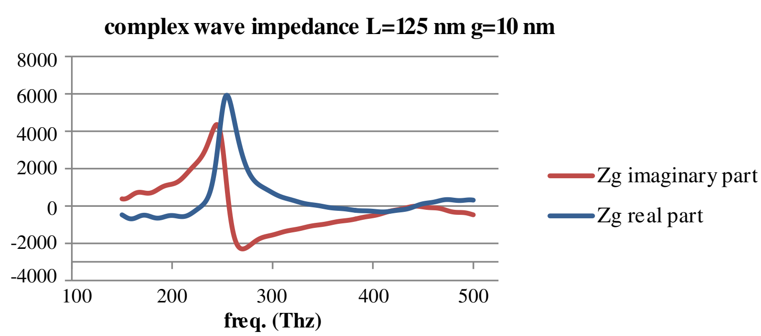

Figure 3: Simulated real and imaginary parts of Z_g versus frequency. Antenna length 'L' = 125 nm and the gap 'g' = 10 nm.

3. A TRANSMISSION LINE MODEL

In this section we attempt to find a simple transmission line model for the Bow-tie antenna to explain the behavior of the resonant frequency with the antenna length and gap. The first resonance of the nano-antenna occurs when the total phase difference between antenna terminals is equal to π radians. The equivalent transmission line of one arm of the antenna is shown in Fig. 5. The T.L has a length l_{eff} and is open circuited at the right-hand terminal, where $l_{eff} = L + \Delta l$. Here Δl accounts for field fringing at the right terminal. The wave phase constant β_r on this T.L is the real part of the TM β given by (1). The gap is accounted for by a series capacitance C connected to the T.L at one end and is grounded at the other end. The resonance condition dictates that the sum of impedances looking right and left of the capacitor must equal zero. Mathematically, this reads:

$$-jZ_0 \mathrm{Cot}\left(\beta_r l_{eff}\right) + (j\omega C)^{-1} = 0, \tag{2}$$

where Z_0 is the characteristic impedance of the T.L. Expecting $\beta_r l_{eff}$ to be close to $\pi/2$, we set $\beta_r l_{eff} = \pi/2 + \delta$; $\delta \ll 1$. Then (2) is approximated by:

$$\tan\delta \triangleq \delta = (\omega C Z_0)^{-1} \tag{3}$$

Hence:

$$k_0 l_{eff} = \frac{1}{n(\omega)}\left[\frac{\pi}{2} + (\omega C Z_0)^{-1}\right] \tag{4}$$

In the above

$$n(\omega) = \frac{\beta_r}{k_0} = \mathrm{Re}\left[\sqrt{\frac{\epsilon_m \epsilon_d}{\epsilon_m + \epsilon_d}}\right] \tag{5}$$

Equation (4) can be solved for the resonant frequency ω for a given l_{eff} and the product $Z_0 C$ (sec). We infer from (4) that as C is reduced, k_0 increases. In other words, as the gap 'g' of the Bow-tie increases, the resonant frequency increases showing a blue shift for the same antenna length. This agrees with the simulation results in Fig. 4. We choose to have $Z_0 C$ a sole function of the gap spacing 'g' while Δl is a sole function of antenna length L. By comparing the simulated results in Fig. 4 with computed resonant frequencies obtained from (4), we optimize $Z_0 C$ and Δl to have the best fit to the simulated results of Fig. 4. A comparison between the computed and simulated resonant frequencies for three values of antenna length is shown in Fig. 6. Close agreement between the results is clear, which proves the adequacy of out T.L. model.

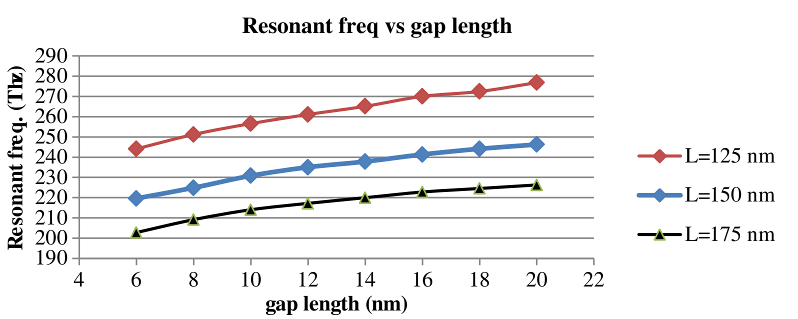

Figure 4: Resonant frequency versus the gap length 'g'. 'L' is a parameter.

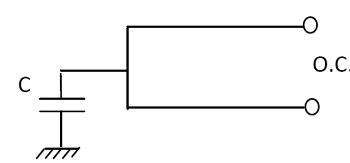

Figure 5: The equivalent transmission line of one arm of the antenna.

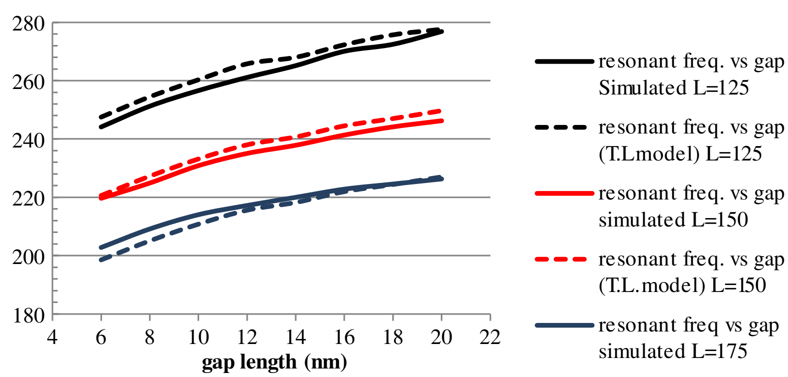

Figure 6: Comparison between antenna resonant frequencies obtained by simulations and those predicted by the T.L. model for $L = 125$, 150 and 175 nm.

4. CONCLUSIONS

A study of a Bow-tie nanoantenna made of gold on glass substrate is performed using the commercial CST software. It has been found that maximum electric field across the nanoantenna gap in the Infra-red range occurs at the resonant frequency that corresponds to a real gap impedance. The latter was defined as the ratio of the longitudinal E-field to the transverse H field in the gap. A simple transmission line model is devised to predict the resonant frequency of the nanoantenna as a function of antenna length and the gap between antenna arms.

REFERENCES

1. Ploschner, M., M. Mazilu, T. F. Krauss, and K. Dholakia, "Optical forces near a nanoantenna," School of Physics and Astronomy, University of St Andrews St Andrews, Fife, KY16 9SS, UK.
2. Gramotnev, D. K. and S. I. Bozhevolnyi, "Plasmonics beyond the diffraction limit," *Nature Photonics*, Vol. 4, Feb. 2010.
3. Biagioni, P., J.-S. Huang, and B. Hecht, "Nanoantennas for visible and infrared radiation," Jan. 2012.
4. Barnes, W. L., A. Dereux, and T. W. Ebbesen, "Surface plasmon subwavelength optics," *Nature*, Vol. 424, 824–830, Aug. 14, 2003.

Redshift by Design for Plasmonic Enhancement of Ultrathin Infrared Detectors

Marko Obradov, **Zoran Jakšić**, **Milija Sarajlić**, **and Danijela Randjelović**
Centre of Microelectronic Technologies and Single Crystals
Institute of Chemistry, Technology and Metallyrgy
University of Belgrade, Njegoševa 12, Belgrade 11000, Serbia

Abstract— In order to maximize sensitivity and specific detectivity of photodetectors, one has to ensure optimal light concentration within the active area. We considered light trapping based on surface plasmon resonance (SPR) in infrared detectors for night vision purposes. We investigated redshifting by the replacement of metal with transparent conductive oxides (TCO) like indium tin oxide and zinc oxide. We considered nanoparticle fillers embedded in a thin dielectric host with increased relative permittivity and located at the detector surface. We used finite element method to perform optimization of our plasmonic light trapping structures. Regarding the infrared detectors, we considered epitaxial mercury cadmium telluride devices with a typical active layer thickness of 4–8 micrometers. Our results show that sensitivity and specific detectivity of narrow-bandgap detectors can be significantly enhanced. Even thinner active areas than those conventionally used can be used. Since the overall level of intrinsic noise in a night vision detector (especially generation-recombination noise due to Auger processes) is dependent on the volume of the active region, in our case this noise is suppressed by the same mechanism that ensures sensitivity enhancement. Thus additional improvement of specific detectivity is achieved, which allows for higher operating temperatures of night vision photodetectors.

1. INTRODUCTION

The performance of any photodetector is determined by the photon flux within the detector active area, the efficiency of the conversion from the flux to useful electrical signal and by the stochastic fluctuations of the signal [1]. In the case of semiconductor infrared detectors operating near room temperature, noise becomes the key limiting factor to the device performance. The reason is that thermal processes causing undesired interband transitions become very strong and start to compete with transitions caused by the useful signal.

In the semiconductor devices for night vision there are three main generation-recombination (g-r) mechanisms that limit the device performance, radiative, Shockley-Read and Auger processes [2]. Among these, the nonradiative Auger processes exert the largest influence and severely limit the signal. Because these processes are dependent on the concentration of charge carriers, which itself is proportional to temperature, this is the reason why semiconductor infrared detectors are cooled, usually by liquid nitrogen.

Thermal g-r processes are also proportional to the volume of the active region, since in a smaller volume a smaller number of undesired g-r acts occurs. Since the active area is usually pre-defined, this means that the photodetector should be as thin as possible. On the other hand, the useful signal is proportional to the thickness of the detector. Thus in order to ensure maximum sensitivity one should increase the thickness, and at the same time to minimize g-r noise one needs to decrease it. This means that one needs to reach a trade-off where both requirements are partially satisfied. In order to decrease the thickness and to retain the maximum photon flux various strategies are used that belong to the light management [3].

Conventional approaches to photon management in photodetectors include increasing the light path within the device, for instance by the use of back-side reflectors, by placing the active area between two dielectric layers or by using the resonant cavity enhancement where the detector is placed between two Bragg-type dielectric mirrors [1, 4].

Recently a novel method for flux localization within the detector active area has been proposed for solar cells, the use of plasmonics [5]. To this purpose one introduces noble metal nanoparticles whose electromagnetic (EM) behavior is described by the Drude model at the front or the back surface of the detector, or alternatively includes them within the active area itself. The EM field is localized around the metal nanoparticles and ensures light localization within the devices, thus allowing for a decrease of the detector thickness. A problem is that the plasma frequency of noble metals (Au, Ag) is around the ultraviolet region and thus is not useful for infrared devices without shifting the spectral range to longer wavelengths — "redshifting".

A method for redshift is the use of designer plasmons ("spoof" plasmons) [6] where a periodic metal-dielectric structure is fabricated (for instance a subwavelength hole array) whose effective plasma frequency is strongly redshifted. Such structures were proposed to improve light management and enhance the sensitivity of night vision detectors [7].

Another method is the use of plasmonic nanoparticles for the enhancement of infrared detector performance, as proposed in Ref. [8]. To this purpose doped transparent conductive oxide (TCO) nanoparticles have been introduced instead of noble metal nanoparticles. The plasma frequency of TCO materials like tin oxide, indium tin oxide (ITO), aluminum doped zinc oxide (AZO), etc. is redshifted compared to that of noble metals [9, 10]. A further redshift is ensured through embedding the nanoparticles in dielectric with increased dielectric permittivity [11].

In this work we propose the use of TCO nanoparticles for simultaneous suppression of thermal noise in semiconductor infrared photodetectors for night vision and enhancement of their sensitivity through infrared radiation localization within the detector. In this way one uses the same mechanism to increase the sensitivity of the detector and to suppress noise. We suggest technological strategies to implement this approach. We utilize electromagnetic modeling by the finite element method to optimize the proposed photodetector structures.

2. THEORY

The noise current of an infrared photodetector due to generation-recombination processes is [1]

$$i_N = qg\sqrt{2\,(G+R)\,dwl\Delta f}, \tag{1}$$

where q is elementary electron charge, g is carrier generation rate, G is thermal generation rate and R thermal recombination rate (both dominated by Auger processes), d is the thickness of the detector active region, w is the width and l the length of the detector active area, while Δf is the operating frequency range.

The specific detectivity of the infrared detector is

$$D^* = \lambda\eta\sqrt{\frac{A_{opt}/wl}{2hcd\,(G+R)}} \tag{2}$$

where λ is the operating wavelength, η is the quantum efficiency, A_{opt} is the optical area (i.e., the area receiving the optical flux; it may differ from the real area determined as lw, for instance if some kind of optical concentrator is used), h is the Planck constant and c is the speed of light in vacuum. It can be seen that the detector volume must be minimized in order to maximize specific detectivity. On the other hand, the quantum efficiency can be approximately written as

$$\eta \approx 1 - e^{-\alpha d} \tag{3}$$

where α is the absorption coefficient of the detector material. Thus detector thickness should be maximized if the lw product is given in advance, as is typically the case.

A possible solution for this contradictory requirement is to minimize the thickness and to ensure maximal localization of electromagnetic field in thus minimized volume. The electromagnetic field is efficiently localized by the use of surface plasmons polaritons (localized plasmons polaritons in the case of nanoparticles) at the interface between materials with positive relative dielectric permittivity (semiconductor) and negative permittivity (TCO).

Figure 1 shows several possible approaches to the enhancement of EM field within the active region using surface plasmon resonance. Figure 1(a) shows a TCO nanoparticle placed directly to the active region surface. Scattering of incident IR radiation in the direction of propagation ensures field enhancement. Figure 1(b) shows a TCo particle enclosed by an core shell of dielectric with high relative dielectric permittivity ε, and Figure 1(c) shows a particle within a homogeneous dielectric host. Figure 1(d) represents a possible way to implement this by mechanically placing a freestanding dielectric membrane [12, 13] onto the surface of a previously fabricated detector. Finally, Figure 1(e) show the situation where mercury cadmium telluride ($Hg_{1-x}Cd_xTe$) narrow-bandgap semiconductor is used; the presented sharply graded profile is typical for the devices fabricated by vapor-phase epitaxy [14].

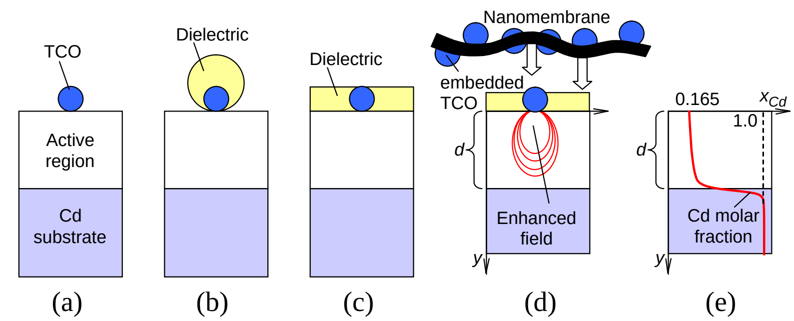

Figure 1: IR detector enhancement by TCO nanoparticles. (a) TCO at the surface. (b) Core-shell TCO with high-ε dielectric. (c) High-ε dielectric with embedded TCO particle. (d) A method of application of embedded TCO nanoparticles to an existing detector by mechanically placing a freestanding membrane. (e) Spatial profile of Cd molar fraction across HgCdTe sample.

3. RESULTS

The field localization due to the introduction of nanoparticle fillers has been calculated by finite element method (FEM) simulations utilizing the Comsol Multiphysics package (RF module). The case shown in Figure 1(c) was assumed, a dielectric layer containing TCO particles applied to the surface of semiconductor. The TCO was indium tin oxide (ITO) [10] with a doping level furnishing a plasma resonance at 700 nm. The TCO particle diameter was $d = 250$ nm.

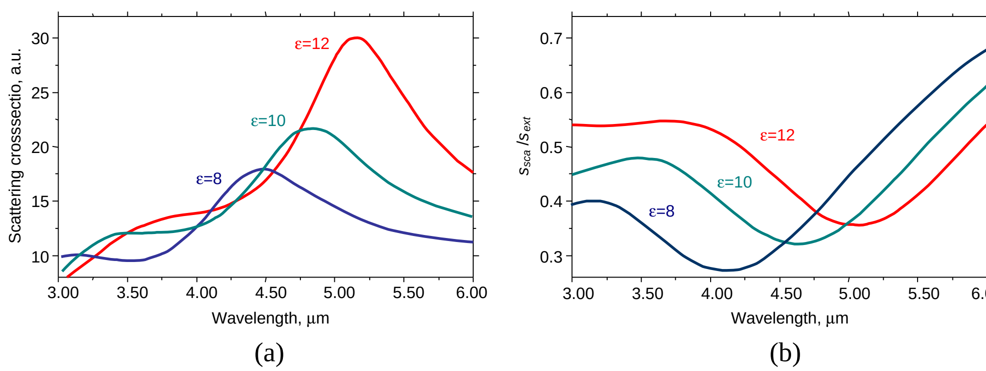

Figure 2: Spectral dependence of scattering S_{scat} and extinction S_{ext} cross-section for an embedded ITO particle, $d = 250$ nm, $\lambda_p = 700$ nm. (a) Scattering cross section. (b) Ratio of scattering S_{scat} and extinction S_{ext} cross section ($S_{ext} = S_{abs} + S_{scat}$).

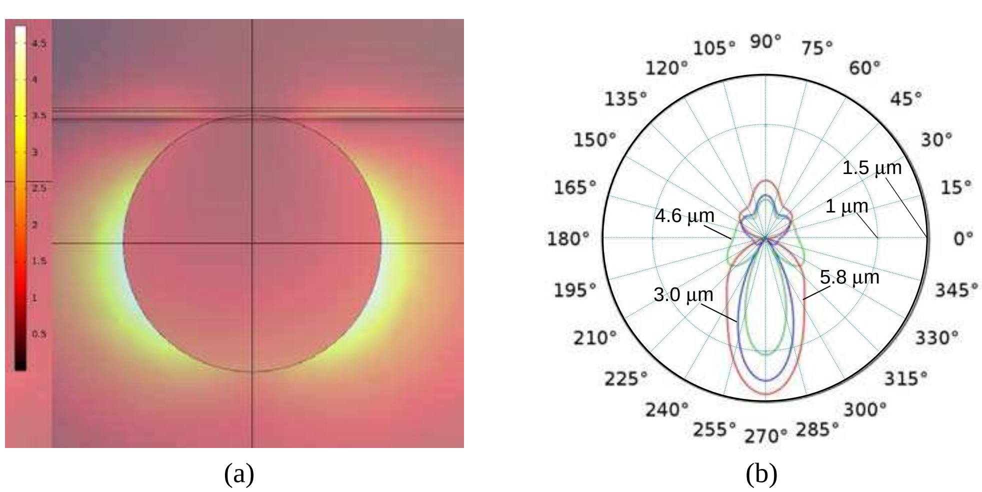

Figure 3: Near and far field around the ITO particle on top of an $Hg_{1-x}Cd_xTe$ sample. Incident EM wave arrives from top. (a) Spatial dependence of near field. (b) Polar diagram of far field distribution.

Figure 2(a) shows the spectral dependence of scattering cross-section for three different values of relative permittivity of the embedding dielectric layer. All cross-section peaks are obtained in the (3–5) μm atmospheric window. As expected, the redshift increases with the increase of the refractive index of the embedding medium.

Figure 2(b) shows the ratio of scattering cross section S_{scat} and extinction cross section S_{ext}. As the wavelength increases and nears resonance a dip of the characteristics appears. This is associated with the mechanism of plasmon resonance and accompanying high losses.

Figure 3(a) shows the near field distribution around a single TCO particle. Strong localization around the bottom part of the particle is readily observed. A polar diagram for far field distribution is shown in Figure 3(b) for three different wavelengths. Peak field is achieved at a distance of about 1 μm to 1.5 μm from the bottom of the TCO sphere. These results suggest that even thinner detector active areas can be used than those encountered in the state of the art devices. Structures with an active area thickness decreased down to 1–3 μm could be utilized. These can be fabricated by depositing $Hg_{1-x}Cd_xTe$ onto CdTe substrate by, e.g., isothermal vapor phase epitaxy [14] or the already existing structures can be thinned by wet etching in bromine-methanol solution [15].

4. CONCLUSION

We described a strategy to improve sensitivity of intrinsic semiconductor infrared detector by using TCO nanoparticles and redshifting approaches that ensure their use in the infrared wavelength range. We utilized numerical approach to simulate our devices. We applied finite element method utilizing Comsol Multiphysics package to model EM scattering on TCO. We show that the method is also useful for suppression of thermal noise, including Auger noise. Thus we conclude that our approach can be used both to improve light management and to decrease noise equivivalent power, thus ensuring operation of conventional infrared detectors at elevated temperatures. An important detail is that the approach is applicable not only during fabrication of infrared detectors, but could be also utilized to improve performance of finished devices. Our further steps will be dedicated to the consideration of our approach within the context of designer plasmon structures applied to the photodetector surface.

ACKNOWLEDGMENT

This work has been partially funded by Serbian Ministry of Education, Science and Technological Development within the framework of the project TR 32008.

REFERENCES

1. Rogalski, A., *Infrared Detectors*, CRC Press, Bocca Raton, 2010.
2. Piotrowski, J. and A. Rogalski, *High-operating Temperature Infrared Photodetectors*, SPIE Press, Bellingham, 2007.
3. Yablonovitch, E. and G. D. Cody, "Intensity enhancement in textured optical sheets for solar cells," *IEEE Transactions on Electron Devices*, Vol. 29, 300–305, 1982.
4. Ünlü, M. S. and S. Strite, "Resonant cavity enhanced photonic devices," *J. Appl. Phys.*, Vol. 78, 607–639, 1995.
5. Atwater, H. A. and A. Polman, "Plasmonics for improved photovoltaic devices," *Nature Mater.*, Vol. 9, 205–213, 2010.
6. Pendry, J. B., L. Martín-Moreno, and F. J. Garcia-Vidal, "Mimicking surface plasmons with structured surfaces," *Science*, Vol. 305, 847–848, 2004.
7. Catchpole, K. R. and A. Polman, "Plasmonic solar cells," *Opt. Express*, Vol. 16, 21793–21800, 2008.
8. Jakšić, Z., M. Milinović, and D. Randjelović, "Nanotechnological enhancement of infrared detectors by plasmon resonance in transparent conductive oxide nanoparticles," *J. Mech. Eng.*, Vol. 58, 367–375, 2012.
9. Boltasseva, A. and H. A. Atwater, "Low-loss plasmonic metamaterials," *Science*, Vol. 331, 290–291, 2011.
10. Franzen, S., C. Rhodes, M. Cerruti, R. W. Gerber, M. Losego, J. P. Maria, and D. E. Aspnes, "Plasmonic phenomena in indium tin oxide and ITO-Au hybrid films," *Opt. Lett.*, Vol. 34, 2867–2869, 2009.
11. Schmid, M., R. Klenk, M. C. Lux-Steiner, M. Topič, and J. Krč, "Modeling plasmonic scattering combined with thin-film optics," *Nanotechnology*, Vol. 22, 025204.1–025204.10, 2010.

12. Jiang, C., S. Markutsya, Y. Pikus, and V. V. Tsukruk, "Freely suspended nanocomposite membranes as highly sensitive sensors," *Nature Mater.*, Vol. 3, No. 10, 721–728, 2004.
13. Jakšić, Z. and J. Matovic, "Functionalization of artificial freestanding composite nanomembranes," *Materials*, Vol. 3, 165–200, 2010.
14. Djurić, Z., Z. Jakšić, Z. Djinović, M. Matić, and Ž. Lazić, "Some theoretical and technological aspects of uncooled HgCdTe detectors: A review," *Microelectron. J.*, Vol. 25, 99–114, 1994.
15. Srivastav, V., R. Pal, and H. P. Vyas, "Overview of etching technologies used for HgCdTe," *Opto-El. Rev.*, Vol. 13, 197–211, 2005.

Gain Assisted Surface Plasmon Polariton Propagation in a Schottky Junction Based Cylindrical Structure

T. M. Wijesinghe and M. Premaratne
Advanced Computing and Simulation Laboratory (AχL)
Department of Electrical and Computer Systems Engineering
Monash University, Clayton, VIC 3800, Australia

Abstract— High propagation losses associated with surface plasmon polariton (SPP) guiding structures are a major problem in plasmonics. We investigate SPP mode propagation in a radial Schottky junction channel where the structure simultaneously provides both a gain medium and a waveguide with high mode confinement. An analytical theory is deduced to describe the possibility of loss compensation of the SPP field. Furthermore, the dependence of modal gain with core radius and applied voltage across the Schottky junction is discussed.

1. INTRODUCTION

Surface plasmon polartions (SPPs) are hybrid transverse magnetic optical waves that are bounded and propagate along metal-dielectric interfaces and oscillate collectively with free electrons in the metal [1, 2]. SPPs have proven to be effective in nanoscale as its ability to confine and manipulate photonic energy through subwavelength structures, overcoming constraints imposed by the fundamental diffraction limit [3]. The fundamental SPP properties have been found applications in fields such as spectroscopy [4], nanophotonics, circuitry [5], bio-sensing and imaging [6].

SPP waveguides considered to be a major topic in photo-electronics which lead to efficient integration of photonics elements with electronic circuitries. Recent studies scaled down the SPP waveguides from metal stripes [5, 7] to nanowires [8] and nanoparticle chains, demonstrating more improved SPP manipulations. However, the inherent losses in metallic elements cause SPP propagation distance limit to few micrometers. The ability of energy gain by interacting SPP with an active media has been studied in recent research literature for different plasmonic structures incorporating active media such as dye molecules, polymers and semiconductor heterostructures [9–13].

In this work we demonstrate a parametric study on partial compensation of SPP power loss in the metal by supplying gain through carrier injection to the SPP mode propagate in the waveguide using a semiconductor active medium in order to improve the mode propagation length. We consider a cylindrical structure which is formed by a metal core and a finite semiconductor shell as shown in Fig. 1(a). The cylindrical SPP modes show tight confinement to the interface than the planer SPP modes [5]. Further, cylindrical structure provides an inherently large surface area to volume ratios, inducing more interface effects [14] hence junction properties can be used more effectively for this system.

2. SPP IN A RADIAL SCHOTTKY JUNCTION

Referring to Fig. 1(a), we assume SPP modes in the metal-semiconductor interface propagate alone z direction. The SPP propagation modes in a cylindrical structure can be solved following a similar procedure used for a planer structure. The SPP modes can be found by using Maxwell's equations in cylindrical coordinates (r, ϕ, z) and applying boundary conditions at the metal-semiconductor interface [See Fig. 1(a)] [1, 15]. The solution of these equations gives the magnetic field component of transverse magnetic SPP mode as,

$$H_{\phi,m} = A_m \frac{i\omega\epsilon_m\epsilon_o}{\gamma} I_0'(r\gamma_m)\exp(i\beta z - i\omega t),$$

and

$$H_{\phi,s} = A_s \frac{i\omega\epsilon_s\epsilon_o}{\gamma} K_0'(r\gamma_s)\exp(i\beta z - i\omega t)$$

where β and $\gamma_{m,s} = \sqrt{\beta^2 - k^2\epsilon_{m,s}\epsilon_o}$ are the longitudinal and transverse SPP wave vectors. The symbols ω, k, ϵ_o, t, $A_{m,s}$ and $\epsilon_{m,s}$ are frequency, wave vector of vacuum, permittivity of vacuum, time, amplitudes and permittivity of metal or semiconductor, respectively. The notations I_0, K_0,

I_1, K_1, I_0', K_0' are modified bessel functions of first and second kind with order zero and one and their derivatives, respectively. The wave vector β is found by solving the dispersion equation given by,

$$\frac{\gamma_s}{\gamma_m}\frac{I_1(r_o\gamma_m)}{I_0(r_o\gamma_m)}\frac{K_0(r_o\gamma_s)}{K_1(r_o\gamma_s)}+\frac{\epsilon_s}{\epsilon_m}=0$$

Accordingly we can find electrical field components (F_r and F_z) of SPP mode using Maxwell's equations and propagation length, $L_{sp}=1/2\mathrm{Im}(\beta)$ [5].

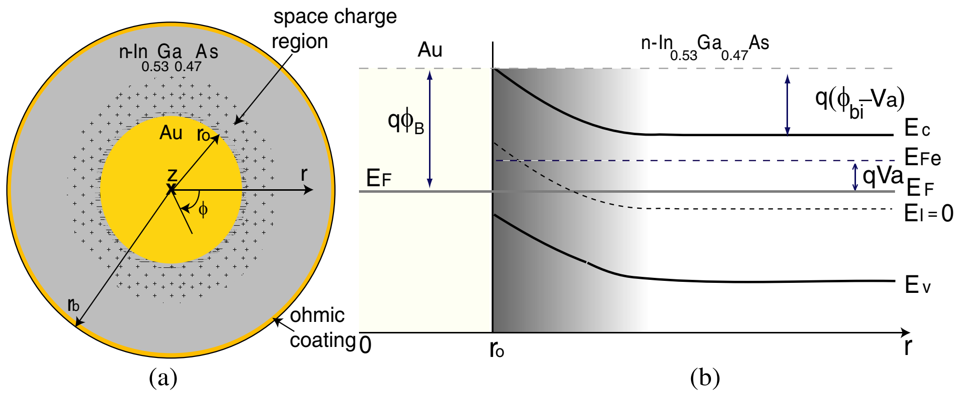

Figure 1: (a) The cross section of the radial Schottky junction waveguide with an active region. (b) The energy band diagram of the Schottky junction along radial direction. The variables are defined in the Section 2.

The energy band diagram along the plane r with fixed ϕ and z is shown in Fig. 1(b). A Schottky barrier, $q\phi_B$ is formed in the Au/n-In$_{0.53}$Ga$_{0.47}$As interface with a space charge region in the semiconductor region [16, 17]. Here E_c and E_v are the conduction and valance energy bands. E_F defines the Fermi energy level while E_{Fe} is the quasi fermi level of electrons. E_I is the intrinsic energy level which is considered as the zero reference level. Inside the semiconductor the normalized potential is defined as $u=(E_F-E_I)/KT$. Here K, T and q are Boltzmann constant, absolute temperature and electron charge. Under degenerate conditions the free hole, p and electron, n distribution in the semiconductor can be found using the the Fermi-Dirac statistics:

$$p=\frac{2}{\sqrt{\pi}}N_v\mathbf{F}_{\frac{1}{2}}\left(\frac{E_v-E_F}{KT}\right) \tag{1}$$

where, N_v and $\mathbf{F}_{\frac{1}{2}}$ are the effective density of states of valance band and Fermi-Dirac integral, respectively [16, 18]. When the junction is forward biased with an applied voltage V_a, the condition for a p-type inversion layer is $p-n\gg N_D$ where N_D defines the donor density. By applying Poisson's equation to radial Schottky junction,

$$\frac{1}{r}\frac{d}{dr}\left(r\frac{du}{dr}\right)=-\frac{q}{KT}\frac{\rho}{\epsilon} \tag{2}$$

Assuming $\rho=\rho_D+q(p-n)$ where ρ_D is donor impurity concentration, we can expand the (2) in to,

$$\frac{1}{r}\frac{du}{dr}+\frac{d^2u}{dr^2}=-\frac{1}{2L_D^2}\left[\frac{N_D}{n_i(1+2e^{(u-w_{D,I})})}+\frac{\mathbf{F}_{\frac{1}{2}}(w_{V,I}-u)}{\mathbf{F}_{\frac{1}{2}}(w_{V,I})}-\frac{\mathbf{F}_{\frac{1}{2}}(u-w_{C,I})}{\mathbf{F}_{\frac{1}{2}}(w_{I,C})}\right], \tag{3}$$

where $L_D=\sqrt{\epsilon_s kT/2q^2 n_i}$ and n_i are the intrinsic Daybe length and intrinsic carrier density. The notation w defines the energy difference between point P and Q by $w_{P,Q}=(E_P-E_Q)/q$. Then, E_D defines the electron energy level of donors. To estimate the potential distribution along the space charge region, (3) is solved by integration. Accordingly we obtained the following expression.

$$\int_{r_o}^{r}\frac{dr}{\sqrt{\ln(r_b/r)-1}}=\sqrt{2}L_D\int_{u_o}^{u}\frac{du}{\sqrt{S}} \tag{4}$$

where,

$$S = \frac{N_D}{n_i} \ln \left[1 + \frac{1}{2} e^{(w_{D,I} - u)} \right]_u^{u_b} - \frac{2}{3} \left[\frac{\mathbf{F}_{\frac{3}{2}}(w_{V,I} - u)}{\mathbf{F}_{\frac{1}{2}}(w_{V,I})} \right]_u^{u_b} + \frac{2}{3} \left[\frac{\mathbf{F}_{\frac{3}{2}}(u - w_{C,I})}{\mathbf{F}_{\frac{1}{2}}(w_{I,C})} \right]_u^{u_b}$$

Then (4) is solved integrating from the interface ($r = r_o$) to the bulk region, where u_o and u_b define the potentials in interface and bulk region [19]. Accordingly, the carrier distributions p and n along r are found.

The material gain spectrum for $In_{0.53}Ga_{0.47}As$ for $N_D = 1 \times 10^{18}\,\mathrm{cm}^{-3}$ and $p = 5 \times 10^{19}\,\mathrm{cm}^{-3}$ is shown in Fig. 2(a) [20]. The material gain can be approximated in terms of minority carrier density in the inversion region by $g_m = g_o[\ln(p/p_o) + 1]$, where g_o and p_o are constant parameters

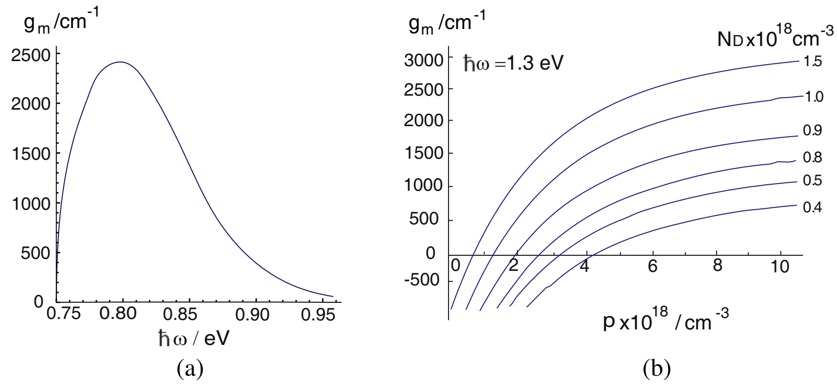

Figure 2: (a) The material gain spectrum of $In_{0.53}Ga_{0.47}As$ for $N_D = 1 \times 10^{18}\,\mathrm{cm}^{-3}$ and $p = 5 \times 10^{19}\,\mathrm{cm}^{-3}$. (b) The material gain variation with minority carrier density, p for different N_D value. Assumed $h\omega = 1.3\,\mathrm{eV}$ and energy gap of $In_{0.53}Ga_{0.47}As$ is $0.75\,\mathrm{eV}$.

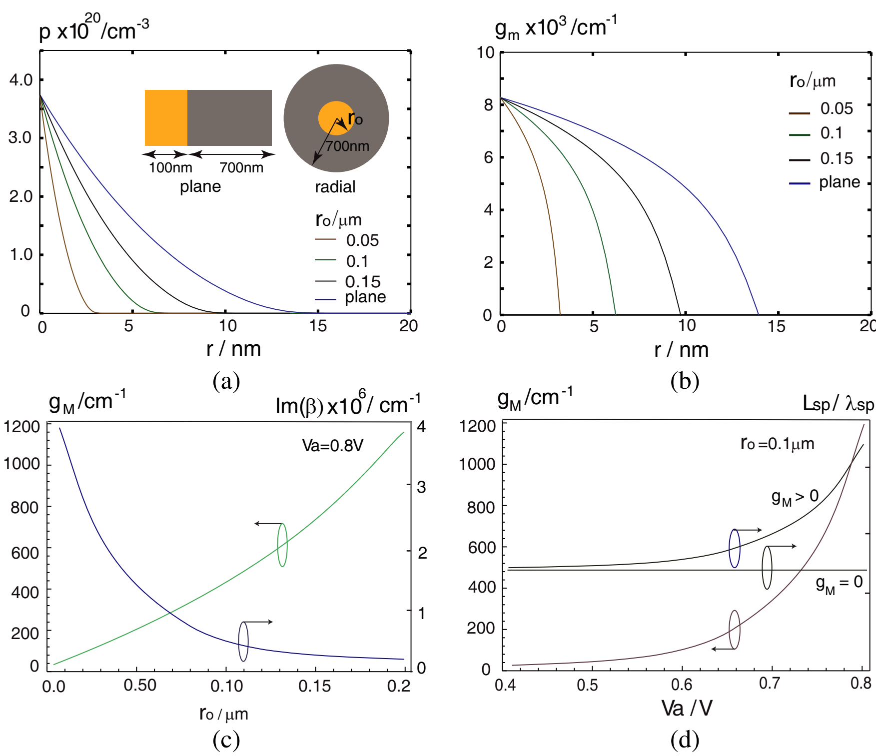

Figure 3: (a) Minority carrier distribution along the radius of the shell, assuming $r = r_o$ at the metal-semiconductor interface. (b) Material gain distribution along the radius of the shell, assuming $r = r_o$ at the interface. (c) Variation of modal gain, g_M and $\mathrm{Im}(\beta)$ with the core radius r_o. (d) Variation of g_M and L_{sp}/λ_{sp} with the applied voltage. Assumed $N_D = 1 \times 10^{18}\,\mathrm{cm}^{-3}$, $\lambda = 1.7\,\mu\mathrm{m}$ and energy gap of $In_{0.53}Ga_{0.47}As$ is $0.75\,\mathrm{eV}$.

[See Fig. 2(b)]. Under the high forward biased conditions the minority carriers are injected to the interface leading an carrier inversion near the Schottky junction which is found using (1). Hence material gain distribution near the interface can be analysed. The Figs. 3(a) and 3(b) illustrate p and g_m distributions near the junction. These variations are compared for different core radii and planer structure with same dimensions [Shown in the inset of Fig. 3(a)]. As the core radius increases, the inversion region width increases towards that of the plane structure. Finally the modal gain g_M experienced by SPP field in this coaxial junction can be calculated by [10, 12],

$$g_M = \frac{k_o\sqrt{\epsilon_s}\int_{r_o}^{r_b} g_m(r)|H_\phi(r)|^2 dr}{\mathrm{Re}(\beta)\int_0^{r_b}|H_\phi(r)|^2 dr}. \tag{5}$$

The variation of g_M and $\mathrm{Im}(\beta)$ with core radius r_o are shown in Fig. 3(c). Smaller r_o shows higher β values and accordingly higher $\gamma_{m,s}$ values. Hence the radial SPP modes are tightly confined to the interface compared to planer structures, but creating higher losses limiting propagation length. Therefore, compensating losses is required. The modal gain, g_M improves with r_o as β decreases and inversion width increases accordingly. Then, the propagation length, L_{sp} can be estimated including modal gain contribution. g_M and L_{sp}/λ_{sp} variation with V_a is shown in Fig. 3(d) where $\lambda_{sp} = 2\pi/\mathrm{Re}(\beta)$. At $Va = 0.8\,\mathrm{V}$, L_{sp}/λ_{sp} for Schottky junction has improved nearly by 50% for the gain assisted case. Compared to the planer Schottky junction, the radial Schottky junction has much smaller space charge width and SPP mode penetration depths to each media. Therefore waveguide can be miniaturized further avoiding bulk structures while providing gain to compensate losses.

3. CONCLUSION

The radial Schottky junction with an ohmic coating in the surface can be used to obtain an improved SPP propagation length under forward biased conditions. A Schottky junction with a high barrier height could form an inversion layer in its space charge region under the forward biased condition. Here carrier injection takes place in the radial direction hence creating much smaller space charge region. This leads to a population inversion in the junction, yielding a stimulation emission process. Hence, gain can be provided to the SPP field to partially compensate propagation losses.

In this work we derived analytical expressions for the carrier behavior in the radial Schottky junction and demonstrated the effect of core radius and externally applied voltage on inversion region and associated material gain distribution in the active region. Further, we defined the modal gain coefficient for TM-SPP mode propagates along the cylindrical structure which is formed using Au core and n-$\mathrm{In}_{0.53}\mathrm{Ga}_{0.47}\mathrm{As}$ shell. Then we analysed the power loss coefficient and estimate the net modal gain experienced by SPPs. Accordingly, we showed a considerable improvement in mode propagation length. This method leads to well confined and miniaturized long range SPP channels having more simple and efficient gain provision by electrical injection. This analysis gives vital information for design and utilization of radial Schottky junction as active waveguides for routing SPPs in integrated circuitry.

ACKNOWLEDGMENT

The authors would like to thank Australian Research Council for the financial support.

REFERENCES

1. Premaratne, M. and G. P. Agrawal, *Light Propagation in Gain Media: Optical Amplifiers*, Cambridge University Press, 2011.
2. Ozbay, E., "Plasmonics: Merging photonics and electronics at nanoscale dimensions," *Science*, Vol. 311, 189–193, 2006.
3. Barnes, W. L., A. Dereux, and T. W. Ebbesen, "Surface plasmon subwavelength optics," *Nature Photonics*, Vol. 424, 824–830, 2003.
4. Kawata, S., Y. Inouye, and P. Verma, "Plasmonics for near-field nano-imaging and superlensing," *Nature Photonics*, Vol. 3, 388–394, 2009.
5. Sarid, D. and W. Challener, *Modern Introduction to Surface Plasmons: Theory, Mathematica Modeling and Applications*, Cambridge University Press, 2010.
6. Anker, J. N., W. P. Hall, O. Lyandres, N. C. Shah, J. Zhao, and R. P. V. Duyne, "Biosensing with plasmonic nanosensors," *Nature Materials*, Vol. 7, 442–453, 2008.

7. Maier, S. A., "Gain-assisted propagation of electromagnetic energy in subwavelength surface plasmon polariton gap waveguides," *Opt. Commun.*, Vol. 258, No. 2, 295–299, 2006.
8. Handapangoda, D., I. D. Rukhlenko, M. Premaratne, and C. Jagadish, "Optimization of gain–assisted waveguiding in metal–dielectric nanowires," *Opt. Lett.*, Vol. 35, No. 24, 4190–4192, Dec. 2010.
9. Gather, M. C., K. Meerholz, N. Danz, and K. Leosson, "Net optical gain in a plasmonic waveguide embedded in a fluorescent polymer," *Nature Photonics*, Vol. 4, 457–462, 2010.
10. Fedyanin, D. Y. and A. V. Arsenin, "Surface plasmon polariton amplification in metal-semiconductor structures," *Opt. Express*, Vol. 19, No. 13, 12524–12531, Jan. 2011.
11. Stockman, M. I., "Loss compensation by gain and spasing," *Phil. Trans. R. Soc*, Vol. 369, 3510–3524, Sep. 2011.
12. Wijesinghe, T. M., and M. Premaratne, "Surface plasmon polaritons propagation through a Schottky junction: Influence of the inversion layer," *IEEE Photon. J.*, Vol. 5, 4800216, 2013.
13. Wijesinghe, T. and M. Premaratne, "Dispersion relation for surface plasmon polaritons on a schottky junction," *Opt. Express*, Vol. 20, No. 7, 7151–7164, Mar. 2012.
14. Kayes, B., H. Atwater, and N. Lewis, "Comparison of the device physics principles of planar and radial p-n junction nanorod solar cells," *J. Appl. Phys.*, Vol. 97, 114301, 2005.
15. Pritz, J. and L. Woods, "Surface plasmon polaritons in concentric cylindrical structures," *Solid State Commun.*, Vol. 146, 345–350, 2008.
16. Sze, S. M. and K. K. Ng, *Physics of Semiconductor Devices*, 3rd Edition, John Wiley and Sons, 2006.
17. Tersoff, J., "Schottky barriers and semiconductor band structures," *Phys. Rev. B*, Vol. 32, 6968–6971, Nov. 1985.
18. Seiwatz, R. and M. Green, "Space charge calculations for semiconductors," *J. Appl. Phys.*, Vol. 29, 1034–1041, Feb. 1958.
19. Lindfield, G. and J. Penny, *Numerical Methods: Using MATLAB*, 3rd Edition, Academic Press Inc., 2012.
20. Chuang, S. L., *Physics of Photonic Devices*, 2nd Edition, John Wiley and Sons, 2009.

Novel, Compact and Multiband Antenna for Mobile and Wireless Communication

Kamel S. Sultan[1], **Haythem H. Abdullah**[1], **Esmat A. Abdallah**[1], **and Essam A. Hashish**[2]

[1]Electronics Research Institute, Dokki, Giza, Egypt
[2]Faculty of Engineering, Cairo University, Giza, Egypt

Abstract— In this paper, an open slot antenna fed by a U shaped monople is introduced. The slot antenna radiates in the range from 1.6 to 3.44 GHz and from 3.8 to 5.7 GHz. The slot is formed by an open ring of quarter wavelength at 900 MHz. Thus, the ring acts as a monopole at 900 MHz in addition to a wideband slot radiator in the high frequency range. In order to serve the LTE700 MHz band, another ringe monopole is added to the antenna. The proposed antenna has a −10 dB bandwidth which extends from 674 to 750 MHz, from 872 to 976 MHz, from 1.6 to 3.44 GHz, and from 3.8 to 5.7 GHz. The antenna size is $23 \times 31 \times 1.5\,\mathrm{mm}^3$. A prototype of the antenna was fabricated using FR4 substrate ($\boldsymbol{\varepsilon}_\mathbf{r} = 4.5$) with 1.5 mm thickness and loss tangent of 0.025. This paper proposes a new mobile handset antenna structure with low SAR values with compact size that cover most of the mobile operating bands and other wireless applications. The covered bands are the GSM900, DCS1800, PCS1900, UMTS2100, and most of the LTE bands including the LTE700 band. Furthermore, it covers the ISM, WIMAX and the WLAN bands. The SAR calculations are done using the CST 2012 commercial package and the voxel head modal. The SAR values are calculated at different operating bands, different distances, and different orientations. The effect of the human body on the performance of the antenna is tested by calculating the radiation pattern in the presence of the body. The simulation results are compared to the experimental measurements and a good agreement is observed.

1. INTRODUCTION

The current development demand of mobile devices is to be smaller, slimmer, lighter, and to have low specific absorption rate (SAR). Also, the future development of the personal communication devices will aim to provide image, voice and data communication at any time. This indicates that mobile devices are required to support different technologies and operate in different frequency bands. The LTE (Long Term Evolution) is a new high-performance air interface standard for cellular mobile communication systems. It is the 4th generation (4G) of radio technologies to increase the capacity and speed of mobile telephone networks [1–6].

In order to include LTE700, Bhatti et al. [2] proposed a new compact dual band antenna that consists of two meander-line monopoles that covers the LTE700 (at −10 dB) with dimensions of $50 \times 87 \times 1\,\mathrm{mm}^3$. Other antennas were designed to include LTE700/LTE2300/LTE2500, e.g., Young et al. [3] introduced an octa band antenna with more compact size of $46 \times 7 \times 11\,\mathrm{mm}^3$. The antenna operating bands are; the LTE700, GSM 850, GSM900, DCS1800, PCS1900, WCDMA2100, LTE2300, and the LTE2500 bands at (−6 dB). Although the antenna proposed by Young et al. [3] has a compact size and covers octa bands of the operating frequencies, still many bands need to be covered. In addition, it consists of multilayers that complicate the fabrication process. Wong and chen [4] recently proposed a small-size printed loop antenna integrated with two stacked coupled-fed shorted strip monopoles for multiband operation in a mobile phone that covers LTE700, LTE2300, LTE2500, GSM850, GSM900, DCS1800, PCS1900, and UMTS bands (at −6 dB) with size reduction compared to [3]. Guo et al. [5] introduced a new compact multiband antenna that covers new bands than [3, 4], GSM900, DCS1800, PCS1900, UMTS2100, and some LTE bands (FDD-LTE band 1–6, 8–10 and TDD-LTE band 19, 20, 33–37) [6] with dimensions of $50 \times 15 \times 4\,\mathrm{mm}^3$.

In this paper, a novel internal antenna consisting of a monopole with two branch lines to cover multibands including the LTE bands is introduced. The proposed antenna has −10 dB bandwidth which extends from 674 to 750 MHz, from 872 to 976 MHz, from 1.6 to 3.44 GHz, and from 3.8 to 5.7 GHz, which means that it supports the following operating bands; GSM900, DCS1800, PCS1900, UMTS2100, ISM2450, most LTE bands (FDD-LTE band 1–4, 7–12, 15–17, 23–25 and TDD-LTE band 33–41), WiMAX (2.3–2.4 GHz, 2.5–2.69 GHz, 5.1–5.7 GHz), and WLAN (2.4–2.5 GHz, 4.8–5 GHz, and 4.825–5.515 GHz), with a size of $23 \times 31 \times 1.5\,\mathrm{mm}^3$. The GSM850, some LTE bands (FDD-LTE band 5, 6, 13, 14, 28–22 and TDD-LTE 42–43) and WiMAX (3.3–3.8 GHz, and 3.4–3.6 GHz) are covered at −6 dB impedance bandwidth.

2. ANTENNA DESIGN

The proposed antenna is a planar microstrip antenna with compact dimensions of $(23 \times 31 \times 1.5)\,\mathrm{mm}^3$. The antenna can be easily integrated in small and sleek mobile device. Fig. 1 shows the geometry of the proposed antenna. All the labeled dimensions are tabulated in Table 1. A prototype of the antenna was fabricated over FR4 substrate ($\epsilon_r = 4.5$) with 1.5 mm thickness and loss tangent of 0.025 as shown in Fig. 2. The proposed antenna is composed of a planar U-shaped monopole and two branch lines. The first branch line acts as a monopole radiator at the 900 MHz and at the same time acts as a cavity resonator fed by the U-shaped monopole that radiates in the upper frequency bands. The two branch lines increase the path over which the surface current flows and that eventually results in lowering the resonant frequency. The electrical length of the first line is optimized to resonate at 900 MHz (872–976 MHz). The optimized length of the first line is 62 mm and the electrical length of the second line is optimize to resonate at 700 MHz (674–750 MHz) with length 82 mm. The antenna parameters are tabulated in Table 1.

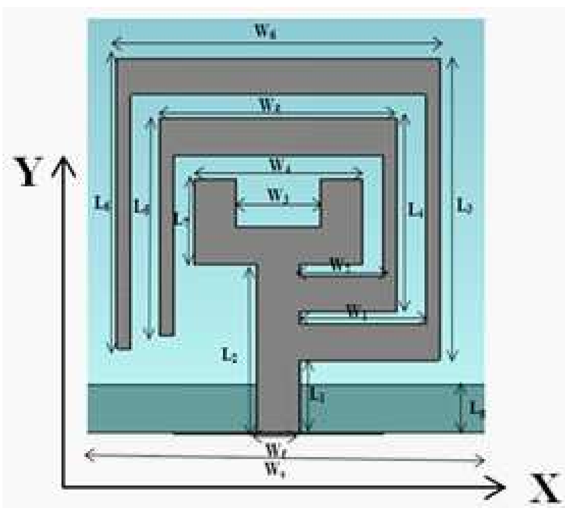

Figure 1: Geometry of the proposed antenna.

Figure 2: Photo of the fabricated antenna.

Table 1: Parameters of the proposed antenna (all dimensions in mm).

Parameter	Value	Parameter	Value	Parameter	Value	Parameter	Value
L_1	3	L_5	18	W_1	9	W_5	17
L_2	15	L_6	24	W_2	6	W_6	23
L_3	25	L_7	7	W_3	6	W_s	25
L_4	16	L_g	4	W_4	12	W_f	3

3. SIMULATION AND MEASURED RESULTS

The proposed antenna is simulated using the CST Microwave Studio 2011. Fig. 3 shows a comparison between the simulated and the measured results of the return loss. The simulated and the experimental results ensure that the antenna covers all the aforementioned mobile and wireless applications bands. Taking the −10 dB return loss reference, the antenna operates in the four bands (674–750 MHz), (872–976 MHz), (1.6–3.44 GHz), and (3.8–5.7 GHz). The first and the second resonant frequency are controlled by adjusting the total length of the second and first lines and the third and fourth resonant are controlled by adjusting the dimensions of monopole radiators and branch lines. The gain of the proposed antenna 1.2 dBi, 2.3 dBi, 2 dBi and 1.8 dBi at the following frequancies 0.7 GHz, 0.9 GHz, 1.8 GHz, and 2.1 GHz, respectivity. Fig. 4 shows the radiation pattern of the proposed antenna at the first resonant frequency (0.7 GHz).

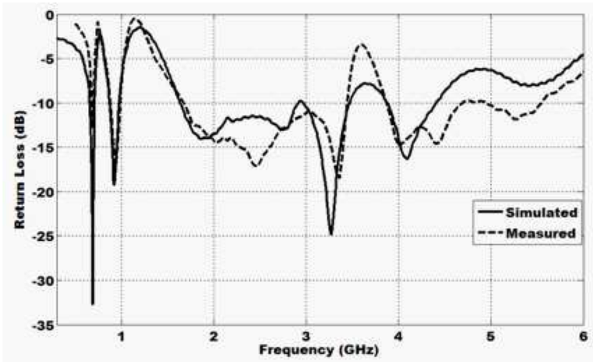

Figure 3: Simulated and measured return loss of the proposed antenna.

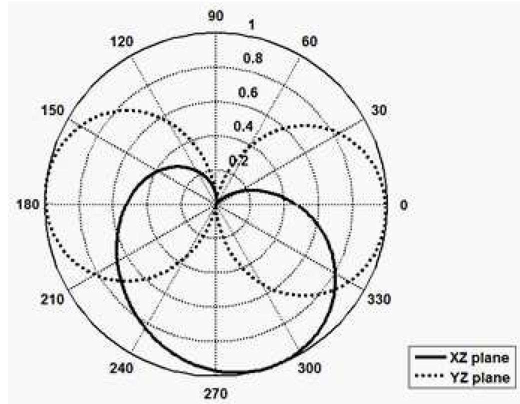

Figure 4: Simulated radiation pattern at 0.7 GHz.

4. SAR CALCULATION

As the use of the mobile phone is increased, the research on the health risk due to the electromagnetic (EM) fields generated from wireless terminals is widely in progress. Many factors may affect the EM interaction while using cellular handset in close proximity to head and hand. One of the most widely used parameters for the evaluation of exposure is SAR, specific absorption rate. Therefore, some regulations and standards have been issued to limit the radiation exposure from the mobile handsets not only to decrease the SAR but also to increase the antenna systems efficiency.

The SAR limit specified in IEEE C95.1: 2005 has been updated to 2 W/kg over any 10-g of tissue [7], which is comparable to the limit specified in the International Commission on Non-Ionizing Radiation Protection (ICNIRP) guidelines [8]. The output power of the cellular phone model need to be set before SAR is simulated. In this paper, the output power of the cellular phone is set to 500 mW at the operating frequencies of 0.7, 0.9, 1.8, and 2.1 GHz. Fig. 5 shows the antenna structure in the vicinity of the human head model (Hugo Voxel model) [9]. The SAR values are calculated according to the 10 gram standard of the human tissue mass. The SAR calculations are done using the CST 2012 commercial package with Hugo model CST Microwave Studio [10]; the tissues that are contained have relative permittivities and conductivities, according to [11]. The tissues frequency dispersive properties are taken into consideration. As expected, the SAR values depend on the operating frequency, the antenna types and the distance between the antenna and the human body. Table 2 shows the averaged 10 g SAR at the aforementioned operating frequencies when the antenna is in close proximity to the body.

It is noticed that the antenna fulfills the IEEE C95.1: 2005 and the ICNIRP standards. Due to the results scalability when the power level changes, the SAR values could be controlled by adjusting the separation between the antenna and the head.

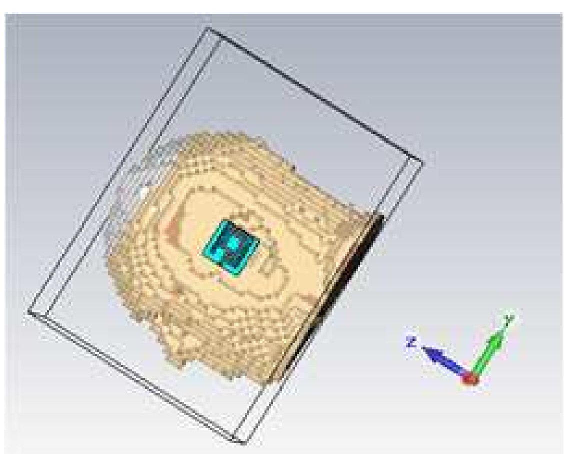

Figure 5: Antenna structure with the human head model (Hugo voxel model).

Table 2: SAR values and the effects of human model on antenna proporties.

F (GHz)	SAR (W/kg) (10 g)	In free space		With human model	
		S_{11} (dB)	Radiation efficiency (%)	S_{11} (dB)	Radiation efficiency (%)
0.7	1.07	−23.11	65	−18.93	54.5
0.9	0.93	−14.7	82	−12.54	69.6
1.8	0.806	−13.5	77.2	−12.6	63
2.1	1.6	−12.5	82.6	−17.4	71.3

5. CONCLUSION

A new compact planar antenna design that supports most of the operating mobile services, ISM applications, and wireless communication services is introduced. The SAR values of the antenna satisfy the standard safety guidelines. The antenna has more compact size when compared to other published antennas. The antenna was simulated using the CST simulator and fabricated using the photolithographic technique. Very good agreement is obtained between the simulated and the experimental results.

ACKNOWLEDGMENT

This work is funded by the National Telecom. Regulatory Authority (NTRA), Ministry of Communication and Information Technology, Egypt.

REFERENCES

1. Sesia, S., I. Toufik, and M. Baker, *LT — The UMTS Long Term Evolution: From Theory to Practice*, Wiley, Chichester, U.K., 2009.
2. Bhatti, R. A., S. Yi, and S. Park, "Compact antenna array with port decoupling for LTE-standardized mobile phones," *IEEE Antennas and Wireless Propagation Letters*, Vol. 8, 1430–1433, 2009.
3. Young, C. W., Y. B. Jung, and C. W. Jung, "Octaband internal antenna for 4G mobile handset" *IEEE Antennas and Wireless Propagation Letters*, Vol. 10, 817–819, 2011.
4. Wong, K. L. and W. Y. Chen, "Small-size printed loop-type antenna integrated with two stacked coupled-fed shorted strip monopoles for eight-band LTE/GSM/UMTS operation in the mobile," *Microwave and Optical Technology Letters*, Vol. 52, No. 7, 1471–1476, Jul. 2010.
5. Guo, Q., S. Member, R. Mittra, L. Fellow, F. Lei, Z. Li, J. Ju, and J. Byun, "Interaction between internal antenna and external antenna of mobile phone and hand effec," *IEEE Trans. Antenna and Propag.*, Vol. 61, No. 2, Feb. 2013.
6. 3GPP, "3rd generation partnership project; Technical specification group radio access networ; Evolved universal terrestrial radio access (E-UTRA); User equipment (UE) radio transmission and reception (Release 10)," 3GPP TS36.101 V10.4.0, Table 5.5-1 E-UTRA, Sep. 2011.
7. IEEE C95.1-2005, "IEEE standards for safety levels with respect to human exposure to radio frequency electromagnetic fields, 3 kHz to 300 GHz," Institute of Electrical and Electronics Engineers, New York, NY, 2005.
8. International Non-Ionizing Radiation Committee of the International Radiation Protection Association, "Guidelines on limits on exposure to radio frequency electromagnetic fields in the frequency range from 100 kHz to 300 GHz," *Health Physics*, Vol. 54, No. 1, 115–123, 1988.
9. CST Microwave Studio Suite 2011 User's Manual, 2011, www.cst.com.
10. Gabriel, S., R. W. Lau, and C. Gabriel, "The dielectric properties of biological tissues II Measurements in the frequency range 10 Hz to 20 GHz," *Phys. Med. Biol.*, Vol. 41, 2251–2269, 1996.
11. Gabriel, C., "Tissue equivalent material for hand phantoms," *Phys. Med. Biol.*, Vol. 52, 4205–4210, 2007.

Gold Plating Carbon Nano Tube Antenna Integrated with Voltage Control Oscillator

Kuan-Ting Lin[1], **Jian-Yu Hsieh**[1], **Yu-Jen Chen**[2], **Shuo-Hung Chang**[2], **Ying-Jay Yang**[1], **and Shey-Shi Lu**[1],

[1]Graduate Institute of Electronics Engineering, National Taiwan University, Taiwan, R.O.C.
[2]Department of Mechanical Engineering, National Taiwan University, Taiwan, R.O.C.

Abstract— In this paper, a gold plating carbon nanotube (CNT) antenna which is integrated with voltage control oscillator (VCO) is proposed. The VCO is fabricated in 65nm CMOS technology and operated from 50.6 to 51.1 GHz with phase noise of −88 dBc/Hz at 1 MHz offset and power consumption of 3 mW. The measurement results of the antenna indicate that the radiation power is −49.9 dBm for 50.7 GHz. The radiation power of the VCO with the CNT antenna is 10 dB larger than the radiation power of the VCO without the CNT antenna.

1. INTRODUCTION

Recently, high-speed wireless applications have become popular, including cloud services, video streaming, and data communications. In order to meet the high data rate requirements, millimeter-wave applications which have wide bandwidth for wireless transmission are the trend to serve the needs. The antenna is the first component in the transceiver and combining the antenna and CMOS chip concurrently in millimeter-wave integrated circuits is difficult [1, 2]. Moreover, substrate loss of an on-chip antenna causes low radiation efficiency at such high frequencies.

Nano materials are proposed to be antennas such as carbon nanotubes (CNTs) and silver nanowires [3–5] for consumer electronics products. Besides, the housing effect on the CNT antenna performance is less affected than the copper antenna [6]. However, the large intrinsic resistance and kinetic inductance of CNTs may degrade the antenna efficiency. Bundled CNTs can reduce intrinsic resistance and kinetic inductance [7, 8]. A monopole antenna may be achieved with a single bundled CNT. In addition, gold plating on CNTs can improve the conductivity of CNTs which reduces the ohmic loss and increases the radiation efficiency of CNT antennas [9]. In this letter, a gold plating of the bundled carbon nano tube antenna which is integrated with a voltage control oscillator (VCO) is proposed for millimeter-wave applications. The experimental design is illustrated in Section 2. The measurement results and discussion are presented in Section 3. Finally, the conclusions are summarized in Section 4.

2. EXPERIMENTAL DESIGN

Figure 1 shows the experimental setup of the gold plating CNT antenna integrated with voltage control oscillator. In order to obtain the antenna properties of the bundled CNT, the measuring equipment includes a V-band horn antenna and spectrum analyzer are used. The detail implementation is described as follows.

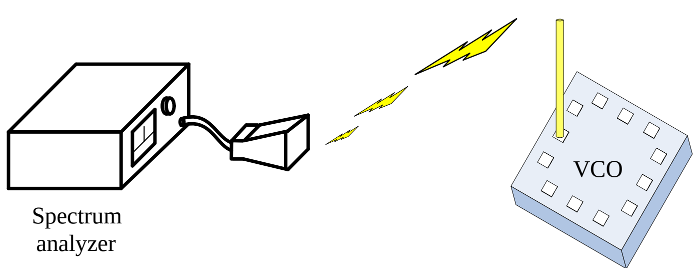

Figure 1: Experimental setup of gold plating carbon nanotube antenna integrated with voltage control oscillator.

Figure 2 shows the scanning electron microscope image of CNT. The length and width of the bundled carbon nano tube are equal to 520 μm and 54 μm, respectively. The characteristics of the CNT can be obtained from [9, 10] and expressed as:

$$R_S = \frac{E_{CNT} + j\omega L_k}{N} \tag{1}$$

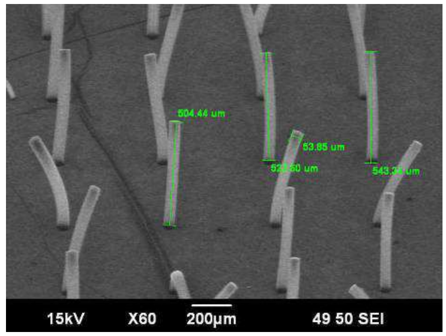

Figure 2: Scanning electron microscope image of CNT.

where N represents the number of CNTs in unit width. The surface resistivity (R_S) of a bundled CNT is proportional to the resistance R_{CNT} and kinetic inductance L_k of a CNT and is inversely proportional to number density of CNTs.

Figure 3 shows the VCO structure adopted in this letter. The complementary oscillator is consisted of both nMOS and pMOS cross-coupled pairs in parallel to generate the negative transconductance. With the same bias current flowing through both nMOS and pMOS devices, the negative transconductance can be twice as larger for the same power consumption. The oscillation frequency of the VCO is simply defined as:

$$f_{osc} = \frac{1}{2\pi\sqrt{LC}} \tag{2}$$

where L and C are the inductance and capacitance in the resonant tank, respectively. According to (2), by varying the value of the inductance or capacitance, the oscillation frequency is able to be changed. However, it is more often that the frequency tuning is achieved by varying the capacitance through varactors, whose capacitance is voltage-dependent. In this work, two accumulation-mode MOS are used as the varactors because varactors in this structure operate in the depletion and accumulation regions only and have larger Cmax to Cmin ratio than other structures to enhance the tuning range of the oscillator.

The integration of the antenna and VCO is performed by silver paste. Silver paste is moistened by a single point DC probe with a 1 μm needle and stuck on the VCO signal out pad which is a 100 pitch GSG pattern. Then a bundled CNT with gold plating is caught by the DC probe. Finally, the gold plating CNT antenna integrated with VCO can be show in Figure 4. This integration not only saves a V-band signal generator but also demonstrates an on-chip antenna implementation. Owing to gold plating, the antenna and radiation efficiency can be improved.

3. MEASUREMENT RESULTS

The design of the V-band complementary VCO is fabricated in 65nm CMOS technology with transistors, varactors, and inductors. Measurements show a 51 GHz VCO operating from 1 V

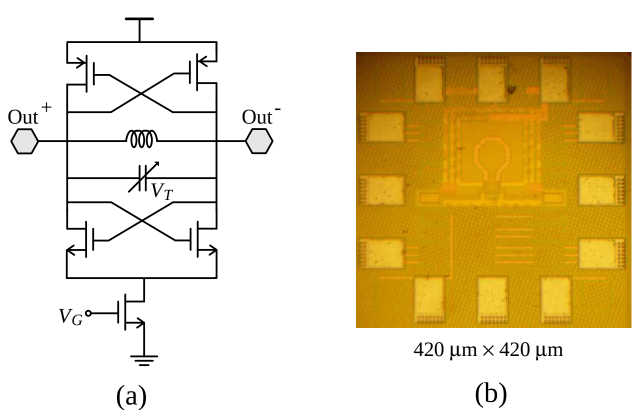

Figure 3: Voltage control oscillator. (a) Schematic. (b) Die photo.

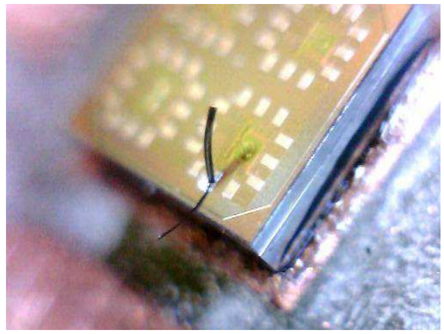

Figure 4: Gold plating CNT antenna integrated with VCO.

with phase noise of −88 dBc/Hz at 1 MHz offset and power consumption of 3 mW, which delivers −15 dBm of differential output power. The figure of merit is −177.4 dBc/Hz for the implemented VCO. Figure 5 shows the phase noise and tuning curve of the VCO.

The measurement results of the antenna indicate that the radiation power is −49.9 dBm for 50.7 GHz. The radiation power is about 10 dB larger than the radiation power of the VCO without the CNT antenna as shown in Figure 6. The experimental results show that the CNT is suitable to be an antenna and may be considered as a useful component in future millimeter-wave applications.

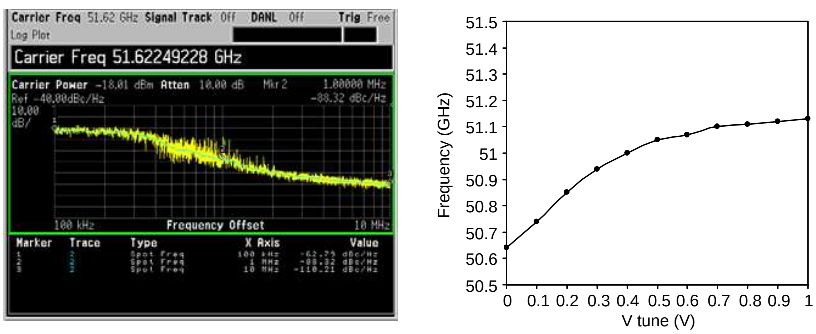

(a) (b)

Figure 5: VCO measurement results. (a) Phase noise. (b) Tuning curve.

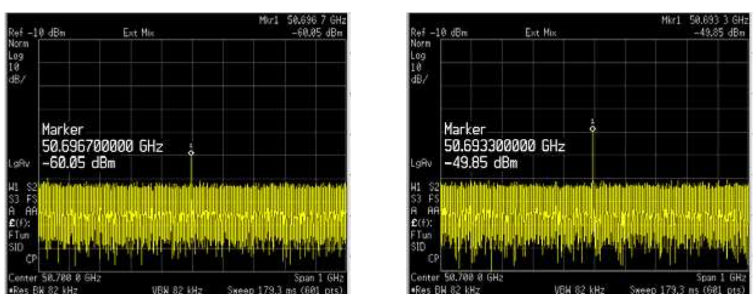

(a) (b)

Figure 6: Measured performance. (a) Without CNT antenna. (b) With CNT antenna.

4. CONCLUSIONS

Fro the 60 GHz WLAN application, the length of CNTs must be longer to achieve a quarter wave antenna and oscillation frequency of the VCO need increasing 10 GHz to meet the feature. Using bundled structure of CNTs can reduce the surface resistance and the gold plating process also enhances the radiation efficiency of the antenna. The dimensions of CNTs are suitable to be an antenna and can be considered as a useful component in future millimeter-wave applications.

ACKNOWLEDGMENT

The authors are grateful to the National Chip Implementation Center in Taiwan for their technical support and the National Science Council under Grant NSC 101-2221-E-002 -023.

REFERENCES

1. Sun, M. and Y. P. Zhang, "100-GHz quasi-Yagi antenna in silicon technology," *IEEE Electron Device Lett.*, Vol. 28, No. 5, 455–457, May 2007.
2. Hsu, S.-S., K.-C. Wei, C.-Y. Hsu, and H.-R. Chuang, "A 60-GHz millimeter-wave CPW-fed Yagi antenna fabricated by using 0.18-CMOS technology," *IEEE Electron Device Lett.*, Vol. 29, No. 6, 625–627, Jun. 2008.
3. Mehdipour, A., I. D. Rosca, A.-R. Sebak, C. W. Trueman, and S. V. Hoa, "Full-composite fractal antenna using carbon nanotubes for multiband wireless applications," *IEEE Antennas Wireless Propag. Lett.*, Vol. 9, 891–894, 2010.
4. Mehdipour, A., T. A. Denidni, A.-R. Sebak, C. W. Trueman, I. D. Rosca, and S. V. Hoa, "Nonmetallic dielectric resonator antenna using carbon nanotube composite materials," *IEEE Antennas Wireless Propag. Lett.*, Vol. 11, 1293–1295, 2012.
5. Rai, T., P. Dantes, B. Bahreyni, and W. S. Kim, "A stretchable RF antenna with silver nanowires," *IEEE Electron Device Lett.*, Vol. 34, No. 4, 544–546, Apr. 2013.
6. Mehdipour, A., I. D. Rosca, A.-R. Sebak, C. W. Trueman, and S. V. Hoa, "Carbon nanotube composites for wideband millimeter-wave antenna applications," *IEEE Trans. Antennas Propag.*, Vol. 59, No. 10, 3572–3578, Oct. 2011.
7. Plombon, J. J., K. P. O'Brien, F. Gstrein, V. M. Dubin, and Y. Jiao, "High-frequency electrical properties of individual and bundled carbon nanotubes," *Applied Physics Lett.*, Vol. 90, 063106-1–063106-3, 2007.
8. Huang, Y. and W.-Y. Yin, "Performance predication of carbon nanotube bundle dipole antenna," *Proc. IEEE Asia-Pacific Microwave Conf. (APMC)*, Vol. 7, No. 3, 331–337, Dec. 2007.
9. Choi, S. and K. Sarabandi, "Design of efficient terahertz antennas: Carbon nanotube versus gold," *Proc. IEEE Antenna Propag. Soc. Int. Symp.*, 1–4, Jul. 2010.
10. Burke, P. J., "An RF circuit model for carbon nanotubes," *IEEE Trans. Nanotechnology*, Vol. 2, No. 1, 55–58, Mar. 2003.

Theoretical Analysis of AC Resistance of Coil Made by Copper Clad Aluminum Wires

C. Kamidaki and N. Guan
Power and Telecommunication Cable System R&D Department, Fujikura Ltd., Japan

Abstract— In this paper, we propose coils made by copper clad aluminum (CCA) in wireless power transfer (WPT) systems, which show lower AC resistance than Cu ones in a certain range of frequencies. Resistance of CCA or Cu coil is formulated by analysis of the skin effect, proximity effect and a shape factor of the coil which describes intensity of magnetic fields created by applied current in the coil itself. Boundary frequencies of the range where CCA coils are superior to Cu ones and corresponding resistances are quantitatively analyzed. The condition where CCA coils show lower resistance compared to Cu ones is clarified as configuration of coils and operation frequency.

1. INTRODUCTION

In a wireless power transfer system using inductive coupling through magnetic fields, power transfer efficiency is significantly influenced by the quality factor $Q = \omega L/R_{ac}$ of its coil, where ω, L and R_{ac} are the angular frequency, inductance and AC resistance, respectively [1]. In order to obtain a higher Q, higher frequency and lower R_{ac} are desirable, but R_{ac} increases quickly with frequency due to the skin effect as well as the proximity effect which comes from the eddy current induced by current flowing in neighbor wires.

We have proposed copper clad aluminum (CCA) wires which are aluminum (Al) wires coated with thin Cu layer via metallic bond, as shown in Fig. 1 [2]. The CCA coils are not only cost-effective, light-weight and solderable as Cu, but also show lower R_{ac} than Cu under certain circumstance. In the study, both the skin and proximity effects for a round metallic wire with multiple layers are theoretically analyzed and the AC resistance is formulated as a summation of an AC resistance caused by the skin effect and a product of a loss caused by the proximity effect and a shape factor of the coil.

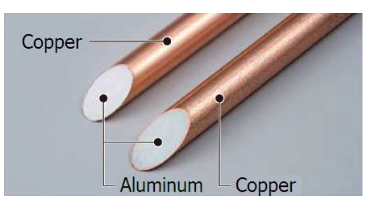

Figure 1: Copper clad aluminum wire.

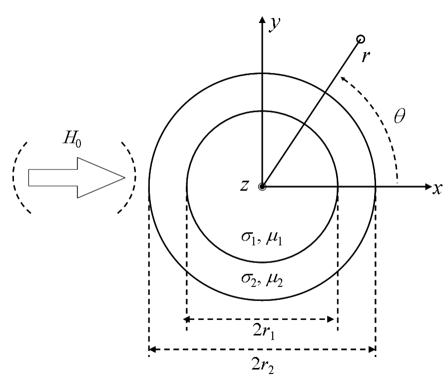

Figure 2: Analysis model of CCA wire.

In this paper, the shape factor of a coil, which was obtained by curve-fitting from measurement, is numerically formulated. Frequencies f_1 and f_2 between which CCA coils have lower R_{ac} than Cu ones and corresponding resistance R_1 and R_2 are quantitatively analyzed. It is demonstrated that our theoretical analysis agrees with measurement very well.

2. FORMULATION OF AC RESISTANCE OF CCA COILS

A CCA wire is modeled as a round wire uniformly distributed along z-direction with two-layers where the i-th layer has a radius of r_i, conductivity of σ_i and relative permeability of μ_i, as shown in Fig. 2. Assuming a time factor of $e^{j\omega t}$, the z-component of electric field E_z at the i-th layer induced by a current in z-direction satisfies the following equation:

$$\frac{\partial^2 E_z}{\partial r^2} + \frac{1}{r}\frac{\partial E_z}{\partial r} - j\omega\mu_i\mu_0\sigma_i E_z = 0 \tag{1}$$

which has a solution of

$$E_z = \begin{cases} A_1 J_0(k_1 r) & (r \leq r_1) \\ A_2 J_0(k_2 r) + B_2 Y_0(k_2 r) & (r_1 < r \leq r_2) \end{cases} \tag{2}$$

where A_i and B_i are constants, J_ν and Y_ν are the Bessel and Neumann functions of the ν-th order, respectively, and $k_i^2 = -j\omega\mu_i\mu_0\sigma_i$. The energy consumption in the wire is equal to the power flow entering the wire from surface and is expressed by surface integration of Poynting vector on the wire. Therefore, when AC current flows in the wire, resistance caused by the skin effect per unit length is given by

$$R_s = \Re\left[\frac{j\omega\mu_2\mu_0}{2\pi\xi} \cdot \frac{A_2 J_0(\xi) + B_2 Y_0(\xi)}{A_2 J_0'(\xi) + B_2 Y_0'(\xi)}\right] \tag{3}$$

where $\xi = k_2 r_2$ and $\Re$ denotes real part.

Assume that an AC magnetic field with intensity of H_0 is applied to the wire along x-direction as shown in Fig. 2, the z-component of magnetic potential A_z satisfies the following equation:

$$\frac{\partial^2 A_z}{\partial r^2} + \frac{1}{r}\frac{\partial A_z}{\partial r} + \frac{1}{r^2}\frac{\partial^2 A_z}{\partial \theta^2} + k_i^2 A_z = 0 \tag{4}$$

which has a solution of

$$A_z = \sin\theta \times \begin{cases} C_1 J_1(k_1 r) & (r \leq r_1) \\ C_2 J_1(k_2 r) + D_2 Y_1(k_2 r) & (r_1 < r \leq r_2) \\ C_3 r + D_3 r^{-1} & (r2 < r) \end{cases} \tag{5}$$

where C_i and D_i are constants. Then the loss due to eddy current in the wire per unit length is calculated by the power flow passing through the surface of the wire and is given by

$$P_p = -\frac{2\pi\left|\xi\right|^2\left|H_0\right|^2}{\sigma_2} \cdot \frac{\xi X Y^*}{\left|Z\right|^2} \tag{6}$$

where

$$\begin{aligned} X &= C_2 J_1(\xi) + D_2 Y_1(\xi) \\ Y &= C_2 J_1'(\xi) + D_2 Y_1'(\xi) \\ Z &= (\mu_2 - 1)X + \xi\left[C_2 J_0(\xi) + D_2 Y_0(\xi)\right] \end{aligned}$$

Noting that magnetic field is generated by current flowing in the wire for a coil, then the magnetic field is proportional to the magnitude of the current, i.e.,

$$|H_0| = \alpha|I| \tag{7}$$

Since eddy current loss is expressed as a product of the AC resistance due to the proximity effect and a square of the applied current, AC resistance of coils wound by litz wire with N wires and length of l is expressed by

$$R_{ac} = \left(R_s + \alpha^2 D_p\right) \times \frac{l}{N} \tag{8}$$

where D_p is associated with the loss caused by the proximity effect per unit length and is given by

$$D_p = -\frac{4\pi\left|\xi\right|^2}{\sigma_2} \cdot \Re\left(\xi\frac{XY^*}{\left|Z\right|^2}\right). \tag{9}$$

Assume that a coil wound with T turns is $N \times T$ concentric circle wires as shown in Fig. 3, the intensity of applied magnetic field to the i-th wire H_i is obtained as a summation of magnetic fields from circular current flowing in all other wires in the case of air core coils, and can be expressed

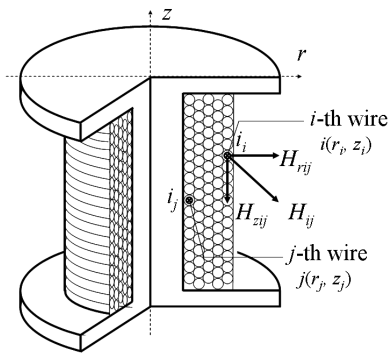

Figure 3: Analysis model of coil.

Figure 4: Picture of measured coil.

by [3]

$$H_i^2 = \left|\sum_{j\neq i}^{N\times T} H_{rij}\right|^2 + \left|\sum_{j\neq i}^{N\times T} H_{zij}\right|^2 \tag{10}$$

$$H_{rij} = \frac{i_j}{2\pi}\frac{z_i - z_j}{r_j\sqrt{(r_i+r_j)^2+(z_i-z_j)^2}}\left[-K(k_c) + \frac{r_i^2+r_j^2+(z_i-z_j)^2}{(r_i-r_j)^2+(z_i-z_j)^2}\cdot E(k_c)\right] \tag{11}$$

$$H_{zij} = \frac{i_j}{2\pi}\frac{1}{\sqrt{(r_i+r_j)^2+(z_i-z_j)^2}}\left[K(k_c) - \frac{r_i^2-r_j^2+(z_i-z_j)^2}{(r_i-r_j)^2+(z_i-z_j)^2}\cdot E(k_c)\right] \tag{12}$$

$$k_c = \sqrt{\frac{4r_i r_j}{(r_i+r_j)^2+(z_i-z_j)^2}} \tag{13}$$

where i_j is the current flowing in the j-th wire, K and E are complete elliptic integrals of the first and second kinds, respectively. Then α is calculated by

$$\alpha = \sqrt{\frac{\sum_{i=1}^{N\times T} 2\pi r_i H_i^2}{\sum_{i=1}^{N\times T} 2\pi r_i i_i^2}} \tag{14}$$

3. NUMERICAL RESULTS

For a coil shown in Fig. 4, where cables are stranded with 14 wires of Φ0.40 mm for 8 layers of 10 turns on a bobbin of Φ20 mm, Fig. 5 shows the measured and calculated R_{ac} of the coil wound by Cu or CCA wire which consists of 5% Cu and 95% Al in area ratio. In the measurement, R_{ac} increases with frequency and R_{ac} of CCA coil is lower than Cu one from 15 to 450 kHz. In the calculation, the shape factor α is obtained as 13.6 mm^{-1} by Eq. (14). This value makes the calculation agree with the measurement very well.

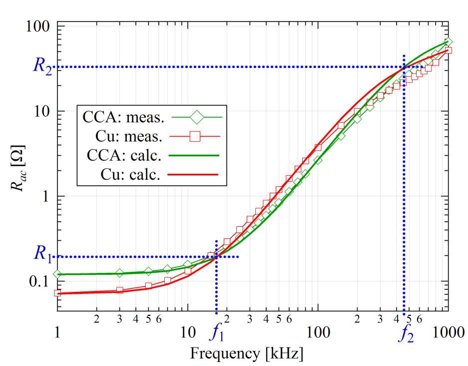

Figure 5: Measured and calculated R_{ac} for $14 \times$ Φ0.40 mm coils.

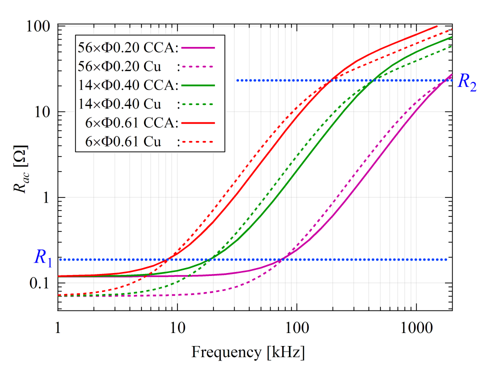

Figure 6: Calculated R_{ac} for different coils.

Figure 6 shows the calculated R_{ac} of coils which are wound by wires with the same sectional area and configuration but different number and thickness of wires. R_{ac} for CCA or Cu coils wound by a litz wire with 56 wires of Φ0.20 mm and one with 6 wires of Φ0.61 mm are added to the calculated result in Fig. 5. Although f_1 and f_2 shift to higher frequency as the wires get thinner, the corresponding R_1 and R_2 are independent on the thickness of wires. This phenomenon is explained as follows.

At a low frequency at which wire radius is smaller enough than the skin depth $\delta = \sqrt{2/\omega\sigma\mu}$, R_s and D_p are approximated by [4]:

$$R_s \simeq \frac{1}{\pi\sigma_2(r_2^2 - r_1^2) + \pi\sigma_1 r_1^2}, \tag{15}$$

$$D_p \simeq \frac{\pi\left(\omega\mu_0\right)^2}{4}\left[\sigma_2\left(r_2^4 - r_1^4\right) + \pi\sigma_1 r_1^4\right]. \tag{16}$$

Then, f_1 and R_1 are easily obtained to

$$f_1 = \frac{1}{\pi\alpha r_1}\sqrt{f_{\mathrm{Cu}} f_{\mathrm{CCA}}} \tag{17}$$

$$R_1 = R_{\mathrm{Cu}} + \frac{r_2^2}{r_1^2} R_{\mathrm{CCA}} \tag{18}$$

where R_{CCA} and R_{Cu} are DC resistances of CCA and Cu coil, f_{Cu} is defined as a frequency at which the radius of wire is equal to the skin depth of Cu, and f_{CCA} a frequency at which the radius of wire is equal to the skin depth of an uniform material with the same DC resistance of CCA wire. They are expressed by

$$f_{\mathrm{Cu}} = \sqrt{\frac{1}{\pi\mu_0\sigma_2}}\frac{1}{r_2}, \tag{19}$$

$$f_{\mathrm{CCA}} = \sqrt{\frac{r_2^2}{\pi\mu_0\left[\sigma_2(r_2^2 - r_1^2) + \sigma_1 r_1^2\right]}}\frac{1}{r_2}. \tag{20}$$

Equation (18) leads to an interesting result that R_1 depends on DC resistance of these coils and sectional area ratio of Al in CCA. Furthermore, R_1 approaches to the summation of DC resistances of wires as the outer layer gets thinner. In the measurement in Fig. 5, R_{CCA}, R_{Cu} and R_1 are 120, 71 and 197 mΩ, respectively. According to Eq. (18), R_1 is 197 mΩ and coincides with the measurement. Frequency f_1 obtained by Eq. (17) is 16.8 kHz which differs a little with the measurement of 15 kHz as shown in Fig. 5.

Since the proximity effect is prominent in R_{ac} at high frequency, f_2 is obtained as the frequency at which D_p's of CCA and Cu show a same value.

4. CONCLUSION

We have proposed an analytical expression of AC resistance of CCA coil by developing an analysis formulation for the skin effect, proximity effect and a shape factor of a coil. The theoretical and experimental results agreed well with each other and both demonstrated the superiority of CCA coil over Cu one regarding on AC resistance in a certain condition. In real applications, it should be easily confirmed whether it is effective or not to make replacement of Cu by CCA for not only saving weight but also decreasing energy loss, by using estimated f_1 and f_2. It will take advantage of these features by applying this phenomenon to WPT systems to save total energy consumption, especially in power charging for electrical vehicles.

REFERENCES

1. Yamanaka, T., Y. Kaneko, S. Abe, and T. Yasuda, "10 kW contactless power transfer system for rapid charger of electric vehicle," *Int. Battery, Hybrid and Fuel Cell Electric Vehicle Symp.*, 1–9, Los Angeles, USA, May 2012.
2. Guan, N., C. Kamidaki, T. Shinmoto, and K. Yashiro, "AC resistance of copper clad aluminum wires," *Proc. of the 2012 Int. Symp. on Antennas and Propagation*, 447–450, Nagoya, Japan, Oct. 2012.

3. Stratton, J. A., *Electromagnetic Theory*, McGraw-Hill, New York, 1941.
4. Sullivan, C. R., "Aluminum windings and other strategies for high-frequency magnetics design in an era of high copper and energy costs," *IEEE Applied Power Electronics Conf.*, 78–84, Anaheim, USA, Feb. 2007.

Wireless Power Transmission by Enlarging the Near Field

Konstantin Meyl
Faculty of Computer and Electrical Engineering, Furtwangen University, Germany

Abstract— Continuing the contribution about "wireless power transmission by scalar waves", presented in Moscow 2012, this paper goes deeper, explaining the different types and properties of waves described by the wave equation. Starting with the wave description of Maxwell an extended version of the Laplace equation is derived, expanding the standard derivations of the near field, showing how to influence the zone, where the longitudinal wave parts occur. We come to the conclusion that the near field zone is enlarging, if the longitudinal parts of a wave or the antenna voltage are accelerated. This relationship is essential for the wireless transmission of energy. In addition this exciting new result could be tested experimentally. The simple experiment will be demonstrated at PIERS 2013 in Stockholm. Only by changing the antenna design, it will be shown how both, the speed of propagation and the near field are enlarging proportional to each other. In all practical applications [1], as discussed in PIERS Proceedings 2012, the extended near field is the key of success.

1. INTRODUCTION

As a starting-point and as approach serve the wave equation derived from the field equations according to Maxwell. On one hand is a transverse electro-magnetic wave [2]:

$$\begin{array}{ccc} \underbrace{-\text{curl curl } \mathbf{E}\cdot c^2} & = & \underbrace{d^2\mathbf{E}/dt^2} + \underbrace{(1/\tau_1)\cdot d\,\mathbf{E}/dt} \\ \text{transverse} & - & \text{wave} + \text{vortex damping} \end{array} \tag{1}$$

On the other hand, there is a damping term in the equation which is responsible for the losses of an antenna. It indicates the wave component, which is converted into standing waves, can also be called field vortices, which produce vortex losses for their part with the time constant τ_1 in the form of heat. But where are the longitudinal wave components proven at close range of an antenna and still used with transponders technically? Are they involved with the vortex damping? A new approach is needed.

2. DERIVATION FROM TEXT BOOK PHYSICS

The time derivation of the electric field vector $\mathbf{E}(\mathbf{r}(t))$ is, according to the rule:

$$\frac{d\mathbf{E}(\mathbf{r}(t))}{dt} = \frac{\partial\mathbf{E}(\mathbf{r}=\mathbf{r}(t))}{\partial\mathbf{r}}\cdot\frac{d\mathbf{r}(t)}{dt} = (\mathbf{v}\text{ grad})\mathbf{E}, \tag{2}$$

if $\mathbf{v} = d\mathbf{r}/dt$ is a non-accelerated relative motion in the x-direction.

Thus the vortex damping factor is now:

$$(1/\tau_1)\cdot d\mathbf{E}/dt = (\mathbf{v}\text{ grad})(\mathbf{E}/\tau_1) \tag{3}$$

The current density $\mathbf{j}$ is a space charge density ρ_{el} consisting of negative charge carriers, which moves with the velocity $\mathbf{v}$ for instance through a conductor (in the x-direction).

The notation in mathematics says:

$$\mathbf{j} = -\mathbf{v}\cdot\rho_{el} = -\mathbf{v}\cdot\text{div}\mathbf{D} \tag{4}$$

By means of Ohm's law

$$\mathbf{j} = \sigma\cdot\mathbf{E} = \mathbf{D}/\tau_1 \tag{5}$$

and the relation of material

$$\mathbf{D} = \varepsilon\cdot\mathbf{E} \tag{6}$$

the current density $\mathbf{j}$ also can be written down as dielectric displacement current with the characteristic relaxation time constant for the eddy currents

$$\tau_1 = \varepsilon/\sigma \tag{7}$$

and:

$$\mathbf{E}/\tau_1 == -\mathbf{v}\ \mathrm{div}\ \mathbf{E} \tag{8}$$

Using the introduced relations involved with a in x-direction propagating wave ($\mathbf{v} = (v_x, v_y = 0, v_z = 0)$) Eq. (3) can be transformed directly into:

$$(1/\tau_1) \cdot d\,\mathbf{E}/dt = -||\mathbf{v}||^2 \cdot \mathrm{grad}\ \mathrm{div}\,\mathbf{E}. \tag{9}$$

The divergence of a field vector (div$\mathbf{E}$) mathematically is seen a scalar, for which reason this term as part of the wave equation founds so-called "scalar waves" and that means that potential vortices, as far as they exist, will appear as a scalar wave. To that extent the derivation prescribes the interpretation [2].

3. UNIVERSAL WAVE EQUATION

$$\begin{array}{c|c|c} ||\mathbf{v}||^2\mathrm{grad\ div}\ \mathbf{E} & - c^2\mathrm{curl\ curl}\ \mathbf{E} & = d^2\mathbf{E}/dt^2 \\ \text{longitudinal} & \text{transverse} & \text{wave} \\ \text{with } v = \text{arbitrary} & \text{with } c = \text{const.} & \text{velocity of} \\ \text{(scalar wave)} & \text{(em. wave)} & \text{propagation} \end{array} \tag{10}$$

This wave equation can be divided into longitudinal and transverse wave parts, which can propagate with different velocity.

Physically seen the vortices have particle nature as a consequence of their structure forming property. With that they carry momentum, which puts them in a position to form a longitudinal shock wave similar to a sound wave. If the propagation of the light one time takes place as a wave and another time as a particle, then this simply and solely is a consequence of the wave equation.

Light quanta should be interpreted as evidence for the existence of scalar waves. Here however also occurs the restriction that light always propagates with the speed of light. It concerns the special case $v = c$. With that the derived wave Equation (10) changes into the inhomogeneous Laplace equation:

$$\Delta\mathbf{E} = \mathrm{grad\ div}\ \mathbf{E} - \mathrm{curl\ curl}\ \mathbf{E} = \left(1/c^2\right) \cdot d^2\mathbf{E}/dt^2 \tag{11}$$

The electromagnetic wave in general is propagating with c. As a transverse wave the field vectors are standing perpendicular to the direction of propagation. The velocity of propagation therefore is decoupled and constant.

Completely different is the case for the longitudinal wave. Here the propagation takes place in the direction of an oscillating field pointer, so that the phase velocity permanently is changing and merely an average group velocity can be given for the propagation. There exists no restriction for v and $v = c$ only describes a special case. It will be helpful to draw, for the results in a mathematical way, a graphical model. High-frequency technology is distinguished between the near-field and the far-field. Both have fundamentally other properties.

4. THE FAR FIELD (ELECTROMAGNETIC WAVE ACC. TO HERTZ)

Heinrich Hertz did experiments in the short wave range at wavelengths of meters. From today's viewpoint his work would rather be assigned the far-field. As a professor in Karlsruhe he had shown that the electromagnetic wave propagates like a light wave and can be refracted and reflected in the same way [3].

It is a transverse wave for which the field pointers of the electric and the magnetic field oscillate perpendicular to each other and both again perpendicular to the direction of propagation. Besides the propagation with the speed of light, it also is characteristic that there occurs *no phase shift* between E-field and H-field.

5. THE NEAR FIELD (SCALAR WAVE ACC. TO TESLA)

In the proximity it looks completely different. The proximity concerns distances to the transmitter of less than the wavelength divided by 2π. Nikola Tesla has broadcasted in the range of long waves, around 100 Kilohertz, in which case the wavelength already is several kilometers. For the experiments concerning the resonance of the earth he has operated his transmitter in Colorado Springs at frequencies down to 6 Hertz. Doing so, the whole earth moves into the proximity of his transmitter [4]. We probably have to proceed from assumption that the Tesla radiation primarily concerns the proximity, which also is called the radiant range of the transmitting antenna.

For the approach of vertical and closed-loop field structures derivations for the near-field are known [5]. The calculation provides the result that in the proximity of the emitting antenna a phase shift exists between the pointers of the E- and the H-field. The antenna current and the H-field coupled with it lag the E-field of the oscillating dipole charges for 90°

The phase shift hints at why an energy transfer is only possible in the near-field, not in the far-field relying on electromagnetic waves. For this purpose the energy density of the wave-field is calculated by:

$$w = \left(\varepsilon \cdot E^2 + \mu \cdot H^2\right)/2 \quad \text{or by the Poynting Vektor :} \quad \mathbf{S} = \mathbf{E} \times \mathbf{H} \tag{12}$$

for the case that for example the electrical field strength E turns zero. In case of the electromagnetic wave (Fig. 1), at this point, the magnetic field strength also turns zero, with a 90° phase shift however (Fig. 2), it then becomes maximal.

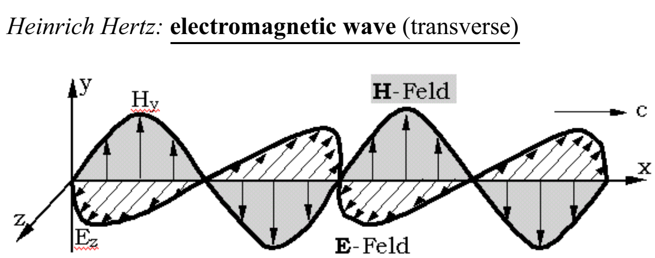

Figure 1: The planar electromagnetic wave in the far zone.

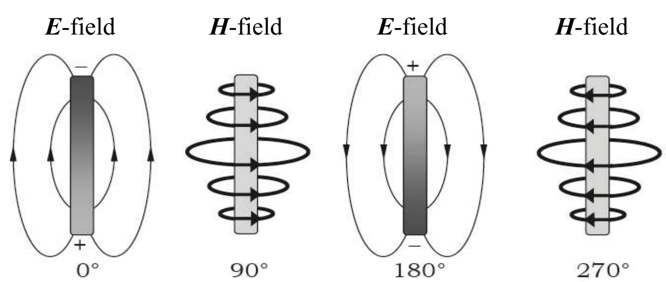

Figure 2: The fields of the oscillating dipole antenna.

6. THE NEAR FIELD AS A VORTEX FIELD

In the text books one finds the detachment of a wave from the dipole accordingly explained. If we regard the structure of the outgoing fields, then we see field vortices, which run around one point, which we can call the vortex center. We continue to recognize in the picture how the generated field structures establish a shock wave as one vortex knocks against the next.

Thus a Hertzian dipole doesn't emit Hertzian waves! An antenna as near-field without exception emits vortices, which only at the transition to the far-field unwind to create electromagnetic waves.

At the receiver the conditions are reversed. Here the wave is rolling up to a vortex, which usually is called and conceived as a standing wave. Only this field vortex causes an antenna current in the rod which the receiver afterwards amplifies and utilizes. The function mode of sending and receiving antennas with the puzzling near field characteristics explain themselves directly from the wave Equation (10).

7. THE VORTEX MODEL OF SCALAR WAVES

What would a useful vortex-model for the rolling up of waves to vortices look like? We proceed from an electromagnetic wave, which does not propagate after the retractor procedure any longer straight-lined, but turns instead with the speed of light in circular motion. Furthermore, it is transverse, because the field pointers of the E-field and the H-field oscillate perpendicular to c. By means of the orbit the speed of light c now has become the vortex velocity.

Wave and vortex turn out to be two possible and *stable field configurations*. For the transition from one into the other no energy is used; it only is a question of *structure*. It is the circumstance that the vortex direction of the ring-like vortex is determined and the field pointers are standing perpendicular to it, as well as perpendicular to each other. This results in two theoretical formation forms for the scalar wave.

In the first case (Fig. 4) the vector of the H-field points into the direction of the vortex centre and that of the E-field axially to the outside. The vortex however will propagate in this direction in space and appear as a scalar wave, so that the propagation of the wave takes place in the direction of the electric field. It may be called an *electric wave*.

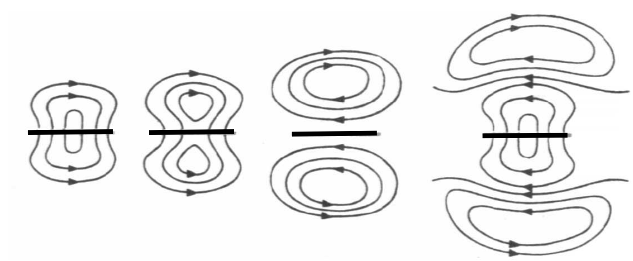

Figure 3: The coming off of the electric field lines from a dipole.

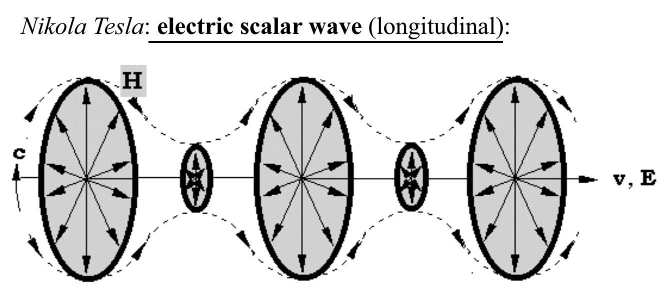

Figure 4: Magnetic ring-vortices form an electric wave.

8. MAGNETIC SCALAR WAVES (ACC. TO MEYL)

In the second case, the field vectors exchange their place. The characteristic of the *magnetic wave* is that the direction of propagation coincides with the oscillating magnetic field pointer (Fig. 5), while the electric field pointer rolls up.

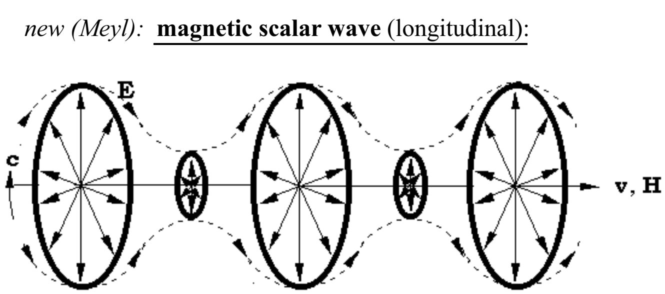

Figure 5: Electric ring-vortices form an magnetic wave.

The vortex picture of the rolled up wave already fits very well, because the propagation of a wave in the direction of its field pointer characterizes a longitudinal wave. Also, because all measurement results are perfectly covered by the vortex model. In the text book of Zinke and Brunswig (German text book about HF-Technology) as one example the near field is computed as exactly this vortex-structure is postulated! [5].

9. THE ANTENNA NOISE

It is well known that longitudinal waves have no firm propagation speed. Since they run toward an oscillating field pointer, also that the speed vector v will oscillate. At so called relativistic speeds within the range of the speed of light the field vortices underlie the *Lorentz contraction*. This means, the faster the oscillating vortex is on its way, the smaller it becomes. The *vortex constantly changes its diameter* as an impulse-carrying mediator of a scalar wave.

Since it is to concern that vortices are rolled up waves, the vortex speed will still be c, with which the wave runs now around the vortex center in circular motion. Hence it follows that with smaller becoming diameter the wave-length of the vortex likewise decreases, while the natural frequency of the vortex increases accordingly.

If the vortex oscillates in the next instant back, the frequency decreases again. The *vortex works as a frequency converter*! The mixture of high frequency signals developed in this way distributed over a broad frequency band is called noise.

Antenna losses concern the portion of radiated field vortices, which did not unroll themselves as waves, which are measured with the help of wide-band receivers as *antenna noise* and in the case of the vortex decay are responsible for heat development.

In the expressions of the field Equation (1) it concerns wave damping. The wave Equation (10) explains besides, why a Hertz signal is to be only received if it exceeds the scalar noise vortices in amplitude.

REFERENCES

1. Meyl, K., "Wireless power transmission by scalar waves," *PIERS Proceedings*, 664–668, Moscow, Russia, Aug. 19–23, 2012.
2. Meyl, K., *Scalar Wave Transponder*, 3rd Edition, Indel Verlag, 2012, www.meyl.eu.
3. Simonyi, K., *Theoretische Elektrotechnik*, Band 20, 7.Aufl., VEB Verlag Berlin, 1979.
4. Tesla, N., "Art of transmitting electrical energy through the natural mediums," US-Patent No. 787, 412, 1905.
5. Brunswig, Z., *Lehrbuch der Hochfrequenztechnik*, 3rd Edition, 335, Band 1, Springer-Verlag, 1986.

Numerical Study on the Radiative Transmission Efficiency of Dipolar Sources

C. L. Moorey, W. Holderbaum, and B. A. Potter
University of Reading, UK

Abstract— A numerical solution for the Radiation Transmission Efficiency (RTE) of electric and magnetic dipoles is obtained, and analysed with respect to frequency and spatial location. The results are compared against the findings of an equivalent analysis that used the closed-form expressions for the electromagnetic fields. It is shown that the two different methods present different findings with respect to the RTE of the dipoles. Conclusions are drawn as to the reason(s) behind the discrepancies between the two models, and provide the basis for future work.

1. INTRODUCTION

Within the context of Wireless Power Transfer (WPT), electric and magnetic dipoles are important objects. Arbitrary radiation patterns may be constructed from, or conversely, decomposed into, a linear superposition of electric and magnetic dipoles [3, 4]. Additionally, their closed-form electromagnetic field solutions are well known [6, 8]. As such, they provide a means by which an electromagnetically complex structure can be broken down and greatly simplified.

An earlier work considered the Radiation Transmission Efficiency (RTE) of electric and magnetic dipoles [9]. This transmission efficiency represented the transmission characteristics of WPT based upon electromagnetic radiation from electric and magnetic dipoles. The details of how this radiation is absorbed by a receiver are simplified in the definition of the RTE, but the simplification allowed an efficiency to be defined that was not restricted to either the near- or far-field zones. This was achieved by using the full-field solutions for the electromagnetic fields of the dipoles to compute the Poynting vector and the total power radiated from each dipole. This however produced a discontinuity in the RTE at a distance $r = \lambda/\sqrt{2}\pi$ (where λ is the radiation wavelength). The nature of this discontinuity is unclear from the closed-form solutions for the fields alone, so further investigations are required.

Numerical methods are commonly applied to electromagnetic problems [2], and are in some cases, the only possible means by which to obtain field solutions. The numerical solution generated can usually be extended over near- to far-field[1] zones, and can produce an almost continuous set of electromagnetic field data if the mesh of the computational domain is set to be fine enough. As such, there is strong motivation for generating numerical data to further analyse the analytic work already undertaken. This paper utilizes XFdtd 7.1.2.1 to numerically investigate the results obtained for the RTE of electric and magnetic dipoles in order to reinforce, or to identify errors in, the findings of its preceeding closed-form analysis. The software is based on a finite-difference approximation which discretizes Maxwell's equations (specifically the laws of Ampére and Faraday) in time and space [1, 10].

Section 2 introduces electric and magnetic dipoles, the definition of the RTE and the main points of interest regarding the RTE of the dipoles. Section 3 presents simulation results and Section 4 concludes the findings of the analysis and briefly describes future work.

2. MOTIVATION

This Section introduces briefly electric and magnetic dipoles, describes how to compute the radiation transmission efficiency, discusses the main characteristics of the RTE for each dipole and motivates the need for the further numerical study presented in this paper.

2.1. Electric and Magnetic Dipoles

An electric dipole consists of two, equal, oppositely-charged, fixed charge distributions, $+q(t)$ and $-q(t)$, separated by a distance l, along which a time-dependent current $I(t)$ flows, shown by Figure 1. The length l must be kept short to ensure that the current is spatially constant; practically, this is satisfied for electric dipoles of length $l \leq \lambda/10$.

[1]By way of near- to far-field transformation methods for these distances, as to avoid the memory problems associated with a computational grid that is large enough to extend to typical far-field zones.

A magnetic dipole can be considered the magnetic "dual" of the electric dipole; rather than having two fixed electrostatic charge distributions at each end, the magnetic dipole has two fixed magnetic poles, like a bar magnet (see Figure 2). A closed, circular loop of wire, of radius a, along which the current $I(t)$ flows can be thought of as a magnetic dipole — the well-known Ampère's loop equivalence principle [6].

2.2. Radiation Transmission Efficiency

The radiation transmission efficiency (RTE), η, is defined as:

$$\eta = \left| \frac{\mathrm{Re}(\mathbf{S}) \times A_r}{P_{rad}} \right| \tag{1}$$

where Re($\mathbf{S}$) denotes the real-part of the Poynting vector, which describes the flow of electromagnetic energy away from a source in the form of radiation. To obtain closed from solutions for $\mathbf{S}$ for each dipole, one makes use of the magnetic vector potential, $\mathbf{A}$, and scalar potential, ϕ, to solve for the electric and magnetic fields (denoted by $\mathbf{E}$ and $\mathbf{H}$ respectively) outside the dipoles. The Poynting vector is equal to the vector cross-product of the fields $\mathbf{E}$ and $\mathbf{H}$, i.e., $\mathbf{S} = \mathbf{E} \times \mathbf{H}$.

P_{rad} is the total power radiated by the source, and is obtained via surface integration of $\mathbf{S}$ *without restricting the solution for* $\boldsymbol{S}$ *to either the near field or the far-field zones* as done throughout the literature [5, 7]. This operation produces an equation for P_{rad} for each dipole that varies with the radial distance r, before settling down to the well known far-field expressions after a wavelength (λ). It is this dependence that causes the discontinuity at $r = \lambda/\sqrt{2}\pi$.

A_r denotes the surface area of the receiver. The reception characteristics of the receiver are simplified in Equation (1); it assumed that the radiation from the source is normally incident up the receiver surface and that no scattering losses are incurred. As such, Equation (1) can be though of as a theoretical upper bound for the overall transfer efficiency of the system.

2.3. Radiation Transmission Efficiency of Electric and Magnetic Dipoles

Analysis into the RTE of electric and magnetic dipoles showed that despite having differing equations for $\mathbf{S}$ and P_{rad}, the RTE was shown to be the same for each dipole. The RTE for the dipoles, η_d, is given by Equation (2)

$$\eta_d = \frac{3A_r \sin^2\theta}{8\pi((\beta r)^2 - 2)r^2} \left(\cos^2\theta \left(8r + 4r^2 - (\beta r)^4 + (\beta r)^2\right) + (\beta r)^4 - 4(\beta r)^2 + 4)\right)^{1/2} \tag{2}$$

where $\beta = \omega/c$ denotes the free-space wavenumber. The total power radiated by each dipole, $P_{rad,e}$ and $P_{rad,m}$, is however not the same. They are given by Equations (3) and (4),

$$|P_{e,rad}| = \frac{((\beta r)^2 - 2)(I_0 l)^2}{12\pi c\epsilon_0 r^2} \tag{3}$$

$$|P_{m,rad}| = \frac{((\beta r)^2 - 2)\omega\beta(a^2\pi I_0)^2}{\epsilon_0 \pi c^2 r^2} \tag{4}$$

I_0 represents the amplitude of the current excitation along each dipole, ϵ_0 is the permittivity of free space and μ_0 is the permeability of free-space. It can be easily verified that Equations (3) and

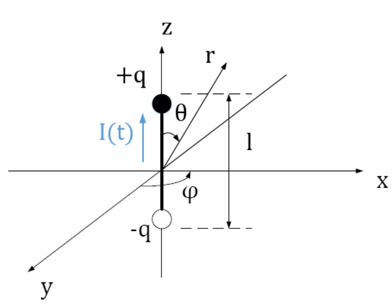

Figure 1: Electric dipole embedded in a spherical coordinate system.

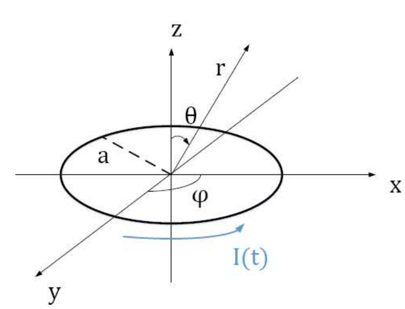

Figure 2: Magnetic dipole embedded in a spherical coordinate system.

(4) reduce to the far-field expressions $P'_{e,rad}$ (5) and $P'_{m,rad}$ (6) for $\beta r \gg 1$:

$$P'_{e,rad} = \frac{\mu_0(\omega I_0 l)^2}{12\pi c} \tag{5}$$

$$P'_{m,rad} = \frac{\mu_0\omega^4(a^2\pi I_0)^2}{12\pi c^3} \tag{6}$$

For a more detailed analysis and derivation of Equations (1)–(6), the reader is referred to [9].

3. RESULTS

The dipoles are oriented as shown in Figures 1, 2, and are subjected to 1 V sinusoidal current excitations at 300 MHz and 3 GHz. The RTE is measured from 0.1–2.5 metres (m) at 0.25 m intervals. The variation of the RTE with respect to polar angle, θ, is considered; at $\theta = 90°$ and $\theta = 45°$. Due to symmetry, there is no field variation with respect to the azimuth angle (initial simulations confirmed this), φ, and so this angle is kept fixed throughout the simulations. The RTE is normalised represent efficiency loss, i.e., $\eta_{norm} = 10\log_{10}(\eta)$ dB.

Figures 3 and 4 show the results of the simulations at 300 MHz and 3 GHz respectively. It can be seen that the RTE for the electric and magnetic dipoles at 300 MHz are different at both $\theta = 45°$ and $\theta = 90°$, with the electric dipole exhibiting the least efficiency loss over the distance range at both angles. At 3 GHz, the RTE of the dipoles is again not the same, but it is the magnetic dipole that exhibits the least efficiency loss over the majority of the distance range. In terms of frequency, the dipoles at 300 MHz show lower efficiency loss than dipoles at 3 GHz. This was observed in the

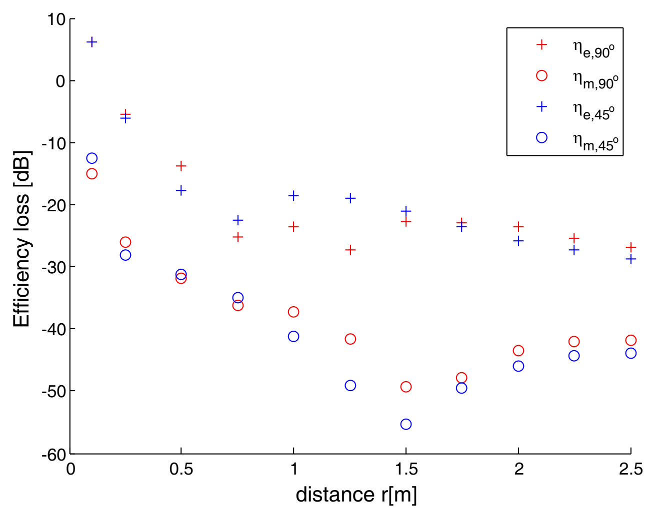

Figure 3: RTE for electric η_e and magnetic η_m dipoles for polar angle $\theta = 90°$ and $\theta = 45°$ at 300 MHz.

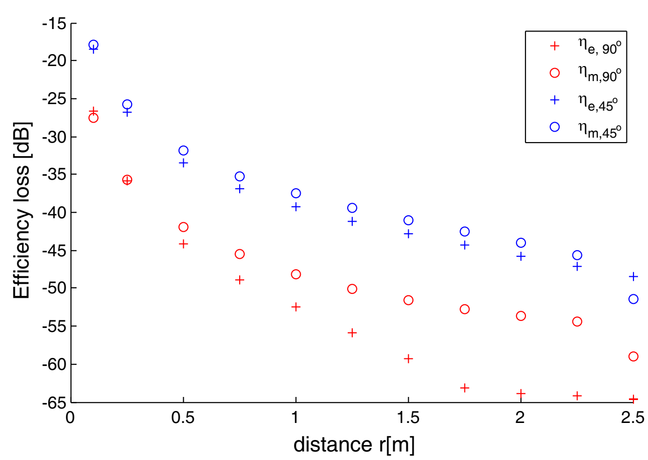

Figure 4: RTE for electric η_e and magnetic η_m dipoles for polar angle $\theta = 90°$ and $\theta = 45°$ at 3 GHz.

closed form analysis, and was concluded to be due to the near-field components that exist over a greater distance range at lower frequencies.

What is clear from the figure at 300 MHz is that the claimed discontinuity from the closed-form analysis at $r = \lambda/\sqrt{2}\pi = 0.225\,\mathrm{m}$ is not apparent, and the points in the region around the discontinuity follow a smooth decay (this has been confirmed in separate simulation by increasing the number numerical data points in this region). This suggests that the closed-form solution is not well defined around the region of the discontinuity. Furthermore, the dipoles do not exhibit the same RTE over the distance range. The discrepancy between this and the closed-form analysis could be due to the simplified view of the dipole models in the closed-form picture, i.e., the simulation takes into account details such as the impedance, dissipative losses and how power is fed to the dipoles. It is possible that the inclusion of these details into the closed-form analysis could provide a better correlation between the two approaches.

Another possible reason for discrepancy is that despite the inclusion of so-called "near-field" terms in the field equations, these are in fact still insufficient to describe the complex behaviour of radiation in near-field regions; this is to be investigated by extending the size of the computational domain in the simulations and considering a higher frequency range (since this will reduce the size of the near-field regions).

4. CONCLUSION

The results of the numerical study have shown that electric and magnetic dipoles exhibit different RTEs and that there is no observed discontinuity at $r = \lambda/\sqrt{2}\pi$, in contrast to what is predicted by the closed-form analysis. The numerical analysis showed that lower frequency dipoles exhibit less loss in efficiency than their higher frequency counterparts, over a distance of several metres. This is in agreement with the closed-form analysis. It has been hypothesised as to why there are discrepancies between the numerical and analytic exercises, and these provide scope for future work.

REFERENCES

1. Berenger, J.-P., "Three-dimensional perfectly matched layer for the absorption of electromagnetic waves," *Journal of Computational Physics*, Vol. 127, No. 2, 363–379, 1996.
2. Davidson, D., *Comptational Electromagnetics for RF and Microwave Engineering*, 2nd Edition, Cambridge University Press, 2005.
3. Drabowitch, S., *Modern Antennas*, 1st Edition, Springer, 1997.
4. Fan, H. and F. Schlagenhaufer, "Far-field approximation of electrically moderate- sized structures by infinitesimal electric and magnetic dipoles," *IEEE Transactions on Electromagnetic Compatibility*, Vol. 52, No. 1, 82–88, 2010.
5. Grant, I. and W. Phillips, *Electromagnetism*, 2nd Edition, John-Wiley & Sons, 2003.
6. Hammond, P., *Applied Electromagnetism*, 1st Edition, Pergamon Press, 1971.
7. Kraus, J. and R. Marheftka, *Antennas*, 3rd Edition, McGraw-Hill, 2003.
8. Li, L.-W., M.-S. Leong, P.-S. Kooi, and T.-S. Yeo, "Exact solutions of electromagnetic fields in both near and far zones radiated by thin circular-loop antennas: A general representation," *IEEE Transactions on Antennas and Propagation*, Vol. 45, No. 12, 1741–1748, 1997.
9. Moorey, C., W. Holderbaum, and B. A. Potter, "Radiative power transmission of dipolar sources," *Proceedings of IEEE Wireless Power Transfer Conference, Technologies, Systems and Applications*, 206–209, 2013.
10. Yee, K. S., "Numerical solution of initial boundary problems involving Maxwell's equations in isotropic media," *IEEE Transactions on Antennas and Propagation*, Vol. 14, No. 3, 302–307, 1966.

An Energy Management Circuit Based on Up-conversion to Power Wireless Sensor Nodes

S. Q. Pan, P. Li, Y. M. Wen, Z. Q. Zhang, D. Lu, and D. F. Sun
Research Center of Sensors and Instruments, Department of Optoelectronic Engineering
Chongqing University, Chongqing 400044, China

Abstract— This paper presents an up-conversion energy management circuit for harvesting electrical energy induced from the current-carrying electric cord and driving wireless sensor nodes. Since the low frequency signal induced from the electric cord is up-converted into a new one focused on a higher frequency by the management circuit the energy harvesting power of the management circuit can be improved. More energy can be accumulated in the storage capacitor and the charging time can also be improved. It is demonstrated that the maximum energy harvesting efficiency of the management circuit can reach to 91.67%. Under 1 A current through the electric cord circumstances, the energy stored in the storage capacitor can be released to drive a wireless sensor node, whose power consumptions are 18 mW in acquiring data mode (199 ms) and 54 mW in transmitting data mode (1 ms) at a communication distance of 20 m, respectively.

1. INTRODUCTION

Nowadays, as indispensable facilities, electric cords need to be monitored for safe and reliable operation. Since electric cords are generally installed in unapproachable environments, it is hard and inconvenient to monitor the electric cords by traditional approaches. Wireless sensor nodes (WSNs) possess many characteristics, such as low power consumption, wireless connection, and handy installation [1]. Hence, it is not complicated to monitor the electric cords by WSNs. The power supplies are significant to the operation lifespan of WSNs. The conventional power supplies are batteries, but batteries have many disadvantages including limited energy and bulky size [2]. Harvesting ambient energy as the power supplies of WSNs is gradually becoming an excellent alternative solution to batteries [3].

Electromagnetic energy distributes around the current-carrying electric cord and can be scavenged as the energy source of WSNs by the energy harvester. An energy management circuit is necessary to store and govern the energy from transducer. Traditional energy management circuit is composed of an ac-dc rectifier, a storage capacitor, and a dc-dc converter [4]. An input voltage of 120 mV can be converted to an output voltage of 1.2 V with a maximum efficiency of about 30% by the proposed circuit [5]. Different kinds of interface circuits based on synchronized switch harvesting on inductor (SSHI) technique are developed to improve energy harvesting efficiency [6, 7]. In these SSHI circuits more power consumptions can be caused by the auxiliary devices including voltage detection sensor and microcontroller. However, due to weak outputs of transducers and poor impedance matching of the aforementioned management circuits, it is difficult to accumulate adequate energy and drive WSNs under weak current through the electric cord circumstances. A high efficiency energy management circuit is necessary to harvest enough power from the current-carrying electric cords for WSNs.

This paper describes an energy management circuit based on up-conversion for scavenging electrical energy induced from the electric cord. The accumulated energy by the proposed management circuit can drive the WSN with the power consumption of 54 mW under 1 A current through the electric cord circumstances.

2. ENERGY MANAGEMENT CIRCUIT

An electromagnetic transducer is proposed to convert electromagnetic energy distributing around the current-carrying electric cord into electrical energy, as shown in Figure 1. The output power and voltage of the harvesting coil (L_2 in Figure 1) change as a function of load resistance under 1 A current through the electric cord circumstances, as shown in Figure 2. The output voltage increases with load resistance and the maximum output power of 0.72 mW can be obtained under a resistance of 8 kΩ. For a large storage capacitor, the output power is weak due to capacitive load. Hence, a high efficiency energy management circuit must be developed to achieve good impedance matching and accumulate more energy.

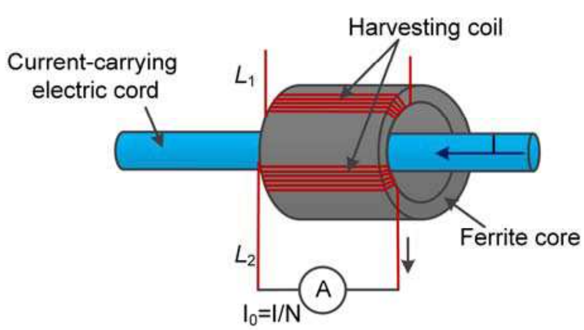

Figure 1: Electromagnetic transducer.

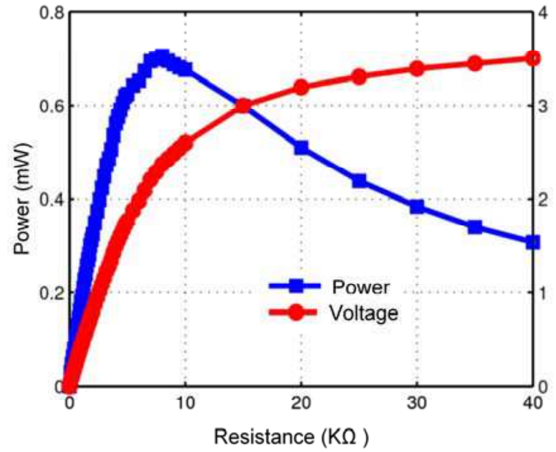

Figure 2: Output power and voltage as a function of load resistance.

The electromagnetic transducers are installed in the 220 V distribution box, as shown in Figure 3(a). The energy management circuit is composed of a matching circuit, an up-conversion circuit, a rectifier, a storage capacitor, and a regulator, as shown in Figure 3(b). The proposed matching circuit can achieve good impedance matching by converting a low frequency signal into a high frequency signal.

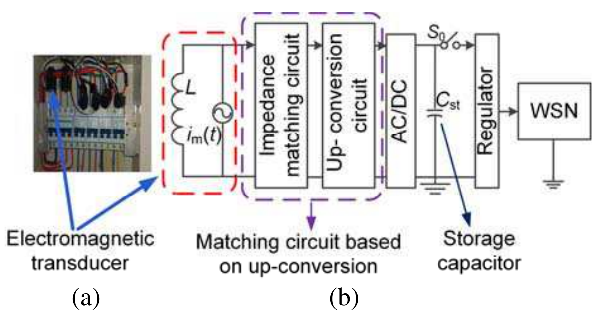

Figure 3: (a) Transducers installed in distribution box. (b) Schematic diagram of management circuit.

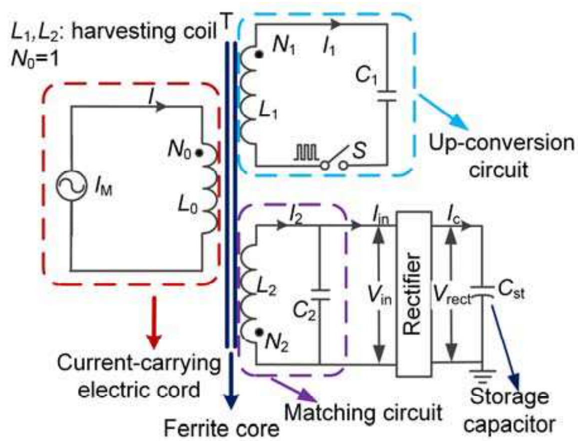

Figure 4: Equivalent management circuit.

The equivalent management circuit is shown in Figure 4. The current-carrying electric cord can be equivalent to a serial circuit with a current source and an inductor with only one turn of coil. S is an ultra-low power consumption bidirectional switch, which is opened or closed by a trigger signal generated by a rectangular wave generating circuit (1 μA). C_2 is the matching capacitor to produce damped oscillating response with inductor L_2. The signal of ω_0 induced from electric cord can be up-converted into a signal focused on new frequencies (ω_0, ω_1, and ω_2). The voltage across capacitor C_2 can be expressed as

$$v_{c2}(t) = \begin{cases} Ae^{-\alpha_1 t}\sin(\omega_1 t + \gamma_1) + \mathrm{C}\sin\omega_0 t. \ S \text{ is on} \\ Be^{-\alpha_2 t}\sin(\omega_2 t + \gamma_2) + D\sin\omega_0 t. \ S \text{ is off} \end{cases} \tag{1}$$

It is evident that $v_{c2}(t)$ contains a damped oscillating signal of ω_1 (or ω_2) and a sinusoidal signal of ω_0 when S is on (or off). When S is controlled by a trigger signal with a frequency of 114 Hz and a duty cycle of 50%, the output voltage across capacitor C_2 is shown in Figure 5. The 50 Hz ac signal is up-converted into a new one mainly focused on 4.72 kHz by the management circuit.

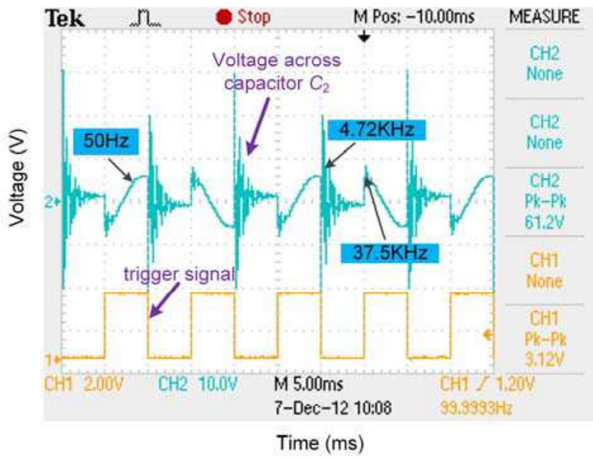

Figure 5: Voltage across capacitor C_2.

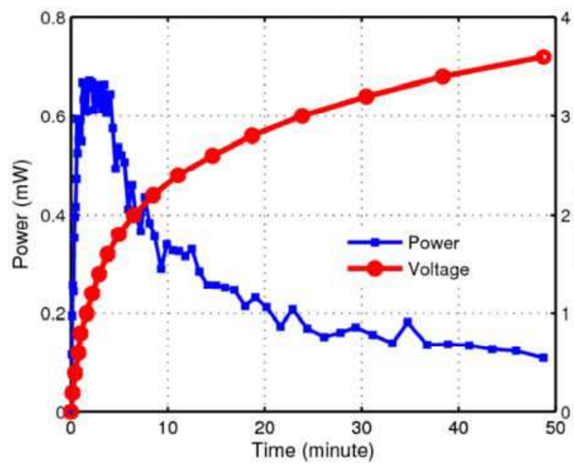

Figure 6: Charging power and voltage of storage capacitor.

3. EXPERIMENT

Under 1 A current through the electric cord circumstances, the charging power and voltage of storage capacitor (0.1 F) are shown in Figure 6. The storage capacitor can be charged to 3.3 V at a charging time of 30 minutes. The maximum charging power of 0.66 mW can be obtained when the voltage across storage capacitor is 1.1 V. Hence, the maximum energy harvesting efficiency of the management circuit is

$$\eta = (0.66\,\mathrm{mW}/0.72\,\mathrm{mW}) \times 100\% = 91.67\% \tag{2}$$

The WSN is composed of a wireless System-on-Chip (nRF24LE1) and sensor units (DS600). The power consumptions of receiving data (199 ms) and transmitting data (1 ms) are 18 mW and 54 mW, respectively. The necessary energy of WSN in an operation period is

$$E_n = 54\,\mathrm{mW} \times 0.001\,\mathrm{s} + 18\,\mathrm{mW} \times 0.199\,\mathrm{s} = 3.64\,\mathrm{mJ} \tag{3}$$

The experimental results show that the voltage across storage capacitor drops from 3.16 V to 3.11 V after transmitting data. Thus, the energy provided by the management circuit in a discharging period is

$$E_o = \left[(3.16\,\mathrm{V})^2 - (3.11\,\mathrm{V})^2\right] \times 0.1\,\mathrm{F}/2 = 15.68\,\mathrm{mJ} \tag{4}$$

From Equations (3) and (4), $E_o > E_n$. Hence, the scavenged energy from the electric cord by the management circuit can drive the WSN under 1 A current through the electric cord circumstances.

4. CONCLUSION

In this paper, an electromagnetic energy management circuit based on up-conversion is proposed to harvest energy from electric cord and drive WSNs. The management circuit can achieve good impedance matching. Under 1 A current through the electric cord circumstances, the maximum energy harvesting efficiency is 91.67% and the storage capacitor can be charged to 3.3 V within 30 minutes. The weak energy from electric cord can be accumulated to drive the WSN with an output power of 54 mW at a distance of 20 m. The proposed approach based on up-conversion technique can also be applied in other energy harvesting circuits to harvest weak energy from transducers.

ACKNOWLEDGMENT

This work is financially supported by the National Natural Science Foundation of China (Grant Nos. 50830202 and 61071042) and the National High Technology Research and Development Program of China (863 Program) (No. 2012AA040602).

REFERENCES

1. Kazmierski, T. K., G. V. Merrett, and L. Wang, "Modeling of wireless sensor nodes powered by tunable energy harvesters: HDL-based approach," *IEEE Sensors J.*, Vol. 12, No. 8, 2680–2690, 2012.
2. Ramachandran, K. and B. Sikdar, "A population based approach to model the lifetime and energy distribution in battery constrained wireless sensor networks," *IEEE J. Sel. Areas Commun.,* Vol. 28, No. 4, 576–586, 2010.
3. Li, P., Y. M. Wen, P. G. Liu, and X. S. Li, "A magnetoelectrical energy harvester and management circuit for wireless sensor network," *Sens. Actuators A*, No. 157, 100–106, 2009.
4. Cao, X. P., W. J. Chang, Y. C. King, and Y. K. Lee, "Electromagnetic energy harvesting circuit with feedforward and feedback DC-DC PWM boost converter for vibration power generator system," *IEEE Trans. Power Electron.*, Vol. 22, No. 2, 679–675, 2007.
5. Richelli, A., S. Comensoli, and Z. M. Vajna, "A DC/DC boosting technique and power management for ultralow-voltage energy harvesting applications," *IEEE Trans. Ind. Electron.,* Vol. 59, No. 6, 2701–2708, 2012.
6. Zhu, L. Y. and R. W. Chen, "A new synchronized switching harvesting scheme employing current doubler rectifier," *Sens. Actuators A*, No. 174, 107–114, 2011.
7. Li, P., Y. M. Wen, C. B. Jia, and X. S. Li, "A magnetoelectric composite energy harvester and power management circuit," *IEEE Trans. Ind. Electron.,* Vol. 58, No. 7, 2944–2951, 2011.

Self-contained Self-powered Wireless Sensing Node for AC Power Supply Cords Monitoring

D. Lu, Y. Wen, P. Li, S. Pan, and Z. Zhang
Research Center of Sensors and Instruments, Department of Optoelectronic Engineering
Chongqing University, Chongqing 400044, China

Abstract— This paper presents a self-contained self-powered wireless sensing node for AC power supply cords monitoring. It consists of an energy harvester, a current sensor, a temperature sensor and a wireless module. The underlying component of the node is a magnetic split-core, which readily embraces the monitored cord in operation. There are two sets of coils wound around the core, one is sensing the current and another is scavenging the magnetic energy originated from the carried-on AC current. The output of the energy harvesting coil is connected with the power management circuit to produce adequate DC supply for the wireless sensing node. The outputs of the current and temperature sensors are connected to the module for wireless transmission. The node is demonstrated to monitor AC power supply cord with carrying current from 1 A to 100 A of electric appliances exclusive of externally physical connections. With the proposed wireless sensing nodes, a wireless sensor network can achieve distributed monitoring of the AC power supply cords.

1. INTRODUCTION

Energy harvesting is thought to be a promising solution for sustainably powering wireless sensors. As a matter of fact, in general ambience, it is quite difficult to sustainably scavenge adequate energy from ambient sources for power supply. However there are guaranteed electric/magnetic fields along power cords carrying AC currents. Based on this fact, quantities of researches have been done on the self-powered sensor systems, which scavenge the electromagnetic energy originated from the carried-on AC current [1].

Harvesting the energy aroused from AC current carrying power lines have been designed for the electric power monitoring systems of power transmission lines [2] and substations [3], in which cases, the line voltage reaches kV-level. There are also self-powered sensors applied in the power supply cords, whose voltage is typically $110\,\mathrm{V} \sim 380\,\mathrm{V}$ [4, 5]. In the case of wireless sensing of power cord condition, a battery usually has to be contained in the wireless node [6, 7]. Here, for wireless monitoring low-voltage AC power supply cords of electric appliances, a self-contained self-powered wireless sensing node is proposed.

The self-contained self-powered wireless sensing node wirelessly transmits the outputs of the current and temperature sensors and scavenges the magnetic energy surrounding the monitored cord for node's operation simultaneously, achieving the wireless monitoring AC power cords exclusive of externally physical connection to a DC power supply. Actual tests have been carried out to verify the validity of the self-contained self-powered wireless sensing node. Furthermore, a wireless sensor network employing the proposed sensing nodes is also constructed for distributed power supply cords monitoring.

2. NODE DESIGN

The architecture of the self-contained self-powered wireless sensing node is shown in Figure 1. There are three parts included, namely an energy harvester, sensors and a wireless module. The energy harvester is composed of an energy harvesting coil and a power management circuit. Sensors consist of a current sensor and a temperature sensor. For easy installation and maintenance, the core is designed as a split-core.

Both the energy harvesting coil and current sensing coil are on the basis of the same principle — electromagnetic induction. The coils couple to the alternating magnetic field produced by an AC current-carrying cord passing through the core, as a result, an alternating electromotive force which is proportional to the AC current is induced across the coils. Two sets of coils both wrap around the magnetic core, consequently, energy harvesting and current sensing can be achieved in the same magnetic path.

However the energy scavenged by harvesting coil exists in AC form, and the instantaneous output power is not always enough for the operating of the node, a power management circuit is

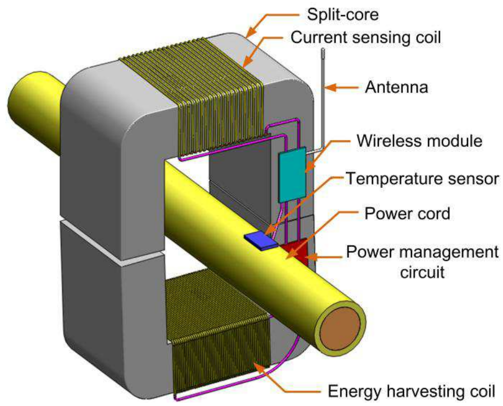

Figure 1: Architecture of the self-contained self-powered wireless sensing node.

designed to accumulate and store energy and provide a high-power DC output to drive the sensing node. The scavenged energy is stored in a storage capacitor/rechargeable battery of the power management circuit. When discharging, the capacitor/battery acts as the power supply for the sensing node with the voltage dropping from U_1 to U_2. The energy stored in the capacitor/battery available for the sensing node is

$$E = \frac{1}{2}C\left(U_1^2 - U_2^2\right) \tag{1}$$

where C is the value of the storage capacitor/rechargeable battery.

In order for wireless communication, a module is required to wirelessly transmit the outputs of the current and temperature sensors. A wireless sensor network with the proposed sensing nodes is essential for multi-point monitoring of AC power supply cords.

To reduce the power consumption of the sensing node for long-time AC power cords monitoring, the node is set to work and sleep alternately. The work duration includes the activity cycle and the transmission interval. During the activity cycle, the node wakes up and acquires current and temperature information. In one period, the energy consumed by the sensing node is

$$E_n = P_{sleep}T_{sleep} + P_{active}T_{active} + P_{trans}T_{trans} \tag{2}$$

where P_{sleep}, P_{active}, P_{trans} are the power consumption of the node in the sleep, active and transmission stage separately and T_{sleep}, T_{active}, T_{trans} are the corresponding time of the three stages respectively.

3. EXPERIMENTS

The fabricated self-contained self-powered wireless sensing node is shown in Figure 2. Because of the compact size and self-contained device architecture, the sensing node can be readily installed to encircle a power cord without interruption of the power supply from the monitored cord. Nordic's nRF24LE1 SOC solution which is comprised of a high performance microcontroller core, 6–12 bit ADC and a transceiver is employed for wireless transmission.

In the experiment, the sleep time of the sensing node is set to be 2 minutes. An activity cycle and a transmission process requires 201 ms and 500 μs respectively. As shown in Figure 3, the

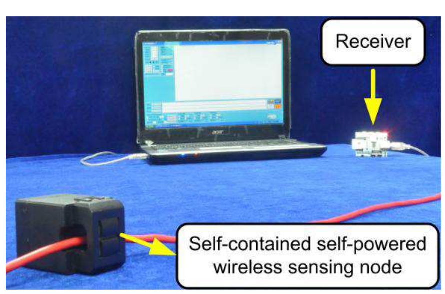

Figure 2: Experimental setup of the self-contained self-powered wireless sensing node.

power consumed by the sensing node in one period is

$$E_n = 6.4\,\mu\text{W} \times 120\,\text{s} + 18\,\text{mW} \times 201\,\text{ms} + 54\,\text{mW} \times 0.5\,\text{ms} \approx 4.42\,\text{mJ} \tag{3}$$

A storage capacitor is used for energy storage element in the test. During the work duration of the sensing node, the voltage of the capacitor drops from 3.43 V to 3.39 V, which is shown in Figure 4, the energy provided by the storage capacitor is

$$E = \frac{1}{2} \times 0.1 \times \left(3.43^2 - 3.39^2\right) = 13.64\,\text{mJ} \tag{4}$$

The normal efficiency of a regulated power supply circuit is more than 70%. Consequently, the energy supplied to the sensing node is at least 13.64 mJ $*$ 70% = 9.548 mJ. It's obvious that the energy provided by the power management circuit can meet the power consumption requirement of the sensing node.

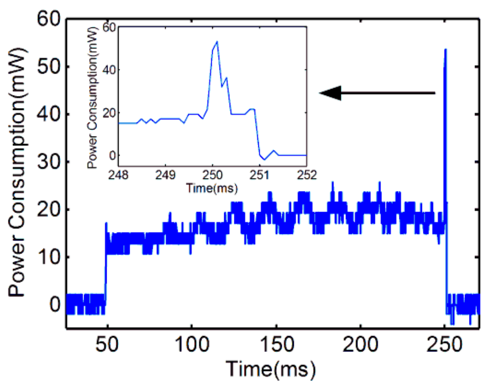

Figure 3: Power consumption of the sensing node.

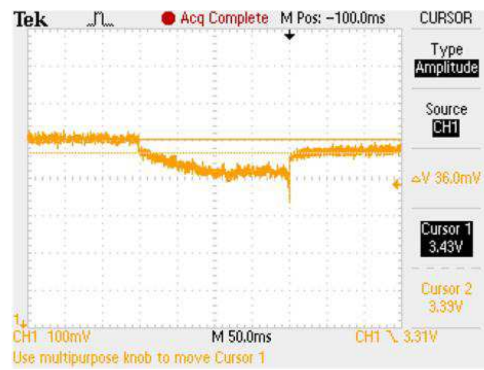

Figure 4: Discharge process of the storage capacitor.

The data loss ratio of the point-to-point communication test is performed in the indoor condition, whose result is shown in Figure 5. According to the figure, the data loss rate of the point-to-point communication is lower than 0.25‰ with communication distance within 10 meters. The data loss rate in the open field is considerably lower than the one in the indoor condition.

The wireless sensor network is constructed in a star topology distributively with the proposed self-contained self-powered sensing nodes, which is shown in Figure 6.

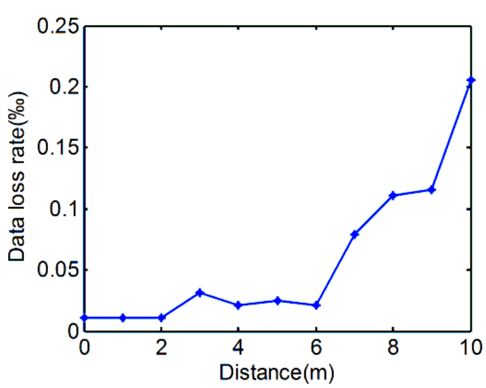

Figure 5: Data loss rate as a function of distance.

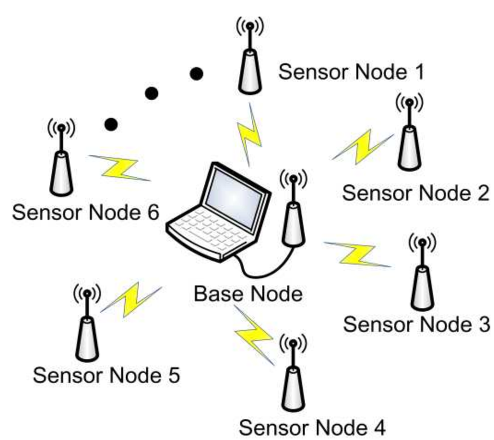

Figure 6: Schema of the wireless sensor network.

4. CONCLUSION

In this paper, the self-contained self-powered wireless sensing node for AC power supply cords monitoring is presented. The energy induced from the magnetic field is transferred to the wireless module by using the power management circuit. It's verified that the self-contained self-powered wireless sensing node can operate while the carried-on current is from 1 A to 100 A with a wireless distance of 10 meters and the sensing data is wirelessly transmitted at a data loss rate of point-to-point communication less than 0.25‰. The wireless sensor network is constructed in a star topology for distributed monitoring with the proposed wireless sensing nodes.

The application fields of the self-contained self-powered wireless sensing node not only can be applied to monitoring of power supply cords, but also can be easily extended to realize intelligent community or intelligent buildings etc., and the concept of "self-contained self-powered wireless sensor" can be applied to almost all "M2M" industries.

ACKNOWLEDGMENT

This work is supported by the National Natural Science Foundation of China (No. 6107104) and National Education Ministry Doctor Foundation of China (No. 20100191110009).

REFERENCES

1. Paprotny, I., E. Leland, C. Sherman, R. M. White, and P. K. Wright, "Self-powered MEMS sensor module for measuring electrical quantities in residential, commercial, distribution and transmission power systems," *IEEE Energy Conversion Congress and Exposition*, 4159–4164, Atlanta, USA, Sep. 2010.
2. Guo, F., H. Hayat, and J. Wang, "Energy harvesting devices for high voltage transmission line monitoring," *Power and Energy Society General Meeting*, 1–8, Detroit, USA, Jul. 2011.
3. Roscoe, N. M. and M. D. Judd, "Harvesting energy from magnetic fields to power condition monitoring sensors," *IEEE Sens. J.*, Vol. 13, No. 6, 2263–2270, 2013.
4. Li, P., Y. Wen, P. Liu, X. Li, and C. Jia, "A magnetoelectric energy harvester and management circuit for wireless sensor network," *Sens. Actuators A*, Vol. 157, No. 1, 100–106, 2010.
5. Leland, E. S., C. T. Sherman, P. Minor, R. M. White, and P. K. Wright, "A new MEMS sensor for AC electric current," *IEEE Sensors*, 1177–1182, Waikoloa, USA, Nov. 2010.
6. Xu, Q., M. Seidel, I. Paprotny, R. M. White, and P. K. Wright, "Integrated centralized electric current monitoring system using wirelessly enabled non-intrusive AC current sensor," *IEEE Sensors*, 1988–2001, Limerick, Ireland, Oct. 2011.
7. Zhang, Y., J. Lu, H. Hiroshima, T. Itoh, and R. Madeda, "Simulation and design of micro inductor for electromagnetic energy scavenging at low AC frequency in wireless sensor network," *PowerMEMS*, 253–256, Washington DC, USA, Dec. 2009.

Design of Ultra Wideband Balanced Antipodal Vivaldi Antenna for Hyperthermia Treatment

Khaled A. Alsulaiman, **Mohammed Al alShaykh**,
Sulaiman Alsulaiman, and **Ibrahim Elshafiey**
Department of Electrical Engineering, King Saud University, Riyadh, Saudi Arabia

Abstract— A hyperthermia applicator for tumor treatment in the head and neck region is introduced. The system is based on an array of UWB, electrically small Vivaldi antenna. The antenna design has dimensions of $80 \times 44 \times 9.2$ mm including the SMA attachments. The antenna is simulated with water background, and the simulation results under SEMCAD X environment shows a reflection coefficient less than -10 dB at a frequency range from 50 MHz to 3.75 GHz. Specific absorption rate (SAR) values of a simulated tumor in a head phantom model exposed to radiation from four antenna are presented. Investigation of the use of nanoparticles to control the electrical conductivity and permittivity of the tumor is presented.

1. INTRODUCTION

Hyperthermia is a technique that depends on thermal therapy by localizing heat to the tumor area. Limited temperature rise from to 41–45°C is typically applied in hyperthermia treatment. Elevated temperature can damage and kill cancer cells, usually with minimal injury to normal tissues, by enhancing blood circulation and hence oxygenation. In regional hyperthermia, large areas of tissue, such as a body cavity, organ, or limb are heated. In local hyperthermia, which is more attractive, yet more challenging, the tumor region is targeted with the thermal energy [1].

Different types of energy may be used to apply heat, including radiofrequency, microwave and ultrasound. The side effects of hyperthermia are minimal compared to standard cancer treatment modalities. Unlike X-rays and gamma rays, applying hyperthermia using radiation of spectrum range of 0.3–3.3 GHz is quite harmless. Hyperthermia can thus be used to increase the effectiveness and reduce the required doses of other treatment modalities such as chemotherapy and radiotherapy. The main concern of hyperthermia is the burn of skin or normal cell damage, and these effects can be limited using cooling water bolus to reduce the temperature of skin affected by radiation.

2. VIVALDI ANTENNA THEORY

Vivaldi antenna is a tapered slot antenna (TSA). Radiating structure is usually exponentially tapered; however, examples of parabolic, hyperbolic or elliptical curves designs exist. TSAs offer qualities such as efficiency, bandwidth, light weight, and geometric simplicity. Utilizing low cost, reproducible, and repeatable designs result. It was first investigated by P. Gibson in 1979 [2] and many improvements to the initial design came later, namely in the works of E. Gazit in 1988 [3] and Langley, Hall and Newham [4] in 1996. Vivaldi antennas are good candidates to use in hyperthermia treatment due to their properties.

3. ANTENNA DESIGN

In the design, we followed the model of Bourqui et al. [5], with optimization performed to enhance the design to match the objectives. The antenna consists of three copper layers. The middle layer is the conductor which is connected to the coaxial transmission line of the SMA connector. The other two ground layers are connected to the SMA connector's ground. The Feed is a gradual transition between stripline to a tri-stripline transmission line. The conductor layer width increases linearly, while the ground layers decrease exponentially to maintain constant impedance. After a short distance the ground layers flares in opposing direction with exponential curves creating the antenna aperture. The feeding layer is separated from the ground layers by two dielectric substrates. Two additional dielectric layers are stacked on each side of the antenna. More than 50 models of different substrates, taper rates, geometric sizes, background materials were simulated and studied until reaching a final design. A significant improvement occurred when the stripline "feeding" part width of the conducting layer was changed from the almost linearly increasing to exponentially decreasing with a larger starting width.

4. EVALUATION METHOD

The modeling of the Vivaldi antenna was done by writing the curve equations using MATLAB and then transforming the data of the curves to a python script. The python scripts are imported in SEMCAD X to be converted into conductive sheets. The matching had to be enhanced and the logical way to tackle this would be by increasing the size of the antenna thereby reducing the reflection coefficient. However, the small size was one of our objectives. A novel way to solve this was by immersing the antenna in distilled water. Most importantly, the water would shift the operating frequency to the required band while maintain the antenna size. It would be used to cool the patient skin & solve the fear of skin burns. It would reduce hot spots and improve the impedance matching between the biological tissue and the antenna. This thus offers a simple, effective and economical solution. We then focused more on grounds layers.

By decreasing the starting width, a significant improvement occurred.The substrate chosen was Rogers RT/duroid 5870 ($\varepsilon_r = 2.33$), each with thickness 1.52 mm. Distilled water ($\varepsilon_r = 78\,\sigma = 2$) was chosen as background. The antenna plot is shown in Figure 1, and the designed model in SEMCAD X is shown in Figure 2. The total geometric size of the antenna is $80 \times 44 \times 9.2$ mm excluding the SMA attachments. After reviewing published papers and searching the literature, this is by far the smallest Vivaldi antenna operating at a frequency of 50 MHz.

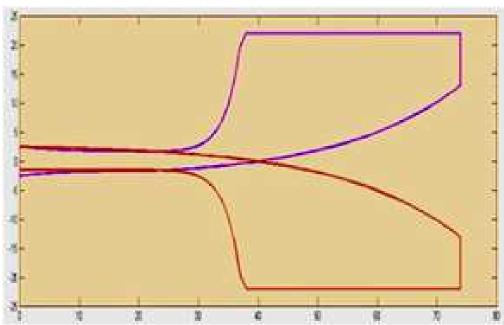

Figure 1: Plot of antenna (red), and ground (blue) outlines.

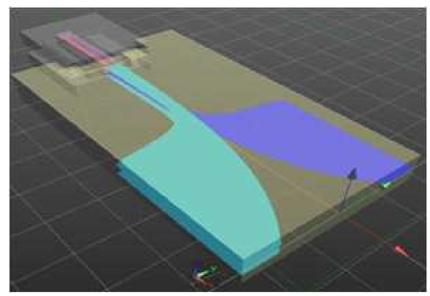

Figure 2: Perspective view of the BAVA SEMCAD X model.

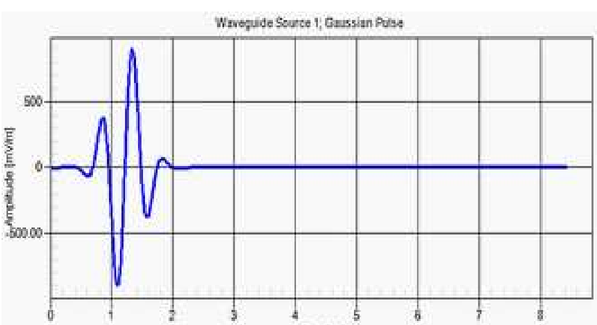

Figure 3: Excitation pulse.

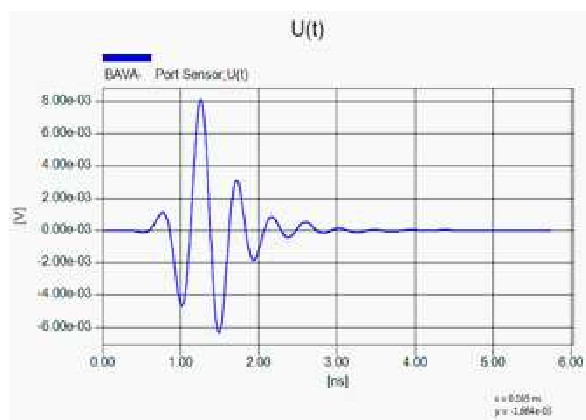

Figure 4: Time domain response.

The feeding was performed by a waveguide source with a Gaussian, TEM mode pulse through a coaxial rod of inner radius 0.635 mm. The excitation pulse is shown in Figure 3. The time domain response of the antenna is shown in Figure 4. The port sensor results show that the antenna is stable and has low distortion. The antenna reaches convergence after 4.5 ns approximately.

5. RESULTS

The antenna RMS electric field on the antenna center plane at frequency values of 0.05, 0.1, 0.2, 0.4, 0.7, 1, 1.5, 2, 2.5, and 3 GHz are shown in Figure 5. The endfire characteristic is clear from the figure. We notice some back radiation which decrease with increasing frequency. A huge refraction or fringing at the substrate-water interface is noticed. This becomes more evident at

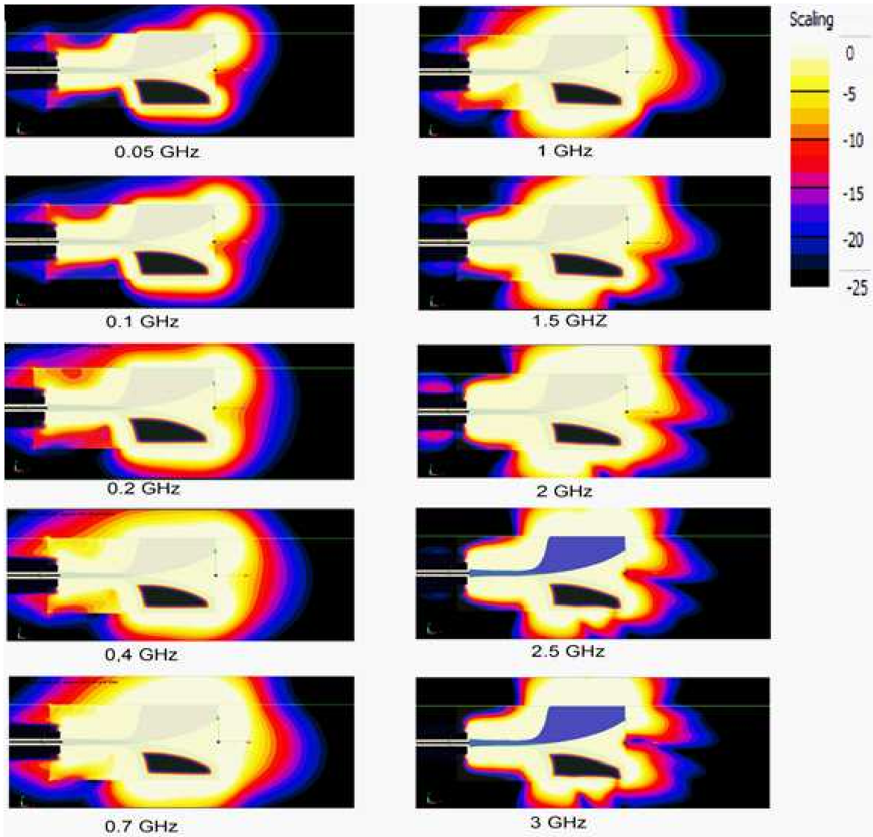

Figure 5: Simulated radiated E-field RMS modulus in the antenna plane.

larger frequencies. However, this fringing can be accounted for and the antenna shouldn't be directed at the head directly. Instead, it could rotatedto counteract this fringing.

The reflection coefficient parameter is shown in Figure 6 the simulation started from a frequency of 50 MHz. The upper frequency of the simulation is 3.75 GHz. No upper or lower limit is known inferred from the simulation. The antenna has an UWB operating range, which covers the required frequency band.

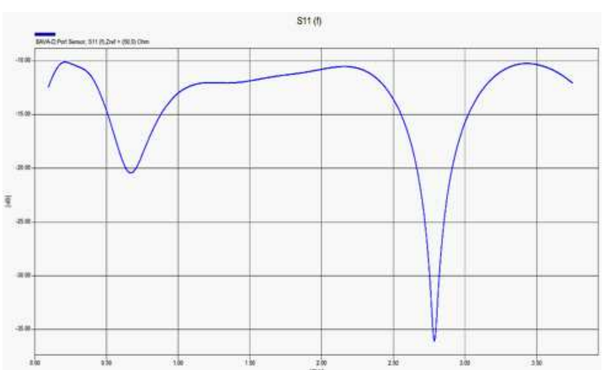

Figure 6: Reflection coefficient.

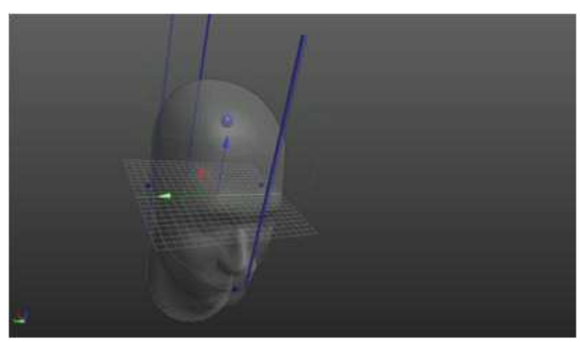

Figure 7: 3D view of the phantom model surrounded by antenna array.

6. ELECTRICAL CHARACTERISTICSOF TUMORS

Recently nanoparticles have been suggested for various biomedical applications. Nanoparticles can thus be thought of as a technique to adjust the electrical properties of the tumor and enhance the performance of hyperthermia treatment. The impact of electrical conductivity σ and the real permittivity ε_r on the energy deposition in the tumor is investigated. The study is given in terms of the specific absorption rate (SAR), which is a measure of the rate at which energy is absorbed by the body when exposed to the radiation. Simulation is performed to determine the optimum values of tumor characteristics, using a parameter sweep. A human head phantom is considered which is surrounded by four dipole antennas operating at 540 MHz as shown in Figure 7. The tumor modeling tissue is located in the center of the brain.

The conductivity range is considered starting from normal human brain white matter conductivity of 0.4 S/m up to 13 S/m. The SAR values are normalized with the maximum obtained value and is illustrated in Figure 8. Nonlinear behavior is noticed of SAR value with the conductivity values. A maxima was found at 5.6 s/m. Random points were studied after 13 s/m, all were found to have less SAR values.

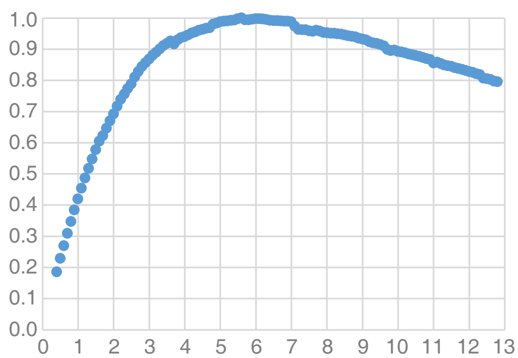

Figure 8: Normalized SAR vs. conductivity.

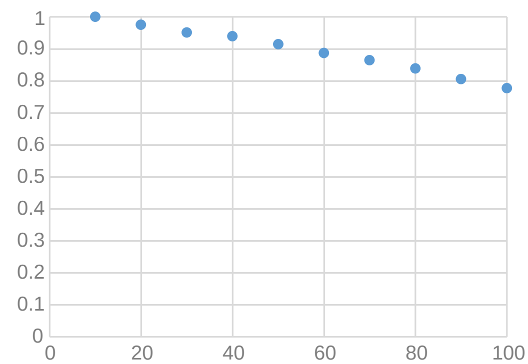

Figure 9: Normalized SAR vs. real permittivity.

Normalized SAR values against variation in the tumor permittivity is presented in Figure 9. The permittivity range studied started from $\varepsilon_r = 10$ up to $\varepsilon_r = 100$. SAR is noticed to have almost inverse linear dependence on the relative permittivity values.

7. CONCLUSIONS

Current state of the art hyperthermia treatment systems operate under single or narrowband frequency utilizing relatively large sized antennas. This limits the number of antennas that could be used in the array system. To achieve a system of wideband spectrum allowing the use of large number of elements array, we designed a balanced antipodal Vivaldi antenna with dimensions of $80 \times 44 \times 9.2$ mm including the SMA attachments. The antenna when immersed in water is shown to operate in the whole simulation bandwidth (50 MHz to 3.75 GHz), which can thus present an attractive design. Furthermore, the electrical characteristics of the tumor was investigated for their effects on SAR values. Optimum value of conductivity is noticed in the range of 5 S/m to about 7 S/m. Reduction in the values of SAR absorbed by the tumor is noticed to behave almost linearly with increase of relative permittivity. Use of phased antenna array with reasonable number of elements, and optimizing the tumor electrical characteristics using novel techniques such as the nanoparticles can have positive impact of the use of microwave hyperthermia treatment.

ACKNOWLEDGMENT

This research work is supported by the National Plan for Science and Technology, Kingdom of Saudi Arabia, under project No.: 10-ELE996-02.

REFERENCES

1. Van der Zee, J., "Heating the patient: A promising approach?," *Annals of Oncology*, Vol. 13, No. 8, 1173–1184, 2002.
2. Gibson, P. J., "The Vivaldi aerial," *Proceedings of the 9th European Microwave Conference*, 1979.
3. Gazit, E., "Improved design of the Vivaldi antenna," *IEE Proceedings*, Vol. 135, 89–92, 1988.
4. Langley, J. D. S., P. S. Hall, and P. Newham, "Balanced antipodal Vivaldi antenna forwide bandwidth phased arrays," *IEE Proc. Microw. Antennas Propag.*, Vol. 143, 97–102, 1996.
5. "Balanced antipodal vivaldi antenna with dielectric director for near-field microwave imaging," Jeremie Bourqui. *IEEE Transactions on Antennas and Propagation*, Vol. 58, No. 7, July 2010.

Label-free Acoustic and Optical Biosensors Playing on Evanescent Waves

Yihui Wu, Guigen Liu, Peng Hao, Junfeng Wu, Yongbo Deng, Yongshun Liu, and Ming Xuan
State Key Laboratory of Applied Optics, Changchun Institute of Optics, Fine Mechanics and Physics
Chinese Academy of Sciences, Changchun 130033, China

Abstract— Development of sensitive, reliable, high-throughput, label-free detection techniques is an issue with increasing emphasis because the labeling strategies that most of the microarray applications have employed, such as fluorescent, chemiluminescent and radioactive labeling, have synthetic challenges, multiple label issues and may exhibit interference with the binding sites. Label-free detection techniques monitor biomolecular interactions and simplify the bioassays by eliminating the need for secondary reactants. Especially, biosensors based on evanescent waves often have high sensitivities by recording the changes caused by the molecule interaction near the sensor surface within the evanescent field, and moreover they provide quantitative information for the binding kinetics.

In this article, we will describe the similarity of sound waves and electromagnetic waves and review the biosensors to which the two types of label-free techniques are related. The theoretical and technical outlines behind the sensing principles, such as the evanescent waves scattering, interference, resonance and tunnel effects, will be summarized. The physical mechanisms to modulate waves by micro/nano structures, which localize the waves, amplify the signal/noise ratio and increase Q factor for high sensitivity and high resolution, will also be discussed. Moreover, the promising acousto-optic sensing mechanism and the possibility of multi-parameter decoupling detection will be mentioned. The potential prospects, merits and challenges of these kinds of biosensors are also indicated.

1. INTRODUCTION

Flourescence microscopy is extremely powerful for biomolecular interactions. But the flourescent labels are often bigger than the biomolecules of interest, which affects the complex molecular interaction [1]. So real-time analyzing the relationship between molecular structure and biological function is still one of the biggest challenges in the life sciences [2].

Biosensors based on waveguides allow the binding of biomolecules on their surfaces within the depth of evanescent field and lead to miniaturized and batch producible devices. The physical parameters change of the waveguides by scattered echoes or absorption of the molecules will be output by all kinds of signals which describe the guided waves. In our opinion, the rationality of the evanescent wave sensor (EMS) is: a) the density of evanescent field is bigger on the surface of the sensor, where the molecules are bound; b) the depth of evanescent field is on wavelength scale, close to the scale of the biological molecules, so the waves beyond this area will have little impact on the signal from the interactions and reduce the background noises; c) different modes will have different depth of evanescent fields and will play different roles, thus, multi-physical-parameter identification is accessible; d) evanescent waves will carry high spatial frequency information which is tuned by nanoscale samples even beyond the diffraction limit. The two aspects of both super-resolution imaging and sensing will help the recognition of biological reactions, especially label-free detections, even it is still difficult to exhibit single-molecular sensitivity in order to produce biological relevance [1].

There have been many reviews about label-free detection techniques and the sensitivities and applications have been presented in detail [3–8]. For example, Valsecchi and Brolo presented the techniques about many types of periodic plasmonic sensors and their performances, they concluded that the Krestchmann-Raether SPR configuration was still the gold standard although several of the periodic plasmonic platforms had reported comparable performance [9]. Fan et al. [6] reviewed the progress in optical biosensors that used the label-free detection protocols. The sensing performance of some optical structures, such as SPR (surface plasmon resonance), waveguide fiber gratings, ring resonators, and photonic crystals have been evaluated and compared in terms of sensitivity and detection limit. Zalyubovskiy et al. [10] wrote about the theoretical limits of localized surface plasmon resonance (LSPR) and compared with conventional SPR. They jumped to a conclusion that sensitivity of the LSPR is on par with SPR for analyte thickness ≤ 10 nm. Because of the localized nature of plasmonic oscillations excited on the nanoparticles, LSPR is immune to the bulk noise sources that plague SPR systems. LSPR will perform $\sim$ 8-fold better in terms of S/N as compared to the classic SPR in the same temperature-controlled environment. Ray et al. [11] reviewed the label-free detection techniques for protein microarrays and so on.

In order to link and provide more insights of the physical concepts into acoustic and optical biosensors, the review will brief describe the similarity of sound waves and electromagnetic waves and the theoretical and technical outlines behind the sensing principles, such as the evanescent wave scattering, interference, resonance and the tunneling effects. The physical mechanisms to modulate waves by micro/nano structures which localize the waves, amplify the signal/noise ratio, and increase Q factor for high sensitivity and high resolution will also be discussed. Discussions ranging from the summary of the current obstacles of accurate detection to potential applications, prospects, and merits are also provided.

2. SENSING BASED ON WAVEGUIDES

2.1. Acoustic and Optical Waveguides

In the opinion of Johnson [12], wave equations, like scalar wave equation, Maxwell's equation, Schrodinger's equation and so on, can all be written abstractly in one form from an algebraic perspective which shares certain common features:

$$\frac{\partial w}{\partial t} = \hat{D}w + s \tag{1}$$

where $w(x;t)$ is some vector-field wave function characterizing the solutions. $\hat{D}$ is some linear operator (using the "hat" notation from quantum mechanics to denote linear operators), neglecting nonlinear effects, and $s(x;t)$ is some source term. It can be written in the form of eigenfunctions with exponential functions e^{ikx} for some k:

$$w(x,t) = W(x)e^{-iwt} = W_0 e^{i(k\cdot x - wt)} \tag{2}$$

For each k, there is a discrete set of eigenfrequencies $\omega_n(\vec{k})$ which are called the dispersion relation or the band structure of the medium.

Acoustic waves are matter waves and the transmission relies on the medium. The coupling oscillator in acoustic waves can be expressed by three parameters: two of them charactering the energy storage and exchange and the third charactering of energy dissipation. The product of the two energy storage parameters determines the propagation velocity of wave in the medium, as the third parameter is zero, the ratio of the two parameters decides the wave impedance of media [13].

Light is electromagnetic wave, described by Maxwell's equations, in terms of the electric field E and magnetic field H, with eigenproblem simplified into two separate Hermitian positive semidefinite eigenproblems for E and H [13]. For most optically transparent polymers, the attenuation can often be neglected, but in some cases, it may be necessary to include an attenuation constant, especially, when light is interacting with an absorption medium.

The existence of evanescent waves in optical or acoustic devices is due to that the tangential electromagnetic field (or pressure gradients) can't be discontinuous at the dielectric boundary. Evanescent waves are particular solutions of the wave equation that decay or decrease exponentially with distance but will not transfer any energy due to the fact that the time average of Poynting vector is zero. And the field decay along the propagation can be considered as the result of interference between elementary oscillating dipole sources rather than point sources [14]. Normally the propagation of a waveguide mode can be extremely affected by local modification of the conditions of the guiding. They are involved in many physical phenomena including coupling in and out waveguides and resonators, near-field optics, tunneling, subwavelength focusing, or surface waves, etc.. At a given frequency, evanescent waves are characterized by the fact that their wave vector, k, is complex valued [15].

2.2. Matter Interaction with Evanescent Waves

When the biomolecules are dissolved in a solvent, both the density and refractive index (RI) are linear functions of the concentration. Thus, the measurement of the density of the absorbed protein layer allows for the determination of RI of the protein layer, and vice versa, according to the following relation [16]:

$$n_{layer} = n_{solvent} + \frac{\rho_{layer} - \rho_{solvent}}{1 - \frac{\rho_{solvent}}{\rho_{protein}}} \frac{dn}{dc} \tag{3}$$

where n_{layer} and $n_{solvent}$ are the refractive indices of protein layer and solvent, respectively, ρ_{layer} and $\rho_{protein}$ are the densities of protein layer and solvent, respectively, dn/dc has the generally accepted value of $0.182\,\mathrm{g/cm^3}$ [17]. The strong dependence of RI on protein density is also reflected by the fact that larger molecules form a less dense layer [16] and thus provides a lower RI.

An acoustic wave is transmitted into a gaseous, liquid or solid medium that undergoes changes due to measurands. The changes in the elastic and viscous constants, and the density of a medium due to the measurand cause the change in the velocity, impedance, and absorption of the acoustic wave. Acoustic biosensors can measure simultaneously both the acoustical/mechanical and electrical/dielectric properties of bio environment which significantly expands their sensing capabilities. In general, the acoustic phase velocity can be affected by many factors, each of which possesses a potential sensor response. M. Hoummady et al. [18] illustrated the perturbation of the acoustic velocity by mass (mass), electrical (elec), mechanical (mech) and environmental (envir) parameter properties through Eq. (4)

$$\frac{\Delta V}{V_{acoustic}} \cong \frac{1}{V_{acoustic}}\left(\frac{\partial V}{\partial mass}\Delta mass + \frac{\partial V}{\partial elec}\Delta elec + \frac{\partial V}{\partial mech}\Delta mech + \frac{\partial V}{\partial envir}\Delta envir\right) \tag{4}$$

One of the most interesting sensing mechanisms of acoustic sensor response is mass loading. The mass sensitivity is defined by a phase velocity for a differential surface mass changeso it's inversely proportional to mass of the oscillator, $S = 1/M$, in which M is closely related to the penetration depth of the evanescent waves. In fact, a sensor responses to a combination of these parameters, hence the problem of overlapping sensitivities needs to be addressed. For example, for lamb wave sensor, the analytical expression for evanescent wave penetration depth of A_0 mode is [19]:

$$\delta = \frac{\lambda}{2\pi}\frac{1}{\sqrt{1-(\frac{v_1}{c_w})^2}} \tag{5}$$

where, C_w is the sound velocity of the liquid; V_l is phase velocity of A_0 mode in liquid. Among some of the integrated acoustic sensors, like surface acoustic wave (SAW), Love wave, and film bulk acoustic resonator (FBAR), Lamb wave sensor is more attractive in biochemical applications for its higher sensitivity and ability to work in liquid and has the potential for multi-parameter measurements at a time. Due to the much longer wavelength comparing to optical wave, it is very suitable for large molecules detection [19].

Similarlythe sensitivity of optical sensor is defined as the rate of change of effective index relative to its cover index change. It has predicted have extended mode which could interact with the surrounding analyses in a much better way than the commonly used evanescent wave sensing (EWS). The shortcomings of EWS are overcome by the introduction of the small optical mode area structure technique [20].

3. ENHANCEMENT OF THE MATTER INTERACTION WITH EVANESCENT WAVES

High performance biosensors are required to detect, specifically and sensitively, biological species that can cause harm to humans at a concentration range well below the harmful threshold level [21]. There have been so many biosensors configurations for their performance enhancement, such as photonic crystal-based [22–24], graphene-based [25], nanostructure-enhanced [21], etc.. Here, we mainly presented the ways to enhance the matter interaction with evanescent waves.

3.1. Adsorption and Absorption

One of the typical optical evanescent biosensors is optical fiber sensor. It has been clear that the sensitivity of the absorption fiber sensor is inversely proportional to the waveguide thickness [26]. The strength and penetration depth of evanescent field may be enhanced by adapting tapered probes. However, thinner and longer probes may be more fragile and difficult to handle. And a small diameter may require light sources with a high intensity and/or better focusing optics to obtain detectable intensity changes at the detector end. Another problem is that this kind of very thin optical fiber fabricated by heating and pulling process has a poor reproducibility and is extremely difficult to package [27, 28]. In addition, detection of analytes of larger volume such as whole cells and very large molecules may be limited by low evanescent field strength and insufficient penetration depths. Hence, evanescent wave absorbance may not change significantly.

In our group the problem is solved by on-chip etching method, in which the diameter of the fibers can be controlled precisely by an online monitoring system [26]. The fabricated optical fiber has two tapered regions (Fig. 1(a)$_1$), it can be applied to distinguish 10 pg/mL abrin (Fig. 1(a)$_2$) and 1 ng/mL ricin (Fig. 1(a)$_3$). Recently, a novel evanescent wave absorption biosensor which combines optical microfibers (OMFs) and gold nanoparticles (GNPs) is proposed [29]. GNPs exhibit strong absorption property in the visible range. For GNPs smaller than 60 nm, the absorption is much stronger than the scattering, which means the imaginary part of RI plays a dominant role. Thus, by utilizing GNPs, the influence of mode interference which is mainly related to the real part of RI can be avoided and the OMFs can response regularly due to power loss caused by absorption. This biosensor can achieve very high sensitivities because OMFs have a large power fraction in the

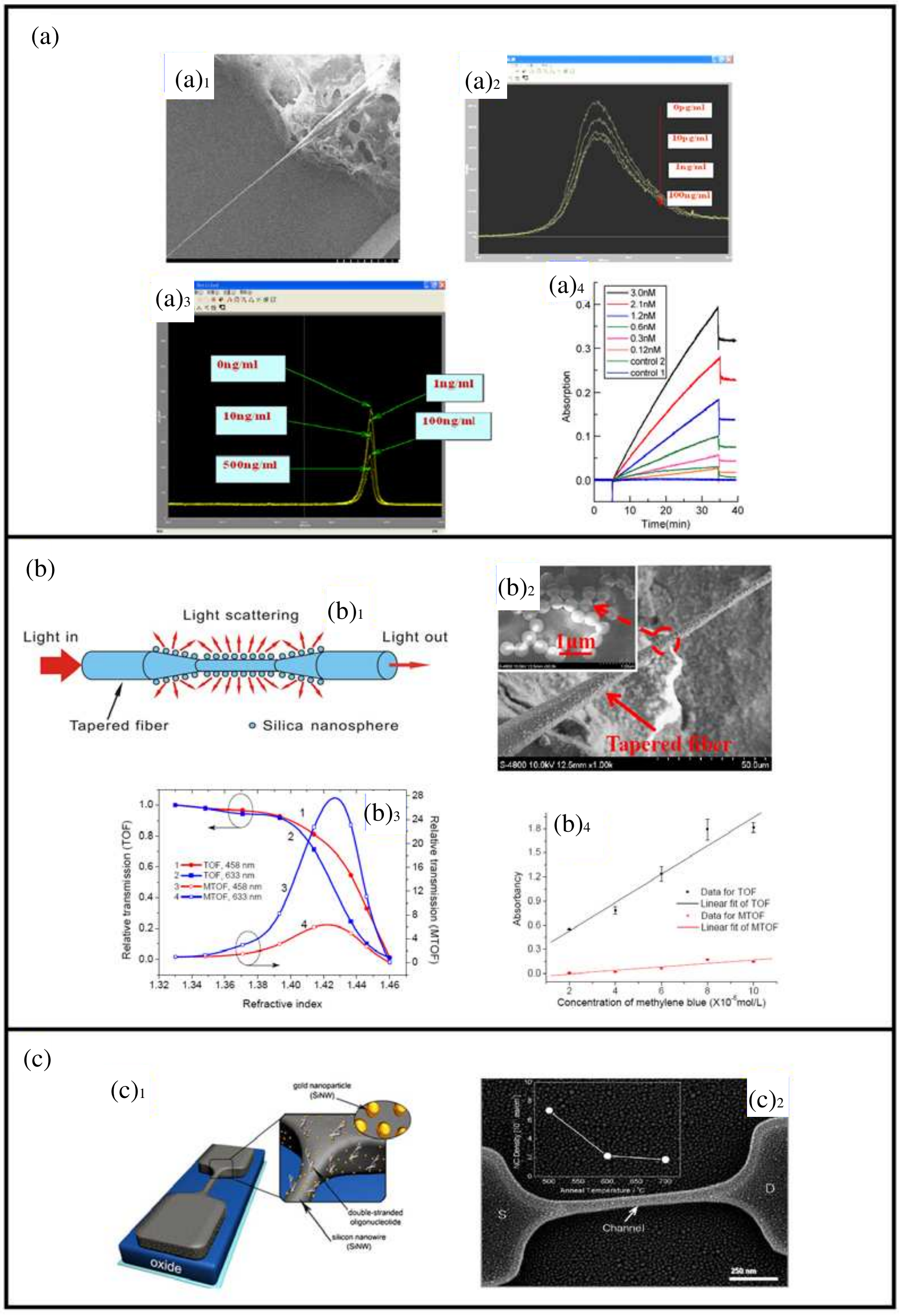

Figure 1: (a) An optical fiber taper fabricated via chemical etching [31], (a)$_1$, SEM image, the response to abrin ((a)$_2$) and ricin ((a)$_3$) with different concentrations, (a)$_4$, linear regressions of the goat IgG concentration dependence for fibers with a waist diameter of 1.5 μm and 4.5 μm, respectively. (b) Silica nanospheres modified tapered optical fiber [32, 33], (b)$_1$, schematic, (b)$_2$, SEM image, the response of TOF and MTOF to RI ((b)$_3$) and methylene blue ((b)$_4$). (c) Gold nanoparticle embedded silicon nanowire biosensor [34], (c)$_1$, schematic, (c)$_2$, SEM image. (Reprinted with permission).

cladding and also the optical cross-sections of GNPs are typically 4 to 5 orders of magnitude higher than that of conventional dyes [30]. In addition, GNPs have the advantage of ease in bio-conjugation and long term stability. Immunoassays were performed to further verify the applicability of this novel fiber optic sensor, and GNP-labeled goat IgG were detected with high sensitivity and good linearity, the selectivity was also improved (Fig. $1(\mathrm{a})_4$). In the immunoassays, a detection limit of 6 pM and a detection range of 6 pM to 300 pM with good linearity for GNP-labeled goat IgG was achieved using a 1.5-µm-thick OMF. A theoretical detection limit in the femtomolar level can be obtained when a 210-nm-thick optical fiber is used [29].

In fact, very small particles exhibit the well-known dipolar surface plasmon resonance at around 365 nm due to collective electron oscillation. Because, in this case, the Mie coefficients of the electric multipoles are much larger than the Mie coefficients of the magnetic multipoles, the TE modes do not appear in the spectra. The polarisation-dependent cross sections for extinction as well as for scattering are for all wavelengths very near to the ratio 1 [35].

For larger silver particles, like $2a = 200\,\mathrm{nm}$, the extinction cross section is strongly enhanced for shorter wavelengths in the case of evanescent wave excitation. This effect is particularly distinct for the case of excitation by a p-polarized evanescent wave. The ratio of the excitation-dependent cross sections now depends on the wavelength, the excitation itself contains stronger contributions from higher multipoles due to the large transverse field gradient of the evanescent wave. Moreover, the optical absorption cross section generally exhibits a stronger contrast between off-resonant and on-resonant conditions than the scattering cross section.

Other nano materials such as gold nanorods and silica-gold nanoshells are also promising labels for this OMF biosensor because the optical cross-sections of these nano particles are one order of magnitude higher than gold nano spheres. Besides, multi-target immunoassay can be realized if we use different nano particles with different absorption bands [36].

Gold nanoparticle (GN) embedded silicon nanowire (SiNW) configuration was proposed as a new biosensor for label-free DNA detection to enhance the sensitivity. The electric current flow between two terminals, a source and a drain electrode, were measured to sense the immobilization of probe oligonucleotides and their hybridization with target oligonucleotides (Fig. 1(c)). After simple immobilization of oligonucleotides by virtue of the chemical affinity with thiol on the gold nanoparticles embedded silicon nanowire, the 23-mer complementary target oligonucleotides corresponding to the breast cancer DNA were detected at a 1 pM concentration. At high concentration (0.1 µM), the current was increased by 100 times after the specific binding of the conjugated oligonucleotide [34].

3.2. Scattering the Evanescent Wave

3.2.1. Homogeneous Dielectric Spheres

The properties of evanescent waves have been long-exploited both experimentally and theoretically using the technique known as attenuated total reflection spectroscopy [37]. Later, the dielectric spheres were used to elastically scatter evanescent fields, and the cross-polarization was discovered for the scattering of evanescent waves due to the damping factor in the incident wave destroying the symmetry, in contrast to the lack of cross-polarization in Lorentz-Mie scattering [38].

Due to the strong transverse intensity gradient of evanescent waves, high-order multipoles are strongly enhanced by scattering and extinction of evanescent waves, compared to plane waves. Even when the sphere is in contact with the surface, the spectra for evanescent-wave excitation differ strongly from those for plane-wave excitation, and resonances with large peak amplitudes are observed for s- as well as p-polarized evanescent waves. The difference in the cross sections for s-polarized and p-polarized evanescent-wave excitation, respectively, for a spherical particle is caused by the different internal structure of the exciting field in both cases. In the case of s-polarization, the electric field of the wave oscillates perpendicular to the plane of incidence, whereas in the p-polarized case, the electric field rotates in the plane of incidence due to the complex phase of the totally reflected wave [12, 39].

In a previous paper from our group [32], a tapered optical fiber (TOF) refractometer was enhanced by modifying the waist region with a coating of SiO_2 nanospheres (Fig. 1(b)). The combination of nanosphere-induced scattering losses and multimode propagation of tapered fiber gave rise to a broadened detection range and improved sensitivity for refractive index sensing. In another paper [33], in contrast to the enhanced refractive index sensing, further experiments showed unexpectedly that this modified TOF (MTOF) was less sensitive to the absorption of surrounding medium than the original TOF without SiO_2. Owing to the higher-order mode filtering, the small remaining cladding power fraction of lower-order modes gave rise to the great sensitivity drop for

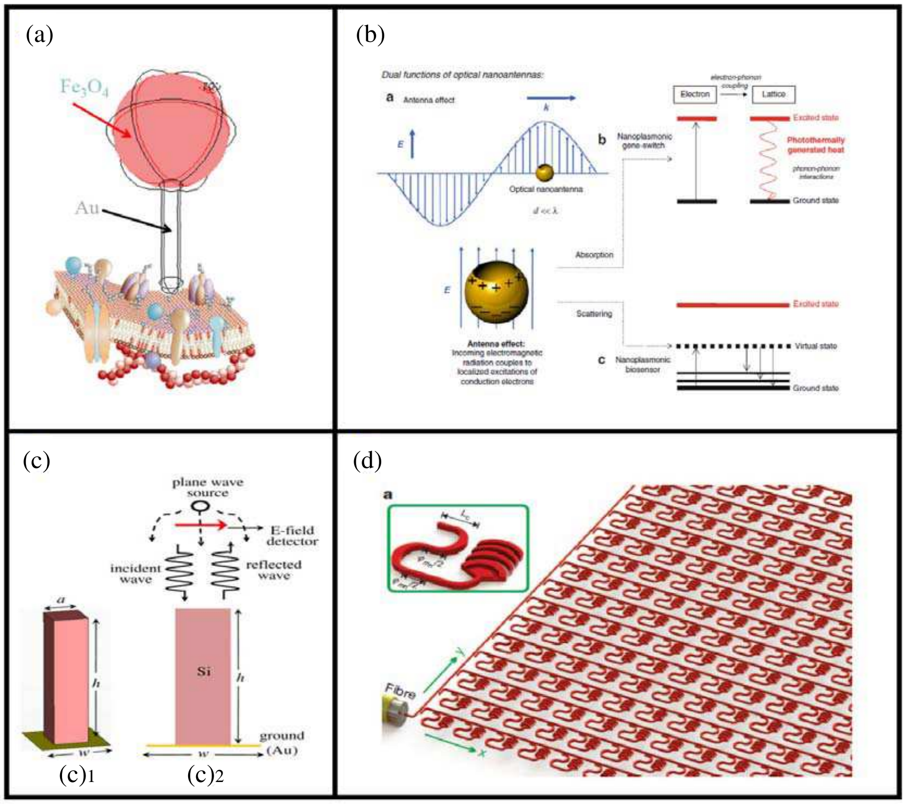

Figure 2: (a) Design of new magneto-plasmonic core-shell nano-antennas [44]. (b) Design and mechanism of the dual functions of optical nanoantennas [36]. (c) Si-based dielectric resonator antenna and simulation setup in CST [43], $(c)_1$, perspective view, and $(c)_2$, side view. (d) Schematic illustration of a 64×64 nanophotonic phased array (NPA) system [45]. (Reprinted with permission).

MTOF as illustrated in Fig. $1(b)_4$. And this MTOF may be a promising tool to extract the RI information with little interference from absorbance properties of the biomolecules.

In fact, subwavelength dielectric structures are able to provide similarly strong, tunable resonant light scattering but less lossy than metals. Compared with plasmonic resonances, which typically involves low modes such as dipole and quandrapole, the resonance in dielectric structures is even more complicated. Unlike traditional analytical or numerical models, which simulate light scattering by rigorously matching electromagnetic fields at boundaries, Yu and Cao [40] considered subwavelength dielectric structures as leaky resonators and evaluate the light scattering as a coupling between incident light and leaky modes of the structure. It provides new intuitive insights into the scattering and the phase shift in the scattered light. It's helpful to understand the light-matter interaction at subwavelength dielectric structures with functions such as scattering inversion, super-resolution imaging, beam steering and so on [41].

3.2.2. Tip-enhanced Nanometer Tools

Tip-enhanced nearfield Surface plasmon resonances enable sub-nanometer and nanometer tools, such as optical antennas, to directly interface with intracellular processes and particularly efficient at selected frequencies. It holds promise as nanoplasmonic gene switches, biosensors, SERS-based biosensing for spectroscopic imaging in living cells as well as in vitro molecular detection [36, 42]. The quantitative approaches should capture dynamic "spectral snapshots" of the intracellular biochemical distribution of living systems that were otherwise previously impossible to detect using conventional methods [43].

A new magneto-plasmonic core-shell nano-antennas was proposed by Mezeme et al. (Fig. 2(a)) [44]. In this configuration the magnetic core is controllable by H and useful for local microwave heating (hyperthermia), the Plasmonic shell induces a localized enhancement of E on 40 nm. It gives the possibility for multiscale modeling of biological cells.

A microdielectric resonator antenna of dimensions ($100 \times 100 \times 500$ mm) designed for biosensing applications were reported in 2011 [43]. The antenna was terminated with a thin layer of gold on the top and bottom of the microstructure for achieving a high Q. On top of the antenna was the sensing region ($100\,\mathrm{mm}^3$) which loaded the antenna depending on the type of material (Fig. 2(c)). The loading in turn changed the antenna reflectance, resonant frequency and polarization, and thus enabled the sensing action. The sensor activation and detection can be done using a far-infrared spectroscopy technique.

Nanoplasmonic resonator antenna functions as an ideal carrier of cargo of biomoleculars with its extraordinarily large surface-to-volume ratio to absorb or scatter light, which enhances the interaction between light and matter and also the spectral information (Fig. 2(b)) [46].

3.3. Plasmonic Field Enhancement

Surface plasmons (SPs) are coherent electron oscillations that exist at the interface between any two materials where the real part of the dielectric function changes sign across the interface (e.g., a metal-dielectric interface, such as a metal sheet in air). SPs have lower energy than bulk (or volume) plasmons which quantize the longitudinal electron oscillations about positive ion cores within the bulk of an electron gas (or plasma). When SPs coupled with a photon, the resulting hybrid excitation is called a surface plasmon polariton (SPP). This SPP can propagate along the surface of a metal until energy is lost either via absorption in the metal or radiation into free-space [47].

The first SPR immunoassay was proposed in 1983 by Liedberg et al. at the Linkoping Institute of Technology [48]. The evanescent tails of propagating surface plasmon resonance (p-SPR) waves are long and represent a long-range average response of the multilayer. It exhibits a large refractive index sensitivity of $2 \times 10^6\,\mathrm{nm/RIU}$ (refractive index unit) [49].

Surface plasmons enable the confinement of the light by electromagnetic excitations coupled to electron charge density waves on metal-dielectric interfaces or localized on metallic nanostructures. It enhances light-matter interactions [50]. Localized SPR (L-SPR) excitations occur around high (nanoscale) radios of curvature metal/dielectric features, consequently, the evanescent tails of L-SPR excitation are typically of this length scale. The use of nanoparticle tags/labels also can result in a dramatic enhancement of sensitivity due to the coupling between the L-SPR of metallic nanoparticles and SPR of the sensing film. The detection sensitivity of the nanorod-conjugated antibody is 25–100 times more sensitive than the SPR biosensor without gold nanorods (GNRs) [51]. Drastic sensitivity enhancement, owing to the electromagnetic interaction between the nanotag and the sensing film, was maximized using the longitudinal plasmonic resonance of the GNRs, and the maximum enhancement effect can be achieved when the longitudinal SPR peak wavelength of GNRs functionally matches the surface plasmon wavelength.

In fact, the above two kinds of sensors are very competitive in terms of sensitivities. The short (and tunable) characteristic decay length, l_d, of the electromagnetic field provides the L-SPR nanosensor with enhanced sensitivity. The overall responses of these two sensors that seem different can be described by the following equation [52]:

$$\Delta\lambda_{\max} = m\Delta n\left(1 - e^{-2d/l_d}\right) \tag{6}$$

where $\Delta\lambda_{\max}$ is the wavelength shift response, m is the refractive index sensitivity, Δn is the change in refractive index induced by an adsorbent, d is the effective thickness of adsorbing layer, and l_d is the characteristic electromagnetic field decay length. These L-SPR nanosensor results indicate that l_d is approximately 5–15 nm or 1–3% of the wavelength and depends on the size, shape, and composition of the nanoparticles. This differs greatly from the 200–300 nm decay length or approximately 15–25% of the wavelength for the SPR sensor. The ultrathin freestanding nanoporous gold (NPG) membranes ("leaf") fabricated using a simple chemical dealloying method was reported [53]. It simultaneously supports both propagating and localized surface plasmon resonances (p-SPR and L-SPR), respectively, two kinds of optical excitations used in state-of-the-art optical sensing technologies. The sensitivity for detecting the biological agents was obviously increased by the SPR biosensor assembled with nano-porous gold membranes [54].

However, hindered by the fact that localized plasmon resonances (LPRs) are broad. Many applications, like biosensor, would get a strong boost from plasmon resonances with a higher quality factor Zou et al. [57] suggested that extremely narrow plasmon resonances are possible in uniform arrays of nanoparticles. The theory of narrow plasmon resonances has been elaborated by Markel [58]. Report an experimental observation of extremely narrow resonances measured in sample absorption and reflection and produced by diffraction coupling of localized plasmons (LPs), similar in nature to Schatz-Markel resonances [55]. They showed experimentally that the reflection from an array of nanoparticles can be completely suppressed at certain wavelengths and their metal nanostructures exhibit jump for the phase of the reflected light (Fig. 3(a)).

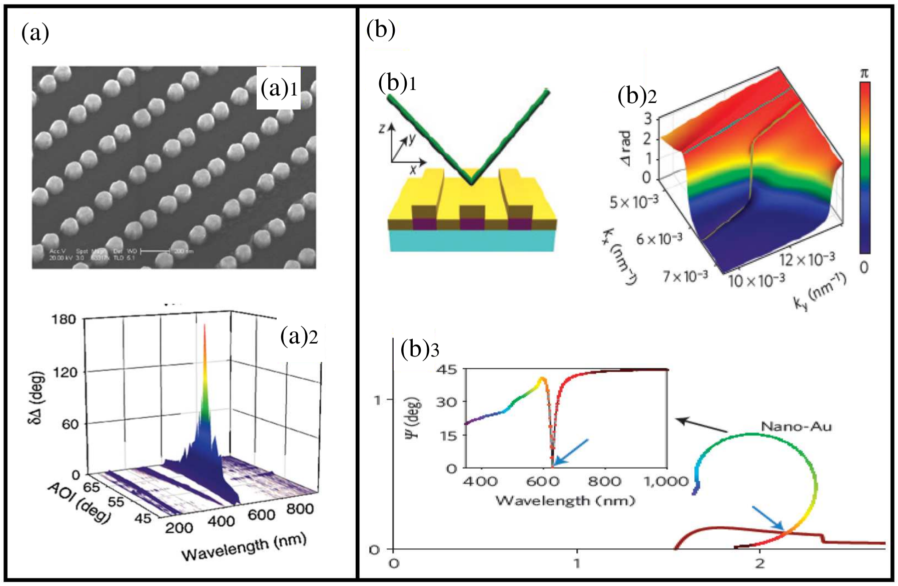

Figure 3: (a) Extremely narrow plasmon resonance based on double-Au nanoarray [55], $(a)_1$, micrograph, $(a)_2$, 3D plot of digital derivative of relative phase. (b) Singular phase nano-optics in plasmonic metamaterials [56], $(b)_1$, schematics of light reflection from nanostructured film, $(a)_2$, phase of p-polarized light as a function of wave vector, $(a)_3$, the brown dispersion curve. (Reprinted with permission).

Recently, Kravets et al. [5, 6] demonstrated the feasibility of singular visible-light nano-optics which exploits the benefits of both plasmonic field enhancement and the peculiarities of the phase of light (Fig. 3(b)). It shows that plasmonic metamaterials exhibit topologically protected zero reflection yielding to sharp phase changes nearby, which can be employed to radically improve the sensitivity of detectors based on plasmon resonances. And an area mass sensitivity at the level of fg/mm^{-2} and detection of individual biomolecules are respectively obtained [43]. Feng et al. demonstrated a biochemical sensor consisting of nanoscale grooves and slits milled in a metal film to form two-arm, three-beam, planar plasmonic interferometers [59]. By integrating thousands of plasmonic interferometers per square millimeter with a microfluidic system, a wavelength sensitivity between 370 and 630 nm/RIU, a relative intensity change between $\sim 10^3$ and 10^6 %/RIU, and a resolution of $\sim 3 \times 10^{-7}$ in refractive index change were experimentally measured using typical sensing volumes as low as 20 fL.

3.4. Intracavity Sensing

When photons are confined in a finite volume, two new physical parameters become relevant: optical mode volume and confined photon number. From a quantum mechanical perspective, the former concept describes the localized nature of the photon quantum state, and the latter concept gives the occupancy number of the quantum state under investigation [60]. When a particle is introduced into the system, two perturbation effects result: modification of the quantum state and hence the polarization energy change of a single photon, as well as the photon occupancy number change dN. And the occupancy number variation dN is generally inversely proportional to the optical mode volume, a conclusion drawn from general perturbation theory.

The concept of intracavity sensing has been demonstrated by Gourly et al. [61]. In their approach an entire cell, e.g., an erythrocyte is introduced to the cavity of a vertical cavity surface-emitting laser (VCSEL). Due to the fact that the cell does not absorb the light at the wavelength of 850 nm, the cell in the cavity will act as a Fabry-Perot etalon.

Consider a laser where the effective refractive index in the cavity is changed by Δn. This implies a change in the oscillation frequency of the laser given by [62]

$$\frac{\Delta n_{eff}}{\langle n_{eff} \rangle} = \frac{\Delta f}{f_0} \tag{7}$$

Very small frequency shifts are preferably detected as shifts relative to a stable reference. Light beating is then applied to obtain the difference frequency. The effective interaction length is then given by the optical propagation length within the mutual coherence time of the two modes. Thus it is essential that the two modes are as closely matched as compatible with the requirement that only one mode is affected by the refractive index change. Being an emerging sensing technology, it has recently been under intensive investigation.

Silicon photonics is a promising platform for high density integration of photonic devices. It is compatible with CMOS fabrication and therefore high volume manufacturing is feasible. In reference [22], Zou et al. (Fig. 4(a)) experimentally demonstrated a silicon photonic crystal (PC) microcavity biosensor with 50 femto-molar detection limit. Our devices have demonstrated sensitivities higher than than competing optical platforms at concentration of 0.1 μg/ml across a range of dissociation constants KD 1 micro-molar to 1 femto-molar. High sensitivities were achieved by slow light engineering which reduced the radiation loss and increased the stored energy in the PC microcavity resonance mode which contributed to high Q as well as enhanced optical mode overlap with the analyte.

In a ring resonator, the light propagates in the form of whispering gallery modes (WGMs) or circulating waveguide modes, which results from total internal reflection of light along the curved boundary between the high and low refractive index (RI) media. The WGM has the evanescent field present at the ring resonator surface and responds to the binding of biomolecules (Fig. 4(c)) [64]. In contrast to the straight waveguide, the effective light–analyte interaction length of a ring resonator sensor is no longer determined by the sensor's physical size, but rather by the number of revolutions of the light supported by the resonator, which is characterized by the resonator quality factor, or the Q-factor.

Armani et al. [66] reported the disc ring resonator arrays whose Q factor can reach 10^8, the minimum detectable concentration of 5×10^{-18} M of a solution of interleukin-2 with this sensor was reported. Vollmer et al. [67] reported the similar single molecule biological sensing technology in 2008. But for commercialization, it still needs to improve the design and fabrication processes.

In our knowledge, the first commercialized acoustic biosensor is Quartz crystal microbalance (QCM) [68–72]. To MEMS based acoustic sensors, the techniques make it possible to extremely decrease the mass of the oscillators and work on MHz $\sim$ GHz high frequency with very high sensitivities and multimode detection [73, 74]. Recently, Ioana Voiculescua et al. presented a review about "Acoustic wave based MEMS devices for biosensing applications" [75]. However, compared with optical biosensors, the Q factors are often very low. The Q factor of the most film acoustic sensors are even lower than QCM. Similar to optical photonic crystal (PC), the localized modes can also be obtained by putting defects in phononic crystals and making their resonate frequencies within the bandgap. Point defect cavity was constructed in a two-dimensional phononic crystal plate in our group in 2008 (Fig. 4(b)) [76]. In this structure, acoustic energy can be confined efficiently in both X and Y directions by PC, which were shown by optical interference measurement. The signal wave propagation is avoided by exciting the defect cavity inside. It is found that the Q factors of PC in vacuum are mainly determined by inner attenuations and are affected by imaginary decay factors. As an example, the breathing mode has highest Q factor in vacuum among nine modes due to low inner attenuation and low energy leakage. The Q factors of all modes decrease due to air damping and breathing mode is less sensitive to air due to less square normal velocity over the total structure. By selectively loading the PC with water on one side, the interactions between liquid and high Q defect cavity were studied. Even all the modes suffer strong liquid damping the point defect modes with shear movement between plate and water surfaces suffer lower attenuation and still have rather high Q factors as high as 49800 (Fig. 4(b)$_2$).

The response of a phononic crystal sensor (PCS) to surface mass is linear, which has been approved by the detection of NaCl in the localized region of the phononic crystal sensor (PCS). A PCS with a thickness of 380 μm has a sensitivity of 9.1 Hz/ng, the detection limit is 0.38 ng (Fig. 4(b)$_3$). Now, the theoretical prediction of a sensitivity of 91 Hz/pg is reached by reducing the thickness and hole diameter by an order of magnitude, this result is better than mass sensors based on acoustic devices, and the experimental investigation is under way [63].

Besides, in our group, a micro-acoustic WGM which were excited and measured by evanescent wave from Lamb wave device was investigated (Fig. 4(d)) [65]. The characters of acoustic WGMs were studied both theoretically and experimentally. The acoustic WGMs exhibited sharp periodic dips due to the resonance of the circular structure of the tube and even have narrow periodic dips as optical WGMs due to the closed circular structure of the tube. Thus the high Q factor of

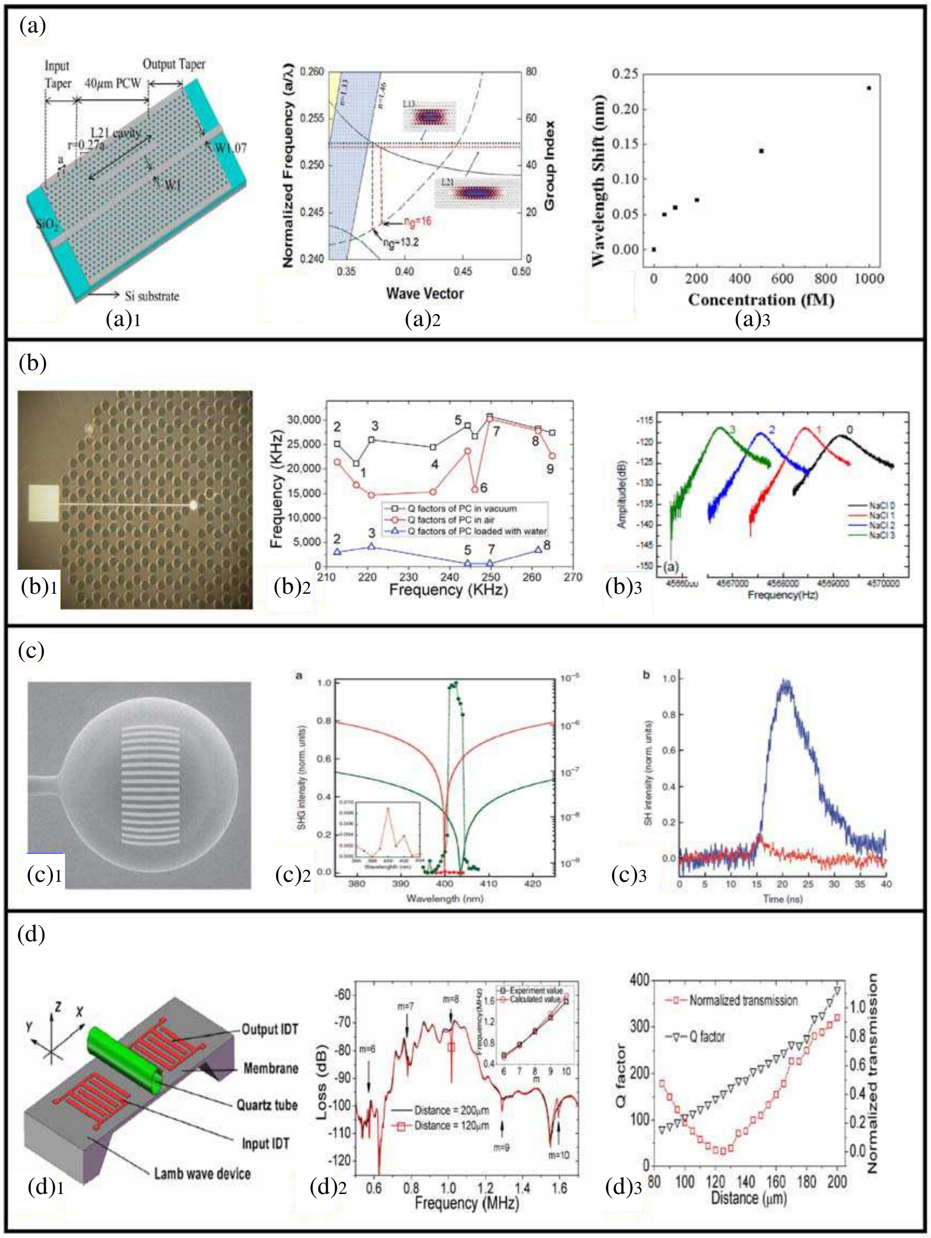

Figure 4: (a) Silicon photonic crystal microcavity biosensors [22], $(a)_1$, a schematic of photonic crystal microcavity device, $(a)_2$, dispersion diagram of W_1 photonic crystal waveguide in water. (b) Point defect phononic crystal [63], $(b)_1$, optical microscope image, $(b)_2$, the Q factor of the point defect mode of phononic crystal in vacuum, air, and water, $(b)_3$, the amplitude of point defect mode versus frequency. (c) Second harmonic light generation based on whispering gallery microresonators [64], $(c)_1$, periodic molecular pattern on the sphere surface, $(c)_2$, second harmonic generation as a function of half the wavelength of the fundamental wave, $(c)_3$, second harmonic intensity as a function of time. (d) The acoustic WGMs [65], $(d)_1$, schematic drawing of principle, $(d)_2$, responses of the acoustic WGMs with different distances between the Lamb wave device and the tube, $(d)_3$, normalized transmission and Q factors with different coupling distances. (Reprinted with permission).

acoustic WGMs was obtained (Fig. $4(d)_2$). Furthermore, the resonance frequency shifts due to the mass changing on the tube surface was measured. These results can be used in designing acoustic resonator, filter and sensors. The Q factor of the acoustic WGMs reaches 380, which is one order higher than that of the Lamb wave device working in liquid. Therefore, the resolution of mass change was improved comparing with traditional Lamb wave sensors.

3.5. Tunneling Effect

The optical tunneling effect refers to the frustration of an evanescent wave which was coined in reference to the electric tunneling effect (Fig. 5(a)) [77]. Indeed, in optics, the inverse of the refractive indexes of the different media can be regarded as analog of the potential barrier. Similarly, in acoustics, if medium A is liquid or gas and medium B a solid, medium A can be regarded as a region of space where the particle's total energy is greater than its potential energy and medium B is the potential barrier.

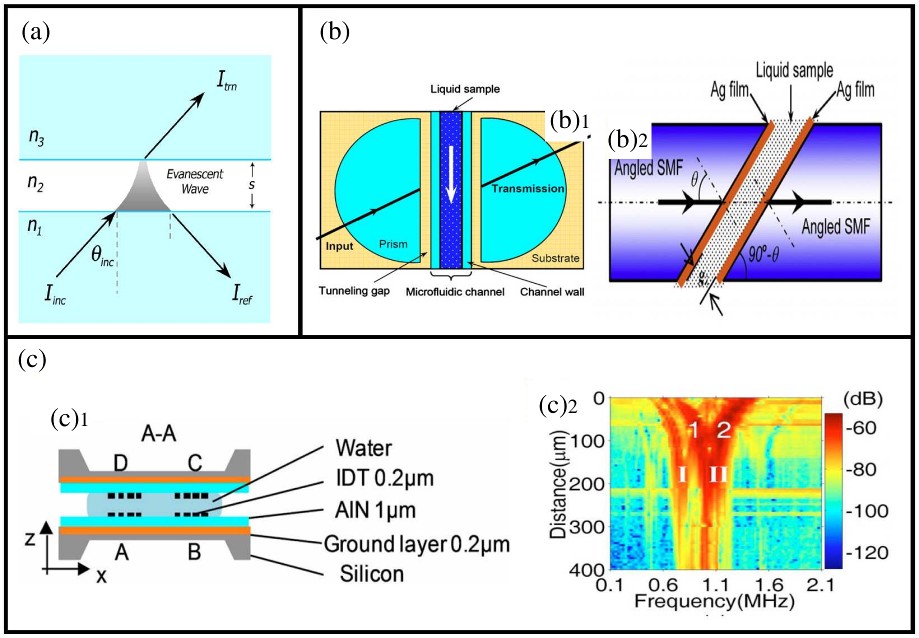

Figure 5: (a) Frustrated internal reflection for a three layer system [77]. (b) Optofluidic refractometer using resonant optical tunneling effect based on, $(b)_1$, prisms [81], and $(b)_2$, angled fibers [82]. (c) Evanescent wave of a Lamb wave sensor [80], $(c)_1$, the measurement setup via a sandwich of Lamb wave devices, $(c)_2$, the amplitude variations with distance at C port. (Reprinted with permission).

For the evanescent waves there is a phase difference of $\pi/2$ between the electric and magnetic fields in the plane perpendicular to the direction of propagation of the evanescent wave. Therefore, there is no flow of energy in the direction of propagation of the evanescent wave or, in other words, the Poynting vector in the propagation direction of the evanescent wave has zero time average [78]. But if another medium with the index higher than the index of medium A, and the distance this medium and medium A is smaller than the penetration depth, an important part of the light energy will transfer into this medium. It has been shown that by locating tip detectors [79].

An acoustic microsensor based on tunnelling effect was proposed in 2008 (Fig. 5(c)) [80]. In which one liquid layer is sandwiched between two Lamb wave sensors which are interacted by evanescent field in liquid.

One example of the practical application of optical tunneling effect is optofluidic refractometer [81, 82]. In [81], the resonant optical tunneling effect (ROTE) realized through a structure consisting of two hemicylindrical prisms, two air gaps, and a microfluidic channel (Fig. 5(b)) is theoretically predicted to achieve a sensitivity of 760 nm/RIU and a detectivity of 85000 RIU^{-1}. In [82], the ROTE is constructed through two angled silver-coated optical fibers (Fig. 5(c)) to detect the RI changes by measuring the intensity variation of transmission intensity or the wavelength shift of transmission peak, theoretically achieving a high sensitivity of 81000 nm/RIU. These ROTE based sensors are believed to be promising for monitoring the tiny change of the biochemical constituents with the ability of real-time and label-free detection.

The response variations at ports B and C of the sandwich Lamb wave sensor with an adjustment in the Z direction were represented in (Fig. $5(c)_1$). Both the amplitudes and the phases show the splitting which appears when the distance becomes small, which shows that the two sensors are coupled in the region of the evanescent field and they begin to work as a sandwich sensor (Fig. $5(c)_2$).

The dispersion curves have been obtained experimentally. The Sandwich sensor is sensitive to the thickness variation due to the evanescent field interaction. It gives the new insight into the measurement of acoustic biosensor in which several parameters, such as the density of liquid, the density and the thickness of the absorbed layer on the membrane, can be gotten respectively and allows precise multi-parameters measurement [80].

Y. Ben-Aryen [78] explained the mechanism that when the detectors had a size much smaller than a wavelength, such as tip and other nanostructures we mentioned above, it was possible to convert part of the evanescent waves into propagating waves and to obtain high-resolution effects. The tunneling of evanescent waves into propagating waves is related to the convolution of the high spatial frequencies of the source with those of the detectors. Such an approach is demonstrated by treating the evanescent waves which are diffracted from very narrow apertures in a plane screen (with dimensions much smaller than the wavelength) and are converted into propagating waves by tip detectors. The mechanism responsible for the conversion of evanescent waves into propagating waves is explained and a general formula for the conversion of evanescent waves into propagating waves is derived. Similarly, we can imagine such kind of biosensors which can get high resolution information, about not only the thickness but also the interaction between the tip and molecules.

3.6. Optomechanical Interaction

Acousto-electromagnetic wave interaction refers to the phenomena occurring when electromagnetic waves scatter from an object in a resonant acoustic mode of vibration. The incident electromagnetic wave is modulated by the object's motion, giving rise to a small Doppler component in the scattered field. The Doppler component contains information specific to the scatterer, independent of the background material.

In general, optomechanical coupling between light and matter is insignificant since a photon does not have rest mass, but its effect can be enhanced for a structure with small mass and strong light confinement. Roh et al. [83] fabricated bilayer PhCs and observed large optomechanical coupling by employing band-edge modes. Furthermore, efficient coupling between optical modes and mechanical modes was confirmed by the observation of Brownian modes in the RF signal of the reflected light. Their result clearly showed that bilayer PhCs can serve strongly coupled optomechanical systems.

Fan and Zhu [84] investigated the optomechanical interaction in two coupled microresonators while utilizing the composite resonances of the system. By taking advantages of the split resonance, they bypassed the requirement of frequency detuning for the input light in a single resonator system. For the external modulation driven system, the power efficiency to obtain the optomechanically-induced transparency (OMIT) phenomenon can be greatly increased. By properly choosing the parameters of the coupled optomechanical system, it shows that an optically controlled mechanical energy transfer between different mechanical oscillators is possible.

Most recently, a photonic-crystal nanocavity has been investigated as an optomechanical accelerometer that makes use of ultrasensitive displacement readout [85], achieving an acceleration resolution of 10 μgHz-1/2 with submilliwatt optical power, a bandwidth greater than 20 kHz and a dynamic range of greater than 40 dB. This nancavity is integrated with a nanotethered test mass of high mechanical Q-factor. The nanogram test masses allow for strong optomechanical backaction and set the stage for a new class of motional sensors. We believe this kind of optomechanical sensors will find applications in biological or chemical recognition techniques. But in our knowledges, it has not been really used. Based on our research works on optical and acoustic biosensors (Fig 4(d)), with the reference of optical whispering gallery modes (WGMs), a biosensor based on acoustic and optical WGMs coupled and excited with Lamb Waves for multi-parameter detection is proposed [86]. The cavity will be stimulated by a tapered optical fiber and a Lamb wave transducer both. The oscillations will be in different wavelengths and the optical and acoustic fields will both interact with the target molecules on the cavity's surface. It is supposed to get high sensitive, high Q factor resonance to improve detection with acoustic signal also.

4. OUTLOOK AND DISCUSSIONS

Sensors based on optical or acoustic transduction distinguish the perturbation of waves, they have notable similarity and specialty, i.e., oscillators (photons and phonons) $\rightarrow$ wave (electromagnetic and mechanical wave) $\rightarrow$ modulation (wavelength, frequency, amplitude, and phase, etc.) $\rightarrow$ electronic signal.

Due to the existence of high-space-frequency signals, evanescent wave sensor in itself is an excellent filter, maintaining the nano scale information of biological targets and obtaining a high signal to noise ratio (SNR). To intensify the modulation of waves by biomolecules and increase the efficiency of the wave translation is the key to obtain higher sensitivity. Obviously, there is need to endow oscillators with more energy or momentum and transfer them to biomolecules. And higher Q factor should be obtained to ensure a higher SNR.

By taking the advantage of localization and resonance, the wave-matter interactions are hugely enhanced and the sensitivity is thus promoted. But the quantitative relationship between field magnification and sensitivity improvement has not been thoroughly analyzed. The defect modes of artificial crystals and other cavities intensify the local fields, meantime, they provide an alternative to high-Q resonance which is the premise of high-resolution detection. However, whether there is a trade-off between high Q and high sensitivity still needs insightful investigation.

Recent advancements in nanotechnology and nanoplasmonics now enable sub-nanometer and nanometer tools to directly interface with intracellular processes. Coupling both of optical and acoustic effects,especially in the size of nano meters, the mutual action would be stronger at higher frequencies,. Moreover, acoustic assistance can provide the condition for momentum matching, acoustic-optic sensing may have real coupling effects. However, owing to the ongoing developments of nano technology, it's still difficult to ensure the repeatability for commercial use.

The development of biosensors always depends on the biorecognition technology. Although label-free detections can have very high sensitivities, single-parameter detections cannot fulfill biological recognition at present. Furthermore, highly sensitive detection, especially single-molecule detection, is prone to the influence from other molecules and surrounding environment. Usually, high sensitivity tends to be susceptible to a variety of background signals, therefore, the calibration of genuine label-free detection remains a big challenge.

Nowadays, the flourishing progress of super-resolution imaging, whether near field or far field, resembles the highly sensitive biorecognition technique, the nano imaging technology would be the next generation biological detection tools.

REFERENCES

1. Rigneault, H. and E. Andresen, "Fast and label-free," *Nature Photon.*, Vol. 6, 2, 2012.
2. Hutchinson, A. M., "Evanescent wave biosensors," *Molecular Biotechnology*, Vol. 3, 8, 1995.
3. Hutter, E. and J. H. Fendler, "Exploitation of localized surface plasmon resonance," *Adv. Mater.*, Vol. 16, 22, 2004.
4. Link, S. and M. A. El-Sayed, "Spectral properties and relaxation dynamics of surface plasmon electronic oscillations in gold and silver nanodots and nanorods," *J. Phys. Chem. B*, Vol. 103, 17, 1999.
5. Leung, A., P. M. Shankar, and R. Mutharasan, "A review of fiber-optic biosensors," *Sens. Actuators B*, Vol. 125, 703, 2007.
6. Fan, X., I. M. White, S. I. Shopova, H. Zhu, J. D. Suter, and Y. Sun, "Sensitive optical biosensors for unlabeled targets: A review," *Anal. Chim. Acta*, Vol. 23, 26, 2008.
7. Lee, B., S. Roh, and J. Park, "Current status of micro- and nano-structured optical fiber sensors," *Opt. Fiber Technol.*, Vol. 15, 221, 2009.
8. Brambilla, G., F. Xu, P. Horak, Y. Jung, F. Koizumi, N. P. Sessions, E. Koukharenko, X. Feng, G. S. Murugan, J. S. Wilkinso, and D. J. Richardson, "Optical fiber nanowires and microwires: Fabrication and applications," *Advances in Optics and Photonics*, Vol. 1, 161, 2009.
9. Valsecchi, C. and A. G. Brolo, "Periodic metallic nanostructures as plasmonic chemical sensors," *Langmuir*, Vol. 29, 12, 2013.
10. Zalyubovskiy, S. J., M. Bogdanova, A. Deinega, Y. Lozovik, A. D. Pris, K. H. An, W. P. Hall, and R. A. Potyrailo, "Theoretical limit of localized surface plasmon resonance sensitivity to local refractive index change and its comparison to conventional surface plasmon resonance sensor," *J. Opt. Soc. Am. A*, Vol. 29, 9, 2012.
11. Ray, S., G. Mehta, and S. Srivastava, "Label-free detection techniques for protein microarrays: Prospects, merits and challenges," *Proteomics*, Vol. 10, 18, 2010.
12. Johnson, S. G., "Notes on the algebraci structure of wave equations," 2010.
13. Pain, H. J., *The Physics of Vibrations and Waves*, 6th Edition, Wiley, 2005.
14. Makris, K. G. and D. Psaltis, "Huygens-Fresnel diffraction and evanescent waves," *Optics Communications*, Vol. 284, 4, 2011.
15. Laude, V., Y. Achaoui, S. Benchabane, and A. Khelif, "Evanescent bloch waves and the complex band structure of phononic crystals," *Phys. Rev. B*, Vol. 4, 2009.
16. Vörös, J., "The density and refractive index of adsorbing protein layers," *Biophysical Journal*, Vol. 87, 9, 2004.

17. Ball, V. and J. J. Ramsden, "Buffer dependence of refractive index increments of protein solutions," *Biopolymers*, Vol. 46, 4, 1998.
18. Hoummady, M., A. Campitelli, and W. Wlodarski, "Acoustic wave sensors: Designs, sensing mechanisms and applications," *Smart Mater. Struct.*, Vol. 6, 11, 1997.
19. Li, F., "Innovative detection methods in liquid for a Lamb wave biosensors," University of Chinese Academy of Sciences, Beijing, 2008.
20. Verma, A., Y. Prajapati, S. Ayub, J. P. Saini, and V. Singh, "Analytical analysis of sensitivity of optical waveguide sensor," *International Journal of Engineering, Science and Technology*, Vol. 3, 5, 2011.
21. Zhang, G., "Nanostructure-enhanced surface acoustic waves biosensor and its computational modeling," *Journal of Sensors*, Vol. 2009, 11, 2009.
22. Zou, Y., S. Chakravarty, W.-C. Lai, C.-C. Hsieh, and R. T. Chen, "High yield silicon photonic crystal microcavity biosensors with 100 fM detection limit," *Proc. of SPIE*, Vol. 8570, 7, 2013.
23. Lee, M. and P. M. Fauchet, "Two-dimensional silicon photonic crystal based biosensing platform for protein detection," *Opt. Express*, Vol. 15, 6, 2007.
24. Chakravarty, S., Y. Zou, W. Lai, and R. Chen, "Slow light engineering for high Q high sensitivity photonic crystal microcavity biosensors in silicon," *Biosens. Bioelectron.*, Vol. 38, 7, 2012.
25. Sreekanth, K. V., S. Zeng, K.-T. Yong, and T. Yu, "Sensitivity enhanced biosensor using graphene-based one-dimensional photonic crystal," *Sens. Actuators B*, Vol. 182, 5, 2013.
26. Wu, Y., X. Deng, F. Li, and X. Zhuang, "Less-mode optic fiber evanescent wave absorbing sensor: Parameter design for high sensitivity liquid detection," *Sensors and Actuators B*, Vol. 122, 127–134, 2007.
27. Sai, V. V. R., T. Kundu, C. Deshmukh, S. Titus, P. Kumar, and S. Mukherji, "Label-free fiber optic biosensor based on evanescent wave absorbance at 280 nm," *Sens. Actuators B Chem.*, Vol. 143, 7, 2010.
28. Leung, A., K. Rijal, P. M. Shankar, and R. Mutharasan, "Effects of geometry on transmission and sensing potential of tapered fiber sensors," *Biosens. Bioelectron.*, Vol. 21, 2210, 2006.
29. Li, K., G. Liu, Y. Wu, P. Hao, W. Zhou, and Z. Zhang, "Gold nanoparticle-enhanced optical microfiber evanescent wave-absorption biosensors with high sensitivity and reproducibility," *Biosens. Bioelectron.*, Submitted, 2013.
30. Jain, P. K., K. S. Lee, I. H. El-Sayed, and M. A. El-Sayed, "Calculated absorption and scattering properties of gold nanoparticles of different size, shape, and composition: Applications in biological imaging and biomedicine," *J. Phys. Chem. B*, Vol. 110, 7238–7249, 2006.
31. Zhuang, X., "Study on the art of fiber-optic evanescent field sensor with high sensitivity," University of Chinese Academy of Sciences, Beijing, 2009.
32. Liu, G., Y. Wu, K. Li, P. Hao, P. Zhang, and M. Xuan, "Mie scattering-enhanced fiber-optic refractometer," *IEEE Photon. Technol. Lett.*, Vol. 24, 3, 2012.
33. Liu, G., Y. Wu, K. Li, P. Hao, and M. Xuan, "Silica nanospheres for filtering higher-order optical fiber modes," *Appl. Opt.*, Vol. 52, 5, 2013.
34. Ryu, S.-W., C.-H. Kim, J.-W. Han, C.-J. Kim, C. Jungb, H. G. Park, and Y.-K. Choi, "Gold nanoparticle embedded silicon nanowire biosensor for applications of label-free DNA detection," *Biosens. Bioelectron.*, Vol. 25, 4, 2010.
35. Quinten, M., A. Pack, and R. Wannemacher, "Scattering and extinction of evanescent waves by small particles," *Appl. Phys. B*, Vol. 68, 6, 1999.
36. Dmitriev, A., *Nanoplasmonic Sensors*, Springer, New York, 2012.
37. Harrick, N. J., *Internal Reflection Spectroscopy*, Interscience-Wiley, New York, 1967.
38. Chew, H., D.-S. Wang, and M. Kerker, "Elastic scattering of evanescent electromagnetic waves," *Appl. Opt.*, Vol. 18, 9, 1979.
39. Quinten, M., A. Pack, and R. Wannemacher, "Scattering and extinction of evanescent waves by small particles," *Appl. Phys. B*, Vol. 68, 6, 1998.
40. Yu, Y. and L. Cao, "The phase shift of light scattering at subwavelength dielectric structures," *Opt. Express*, Vol. 21, 11, 2013.
41. Chang, Y.-K., Z.-X. Lou, K.-D. Chang, and C.-W. Chang, "Universal scaling of plasmonic refractive index sensors," *Opt. Express*, Vol. 21, 8, 2013.
42. Novotny, L. and N. V. Hulst, "Antennas for light," *Nature Photon.*, Vol. 5, 8, 2011.

43. Pal, A., A. Mehta, M. E. Marhic, K. C. Chan, and K. S. Teng, "Microresonator antenna for biosensing applications," *Micro. Nano. Lett.*, Vol. 6, 3, 2011.
44. Mezeme, M. E. and C. Brosseau, "Design of magnetoplasmonic resonant nanoantennas for biosensing applications," *COMSOL Conference 2010*, Paris, 2010.
45. Sun, J., E. Timurdogan, A. Yaacobi, E. S. Hosseini, and M. R. Watts, "Large-scale nanophotonic phased array," *Nature*, Vol. 493, 5, 2013.
46. Lee, S. E. and L. P. Lee, "Biomolecular plasmonics for quantitative biology and nanomedicine," *Current Opinion in Biotechnology*, Vol. 21, 9, 2010.
47. Barnes, W. L., A. Dereux, and T. W. Ebbesen, "Surface plasmon subwavelength optics," *Nature*, Vol. 424, 7, 2003.
48. Liedberg, B., C. Nylander, and I. Lunström, "Surface plasmon resonance for gas detection and biosensing," *Sens. Actuators*, Vol. 4, 1983.
49. Haes, A. J. and R. P. V. Duyne, "A unified view of propagating and localized surface plasmon resonance biosensors," *Analytical and Bioanalytical Chemistry*, 2004.
50. Barnes, W. L., "Fluorescence near interfaces: The role of photonic mode density," *Journal of Modern Optics*, Vol. 45, 39, 1998.
51. Hao, P., Y. Wu, and F. Li, "Improved sensitivity of wavelength modulated SPR biosensor using gold nanorods," *Appl. Opt.*, Vol. 50, 4, 2011.
52. Jung, L. S., C. T. Campbell, T. M. Chinowsky, M. N. Mar, and S. S. Yee, "Quantitative interpretation of the response of surface plasmon resonance sensors to adsorbed films," *Langmuir*, Vol. 14, 13, 1998.
53. Yang, Y., "Research on the role of enhancing SPR sensor sensitivity by nano-porous gold membrane," University of Chinese Academy of Sciences, Beijing, 2009.
54. Yang, Y., Y. Wu, P. Hao, and Z. Zhang, "A new type of nano-porous gold membrane for surface plasmon resonance biosensor," *Spectroscopy and Spectral Analysis*, Vol. 30, 4, 2010.
55. Kravets, V. G., F. Schedin, and A. N. Grigorenko, "Extremely narrow plasmon resonances based on diffraction coupling of localized plasmons in arrays of metallic nanoparticles," *Phys. Rev. Lett.*, Vol. 101, 4, 2008.
56. Kravets, V. G., F. Schedin, R. Jalil, L. Britnell, R. V. Gorbachev, D. Ansell, B. Thackray, K. S. Novoselov, A. K. Geim, A. V. Kabashin, and A. N. Grigorenko, "Singlular phase nano-optics in plasmonic metamaterials for label-free single-molecule detection," *Nature Materials*, Vol. 12, 6, 2013.
57. Zou, S., N. Janel, and G. C. Schatz, "Silver nanoparticle array structures that produce remarkably narrow plasmon lineshapes," *J. Chem. Phys.*, Vol. 120, 5, 2004.
58. Markel, V. A., "Divergence of dipole sums and the nature of non-Lorentzian exponentially narrow resonances in one-dimensional periodic arrays of nanospheres," *J. Phys. B: At. Mol. Opt. Phys.*, Vol. 38, 7, 2005.
59. Feng, J., V. S. Siu, A. Roelke, V. Mehta, S. Y. Rhieu, G. T. R. Palmore, and D. Pacifici, "Nanoscale plasmonic interferometers for multispectral, high-throughput biochemical sensing," *Nano Lett.*, Vol. 12, 8, 2011.
60. Hu, J., S. Lin, L. C. Kimerling, and K. Crozier, "Optical traping of dielectric nanoparticals in resonant cavities," *Phys. Rev. B*, Vol. 82, 8, 2010.
61. Gourley, P. L., D. Y. Sasaki, and R. K. Naviaux, "Nanolaser spectroscopy for studying novel biomaterials," *Proc. of SPIE*, Vol. 6859, 10, 2008.
62. Lindvold, L. and L. Lading, "Evanescent field sensing: Cavity-coupled refractive index sensor (CRIS)," *Proc. of SPIE*, Vol. 3276, 8, 1998.
63. Liu, J., "The theoretical and experimental investigation of phononic crystals for high Q acoustic sensing," University of Chinese Academy of Sciences, Beijing, 2013.
64. Dominguez-Juarez, J. L., G. Kozyreff, and J. Martorell, "Whispering gallery microresonators for second harmonic light generation from a low number of small molecules," *Nature Communications*, Vol. 1253, 8, 2013.
65. Li, F., M. Xuan, Y. Wu, and F. Bastien, "Acoustic whispering gallery mode coupling with Lamb waves," *Sens. Actuators A*, Vol. 189, 4, 2013.
66. Armani, A. M., R. P. Kulkarni, S. E. Fraser, R. C. Flagan, and K. J. Vahala, "Label-free, single-molecule detection with optical microcavites," *Science Express*, Vol. 10, 6, 2007.
67. Vollmer, F. and S. Arnold, "Whispering-gallery-mode biosensing: Label-free detection down to single molecules," *Nature Methods*, Vol. 5, 6, 2008.

68. King, J. W. H., "Piezoelectric sorption detector," *Anal. Chem.*, Vol. 36, 5, 1964.
69. Sauerbrey, G., "Verwendung von schwingquarzen zur wägung dünner schichten und zur mikrowägung," *Z. Phys.*, Vol. 155, 17, 1959.
70. Lu, C. and A. W. Czanderna, *Applications of Piezoelectric Quartz Crystal Microbalances*, Elsevier, 1984.
71. Grate, J. W., "Acoustic wave microsensor arrays for vapor sensing," *Chem. Rev.*, Vol. 100, 22, 2000.
72. Bruckenstein, S. and M. Shay, "Experimental aspects of use of the quartz crystal microbalance in solution," *Electrochim. Acta*, Vol. 20, 6, 1985.
73. Vellekoop, M. J., "Acoustic wave sensors and their technology," *Ultrasonics*, Vol. 36, 8, 1998.
74. Zhdanov, V. P., M. Edvardsson, Fredrik Höök, and B. Kasemo, "Suppression of binding events via external perturbation with emphasis on QCM," *Chemical Physics Letters*, Vol. 424, 4, 2006.
75. Lin, R.-C., Y.-C. Chen, W.-T. Chang, C.-C. Cheng, and K.-S. Kao, "Highly sensitive mass sensor using film bulk acoustic resonator," *Sens. Actuators A*, Vol. 147, 5, 2008.
76. Li, F., J. Liu, and Y. Wu, "The investigation of point defect modes of phononic crystal for high Q resonance," *J. Appl. Phys.*, Vol. 109, 4, 2011.
77. Clark, S. C., "Development of the evanescent wave atomic force microscope," Virginia Polytechnic Institute and State University, Blacksburg, 2005.
78. Ben-Aryeh, Y., "Tunneling of evanescent waves into propagating waves," *Appl. Phys. B*, Vol. 84, 4, 2006.
79. Fornel, F. D., *Evanescent Waves*, Springer, Berlin, 2001.
80. Li, F., J.-F. Manceau, Y. Wu, and F. Bastien, "Measurements of evanescent wave in a sandwich Lamb wave sensor," *Appl. Phys. Lett.*, Vol. 93, 3, 2008.
81. Jian, A. Q., X. M. Zhang, W. M. Zhu, and M. Yu, "Optofluidic refractometer using resonant optical tunneling effect," *Biomicrofluidics*, Vol. 4, 11, 2010.
82. Jian, A. Q., X. M. Zhang, W. M. Zhu, and A. Q. Liu, "Liquid refractive index sensors using resonant optical tunneling effect for ultra-high sensitivity," *Sens. Actuators A*, Vol. 169, 5, 2011.
83. Roh, Y.-G., T. Tanabe, A. Shinya, H. Taniyama, E. Kuramochi, and S. Matsuo, "Strong optomechanical interaction in a bilyaer photonic crystal," *Phys. Rev. B*, Vol. 81, 4, 2010.
84. Fan, J. and L. Zhu, "Enhanced optomechanical interaction in coupled microresonators," *Opt. Express*, Vol. 20, 10, 2012.
85. Krause, A. G., M. Winger, T. D. Blasius, Q. Lin, and O. Painter, "A high-resolution microchip optomechanical accelerometer," *Nature Photon.*, Vol. 6, 5, 2012.
86. Wu, Y., F. Li, G. Liu, and X. Ming, "Single molecule identification — The opto-acoustic coupling cavity shows its potential," *International Conference on Micro/Nano Optical Engineering (ICOME)*, Changchun, China, 2011.

The Estimation of a Gold Nanoparticles Distribution Using the Evanescent Electric Field in Gold Nanoparticles Filled Surface Plasmon Resonance Biosensing

Chardchai Korjittavanit[1], **Rardchawadee Silapunt**[1], **and Boonsong Sutapun**[2]

[1]Department of Electronic and Telecommunication
King Mongkut's University of Technology Thonburi, Bangkok 10140, Thailand
[2]School of Telecommunication Engineering
Suranaree University of Technology, Nakhon Ratchasima, Thailand

Abstract— The estimation of a gold nanoparticles (AuNPs) distribution using the evanescent electric field in AuNPs filled surface plasmon resonance (SPR) biosensing is proposed here.

The average evanescent electric fields in the 2-dimensional (2D) sensing structure containing thin gold and saline layers are determined. The location of AuNPs from the gold/saline interface has a great influence on the shift of the evanescent field profile. The results also indicate that higher number of AuNPs with preferably uniform distribution provides very strong profile shift. The shifts observed in most profiles are well correlated with those of the surface plasmon resonance (SPR) curves.

1. INTRODUCTION

Surface plasmon resonance (SPR) has been widely adopted for sensing applications [1, 2]. Monitoring reflected light intensity associated with dielectric changes of biomolecules is considered a key to identify types of biomolecules as well as their density The sensitivity of the SPR sensor has later been improved by filling gold nanoparticles (AuNPs) in the dielectric layer to enhance field couplings induced by localized surface plasmons (LSPs) of AuNPs [3, 4]. It is believed that the sensing capability depends significantly on AuNPs distributions.

In this paper, the evanescent field profile monitoring is proposed to determine AuNP distributions in the AuNPs filled SPR sensing system. The case studies include uniform and non-uniform arrays of AuNPs in 1- and 2-row structures. The SPR curves are created for comparison,by including the effects of AuNPs using widely known modified Maxwell-Garnett (MG) model [5].

2. RESEARCH APPROACH

2.1. Evanescent Electric Field Calculation

The 2D single interface structure filled with AuNPs is shown in Figure 1. The lower ($z < 0$) and upper ($z > 0$) half spaces contain gold (Au) and dielectric layers, respectively. The general TM solutions for the evanescent electric fields using Maxwell's equations in the upper half space, assuming a flat interface is shown as

$$E_x(z) = -iA\frac{1}{\omega\varepsilon_0\varepsilon_d}k_d e^{i\beta x}e^{-k_d z} \tag{1}$$

$$E_z(z) = -A\frac{\beta}{\omega\varepsilon_0\varepsilon_d}e^{i\beta x}e^{-k_d z}, \tag{2}$$

where A is the amplitude constant, ω is the angular frequency (rad/s), ε_d is saline dielectric constant, ε_o is the free space permittivity β is the propagation constant of the surface plasmon polariton (SPP) $= \frac{\omega}{c}\sqrt{\frac{\varepsilon_d\varepsilon_m(\omega)}{\varepsilon_d+\varepsilon_m(\omega)}}$, where c is the light velocity and ε_m is the complex dielectric constant of the metal layer, and $k_d = \alpha_d + ip_d$ is the component of the wave vector with the attenuation constant α_d (S/m) and the phase constant p_d (rad/m), respectively.

The evanescent electric fields are computed using MATLAB at every point in the model space and ones at AuNPs locations are employed to determine the fields induced by LSPs of AuNPs. The magnitudes of the vector sums of the evanescent electric fields in (1) and (2) are superposed with those induced by AuNPs. These evanescent electric field values, $|E_0|$, are averaged out to obtain the average decay field, $|E_0|_{ave}$, as a function of the distance z.

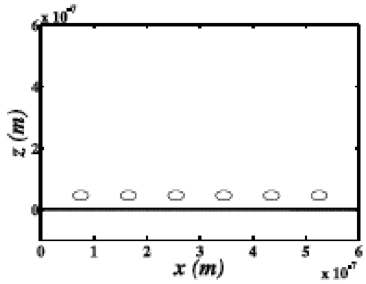

Figure 1: AuNPs filled SPR structure.

2.2. Setup Parameters

The size of the 2D SPR model structure is $1600 \times 500\,\text{nm}^2$. The p-polarized light of 820 nm wavelength is employed. The saline layer has $\varepsilon_d = 1.904$. The gold layer is 50 nm thick and has $\varepsilon_m = -25.5782 + 1.6106i$ at this wavelength. All AuNP shave equally 15 nm radius. Their dielectric function is determined by the Drude model. The average decay electric field profiles are determined for uniform and non-uniform arrays of AuNPs in 1- and 2-row structures. Ten is set as a default number of AuNPs per row. The modified MG equations are then employed to calculate for effective dielectric constants of the AuNPs filled dielectric layers in all cases. SPR data are then computed using WINSPALL. Note that, the interaction between NPs in the same row is assumed negligible.

3. RESULTS AND DISCUSSION

An example of the $|E_0|$ distribution of the 1-row uniform AuNPs array located at $z = 50\,\text{nm}$ is shown in Figure 2(a). These average evanescent electric field profiles at different array heights are plotted as related power density term, $|E_0|^2_{ave}$, for better visualization as shown in Figure 2(b). The valley in each profile indicates the location of the AuNPs array. The electromagnetic (EM) couplings between AuNPs and surround medium can easily be observed by vertical profile shifts from the conventional or no AuNPs baseline. As expected, the coupling becomes weaker as the height increases due to field attenuation in the saline layer. The SPR shifts of the AuNPs filled

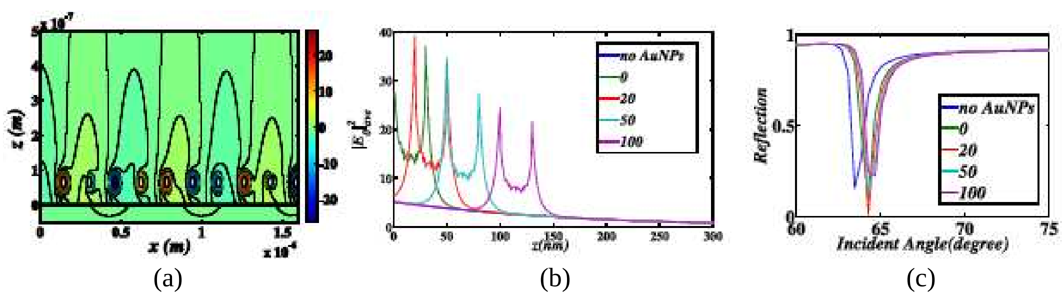

Figure 2: (a) The $|E_0|$ distribution of 1-row uniform AuNPs array located at $z = 50\,\text{nm}$, (b) $|E_0|^2_{ave}$ profiles as a function of height, and (c) corresponding SPR profiles.

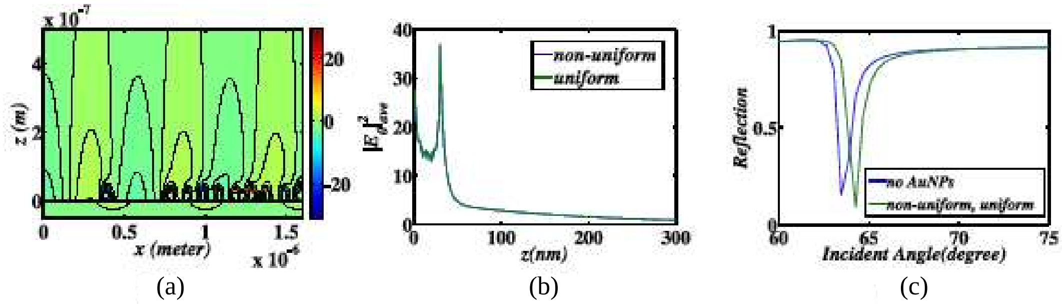

Figure 3: (a) The $|E_0|$ distribution of 1-row non-uniform AuNPs array located at $z = 0\,\text{nm}$, (b) $|E_0|^2_{ave}$ profiles comparison, and (c) SPR profiles comparison.

sensing structure in Figure 2(c) are easily distinguished from that of the conventional curve but exhibit very little difference from one another. Figure 3(a) shows the $|E_0|$ distribution of the 1-row non-uniform AuNPs array located at $z = 0$ nm. The associated $|E_0|^2_{ave}$ profile is compared with the uniform array at the same location as shown in Figure 3(b). Both profiles are quite similar, implying that the AuNPs uniformity is unlikely an important factor at this stage. The results are confirmed with SPR profile shifts in Figure 3(c).

The $|E_0|$ distribution in the structure containing the 2-row uniform AuNPs array with 20 nm gap between rows are shown in Figure 4(a). The field couplings between rows are clearly observed. The $|E_0|^2_{ave}$ profiles at different gap sizes are shown in Figure 4(b). The strongest coupling is observed at zero gap as expected. The inset shows zoomed in profiles at 20, 50, and 100 nm gap. Compared with the conventional and one-row cases, these 2-row profiles shift up much more significantly, agree with SPR profiles in Figure 4(c). These results suggest that additional AuNPs and interactions between rows may have a strong influence to the total field coupling. This 2-row or pair formation is thus definitely useful for SPR sensitivity improvement.

Figure 5(a) shows the $|E_0|$ distribution in the 2-row non-uniform AuNPs array with only 5 AuNPs in the upper row, and 20 nm gap between rows. The interaction between rows is clearly subsided as shown in Figure 5(b), compared with that of the 2-row uniform array case. The smaller

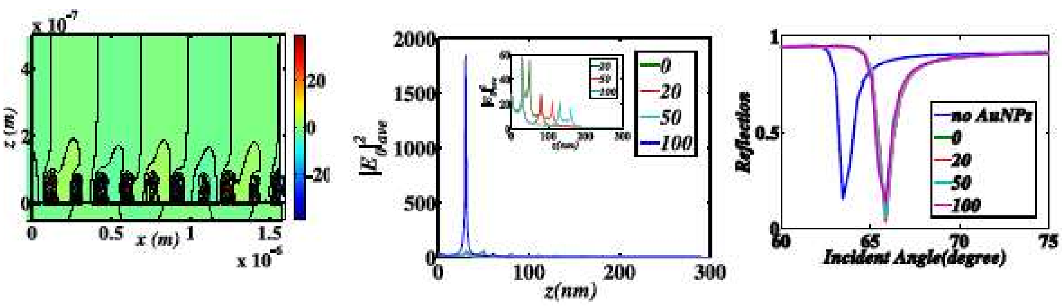

(a) (b) (c)

Figure 4: (a) The $|E_0|$ distribution of 2-row uniform AuNPs array with 20 nm gap, (b) $|E_0|^2_{ave}$ profiles as a function of gap sizes, and (c) SPR profiles.

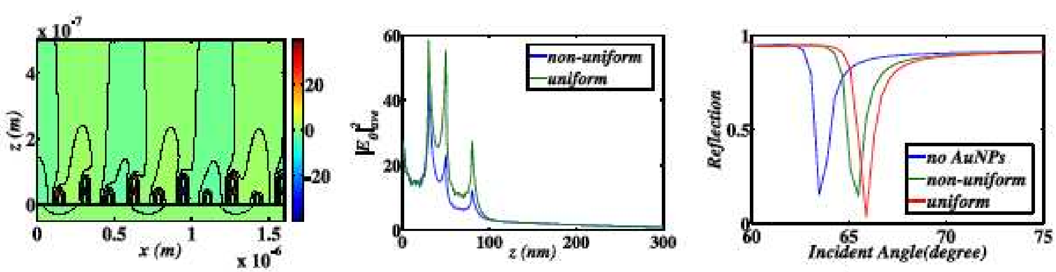

(a) (b) (c)

Figure 5: (a) 2-row array with unequal number of AuNPs at 20 nm gap, (b) $|E_0|^2_{ave}$ profiles, and (c) SPR profiles.

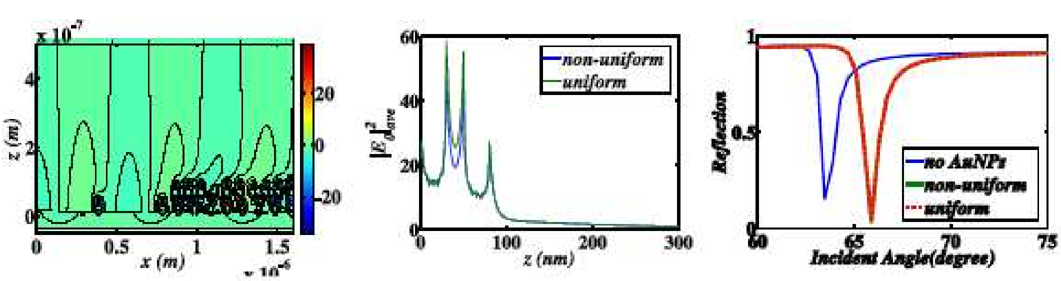

(a) (b) (c)

Figure 6: (a) 2-row non-uniform array with different AuNPs distribution at 20 nm gap, (b) $|E_0|^2_{ave}$ profiles, and (c) SPR profiles.

number of AuNPs in the upper row is indicated by smaller side peaks of the upper AuNPs valley. The result is well correlated with the smaller SPR shift shown in Figure 5(c).

Finally, the $|E_0|$ distribution in the structure containing the 2-row non-uniform AuNPs array with different AuNPs distributions in both rows and a 20 nm gap, is shown in Figure 6(a). The extreme distributions of most AuNPs in both rows locating on the right half of the model space are selected for the demonstration purpose. Figure 6(b) shows the corresponding $|E_0|^2_{ave}$ profile compared with that of the 2-row uniform AuNPs array. The smaller shift of the middle valley including the reduction in its side peaks indicates the overall decrease in row-to-row coupling due to non-uniform AuNPs distributions. However, the SPR profile shift shown in Figure 6(c) is similar to that of the uniform case since the calculation of the SPR curve is actually based on the AuNPs density, not their distribution.

4. CONCLUSIONS

The $|E_0|^2_{ave}$ profile shift for the 1-row uniform AuNPs array structure decreases as the array height increases. The $|E_0|^2_{ave}$ profile and SPR profile shifts in the structures containing 1-row non-uniform AuNPs arrays are barely distinguished from those of the uniform array. It is found later that both $|E_0|^2_{ave}$ and SPR profile shifts in the 2-row uniform AuNPs array structure are much higher due to stronger coupling induced by additional AuNPs. This finding is well supported by the profiles observed in the 2-row unequal number of AuNPs array. However for the case of the 2-row non-uniform array, there is no change in the SPR profile shift since the calculation of the SPR curve is actually based on the AuNPs density, not their distribution. These results suggest that the evanescent field approach is quite useful for estimating AuNPs distributions when the sufficient number of AuNPs is considered.

REFERENCES

1. Abdulhalim, I., M. Zourob, and A. Lakhtakia, "Surface plasmonresonance for biosensing: A mini-review," *Electromagnetics*, Vol. 28, No. 3, 214–242, 2008.
2. Kumar, S., G. Sharma, and V. Singh, "Sensitivity modulation of surface plasmonresonance sensor configurations in optical fiber waveguide," *Progress In Electromagnetics Research Letters*, Vol. 37, 167–176, 2013.
3. Tamada, K., F. Nakamura, M. Ito, X. Li, and A. Baba, *SPR-based DNA Detection with Metal Nanoparticles*, Springer, Plasmonics, 2007.
4. Golden, M. S., A. C. Bjonnes, and R. M. Georgiadis, "Distance- and wavelength-dependent dielectric function of Au nanoparticles by angle-resolved surface plasmon resonance imaging," *Journal of Physical Chemistry C*, 8837–8843, 2010.
5. Koledintseva, M. Y., R. E. DuBroff, and R. W. Schwartz, "A Maxwell Garnet model for dielectric mixtures containing conducting particles at optical frequencies," *Progress In Electromagnetics Research*, Vol. 63, 223–242, 2006.

Numerical Analysis of Passively Q-switched Er and Yb Doped Fiber Laser

Dan Savastru, Roxana Savastru, Sorin Miclos, and Ion Lancranjan
National Institute of R&D for Optoelectronics — INOE 2000
409 Atomistilor St., Magurele, Ilfov RO-077125, Romania

Abstract— We present simulation results of an analysis of linear and ring structures of single or double cladding fiber laser using Er^{3+}, Yb^{3+}, Er^{3+}/Yb^{3+} or $Er^{3+}/Yb^{3+}/Cr^{3+}$ as active lasing centers and operated in passive Q-switching regime. Several types of passive Q-switch cells made of materials such as Co^{2+}:$MgAl_2O_4$ bulk crystals or nano-crystals embedded in phosphate glass, Co^{2+}:ZnSe, Co^{2+}:ZnS, UO^{2+} embedded in phosphate glass, Cr^{4+}:YAG bulk crystal and LiF:F_2^- (lithium fluoride with F_2^- color centers) are considered. The use of an un-pumped Er^{3+} doped fiber optic as a passive Q-switch cell is also analyzed. Both doped fiber optic active medium and passive Q-switch cell spectroscopic characteristics are analyzed concerning the lasing function. The saturation dynamics of the analyzed passive Q-switch cells is separately done by a FTDT method. The simulation results are obtained by solving the coupled rate equations describing the laser dynamics, considering as accurate as possible the differential equation coefficients describing laser systems. The linear and ring fiber laser structures simulations are performed considering the influence of various factors including ASE on power and temporal output characteristics of eye-safe erbium laser. Also the thermal effects occurring in the passive Q-switch cells during laser operation are investigated. Presented simulation results are part of a design procedure of linear or ring fiber laser emitters, including the "Eye Safe" ones operated at approximately 1550 nm for various industrial, laboratory or military applications.

1. INTRODUCTION

Compact high efficiency diode pumped lasers, such as passively Q-switched Er^{3+} and Yb^{3+} fiber lasers are required for various applications, such as medical, material micro-processing, eye-safe range-finding, target designating and remote sensing [1–6]. The basic reason for this interest relies on excellent beam quality, high efficiency, compactness and reliability. This made the diode-pumped rare-earth-doped double-cladding fiber lasers become very important light sources [6–8]. Development and optimization of passively Q-switched Er^{3+} and Yb^{3+} fiber lasers with specified output radiation dynamical characteristics require adequate modeling of the laser mode evolution within the cavity [7–12]. There are several effects, as laser medium thermalization, slow Q-switching or effects of absorber lifetime, that are considered during the numerical modeling of passively Q-switched laser operation [12–15]. Among these effects the amplified spontaneous emission (ASE), often referred to as amplified luminescence, is one of the factors that can significantly affect the laser threshold, the power and the temporal characteristics [9–13]. Passive Q-switches made of Co^{2+}:$MgAl_2O_4$ bulk crystals or nano-crystals embedded in phosphate glass, Co^{2+}:ZnSe, Co^{2+}:ZnS, UO^{2+} embedded in phosphate glass (used for Er^{3+} based fiber lasers), Cr^{4+}:YAG bulk crystal and LiF:F_2^-, lithium fluoride with F_2^- color centers (used for Yb^{3+} based lasers) are considered in this analysis [16–18].

2. THEORY

In Fig. 1 is presented the schematic of the fiber laser using Er^{3+} or Yb^{3+} ions doped optic fiber [19]. It is a common Er^{3+} or Yb^{3+} fiber laser setup.

The coupled rate equations usually used to model passively Q-switched lasers are generally based on the approximations of the uniform pumping of the gain medium, the intra-cavity optical intensity as axially uniform, and the complete recovery of the saturable absorber [17–21]. Including the focusing effect, the coupled equations for a three-level or four-level saturable absorber are given

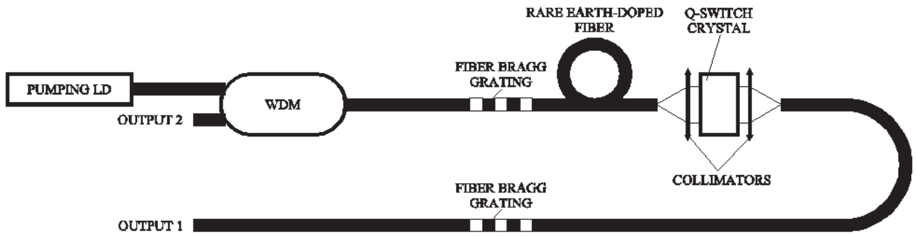

Figure 1. Passively Q-switched fiber laser. PUMPING LD — pumping laser diode (emitting at 980 nm in the case of Er^{3+} fiber lasers; emitting at 941 nm in the case of Yb^{3+} fiber lasers); WDM — wavelength division multiplexor; FIBER BRAGG GRATINGs act as laser resonator mirrors; Q-SWITCH CRYSTAL — the passive optical Q-switch cell; COLLIMATORS — two collimating lenses producing a parallel beam for the Q-switch cell; RARE EARTH-DOPED FIBER — Er^{3+} or Yb^{3+} laser active medium.

by [17–21]:

$$\frac{d\Phi(t)}{dt} = \frac{\Phi(t)}{t_r}\left[2\sigma_{am} n(t)\, l_{am} - 2\sigma_{gs} n_{gs}(t)\, l_{sa} - 2\sigma_{es} n_{es}(t)\, l_{sa} - \left(\ln\left(\frac{1}{R}\right) + L_{loss}\right)\right] \quad (1)$$

$$\frac{dn(t)}{dt} = R_p - \gamma \cdot c \cdot \sigma_{am} \cdot \Phi(t) \cdot n(t) - \frac{n(t)}{\tau_{am}} \quad (2)$$

$$\frac{dn_{gs}(t)}{dt} = -\frac{A}{A_{sa}} c \cdot \sigma_{gs} \cdot \Phi(t) \cdot n_{gs}(t) \quad (3)$$

It was considered the condition (4) imposed by the constant population density of the saturable absorber centers:

$$n_{gs}(t) + n_{es}(t) = n_{s0} \quad (4)$$

In the above equations $\Phi(t)$ is the intra-cavity photon density in the cross-sectional area of the laser beam in the gain medium; n is the population density of the gain medium; n_{s0} is the total population density of the saturable absorber centers; n_{gs} and n_{es} are the instantaneous population densities in the ground and excited states of the saturable absorber, respectively; σ_{am} is the active medium emission cross section; σ_{gs} and σ_{es} are the ground-state absorption and excited-state absorption cross sections of the saturable absorber, respectively; l_{am} is the length of the active medium; τ_{am} is the fluorescence lifetime of the upper laser level; l_{sa} is the length of the saturable absorber, A/A_s is the ratio of the laser beam average area in the gain medium and in the saturable absorber; R is the reflectivity of the output mirror (actually the product of the two mirrors reflectivity, R_1 and R_2), L_{loss} is the round-trip dissipative optical losses, γ is the inversion reduction factor, $\gamma = 1$ and $\gamma = 2$ correspond to four-level and three-level systems respectively), and t_r is the round-trip transit time of light in the cavity optical length l; c is the speed of light. R_p represents the pumping rate, proportional to the pumping power, P_p, defined as:

$$R_p \approx \frac{P_p}{h\nu A l_{am}} \quad (5)$$

In Eq. (5), $h\nu$ is the pumping quanta energy. T_2, is defined as in [19].

3. RESULTS

The differential equation system (1)–(3) is solved by using Runge-Kutta-Fehlberg 45 method. The inversion reduction factor is $\gamma = 1$ in the Er^{3+} case and $\gamma = 2$ for the Yb^{3+} case. The active medium length is $l_{am} = 2.5$ m for both types of fiber laser. The resonator length is $l_r = 3.0$ m for both types of fiber laser. $\sigma_{am} = 0.575 \cdot 10^{-20}\,\mathrm{cm}^2$ and $\tau_{am} = 5.545 \cdot 10^{-3}$ s in the case of Er^{3+} ions doped fiber laser. $\sigma_{am} = 0.241 \cdot 10^{-21}\,\mathrm{cm}^2$ and $\tau_{am} = 0951 \cdot 10^{-3}$ s in the case of Yb^{3+} ions doped fiber laser. $R_1 = 0.995$ and $R_2 = 0.925$ for both types of fiber laser. The pumping rate was considered to vary in the range 0.5–$2.5 \cdot 10^{21}\,\mathrm{cm}^{-3}$ for both types of fiber laser. The concentrations of saturable absorber centers are adjusted to impose an initial, zero signal transmittance of 0.90 for 2 mm thickness.

In Table 1 the parameters of the passive Q-switches considered for Er^{3+} fiber laser operation are presented. It can be noticed that passive optical Q-switch cells commonly used in the case of Er^{3+} fiber lasers have no residual absorption from excited electronic levels.

Table 1.

Q-Switch	σ_{sa} [cm^2]	τ_{sa} [s]	n_{s0} [cm^{-3}]	n
Co^{2+}:ZnSe	$5.31 \cdot 10^{-19}$	$2.9 \cdot 10^{-4}$	$5.914 \cdot 10^{19}$	2.45551
Co^{2+}:$MgAl_2O_4$ (nanocrystals)	$3.85 \cdot 10^{-19}$	$6.0 \cdot 10^{-7}$	$9.053 \cdot 10^{19}$	2.16416
Co^{2+}:$MgAl_2O_4$	$3.51 \cdot 10^{-19}$	$1.8 \cdot 10^{-7}$	$1.152 \cdot 10^{20}$	1.69416
U^{2+}:CaF_2	$7.05 \cdot 10^{-20}$	$2.0 \cdot 10^{-7}$	$6.139 \cdot 10^{20}$	1.42601
U^{2+}:Phosphate Glass	$5.56 \cdot 10^{-20}$	$1.0 \cdot 10^{-7}$	$7.622 \cdot 10^{20}$	1.51647

Table 2 summarizes the simulation results for Er^{3+} fiber laser: the output laser pulse width, t_p, and the repetition frequency, f_r,.

Table 2.

Q-Switch	Co^{2+}:ZnSe	Co^{2+}:$MgAl_2O_4$ (nanocrystals)	Co^{2+}:$MgAl_2O_4$	UO^{2+}:CaF_2	UO^{2+}:Phosphate Glass
t_p [ns]	75.2	89.4	93.9	72.1	79.3
f_r [kHz]	39.54	41.11	42.27	34.35	40.55

In Table 3 the parameters of the passive Q-switches considered for Yb^{3+} fiber laser operation are presented. It can be noticed that passive optical Q-switch cells commonly used in the case of Yb^{3+} fiber lasers have no residual absorption from excited electronic levels.

Table 3.

Q-Switch	σ_{gs} [cm^2]	σ_{es} [cm^2]	τ_{sa} [s]	n_{s0} [cm^{-3}]	n
Cr^{4+}:YAG	$8.75 \cdot 10^{-19}$	$2.25 \cdot 10^{-19}$	$2.9 \cdot 10^{-4}$	$3.014 \cdot 10^{19}$	1.85551
LiF:F_2^-	$1.85 \cdot 10^{-19}$	-	$6.0 \cdot 10^{-7}$	$9.053 \cdot 10^{19}$	1.16416

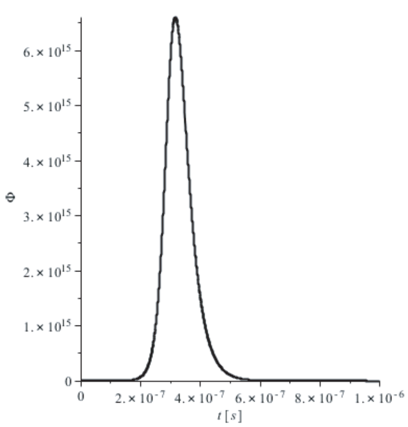

Figure 2. Shape of a singular pulse for Co^{2+}:ZnSe.

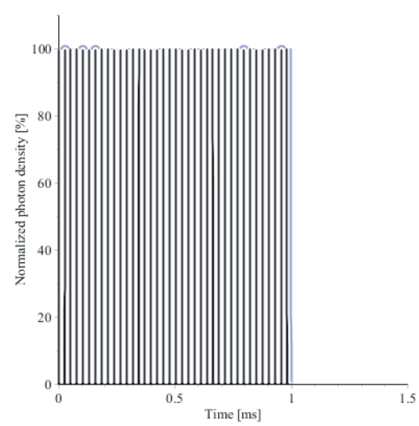

Figure 3. Shape of a pulse train for Co^{2+}:ZnSe.

Table 4 summarizes the simulation results for Yb^{3+} fiber laser: the output laser pulse width, t_p, and the repetition frequency, f_r.

Transmittance vs. incident power, as resulted from simulation using the FDTD method is displayed in Fig. 6 (for Cr:ZnSe) and Fig. 7 (for Cr:ZnS).

Table 4.

Q-Switch	Cr^{4+}:YAG	LiF:F_2^-
t_p [ns]	85.2	90.4
f_r [kHz]	29.54	42.11

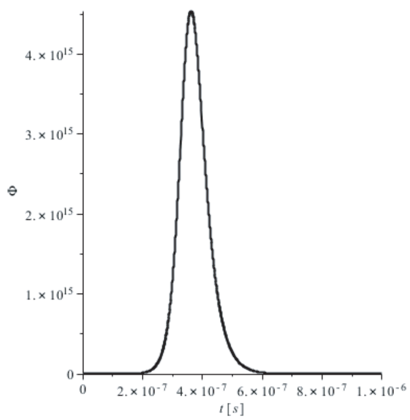

Figure 4. Shape of a singular pulse for Cr^{4+}:YAG.

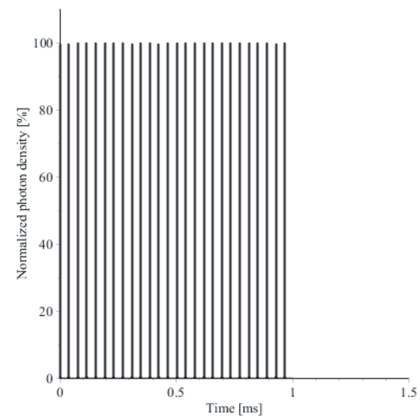

Figure 5. Shape of a pulse train for Cr^{4+}:YAG.

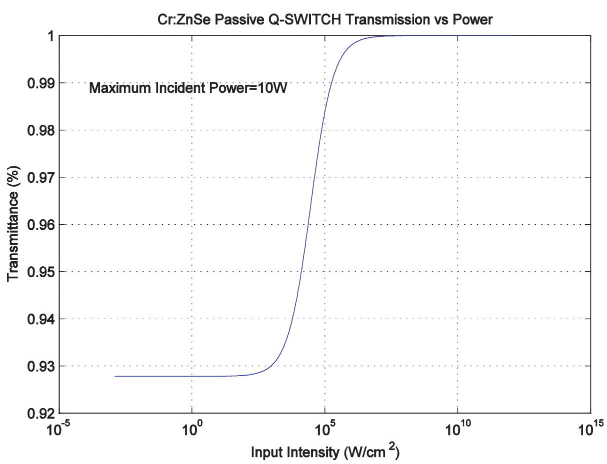

Figure 6. Transmittance for Cr:ZnSe.

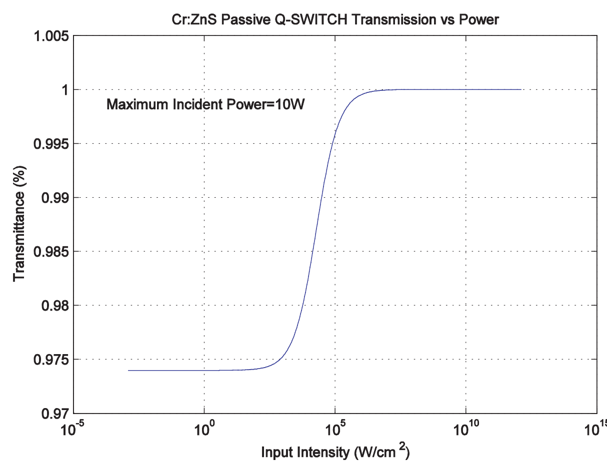

Figure 7. Transmittance for Cr:ZnS.

4. CONCLUSIONS

For Er^{3+} fiber laser five types of passive Q-switch cells were analyzed. Regarding the functionality, the narrowest pulses are given by UO^{2+}:CaF_2 ($t_p = 72.1$ ns) and Co^{2+}:ZnSe ($t_p = 75.2$ ns). But their thermo-mechanical reliability is poor, so we consider the best choice to be Co^{2+}:$MgAl_2O_4$ (nanocrystals), which gives larger pulses (89.4 ns), but has a good thermo-mechanical reliability.

For Yb^{3+} fiber laser only two types of passive Q-switch cells were analyzed: Cr^{4+}:YAG and LiF:F_2^-. In this case, the choice is simpler: Cr^{4+}:YAG is better ($t_p = 72.1$ ns and $f_r = 29.54$ kHz), while its thermo-mechanical reliability is good.

This analysis serves improving passive Q-switched fiber lasers design. The Er^{3+} and Yb^{3+} passive Q-switched fiber lasers are dedicated to different applications. Er^{3+} fiber laser are used for remote sensing, for "Eye Safe" range finding target designation. Yb^{3+} is used for microprocessing applications, for medical applications. The analysis for Er^{3+} fiber laser was intended for an "Eye Safe" laser emitter operated in passive optical Q-switching regime.

ACKNOWLEDGMENT

These results were obtained in the frame of Romanian National Authority for Scientific Research "PARTNERSHIP IN PRIORITY DOMAINS" Programme Contract nr. 184/2012 "MOIST".

REFERENCES

1. Abazadze, A. Yu., V. N. Bykov, G. M. Zverev, A. A. Pleshkov, and V. A. Simakov, "Highly efficient minilaser with transverse pulsed semiconductor pumping for eye-safe laser range-finding," *Quantum Electron*, Vol. 32, No. 3, 210–212, 2002.
2. Nettleton, J. E., B. W. Schilling, D. N. Barr, and J. S. Lei, "Monoblock laser for a low-cost, eyesafe, microlaser range finder," *Appl. Opt.*, Vol. 39, No. 15, 2428–2432, 2000.
3. Zendzian, W., L. Galecki, J. K. Jabczynski, J. Kwiatkowski, L. Gorajek, M. Nemec, H. Jelinkova, and J. Sulc, "Resonantly pumped, high peak power Er:YAG laser," *Laser Phys.*, Vol. 20, No. 2, 470–473, 2010.
4. McGrath, A. J., J. Munch, G. Smith, and P. Veitch, "Injection-seeded, single-frequency, Q-switched erbium: Glass laser for remote sensing," *Appl. Opt.*, Vol. 37, No. 24, 5706–5709, 1998.
5. Zenteno, L, "High-power double-cladding fiber lasers," *J. Lightwave Technol.*, Vol. 11, 1435–1446, 1993.
6. Digonnet, M. J. F., *Rare-Earth-Doped Fiber Lasers and Amplifiers*, 2nd Edition, Marcel Dekker, 2001.
7. Chen, Z. J., A. B. Grudinin, J. Porta, and J. D. Minelly, "Enhanced Q switching in double-cladding fiber lasers," *Opt. Lett.*, Vol. 23, 454–456, 1998.
8. Alvarez-Chavez, J. A., H. L. Offerhaus, J. Nilson, P. W. Turner, W. A. Clarkson, and D. J. Richardson, "High-energy high-power ytterbium-doped Q-switched fiber laser," *Opt. Lett.*, Vol. 25, 37–39, 2000.
9. Fan, Y. X., F. Y. Lu, S. L. Hu, K. C. Lu, H. J. Wang, X. Y. Dong, J. L. He, and H. T. Wang, "Tunable high-peak-power, high-energy hybrid Q-switched double-cladding fiber laser," *Opt. Lett.*, Vol. 29, 724–726, 2004.
10. Wang, Y. and C. Q. Xu, "Modeling and optimization of Q-switched double-cladding fiber lasers," *Appl. Opt.*, Vol. 45, 2058–2071, 2006.
11. Tordella, T., H. Djellout, B. Dussardier, A. Saïssy, and G. Monnom, "High repetition rate passively Q-switched Nd^{3+}:Cr^{4+} all-fibre laser," *Electron. Lett.*, Vol. 39, 1307–1308, 2003.
12. Fotiadi, A., A. Kurkov, and I. Razdobreev, "All-fiber passively Q-switched ytterbium laser," *CLEO/Europe-EQEC 2005, Technical Digest*, CJ 2-3, Munich, Germany, 2005.
13. Adel, P., M. Auerbach, C. Fallnich, S. Unger, H.-R. Müller, and J. Kirchhof, "Passive Q-switching by Tm^{3+} co-doping of a Yb^{3+}-fiber laser," *Opt. Express*, Vol. 11, 2730–2735, 2003.
14. Laroche, M., A. M. Chardon, J. Nilsson, D. P. Shepherd, W. A. Clarkson, S. Girard, and R. Moncorge, "Compact diode-pumped passively Q-switched tunable Er-Yb double-cladding fiber laser," *Opt. Lett.,* Vol. 27, 1980–1982, 2002.
15. Philippov, V. N., A. V. Kiryanov, and S. Unger, "Advanced configuration of erbium fiber passively Q-switched laser with Co^{2+}:ZnSe crystal as saturable absorber," *IEEE Photon. Technol. Lett.*, Vol. 16, 57–59, 2004.
16. Qamar, F. Z. and T. A. King, "Passive Q-switching of the Tm-silica fiber laser near 2 μm by Cr^{2+}:ZnSe saturable absorber crystal," *Opt. Commun.*, Vol. 248, 501–505, 2005.
17. Dong, S. L., Q. T. Lu, and I. Lancranjan, "220-W average output power from a Q-switching Nd:YAG slab laser with a LiF:F_2^- crystal," *Optics and Laser Technology*, Vol. 25, No. 3, 175–178, 1993.
18. Lancranjan, I., S. Miclos, and D. Savastru, "Numerical simulation of a passive optical Q-switched solid state laser-high brightness Nd:YAG laser case," *J. Optoelectron. Adv. Mater.*, Vol. 13, No. 5, 477–484, 2011.
19. Lancranjan, I., D. Savastru, S. Miclos, and R. Savastru, "Analysis of a passively Q-switched Nd:YAG slab laser oscillator/amplifier system," *Proc. SPIE*, Vol. 8547, 854712, 2012, doi:10.1117/12.974453.
20. Sennaroglu, A., *Solid-state Lasers and Applications*, Chap. 2, Chap. 5, CRC Press Taylor & Francis Group, 2007.
21. Koechner, W., *Solid-state Laser Engineering*, Springer Series in Optical Sciences, 6th Edition, Vol. 1, Springer, Berlin, 2006.

Design of Multiband Reflection Filters with Dielectric Frequency Selective Surfaces

A. Coves[1], **B. Gimeno**[2], **and M. V. Andrés**[2]

[1]Departamento de Ingeniería de Comunicaciones, Universidad Miguel Hernández de Elche
Elche, Alicante 03202, Spain
[2]Departamento de Física Aplicada y Electromagnetismo, Instituto de Ciencia de los Materiales
Universidad de Valencia, Burjassot, Valencia 46100, Spain

Abstract— In this work, a double-band reflection filter is theoretically demonstrated using a dielectric frequency-selective surface (DFSS) under normal TE plane wave excitation. A formulation based on a vectorial modal method is applied to the study of scattering of plane waves in a multilayered DFSS containing several dielectric gratings with different grating periods. It is shown that this structure can act as a multi-band reflection filter at normal incidence. The central frequencies of the filter are determined by the resonances of the individual single-layer waveguide gratings, so they can be tuned by choosing adequate periodicities of the periodic layers. Finally, an example of a double-band reflection filter is obtained for TE normal plane-wave excitation.

1. INTRODUCTION

The frequency selectivity behavior of multilayered periodic structures, both dielectric and metallic, has led to a growing interest in the study and application of this type of structures at microwave frequencies and in the visible range. Thus, multilayered structures formed by the cascade connection of periodic metallic surfaces printed on dielectric homogeneous layers have found a wide field of application in antennas and satellite communication systems as reflection and transmission filters [1]. On the other side, a recent interest has arisen in the application of thin dielectric structures that combine the use of homogeneous and periodic layers [2–4] which have a periodic variation along some layers. At millimeter frequencies, these structures have the advantage of having low absorption losses compared to metal surfaces. These structures have been given multiple applications including transmission and reflection filters, antenna reflectors, couplers, multiplexers, holograms, optical sensors, Bragg gratings, etc..

This work focuses on the study and design of reflection filters, using multilayered periodic dielectric structures with periodicity in one dimension, under plane wave excitation. To this end, the formulation developed in [4, 5] based on a vectorial modal method is used. These structures have already been previously designed as reflection filters under plane wave excitation [3], using a single periodic dielectric grating with a rectangular modulation of the dielectric permittivity. The frequency response of the periodic grating is determined by the resonance effect of guided modes in the grating, giving rise to strong reflections (total reflection) at certain frequencies, with practically no reflection in the frequency bands adjacent to the resonant frequency. The position of the resonance frequency of the grating is determined by the phase matching condition in the periodic layer [2, 4].

This paper demonstrates that it is possible to design multiband reflection filters using structures containing various periodic gratings with different period, where the resonant frequencies are determined by the resonances of the individual periodic gratings. It has been found that the frequency shift between the total reflection peaks of the filter can be adjusted by changing the periods of the different periodic gratings.

2. PRINCIPLES OF MULTIBAND REFLECTION FILTERS

Figure 1 shows a DFSS constituted by several dielectric gratings with different periods separated by air layers. Each dielectric grating of period D_i and thickness h_{pi} is composed of two dielectric materials with relative permittivities ε_{Hi} and ε_{Li}, and widths $l_{Hi} = l_{Li} = D_i/2$. This structure can act as a multiband reflection filter under normal incidence. In order to obtain the spectral response of the system the Generalized Scattering Matrix technique has been employed, that allows analyzing the junction between different guiding regions, which in our case will be the transitions between the periodic dielectric layers and the air layers. Finally, the cascade connection of the different

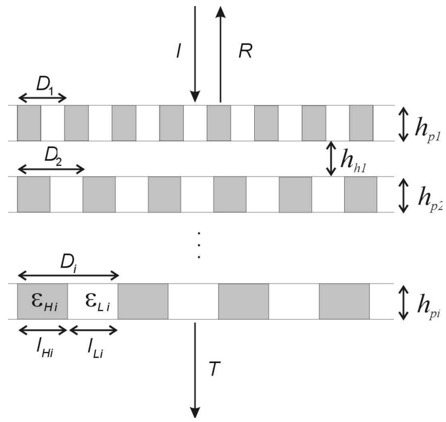

Figure 1: Multiband reflection filter using several dielectric gratings with different period under normal plane wave excitation.

individual scattering matrices is performed by using the scattering matrices corresponding to the propagation along each section connecting such transitions. The application of this method requires the knowledge of the modal spectrum in each media. In the air region we have chosen as solution the Floquet modes corresponding to a homogeneous medium [1]. On the other hand, the modal spectrum in each periodic dielectric media has been obtained by using a vectorial modal method developed by the authors, which is described in [4, 5]. When analyzing an structure constituted by several DFSS of different period separated by air layers, the study of a new type of transition has been added between two regions of different period, which for simplicity has been chosen inside the homogeneous region, i.e., between Floquet modes in the air region with different period. This kind of structure can be designed appropriately to present a number of reflection peaks (zero transmission) in the frequency band of interest when excited by a normal incident plane wave. In this way, it can be used as a multiband reflection filter under normal plane wave incidence. The frequencies at which the structure shows total reflection are determined by the resonances of the individual periodic dielectric layers, which depend on the periodicity and thickness of each periodic layer [4]. On the other hand, the air layers connecting periodic dielectric layers must be thick enough in order to avoid the coupling of evanescent waves of the adjacent periodic layers [6].

3. DOUBLE BAND REFLECTION FILTER

Figure 2 shows the spectral response of the double band reflection filter which has been designed using a DFSS consisting of two dielectric gratings with dielectric materials of relative permittivities $\varepsilon_{H1} = \varepsilon_{H3} = 2.56$ and $\varepsilon_{L1} = \varepsilon_{L3} = 1.0$. The periods of the dielectric gratings are $D_1 = 30.0\,\text{mm}$ and $D_2 = 29.0\,\text{mm}$, being the thickness of both periodic layers of $h_{p1} = h_{p2} = 25.8\,\text{mm}$. The two dielectric gratings are separated by an air layer of thickness $h_{h1} = 52.0\,\text{mm}$. This DFSS has been designed for excitation of normal incident plane wave with TE polarization, so it behaves as a double band reflection filter, whose total reflection frequencies are given by the resonances of the individual dielectric gratings. Figure 2 shows the reflection response of this structure, where two

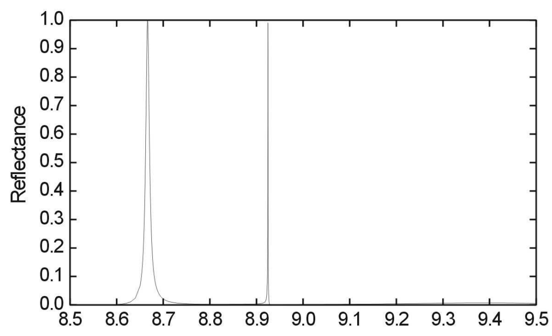

Figure 2: Spectral response of the designed double band reflection filter.

peaks of total reflection can be observed, with a frequency separation of 258.4 MHz (corresponding to a wavelength difference of 0.1 cm, which coincides with the difference between the two periods of the dielectric gratings). This separation can be adequately adjusted varying the periods of the dielectric gratings. Following the procedure described in the design process of this kind of filters, it can be checked that adding additional dielectric gratings of slightly different successive periods, these structures can also be employed as a new mechanism of band broadening in this type of reflection filters.

4. CONCLUSION

In this work, it is described a new procedure for the design of multiband reflection filters based on DFSS constituted by several dielectric gratings of different period separated by air layers. It has been checked that the frequency separation between the total reflection peaks of the filter can be adjusted modifying the periods of the different dielectric gratings. Finally, it is shown an example of a double band reflection filter designed for normal TE plane wave incidence using a DFSS constituted by two dielectric gratings with slightly different periods, separated by an air layer. It is demonstrated that the frequency separation between the two reflection peaks is directly related to the difference of the employed periodicities.

ACKNOWLEDGMENT

This work was supported by the Ministerio de Ciencia e Innovación, Spanish Government, under the coordinated project TEC2010-21520-C04-02.

REFERENCES

1. Mittra, R., C. H. Chan, and T. Cwik, "Techniques for analyzing frequency selective surfaces — A review," *Proceedings of the IEEE*, Vol. 76, No. 12, 1593–1615, Dec. 1988.
2. Bertoni, H. L., L. H. S. Cheo, and T. Tamir, "Frequency-selective reflection and transmission by a periodic dielectric layer," *IEEE Transactions on Antennas Propagat.*, Vol. 37, No. 1, 78–83, Jan. 2006.
3. Tibuleac, S., R. Magnusson, T. A. Maldonado, P. P. Young, and T. R. Holzheimer, "Dielectric frequency-selective structures incorporating waveguide gratings," *IEEE Transactions on Microwave Theory and Tech.*, Vol. 48, No. 4, 553–561, Apr. 2000.
4. Coves, A., B. Gimeno, J. Gil, M. V. Andrés, A. A. San Blas, and V. Boria, "Full-wave analysis of dielectric frequency-selective surfaces using a vectorial modal method," *IEEE Transactions on Antennas Propagat.*, Vol. 52, No. 8, 2091–2099, Aug. 2004.
5. Coves, A., B. Gimeno, A. A. San Blas, A. Vidal, V. E. Boria, and M. V. Andrés, "Three-dimensional scattering of dielectric gratings under plane-wave excitation," *IEEE Antennas Wirel. Propagat. Lett.*, Vol. 2, 215–218, 2003.
6. Coves, A., B. Gimeno, and M. V. Andrés, "Oblique incidence and polarization effects in coupled gratings," *Opt. Express*, Vol. 20, No. 23, 25454–24560, Nov. 2012.

A 12-cavity Relativistic Magnetron with Optimized Design of Diffraction Output

M. Liu[1], **C. Liu**[1], **and E. Schamiloglu**[2]

[1]Key Laboratory of Physical Electronics and Devices of the Ministry of Education
Xi'an Jiaotong University, Xi'an 710049, China
[2]Department of Electrical and Computer Engineering
University of New Mexico, Albuquerque, NM 8713-0001, USA

Abstract— The possibility of mode switching from one pulse to the next in a 6-cavity gigawatt and 12-cavity gigawatt magnetron with diffraction output (MDO) using a single frequency RF signal was demonstrated using particle-in-cell (PIC) simulations in our earlier work [1–3]. For the 12-cavity gigawatt magnetron, a splitting of the radiation frequency for each eigenmode owing to its different longitudinal distribution was also demonstrated. In this paper we optimize the 12-cavity gigawatt magnetron to improve the electronic efficiency and output power, and calculate the eigenmodes for the optimized 12-cavity gigawatt magnetron. When the relativistic magnetron is operated using an applied 400 kV voltage pulse, electrons emitted from the cathode with high energy strike the anode block and secondary electron and backscattering electron emission occurs. The emitted secondary current will lower the output power of the 12-cavity relativistic magnetron and will complicate the spectrum when the applied magnetic field approaches the boundary of neighboring modes. This is especially the case for a short applied voltage pulse. This phenomenon changes the boundary between neighboring modes as well as the boundary between splitting neighboring longitudinal modes with the same transverse field structure. Also, this makes choosing stable modes complicated when considering a boundary for mode switching.

The result of this paper will provide reference for 12-cavity gigawatt magnetron mode switching experiments when selecting the boundary between neighboring modes.

1. INTRODUCTION

In a relativistic MDO any mode can be used as the operating mode. There is also the possibility of using a weak RF signal to switch adjacent modes or neighboring longitudinal modes. Mode switching from one pulse to the next pulse in a highly efficient 6-cavity gigawatt MDO [2] can be achieved using a weak ($\sim 10^5$ W), short ($\sim 10^{-8}$ s), single frequency microwave signal. In a 12-cavity relativistic magnetron, mode switching between modes that have the same transverse field structure, but different axial distributions can be achieved using a weak ($\sim 10^5$ W), short ($\sim 10^{-8}$ s) microwave signal. In this paper a voltage of 400 kV is applied to an optimized configuration of a 12-cavity relativistic magnetron to radiate the TE_{41} mode with frequency 2.52 GHz and power that can be increased from 1.3 GW to 1.5 GW. For a higher frequency of 2.72 GHz the output power can be increased from 1.5 GW to 1.75 GW. The electronic efficiency of low frequency operation can be improved from $\eta_e \sim 50\%$ to $\eta_e \sim 60\%$, while the electronic efficiency of high frequency operation can be improved from $\eta_e \sim 63.5\%$ to $\eta_e \sim 72\%$ compared to the un-optimized configuration described in [4]. When a voltage of 400 kV is applied, the PIC simulations show that energetic electrons emitted from the cathode strike the anode block such that secondary electron and backscattered electron emission occur.

In this paper we show that for a 12-cavity relativistic MDO, secondary electron emission and backscattered electron emission from the anode will alter the boundary between neighboring modes, as well as different longitudinal modes for the same transverse mode.

2. SIMULATION SET-UP

The 12-cavity relativistic MDO uses the configuration in [4] driven by a transparent cathode [3]. The optimized 12-cavity magnetron in which $\beta \sim 31.8$, $\alpha \sim 12.6$, $L = 8.9$ cm, and the length of cathode is about 1.8 times the anode length, as shown in Fig. 1 (these parameters are shown in the figure as well). In this paper we use the HFSS code [5] to compute the eigenmodes of a 12-cavity relativistic MDO and found that for one mode there are several eigenmode branches. For example, for the TE_{41} mode, between the low frequency ~ 2.52 GHz mode and one high frequency ~ 2.72 GHz mode there is still an additional mode at 2.68 GHz. However, for ease of comparison, we use the same low frequency and high frequency modes as in [4]. We use the UNIPIC code [6] to show that, after optimizing the 12-cavity magnetron in the axial direction in the anode block,

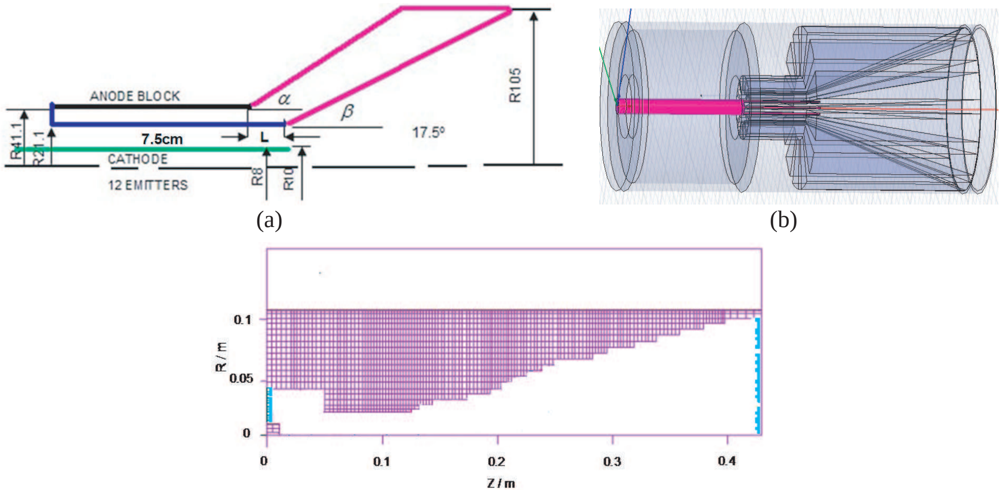

(a) (b) (c)

Figure 1: The longitudinal section of the 12-cavity MDO: (a) view in r-z plane; (b) view in r-z plane in HFSS; (c) view in r-z plane in UNIPIC.

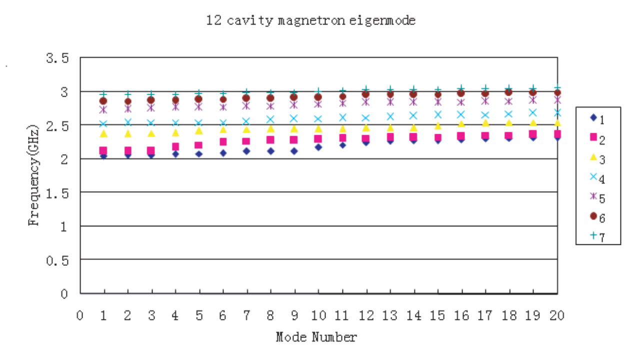

Figure 2: Eigenmodes of a 12-cavity relativistic MDO.

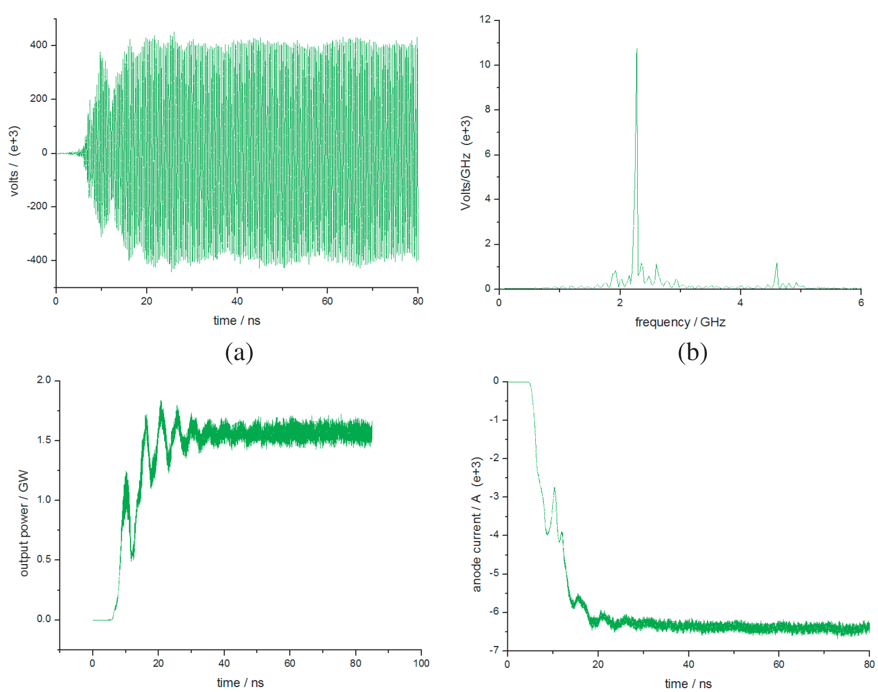

(a) (b) (c) (d)

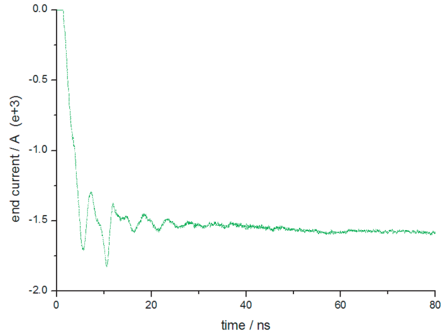

(e)

Figure 3: TE_{41} mode generated at $f = 2.52\,\text{GHz}$: (a) output electric field; (b) spectrum; (c) output power; (d) anode current; (e) end current.

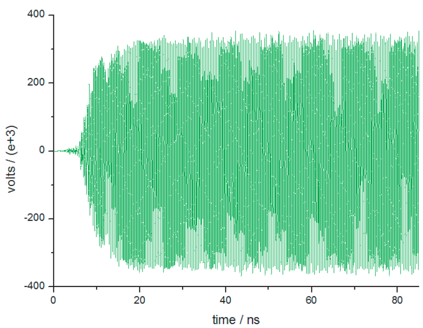

(a)

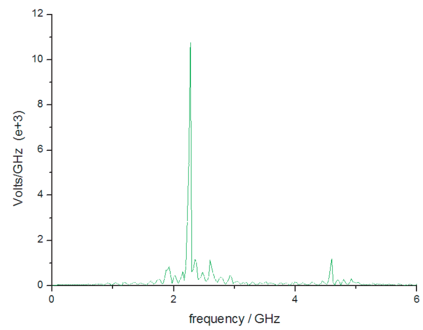

(b)

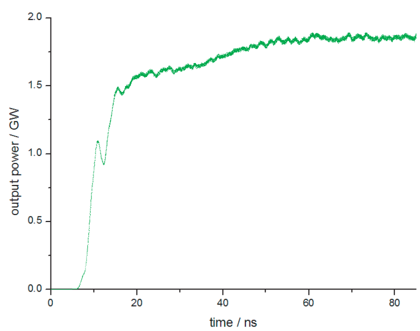

(c)

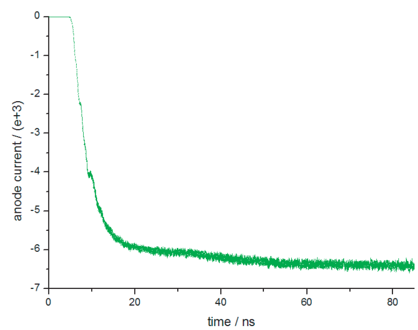

(d)

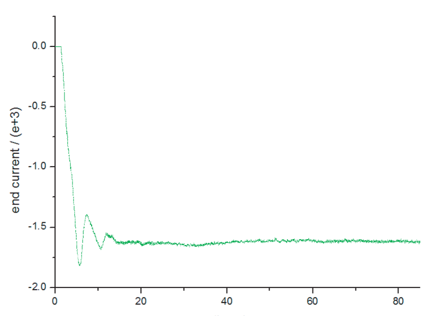

(e)

Figure 4: TE_{41} mode generated at $f = 2.72\,\text{GHz}$: (a) output electric field; (b) spectrum; (c) output power; (d) anode current; (e) end current.

the efficiency can be improved by 10% and the output power for the TE_{41} mode with one low frequency $\sim 2.52\,\text{GHz}$ and one high frequency $\sim 2.72\,\text{GHz}$ mode is at the GW-level. The electric field, output power, operating frequency, anode current, end current for the TE_{41} mode with high frequency ($f = 2.52\,\text{GHz}$) and the TE_{41} mode ($f = 2.72\,\text{GHz}$) are shown in Figs. 3 and 4. The electron particle plot [7] for the TE_{41} mode and the electric field contour in the φ-plane are shown in Fig. 5.

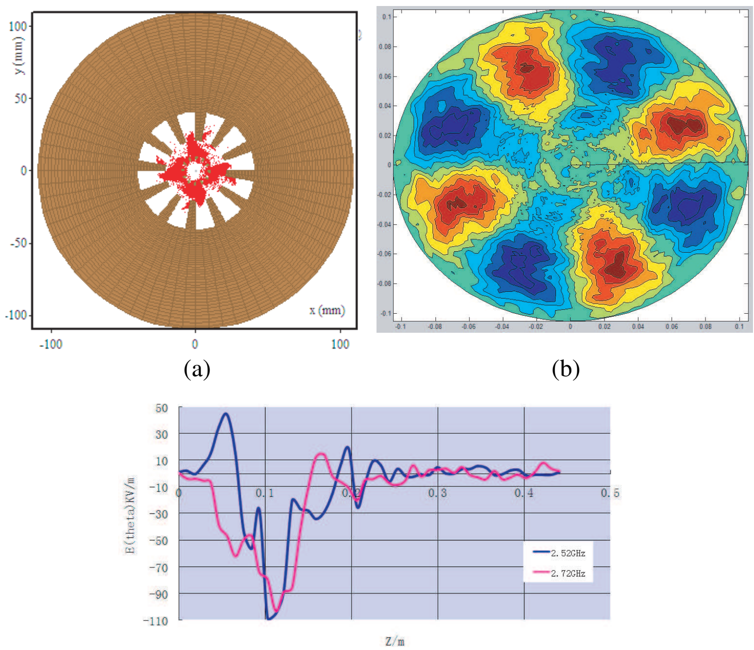

Figure 5: TE_{41} mode with low frequency $f = 2.52\,\text{GHz}$ and high frequency $f = 2.72\,\text{GHz}$ generation: (a) electron particle plot; (b) electric field contour in the φ-plane; (c) low frequency $f = 2.52\,\text{GHz}$ and high frequency $f = 2.72\,\text{GHz}$ electric-field distribution in the z direction.

3. RESULTS

The UNIPIC code [6] simulation results shown in Fig. 6 indicate that when the applied voltage is 400 kV, the energetic electrons emitted from cathode strike the relativistic magnetron anode block and secondary electrons and backscattered electrons are emitted. The secondary current formed complicates neighboring modes. This phenomenon is more apparent when in the usual relativistic A6 MDO or the relativistic A6 magnetron with radial output, especially more apparent in 12-cavity relativistic MDO since more longitudinal modes exist and mode separation becomes smaller. In Fig. 6, the purple electrons represent the explosive emission electrons with high energy while the blue electrons represent the secondary and backscattered electrons for an applied voltage of 400 kV and magnetic field 0.43 T.

The UNIPIC code [6] simulation shown in Fig. 6 is for a 12-cavity relativistic MDO with one cavity driven by a transparent cathode and an applied voltage pulse of 400 kV.

Furthermore, in a 12-cavity relativistic MDO the splitting of the frequency occurs when sec-

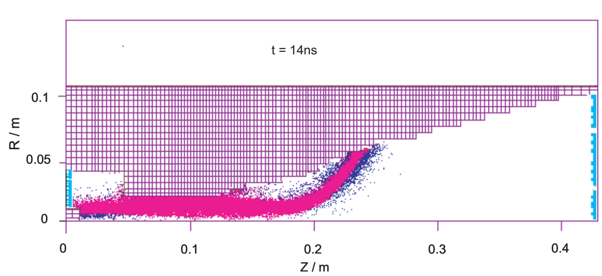

Figure 6: Particle plot of explosive emission electrons (blue) together with secondary and backscattered electrons (purple) in a 12-cavity relativistic MDO.

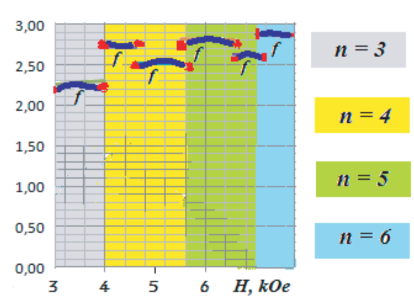

Figure 7: Secondary electron emission and backscattered electron emission in a 12-cavity relativistic MDO leads to complications for the boundary between neighboring modes and more complicated boundaries for longitudinal modes for a fixed transverse mode (the red colored portion shows the complicated boundaries).

ondary and backscattered electron emission occur, and the boundary shown in red in Fig. 7 becomes more complicated. This phenomenon is more important for RF priming [5] and mode switching using a short applied voltage pulse when choosing stable operating modes [6, 7].

4. DISCUSSIONS

Simulations using the UNIPIC code show that when a 12-cavity relativistic MDO is driven with a 400 kV voltage pulse the operating characteristics of such a device is affected by the emission of secondary and backscattered electrons from the anode block. The emission of secondary and backscattered electrons causes mode competition between neighboring modes, as shown, for example, in Fig. 7 when the applied voltage $V = 400\,\mathrm{kV}$.

5. CONCLUSIONS

Simulations using the UNIPIC code show that a 12-cavity relativistic MDO driven by a transparent cathode operates in the TE_{41} mode with one low frequency $f \sim 2.52\,\mathrm{GHz}$ and one high frequency $f \sim 2.72\,\mathrm{GHz}$ mode. The output power of the $f \sim 2.52\,\mathrm{GHz}$ mode can be increased from 1.3 GW to 1.5 GW while its electronic efficiency can be improved from 50% to 60%. The output power of the $f \sim 2.72\,\mathrm{GHz}$ mode can be increased from 1.5 GW to 1.75 GW while its electronic efficiency can be improved from 63.5% to 72%. When a 400 kV voltage pulse is applied, the PIC simulations show that energetic electrons emitted from the cathode strike the anode block such that secondary and backscattered electron emission occur. This phenomenon makes mode switching technology more complicated when choosing a stable mode and its critical boundary.

ACKNOWLEDGMENT

Work at Xi'an Jiaotong University was supported in part by the Foundation of Science and Technology on High Power Microwave Laboratory, Central University Foundation, and 2013KW07. Work at the University of New Mexico was supported in part by ONR Grant N00014-13-1-0565.

REFERENCES

1. Fuks, M. I. and N. F. Kovalev, "Relativistic magnetron with diffraction output," *Program and Abstracts of XI Int. Conf. on High-power Electromagnetics*, 18, 1998.
2. Liu, M., C. Michel, S. Prasad, M. Fuks, E. Schamiloglu, and C. L. Liu, *Appl. Phys. Lett.*, Vol. 97, 251501-3, 2010.
3. Fuks, M. and E. Schamiloglu, *IEEE Trans. Plasma Sci.*, Vol. 38, 1302–1312, 2010.
4. Liu, M., M. Fuks, E. Schamiloglu, and C. L. Liu, "Frequency switching in a 12-cavity relativistic magnetron with axial extraction of radiation," *IEEE Trans. Plasma Sci.*, Vol. 40, 1569–1574, 2012.
5. http://www.ansys.com/Products/Simulation+Technolo/Electromagnetics/HighPerformance+Electronic+Design/ANSYS+HFSS.
6. Wang, J. G., D. H. Zhang, and C. L. Liu, "UNIPIC code for simulations of high power microwave devices," *Phys. Plasmas*, Vol. 16, 033108.1–3, 2009.
7. Goplen, B., L. Ludeking, D. Smithe, and G. Warren, *Comp. Phys. Commun.*, Vol. 87, 54–86, 1995.
8. White, W., R. M. Gilgenbach, M. C. Jones, V. B. Neculaes, Y. Y. Lau, P. Pengvanich, N. M. C. Jordan, B. W. Hoff, R. Edgar, T. A. Spencer, and D. Price, "Radio frequency priming of a long-pulse relativistic magnetron," *IEEE Trans. Plasma Sci.*, Vol. 34, 627–634, 2006.
9. Liu, M., C. Michel, S. Prasad, M. Fuks, E. Schamiloglu, and C.-L. Liu, "RF mode switching in a relativistic magnetron with diffraction output," *Appl. Phys. Lett.*, Vol. 97, 251501–251503, 2010.
10. Liu, M., M. Fuks, E. Schamiloglu, and C. L. Liu, "Frequency switching in a 12-cavity relativistic magnetron with axial extraction of radiation," *IEEE Trans. Plasma Sci.*, Vol. 40, 1569–1574, 2012.

Narrow-band Wave Block by Chiral Metamaterials

Nantakan Wongkasem and Amornthep Sonsilphong
Metasolver Laboratory, Department of Electrical Engineering
Faculty of Engineering, Khon Kaen University, Khon Kaen 40002, Thailand

Abstract— EM wave block design using double-layer chiral metamaterials in microwave regimes is proposed. One of the well-known chiral structures, C_8, proven to have low loss narrow bandwidth, is employed in this design. The first layer is used to block one of the CP waves, while the other CP wave is filtered out by the same chiral structure with opposite handedness. Different distances between the two chiral layers are observed for the stopband location. These proposed designs are additional promising candidates in EM wave block applications.

1. INTRODUCTION

Based on optical activity or optical rotary dispersion (ORD), as an arbitrary polarized electromagnetic (EM) wave propagates through lossy chiral media, the wave splits into two waves with different phase velocities. These two eigenmodes, left and right circularly polarized waves (LCP and RCP wave), with different refractive indices, cause the rotation of the polarization plane. At the chiral-end, the two CP waves are then coupled and exit the media in one polarization configuration, typically as an elliptically polarized wave due to the circular dichroism (CD) or absorption loss.

Chiral metamaterials have been proposed for broadband [1–3] and multi-band circular polarizers [4, 5], where different transformation responses for the LCP and RCP waves have been investigated. A designated CP wave of the two CP waves is blocked or filtered out depending on the handedness or enantiomer orientation of the chiral structures [6]. However, when high values of chirality index are generated, low loss circular birefringence is found [7, 8]. In this study, we propose an EM wave block design using double-layer chiral metamaterials in microwave regimes One of the well-known chiral structures, C_8 [8, 9], proven to have low loss narrow bandwidth, is employed in this design. The first layer is used to block one of the CP waves while the other CP wave is filtered out by the same chiral structure with opposite handedness. Different distances between the two chiral layers are observed for the resonance location of the composite. These proposed designs are additional promising candidates in EM wave block applications.

2. WAVE BLOCK BY C_8 STRUCTURE

A low loss isotropic chiral structure, C_8 [9], shown in Figure 1(a), is used in this study. An earlier report has shown that chirality and refractive index can be controlled effectively by the structure geometry [7]. H_1 and H_2, respectively, are the main axis and the arm of the structure; w is the linewidth, A° is the angle between the main axis and the connected arms, and B° is the angle between the adjacent main axis. With regard to its well-defined chiral orientation, a non-twisted C_8 structure with opposite arm illustrated in Figure 1(b) is employed to generate handedness properties. The two structures with opposite arms are placed on top of each other; hence, there is no twisted angle. The bi-layer structures are set using a periodic boundary. A double copper-clad Arlon Di 880 board is used as a substrate. The dielectric constant of the substrate board, ε_r, is 2.2, with a dielectric loss tangent of 0.0001. The dimension parameters are given as follows:

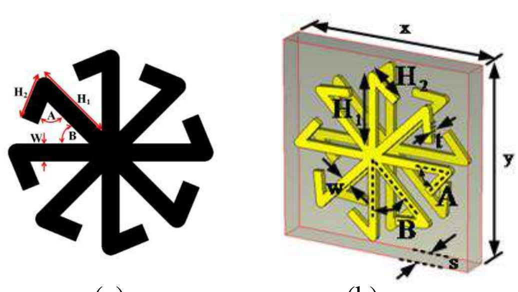

(a) (b)

Figure 1: (a) C_8 structure and (b) a unit cell of the conjugated bi-layer C_8 structures [7].

$a_x = a_y = 37$ mm, $w = 2.8$ mm, $H_1 = 15.7$ mm, $s = 0.254$ mm and $B = 360°/\text{n}$. The copper thickness, t_m, is 0.03 mm.

A unit cell of left-handed (LH) and right-handed (RH) conjugated bi-layer C_8 structures are presented in Figure 2. The excitation is launched along $-z$ axis. Electric field, $\vec{E}$, and magnetic field, $\vec{H}$, are set along $+y$ and $+x$ axis, respectively. Figure 3 shows scattering (S) parameters of the LH and the RH conjugated bi-layer C_8 structures. The LCP wave can propagate through the RH structures at the operating frequency $f = 3.43$ GHz; while the RCP wave is truncated. Opposite results are found from the LH structures.

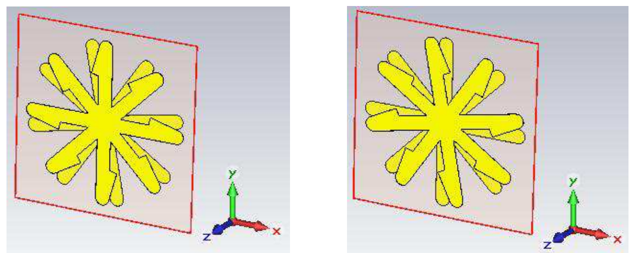

(a) (b)

Figure 2: A unit cell of (a) LH and (b) RH conjugated bi-layer C_8 structures.

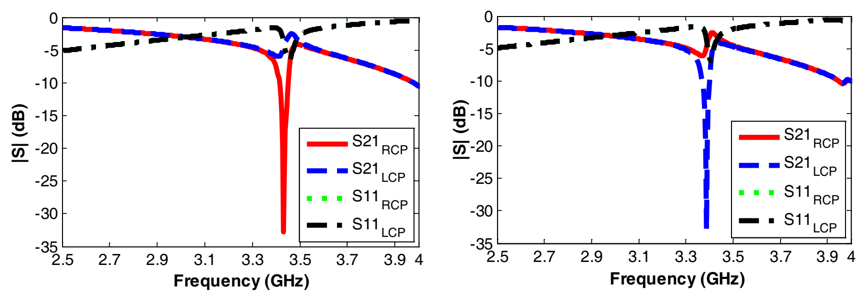

(a) (b)

Figure 3: S parameters of (a) left-handed and (b) right-handed conjugated bi-layer C_8 structures.

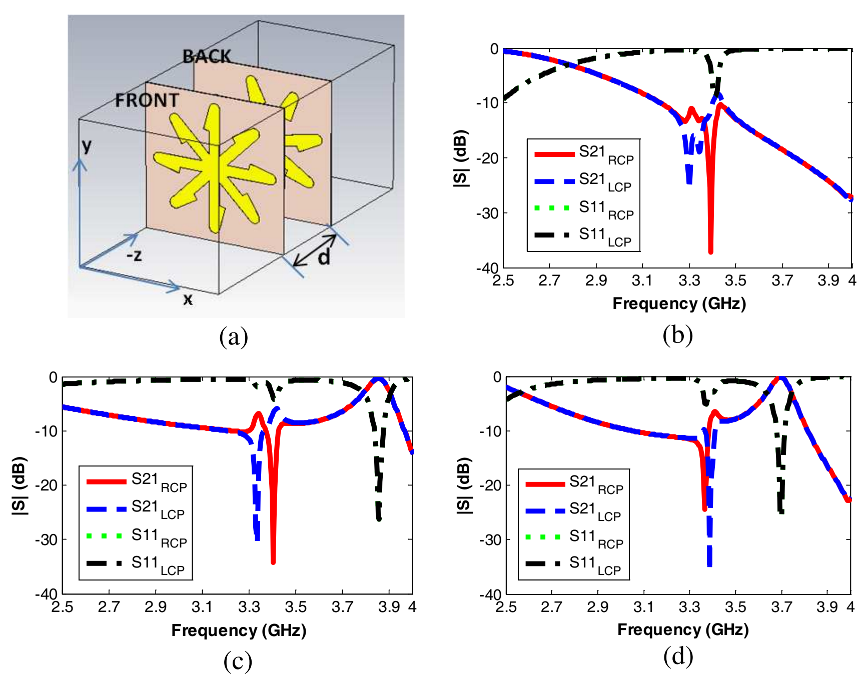

(a) (b)

(c) (d)

Figure 4: (a) CMM wave block and S parameters of the CMM wave block where (b) $d = \lambda/4$, (c) $d = \lambda/2$ and (d) $d = \lambda$.

The LH and the RH conjugated bi-layer C_8 structures are combined to perform as a CMM wave block. The two bi-layers are separated by a distance, d, as shown in Figure 4(a). S parameters of the CMM wave block are investigated when $d = \lambda/4$, $d = \lambda/2$ and $d = \lambda$. The resonances (S_{21}) of the LCP and RCP wave are almost overlapped when $d = \lambda$, confirming the complete CP wave block at the composite resonance frequency $f = 3.40\,\text{GHz}$.

3. CONCLUSIONS

Double-layer LH/RH chiral metamaterials are designed as EM wave block. The conjugated bi-layer C_8 structures are selected as low loss chiral metamaterials. The composite structure is composed of an array of LH and an array of RH chiral metamaterials. RCP wave is blocked by the LH set while LCP wave is filtered out by the RH set. The complete CP block is found when the distance between the two layers equals a wavelength at the operating frequency.

ACKNOWLEDGMENT

This project is financially supported by the Thailand Research Fund (RSA5480010) and the Faculty of Engineering, Khon Kaen University, Thailand. We also thank the Office of the National Broadcasting and Telecommunications Commission (NBTC) for funding the CST Microwave Studio® software applied in the simulations.

REFERENCES

1. Gansel, J. K., M. Thiel, M. S. Rill, M. Decker, K. Bade, V. Saile, G. V. Freymann, S. Linden, and M. Wegener, "Gold helix photonic metamaterial as broadband circular polarizer," *Science,* Vol. 325, 1513, 2009.
2. Gansel, J. K., M. Wegener, S. Burger, and S. Linden, "Gold helix photonic metamaterials: A numerical parameter study," *Optics Express*, Vol. 18, 1059, 2010.
3. Yang, Z. Y., M. Zhao, P. X. Lu, and Y. F. Lu, "Ultrabroadband optical circular polarizers consisting of double-helical nanowire structures," *Optics Letters,* Vol. 35, 2588–2590, 2010.
4. Ma, X., C. Huang, M. Pu, Y. Wang, Z. Zhao, C. Wang, and X. Luo, "Dual-band asymmetry chiral metamaterial based on planar spiral structure," *Appl. Phys. Lett.*, Vol. 101, 161901, 2012.
5. Wang, B., T. Koschny, and C. M. Soukoulis, "Wide-angle and polarization independent chiral metamaterials absorbers," *Phys. Rev. B*, Vol. 80, 033108, 2009.
6. Wongkasem, N., C. Kamtongdee, A. Akyurtlu, and K. Marx, "Artificial multiple helices: EM and polarization properties," *J. Opt.*, Vol. 12, 075102, 2010.
7. Panpradit, W., A. Sonsilphong, C. Soemphol, and N. Wongkasem, "High negative refractive index chiral metamaterials," *J. Opt.*, Vol. 14, 075101, 2012.
8. Sonsilphong, A. and N. Wongkasem, "Three-dimensional artificial double helices with high negative refractive index," *J. Opt.*, Vol. 14, 105103, 2012.
9. Matra, K. and N. Wongkasem, "Left-handed chiral isotropic metamaterials: Analysis and detailed numerical study," *J. Opt. A: Pure and Applied Optics*, Vol. 11, 074011, 2009.

Ray Tracing in an Arbitrary Cloak in Two Dimensions

H. H. Sidhwa[1], **R. P. Aiyar**[2], **and S. V. Kulkarni**[1]

[1]Department of Electrical Engineering, Indian Institute of Technology, Bombay, India
[2]CRNTS, Indian Institute of Technology, Bombay, India

Abstract— Electromagnetic wave behaviour in an anisotropic medium with a two dimensional arbitrary geometry is studied. The aim is to trace the path of a ray in such a complex medium for the purpose of achieving cloaking (invisibility). A coordinate transformation is carried out for the formulation of an annular region at the centre of the structure whose topology is a scaled geometry of outer boundary of the structure.

1. INTRODUCTION

The idea of invisibility has intrigued and fascinated mankind for thousands of years. The motive is to bend the path of a ray around the body of interest so as to give an impression that the ray is travelling in a straight line uninterrupted by any obstacle. The idea of using coordinate transformation for altering the material characteristics, which would in turn cause a change in the formulation of Maxwell equations, was first espoused by Pendry et al. [1] and Leonhardt [2] in 2006. A process of ray tracing in transformed media for spherical and cylindrical cloaks using Cartesian tensors was carried out by Pendry et al. [3]. A generalized method for designing arbitrarily shaped cloaks using transformation of coordinates approach has been discussed by Li and Li [4]. A full wave simulation using a commercial software is carried out to verify the method.

In this paper, an attempt has been made to carry out a ray tracing process for an arbitrary two dimensional cloak. The region to be cloaked is represented as an arbitrary closed curve in a two dimensional space. For the purpose of cloaking the region inside the domain is to be mapped to an annular region similar to the approach given by Li and Li [4]. A coordinate transformation is carried out for the formulation of an annular region at the centre of the structure with outer and inner boundaries having same shape. The formulation for the Hamiltonian is done as reported in [3]. Expressions for permittivity and permeability in the anisotropic medium in the transformed medium are calculated. For verification of the method, it is assumed that the arbitrary geometry is elliptical in nature. The Hamiltonian is formulated by including terms dependent on cylindrical polar coordinate, θ.

2. ANALYSIS OF TWO DIMENSIONAL ARBITRARY CLOAK

A point in space can be expressed by (r, θ, z) in cylindrical coordinates [4].

$$x = r\cos\theta \quad y = r\sin\theta$$

In a 2 dimensional geometry, let the shape of the outer contour be arbitrary in nature. Let $r = R(\theta)$ define the outer contour. We can define a normalised parameter as:

$$\rho = \frac{r}{R(\theta)} = \frac{\sqrt{x^2+y^2}}{R(\theta)}$$

For a given path, ρ remains constant while the wave traverses path of 360°.

The coordinates can now be expressed as

$$x = \rho R(\theta)\cos\theta \quad y = \rho R(\theta)\sin\theta \tag{1}$$

For the process of cloaking, we define a transformation which compresses any point lying in the region $0 \le \rho \le 1$ to $\tau \le \rho' \le 1$. The new region formed is an annular surface with coordinate system (ρ', θ', z'). The relationship between the original and transformed coordinate systems can be expressed as:

$$0 < \rho < 1 \Rightarrow \tau < \rho' < 1 \qquad \therefore \rho' = \tau + (1-\tau)\rho \quad \theta' = \theta \quad z' = z$$

Outside the cloaked region lies free space for which corresponding characteristics can be used. The corresponding transformed Cartesian coordinates can now be expressed as [4]:

$$x' = r' \cos\theta' = \rho' R(\theta') \cos\theta \tag{2}$$
$$y' = r' \sin\theta' = \rho' R(\theta') \sin\theta \tag{3}$$
$$x' = \left[\tau R(\tan^{-1}\frac{y}{x}) + (1-\tau)\sqrt{x^2+y^2}\right]\frac{x}{\sqrt{x^2+y^2}} \tag{4}$$
$$y' = \left[\tau R(\tan^{-1}\frac{y}{x}) + (1-\tau)\sqrt{x^2+y^2}\right]\frac{y}{\sqrt{x^2+y^2}} \tag{5}$$
$$z' = z \tag{6}$$

Relative permittivity and permeability tensors can also be transformed as [6]:

$$\epsilon^{i'j'} = |\Lambda_i^{i'}|^{-1}\Lambda^{i\prime}{}_i\Lambda^{j\prime}{}_j\epsilon^{ij} \tag{7}$$
$$\mu^{i'j'} = |\Lambda_i^{i'}|^{-1}\Lambda^{i\prime}{}_i\Lambda^{j\prime}{}_j\mu^{ij} \tag{8}$$
$$\epsilon^{x'x'} = |\Lambda_i^{x'}|^{-1}\Lambda^{x\prime}{}_i\Lambda^{x\prime}{}_j\epsilon^{ij} = |\Lambda_x^{x'}|^{-1}\Lambda^{x\prime}{}_x\Lambda^{x\prime}{}_x\epsilon^{xx} + |\Lambda_y^{x'}|^{-1}\Lambda^{x\prime}{}_y\Lambda^{x\prime}{}_y\epsilon^{yy} \tag{9}$$
$$\epsilon^{x'y'} = |\Lambda_i^{x'}|^{-1}\Lambda^{x\prime}{}_i\Lambda^{y\prime}{}_j\epsilon^{ij} = |\Lambda_x^{x'}|^{-1}\Lambda^{x\prime}{}_x\Lambda^{y\prime}{}_x\epsilon^{xx} + |\Lambda_y^{x'}|^{-1}\Lambda^{x\prime}{}_y\Lambda^{y\prime}{}_y\epsilon^{yy} \tag{10}$$
$$\epsilon^{y'y'} = |\Lambda_i^{y'}|^{-1}\Lambda^{y\prime}{}_i\Lambda^{y\prime}{}_j\epsilon^{ij} = |\Lambda_x^{y'}|^{-1}\Lambda^{y\prime}{}_x\Lambda^{y\prime}{}_x\epsilon^{xx} + |\Lambda_y^{y'}|^{-1}\Lambda^{y\prime}{}_y\Lambda^{y\prime}{}_y\epsilon^{yy} \tag{11}$$
$$\mu^{x'x'} = \epsilon^{x'x'} \tag{12}$$
$$\mu^{x'y'} = \epsilon^{x'y'} \tag{13}$$
$$\mu^{y'y'} = \epsilon^{y'y'} \tag{14}$$

The final expressions for the permittivity in the transformed coordinate system can be seen in [4].

3. CALCULATION OF HAMILTONIAN

Since there is no loss of energy while the wave propagates through the medium, the Hamiltonian (given by the following expression) can be found in order to trace the path of the wave in the cloaked medium [3].

$$H = \frac{1}{2}(1-\tau)(\mathbf{knk} - |\mathbf{n}|) \tag{15}$$
$$|\mathbf{n}| = |\boldsymbol{\epsilon}| = \frac{1}{(1-\tau)^2}\frac{r'-\tau R}{r'} \tag{16}$$
$$H = k_x^2\epsilon^{x'x'} + 2k_xk_y\epsilon^{x'y'} + k_y^2\epsilon^{y'y'} + k_z^2\epsilon^{z'z'} - |\epsilon| \tag{17}$$

where $\mathbf{n}$ is the refractive index of the medium and $\mathbf{k}$ is the propagation vector. The path can be parametrised as [5]:

$$\frac{d\mathbf{x}}{d\varsigma} = \frac{\partial H}{\partial \mathbf{k}} \qquad \frac{d\mathbf{k}}{d\varsigma} = -\frac{\partial H}{\partial \mathbf{x}}$$

where ς is the parameterising varaible and $\mathbf{x}$ is the position vector.

The Hamiltonian can be solved as per [5] as:

$$\frac{\partial H}{\partial k_x} = 2k_x\epsilon^{x'x'} + 2k_y\epsilon^{y'y'} \tag{18}$$
$$\frac{\partial H}{\partial k_y} = 2k_x\epsilon^{x'y'} + 2k_y\epsilon^{y'y'} \tag{19}$$
$$\frac{\partial H}{\partial k_z} = 2k_z\epsilon^{z'z'} \tag{20}$$

$$\frac{\partial H}{\partial x} = k_x^2 \frac{\partial \epsilon^{x'x'}}{\partial x} + 2k_x k_y \frac{\partial \epsilon^{x'y'}}{\partial x} + k_y^2 \frac{\partial \epsilon^{y'y'}}{\partial x} + k_z^2 \frac{\partial \epsilon^{z'z'}}{\partial x} - \frac{\partial |\boldsymbol{\epsilon}|}{\partial x} \tag{21}$$

$$A = \left[(r' - \tau R)^2 + \tau^2 (\frac{\partial R}{\partial \theta})^2 \right] \cos^2\theta - 2\tau r' \frac{\partial R}{\partial \theta} \sin\theta \cos\theta + r'^2 \sin^2\theta \tag{22}$$

$$\epsilon^{x'x'} = \frac{1}{r'(r' - \tau R)} A \tag{23}$$

$$\frac{\partial \epsilon^{x'x'}}{\partial x} = \sin\theta \frac{1-\tau}{r'(r'-\tau R)^2} \left[\frac{\partial R}{\partial \theta} \frac{\rho' - \tau}{r' - \tau R} 2A - \frac{\partial A}{\partial \theta} \right] \tag{24}$$

The expressions for $\partial\epsilon^{x'x'}/\partial y$, $\partial\epsilon^{y'y'}/\partial x$, $\partial\epsilon^{y'y'}/\partial y$, $\partial\epsilon^{x'y'}/\partial x$ and $\partial\epsilon^{x'y'}/\partial y$ can be calculated in a similar way for the calculation of $\partial H/\partial y$.

For the verification of the above algorithm, the outer contour is considered to have the shape of an ellipse with major axis a and minor axis b.

$$R = \frac{ab}{\sqrt{b^2\cos^2\theta + a^2\sin^2\theta}} \tag{25}$$

$$\frac{\partial R}{\partial \theta} = \frac{\sin\theta cos\theta \left(b^2 - a^2\right) ab}{\left(b^2\cos^2\theta + a^2\sin^2\theta\right)^{3/2}} \tag{26}$$

$$\frac{\partial^2 R}{\partial \theta^2} = \left(b^2 - a^2\right) ab \left(\frac{\cos 2\theta}{(b^2\cos^2\theta + a^2\sin^2\theta)^{3/2}} + \frac{3}{4} \frac{(b^2 - a^2)\sin^2 2\theta}{(b^2\cos^2\theta + a^2\sin^2\theta)^{5/2}} \right) \tag{27}$$

On substituting for R and its derivatives in Eq. (17) for the Hamiltonian, and solving for position vector x and propagation vector k, the path of the ray inside the cloaked medium is traced.

4. RESULTS FOR AN ELLIPTICAL CLOAK

- The elliptical cloak in Fig. 1 shows that a medium with properties defined by Eq. (23) would exhibit cloaking for electromagnetic waves in geometric limit (the wavelength $\lambda \ll a$ and $\lambda \ll b$ in the case of ellipse).
- Experimentally, these structures cannot be realized using naturally occurring materials. Metamaterials which have properties like Eq. (23), i.e., variable ϵ_r, $0 < \epsilon_r < 1$, etc., can realise such characteristics through split ring resonators or complementary split ring resonators.

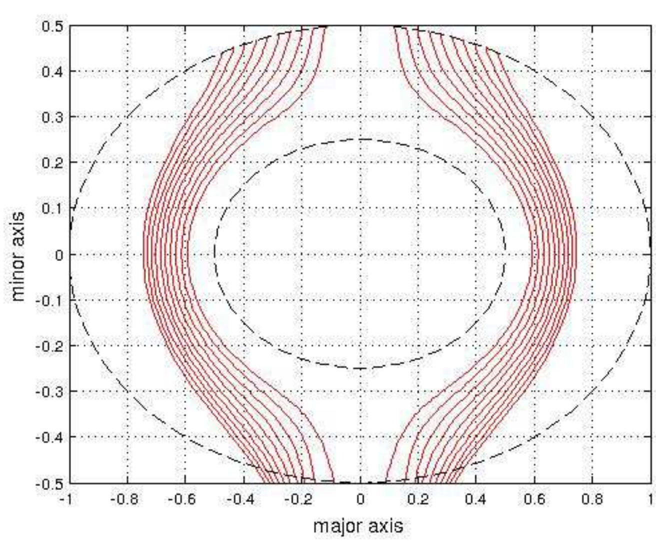

Figure 1: Plot of elliptical cloak in an X-Y plane for $\frac{a}{b} = 2$, $\tau = 0.5$.

5. CONCLUSION

A generalized method for ray tracing of an arbitrarily shaped cloak in two dimensions by finding the corresponding Hamiltonian is illustrated. In the existing literature, formulations have been given for specific shaped cloaks and verified by ray tracing. Recently, algorithms have been proposed for arbitrarily shaped cloaks, but these algorithms have not been tested through ray tracing method. In this paper, one such algorithm has been used for realizing an arbitrarily shaped cloak. The method has been verified through ray tracing. Any arbitrary two dimensional closed curve can be parameterized by specifying ρ as a function of θ. The function $\rho(\theta)$ must be a single valued function of θ for the described algorithm to work efficiently. Thus, any curve satisfying the above characteristics can be cloaked and verified by the process of ray tracing.

ACKNOWLEDGMENT

The authors would like to thank Prof. R. K. Shevgaonkar for his valuable suggestions throughout this work. The help given by Mr. Chinmay Rajhans towards the mathematical formulation is also appreciated.

REFERENCES

1. Pendry, J. B. and D. Schurig, "Controlling electromagnetic fields," *Sciencemag.*, Vol. 312, 1779–1782, 2006.
2. Leonhardt, U., "Optical conformal mapping," *Science Express*, Vol. 312, 1777–1780, 2006.
3. Shurig, D., J. B. Pendry, and D. R. Smith, "Calculation of material properties and ray tracing in transformation media," *Optics Express OSA*, Vol. 14, No. 21, 9794–9804, 2006.
4. Li, C. and F. Li, "Two-dimensional electromagnetic cloaks with arbitrary geometries," *Optics Express OSA*, Vol. 34, No. 10, 1064–1076, 2008.
5. Kravtsov, Y. A. and Y. I. Orlov, *Geometric Optics of Inhomogeneous Media*, Springer-Verlag, Berlin, 1990.
6. Post, E. J., *Formal Structure of Electromagnetics*, Wiley, New York, 1962.

Electromagnetic Behavior of SRR Loaded Microstrip Transmission Lines: Investigation for Different SRR Types and Array Topologies

G. Disken, F. Pala, E. Demir, H. D. Korucu, and E. Ekmekci
Department of Electronics and Communication Engineering
Suleyman Demirel University, Isparta, Turkey

Abstract— We study on microstrip transmission lines loaded by SRR structures in various types, numbers and topologies. We basically observe the effects of SRR number, SRR geometry and the other design parameters on insertion loss (i.e., magnitude of S_{21} in dB). We present that SRR loaded transmission lines behave as a band stop filter and increasing number of elements decreases the insertion loss. Moreover, changing SRR design parameters effects the location of the resonance frequency.

1. INTRODUCTION

Metamaterials are artificial structures that show unique properties such as negative effective permittivity/permeability, negative refractive index, reversed Doppler effect and reversed Cerenkov radiation [1]. These artificial structures promise very effective solutions for many engineering problems in microwave, terahertz and optic regions [1, 2]. Split Ring Resonator (SRR) is the well-known metamaterial structure that is widely used in many metamaterial applications. Recently, filtering applications of SRRs have also become popular [3–10]. These studies are basically composed of SRR loaded microstrip transmission lines [3–10].

In this study, we investigate the electromagnetic behavior of microstrip transmission lines loaded by different SRR geometries and array topologies. Firstly, we load $50\,\Omega$ microstrip transmission lines by single, double and quadruple SRR structures whose geometries are shown in Figure 1. Following, we investigate the effects of some important design parameters on insertion loss. The design parameters under investigation are SRR line width w, SRR gap orientations, separation distance from feed line s_f, separation distance between adjacent elements along propagation direction s_{int} and lastly separation distance between inner and outer rings of the SRR.

2. DESIGN AND SIMULATIONS

The schematic views for the unit cell structures investigated in this study are given in Figure 1. These are square-shaped single ring SRR (structure A), square-shaped single ring SRR smoothened at the corners (structure B), circular-shaped single ring SRR (structure C), square-shaped double ring SRR (structure D), square-shaped double ring SRR smoothened at the corners (structure E), circular-shaped double ring SRR (structure F). The design parameters for all these structures are

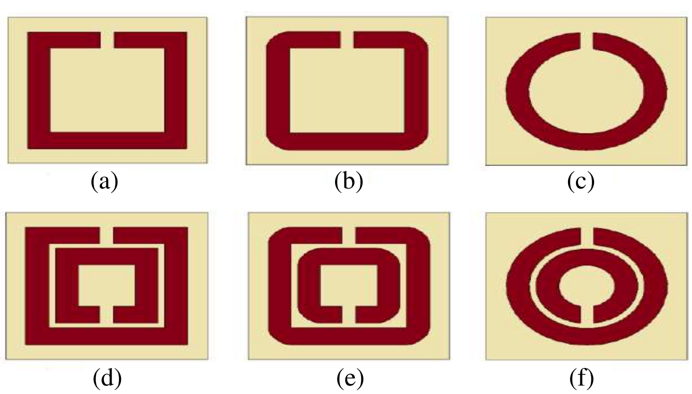

Figure 1: The SRR structures that are used in this study. (a) Square-shaped single ring SRR (structure A), (b) smoothened square-shaped single ring SRR (structure B), (c) circular-shaped single ring SRR (structure C), (d) square-shaped double ring SRR (structure D), (e) smoothened square-shaped double ring SRR (structure E), (f) circular-shaped double ring SRR (structure F).

given schematically in Figure 2 on a microstrip transmission line loaded by four identical structure D resonators. Herein, the microstrip transmission line width w_f is set to 2.11 mm to provide 50 Ω line impedance. The ring gap $g = 0.5$ mm and one side length of the ring (outer diameter for the circular structures) $L = 4$ mm are constants. The SRR line width w, separation distance between inner and outer rings s (if exists), separation distance between SRR and feed line s_f, separation distance between two SRR structure along propagation direction S_{int} (if exists) are set as variables to investigate their effects on insertion loss. All structures in this study are constructed on 20 mm × 30 mm Arlon AD250 substrate having dielectric constant $\varepsilon_r = 2.5$, dielectric loss tangent $\tan\delta = 0.0018$, dielectric thickness $t_{sub} = 0.762$ mm, copper thickness $t_m = 0.035$ mm.

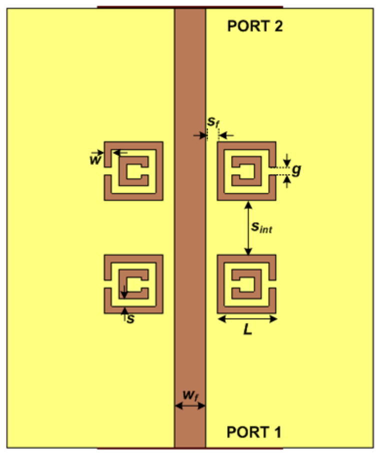

Figure 2: The design parameters on quadruple SRR loaded microstrip transmission line.

3. RESULTS

First of all, we investigate the effects of SRR geometry and SRR number on insertion loss (i.e., $|S_{21}|$ in dB). The computed results are presented in Figures 3, 4 and 5. We observe that the SRR geometry effects the location of the resonance frequency as we expected, hence all structures resonate at different frequencies. Moreover we observe higher insertion losses in circular resonator structures (i.e., in structures C and F in Figures 1, 2 and 3). In other words, square shaped structures promise better filtering performances (i.e., structures A, B, D and E in Figures 1, 2 and 3). Besides, increasing the number of rings from 1 to 4, decreases the insertion loss from −4.6 dB level to −15.8 dB level for structures A, B, D and E, on the other hand it decreases insertion loss from −3.8 dB level to −12 dB level for structures C and F. Among all, structure D provides lower resonance frequency although it has nearly the same physical dimensions among all. This reveals that structure D is the electrically smallest one.

In Figure 6, we investigate the effects of w on resonance frequency for transmission line loaded by quadruple structure D. The graph shows that increasing w increases the resonance frequency.

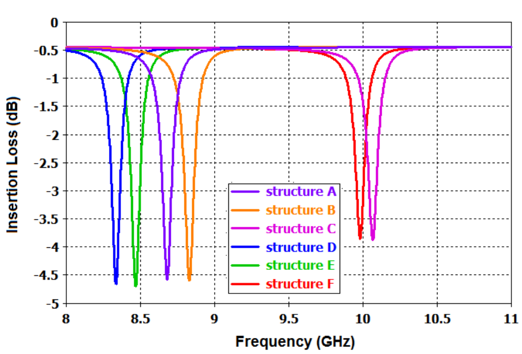

Figure 3: Insertion loss simulations for the transmission line loaded by single SRR type structures. $L = 4$ mm, $w = 0.5$ mm, $g = 0.5$ mm, $s = 0.5$ mm, $s_{int} = 3.71$ mm, $s_f = 0.8$ mm.

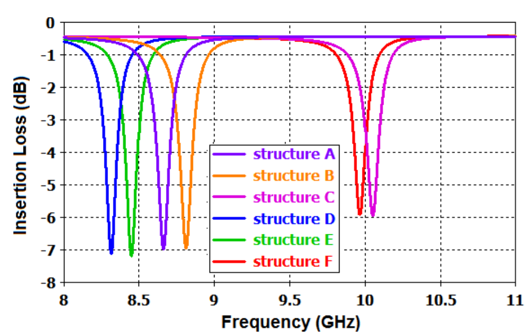

Figure 4: Insertion loss simulations for the transmission line loaded by double SRR type structures. $L = 4$ mm, $w = 0.5$ mm, $g = 0.5$ mm, $s = 0.5$ mm, $s_{int} = 3.71$ mm, $s_f = 0.8$ mm.

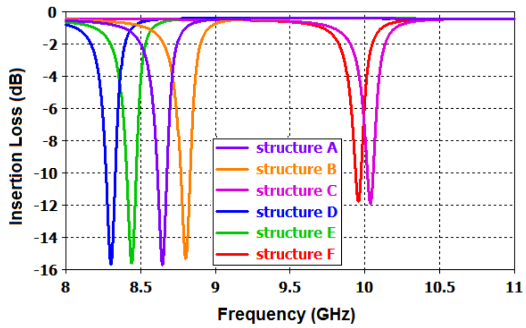

Figure 5: Insertion loss simulations for the transmission line loaded by quadruple SRR type structures. $L = 4\,\text{mm}$, $w = 0.5\,\text{mm}$, $g = 0.5\,\text{mm}$, $s = 0.5\,\text{mm}$, $s_{int} = 3.71\,\text{mm}$, $s_f = 0.8\,\text{mm}$.

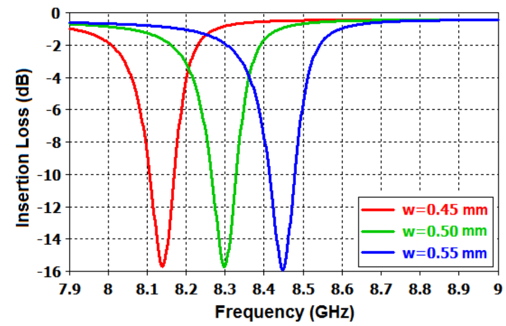

Figure 6: Insertion loss simulations for the transmission line loaded by quadruple structure D. $L = 4\,\text{mm}$, $g = 0.5\,\text{mm}$, $s = 0.5\,\text{mm}$, $s_{int} = 3.71\,\text{mm}$, $s_f = 0.8\,\text{mm}$ and w is variable.

Figure 7 shows the effects of gap orientation for transmission line loaded by quadruple SRR structures. These quadruple structures composed of structure D (i.e., angle $= 0°$, the red SRR given in the inset), structure D whose inner ring is rotated 90 degrees (i.e., angle $= 90°$, the green SRR given in the inset), structure D whose inner ring is rotated 180 degrees (i.e., angle $= 180°$, the blue SRR given in the inset). The red one has the lower resonance frequency hence it has the highest inter ring capacitances and the blue one has the highest resonance frequency hence it has the lowest inter ring capacitances.

Figure 9 shows the effects of inter element spacing s_{int} along the propagation direction for transmission line loaded by quadruple structure D. For this study, increasing s_{int} does not affect

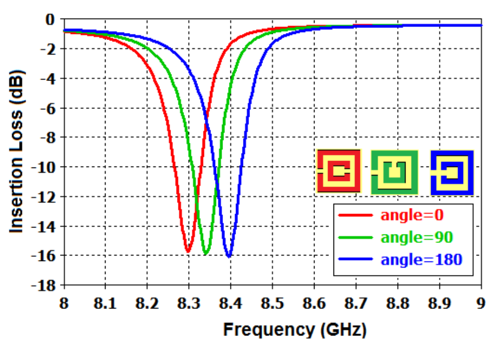

Figure 7: Insertion loss simulations for the transmission line loaded by quadruple structure D. $L = 4\,\text{mm}$, $w = 0.5\,\text{mm}$, $g = 0.5\,\text{mm}$, $s = 0.5\,\text{mm}$, $s_{int} = 3.71\,\text{mm}$, $s_f = 0.8\,\text{mm}$.

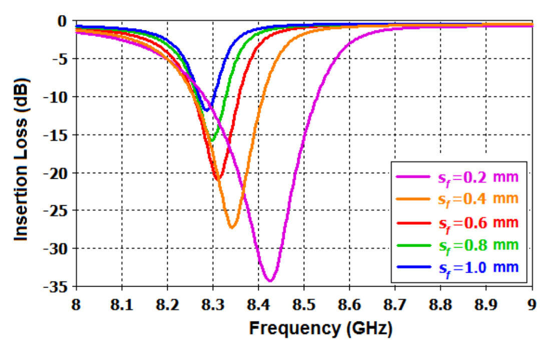

Figure 8: Insertion loss simulations for the transmission line loaded by quadruple structure D. $L = 4\,\text{mm}$, $w = 0.5\,\text{mm}$, $g = 0.5\,\text{mm}$, $s = 0.5\,\text{mm}$, $s_{int} = 3.71\,\text{mm}$, s_f is variable.

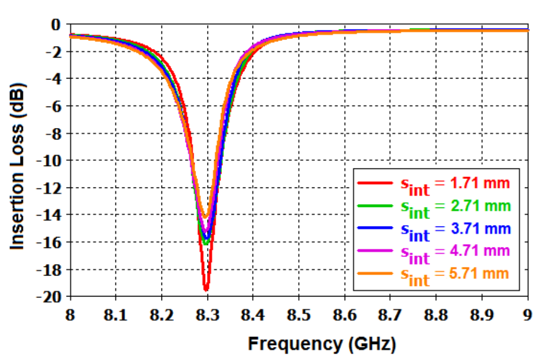

Figure 9: Insertion loss simulations for the transmission line loaded by quadruple structure D. $L = 4\,\text{mm}$, $w = 0.5\,\text{mm}$, $g = 0.5\,\text{mm}$, $s = 0.5\,\text{mm}$, $s_f = 0.8\,\text{mm}$, s_{int} is variable.

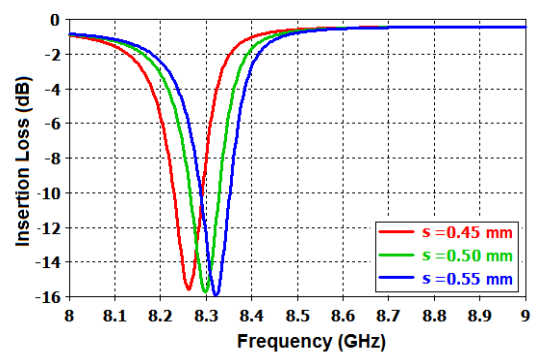

Figure 10: Insertion loss simulations for the transmission line loaded by quadruple structure D. $L = 4\,\text{mm}$, $w = 0.5\,\text{mm}$, $g = 0.5\,\text{mm}$, $s_f = 0.8\,\text{mm}$, $s_{int} = 3.71\,\text{mm}$, s is variable.

the location of the resonance frequency; however it increases the insertion loss.

Figure 10 shows the effects of inter ring spacing s along for transmission line loaded by quadruple structure D. The figure shows that increasing s increases the location of the resonance frequency since it lower the inter ring capacitance.

4. CONCLUSIONS

In this study, we investigated the electromagnetic behavior of microstrip transmission lines loaded by different SRR types and array topologies. We conclude that SRR loaded microstrip transmission line provides a band stop filtering effect, besides SRR geometry and number have effects on the location and the strength of the filter's resonance frequency, respectively. The electrically smallest structure under investigation was structure D, and the lowest insertion losses observed for square shaped structures. Increasing number of SRR structures, decreasing s_f and decreasing s_{int} decreased the insertion losses.

REFERENCES

1. Caloz, C. and T. Itoh, *Electromagnetic Metamaterials, Transmission Line Theory and Microwave Applications*, Wiley-IEEE Press, Hoboken, NJ, 2006.
2. Eleftheriades, G. V. and K. G. Balmain, *Negative-refraction Metamaterials: Fundamental Principles and Applications*, Wiley-IEEE Press, Hoboken, NJ, 2005.
3. Aznar, F., M. Gil, J. Bonache, J. García-García, and F. Martín, "Metamaterial transmission lines based on broad-side coupled spiral resonators," *Electronics Letters*, Vol. 43, No. 9, 2007.
4. García-García, J., F. Aznar, M. Gil, J. Bonache, and F. Martín, "Size reduction of SRRs for metamaterial and left handed media design," *PIERS Online*, Vol. 3, No. 3, 266–269, 2007.
5. García-García, J., F. Martín, F. Falcone, J. Bonache, J. D. Baena, I. Gil, E. Amat, T. Lopetegi, M. A. G. Laso, J. A. M. Iturmendi, M. Sorolla, and R. Marqués, "Microwave filters with improved stopband based on sub-wavelength resonators," *IEEE Transactions on Microwave Theory and Techniques*, Vol. 53, No. 6, 2005.
6. Withayachumnankul, W., K. Jaruwongrungsee, C. Fumeaux, and D. Abbott, "Metamaterial-inspired multichannel thin-film sensor", *IEEE Sensors Journal*, Vol. 12, No. 5, 1455–1458, 2012.
7. Lee, H.-J., J.-H. Lee, and H.-I. Jung, "A symmetric metamaterial element-based RF biosensor for rapid and label-free detection," *Applied Physics Letters*, Vol. 99, 163703, 2011.
8. Puantes, M., M. Maasch, M. Schüßler, and R. Jakoby, "Frequency multiplexed 2-dimensional sensor array based on split-ring resonators for organic tissue analysis," *IEEE Transactions on Microwave Theory and Techniques*, Vol. 60, No. 6, 2012.
9. Wiwatcharagoses, N., K. Y. Park, and P. Chahal, "Metamaterial-inspired miniaturized microwave sensing probes," *IEEE 62nd Electronic Components and Technology Conference (ECTC)*, 2106–2111, 2012.
10. Korucu, H. D. and E. Ekmekci, "Researches on metamaterial based dual-band microstrip band stop filter design," *İlk Bildiriler Konferansı*, 64–67, Ankara, Turkey, Jun. 2013.

Microwave Focusing by a Wire Medium

Joaquim J. Barroso[1], **Antônio Tomaz**[2], **Ugur C. Hasar**[3], **and Alberto J. Faro Orlando**[2]

[1]Instituto Nacional de Pesquisas Espaciais (INPE), São José dos Campos, SP, Brazil
[2]Instituto Tecnológico de Aeronáutica (ITA), São José dos Campos, SP, Brazil
[3]University of Gaziantep, Gaziantep 27310, Turkey

Abstract— Through numerical simulation, the present paper demonstrates the ability of a wire medium to focus microwave radiation in the 8–14 GHz frequency range. Microwave focusing is achieved in a small volume to produce localized energy dissipation processes and high-temperature gradients. The wire medium is implemented with 0.5-mm-diameter metallic wires symmetrically arranged in a square lattice with spacing constant of 10.0 mm.

1. INTRODUCTION

As a versatile electroheat method, microwave heating offers advantages over conventional heating because energy is directly transferred into the absorbing material without thermal conductivity delay and without passing through an interface [1, 2]. In this regard, the present paper demonstrates the ability of a wire medium to focus microwave radiation in the 8–14 GHz frequency range. Despite the considerable operating wavelength, microwave focusing is achieved in a small volume to produce localized energy dissipation processes and high-temperature gradients. Such a structure allows the realization of a refracting medium with refractive index less than unity, thus being referred to as a phase-advance dielectric. The idea that near-zero refractive index media could be artificially realized from metals was originated by Koch in 1948 [3], even before the delay dielectrics [4]. The concept of artificial dielectric has later expanded on by pioneering researchers, with most of the work occurring in the 1950s [5–7]. Renewed interest in wire media was sparked with the advent of materials in the 2000s, leading to a range of new applications such as subwavelength imaging in the visible spectrum, transport of near-field images, and directive emission [8–10].

2. RESULTS AND DISCUSSION

The wire medium is implemented with 0.5-mm-diameter metallic wires symmetrically arranged in a square lattice (spacing constant of 10.0 mm) to build a rectangular parallelepiped 17-wire long and 15-wire wide; then a square of 5×5 wires is removed from the downstream edge to form a reentrant slab symmetric along its length, as shown in Fig. 1. By using the finite-integration-technique software CST MWS [11], full-wave electromagnetic simulation is carried out on the rectangular bounding box, with boundary conditions the top and bottom faces set as perfectly conducting metallic planes, while the lateral walls are magnetic surfaces. The upstream red colored end face [Fig. 1(a)], is used as an input port from which a normally incident plane wave is launched into the medium with the electric field polarized along the wires. The simulated return loss (S_{11} scattering parameter) is shown in Fig. 2, where 16 sharp dips appear in the first pass band. Such peaks are related to the 16 resonant eigenmodes supported by the periodic medium thus constructed with 17 rows. Above the pass band there extends a Bragg stopband starting from 15 GHz, the frequency at which its half wavelength is just the periodic distance $p = 10.0$ mm. In the second pass band, above the band gap ($\lambda/2 < p$), the wire medium behaves as a photonic crystal, where diffraction

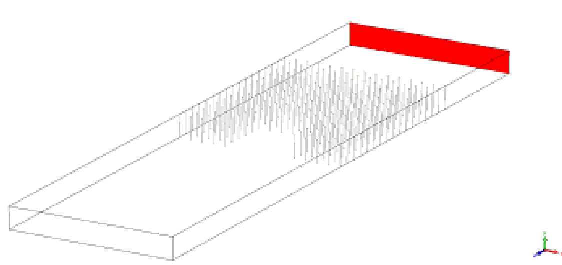

Figure 1: A perspective view of the wire medium.

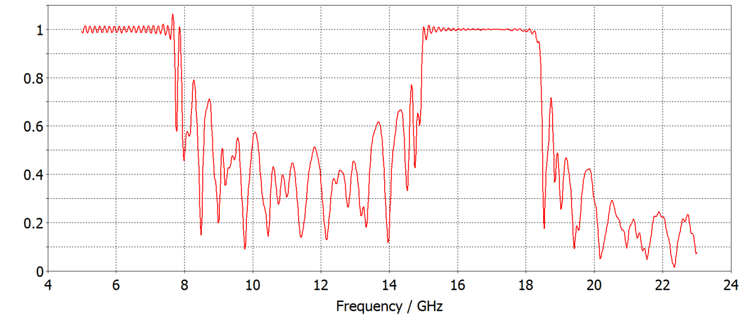

Figure 2: The return loss (scattering S_{11} parameter) of the wire medium at 8.45 GHz.

and scattering phenomena dominate, and as such the periodic structure cannot be characterized by an effective refractive index.

On the other hand, in the first passband ($\lambda/2 > p$), the propagating fields see the structure as a homogeneous and refractive medium. In fact, at 9.77 GHz we see in Fig. 3 that the parallel wavefronts of the input plane wave converge to a focal line after passing through the reentrant region in the wire medium. Other frequencies corresponding to the resonance dips in Fig. 2 would give similar electric-field patterns. Moreover, the resonance frequency can be tuned by removing or adding extra rows of wires. For instance, by adding two short rows of five wires on the leading edges of the structure, the third dip from the left at 8.49 GHz in Fig. 2 shifts down to 8.45 GHz. In the corresponding electric-field pattern shown in Fig. 4, we see that the incoming plane wave is focused on a circular spot, thus demonstrating the focusing action of the wire medium designed. By reciprocity, a source line placed in the focal spot will create an outgoing plane wave propagating outward through the wire medium.

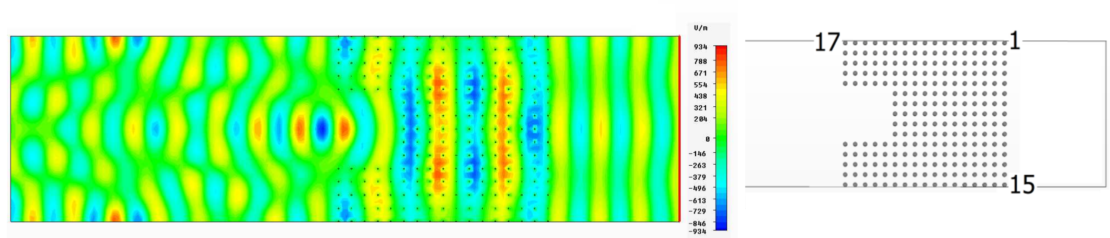

Figure 3: Top view of the electric-field pattern at 9.77 GHz.

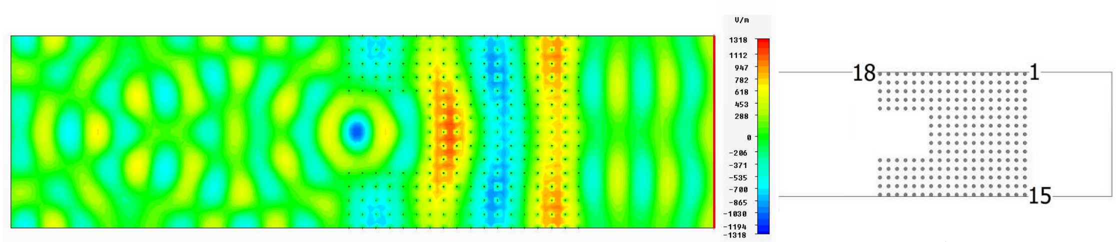

(a) (b)

Figure 4: Electric-field pattern at 8.45 GHz. (b) the corresponding wire arrangement.

As an indicator of the electromagnetic response of a material, the refractive index, n, relates to the relative values of the electrical permittivity, ε, and magnetic permeability, μ, by $n = \sqrt{\mu\varepsilon}$. These two parameters quantify the degree of the responses of the characteristic motions of the electrons in the metallic wires. The permeability quantifies how much the electrons respond to the magnetic field, while ε describes the electrons' degree of response to the electric field component of the driving field. Since the incoming electric field is polarized parallel to the thin wires, the accompanying magnetic is practically undisturbed, and thus $\mu \approx 1$. On the other hand, in the 8–14 GHz range, which is above the plasmonic frequency of the free electrons inside the wires, the electrons resist the push of the electric force and move in the opposite direction of the electric field, such that the motion of the electrons goes out of phase with respect to the oscillating electric field, thus yielding $\varepsilon < 1$. Therefore the resultant electromagnetic response of the wire medium produces $n < 1$, meaning that the structure is a phase-advance medium, in which the wave phase velocity is greater than that in free space.

This heuristic discussion is pictured is Fig. 5. The incoming phase front AD upon reaching the reentrant side of the wire structure is separated in three parts, with the central segment BC moving more slowly than the segments AB and CD which propagate faster across the wires. The net lens effect is seen by the three separated branches which form, albeit segmented, a concave cylindrical surface.

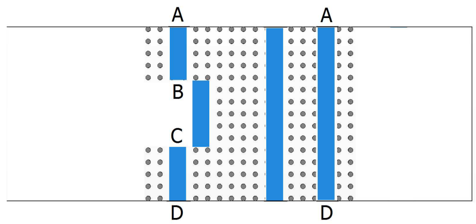

Figure 5: Wave front transformation in the wire medium.

3. CONCLUSION

With the electric field of the impinging wave being polarized along the metallic wires there is no charge accumulation on the wires, implying that spatial dispersion effects are negligible and therefore a local model can be used for describing the refractive properties of the medium. The fundamental mechanism underlying the interaction of the wires with the electromagnetic wave is that the electrons moving in the metallic wire uses up some energy of the wave, thus affecting how the wave propagates across the wires.

Because the lattice constant of the periodic structure is significantly smaller than the usable wavelength, the wire medium discussed here is regarded as large-scale model of a homogeneous dielectric slab, which acts as phase front transformer by converting an incoming plane wave into a cylindrical wave, and also by redirecting the incoming energy toward a focal spot. The results demonstrate the ability of the wire medium in controlling plane-wave phase fronts as desired. Regarding its implementation as a microwave applicator, the structure offers manufacturing flexibility to specified variations in the refractive index by easily altering the geometric parameters and dimensions of the periodic structure.

REFERENCES

1. Metaxas, A. C., *Foundations of Electroheat*, Wiley, New York, 1966.
2. Rassaei, L. and F. Marken, "Focusing microwaves at electrodes. A review: Localised microwave effects at electrochemical sensors," *Chemistry Today*, Vol. 27, 14–16, Jul.–Aug. 2009.
3. Kock, W. E., "Metallic delay lenses," *Bell Tech. J.*, Vol. 27, 58–82, 1948.
4. Brown, J., "Lens antennas," Chap. 18, *Antenna Theory, Part 2*, R. E. Collin and F. J. Zucker, Eds., McGraw-Hill, New York, 1969.
5. Brown, J., "Artificial dielectrics having refractive indices less than unity," *Proc. IEE,* Vol. 100, 51–62, London, 1953.
6. Cohn, S. B., "Experimental verification of the metal-strip delay-lens theory," *J. Appl. Phys.*, Vol. 24, 839–841, 1953.
7. Rotman, W., "Plasma simulation by artificial dielectrics and parallel-plate media," *IRE Trans. Antennas Propag.*, Vol. 1, 82–95, 1962.
8. Hudlicka, M., J. Machac, and I. S. Nefedov, "A triple wire medium as an anisotropic negative permittivity metamaterial, *Progress In Electromagnetics Research*, Vol. 65, 233–246, 2006.
9. Simovski, C. R., P. A. Belov, A. V. Atrashchenko, and Y. S. Kivshar, "Wire metamaterials: Physics and applications," *Adv. Mater.*, Vol. 24, 4229–4248, Aug. 2012.
10. Barroso, J. J., A. Tomaz, and U. C. Hasar, "Wire grid metamaterial for directive emission," *SBMO/IEEE MTT-S International Microwave and Optoelectronics Conference*, Rio de Janeiro, Aug. 2013.
11. CST Microwave Studio, Version 2005, CST GmbH, Darmstadt, Germany, 2005.

Novel Rectenna Using Modified Ground Plane for RF Energy Harvesting

Jung-Ick Moon, In-Kui Cho, Seong-Min Kim, Soon-Ik Jeon, and Jae Ick Choi
Radio Technology Research Department
Electronics and Telecommunications Research Institute (ETRI), Korea

Abstract— In this paper, a novel antenna using modified ground plane for RF energy harvesting was proposed. This antenna is composed of the main radiator and the modified ground plane. The main radiator designed as a dipole type covers WCDMA-band in Korea and the ground plane is used to harvest the RF energy from the main radiators, which don't disturb the main radiator's electrical performance. The ground plane has a rectangular structure with vertical metallic walls in order to suppress and harvest the back-lobe of the antenna. The amount of the harvested energy from this rectenna is approximately 1% of the originally radiated power. The simulated gain of the proposed antenna is almost same with that of the printed dipole without the metallic walls. And the back-lobe of the proposed rectenna was reduced to 7.0 dB.

1. INTRODUCTION

Energy harvesting is the process of accumulating and storing ambient energy from various sources in surroundings to energy storage components. Although many researchers have an effort to increase the receiving RF power, the RF harvested energy from the base station and repeater for mobile communications is less than $0.1\,\mu\mathrm{W/cm}^2$ [1, 2]. This value shows miniscule amounts, about from a 1,000 to 10,000 of other ambient energy sources. Therefore more reasonable solution to harvest RF energy should be needed. Generally, the rectenna to receive RF energy in free space was near and the line of sight of the antenna transmitting high power. In this case the resonant frequencies of them are very similar to each other. Due to the same frequency, the strong coupling is happened and has much effect on the performance of the antenna. In this paper, a novel rectenna design using the antenna with the modified ground plane to harvest RF energy is presented and its performance is verified with the simulated results.

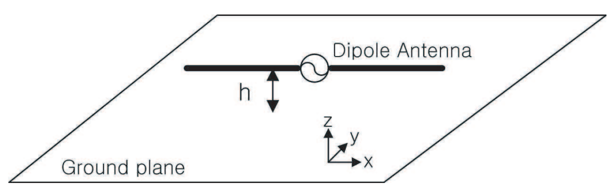

Figure 1: High gain dipole antenna with a rectangular ground plane.

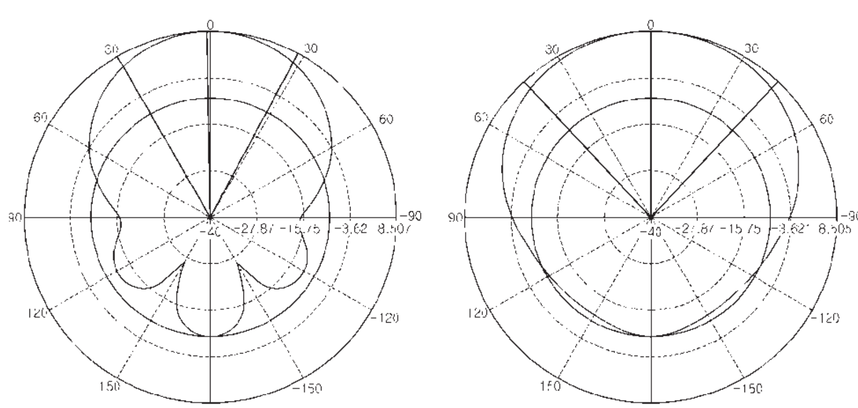

(a) (b)

Figure 2: The radiation gains and patterns of the high gain dipole antenna shown in Figure 1. (a) E-plane. (b) H-plane.

2. DESIGN OF THE NOVEL RECTENNA FOR RF ENERGY HARVESTING

Figures 1 and 2 show a dipole antenna with the rectangular ground plane and the simulated performances. The dimensions and height, h, of the ground plane are $15 \times 15\,\mathrm{cm}^2$ with $h = 30\,\mathrm{mm}$. As shown in Figure 2, the ground plane was used to reduce the back-lobe and increase the gain of antenna. The gain and FBR (Front Back Ratio) of antenna are about 8.5 dBi and 17.2 dB, respectively. And this antenna covers the range 2110 MHz to 2170 MHz for WCDMA-band in Korea.

In order to harvest RF energy from this antenna, a conventional technique such as the additional antennas or parasitic patches with the similar resonance frequency can be used. However, it is possible that this technique has bad effect on the performance of the origin antenna. Therefore a novel design with non-resonant structures should be needed.

Figure 3 shows the novel rectenna design with the modified ground plane. Even though the vertically metallic walls on the ground plane to reduce the back-lobe were already presented [3, 4], the previous metallic walls were on the edge of the ground plane and had no the harvesting function. As shown in Figure 3, the vertically metallic grounded walls with coaxial cable are added to suppress

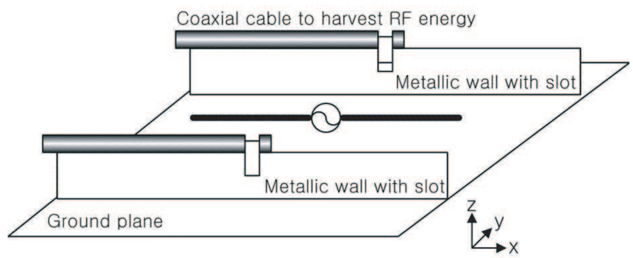

Figure 3: The proposed rectenna structure.

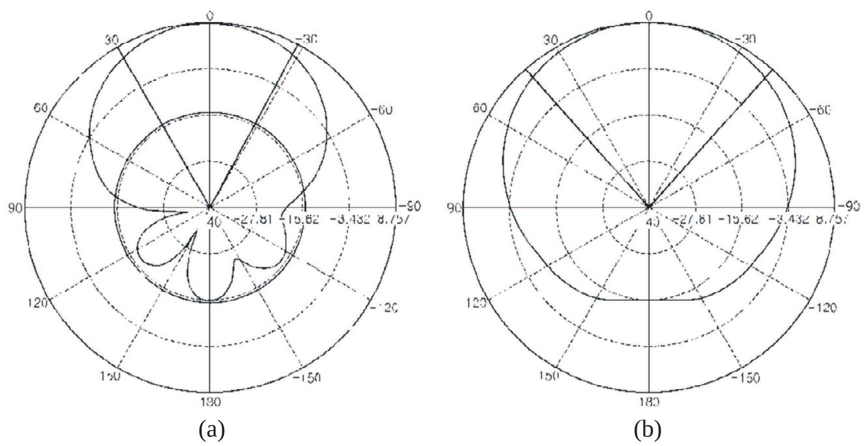

Figure 4: The radiation patterns of the high gain dipole antenna shown in Figure 1. (a) E-plane. (b) H-plane.

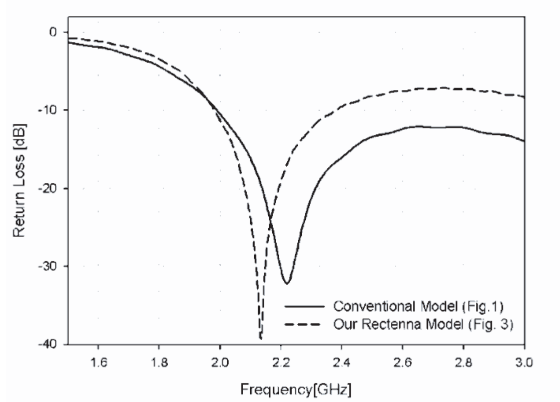

Figure 5: The comparison between the conventional antenna model and the proposed rectenna model.

and harvest the back-lobe of antenna which has little effect on the forward radiation performance. The coupling between the main radiator and the metallic wall is about 20 dB and can be controlled by the locations of the slot and walls. Figure 4 shows the radiation gains and patterns of the proposed rectenna. As shown in Figure 4, the gain and FBF of the proposed model is much improved. Figure 5 compares the return loss of the origin antenna and the proposed rectenna. And Table 1 presents the summary of the comparison between the conventional model and our model.

Table 1: The summary of the performance.

	Conventional Model	Our Rectenna Model
Frequency Range [MHz] (Return loss < -15 dB)	$2080 \sim 2430$	$2040 \sim 2240$
Radiation Gain [dBi]	8.5	8.75
FBR (Front Back Ratio) [dB]	17.2	24.0
Beamwidth (E-plane, H-plane) [deg]	58.0 (E), 86.7 (H)	57.7 (E), 84.1 (H)

3. CONCLUSIONS

This paper presented the design and analysis of a novel antenna using modified ground plane that is effective for RF energy harvest. The metallic walls with the slot and coaxial cables were used to suppress and harvest the back-lobe of the origin antenna. Using the proposed harvesting technique, the back-lobe of the rectenna was reduced to 7.0 dB and the gain of that was improved. These results show that this proposed rectenna is useful for RF energy harvest applications. In addition, it would be very useful in practical and efficient antenna design.

ACKNOWLEDGMENT

This research was funded by the MSIP (Ministry of Science, ICT & Future Planning), Korea in the ICT R&D Program 2013.

REFERENCES

1. Fiorini, P., "Micropower energy scavenging," *Solid-State Circuits Conference*, 2008.
2. Heo, S., "Efficient maximum power tracking of energy harvesting using a μ controller for power savings," *ETRI Journal*, Vol. 33, No. 6, Dec. 2011.
3. Siu, L. and K.-M. Luk, "Unidirectional antenna with loaded dielectric substrate," *IEEE Antenna and Wireless Propagation Letters*, Vol. 7, 2008.
4. Wong, T. P. and K. M. Luk, "A wide bandwidth and wide beamwidth CDMA/GSM base station antenna array with low backlobe radiation," *IEEE Transactions on Vehicular Technology*, Vol. 54, No. 3, 903–909, 2005.

A High-efficiency Matching Technique for Low Power Levels in RF Harvesting

I. Anchustegui-Echearte[1], **D. Jiménez-López**[1], **M. Gasulla**[1], **F. Giuppi**[2], **and A. Georgiadis**[2]

[1]Department of Electronic Engineering, Universitat Politècnica de Catalunya, Catalonia, Spain
[2]Centre Tecnològic de Telecomunicacions de Catalunya, Catalonia, Spain

Abstract— Radiofrequency (RF) energy can be harvested in order to power autonomous sensors either from the surrounding environment or from dedicated sources. A conventional RF harvester is mainly composed by an antenna, a matching network and a rectifier. At low power levels, e.g., -10 dBm and below, the corresponding voltage amplitude at the antenna is low and comparable to the voltage drop of the diodes used in the rectifier. In order to boost the voltage at the rectifier input and thus the rectifier efficiency, an L-network optimized for an input power of -10 dBm at 868 MHz is proposed in this work. As for the rectifier, a half-wave rectifier with a single zero-bias Schottky diode (HSMS2850) was selected. First, a theoretical analysis was performed followed by simulations with ADS (Harmonic Balance). Simulations show efficiencies of 75% for an input power of -10 dBm with ideal components but using the actual model of the diode rectifier. The incorporation of the PCB layout effects and the actual components decreases the efficiency to below 50%. Finally, a PCB implementation was performed using a 0.5 pF capacitor and a 27 nH inductor for the L network. The input power was generated by an RF generator. The RF-to-DC efficiency was of 45% at 868 MHz with an optimum load of 2.5 kΩ. Efficiencies of 34.5% and 22.5% were achieved at -15 dBm and -20 dBm, respectively.

1. INTRODUCTION

The possibility of powering low power devices (e.g., RFID tags/sensors or autonomous sensors) from electromagnetic waves has been widely proposed in the literature [1–13]. Radiofrequency (RF) energy can be harvested either from the surrounding environment or from dedicated sources. Fig. 1 shows the main building blocks of a conventional RF energy harvester, which is composed of an antenna, an impedance matching block, and a rectifier.

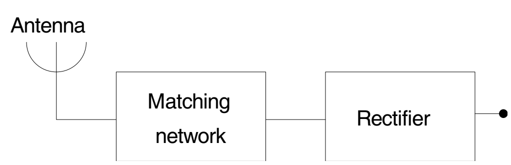

Figure 1: A conventional RF energy harvester.

An antenna can be roughly modelled as an AC voltage source (v_s) with a series impedance. The series impedance basically comprises a radiation resistance (R_s), a loss resistance and a reactive part. The amplitude of the voltage generated on the antenna is given by [6]

$$\hat{v}_\mathrm{s} = 2\sqrt{2R_\mathrm{s}P_\mathrm{AV}} \tag{1}$$

where P_AV is the available power at the antenna. As can be deduced, lower values of P_AV lead to lower values of v_s.

Rectifier circuits provide a dc output voltage. Several topologies have been reported such as a single series- or shunt-mounted diode [3, 4, 8, 9, 13], a bridge rectifier [3] and single or multistage voltage doubler structures [2, 5–7, 10–13]. The input impedance of the rectifier can be modelled as a capacitance (C_in) in parallel with a resistance (R_in) [1, 6, 7, 11–13]. Accurate expressions of the input impedance are not straightforward [11]. As an approximation, C_in, apart from the parasitic capacitances introduced from the layout, is mainly given by the addition of the parasitic capacitances of the diodes [6, 7] whereas R_in is proportional to the output load [6, 13].

The objective of the impedance matching network is to match the input impedance of the rectifier to the antenna impedance so that maximum power may be transferred. In this condition, the antenna sees at its output the complex conjugate of the antenna impedance. Fig. 2 shows three different types of matching networks where v_s and R_s model the antenna and R_{in}-C_{in} model the input impedance of the rectifier plus the ensuing load (e.g., autonomous sensor) to be powered.

In Fig. 2(a) a shunt inductor (L_{shunt}) is placed in parallel with the input of the rectifier, whose value is given by

$$L_{shunt} = \frac{1}{\omega_r^2 \cdot C_{in}} \tag{2}$$

whereby ω_r is the angular resonant frequency. A shunt inductor is used in [11, 13]. Maximum power will be transferred for $R_{in} = R_s$, being the voltage at the rectifier input (v_{in}) half v_s. From (1), low values of P_{AV} (e.g., < 0 dBm) lead to low values of v_s and thus of v_{in}. Thus, due to the voltage drop of the diodes the rectifier efficiency will be low. This issue can be partialy solved by using antennas with higher radiation resistance (e.g., a folded dipole has a radiation resistance of roughly 300 Ω) which, from (1), lead to a higher value of v_{in}. Another approach is to use an L-matching network, an example of which is shown in Fig. 2(b). Here, a voltage boosting in v_{in} can be achieved whenever using a relative high-Q network, which results in higher efficiencies of the rectifier [10–12]. These types of matching networks have been used, for example, in [6, 7, 12]. In order to achieve the same effect, transformers have also been proposed (Fig. 2(c)), as in [1].

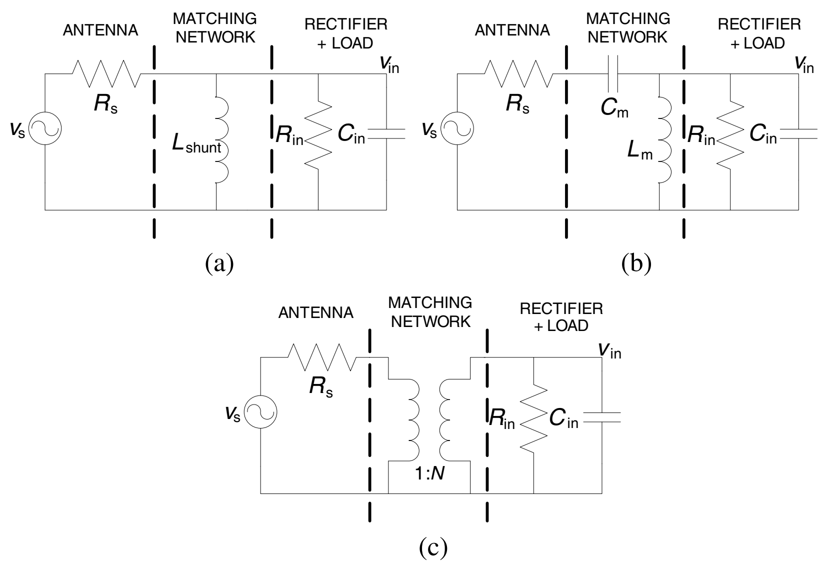

Figure 2: Three types of matching networks: (a) shunt inductor, (b) L network, (c) transformer.

In this work, in order to achieve high efficiencies at low RF input powers, the use of the matching network of Fig. 2(b) is proposed. A series-configured Schottky diode (HSMS2850, Avago Technologies) with a low threshold voltage will be used for the rectifier. The circuit will be optimized for an input power of −10 dBm at a resonant frequency of 868 MHz (ISM band).

2. L-MATCHING NETWORK

For the circuit of Fig. 2(b), the required values of the matching network are given by

$$C_m = \frac{1}{\omega_r R_s}\sqrt{\frac{R_s}{R_{in}-R_s}} \tag{3}$$

$$L_m = \frac{R_{in}}{\omega_r}\frac{1}{\omega_r R_{in} C_{in} + \frac{1}{\sqrt{\frac{R_s}{R_{in}-R_s}}}} \tag{4}$$

being the voltage gain [1, 12]

$$G = \frac{v_{in}}{v_s} = \frac{1}{2} \cdot \sqrt{\frac{R_{in}}{R_s}} \tag{5}$$

Thus, for $R_{\rm in} > R_{\rm s}$, the voltage will be boosted. The drawback is that the circuit becomes more selective since the circuit Q is given by [7]

$$Q = \sqrt{\frac{R_{\rm in}}{R_{\rm s}} - 1} \tag{6}$$

In order to maximize the power efficiency, the following procedure will be followed. First, a suitable gain will be selected in order to achieve a relative high value of $v_{\rm in}$. Then, from (5), and assuming a given value of $R_{\rm s}$, the value of $R_{\rm in}$ will be obtained. Finally, for given values of $\omega_{\rm r}$ and $C_{\rm in}$, the component values of the matching network will be obtained from (3) and (4).

3. SIMULATIONS AND EXPERIMENTAL RESULTS

Figure 3 shows the circuit schematic of the simulated circuit. Simulations were carried out using the Harmonic Balance module of ADS software (Agilent). As can be seen, the antenna is modelled by $v_{\rm s}$ and $R_{\rm s}$ and ideal lumped components were used for rest with the exception of the diode, where the actual model has been used. The output load is composed by a filter capacitor of 1 nF ($C_{\rm Load}$) in parallel with a resistive load ($R_{\rm Load}$).

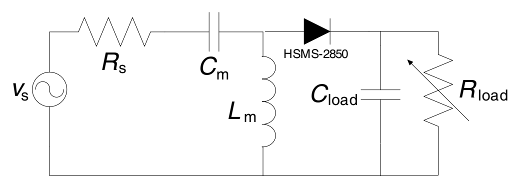

Figure 3: Circuit schematic with ADS of the RF harvester.

The design was optimized for $P_{\rm AV} = -10\,\text{dBm}$ at 868 MHz (ISM band) and $R_{\rm s} = 50$. From (1), $\hat{v}_{\rm s} = 0.2\,\text{V}$. Then, in order to boost $v_{\rm in}$ to a suitable voltage, we selected $G = 5$, which leads to $\hat{v}_{\rm in} = 1\,\text{V}$, high enough compared to the voltage drop of the diode (0.15 V for a forward current of 0.1 mA). Thus, from (5), $R_{\rm in} = 5\,\text{k}\Omega$ will be required. From the manufacturer data, the diode presents a parasitic capacitance of 0.18 pF, which for this circuit will be assumed as $C_{\rm in}$. Thus, from (3) and (4) the following values for the L-matching network are obtained: $C_{\rm m} = 0.368\,\text{pF}$ and $L_{\rm m} = 61.7\,\text{nH}$.

As for $L_{\rm m}$ and $R_{\rm Load}$, a parametric sweep was performed in order to find the best performance in terms of efficiency (η), where

$$\eta = \frac{P_{\rm Load}}{P_{\rm AV}} \tag{7}$$

being $P_{\rm Load}$ the power dissipated at $R_{\rm Load}$. Fig. 4 shows the results where a sweep of $L_{\rm m}$ from 55 nH to 65 nH with steps of 1 nH was performed. A maximum efficiency of nearly 75% was found for $L_{\rm m} = 60\,\text{nH}$ and $R_{\rm Load} = 8.5\,\text{k}\Omega$. The value of $L_{\rm m}$ nearly matches that found theoretically. On the other hand, as the value of $R_{\rm Load}$ directly influences the equivalent resistance $R_{\rm in}$, an optimum value is also found. Techniques for automatically controlling the value of $R_{\rm in}$ have been presented in [8] but are outside the scope of this paper.

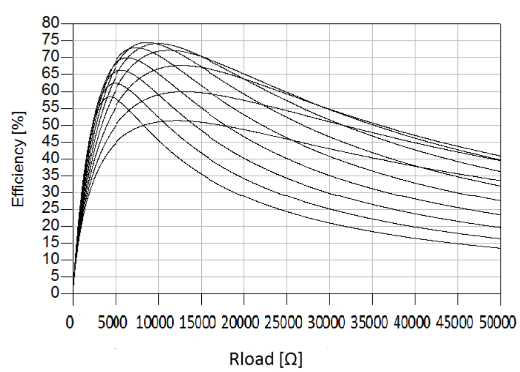

Figure 4: Efficiency versus $L_{\rm m}$ and $R_{\rm Load}$ with ideal lumped components.

Then, a FR4 PCB was designed (Fig. 5) and the S parameters corresponding to the layout were incoporated into the simulation. Commercial components were also added. As for C_{Load}, a capacitor of value 1 nF (ATC) was selected. As for L_{m} and C_{m}, a trial and error procedure was followed, starting from the values found before, in order to achieve the highest efficiency. Finally, $C_{\mathrm{m}} = 0.5$ pF (AVX) and $L_{\mathrm{m}} = 27$ nH (Coilcraft) were selected. Fig. 6 shows the simulated efficiency versus R_{Load}, where a maximum efficiency of 48% was achieved for $R_{\mathrm{Load}} = 3.1\,\mathrm{k}\Omega$.

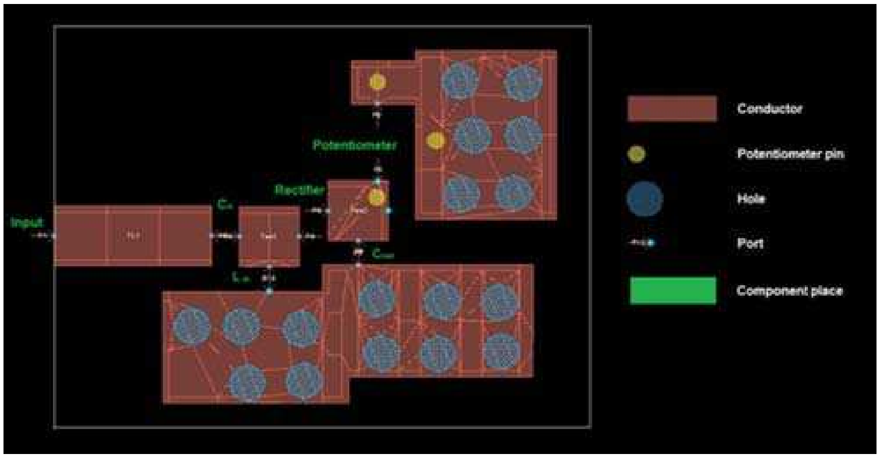

Figure 5: PCB layout.

The designed circuit was implemented using a potentiometer for R_{Load}, in order to find out the optimum load. An RF signal generator was used at the input in order to emulate the antenna. Fig. 7 shows the results for an input power of −10 dBm, where an efficiency of 45% was achieved for a load of 2.5 kΩ. So, experimental results largely agree with simulations. Bandwidth (half-power) was found to be 122 MHz. Efficiency drecreased to 34.5% and 22.5% at −15 dBm and −20 dBm, respectively. A fair comparison with other works is rather difficult but measured efficiencies are among the highest achieved in the literature at that power levels.

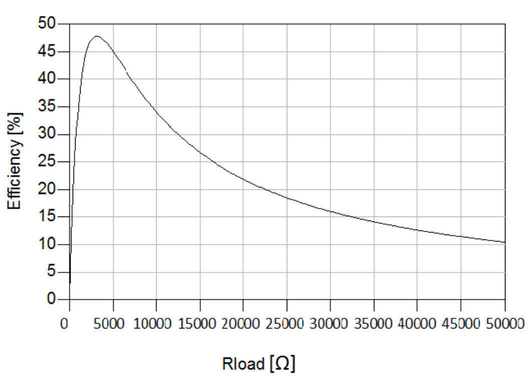

Figure 6: Efficiency vs R_{Load} with commercial components and layout effects.

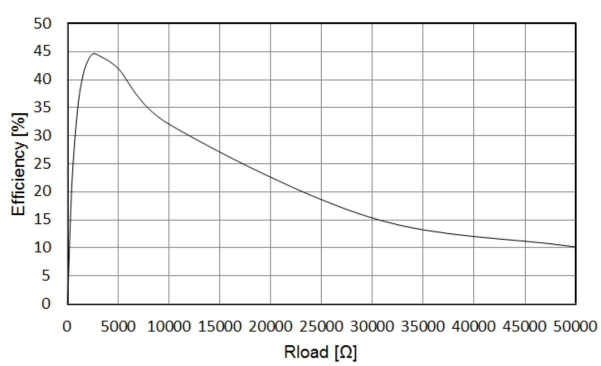

Figure 7: Measured efficiency vs R_{Load}.

4. CONCLUSIONS

A matching technique using a simple L-network has been proposed in order to boost the efficiency of RF harvesters at low power levels. A theoretical approach in order to find out suitable values of the capacitance and inductance of the matching network has been presented. Simulations have shown efficiencies of 75% for an input power of −10 dBm with ideal components but using the actual model of the diode rectifier. The incorporation of the PCB layout effects and the actual components decreases the efficiency to below 50%. Experimental results largely agree with simulations showing an efficiency of 45% at −10 dBm. Efficiency decreases to 34.5% and 22.5% at −15 dBm and −20 dBm, respectively.

ACKNOWLEDGMENT

The work of I. Anchustegui-Echearte, D. Jiménez-López and M. Gasulla was supported by the Spanish Ministry of Economy and Competitivity under Project TEC2011-27397. The work of A. Georgiadis and F. Giuppi was supported by the Spanish Ministry of Economy and Competitivity under Project TEC2012-39143 and by EU Marie Curie project FP7-PEOPLE-2009-IAPP 251557.

REFERENCES

1. Soltani, H. N. and F. Yuan, "A high-gain power-matching technique for efficient radio-frequency power harvest of passive wireless microsystems," *IEEE Trans. Circuits Syst. I*, Vol. 57, No. 10, 2685–2695, 2010.
2. Nintanavongsa, P., U. Muncuk, D. R. Lewis, and K. R. Chowdhury, "Design optimization and implementation for RF energy harvesting circuits," *IEEE J. Emerg. Sel. Topic Circuits Syst.*, Vol. 2, No. 1, 24–33, 2012.
3. Marian, V., B. Allard, C. Vollaire, and J. Verdier, "Strategy for microwave energy harvesting from ambient field or a feeding source," *IEEE Trans. Power Electron.*, Vol. 27, No. 11, 4481–4491, 2012.
4. Pinuela, M., P. D. Mitcheson, and S. Lucyszyn, "Ambient RF energy harvesting in urban and semi-urban environments," *IEEE Trans. Microw. Theory Techn.*, Vol. 61, No. 7, 2715–2726, 2013.
5. Georgiadis, A., G. Andia, and A. Collado, "Rectenna design and optimization using reciprocity theory and harmonic balance analysis for electromagnetic (EM) energy harvesting," *IEEE Antennas Wireless Propag. Lett.*, Vol. 9, 444–446, 2010.
6. Curty, J. P., N. Joehl, F. Krummenacher, C. Dehollaini, and M. J. Declercq, "A model for μ-power rectifier analysis and design," *IEEE Trans. Circuits Syst. I, Reg. Papers*, Vol. 52, No. 12, 2771–2779, 2005.
7. De Vita, G. and G. Iannaccone, "Design criteria for the RF section of UHF and microwave passive RFID transponders," *IEEE Trans. Microw. Theory Techn.*, Vol. 53, No. 9, 2978–2990, 2005.
8. Paing, T., J. Shin, R. Zane, and Z. Popovic, "Resistor emulation approach to low-power RF energy harvesting," *IEEE Trans. Power Electron.*, Vol. 23, No. 3, 1494–1501, 2008.
9. Takhedmit, H., L. Cirio, S. Bellal, D. Delcroix, and O. Picon, "Compact and efficient 2.45 GHz circularly polarised shorted ring-slot rectenna," *Electron. Lett.*, Vol. 48, No. 5, 253–254, 2012.
10. Le, T., K. Mayaram, and T. Fiez, "Efficient far-field radio frequency energy harvesting for passively powered sensor networks," *IEEE J. Solid-State Circuits*, Vol. 43, No. 5, 1287–1302, 2008.
11. Barnett, R. E., J. Liu, and S. Lazar, "A RF to DC voltage conversion model for multi-stage rectifiers in UHF RFID transponders," *IEEE J. Solid-State Circuits*, Vol. 44, No. 2, 354–370, 2009.
12. Shameli, A., A. Safarian, A. Rofougaran, M. Rofougaran, and F. De Flaviis, "Power harvester design for passive UHF RFID tag using a voltage boosting technique," *IEEE Trans. Microw Theory Techn.*, Vol. 55, No. 6, 1089–1097, 2007.
13. Penella-López, M. T. and M. Gasulla-Forner, "Radiofrequency energy harvesting," *Powering Autonomous Sensors*, 125–147, Springer, Dordretch, 2011.

Phase Characterization of X-band Minkowski Reflectarray Antennas Using 3-D CST Microwave Studio-based Neural Network Model Included Dielectric Properties

Selahattin Nesil[1], **Filiz Güneş**[2], **and Salih Demirel**[2]

[1]Department of Electrical and Electronics Engineering, Fatih University, Istanbul, Turkey
[2]Department of Electronics and Communication Engineering
Yıldız Technical University, Istanbul, Turkey

Abstract— This paper presents a complete MLP NN model including the dielectric property ε_r of the substrate is built to be used in both the design and performance analysis of the Minkowski RAs for the X-band applications. For this purpose, 3-D simulations by Computer Simulation Technology Microwave Studio (CST) are generated from Minkowski radiating element placed at the end of a standard X-band waveguide, by varying the geometrical parameters of the patch for each substrate $(\varepsilon_r - h)$ at each operation frequency f within the defined input domain. Thus, a data set is composed. After the training and validation data sets are determined, the MLP NN with the Levenberg-Marquardt algorithm is applied to the actual data. In the final stage, the reflection phase characterization of the MLP ANN model for a Minkowski patch is presented as the numerous graphics depicting the some variations of the geometry parameters and substrate parameters $(\varepsilon_r - h)$ as compared with analysis of the 3-D EM simulator CST and interpreted in terms of design parameters.

1. INTRODUCTION

Modern wireless communication system requires low profile, light weight, high gain, and simple structure antennas to assure reliability, mobility, and high efficiency characteristics. Microstrip reflectarray (RA) antenna satisfies all of these requirements. Thus, printed microstrip reflectarray antennas may be accepted as a fairly new antenna type. These antennas provide all of the advantages of printed circuit technology. In addition, they do not require any complicated feeding network. The flat-plate microstrip reflectarray offers advantage of profile size reduction as compared to its counterpart parabolic reflector. The limitations of microstrip RA antennas are narrow frequency band and disability to operate at high power levels of waveguide, coaxial line or even strip line. Therefore, the challenge in microstrip RA antenna design is to increase the bandwidth and gain that necessitates the design optimization of the unit element together with the substrate The phasing method using variable size patches is a preferable choice in many designs due to its simplicity. To meet the larger phasing range on a single layer substrate, the novel, complicated patch configurations are needed to be worked in which the structure to be optimized presents a lot of degrees of freedom and all concur to the performances of the whole antenna [1]. Since a 3-D EM simulator is very inefficient to be used within an optimization procedure, the accurate and rapid models are desperately needed in the design optimization of the reflectarrays. In recent years, Multilayer Perceptron (MLP) type of Artificial Neural Network (ANN) has been used in the modeling of microstrip (RA) [2]. Our research group has worked with the Minkowski shape [3, 4] which is from the 1st iteration of fractals and the Minkowski radiator is shown to have an optimum phasing characteristic with the fairly large linear region and easy fabrication.

In this paper, the analysis stage of the reflection behavior for a reflectarray element has been briefly summarized Thus the reflection phase of an independent Minkowski element has been established as a highly nonlinear function within the continuous domain of the element geometry and substrate parameters $(\varepsilon_r - h)$ in a defined bandwidth centered the resonant frequency (11 GHz) frequency employing the 3-D (CST MWS). In the final step, radiation features of the designed reflectarray are obtained and discussed employing the 3-D Computer Simulation Technology Microwave Studio (CST MWS) simulations.

2. THE REFLECTION PHASE CHARACTERIZATION

Because of numerous factors which impact on the design of reflectarray, it is very important to select the type and geometry of reflective element as well as the substrate properties chosen. In this section, different sizes of reflectarray radiating element is designed on a single layer substrate within X-band frequency range. Element geometry has been proposed to be a resonant element shape for periodic reflectarray structure. This geometry shape is depicted in (Fig. 1(a)), which is a first fractal type, as called Minkowski shape [3–5].

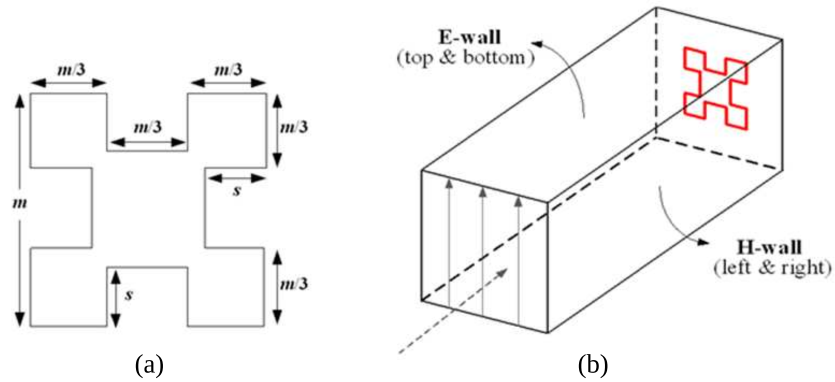

Figure 1: (a) Minkowski patch geometry. (b) Boundary conditions for TEM mode waveguide propagation.

The relationship between the Minkowski parameters is formulated as:

$$n = \frac{s}{m/3}, \qquad 0 \leq n \leq 1 \tag{1}$$

In (1), s is the cavity and m is the edge length of patch and n refers the ratio of the cavity to edge length of the patch. The reflection response of unit element and phase of reflected wave are generated from the theoretical analysis implemented by the H-wall waveguide simulator running available full-wave simulation tool (CST MWS). The infinite array approach by using H-wall waveguide simulator, also called parallel-plate waveguide simulator, is one of the most popular techniques for calibrating the reflection phase. (Fig. 1(b)) represents the geometry of rectangular waveguide that has been used to design a unit element and the TEM-mode propagation boundary conditions in the simulation setup [3–5]. The top and bottom surfaces of the waveguide are selected as perfectly electric conducting walls, while the right and left walls are selected as perfectly magnetic field walls. The vertically polarized incoming waves will see the element at the end of the waveguide at the broadside direction and then scattered back also at the broadside direction with a set of amplitude and phase information.

The sampling process of our model can be ordered as follows: the operation bandwidth (8–12 GHz) is swept at intervals of 1 GHz and the number of the sample frequencies is $fs = 5$. Thus, Minkowski configuration set are generated as $ns \times ms$ for each sampled substrate properties $(\varepsilon_r - h)$ at each sampling frequency where $ns = 6$ and $ms = 5$ are the number of samples for the indention relation and patch width, respectively. The patch width value, m is swept by $\pm\%10$ and $\pm\%2$ around the resonant length $((m = 5.41\,\text{mm}))$ which is m while n is swept by an interval of 0.15 between 0.15 and 0.90. Simultaneously the substrate thickness is sampled at intervals of 0.5 mm between the 0.5 and 3 mm range and the total number of the thickness sampling is $hs = 6$. In addition, dielectric permittivity of substrate (ε_r) varied between 1 and 6 at intervals of 1, thus, the dielectric permittivity sampling is $\varepsilon s = 6$. Thus the entire Minkowski space is discretized totally into the $fs \times \varepsilon s \times hs \times ms \times ns = 5400$ Minkowski configurations.

3. APPLICATION OF MLP ANN MODEL

In this stage, the most common neural network architecture called as Multilayer Perceptron (MLP) is applied A Multilayer Perceptron (MLP) is a feed forward artificial neural network model that maps sets of input data onto a set of appropriate output [6]. The MLP network consists of multiple layers of nodes in a directed graph, with each layer fully connected to the next one. The layers of a multilayer network have different roles. If the layer is generated by the network output, this layer is called as an output layer. All other layers are called hidden layers. These layers have the weight matrix, the summation and multiplication operations, the bias vector b, the transfer function boxes and the output vector.

When the training is performed, the rms errors of both the training and validation processes decrease with increasing iterations. The ith output for the Pth training pattern expressed by:

$$Y_p(i) = \sum_{k=1}^{N+1} W_{oi}(i,k) X_P(k) + \sum_{j=1}^{N_h} W_{oi}(i,j) O_P(j) \tag{2}$$

In (2), $W_{oi}(i,k)$ represents the weight from the input nodes to the output nodes and $W_{oi}(i,j)$ represents the weight from the hidden nodes to the output nodes.

In order to design of our MLP model, first we have been composed a Black-Box analysis model (Fig. 4(a)) for geometrical parameters of Minkowski radiating element and substrate properties. This analysis model covers the 5-dimensional Minkowski spaces are mapped into the 1-dimensional reflection phase space by the ANN. In the Black-box of analysis model, m, n, ε_r, h, f are used as input parameters which refer patch width, the cavity to edge of Minkowski, dielectric permittivity of substrate, thickness of substrate, and frequency respectively. Hence, the reflection phase of unit element is defined as output of this analysis model. The structure of our ANN model consists of an input layer, two hidden layer, and an output layer which is depicted in (Fig. 4(b)). For network training, a data set of geometrical configurations of the patch and properties of substrate ($\varepsilon_r - h$) is

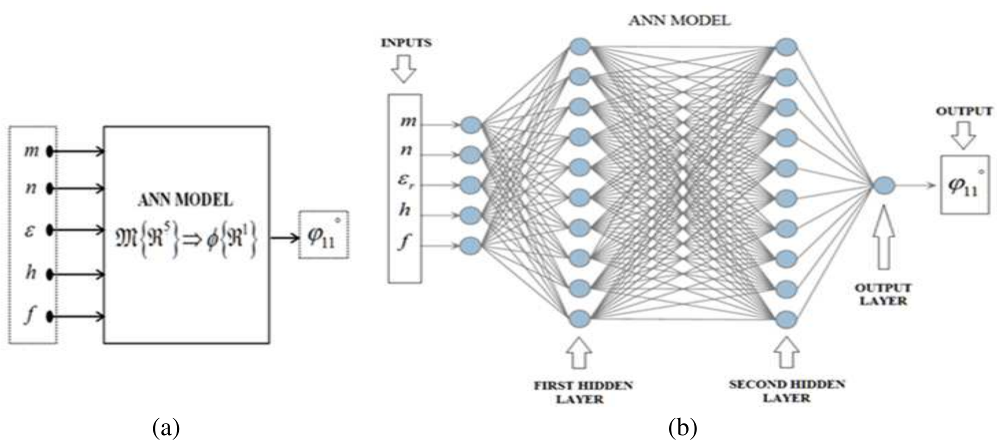

Figure 2: (a) Black-box model of unit cell with MLP model. (b) The structure of artificial neural network model for minkowski patch with 5 input and 1 output neurons and 2 hidden layers both of 10 neurons.

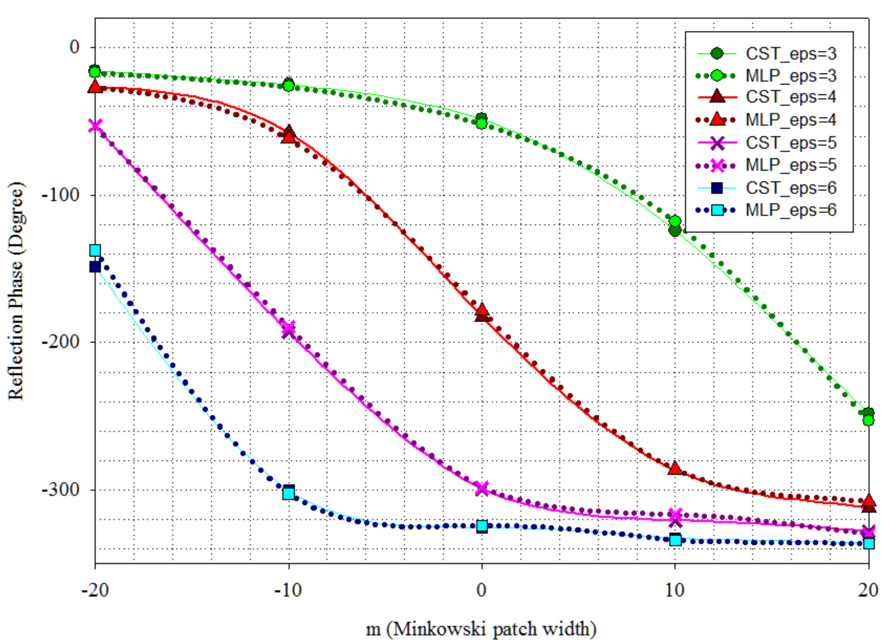

Figure 3: Two dimensional graphs for reflection phase values for target and predicted data versus m (patch width) variation due to the various ε_r (relative permittivity of substrate) values at fixed conditions ($n = 0.6$, $h = 1.5$ mm, $f = 11$ GHz).

generated and the corresponding reflection phase is estimated. The hyperbolic tangent function is applied as activation function for both two hidden layers of our model with 10 neurons. Levenberg Marquart algorithm is applied as an output layer.

4. RESULTS AND DISCUSSIONS

The data, which is used for training the network, are generated from by the H-wall waveguide simulator using CST MWS. The overall performance of the MLP is measured by the mean square error In our model, the mean square errors for training and testing are calculated as 9.9564×10^{-5} and 1.7264×10^{-4}, respectively. It is observed that both the target and reconstructed data matched, thus one can decide the modeling process results in an accurate model. Two dimensional view of the reflection phase alteration is depicted in (Fig. 3) with respect to the patch width variation at

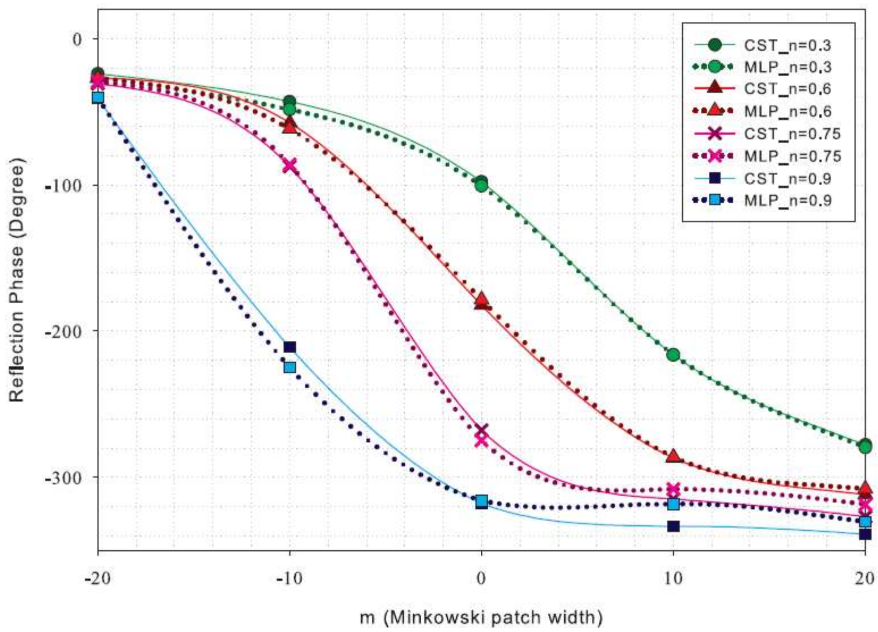

Figure 4: Two dimensional graphs for reflection phase values for target and predicted data versus m (patch width) variation due to the various n (indention relation) values at fixed conditions ($\varepsilon_r = 4$, $h = 1.5$ mm, $f = 11$ GHz).

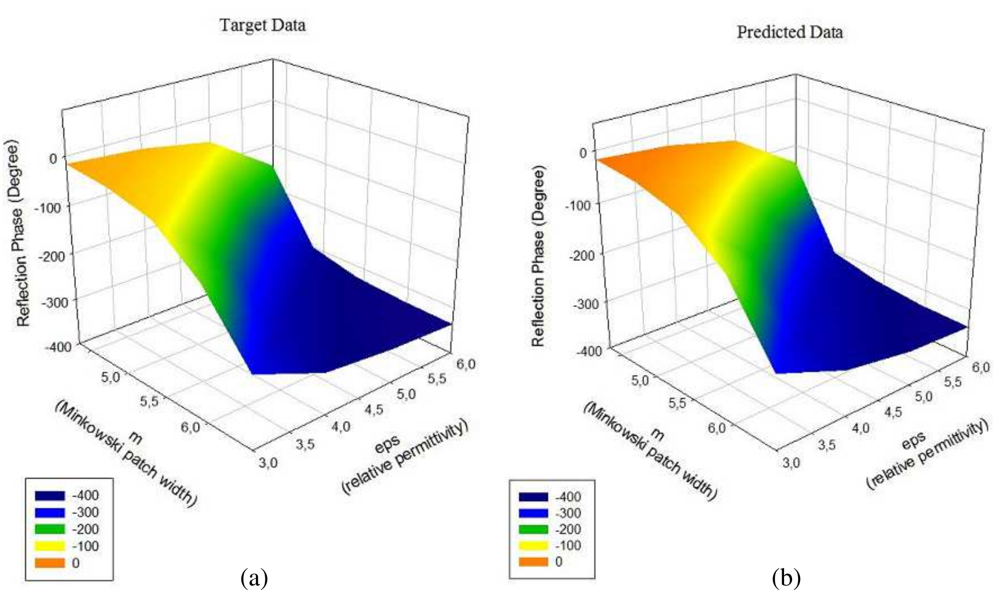

Figure 5: Three dimensional view for reflection phase values versus m (patch width) and ε_r (relative permittivity of substrate) values on fixed conditions ($n = 0.6$, $h = 1.5$ mm, $f = 11$ GHz) for (a) target and (b) predicted data.

11 (GHz) that for various dielectric permittivity (ε_r) values due to the fixed substrate thickness $h = 1.5$ (mm) and indentation relation $n = 0.6$. Furthermore, it can be seen in (Fig. 4) that two dimensional view of the reflection phase alteration with respect to the patch width variation at 11 (GHz) that for various indentation relation, n values due to the fixed substrate thickness $h = 1.5$ (mm) and dielectric permittivity $\varepsilon_r = 4$. The straight lines refer target data, the dotted lines are used for predicted data. Finally, (Fig. 5) depicts the different viewpoint of Fig. 3 as 3D representation of comparison between the target and predicted data on same conditions. In comparison with the target and predicted the reflection phase values, it can be understood that MLP NN model is very efficient to predict the real values implemented by the CST simulations.

5. CONCLUSION

In this paper, a complete, accurate and fast MLP ANN model is presented based on the 3-D (CST MWS) to be employed in both design and analysis of the Minkowski RA. All the stages of building the MLP ANN model and its utilization in design and analysis of a Minkowski RA are given in details. When the outputs of performed MLP ANN model and 3-D simulations are compared, it is proven that the MLP is very accurate and fast solution method to solve the complex relationship between the geometrical parameters of reflectarray and its reflection characteristics. Thus, the optimum Minkowski geometry can be obtained not only on a defined substrate, at the same time, on the most suitable substrate with the optimum dielectric property ε_r and thickness h.

REFERENCES

1. Huang, J. and J. A. Encinar, *Reflectarray Antennas*, Wiley — IEEE Press, 2007, ISBN: 978-0 470-08491-4.
2. Caputo, D., et al., "Neural network characterization of microstrip patches for reflectarray optimization," *Proceedings of the European Conference on Antennas and Propagation, EuCAP*, 2520–2522, March 23–27, 2009.
3. Nesil, S., F. Gunes, and U. Ozkaya, "Phase characterization of a reflectarray unit cell with Minkowski shape radiating element using multilayer perceptron neural network," *7th International Conference on Electrical and Electronics Engineering (ELECO)*, II-219, II-222, Dec. 1–4, 2011.
4. Nesil, S., F. Gunes, and G. Kaya, "Analysis and design of X-band reflectarray antenna using 3-D EM-based artificial neural network model," *IEEE International Conference on Ultra-Wideband (ICUWB)*, 532, 536, Sep. 17–20, 2012.
5. Zubir, F., M. K. A. Rahim, O. Ayop, A. Wahid, and H. A. Majid, "Design and analysis of microstrip reflectarray antenna with minkowski shape radiating element," *Progress In Electromagnetics Research B*, Vol. 24, 317–331, 2010.
6. Burrascano, P., S. Fiori, and M. Mongiardo, "A review of artificial neural networks applications in microwave computer-aided design (invited article)," *Int. Journal of RF and Microwave CAE Special Issue: Applications of Artificial Neural Networks to RF and Microwave Design*, Vol. 9, 158–174, 1999.

Antenna Array Synthesis, Using Method of Compressed Cosines

Peter Apostolov
High school "College of Telecommunications and Post", Student City
Street "Academician Stefan Mladenov", No. 1, Sofia, Bulgaria

Abstract— In the paper, an application of the method of compressed cosines is shown for synthesis of a three-element linear equidistant antenna array (LEAA). The synthesis is performed by an approximation of a Kronecker Delta function. Two cases of approximations by optimal third-degree polynomials are considered. As a result, directivity diagrams with a high selectivity are obtained. Functional and gain diagrams for realization of a three-element LEAA and a five-element, two-dimensional LEAA are proposed.

1. INTRODUCTION

The purpose of an LEAA is the reception/transmission of far-field signals. The LEAA is a spatial filter. In theory, it is assumed to consist of n, uniformly and linearly placed isotropic radiators (sensors). A main task in construction is creating a LEAA with the fewest possible antennas with a narrowband gain diagram (GD) and low levels of side lobes. An ideal GD is the Kronecker delta function

$$\delta(\theta) = \begin{cases} 1, & \theta = 0 \\ 0, & \theta \neq 0 \end{cases}, \quad \theta \in [-\pi/2, \pi/2]. \tag{1}$$

This is a GD with a main lobe having a width of 0 degrees and an infinite attenuation outside it. Such an antenna array cannot be realized. That's why the LEAA synthesis is based on approximating functions. Many methods are known in the literature. The best optimal LEAA diagrams are obtained by the method of Dolph-Chebyshev and its modification proposed by Riblet [1]. New methods for LEAA synthesis have been created during the last decades, whose theoretical basis is associated with digital FIR filter synthesis [2]. The following dependence exists in all the mentioned methods: the increase of the selectivity of the GD is associated with the increase of the number of the sensors of the LEAA.

The present paper considered a method that continues the research in this area. The theoretical basis are published in [3, 4]. The approximation with a cosine function lies on its basis, which argument contains S-curve modulating function, hence the name "approximation with compressed cosines". With the method, trigonometric polynomials are obtained of a low order and a small approximation error. An application of the method will be shown for synthesis of a 3-element LEAA and a 5-element two-dimensional LEAA with parameters close to the ideal GD — the Kronecker delta function.

2. THEORETICAL BASIS

2.1. Case A: LEAA with Side Lobes

The approximation with compressed cosines is performed by an optimal trigonometric polynomial of the form

$$P_3(\theta) = \sum_{k=1}^{4} b_k \cos[(k-1)\varphi(\theta)], \tag{2}$$

with coefficients:

$$b_1 = 0.5 - \varepsilon; \quad b_2 = b_4 = 0; \quad b_3 = 0.5, \tag{3}$$

where ε is the approximation error. The modulating function is

$$\varphi(\theta) = \pi \mathrm{erf}(\beta k d \sin\theta), \quad \theta \in [-\pi/2, \pi/2], \tag{4}$$

where d is the interelement distances, $k = 2\pi/\lambda$ is the wavenumber, $\beta > 0$ is a parameter, erf(.) is the integral Gauss error function. After substituting of the coefficients in (2) the following is obtained:

$$P_3(\theta) = 0.5 + 0.5\cos(\varphi(\theta)) - \varepsilon. \tag{5}$$

The exciting currents of the antenna array are determined by the non-zero coefficients of the polynomial:

$$I_k = b_3/2, b_1, b_3/2; \quad k = 1, 2, 3, \tag{6}$$

after which they are normed with respect to I_1. The array factor has the form

$$A(\theta) = 1 + (2 - 4\varepsilon)\exp(j\varphi(\theta)) + \exp(j2\varphi(\theta)). \tag{7}$$

Figure 1(a) shows an approximation of a δ-Kronecker by an optimal third-degree polynomial. This is an optimal approximation with an error ε. Fig. 1(b) shows the LEAA array factor. The array factor is identical to the LEAA gain diagram, because isotropic radiators are used. The LEAA selectivity depends on parameter β. It is possible to obtain an approximation very close to the ideal one for large values of the parameter β. Fig. 2 shows a GD with the following specification: number of radiators $n = 3$, distance $d = \lambda/2$, width of the GD at a level of $-3\,\mathrm{dB}$ $\Delta\theta_{-3\,\mathrm{dB}} = 0.12°$, power's attenuation of the side lobes $A_S = 60\,\mathrm{dB}$. The analogy with the Kronecker delta function is obvious.

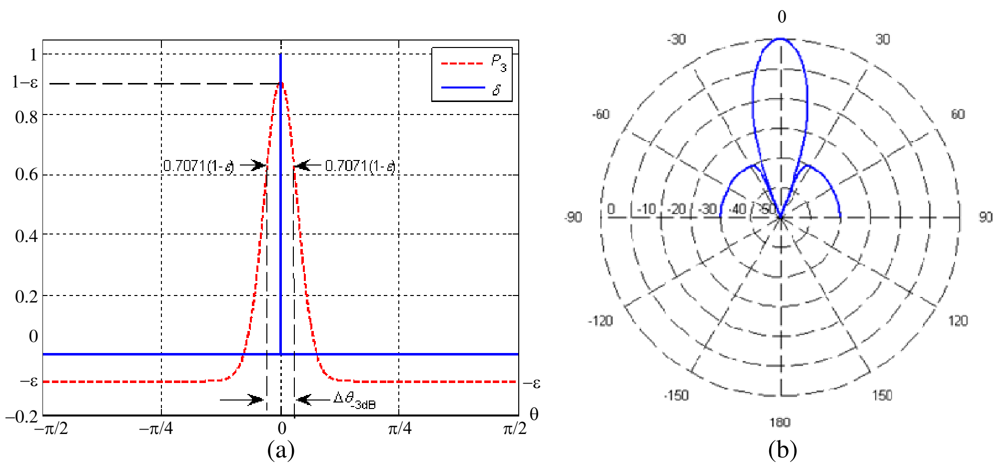

Figure 1: (a) Approximation of a δ-Kronecker. (b) Array factor/gain diagram.

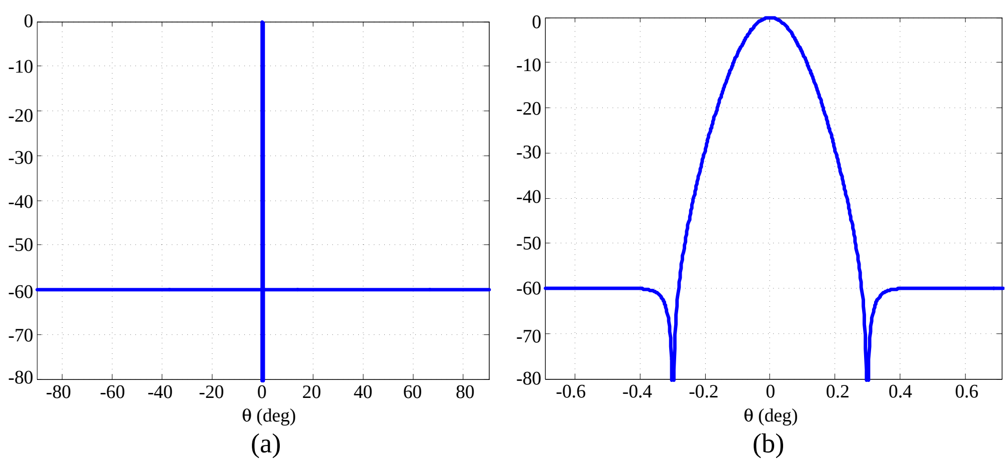

Figure 2: GD close to the ideal function. Fragment of the main lobe.

2.2. Case B: LEAA without Side Lobes

From (5) it is seen that the third term $(-\varepsilon)$ does not depend on the spatial angle θ. Its meaning in this dependence is to translate the function in negative vertical direction by the value ε, as seen from Fig. 1(a). The maximum value of the function is $(1 - \varepsilon)$, and the minimum is $(-\varepsilon)$. Therefore, if it is assumed that $\varepsilon = 0$, a polynomial will be obtained with the same approximation properties, and its plot is translated by ε in vertical positive direction — Fig. 3(a). In this case, the polynomial coefficients are constants:

$$b_1 = 0.5; \quad b_2 = b_4 = 0; \quad b_3 = 0.5. \tag{8}$$

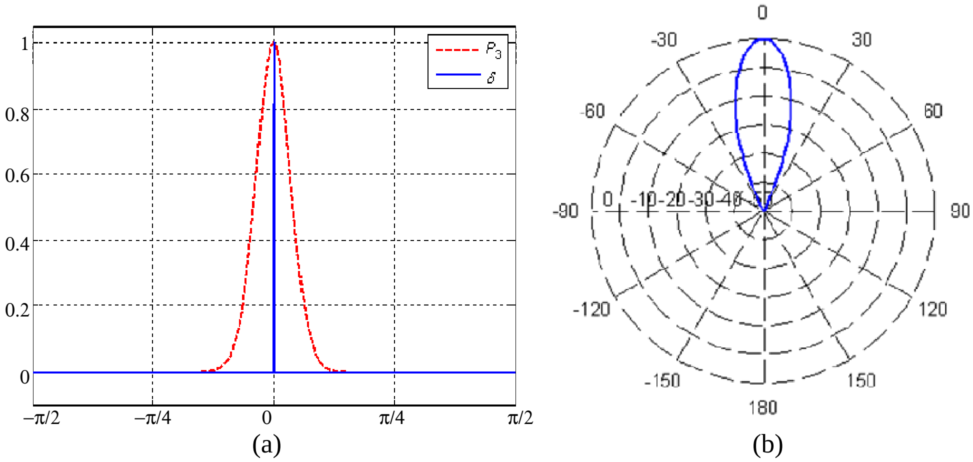

Figure 3: (a) Approximation with a translated third-degree polynomial. (b) Array factor/GD.

The analytical expression of the polynomial is

$$P_3(\theta) = 0.5 + 0.5\cos(\varphi(\theta)), \tag{9}$$

and the array factor is

$$A(\theta) = 1 + 2\exp(j\varphi(\theta)) + \exp(j2\varphi(\theta)). \tag{10}$$

Figure 3(b) shows a GD of an antenna array — case B.

3. LEAA REALIZATION

From the equations for the array factor (7) and (10) it is seen that the exciting currents can be easily realized — it is necessary to amplify the signal from the second antenna. The exponents of the second and the third term reflect the phase change of the signals. LEAA with Luneberg lens is realized. We assume that the lens has a unit gain, similarly to an isotropic radiator. The Luneberg lens is a sphere with variable dielectric constant ε_r. The refraction coefficient does not depend on the wavelength λ. Therefore, the focusing properties of the Luneberg lens are in the entire

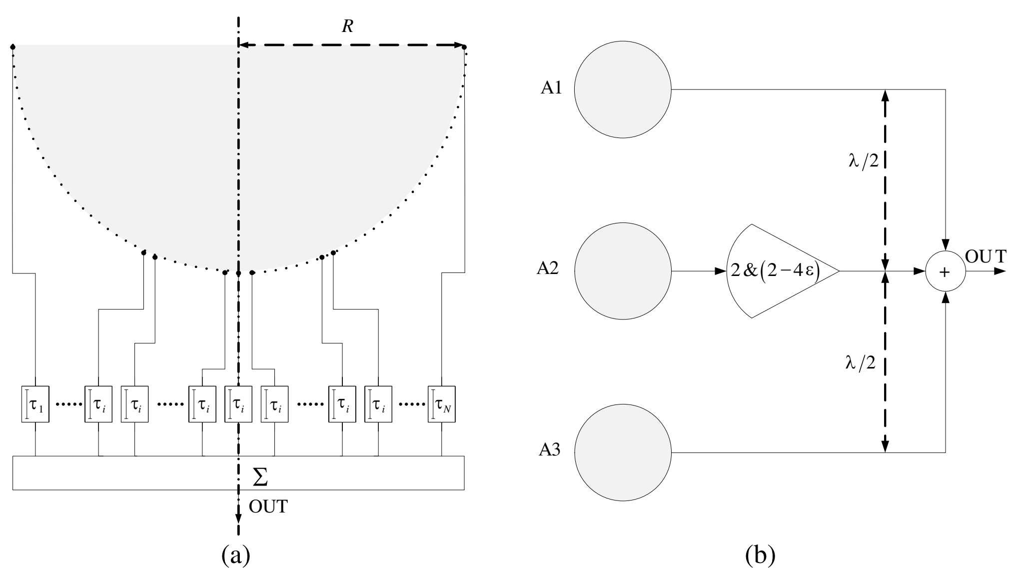

Figure 4: (a) Lower hemisphere of a Luneberg lens antenna with delay lines. (b) LEAA structure.

radiofrequency band. The lens has the property to focus the parallel rays from all the directions of the azimuthal angle θ in points placed on one semicircle in the azimuthal plane. The phase function $\varphi(\theta)$ with delay lines is realized — in Fig. 4(a).

Figure 4(b) shows the structure of a three-element LEAA with the same Luneberg lenses with delay lines. The signal from the second antenna is amplified 2 or $2 - 4\varepsilon$ times. At the output, all the signals are added. Fig. 5(a) shows the values of the time delays for the three antennas, where $\tau_{\max} = \lambda/2c$; c — light velocity.

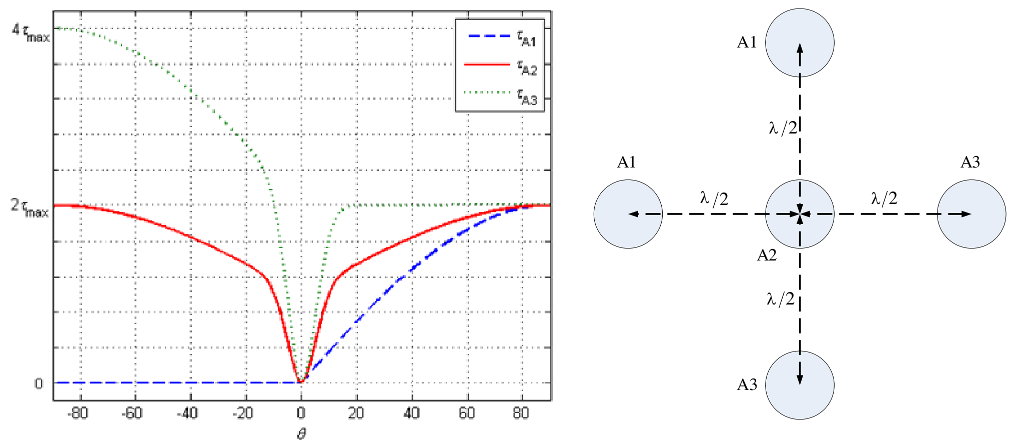

(a) (b)

Figure 5: (a) Time delay functions. (b) Five element two dimensional LEAA.

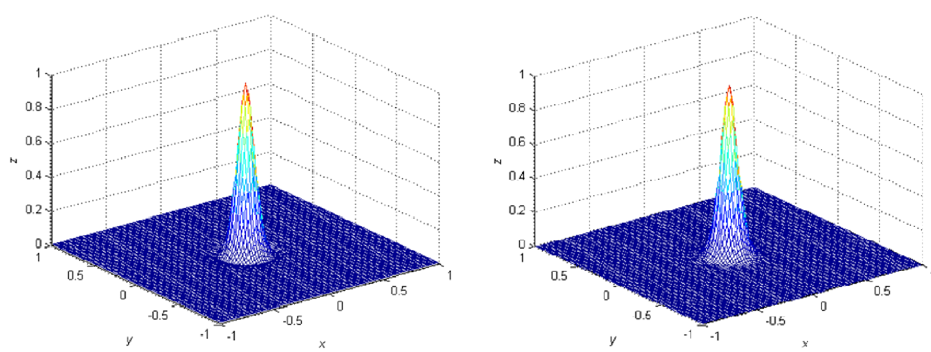

(a) (b)

Figure 6: Two-dimensional GD — case A and B.

4. TWO-DIMENSIONAL LEAA WITH 5 SENSORS

It is known that LEAA is selective in the azimuthal angle θ only. To obtain 2-D selectivity a combination has to be realized of two orthogonally placed linear LEAAs with three sensors each, as shown in Fig. 5(b). The sensors for the delay lines of the central common antenna A2 are placed on the two mutually perpendicular focal semicircles. The signal from A2 is amplified 2 or $2 - 4\varepsilon$ times. At the output, all the signals are added. Fig. 6 shows theoretical GDs of two-dimensional LEAAs, corresponding to the one-dimensional ones from case A and case B.

5. CONCLUSION

In the proposed method, the number of sensors is constant: 3 for a one-dimensional LEAA and 5 for a two-dimensional LEAA. The change in the width of the main lobe of the GD depends on the parameter β, and the level of the side lobes (for case A) — on the approximation error ε. The time delays of the delay lines are changed by β, and the gain in the circuit of the second antenna is changed by ε. The values of the parameter β can be arbitrarily large. This means that with three lens antennas, an arbitrary specification can be realized with respect to the width of the main lobe and the attenuation level of the side lobes. The proposed method possesses one noticeable property. The change of the interelement distance d, or the wavelength λ (4) can be compensated by the parameter β (resp. time delays) and it does not affect the main lobe width and the LEAA selectivity. The aforementioned advantage of the method gives very good opportunities for constructing receiver LEAAs with digital signal processing. For a fixed interelement distance, the antenna array can work simultaneously and in real time in a very broad frequency band, since the change of the time delays in the delay lines and the gain in the second antenna are programmable.

REFERENCES

1. Riblet, H. J., "Discussion on a current distribution for broadside arrays which optimizes the relationship between beamwidth and side-lobe level," *Proc. IRE*, 489–492, May 1947.
2. Van Trees, H. L., *Optimum Array Processing*, John Wiley & Sons, 2002.
3. Apostolov, P. S., "Linear equidistant antenna array with improved selectivity," *IEEE Transaction on Antennas and propagation*, Vol. 59, No. 10, 3940–3943, August 2011.
4. Apostolov, P. S., *Apprpximations with Compressed Cosines and Their Applications*, Prof. M. Drinov, Academic Press, Sofia, 2012.

High-gain S-band Slotted Waveguide Antenna Arrays with Elliptical Slots and Low Sidelobe Levels

M. Al-Husseini[1], **A. El-Hajj**[2], **and K. Y. Kabalan**[2]

[1]Lebanese Center for Studies and Research, Beirut 2030 8303, Lebanon
[2]American University of Beirut, Beirut 1107 2020, Lebanon

Abstract— Slotted waveguide antenna arrays offer clear advantages in terms of their design, weight, volume, power handling, directivity and efficiency. Slots with rounded corners are more robust for high power applications. This paper presents a slotted waveguide antenna with elliptical slots made to one broadwall of an S-band rectangular waveguide. The antenna is designed for operation at 3 GHz. The slots length and width are optimized for this frequency, and their displacements are determined for a 20 dB sidelobe level ratio. Two rectangular metal sheets are then symmetrically added as reflectors to focus the azimuth plane beam and increase the gain.

1. INTRODUCTION

Slotted waveguide antennas (SWAs) [1] radiate energy through slots cut in a broad or narrow wall of a rectangular waveguide. They are attractive due to their design simplicity, since the radiating elements are an integral part of the feed system, that is the waveguide itself. This removes the need for baluns or matching networks. They also offer significant advantages in terms of weight, volume, high power handling, high efficiency and good reflection coefficient [2]. Thus, they have been ideal solutions for many radar, communications, navigation, and high power microwave applications [3].

SWAs can be realized as resonant or non-resonant according to the wave propagation inside the waveguide (respectively standing or traveling wave) [4, 5]. The design of a resonant SWA is generally based on the procedure described by Elliot [4, 6, 7], by which the waveguide end is short-circuited at a distance of a quarter-guide wavelength from the center of the last slot, and the inter-slot distance is one-half the guide wavelength. For rectangular slots, the slot length should be about half the free-space wavelength. Slot shapes that avoid sharp corners are more suitable for high power applications, since sharp corners aggravate the electrical breakdown problems. Elliptical slots are an excellent candidate for such applications [8].

As with all antenna arrays, the resulting sidelobe level is related to the excitations of the individual elements. In SWAs, the excitation of each slot is proportional to its conductance. For the case of longitudinal slots in the broadwall of a waveguide, a slot conductance is controlled by its displacement from the broadface centerline [9]. Thus, for a desired sidelobe level, the corresponding set of slots displacements should be determined.

In this paper, an SWA designed for operation at 3 GHz is presented, where ten elliptical slots are made to one broadface of an S-band rectangular waveguide. The slot displacements from the centerline are determined to obtain a sidelobe level ratio of 20 dB. Later, two metals sheets are attached to the SWA edges to focus its azimuth plane beam. The reflection coefficient, pattern plots and gain results of the antenna are reported.

2. ANTENNA CONFIGURATION

The target frequency is 3 GHz, so a WR-284 waveguide having $a = 2.84''$ and $b = 1.37''$ is used to construct the SWA. The waveguide is shorted at one end and fed at the other. Ten elliptical slots are cut into one of its broadsides. The slots are spaced at half the guide wavelength, center to center, where in this case the guide wavelength $\lambda_g = 138.5$ mm. The slots are positioned such that the center of the first one, $Slot1$, is at a distance of $\lambda_g/4$ from the waveguide feed, and the center of the last slot, $Slot10$, is at $\lambda_g/4$ from the waveguide's short-circuited side. The total length of the waveguide is thus $5\lambda_g$.

The width of each slot, which is 2 times the minor radius of the ellipse, is fixed at 5 mm. This is calculated as follows: for X-band SWAs, which the literature if full of, the adopted width of a rectangular slot is $0.0625''$, corresponding to $a = 0.9''$. By proportionality, the width of the elliptical slot for this S-band SWA is computed from $2.84'' \times 0.0625/0.9$, which is $0.197''$ or 5 mm. Because of their elliptical shape, the length of the slots (double the major radius) is expected to be larger than half the free space wavelength. Simulations using ANSYS HFSS are done to optimize the slot length for resonance at 3 GHz. For these simulations, it is assumed that all slots are at the same spacing from the broadside centerline, in an alternating fashion. The resonant slot length is found to be 54.25 mm.

For a desired sidelobe level ratio (SLR) of 20 dB, a heuristic method is used to obtain the required set of slots displacements. The slots near the two waveguide edges are closest to the broadface centerline, whereas those toward the waveguide center have the largest displacement. The detailed displacements values are given in Section 3.

Two metal sheets are then attached symmetrically, as shown in Fig. 1, at an angle of 60° with respect to the XZ plane. These 2 sheets act as reflectors, thus leading to beam focusing in the azimuth plane and as a result to a gain increase. The width of each metal sheet, L, is 3″.

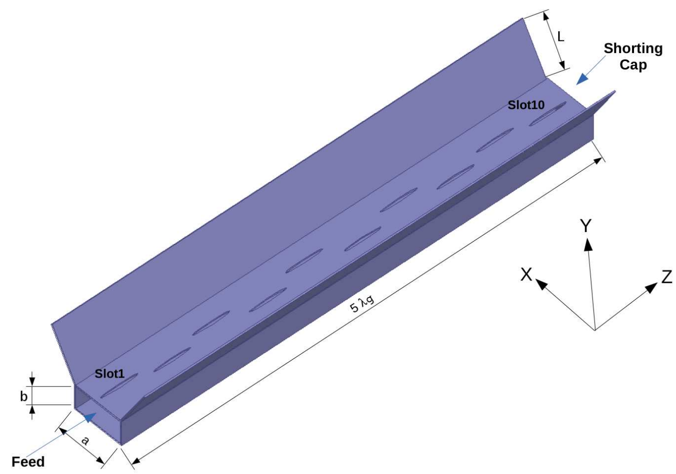

Figure 1: Slotted waveguide with 10 elliptical slots with two re ectors added.

3. RESULTS

The uniform slots displacement that leads to a good reflection coefficient at 3 GHz is calculated using

$$d_u = \frac{a}{\pi}\sqrt{\arcsin\left[\frac{1}{N \times G}\right]}, \tag{1}$$

where

$$G = 2.09 \times \frac{a}{b} \times \frac{\lambda_0}{\lambda_g} \times \left[\cos(0.464\pi \times \lambda_0/\lambda_g) - \cos(0.464\pi)\right]^2. \tag{2}$$

In (1), N is the number of slots, which is equal to 10, and in (2), λ_0 is the free-space wavelength. At 3 GHz, $\lambda_0 = 100$ mm. For this SWA, $d_u = 7.7$ mm. This displacement value is used in the HFSS simulations to obtain the resonant elliptical slot length, which is found to be 54.25 mm. For this slot length and this uniform displacement of all ten slots, the resulting SLR is around 13 dB, which is as expected. The reflection coefficient S_{11} and the YZ-plane gain pattern in this case are given in Fig. 2. A peak gain of about 17 dB and an SLR of 13.2 dB are recorded. The half-power beamwidth (HPBW) in this plane is 7.2 degrees. These values are obtained using CST Microwave Studio, but are also verified with HFSS.

Since better SLRs are desirable, the slots displacements are changed, to non-uniform, using a heuristic method, which will not be detailed in this paper. For an example SLR of 20 dB, the displacement values are given in Table 1. The alternating pattern about the centerline is respected. The length of all slots is kept at 54.25 mm, as in the uniform case. Simulations have proven that the resonating length of these elliptical slots is not very sensitive to the distance from the centerline. For these values, the antenna still resonates at 3 GHz, the SLR is 20 dB, the peak gain is 16.8 dB, and the YZ-plane HPBW increases to 8.4 degrees. The broadening of the main beam is expected when the sidelobes are forced to go lower.

When the two reflectors are added, a gain increase of about 3 dB is obtained due to a focus of the azimuth plane beam. The antenna retains its resonance at 3 GHz, and the SLR remains around

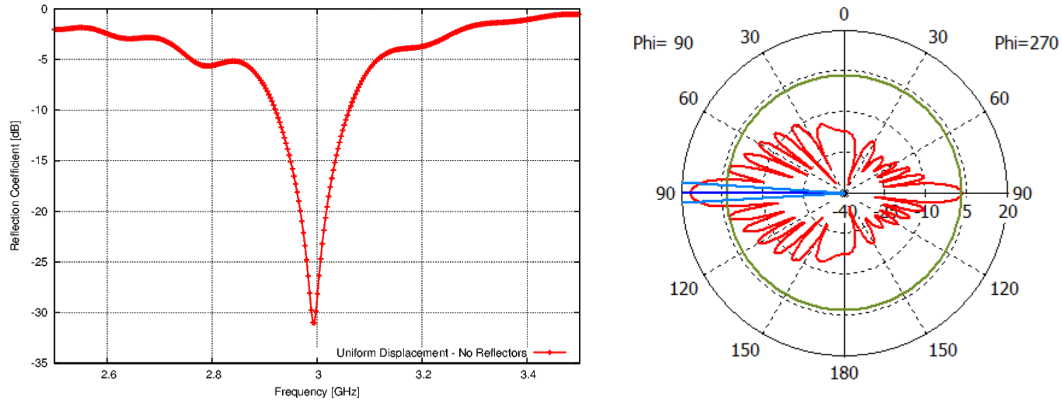

(a) S_{11} for uniform slots displacement

(b) Pattern in the *YZ* plane

Figure 2: Antenna's reflection coefficient and YZ-plane pattern for the case of uniform slot displacement and before attaching the two reflectors.

Table 1: Displacement of slot centers for an SLR of 20 dB.

Slot number	1	2	3	4	5	6	7	8	9	10
Displacement (mm)	3.74	5.42	7.11	8.4	9.11	9.11	8.4	7.11	5.42	3.74

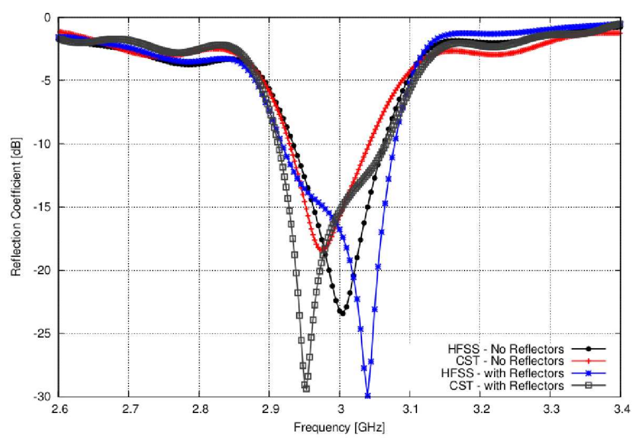

Figure 3: Reflection coefficient without and with the reflectors.

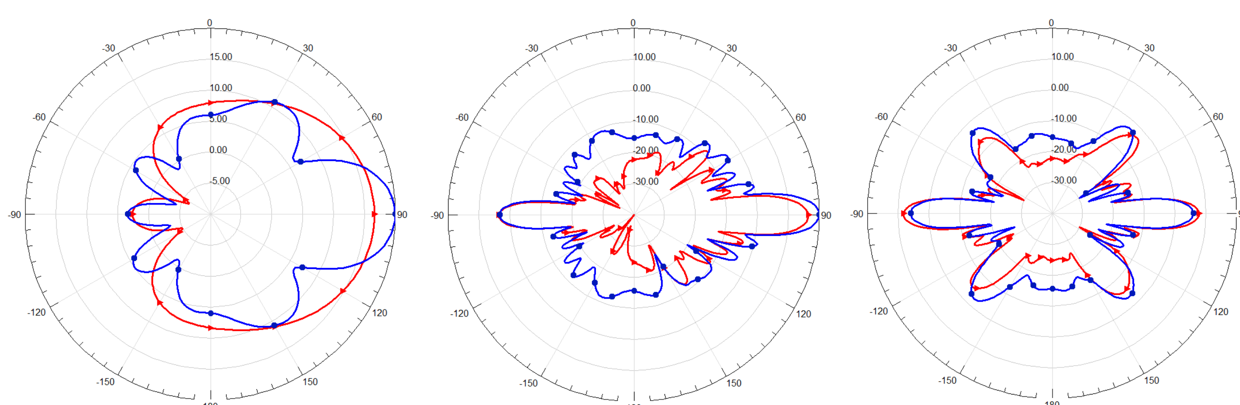

(a) Patterns in the azimuth plane

(b) Patterns in the *YZ* plane

(c) Patterns in the *XZ* plane

Figure 4: Antenna's gain patterns in the three principal planes (red line: no reflectors, blue line: with reflectors).

20 dB. The back lobe level stays about the same, so the main-to-back lobe level ratio also increases by about 3 dB. The S_{11} and pattern results of the two cases, with and without the reflectors, are shown in Fig. 3 and Fig. 4, respectively. All results generated in HFSS were verified in CST Microwave Studio, where a good match is observed.

4. CONCLUSION

A 3 GHz slotted waveguide antenna was presented. It has 10 elliptical slots, with optimized dimensions, made to one broadwall and displaced around its centerline so as to obtain a 20 dB sidelobe level ratio. The antenna has a very broad azimuth plane beam and a peak gain of about 17 dB. Upon adding two reflectors to the antenna's edges, the beam is focused and the gain is increased to about 20 dB.

REFERENCES

1. Gilbert, R. A., "Waveguide slot antenna arrays," *Antenna Engineering Handbook*, 4th Edition, J. L. Volakis, Ed., McGraw-Hill, 2007.
2. Mailloux, R. J., *Phased Array Antenna Handbook*, Artech House, 2005.
3. Rueggeberg, W., "A multislotted waveguide antenna for high-powered microwave heating systems," *IEEE Trans. Ind. Applicat.*, Vol. 16, No. 6, 809–813, 1980.
4. Elliott, R. S. and L. A. Kurtz, "The design of small slot arrays," *IEEE Trans. Antennas Propagat.*, Vol. 26, 214–219, Mar. 1978.
5. Elliott, R. S., "The design of traveling wave fed longitudinal shunt slot arrays," *IEEE Trans. Antennas Propagat.*, Vol. 27, No. 5, 717–720, Sep. 1979.
6. Elliott, R. S., "An improved design procedure for small arrays of shunt slots," *IEEE Trans. Antennas Propagat.*, Vol. 31, 48–53, Jan. 1983.
7. Elliott, R. S. and W. R. O'Loughlin, "The design of slot arrays including internal mutual coupling," *IEEE Trans. Antennas Propagat.*, Vol. 34, 1149–1154, Sep. 1986.
8. Baum, C. E., "Sidewall waveguide slot antenna for high power," Sensor and Simulation Note 503, Aug. 2005.
9. Stevenson, A. F., "Theory of slots in rectangular waveguides," *Journal of Applied Physics*, Vol. 19, 24–38, 1948.

Large Impedance Ground Plane Antennas for mm-accuracy of GNSS Positioning in Real Time

D. V. Tatarnikov and A. V. Astakhov
Topcon Positioning Systems, Russia

Abstract— Accuracy of differential positioning with the Global Navigation Satellite Systems (GNSS) is currently about $+/-1\ldots 2$ cm in real time; unavoidable multipath reflections from the Earth surface undelaying the receiver antenna remains the largest error source. To suppress said reflections antenna is to have a cut-off type pattern in the elevation plane. This calls for the antenna size to be sufficiently large in the wavelength scale. Results of antenna system development employing large impedance ground plane are presented. High capacitive impedance pins surface has been used. Antenna samples with the ground plane of 3 meters in diameter have been built. Multipath error is shown to fall below phase noise of the receiver. By filtering out said noise a real-time positioning accuracy of $+/-1.5\ldots 2$ mm in vertical has been achieved.

1. INTRODUCTION

Currently, accuracy of differential positioning with the Global Navigation Satellite Systems (GNSS) is about $+/-1$–2 cm in real time. This has allowed for broad use of GNSS for land survey, geodesy, automated machines for construction and agriculture and for planetary research. Multipath reflections of satellite signals from the terrain that is undelaying the receiver antenna remains the largest error source. The only mean to mitigate the reflections is to decrease the receiver antenna gain for directions below local horizon. With practice, it is common to use elevation mask of 10–12 degrees that is to exclude satellites below said elevation angle from processing. However, signals of satellites even slightly above said mask are necessary to support geometrical DOP factor [1]. Said implies that the receiver antenna pattern is to be homogeneous within the entire top semi-sphere up to 10–12 degrees elevation with a sharp drop (cut-off) then. Common antennas with up to 1–2 wavelength ground planes do not possess this property. This results in arising the mentioned error.

To achieve cut-off type of the pattern the receiver antenna is to be sufficiently large in the wavelength scale. Two GNSS antenna types with the cut-off pattern have been presented:a cross-dipole antenna over a flat conductive ground plane [2] and a vertical antenna array of 10–15 wavelengths (2–3 meters) total height (length) [3]. However, to the best of the authors of this paper knowledge,characterization of said antennas in regards to high precision GNSS practice has not been published.

This paper presents a newly done development of a large impedance ground plane. In what follows the antenna placed on top of the ground plane is referred to as "antenna element"; the combination of an antenna element and a ground plane is referred to as an "antenna system"; to distinguish antenna ground plane from the "ground surface" of the terrain the latter is referred to as the Earth surface. The newly developed ground plane allows for commercially available GNSS antennas to be used as antenna elements. Thus the design could be viewed as a reference or a test bench for various purposes. The ground plane allows to achieve a regular typical antenna gain from zenith up to 10–12 degrees above the local horizon with at least 20 dB multipath suppression for directions starting from 10–12 degrees below the horizon. It is worth mentioning that current GNSS signals occupy two subbands of L-band; namely 1150–1300 MHz and 1540–1610 MHz with slightly over 30% total bandwidth. The satellite signals are right-hand circular polarized (RHCP).

The ground plane under consideration is to possess a high capacitive impedance surface (HCIS). Although certain advantages of a surface wave excitation for GNSS antenna ground planes of common size has been demonstrated [4], for size ranges exceeding 5 wavelengths assuming broadband functionality the cut-off frequency response of HCIS seemed preferable. A variety of structures is known to compose HCIS. Widely used is a Choke Ring ground plane [5]. Another type is mushrooms structure [6] employed in [7]. However, straight pins structure similar to [8] has been chosen for the sake of broadband functionality and manufacturing simplicity. It is assumed that pins diameter is $0.03\ldots 0.04\lambda$ ($6\ldots 8$ mm for GNSS frequencies). Here λ is the wavelength. Pins are arranged in a regular grid with $0.1\ldots 0.2\lambda$ spacing. Pins length slightly exceeds a quarter of the wavelength at the lowest frequency (1150 MHz). With such a structure, TEM wave with respect to the coordinate along the pins is dominating. This leads [8] to the derivate of impedance versus frequency decrease if compared to concentric grooves of a Choke Ring and thus to potentially smoother frequency response. An incident TE-type field with respect to the coordinate along the pins would not excite currents over the pins. Thus in the H-plane of a linear polarized antenna the incident field would not be interfered by the pins and would be reflected by the metal base of the ground plane. This is to be accounted for as shown below. In Section 2 the main ground plane design considerations are discussed. In Section 3, the ground plane implementation and performance characterization is provided.

2. GROUND PLANE DESIGN GUIDELINES

Consider two-dimensional problem of Figure 1. Excitation sources in the form of four magnetic line currents are shown by thick dots. Currents are placed over HCIS of a size L. Elevation angle θ is counted from the HCIS plane such that $0 \leq \theta \leq \pi/2$ indicates directions in the top demi-sphere and $-\pi/2 \leq \theta \leq 0$ is for the bottom semi-sphere. These four line currents are to model antenna element pattern. The currents are grouped by two, 1, $1'$ and 2, $2'$. Each pair is to model antenna element directivity with respect to zenith ($\theta = \pi/2$) and nadir ($\theta = -\pi/2$) directions. Namely, for the pair 1, $1'$ the magnetic line currents are

$$\vec{j}^m_{1'} = -\alpha e^{-ik\Delta} \vec{j}^m_1 \tag{1}$$

and similar for the second pair. Here $k = 2\pi/\lambda$ is the wavenumber, distance Δ in between currents is much smaller than the wavelength, time dependence is $\exp(i\omega t)$. If $\alpha = 1$ holds, currents 1, $1'$ will form an ideal cardioid pattern with a null in the direction towards HCIS ground plane. Respective currents of pairs 1, $1'$ and 2, $2'$ are of same magnitudes and phases. Radiation patterns of the four currents for the distance a in between pairs equal to 0.4λ and two values of α are shown in Figure 2. These are realistic approximations to common GNSS antenna patterns.

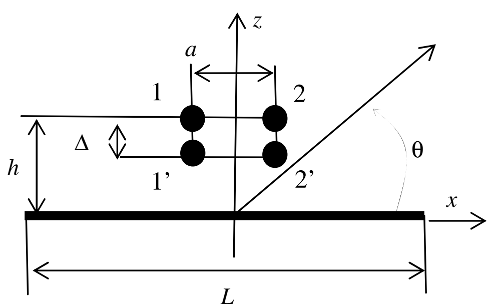

Figure 1: Two dimensional problem (calculated).

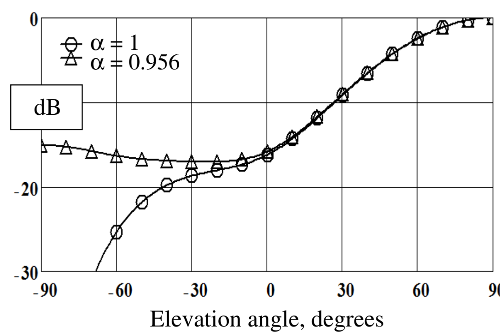

Figure 2: Excitation source pattern.

The advantage of HCIS is that the fields decay as $(kx)^{-3/2}$ with x growth as opposed to $(kx)^{-1/2}$ for a perfect electric conductor case. Here x is a distance from the source counted along the ground plane However, HCIS leads to narrowing of the radiation pattern of the source. In the limit of an infinitely large L the radiation pattern would have a null in the direction grazing to HCIS ($\theta = 0$). Such narrowing is undesirable for GNSS applications as it may result in the difficulties of tracking low elevated satellites by the receiver. To estimate the pattern for certain h and L one may employ physical optics approximation to the fields along HCIS assuming that the fields are an excerption of those of an infinite plane. Due to fields decay along the ground plane, edge waves [9] provide with comparatively small correction to the pattern even with the perfect electric conductor plane as was estimated in [10].

To simplify the estimate further one may assume that HCIS is a perfect magnetic conductor; the finite value of the surface impedance would not affect the resulting pattern significantly if said value is large enough [10]. For the perfect magnetic conductor, a surface magnetic current excited by a magnetic line source located at $x = a/2$ is

$$\vec{j}^m = \vec{y}_0 2U \frac{k}{4i} H_1^{(2)} \left(k\sqrt{h^2 + (x-a/2)^2}\right) \sin\left(\mathrm{acrtg}\left(h/\left|x - a/2\right|\right)\right); \quad -L/2 \leq x \leq L/2 \tag{2}$$

Here U is the voltage across magnetic line current, $H_1^{(2)}(x)$ is the Hankel function of the first order and second kind, $\vec{y}_0$ is the unit vector of y-axis (perpendicular to the drawing plane of Figure 1).

Radiation pattern calculation of the current (2) is straightforward. Complete pattern $F(\theta)$ is a sum of that of the currents (2) associated with each of the four sources and source patterns in free space. We assume the total pattern is normalized to zenith reading.

Within the specular reflections model the quantity of interest is a down-up ratio $DU(\theta^e) = F(-\theta)/F(\theta)$. Antenna system height over the Earth surface is 2–3 meters typically. Then, the footprint at the Earth surface of the first Fresnel zone for the reflected signal is about 10 meters which suggests for the specular reflections model to be realistic. Assuming elevation mask of 12 degrees notations $F_{+12} = F(+12^\circ)$ and $DU_{12} = DU(12^\circ)$ are adopted for short.The first quantity indicates the worst case from satellite tracking standpoint while the second is the worst (the weakest) case from multipath rejection standpoint. With Figures 3(a), (b) said quantities are plotted versus height h for HCIS ground planes of two sizes L. As seen, with the height h increase within the range $0.1\lambda \leq h \leq 0.6\lambda DU_{12}$ stays almost constant while F_{+12} is rapidly decreasing in absolute value (improving). Said F_{+12} reaches $-12 \ldots -15$ dB for $h \approx 0.5 \ldots 0.6\lambda$ which is sufficient for reliable tracking of low elevated satellites. The value DU_{12} is increasing in absolute value (improving) with the size L growth. Thus target design figures could be achieved (at least in principle) by choosing appropriate h and L. For further implementation $L \approx 13\lambda$ has been chosen. Here the value of DU_{12} is -20 dB.

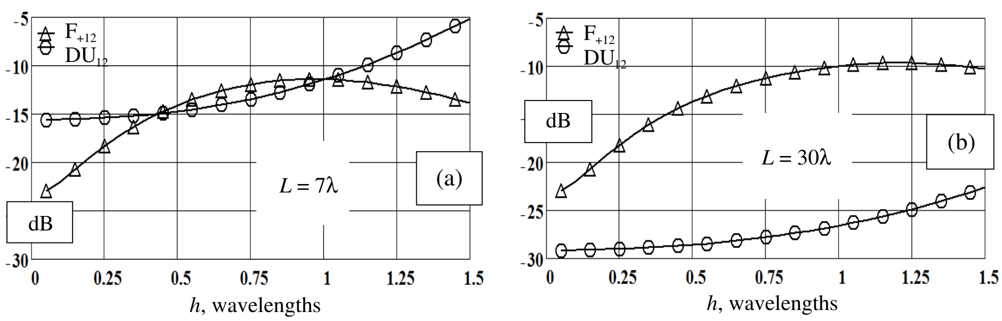

Figure 3: F_{+12} and DU_{12} values versus antenna element height over HCIS of two sizes (calculated).

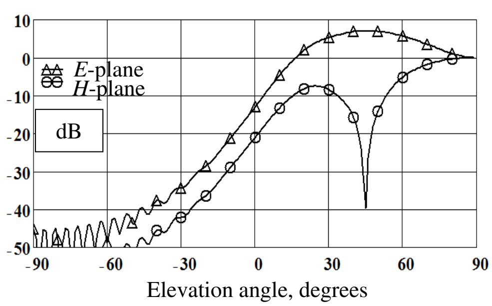

Figure 4: Radiation patterns in E- and H-planes of a linear polarized source (calculated).

In Figure 4 radiation patterns for E- and H-planes of a linear polarized antenna element are illustrated. Here $h \approx 0.45\lambda$ and $L \approx 13\lambda$. The E-plane pattern is calculated using considerations of above. The H-plane pattern is calculated using electric line sources placed over a perfect electric conductor ground plane. Expressions for the radiation patterns in these two cases coincide due to the duality principle. With the H-plane, the height of the sources over the ground plane is assumed to be $h + \lambda/4$. This is because with this plane the incident field is being reflected by the plane metal base of the ground plane as has been mentioned above. The plots of Figure 4 are calculated assuming that the sources $1'$ and $2'$ are removed thus the antenna element pattern is symmetrical with respect to the direction of $\theta = 0$. As seen, in the H-plane, a null is being formed for a certain direction within the top semi-sphere. Said null affects RHCP antenna polarization properties. However, calculations have shown that if an antenna element possesses at least $-12 \ldots -15$ dB of suppression of radiation in the direction towards the ground plane, said null is (being) smoothed out. Said antenna element pattern property is typical with today commercially available GNSS antennas.Estimates of above are done with two-dimensional models considerations. However, within physical optics approximations to the ground plane currents, E- and H-plane radiation patterns for three-dimensional problem (disk) coincide with those of above if the ground plane is large enough.

3. IMPLEMENTATION EXAMPLE AND FIELD TEST RESULTS

Antenna pattern realization has been checked by scaling approach first. For this purpose an antenna system operating at 5700 MHz has been constructed (Figure 5(a)). Here the diameter of the ground plane is about 71 cm (13.5λ). A microstrip patch antenna with local flat ground plane was used as antenna element. Such an antenna element has a down/up ratio of -15 dB in the direction towards the impedance surface. Figure 5(b) shows measured plots of the antenna system patterns for two different values of the height h. As seen,said plots almost coincide. F_{+12} is about -11 dB to about -9 dB; DU_{12} is better than -20 dB; and $F(-\pi/2)$ is less than -40 dB. The antenna system for GNSS operation is shown in Figure 6. Antenna system comprises a straight pins ground plane with total diameter of 3 meters and an antenna element mounted at the height of about 7 ... 8 cm. Different types of commercially available GNSS receiver antennas were tested as antenna elements with practically the same results. Shown in photopicture is Topcon MGA8 compact dual frequency RTK antenna. Antenna system is mounted on a support frame at a height of about 2 meters above the Earth surface.

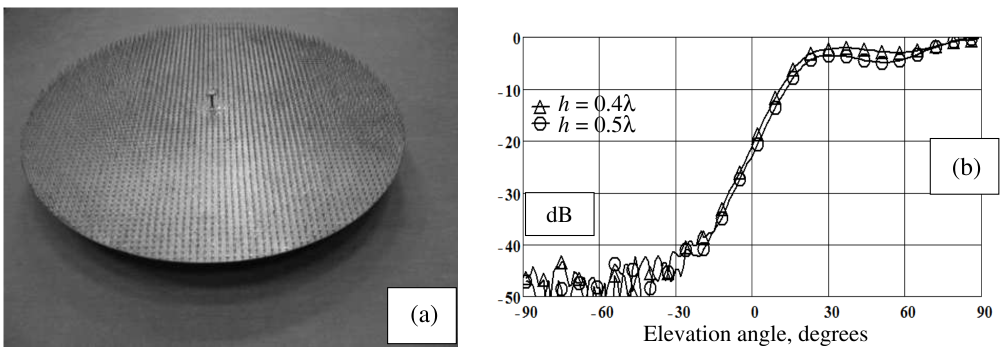

Figure 5: Antenna system model operating at 5700 MHz and corresponding antenna patterns (measured).

Figure 6: GNSS antenna sample (measured).

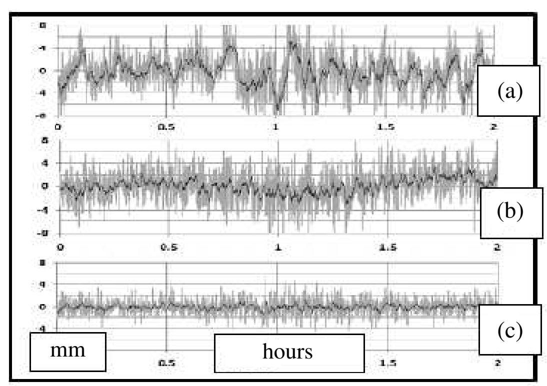

Figure 7: Vertical coordinate readings in real time.

Achievable precision of differential satellite positioning was tested at open sky test range. Three short (about 10 meters length) baselines were used: a) in between two standard Choke Ring antennas as base and rover; b) in between two large impedance ground plane antennas; and c) is of so-called zero type. This last one means two GNSS receivers connected to one antenna via a splitter. Zero baseline is free from multipath errors and illustrates system noise level. Topcon survey grade receivers have been used for data collection. Real time readings for vertical coordinate for these 3 cases are shown in Figures 7(a), (b), (c) respectively. Observation session lasted for 2 hours, data sampling rate was 5 seconds. In each plot,the results of system noise smoothing by moving window of 10 samples are illustrated by a thick line. As seen with the plots, typical multipath error-induced time line with Choke Ring antennas has been smoothed out with large impedance ones. For this last case the remaining multipath error falls below system noise and is estimated to be $+/-1.5\ldots2\,\mathrm{mm}$.

4. CONCLUSION

GNSS antenna system with large impedance ground plane has been developed. Antenna system has a cut-off pattern in elevation plane providing with multipath suppression of 20 dB or better staring from 10–12 degrees elevation. Multipath error to positioning in real time is shown to fall below the system noise level and is estimated to be $+/-1.5\ldots2\,\mathrm{mm}$ in vertical coordinate.

REFERENCES

1. Leick, A., *GPS Satellite Surveying*, 2nd Edition, Wiley & Sons, New York, 1995.
2. Counselman, C. C., "Multipath-rejecting GPS antennas," *Proceedings of the IEEE*, Vol. 87, No. 1, 86–91, 1999.
3. Lopez, A. R., "GPS landing system reference antenna," *IEEE Antennas and Propagation Magazine*, Vol. 52, No. 1, 105–113, 2010.
4. Scire-Scappuzzo, F. and S. N. Makarov, "A low-multipath wideband GPS antenna with cutoff or non-cutoff corrugated ground plane," *IEEE Trans. AP*, Vol. 57, No. 1, 33–46, 2009.
5. Tranquilla, J. M., J. P. Carr, and H. M. Al-Rizzo, "Analysis of a choke ring ground plane for multipath control in global positioning system (GPS) applications," *IEEE Proc. AP*, Vol. 42, No. 7, 905–911, 1994.
6. Sievenpiper, D. F., "High impedance electromagnetic surfaces," Ph.D. Dissertation, University of California, Los Angeles, 1999.
7. McKinzie, W. E., R. B. Hurtado, B. K. Klimczak, and J. D. Dutton, "Mitigation of multipath through the use of an artificial magnetic conductor for precision GPS surveying antennas," *Proceedings of IEEE AP International Symposium*, Vol. 4, 640–643, 2002.
8. Tatarnikov, D. V., A. V. Astakhov, and A. P. Stepanenko, "Broadband convex impedance ground planes for multi-system GNSS reference station antennas," *GPS Solutions*, Vol. 15, No. 2, 101–108, 2011.
9. Ufimtsev, P. Ya., *Fundamentals of the Physical Theory of Diffraction*, Wiley & Sons, New Jersey, 2007.
10. Tatarnikov, D. V., "Ground planes for high precision GNSS antennas. Part I. Flat conductive and impedance ground planes," *Antennas, Moscow, Raditechnika*, No. 4 (131), 6–19, 2008 (in Russian).

Omni-directional Leaky-wave Coaxial Antenna

Ahmed M. Attiya
Microwave Engineering Department, Electronics Research Institute, Egypt

Abstract— In this paper, we present modal analysis of a coaxial leaky wave antenna composed of an inner perfect electric conductor and an outer artificial partially reflecting impedance surface separated by a dielectric layer. The artificial impedance surface can be implemented by periodic slits with periodicity much less than the operating wavelength. The equivalent surface impedance of this surface is obtained by analytical form. Simple design steps based on this modal analysis are presented. These design steps are used to design a coaxial leaky wave antenna. This design is verified by comparing results with full wave analysis based on finite element simulator.

1. INTRODUCTION

There is an increasing interest in directive omni-directional antennas with a conical radiation pattern in different applications like satellite communication, wireless systems and mobile base stations. Different configurations can be used for these applications like metamaterial shell waveguide, cylindrical dielectric rod, corrugated dielectric rod, and coaxial structure with periodic perturbation on its outer side [1–4].

For a special case where the periodic perturbation has a periodicity which is much smaller than the operating wavelength, this periodic structure can be treated as an equivalent partially reflecting impedance surface [5]. Figure 1 shows the cross section of the proposed antenna structure where a and b are the inner and outer radii respectively, ε_1 is the permittivity of the dielectric material between the inner and the outer surfaces, and θ_0 is the direction of the main beam. The inner surface is assumed to be perfectly electric conductor while the outer surface is partially reflecting surface which can be presented as a reactive surface impedance Z_S.

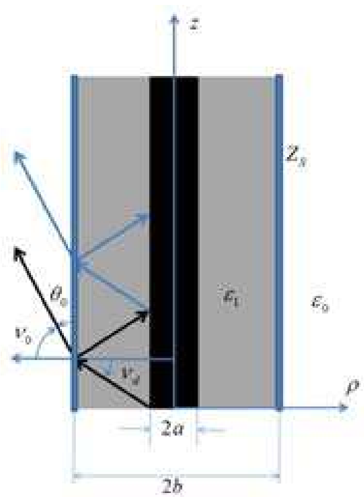

Figure 1: Geometry of a coaxial leaky wave antenna with inner conductor and partially reflecting outer surface.

Zhao et al. [6] introduced simplified modal analysis and design procedure for planar leaky wave antenna based on transverse equivalent network of a planar waveguide composed of a grounded dielectric substrate and covered with a partially reflecting artificial impedance surface. They compared this analysis with full wave analysis based on MoM [7, 8] and they showed excellent accuracy with much less computational complexity. They also used this simplified modal analysis to introduce physical interpretations to the main properties of the introduced leaky wave antenna.

In this paper, the analysis of [6] for the planar leaky wave antenna is applied to the case of a coaxial leaky wave antenna with an impedance outer surface. This analysis is used to introduce design steps for this coaxial leaky wave antenna. These design steps are used to obtain the physical parameters of this coaxial structure like the outer radius and the surface impedance of the outer surface for specific values of inner radius and dielectric material to obtain certain scanning angle at a certain operating frequency. The artificial impedance surface is implemented by periodic slits in a conducting sheet. The dimensions of these slits which satisfy the required impedance surface are obtained by analytical form. All these parameters are combined together and compared with the results of a full wave numerical simulation by using HFSS simulator.

2. THEORY AND ANALYSIS

To obtain an omni-directional radiation pattern, it would be required to use zero order modes in ϕ direction. The fields inside the structure can be presented as multiple reflected rays as shown in Figure 1. Thus, the proposed coaxial leaky wave antenna should support either TM_{0n} or TE_{0n} mode. To obtain an oblique beam the lowest order mode corresponds to $n = 1$. The present analysis of coaxial leaky wave antenna is based on TM_{01}. Similar steps can be used for TE_{01}.

The TM Hertzian potentials for the zero order modes in ϕ direction inside and outside the coaxial structure are given by:

$$\Pi'_{1z} = \left[A'_1 J_0\left(\gamma'_{1\rho}\rho\right) + B'_1 Y_0\left(\gamma'_{1\rho}\rho\right)\right] e^{-j\gamma'_z z} \quad \text{where } a \leq \rho \leq b. \tag{1a}$$

$$\Pi'_{0z} = A'_0 H_m^{(2)}\left(\gamma'_{0\rho}\rho\right) e^{-j\gamma'_z z} \quad \text{where } b \leq \rho \leq \infty. \tag{1b}$$

By using these Hertzian potentials, one can obtain the fields inside and outside the coaxial structure. These fields are used to obtain the corresponding dispersion equation of this coaxial structure by applying the boundary conditions on the inner and outer interfaces as follows:

$$\frac{\gamma_\rho^d \gamma_\rho^0 H_0^{(2)}\left(\gamma_\rho^0 b\right)\mathbf{\Phi}}{\varepsilon_r \gamma_\rho^0 H_0^{(2)}\left(\gamma_\rho^0 b\right)\mathbf{\Psi} + \gamma_\rho^d H_1^{(2)}\left(\gamma_\rho^0 b\right)\mathbf{\Phi}} - j\frac{Z_S k_0}{\eta_0} = 0 \tag{2a}$$

where

$$\mathbf{\Phi} = \left[Y_0\left(\gamma_\rho^d a\right) J_0\left(\gamma_\rho^d b\right) - J_0\left(\gamma_\rho^d a\right) Y_0\left(\gamma_\rho^d b\right)\right] \tag{2b}$$

and

$$\mathbf{\Psi} = \left[J_0\left(\gamma_\rho^d a\right) Y_1\left(\gamma_\rho^d b\right) - Y_0\left(\gamma_\rho^d a\right) J_1\left(\gamma_\rho^d b\right)\right] \tag{2c}$$

By solving this dispersion equation one can obtain the longitudinal complex propagation constant which can be used to obtain peak direction and the beamwidth of the radiation pattern [4].

3. STEPS OF DESIGNING A COAXIAL LEAKY WAVE ANTENNA WITH AN OUTER IMPEDANCE SURFACE

To design a coaxial leaky wave antenna the input parameters are the operating frequency, the inner radius, the dielectric material between the inner and the outer surfaces, the required scanning angle and the required beamwidth. On the other hand, the parameters required to be determined are the outer radius, the outer surface impedance and how to implement this surface impedance.

The first step to design a coaxial leaky wave antenna with a certain inner radius and dielectric material is to determine the outer radius which would be suitable to introduce leaky wave radiation in the required direction of the main beam. To obtain an initial guess of this outer radius, we assume a coaxial structure with a perfect conducting outer layer. The main beam is tilted with an angle $v_0 = \frac{\pi}{2} - \theta_0$ in free space with respect to the normal direction on the interface between the outer of the dielectric layer and free space as shown in Figure 1. Thus the corresponding angle inside the dielectric medium can be directly obtained by using Snell's law as $v_d = \sin^{-1}(\frac{\sin v_0}{\sqrt{\varepsilon_r}})$. For the case of a coaxial structure with an outer perfect conductor, the propagation constant is pure real since there is no leakage of the guided wave. Thus the transverse propagation constant is simply $\gamma_\rho^d = k_1 \cos v_d$. The problem now is to find the outer radius b_{PEC} that satisfies the eigenvalue equation of the coaxial structure with perfect conductor outer surface to determine the thickness of the dielectric layer as follows:

$$Y_0\left(k_1 a \cos v_d\right) J_0\left(k_1 b_{\mathrm{PEC}} \cos v_d\right) - J_0\left(k_1 a \cos v_d\right) Y_0\left(k_1 b_{\mathrm{PEC}} \cos v_d\right) = 0 \tag{3}$$

The next step is to determine the required complex longitudinal propagation constant of the proposed leaky wave structure which satisfies the required scanning angle and beamwidth by using the relations in [4]. Thus we obtain γ_z, γ_ρ^0 and γ_ρ^d. By using the values of γ_ρ^0, γ_ρ^d, b_{PED} and the remaining input parameters in Eq. (2a) one can obtain the surface impedance Z_S which satisfies the dispersion equation. However, the obtained surface impedance in this case is usually complex value which represents a combination between resistive and a reactive sheet impedance. Implementation of equivalent pure reactive impedance sheet can be obtained directly by using an periodic patches or slits. Thus it is required to tune the outer radius in Eq. (2a) to obtain a pure reactive surface impedance. This can be obtained by a simple search algorithm for different values of the outer radius around the initial guess b_{PEC} to obtain b_{Z_S} which satisfies the same complex propagation coefficient and satisfies at the same time pure reactive surface impedance. The resulting outer radius b_{Z_S} which satisfies pure reactive surface impedance is slightly larger than b_{PEC} and the resulting reactive surface impedance $Z_S = -jX_S$ is capacitive. This capacitive surface impedance on the interface between a dielectric layer and free space can be implemented by an array of narrow slits on the interface. The equivalent surface impedance on narrow slits is given by [5]

$$\frac{Z_S}{\eta_0} = -j\frac{\pi}{k_0 d(\varepsilon_r + 1)\ln\left(1/\sin\frac{\pi g}{2d}\right)} \tag{4}$$

where d and g are the period and the width of the slits respectively. By fixing the period of the slits at a certain value, one can solve Eq. (4) to obtain the slit width which satisfies the required surface impedance.

4. RESULTS AND DISCUSSIONS

In this section, we show the detailed steps for designing a coaxial leaky wave antenna based on the above discussions. The operating frequency is assumed to be 10 GHz. The length of the antenna is assumed to be 300 mm which is ten times the free space wavelength at the operating frequency. The radius of the inner conductor is assumed to be 10 mm which corresponds one third the free space wave. The dielectric layer between the inner and outer surfaces are assumed to be tefelon of $\varepsilon_r = 2.2$. The required scanning angle is assumed to be $\theta_0 = 60°$ and the required 3 dB beamwidth is assumed to be 10°. For this scanning angle and beamwidth the required complex longitudinal propagation coefficient is obtained by [4] as $\gamma_Z/k_0 = 0.5 - j0.075$.

By using the above parameters, Eq. (3) is solved numerically to obtain the initial guess of the outer radius based on PEC outer surface. For the present scanning angle, the initial guess of the outer radius is found to be nearly 20.6773 mm. The resulting outer radius in the previous step combined with the complex longitudinal propagation constant and the remaining parameters are used in Eq. (2) to obtain the required normalized surface impedance of the outer surface It is found that this normalized surface impedance should be $Z_S/\eta_0 = 0.0395 - j0.0038$ to obtain the required scanning angle. A simple search is performed on different values of outer radius to obtain a pure reactive surface impedance. It is found that for the above parameters, the required outer radius is found to be nearly 22 mm which is slightly larger than the initial guess obtained by PEC outer surface. For this outer radius, the normalized surface impedance of the outer surface should be $Z_S/\eta_0 = -j0.2064$. Thus, the parameters of the proposed coaxial leaky wave antenna in the present design are = 10 mm, $b = 22$ mm, $\varepsilon_r = 2.2$, and $Z_S/\eta_0 = -j0.2064$ which corresponds to slit width 75 µm for a periodicity of 6 mm. These parameters are used in full wave simulation by using HFSS as shown in Figure 2. This coaxial structure is fed by using a wave port at one end and is terminated by a matched lumped load at the other end such that the simulated reflection coefficient at the feeding end is less than −30 dB at the operating frequency. Figure 3 shows the simulated radiation pattern of this coaxial leaky wave antenna. It can be noted the good agreement

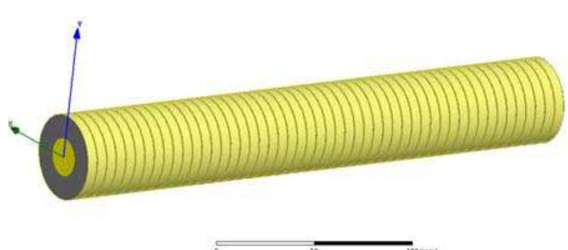

Figure 2: Geometry of the simulated coaxial leaky wave antenna.

with the proposed scanning angle and beamwidth.

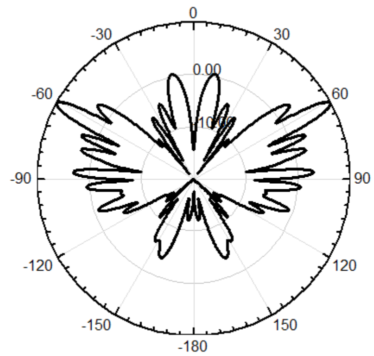

Figure 3: Simulated radiation pattern as function of angle θ in degrees. The parameters of the coaxial leaky wave antenna are $L = 300\,\text{mm}$, $a = 10\,\text{mm}$, $b = 22\,\text{mm}$, $\varepsilon_r = 2.2\,\text{mm}$, $d = 6.0\,\text{mm}$ and $w = 5.25\,\text{mm}$. The operating frequency is $f = 10\,\text{GHz}$.

5. CONCLUSION

In this paper, we presented analysis of a coaxial leaky wave antenna composed of an inner perfect electric conductor and an outer impedance surface separated by a dielectric layer. This analysis is used to introduce detailed design steps for this leaky wave antenna. These design steps are used to obtain the physical parameters of this coaxial structure like the outer radius and the surface impedance of the outer surface for specific values of inner radius and dielectric material to obtain the required peak radiation angle at the design operating frequency. The impedance surface is implemented by periodic slits in a conducting sheet. Primary estimates for the dimensions of these slits which satisfy the required impedance surface are obtained by simple analytical form suitable for planar interface and normal incidence. All these parameters are combined together in a full wave numerical simulation by using HFSS. The results of the numerical simulation shows good agreement with proposed design requirements.

REFERENCES

1. Kim, D. H. and H. J. Eom, "Radiation of a leaky coaxial cable with narrow transverse slots," *IEEE Trans. Antennas Propag.*, Vol. 55, No. 1, 107–110, Jan. 2007.
2. Xu, S., J. Min, S.-T. Peng, and F. K. Schwering, "A millimeter-wave omnidirectional circular dielectric rod grating antenna," *IEEE Trans. Antennas Propag.*, Vol. 39, No. 7, 883–891, Jul. 1991.
3. Alu, A., F. Bilotti, N. Engheta, and L. Vegni, "Theory and simulations of conformal omnidirectional subwavelength metamaterial leaky-wave antenna," *IEEE Trans. Antennas Propag.*, Vol. 55, No. 6, 1698–1708, Jun. 2007.
4. Kim, J.-P. and C.-W. Lee, "Radiation characteristics of strip-loaded dielectric-coated conducting cylinder," *Int. J. RF Microw. Comput.-Aided Eng.*, Vol. 18, No. 1, 32–41, Jan. 2008.
5. Tretyakov, S., *Analytical Modeling in Applied Electromagnetics*, Artech House, Inc., 2003.
6. Zhao, T., D. R. Jackson, J. T. Williams, and A. A. Oliner, "General formulas for 2-D leaky-wave antennas," *IEEE Trans. Antennas Propag.*, Vol. 53, No. 11, 3525–3533, Nov. 1993.
7. Zhao, T., D. R. Jackson, J. T. Williams, H. Y. Yang, and A. A. Oliner, "2-D periodic leaky-wave antennas — Part I: Metal patch design," *IEEE Trans. Antennas Propag.*, Vol. 53, No. 11, 3505–3514, Nov. 2005.
8. Zhao, T., D. R. Jackson, and J. T. Williams, "2-D periodic leaky-wave antennas — Part II: Slot design," *IEEE Trans. Antennas Propag.*, Vol. 53, No. 11, 3515–3524, Nov. 2005.

Robust Beamforming Using Weighted Directional Constraints and Wavelet Blocking Matrix

Said E. El-Khamy, Mohamed R. M. Rizk, and Roshdy K. Korayem
Department of Electrical Engineering, Faculty of Engineering
Alexandria University, Alexandria, Egypt

Abstract— Constrained Least Mean Square (CLMS) beamformer is sensitive to the direction estimation error. Bayesian based modifications are used to add robustness to the CLMS beamformer. In this paper, Bayesian Beamformer is implemented using a Generalized Sidelobe Canceller (GSLC), one of the CLMS implementation techniques. The proposed robust GSLC reduces the computational complexity and saves degrees of freedom than other conventional robust designs. The released degrees of freedom grant more efficiency to the interferers' rejection process.

1. INTRODUCTION

The Constrained Least Mean Square (CLMS) [1, 2] algorithm minimizes the output power of the antenna array and satisfies some constraints (e.g., directional constraints). In the case of directional constraints, CLMS algorithms (e.g., sidelobe canceller [3]) fail to capture the Signal Of Interest (SOI) if there is an error in the Direction Of Arrival (DOA) estimation. Moreover it will consider the SOI as an interferer and create null in the SOI direction. The large gain will be toward the wrong (detected) direction. Several techniques may be used to overcome this problem. We are interested in two of them. First, constraining the pattern derivative(s) to be equal to zero at the DOA to create constant gain around the detection angle [4]. The second is dividing the interval of uncertainty into smaller intervals. The desired beamformer is the sum of the ideal beamformers of the mid-points of the intervals weighted by some weights. Fuzzy logic based weights are an efficient scenario [5] for the offline adaptation, more efficient version is in [6]. Probability density function of the random variable θ namely Bayesian weights, θ is the DOA, are one of the efficient weights may be used for the online adaptation [7].

The Generalized Sidelobe Canceller (GSLC) is one of the efficient techniques to implement CLMS. It consists of quiescent filter, blocking matrix and variable weights. The GSLC with wavelet based blocking matrix [8, 9] employs the wavelet property of vanishing moments to block wide interval. This needs to bypass the same interval in the quiescent filter. Normally, derivative constraints are used in the quiescent filter. The pass interval through the derivative constraints does not employ the whole blocked interval.

In this paper, The Bayesian based beamformer has been implemented using GSLC. The proposed GSLC has the ability of flexible design (quiescent filter can be wider band) using fewer degrees of freedom than the derivative constraints and less computational complexity than the previous Bayesian beamformer. The paper is organized as follows. Section 2, optimization techniques revision reviews CLMS and GSLC, Chapter 3 reviews the Bayesian based beamformer, Chapter 4 introduces the proposed algorithm, Chapter 5 shows the simulation results and Chapter 6 concludes the paper.

2. OPTIMIZATION TECHNIQUES REVISION

In the case that the communication system has the ability to destroy a portion of the bandwidth to send a reference signal, the Least Mean Square (LMS) can be used to adapt the antenna array. Ifthe reference signal is d, the array output $y = w^H x$ (x is the array input vector, w is the weight vector) the error signal $e = d - y$. LMS minimizes the power in the error signal $e = d - y$. It is a quadratic problem in w, its solution is given in [1, 8]

$$w_{LMS} = R_{xx}^{-1} R_{xd}, \tag{1}$$

R_{xx} is the autocorrelation matrix of the input, R_{xd} is the crosscorrelation matrix of the input and reference signal.

If there is no reference signal in the system then the Constrained Least Mean Square (CLMS) is one of the solutions to adapt the array. It minimizes the output power while constraining the solution to satisfy the linear constraints set $C^H w = f$, C is the constraint matrix, f is the response vector. The solution is given by [2]

$$W_{CLMS} = R_{xx}^{-1} C \left(C^H R_{xx}^{-11} C \right)^{-1} f \tag{2}$$

For a simple beamformer with one directional constraint which is unity gain in the desired DOA and nulling the interferers by minimization, the constraint matrix C tends to a vector and $(C^H R_{xx}^{-1} C)$ tends to a scalar. From thissolution one can show that CLMS is sensitive to the constraints' (e.g., directional) errors. Derivative constraint(s) is one of the mostfamous techniques used to create robust beamformer with respect to direction estimation errors. It depends on forcing the beam-pattern derivative(s) to be zero at the direction of arrival. Higher order zero derivatives are more robustness. The column $[1^n \; 2^n \; \ldots \; M^n]^T$ in the constraint matrix C creates zero derivative constraints of order nif the corresponding element in the response vector f is zero [4].

To simplify the problem of CLMS, GSLC (Generalized Sidelobe Canceller) [3] may be used. It depends processing the input into two branches. The first branch is a quiescent filter F, designed to hold the constraints. The second branch is a blocking matrix B which is designed to block the SOI, w_{SLC} is a weight vector located after the blocking matrix to optimize the GSLC. w_{SLC} is optimized using LMS to minimize the difference power between the output of the two branches. Minimization of this difference power is equivalent to solving the CLMS problem with CLMS equivalent weight $w_{eq} = F - Bw$.

The design problem of the GSLC is the design of F & B. In [3], $F = C(C^H C)^{-1} f$ holds the constraints set $C^H w = f$. To design derivative constraints based robust GSLC we choose C and f like the CLMS case. B is designed to block the derivative constraints around the DOA. There are a lot of research to design B. We are interested in the wavelet based one which introduced in [8] regarding its low computational cost due to its sparse construction

$$B = \begin{bmatrix} H_1 \\ H_2 \\ \vdots \\ H_{M-1} \end{bmatrix}, \quad H_m = \begin{bmatrix} h_{m1} & h_{m2} & \ldots & h_{m(MK)} & 0 & \ldots & 0 \\ o_d & h_{m1} & h_{m2} & \ldots & h_{m(MK)} & \ldots & 0 \\ \vdots & & \vdots & & \ddots & \ddots & \\ o_d & \ldots & o_d & h_{m1} & h_{m2} & \ldots & h_{m(MK)} \end{bmatrix} \tag{3}$$

h_i is the ith filter in an M-band K-regular wavelet filters system. h_{ij} indicates the element j in the filter i. o_d is a zero row vector of d zeros. This matrix blocks the SOI and $K-1$ derivatives using its regularity K, proved in [8]. Concerning this design, F destroys a number of degrees of freedom equal to the number of derivative constraints plus one directional constraint. We will show in our beamformer how to reduce this number of degrees of freedom to give them the opportunity to be used by the minimization technique.

3. BAYESIAN BASED BEAMFORMER

Suppose that the SOI impinges the array from the desired angle θ_{des}. Assuming detection error, the detected angle of arrival is θ_{det}. Using the CLMS beamformer with one directional constraint will consider the SOI from the direction θ_{des} as an interferer and discard it. To prevent that, the technique used in [7] assumes θ as a random variable with a given a priori probability density function (pdf). The a priori pdf is used to calculate the a posteriori pdf, $p(\theta/x)$. The interval of uncertainty is divided into L intervals, the desired beamformer is the sum of the beamformers of each interval multiplied by its a posteriori probability value. The a posteriori pdf has been found in [7] and can be approximated to

$$p(\theta_i | x) = c p_i e^{K\gamma \frac{1}{a_i^H R_K^{-1} a_i}} \tag{4}$$

K is the number of samples, p_i is the a priori probability, c is a constant to hold the sum of the probabilities to 1, γ: a constant controls the behavior of the algorithm, and R_K is the sample covariance matrix equal $E(xx^H)$. Then the desired beamformer is

$$w_{Bay} = \sum_{i=1}^{L} w_i p(\theta_i | x) \tag{5}$$

w_i is the weight at angle θ_i calculated from Equation (2).

4. WAVELET BLOCKING MATRIX WITH BAYESIAN BASED CONSTRAINTS AS A ROBUST BEAMFORMER

In our proposed technique we used th esidelobe canceller to design the Bayesian based beamformer reviewed in Section 3. Wavelet based blocking matrix shown in Equation (3) was used to block derivative constraints around the DOA. To design the quiescent filter the interval of uncertainty is divided into L small intervals like Bayesian beamformer. The quiescent filter of each interval is calculated using the conventional form with one directional constraint. Substituting the equivalent CLMS weight in Equation (5) we get

$$w_{Bay} = \sum\nolimits_{i=1}^{L} (F_i - Bw) p(\theta_i|x), \quad F_i = \frac{1}{M} a_i \tag{6}$$

$$w_{Bay} = \sum_{i=1}^{L} \left(\frac{1}{M} a_i - Bw \right) p(\theta_i|x) \tag{7}$$

Note that the blocking matrix blocks the whole interval of uncertainty, so it is considered the same for all intervals

$$w_{Bay} = \frac{1}{M} \sum\nolimits_{i=1}^{L} a_i p(\theta_i|x) - Bw \sum\nolimits_{i=1}^{L} p(\theta_i|x) = \frac{1}{M} \sum\nolimits_{i=1}^{L} a_i p(\theta_i|x) - Bw \tag{8}$$

Comparing this equation with the CLMS equivalent weight we can get

$$F = \frac{1}{M} \sum_{i=1}^{L} a_i p(\theta_i|x) \tag{9}$$

From this result, we see that the quiescent filter is a direct algebraic sum of the mid-points steering vectors multiplied by their Bayesian weights. This gives the ability of controlling the quiescent filter band; the Bayesian weights contribute the high directivity keeping the advantage of the Bayesian beamformer. From the analogy between this result and the conventional case we can verify that only one degree of freedom is destroyed to get the result, allowing more constraints to the minimization process to create deeper nulls. We can conclude that we got the advantage of the derivative constraints (robustness), the advantages of Bayesian weights (directivity) and advantage of multiple beamformers (fewer degrees of freedom than derivative constraints).

5. SIMULATION RESULTS

Assume a uniform linear 12 elements sensor array. Four signals impinge the array from angles −75, −55, 20, 45 degrees. The 20 degree is the desired direction. The Sidelobe canceller with wavelet based blocking matrix 4 bands 3 regular was simulated in the case of simple second order derivative constraints [8] and with the proposed quiescent filter. The results were averaged over 10 trails Figure 1–Figure 4 show the beampattern of both beamformers for the case of no error, 4, 8 and 10 degrees estimation error. We can see in the case of 10 degrees error that the conventional derivative constraints created a null toward the desired DOA while the proposed beamformer maintains high

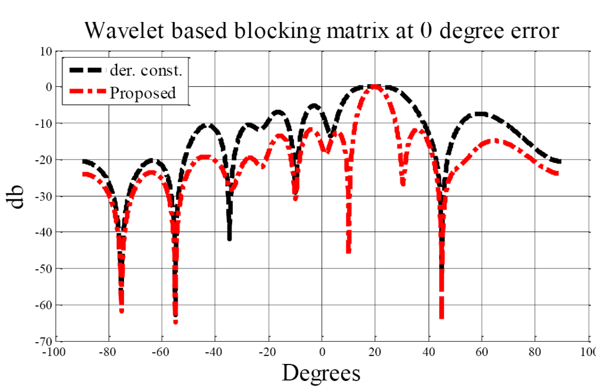

Figure 1: Beampattern in the case of no error.

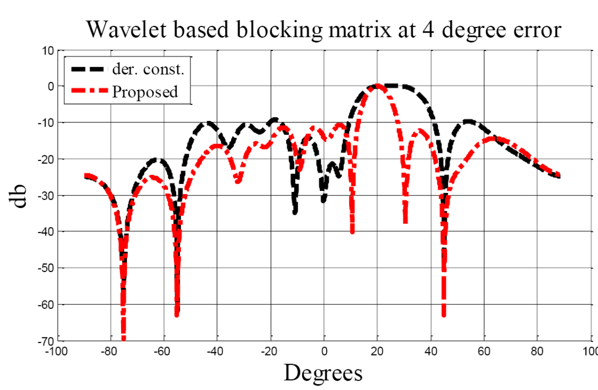

Figure 2: Beampattern with 4 degrees detection error.

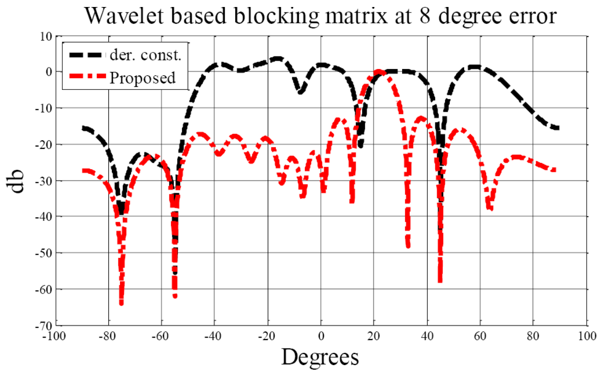

Figure 3: Beampattern with 8 degrees detection error.

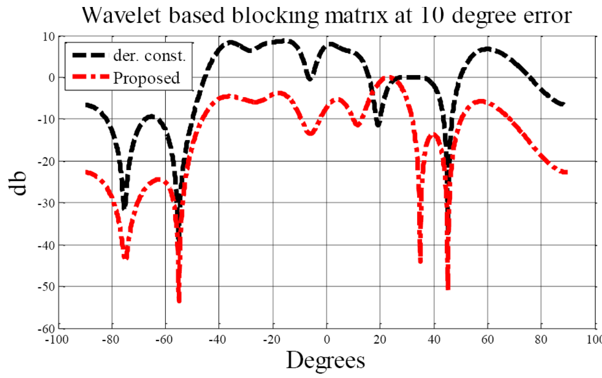

Figure 4: Beampattern with 10 degrees detection error.

gain. Conventional derivative constraints cover the uncertainty interval with wide beam while the proposed beamformer covers it with high directivity. The proposed beamformer creates deeper nulls due to the more degrees of freedom available for the minimization process. The computational complexity is less due to the fact that we optimize only one branch and one quiescent filter instead of L beamformers in the conventional Bayesian beamformer.

6. CONCLUSIONS

In the paper which we introduce an abstract, sidelobe canceller based Bayesian beamformer has been designed. In the conventional Bayesian beamformer the beamformer is calculated multiple times for different signal of interest locations while the interferers are the same for all the patterns. This makes an extra computational load. Given the fact that the sidelobe canceller divides the problem into two branches, one branch is for the signal of interest while the other is for the interferers, this contributes the opportunity to calculate the interferers' related part only once in the new design. The new design contributes more flexibility to control the sidelobe canceller components as well as saving degrees of freedom comparing with the derivative constraints case. Also, it can track the user with high directivity although there is an error in the direction of arrival estimation.

REFERENCES

1. Monzingo, R. A. and T. W. Miller, *Introduction to Adaptive Arrays*, John Wiely & Sons, 1980.
2. Frost, III, O. L., "An algorithm for linearly constrained adaptive array processing," *Proceedings of the IEEE*, Vol. 60, No. 8, 926–935, Aug. 1972.
3. Griffiths, L. and C. Jim, "An alternative approach to linearly constrained adaptive beamforming," *IEEE Transactions on Antennas and Propagation*, Vol. 30, No. 1, 1982.
4. Er, M. H. and A. Cantoni, "Derivative constraints for broad-band element space antenna array processors," *IEEE Transactions on Acoustics. Speech, Signal Processing*, Vol. 31, 1378–1393, Dec. 1983.
5. Morell, A., A. Pascual-Iserte, and A. I. Perez-Neira, "Fuzzy inference based robust beamforming," *Elsevier Signal Processing*, Vol. 85, 2014–2029, 2005.
6. El-Khamy, S. E., M. M. Rizk, and R. K. Korayem, "Fuzzy inference based wavelet robust sidelobe canceller," *International Conference on High Performance Computing and Simulation*, Helsinki, Finland, Jul. 1005, 2013, Accepted for Publication.
7. Bell, K. L., Y. Ephraim, and H. L. Van Trees, "A Bayesian approach to robust adaptive beamforming," *IEEE Trans. Signal Process.*, Vol. 48, 386–398, Feb. 2000.
8. Chu, Y. and W. H. Fang, "A novel wavelet-based generalized sidelobe canceller," *IEEE Transactions on Antennas and Propagation*, Vol. 47, 1485–1494, Sep. 1999.
9. El-Khamy, S. and A. F. El-Keyi, "Wavelet domain processing of Generalized sidelobe canceller for wideband smart arrays," *URSI*, 2004.
10. Widrow, B., P. E. Mantey, L. J. Griffiths, and B. B. Goode, "Adaptive antenna systems," *Proceedings of the IEEE*, Vol. 55, No. 12, Dec. 1967.

Design of Elliptic-Function Microstrip Filters with Defected Ground Structures

A. O. Ertay and S. Şimşek
Electrical and Electronics Eng. Faculty, Istanbul Technical University, Istanbul, Turkey

Abstract— In this study, a design procedure which includes three steps is proposed to improve the frequency characteristics of elliptic function microstrip filters with defected ground structures. Firstly, a conventional filter design is presented using elliptic filter prototype. Following the first step, normalized element values of elliptic low pass filter prototype are used and desired filter transformation is carried out. Secondly, microstrip filter transformation of obtained elliptic low pass filter is attained. Lastly, ground plane is etched with different shapes like square-dumbbell, interdigital and fractal versions of different geometries. In this case, an improvement of microstrip filter design is achieved using Defected Ground Structures (DGSs). MATLAB and full wave electromagnetic simulators are used to model the proposed filters. Scattering parameters of microstrip elliptic filter are extracted and plotted via commercial EM design environments. Modifications of ground plane with different geometries are applied to the microstrip elliptic filter via EM software tools and consistent simulation results are obtained.

1. INTRODUCTION

Determination of design objectives of microwave filters is one of the most important points in filter design concerning practical requirements. Microwave filter designers follow specific design procedures to meet design objectives [1].

Filters may have frequency characteristics like bandpass, low pass, high pass and bandstop responses. Practically, any filter has no ideal characteristics such as infinite attenuation at stopband, zero insertion loss at passband [2] and steep transition region from passband to stopband. In addition, some of designer's goals may be compacting of the design structure for smooth curve of group delay, broad bandwidth or stopband. Therefore, it is desired to approach these ideal cases for proposed filter characteristics.

Recently, a spreading attention is given for defected ground structures due to demonstrating of their multi-electromagnetic band gaps (EBGs) or stop bands in frequency responses. There is an etch or slot on the ground plane of planar microstrip which permits interaction between microstrip and defected ground plane [3].

Many applications such as power dividers, microstrip antennas and microwave filters are based on defected ground structures. In power divider applications, etching ground plane can provide size reduction [4] at lower microwave frequencies. Furthermore, DGSs are used for compactness [5, 6], harmonic control in active microstrip antennas [7], impedance matching at feed line [8], improving and controlling radiation properties of patch antennas [9] and suppression of cross-polarized radiation from microstrip arrays [10]. DGSs find more common usage interest in microwave filter applications [11]. Various kinds of design are available in literature for different filter types and specific properties like small size [12, 13], sharp rejection [14], wide stopband [15], multi-band response [16]. In some applications, sharper transition region is vital important role and sharpness factor should be analyzed for this applications [17, 18].

2. DESIGN PROCEDURE

Achieving an elliptic microstrip filter design is the first step of design objectives. To do this, it is needed to have normalized element values and some important parameters like minimum stopband insertion loss (IL) value for elliptic low pass prototype filter. Table 1 shows desired design values for elliptic function low pass prototype filter design. Because of no simple formulation for determining element values of the elliptic-function lowpass prototype filters, element values in [3] are used in the design. For more information about element values of elliptic function low pass prototype filters are available in [19, 20].

In Table 1, n, Ω_C, Ω_s, L_{As}, L_{Ar} are order of filter, normalized cutoff frequency, the equal-ripple stopband starting frequency, minimum stop band insertion loss and pass band ripple, respectively. Normalized element values of elliptic function low pass filter prototype are g_0 to g_7. It is needed to find L-C element values of passive elements shown in Figure 1. In this design input/output

Table 1: Element values of elliptic function low pass prototype filter for $g_0 = g_7 = 1$, $\Omega_C = 1$.

n	Ω_s	L_{As} [dB]	L_{Ar} [dB]	$g_{L1} = g_1$	$g_{C2} = g_2$	$g_{L2} = g_2$	$g_{L3} = g_3$	$g_{C4} = g_4$	$g_{L4} = g_4$	$g_{L5} = g_5$	$g_{C6} = g_6$
6	1.2503	39.9773	0.1	0.7422	1.1189	0.3313	1.2276	0.9746	0.6260	1.1413	1.0273

terminal impedance, relative dielectric permittivity, substrate thickness are chosen as $Z_0 = 50\,\Omega$, $\varepsilon_r = 10.8$ and $h = 1.27\,\text{mm}$ respectively. In addition to these parameters, it is desired to design a low-pass filter with a cut-off frequency of 1.6 GHz using DGS. According to our simulation results, DGS structure reduces cut-off frequency of designed filter. Therefore, cut-off frequency should be chosen greater than desired frequency. It is appropriate to start the design with a cut-off frequency which is 30% or 40% greater than desired frequency. In these simulations, cut-off frequency of low-pass filter is assumed as 2 GHz. The L-C element values, which are scaled to Z_0 and f_c, can be determined as given in [3].

$$\begin{aligned} L_i &= \frac{1}{2\pi f_c} Z_0 g_{L_i} \\ C_i &= \frac{1}{2\pi f_c} \frac{1}{Z_0} g_{C_i} \end{aligned} \tag{1}$$

Calculated element values are given in Table 2.

Table 2: L-C Element values of desired design.

L_1	L_2	C_2	L_3	L_4	C_4	L_5	C_6
2.9531 nH	1.3182 nH	1.7807 pF	4.8844 nH	2.4907 nH	1.5511 pF	4.5410 nH	1.6256 pF

In this design, stepped impedance low pass filter, which use a cascaded structure of alternating high- and low-impedance transmission lines, is used to realize microstrip structure. Inductors behave high impedance lines and capacitors are modeled low impedance ones. Because of stepped impedance design is valid only short transmission line $l < \lambda/8$, it is needed to be careful at each step. For the design of low impedance and high impedance line $Z_{0L} = 14\,\Omega$ and $Z_{0H} = 93\,\Omega$ are taken. Design Equation (2) can be used to find physical lengths of high and low impedance lines with respect to the desired element values.

$$\begin{aligned} l_{L_i} &= \frac{\lambda_{gL}(f_c)}{2\pi} \sin^{-1}\left(2\pi f_c \frac{L_i}{Z_{0L}}\right) \\ l_{C_i} &= \frac{\lambda_{gC}(f_c)}{2\pi} \sin^{-1}\left(2\pi f_c Z_{0C} C_i\right) \end{aligned} \tag{2}$$

Table 3 lists all relevant microstrip design parameters calculated using the microstrip design equations.

Table 3: Microstrip design parameters of desired elliptic low pass filter.

$Z_{oH} = 93\,\Omega$	$W_L = 0.2\,\text{mm}$	$\varepsilon_{eff} = 6.4577$	$\lambda_{gL}(f_c) = 59.02\,\text{mm}$
$l_{L1} = 3.85\,\text{mm}$, $l_{L2} = 1.682\,\text{mm}$, $l_{L3} = 6.771\,\text{mm}$, $l_{L4} = 3.224\,\text{mm}$, $l_{L5} = 6.206\,\text{mm}$			
$Z_{oL} = 50\,\Omega$	$W_0 = 1.1\,\text{mm}$	$\varepsilon_{eff} = 7.1714$	$\lambda_{g0}(f_c) = 56.01\,\text{mm}$
$Z_{oL} = 14\,\Omega$	$W_C = 8\,\text{mm}$	$\varepsilon_{eff} = 8.7749$	$\lambda_{gC}(f_c) = 50.63\,\text{mm}$
$l_{C2} = 2.56\,\text{mm}$, $l_{C4} = 2.22\,\text{mm}$, $l_{C6} = 2.33\,\text{mm}$			

Figure 2 shows microstrip realization of desired design. Scattering parameters of Figure 2 are attained with the help of SONNET electromagnetic simulation program. Figure 3(a) illustrates scattering parameters of required design both HFSS and SONNET EM simulation environments. Because of undesired reactance/susceptance and microstrip discontinuities, -3 dB cut off frequency reveals at 1.62 GHz in HFSS and at 1.65 GHz in SONNET. Resonant frequency and sharpness factor are obtained as 2.05 GHz and 0.8048 via SONNET.

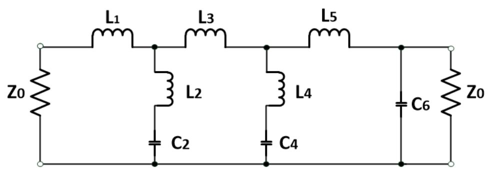

Figure 1: An elliptic-function, lumped-element low pass filter.

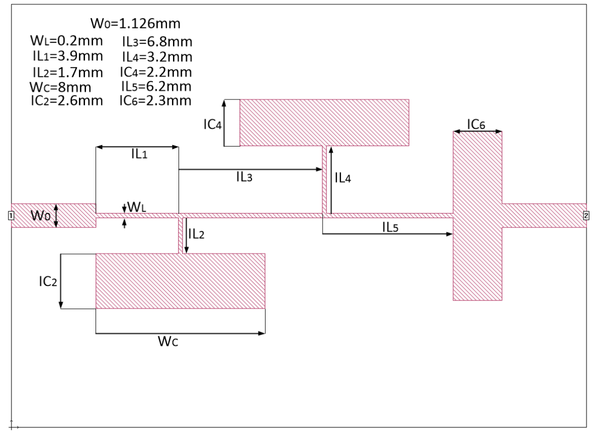

Figure 2: Microstrip realization of desired design.

3. NUMERICAL RESULTS

Last step is to etch ground plane and investigate of different frequency characteristics of the design. In the design procedure, some kind of different geometries like square dumbbell, fractal dumbbell and meander DGSs are applied to ground plane (Figure 3). Figures 3(b) and 3(c) show square dumbbell and fractal DGS at the bottom of the designed filter.

Figure 3(d) gives comparison of S-parameters of designed filters with dumbbell square DGS, fractal DGS and without DGS. Figure 3(d) shows that etching ground plane with dumbbell square DGS increases cut off and resonant frequency with respect to without DGS case. Fractal DGS

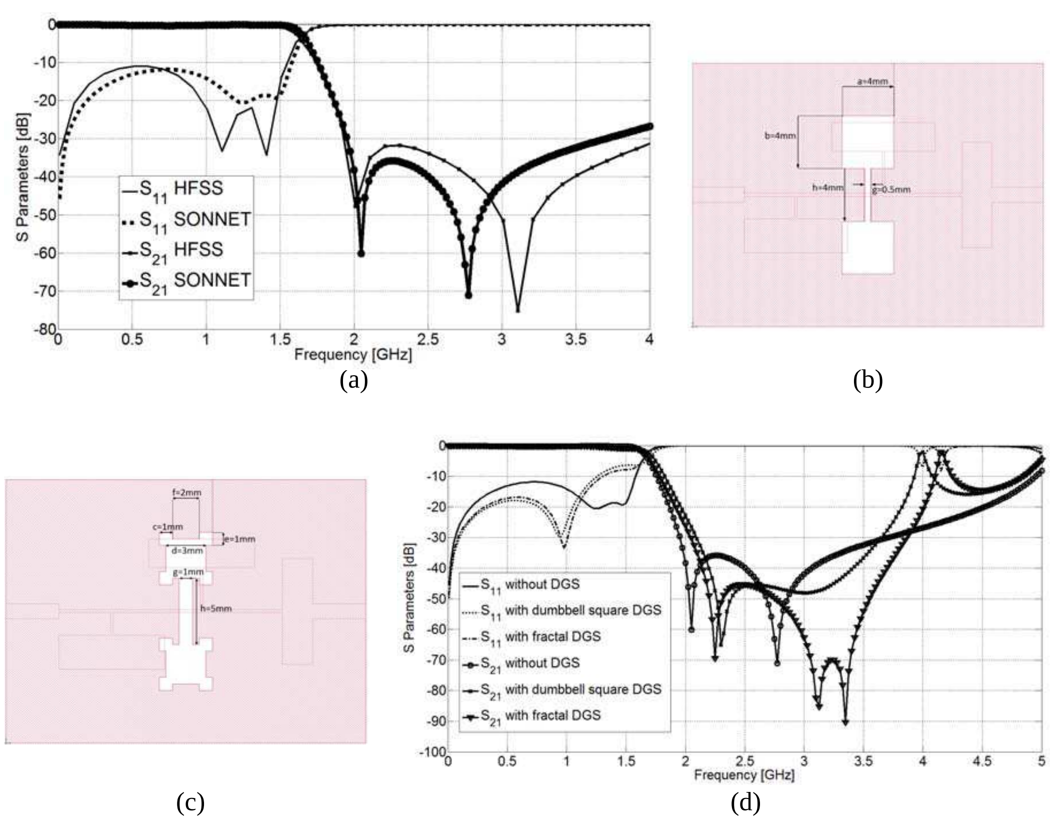

Figure 3: (a) S parameters of elliptic function microstrip low pass filter. (b) Bottom of the designed filter (square dumbbell). (c) Bottom of the designed filter (Fractal Dumbbell). (d) S parameters of elliptic function microstrip low pass filter with square dumbbell and fractal dumbbell.

shape in ground plane decreases cut off and resonant frequency to the square dumbbell DGS case. Transmission peak occurs in dumbbell square DGS case at 4 GHz as well as in fractal DGS case at 4.15 GHz. Another case of designed filters is etching ground plane with having meander DGS. Figure 4(a) and 4(b) show view of meander DGS shape and its design parameters. As it is seen in Figure 4(b) and 4(d) design parameter like conductor spacing (cs) and finger numbers of meander DGS shape are varied and compared to each other. Figure 4 also shows that sharpness factor decreases when finger number increases for meander DGS.

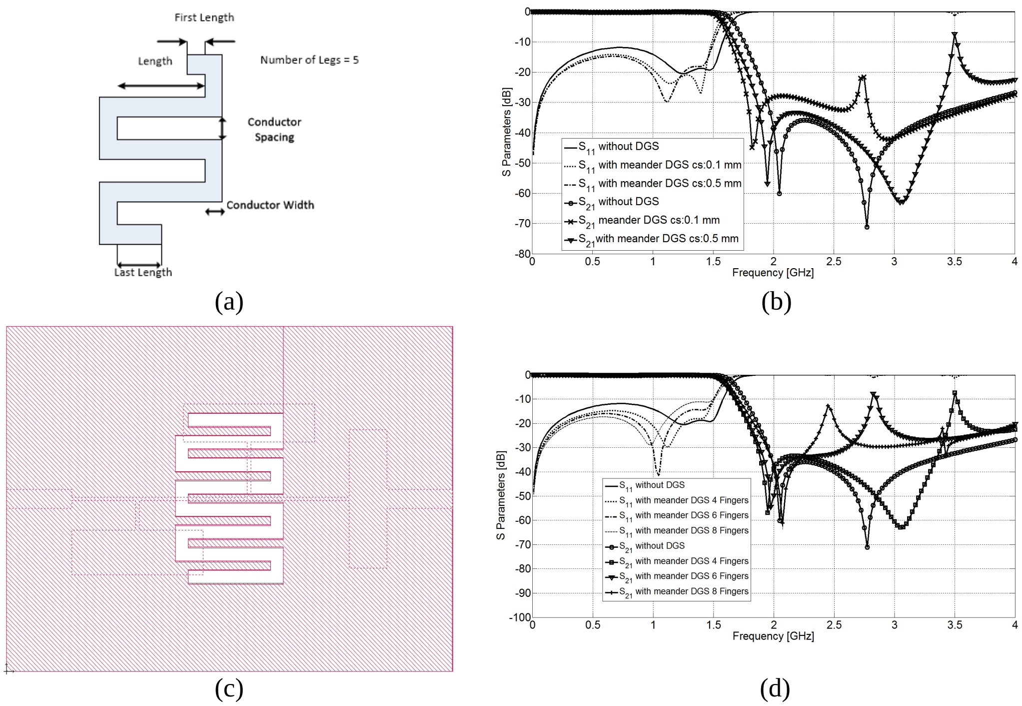

Figure 4: (a) Meander DGS Geometry. (b) Comparison of S parameters both included meander DGS having different conductor spacing (cs = 0.1 mm, 0.5 mm) values and without DGS case, (Lengt = 9 mm, Final Length = 5 mm, Conductor width = 0.8 mm, First Length = 5, Number of Fingers = 4. (c) Bottom view of designed filter with meander DGS. (d) Comparison of S parameters both included meander DGS having different fingers (f = 4, 6, 8) values and without DGS case, (Length = 9 mm, Final Length = 5 mm, Conductor width = 0.8 mm, First Length = 5 mm, Conductor Spacing = 0.5 mm).

Table 4 lists variation of cut off (f_c), resonant frequency (f_0) and sharpness factor (f_c/f_0) values when different DGS cases are applied. Furthermore, variation of length value of meander DGS case is also analyzed. It shows that when the length value is increased sharpness factor value increases for meander DGS case.

Table 4: Comparison of different filter designs with DGS.

Design Types	f_c (GHz)	f_0 (GHz)	Sharpness Factor: f_c/f_0
without DGS	1.65	2.05	0.8048
with SD DGS	1.709	2.3	0.743
with fractal DGS	1.672	2.25	0.743
with meander DGS Finger: 4	1.58	1.95	0.8102
with meander DGS Finger: 6	1.582	1.97	0.8030
with meander DGS Finger: 8	1.602	2.075	0.772
with meander DGS Length: 5	1.602	2.075	0.772
with meander DGS Length: 9	1.545	1.825	0.846
with meander DGS conductor spacing: 0.1 mm	1.556	1.825	0.852
with meander DGS conductor spacing: 0.5 mm	1.58	1.95	0.810

4. CONCLUSION

In this paper, an elliptic-function low pass microstrip filter is designed with defected ground structures using full-wave electromagnetic design environments. Different DGS shapes like square dumbbell DGS, fractal dumbbell DGS, meander DGS are etched on ground plane separately and sharpness factor values of these different designs are compared. Our design objectives are achieved and it is shown appropriate DGS shapes on ground plane could be important parameter to improve better sharpness factor.

REFERENCES

1. Şimşek, S., E. Topuz, and E. Niver, "A novel design method for electromagnetic bandgap based waveguide filters with periodic dielectric loading," *AEU Int. J. Electron. Commun.*, Vol. 66, No. 3, 228–234, 2012.
2. Pozar, D. M., *Microwave Engineering,* 4th Edition, John Wiley, 2012
3. Hong, J. S., *Microstrip Filters for RF/Microwave Applications*, 2nd Edition, John Wiley, 2011.
4. Oraizi, H. and M. S. Esfahlan, "Miniaturization of wilkinson power dividers by using defected ground structures," *Progress In Electromagnetics Research Letters*, Vol. 4, 113–120, 2008.
5. Liu, J. X., W. Y. Yin, and S. L. He, "A new defected ground structure and its application for miniaturized switchable antenna," *Progress In Electromagnetics Research Letters*, Vol. 107, 115–128, 2010.
6. Wang, T., Y.-Z. Yin, J. Yang, Y.-L. Zhang, and J.-J. Xie, "Compact triple-band antenna using defected ground structure for WLAN/WiMAX applications," *Progress In Electromagnetics Research Letters*, Vol. 35, 155–164, 2012.
7. Horri, Y. and M. Tsutsumi, "Harmonic control by photonic bandgap on microstrip patch antenna," *IEEE Microwave Guided Lett.*, Vol. 9, 13–15, Jan. 1999.
8. Thakur, J. P. and J. Park, "An advance design approach for circular polarization of the microstrip antenna with unbalance DGS feedlines," *IEEE Antennas Wireless Propag. Lett.*, Vol. 5, 101–103, 2006.
9. Sung, Y. J. and Y.-S. Kim, "An improved design of microstrip patch antennas using photonic bandgap structure," *IEEE Trans. Antennas Propagat.*, Vol. 53, No. 5, 1799–1803, May 2005.
10. Guha, D., M. Biswas, and Y. M. M. Antar, "Microstrip patch antenna with defected ground structure for cross polarization suppression," *IEEE Antennas Wireless Propag. Lett.*, Vol. 4, 455–458, 2005.
11. Ahn, D, J. S. Park, C. S. Kim, J. Kim, Y. Qian, and T. Itoh, "A design of the low-pass filter using the novel microstrip defected ground structure," *IEEE Transactions on Microwave Theory and Techniques*, Vol. 49, No. 1, Jan. 2001.
12. Chen, J. X., J. L. Li, K. C. Wan, and Q. Xue, "Compact quasi-elliptic function filter based on defected ground structure," *IEE Proc. — Microw. Antennas Propag.*, Vol. 153, No. 4, Aug. 2006.
13. Abdel-Rahman, A., A. K. Verma, A. Boutejdar, and A. S. Omar, "Compact stub type microstrip bandpass filter using defected ground plane," *IEEE Microwave and Wireless Components Letters*, Vol. 14, No. 4, Apr. 2004.
14. Tu, W.-H. and K. Chang, "Compact microstrip low-pass filter with sharp rejection," *IEEE Microwave and Wireless Components Letters*, Vol. 15, No. 6, Jun. 2005.
15. Al Sharkawy, M., A. Boutejdar, and E. Galal, "Design of ultra-wide stop-band DGS low-pass filter using meander- and multilayer techniques," *Microwave and Optical Technology Letters*, Vol. 55, No. 6, Jun. 2013.
16. Chang, C., W. Chen, and Z. Zhang, "A novel dual-mode dual-band bandpass filter with DGS," *PIERS Proceedings*, 1723–1726, Marrakesh, Morocco, Mar. 20–23, 2011.
17. Adel, B., A. Abdel-Rahman, and K. Verma, A. Boutejdar, and A. S. Omar, "Control of bandstop response of Hi-Lo Microstrip low-pass filter using slot in ground plane," *IEEE Transactions on Microwave Theory and Techniques*, Vol. 52, No. 3, Mar. 2004.
18. Kumar, A., A. Sawant, and M. V. Kartikeyan, "Investigation of fractal DGS microwave filters," *2013 National Conference on Communications (NCC)*, Feb. 15–17, 2013.
19. Saal, R. and E. Ulbrich, "On the design of filters by synthesis," *IRE Trans. Circuit Theory*, Vol. 5, 284–327, 1958.
20. Saal, R., "Der entwurfvon filternmit hilfedes kataloges normierter tiefpasse," Telefunkn GmbH, Backnang, Germany, 1961.

Electromagnetic Stimulation of Transport in Water for Geoenvironmental Applications

A. Farid, M. Azad, J. Browning, and E. Barney-Smith
Boise State University, USA

Abstract— Air sparging is a popular soil remediation technique that enables the removal of contaminants by diffusing air into saturated zones of soil. The removal process is, however, slow. The goal of this work is to study the effect of electromagnetic (EM) waves — with minimal heat generation — on transport mechanisms such as diffusion, in order to improve airflow or contaminant transport and expedite the cleanup process using air sparging or similar technologies. This effect is studied through an experimental setup that examines the diffusion of a nonreactive dye in water under EM waves at a range of frequencies between 50 and 200 MHz. The electric field was simulated using COMSOL Multiphysics for better 3D visualization and analysis and then validated using experimental measurements. A dielectrophoretic study was performed using the simulated electric field. Various dye flow under EM stimulation at different frequencies were compared. At 65 MHz and 76 MHz, the dye flow was in the direction of the dielectrophoretic forces, which is believed to be the governing mechanism for dye transport.

1. INTRODUCTION

Remediation of contaminated soil/groundwater has become an area of interest in recent decades. Several remediation techniques have been used for removal of the contaminants, among which air sparging [1] is very popular. In-situ air sparging (AS) is a technique in which air or oxygen is injected into water-saturated zones in order to remove organic contaminants by a combination of volatilization and aerobic biodegradation processes. The contaminant-free air injected into the saturated zones of the subsurface enables the phase transfer of organic contaminants from a dissolved or adsorbed state to a vapor phase. Despite the impressive results, the effectiveness of air sparging is limited because of its semi-random remediation process [2]. Air can flow more easily in partially saturated media compared to water-saturated ones, resulting in airflow limited to initial randomlyformed air channels. An advantage of EM over other enhancement methods, such as the use of direct or alternating current (DC or AC), is that EM waves can be applied at proper frequencies (lower MHz) and lower EM power and, therefore, would dissipate a small amount of energy in the medium and would not alter the pH of the environment. The transport of a nonreactive inert dye in water is studied as a visible analogy to the air or contaminant flow in saturated media. The goal of this work is to study the effect of electromagnetic waves on transport mechanisms in saturated media at frequencies where heat generation is minimal. The main objective of this work is to find the governing phenomenon that directs the flow of the dye when EM stimulation is applied. Dielectrophoresis [3] is specifically investigated as a potential governing mechanism behind this effect. Studying the relationship between the magnitude of the EM power and the transport rate, as a representative of the transport rate, is another objective of this work.

2. METHODOLOGY, EXPERIMENTATION, AND SIMULATION

The experimental setup consists of a 40-cm $\times$ 40-cm $\times$ 40-cm acrylic box (Figure 1) and a 38-cm $\times$ 38-cm $\times$ 38-cm RF (radio-frequency) resonant cavity, filled with water. The cavity structure is built using copper mesh screens instead of solid copper plates to enable imaging and visualization. The opening diameter of the copper mesh is ~ 3 mm (1/8 inch), which is much smaller than the wavelength of the applied 50–200 MHz frequency waves in water (≈ 160 mm–660 mm). A coaxial loop antenna coupled to the resonant cavity and connected to the EM source launches EM waves into the medium. The antenna is made of an RG8 coaxial cable. The outer conductor of the cable is electrically grounded at both ends of the cable, sharing the same electric ground as the cavity. The inner conductor passes through a brass piece soldered to the top copper boundary, hence, sharing the same electric ground as the outer conductor, to provide electrical continuity to the resonant cavity. A continuous wave (CW) radio-frequency signal was generated using an HP E4400B signal generator and amplified using a Model 100 LMB amplifier, manufactured by Amplifier Research. To maximize the amplifier output forward power to be input into the testing medium, a matching network was used (See [4] for more information).

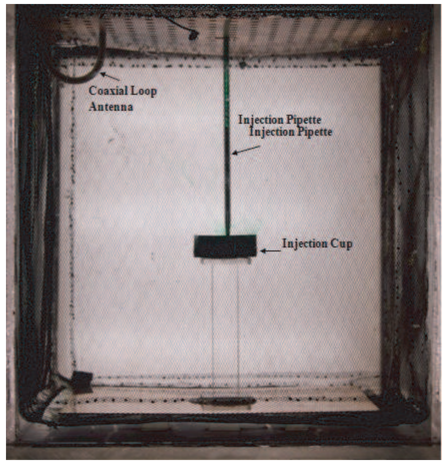

Figure 1: Medium under test for the modified setup showing the acrylic box, resonant cavity filled with water, injection cup, injection pipette, and loop antenna.

An inert, nonreactive, water-based dye (a green McCormick food-coloring dye) was used as the diffusing matter to allow the visualization of the transport inside the medium. A clear acrylic table was built to allow the introduction of the dye close to the center of the medium (far from the cavity boundaries). A circular plastic cup with a radius of 30 mm was glued to the top plate of the injection table. The cup is used to hold the dye during the initial injection and prevent the dye from descending off the injection table down to the bottom of the box. Digital imaging was used to analyze the transport of the dye to determine the EM-stimulation effect. Images were taken using a Cannon Rebel T2i 18-MegaPixel digital camera. Images were taken at 30-second intervals for this experiment. The pixel values of the two-dimensional (2D) digital images correlate to the dye concentration integrated along corresponding lines of sight.

The electric field is mapped in the region under test using a 50-Ω, RG-402, coaxial probe controlled by a three-dimensional (3D) translation table. The probe is connected to a spectrum analyzer and is moved to the nodes of a desired 3D grid. The monopole probe is vertically polarized. However, a full 3D vector electric field is necessary to understand the correlation between the

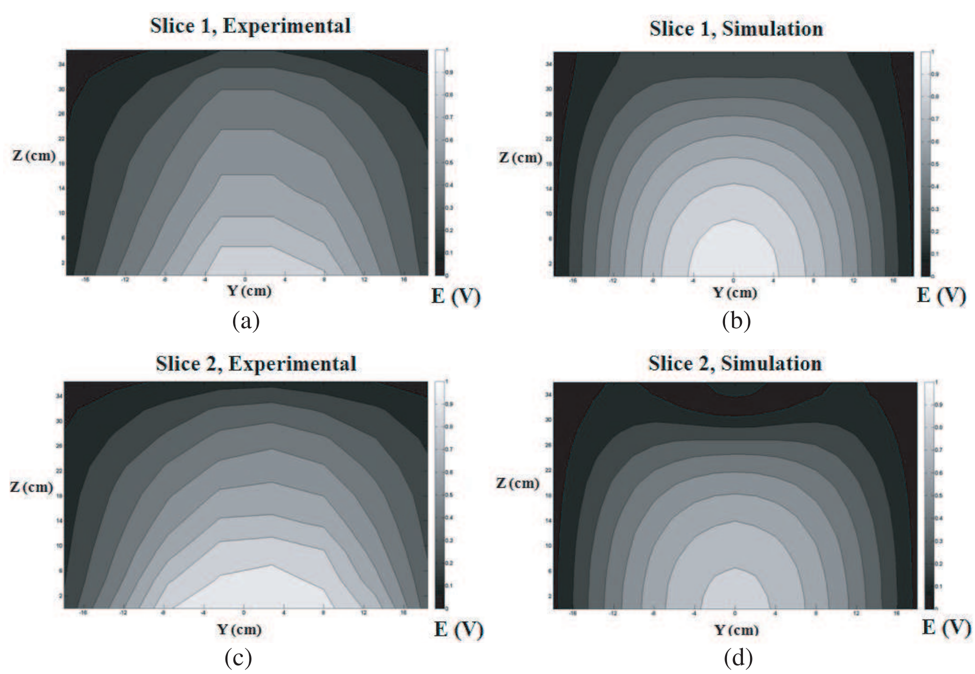

Figure 2: Normalized electric field map: (a) Slice 1, experimentally measured; (b) Slice 1, simulated; (c) Slice 2, experimentally measured; and (d) Slice 2, simulated.

RF radiation pattern and the dye transport. Therefore, the electric field pattern is simulated at various frequencies using the COMSOL software, and its Z component is validated against the experimentally mapped electric field. Figure 2 shows the measured and simulated contour maps on two depth slices at 65 MHz. In order to investigate the effect of temperature on the dye flow, the temperature of the water close to the antenna body was recorded at different EM-stimulation frequencies.

3. RESULTS AND DISCUSSION

3.1. Unstimulated Tests

After complete injection of the dye, small portions of the dye rose from the cup and then descended downward because the dye density was slightly larger than that of water ($1\,\mathrm{g/cm^3}$). There was a relatively random time interval (5 to 12 minutes) at which the dye rose out of the cup. However, approximately 1 hour past the beginning of the experiment, this time interval decreased, and more continuous risings were observed. Figure 3(a) shows an example of the dye transport in an unstimulated test.

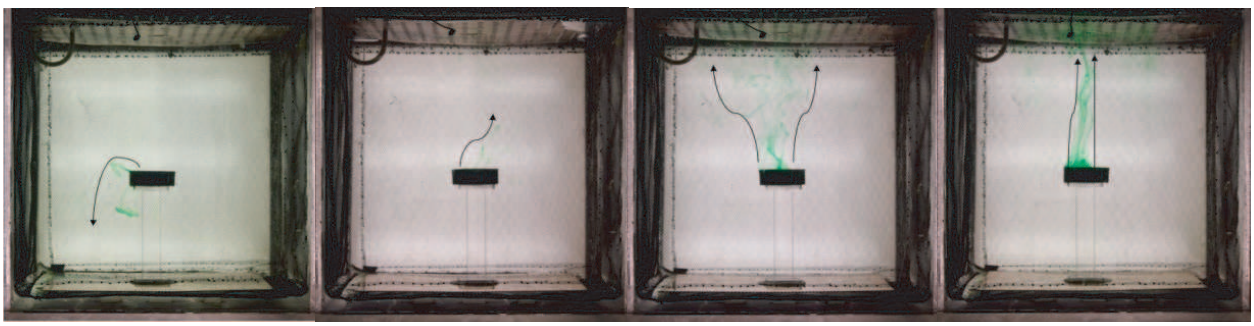

(a) (b) (c) (d)

Figure 3: (a) Dye transport during: (a) an unstimulated test; dye randomly rises out of injection cup and descends; and dye flow in an EM-stimulated experiment at 65 MHz frequency after 20 minutes of stimulation and at the power level of: (b) 10 W, (c) 20 W, and (d) 30 W. Dye rises out of injection cup toward top boundary.

3.2. Stimulated Tests

When the medium was stimulated at the frequency of 65 MHz, there was an upward flow of the dye. Portions of the dye rose out of the cup and moved upward toward the top boundary of the resonant cavity. After reaching the top boundary, the dye spread horizontally in random directions. The stimulated experiment was performed at 10, 20, and 30 W to investigate the effect of the power level. Increasing the EM power increased the upward dye flow. Figures 3(b), 3(c), and 3(d) illustrate the flow of the dye 20 minutes after the dye injection at power magnitudes of 10, 20, and 30 W, respectively. The threshold of power needed to electromagnetically induce the upward dye transport is $P = 10\,\mathrm{W}$ at the frequency of $f = 65\,\mathrm{MHz}$.

3.3. Frequency Effect

Although only the 65 MHz simulation was successfully validated experimentally, the experiment was repeated for other frequencies as well. The choice of the frequency was based on the quality of the impedance-matching achieved that was monitored by the spectrum analyzer. As a result, several tests were performed at 60, 69, 75, and 77 MHz at an RF power of 30 W. Unlike the tests performed at 65 MHz, during the stimulation at these other frequencies — except for 75 MHz — the flow of the dye was observed to be similar to the unstimulated tests. In other words, the stimulation had no apparent effect on the flow of the dye. At 75 MHz, the dye remained inside the cup for as long as the medium was stimulated and the power was above 3 W. The simulated electric-field pattern seems to support this phenomenon according to a potential dielectrophoretic nature. However, the experimental electric-field measurements showed no consistency with the simulation.

3.4. Temperature Effect

The change of temperature over time was monitored at various frequencies at a point 1 cm from the center of the loop antenna, where the strongest temperature rise was expected due to resistive heat generation at the proximity to the heat source (i.e., loop antenna). As expected, the temperature slightly increased for all the frequencies over time. The maximum change in temperature within the period of stimulation was less than 1°C for all frequencies. The observed pattern of rise in the temperature was the same for all frequencies, while the electric-field radiation pattern and dye flow were different for 65 MHz, 75 MHz, and other frequencies. This suggests that the flow of the dye is not dominated by a convective flow (due to thermal effects) and is due to the electromagnetic field.

3.5. Electric-field Pattern Effect and Governing Mechanism

The validated simulated electric field, containing the X, Y, and Z components of the electric field at nodes spaced on a 2-cm grid within the cavity, was exported into MATLAB. A script (*m.file*) was developed in MATLAB using a forward finite difference method to calculate the dielectrophoretic force based on Equation (1).

$$\begin{aligned}\vec{F}_{DEF} &= 2\pi r^3 \varepsilon_m^* \mathrm{Re}\left\{\frac{\varepsilon_p^* - \varepsilon_m^*}{\varepsilon_m^*}\right\} \vec{\nabla}\,|E|^2_{(i,j,k)} \\ &= 2\pi r^3 \varepsilon_m^* \mathrm{Re}\left\{\frac{\varepsilon_p^* - \varepsilon_m^*}{\varepsilon_m^*}\right\}\left(\frac{|E|^2_{i,j+1,k} - |E|^2_{i,j-1,k}}{2dx} + \frac{|E|^2_{i+1,j,k} - |E|^2_{i-1,j,k}}{2dy} + \frac{|E|^2_{i,j,k+1} - |E|^2_{i,j,k-1}}{2dz}\right) \end{aligned} \quad (1)$$

Three matrices of the three components of the gradient of the squared electric field ($\nabla|E|^2$) were computed. However, the dye concentration at each node within images represents the concentration integrated over the line of sight (in the Y direction, i.e., perpendicular to the image). Hence, the X and Z components of the gradient of the squared electric field were integrated over the Y-axis. Figures 4(a) and 4(b) represent the contour map of the Z and X components of the $\nabla|E|^2$ vector, respectively.

According to Figure 4(a), the Z-component of $\nabla|E|^2$ is negative with an increasing magnitude toward the top. As a result, because of the smaller dielectric constant of dye compared to that of water, the direction of the dielectrophoretic forces are in the positive Z direction (i.e., upward) at 65 MHz. This result is in agreement with the results from the experimental field investigation as well.

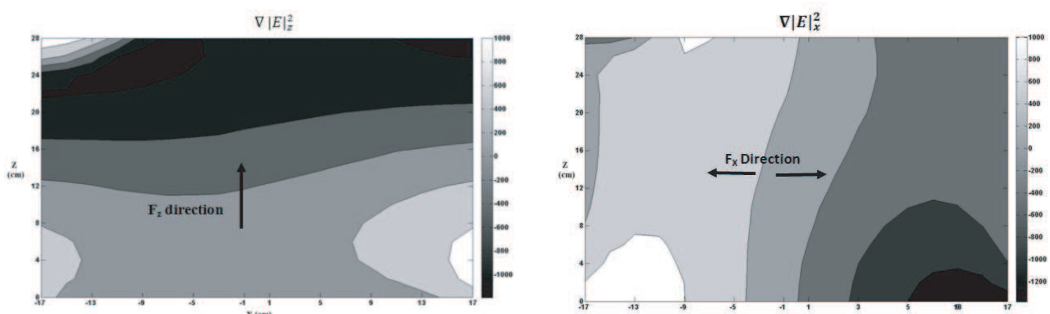

(a) (b)

Figure 4: Contour map of the simulated $\nabla|E|^2$ (V^2/m^3) according to COMSOL Multiphysics results at 65 MHz: (a) Z component and (b) X component.

On the other hand, the X-component of the $\nabla|E|^2$ vector creates a force dragging the dye toward the side walls of the cavity. However, the magnitude of the forces in the X direction is almost 1/2 of the magnitude of the vertical forces. As a result, the upward flow of the dye dominates the horizontal flow except near the top boundary, where the upward flow has slowed or stopped. Since the dye has a flow moving both right and left after it reaches the top boundary, the observed flow near the top boundary can be interpreted as a mix of dielectrophoresis and diffusion.

3.6. Digital Analysis and Evaluation

Digital-image analysis was performed to extract quantifiable information from images of dye transport in RAW format. RAW-format images were then converted into the TIFF format and imported into MATLAB in matrix format. The averaged, background image (containing everything but the dye) was subtracted from every other image, leaving only the transporting dye. The elements of the resulting matrices represent the intensity of pixels at different locations in the box as a representative of dye concentration. Following analyses were then performed.

3.6.1. Pixel Intensity Summation

A zone shown in Figure 5(a) was selected to measure the amount of dye that had left the injection cup or the main finger formed in each test. The summation was performed on the set of the experiments performed at 65 MHz (10 W, 20 W, and 30 W) as well as for the test performed at 75 MHz (30 W) and the unstimulated test. Figure 6 shows the plot of the summation of pixel intensities over time for these tests. Because no dye transport was observed for the tests performed at 75 MHz, it was, hence, expected that the summation of pixel values for this test be constant over time. However, the plot shows some variation over time attributed to the errors associated with the background noise. In general, the average value did not increase or decrease. The similar range of concentration data associated with the unstimulated test and the stimulated test at 10 W proves that the amount of the dye entering this zone was not large enough to overcome the noise. In summary, the change of the sum of pixel intensities over time for the unstimulated test, stimulated test at 75 MHz (even at 30 W of power), and 65 MHz (with a power less than 10 W) followed the same pattern with the average unchanged. The plot of pixel values over time for the stimulated tests of 65 MHz at 20 W and 30 W, on the other hand, shows different results. The sum of adjusted pixel intensities increased over time for these two tests, meaning pixels became darker. This refers to the presence of more dye in the upper region. In order to quantify the variations in the sum of pixel values over time for each test, the relative change (%) of the summation was also calculated. Therefore, the last three datasets (at $t = 105$ min., 106.5 min., and 108 min. after the beginning of the stimulation) were averaged and subtracted from the initial dataset ($t = 0$ min.) of the curves of Figure 6(a). The relative change (%) was calculated and plotted versus power (Figure 6(b)).

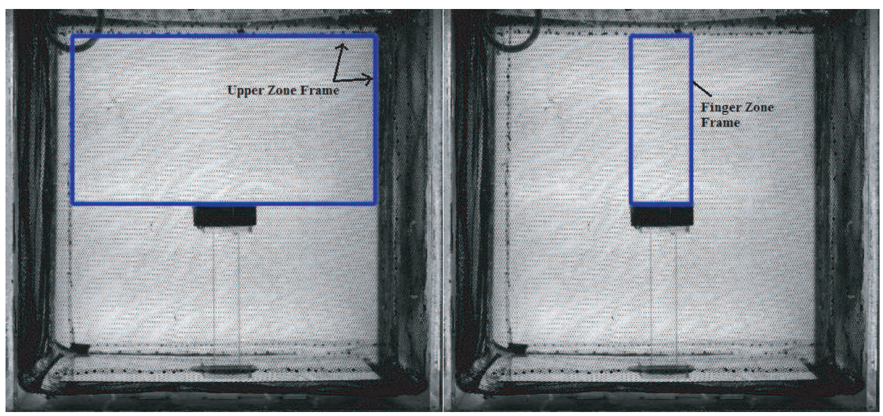

(a) (b)

Figure 5: (a) Study zone, referred to as upper zone, in Intensity Summation Analysis and (b) study zone, referred to as finger zone, in the "finger-height analysis".

3.6.2. Fingers' Characteristics

Several other characteristic parameters were calculated to understand the shape of each finger. These characteristic parameters include finger height and width. A finger zone is defined in images (e.g., Figure 3(b)), which includes the main dye finger for the majority of the time during the upward flow of the dye, when the medium is electromagnetically stimulated at 65 MHz (at 10, 20, and 30 W power levels). This study is limited to the tests performed at 65 MHz because of stronger, more controlled finger movements at this specific frequency. The number of pixels containing enough dye (above a consistent threshold representing visible fingers) was recorded versus elevation within the selected zone at different times. The number represents the width of the finger. This method enabled a study of the finger-width profile for each test over time.As seen in Figure 6(c), the finger for the test performed at 65 MHz at 10 W of power was almost constant at all elevations and was always smaller than the number for 20 and 30 W power levels. For the 20-W case, the finger width was almost constant at all elevations as well but was larger than that of the 10-W case. This was a representative of a more concentrated upward dye flow compared to the 10-W case that was not focused and dispersed gradually. For the test at 30 W, the plot shows that the width decreased rapidly with increasing elevation above the injection cup. However, the fingers became darker (the intensity of these pixels increased drastically). The digital pictures associated with this test confirms much darker, yet more focused, fingers tend to move faster and in a more straight, focused, and robust shape at 30 W.

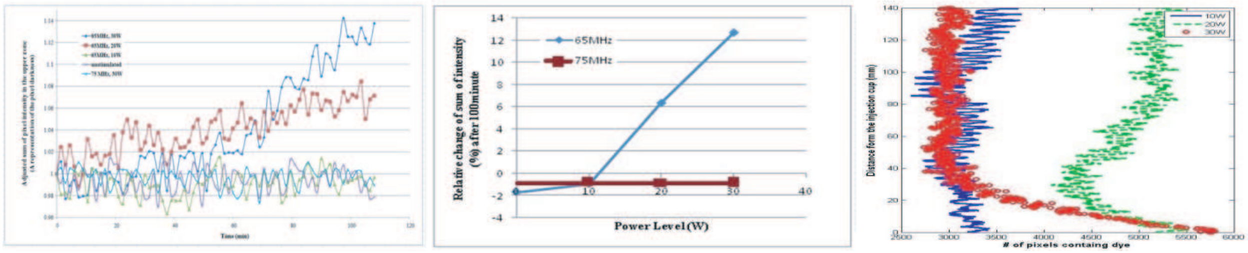

(a) (b) (c)

Figure 6: Plot of adjusted sum of image pixel intensities (representing transported dye amounts) for an unstimulated test; three stimulated tests at 65 MHz at power levels of 10 W, 20 W, and 30 W; and a stimulated test at 75 MHz and 30 W of power versus: (a) time and (b) power (summation performed over highlighted upper zone in digital images); and (c) Plot of total number of pixels containing enough dye to be considered a finger accumulated over time versus elevation above injection cup.

ACKNOWLEDGMENT

This project was supported by the National Science Foundation through the Interdisciplinary Research (IDR) program, CBET Award No. 0928703.

REFERENCES

1. Johnson, R. L., P. C. Johnson, D. B. McWhorter, R. E. Hinchee, and I. Goodman, "An overview of in-situ air sparging," *J. of Groundwater Monitoring and Remediation*, Vol. 13, No. 4, 127–135, 1998.
2. Braida, W. and S. K. Ong, "Air sparging Effectiveness: Laboratory characterization of air-channel mass transfer zone for VOC volatilization," *J. of Hazardous Materials*, Vol. B87, 241–258, 2001.
3. Jones, T. B., "Basic theory of dielectrophoresis and electrorotation," *IEEE Eng. Med. Biol. Mag.*, Vol. 22, No. 6, 33–42, Nov.–Dec. 2003.
4. Azad, M., H. Sangrey, A. Farid, J. Browning, and E. Barney-Smith, "Electromagnetic stimulation of two-phase transport in water-saturated media for geoenvironmental applications," *ASTM, Geotechnical Testing Journal,* Vol. 13, No. 1, 97–106, January 2013.

Modeling of Ultra Wideband Antenna Arrays

Yvan Duroc
Grenoble Alpes University, LCIS, F-26900, Valence, France

Abstract— This paper presents system approaches for modeling the antenna arrays and the mutual coupling. The modeling based on the characterization of linear time invariant systems can be exploited in the case of UWB antenna arrays for different issues: the expression of the beampattern of an array of N-antennas, the determination of a time-frequency model of TX antenna arrays, and the characterization of the mutual coupling between two elements.

1. INTRODUCTION

Even if the concept of antennas arrays is not new with early work in the 1920s, Multiple Input Multiple Output communication systems using antenna arrays have recently emerged as a breakthrough for wireless systems of revolutionary importance [1]. Otherwise, Ultra Wideband (UWB) technology is a potential candidate in the race of the wireless world since the Federal Communications Commission (FCC) released a report approving its use. However, this technology is limited by an extremely low allowable transmitted power, i.e., $-41.3\,\text{dBm/MHz}$ [2]. To overcome this limitation, the combination of MIMO techniques with UWB technology emerges as a relevant solution. Moreover, the known advantages of the antenna arrays for the narrowband systems always exist for the UWB systems [3].

In this context, a lot of works concerned the design of UWB MIMO antennas [4–6], as well as the description of their properties [7–10]. The direct transposition of narrowband approaches is not adequate and too incomplete for the UWB antenna array description, as is the case of single element [10–12]. With a model point of view, the transfer function (i.e., frequency response) and the impulse response (i.e., time response) have been found as relevant description of the single UWB antennas [13]. They are derived from the effective lengths which first have been considered to describe and specify the transient radiation and reception characteristics of antennas [14, 15]. Therefore, the single UWB antennas can be modeled as Linear and Time Invariant (LTI) systems. As presented in the next sections, this system modeling based on the characterization of LTI systems can be exploited in the case of UWB antenna arrays for different issues: the characterization of the mutual coupling between two elements, the expression of the beampattern of an array of N-antennas, and the determination of a time-frequency model of TX antenna arrays.

2. SYSTEM MODEL OF UWB ANTENNA ARRAYS

2.1. Presentation

Figure 1 illustrates a model of the wireless communication systems. The radio link decomposed into three functional blocs provides a useful modeling: the channel of propagation $H_{ch}(f)$, the TX and RX antennas (which can be single or multiple) each described by a transfer function, $\vec{H}_{TX}(f, \theta_{TX}, \varphi_{TX})$ and $\vec{H}_{RX}(f, \theta_{RX}, \varphi_{RX})$, and the associated impulse response $\vec{h}_{TX}(t, \theta_{TX}, \varphi_{TX})$ and $\vec{h}_{RX}(t, \theta_{RX}, \varphi_{RX})$ where f is the frequency, t is the time, and θ and φ are the polar and azimuth angles. Therefore, the characterization is very complete, because it includes the frequency dependence, the phase information, and the polarization and the directional properties. Under far-field propagation conditions, it can be shown that the transfer functions and the impulse responses modeling the antennas present analytical expressions, which are functions of the effective length of the antennas expressed in frequency domain or time domain respectively [16].

Moreover, assuming a wireless channel with only one direct path between the transmitter and receiver (i.e., Line-Of-Sight, LOS propagation), the transfer between the output s and the input e can also be deduced. The characterization of antennas as LTI systems presents the advantage to achieve time-frequency models, especially suitable for UWB antennas, and for example, allows the determination of the radiated and received transient waveforms of any arbitrary waveform excitation and antenna orientation.

2.2. Transfer Function of Antenna Array in Emission Mode

Using the concept of array factor and conjointly the approaches developed for achieving the system models of UWB antennas, an UWB array system model can be achieved. Considering the above

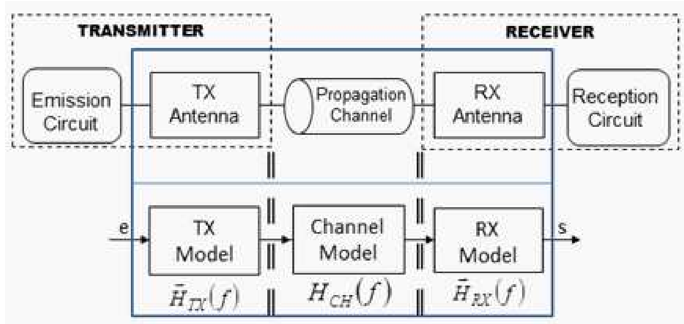

Figure 1: Block diagram of wireless communication systems.

assumptions, the radiated field in transmission $\vec{E}^{rad}$ can be defined in the frequency domain from the effective length $\vec{L}_{eTX}$ of the TX antenna as:

$$\vec{E}^{rad}(f,\theta_{TX},\varphi_{TX}) = j\frac{f}{c}Z_0\frac{\exp\left(-j\omega\frac{dr}{c}\right)}{2r}I(f)\vec{L}_{eTX}(f,\theta_{TX},\varphi_{TX}) \tag{1}$$

where r is the radiation distance, Z_0 is the free space impedance, I is the excitation current. This expression can be rewritten introducing the transverse part of the radiation vector $\vec{F}_\perp$ as follows:

$$\vec{E}^{rad}(f,\theta_{TX},\varphi_{TX}) = -j\frac{f}{c}Z_0\frac{\exp\left(-j\omega\frac{dr}{c}\right)}{2r}\vec{F}_\perp(f,\theta_{TX},\varphi_{TX}) \tag{2}$$

The vector $\vec{F}_\perp$ includes both the characteristics of the antenna via the effective length $\vec{L}_{eTX}$ and the properties of the emitted signal via the spectral form of the current $I(f)$. Under the same assumptions and considering an antenna array (with N elements), the total radiated field $\vec{E}^{tot}_{rad}$ is:

$$\vec{E}^{rad}_{tot}(f,\theta_{TX},\varphi_{TX}) = -j\frac{f}{c}Z_0\frac{\exp\left(-j\omega\frac{dr}{c}\right)}{2r}\vec{F}_{tot,\perp}(f,\theta_{TX},\varphi_{TX}) \tag{3}$$

with

$$\vec{F}_{tot,\perp}(f,\theta_{TX},\varphi_{TX}) = A(f,\theta_{TX},\varphi_{TX})\cdot\vec{F}_\perp(f,\theta_{TX},\varphi_{TX}) \tag{4}$$

Consequently, an equivalent effective length $\vec{L}_{etot,TX}$, called total effective length by analogy with the total radiation vector, for the antenna array can be introduced as:

$$\vec{L}_{etot,TX}(f,\theta_{TX},\varphi_{TX}) = A(f,\theta_{TX},\varphi_{TX})\cdot\vec{L}_{eTX}(f,\theta_{TX},\varphi_{TX}) \tag{5}$$

The array factor $A(f,\theta_{TX},\varphi_{TX})$ is easily defined by the traditional approaches. Furthermore, the study remains general as shown in the previous section; the antenna array can be constituted of all types of the similar antennas, narrowband or UWB antennas.

An extension of the system modeling for the UWB antenna arrays can now be deduced. As presented in [16], several formulations are possible according to the chosen way for the modeling. For illustrating the concept, the Figure 1 being considered, a TX model can be established. The TX antenna assumed to be an antenna array, the transfer function $\vec{H}_{TX}(f,\theta_{TX},\varphi_{TX})$ and the associated impulse response $\vec{h}_{TX}(f,\theta_{TX},\varphi_{TX})$ can be expressed in function of the total effective length as shown below. Therefore, the function transfer of an antenna array in transmission mode can be written in a very general form as:

$$\vec{H}_{TX}(f,\theta_{TX},\varphi_{TX}) = \alpha\vec{L}_{etot,TX}(f,\theta_{TX},\varphi_{TX}) \tag{6}$$

where the coefficient α is a scalar, frequency dependent, which includes the modeling approach and the generator and antenna impedances (for more details about α, see for example [16]).

Finally, it should be noted that for this study, it was assumed that the coupling between adjacent radiation elements is not taken into consideration.

3. SYSTEM MODEL FOR CHARACTERIZING THE MUTUAL COUPLING

3.1. Presentation

The main idea behind antenna diversity techniques is to produce different replicas of the transmitted signal to the receiver. If these replicas are sent over the propagation channel such that their statistics are independent, when one of them fades, it is less likely that the other copies of the transmitted signal will be in feed fade simultaneously. Thanks to this redundancy, the receiver can decode the transmitted signal even in fading conditions, as long as they all do not fade simultaneously. In consequence when antenna diversity is desired, the signals transmitted by multiple antenna elements are generally supposed independent or uncorrelated. However, the current induced on one antenna produces a voltage at the terminals of nearby elements, termed as mutual coupling [17]. It means there is always mutual coupling present between nearby antenna elements. For MIMO applications, the mutual coupling should be minimized to as low value possible.

3.2. Modeling of the Mutual Coupling

In order to illustrate the mutual coupling, let two TX antennas which are confined. The radiated field by one of these antennas will be modified due to the presence of the second. So the received field will also be affected! This problem is illustrated in Figure 2: the received signals, $s_1(t)$ and $s_2(t)$, will be different, even if the emitted signal $e_1(t)$ is the same in the considered cases.

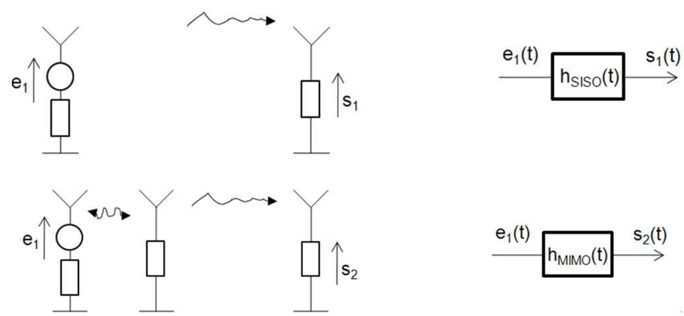

Figure 2: Effect of the mutual coupling generated by MIMO antenna system.

Consider the illustrated example by Figure 1, the corresponding output signals can be described in the time domain by:

$$s_1(t) = h_{\mathrm{SISO}}(t) * e_1(t) \tag{7}$$

$$s_2(t) = h_{\mathrm{MIMO}}(t) * e_1(t) \tag{8}$$

where $e_1(t)$ is the input of the system, $s_1(t)$ is the output signal in the case of SISO, $s_2(t)$ is the output signal in the case of MIMO, $h_{\mathrm{SISO}}(t)$ is the impulse response of the SISO system, $h_{\mathrm{MIMO}}(t)$ is the impulse response of the MIMO system. With the associative property of the convolution product, the mutual coupling can be modeled in the following way:

$$s_2(t) = (h_{\mathrm{SISO}}(t) * e_1(t)) * h_C(t) \tag{9}$$

with

$$h_{\mathrm{MIMO}}(t) = h_{\mathrm{SISO}}(t) * h_C(t) \tag{10}$$

In consequence, the introduced impulse response $h_C(t)$ (subscript C denotes coupling) translates precisely the effects of the second antenna on the radiations in time domain. From simulation or measurement, the associated frequency response $H_C(f)$ can be easily determined. Hence

$$H_C(f) = H_{\mathrm{MIMO}}(f) / H_{\mathrm{SISO}}(f) \tag{11}$$

where

$$H_{\mathrm{SISO}}(f) = S_1(f)/E_1(f) \tag{12}$$

$$H_{\mathrm{MIMO}}(f) = S_2(f)/E_1(f) \tag{13}$$

where $E_1(f)$, $S_1(f)$, $S_2(f)$, $H_{\mathrm{SISO}}(f)$, $H_{\mathrm{MIMO}}(f)$, $H_C(f)$ are the frequency responses of $e_1(t)$, $s_1(t)$, $s_2(t)$, $h_{\mathrm{SISO}}(t)$, $h_{\mathrm{MIMO}}(t)$, $h_C(t)$, respectively.

Therefore, the effects of the mutual coupling can be described by a LTI model. The proposed approach offers several advantages: an analytical model can be derived, and from this description, it is possible to envisage the reduction of the coupling using a matched pulse [18].

4. CONCLUSION

This paper emphasized system approaches for modeling the antenna arrays and the mutual coupling. The proposed concepts lead to general and elegant models including the cases of single antennas and antenna arrays, which are valuable for narrowband and UWB wireless communication systems.

REFERENCES

1. Wilmotte, R. M. and J. McPetrie, "A theoretical investigation of the phase relations in beam systems," *Wireless Section, Proc. of the Institute of Electrical Engineers*, Vol. 3, No. 9, 182–187, 1928.
2. Federal Communications Commission (FCC), "Revision of part 15 of the commission rules regarding ultra-wideband transmission systems," ET Docket 98-153, FCC 02-48, First Report and Order, 2002.
3. Kaiser, T., F. Zheng, and E. Dimitrov, "An overview of ultra-wide-band systems with MIMO," *Proceedings of the IEEE*, Vol. 97, No. 2, 285–312, 2009.
4. Hong, S., K. Chung, J. Lee, S. Jung, S. S. Lee, and J. Choi, "Printed diversity antenna with stubs for UWB applications," *Microwave Optical Technology Letters*, Vol. 5, No. 5, 1352–1356, 2008.
5. Zhang, S., Z. Ying, J. Xiong, and S. He, "Ultrawideband MIMO/diversity antennas with a tree-like structure to enhance wideband isolation," *IEEE Antennas and Wireless Propagation Letters*, Vol. 8, 2009.
6. Najam, A. I., Y. Duroc, and S. Tedjini, "Design & characterization of an antenna system for UWB-MIMO communication systems," *Proceedings of European Conference on Antennas and Propagation*, 2010.
7. Hussain, M. and A. Al-Zayed, "Aperture-sparsity analysis of ultrawideband two-dimensional focused array," *IEEE Transactions on Antennas and Propagation*, Vol. 56, No. 7, 1908–1918, 2008.
8. Shlivinski, A., "Kinematic properties of short-pulsed sparse transmitting arrays," *Progress In Electromagnetic Research*, Vol. 115, 11–33, 2011.
9. Sipal, V., D. Edwards, and B. Allen, "Descriptor choice for UWB antenna arrays," *Proceedings of European Conference on Antennas and Propagation*, 2012.
10. Farr, E. G. and C. E. Baum, "Extending the definitions of antenna gains and radiation pattern into the time domain," Sensor and Simulation Note 350, 1992.
11. Wiesbeck, W., G. Adamiuk, and C. Sturm, "Basic properties and design principles of UWB antennas," *Proceedings of the IEEE*, Vol. 97, No. 2, 372–385, 2009.
12. Duroc, Y., A. Ghiotto, T. P. Vuong, and S. Tedjini, "On the characterization of UWB antennas," *International Journal of RF and Microwave Computer-Aided Engineering*, Vol. 19, No. 2, 258–269, 2009.
13. Duroc, Y., A. Ghiotto, T. P. Vuong, and S. Tedjini, "UWB antennas: Systems with transfer function and impulse response," *IEEE Transactions on Antennas and Propagation*, Vol. 55, No. 5, 1449–1451, 2007.
14. Baum, C. E., "Time domain characterization of antennas with TEM feeds," Sensor and Simulation Notes, Note 426, Oct. 1998.
15. Shlivinski, A., E. Heyman, and R. Kastner, "Antenna characterization in the time domain," *IEEE Transactions on Antenna and Propagation*, Vol. 45, No. 7, 1140–1147, 1997.
16. Duroc, Y., "On the system modeling of antennas," *Progress In Electromagnetics Research B*, Vol. 21, 69–85, 2010.
17. Wallace, J. W. and M. A. Jensen, "Mutual coupling in MIMO wireless systems: A rigorous network theory and analysis," *IEEE Transactions on Wireless Communications*, Vol. 3, No. 4, 1317–1325, 2004.
18. Duroc, Y., A. I. Najam, and R. Siragusa, "System model for characterizing and reducing the mutual coupling in multiple-input multiple-output antennas," *Microwave and Optical Technology Letters*, Vol. 53, No. 3, 2011.

A Method of Dual-frequency Decoupling for Two-element MIMO Antenna

Hiroshi Sato[1,2], **Yoshio Koyanagi**[2], **Koichi Ogawa**[3], **and Masaharu Takahashi**[1]

[1]Chiba University, Japan
[2]Panasonic Mobile Communications Co., Ltd., Japan
[3]Toyama University, Japan

Abstract— This paper presents a method of dual-frequency antenna decoupling between closely spaced 2-element monopole. The method utilizes a newly developed decoupling circuit between two elements, realizing a reduction of mutual coupling in the two frequency bands simultaneously. It is confirmed that MIMO antennas using the proposed decoupling technique provide higher antenna efficiency, lower antenna correlation and higher multiplexing efficiency.

1. INTRODUCTION

MIMO technologies [1] using multiple antennas have been implemented in many wireless terminals, for the purpose of an increase in transmission rate. There is a limited space available for installing a number of antenna elements in these wireless terminals, and consequently mutual coupling has a great impact on antenna efficiency and antenna correlation, resulting in reduction of transmission rate, due to a small distance between antenna elements. If closely spaced MIMO antennas are placed without mutual coupling, antennas get low volume, and can give a freedom of designing a wireless terminal in terms of a good appearance and compactness of the terminal. In previous studies, most of them were considered only on a single frequency [2] or used many circuit components on multiple frequencies [3].

This paper presents a method of dual-frequency antenna decoupling between closely spaced 2-element monopole [4]. The method utilizes a newly developed decoupling circuit between two elements, realizing a reduction of mutual coupling in the two frequency bands simultaneously. It is confirmed that MIMO antennas using the proposed decoupling technique provide higher antenna efficiency, lower antenna correlation and higher multiplexing efficiency than those without decoupling.

2. ANALYSIS MODEL

In this paper, decoupling circuits for port isolation of 2-element monopole 2×2 MIMO antenna at dual-frequency is proposed. Fig. 1 shows 2-element monopole 2×2 MIMO antenna. Desired frequencies are 1.5 and 2.5 GHz. This antenna is implemented on $100 \times 50 \times 0.8$ mm one side Copper plate FR4 substrate. Size of monopole is 26×1.4 mm, and interval is 4.6 mm. Antennas are placed middle of ground plane. Both elements have feed points and matching circuits, and decoupling circuit is placed between feed points. All antennas in this paper were calculated by CST Microwave studio [5].

Figure 2 shows S-parameter of Fig. 1's 2-element antenna with matching circuits without decoupling circuits by simulation and measurement. Matching circuits use Murata's LQG15 inductor and GRM15 capacitor [6]. And S_{11} is under -10 dB at 1.5 and 2.5 GHz. Fig. 2 shows strong coupling of -1.9 dB at 1.5 GHz and -4.4 dB at 2.5 GHz, because antennas are disposed close. For this reason, antenna efficiencies of 2-element without decoupling are 6.7 dB at 1.5 GHz and 5.0 dB at 2.5 GHz less than 1-element. Therefore, to remove coupling and to improve antenna efficiency, decoupling circuit for dual-frequency is derived by evolving single frequency method [2].

3. DECOUPLING METHOD FOR SINGLE FREQUENCY

$$[S_B] = \begin{bmatrix} S_{B11} & S_{B12} \\ S_{B21} & S_{B22} \end{bmatrix} = \begin{bmatrix} 0 & \alpha e^{-j(\varphi+2\theta)} \\ \alpha e^{-j(\varphi+2\theta)} & 0 \end{bmatrix} \tag{1}$$

$$Y_{C21} = Y_{C12} = Y_0 \left[\frac{-2\alpha e^{-j(\varphi+2\theta)}}{1 - \alpha^2 e^{-j(\varphi+2\theta)}} \right] - jB \tag{2}$$

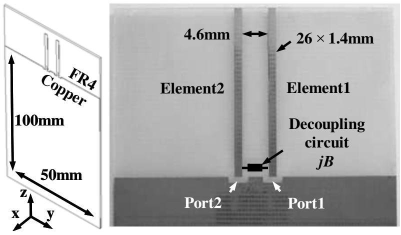

Figure 1: 2-element monopole 2×2 MIMO antenna.

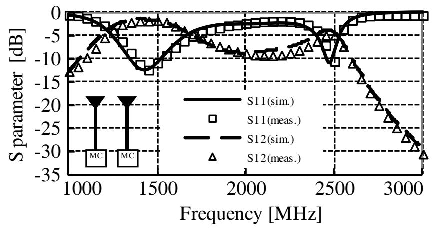

Figure 2: S-parameter.

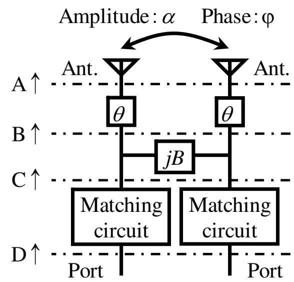

Figure 3: Block diagram for decoupling method.

$$S_{C21} = S_{C12} = \frac{-2Y_{C21}Y_0}{Y_0^2 + 2Y_{C11}Y_0 + (Y_{C11})^2 - (Y_{C21})^2} \tag{3}$$

Already Single frequency decoupling method between 2-element antenna was shown by [2]. Fig. 3 is block diagram of 2-element antenna with decoupling circuit. Decoupling circuit jB for single frequency is derived.

α and φ are amplitude and phase difference of coupling coefficient between antennas at observation plane A. The phase shifters of θdeg are added after observation plane A. Susceptance jB is placed between the antenna after observation plane B. In particular, Susceptance jB is referred to as the decoupling circuit. Finally, matching circuits are added after observation plane C. For sake of simplicity, structure and circuit value in this diagram are assumed symmetric, and assume that these antenna elements and phase shifters are obtained impedance matching. For this reason, miss match doesn't occur at observation plane A. Phase difference of the coupling between antennas is φ and one phase shifter has electrical length θ. Therefore, Coupling phase difference between ports at observation plane B is $\varphi + 2\theta$. Thus S-matrix at observation plane B can be expressed as (1). Y_{21} at observation surface C is shown by decoupling circuit jB and Y-parameter which is converted from S-matrix (1), and is expressed as (2). S_{21} at observation surface C is shown by conversion formula to S-parameter from Y-parameter, and can thus be expressed as (3).

When numerator is zero of (3), decoupling ($S_{C21} = 0$) is obtained. This means that, $Y_{C21} = 0$ is a condition of decoupling, and the susceptance job of decoupling circuit and θ of the phase shifter have to be derived as to satisfy $Y_{C21} = 0$. When $(\varphi + 2\theta)$ is 90 deg at (2), [ ] at (2) is a pure imaginary number. Furthermore Y_{C21} gets zero by using a jB to offset that imaginary. Thus, $S_{C21} = S_{C12} = 0$ and Coupling are removed. Therefore, one of conditional expression using phase shifter for decoupling is shown in (4).

By substituting (4) for (2), conditional expression for decoupling using jB is shown in (5). Further, If B of (5) is positive, decoupling circuit is capacitor. If B is negative, decoupling circuit is inductor. θ in (4) and jB in (5) are conditions of decoupling. Finally, matching circuits are placed at observation plane D.

$$\varphi + 2\theta = \pm\pi/2 \Rightarrow \theta = (\pm\pi/2 - \varphi)/2 \tag{4}$$

$$Y_0 \left[\frac{-2\alpha \times \pm j}{1+\alpha^2}\right] - jB = 0 \Rightarrow B = \frac{\pm 2\alpha}{1+\alpha^2} Y_0 \tag{5}$$

4. DECOUPLING METHOD FOR DUAL-FREQUENCY

Dual-frequency decoupling method is evolved from single frequency method.

Only the susceptance jB between feed ports is used when the decoupling performs at dual-frequency. Because it is difficult to make two suitable phases for dual-frequency by one circuit, the phase shifter should not be derived. And non-phase shifter structure is good for the volume and cost reduction. Without phase shifter, coupling phase difference φ on Fig. 3's observation surface B is not 90 deg strictly. Therefore, Y_{C12} in (2) has real part occasionally, and coupling is not removed at that time. To solve this problem, the impedance of both antenna elements is controlled such as real parts of Y_{C12} become zero at dual-frequency. By this approach, antennas can be decoupled without phase shifters. With respect to the imaginary part of Y_{12}, decoupling circuits have to have same susceptance of antenna's $\mathrm{Im}(Y_{12})$ at a dual-frequency, and this circuit is placed between feed points. These are dual-frequency decoupling techniques. Fig. 4 shows admittance Y_{12} of only 2-element antenna in Fig. 1. $\mathrm{Re}(Y_{12})$ has value that is significantly different from 0 mS near 1.8 GHz. Therefore decoupling is performed at 1.5 and 2.5 GHz which avoid around 1.8 GHz.

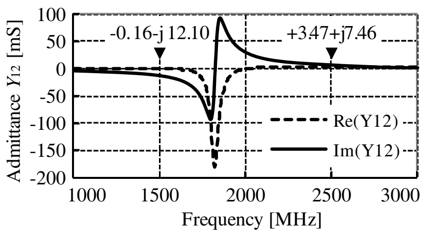

Figure 4: Admittance Y_{12} (2-element only).

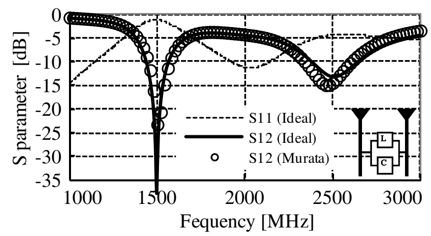

Figure 5: S-parameter. ($L = 4.1\,\mathrm{nH}$, $C = 1.5\,\mathrm{pF}$).

Dual-frequency decoupling circuit is composed from parallel of an inductor for 1.5 GHz and a capacitor for 2.5 GHz. Relationships among susceptance B, inductor L and capacitor C are represented by (6). Capacitor C and inductor L of the parallel circuit have to be satisfied susceptance and angular frequency ω at these dual-frequency simultaneously.

$$B = \omega C - \frac{1}{\omega L} \tag{6}$$

$$L = \frac{(\omega_2 + \omega_1)(\omega_2 - \omega_1)}{\omega_1 \omega_2 (\omega_1 B_2 - \omega_2 B_1)} \qquad C = \frac{\omega_2 B_2 - \omega_1 B_1}{(\omega_2 + \omega_1)(\omega_2 - \omega_1)} \tag{7}$$

Decoupling circuit for dual-frequency is calculated in (7). Susceptance of desired frequency 1 and 2 are defined as B_1 and B_2. And angular frequency of desired frequency 1 and 2 are defined as ω_1 and ω_2. $L = 4.1\,\mathrm{nH}$ and $C = 1.5\,\mathrm{pF}$ of decoupling circuits are calculated from (7). When these ideal parallel circuits are disposed between the feed points, S_{12} are -32.9 dB at 1.5 GHz and -12.4 dB at 2.5 GHz in Fig. 5. Same decoupling performance as single frequency is realized at dual-frequency.

In conclusion, at first the antenna structure is selected such as $\mathrm{Re}(Y_{12}) \fallingdotseq 0$ at desired two frequencies. Furthermore, a decoupling circuit of same susceptance value as antenna's $\mathrm{Im}(Y_{12})$ at desired frequency is placed between feed points. Finally, effect of dual-frequency decoupling circuit was demonstrated.

5. ANTENNA EFFICIENCY

S-parameters, which obtained using decoupling and matching circuits at dual-frequency is shown in Fig. 7. And these circuit configurations are shown in Fig. 6. Matching and coupling are lower than -10 dB at dual-frequency. Compared case of without decoupling in Fig. 2(b) to with decoupling in Fig. 7, S_{12} are improved 10.6 dB at 1.5 GHz and 7.1 dB at 2.5 GHz.

In Fig. 8, antenna efficiency by simulation and measurement in circuit configuration of Fig. 6 is shown. These experimental results have the same simulation trends, and validity of the analysis result is revealed. In comparison of the case without decoupling in Fig. 2(b) and the case with decoupling in Fig. 7, antenna efficiency is improved 4.8 dB and 3.6 dB at 1.5 GHz and 2.5 GHz, respectively.

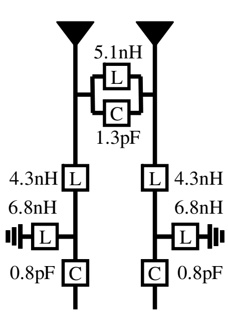

Figure 6: Circuit constants.

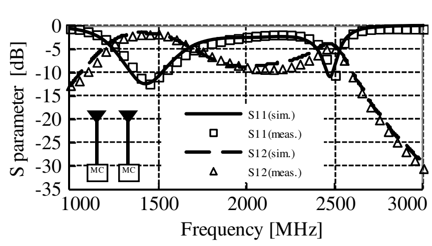

Figure 7: S-parameter.

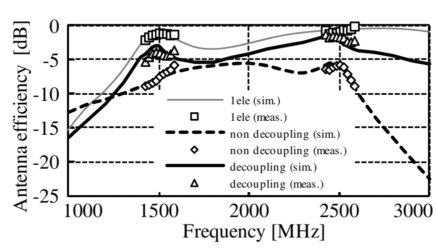

Figure 8: Antenna efficiency.

6. CORRELATION COEFFICIENT

Correlation coefficient ρ_e is a figure of merit for MIMO performance and a measure for the similarity between two radiation patterns. It is important as well as antenna efficiency for MIMO system. Using (8) [7], Correlation coefficient is calculated from both antennas of amplitude and phase radiation pattern E in all angle. Cross-polarization power ratio (XPR) is calculated as $XPR = 1$ (0 dB). Power density function P_θ and P_φ are defined as $P_\theta = P_\varphi = 1/(4\pi)$. Namely, incoming wave is assumed uniform distribution as with antenna efficiency.

Figure 9 shows correlation coefficient ρ_e of 2-element with and without decoupling circuit. When using decoupling circuit, correlation coefficient is improved from 0.63 to 0.60 at 1.5 GHz from 0.46 to 0.11 at 2.5 GHz. It is reduced at dual-frequency. The reason is that the both antenna has a different radiation pattern with the opposite direction in decoupling model.

$$\rho_e = |r|^2 = \frac{\left|\int_0^{2\pi}\int_0^{\pi}\left(XPR\cdot E_{\theta 1}\cdot E_{\theta 2}^*\cdot P_\theta + E_{\varphi 1}\cdot E_{\varphi 2}^*\cdot P_\varphi\right)d\Omega\right|^2}{\begin{array}{l}\int_0^{2\pi}\int_0^{\pi}\left(XPR\cdot E_{\theta 1}\cdot E_{\theta 1}^*\cdot P_\theta + E_{\varphi 1}\cdot E_{\varphi 1}^*\cdot P_\varphi\right)d\Omega\\ \times\int_0^{2\pi}\int_0^{\pi}\left(XPR\cdot E_{\theta 2}\cdot E_{\theta 2}^*\cdot P_\theta + E_{\varphi 2}\cdot E_{\varphi 2}^*\cdot P_\varphi\right)d\Omega\end{array}} \tag{8}$$

7. MIMO PERFORMANCE

The multiplexing efficiency [8] which is calculated by antenna efficiency and correlation coefficient is one of performance MIMO antenna's index. MIMO performance of decoupling antenna is compared by this value.

The multiplexing efficiency η_{mux} defines the loss of power efficiency when using a decoupling antenna to achieve the same channel capacity as that of an ideal MIMO antenna with 100% total antenna efficiencies and zero correlation for same reference propagation channel with uniform 3D angular power spectrum in high signal-to-noise ratio. Using (9), the multiplexing Efficiency η_{mux} in Fig. 10 is calculated from both antennas efficiency η_1 and η_2 in Fig. 8 and correlation coefficient $|r|^2$ with uniform 3D angular power spectrum in Fig. 9.

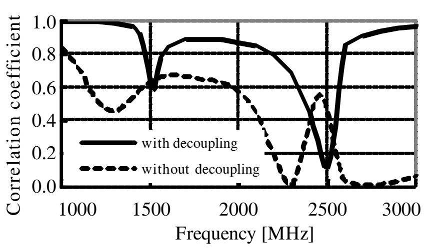

Figure 9: Correlation coefficient.

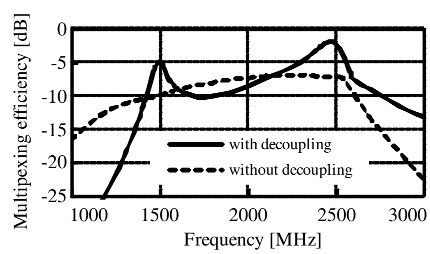

Figure 10: Multiplexing efficiency.

The multiplexing efficiencies of decoupling antenna are 4.9 dB at 1.5 GHz and 4.7 dB at 2.5 GHz higher than without decoupling model. So the performance of MIMO communication using decoupling antenna will be higher than without decoupling.

$$\eta_{mux} = \sqrt{\eta_1\eta_1\left(1-|r|^2\right)} \tag{9}$$

8. CONCLUSIONS

This paper presented a design method and effect of dual-frequency antenna decoupling between closely spaced 2-element monopole. When decoupling circuits which is a parallel circuit composed of inductor and capacitor for dual-frequency is placed between feed points, couplings were reduced 10.6 dB at 1.5 GHz and 7.1 dB at 2.5 GHz. And antenna efficiencies are improved 4.8 dB at 1.5 GHz and 3.6 dB at 2.5 GHz. Furthermore, correlation coefficients are reduced, and low correlation coefficient 0.60 and 0.11 were obtained at 1.5 and 2.5 GHz. As a result, decoupling antenna gets higher multiplexing efficiencies than MIMO antenna without decoupling. Low coupling, high antenna efficiency and low correlation coefficient mean that this decoupling technique may realize MIMO antenna which is obtained high throughput.

REFERENCES

1. Teletar, I. E., "Capacity of multi-antenna Gaussian channels," *Tech. Rep.*, AT&T-Bell Labs, Jun. 1995.
2. Chen, S.-C., Y.-S. Wang, and S.-J. Chung, "A decoupling technique for increasing the port isolation between two strongly coupled antennas," *IEEE Trans. Antennas Propag.*, Vol. 56, No. 12, 3650–3658, 2008.
3. Bhatti, R. A., S. Yi, and S. O. Park, "Compact antenna array with port decoupling for LTE-standardized mobile phones," *IEEE Antennas and Wireless Propagation Letters*, Vol. 8, 1430–1433, 2009.
4. Sato, H., Y. Koyanagi, K. Ogawa, and M. Takahashi, "A method of dual-frequency decoupling for closely spaced two small antennas," *IEICE Trans. B*, Vol. J94-B-II, No. 9, 1104–1113, Sep. 2011 (in Japanese).
5. CST STUDIO SUITE, 2012, http://www.cst.com/.
6. Murata Chip *S*-Parameter and Impedance Library, http://www.murata.com/products/design_support/mcsil/.
7. Ogawa, K., T. Matsuyoshi, and K. Monma, "An analysis of the performance of a handset diversity antenna influenced by head, hand, and shoulder effects at 900 MHz. Part II: Correlation characteristics," *IEEE Trans. Vehicular Technology*, Vol. 50, No. 3, 845–853, May 2001.
8. Tian, R., B. K. Lau, and Z. Ying, "Multiplexing efficiency of MIMO antennas," *IEEE Antennas and Wireless Propagation Letters*, Vol. 10, 183–186, 2011.

Body-effect-adaptive Compact Wideband LTE MIMO Antenna Array with Quad Elements for Mobile Terminals

Shuai Zhang[1,2], **Kun Zhao**[1,3], **Zhinong Ying**[3], **and Sailing He**[1,2]

[1]School of Electrical Engineering, KTH-Royal Institute of Technology, Stockholm SE-100 44, Sweden
[2]Centre for Optical and Electromagnetic Research, Zhejiang University, Hangzhou 310058, China
[3]Research and Technology, Corporate Technology Office
Sony Mobile Communications AB, Lund SE-221 88, Sweden

Abstract— A body-effect-adaptive compact wideband LTE MIMO antenna array with quad elements for mobile terminals is proposed in this paper. It can cover the bands of 750–960 and 1700–2700 MHz with a low envelope correlation coefficient. Through different combinations two of the four elements can be utilized as dual element LTE MIMO antenna array to reduce three kinds of body effects (head and hand; single hand; dual hands) with the other two ports open. Some common rules about the body effects are introduced. The conclusions about the optimal chassis locations of LTE MIMO antenna elements to improve MIMO performance are also presented.

1. INTRODUCTION

As an effective way to increase channel capacity without more spectrum efficiency and power, the long-term evolution (LTE) MIMO system has become a research hotspot. In order to guarantee a high performance of LTE MIMO systems the envelope correlations between MIMO antenna elements should be low and the efficiency of each element has to be as high as possible. At the same time, since the space of mobile terminals is limited, the LTE MIMO antenna array should be compact and cover a wideband. Small wide band antenna elements have been studied in [1, 2] Compact MIMO antennas have been investigated in [3, 4]. In practical applications, the human body (as a lossy material) will highly affect the channel capacity of LTE MIMO systems and how to reduce the channel capacity loss due to body has become an though problem. Actual diversity performance of a multiband diversity antenna with hand and head effects has been studied in [5]. In this paper, a compact quad-element LTE MIMO antenna array has been proposed for mobile terminals, which can cover a wide band of 750–960 and 1700–2700 MHz. With the help of different locations of the four LTE MIMO antenna elements, when only two of them are selected to operate with the other two ports open, three kinds of the body effects (head and hand; single hand; dual hand) on MIMO channel capacity can be reduced efficiently. Some conclusions about the body effects on the chassis locations of LTE MIMO antennas can also be obtained.

2. COMPACT ADAPATIVE WIDEBAND LTE MIMO ANTENNA ARRAY WITH QUAD ELEMENTS

Figure 1(a) shows the compact qual-element wideband LTE MIMO antenna array. Some detailed descriptions about the LTE MIMO antenna can be found in [6], and some related single LTE

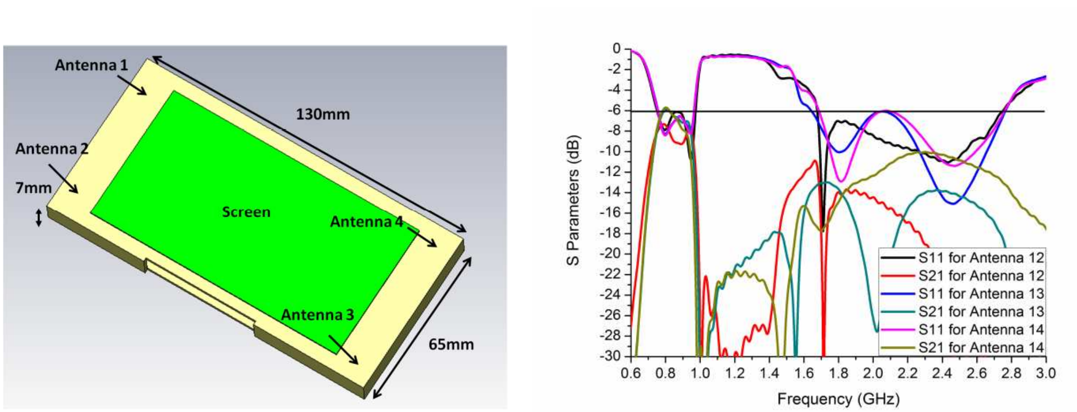

(a) (b)

Figure 1: (a) Configurations and (b) the S parameters of the compact adaptive LTE MIMO antenna array.

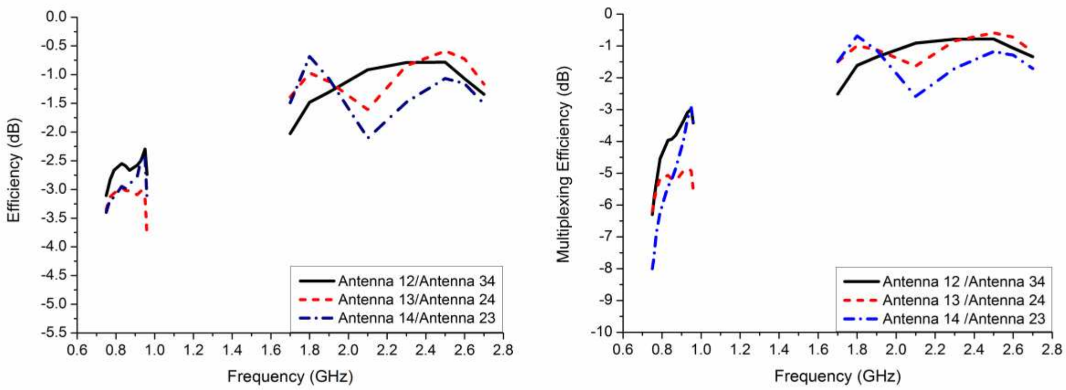

(a) (b)

Figure 2: (a) Efficiency and (b) multiplexing efficiency, of the different LTE MIMO antenna element combinations.

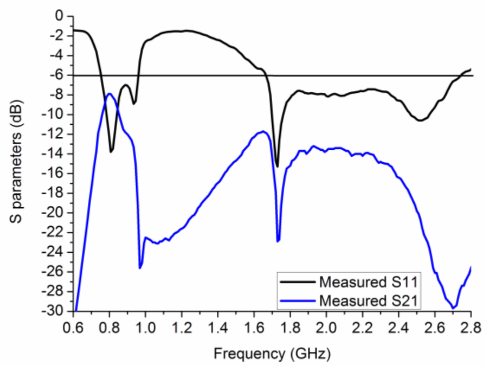

Figure 3: Measured S parameters when Antennas 1 and 2 are operating.

wideband antennas can be found in [7, 8]. In the application, only two of the four antenna elements will be selected to work with the ports and grounding points of the other two elements open, to realize the adaptive function. In order to describe the dual-element combinations easier, Antenna ij will be used to represent the Antenna 1 (see Fig. 1(a)) and Antenna 2 are operating with the grounding points and ports of Antenna 3 and Antenna 4 open. The S parameters and efficiency of different dual-element combinations are shown in Fig. 1(b) and Fig. 2(a), respectively. It can be observed that each combination can cover the bands of 750–960 and 1700–2700 MHz with a high efficiency. Multiplexing efficiency (ME) is a useful parameter to estimate the MIMO channel capacity and can be calculated simply through the following formula [9]:

$$\text{Multiplexing Efficiency} = \sqrt{(1-\rho_e)\eta_1\eta_2} \tag{1}$$

where η_1 and η_2 are the total efficiency of the first and the second antenna, respectively. ρ_e is the envelope correlation coefficient between the first and the second antenna. Fig. 2(b) shows the ME of each combination. We found in the low band the MIMO performance of Antennas 1 and 2 is better than that of Antennas 3 and 4. This is because the combination of Antennas 1 and 2 has a lower mutual coupling as well as a lower envelope correlation coefficient than the combination of Antennas 3 and 4.

In order to verify the simulation, the measured s parameters are shown in Fig. 3 when Antenna 1 and Antenna 2 are operating.

3. BODY EFFECTS REDUCTION WITH THE PROPOSED ADAPTIVE QUAD-ELEMENT LTE MIMO ANTENNA ARRAY

In the following, three kinds of body effects will be studied with different dual-element combinations in the proposed quad-element LTE MIMO antennas. All the simulations are carried out using commercial software CST [10].

Figures 4(a) and (b) show the model of CTIA head PDA hand and the ME, respectively. The ME is calculated through the envelope correlation coefficients and total efficiencies. It can be observed that in the low band the combination of Antennas 3 and 4 (located on the bottom part of the chassis) has a better ME than the combination of the others. In the high band the combination of Antennas 1 and 3, which has less coverage of head and hand, performs quite outstandingly. Therefore, in the applications combination of Antennas 3 and 4 and the combination of Antennas 1 and 3 can be utilized for the low and high bands, respectively. Figs. 5(a) and (b) show the PDA hand (browsing mode) model and ME, respectively. The results are quite similar to hand and head case. In the low band of 750–900 MHz the combination of Antennas 3 and 4 (with more hand coverage) has a better performance while in the high band the combination of Antennas 1 and 2 with less hand coverage performs better. The rules are also the same in the situation of dual bands in Fig. 6(b), the combination of Antennas 1 and 4 (the most coverage of dual hand) and the combination of Antennas 2 and 3 (the least coverage of dual hand) will be used for low band and high bands, respectively.

From the ME results for different body effect cases, we can find the following rules:

1). In the band from 750 MHz to 900 MHz, the dual-element combination with the most human body coverage perform more outstanding than the other combination. This is a little contrary to our common thinking. Low body coverage does not always give a good result.

2). In the bands of 900–960 MHz and 1.7–2.7 MHz, the best performance should belong to the combination with the least body coverage.

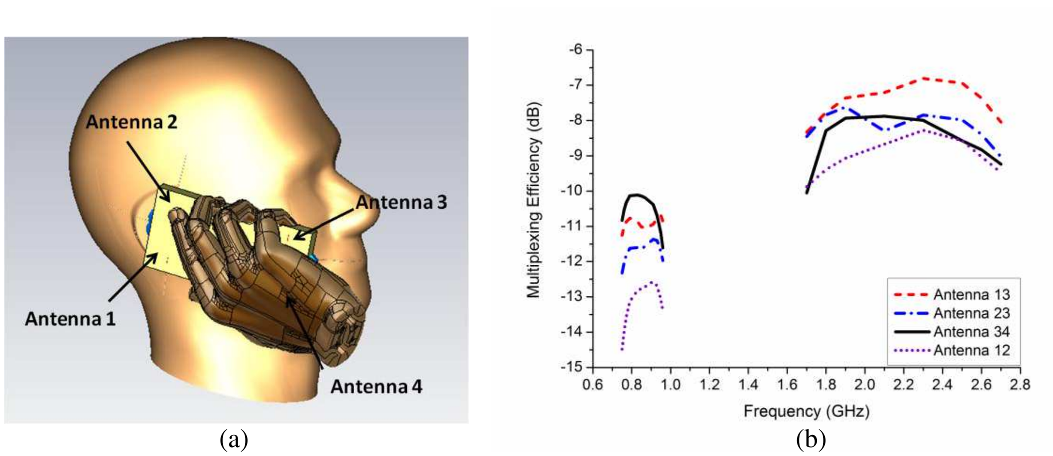

Figure 4: (a) Model and antenna locations of CTIA head and PDA hand, (b) multiplexing efficiency of the different LTE MIMO antenna element combinations in CTIA head and PDA hand case.

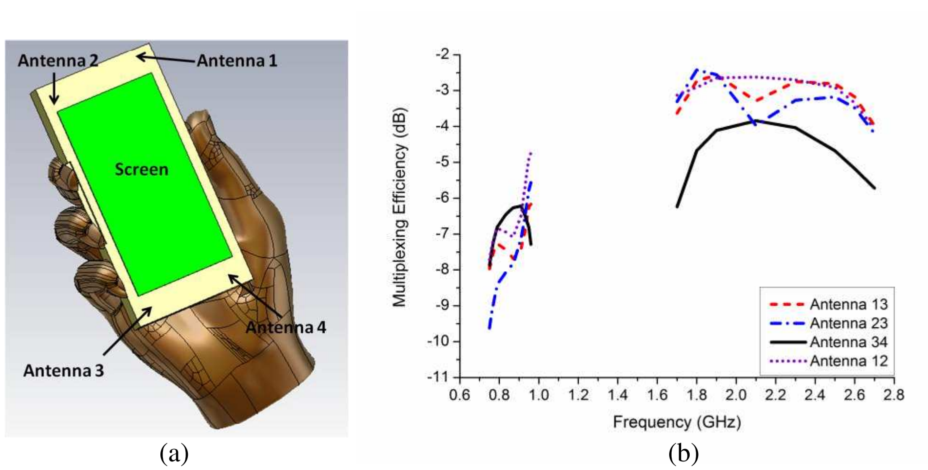

Figure 5: (a) Model and antenna locations of PDA hand (browsing mode), (b) multiplexing efficiency of the different LTE MIMO antenna element combinations in PDA hand case (browsing mode).

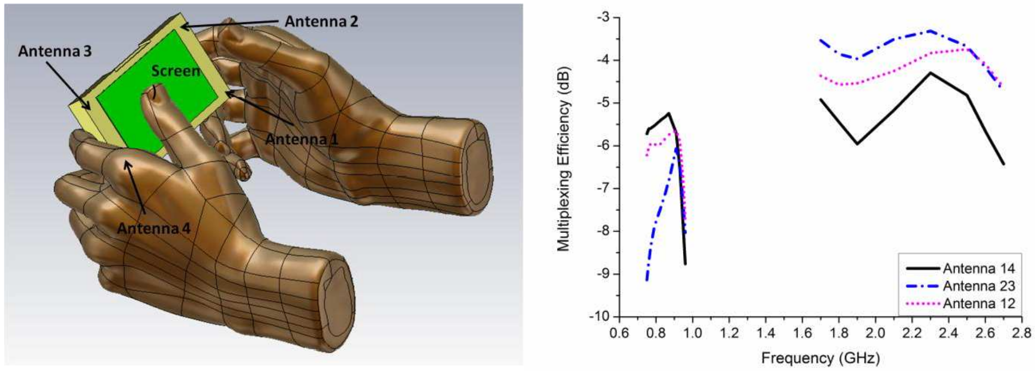

(a) (b)

Figure 6: (a) Model and antenna locations of dual hands, (b) multiplexing efficiencies of the different LTE MIMO antenna element combinations in dual hands case.

4. CONCLUSION

A compact adaptive wideband collocated LTE MIMO antenna array with quad elements for mobile terminals has been introduced, which can cover the bands of 750–960 and 1700–2700 MHz. Through different selections of two MIMO antenna elements in four, the three kinds of body effects (head and hand; single hand; dual hands) can be reduced efficiently. For the low band, Antenna pair (3, 4), Antenna pair (3, 4), and Antenna pair (1, 4) can be utilized for the CTIA head and PDA hand, PDA hand (browsing mode), and dual hand cases, respectively. And for the high band, Antenna pair (1, 3), Antenna pair (1, 2), and Antenna pair (2, 3) can be utilized for the CTIA head and PDA hand, PDA hand (browsing mode), and dual hand cases, respectively. Some rules have been provided to improve the MIMO channel capacity through selecting different dual-element combinations with the different chassis locations.

REFERENCES

1. Khan, S. N., S. Zhang, and S. He, "Low profile and compact size coplanar UWB antenna working from 2.8 GHz to over 40 GHz," *Microw. Opt. Technol. Lett.,* Vol. 51, 408–411, 2009.
2. Ni, W., N. Nakajima, and S. Zhang, "A broadband compact folded monopole antenna for WLAN/WiMAX communication applications," *Journal of Electromagnetic Waves and Applications*, Vol. 24, No. 7, 921–930, 2010.
3. Zhang, S., B. K. Lau, Y. Tan, Z. Ying, and S. He, "Mutual coupling reduction of two PIFAs with a T-shape slot impedance transformer for MIMO mobile terminals," *IEEE Trans. Antennas Propag.*, Vol. 60, No. 3, 1521–1531, Mar. 2012.
4. Lee, J., et al., "Miniature long-term evolution (LTE) MIMO ferrite antenna," *IEEE Antennas Wireless Propag. Lett.,* Vol. 10, 603–606, 2011.
5. Plicanic, V., B. K. Lau, A. Derneryd, and Z. Ying, "Actual diversity performance of a multiband diversity antenna with hand and head effects," *IEEE Trans. Antennas Propag.*, Vol. 57, No. 5, 1547–1556, May 2009.
6. Zhang, S., S. He, K. Zhao, and Z. Ying, "Multi-band wireless terminals with multiple antennas along an end portion, and related multi-band antenna systems," Sonyericsson Patent Pending and Filed by USA, Sep. 2011.
7. Ying, Z., "Simple compact LC loading wideband antenna for LTE and other bands," Sonyericsson Patent Pending and Filed by USA, Oct. 2010.
8. Ying, Z., "Ground free type compact LC loading dual loop more than 10 bands antenna for cellular and non-cellular wireless terminals," Sonyericsson Patent Pending and Filed by USA, Mar. 2010.
9. Tian, R., B. K. Lau, and Z. Ying, "Multiplexing efficiency of MIMO antennas," *IEEE Antennas Wireless Propag. Lett.*, Vol. 10, 183–186, 2011.
10. CST Microwave Studio2011 by Computer Simulation Technology [Online] Available: http://www.cst.com.

Multiple-feed Coupling Measurements for Luneburg Lens Antenna

D. Franco-Vazquez, M. Vera-Isasa, and E. de Lorenzo Rodríguez
Universidade de Vigo, Spain

Abstract— Mutual coupling measurements between two feeds of a Luneburg lens are presented in this paper. A 356 mm diameter Luneburg lens with two WR90 feeds is used to perform measurements within the 8–11 GHz frequency range. Results of mutual coupling with and without lens are presented for different spacing between the feeds for both vertical and horizontal polarization. Measurements with four feeds are also presented.

1. INTRODUCTION

Luneburg lens has being studied extensively since 1944 [1] but, recently, the use of new materials avoids the weight inconvenient of this kind of antennas [2, 3]. The Luneburg lens is a very interesting solution, when simultaneous reception from several different directions is desired, in relation to other alternatives like arrays that require a complicated beamforming network. Simultaneous beams are achieved by using as many feeds as beams required. The lens concentrates the feed radiated field in a narrow beam in the direction of interest. Limitations in the number of beams or proximity between them are imposed by the system geometry: the size of the feeds, the mutual coupling and the blocking between them. Despite this drawback, few studies of mutual coupling between feeds illuminating a Luneburg lens can be found in literature [4].

In this contribution, coupling measurements obtained between 8 and 11 GHz for a 356 mm diameter Luneburg lens with two and four slightly flared WR90 feeds are shown. In the following section a description of the antenna, the measurement scheme and the equipment are provided. Results for different angular feed separation and polarization in the mentioned frequency range can be found in the third section and the conclusions close the paper.

2. MEASUREMENT SYSTEM

The antenna under test consists of a 356 mm diameter Luneburg lens illuminated at 193 mm focal distance by vertical polarized WR90 waveguides with aperture dimensions 2.6×1.3 cm. Figure 1 depicts the waveguide azimuth and elevation radiation pattern at 8 and 10 GHz, and Figure 2 shows a picture of the waveguide used in the measurements.

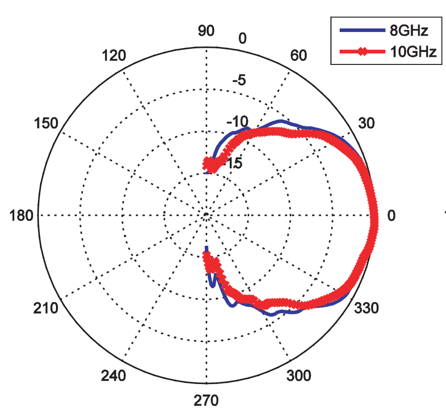

(a)

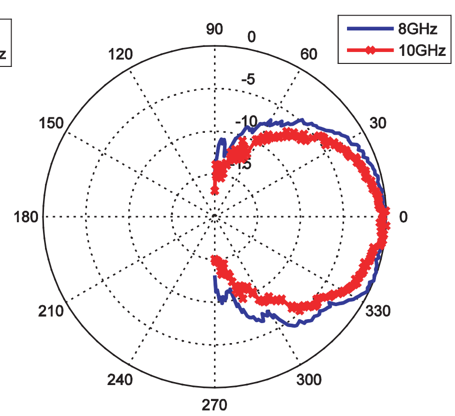

(b)

Figure 1: Waveguide radiation pattern (a) azimuth, and (b) elevation.

The antenna under test is placed inside an anechoic chamber to perform the coupling measurements. In a first step, measurements involve only two waveguides placed around the lens at the focal point, one in a fixed angular position (fixed waveguide) whereas the other (mobile waveguide) is initially placed as close to the fixed waveguide as possible and then it is moved away around the lens with a step of one degree. The fixed waveguide is connected to the port 1 of a four-port Rhode & Schwartz ZVA-67 network analyzer, and the mobile waveguide is connected to the port 2. The

Figure 2: Picture of the waveguide WR90 used in the measurements.

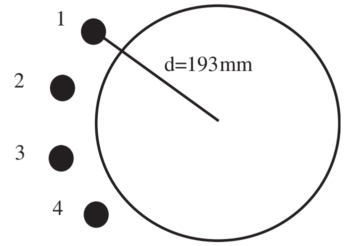

Figure 3: Scheme of four elements placed simultaneously around the lens.

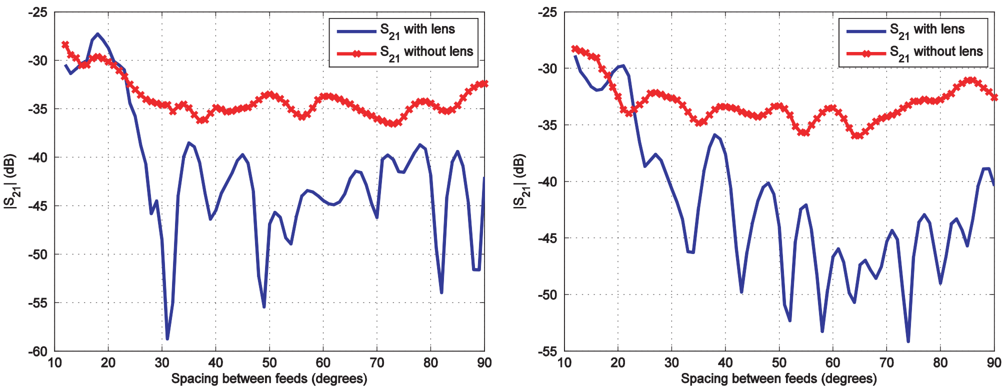

(a) (b)

Figure 4: Mutual coupling at 8 GHz between two feeds with and without lens. (a) Vertical polarization. (b) Horizontal polarization.

S_{21} parameter given by the network analyzer is recorded for further processing at every angular separation between feeds for both vertical and horizontal polarizations within the frequency range 8–11 GHz.

In a second step, the coupling between four elements placed simultaneously around the lens is measured. In the initial position the feeds are placed at the focal point around the lens as close as possible to each other. The feeds are sequentially numbered as it is shown in Figure 3, and each one is connected to its respectively port of the network analyzer according to its label. The following feeds arrangement positions are achieved increasing one degree the spacing between feeds. The scattering parameters involving every pair of feeds gathered from the network analyzer for both vertical and horizontal polarizations within the frequency range 8–11 GHz are recorded for further processing.

3. MEASUREMENT RESULTS

Vertical and horizontal polarization mutual coupling between two feeds at 8 GHz is shown in Figure 4 where measured coupling without lens is also included. Both images show an abruptly decreasing of the mutual coupling from 20° of spacing between feeds, therefore two zones delimited by 20° of separation between feeds (coupled and uncoupled zone) are defined. The difference in the mean value of S_{21} between the coupled and uncoupled zone for vertical polarization is around 13 dB. The abruptly decrease in the mutual coupling is clearly due to the collimating effect of the Luneburg lens, given that the results for mutual coupling without the lens present in the measurement system remains relatively constant, with differences in the mean value of S_{21} between the coupled and uncoupled zone of 4.74 dB for vertical polarization and 3.26 dB for horizontal one. The difference in the mutual coupling level due to the presence of the lens is close to 9 dB. Besides, results obtained for both polarizations are consistent, although horizontal polarization provides a slightly lower coupling due to the narrower waveguide 3 dB-beamwidth for horizontal polarization. Mean values of S_{21} for coupled and uncoupled zone are presented in Table 1.

Mutual coupling between two feeds with an angular spacing of 20° from 8 GHz to 11 GHz for vertical and horizontal polarization is shown in Figure 5. Again, horizontal polarization provides smaller coupling for the complete frequency range.

Table 1: Mean value of the mutual coupling at 8 GHz.

	Polarization	**Mean (S_{21}) (dB) coupled zone**	**Mean (S_{21}) (dB) uncoupled zone**	**Difference (dB)**
Without lens	Vertical	−29.78	−34.52	4.74
	Horizontal	−30.40	−33.66	3.26
With lens	Vertical	−29.44	−43.31	13.87
	Horizontal	−30.77	−43.53	12.76

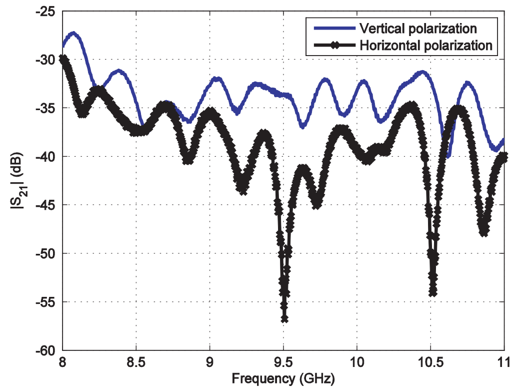

Figure 5: Mutual coupling vs. frequency between two feeds with an angular separation of 20°.

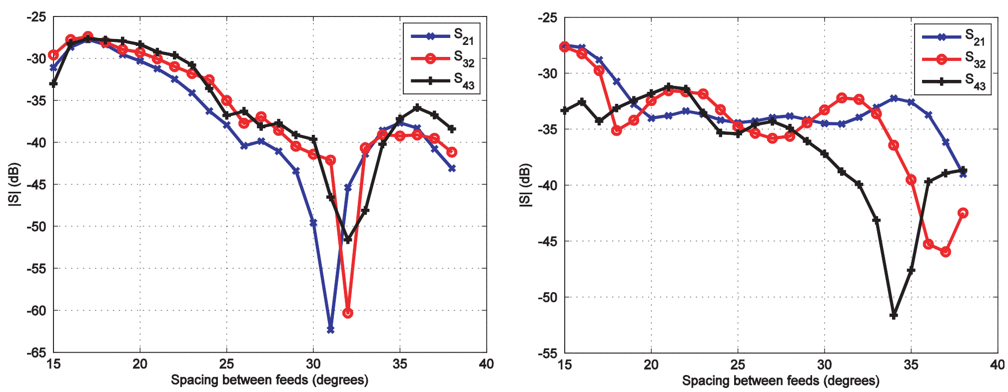

(a) (b)

Figure 6: Mutual coupling at 8 GHz between two contiguous feeds with four feeds present. (a) Vertical polarization. (b) Horizontal polarization.

Results for the coupling between two contiguous feeds at 8 GHz when four elements are placed around the lens simultaneously are presented in Figure 6 for vertical and horizontal polarization. According to the results depicted, the same trend can be appreciated for the coupling between the three pairs of feeds studied (feeds 1–2, 2–3 and 3–4). Therefore, coupling between a pair of contiguous feeds is strongly determined by the spacing between feeds and not for the relative position of the pair into the 4-feeds arrangement.

4. CONCLUSIONS

Vertical and horizontal polarization measurements of the mutual coupling between two waveguides feeding a Luneburg lens, for both two and four-feeds arrangements, have been carried out for frequencies in the range 8–11 GHz. Measurements performed without lens show the mutual coupling inherent to the feed system.

Mutual coupling in the two-feeds arrangement, with and without lens are similar up to 20 degrees of separation. An abrupt decrease is observed for greater separations due to the collimating effect of the lens. Results obtained for both polarizations are consistent, although horizontal polarization provides a slightly lower coupling for the complete frequency range due to the narrower waveguide 3 dB-beamwidth for this polarization.

When four waveguides are simultaneously placed around the Luneburg lens, the relative position of a particular pair of contiguous feeds is not a determinant factor in mutual coupling. The critical parameter is the angular separation between the feeds.

ACKNOWLEDGMENT

This research is partially supported by the European Regional Development Fund (ERDF) and the Galician Regional Government under project CN 2012/260 "Consolidation of Research Units: AtlantTIC" and the Spanish State Secretary for Research under project TEC2011-28789-C02-02.

REFERENCES

1. Luneburg, R. K., *Mathematical Theory of Optics,* 189–213, Brown University Press, 1944.
2. Matytsine, L., P. Lagoiski, M. Matytsine, and S. Matitsine, "Large size, lightweight, Luneburg Lenses for multi-beam antenna applications," *2012 6th European Conference on Antennas and Propagation (EUCAP)*, 2266–2270, March 26–30, 2012.
3. Liang, M., X. Yu, R. Sabory-Garcia, W.-R. Ng, M. E. Gehm, and H. Xin, "Direction of arrival estimation using Luneburg lens," *2012 IEEE MTT-S International Microwave Symposium Digest (MTT)*, 1–3, June 17–22, 2012.
4. Nikolic, N. and J. S. Kot, "Analysis of mutual coupling in a multi-beam Luneburg lens antenna using a hybrid method," *2007 IEEE Antennas and Propagation Society International Symposium*, 4999–5002, June 9–15, 2007.

Asymetrical Interdigital Dual-band Bandpass Filter Using Grounded inside Arms with via Holes

Ram Krishna Maharjan and Nam-Young Kim
RFIC Center, Kwangwoon University, 447-1 Wolgye-dong, Nowon-ku, Seoul 139-701, Korea

Abstract— A planar novel asymmetrical interdigital dual-band bandpass filter (BPF) based on the bended-inside arms' using via ground holes is presented for C-band and other wireless applications. By optimizing the orientation of internal and external interdigital-arms with via holes, as well as consequently analyzing the transmission and reflection coefficients in scattering parameters, a useful dual-band filter response is realized. The designed interdigital resonator-based dual-band filter is fed by asymmetric feeder lines, and four transmission zeros are obtained at the both sides of bands in order to improve the band selectivity and spurious suppression. The grounded arms enhance to flow electric and magnetic field significantly. Hence the orientation of the both arms helps to build up strong electromagnetic (EM) coupling effectively through the open gaps and via holes themselves with maintaining adequate transmission and reflection coefficients for dual-band frequencies. The first and second band resonant frequencies were measured at 3.7 GHz and 5.7 GHz, respectively.The measured return losses (S_{11}) of the fabricated filter are of -18.6 dB and -19.2 dB; and insertion losses (S_{21}) are of -0.48 dB and -1.02 dB, at the first and the second resonant frequencies of the dual-band bandpass filter. The spurious suppression was measured to be less than -32 dB at out-band frequencies in all of four transmission zeros. This BPF is compared and demonstrated by the predicted simulation and measurement results that the proposed dual-band filter has both good performance and selectivity. The designed filter can be useful to the C-band application in satellite communication systems.

1. INTRODUCTION

With the rapid development of modern satellite communications, dual-band filters have been more attractive foruplink/downlink global system in fixed satellite service (FSS) using geostationary satellites.Recently, compact size, high-performance and low cost dual-band filter is in great demand for enhancing system performances. For requirement of application,dual-band bandpass filter has been widely studied in many papers [1–11]. In [1–3], dual-band filters were implemented by combination of two single band filters and each of these bands was designed separately [3]. The satellite communication system used C-band downlink is in geostationary earth orbit and carries usually 24 transponders, each with a bandwidth of 36 GHz, therefore the satellite uses orthogonal circular polarizations to provide an effective RF bandwidth of 864 MHz. The communications C-band was the first frequency band that was allocated for commercial telecommunications via satellites. The same frequencies were already in use for terrestrial microwave radio relay chains. Nearly all C-band communication satellites use the band of frequencies from 3.7 to 4.2 GHz for their downlinks. Center frequency of 5.7 GHz is used for wireless communication such as in microwave links, RFID, Wi-Fi, etc..

In this paper, a dual-band BPF is presented by applying asymmetric interdigital arms with via holes. The lower passband is mainly affected by short stub using via and the higher passband is mainly affected by the spacing the arms. Besides, two pairs of transmission zeros are introduced to improve selectivity and suppression.The proposed filter can be used for C-band downlink and terrestrial microwave link communication effectively. Such type of planar filter can be a desired size and is easily mounted on a dielectric substrate using printed circuit technology. This BPF can be very useful to the system by reducing the cost and size, as well as enhancing the overall system performance. These planar filters have the advantages of a low profile, high selectivity and good reliability.

2. DESIGN ANALYSIS OF BPF

In this design, the proposed filter was designed, simulated analyze on a common Teflon substrate with a thickness of 0.504 mm and a relative dielectric constant, ε_r of 2.52. A commercially available Sonnet EM simulator is utilized for realizing the desired dual-band filter characteristics. Fig. 1 shows the schematic design layout of the dual-band BPF with the appropriate dimensions. Two similar types of resonators are inter-coupled to make asymmetrical interdigital structure. The shorted via holes connecting into a common ground substrate build up dual-band characteristics. The mutual inductance between two corresponding arms of interdigital structure and parasitic capacitance due to gap distances in resonators enhances the total value of overall inductance and capacitance of the resonators. With input/output devices 50 Ω impedance are matched and characterized using asymmetric port terminals as Refs. [12–14]. A simple planar interdigital topology is proposed with low cost dielectric material like Teflon having a low dielectric constant. Each of inside arms in the structure is short-circuited using via ground holes at one end and both of outside arms are open-circuited at the opposite sides. The interdigital arms also called resonator elements are seemed those open-circuited arms being arranged in a parallel array with the positions of the short-circuited ends. Two pass-bands are produced by a pair of grounded via holes into the bended ends of the inside arms of the asymmetrical interdigital structure. The design and use of compact interdigital structure with opposite vias are critical to ensure successful circuit design and desired bandpass characteristics. The dual self-resonant frequencies depend on the physical interdigital arms and bended geometry with vias as well as material properties. The number of arms, via diameter, gaps and the metal trace width values highly affect the self-resonance frequency.

The photograph of the proposed design layout of the dual-band filter is depicted in Fig. 1(a). The filter was fabricated using photolithographic techniques and a wet etching process in printed circuit technology. The overall size of the filter dimensions is $14.6 \times 25\,\text{mm}^2$. By using the Sonnet EM simulation tool, after design analysis and optimization, the geometric dimensions of the filter were determined to be: $L_1 = 5.8\,\text{mm}$, $L_2 = 12.6\,\text{mm}$, $W_1 = 11.6\,\text{mm}$, $W_2 = 1.4\,\text{mm}$, $X = Y = 2.2\,\text{mm}$, $\varnothing = 1.0\,\text{mm}$, $a = b = 1.4\,\text{mm}$, $S = 0.2\,\text{mm}$, $d_1 = 0.4\,\text{mm}$, $d_2 = 1.0\,\text{mm}$, $g_1 = 0.2\,\text{mm}$, $g_2 = 1.0\,\text{mm}$, and $p_1 = p_2 = 2.0\,\text{mm}$. p_1 and p_2 are the port reference distances for connecting connectors with the fabricated device.

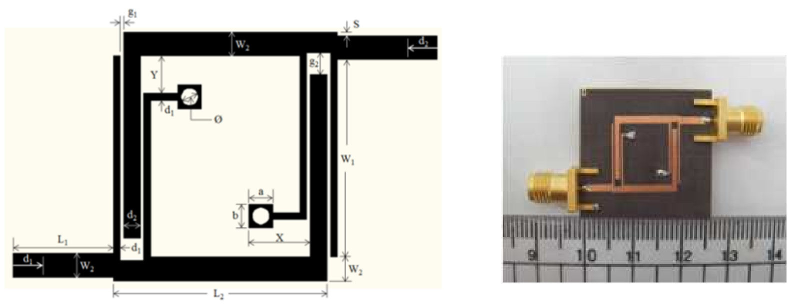

(a) (b)

Figure 1: (a) Schematic design layout, (b) photograph of the proposed filter.

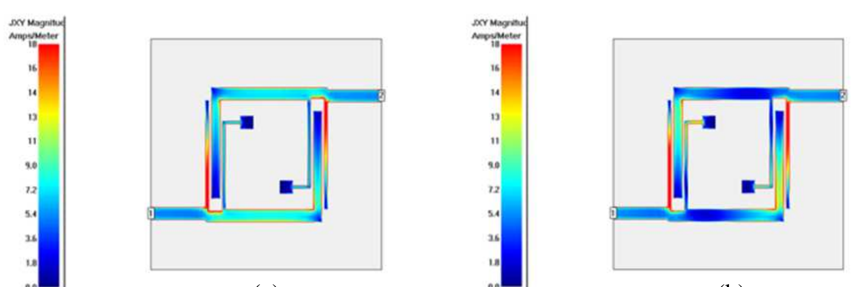

(a) (b)

Figure 2: Surface current distributions at (a) 3.5 GHz and (b) 5.55 GHz.

3. SIMULATED AND MEASURED RESULTS

The surface current distributions at both resonant frequency bands are presented in Fig. 2. The current distributions at the resonant frequencies are illustrated and nearby adjacent frequencies were also simulated, but they are not shown here. The current distributions were observed randomly at different frequencies nearby resonance conditions. The simulation results show the current density of the proposed filter at the significant states around the resonant condition as given in Figs. 2(a) and 2(b). These figures show the essential state of equal and quite good current distribution at both frequencies of 3.5 GHz and 5.55 GHz frequencies compared to the other adjacent frequencies.

In fact, the reactive components cancel each other and leave only the resistance at resonant states, resulting in the maximum current flowing in those conditions rather than which found in the other bands of non-resonant frequencies.

The structural design layout with the major dimensions of the proposed filter is illustrated in Fig. 1(b). The fabricated filter was tested and characterized by using the Agilent 8510C vector network analyzer (VNA). To verify the predictions, the experimental results were analyzed and compared to the simulated parameters. The measured and simulated results of the insertion loss (S_{21}) and the return loss (S_{11}) are compared in Fig. 3. The proposed filter was designed and simulated at 3.5 GHz and 5.55 GHz resonant frequencies. In the measurement results, the resonant frequencies were shifted above and resonated at 3.7 GHz and 5.7 GHz. The reasons of frequency shift can be due to dielectric substrate loss, the limitation of the accuracy in physical dimension and lack of accurate connection orientation while connectors soldered with the device. The maximum allowable fabrication tolerance especially in sensitive geometrical gap can also affect while chemical etching and cleaning processes were completed [15]. The first and second band resonant frequencies were measured at 3.7 GHz and 5.7 GHz, respectively. The measured return losses (S_{11}) of the fabricated filter are of -18.6 dB and -19.2 dB; and insertion losses (S_{21}) are of -0.48 dB and -1.02 dB, at the first and the second resonant frequencies of the dual-band bandpass filter, respectively. The spurious suppression was measured to be less than -32 dB at out-band frequencies in all of four transmission zeros. To validate the methods applied in the design, the proposed filter is fabricated and measured.

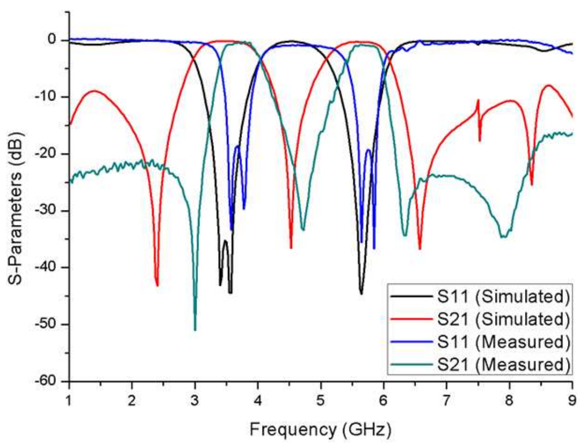

Figure 3: Comparison of S-parameter responses.

4. CONCLUSIONS

The proposed BPF was designed, fabricated, measured and compared with the simulated results. It is compared and demonstrated by the predicted simulation and measurement results that the proposed dual-band filter has both good performance and selectivity. The designed filter can be useful to the C-band application in satellite communication and other wireless communication systems.Due to the shorted arm of interdigital structure using via holes the proposed filter can have a dual-band characteristics with four transmission zeros These types of BPF can be attractive for satellite communications and terrestrial microwave links.

ACKNOWLEDGMENT

This research work was supported by the National Research Foundation of Korea (NRF) and a Grant supported from the Korea government (MESH) (No. 2012-0009224) and (No. 2012R1A1A2004 366). This work was also supported by a Research Grant of Kwangwoon University in 2013.

REFERENCES

1. Lee, J. and Y. Lim, "Dual-band bandpass filter using dual-mode resonators," *Microwave and Optical Technology Letters*, Vol. 53, No. 11, 2515–2517, 2011.
2. Wu, B., C.-H. Liang, P.-Y. Qin, and Q. Li, "Compact dual-band filter using defected stepped impedance resonator," *IEEE Microwave and Wireless Components Letters*, Vol. 18, No. 10, 674–676, 2008.

3. Wu, B., C.-H. Liang, Q. Li, and P.-Y. Qin, " Novel dual-band filter incorporating defected SIR and microstrip SIR," *IEEE Microwave and Wireless Components Letters*, Vol. 18, No. 6, 392–394, 2008.
4. Zhou, M.-Q., X.-H. Tang, and F. Xiao, "Compact dual band transversal bandpass filter with multiple transmission zeros and controllable bandwidths," *IEEE Microwave and Wireless Components Letters*, Vol. 19, No. 6, 347–349, 2009.
5. Hong, J.-S., S. Hussein, and Y.-H. Chun, "Dual-mode microstrip open-loop resonators and filters," *IEEE Transactions on Microwave Theory and Techniques*, Vol. 55, No. 8, 1764–1770, 2007.
6. Zhang, X.-Y., J.-X. Chen, Q. Xue, and S.-M. Li, "Dual-bandbandpass filters using stub-loaded resonators," *IEEE Microwaveand Wireless Components Letters*, Vol. 17, No. 8, 583–585, 2007.
7. Chu, Q.-X. and F.-C. Chen, "A compact dual-band bandpass filter using meandering stepped impedance resonators," *IEEE Microwave and Wireless Components Letters*, Vol. 18, No. 5, 320–322, 2008.
8. Mondal, P. and M. K. Mandal, "Design of dual-band bandpass filters using stub-loaded open-loop resonators," *IEEE Transactions on Microwave Theory and Techniques,*, Vol. 56, No. 1, 150–155, 2008.
9. Weng, M.-H., H. W. Wu, and Y.-K. Su, "Compact and low loss dualbandbandpass filter using pseudo-interdigital stepped impedanceresonators for WLANs," *IEEE Microwave and Wireless Components Letters*, Vol. 17, No. 3, 187–189, 2007.
10. Li, Y.-C., H. Wong, and Q. Xue, "Dual-mode dual-band bandpassfilter based on a stub-loaded patch resonator," *IEEE Microwave and Wireless Components Letters*, Vol. 21, No. 10, 525–527, 2011.
11. Sung, Y.-J., "Dual-mode dual-band filter with band notch structures," *IEEE Microwave and Wireless Components Letters*, Vol. 20, No. 2, 73–75, 2010.
12. Maharjan, R. K., B. Shrestha, and N. Y. Kim, "Compact microstrip square open-loop bandpass filter using open-stub," *IET Electron. Lett.*, Vol. 48, No. 6, 333–334, 2012.
13. Maharjan, R. K. and N. Y. Kim, "Microstrip dual I-band bandpass filter with symmetrical twininductor resonators," *Microw. and Optical Techn. Lett.*, Vol. 54, No. 3, 638–641, 2012.
14. Maharjan, R. K. and N. Y. Kim, "Compact stub-coupled square open-loop bandpass filter for Ku-band applications," *Journal of Electromagnetic Waves and Applications*, Vol. 26, Nos. 5/6, 603–614, 2012.
15. Bogatin, E., "Design rule for microstrip capacitance," *IEEE Trans. on Components, Hybrids and Manufacturing*, Vol. 11, No. 3, 253–259, 1988.

Systematic Study of the Effective Permittivity in a Periodically Drilled Substrate Integrated Waveguide

R. Isidro[1], **A. Coves**[1], **M. A. Sánchez-Soriano**[2], **G. Torregrosa**[1], **E. Bronchalo**[1], and **M. Bozzi**[3]

[1]Departamento de Ingeniería de Comunicaciones
Universidad Miguel Hernández de Elche, Elche, Alicante 03202, Spain
[2]Lab-STICC, Université Bretagne Occidentale, Brest, France
[3]Department of Electrical, Computer and Biomedical Engineering
University of Pavia, Pavia, Italy

Abstract— This paper presents the results of a systematic study of the effective permittivity in a Substrate Integrated Waveguide (SIW) in which arrays of air holes are added along the waveguide in order to synthesize a lower effective permittivity. The study has been performed with the commercial software tool HFSS. For each geometry analyzed, one period along the propagation direction has been simulated, and by applying periodic conditions, the obtained cutoff frequency of the waveguide provides its effective permittivity. Different hole patterns have been analyzed, and for each one, the effect of the variation of the hole diameters has also been studied. Such study demonstrates that the effective permittivity in the drilled guide cannot be rigorously approximated by a surface weighted average, mainly due to the drilling of the metal surfaces. The radiation by the air holes in the drilled SIW has also been studied, concluding that radiation losses are not important if some design considerations are followed.

1. INTRODUCTION

In recent years, many papers have been published on a new type of transmission line called SIW [1, 2]. This low-cost realization of the traditional rectangular waveguide takes the advantages of planar lines for easy integration with other circuits, and low radiation losses of waveguides. Furthermore, this new technology has been used for making a large number of microwave devices such as filters, antennas, multiplexers, etc. [3–5]. On the other hand, the use of different dielectric materials along a rectangular guide [6] can be applied to the design of filtering structures.

This paper presents the results of a systematic study of the effective permittivity in a SIW in which arrays of air holes are added along the waveguide in order to synthesize a lower effective permittivity. To this end, different hole patterns have been analyzed, and for each one, the effect of the variation of the hole diameters has also been studied. The study shows that, although in shielded drilled waveguides the effective permittivity can be approximated by a surface weighted average between the drilled and undrilled surface, this approximation is no longer valid in unshielded drilled waveguides, mainly due to the drilling of the metal surfaces. The radiation effect by the air holes in the drilled SIW has also been studied, concluding that radiation losses are not important if some design considerations are followed. The results of this study will be used in a new topology of bandpass filters in SIW technology based on coupled cavities of different permittivity, which is achieved by the introduction of air holes in the lower relative permittivity sections, where a decrease of the dielectric losses is expected due to the removal of material.

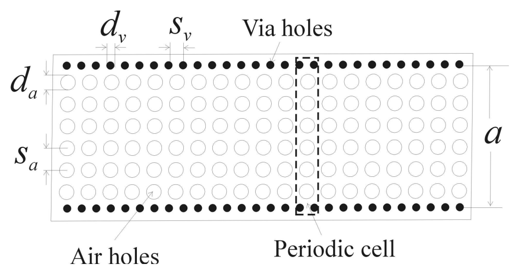

Figure 1: Scheme of a SIW with periodic air holes.

2. STUDY OF THE EFFECTIVE PERMITTIVITY OF A SIW WITH PERIODIC AIR HOLES

Figure 1 shows the scheme of a section of the waveguide under study, consisting of a conventional SIW in which arrays of air holes are added along the waveguide, in this case following a rectangular pattern. This waveguide is constituted by two rows of parallel metallic posts (or via holes) delimiting the area of propagation of the fundamental TE_{10} mode of the SIW. The metallic posts are characterized by their separation s_v, and by their diameter d_v, whose values must be appropriately chosen [1] in order to avoid radiation losses, so they must fulfill the following conditions:

$$d_v < \lambda_g/5, \quad s_v \leq 2d_v \tag{1}$$

where λ_g is the guided wavelength. On the other hand, the propagation constant of this guide is determined by the width a of the SIW, and also by the effective permittivity obtained after making the air holes in the propagation area. The air holes are characterized by their diameter d_a, and by their separation s_a, whose choice will be delimited by the availability of drills in the manufacturing process on one hand, and by the minimum separation between the edges of adjacent holes, which we'll fix to 200 µm, in order to avoid the breaking the substrate. A previous study of this type of guide [2] demonstrates that a SIW can be analyzed as an equivalent rectangular waveguide of effective width a_{eff} given by:

$$a_{\mathit{eff}} = a - \frac{d_v^2}{0.95 s_v} \tag{2}$$

Then, all the study followed in this section is carried out with the equivalent waveguide of width a_{eff}.

In a first approximation, the effective relative permittivity of the waveguide can be calculated as an averaged function weighted by the drilled and undrilled surface in a periodic cell (dashed box in Figure 1):

$$\epsilon_{r\ \mathit{eff}} = \frac{\epsilon_{r\,air} S_{air} + \epsilon_{r\,subs}\left(S_{cell} - S_{air}\right)}{S_{cell}} \tag{3}$$

being $\epsilon_{r\,air} = 1$. According to Equation (3), the effective permittivity will be lower for a higher ratio between the air surface and the surface of the periodic cell S_{air}/S_{cell}. Figure 2 shows some particular

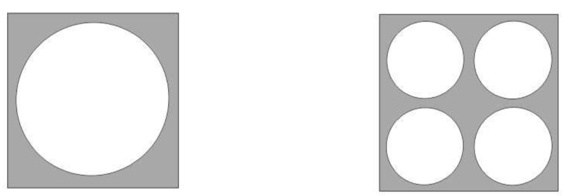

(a) $S_{air}/S_{cell} = 0.669$ (b) $S_{air}/S_{cell} = 0.577$

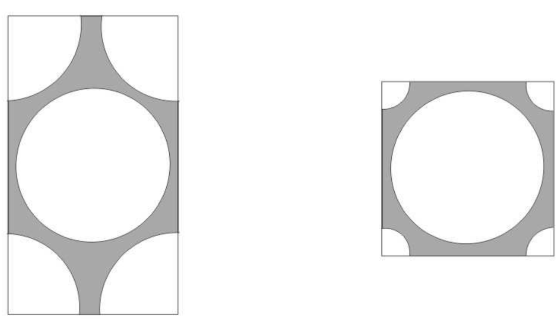

(c) $S_{air}/S_{cell} = 0.773$ (d) $S_{air}/S_{cell} = 0.751$

Figure 2: Comparison of the ratio S_{air}/S_{cell} obtained with different hole patterns: (a) Rectangular pattern with $d_a = 1.2$ mm, (b) rectangular pattern with $d_a = 0.6$ mm, (c) triangular pattern with $d_a = 1.2$ mm, (d) triangular pattern with multiple air hole sizes ($d_{a1} = 1.2$ mm and $d_{a2} = 0.6$ mm).

cases of the ratio S_{air}/S_{cell} obtained with different hole patterns. Comparison of Figures 2(a) and (b) show that when using a rectangular pattern, the air surface is maximized for bigger holes. Figures 3(a) and (c) show that for a fixed hole diameter, the triangular pattern provides a greater air/cell surface ratio than the rectangular pattern (see Figure 3). However, not all drills are available in the manufacturing process. Moreover, the fixed size of the waveguide is an additional constraint in the choice of the hole size. With all these constraints, another way to increase the air surface is to use different hole diameters. Figure 2(d) shows that by using different hole sizes, an air/cell surface ratio close to that of the triangular pattern can be obtained. Finally, it is important to note that the results provided in Figures 2 and 3 correspond to a minimum separation between air holes, so that for larger separations we won't be able to obtain such high values of air/cell surface ratios.

In Figure 3 it is compared, for the different diameters of drills available in our laboratory, the air/cell surface ratio S_{air}/S_{cell} in the case of a rectangular and triangular hole pattern (see Figure 2 for a minimum separation between air holes of 200 μm).

On the other hand, in order to obtain the effective permittivity of the drilled waveguide more accurately, i.e., having into account the fact that the top and bottom metallic layers are drilled, the electromagnetic analysis commercial tool HFSS [7] has been employed. This analysis tool yields the cutoff frequencies of the modes of the structure in the propagation direction. In this case, we'll restrict our study to the monomode regime of the waveguide, so that it is possible to relate the effective permittivity of the waveguide with the cutoff frequency of the TE_{10} mode through the following expression:

$$\epsilon_{r\ eff} = \frac{c^2}{4a_{eff}^2 f_c^2} \tag{4}$$

where c is the speed of light in free space and f_c is the cutoff frequency of the first mode of the waveguide provided by the program. For each air hole pattern analyzed, given that periodic conditions are met along the waveguide, we only need to analyze a periodic cell along the direction of propagation.

3. RESULTS

Using Equations (3) and (4) derived in the previous section, we have obtained the effective relative permittivity of a waveguide of dimensions $a_{eff} = 7.9$ mm and $b = 0.63$ mm in which a series of air holes have been periodically made on a metalized substrate of $\epsilon_r = 10$ for different ratios S_{air}/S_{cell}, varying the hole diameters. First, in Figure 4 it is represented the effective relative permittivity $\epsilon_{r\ eff}$ given by Equation (4) for a different number of air holes in the unit cell equally spaced across the width of the guide following a rectangular pattern for the different possible diameters. In all cases a minimum separation between air hole columns in the direction of propagation of 200 μm has been kept. Thus, for this guide width, such curves can be employed as a way of determining the drill diameter to employ for obtaining a desired value of $\epsilon_{r\ eff}$. In this figure it can be checked

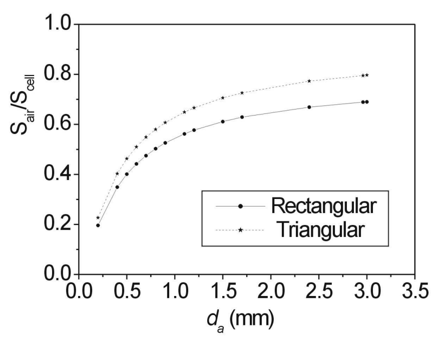

Figure 3: Comparison of the ratio S_{air}/S_{cell} of a rectangular and triangular hole pattern for different hole diameters.

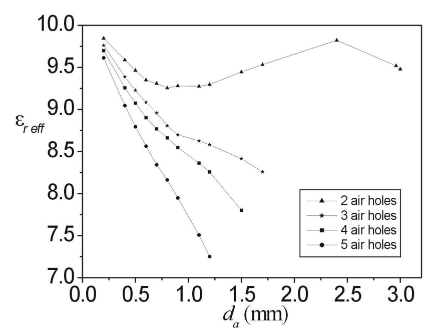

Figure 4: Effective relative permittivity $\epsilon_{r\ eff}$ obtained with Equation (5) for different numbers of air holes in the unit cell equally spaced across the width of the guide following a rectangular pattern for the different possible diameters.

that, contrary to what it is predicted by Equation (3), the $\epsilon_{r\,eff}$ obtained in each case not always decreases with increasing radius of the air holes. This fact is more evident in the case of two air holes along the guide width, which represents a higher inhomogeneity in the guide, thus further away from the equivalent case of a waveguide filled with a uniform material of $\epsilon_{r\,eff}$.

In order to check it, Table 1(a) shows, for the case of two air holes in the unit cell and different diameters, the ratio S_{air}/S_{cell} and the value of $\epsilon_{r\,eff}$ given by Equation (3) and that provided by Equation (4). In such table it can be observed that the results provided by Equation (3) differ more to that given by Equation (4) with increasing air hole diameter. This is because Equation (3) does not take into account the non-uniform field distribution of the fundamental mode in the guide on one hand, nor does the fact that the top and bottom metallic layers are drilled. In order to see this last effect in a separated way, the last column in Table 1(a) shows the $\epsilon_{r\,eff}$ obtained in an equivalent drilled and shielded guide. In view of the obtained results, it can be concluded that this last effect is quite relevant, depending of the air hole diameter. In fact, for the unshielded waveguide, it has been checked that the electric field is mainly confined in the dielectric material, and then the $\epsilon_{r\,eff}$ is close to that of the substrate. However, for the shielded waveguide, the electric field distributes transversely through the air holes following the TE_{10} mode profile, which implies a considerable reduction of its effective permittivity.

Table 1: (a) Comparison of $\epsilon_{r\,eff}$ of a guide of dimensions $a_{eff} = 7.9$ mm and $b = 0.63$ mm with two air holes in the unit cell. (b) $\epsilon_{r\,eff}$ obtained with Equation (4) for different triangular patterns using 2 different diameters.

(a)

d_a (mm)	S_{air}/S_{cell}	$\epsilon_{r\,eff}$ (3)	$\epsilon_{r\,eff}$ (4)	$\epsilon_{r\,eff}$ (4) shielded
0.2	0.020	9.821	9.846	9.825
0.4	0.053	9.523	9.588	9.512
0.5	0.071	9.361	9.464	9.344
0.6	0.089	9.195	9.349	9.172
0.7	0.108	9.026	9.310	8.997
0.8	0.127	8.855	9.255	8.821
0.9	0.146	8.682	9.280	8.644
1.1	0.185	8.334	9.275	8.288
1.2	0.205	8.159	9.297	8.109
1.5	0.263	7.632	9.446	7.571
1.7	0.302	7.278	9.532	7.211
2.4	0.440	6.036	9.822	5.937
2.96	0.551	5.038	9.519	4.902
3.0	0.559	4.967	9.479	4.828

(b)

n	d_{a1} (mm)	d_{a2} (mm)	S_{air}/S_{cell}	$\epsilon_{r\,eff}$
5	1.1	0.6	0.484	6.755
5	0.9	0.8	0.427	6.759
5	0.8	0.9	0.416	6.679
5	0.6	1.1	0.429	6.358
5	0.5	1.2	0.453	6.101
4	1.7	0.6	0.653	6.325
4	1.5	0.8	0.564	6.508
4	1.2	1.1	0.485	6.385
4	1.1	1.2	0.473	6.274
4	0.8	1.5	0.481	5.776
4	0.6	1.7	0.522	5.169
3	1.7	1.5	0.510	6.242
3	1.5	1.7	0.485	6.008
2	3.0	1.7	0.539	7.335
2	1.7	3.0	0.382	5.358

A possible way to reduce the $\epsilon_{r\,eff}$ in the guide is to use different hole diameters. Thus, Table 1(b) shows the ratio S_{air}/S_{cell} and $\epsilon_{r\,eff}$ given by Equation (4) for different triangular patterns using 2 different diameters, for different number n of air holes of diameter d_{a1} equally spaced in the guide width. In this table it can be checked that the lowest value of $\epsilon_{r\,eff}$ is not obtained for the highest S_{air}/S_{cell} ratio. This is due to the finite size of the waveguide, so when the greater holes are drilled in the center of the guide (where the field of the fundamental mode is more intense), a lower value of $\epsilon_{r\,eff}$ is achieved.

The last part of this study is devoted to the estimation of radiation losses through the air holes. The side losses through the metallic posts have not been considered, since they have already been studied in other works [1]. Furthermore, an infinite conductivity has been assumed in the metallic walls and a zero loss tangent in the dielectric substrate. In order to obtain the radiation losses, the guide has been placed inside an empty box with radiation conditions on the walls. Radiation losses in a periodic cell have been obtained from its scattering parameters as:

$$L_R = -10\log_{10}\left(|S_{11}|^2 + |S_{21}|^2\right) \tag{5}$$

Figure 5 shows the radiation losses per unit cell in the drilled guide of dimensions $a_{eff} = 7.9$ mm and $b = 0.63$ mm in the case of two air holes in the guide width for the 3 biggest available drills. As it can be observed, radiation losses increase with frequency on one hand, and with hole diameter on the other hand. Also, it has been found that radiation losses linearly increase with the number of cells. In view of the results, we can conclude that radiation losses through the air holes won't be important in the future filters to be implemented, if we use diameters smaller than 2 mm.

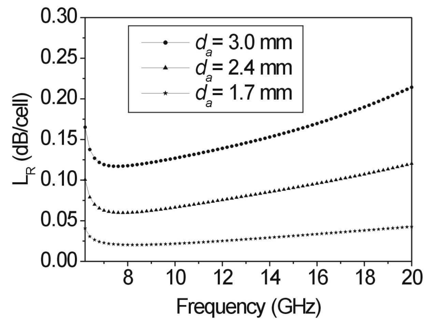

Figure 5: Radiation losses per unit cell in a drilled guide with two air holes for the 3 biggest available drills.

4. CONCLUSION

A systematic study of the effective permittivity in a SIW in which arrays of air holes are added in order to synthesize a lower effective permittivity has been made, which is derived from the cutoff frequency of its fundamental mode. Different hole patterns have been analyzed, and also the effect of the variation of the hole diameters. Such study demonstrates that the effective permittivity in the drilled waveguide cannot be rigorously approximated by a surface weighted average, mainly due to the drilling of the metal surfaces. It has also been checked that there are nearly no radiation losses through the air holes, if we use diameters smaller than 2 mm.

ACKNOWLEDGMENT

This work was supported by the Ministerio de Ciencia e Innovación, Spanish Government, under the coordinated project TEC2010-21520-C04-02.

REFERENCES

1. Deslandes, D. and K. Wu, "Design consideration and performance analysis of substrate integrated waveguide components," *32nd European Microwave Conference Proceedings*, Vol. 2, 881–884, Sep. 2002.
2. Cassivi, Y., L. Perregrini, P. Arcioni, M. Bressan, K. Wu, and G. Conciauro, "Dispersion characteristics of substrate integrated rectangular waveguide," *IEEE Microw. Wirel. Compon. Lett.*, Vol. 12, No. 9, 333–335, Sep. 2002.
3. Yan, L., W. Hong, G. Hua, J. Chen, K. Wu, and T. J. Cui, "Simulation and experiment on SIW slot array antennas," *IEEE Microw. Wirel. Compon. Lett.*, Vol. 14, No. 9, 446–448, Sep. 2004.
4. Chen, X. P., K. Wu, and Z. L. Li, "Dual-band and triple-band substrate integrated waveguide filters with Chebyshev and quasielliptic responses," *IEEE Trans. Microw. Theory Tech.*, Vol. 55, No. 12, 2569–2578, Sep. 2007.
5. Bozzi, M., A. Georgiadis, and K. Wu, "Review of substrate integrated waveguide (SIW) circuits and antennas," *IET Microw. Antennas Propagat.*, Vol. 5, No. 8, 909–920, Jun. 2011.
6. Gómez, A., A. Lakhtakia, A. Vegas, and M. A. Solano, "Band-gaps electromagnéticos unidimensionales en guía de onda rectangular," *Actas del XVIII Simposium Nacional de la Unión Científica Internacional de Radio*, La Coruña, España, Sep. 2008.
7. "HFSS: 3D full-wave electromagnetic field simulation," available: http://www.ansoft.com/products/hf/hfss, 2007.

A Compact Hybrid EBG Microstrip Bandstop Filter for Digital Clock Suppression in a Power Supply System

R. Peña-Rivero, **A. Mendoza-Tellez**, **R. Linares y Miranda**, **and J. A. Tirado-Mendez**
Laboratorio de Compatibilidad Electromagnetica Escuela Superior de Ingeniería Mecanica y Electrica
Instituto Politécnico Nacional, UPALM. Av. IPN s/n Col. Lindavista, México DF 07738, Mexico

Abstract— In this paper, a compact novel wide band microstrip bandstop filter for digital clock suppression in power supply systems is presented. Filter combines the effects of electromagnetic bandagap structure (EBG) with surface mount technology (SMT) capacitor. Parameters are optimized via numerical simulations to achieve a stopband of 12 GHz for a reject of the first nine harmonics of a 1.35 GHz digital clock frequency. A FR4 substrate of relative permittivity 4.7 is used, where mushrooms like EBG structure of rectangular patches connected to ground by vias are built. Four SMT capacitor of 1 pF to the EBG structure are added. With this is possible to obtain a rejection band at -3 dB form 1 GHz to 13.1 GHz within a small circuit area of 225 mm^2

1. INTRODUCTION

Advances in integrated circuit technology have been essential for the rapid development of modern digital computers and high-speed digital circuits, but as time passes, the increasing need for faster processing capability, the growing number of devices that have been integrated on a single chip and the reduction on voltage levels make the digital systems more sensitive to power-ground noise [1]. Simultaneous switching noise (SSN) also known as ground bounce (GBN) or ΔI-noise and is one of the biggest concerns during the design of digital circuits [2]. The term simultaneous switching noise is used to describe fluctuations in the reference power plane that occur when most of the bits in the data bus switch at the same time. This can cause several Power and Signal Integrity (PI/SI) problems during circuits operation [1–3] due to the increase in switching speeds and clock frequencies. In this context several researchers published different methods for SSN reduction which include the use of discrete decoupling capacitors to provide grounding paths for the voltage fluctuations on the reference planes [4, 5], but this method is limited only to low frequencies due to the capacitor's series lead inductance. In the last decade there has been an increasing interest in the use of electromagnetic bandgap structures (EBG) [7, 8] for suppression of SSN [9–15] in high digital data rates (above 1 GHz). The use of EBG has been proposed in different papers to suppress fluctuations in the reference power planes [9–12], however, these planes need large areas to get a filtering effect with a narrow suppression band. Another proposed structure was built using mushroom-like EBG structures between the power and return signal planes [13–15]. The drawback with this kind of structure is the complexity due to the need of three layers which difficulties the manufacturing process. Both options need large areas to get a wideband noise suppression, which implies a serious limitation to implement these techniques in real applications within small printed circuit board (PCB) areas.

2. BANDSTOP FILTER

2.1. Proposed EBG Structure Used as Reference

Figure 1 depicts a scheme of the proposed bandstop EBG filter which is built in a two layer PCB From de SI point view the structure has a uniform return plane (at the back) in order to have a good signal quality. Four rectangular metallic patches have been added on each side of the power trace and connected to the return plane by cylindrical vias set at the center of each patch.

The resulting EBG cells contribute with parasitic capacitive and inductive effects which create a resonant structure that in combination with the microstrip line presents a filtering effect [16]. The parasitic effects present in these structures are numerous and it would be difficult to analyze them all. Figure 2 depicts a diagram which illustrates the presence of the LC effects with more influence on the response of the proposed EBG filter. In the scheme shown the capacitance Cp is due to the separation between the power trace (signal path) and the neighbor patch. Cv represents the capacitive effect between the patch and the return power plane (also known as return signal path) [15, 17], which depends on thickness and permittivity of the substrate and the patch area. The parasitic inductive effects depend on the elements that form the current loop. The diameter used in each via is the parameter with more contribution in the parasitic inductance effects.

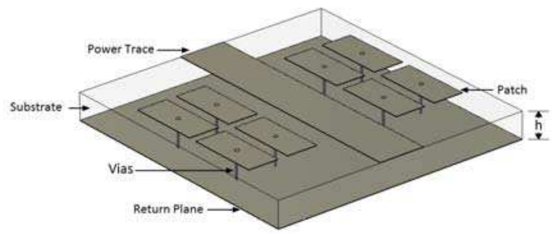

Figure 1: 3-D view of the proposed bandstop EBG filter.

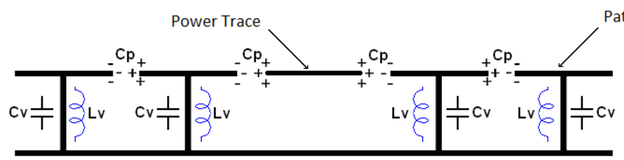

Figure 2: EBG filter cross-sectional view showing the parasitic effects present in the structure.

2.2. EBG Filter Design

Figure 3(a) depicts a top view from the proposed EBG filter. The geometrical parameters of the unit cell are denoted as (a, b), d is the separation between the patches and s is the separation between the signal path and the frontal patches.

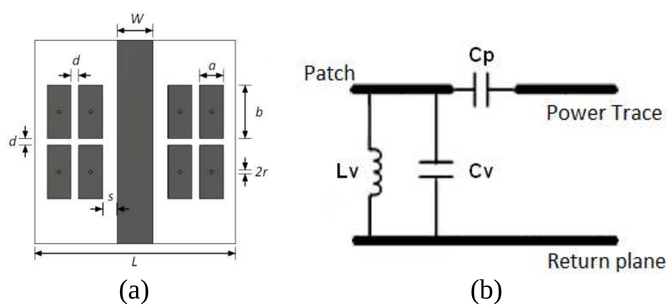

Figure 3: (a) Top view of proposed bandstop EBG filter. (b) Simplified electric equivalent circuit.

A large patch area implies an increase in the parasitic capacitance which reduces the resonant frequency. However, as mentioned above, the limiting factor lies on the maximum filter size. A low frequency filter needs bigger patch areas, which may be difficult to implement in compact electronic designs. Vias radius is another important parameter on filter design since it has considerable influence on the parasitic inductance effect. Thus, this allows the designer to manipulate easily the filter's resonant frequency. So if it is necessary to work on low operation frequencies, the vias diameter would have to be quite small. In order to quantify the LC parasitic effects present in the structure and predict the center frequency of the rejection band, Figure 3(b) shows a simplified equivalent circuit model where the circuit elements can be calculated by:

$$Cp = \varepsilon_0 \varepsilon_r \frac{a \cdot t}{s} \tag{1}$$

$$Cv = \varepsilon_0 \varepsilon_r \frac{a \cdot b}{h} \tag{2}$$

$$Lv = \mu_0 \frac{h}{2\pi} \left[\ln \frac{2h}{r} + \alpha \right] \tag{3}$$

where the constant α can be determined empirically using simulation results [15]. The filter's resonant frequency is given by

$$f_0 = \frac{1}{2\pi\sqrt{Lv\,(Cp + Cv)}} \tag{4}$$

The equivalent circuit model considers only the parasitic capacitive effects between the signal path and the frontal patch. The external patch effects are neglected since the capacitance between neighbor patches is very small. By simulation, we have noted that its effect is not decisive for the filter's resonant frequency. It is desirable to have a small filter size in order to implement in compact electronic designs. Therefore, a structure size of 15 mm × 15 mm was proposed. Once the filter size was defined ($L = 15$ mm), several simulations were performed varying the geometrical parameters shown in Figure 3 in order to find the lowest stop band frequency range. According to simulation results and using the Equation (4) the lower stop band frequency obtained was 8.5 GHz. To shift the stop band frequency range near to 1 GHz four 1 pF chip monolithic capacitors were placed in the front patches (near the signal path) because; in this zone the current distribution in the microstrip line is higher at high frequencies. This allowed us to increase Cp capacitance, which in turn is useful to expand the rejection bandwidth and reduce the lower cutoff frequency without increasing the structure size. The signal path (power trace) width W may have different dimensions in a real-life application; however, in this case a designed trace for 50 Ω impedance was used to have a good coupling with the measurement equipment. Figure 4 shows a top view of the EBG structure with its dimensions. The patches were defined with a rectangular shape, their dimensions were $a = 2$ mm and $b = 4$ mm with a separation $d = 0.5$ mm and a distance between the frontal patches and the signal path $s = 1$ mm. The vias radius r used was 0.127 mm, and $w = 2.8$ mm to obtain a characteristic impedance of 50 Ω. The filter was built on fiberglass substrate (equivalent to FR-4) with a relative permittivity of 4.7, with a thickness of 1.6 mm according to the IPC-4101 standard. Figure 5(a) depicts a photography of the EBG filter constructed.

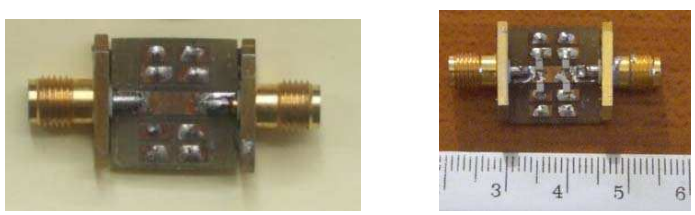

(a) (b)

Figure 4: Bandstop small size EBG filter. (a) Without capacitors. (b) With chip capacitors.

SMA connectors with a maximum operating frequency of 18 GHz were used to connect the structure with the measurement equipment. Each via was built by drilling a hole in the patch (at center) and introducing 0.127 mm gauge copper to connect all of them to the return signal path This filter was used as reference (Figure 4(a)). Then, four Murata-GRM40 1 pF ceramic chip capacitors were added to the four front patches, as shown in Figure 4(b).

3. EXPERIMENTAL AND SIMULATION RESULTS

The S_{21} parameter results, obtained by measurement and simulation, for the proposed bandstop EBG filter (used as reference) are shown in Figure 5(a) (red graph). As can be seen the lower cutoff frequency obtained was 7.7 GHz with a rejection bandwidth of 1.9 GHz. It is limited in its rejected bandwidth in comparison with other filters reported. It has a narrower rejected bandwidth and the maximum attenuation obtained was −15 dB and there is no attenuation in low frequencies. When 1 pF chip capacitors are used, a notable improvement in filter response is observed. Due to the combined effects of the capacitors and the EBG structure, both the filter rejection band and attenuation level increases. One can see that the maximum attenuation has an increase of about 30 dB in a wide frequency range, as can be seen in Figure 5(a) (blue graph).

Figure 5(b) depicts the Hybrid EBG filter response measured using a NVA from 500 MHz to 18 GHz. In Table 1 can be seen the fundamental frequency of 1.35 GHz and the attenuation levels for the next nine harmonics.

As can be seen in Table 1 is possible to attenuate the 1.35 GHz frequency and the next nine harmonics with attenuation levels above −3 dBm.

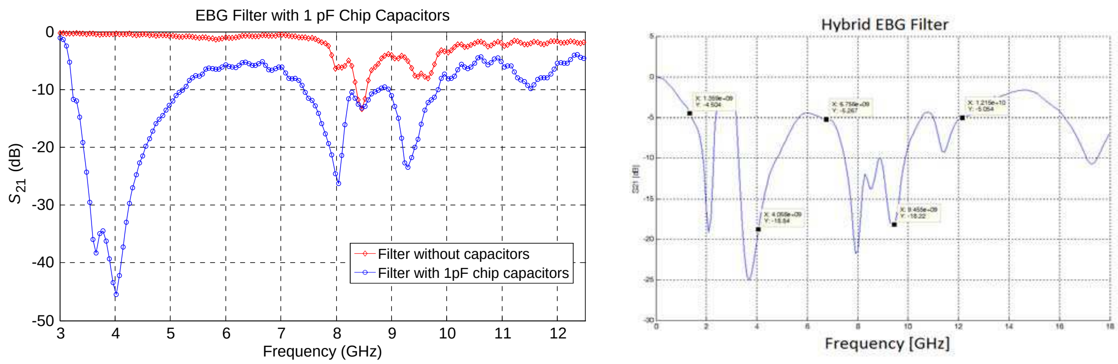

(a) (b)

Figure 5: Measurement results (a) EBG filter with and without chip capacitors and (b) EBG filter with capacitors from 500 MHz to 10 GHz.

Table 1: Cursor data point from Figure 5(b).

Frequency [GHz]	Attenuation level [dBm]	Frequency [GHz]	Attenuation level [dBm]
1.35	−4.50	9.45	−18.22
4.05	−18.84	12.1	−5.05
6.75	−5.26	-	-

4. CONCLUSION

In this article the implementation of a small size filter built in microstrip using mushroom-like EBG structures is presented. With this structure, a suppression band of 1.9 GHz with maximum attenuation of 15 dB in the resonance frequency was achieved. In addition, four 1 pF chip capacitors were added to the filter to combine the effects of the EBG structure with the effects of capacitors to increase the rejection bandwidth and reduce the lower cutoff frequency without increasing the size of the filter. By placing chip capacitors on the filter, a 9.5 GHz rejection band and a maximum attenuation of 45dB were achieved. This means a significant improvement compared to the EBG filter without capacitors. Using 1 pF chip capacitors not only allows the filter to operate from lower frequencies but also increases the attenuation in the EBG structure operating frequencies. This shows that by combining EBG structures and chip capacitors it is possible to build small-size filters with rejection bands and attenuation levels similar to those of larger structures. The main advantage of this EBG filter design is its size, which is smaller than other structures presented in previous works. Despite the size reduction, in this type of EBG structure design there is no decrease in attenuation levels and rejected bandwidth. In this way the Hybrid EBG filter with a 15mmx15mm area can cover a wide rejection bandwidth in a similar way to other bigger structures [10–13].

ACKNOWLEDGMENT

This study was carried out with the support of Secretaria de Investigacion y PosgradoInstituto Politécnico Nacional (Grant Nos. SIP20121332 and SIP10130298)

REFERENCES

1. Chen, C.-T., J. Zhao, and Q. Chen, "A simulation study of simultaneous switching noise," *2001 Electronic Components and Technology Conference*, 2001.
2. Ott, H. W., *Electromagnetic Compatibility Engineering*, John Wiley & Sons, 2009.
3. Backenius, E., M. Vesterbacka, and R. Hägglund, "Effect of simultaneous switching noise on an analog Filter," *13th IEEE International Conference on Electronics, Circuits and Systems, ICECS '06*, 898–901, 2006.
4. Hubing, T., "Effective strategies for choosing and locating printed circuit board decoupling capacitors," *2005 International Symposium on Electromagnetic Compatibility*, 632, 2005.
5. Shim, H. W., T. Zeeff, and T. H. Hubing, "Decoupling strategies for printed circuit boards without power planes," *IEEE International Symposium on Electromagnetic Compatibility, EMC 2002*, Vol. 1, 258–261, 2002.

6. Paul, C. R., *Introduction to Electromagnetic Compatibility,* 2nd Edition, John Wiley & Sons, New Jersey, 2006.
7. Sievenpiper, D. F., L. Zhang, R. F. Jimenez Broas, N. G. Alexopolous, and E. Yablonovitch, "High-impedance electromagnetic surfaces with a forbidden frequency band," *IEEE Transactions on Microwave Theory and Techniques*, Vol. 47, No. 11, 2059–2074, Nov. 1999.
8. Yang, F. and Y. Rahmat-Samii, "Electromagnetic band gap structures in antenna engineering," Chapter 6, 1–11, Cambridge University Press, New York, 2009.
9. Kamgaing, T. and O. M. Ramahi, "A novel power plane with integrated simultaneous switching noise mitigation capability using high impedance surface," *IEEE Microwave and Wireless Components Letters*, Vol. 13, No. 1, 21–23, Jan. 2003.
10. Shahparnia, S. and O. M. Ramahi, "Simultaneous switching noise mitigation in PCB using cascaded high-impedance surfaces," *Electronics Letters*, Vol. 40, No. 2, Jan. 2004.
11. Wu, T.-L., Y.-H. Lin, T.-K. Wang, C.-C. Wang, and S.-T. Chen, "Electromagnetic bandgap power/ground planes for wideband suppression of ground bounce noise and radiated emission in high-speed circuits," *IEEE Transactions on Microwave Theory and Techniques*, Vol. 53, No. 9, Sep. 2005.
12. Abhari, R. and G. V. Eleftheriades, "Metallo-dielectric electromagnetic bandgap structures for suppression and isolation of the parallel-plate noise in high-speed circuits," *IEEE Transactions on Microwave Theory and Techniques*, Vol. 51, No. 6, 1629–1639, Jun. 2003.
13. Shahparnia, S. and O. M. Ramahi, "Design, implementation, and testing of miniaturized electromagnetic bandgap structures for broadband switching noise mitigation in high-speed PCBs," *IEEE Transactions on Advanced Packaging*, Vol. 30, No. 2, 171–179, May 2007.
14. Shahparnia, S. and O. M. Ramahi, "Miniaturised electromagnetic bandgap structures for broadband switching noise suppression in PCBs," *Electronics Letters*, Vol. 41, No. 9, Apr. 2005.
15. Wang, C.-L., G.-H. Shiue, W.-D. Guo, and R.-B. Wu, "A systematic design to suppress wideband ground bounce noise in high-speed circuits by electromagnetic bandgap enhanced split powers," *IEEE Transactions on Microwave Theory and Techniques*, Vol. 54, No. 12, 4209–4217, Dec. 2006.
16. Huang, S. Y. and Y. H. Lee, "A tapered small-size EBG microstrip bandstop filter design with triple EBG structures," *Microwave and Optical Technology Letters*, Vol. 46, No. 2, 154–158, Jul. 2005.
17. Shahparnia, S. and O. M. Ramahi, "A simple and effective model for electromagnetic bandgap structures embedded in printed circuit boards," *IEEE Microwave and Wireless Components Letters*, Vol. 15, No. 10, 621–623, Oct. 2005.

Switchable Band-stop to All Pass Filter Using Stepped Impedance Resonator

A. A. Bakhit and W. P. Wong
Universiti Teknologi PETRONAS, Bandar Seri Iskandar, 31750 Tronoh, Perak, Malaysia

Abstract— The exponential growth of the modern wireless communications market creates an unprecedented demand for compact-size, low-cost, high-performance and a reconfigurable filter. Due to this recent development, much attention has been devoted to compact microwave reconfigurable filters. This paper discusses and delves into the design of novel switchable band-stop to all pass filters. This filter is realized by using a stepped impedance resonator, by incorporating the PIN diodes into the topology as switching elements. It results in two modes of operation under two conditions; in the first condition, the filter will produce a band-stop response when the PIN diodes are switched 'ON', and in the second condition, the filter will produce an all pass response when the PIN diodes are switched 'OFF'. Theoretical analysis of the approach is presented in this paper, and its feasibility has been experimentally verified with a micro-strip circuit prototype. The measured result shows that the insertion loss $S(1,2)$ in band-stop mode of an operation is around 38 dB, while the return loss $S(1,1)$ is around 27 dB. For the all-pass mode of operation, the insertion loss is totally flat at 0 dB, while the return loss is around 17 dB, making it suitable for wireless communication.

1. INTRODUCTION

As modern wireless and microwave systems progress toward spectral cognitive systems, more and more filter re-configurability will be necessary so as to enable the full potential of the system performance [1]. The first condition that must be met by a reconfigurable filter is that it must be capable of inducing microwave transmitters and receivers to be adaptable to multi-band operations using a single filter, which is highly desirable in the current wireless communication technology. Among the many techniques found in recent literature, reconfigurable filters for cognitive system prove to be a popular technique.

I. Hunter et al. in [2] posit that quite a number of microwave front ends are primarily designed with bandpass filters in order to prevent it from generating or receiving unwanted interference. The omnipresence of bandpass filters is due to the fact that most microwave systems are rendered unaware of the spectrum they are operating in, which creates a need for a fear-based front-end architecture attenuating all frequencies except the band of interest's. However, a front-end architecture based on bandpass filters results in a significant insertion loss in the frequency band of interest, which scuttle the system's performance. There is an embedded tradeoff between the given resonator quality factor (Q), bandpass's filter bandwidth, order, and the pass band insertion loss [3]. Therefore, the greater the protection from generating or receiving interference in the adjacent frequency bands, the higher the insertion loss will be in the band of interest. When it is compared to bandpass filters, the band-stop filters exhibit lower pass band insertion losses, which minimizes the degradation of the receiver's noise figure, while providing a high rejection level for removing spurious signals. Therefore, recent interest in tunable band-stop filter for cognitive system is skyrocketing [4–9]. These band-stop filters are salient in spectral-dense environment, where high power interference signal is of a primary concern.

Microwave system that is cognizant of the spectrum in which it is operating [1], would not need to operate in the fear-based mode of operation described above. In fact, it could operate without a filter if there was not any strong interference. This would greatly benefit lower insertion loss than bandpass-centric front ends.

Wide band systems [10], and systems with highly linear low-noise amplifiers (LNAs) [11] could reap the most benefit from such an interference mitigation strategy; which allows a receiver to take advantage of the benefits of a band-stop filter-centric front end, while dynamically allowing for a mode of operation that allows signals at all frequencies to be received when there are no interferences.

Until recently, different structures of micro-strip reconfigurable band-stop filters have been proposed [12–14]. These structures are innovative, however, a switchable band-stop to all pass filters suitable for the integration into a switchable, narrow band system has not been demonstrated as of yet. This paper is concerned with the design of a novel switchable band-stop to all pass filters, with new capabilities not found in previous designs.

This paper is organized as follows; Section 2 presents the theory describing the proposed prototype, while Section 3 discusses the microstrip prototype and measurements. Finally, the work is summarized in Section 4.

2. PROPOSED DESIGN METHOD

In cognitive radio spectrum utilization scheme, it is useful to switch off the band-stop filter in case no interference is present; when the filter is switched "OFF", additional channel loss introduced by the filter will be minimized and the available spectrum will be fully utilized [17].

In this work, PIN diode switches are incorporated into the miniaturized matched band-stop filter topology [16, 18] in order to realize the design of a band-stop to all pass filters. Therefore, the novel capacitive coupling structure type of filter is shown in the circuit of Figure 1. It can be seen in Figure 1(a) that the low Z sections of both left and right side have an electrical length of θ_x and a characteristic impedance of Z_2. The high Z sections of both left and right side have an electrical length of θ_y and characteristic impedance of Z_1. Moreover, the resonator is loaded with lump coupling element L, where the lump inductor is shunted at the midpoint of the transmission line section. Finally, the input and output is coupled by an inverter $K = j$.

This coupling structure provides two modes of operation under two conditions. In the first condition, the PIN diodes are switched "ON". During the "ON" state, the PIN diode behaves like a variable resistor R_s for high-frequency signal. Therefore, the new capacitive coupling structure for this mode of operation along with its generalized coupled resonator model, is displayed in Figure 2(a) and Figure 2(b) respectively. This topology is a symmetrical structure with respect to the plane AA', ensures that the resonance condition can be derived by utilizing the classical method for odd and even mode analysis.

The even and odd mode admittances of the generalized coupled resonator model shown in Figure 2(b) are derived as follows:

$$Y_{even}(p) = -j + R_s K_1^2 + \frac{K_1^2}{Y_{sub} + jK_2} \tag{1}$$

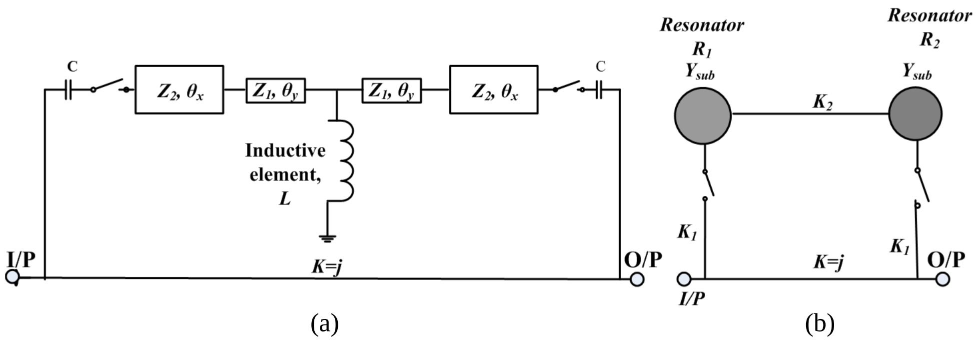

Figure 1: (a) Coupling structure of band-stop to all pass filter, (b) generalized coupled resonator model for band-stop to all pass filter.

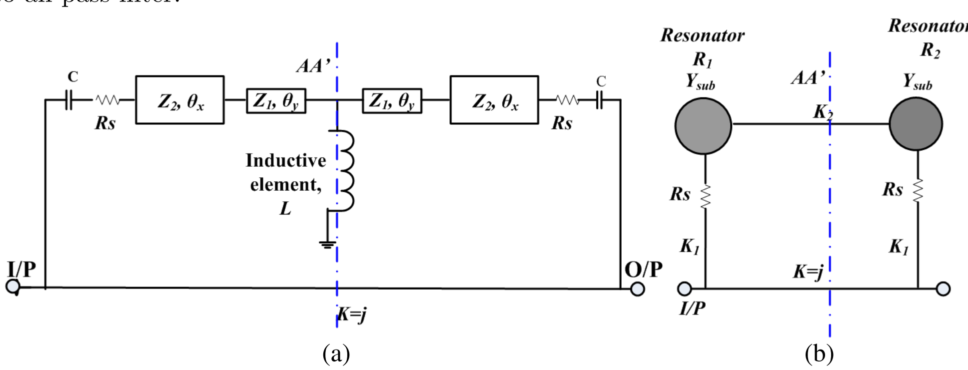

Figure 2: (a) Coupling structure of the miniaturized matched band-stop mode of operation, (b) generalized coupled resonator model for band-stop mode of operation.

and

$$Y_{odd}(p) = j + R_s K_1^2 + \frac{K_1^2}{Y_{sub} - jK_2} \tag{2}$$

The transmission and reflection function of the filter can be calculated from the derived odd and even-mode admittances and are given in [15].

$$S(1,2) = \frac{Y_{odd}(p) - Y_{even}(p)}{(1 + Y_{odd}(p))(1 + Y_{even}(p)} \tag{3}$$

$$S(1,1) = \frac{1 - Y_{odd}(p)Y_{even}(p))}{(1 + Y_{odd}(p))(1 + Y_{even}(p))} \tag{4}$$

for a perfectly matched system at resonance,

$$S(1,2)|_{\omega_0} = 0 \Rightarrow Y_{odd}(p) - Y_{even}(p) = 0 \tag{5}$$

and

$$S(1,1)|_{\omega_0} = 0 \Rightarrow Y_{odd}(p) = 1/Y_{even}(p) \tag{6}$$

The expression of K_1 and K_2 are derived from Equation (5) and Equation (6) as follows:

$$K_2 = \mp\frac{1}{2}\frac{-1 + \sqrt{1 - 4R_s^2G^2 - 4R_sG}}{R_s} \tag{7}$$

and

$$K_1 = \mp\frac{\sqrt{-K_2(2 + 4R_sG + 2R_s^2G^2 + 2R_s^2K_2^2)}}{1 + 2R_sG + R_s^2G^2 + R_s^2K_2^2} \tag{8}$$

The theoretical transmission and reflection responses of the band-stop mode of operation when $Rs = 0$ and $Rs = 0.02$ ohm are shown in Figure 3(c), and the simulation is performed with Mathlab software. When the forward resistance Rs is equal to zero; the generalized coupling resonator model shown in Figure 2(b) will have the same structure as the Generalized coupled resonator model of a matched notch filter, displayed in [18, 19], and the expression of K_1 and K_2 in Equation (7) and Equation (8) are simplified as follows:

$$K_1 = \mp\sqrt{2G} \tag{9}$$
$$K_2 = \pm(G) \tag{10}$$

It can be observed in Figure 3(c) that the insertion loss and the return loss are infinite when the forward resistance Rs approaching zero.

When the forward resistance $Rs = 0.02$ ohm, it is observed that the insertion loss is infinite and the return loss is around 80 dB in the pass band of interest, and infinite at resonance.

In the second condition, the PIN diodes are switched "*OFF*". During the "*OFF*" state, the PIN diode acts as a low capacitance C_d. So the capacitive coupling structure of this mode of operation along with its generalized coupled resonator model are displayed in Figure 3(a) and Figure 3(b). This mode of operation gives an all pass responses.

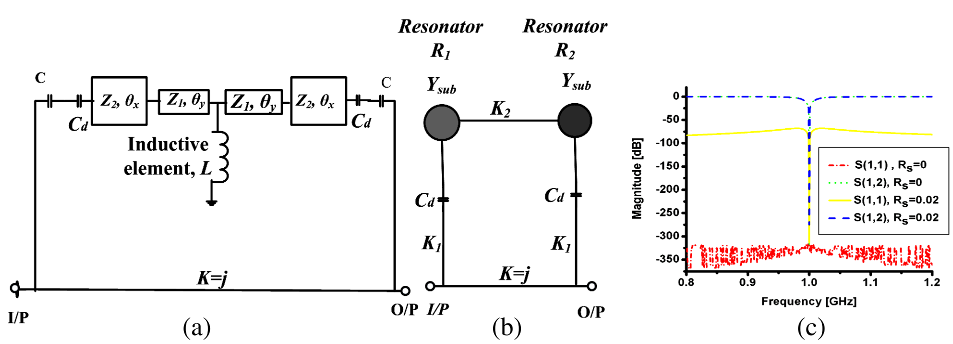

Figure 3: (a) Coupling structure for an All pass mode of operation, (b) generalized coupled resonator model for an All pass mode of operation, (c) theoretical response of band-stop mode of operation.

3. MICRO-STRIP PROTOTYPE AND MEASUREMENTS

The switchable band-stop to all pass filter was designed and fabricated on Rogers/Duroid 5880 substrate, with a dielectric constant of 2.2 and a thickness of 787 µm. The micro-strip circuit prototype is shown in Figure 4(a).

The switch elements used in this design are sky-work SMP1345 in an SC79 package. They have a frequency range of 10 MHz to 6 GHz, a low forward resistance (1.5 ohm at 10 mA), and very low capacitance (0.15 pF) in reverse bias mode. The inductive element is realized by a short circuit via a hole shunted at the mid-point of the resonator. The high-impedance quarter-wave-length transmission-line elements of 200 µm-wide (100 ohm) microstrip traces are implemented in order to provide bias to the Pin diodes, in conjunction with 1 kohm resistance, and 100 pF chip capacitors. It is worth to note that the chip capacitor packages parasitic are relatively insignificant at low frequencies, and its effects are rather negligible. The coupling between the input/output and the resonator of the proposed prototype is obtained by an interdigital capacitor available in Agilent Advanced Design System (ADS).

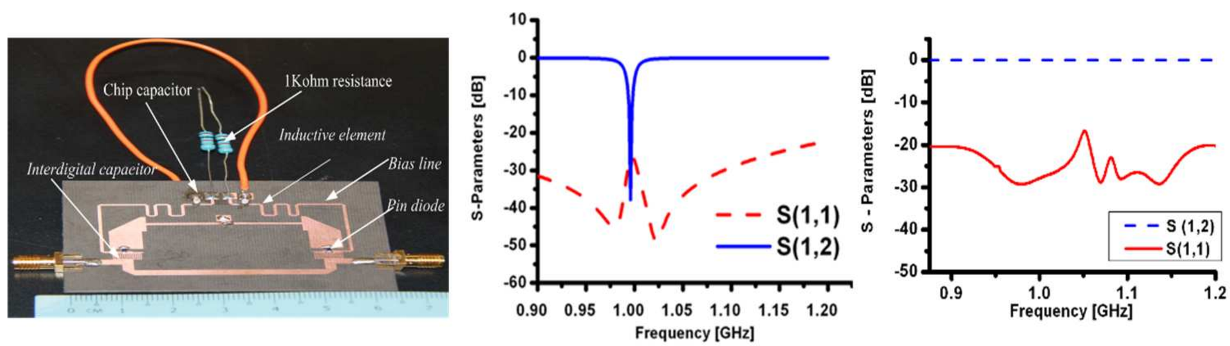

(a) (b) (c)

Figure 4: (a) Photography of switchable band-stop to all pass filter, (b) band-stop mode of operation, (c) all pass mode of operation.

3.1. Pin Diodes Are Switched "*ON*"

The operation of the filter is based on the PIN diode's "*ON*" and "*OFF*" mode. When the pin diodes are switched "*ON*", the filter produces a matched band-stop response. The diodes are turned "*ON*" when 10 V is connected to the bias line. The measured frequency responses of insertion loss $S(2,1)$ and return loss $S(1,1)$ are shown in Figure 4(b). The insertion loss is around 38 dB and the return loss is around 27 dB.

3.2. Pin Diodes Are Switched "*OFF*"

When the pin diodes are turned "OFF", the filter produces an All Pass response. The measured frequency responses of $S(2,1)$ and $S(1,1)$ magnitudes are shown in Figure 4(c). It can be seen that the transmission response is totally flat at 0 dB, and the reflection coefficient response is around -17 dB.

4. CONCLUSION

A switchable matched band-stop filter has been implemented and its hardware verified. The theoretical and measurement analysis are proven by confirming that the miniaturized matched band-stop filter permits the construction of a switchable filter via the incorporation of a tuning element into the filter's topology.

The benefits and applications of a switchable band-stop to an all-pass filter are envisioned to include general system flexibility, at no cost of physical space. In wireless communication and cognitive radio environments, these filters would be invaluable to radio systems, as it allows the receiver to take advantage of the benefits of a band-stop filter centric front end, while dynamically allowing for a mode of operation, which allows signal at all frequencies to be received in low-power environments. Potential future application includes increasing the filter's performance in tandem with an increasing power level.

REFERENCES

1. Perlman, B., J. Laskar, and K. Lim, "Fine-tuning commercial and military radio design," *IEEE Microw. Mag.*, Vol. 9, No. 4, 95–106, Aug. 2008.
2. Hunter, I., R. Ranson, A. Guyette, and A. Abunjaileh, "Microwave filter design from a systems perspective," *IEEE Microw. Mag.*, Vol. 8, No. 5, 71–77, Oct. 2007.
3. Hunter, I. C., *Theory and Design of Microwave Filters*, Chapter 4, 125–131, Inst. Electr. Eng., London, UK, 2001.
4. Jachowski, D. R. and C. Rauscher, "Frequency-agile bandstop filter with tunable attenuation," *IEEE MTT-S Int. Microw. Symp. Dig.*, 649–652, Boston, MA, Jun. 2009.
5. Naglich, E. J., J. Lee, D. Peroulis, and W. J. Chappell, "A tunable bandpass-to-bandstop reconfigurable filter with independent bandwidths and tunable response shape," *IEEE Transactions on Microwave Theory and Techniques*, Vol. 58, No. 12, 3770–3779, Dec. 2010.
6. Reines, I., S.-J. Park, and G. Rebeiz, "Compact low-loss tunable -band bandstop filter with miniature RF-MEMS switches," *IEEE Trans. Microw. Theory Tech.*, Vol. 58, No. 7, 1887–1895, Jul. 2010.
7. Yan, W. and R. Mansour, "Compact tunable bandstop filter integrated with large deected actuators," *IEEE MTT-S Int. Microw. Symp. Dig.*, 1611–1614, Jun. 2007.
8. Tsai, C., G. Qiu, H. Gao, L. Yang, G. Li, S. Nikitov, and Y. Gulyaev, "Tunable wideband microwave band-stop and bandpass filters using YIG/GGG-GaAs layer structures," *IEEE Trans. Magn.*, Vol. 41, No. 10, 3568–3570, Oct. 2005.
9. Rauscher, C., "Varactor-tuned active notch filter with low passband noise and signal distortion," *IEEE Trans. Microw. Theory Tech.*, Vol. 49, No. 8, 1431–1437, Aug. 2001.
10. Rodenbeck, C., S.-G. Kim, W.-H. Tu, M. Coutant, S. Hong, M. Li, and K. Chang, "Ultra-wideband low-cost phased-array radars," *IEEE Trans. Microw. Theory Tech.*, Vol. 53, No. 12, 3697–3703, Dec. 2005.
11. Kobayashi, K., Y. C. Chen, I. Smorchkova, R. Tsai, M. Wojtowicz, and A. Oki, "A 2 watt, sub-dB noise figure GaN MMIC LNA-PA amplifier with multi-octave bandwidth from 0.2–8 GHz," *IEEE MTT-S Int. Microw. Symp. Dig.*, 619–622, Jun. 2007.
12. Tu, W.-H., "Switchable microstrip bandpass filters with reconfigurable on-state frequency responses," *IEEE Microw. Wireless Compon. Lett.*, Vol. 20, No. 5, 259–261, May 2010.
13. Karim, M. F., A. Q. Liu, A. Alphones, and A. B. Yu, "A novel reconfigurable filter using periodic structures," *IEEE MTT-S Int. Microw. Symp. Dig.*, 943–946, San Francisco, CA, Jun. 2006.
14. Chen, Y.-M., S.-F. Chang, C.-Y. Chou, and K.-H. Liu, "A reconfigurable bandpass-bandstop filter based on varactor-loaded closed-ring resonators," *IEEE Microw. Mag.*, Vol. 10, No. 1, 138–140, Feb. 2009.
15. Hunter, I. C., *Theory and Design of Microwave Filters*, IEE, London, UK, 2001.
16. Adoum, B. A. and W. P. Wen, "Miniaturized matched band-stop filter based dual mode resonator," *National Postgraduate Conference (NPC)*, 1–3, Perak, Malaysia, Sep. 2011.
17. Wu, Z., Y. Shim, and M. Rais-Zadeh, "Switchable wide tuning range bandstop filters for frequency-agile radios," *IEEE International Electron Devices Meeting (IEDM)*, 2051–2054, Dec. 2011.
18. Bakhit, A. A. and P. W. Wong, "A novel single and dual-band miniaturized matched band-stop filter using stepped impedance resonator," *Progress In Electromagnetics Research C*, Vol. 33, 229–241, 2012.
19. Wong, P. W., I. C. Hunter, and R. D. Pollard, "Matched bandstop resonator with tunable K-inverter," *Microwave Conference*, 664–667, European, Oct. 9–12, 2007.

Effect of the Ionizing Radiation on the Harmonic and Intermodulation Performance of the CMOS Inverting Amplifier

Muhammad Taher Abuelma'atti
King Fahd University of Petroleum and Minerals, Box 203, Dhahran 31261, Saudi Arabia

Abstract— This paper presents a simple mathematical model for the transfer characteristic of the CMOS inverting amplifier. The model, basically a Fourier series, can accommodate the influence of the irradiation and can yield closed-form expressions for the amplitudes of the harmonic and intermodulation components of the output voltage resulting from a two-tone input voltage. The results show that the harmonic and intermodulation performance of the CMOS inverter is strongly dependent on the irradiation condition and the amplitudes of the input tones.

1. INTRODUCTION

Over the years researchers have observed the effect of radiation on the performance of CMOS-based inverters; see for example [1–6] and the references cited therein. It is well established that large changes in threshold voltage, current drive and transconductance of the basic MOSFET components are attributed to radiation effects. Also, it is well established that these effects will cause variation in the transfer characteristics of the un-irradiated and irradiated CMOS inverters; see for example [1–3, 5].

On the other hand, it is well known that properly biased CMOS inverters can be used as analog inverting amplifiers. However, because of the inherent nonlinear characteristic of the CMOS inverter, a two-tone input voltage would result, in output voltage comprising fundamental components, harmonics and combinations of harmonics of different frequencies that is intermodulation components. In analog circuit design it is essential to predict the harmonic and intermodulation performance of the amplifier. Obviously, by virtue of their origin, these harmonics and intermodulation products will be affected by the nonlinear characteristic of the inverter circuit. And since this nonlinear characteristic is affected by radiation effects then it is obvious that harmonic and intermodulation performance of an irradiated CMOS inverter will be different from that of an un-irradiated one. While very few attempts have been reported on the radiation effects on the intermodulation performance of GaAs MESTET amplifiers [7, 8], no attempt has been reported so far on the radiation effects on the harmonic and intermodulation performance of CMOS inverters. It is the major intention of this paper to present such a study.

2. PROPOSED MODEL

Figure 2 shows the typical irradiated and un-irradiated transfer characteristics of the CMOS inverter circuit shown in Fig. 1 [5]. It is obvious from Fig. 2 that, if properly biased in the linear region, the inverter circuit of Fig. 1 can be used as an analog amplifier with voltage gain around 20. It is also obvious that the transfer characteristic of the inverter is nonlinear. Thus, a two-tone input signal will result in output harmonics and intermodulation components. As a pre-requisite to predict the harmonic and intermodulation performance of the inverter a mathematical model is needed. Here we propose to model the un-irradiated inverter transfer characteristic of Fig. 2 by the model of Equation (1).

$$V_{out} = V_{outoffset} + \sum_{m=1}^{M} \left[a_m \cos\left(\frac{2n\pi}{D}(V_{in} - V_{inoffset})\right) + b_m \sin\left(\frac{2n\pi}{D}(V_{in} - V_{inoffset})\right)\right] \quad (1)$$

In Equation (1), $V_{inoffset}$ and $V_{outoffset}$, are the values of V_{out} and V_{in} at the threshold point and $a_m, b_m, m = 1, 2, \ldots, M$ are fitting parameters that can be obtained using the procedure described in [9]. This procedure is simple and does not require extensive computing facilities or well-developed software. For convenience, a brief description of this procedure is given here. First, the offsets of the characteristic of Fig. 1, $V_{inoffset} = 2.43\,\mathrm{V}$ and $V_{outoffset} = 2.17\,\mathrm{V}$, are removed and the resulting characteristic is mirror-imaged to produce periodic functions with a complete period $= D$.

Second, these characteristics are approximated by a number of straight-line segments joined end to end. Using the slopes of these segments, it is easy to obtain the parameters $a_m, b_m, m =$

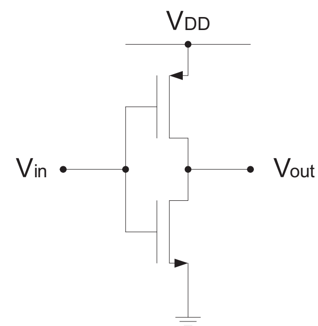

Figure 1: CMOS inverter circuit [5].

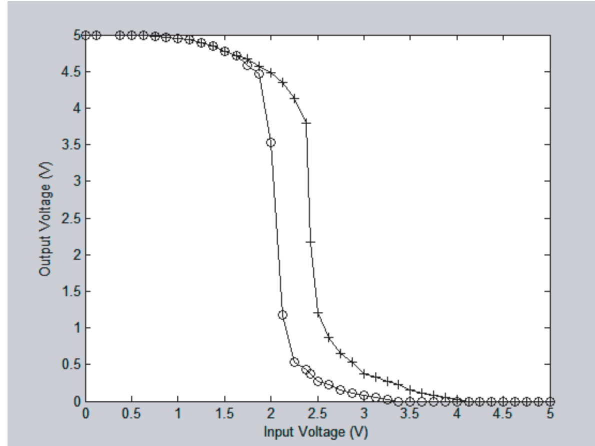

Figure 2: Transfer characteristics of the CMOS inverter of Fig. 1 [5]. +: Pre-irradiation ($D = 0$ krad (Si), ∘: Post-irradiation ($D = 500$ krad (Si).

$1, 2, \ldots, M$ using simple algebraic calculations. The results show that a very small value of the relative root-mean-square error (RRMSE) less than 0.4% can be achieved. This confirms the validity of Equation (1) for the approximating the $V_{out} = f(V_{in})$ characteristic of the un-irradiated MOSFET inverter transfer characteristic of Fig. 2.

3. HARMONIC AND INTERMODULATION PERFORMANCE

Equation (1) can be used for predicting the amplitudes of the harmonics and intermodulation components of the CMOS inverter output voltage, V_{out}, resulting from a two-tone equal-amplitude input voltage of the form

$$V_{in}(t) = V_{inbias} + V(\sin\omega_1 t + \sin\omega_2 t) \tag{2}$$

where ω_1, ω_2 and V represent the frequencies and the amplitude of the two input tones. In Equation (2) the input bias voltage, V_{inbias}, can be expressed as

$$V_{inbias} = V_{offset} + V_{inshift} \tag{3}$$

where $V_{inshift} = 0$ for the un-irradiated characteristic of Fig. 1 and $V_{inshift} \neq 0$ for the irradiated characteristic and it represents the DC shift in the un-irradiated characteristic resulting from the irradiation.

Combining Equations (1)–(3) and using the trigonometric identities

$$\begin{aligned}\sin(\beta\sin\theta) &= 2\sum_{l=0}^{\infty} J_{2k+1}(\beta)\sin(2l+1)\theta\\ \cos(\beta\sin\theta) &= J_0(\beta) + 2\sum_{l=1}^{\infty} J_{2l}(\beta)\cos(2l)\theta\end{aligned}$$

where $J_l(\beta)$ is the Bessel function of order l, and after simple mathematical manipulations, it is easy to show that the amplitude of the output voltage components of frequencies ω_1 and ω_2 will be given by

$$\begin{aligned}V_{out1,0} &= 2\sum_{m=1}^{M} b_m \cos\left(\frac{2m\pi}{D}V_{shift}\right) J_1\left(\frac{2m\pi}{D}X\right) J_0\left(\frac{2m\pi}{D}X\right)\\ &\quad +2\sum_{m=1}^{M} a_m \sin\left(\frac{2m\pi}{D}V_{shift}\right) J_1\left(\frac{2m\pi}{D}X\right) J_0\left(\frac{2m\pi}{D}X\right)\end{aligned} \tag{4}$$

The amplitude of the third-harmonic components of frequencies $3\omega_1$ and $3\omega_2$

$$\begin{aligned} V_{out3,0} &= 2\sum_{m=1}^{M} b_m \cos\left(\frac{2m\pi}{D}V_{shift}\right) J_3\left(\frac{2m\pi}{D}X\right) J_0\left(\frac{2m\pi}{D}X\right) \\ &\quad +2\sum_{m=1}^{M} a_m \sin\left(\frac{2m\pi}{D}V_{shift}\right) J_3\left(\frac{2m\pi}{D}X\right) J_0\left(\frac{2m\pi}{D}X\right) \end{aligned} \tag{5}$$

The amplitude of the output third-order intermodulation components of frequencies $2\omega_1 - \omega_2$ and $2\omega_2 - \omega_1$ will be given by

$$\begin{aligned} V_{out2,1} &= 2\sum_{m=1}^{M} b_m \cos\left(\frac{2m\pi}{D}V_{shift}\right) J_2\left(\frac{2m\pi}{D}X\right) J_1\left(\frac{2m\pi}{D}X\right) \\ &\quad +2\sum_{m=1}^{M} a_m \sin\left(\frac{2m\pi}{D}V_{shift}\right) J_2\left(\frac{2m\pi}{D}X\right) J_1\left(\frac{2m\pi}{D}X\right) \end{aligned} \tag{6}$$

The amplitude of the second-harmonic components of frequencies $2\omega_1$ and $2\omega_2$ will be given by

$$\begin{aligned} V_{out2,0} &= 2\sum_{m=1}^{M} a_m \cos\left(\frac{2m\pi}{D}V_{shift}\right) J_2\left(\frac{2m\pi}{D}X\right) J_0\left(\frac{2m\pi}{D}X\right) \\ &\quad +2\sum_{m=1}^{M} b_m \sin\left(\frac{2m\pi}{D}V_{shift}\right) J_2\left(\frac{2m\pi}{D}X\right) J_0\left(\frac{2m\pi}{D}X\right) \end{aligned} \tag{7}$$

And the amplitude of the third-harmonic components of frequencies $3\omega_1$ and $3\omega_2$ will be given by

$$\begin{aligned} V_{out1,1} &= 2\sum_{m=1}^{M} a_m \cos\left(\frac{2m\pi}{D}V_{shift}\right) J_1\left(\frac{2m\pi}{D}X\right) J_1\left(\frac{2m\pi}{D}X\right) \\ &\quad +2\sum_{m=1}^{M} b_m \sin\left(\frac{2m\pi}{D}V_{shift}\right) J_1\left(\frac{2m\pi}{D}X\right) J_1\left(\frac{2m\pi}{D}X\right) \end{aligned} \tag{8}$$

Using Equations (4)–(8) the harmonic and intermodulation performance of the un-irradiated ($V_{shift} = 0$) and radiated ($V_{shift} = -0.38\,\mathrm{V}$) CMOS inverter of Fig. 2 was calculated and the results are shown in Figs. 3 and 4. Inspection of Figs. 3 and 4 clearly shows that the harmonic and intermodulation performances of the CMOS inverter are strongly affected by the irradiation which causes a shift in the inverter transfer function. For example, for the un-irradiated CMOS inverter characteristic of Fig. 4, the fundamental and the odd-order harmonic and intermodulation products are monotonically increasing with the amplitude of the input voltage. Moreover, it appears that the odd-order harmonic and intermodulation products are dominant with respect to the even-order components. For example, for input voltage amplitude = 1.25 V, the amplitude of the fundamental output component is 0.96 V, while the amplitudes of output the second-harmonic, third-order intermodulation, third-harmonic and second-order intermodulation components are 0.003 V, 0.27 V, 0.056 V and 0.003 V respectively. This implies that the third-order intermodulation component is about 39 dB higher than the second-order intermodulation.

However, for the irradiated CMOS inverter characteristic the variations of the output components with the input voltage amplitude follow a different pattern as shown in Fig. 3. While the fundamental output component is monotonically increasing, the second-order intermodulation and the second-harmonic components first increase with the increase of the input voltage amplitude until a maximum value reached at about 0.5 V for the second-order intermodulation and 0.25 V for the second-harmonic component. Moreover, it appears also that the second-order intermodulation is always dominant over all other components including the third-order intermodulation. This implies that the voltage shift resulting from irradiation will increase the even-symmetry of the transfer characteristic. For the sake of comparison with the performance of the un-irradiated CMOS inverter, Fig. 3 shows that for the input voltage amplitude = 1.25 V, the amplitude of the fundamental

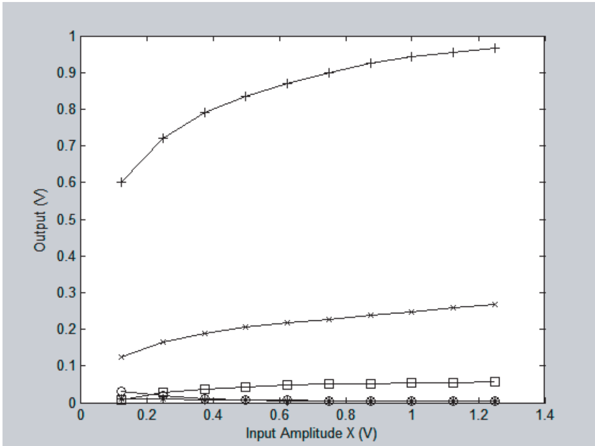

Figure 3: Fundamental, harmonic and intermodulation performance of the CMOS inverter ($D = 0\,\mathrm{krad}$ (Si)), $+$: Fundamental, $*$: Second-harmonic, $\times$: Third-order intermodulation, $\square$: Third-harmonic, $\circ$: Second-order intermodulation.

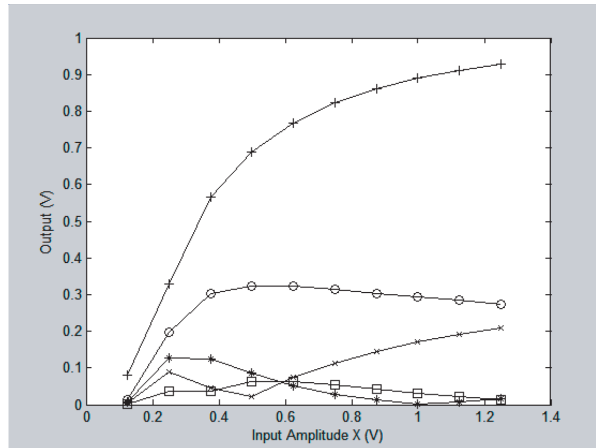

Figure 4: Fundamental, harmonic and intermodulation performance of the CMOS inverter ($D = 500\,\mathrm{krad}$ (Si)), $+$: Fundamental, $*$: Second-harmonic, $\times$: Third-order intermodulation, $\square$: Third-harmonic, $\circ$: Second-order intermodulation.

output component is 0.93 V, while the amplitudes of output the second-harmonic, third-order intermodulation, third-harmonic and second-order intermodulation components are 0.016 V, 0.21 V, 0.012 V and 0.27 V respectively. In contrast with the un-irradiated CMOS inverter performance it appears that the second-order intermodulation component is about 4 dB higher than the third-order intermodulation output component. These results clearly demonstrate the effect of irradiation on the harmonic and intermodulation performance of CMOS analog inverting amplifier.

4. CONCLUSIONS

In this paper a simple mathematical model for the transfer characteristic, $V_{out} = f(V_{in})$, of the CMOS inverting amplifier has been presented. Using this model, simple closed-form expressions were obtained for the harmonic and intermodulation performance of the CMOS inverting amplifier and excited by a multisinusoidal input voltage plus a bias voltage. Since irradiation will result in shifting the transfer characteristic, the same model can be used for predicting the influence of irradiation on the harmonic and intermodulation performance of the CMOS inverter with the shift resulting from the irradiation considered as part of the bias voltage. Using these expressions the harmonic and intermodulation performance of the CMOS inverting amplifier can be studied for any scenario of the input voltage amplitudes. The special case of a two-tone equal-amplitude input voltage was considered in detail. The results reveal that the harmonic and intermodulation performance of the CMOS inverting amplifier is strongly dependent on the irradiation conditions. Using the results reported in this paper it is possible to study the influence of irradiation on the harmonic and intermodulation performance of the CMOS inverting amplifier and to define the working dynamic range pre-specified harmonic and/or intermodulation performance. This is very essential for any potential application of the CMOS inverting amplifier in electronic circuits subjected to irradiation.

ACKNOWLEDGMENT

The author acknowledges with thanks the support of King Fahd University of Petroleum and Minerals.

REFERENCES

1. Gautam, R., M. Saxena, R. S. Gupta, and M. Gupta, "Numerical analysis of localised charges impact on static and dynamic performance of nanoscale cylindrical surrounding gate MOSFET based CMOS inverter," *Microelectronics Reliability*, 2012, htto://dx.doi.org/10.1016/j.microel.2012.08.009.
2. Estep, N. A., J. C. Petrosky, J. W. McClory, Y. Kim, and A. J. Terzuoli, Jr., "Electromagnetic interference and ionizing radiation effects on CMOS devices," *IEEE Transactions on Plasma Science*, Vol. 40, 1495–1501, 2012.

3. Dahl, K. R., "Combined effects of radio frequency and electron radiation on CMOS inverters," Thesis, Air Force Institute of Technology, 2011.
4. Barnaby, H. J., "Total-ionizing-dose effects in modern CMOS technologies," *IEEE Transactions on Nuclear Science*, Vol. 53, 3103–3121, 2006.
5. Chauhan, R. K., S. Dasgupta, and P. Chakrabarti, "Influence of ionising radiation on the performance of CMOS inverter," *Microelectronics Journal*, Vol. 32, 615–620, 2001.
6. Chen, C.-C., S.-C. Liu, C.-C. Hsiao, and J.-G. Hwu, "A circuit design for improvement of radiation hardness in CMOS digital circuits," *IEEE Transactions on Nuclear Science*, Vol. 39, 272–277, 1992.
7. Moghe, S. B., R. J. Gutmann, and J. M. Borrego, "Radiation effects on distortion characteristics of power GaAs MESFET amplifiers," *IEEE Transactions on Nuclear Science*, Vol. NS-29, 1545–1550, 1982.
8. Moghe, S. B., R. J. Gutmann, and J. M. Borrego, "Radiation effects on power GaAs MESFET amplifiers," *IEEE Transactions on Nuclear Science*, Vol. NS-29, 1010–1013, 1982.
9. Abuelma'atti, M. T., "Simple method for calculating Fourier coefficients of experimentally obtained waveforms," *Proceedings IEE-Science Measurement, Technology*, Vol. 141, 177–178, 1994.

Design Optimization of Microstrip Matching Circuits Using a Honey Bee Mating Algorithm Subject to the Transistor's Potential Performance

Peyman Mahouti, Salih Demirel, and Filiz Güneş
Department of Electronics and Communication Engineering, Yıldız Technical University Istanbul, Turkey

Abstract— In this work, the same Honey Bee Mating Optimization as in [1], this time is applied to design of the input and output microstrip matching circuits to provide the source Z_S and load Z_L terminations ensuring the selected performance quadrate to the transistor, respectively for the desired performance triplets (V_{in}, $F(f)$, G_T) [1, 2]. In this implementation, the populations of the Queen Candidates and Drones are defined in terms of the widths $\vec{W}$ and lengths $\vec{\ell}$ of the input and output microstrip matching circuits to determine the fitness values or estrogen values of the bees. Among the female bees probabilistically mating with the drones, the one with the fittest gens or estrogen level will be chosen as the Queen bee, in the other words, the best solution for optimization problem. On the other hand, the multi-objective design optimization procedure of the amplifier is reduced into the single objective design procedures of the input/output matching circuits using Darlington realizations of the quadrate Z_S, Z_L terminations. It can be concluded that in this work, all the constituents of the HBMO design optimization are defined rigorously and at the output, all the microstrip lengths and widths of the input and output matching circuits are obtained to be printed on a selected dielectric substrate. Finally as a work example the design of a typically ultra-wide band low noise amplifier with NE3512S02 is presented on a substrate of Rogers 4350 ($\varepsilon_r = 3.48$, $h = 1.524\,\mathrm{mm}$, $\tan\delta = 0.003$, $t = 0.001\,\mathrm{mm}$) within 2–5 GHz satisfying ($V_{in} = 1.5$, $F = F_{\min}(f)$, $G_T = 10\,\mathrm{dB}$) triplet using the T type of microstrip matching circuit and verified using the circuit simulator AWR.

1. INTRODUCTION

Honey Bee Mating Optimization (HBMO) is a recent swarm-based optimization algorithm to solve highly nonlinear optimization problems, in which the search algorithm is inspired by the process of honey bee mating in real life where the Queen of the colony is the most important member with the duty of giving birth to the new members of the hive by mating with a series of Drone Bees. In honey bee colonies, female bees that have the most amount of estrogen will be chosen as the Queen Bees. In open literature, HBMO is applied firstly to the optimal reservoir operation by Afshar, Haddad, Marino and Adams [3]. To the best knowledge of the authors, the HBMO algorithm is built as a simple and efficient optimization tool and applied as a first time to determine the Feasible Design Target Space (FDTS) for a front-end microwave amplifier and the resulted numerical solutions are compared with their analytical counterparts [1]. This FDTS covers all the compatible (Input VSWR $V_{inreq} \geq 1$, Noise Figure $F_{req} \geq F_{\min}(f)$, Gain $G_{Treq} \leq G_{T\max}$, Bandwidth B) quadrates and their corresponding source Z_S and Load Z_L terminations within the continuous operation (V_{DS}, I_{DS}, f) parameter domain of the microwave transistor In this work, it is aimed to find the widths and lengths of the microstrip transmission lines of matching circuits. The proposed algorithm will try to find these dimension values for T type matching circuit for input or output of a LNA design. In the next section, matching circuits design with microstrip transmission lines and Darlington theorem will be described. In the Section 3, HBMO algorithm its parameters and its cost function for our optimization problem will be presented. In the last section, an example work for the proposed algorithm is done for an ultra-wide band low noise amplifier.

2. MATCHING CIRCUIT DESIGN

In order to make an ultra-wide application design one of the most hard challenges is to design the matching circuit for the application in order to have the low return loss in input of the structure.

Matching circuits are two port structures that change the impedance value of a certain load to the impedance value of the source. Briefly, it is desired that the input impedance of the two port network is equal to the conjugate or to the value of the source impedance. The value of the input impedance can be obtained as follows:

$$Z_{in} = \frac{AZ_L + B}{CZ_L + D} \tag{1}$$

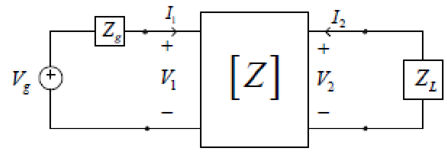

Figure 1: Schematic of a two port matching circuit.

In this work, our two port matching circuit is a T type microstrip matching circuit. The chain ($ABCD$) parameters of the T type matching circuit can be shown as follow:

$$\begin{bmatrix} 1+Z_1Y_2 & Z_3+Z_1(Y_2Z_3+1) \\ Y_2 & 1+Y_2Z_3 \end{bmatrix} \tag{2}$$

The optimization problem or the cost function for this work is the difference between the required input impedance value and the values of the T type matching network with 50 ohm termination as the source or load impedance for input or output of the LNA.

$$Cost = \sum_{i}^{m} |R_{in}(f_i) - R_{inreq}(f_i)| + |X_{in}(f_i) - X_{inreq}(f_i)| \tag{3}$$

3. HONEY BEE MATING OPTIMIZATION

As it is mentioned before HBMO is a recent swarm-based optimization algorithm to solve highly nonlinear optimization problems, in which the search algorithm is inspired by the process of honey bee mating in real life where the Queen of the colony is the most important member with the duty of giving birth to the new members of the hive by mating with a series of Drone Bees.

For our optimization problem these bees will be taken in terms of widths and lengths of a microstrip transmission line. The Queen and Drone Population are defined in terms of the optimization variables respectively as below:

$$Q_i \begin{bmatrix} w_{1Qi}, & w_{2Qi}, & w_{3Qi} \\ l_{1Qi}, & l_{2Qi}, & l_{3Qi} \end{bmatrix}_{2x3} \quad D_j = \begin{bmatrix} w_{1Dj}, & w_{2Dj}, & w_{3Dj} \\ l_{1Dj}, & l_{2Dj}, & l_{3Dj} \end{bmatrix}_{2x3} \tag{4}$$

Furthermore Genetic inheritance belonging to each Queen Qi and Drone Dj are expressed in terms of the optimization variables as follows:

$$Q_{iGen} = \begin{bmatrix} W_1, & W_2, & W_3 \\ L_1, & L_2, & L_3 \end{bmatrix}_{2x3} \tag{5}$$

$$D_{jGen} = \begin{bmatrix} W_1, & W_2, & W_3 \\ L_1, & L_2, & L_3 \end{bmatrix}_{2x3} \tag{6}$$

$$W_i = [w_i]_{m\times1} \quad L_i = [\ell_i]_{m\times1}, \quad i = 1,2,3 \tag{7}$$

$m = 5000$ for Queens and $m = 100$ for each Drone bee as the predefined parameters.

The Queen bee and the Drones will take mating flights just as like in [2] in order to create a genetic pool for next generations. The created genetic pool can be simply described as follow:

$$GP = \begin{bmatrix} W_{1GP}, & W_{2GP}, & W_{3GP} \\ L_{1GP}, & L_{2GP}, & L_{3GP} \end{bmatrix}_{2x3} \tag{8}$$

$$W_{iGP} = [w_i]_{m\times1} \quad L_{iGP} = [\ell_i]_{m\times1} \quad i = 1,2,3 \tag{9}$$

$m = 1000+100\,N_{Drs}$ and $N_{Drs} \leq N_{Drone}$ is the number of the drones each of which had a successful mating flight with the Master Queen Bee.

In the proposed HBMO algorithm, gender of all new born members of the colony will be assumed as female, thus each solution can be considered as a potential Master Queen Bee candidate.

$$Egg\_population = [Egg_1\, Egg_2 \ldots Egg_{N_{Egg}}] \quad Egg_i = \begin{bmatrix} w_{1Egg_i}, & w_{2Egg_i}, & w_{3Egg_i} \\ \ell_{1Egg_i}, & \ell_{2Egg_i}, & \ell_{3Egg_i} \end{bmatrix}_{2x3} \tag{10}$$

$i = 1, \ldots, N_{egg}$, which is generated by random selection by crossing over among the corresponding elements of the genetic pool.

In the next step, the cost value of each egg will be calculated according to Eq. (3), and the best member of the Bee colony will be taken as the final solution just like it is done in [2]. In the next section, a worked example for our proposed algorithm has been done and its success rate is conformed in AWR.

4. WORKED EXAMPLE

In this section of the work, NE3512S02 had been used as a high technology transistor for our ultra-wide band low noise amplifier. In Figure 2 the designed LNA structure with its microstrip matching circuits are shown. The matching circuits are designed in order to satisfied the required impedance values for $V_{in} = 1.5$, $F = F_{\min}(f)$ and $G_T = 10\,\mathrm{dB}$ for 3–5 GHz bandwidth.

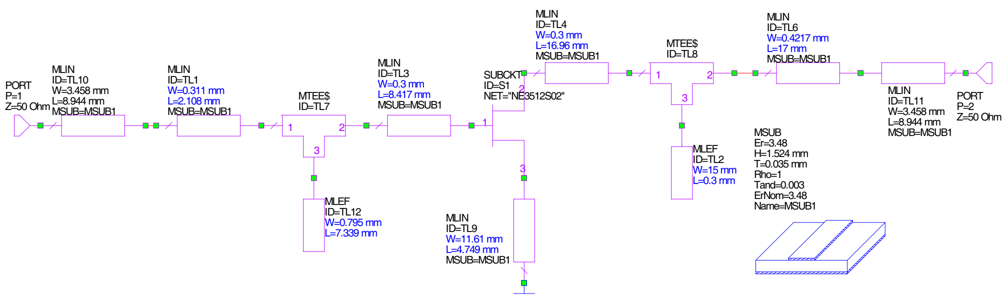

Figure 2: Schematic of the designed microstrip LNA.

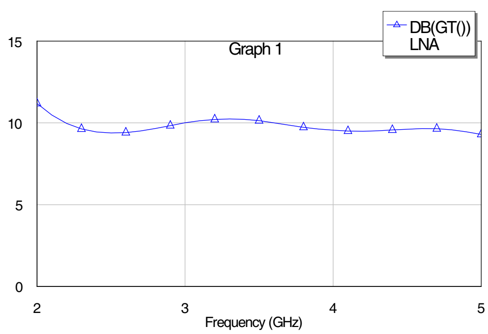

Figure 3: G_T results of the designed microstrip LNA.

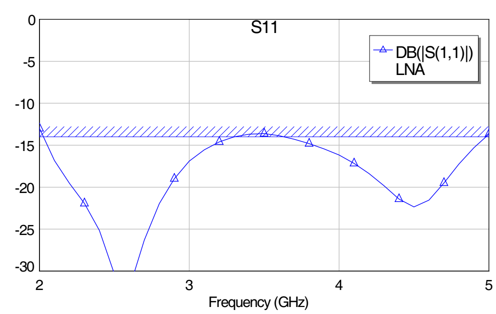

Figure 4: Return loss results of the designed microstrip LNA.

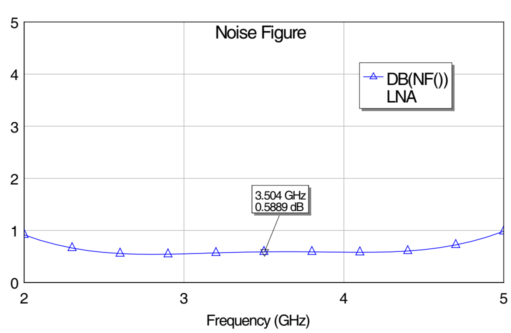

Figure 5: Noise results of the designed microstrip LNA.

As it is seen in previous figures, the proposed algorithm is an effective and successful algorithm for our designed problem. By simply giving the required impedance values for the input and output of the transistor for $V_{in} = 1.5$, $F = F_{\min}(f)$ and $G_T = 10\,\mathrm{dB}$ for 3–5 GHz the algorithm can easily make the design with microstrip transmission lines.

REFERENCES

1. Mahouti, P., F. Güneş, and S. Demirel, "Honey-bees mating algorithm applied to feasible design target space for a wide-band front-end amplifier," *2012 IEEE International Conference on Ultra-wideband*, 251–255, 2012.
2. Güneş, F., M. Güneş, and M. M. Fidan, "Performance characterisation of a microwave transistor," *IEE Proceedings — Circuits, Devices and Systems*, Vol. 141, No. 5, 337–344, 1994.
3. Afshar, A., O. B. Haddad, M. A. Marino, and B. J. Adams, "Honey — Bee mating optimization (HBMO) algorithm for optimal reservoir operation," *Journal of the Franklin Institute*, Vol. 344, 452–462, 2007.

Electromagnetic Information Delivery as a New Perspsctive in Medicine

Alberto Foletti[1,2], **Settimio Grimaldi**[2], **Mario Ledda**[2], **and Antonella Lisi**[2]

[1]Department of Innovative Technologies
University of Applied Sciences of Southern Switzerland-SUPSI, Galleria, Manno 2,6928, Switzerland
[2]Institute of Translational Pharmacology, National Research Council-CNR
Via Fosso del Cavaliere, 100, Rome 00133, Italy

Abstract— Since the time of Hyppocrates it is very well known that is possible to transfer biochemical information for the treatment of human diseases by using molecules as active principle.

This strategy has been the most efficient one until the time of Becker and Fröhlich when we become aware that it was also possible transfer effective information to biological target by the use of electromagnetic field in the ELF range. Later on Benveniste suggested that for every chemical molecule there is only and only one electromagnetic image a kind of electromagnetic signature. Benveniste and coworkers demonstrated that picking up the physical signals of a chemical compound and transferring it to an aqueous system by mean of an electronic device this procedure was mimicking the same effect of the chemical source molecule. The transfer of the physical activity is probably mediated and can be amplified by water biophysical re-patterning. Electromagnetic Information Transfer of Specific Molecular Signals according to previous report and ours was performed in order to understand the possible role of water in mediating the electro-magnetic information transfer of biological active molecules such as retinoic acid (RA). The electromagnetic information signals from the retinoic acid solution (RA-EMIT) was captured and transferred to the target by a commercially available oscillator (Vega Select 719). The retinoic acid signals was transferred to a cell culture medium (RPMI). Neuroblastoma Cell Line (LAN-5) was seeded and grown up for four days in presence of Retinoic Acid signal and/or chemical molecule. The experimental findings demonstrated that the RA signal shows the tendency to behave as a differentiating agent such as the original molecule.

1. INTRODUCTION

Aqueous system is universally assumed as the basis for any living process. Someone suggested that water could be considered as the forgotten matrix of life [1]. As a matter of fact Tales of Miletus was the first philosopher assuming water as the primary essence of nature. Nevertheless only recently the role of water has been reconsidered as more than a simple solvent and has been established that aqueous system could play an active role in the architecture and function of cell and tissues [2–5]. Moreover an additional role of aqueous system has been outlined in their ability of processing, storing and retrieving electro-magnetic information [6, 7].Our hypotheses is that an aqueous system, such one of those enfolded in livings, could play an additional role in modulating biological functions providing basis for processing, storing and retrieving information mediated by electro-magnetic signals mimicking the effect of a specific drug or driving a specific endogenous function.Liquid water shows many anomalies in its thermodynamics properties such as compressibility, density variation and many others. Some of these features are more evident at low temperatures but they are still present at room temperature were living systems exert their biological activities. At ambient conditions our traditional view of water is an homogeneous distribution of tetrahedral structure hydrogen bonded. In spite of this very simple description a more complex picture arise from recent report identifying inhomogeneous structures at ambient condition [8-10] that could fit the concept of coherent domains as previously described by the Italian physicist Giuliano Preparata applying the Quantum Electrodynamic Theory (QED) to the understanding

of water and of biological systems behavior [11]. According to QED liquid water can be viewed as an equilibrium between two components: coherent and incoherent ones. The coherent component is contained within spherical, so called "Coherence Domain" (CD), where all water molecules synchronously oscillate with the same phase. Coherence Domains are surrounded by the incoherent component where water molecules oscillate in random phases regardless each other. In this framework an aqueous system such one enfolded in livings could play an additional role in modulating biological functions by generating dissipative structure providing basis for processing, storing and retrieving information mediated by electro-magnetic signals [6, 7, 11, 12]. Any electro-magnetic signals, both endogenous and exogenous, when became resonant with some of the coherent domains of water can induce a dipole moments re-patterning therefore inducing these structure to oscillate coherently each other generating a new phase correlation described as a super-coherent [13]. This procedure could allows to an external pattern of electro-magnetic signals to be stored,translated and transferred by the water structure of the aqueous systems toward the biological target selectively modulating their activity. Some experimental evidence of the process defined as electro-magnetic information delivery mediated through aqueous system has accumulated in the last two decades (14–22). In order to test the hypotheses that aqueous system could be able to store and transfer specific information to a biological target we design the following "in vitro"experimental procedure.

2. MATERIAL AND METHODS

2.1. Cell Cultures

LAN-5 human neuroblastoma cells were grown in RPMI (Gibco Laboratories, Scotland) supplemented with 10% Fetal Calf Serum (Gibco Laboratories, Scotland)and antibiotics (110 IU/ml of penicillin and 0.1 mg/ml of streptomycin) at $37 \pm 0.3^\circ$C, and 5% CO_2 as carbon source and subcultured twice a week at a 1 : 5 ratio. In our paper the cells were cultured and treated for 4 days in 3 different conditions: they were grown in absence (control) and in presence of electro-magnetic signal of the Retinoic Acid (RA emmitas) and also treated with chemical Retinoic Acid (RA, 5 μM Sigma) which was used as positive control.

2.2. Transmission Apparatus

For the transmission experiments to cell's medium, the input coil was operated at room temperature and was coupled via a homemade amplifier (Gain 0.25 dB from 1 to 100 Hz maximum output voltage 20 V p-p, maximum output current 1 A, Max Power 20 W rms) to a commercial available wave generator (VEGA Select 719). Into the output (target) coil was placed the cell's culture medium. The target coil was made of 85 turns of 2 mm copper wire, 17 cm long and 9.5 cm width and fed at100mV from the wave generator. The source tube containing 5 μM RA was placed

inside the input coil. The signal from the Retinoic Acid (RA) solution in the coil was fed into the electronic amplifier, then from the electronic amplifier the signal was transferred to the wave generator. In the wave generator the electronic signal corresponding to RA was superimposed over a 7 Hz sinusoidal frequency carrier modulated at 3 kHz as previously reported [19–22]. From the wave generator then, the signal was delivered to the culture medium. During the entire experimental procedure all the electrical parameters remained constant.

2.3. Cell Medium Conditioning

Retinoic Acid, a well known chemical differentiating agent, were placed at room temperature in the input coil connected to an oscillator (Vega Select 719), while culture medium for LAN-5 neuroblastoma human cells was placed into the output coil and exposed to RA electro-magnetic signals for one hour. At the end of the exposure time the oscillator was switched off and LAN-5 neuroblastoma cells seededon petri dish, cultured using this previously conditioned medium and placed, as usual, into a cell incubator under controlled growing conditions.

2.4. Cell Growth and Mortality Analysis

For each experimental condition, cells were grown for 4 days. At day 1, 2, 3 and 4, cells were harvested with 0.1% trypsin-EDTA (Sigma), washed twice with PBS andthe total number of nucleated and viable cells was counted by Trypan Blue dye (0.4%) (Sigma) exclusion assay using a Bürkerhemocytometer chamber.

2.5. Cell Metabolic Activity Analysis

The quantification of LAN-5 metabolic activity, as an index of cellular proliferation, was performed by a colorimetric assay based on oxidation of tetrazolium salts (Cell Proliferation Reagent water soluble tetrazolium salt (WST)-1; Roche Diagnostics Basel, Switzerland). The LAN-5 cells were seeded on in 96-well plates and grown in the three different conditions (Ctr, RA and RA emittas) up to 4 days. Water soluble Tetrazolium salt (WST-1) reagent diluted to 1 : 10 was added in the medium at 1, 2, 3and 4 days and then incubated for 2 h in humidified atmosphere (378C, 5% CO_2). The quantification of LAN-5 metabolic activity was performed by absorbance measurement at 450 nm with a scanning multiwell spectrophotometer (Biotrack II; Amersham Biosciences).

3. ANALYSIS OF NEURITE OUTGROWTH

The LAN-5 cells were seeded on Petri dishes and grown for 4 days in the three different conditions. At the end of these treatments the cells were, washed in PBS, fixed in paraformaldeyde 4% in PBS for 15 min, and tested by phase contrast microscopy to observe cell morphology and to visualize the presence of neuritic structures that were counted to obtained the percentage of cells having neurite

outgrowth. Phase contrast analysis were performed using an inverted microscope(Olympus IX51, RT Slider SPOT — Diagnostic instruments) equipped with a 20X, 40X and 60X objective and with a cooled CCD camera (Spot RT Slider, Diagnostic Instruments).

4. RESULTS AND DISCUSSION

In this study, we demonstrated that the electro-magnetic signals of the Retinoic Acidmolecule can be recorded and stored by the aqueous system of the cell culture medium. Neuroblastoma cell line (LAN-5) was grown up to 4 days in standard medium (Control = CTR) or in the presence of

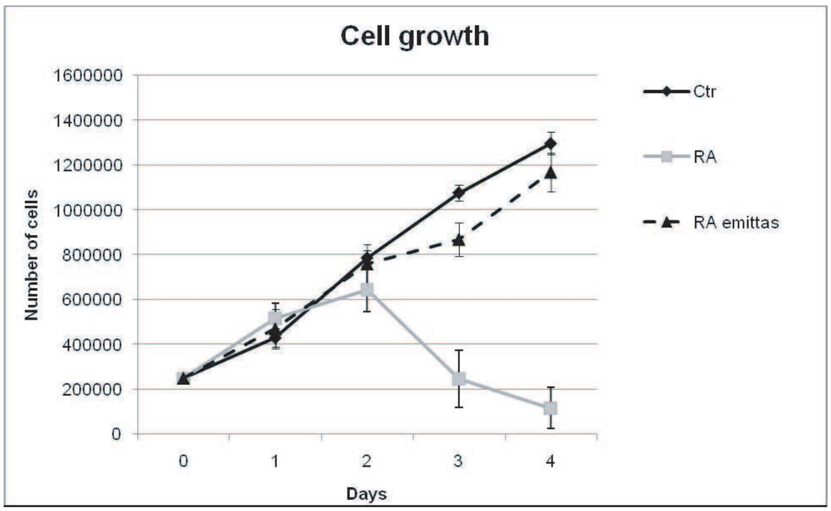

Figure 1: Cell growth analysis: $^{*}p < 0.05$.

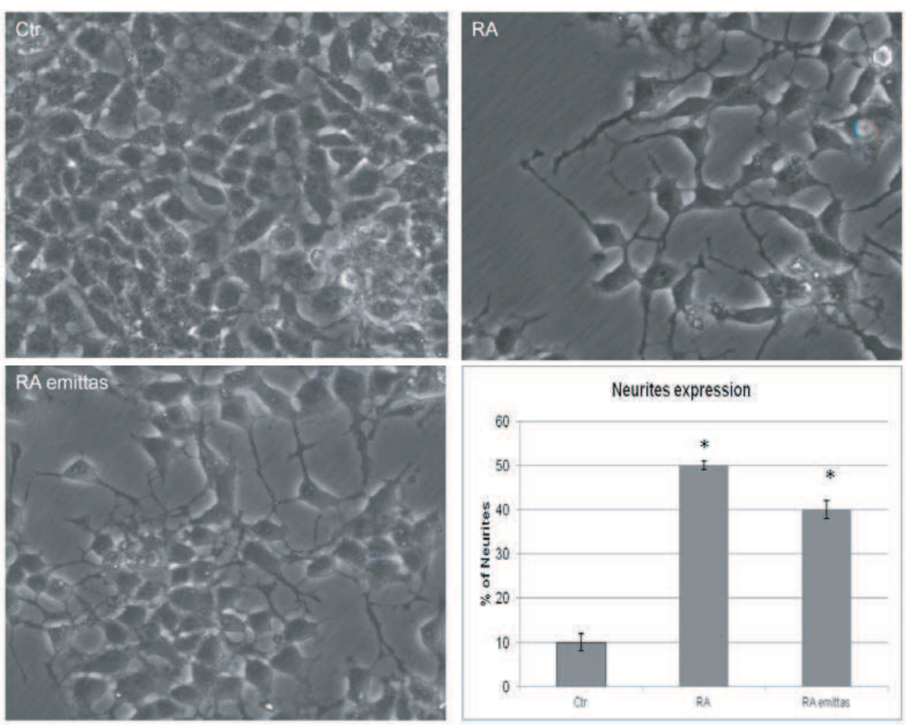

Figure 2: Analysis of neurite outgrowth expression: $^{*}p < 0.05$.

Retinoic Acid signal (RA-emittas). The treated cell with chemical Retinoic Acid molecule was also used as positive control (RA). Cell growth and mortality, analysed by direct cell count using Trypan Blue dye exclusion assay, showed that treatment with chemical Retinoic Aciddramatically decreased LAN-5 cell growth and increased cell mortality compared tocontrol one (Fig. 1). Interestingly, cells grown in presence of the electromagnetic signal of the RA (RA emmitas), showed a statistically significant decrease of cell growth, similarly to RA treatment, but no changes in cellular mortality as compared to control cells (Fig. 1). This findings demonstrate that the electromagnetic information system is able to induce the decrease of cell growth without affecting cell viability. WST-1 assay confirmed these results, also highlighting a metabolic activity reduction in the LAN-5 cells grown in the presence of electro-magnetic signals of RA (RA emmitas), compared to control ones (Fig. 3). The neurite outgrowth was also studied by phase contrast microscopy analysis and the number of neuritic structures developed by LAN-5 cells cultured in the three different conditions (Ctr, RA and RA emittas) for 4 days, was counted (Fig. 2). The control cells grew as a monolayer of confluent cells, with very few neuritic-like structures. Instead, the LAN-5 cells, treated with electromagnetic signal of RA (RA emmitas), increased the number of neuritic structures, that are typically expressed in differentiated neuronal cells. The same structures, having a well organized neuronal network, were observed in our positive control, the LAN-5 cells treated with chemical Retinoic Acid, as reported in Fig. 4. These results provide further evidence that aqueous system can be tuned in a resonant manner by an appropriate electro-magnetic information delivery procedure. These data suggest a possible future application of electro-magnetic information delivery protocols for the synergic treatment of a wide range of human diseases by means of specific informative frequency patterns, delivered through and to aqueous systems, providing an important integrative tool in clinical practice.

REFERENCES

1. Voeikov, V. L. and E. Del Giudice, "Water respiration — The basis of the living state," *Water*, Vol. 1, 52–75, 2009.
2. Szent-Gyorgyi, A., "Biology and the pathology of water," *Persp. Biol. Med.*, Vol. 14, No. 2, 239, 1971.
3. Ball, P., "Life's matrix: Water in the cell," *Cell Mol. Biol. (Noisy-le-grand)*, Vol. 47, N. 5, 717–720, 2001.
4. Ball, P., "Water and life: Seeking the solution," *Nature*, Vol. 436, No. 7054, 1084–1085, 2005.
5. Ball, P., "Water as an active constituent in cell biology," *Chem. Rev.*, Vol. 108, No. 1, 74–108, 2008.
6. Montagnier, L., J. Aissa, S. Ferris, J.-L. Montagnier, and C. Lavallée, "Electromagnetic signals are produced by aqueous nanostructures derived from bacterialDNA sequences," *Interdiscip. Sci.*, Vol. 1, No. 2, 81–90, 2009.
7. Montagnier, L., J. Aissa, E. Del Giudice, C. Lavallée, A. Tedeschi, and G. Vitello, "DNA waves and water," *J. Phys.: Conf. Ser.*, Vol. 306, 012007, 2011.
8. Bernal, J. D. and R. H. Fowler, "A theory of water and ionic solution, with particularreference to hydrogen and hydroxyl ions," *J. Chem. Phys.*, Vol. 1, No. 8, 515, 1933.
9. Huang, C., K. T. Wikfeldt, T. Tokushima, D. Nordlund, Y. Harada, U. Bergmann, M. Niebhur, T. M. Weiss, Y. Horikawa, M. Leetmaa, M. P. Ljungberg, O. Takahaschi, A. Lenz, L. Ojamäe, A. P. Lyubartsev, S. Shin, L. G. Petterson, and A. Nilsson, "The inhomogeneous structure of water at ambient conditions," *Proc. Natl. Acad. Sci.*, Vol. 106, No. 36, 15214–15218, USA, 2009.
10. Lo, S. Y., X. Geng, and D. Gann, "Evidence for the existence of stable-water-cluster atroom temperature and normal pressure," *Physics Letters A*, Vol. 373, 3872–3876, 2009.
11. Preparata, G., "QED and medicine," *Riv. Biol.*, Vol. 93, 467–512.
12. Marchettini, N., E. Del Giudice, V. Voeikov, E. Tiezzi, 2010, "Water: A medium in wheredissipative structures are produced by a coherent dynamics," *J. Theor. Biol.*, Vol. 265, No. 4, 511–516, 2000.
13. Del Giudice, E. and A. Tedeschi, "Water and autocatalysis in living matter," *Electomagn. Biol. Med.*, Vol. 28, No. 1, 46–52, 2009.
14. Endler, P. C., M. Citro, W. Pongratz, C. W. Smith, C. Vinattieri, and F. Senekowitsch, "Transfer of molecular information using a bioresonance instrument (BICOM) in amphibiantrial," *Acta Medica Empirica*, Vol. 44, No. 3, 1–16, 1995.

15. Kreisl, P., "Test on the transduction of acetic acid information via an electronicamplifier," *Acta Medica Empirica*, Vol. 47, No. 3, 17–24, 1998.
16. Thomas, Y., M. Schiff, L. Belkadi, P. Jurgens, L. Kahhak, and J. Benveniste, "Activation of human neutrophils by electronically transmitted phorbol-myristate acetate," *Medical Hypotheses*, Vol. 54, 33–39, 2000.
17. Calzoni, G. L., F. Borghini, E. Del Giudice, L. Betti, F. Dal Rio, M. Migliori, G. Trebbi, and A. Speranza, "Weak extremely high frequency microwaves affect pollen-tubeemergence and growth in kiwifruit: Pollen grain irradiation and water mediated effect," *J. Altern. Complement. Med.*, Vol. 9, No. 2, 217–218, 2003.
18. Smith, C. W., "Quanta and coherence effects in water and living systems," *J. Altern. Complement. Med.*, Vol. 10, No. 1, 69–78, 2004.
19. Foletti, A., S. Grimaldi, E. D'Emilia, M. Ledda, and A. Lisi, "Electronically transmitted (EMIT) retinoic acid (RA) signals on LAN-5 neuroblastoma cells as a possibile model of aspecific informative effect in biology," *6th International Workshop on Biological Effect of Electromagnetic Fields Proceedings*, 32–33, Bodrum, Turkey, October 10–14, 2010.
20. Heredia-Rojas, J. A., A. C. Torres-Flores, A. O. Rodriguez-De la Fuente, B. D. Mata-Cardenas, L. E. Rodriguez-Flores, M. P. Barron-Gonzales, A. C. Torres-Pantoja, G. M. Alcocer-Gonzales, "Entamoebahistolytica and Trichomonasvaginalis: Trophozoitegrowth inhibition by metronidazole electro-transferred water," *Expparasitol.*, Vol. 127, No. 1, 80–83, 2011.
21. Foletti, A., M. Ledda, E. D'Emilia, S. Grimaldi, and A. Lisi, "Differentiation of human LAN-5 neuroblastoma cells induced by extremely low frequency electronically trasmitted retinoic acid," *J. Altern. Complement. Med.*, Vol. 17, No. 8, 701–704, 2011.
22. Foletti, A., M. Ledda, E. D'Emilia, S. Grimaldi, and A. Lisi, "Eperimental finding onthe electromagnetic information transfer of specific molecular signals mediated through aqueous system on two human cellular models," *J. Altern. Complement. Med.*, Vol. 18, No. 3, 258–261, 2012.

A Novel Conformal Antenna for Ingestible Capsule Endoscopy in the MedRadio Band

Konstantinos A. Psathas, Asimina Kiourti, and Konstantina S. Nikita
Biomedical Simulations and Imaging Laboratory (BIOSIM)
School of Electrical and Computer Engineering
National Technical University of Athens
9 Iroon Polytechniou Str., Athens 15780, Greece

Abstract— In this paper, a miniature conformal antenna is proposed for ingestible capsule endoscopy in the Medical Device Radiocommunication Services (MedRadio) band (401–406 MHz). Finite Element (FE) numerical simulations are performed assuming the capsule to be surrounded by muscle tissue. The antenna resonates at 402 MHz with a wide 10 dB-bandwidth of 39.95 MHz, and exhibits nearly omni-directional radiation with a maximum far-field gain of −29.64 dB. Maximum powers of 3.83 mW and 23.35 mW may be set as input to the proposed ingestible antenna in order to guarantee compliance with the IEEE C95.1-1999 and IEEE C95.1-2005 safety standards, respectively.

1. INTRODUCTION

The last century advances in telecommunications and microelectronics have contributed a number of benefits in the field of medical applications. In the field of Ingestible Medical Devices (IMDs), significant research efforts are currently carried out, which aim to develop extremely small IMDs with wireless telemetry capabilities. IMDs may be used as diagnostic tools, monitoring devices or even drug-delivery systems, with the utmost goal being to enhance medical treatment and the patients' quality of life.

Traditional wired endoscopy methods do not allow the entire examination of the small intestine (length of 6.5–7.5 m) and offer limited diagnostic capabilities [1]. Nowadays, the development of ingestible microcapsules with imaging capabilities and embedded sensors and antennas enables non-invasive wireless capsule endoscopy (WCE), and has the potential to revolutionize wireless medical telemetry. Such endoscopy capsules are designed to send images of the gastrointestinal (GI) tract in real-time and at high data rates, thus requiring transmitting antennas with wide-bandwidth capabilities. Omni-directivity is also a pre-requisite for ingestible antennas in order to transmit signals regardless of their position and orientation which are, in principle, unknown. Given the miniature dimensions of the capsule and the limited space left after the integration of sensors, electronics and batteries [1, 2], size becomes yet another significant concern for ingestible antennas. Miniaturization becomes even more intriguing in the widely-used low-frequency band of Medical Device Radiocommunication Services (MedRadio, 401–406 MHz) [3]. In the past, several frequency bands have been utilized for ingestible antenna (e.g., ISM [4], WMTS [5] or even lower frequencies (40 MHz) [6]). However, the MedRadio band is hereafter selected because it exhibits some unique advantages: it is available worldwide and it is exclusively used for medical services, thus eliminating interferences with other applications.

In this paper, a novel conformal antenna with miniature dimensions is proposed for ingestible capsule endoscopy in the MedRadio band. The antenna exhibits a microstrip meandered structure with a shorting pin and is printed on a flexible substrate material which allows its conformance to the shape of the capsule. Antenna design and performance investigations are carried out in ANSYS HFSS Software using the Finite Element (FE) method [7].

2. NUMERICAL METHOD AND TISSUE MODEL

The FE solver performs iterative tetrahedron-meshing refinement automatically with the mesh being perturbed by 30% between each pass. The mesh refinement procedure has been set to stop when the maximum change in the reflection coefficient magnitude ($|S_{11}|$) between two consecutive passes is less than 0.02, or when the number of passes exceeds 15. The solver performs an 800 point-frequency sweep by ±100 MHz around the center frequency of 400 MHz.

Antenna design and performance investigations are performed inside a cubic homogeneous model of the human trunk (Fig. 1). The cube simulates muscle tissue properties at 402 MHz (permittivity, $\varepsilon_r = 57$, conductivity, $\sigma = 0.8$ S/m [8]), and exhibits dimensions of 100 mm × 100 mm × 100 mm. The antenna is placed in the center of the model, as shown in Fig. 1. A single-layer tissue model has been chosen because it is simple to model, and exhibits much faster computational times compared to more complex tissue models (e.g., multi-layer canonical or anatomical tissue models). Furthermore, single-layer tissue models exhibit comparable performance to more complex tissue models when it comes to antenna design, as indicated by the authors in [9, 10]. For initial studies and prototype measurements, use of a simple canonical tissue model can prove to be a reliable first-pass proof of concept.

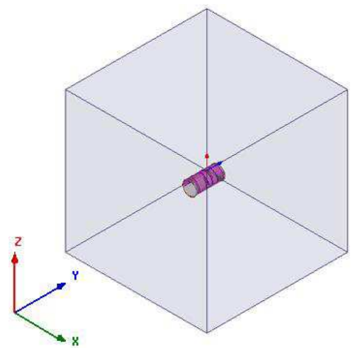

Figure 1: Single-layer canonical muscle box used to design the ingestible antenna.

3. NUMERICAL RESULTS

3.1. Antenna Design

Strict specifications are set during the antenna design process, which can be summarized as follows. Antenna miniaturization is set as the number one goal for this study. Given the fact that the antenna is intended to operate in the low-frequency MedRadio band (401–406 MHz) and that the pill size should not, in average, exceed 24 mm in length and 10 mm in thickness (e.g., 26×11 mm [5], 32.1×10 mm [11]) that goal is generally not easy to achieve. Omni-directivity of the ingestible antenna is also important in order to enhance the quality of the communication link which is formed between the ingestible capsule and exterior monitoring/control equipment. Last but not least, optimization of the antenna design has been performed bearing in mind the requirement for increased bandwidth, as imposed by the high-data rates of WCE applications and the detuning effects which might be caused by the surrounding human tissue environment.

The proposed antenna exhibits a microstrip geometry, with the patch being printed on a flexible substrate material (Rogers RT/duroid 5880, $\varepsilon_r = 2.2$) which allows its conformance to the shape of the capsule. The goal is to maximize the available space for electronics, sensors, and batteries. Low-permittivity substrate materials, like RT/Duroid 2880, help increase the bandwidth of the antenna [12]. Thickness of the substrate layer is limited to 0.127 mm for miniaturization purposes. The antenna incorporates a ground plane under the substrate, which can be used as the reference ground of all electronic devices that are integrated inside the capsule. The antenna is coated by a 0.1 mm-thick polyethylene coating ($\varepsilon_r = 2.25$, loss tangent, $\tan\delta = 0.001$), which preserves the biocompatibility of the ingestible capsule. The conformal radiating patch is of square shape, with meanders being inserted to increase the length of the current flow and decrease its size to 18 mm × 18 mm. A shorting pin connects the patch to the ground plane in order to further shrink the antenna size and assist in antenna matching. Design of the proposed antenna while wrapped around a miniature cylindrical capsule (radius of 5 mm, height of 18 mm) is shown in Fig. 2. The antenna is fed by an L-shape 50 Ohm coaxial cable (Fig. 1(a)), which has been chosen as the most feasible choice for potential future fabrication purposes.

The radiating patch of the antenna consists of seven meanders, as shown in Fig. 2(a). Length and width of the meanders are considered as optimization parameters which help achieve antenna tuning in the MedRadio band. Furthermore, length and width of the meanders help re-tune the antenna in the presence of detuning effects (e.g., variations in tissue electrical properties, presence of surrounding electronic components and batteries inside the capsule, etc.). Optimized parameter values are given in Table 1. The feeding point is located at (0 mm, 0 mm) while the shorting pin is located at (0 mm, −9.2 mm).

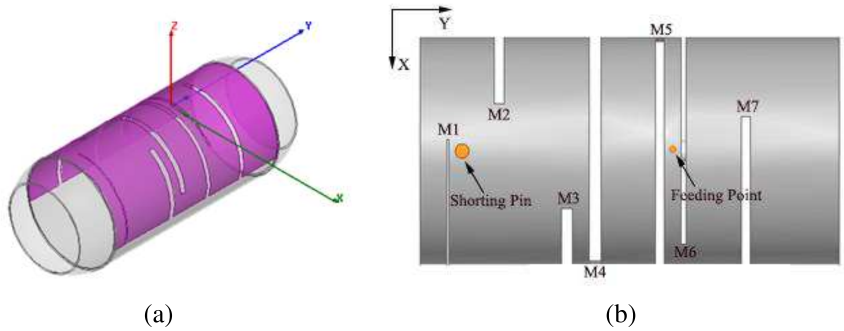

Figure 2: (a) Ingestible antenna model 3-D view. (b) Radiating patch geometry top view.

Table 1: Optimized meanders parameters to achieve antenna resonant frequency inside MedRadio band.

Values	**M1**	**M2**	**M3**	**M4**	**M5**	**M6**	**M7**
Length (mm)	9.5	6.9	6.4	16.1	17.1	13.7	10.5
Width (mm)	0.1	0.4	0.5	0.5	0.4	0.2	0.4

3.2. Antenna Performance

The reflection coefficient ($|S_{11}|$) frequency response of the proposed antenna inside the single-layer model of Fig. 1 is shown in Fig. 3(a). The antenna resonates at 402 MHz with a reflection coefficient magnitude ($|S_{11}|$) of -37.51 dB and a wide 10 dB-bandwidth of 39.95 MHz (or 9.9% of MedRadio). The radiated far-field gain radiation pattern (Fig. 3(b)) is omni-directional, and the maximum far-field gain value is found to equal -29.64 dB. Fig. 4 shows the current distribution on the radiating patch at 403 MHz. This indicates that the effective current path which is responsible for the antenna operation in the MedRadio band is the one between the feeding point and the shorting pin.

Assuming a net input power of 1 W incident to the antenna, the maximum 1-g-averaged (1-g-avg) and 10-g-averaged (10-g-avg) specific absorption rate (SAR) values are found to be equal to 417.55 and 86.65 W/kg, respectively. Therefore, in order to guarantee conformance with the IEEE C95.1-

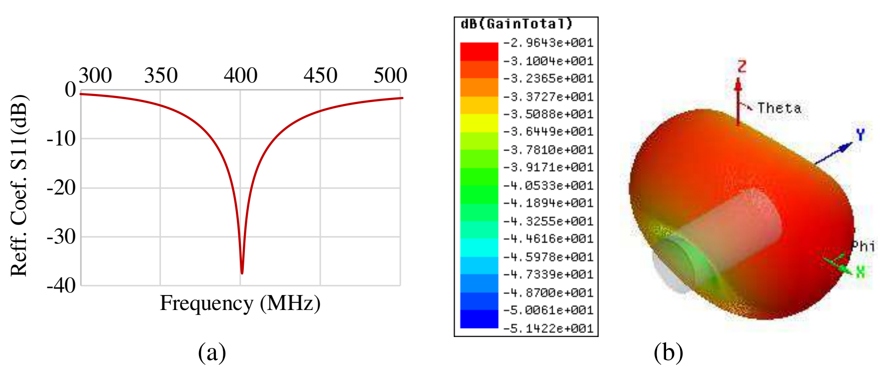

Figure 3: (a) Reflection coefficient frequency response of the proposed optimized antenna, and (b) far-field gain radiation pattern.

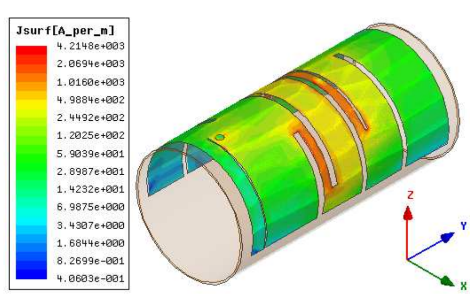

Figure 4: Surface current distribution at 403.5 MHz.

1999 (1-g-avg SAR $\leq$ 1.6 W/kg [13]) and IEEE C95.1-2005 (10-g-avg SAR $\leq$ 2 W/kg [13]) safety standards, the maximum allowed net input power has to be limited to 3.83 mW and 23.35 mW, respectively.

4. CONCLUSIONS

In this study, a novel conformal ingestible antenna was introduced for operation in the MedRadio band. Conformity of the antenna to the shape of the ingestible capsule maximizes the available space for other electronic embedded systems and batteries inside the capsule. Several techniques were applied to minimize the occupied volume of the designed antenna ($18 \times 18 \times 0.127$ mm), while still maintaining an adequate radiation and safety performance. Based on FEM simulations carried out in ANSYS HFSS, the antenna was designed to resonate at 402 MHz with a wide 10 dB bandwidth of 39.95 MHz, and exhibit a maximum far-field gain of -29.64 dB. The IEEE C95.1-1999 and IEEE C95.1-2005 standards were found to limit the maximum allowable net input power to 3.83 mW and 23.35 mW, respectively.

Future work will include the fabrication and experimental testing of a prototype antenna. The goal will be to verify agreement between simulations and measurements regarding the resonance, radiation, and safety performance of the antenna.

REFERENCES

1. Ciuti, G., A. Menciassi, and P. Dario, "Capsule endoscopy: From current achievements to open challenges," *IEEE Reviews in Biomedical Engineering*, Vol. 4, 59–72, 2011.
2. Izdebski, P. M., H. Rajagopalan, and Y. Rahmat-Samii, "Conformal ingestible capsule antenna: A novel chandelier meandered design," *IEEE Transactions on Antennas and Propagation*, Vol. 57, No. 4, 900–909, Apr. 2009.
3. Kiourti, A. and K. S. Nikita, "A review of implantable patch antennas for biomedical telemetry: Challenges and solutions," *IEEE Magazine on Antennas and Propagation*, Vol. 54, No. 3, 210–228, Jun. 2012.
4. Cheng, X., D. E. Senior, C. Kim, and Y. Yoon, "A compact omnidirectional self-packaged patch antenna with complementary split-ring resonator loading for wireless endoscope applications," *IEEE Antennas and Wireless Propagation Letters*, Vol. 10, 1532–1535, 2011.
5. Rajagopalan, H. and Y. Rahmat-Samii, "Wireless medical telemetry characterization for ingestible capsule antenna designs," *IEEE Antennas and Wireless Propagation Letters*, Vol. 11, 1679–1682, 2012.
6. Fatiha, E. H., G. Marjorie, S. Protat, and O. Picon, "Link budget of magnetic antennas for ingestible capsule at 40 MHz," *Progress In Electromagnetics Research*, Vol. 134, 111–131, 2013.
7. Ansoft High Frequency Structure Simulator (HFSS), ver. 11, Ansoft Corporation, Canonsburg, PA, USA, 2008.
8. Gabriel, S., R. W. Lau, and C. Gabriel, "The dielectric properties of biological tissues: II. Measurements in the frequency range 10 Hz to 20 GHz," *Physics in Medicine and Biology*, Vol. 41, No. 11, 2251–2269, 1996.
9. Kiourti, A. and K. S. Nikita, "Miniature scalp-implantable antennas for telemetry in the MICS and ISM bands: Design, safety considerations and link budget analysis," *IEEE Transactions on Antennas and Propagation*, Vol. 60, No. 8, 3568–3575, Aug. 2012.
10. Kiourti, A. and K. S. Nikita, "Accelerated design of optimized implantable antennas for medical telemetry," *IEEE Antennas and Wireless Propagation Letters*, Vol. 11, 1655–1658, 2012.
11. Merli, F., L. Bolomey, J. Zurcher, G. Corradini, E. Meurville, and A. K. Skriverviky, "Design, realization and measurements of a miniature antenna for implantable wireless communication systems," *IEEE Transactions on Antennas and Propagation*, Vol. 59, No. 10, 3544–3555, Oct. 2011.
12. Volakis, J., *Antenna Engineering Handbook*, 4th Edition, McGraw-Hill Companies, Incorporated, 2007.
13. "IEEE standard for safety levels with respect to human exposure to radiofrequency electromagnetic fields, 3 kHz to 300 GHz," IEEE Standard C95.1 (1999) (2005).

Impact of Electromagnetic Field Generated by Mobile Phone on Prooxidant-antioxidant Balance in Selected Internal Organs of Rats

P. Sowa[1], K. Sieron-Stoltny[2], G. Cieslar[3], and A. Sieron[3]

[1]Institute of Power System and Control, Silesian University of Technology, Poland
[2]Department of Physical Medicine, Chair of Physiotherapy
Medical University of Silesia in Katowice, Poland
[4]Department and Clinic of Internal Diseases, Angiology and Physical Medicine
Silesian Medical University, Poland

Abstract— In the study the impact of whole-body exposure to electromagnetic field with a frequency of 900 MHz generated by mobile phone on prooxidant/antioxidant balance in selected internal organs of male rats was estimated, by means of analysis of the contents of markers of membrane lipid peroxidation and oxidative stress: malone dialdehyde (MDA) and total oxidant capacity (TOC), respectively, as well as the activity of antioxidant enzymes: superoxide dismutase (SOD), catalase (CAT), glutathione peroxidase (GPx), glutathione reductase (GR) and glutathione S-transferase (GST), in homogenates of kidney, heart and lung. The experiment was performed on 20 male Wistar rats, in mean age of 10 weeks, divided into 2 equal groups (consisting of 10 animals), subjected to long-term exposure to electromagnetic field or to sham-exposure, respectively. Rats from examined group were exposed for 28 succeeding days to electromagnetic field with frequency of 900 MHz generated by mobile phone Nokia 5110, that was turned on every 1/2 hour by 8 hours daily and emitted signal for 15 s. The mean value of power density of the electromagnetic field registered during initializing of connection was $85.3\,\mu\mathrm{W/m}^2$, and during lasting connection was $17.0\,\mu\mathrm{W/m}^2$. Rats from control group were exposed for 28 succeeding days to sham-exposure, during which they stayed in identical as examined animals environmental conditions, excluding the influence of electromagnetic field. During the exposure the mobile phone was placed under a cage with animals. After the end of a cycle of 28 daily exposures to electromagnetic field or sham-exposures (control rats), animals were starved by 24 hours, then anaesthetized and next the abdominal cavity was opened and samples of kidney, heart and lung were taken. In the homogenates prepared from the obtained samples the contents of TOC and MDA, as well as the activity of SOD, CAT, GPx, GR and GST were measured. The biochemical analyses were performed by means of routine spectrophotometric and kinetic methods. As a result of repeated exposures, in electromagnetic field-exposed group of rats, in kidney tissue homogenates a significant increase in the contents of TOC, as well as a significant decrease in the activity of GR and GST was observed, in heart tissue homogenates a significant decrease in the contents of MDA and in the activity of SOD, CAT, GR and GST was found, while in lung tissue homogenates a significant increase in the contents of TOC and in the activity of GR, as well as a significant decrease in the activity of SOD and CAT was confirmed, as compared to control sham-exposed rats. On the basis of the obtained results it was found, that 4-week lasting exposure of rats to electromagnetic field with physical parameters generated by mobile phone working in a frequency range of 900 MHz, causes a slight intensification of oxidant processes in the tissue of examined internal organs with accompanying compensatory, multidirectional changes of antioxidant enzymes activity, enabling the maintenance of prooxidant/antioxidant balance only in heart tissue.

1. INTRODUCTION

In recent years people are commonly exposed to electromagnetic fields with frequency of 900–1800 MHz generated by mobile phones. Many experimental studies confirmed that electromagnetic fields with various physical parameters could intensify a generation of reactive oxygen species with subsequent disturbances of a balance between an intensity of oxidant processes and capacity of antioxidant defense system depending on the activity of antioxidant enzymes [1–6]. This toxic phenomenon called oxidative stress, results in stimulation of the process of membrane lipids peroxidation, leading in a consequence to development of apoptosis and cell death [7–11].

As in attainable literature there are lacking papers dealing with the influence of systems of mobile telecommunication on the intensity of prooxidant processes and the activity of antioxidant enzymes in tissues of internal organs of living organisms, the aim of the study was to estimate the impact of whole-body exposure to electromagnetic field with a frequency of 900 MHz generated by mobile phone on prooxidant/antioxidant balance in kidney, heart and lung of male rats, by means of analysis of the contents of markers of membrane lipid peroxidation and oxidative stress: malone dialdehyde (MDA) and total oxidant capacity (TOC), respectively, as well as the activity of antioxidant enzymes: superoxide dismutase (SOD) (EC 1.15.1.1), catalase (CAT) (EC 1.11.1.6), glutathione peroxidase (POX) (EC 1.11.1.9.), glutathione reductase (GR) (EC 1.6.4.2) and glutathione S-transferase (GST) (EC 3.1.2.7.) in homogenates of those organs.

2. MATERIAL AND METHODS

The experiment was performed on 20 male Wistar rats, in mean age of 10 weeks with mean initial body mass of 180 $\pm$ 7.5 g before the beginning of the experiment. In order to estimate the impact of electromagnetic field with frequency of 50 Hz generated between two electrodes of experimental system supplied with an alternating current rats were divided into 2 equal groups (consisting of 10 animals) subjected to long-term exposure to electromagnetic field or to sham-exposure, respectively. During the experiment the animals were kept in a special plastic cages, in optimal environmental conditions (stable humidity of air: 60% and temperature: 21°C, 12-hour light-dark cycle). They were fed with standard laboratory pellet food for rodents Labofed B and had unlimited access to drinkable water.

All procedures involving animals were carried out in accordance with the Animals Scientific Procedures Act, published by the U.S. National Institute of Health (1985) and were accepted by the Committee of Bioethics of Medical University of Silesia in Katowice (permission No. 65/2008).

During the exposure animals were placed in a special plastic cage (10 animals in one cage), that did not disturb applied electromagnetic field and allowed the possibility of free movement. Rats from examined group were exposed for 28 succeeding days to electromagnetic field with frequency of 900 MHz generated by mobile phone Nokia 5110, placed directly under the cage, that was turned on every 1/2 hour by 8 hours daily and emitted signal for 15 s. The mean value of power density of the electromagnetic field registered during initializing of connection was 85.3 $\mu W/m^2$, and during lasting connection was 17.0 $\mu W/m^2$.

Rats from control group were subjected for 28 succeeding days to sham-exposure, during which they stayed in identical as examined animals environmental conditions, excluding the influence of electromagnetic field.

After the end of a cycle of 28 daily exposures to electromagnetic field or sham-exposures (control rats), animals were starved by 24 hours and then anaesthetized with use of a mixture of *xylazine* (10 mg/kg *ip*) and *ketamine* (100 mg/kg *ip*). Next after surgical opening of chest and collecting total amount of blood from the left heart ventricle, the abdominal cavity was opened and samples of kidney, heart and lung were taken. In the homogenates prepared from the obtained samples the contents of markers of oxidative stress (TOC) and membrane lipid peroxidation (MDA), as well as the activity of selected antioxidant enzymes: SOD, CAT, POX, GR and GST were measured.

The biochemical analyses were performed by means of kinetic and spectrophotometric methods by: Ohkawa, Ohishi and Yagi [12], Erel [13], Oyanagui [14], Aebi [15], Paglia and Valentine [16], Meister and Anderson [17] and Habich [18], respectively.

3. RESULTS

The results of measurements of the contents of markers of oxidant processes and activities of antioxidant enzymes in homogenates of tissues of particular internal organs (kidney, heart and lung) in both groups of rats, with statistical analysis are presented in Tables 1–6.

In electromagnetic field-exposed group of rats in kidney tissue homogenates a significant increase in the contents of TOC, as well as a significant decrease in the activity of GR and GST was observed, as compared to control sham-exposed rats. No significant changes in the contents of MDA and in the activity of SOD, CAT and POX were noticed.

In electromagnetic field-exposed rats in heart tissue homogenates a significant decrease in the contents of MDA and in the activity of SOD, CAT, GR and GST was observed, as compared to control, sham-exposed rats. No statistically significant changes in the contents of TOC and in the activity of POX were noticed.

In electromagnetic field-exposed rats in lung homogenates a significant increase in the contents of TOC and in the activity of GR, as well as a significant decrease in the activity of SOD and CAT was observed, as compared to control, sham-exposed rats. No statistically significant changes in the contents of MDA and in the activity of POX and GST were noticed.

Table 1: The contents of markers of oxidant processes: MDA and TOC in homogenates of kidney tissue in electromagnetic field-exposed rats and in control, sham-exposed rats, with statistical analysis.

Parameter	**Electromagnetic field-exposed group of rats**	**Control sham-exposed group of rats**	**Statistical significance**
	Mean value ± SD	Mean value ± SD	
Malone dialdehyde MDA [μmol/g protein]	4.78 ± 0.93	3.45 ± 1.41	$p = 0.056$
Total Oxidant Capacity TOC [μmol/g protein]	$\mathbf{11.72 \pm 2.52}$	10.13 ± 1.82	$\boldsymbol{p < 0.001}$

Table 2: The activity of antioxidant enzymes: SOD, CAT, POX, GR and GST in homogenates of kidney tissue in electromagnetic field-exposed rats and in control, sham-exposed rats, with statistical analysis.

Parameter	**Electromagnetic field-exposed group of rats**	**Control sham-exposed group of rats**	**Statistical significance**
	Mean value ± SD	Mean value ± SD	
Superoxide dismutase SOD [NU/mg protein]	216.27 ± 24.84	217.00 ± 16.69	$p = 0.939$
Catalase CAT [kIU/g protein]	143.21 ± 16.21	141.80 ± 15.27	$p = 0.840$
Glutathione peroxidase POX [IU/g protein]	41.87 ± 5.57	40.88 ± 3.58	$p = 0.612$
Glutathione reductase GR [IU/g protein]	$\mathbf{42.42 \pm 6.70}$	92.72 ± 2.78	$\boldsymbol{p < 0.001}$
Glutatione S-transferase GST [IU/g protein]	$\mathbf{1.31 \pm 0.30}$	2.91 ± 0.27	$\boldsymbol{p < 0.001}$

Table 3: The contents of markers of oxidant processes: MDA and TOC in homogenates of heart tissue in electromagnetic field-exposed rats and in control, sham-exposed rats, with statistical analysis.

Parameter	**Electromagnetic field-exposed group of rats**	**Control sham-exposed group of rats**	**Statistical significance**
	Mean value ± SD	Mean value ± SD	
Malone dialdehyde MDA [μmol/g protein]	$\mathbf{2.82 \pm 0.53}$	4.58 ± 0.97	$\boldsymbol{p < 0.001}$
Total Oxidant Capacity TOC [μmol/g protein]	1.37 ± 0.31	1.60 ± 0.36	$p = 0.110$

Table 4: The activity of antioxidant enzymes: SOD, CAT, POX, GR and GST in homogenates of heart tissue in electromagnetic field-exposed rats and in control, sham-exposed rats, with statistical analysis.

Parameter	**Electromagnetic field-exposed group of rats**	**Control sham-exposed group of rats**	**Statistical significance**
	Mean value ± SD	Mean value ± SD	
Superoxide dismutase SOD [NU/mg protein]	**43.36 ± 3.74**	65.26 ± 7.56	$\boldsymbol{p = 0.002}$
Catalase CAT [kIU/g protein]	**39.60 ± 6.17**	62.46 ± 12.39	$\boldsymbol{p < 0.001}$
Glutathione peroxidase POX [IU/g protein]	1.27 ± 0.14	1.15 ± 0.20	$p = 0.077$
Glutathione reductase GR [IU/g protein]	**13.67 ± 0.53**	19.82 ± 1.98	$\boldsymbol{p = 0.002}$
Glutatione S-transferase GST [IU/g protein]	**0.14 ± 0.06**	0.30 ± 0.91	$\boldsymbol{p < 0.001}$

Table 5: The contents of markers of oxidant processes: MDA and TOC in homogenates of lung tissue in electromagnetic field-exposed rats and in control, sham-exposed rats, with statistical analysis.

Parameter	**Electromagnetic field-exposed group of rats**	**Control sham-exposed group of rats**	**Statistical significance**
	Mean value ± SD	Mean value ± SD	
Malone dialdehyde MDA [μmol/g protein]	1.37 ± 0.28	1.50 ± 0.29	$p = 0.370$
Total Oxidant Capacity TOC [μmol/g protein]	**9.52 ± 2.59**	4.48 ± 1.70	$\boldsymbol{p < 0.001}$

Table 6: The activity of antioxidant enzymes: SOD, CAT, POX, GR and GST in homogenates of lung tissue in electromagnetic field-exposed rats and in control, sham-exposed rats, with statistical analysis.

Parameter	**Electromagnetic field-exposed group of rats**	**Control sham-exposed group of rats**	**Statistical significance**
	Mean value ± SD	Mean value ± SD	
Superoxide dismutase SOD [NU/mg protein]	**30.67 ± 1.85**	39.39 ± 6.14	$\boldsymbol{p < 0.001}$
Catalase CAT [kIU/g protein]	**16.61 ± 2.89**	20.80 ± 3.40	$\boldsymbol{p = 0.029}$
Glutathione peroxidase POX [IU/g protein]	4.36 ± 1.13	4.50 ± 1.17	$p = 0.747$
Glutathione reductase GR [IU/g protein]	**42.65 ± 4.21**	35.40 ± 6.37	$\boldsymbol{p = 0.003}$
Glutatione S-transferase GST [IU/g protein]	2.70 ± 0.69	4.03 ± 0.91	$p = 0.222$

4. CONCLUSIONS

Long-term, 4-week lasting exposure of rats to electromagnetic field with physical parameters generated by mobile phone working in a frequency range of 900 MHz, causes a slight intensification of oxidant processes in the tissue of examined internal organs with accompanying compensatory, multidirectional changes of antioxidant enzymes activity, enabling the maintenance of prooxidant/antioxidant balance only in heart tissue.

ACKNOWLEDGMENT

This project was supported by grant No. N N511 351737 from the Polish Ministry for Science and Higher Education.

REFERENCES

1. Paluszak, J., P. Sosnowski, and K. Mikrut, "Influence of variable magnetic field on antioxidant enzymes activity in rat blood," *Acta Bio-optica et Informatica Medica,* Vol. 5, No. 1, 1–5, 1999.
2. Del Carratore, R., E. Morichetti, C. Della Croce, and G. Bronzetti, "Effect of magnetic fields on rodent monooxygenase enzymes," *Bioelectromagnetics,* Vol. 16, No. 5, 324–329, 1995.
3. Kula, B., A. Sobczak, and R. Kuska, "Effects of static and ELF magnetic fields on free radical processes in rat liver and kidney," *Electromagnetic Biology and Medicine,* Vol. 19, No. 1, 99–105, 2000.
4. Kula, B., A. Sobczak, and R. Kuska, "A study of the effects of static and extremely low frequency magnetic fields on lipid peroxidation products in subcellular fibroblast fractions," *Electromagnetic Biology and Medicine,* Vol. 21, No. 2, 161–168, 2002.
5. Cieslar, G., J. Malyszek-Tumidajewicz, P. Sowa, and A. Sieron, "Impact of static electric field on prooxidant-antioxidant balance in rats," *COMPEL,* Vol. 31, No. 4, 1212–1223, 2012.
6. Cieslar, G., J. Zalejska-Fiolka, E. Birkner, S. Kasperczyk, and A. Sieron, "Influence of long-lasting exposure to weak variable magnetic field on activity of antioxidant enzymes in rats," *Physica Medica,* Vol. 20, Suppl. 1, 25–27, 2004.
7. Itoh K., T. Ishii, N. Wakabayashi, and M. Yamamoto, "Regulatory mechanisms of cellular response to oxidative stress," *Free Radical Research,* Vol. 31, No. 4, 319–324, 1999.
8. Cadenas E. and K. Davies, "Mitochondrial free radical generation, oxidative stress and aging," *Free Radical Biology and Medicine,* Vol. 29, Nos. 3–4, 222–230, 2000.
9. Burcham P. C., "Genotoxic lipid peroxidation products: Their DNA demaging properties and role in formation of endogenous DNA adducts," *Mutagenesis,* Vol. 13, No. 3, 287–305, 1998.
10. Hisamitsu, T., K. Narita, and T. Kasahara, "Induction of apoptosis in human leucemic cells by magnetic fields," *Japan Journal of Physiology*, Vol. 47, No. 3, 307–310, 1997.
11. Wolf, F. I., A. Torsello, B., Tedesco, S. Fasanella, A. Boninsegna, M. D'Ascenzo, C. Grassi, G. B. Azzena, and A. Cittadini, "50-Hz extremely low frequency electromagnetic fields enhance cell proliferation and DNA damage: Possible involvement of a redox mechanism," *Biochimica et Biophysica Acta,* Vol. 1743, Nos. 1–2, 120–129, 2005.
12. Ohkawa, H., N. Ohishi, and K. Yagi, "Assay for peroxides in animal tissues by thiobarbituric acid reaction," *Analytical Biochemistry*, Vol. 95, No. 2, 351–358, 1979.
13. Erel, O., "A new automated colorimetric method for measuring total oxidant status," *Clinical Biochemistry,* Vol. 38, No. 12, 1103–1111, 2005.
14. Oyanagui, Y., "Evaluation of assay methods and establishment of kit for superoxide dismutase activity," *Analytical Biochemistry*, Vol. 142, No. 2, 290–296, 1984.
15. Aebi, H., "Catalase in vitro," *Methods in Enzymology,* Vol. 105, 121–126, 1984.
16. Paglia, D. and W. Valentine, "Studies on the quantities and qualitative characterization of erythrocyte glutathione peroxidase," *Journal of Laboratory and Clinical Medicine*, Vol. 70, No. 1, 158–169, 1967.
17. Meister, A. and M. E. Anderson, "Glutathione," *Annual Review of Biochemistry,* Vol. 52, 711–760, 1983.
18. Habig, W. H. and W. B. Jakoby, "Assays for differentiation of glutathione S-transferases," *Methods in Enzymology*, Vol. 77, 398–405, 1981.

Electric and Magnetic Fields Due to the Operation of Roof Mounted Photovoltaic Systems

A. S. Safigianni and A. M. Tsimtsios
Electrical and Computer Engineering Department
Democritus University of Thrace, Xanthi, Greece

Abstract— This paper investigates the electric and magnetic fields due to the operation of roof mounted photovoltaic units. In this framework, firstly, basic topological, constructional and operational data of these systems have been provided. Electric and magnetic field measurements in roof mounted photovoltaic systems having different nominal power and inverter types (single or three-phase) have been performed. The main measurement results have been evaluated according to the reference levels for safe public exposure given by international guidelines and relevant conclusions have been finally derived.

1. INTRODUCTION

Exposure to man-made electromagnetic fields has been steadily increasing during the previous century. The benefits of using electricity in everyday life and health care are unquestioned, but during the last years the scientific community as well as the general public have become increasingly concerned about potential health hazards of exposure to electric and magnetic fields (EMFs) at extremely low frequencies (ELF).

These fields have been suspected of causing or contributing to adverse health effects. Although some health effects have been statistically related to ELF EMFs exposure, these effects are poorly understood and may exist only as statistical or scientific errors. The final conclusion of the relevant work done by several expert working groups all over the world is that more research is required in order to give an accurate answer to the question "do ELF EMFs present a human health hazard?"

Nowadays, national standards as well as generally accepted guidelines define reference levels for safe public and occupational exposure to ELF EMFs. Specifically, according to the International Commission on Non-Ionizing Radiation Protection (ICNIRP) [1] guidelines, these levels for safe general public exposure and for the frequency of 50 Hz are:

- For electric field strength, $E < 5\,\mathrm{kV\ m^{-1}}$
- For magnetic flux density, $B < 200\,\mu\mathrm{T}$

The relevant levels for safe occupational exposure are:

- For electric field strength, $E < 10\,\mathrm{kV\ m^{-1}}$
- For magnetic flux density, $B < 1000\,\mu\mathrm{T}$

In Greece, during the last years a huge number of independent producer applications have been submitted and approved, concerning ground and roof mounted photovoltaic (PV) systems connected to the power distribution network. The Greek Government subsidises the production of these 'green' kWhs in order to meet the environmental constraints established by the Kyoto Protocol and other government initiatives primarily concerning fuel saving.

Various researchers have treated extensively the EMFs generated by transmission lines [2, 3], power stations and substations [4–9] of various voltage levels, domestic appliances etc.. Limited data are yet available about the fields of PV units. In particular, the authors of [10] give magnetic field measurements on an alternating current PV module with attached inverters while the authors of [11] give sound pressure level and EMF measurements at three utility-scale sites with solar PV arrays as well as at one residential PV installation but only inside the house. The measured field values in these papers are far below the safe exposure levels.

This paper investigates the EMFs due to the operation of roof mounted PV units. The close proximity of these units to houses and work places causes anxiety among people over possible health hazards from the resultant EMFs. Therefore, first of all, basic topological, constructional and operational data of these systems are provided. EMF measurements in roof mounted PV systems having different nominal power and inverter types (single or three-phase) have been performed. The main measurement results have been evaluated according to the ICNIRP guidelines. Conclusions, concerning safe public exposure to these fields have been finally derived.

2. ROOF MOUNTED PV UNITS AND EMF MEASUREMENTS

The EMF measurements were performed in PV systems mounted on the roof of three residences in the region of Xanthi, Greece which corresponds to the latitude of 41°. These residences are denoted below with the letters A, B and C. The measurements were performed on March 3rd 2013, between 10 : 30 am and 14 : 00 pm. The ambient temperature was around 12°C. The instrument used for the EMF measurements was the EFA — 3 analyser constructed by the Wandel & Goltermann Company, which is able to take field measurements at the frequency range from 5 Hz to 30 kHz. The same instrument was used in [4] where its characteristics are given in detail.

The PV unit mounted on the roof of the residence A has a nominal power of 8.05 kW, it consists of 35 polycrystalline silicon solar panels, with a nominal power of 230 W each and is connected to the distribution network via three single-phase inverters, each one equipped with an isolation transformer and located also on the roof of the residence. The PV unit of the residence B has a nominal power of 4.8 kW, it consists of 20 polycrystalline silicon solar panels with a nominal power of 240 W each and is connected to the distribution network via one single-phase inverter outside the roof. Finally, the PV unit of the residence C has a nominal power of 9.84 kW, it consists of 41 polycrystalline silicon solar panels with a nominal power of 240 W each and is connected to the distribution network via one three-phase inverter outside the roof.

The initial intention was to take magnetic field measurements every 2 m (horizontally and vertically), within the range of frequencies and for three different heights: head height (2 m), waist height (1 m) and roof surface. Indicative measurements carried out showed that the 50 Hz component is dominant making the harmonic components negligible.

The measurement process for the residence A is the following. Figure 2 shows the ground plan of the roof of the Residence A with the positions where it was scheduled to obtain EMF measurements. As shown, three additional positions (A44, A45 and A46) are identified in the inverters, for more detailed measurements, apart from the basic measurement positions (A0–A43). Table 1 shows the measured magnetic flux density values on the roof of the residence A. These values are below the reference level for safe public exposure, which is equal to 200 μT, in all the measurement positions. In most of these positions the magnetic flux density value is extremely low. Specifically, it does not exceed the value of 1 μT whilst the maximum magnetic flux density value was measured in the site of the inverters and it was equal to 118 μT. The isolation transformers of these inverters are an additional reason for the increased magnetic flux density value in this case. Only in four positions and for the height of 2 m, it was impossible to take field measurements because solar panels exist there. No serious differentiation was noted in the measured magnetic flux density values in relation to the height, as Table 1 shows. As a consequence, the only measurements performed thereafter in the residences B and C correspond to the height of 1 m. Magnetic field measurements were also performed in other places of the residence where its residents have activities, but the resulting values were negligible. During the measurement process in the residence A, the power of the PV unit was equal to 6.4 kW.

All the measured magnetic flux density values in residences B and C were far below the reference level for safe public exposure. In particular, in the residence B, the measured values at the grid positions on the roof were between 0.32 μT and 0.52 μT, whilst the maximum magnetic flux density value was measured at the inverter position, outside the roof and it was equal to 24 μT. In the

Figure 1: Photo view of the roof of the residence A.

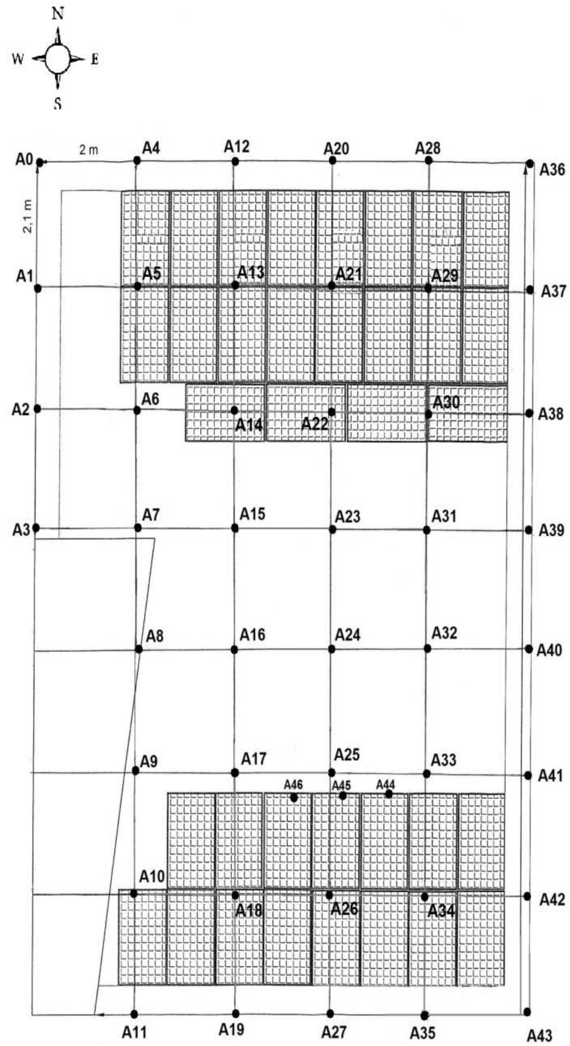

Figure 2: Ground plan of the roof of the residence A with the measurement positions.

	rms magnetic flux density values *B*, (μT)		
Measurement position	0m	1m	2m
A0	0.37	0.30	0.33
A1	0.32	0.38	0.38
A2	0.37	0.33	0.33
A3	7	0.31	0.35
A4	0.36	0.30	0.33
A5	0.36	0.36	-
A6	0.43	0.32	0.52
A7	0.35	0.37	0.38
A8	0.44	0.30	0.35
A9	0.30	0.34	0.34
A10	0.35	0.36	0.34
A11	0.35	0.36	0.34
A12	0.32	0.35	0.38
A13	0.36	0.38	-
A14	0.35	0.36	0.41
A15	0.35	0.37	0.35
A16	0.44	0.30	0.35
A17	0.40	0.32	0.34
A18	0.35	0.36	0.34
A19	0.35	0.36	0.34
A20	0.29	0.28	0.39
A21	0.37	0.32	-
A22	0.47	0.49	0.33
A23	0.43	0.39	0.41
A24	0.44	0.30	0.35
A25	0.44	4.20	1.80
A26	0.35	0.36	0.34
A27	0.35	0.36	0.34
A28	0.30	0.33	0.36
A29	0.33	0.34	-
A30	0.45	0.33	0.37
A31	0.43	0.32	0.41
A32	0.44	0.30	0.35
A33	0.35	3.50	0.45
A34	0.35	0.36	0.34
A35	0.35	0.36	0.34
A36	0.41	0.29	0.28
A37	0.37	0.31	0.30
A38	0.30	0.33	0.36
A39	0.43	0.32	0.41
A40	0.53	0.55	0.33
A41	0.64	0.66	0.38
A42	0.35	0.36	0.34
A43	0.35	0.36	0.34
A44	0.34	118	0.85
A45	0.34	113	0.85
A46	0.34	108	0.85

Table 1: Magnetic flux density values in the PV unit of the residence A.

residence C, the measured values at the grid positions on the roof were between 0.32 μT and 1.2 μT, whilst the maximum magnetic flux density value was also measured at the inverter position, outside the roof and it was equal to 12 μT. The measured magnetic flux density values in other positions inside the residences B and C were negligible. During the measurement process in residences B and C, the power of the PV units was 4.6 kW and 8.4 kW respectively.

Concerning the electric field strength measurements, the electric field sensor was placed on a tripod at the height of 1.7 m, at several measurement positions in each residence and it was connected to the main instrument with a 10 m fiber optic cable. This connection and the distance between the sensor and the main instrument were necessary in order to ensure that the electric field strength would not be perturbed by the presence of persons. In none of the residences the total number of scheduled electric field strength measurements was performed, because indicative measurements that were taken showed that the electric field strength was not differentiated significantly with the measurement position. The measured electric field strength values in all the residences were extremely lower than the reference level for safe public exposure, which is equal to 5 kV/m. Specifically, in the residence A, the entire electric field strength values were around 2 V/m, except for one point, where a cable passes and this value was equal to 28.9 V/m. In the residence B the entire measured electric field strength values were between 22 and 36 V/m. In this case, the electric field was relatively higher because a low voltage distribution network exists very close to this residence. The measured values at the inverter position were very low. In the residence C the entire measured electric field strength values were between 2.2 and 3 V/m, while at the inverter position 2 V/m were measured. Electric field measurements were also performed in other places of the residences, but the resulting values were negligible.

During the measurement process, all three examined PV units were operating close — but lower than their nominal power. However, even if the measured magnetic flux density values were extrapolated to the nominal power of the PV units, the resulting values would also remain far below the relevant reference level for safe public exposure.

3. CONCLUSIONS

In recent years, the general public and working personnel have become increasingly concerned about the health hazards of exposure to ELF EMFs. National and international guidelines have enacted reference levels for safe exposure, while researchers from different areas of expertise deal with the above-mentioned health effects.

This paper reports the results of electric and magnetic field measurements in roof mounted PV systems having different nominal power and inverter types. The measurements have been performed in order to determine whether internationally accepted reference levels for safe public exposure are violated. Both these measurements and the elaboration of the relevant results showed that the magnitudes of the measured field values are within recognized guidelines, suggesting that these fields are not dangerous and, therefore, are no cause of concern among the public.

REFERENCES

1. International Commission of Non Ionizing Radiation Protection (ICNIRP), "ICNIRP statement-guidelines for limiting exposure to time-varying electric and magnetic fields (1 Hz to 100 kHz)," *Health Physics*, Vol. 99, No. 6, 818–836, 2010.
2. Filippopoulos, G. and D. Tsanakas, "Analytical calculation of the magnetic field produced by electric power lines," *IEEE Trans. on Power Delivery,* Vol. 20, No. 2, 1474–1482, 2005.
3. Faria, J. A. and M. E. Almeida, "Accurate calculation of magnetic-field intensity due to overhead power lines with or without mitigation lops with or without capacitor compensation," *IEEE Trans. on Power Delivery*, Vol. 22, No. 2, 951–959, 2007.
4. Safigianni, A. S. and C. G. Tsompanidou, "Measurements of electric and magnetic fields due to the operation of indoor power distribution substations," *IEEE Trans. on Power Delivery*, Vol. 20, No. 3, 1800–1805, 2005.
5. Joseph, W., L. Verloock, and L. Martens, "General public exposure by ELF fields of 150-36/11-kV substations in urban environment," *IEEE Trans. on Power Delivery*, Vol. 24, No. 2, 642–649, 2009.
6. Paraskevopoulos, A. P., P. D. Bourkas, and C. G. Karagianopoulos, "Magnetic induction measurements in high voltage centers of 150/20 kV," *Measurement*, Vol. 42, No. 8, 1188–1194, 2009.
7. Safigianni, A. S. and C. G. Tsompanidou, "Electric and magnetic field measurements in an outdoor electric power substation," *IEEE Trans. on Power Delivery*, Vol. 24, No. 1, 38–42, 2009.
8. Korpinen, L., H. Kuisti, R. Pääkköen, P. Vanhala, and J. Elovaara, "Occupational exposure to electric and magnetic fields while working at switching and transforming stations of 110 kV," *Annals of Occupational Hygiene*, Vol. 55, No. 5, 526–536, 2011.
9. Safigianni, A. S., A. I. Spyridopoulos, and V. L. Kanas, "Electric and magnetic field measurements in a high voltage center," *Annals of Occupational Hygiene*, Vol 56, No. 1, 18–24, 2012.
10. Jennings, C., G. Chang, A. Reyes, and C. Whitaker, "AC photovoltaic module magnetic fields," *26th Photovoltaic Specialists Conference*, Anaheim, USA, Sept. 30–Oct. 3, 1997.
11. Guldberg, P. H., "Study of acoustic and EMF levels from solar photovoltaic projects," INCE, CCM, Tech. Environmental Inc. for Massachusetts Clean Energy Center, 2012.

Experimental Study about the Thermal Effects of EM Sources on Human Skin Tissue

A. Yasin Citkaya[1], **S. Selim Seker**[1], **and Osman Cerezci**[2]

[1]Department of Electrical-Electronics Engineering, Bogazici University
Bebek, Istanbul 34342, Turkey
[2]Department of Electrical-Electronics Engineering, Sakarya University
Esentepe, Sakarya 54187, Turkey

Abstract— Analyzing possible range of the induced thermal effects on biological tissues due to exposure with different light sources requires an extensive effort with experimental methods. This experimental study about thermal effects of light sources on living species is studied to provide reference data for scientists who utilize lighting sources in specific medical treatments and industrial applications. Subsequently, risk management policies can be established utilizing the thermal response of skin tissue and the associated health hazards.

1. INTRODUCTION

Interaction of light with tissue is widely investigated in different perspectives: physics of propagation of light through media and its biological effects to the absorbing media. However, despite the abundance of studies in literature focusing on utilizing light sources for medical treatment, there is a crucial need in literature for investigation about the negative health effects humans are exposed, so that awareness can give birth to protective limits establishment by international organizations.

Optical radiation from artificial sources is used in a wide variety of applications, including consumer, scientific, industrial and medical purposes [1]. Never though, certain exposures remain potentially hazardous and require specific attention in terms of safety standards.

Interactions of light and heat sources with biological tissues should be subject to dosimetric studies with the aim of quantification. No matter which model, either numerical or experimental, is chosen for a study, power of source and duration of exposure will obviously play the most important roles.

2. THEORETICAL BACKGROUND AND METHODOLGY

The principles used in toxicological risk assessment, are: (i) hazard identification, (ii) dose-response, and (iii) exposure [2]. On the minimum health and safety requirements, the European Parliament and the Council of European Union has published a directive (19th individual Directive within the meaning of Article 16 (1) of Directive 89/391/EEC) to specify the exposure of workers to risks arising from physical agents, in other words artificial optical radiation. This well-organized directive [3] provides both exposure determination and risk assessments, together with provisions aimed at avoiding or reducing risks.

Thermoregulation is vital process that skin is thermally responsible for through heat generation, absorption, transmission, conduction, radiation, and vaporization [4]. These crucial role of skin makes it the subject for our experimental study to inspect its thermal response under artificial light and heat sources. Since skin is an inhomogeneous organ with complex optical properties [4], comprehensive numerical study of thermal behavior in real skin tissue is rather complicated, almost impossible and multidisciplinary, this experimental study will provide valuable basis for further numerical studies in literature about thermal interaction of skin with light sources and also may widen the horizons on in-vivo experimental studies.

3. EXPERIMENTAL STUDY

Analyzing possible range of the induced thermal effects on biological tissues due to exposure with different light sources requires an extensive effort with numerical methods, since parameters of both tissue and the light sources chosen show quite variations. In order to make more and meaningful contributions with this study, different light sources from everyday usage are chosen in order to illustrate the effects of spectral variations and also the durational impact on temperature increases. The experimental setup, graphically shown in Figure 1, consists of a light source directed to live human arm, and the thermal interaction between them is monitored via a thermal camera. Distance between tissue and light source, d_1, is set to 30 cm for CFL, LED and Halogen lamps, and thermal camera is held at a distance d_2 of 80 cm for the best visual results, because of the limitation from the focus distance of camera which is 40 cm.

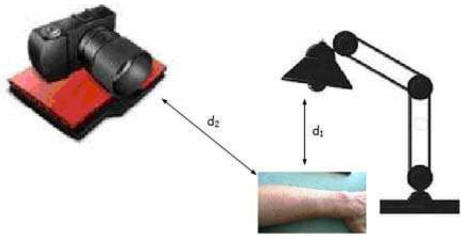

Figure 1: Graphical representation of the experimental setup.

First experiments are done with the CFL, LED and Halogen lamps, which are held at 30 cm distance from human arm. These experiments are followed with Infrared heater studies where the distance of light is increased to 50 cm and distance of thermal camera is kept constant. Nevertheless, 50 cm distance of IR lamp has a probable harmful effect on skin which cause the subject of the experiment to get burn feeling. Then distance d_1 and d_2 are increased to 100 cm and 120 cm respectively, since $d_1 = 100$ cm is officially suggested by the IR heater producer as the minimum safety distance. Next, infrared heaters with different power specifications are chosen to illustrate the results for various thermally induced human skin tissues.

4. DISCUSSION

People are exposed to various kinds of light sources in everyday life, so studying the effects of different artificial light sources will demonstrate realistic conclusions for the daily exposure; and this data can be utilized to draw conclusions on the possible health effects. To reach the ultimate goal, several experiments are conducted with different lamps and heat sources, and thermal behavior of human arm skin tissue is monitored via thermal camera, as in Figures 2 to 5.

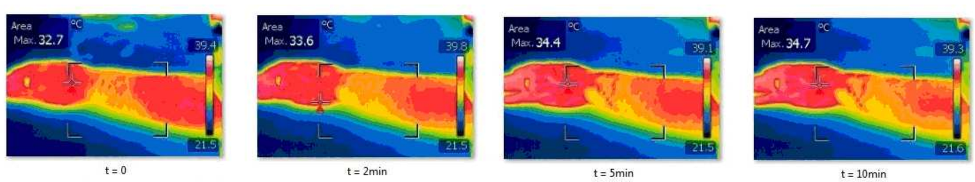

Figure 2: Thermal view of human arm exposed to 12 W LED Lamp at 30 cm distance.

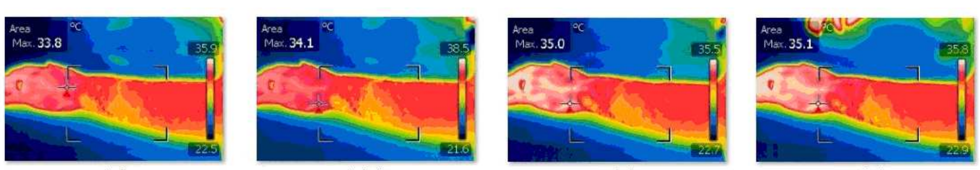

Figure 3: Thermal view of human arm exposed to 15 W CFL (Compact Fluorescent Lamp) at 30 cm distance.

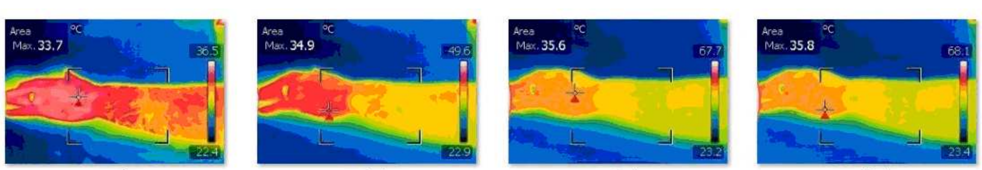

Figure 4: Thermal view of human arm exposed to 100 W Halogen Lamp at 30 cm distance.

From Figure 6, experimental results can be used to compare the thermal effects of different light sources in ambient temperature of 24°C. Initial skin temperature for the human arm, subject of

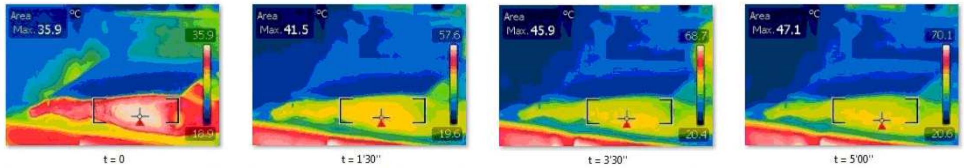

Figure 5: Thermal view of human arm exposed to 2500 W Infrared Heater at a distance of 100 cm.

experiment, is held stable around 33°C and the light sources are positioned at a 30 cm distance. Basically, as it can be expected from daily life, even the power specifications of light sources are smaller relatively than heat sources, these light sources also cause temperature increase on skin tissue. The LED lamp whose power is at the minimum level induces a 2°C increase on live skin in a 10 minutes duration.

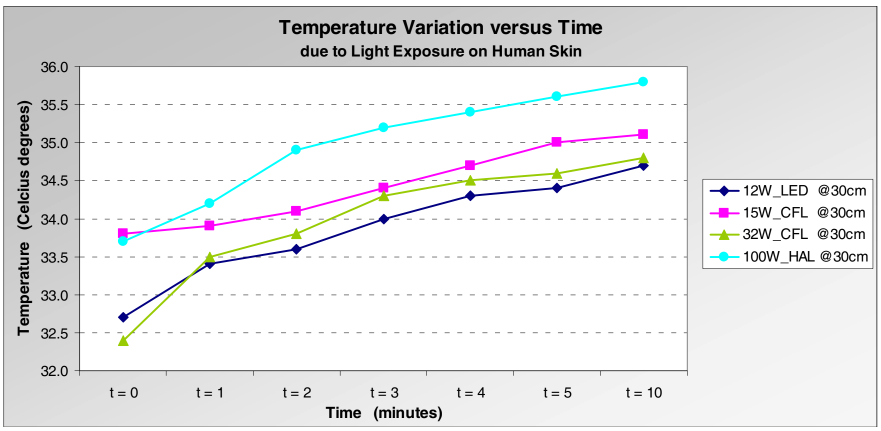

Figure 6: Maximum temperatures induced on human skin by various light sources.

When it comes to comparing the effects of different Compact Fluorescent Lamps with various power specifications, it is clearly visible that 32 W CFL causes higher temperature increase on skin than 15 W CFL. On point that needs to be explained is the fact that the reason why 15 W CFL ends up with higher skin temperature in 10 minutes than 32 W CFL is the higher initial skin temperature for the case of 15 W CFL. For the 32 W CFL experimental study, initial skin temperature is 1.4°C lower than that of 15 W CFL case, and this difference takes about 2 minutes of exposure to be catch up. Looking solely to differential temperatures in both cases, 15 W CFL causes 1.3°C whereas 32 W CFL causes 2.4°C increase. Hence, the aim of choosing two CFLs with different power values has been accomplished in such a way that as the output power of the same light source is increased, induced thermal increase on tissue shows a similar trend, where the effect of power can be clearly differentiated.

Additionally, 100 W Halogen lamp induces about 2.1°C temperature increase on skin tissue whose initial temperature is 33.5°C. Questions may arise here about the difference in experimental results from expectations on the fact that from a constant distance Halogen lamp whose output power is quite high than the CFL should cause relatively higher temperature increase on skin after same duration of exposure. Nevertheless, one should also take the effect of tissue initial temperature into consideration. For this reason, it would be better and more reasonable to compare the effects of Halogen lamp with 15 W CFL, since for both experiments initial tissue temperatures can be taken to be the same.

What is more, from Figure 6, it can be inferred that as duration of exposure is increased from 1 min, to 5 min and 10 minutes, the maximum temperature increase rate gets smaller, that is to say induced maximum temperatures will eventually reach to steady state level as a result of continuous exposure.

In the experiments, it has also been observed that some light sources caused temperature increase in the surrounding air, which has also affected the thermal induction in skin tissue. This factor is also expected and taken into account in the study, because in everyday life occupational exposure media contains surrounding air; hence there is no point in trying to configure an experimental setup which can exclude this effect.

Distance variation will illustrate obvious and expected results on thermal effects of exposure. For this purpose, one experiment is carried out at 50 cm distance between tissue and Infrared heater, whereas others with Infrared heater are carried out at 100 cm distance in accordance with the manufacturer firm's suggestions. The experiment at the 50 cm distance cannot be continued for a duration more than 1 minute, because the subject of experiment starts to get high skin burn feeling immediately. It is clear from the skin temperature obtained after 1st minute that under such a low exposure distance skin begins to get thermal damage. Consequently, minimum suggested safety distance is the most crucial specification to prevent possible health hazards. Previous experiments are done with different light sources to show the effect of variation under constant exposure distance. Then, the effect of distance is observed with Infrared heater whose output power is 2500 W. Lastly, it is now necessary to examine the effect of power variation of Infrared heat sources at a constant distance of 100 cm. Figure 7 Infrared heaters causes continuous temperature increase on human tissue whose initial temperature is held around 36°C. It can be inferred from Figure 7 that with higher power specifications of an Infrared heater, induced temperature increase rate is much higher. For instance, after first 3 minutes of exposure, 2500 W IR heater causes around 10°C increase while 1750 W IR heat source causes only about 6.5°C increase.

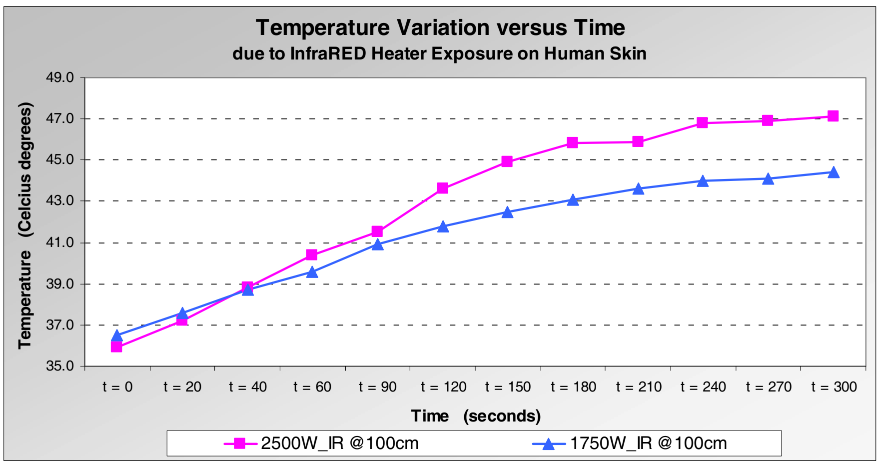

Figure 7: Maximum temperatures induced on human skin by various IR Heaters.

5. CONCLUSION

Since the primary biological effects of interaction of light with tissues are related to heat problems, over the past decades temperature prediction on biological bodies has attracted great attention. Nevertheless, in literature it is almost impossible to find a study focused on thermal effects of commonly-used artificial light and heat sources. **With the experiments made in this study, we have reached real-time data on human living tissues which are all consistent with theory and hereby can be used to compare and verify results of any further numerical methods.** From a detailed analysis of the outputs, it can be stated that at certain times the maximum temperature increase induced on the tissue can reach very high and dangerous levels. This exposure level, furthermore, can be reduced by increasing the distance between tissue and source.

ACKNOWLEDGMENT

This work is supported by Bogazici University Research Foundation Project Code: 5698.

REFERENCES

1. International Commission on Non-ionizing Radiation and Protection, "Guidelines on limits of exposure to broad-band incoherent optical radiation (0.38 to 3 μm)," *Health Physics*, Vol. 73, No. 3, 539–554, 1997.
2. Ahluwalia, G. S., *Cosmetic Applications Laser and Light-based Systems*, William Andrew, 2009.
3. "Directive 2006/25/EC of the European Parliament and of the council of 5 April 2006 on the minimum health and safety requirements regarding the exposure of workers to risks arising

from physical agents (artificial optical radiation) (19th individual directive within the meaning of article 16 (1) of directive 89/391/EEC)," *Official Journal L*, Vol. 114, 38–59, Apr. 27, 2006. http://eur-lex.europa.eu/LexUriServ/LexUriServ.do?uri=CELEX:32006L0025:EN:HTML.
4. L'Etang, A. and Z. Huang, "The effect of laser wavelength in the simulation of laser generated surface waves in human skin model," *Proceedings of the 28th IEEE EMBS Annual International Conference*, 4140–4143, New York City, USA, 2006.

Optimized Nanocage for Cancer Photothermal Therapy and Comparison with Other Nanoparticles

Sameh Kessentini and Dominique Barchiesi
Project Group for Automatic Mesh Generation and Advanced Methods
Gamma3 Project (UTT-INRIA), University of Technology of Troyes, France

Abstract— The purpose of this study is to get more efficient gold nanocages for photothermal therapy (PTT) of cancer. Therefore a numerical maximization of the absorption efficiency (generating heat) is achieved. Two therapeutic cases (using visible and infrared laser) are considered. The optimization leads to an improved absorption of the nanocages compared with previous studies. The optimized nanocages are also compared with other gold nanoparticles (nanorods, hollow nanospheres and nanoshells) and are shown to be more efficient when infrared light is used.

1. INTRODUCTION

The progress and breakthrough of nanotechnology are offering small size nanoparticles that can penetrate small cell capillaries and hence be used for drug delivery and therapeutics. An increasing number of works are showing the use of these nanoparticles for both in vitro and in vivo cancer treatment via localized heat delivery [1–3]. Such treatment is commonly known as photothermal therapy (PTT) using gold nanoparticles which is based on the interaction of a suitable light source with gold nanoparticles embedded in cells to absorb large amount of light. The absorbed energy induces (via non radiative process) a sufficient elevation of temperature leading to the cells necrosis.

The predominating benefits of PTT with gold nanoparticles conjugated to antibodies are both safety and efficiency as PTT limits the possible damage of healthy cells unlike other treatments [4]. Huang et al. [2] found that the laser energy threshold for cell death of the malignant cells using gold nanorods with aspect ratio of 3.9 ($10\,\mathrm{W/cm^2}$) is about half that needed to cause cell death of the nonmalignant cells (that start to be injured at $15\,\mathrm{W/cm^2}$ and are obviously injured at $20\,\mathrm{W/cm^2}$). Au et al. [5] showed that the damage for cancer cells (percentage of cellular damage) treated with the immuno gold nanocages increases linearly as power densities (from $1.6\,\mathrm{W/cm^2}$ to $6.4\,\mathrm{W/cm^2}$). These results suggest that nanoparticles can be used as a selective and efficient photothermal agent for cancer therapy using a low-energy laser.

The laser energy threshold for death of the malignant cells could be reduced provided that more absorbent nanoparticles are used and thus the treatment would be more selective (less damage to healthy cells). The absorption efficiency of gold nanoparticles (that characterizes their ability to absorb electromagnetic radiation) depends on their shape, size and treatment conditions (e.g., laser illumination). Therefore, maximizing the absorption of nanoparticles can be achieved by tailoring their shape and size for a given therapy.

In a previous study [6] we optimized nanorods, nanoshells and hollow nanospheres for targeted photothermal therapy cases. The optimization yielded improved results compared to those reported in other studies, and the above optimized nanoparticles are compared to each other. In this study, we complete the comparison by considering the gold nanocage [3, 5, 7]. The purpose of this study is to optimize nanocage absorption efficiency and compare it with that of other nanoparticles.

The paper is organized as follows: in the second section, the numerical methods used to compute the absorption efficiency and the optimization tool are brie y described. In the third section, the different therapeutic cases and the assumptions for simulations are presented, before carrying comparisons of optimized nanocages with the other nanoparticles. Finally, concluding remarks are given in the fourth section.

2. NUMERICAL AND OPTIMIZATION TOOLS

The discrete dipole approximation (DDA) is used to compute the absorption efficiency Q_{abs} of nanocage. Then, Q_{abs} can be maximized using an adequate optimization algorithm based on the results of the comparison between different optimization algorithms for plasmonic applications [8]. In what follows, a brief description of DDA and the algorithm used for optimization.

The DDA, firstly developed by Devoe [10, 11], is based on discretizing the geometry of the nanoparticle into a set of N elements ($j = 1 \ldots N$) with polarizabilities α_j, located at $\mathbf{r}_j$. Each dipole has a polarization $\mathbf{P}_j = \alpha_j \mathbf{E}_j$, where $\mathbf{E}_j$ is the electric field at $\mathbf{r}_j$ induced by the incident wave and the sum of the dielectric fields induced by interaction with other dipoles (see [12] for more details). The method is widely used for absorption and scattering calculations by nanoparticles used in PTT (the computing time being reduced for small size targets). Moreover, the accuracy of the method was checked by comparison with the experimentally measured SPR peak of nanocage [9]. The Fortran code DDSCAT 7.1 is used to calculate scattering and absorption of light by irregular particles based on the DDA [13]. We edit the Fotran code to present nanocage shape. Then, to discretize the target an inter-dipole distance of 1 nm as this distance was shown to yield accurate results compared to Mie theory [6, Figure 3].

The optimization goal is to maximize Q_{abs} within a search space of the size parameters. Computing Q_{abs} using the DDA can sometimes exceed half an hour for a unique wavelength depending on some parameters: the size of the target, the discretization used, the error tolerance, the optical index, and the performance of the computer. Therefore a deterministic sweep of the search space may be prohibitive, and an adequate optimization algorithm must be used. As suggested in the comparative study [8], we use the improved adaptive particle swarm optimization (PSO) [14, 15]. The PSO, an iterative nature inspired algorithm, uses a population of candidate solutions that collaborates (mimicking the movement of organisms in a bird ock or fish school [16]) to improve these solutions. A brief and concise description of the used algorithm can be found in [6].

3. ASSUMPTIONS, RESULTS AND DISCUSSION

3.1. Assumptions and Therapeutic Cases

The gold nanoparticles should be small enough to penetrate small capillaries and get fixed to cells, typically 10–100 nm or smaller [17, 18]. Therefore we consider nanocage with edge length $a \in [5, 100]$ nm and wall thickness $e \in [1, 50]$ nm. The lower bounds are somewhat dictated by the fabrication precisions of similar nanoparticles [6].

The SEM and TEM image of nanocage show that the corners could be truncated and that the wall is porous but rigid [19, 20]. According to Chen calculation [20], the peak position is sensitive to truncation of corners but not to the number and size of pores on the wall of gold nanocages. Therefore, we consider in this study both nanocage and nanocage with truncated corners as illustrated by Figure 1. The removed part is tetradic with side length equal to $2e$.

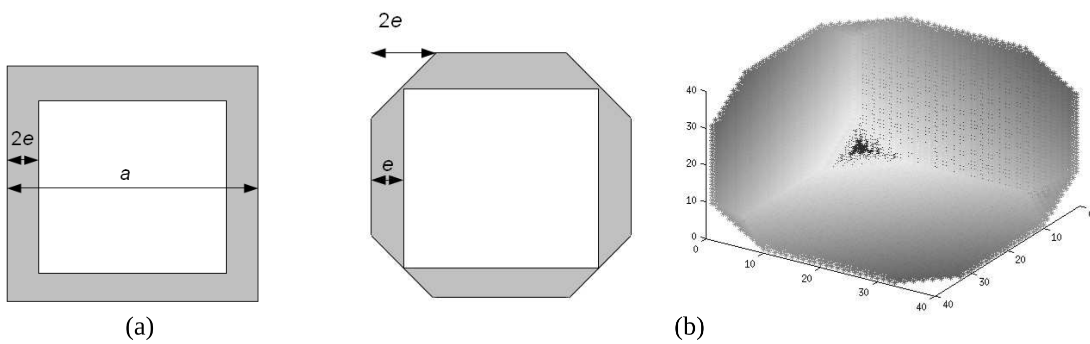

Figure 1: Nanocage: edge length a and wall thickness e, with entire or truncated corners (tetradic removed part with side length equal to $2e$). (a) Nanocage with entire corners. (b) Nanocage with truncated corners.

The choice of the illumination conditions is dictated by the therapeutic application. Two optical windows exist in tissue, as it is mainly transparent within these regions of wavelengths. The main one lies between 600 and 1300 nanometers (nm) and a second one from 1600 to 1850 nm [21]. In these windows, the gold nanoparticles absorb the light more than the organic molecules [4]. PTT in the visible region is suitable for shallow cancer (e.g., skin cancer). Whereas for in vivo therapy of tumors deeply seated under skin, Near Infra Red (NIR) light is required because of its deep penetration. In fact, the hemoglobin and water molecules in tissue have minimal absorption and a limited attenuation of scattering in this spectral region. Both the visible (VIS) and NIR regions are therefore investigated. As in a previous study [6], we consider the two followings cases:

- **case 1:** treatment of shallow cancer assuming the skin dermis as surrounding tissue (refractive index 1.55 [21]) under illumination $\lambda = 633$ nm (VIS).

- **case 2:** treatment of deep cancer assuming subcutaneous fat as surrounding tissue (refractive index 1.44 [21]) under illumination $\lambda = 800$ nm (NIR).

We use the bulk optical index of Johnson and Christy for gold and the inner part of nanocage is supposed to have the same refractive index as tissue (the wall of nanocage being porous).

3.2. Results and Discussion

3.2.1. Optimized Results

The optimal size parameters, that ensure the maximum absorption efficiency Q_{abs}, are reported in Table 1.

Table 1: Optimized shape parameters of gold nanocage in the two therapeutic cases: case 1, the nanoparticles are embedded in skin dermis, using 633 nm illumination wavelength; case 2, the nanoparticles are embedded in subcutaneous fat, using 800 nm illumination wavelength.

Shape		Case 1	Case 2
Nanocage	a (nm)	32	50
	e (nm)	9	5
	Q_{abs}	7.8	17.9
Nanocage with truncated corners	a (nm)	45	52
	e (nm)	10	5
	Q_{abs}	4.9	16.3

3.2.2. Comparison with Previous Studies

Comparing our results with the previous studies where no optimization tools were used, the optimization tools yield better results. To illustrate, for an illumination laser wavelength of 800 nm and assuming truncated corners, the absorption efficiency reach 16.3, whereas:

- Au et al. [5] used nanocage with edge $a = 65$ nm and wall thickness $e = 7.5$ nm which yields an absorption efficiency $Q_{abs} = 9.4$.
- Khlebtsov et al. [7] used nanocage with edge $a = 45$ nm and wall thickness $e = 5$ nm which yields an absorption efficiency Q_{abs} of 5.
- Chen et al. [20] used nanocage with edge $a = 60$ nm and wall thickness $e = 5$ nm which yields an absorption efficiency $Q_{abs} = 6.6$ (at 810 nm laser).

The improved results show that the laser power could be reduced for targeted therapy cases (typically lower than the reported 1.5–5 W/cm^2 [5, 9]) enabling more control (less damage to surrounding healthy cells).

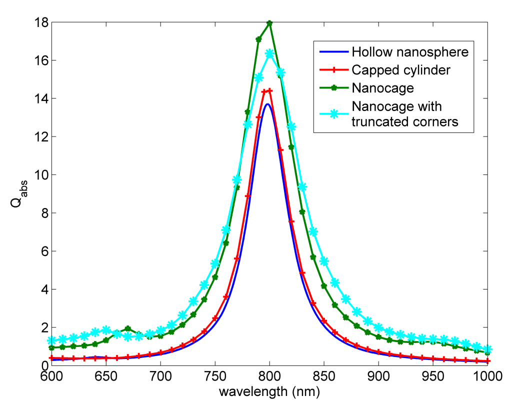

Figure 2: Absorption spectra of optimized capped cylinder and hollow nanosphere [6] and nanocage in therapeutic case 2 (the nanoparticles are embedded in subcutaneous fat, using 800 nm illumination wavelength).

3.2.3. Comparison with Other Nanoparticles

In a previous study [6], we compared optimized nanoshell, hollow nanosphere and nanocage. The nanoshell were found to be the more absorbent in the first therapy case: $Q_{abs} = 10.1$. Therefore, we can conclude that even optimized, nanocages are not as efficient as hollow nanospheres when dealing with shallow cancer. In the second therapeutic case, the absorption efficienciencies of optimized nanoshell, hollow nanosphere and nanorod (with shape of capped cylinder) are 11.8, 13.6 and 14.4, respectively. It seems that the nanocage is more absorbent as illustrated in Figure 2, where $Q_{abs} = 16.3$ for nanocage with truncated corners and $Q_{abs} = 17.9$ for nanocage with entire corners. It should be noticed that the truncation of corners has less influence on the absorption than the shape of nanoparticles (Figure 2).

4. CONCLUSIONS

To get the maximum absorption efficiency in two therapeutic cases, the theoretical optimization of the size parameters of nanocages was carried out. The optimization of the absorption efficiency (computed with the discrete dipole approximation) is achieved by an adequate optimization algorithm (improved PSO algorithm). The results show an improved efficiency compared with previous studies: the absorption efficiency is at least twice.

The nanocages were optimized assuming both non-truncated and truncated corners. The influence of corners' shape on the absorption is less important than the entire shape of nanoparticles. Indeed, the optimized nanocages are compared with other optimized nanoparticles (nanorods, nanoshells and hollow nanospheres). They are the most absorbent when a near infra red illumination is used. Therefore, with such nanocages, the laser power used in therapeutics could be reduced for more control (avoiding any possible injury of surrounding cells).

ACKNOWLEDGMENT

This work was supported by the "Conseil régional de Champagne Ardenne", the "Conseil général de l'Aube" and the Nanoantenna European Project (FP7 Health-F5-2009-241818).

REFERENCES

1. Hirsch, L. R., R. J. Stafford, J. A. Bankson, S. R. Sershen, B. Rivera, R. E. Price, J. D. Hazle, N. J. Halas, and J. L. West, "Nanoshell-mediated near-infrared thermal therapy of tumors under magnetic resonance guidance," *Proc. Natl. Acad. Sci.*, Vol. 100, 13549–13554, USA, 2003.
2. Huang, X., I. H. El-Sayed, W. Qian, and M. A. El-Sayed, "Cancer cell imaging and photothermal therapy in the near-infrared region by using gold nanorods," *J. Am. Chem. Soc.*, Vol. 128, 2115–2120, 2006.
3. Von Maltzahn, G., J.-H. Park, A. Agrawal, N. K. Bandaru, S. K. Das, M. J. Sailor, and S. N. Bhatia, "Computationally guided photothermal tumor therapy using long-circulating gold nanorod antennas," *Cancer Res.*, Vol. 69, 3892–3900, 2009.
4. Liu, C., C. C. Mi, and B. Q. Li, "Energy absorption of gold nanoshells in hyperthermia therapy," *IEEE Trans. in Nanobioscience*, Vol. 7, 206–214, 2008.
5. Au, L., D. Zheng, F. Zhou, Z.-Y. Li, X. Li, and Y. Xia, "A quantitative study on the photothermal effect of immuno gold nanocages targeted to breast cancer cells," *ACS Nano.*, Vol. 2, 1645–1652, 2008.
6. Kessentini, S. and D. Barchiesi, "Quantitative comparison of optimized nanorods, nanoshells and hollow nanospheres for photothermal therapy," *Biomed. Opt. Express*, Vol. 3, 590–604, 2012.
7. Khlebtsov, B. N., V. A. Khanadeev, I. L. Maksimova, G. S. Terentyuk, and N. G. Khlebtsov, "Silver nanocubes and gold nanocages: fabrication and optical and photothermal properties," *Nanotechnologies in Russia*, Vol. 5, 454–468, 2010.
8. Kessentini, S., D. Barchiesi, T. Grosges, and M. Lamy de la Chapelle, "Particle swarm optimization and evolutionary methods for plasmonic biomedical applications," *IEEE Congress on Evolutionary Computation (CEC)*, 2315–2320, New Orleans, 2011.
9. Chen, J., D. Wang, J. Xi, L. Au, A. Siekkinen, A. Warsen, Z.-Y. Li, H. Zhang, Y. Xia, and X. Li, "Immuno gold nanocages with tailored optical properties for targeted photothermal destruction of cancer cells," *Nano Letters*, Vol. 7, 1318–1322, 2007.

10. Devoe, H., "Optical properties of molecular aggregates. I. Classical model of electronic absorption and refraction," *J. Chem. Phys.*, Vol. 41, 393–400, 1964.
11. Devoe, H., "Optical properties of molecular aggregates. II. Classical theory of the refraction, absorption, and optical activity of solutions and crystals," *J. Chem. Phys.*, Vol. 43, 3199–3208, 1965.
12. Draine, B. T. and P. J. Flatau, "Discrete-dipole approximation for scattering calculations," *J. Opt. Soc. Am. A*, Vol. 11, 1491–1499, 1994.
13. Draine, B. T. and P. J. Flatau, "User guide to the discrete dipole approximation code DDSCAT 7.1," http://arXiv.org/abs/1002.1505v1, 2010.
14. Zhan, Z.-H., J. Zhang, Y. Li, and H. S.-H. Chung, "Adaptive particle swarm optimization," *IEEE Trans. on Systems, Man, and Cybernetics — Part B: Cybernetics*, Vol. 39, 1362–1381, 2009.
15. Kessentini, S. and D. Barchiesi, "A new strategy to improve particle swarm optimization exploration ability," *Global Congress on Intelligent Systems (GCIS)*, 27–30, 2010.
16. Kennedy, J. and R. Eberhart, "Particle swarm optimization," *IEEE International Conference on Neural Networks*, 1942–1948, 1995.
17. Chen, P. C., S. C. Mwakwari, and A. K. Oyelere, "Gold nanoparticles: From nanomedicine to nanosensing," *Nanotechnology, Science and Applications*, Vol. 1, 45–66, 2008.
18. Patra, C. R., R. Bhattacharya, D. Mukhopadhyay, and P. Mukherjee, "Fabrication of gold nanoparticles for targeted therapy in pancreatic cancer," *Advanced Drug Delivery Reviews*, Vol. 62, 346–361, 2010.
19. Chen, J., F. Saeki, B. J. Wiley, H. Cang, M. J. Cobb, Z.-Y. Li, L. Au, H. Zhang, M. B. Kimmey, X. Li, and Y. Xia, "Gold nanocages: Bioconjugation and their potential use as optical imaging contrast agents," *Nano Letters*, Vol. 5, 473–477, 2005.
20. Chen, J., B. J. Wiley, Z.-Y. Li, D. Campbell, F. Saeki, H. Cang, L. Au, J. Lee, X. Li, and Y. Xia, "Gold nanocages: engineering their structure for biomedical applications," *Adv. Mater.*, Vol. 17, 2255–2261, 2005.
21. Duck, F. A., *Physical Properties of Tissue A Comprehensive Reference Book*, Academic Press, London, 1990.

Gap Solitons in Coupled Bragg Gratings with Cubic-quintic Nonlinearity

Md. Jahedul Islam and Javid Atai
School of Electrical and Information Engineering, The University of Sydney, NSW 2006, Australia

Abstract— The existence and stability of gap solitons in coupled Bragg gratings with cubic-quintic nonlinearity are investigated. The effect of quintic nonlinearity and coupling coefficient on the stability of asymmetric gap solitons are analyzed.

1. INTRODUCTION

It is well known that the effective dispersion induced by a fiber Bragg grating (FBG) can be up to six orders of magnitude greater than the chromatic dispersion of the medium [1]. At sufficiently high intensities, nonlinearity and the grating-induced dispersion can be balanced giving rise to gap solitons (GSs). Over the past two decades, GSs in Kerr nonlinearity have been studied extensively both theoretically and experimentally [1–7]. Theoretical studies have shown that in a single fiber Bragg grating (FBG), GSs form a two-parameter family [3]. One of these parameters is the soliton's velocity, which can range between zero and the speed of light in the medium. The other parameter is dependent on the detuning frequency, peak power and soliton width. Experimental studies have focused on the generation of very slow or zero velocity gap solitons due to their potential applications in optical signal processing. Thus far, gap solitons with a velocity of $0.23c$ (where c is the speed of light in the medium) have been experimentally observed [8].

Gap solitons have also been investigated in more sophisticated nonlinear systems such as gratings written in quadratic nonlinearity [9, 10], nonuniform gratings [11, 12], grating assisted couplers with Kerr nonlinearity [13–15], and cubic-quintic nonlinearity [16–18]. In this paper, we investigate the existence and stability of GSs in a model of coupled FBGs with cubic-quintic nonlinearity.

2. THE MODEL

Starting from Maxwell's equations and following a similar procedure as outlined in Ref. [13], one can derive the following set of normalized equations:

$$iu_{1t} + iu_{1x} + \left(\frac{1}{2}|u_1|^2 + |v_1|^2\right) u_1 - \eta \left(\frac{1}{4}|u_1|^4 + \frac{3}{2}|u_1|^2|v_1|^2 + \frac{3}{4}|v_1|^4\right) u_1 + v_1 + \lambda u_2 = 0 \quad (1)$$

$$iv_{1t} - iv_{1x} + \left(\frac{1}{2}|v_1|^2 + |u_1|^2\right) v_1 - \eta \left(\frac{1}{4}|v_1|^4 + \frac{3}{2}|v_1|^2|u_1|^2 + \frac{3}{4}|u_1|^4\right) v_1 + u_1 + \lambda v_2 = 0 \quad (2)$$

$$iu_{2t} + iu_{2x} + \left(\frac{1}{2}|u_2|^2 + |v_2|^2\right) u_2 - \eta \left(\frac{1}{4}|u_2|^4 + \frac{3}{2}|u_2|^2|v_2|^2 + \frac{3}{4}|v_2|^4\right) u_2 + v_2 + \lambda u_1 = 0 \quad (3)$$

$$iv_{2t} - iv_{2x} + \left(\frac{1}{2}|v_2|^2 + |u_2|^2\right) v_2 - \eta \left(\frac{1}{4}|v_2|^4 + \frac{3}{2}|v_2|^2|u_2|^2 + \frac{3}{4}|u_2|^4\right) v_2 + u_2 + \lambda v_1 = 0 \quad (4)$$

where $u_{1,2}$ and $v_{1,2}$ are the amplitudes of the forward- and backward-propagating waves in the cores 1 and 2, respectively. $\eta > 0$ is a real parameter and accounts for the strength of the quintic nonlinearity. λ is the coefficient of the linear coupling between two cores.

Substituting $u_{1,2}, v_{1,2} \sim \exp(ikx - i\omega t)$ into the system of Eqs. (1)–(4) and linearizing, the following two branches of the dispersion relation are obtained:

$$\omega^2 = 1 + \lambda^2 + k^2 \pm 2\lambda\sqrt{1 + k^2} \quad (5)$$

The dispersion relation (5) leads to the bandgap is $|\omega| < (1 - |\lambda|)$.

3. QUIESCENT SOLUTIONS AND THEIR STABILITY

We sought for stationary solutions of Eqs. (1)–(4) as $\{u(x,t), v(x,t)\} = \{U(x), V(x)\} \exp(-i\omega t)$. Substituting these expressions into Eqs. (1)–(4) we arrive at a set of ordinary differential equations which can be solved by the relaxation algorithm. It is found that Eqs. (1)–(4) admit both symmetric

($u_1 = u_2$, $v_1 = v_2$) and asymmetric soliton ($u_1 \neq u_2$, $v_1 \neq v_2$) solutions. It is also found that within each of these categories there exist two disjoint families of solitons. The soliton families differ in their amplitudes, phase structures and parities. In one of the families $\Re(u(x))$ and $\Re(v(x))$ are even, and $\Im(u(x))$ and $\Im(v(x))$ are odd functions of x. In the other family, the parities of the real and imaginary parts of the solutions are opposite. The soliton families are separated by the curve $1 - \omega - \lambda = 27/(160\eta)$ in the (η, ω) plane.

To test the stability of the gap solitons, we have solved Eqs. (1)–(4) by means of the symmetrized split-step Fourier method. Figure 1 displays the stability diagram for asymmetric solitons in the

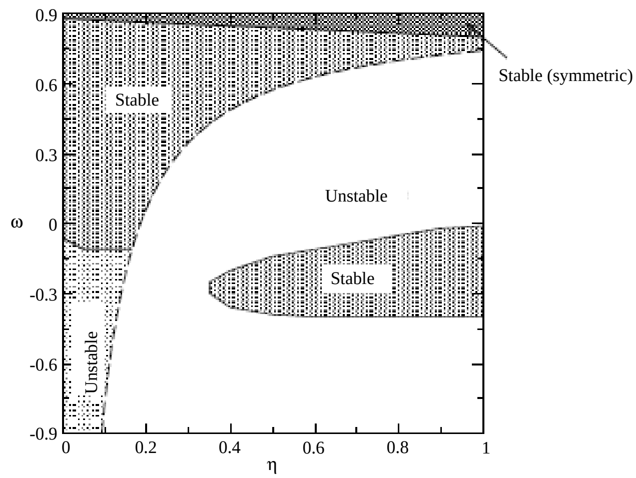

Figure 1: Stability diagram for asymmetric gap solitons for $\lambda = 0.1$. The dashed curve separates the two families of asymmetric solitons.

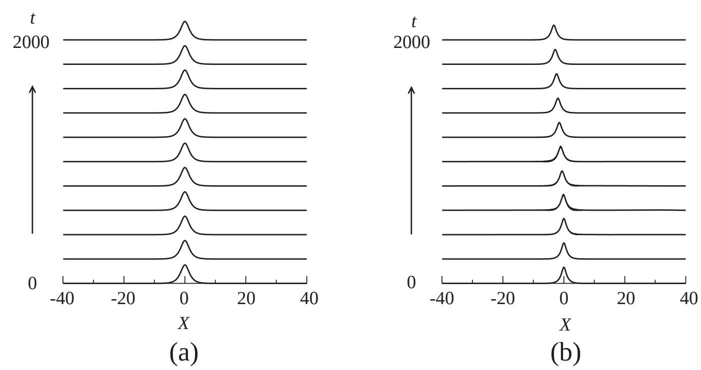

Figure 2: Examples of the evolution of asymmetric gap solitons belonging to the region above the dashed line in Figure 1. (a) A stable soliton with $\lambda = 0.1$, $\eta = 0.2$, $\omega = 0.6$ and (b) an unstable soliton with $\lambda = 0.1$, $\eta = 0.05$, $\omega = -0.19$. In this figure and all the figures that follow, only u_1-component is shown.

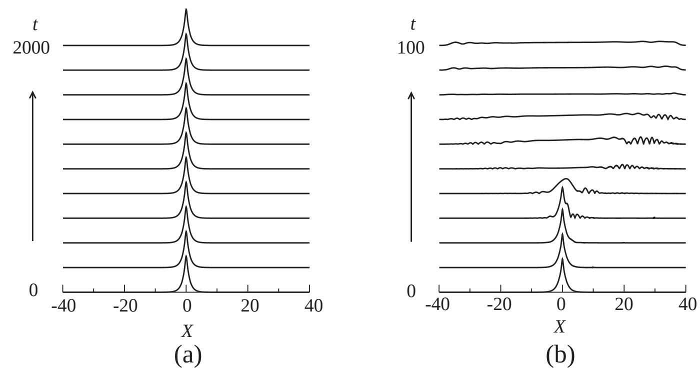

Figure 3: Examples of the evolution of asymmetric gap solitons belonging to the region below the dashed line in Figure 1. (a) A stable soliton with $\lambda = 0.1$, $\eta = 0.6$, $\omega = -0.3$ and (b) an unstable soliton with $\lambda = 0.1$, $\eta = 1.0$, $\omega = 0.4$.

(η, ω) plane for $\lambda = 0.1$. The dashed curve in Figure 1 separates the two families of asymmetric solitons. A notable feature of Figure 1 is that, compared with the dual-core FBG in cubic media (i.e., $\eta = 0$), the presence of quintic nonlinearity results in the expansion of the stable region in the range $0 < \eta < 0.1$. In the case of the other family of asymmetric solitons (i.e., the family to the right of the dashed curve in Figure 1) the stable region expands as η increases. Examples of the evolution of stable and unstable asymmetric solitons for both families are shown in Figures 2 and 3.

4. CONCLUSION

We have numerically investigated the existence and stability of quiescent gap solitons in a model of two linearly coupled Bragg gratings with cubic-quintic nonlinearity. The model supports both symmetric and asymmetric soliton solutions, and in each category there exist two disjoint families of solitons. It is also found that the presence of quintic nonlinearity results in the expansion of the stability region.

REFERENCES

1. De Sterke, C. M. and J. E. Sipe, *Prog. Opt.* Vol. 33, 203, 1994.
2. Eggleton, B. J., R. E. Slusher, C. M. de Sterke, P. A. Krug, and J. E. Sipe, *Phys. Rev. Lett.* Vol. 76, 1627, 1996.
3. Aceves, A. B. and S. Wabnitz, *Phys. Lett. A*, Vol. 141, 37, 1989.
4. Christodoulides, D. N. and R. I. Joseph, *Phys. Rev. Lett.* Vol. 62, 1746, 1989.
5. Barashenkov, I. V., D. E. Pelinovsky, E. V. Zemlyanaya, *Phys. Rev. Lett.*, Vol. 80, 5117, 1998.
6. Mak, W. C. K., B. A. Malomed, and P. L. Chu, *Phys. Rev. E*, Vol. 68, 026609, 2003.
7. Neill, D. R. and J. Atai, *Phys. Lett. A*, Vol. 353, 416, 2006.
8. Mok, J. T., C. M. de Sterke, I. C. M. Littler, and B. J. Eggleton, *Nature Phys.*, Vol. 2, 775, 2006.
9. Conti, C., S. Trillo, and G. Assanto, *Phys. Rev. Lett.* Vol. 78, 2341–2344, 1997.
10. He, H. and P. D. Drummond, *Phys. Rev. Lett.* Vol. 78, 4311-4315, 1997.
11. Atai, J. and B. A. Malomed, *Phys. Lett. A*, Vol. 342, 404, 2005.
12. Neill, D. R., J. Atai, and B. A. Malomed, *J. Opt. A: Pure Appl. Opt.* Vol. 10, 085105, 2008.
13. Mak, W. C. K., P. L. Chu, and B. A. Malomed, *J. Opt. Soc. Am. B*, Vol. 15, 1685, 1998.
14. Atai, J. and B. A. Malomed, *Phys. Rev. E*, Vol. 62, 8713, 2000.
15. Baratali, B. H. and J. Atai, *J. Opt.*, Vol. 14, 065202, 2012.
16. Atai, J. and B. A. Malomed, *Phys. Lett. A*, Vol. 284, 247, 2001.
17. Atai, J., *J. Opt. B: Quantum Semiclass. Opt.*, Vol. 6, S177, 2004.
18. Dasanayaka, S. and J. Atai, *Phys. Rev. E*, Vol. 84, 026613, 2011.

Dual Wavelength Switching by a Bare Fiber Butt Joint in an Erbium-doped Fiber Ring Laser

Fang-Wen Sheu and Yu-Han Kao
Department of Electrophysics, National Chiayi University, Chiayi 60004, Taiwan

Abstract— We construct an erbium-doped fiber ring laser with a bare fiber butt joint. The output wavelength can be switched from 1558 nm to 1531 nm approximately if we transversely or longitudinally displace the bare fiber ends. It is related to the loss-dependent dynamic variation in the nonlinear gain characteristics of erbium-doped fiber.

1. INTRODUCTION

The wavelength tunable erbium-doped fiber ring laser using a tapered single mode fiber tip as a tunable bandpass spatial filter [1] has been proposed and demonstrated [2]. Due to the multibeam interference of the cladding modes in the near field, the tapered fiber tip can be used as a high resolution filter device. Here, we try to alternatively make use of a bare fiber butt joint to realize the wavelength switching in a similar ring-cavity structure. The dual wavelength switching can be achieved by this proposed simple technique.

2. EXPERIMENTAL SETUP AND MEASUREMENT RESULTS

2.1. Experimental Setup

The experimental setup is shown in Figure 1. The two bare fiber ends of two optical fibers form a butt joint, as indicated by the inset enclosed by a dashed box in Figure 1. The other end of the transmitting-end optical fiber is connected to the output port of an erbium-doped fiber amplifier (EDFA, SDO EFAS1P112PP02). The other end of the receiving-end optical fiber is further connected to two successive fiber couplers in order to measure the optical power and optical spectrum of the fiber laser output light with the power meter (ADVANTEST TQ8215) and the optical spectrum analyzer (OSA, ADVANTEST Q8384), respectively. An additional optical fiber is used to guide the laser light emanating from the first fiber coupler to the input port of the EDFA, forming a ring-type resonant cavity. The drive current of the EDFA is first set at 190 mA. The relative positions of the bare fiber ends are initially tuned to achieve maximum laser output power. At this condition, the output wavelength peak is around 1558 nm and the output optical power is 114.39 μW approximately. As the drive current of the EDFA is further reduced, the output optical power will decay linearly and the output wavelength peak will keep being around 1558 nm. When

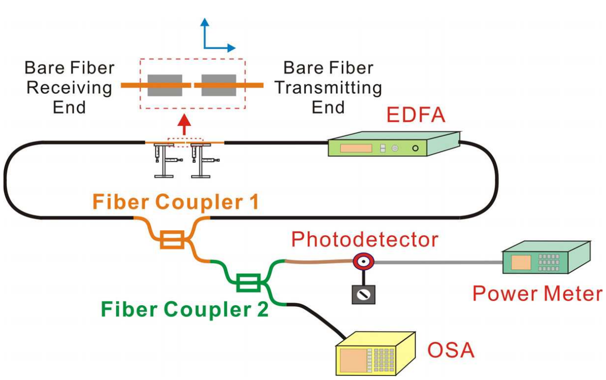

Figure 1: The experimental setup. Inset: The two bare fiber ends.

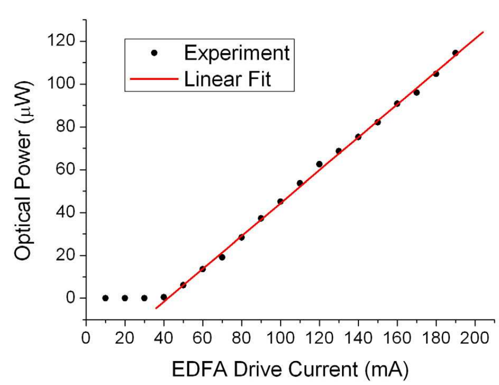

Figure 2: The relationship between the optical power of the fiber laser output light and the drive current of the EDFA.

the drive current reaches 40 mA, the output wavelength peak disappears. The relationship between the optical power of the fiber laser output light and the drive current of the EDFA is shown in Figure 2, which depicts a lasing characteristic LI curve. From the linear fit to the inclined part of this LI curve, we can find that the lasing threshold of the EDFA drive current for this erbium-doped fiber ring laser is 42.07 mA approximately.

2.2. Measurement Results

The drive current of the EDFA is then set again at 190 mA. The relative positions of the bare fiber ends are initially tuned to achieve maximum laser output power. Figure 3 shows the measured output spectra of the erbium-doped fiber ring laser when we transversely displace the bare fiber ends at the butt joint with a precision translator. The original wavelength peak around 1558 nm will weaken gradually and another wavelength peak around 1531 nm will grow gradually inversely, forming a two-wavelength output. If the bare fibers are further transversely displaced, the fiber laser output wavelength can be switched to the peak around 1531 nm.

As shown in Figure 4, when we longitudinally displace the bare fiber ends at the butt joint, the output spectra of the erbium-doped fiber ring laser have similar variation trend. Yet, the required spatial displacement of the bare fiber ends at the butt joint is greater than that required in the previous case, because the longitudinal variation in the laser beam optical intensity is less intense than the transverse one.

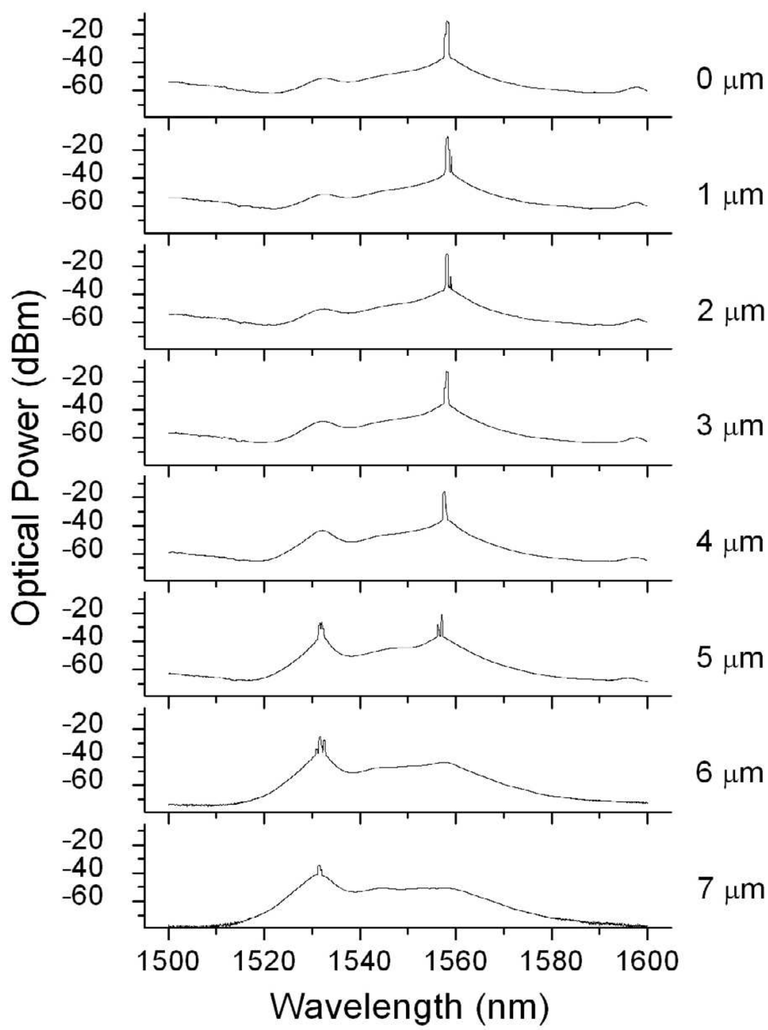

Figure 3: The output spectra of the erbium-doped fiber ring laser when we transversely displace the bare fiber ends at the butt joint. The displacement is indicated at the right place of each sub figure.

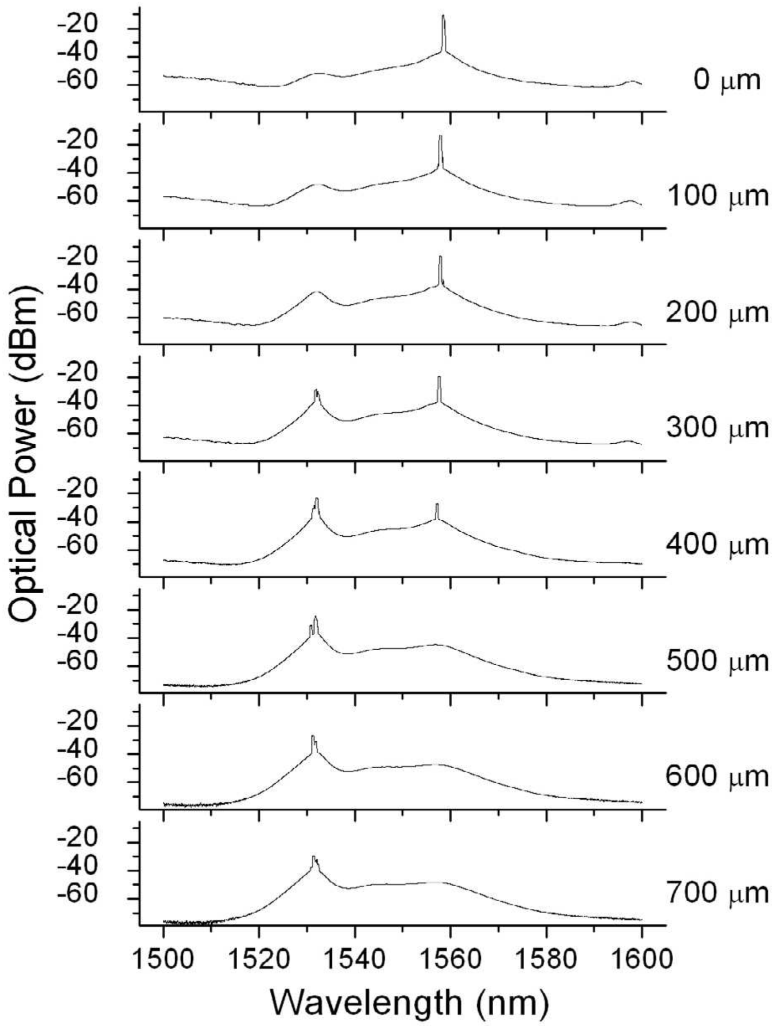

Figure 4: The output spectra of the erbium-doped fiber ring laser when we longitudinally displace the bare fiber ends at the butt joint. The displacement is indicated at the right place of each sub figure.

3. CONCLUSIONS

The output wavelength of an erbium-doped fiber ring laser with a bare fiber butt joint can be switched from 1558 nm to 1531 nm approximately by transversely or longitudinally displacing the butt-joint bare fiber ends. We attribute the possible mechanism to the dynamic variation in the nonlinear gain characteristics (population inversion) of erbium-doped fiber [3], which is modulated by the variation in the resonant cavity loss and still needs further experimental investigation. This dual wavelength switchable erbium-doped fiber ring laser with a simple setup might find useful application if a fast spatial tuning device can be incorporated into the system.

ACKNOWLEDGMENT

This work was supported by the National Science Council, Taiwan, through Projects NSC 98-2815-C-415-004-M and NSC 100-2112-M-415-002-MY3.

REFERENCES

1. Li, Y. and X. Bao, "The observation of comblike transmission spectrum from a tapered single mode fiber tip," *Appl. Phys. Lett.*, Vol. 93, 261107, 2008.
2. Wang, X., Y. Li, and X. Bao, "Tunable ring laser using a tapered single mode fiber tip," *Appl. Opt.*, Vol. 48, 6827–6831, 2009.
3. Desurvire, E., D. Bayart, B. Desthieux, and S. Bigo, *Erbium-doped Fiber Amplifiers Device and System Developments*, John Wiley and Sons, Inc., New York, USA, 2002.

GNSS-based Bistatic Synthetic Aperture Radar Image Formation via Compressive Sensing

Chunyang Dai, **Liangjiang Zhou**, **Xingdong Liang**, **and Yirong Wu**
Institute of Electronics, Chinese Academy of Sciences, Beijing, China

Abstract— Global Navigation Satellite System (GNSS) based bistatic synthetic aperture Radar (BiSAR) is a promising non-cooperative radar imaging system, and becomes a hot research topic in passive remote sensing area. This paper proposed a novel imaging configuration with multiple GNSS transmitters and one receiver, which can be equivalent to a large sparse two-dimensional antenna arrays. By this configuration, we can obtain focused sparse targets on the Earth's surface via compressive sensing (CS) even in zero coherent integration time. Simulations are also been performed to validate the effectiveness of our proposed imaging scheme. Corresponding results show that, our CS image formation algorithm can generate improved focused performance compared with traditional matching filtering method.

1. INTRODUCTION

Bistatic Synthetic Aperture Radar (BiSAR), in which the transmitter and receiver are separated, is a useful tool for remote sensing of the Earth's surface. The transmitter could be non-cooperative or a dedicated radar satellite, while the receiver could be either mounted on a moving platform or fixed on the earth [1]. BiSAR based on Global Navigation Satellite System (GNSS), including the Global Positioning Systems (GPS) [2], GLObal Navigation SAtellite System (GLONASS) [3], the forthcoming Galileo [4] and Beidou [5] system, is a subclass of BiSAR which makes it suitable for applications with a limited power and weight budget.

Our research focused on the imaging configuration with multiple GNSS satellites. In this novel configuration, multiple transmitters mounted on navigation satellites and one receiver fixed near the Earth's surface can be equivalent to a large sparse antenna arrays. To focus the echo data from multiple transmitters, we investigated the compressive sensing method, such as Basis Pursuit (BP) and Matching Pursuit (MP). Based on compressive sensing method, the sparse targets echo data can be focused with overwhelming probability under the restricted isometry property (RIP) condition [6].

The organization of this paper is as follows. Section 2 contains the signal model of our proposed image formation configuration. In Section 3, the image formation algorithm based on compressive sensing is discussed in detail. The numerical simulation to verify the proposed processing method is performed in Section 4. Finally, Section 5 concludes this paper.

2. SIGNAL MODEL

The data acquisition geometry of the GNSS-based BiSAR configuration is shown in Figure 1. This novel imaging configuration consists of several satellite transmitters and one receiver near the Earth's surface. Without loss of generality, the receiver is mounted at $\mathbf{P}_R$; the k-th transmitter ($k = 1, 2, \ldots, K$) is mounted at $\mathbf{P}_T(k)$; the n-th target ($n = 1, 2, \ldots, N$) is mounted at $\boldsymbol{\xi}_n$ on the Earth's surface. Thus, the slant range $R(k, n)$ is the sum of the slant ranges from point target $\boldsymbol{\xi}_n$ to the T/R platforms, i.e.,

$$R(k,n) = \|\mathbf{P}_T(k) - \boldsymbol{\xi}_n\|_2 + \|\boldsymbol{\xi}_n - \mathbf{P}_R\|_2 \tag{1}$$

After demodulation to the baseband, the received signal can be written in terms of the time t and the transmitter index k,

$$s_R(t,k) = \sum_{n=1}^{N} \sigma_n p_k \left(t - \frac{R(k,n)}{c}\right) \exp\left(-j2\pi f_c \frac{R(k,n)}{c}\right) \tag{2}$$

where f_c denotes the carrier frequency; c denotes the wave propagation speed; σ_n denotes the scatterer coeffcient of the n-th target; and $p_k(t)$ denotes the C/A code of k-th satellite. Applying a Fourier transform along t, we get

$$S_R(f,k) = \int s_R(t,k) \exp(-j2\pi ft) dt = \sum_{n=1}^{N} \sigma_n P_k(f) \exp\left(-j2\pi \frac{f_c + f}{c} R(k,n)\right) \tag{3}$$

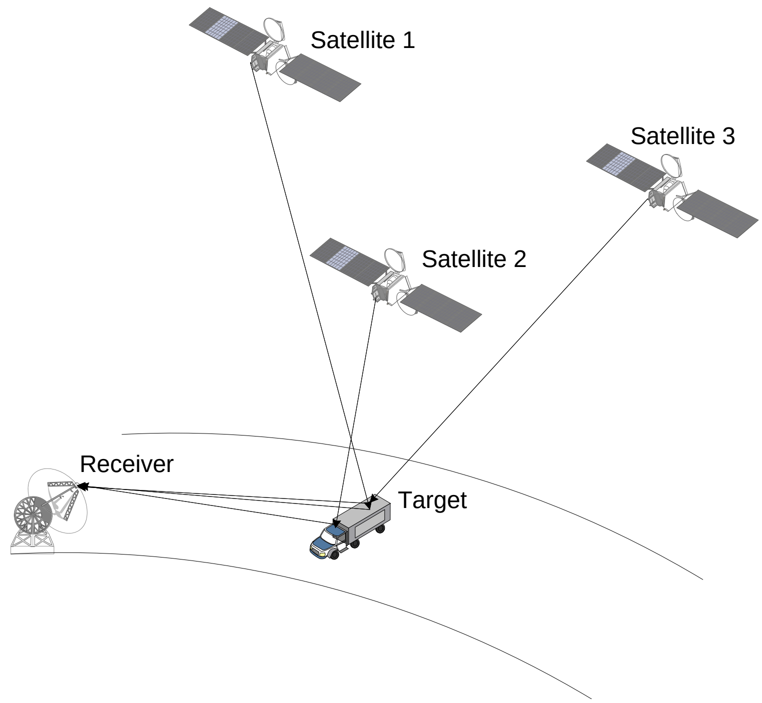

Figure 1: GNSS-based imaging configuration.

where f denotes the range frequency, and $P_k(f)$ denotes the frequency spectrum of C/A code $p_k(t)$. Subsequently, after performing range compressing, i.e., multiplying the complex conjugate of C/A frequency spectrum, we have

$$S_C(f,k) = \left[\text{rect}\left(\frac{f}{B}\right) \cdot \frac{P_k^*(f)}{|P_k(f)|^2}\right] \cdot S_R(f,k) = \sum_{n=1}^{N} \sigma_n \exp\left(-j2\pi \frac{f_c+f}{c} R(k,n)\right) \tag{4}$$

where $B = 1.023\,\text{MHz}$ denotes the bandwidth of C/A code.

3. IMAGE FORMATION VIA COMPRESSIVE SENSING

The first step is to rewrite Equation (4) to the matrix form,

$$\mathbf{S}_k = \mathbf{A}_k \boldsymbol{\sigma} \tag{5}$$

where

$$\mathbf{S}_k = \{S_C(f_m,k)\} \in \mathbb{C}^{M\times 1} \tag{6}$$

$$\mathbf{A}_k = \left\{\exp\left(-j2\pi \frac{f_c+f_m}{c} R(k,n)\right)\right\} \in \mathbb{C}^{M\times N} \tag{7}$$

$$\boldsymbol{\sigma} = \{\sigma_n\} \in \mathbb{C}^{N\times 1} \tag{8}$$

where f_m denotes the m-th sampling point in range frequency axis f, and $m = 1, 2, \ldots, M$. Concatenating all equations such as (5) for $k = 1, 2, \ldots, K$, we have

$$\mathbf{S} = \mathbf{A}\boldsymbol{\sigma} \tag{9}$$

where

$$\mathbf{S} = \begin{bmatrix} \mathbf{S}1 \\ \mathbf{S}2 \\ \vdots \\ \mathbf{S}_K \end{bmatrix} \in \mathbb{C}^{KM\times 1} \tag{10}$$

$$\mathbf{A} = \begin{bmatrix} \mathbf{A}1 \\ \mathbf{A}2 \\ \vdots \\ \mathbf{A}_K \end{bmatrix} \in \mathbb{C}^{KM\times N} \tag{11}$$

For the convenience of processing by compressive sensing, the complex matrix Equation (9) should be transformed to the real matrix equation, i.e.,

$$\tilde{\mathbf{S}} = \tilde{\mathbf{A}}\tilde{\boldsymbol{\sigma}} \tag{12}$$

where

$$\tilde{\mathbf{S}} = \begin{bmatrix} \mathrm{Re}(\mathbf{S}) \\ \mathrm{Im}(\mathbf{S}) \end{bmatrix} \in \mathbb{R}^{2KM\times 1} \tag{13}$$

$$\tilde{\mathbf{A}} = \begin{bmatrix} \mathrm{Re}(\mathbf{A}) & -\mathrm{Im}(\mathbf{A}) \\ \mathrm{Im}(\mathbf{A}) & \mathrm{Re}(\mathbf{A}) \end{bmatrix} \in \mathbb{R}^{2KM\times 2N} \tag{14}$$

and

$$\tilde{\boldsymbol{\sigma}} = \begin{bmatrix} \mathrm{Re}(\boldsymbol{\sigma}) \\ \mathrm{Im}(\boldsymbol{\sigma}) \end{bmatrix} \in \mathbb{R}^{2N\times 1} \tag{15}$$

It is natural to think of the matrix Equation (12) as a problem dual to sparse approximation. Since $\tilde{\boldsymbol{\sigma}}$ has only a few of nonzero components, the echo $\tilde{\mathbf{S}}$ is a linear combination of a few columns from $\tilde{\mathbf{A}}$. To identify the ideal image $\tilde{\boldsymbol{\sigma}}$, we need to determine which columns of $\tilde{\mathbf{A}}$ participate in the echo $\tilde{\mathbf{S}}$. The idea for this problem is to pick columns in a greedy fashion. At each iteration, we choose the column of $\tilde{\mathbf{A}}$ that is most strongly correlated with the remaining part of $\tilde{\mathbf{S}}$. Thus, we consider the OMP algorithm for the recovery of the image $\tilde{\boldsymbol{\sigma}}$. The procedure of OMP is listed as Algorithm [7].

4. NUMERICAL SIMULATION

In this section, we perform a numerical simulation to verify the validity of the proposed image formation method. The imaging zone consists of four point targets, which are shown in Figure 2. The GPS satellite orbit data can be found from the file named "igrs17386.sp3" in website [8]. We choose the nearest 6 satellites from the center of imaging zone as the transmitter. The other simulation parameters are listed in Table 1.

Imaging results by our proposed method are shown in Figure 3. From this figure, we can see that all four targets are arranged in their correct position in the Earth's surface, which means that the sparse targets could be focused according compressive sensing method. While the imaging results generated by the traditional matching filtering technology are shown in Figure 4. It is obvious that the GNSS-based echo data can not be focused by traditional MF method.

Algorithm 1 Procedure of Orthogonal Matching Pursuit.

- **Input:**
  1. The range compressed signal vector $\tilde{\mathbf{S}} \in \mathbb{R}^{2KM\times 1}$;
  2. The dictionary matrix $\tilde{\mathbf{A}} \in \mathbb{R}^{2KM\times 2N}$;
  3. The iteration times H.
- **Procedure:**

Table 1: Simulation parameters.

Parameter	Value	Unit
Carrier frequency	1575.42	MHz
Bandwidth	1.023	MHz
Number of GPS in use	6	1
Center of imaging zone (latitude)	0	deg
Center of imaging zone (longitude)	0	deg
Center of imaging zone (altitude)	0	m
Receiver (latitude)	0	deg
Receiver (longitude)	0.5	deg
Receiver (altitude)	10	Km

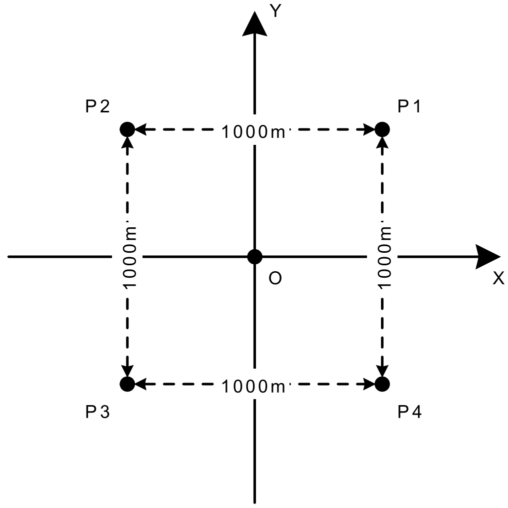

Figure 2: Four targets in zero amplitude plane.

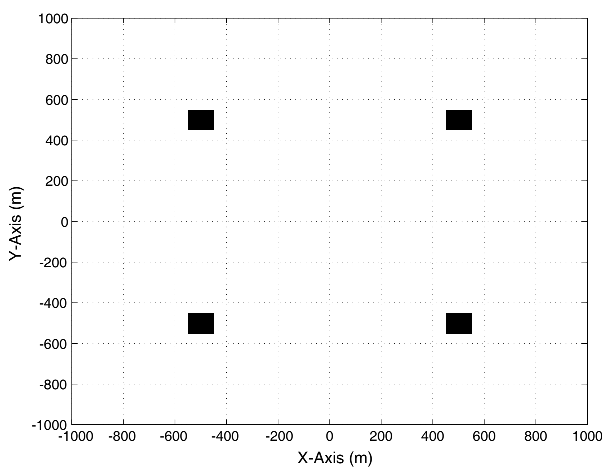

Figure 3: Focused image by OMP.

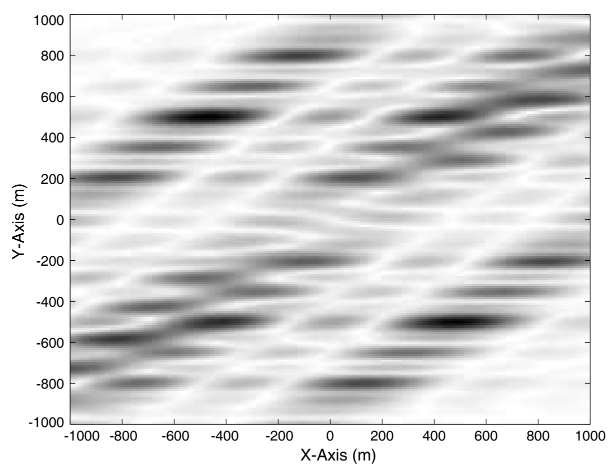

Figure 4: Focused image by MF.

1. Initialize the residual $\mathbf{r}_0 = \tilde{\mathbf{S}}$, the index set $\boldsymbol{\Lambda}_0 = \emptyset$, and the iteration counter $h = 1$, and the empty matrix $\tilde{\mathbf{A}}_0$;
2. Find the index λ_h that solves the easy optimization problem:

$$\boldsymbol{\lambda}_h = \arg \max_{i=1,\,2,\,\ldots,\,2N} |\langle \mathbf{r}_{h-1}, \tilde{\mathbf{a}}_i \rangle| \tag{16}$$

   where $\tilde{\mathbf{A}}_i$ is the ith column vector of the dictionary matrix $\tilde{\mathbf{A}}$;
3. Augment the index set and the matrix of chosen atoms: $\boldsymbol{\Lambda}_h = \boldsymbol{\Lambda}_{h-1} \cup \{\boldsymbol{\Lambda}_h\}$ and $\tilde{\mathbf{A}}_h =$

$[\tilde{\mathbf{A}}_{h-1} \quad \tilde{\mathbf{a}}_{\boldsymbol{\lambda}_h}]$;

4. Solve a least squares problem to obtain a new signal estimate:

$$\mathbf{x}_h = \arg\min_{\mathbf{x}} \left\| \tilde{\mathbf{S}} - \tilde{\mathbf{A}}_h \mathbf{x} \right\|_2 . \tag{17}$$

5. Calculate the new approximation of the data and the new residual:

$$\mathbf{r}_h = \tilde{\mathbf{S}} - \tilde{\mathbf{A}}_h \mathbf{x}_h \tag{18}$$

6. Increment h and return to Step 2, if $h < H$;
7. The final solution $\tilde{\boldsymbol{\sigma}}$ has nonzero indices at the components listed in $\boldsymbol{\Lambda}_H$. The value of the solution $\tilde{\boldsymbol{\sigma}}$ in component λ_h equals the hth component of $\mathbf{x}_h$.

5. CONCLUSION

This paper proposed a novel imaging configuration with multiple GNSS transmitter and one receiver mounted near the Earth's surface. The echo signal is expressed as the linear combination of the column vectors in dictionary matrix. For the sparse targets, we can obtain the focused image using compressive sensing method in zero coherent integration time. The responding numerical simulations are also performed to valid our proposed image formation algorithm.

REFERENCES

1. Zuo, R., *Bistatic Synthetic Aperture Radar Using GNSS as Transmitters of Opportunity,* phdzuo2012bistatic, University of Birmingham, 2012.
2. Wikipedia, "Global positioning system," Wikipedia, 2013, Online accessed May 8, 2013.
3. Wikipedia, "Glonass," Wikipedia, 2013, Online accessed May 8, 2013.
4. Wikipedia, "Galileo (satellite navigation)," Wikipedia, the Free Encyclopedia, 2013, Online accessed May 8, 2013.
5. Wikipedia, "Beidou navigation satellite system," Wikipedia, the Free Encyclopedia, 2013, Online accessed May 8, 2013.
6. Wang, J. and B. Shim, "On the recovery limit of sparse signals using orthogonal matching pursuit," *IEEE Transactions on Signal Processing*, Vol. 60, No. 9, 4973–4976, 2012.
7. Tropp, J. A. and A. C. Gilbert, "Signal recovery from random measurements via orthogonal matching pursuit," *IEEE Transactions on Information Theory*, Vol. 53, No. 12, 4655–4666, 2007.
8. IGS, International GNSS Service, 4, 2013.

Monocrystalline-silicon Microwave MEMS

Joachim Oberhammer, Umer Shah, Zargham Baghchehsaraei, Fritzi Töpfer, Mikael Sterner, Nutapong Somjit, and Nikolai Chekurov
School of Electrical Engineering, KTH Royal Institute of Technology, Stockholm, Sweden

Abstract— This paper gives an overview of recent achievements in microwave micro-electrome chanical systems (microwave MEMS) at KTH Royal Institute of Technology, Stockholm, Sweden. The first topic is a micromachined W-band phase shifter based on a micromachined dielectric block which is vertically moved by integrated MEMS actuators to achieve a tuning of the propagation constant of a micromachined transmission line. The second topic is W-band MEMS-tuneable microwave high-impedance metamaterial surfaces conceptualized for local tuning of the electromagnetic resonance properties of surface waves on a high-impedance surface. The third topic covers 3-dimensional micromachined coplanar transmission lines with integrated MEMS actuators which move the sidewalls of these transmission lines. Multi-stable switches, tuneable capacitors, tuneable couplers, and tuneable filters have been implemented and characterized for 1–40 GHz frequencies. As a forth topic, micromachined waveguide switches are presented. Finally, silicon-micromachined near-field and far-field sensor and antenna interfaces are shown, including a micromachined planar lens antenna and a tapered dielectric rod measurement probe for medical applications.

1. INTRODUCTION

Micro-electromechanical systems (MEMS) are integrated microdevices combining electrical components with passive (sensing) and active (actuation) interface functions to their physical surroundings. Radiofrequency (RF) MEMS are MEMS devices that are interacting with electrical signals from DC up to THz frequencies, by switching, modulating, matching, tuning, and filtering. Typical devices ares witches, mechanically tunable capacitors, micromachined inductors, micromechanical resonators for filters and as frequency base, tunable loaded lines for phase shifters or impedance-matching circuits, reconfigurable antennas, and three-dimensional (3D) micromachined transmission lines. In general, RF MEMS devices are characterized by near-ideal signal handling performance in terms of insertion loss, isolation, linearity, large tuning range, and by keeping these performance parameters over a very large bandwidth [4, 13]. Microwave MEMS are RF MEMS devices that operate with signal frequencies above 30 GHz. With applications moving to higher frequencies, the performance advantages of MEMS devices over their competitors are getting larger. Also, at frequencies where the signal wavelengths are getting closer to the device dimensions, it is possible to miniaturize a complete RF system on a chip, and different ways of interaction between the microwave signals and the micromechanics lead to new possibilities of RF MEMS devices [1].

Operational reliability, i.e., the ability of devices to work as specified over the whole lifetime, and robustness to process parameter variations, are key issues in RF MEMS design [2, 3]. Conventional RF MEMS designs are still characterized by some fundamental problems. Thin metallic bridges, for instance, found in many RF MEMS devices, such as switches and phase shifters, are susceptible to temperature-accelerated creep and fatigue, limiting the device life-time [3]. Dielectric charging is another major reliability issue in electrostatically actuated RF MEMS [4, 5].

In contrast, monocrystalline silicon as used for the devices in this paper results in very robust and reliable MEMS devices, both when used as structural material but also as RF dielectric material if high-resistivity silicon (HRS) is used [6–8]. Instead of isolation layers which are susceptible to dielectric charging, all-metal designs with stoppers [9] are utilized for the devices in this paper to eliminate charging influence.

2. MONOCRYSTALLINE SILICON AS STRUCTURAL AND DIELECTRIC MATERIAL

Even though micromachining has been rapidly augmented with new material and processes [10], monocrystalline silicon, besides silicon carbide, still is the most robust and reliable structural material for micromachined devices [11]. Its yield strength exceeds steel by a factor of 2–3, and maintains elastic properties under high stress levels even when exposed to elevated temperatures, is very well characterized [6], and offers the largest variety of stable and standardized wafer-scale micromachining processes and manufacturing tools. Monocrystalline silicon has been successfully applied to a variety of MEMS devices including pressure sensors, accelerometers, undeformable sub-nm-flatness micromirror arrays, and robust micro-relays.

Besides silicon being an excellent structural material for MEMS moving elements, high-resistivity silicon (HRS), with a bulk resistivity up to 8 kΩcm, and low dielectric losses $\tan\delta$ of 6×10^{-4}, is an excellent substrate and structural dielectric material for radio frequency integrated circuit (RFIC) technology.

3. RF/MICROWAVE MEMS DEVICE EXAMPLES BASED ON MONOCRYSTALLINE SILICON

3.1. Monocrystalline-silicon Dielectric-block Phase-shifters

This section shows a novel multistage all-silicon microwave MEMS phase-shifter concept [12–14]. The concept is based on multiple-step deep-reactive-ion-etched monocrystalline-silicon dielectric blocks that are transfer bonded to an RF substrate containing a 3D micromachined coplanar-waveguide (CPW) transmission line, as shown in Figure 1. As compared to conventional MEMS phase shifters based on thin metallic bridges, including DMTL phase shifters and MEMS switched true time-delay (TTD) networks, the novel concept features the following design elements for improved reliability:

- All mechanical parts, including the moving block, mechanical springs, and support anchors, are etched out of the same, continuous monocrystalline silicon bulk layer for best mechanical reliability, in contrast to thin metallic bridges prone to plastic deformation.
- The dielectric constant of the moving block can be tailor-made in a wide range by varying the etch hole size.
- As dielectric blocks are used for the tuning, the power handling is only limited by the transmission line, in contrast to conventional phase shifters where currents induced in the thin bridges result in substantial device heating and thus power limitation.
- No detectable dielectric charging as no closed dielectric isolation layer is used.
- Reduced substrate losses and substrate charging bydeep-etched grooves in the transmission line.

A single stage of the novel phase shifter concept is depicted in Figure 1, showing a monocrystalline HRS (4 kΩcm) dielectric block on top of a 1-μm thick gold coplanar waveguide (CPW). The relative phase shift is achieved by vertically moving the dielectric block above the transmission line by electrostatic actuation, which results, due to the modulation of the capacitive load of the line, in varying propagation constants of the microwave signal in the transmission line.

Silicon is a very suitable material for this task because of its high dielectric constant of 11.9, resulting in high sensitivity to the block position. The silicon blocks are fabricated by polymer transfer bonding of a complete 30 μm-thick silicon device layer from an SOI wafer to the target wafer, by subsequent removing of the SOI handle wafer and by structuring the block with its mechanical springs by different deep-reactive-ion etching steps. With such a process flow, all mechanical parts (block, spring, anchors) are fabricated out of the same monocrystalline silicon block which guarantees for optimum reliability. Dielectric charging of the block in the down-state is avoided by small SiN distance keepers. When properly choosing the etch-hole sizes, the effective

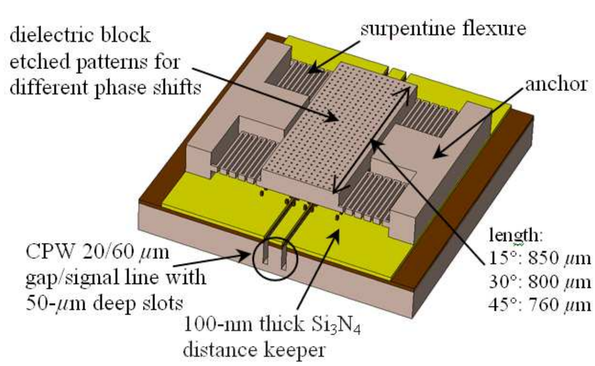

Figure 1: Concept of dielectric-block MEMS phase shifter.

dielectric constant of the block can be tailor-made, giving the possibility of designing phase-shifter stages of different relative phase shifts out of the same material layer. Figure 2(a) shows an SEM picture of a multi-stage device with stages of different effective permittivities, resulting in a 4.25-bit binary-coded multi-stage phase shifter constructed with these stages with 15° resolution and a maximum phase shift of 270° at 75 GHz, consisting of $5 \times 45° + 1 \times 30° + 1 \times 15°$ stages.

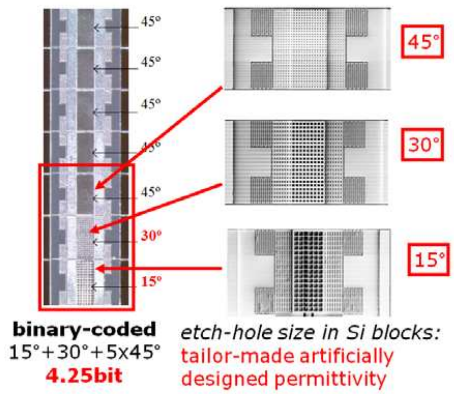

Figure 2: 4.25-bit phase shifter implemented with binary-coded phase-shifter stages.

The maximum insertion loss and return loss at the design frequency of 75 GHz is −3.5 and −17 dB, respectively, and the maximum insertion andre turn loss in the whole 75–110 GHz band are better than −4 and 12 dB. The phase shift per loss is 71.05 and 98.38°/dB at 75 and 110 GHz, respectively, and the phase shift per length is 490 and 7168°/cm at these frequencies. These results are the best maximum loss per bit, phase-shift per loss, and return loss ever reported for the whole W-band. The phase error at a 35 dBm signal power is still below 2%, but reaches quickly 4% at 40 dBm. This behavior results in an intermodulation intercept pointof third order of 48 dBm up to a signal power of 30 dBm, which emphasizes the excellent linearity behavior of the device [12, 13].

All tested devices could be actuated to 1 billion cycles in a non-hermetic environment without any failure or observed change in pull-in voltage, and after which the tests were discontinued. Also, in contrast to conventional MEMS phase shifters, where the power handling is limited by the critical current density in the thin metallic bridges, the power handling of this phase shifter concept is not limited by the moving parts, but just by the actual transmission lines and the substrate as a heat sink. For the novel dielectric-block phase shifter (45° stage), the maximum temperature rise is only 30°C, whereas the maximum temperature rises for aconventional TTD switch and DMTL phase shifter (45°) are as high as 65° and 300°C, respectively, which is by a factor of more than 20 and 10 times more than the novel dielectric-block phase shifter, respectively. Unique for an RF MEMS device, the power handling is only limited by the transmission line itself, rather than by the MEMS elements as in the conventional concepts [14].

3.2. Stress-compensated Metalized Monocrystalline-silicon Membranes for MEMS Tunable Microwave Surfaces

This section shows a novel concept of MEMS tunable micro-wave surfaces [15, 16], specifically high-impedance metamaterial surfaces and leaky-wave antennas, featuring (a) high-reliability monocrystalline silicon membranes not prone to plastic deformation over time and temperature and thus with highly reproducible actuation behavior, and (b) stress and temperature compensated membranes for zero-curvature thick reflective coating using double-side metallization with symmetrical processing from both sides for process parameter robustness [15].

High-impedance surfaces (HIS) exhibits unnaturally high surface impedance at their resonance frequency and have attracted attention because of their promising applications in improvement of antenna radiation patterns, suppression of surface waves [17] and phase shifting [18].

The concept of using distributed electrically small MEMS actuators for local tuning of the surface resonance frequency is illustrated in Figure 3(a). The micromachined elements uniquely unify electromechanical tunability with microwave functionality in one and the same distributed high-impedance surface elements, thus presenting a new class of microsystems interacting with microwaves.

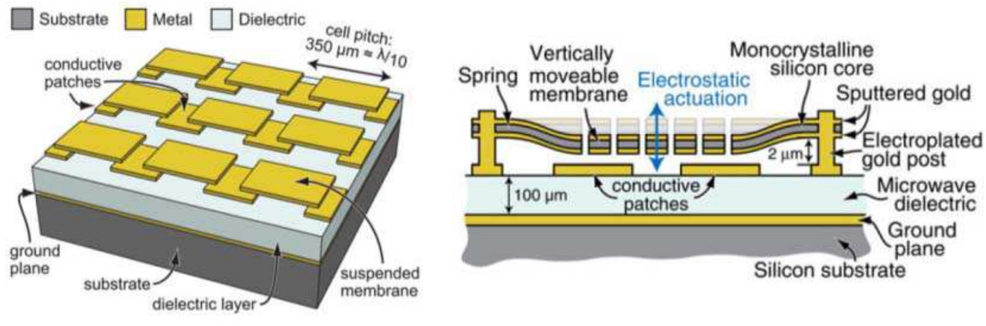

(a) (b)

Figure 3: (a) Illustration of MEMS-tuneable high-impedance surface; (b) cross-section of a single element.

The HIS presented in this section are composed of an array of electrostatically tunable elements, based on vertically moveable conductive membranes and conductive patches on the surface of a ground-backed 100 mm-thick HRS substrate (Figure 3(b)).

The process design of the membranes is quite unique in contrast to conventional MEMS tunable capacitors that are based on thin metallic bridges. A 1 μm-thick monocrystalline silicon core is used for the membrane to provide mechanical robustness and for optimized membrane flatness, and is transfer-bonded to the target substrate by adhesive bonding. The target substrate consists of a 100 μm-thick HRS layer bonded to a handle wafer with a ground plane. For electrical purpose, the transferred membrane is clad on both sides by 0.5 mm gold, the top layer before and the bottom layer after the transfer bonding. This symmetric deposition is designed for high process robustness, since it guarantees a stress-free sandwich structure without having to tune the stress in the metallic layers. The membrane is electrically and mechanically connected by meander-shaped springs to the supporting metal posts, before free-etching of the membranes by plasma-etching the polymer bonding layer is done. Figure 4 shows SEM pictures of a fabricated device, an array of a size of $70 \times 18.5\,\mathrm{mm}^2$ with 200×52 elements designed for car radar applications [11, 19]. The reflective properties of the surfaces were evaluated by back-short termination of a rectangular WR-10 waveguide, showing the characteristic phase transition of over 245° at 112 GHz. The reliability of the membranes has been investigated by monitoring the curvature during lifecycle measurements over 100 million cycles, demonstrating excellent long-term stability with virtually no degradation neither in curvature nor in repeatability of the actuated deflection [15].

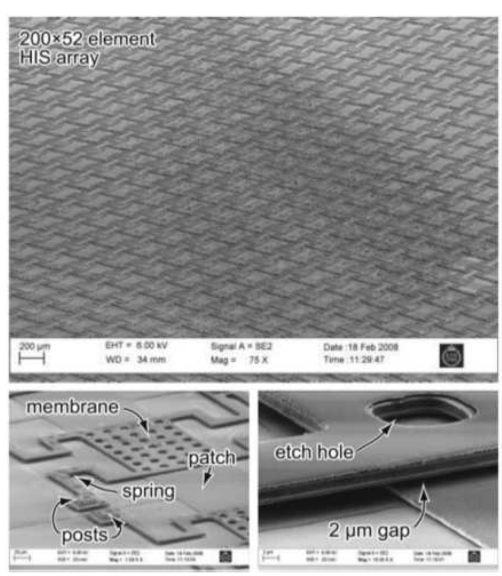

Figure 4: SEM pictures of implemented MEMS-tuneable high-impedance surface arrays.

3.3. Lateral Transmission Line Embedded Multistable Switches and Tunable Capacitors

This section reports on novel electrostatically actuated dc-to-RF metal-contact MEMS switches, multi-position RF MEMS digitally tunable capacitors, and tuneable couplers integrated inside coplanar transmission lines. The devices have in common that they are based on a 3D-micromachined coplanar waveguide (CPW), etched in an RF MEMS SOI process [20] into the 30 μm thick device layer of an SOI wafer, with integrated moveable ground and/or signal line sidewalls, which can be mechanically reconfigured by integrated MEMSeletrostatic actuators. All devices in this section feature an all-metal actuator design without dielectric isolation layers, eliminating actuator-charging problems, arefully stress and temperature compensated since all moving parts are made from monocrystalline silicon with gold metallization of similar thickness on both sides, and are implemented by a simple fabrication process in a single photolithographical process.

Figure 5 shows the concept of a mechanically bi-stable MEMS switch implemented by interlocking cantilevers, which achieves zero power consumption in the on and the off state, and is thus able to maintain its actuation state even at power failure. More information on the bistable mechanism and the device performance is published in [20]. Figure 6 shows SEM pictures of implemented RF switches, and close-up views of the interlocking cantilevers.

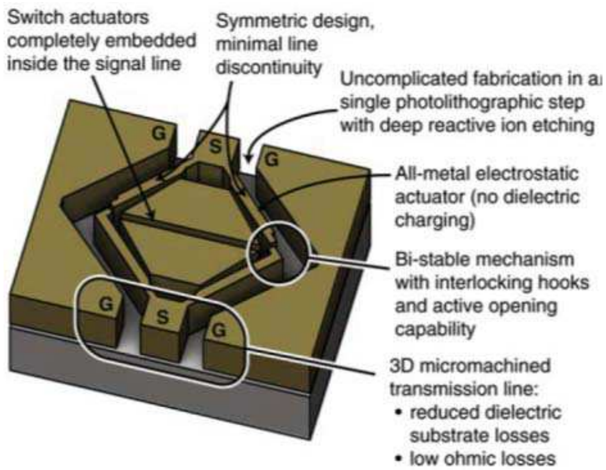

Figure 5: MEMS bistable RF switch concept based on a 3D-micromachined SOI RF MEMS process.

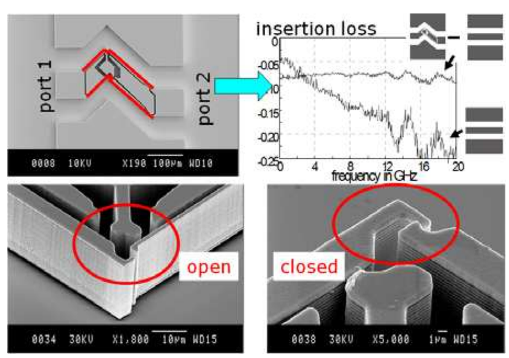

Figure 6: SEM picture and performance of MEMS bistable RF switch based on a 3D SOI RF MEMS process.

Figure 7 shows the concept of tuneable capacitors based on the MEMS-moveable sidewalls of a 3D-micromachined transmission line, and Figure 8 shows SEM pictures of implemented devices. Multi-step actuators have been implemented to achieve a multi-position tuneable capacitance in discrete, well-defined steps. A Q-factor of 88 was measured by a transmission-line resonator for such a device at 40 GHz, which is the so far best frequency-Q performance of a tuneable capacitor ever published. More information on the device can be found in [21].

Furthermore, tuneable couplers have been implemented based on this fabrication concept, which achieved an extraordinary large bandwidth due to a new tuning concept which varies both the

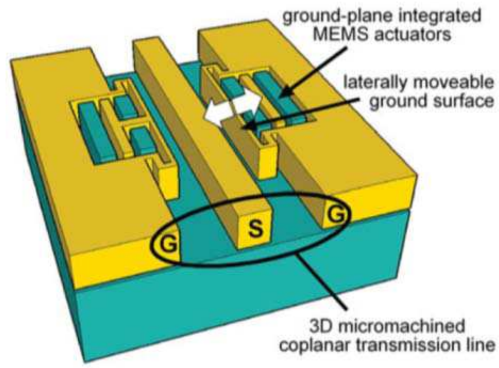

Figure 7: Tuneable capacitor concept based on the moving sidewalls in a 3D SOI RF MEMS process.

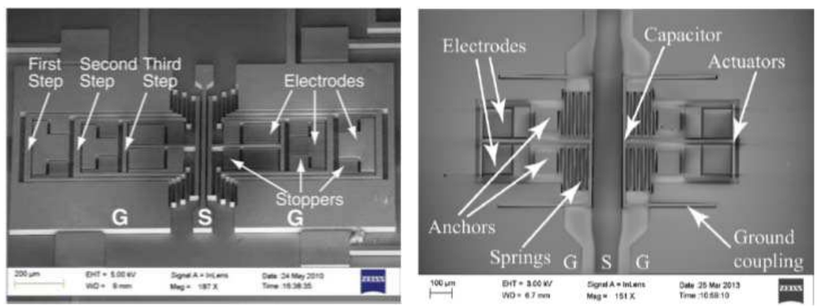

(a) (b)

Figure 8: SEM pictures of MEMS tuneable capacitors: (a) 7-step and (b) 3-step discrete tuneable capacitors.

signal-to-signal and the signal-to-ground capacitances of the the coupled coplanar transmission lines [22].

3.4. Micromachined Waveguide Switches

At frequencies approaching and beyond 100 GHz, transmission line losses are increasing and wavegui de-based solutions are often favourable. Due to the small waveguide dimensions, MEMS chips can be integrated into the waveguides and provide with miniaturized, low-loss reconfiguration functions. A waveguide switch has been implemented, which is based on a reconfigurable, transmissive surface which can be switched between a blocking and a non-blocking state, by reconfiguring vertical bar sections in a way that they short-circuit the electrical field lines of the dominant TE10 mode in the blocking state, as shown in Figure 9. Devices with 9–21 horizontal suspension bars and 20–30 vertical columns have been implemented. Figure 10 shows an SEM picture of a fabricated device

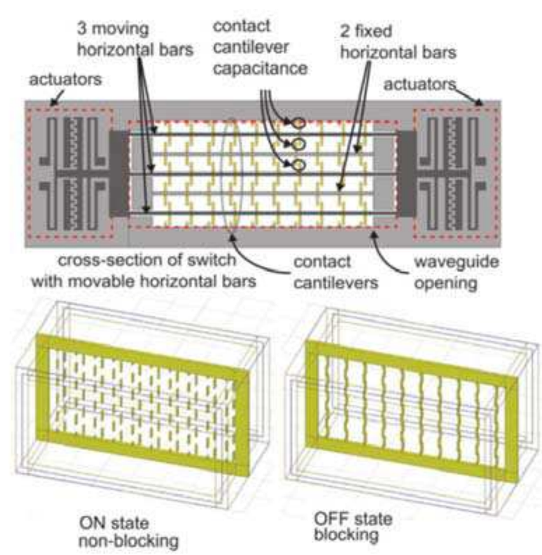

Figure 9: Concept of MEMS waveguide switch based on a reconfigurable transmissive surface.

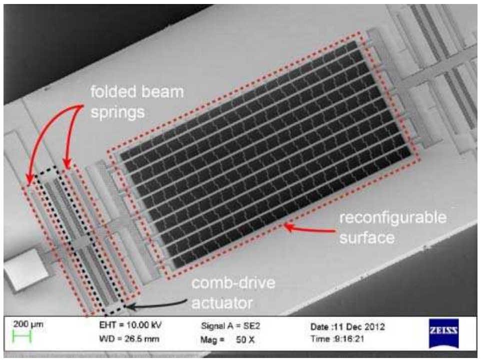

(a)

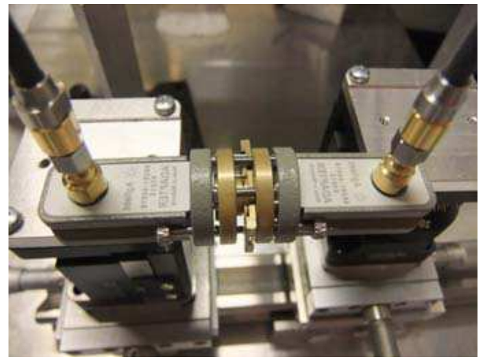

(b)

Figure 10: SEM-picture of waveguide switch, and assembled test setup of the chip between two tailor-made waveguide flanges.

and the assembled test setup. The measured isolation, i.e., S_{21} in blocking state, is $-40\,\mathrm{dB}$ for the best device implementation, and the measured insertion loss, i.e., S_{21} in the non-blocking state, is as low as $-0.5\,\mathrm{dB}$ from 60–65 GHz, where the waveguide assembly alone (reference measurement) contributes to $-0.4\,\mathrm{dB}$ loss in that frequency range [23].

3.5. Micromachined Millimeter-wave Sensor and Antenna Interfaces

Figure 11 shows a concept drawing and a photograph of a micromachined medical near-field sensor interface [24]. The probe has been developed for skin-cancer diagnosis, and is designed for high lateral resolution for resolving small skin cancer speckles as well as for vertically discriminating shallow tissue-layer anomalies. A tip size as small as $0.18\,\mathrm{mm}^2$, which is 18 times smaller than conventional measurement tips for the design frequency of 100 GHz, rs achieved by micromachining a silicon-core tapered dielectric-rod waveguide. This metallized dielectric probe is positioned centrally into a standard WR-10 waveguide by a micromachined holder which allows for easily exchanging the probes at high reproducibility. The dielectric-wedge transition between the waveguide and the probe is optimized for 100–105 GHz. The probe has a measured responsivity of $S_{11}/\varepsilon_r = 0.47\,\mathrm{dB}$ in the permittivity range of cancer/healthy tissue at 100 GHz, a reproducibility better than 1.4% (1σ), long-term stability better than 0.6% (1σ) for 8 h, and a lateral scanning resolution $\sim 100\,\mu\mathrm{m}$ for a $600 \times 300\,\mu\mathrm{m}^2$ probe [25]. For the responsivity analysis, shown in Figure 12, silicon-samples with different etch-hole sizes resulting in a tailor-made permittivity were fabricated, resulting in a long-term stable and reproducible test sample standard [24].

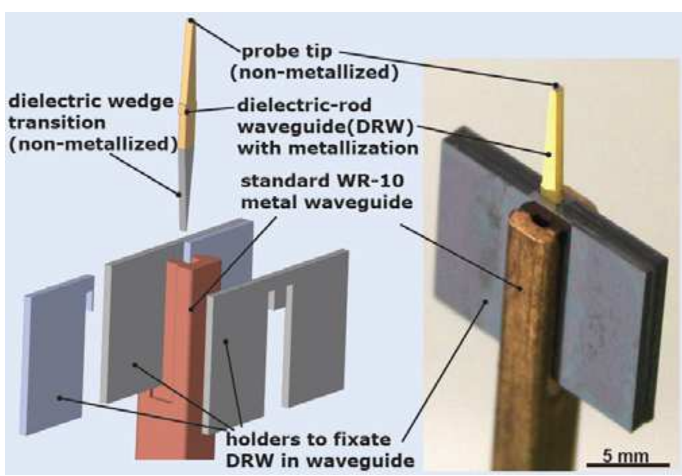

Figure 11: Microwave near-field sensor, based on a micromachined tapered dielectric rod, developed as a 100 GHz skin cancer sensor.

Figure 13, finally, shows a micromachined silicon planar-lens antenna designed for 100 GHz, which, at a lens radius of 11 mm, achieves a half-power beam-width of 13°. The edge of the lens is endowed with an impedance-matching layer, which minimizes reflections between the high-

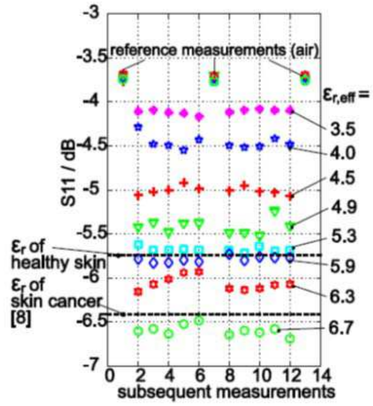

Figure 12: Responsivity analysis of micromachined millimeter-wave skin cancer sensor.

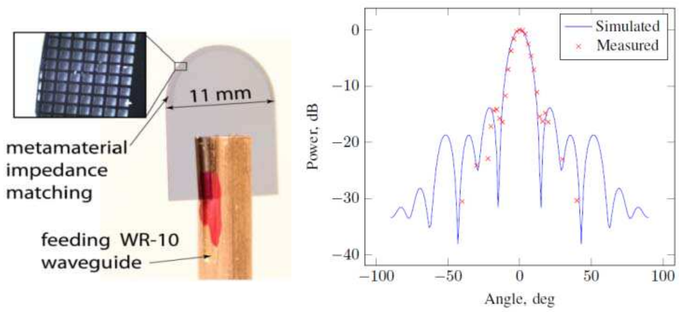

Figure 13: Silicon-micromachined planar-lens antenna.

permittivity silicon and the low-permittivity free-space, and is achieved by etching holes into the silicon structure for getting a local permittivity variation [26].

4. CONCLUSIONS

This paper presented recent achievements in mono-crystalline silicon micromachined RF and microwave MEMS devices, and demonstrates the performance of silicon MEMS in the RF and microwave world, in terms of RF performance, reliability, and also in enabling miniaturized, complex 3-dimensional structures not possible to implement with other fabrication techniques.

ACKNOWLEDGMENT

The authors would like to thank to Jan Åberg, MicroComp Nordic AB, for providing the tailor-made waveguide flanges and modified waveguides for the waveguide switch, and the millimeter-wave antenna and sensor interfaces.

REFERENCES

1. Sterner, M., D. Chicherin, A. V. Räisänen, G. Stemme, and J. Oberhammer, “RF MEMS high-impedancetuneable metamaterials for millimeter-wavebeamsteering,” *Proc. IEEE/ASME Micro-Electro-Mechanical Sytems MEMS 2009*, 896–899, Sorrento, Italy, Jan. 2009.
2. Hartzell, A. L., M. G. da Silva, and H. R. Shea, *MEMS Reliability*, SpringerLink, 2011.
3. DeNatale, J. and R. Mihailovich, “RF MEMS reliability,” *Proc. Transducers 2003*, 943–946, Boston, MA, USA, Jun. 2003.
4. Wibbeler, J., G. Pfeifer, and M. Hietschold, “Parasitic charging of dielectric surfaces in capacitive microelectromechanical systems (MEMS),” *Sensors Actuators A: Phys.*, Vol. 71, No. 1–2, 74–80, 1998.
5. Goldsmith, C., J. Ehmke, A. Malczewski, B. Pillans, S. Eschelmann, Z. Yao, J. Brank, and M. Eberly, “Life time characterization of capacitive RF MEMS switches,” *Proc. IEEE MTT-S Int. Microwave Symp.*, 779–808, Phoenix, AZ, USA, May 2001.
6. Petersen, K., “Silicon as a mechanical material,” *Proc. IEEE*, Vol. 70, No. 5, 420–457, 1982.
7. Lederer, D. and J.-P. Raskin, “New substrate passivation method dedicated to HR SOI wafer fabricationwithincreasedsubstrateresistivity,” *IEEE Electron Dev. Lett.*, Vol. 26, No. 11, 805–807, 2005.

8. Sterner, M., N. Somjit, U. Shah, S. Dudorov, D. Chicherin, A. Räisänen, and J. Oberhammer, "Microwave MEMS devices designed for process robustness and operational reliability," *Int. Journal of Microwave and Wireless Technologies*, Vol. 3, No. 5, 547–563, Oct. 2011.
9. Mardivirin, D., A. Pothier, A. Crunteanu, B. Vialle, and P. Blondy, "Charging in dielectricless capacitive RF-MEMS switches," *IEEE Trans. on Microw. Theory and Tech.*, Vol. 57, No. 1, 231–236, 2009.
10. Liu, C., *Foundations of MEMS*, Pearson Prentice Hall, 2006.
11. Oberhammer, J., M. Sterner, and N. Somjit, "Monocrystalline-silicon microwave MEMS devices: Multi-stable switches, W-band phase shifters, and MEMS tuneable frequency-selective surfaces," *Springer NATO Series: Advanced Materials and Technologies for Micro/Nano Devices, Sensors and Actuators*, Springer, Berlin, 2009.
12. Somjit, N., G. Stemme, and J. Oberhammer, "Deep-reactive ion-etched wafer-scale-transferred all-silicon dielectric-block millimeter-wave MEMS phase shifters," *J. Microelectromech. Syst.*, Vol. 19, 120–128, 2010.
13. Somjit, N., G. Stemme, and J. Oberhammer, "Binary-coded 4.25-bit w-band monocrystalline-silicon MEMS multi-stage dielectric-block phase shifters," *IEEE Trans. on Microw. Theory and Tech.*, Vol. 57, 2834–2840, 2009.
14. Somjit, N., G. Stemme, and J. Oberhammer, "Power-handling analysis of high-power W-band all-silicon MEM sphase shifters," *IEEE Trans. on Electron Dev.*, Vol. 58, No. 5, 1548–1555, 2011.
15. Sterner, M. and J. Oberhammer, "Symmetrical anti-directional metallization for stress-compensation of transfer-bonded monocrystalline silicon membranes," *IEEE/ASME Journal of Microelectromechanical Systems*, Vol. 22, No. 1, 195–205, Feb. 2013.
16. Chicherin, D., M. Sterner, D. Lioubtchenko, J. Oberhammer, and A. V. Räisänen, "Analogue type millimetre wave phase shifters based on MEMS tuneable high-impedance surface and dielectric rod waveguide," *Int. Journal of Microwave and Wireless Technologies*, Vol. 3, No. 5, 533–538, Oct. 2011.
17. Sievenpiper, D., "High-impedance electromagnetic surfaces," Ph.D. dissertation, Department Electrical Engineering, Universtiy of California, Los Angeles, 1999.
18. Higgins, J., H. Xin, A. Sailer, and M. Rosker, "Ka-band waveguide phase shifter using tunable electromagnetic crystal sidewalls," *IEEE Trans. on Microw. Theory and Tech.*, Vol. 51, No. 4, 1281–1288, 2003.
19. Sterner, M., G. Stemme, and J. Oberhammer, "Nanometer-scale flatness and reliability investigation of stress-compensated symmetricallymetallized monocrystalline-silicon multi-layer membranes," *5th IEEE Int. Conf. on Nano/Micro Engineered and Molecular Systems (NEMS)*, 959–962, Jan. 2010.
20. Sterner, M., N. Roxhed, G. Stemme, and J. Oberhammer, "Static zero-power-consumption coplanar-waveguide integrated DC-to-RF metal-contact MEMS switches in two-port and three-port configuration," *IEEE Trans. on Electron Dev.*, Vol. 57, No. 7, 1659–1669, Jul. 2010.
21. Shah, U., M. Sterner, and J. Oberhammer, "Multi-position RF MEMS tunable capacitorsusing laterally-moving sidewalls of 3D-micromachined transmission lines," *IEEE/MTT-S Transactions on MicrowaveTheory and Techniques*, Vol. 61, No. 6, 2340–2352, Jun. 2013.
22. Shah, U., M. Sterner, and J. Oberhammer, "Compact MEMS reconfigurable ultra-wideband 10–18 GHz directional couplers," *Proc. IEEE/ASME Micro Electro Mechanical Systems 2012*, 684–687, Paris, France, Jan. 29–Feb. 2, 2012, Poster Presentation.
23. Baghchehsaraei, Z., U. Shah, S. Dudorov, J. Åberg, G. Stemme, and J. Oberhammer, "MEMS reconfigurable millimeter-wavesurface for V-band rectangular-waveguide switch," *Int. Journal of Microwave and Wireless Technologies*, 341–349, in print, 2013.
24. Töpfer, F., S. Dudorov, and J. Oberhammer, "Micromachined 100 GHz near-field measurement probe for high-resolution microwave skin-cancer diagnosis," *Proc. IEEE MTT-S International Microwave Symposium 2012*, 1–3, Montréal, Canada, Jun. 17–22, 2012.
25. Töpfer, F., S. Dudorov, and J. Oberhammer, "2-dimensional near-field millimeter-wave scanning with micromachined probe for skin cancer diagnosis," *Proc. IEEE/ASME Micro Electro Mechanical Systems 2013*, 1057–1060, Taipei, Taiwan, Jan. 20–23, 2013.
26. Dudorov, S., F. Töpfer, and J. Oberhammer, "Micromachined-silicon W-band planar-lens antenna with metamaterial free-space matching," *Proc. IEEE MTT-S International Microwave Symposium 2012*, 1–3, Montréal, Canada, Jun. 17–22, 2012.